

Alberto Sanfeliu  
José Ruiz-Shulcloper (Eds.)

LNCS 2905

# Progress in Pattern Recognition, Speech and Image Analysis

8th Iberoamerican Congress on Pattern Recognition, CIARP 2003  
Havana, Cuba, November 2003  
Proceedings



Springer

Lecture Notes in Computer Science  
Edited by G. Goos, J. Hartmanis, and J. van Leeuwen

2905

**Springer**

*Berlin*

*Heidelberg*

*New York*

*Hong Kong*

*London*

*Milan*

*Paris*

*Tokyo*

Alberto Sanfeliu José Ruiz-Shulcloper (Eds.)

# Progress in Pattern Recognition, Speech and Image Analysis

8th Iberoamerican Congress  
on Pattern Recognition, CIARP 2003  
Havana, Cuba, November 26-29, 2003  
Proceedings



Springer

Series Editors

Gerhard Goos, Karlsruhe University, Germany  
Juris Hartmanis, Cornell University, NY, USA  
Jan van Leeuwen, Utrecht University, The Netherlands

Volume Editors

Alberto Sanfeliu  
Universitat Politècnica de Catalunya  
Institut de Robòtica i Informàtica Industrial (IRI)  
Parc Tecnològic de Barcelona, Edifici U  
Llorens i Antigas, 4-6, 2<sup>o</sup>, 08028 Barcelona, Spain  
E-mail: asanfeliu@iri.upc.es

José Ruiz-Shulcloper  
Research Center on Pattern Recognition, MINBAS  
7a #21812 e/ 218 y 222, Rpto. Siboney, Playa, Ciudad de la Habana, Cuba  
E-mail: recpat@cidet.icmf.inf.cu

Cataloging-in-Publication Data applied for

A catalog record for this book is available from the Library of Congress.

Bibliographic information published by Die Deutsche Bibliothek  
Die Deutsche Bibliothek lists this publication in the Deutsche Nationalbibliografie;  
detailed bibliographic data is available in the Internet at <<http://dnb.ddb.de>>.

CR Subject Classification (1998): I.5, I.4, I.2.10, I.2.7

ISSN 0302-9743  
ISBN 3-540-20590-X Springer-Verlag Berlin Heidelberg New York

This work is subject to copyright. All rights are reserved, whether the whole or part of the material is concerned, specifically the rights of translation, reprinting, re-use of illustrations, recitation, broadcasting, reproduction on microfilms or in any other way, and storage in data banks. Duplication of this publication or parts thereof is permitted only under the provisions of the German Copyright Law of September 9, 1965, in its current version, and permission for use must always be obtained from Springer-Verlag. Violations are liable for prosecution under the German Copyright Law.

Springer-Verlag is a part of Springer Science+Business Media  
[springeronline.com](http://springeronline.com)

© Springer-Verlag Berlin Heidelberg 2003  
Printed in Germany

Typesetting: Camera-ready by author, data conversion by PTP-Berlin, Protago-TeX-Production GmbH  
Printed on acid-free paper SPIN: 10973301 06/3142 5 4 3 2 1 0

## Preface

CIARP 2003 (8th Iberoamerican Congress on Pattern Recognition) was the eighth event in a series of pioneering congresses on pattern recognition in the Latin American community of countries. This year, however, the forum was extended to include worldwide participation. The event has been held in the past in Mexico, Cuba, Brazil and Portugal; it took place this year in Havana (Cuba). The aim of the congress was to promote and disseminate ongoing research into mathematical methods for pattern recognition, computer vision, image analysis, and speech recognition, as well as the application of these techniques in such diverse areas as robotics, industry, health, entertainment, space exploration, telecommunications, data mining, document analysis, and natural language processing and recognition to name a few. Moreover it was a forum for scientific research, experience exchange, the sharing of new knowledge, and establishing contacts to improve cooperation between research groups in pattern recognition, computer vision and related areas.

The congress was organized by the Institute of Cybernetics, Mathematics and Physics of Cuba (ICIMAF) and the Center for Computing Research (CIC) of the National Polytechnic Institute of Mexico, and was sponsored by the University of La Salle, Mexico, the University of Oriente, Cuba, the Polytechnic Institute "José A. Echevarría," Cuba, the Central University of Las Villas, Cuba, the National Center of Scientific Research, Cuba, the Cuban Association for Pattern Recognition (ACRP), the Portuguese Association for Pattern Recognition (APRP), the Spanish Association for Pattern Recognition and Image Analysis (AERFAI), the Mexican Society for Artificial Intelligence (SMIA), and the International Association for Pattern Recognition (IAPR).

This year the event captured the attention of a significant group of researchers who contributed with over 140 full papers from 19 countries. Out of these, 82 papers were accepted as full papers and are included in this proceedings volume, and 28 papers were accepted as poster presentations. The review process was carried out by the Program Committee, each paper being assessed by at least two reviewers who, in conjunction with other reviewers, prepared an excellent selection dealing with ongoing research. We are especially indebted to them for their efforts and the quality of the reviews.

Three professors were invited to give keynote addresses on topics in computer vision, robot vision and pattern classification: Dr. Rangachar Kasturi, IAPR President, and a professor in the Department of Computer Science and Engineering at Pennsylvania State University, Dr. Gerhard Ritter, Chairman of the Computer and Information Science and Engineering Department at the University of Florida, and Dr. Alberto Sanfeliu, past President of AERFAI, and a professor at the Technical University of Catalonia.

We appreciate very much all the intense work done by the members of the organizing committee that allowed for an excellent conference and proceedings. We hope that this congress was a fruitful precedent for future CIARP events.

# Organization

CIARP 2003 was organized by the Institute of Cybernetics, Mathematics and Physics of Cuba (ICIMAF) and the Center for Computing Research (CIC) of the National Polytechnic Institute of Mexico.

## General Conference Co-chairs

José Ruiz-Shulcloper

Grupo de Reconocimiento de Patrones Lógico-Combinatorios, Instituto de Cibernetica, Matemática y Física, Cuba

Alberto Sanfeliu

Institut de Robòtica i Informàtica Industrial,  
Universitat Politècnica de Catalunya, Spain  
Centro de Investigación en Computación,  
Instituto Politécnico Nacional, Mexico

Juan Luis Díaz de León

## Iberoamerican Committee

Roberto Rodríguez Morales

Instituto de Cibernetica, Matemática y Física, Cuba  
Universidad de Granada, Spain

Nicolás Pérez de la Blanca

Instituto Superior Técnico, Portugal

Jorge Salvador Marques

Centro de Investigaciones en Computación, IPN,  
Mexico

Juan Humberto Sossa

Universidad La Salle, Mexico

Eduardo Gómez Ramírez

Universidad Central de Venezuela, Venezuela

Rina Suros

Pontificia Universidad Católica de Chile, Chile

Gonzalo Rojas

Universidad de la República, Uruguay

Gregory Randall

Universidade Federal de São Carlos, Brazil

Nelson D.A. Mascarenhas

Université des Antilles et de la Guyane, Guadeloupe

Bertille Adelaïde Louviers

Institut de Robòtica i Informàtica Industrial, Spain

Juan Andrade Cetto

Institut de Robòtica i Informàtica Industrial, Spain

Francesc Moreno Noguer

Institut de Robòtica i Informàtica Industrial, Spain

Teresa Vidal

Universitat Politècnica de Catalunya, Spain

Antoni Grau

## Local Committee

Manuel Lazo Cortés

ICIMAF, Cuba

Carmen Seara

ICIMAF, Cuba

Margarita Pie

ICIMAF, Cuba

Regina Peddie

ICIMAF, Cuba

Beatriz Moreno

ICIMAF, Cuba

Carlos Cabal-Mirabal

Universidad de Oriente, Cuba

Isneri Talavera Bustamante

CRP, Cuba

## Program Committee

Alquézar Mancho, R.	Universitat Politècnica de Catalunya, Spain
Araújo, H.	Universidade de Coimbra, Portugal
Baeza Yatez, R.	Universidade de Chile, Chile
Bloch, I.	École Nationale Supérieure des Telecomm., France
Caldas Pinto, J.R.	Instituto Superior Técnico, Portugal
Campilho, A.	Universidade de Porto, Portugal
Cano, Ortiz	S.D. Universidad de Oriente, Cuba
d'Ávila Mascarenhas, N.D.	Universidade Federal de São Carlos, Brazil
Del Bimbo, A.	Università di Firenze, Italy
Desachy, J.	Université des Antilles et de la Guyane, Guadeloupe
Escalante, Ramírez B.	Universidad Nacional Autónoma de México, Mexico
Facon, J.	Pontifícia Universidade Católica do Paraná, Brazil
Goldfarb, L.	University of New Brunswick, Canada
Gómez Gil, M.P.	Universidade de las Américas, Mexico
Gomez Ramirez, E.	Universidad La Salle, Mexico
Gordillo, J.L.	ITESM, Mexico
Grau, A.	Universitat Politècnica de Catalunya, Spain
Guzmán Arenas, A.	Centro de Investigación en Computación, IPN, Mexico
Kasturi, R.	University of Pennsylvania, USA
Kittler, J.	University of Surrey, UK
Koschan, A.	University of Tennessee, USA
Lazo Cortés, M.	Instituto de Cibernética, Matemática y Física, Cuba
Levashkin, S.	Centro de Investigación en Computación, IPN, Mexico
Lira, Chávez J.	Universidad Nacional Autónoma de México, Mexico
Lorenzo Ginori, J.V	Universidad Central de Las Villas, Cuba
Marques, J.S.	Instituto Superior Técnico, Portugal
Medioni, G.	University of Southern California, USA
Moctezuma, M.	Universidad Nacional Autónoma de México, Mexico
Montilla, G.	Universidad de Carabobo, Venezuela
Padilha, A.J.M.N.	Universidade de, Portugal
Pérez de la Blanca, N.	Universidad de Granada, Spain
Petrou, M.	University of Surrey, UK
Pina, P.	Instituto Superior Técnico, Portugal
Pla, F.	Universitat Jaume I, Spain
Randall, G.	Universidad de la República, Uruguay
Riazanov, V.	Russian Academy of Sciences, Russia
Ritter, G.	University of Florida, USA
Rodríguez, R.	Instituto de Cibernética, Matemática y Física, Cuba
Rojas Costa, G.M.	Pontificia Universidad Católica de Chile, Chile
Ruiz Shulcloper, J.	Instituto de Cibernética, Matemática y Física, Cuba
Sanfeliu, A.	Universitat Politècnica de Catalunya, Spain
Sanniti di Baja, G.	Instituto di Cibernetica, CNR, Italy

Serra, J.	École des Mines de Paris, France
Shirai, Y.	Osaka University, Japan
Sossa Azuela, J.H.	Centro de Investigación en Computación, IPN, Mexico
Suros, R.	Universidad Central de Venezuela, Venezuela
Taboada Crispí, A.	Universidad Central de las Villas, Cuba
Valdes Sosa, P.A.	Centro Nacional de Investigaciones Científicas, Cuba
Valev, V.	Saint Louis University, USA
Vidal, E.	Universitat Politècnica de Valencia, Spain
Villanueva, J.J.	Universitat Autònoma de Barcelona, Spain

## Sponsoring Institutions

Universidad La Salle, Mexico  
Universidad de Oriente, Cuba  
Instituto Politécnico “José A. Echevarría,” Cuba  
Universidad Central de las Villas, Cuba  
Centro Nacional de Investigaciones Científicas, Cuba  
Cuban Association for Pattern Recognition (ACRP)  
Portuguese Association for Pattern Recognition (APRP)  
Spanish Association for Pattern Recognition and Image Analysis (AERFAI)  
Mexican Society for Artificial Intelligence (SMIA)  
International Association for Pattern Recognition (IAPR)

# Table of Contents

Neurons, Dendrites, and Pattern Classification .....	1
<i>G.X. Ritter, L. Iancu, G. Urcid</i>	
Robot Vision for Autonomous Object Learning and Tracking .....	17
<i>A. Sanfeliu</i>	
Graduated Scale Inspection Using Computer Vision .....	29
<i>B. Valera, S. Padilla, G. Chávez, V. García Garduño</i>	
Vision System for Subpixel Laser Stripe Profile Extraction with Real Time Operation .....	38
<i>U. Martínez, B. Valera, J. Sánchez, V. García</i>	
Multi-channel Reconstruction of Video Sequences from Low-Resolution and Compressed Observations .....	46
<i>L.D. Alvarez, R. Molina, A.K. Katsaggelos</i>	
3D Rigid Facial Motion Estimation from Disparity Maps .....	54
<i>N. Pérez de la Blanca, J.M. Fuertes, M. Lucena</i>	
Robust Techniques in Least Squares-Based Motion Estimation Problems .....	62
<i>R. Montoliu, F. Pla</i>	
Inexact Graph Matching for Facial Feature Segmentation and Recognition in Video Sequences: Results on Face Tracking .....	71
<i>A.B.V. Graciano, R.M. Cesar Jr., I. Bloch</i>	
Crater Marking and Classification Using Computer Vision .....	79
<i>A. Flores-Méndez</i>	
Using Optical Flow for Tracking .....	87
<i>M. Lucena, J.M. Fuertes, N. Perez de la Blanca</i>	
Another Paradigm for the Solution of the Correspondence Problem in Motion Analysis .....	95
<i>A. Al-Hamadi, R. Niese, B. Michaelis</i>	
Improvement of the Fail-Safe Characteristics in Motion Analysis Using Adaptive Technique .....	104
<i>A. Al-Hamadi, R. Mecke, B. Michaelis</i>	
Spatially Adaptive Algorithm for Impulse Noise Removal from Color Images .....	113
<i>V. Kober, M. Mozerov, J. Álvarez-Borrego</i>	

Improving Phase-Congruency Based Feature Detection through Automatic Scale-Selection .....	121
<i>V.U.B. Schenk, M. Brady</i>	
Robust Estimation of Roughness Parameter in SAR Amplitude Images .....	129
<i>H. Allende, L. Pizarro</i>	
Two New Scale-Adapted Texture Descriptors for Image Segmentation ...	137
<i>M.A. Lozano, F. Escolano</i>	
Topological Query in Image Databases .....	145
<i>M. Scuturici, J. Clech, D.A. Zighed</i>	
Reconstructing 3D Objects from Silhouettes with Unknown Viewpoints: The Case of Planar Orthographic Views .....	153
<i>A. Bottino, L. Jaulin, A. Laurentini</i>	
Enforcing a Shape Correspondence between Two Views of a 3D Non-rigid Object .....	163
<i>M.B. Dias, B.F. Buxton</i>	
A Colour Constancy Algorithm Based on the Histogram of Feasible Colour Mappings .....	171
<i>J. Vergés-Llahí, A. Sanfeliu</i>	
Reconstruction of Surfaces from Cross Sections Using Skeleton Information .....	180
<i>J. Pina Amargós, R. Alquézar Mancho</i>	
Extension of a New Method for Surface Reconstruction from Cross Sections .....	188
<i>J. Pina Amargós, R. Alquézar Mancho</i>	
Imposing Integrability in Geometric Shape-from-Shading .....	196
<i>M. Castelán, E.R. Hancock</i>	
Correcting Radial Lens Distortion Using Image and Point Correspondences .....	204
<i>L. Romero, F. Calderon</i>	
Characterization of Surfaces with Sonars Using Time of Flight and Triangulation .....	212
<i>C. Albores, J.L. Gordillo</i>	
Non-speech Sound Feature Extraction Based on Model Identification for Robot Navigation .....	221
<i>Y. Bolea, A. Grau, A. Sanfeliu</i>	

Enhancement of Noisy Speech Using Sliding Discrete Cosine Transform .....	229
<i>V. Kober</i>	
Integrating High and Low Smoothed LMs in a CSR System .....	236
<i>A. Varona, I. Torres</i>	
Selection of Lexical Units for Continuous Speech Recognition of Basque .....	244
<i>K. López de Ipiña, M. Graña, N. Ezeiza, M. Hernández, E. Zulueta, A. Ezeiza, C. Tovar</i>	
Creating a Mexican Spanish Version of the CMU Sphinx-III Speech Recognition System .....	251
<i>A. Varela, H. Cuayáhuitl, J.A. Nolazco-Flores</i>	
Decision Tree-Based Context Dependent Sublexical Units for Continuous Speech Recognition of Basque .....	259
<i>K. López de Ipiña, M. Graña, N. Ezeiza, M. Hernández, E. Zulueta, A. Ezeiza</i>	
Uniclass and Multiclass Connectionist Classification of Dialogue Acts ...	266
<i>M.J. Castro, D. Vilar, E. Sanchis, P. Aibar</i>	
A Technique for Extraction of Diagnostic Data from Cytological Specimens .....	274
<i>I.B. Gurevich, A. Khilkov, D. Murashov</i>	
Segmentation and Morphometry of Histological Sections Using Deformable Models: A New Tool for Evaluating Testicular Histopathology .....	282
<i>M.A. Guevara, A. Silva, H. Oliveira, M. de Lourdes Pereira, F. Morgado</i>	
Robust Markers for Blood Vessels Segmentation: A New Algorithm .....	291
<i>R. Rodríguez, T.E. Alarcón, O. Pacheco</i>	
Discriminative Power of Lymphoid Cell Features: Factor Analysis Approach .....	298
<i>I.B. Gurevich, D. Harazishvili, I. Jernova, A. Nefyodov, A. Trykova, I. Vorobjev</i>	
Retinal Angiography Based Authentication .....	306
<i>C. Mariño, M.G. Penedo, M.J. Carreira, F. González</i>	
Suboptimal Classifier for Dysarthria Assessment .....	314
<i>E. Castillo Guerra, D.F. Lovely</i>	

Approximate Nearest Neighbour Search with the Fukunaga and Narendra Algorithm and Its Application to Chromosome Classification .....	322
<i>F. Moreno-Seco, L. Micó, J. Oncina</i>	
Characterization of Viability of Seeds by Using Dynamic Speckles and Difference Histograms .....	329
<i>M. Fernández, A. Mavilio, H. Rabal, M. Trivi</i>	
An Adaptive Enhancer with Modified Signal Averaging Scheme to Detect Ventricular Late Potentials .....	334
<i>A. Taboada-Crispí, J.V. Lorenzo-Ginori, D.F. Lovely</i>	
A Study on the Recognition of Patterns of Infant Cry for the Identification of Deafness in Just Born Babies with Neural Networks .....	342
<i>J. Orozco-García, C.A. Reyes-García</i>	
Patients Classification by Risk Using Cluster Analysis and Genetic Algorithms .....	350
<i>M. Chacón, O. Luci</i>	
Mathematical Morphology on MRI for the Determination of Iberian Ham Fat Content .....	359
<i>A. Caro, M. Durán, P.G. Rodríguez, T. Antequera, R. Palacios</i>	
Automatic Dark Fibres Detection in Wool Tops .....	367
<i>J. Bazerque, J. Ciambelli, S. Lafon, G. Randall</i>	
Musical Style Identification Using Grammatical Inference: The Encoding Problem .....	375
<i>P.P. Cruz-Alcázar, E. Vidal-Ruiz, J.C. Pérez-Cortés</i>	
New Distance Measures Applied to Marble Classification .....	383
<i>J. Caldas Pinto, J.M. Sousa, H. Alexandre</i>	
Online Handwritten Signature Verification Using Hidden Markov Models .....	391
<i>Juan J. Igarza, I. Goirizelaia, K. Espinosa, I. Hernández, R. Méndez, J. Sánchez</i>	
Fast Handwritten Recognition Using Continuous Distance Transformation .....	400
<i>J. Arlandis, J.-C. Perez-Cortes</i>	
Stroke Boundary Analysis for Identification of Drawing Tools .....	408
<i>P. Kammerer, G. Langs, R. Sablatnig, E. Zolda</i>	
Solving the Global Localization Problem for Indoor Mobile Robots .....	416
<i>L. Romero, E. Morales, E. Sucar</i>	

Restricted Decontamination for the Imbalanced Training Sample Problem .....	424
<i>R. Barandela, E. Rangel, J.S. Sánchez, F.J. Ferri</i>	
An Entropy Maximization Approach to Optimal Model Selection in Gaussian Mixtures .....	432
<i>A. Peñalver, J.M. Sáez, F. Escolano</i>	
Gaussian Mixture Models for Supervised Classification of Remote Sensing Multispectral Images .....	440
<i>A.C. Oliveira de Melo, R. Marcos de Moraes, L. dos Santos Machado</i>	
Fast Multistage Algorithm for K-NN Classifiers .....	448
<i>I. Soraluze, C. Rodriguez, F. Boto, A. Cortes</i>	
Some Improvements in Tree Based Nearest Neighbour Search Algorithms .....	456
<i>E. Gómez-Ballester, L. Micó, J. Oncina</i>	
Impact of Mixed Metrics on Clustering .....	464
<i>K. Gibert, R. Nonell</i>	
A Comparison between Two Fuzzy Clustering Algorithms for Mixed Features .....	472
<i>I.O. Ayaquica-Martínez, J.F. Martínez-Trinidad</i>	
Extended Star Clustering Algorithm .....	480
<i>R.J. Gil-García, J.M. Badía-Contelles, A. Pons-Porrata</i>	
Two New Metrics for Feature Selection in Pattern Recognition .....	488
<i>P. Piñero, L. Arco, M.M. García, Y. Caballero, R. Yzquierdo, A. Morales</i>	
Conditions of Generating Descriptive Image Algebras by a Set of Image Processing Operations .....	498
<i>I.B. Gurevich, V. Yashina</i>	
Completeness Conditions of a Class of Pattern Recognition Algorithms Based on Image Equivalence .....	506
<i>I.B. Gurevich, I.A. Jernova</i>	
Typical Segment Descriptors: A New Method for Shape Description and Identification .....	512
<i>N.A. Alvarez-Roca, J. Ruiz-Shulcloper, J.M. Sanchiz-Martí</i>	
A New Approach That Selects a Single Hyperplane from the Optimal Pairwise Linear Classifier .....	521
<i>L. Rueda</i>	

A Characterization of Discretized Polygonal Convex Regions by Discrete Moments . . . . .	529
<i>J. Žunić</i>	
Learning Probabilistic Context-Free Grammars from Treebanks . . . . .	537
<i>J.L. Verdú-Mas, J. Calera-Rubio, R.C. Carrasco</i>	
Simulated Annealing for Automated Definition of Fuzzy Sets in Human Central Nervous System Modeling . . . . .	545
<i>F. Mugica, A. Nebot</i>	
Automatic Tuning of Fuzzy Partitions in Inductive Reasoning . . . . .	554
<i>A. Nebot</i>	
Kernel Computation in Morphological Bidirectional Associative Memories . . . . .	563
<i>G. Urcid, G.X. Ritter, L. Iancu</i>	
Improving Still Image Coding by an SOM-Controlled Associative Memory . . . . .	571
<i>G. Krell, R. Rebmann, U. Seiffert, B. Michaelis</i>	
A Morphological Methodology for Features Identification in Satellite Images for Semi-automatic Cartographic Updating . . . . .	580
<i>M. Mengucci, F. Muge</i>	
Morphological Neural Networks with Dendrite Computation: A Geometrical Approach . . . . .	588
<i>R. Barrón, H. Sossa, H. Cortés</i>	
A Method for the Automatic Summarization of Topic-Based Clusters of Documents . . . . .	596
<i>A. Pons-Porrata, J. Ruiz-Shulcloper, R. Berlanga-Llavori</i>	
Improving Prepositional Phrase Attachment Disambiguation Using the Web as Corpus . . . . .	604
<i>H. Calvo, Alexander Gelbukh</i>	
Determination of Similarity Threshold in Clustering Problems for Large Data Sets . . . . .	611
<i>G. Sánchez-Díaz, J.F. Martínez-Trinidad</i>	
Content-Based Retrieval Using Color, Texture, and Shape Information . . . . .	619
<i>R.S. Choras</i>	
Off the Shelf Methods for Robust Portuguese Cadastral Map Analysis . . . . .	627
<i>T. Candeias, F. Tomaz, H. Shahbazkia</i>	

Simultaneous Segmentation-Recognition-Vectorization of Meaningful Geographical Objects in Geo-Images .....	635
<i>S. Levachkine, M. Torres, M. Moreno, R. Quintero</i>	
Geomorphometric Analysis of Raster Image Data to Detect Terrain Ruggedness and Drainage Density .....	643
<i>M. Moreno, S. Levachkine, M. Torres, R. Quintero</i>	
Morphological Applications for Maps Construction in Path Planning Tasks .....	651
<i>J. Azorín, G. De Miguel, F.A. Pujol, J.M. García, M. Pujol, R. Rizo</i>	
Compact Mapping in Plane-Parallel Environments Using Stereo Vision .....	659
<i>J.M. Sáez, A. Peñalver, F. Escolano</i>	
An Oscillatory Neural Network for Image Segmentation .....	667
<i>D. Fernandes, P.O.A. Navaux</i>	
Generating Three-Dimensional Neural Cells Based on Bayes Rules and Interpolation with Thin Plate Splines .....	675
<i>R.C. Coelho, O. Vargas Jaques</i>	
A Maximum Entropy Approach to Sampling in EDA – The Single Connected Case .....	683
<i>A. Ochoa, R. Höns, M. Soto, H. Mühlenbein</i>	
<b>Author Index .....</b>	<b>691</b>

# Neurons, Dendrites, and Pattern Classification

Gerhard X. Ritter<sup>1</sup>, Laurentiu Iancu<sup>1</sup>, and Gonzalo Urcid<sup>2</sup>

<sup>1</sup> CISE Dept., University of Florida, Gainesville, FL 32611-6120, USA

{ritter, liancu}@cise.ufl.edu

<sup>2</sup> Optics Dept., INAOE, Tonantzintla, Pue. 72000, Mexico

gurcid@inaoep.mx

**Abstract.** Computation in a neuron of a traditional neural network is accomplished by summing the products of neural values and connection weights of all the neurons in the network connected to it. The new state of the neuron is then obtained by an activation function which sets the state to either zero or one, depending on the computed value. We provide an alternative way of computation in an artificial neuron based on lattice algebra and dendritic computation. The neurons of the proposed model bear a close resemblance to the morphology of biological neurons and mimic some of their behavior. The computational and pattern recognition capabilities of this model are explored by means of illustrative examples and detailed discussion.

## 1 Introduction

Various artificial neural networks (ANNs) that are currently in vogue, such as radial basis function neural networks and support vector machines, have very little in common with actual biological neural networks. A major aim of this paper is to introduce a model of an artificial neuron that bears a closer resemblance to neurons of the cerebral cortex than those found in the current literature. We will show that this model has greater computational capability and pattern discrimination power than single neurons found in current ANNs. Since our model mimics various biological processes, it will be useful to provide a brief background of the morphology of a biological neuron.

A typical neuron of the mammalian brain has two processes called, respectively, *dendrites* and *axons*. The axon is the principal fiber that forms toward its ends a multitude of branches, called the *axonal tree*. The tips of these branches, called *nerve terminals* or *synaptic knobs*, make contact with the dendritic structures of other neurons. These sites of contact are called *synaptic sites*. The synaptic sites of dendrites are the places where synapses take place. Dendrites have many branches that create large and complicated trees and the number of synapses on a *single* neuron of the cortex typically ranges between 500 and 200,000. Figure 1 provides a simplified sketch of the processes of a biological neuron. It is also well-known that there exist two types of synapses; *excitatory synapses* that play a role in exciting the postsynaptic cell to fire impulses, and

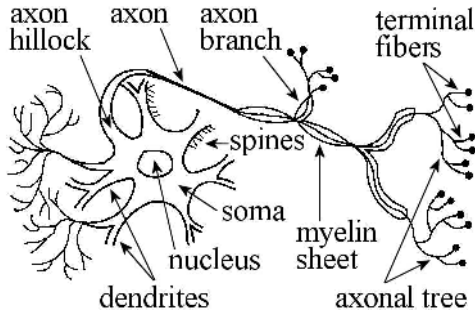


**Fig. 1.** Simplified sketch of the processes of a biological neuron

*inhibitory synapses* that try to prevent the neuron from firing impulses in response to excitatory synapses. The postsynaptic membranes of the dendrites will thus either accept or inhibit the received input from other neurons.

It is worthwhile to note that dendrites make up the largest component in both surface area *and* volume of the brain. Part of this is due to the fact that dendrites span all cortical layers in all regions of the cerebral cortex [1–3]. Thus, when attempting to model artificial brain networks, one cannot ignore dendrites, which make up more than 50% of the neuron's membrane. This is especially true in light of the fact that some researchers have proposed that dendrites, and not the neurons, are the elementary computing devices of the brain, capable of implementing such logical functions as AND, OR, and NOT [1–9].

Current ANN models, and in particular perceptrons, do not include dendritic structures. As a result, problems occur that may be easily preventable when including dendritic computing. For example, M. Gori and F. Scarselli have shown that multilayer perceptrons (MLPs) are not adequate for pattern recognition and verification [10]. Specifically, they proved that multilayer perceptrons with sigmoidal units and a number of hidden units less than or equal to the number of input units, are unable to model patterns distributed in typical clusters. The reason is that these networks draw open separation surfaces in pattern space. In this case, all patterns not members of the cluster but contained in an open area determined by the separation surfaces will be misclassified. This situation is depicted in Fig. 2. When using more hidden units than input units, the separation *may* result closed but, unfortunately, determining whether or not the perceptron draws closed separation surfaces in pattern space is NP-hard. This is quite opposite to what is commonly believed and reported in the literature. The network model described in this paper does not suffer from these problems.

Gori's and Scarselli's result was one reason for trying to use lattice algebra operations in perceptrons. Another reason is that lattice operations have proven quite successful in the area of associative memories as well as some pattern classification tasks [11–22]. Earlier attempts at morphological perceptrons did not include the notion of dendritic computing and were restricted to two-class problems. The lack of dendrites required hidden layers and computationally intensive

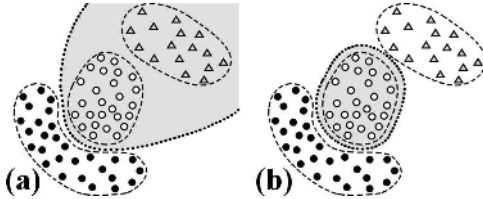


**Fig. 2.** In a trained MLP, the separation surface (dotted) between two clusters (black and white circles) may result open and include impostor patterns (triangles) (a). A closed surface avoids this problem and is desired (b)

algorithms that did not provide for easy generalization to multiclass pattern separation. In contrast, the model defined in this paper uses dendritic computation, requires no hidden layers, is capable of multi-class separation to within any desired degree of accuracy, has the ability to produce closed separation surfaces between pattern clusters, and generalizes to fuzzy pattern recognition.

## 2 Morphological Perceptrons Based on Dendritic Computation

Let  $N_1, \dots, N_n$  denote a collection of neurons with morphology as shown in Fig. 1. Suppose these neurons provide synaptic input to another collection  $M_1, \dots, M_m$  of neurons also having processes as depicted in Fig. 1. The value of a neuron  $N_i$  ( $i = 1, \dots, n$ ) propagates through its axonal tree all the way to the terminal branches that make contact with the neuron  $M_j$  ( $j = 1, \dots, m$ ). The weight of an axonal branch of neuron  $N_i$  terminating on the  $k$ th dendrite of  $M_j$  is denoted by  $w_{ijk}^\ell$ , where the superscript  $\ell \in \{0, 1\}$  distinguishes between *excitatory* ( $\ell = 1$ ) and *inhibitory* ( $\ell = 0$ ) input to the dendrite. The  $k$ th dendrite of  $M_j$  will respond to the total input received from the neurons  $N_1, \dots, N_n$  and will either accept or inhibit the received input. The computation of the  $k$ th dendrite of  $M_j$  is given by

$$\tau_k^j(\mathbf{x}) = p_{jk} \bigwedge_{i \in I(k)} \bigwedge_{\ell \in L(i)} (-1)^{1-\ell} x_i + w_{ijk}^\ell , \quad (1)$$

where  $\mathbf{x} = (x_1, \dots, x_n)$  denotes the input value of the neurons  $N_1, \dots, N_n$  with  $x_i$  representing the value of  $N_i$ ,  $I(k) \subseteq \{1, \dots, n\}$  corresponds to the set of all input neurons with terminal fibers that synapse on the  $k$ th dendrite of  $M_j$ ,  $L(i) \subseteq \{0, 1\}$  corresponds to the set of terminal fibers of  $N_i$  that synapse on the  $k$ th dendrite of  $M_j$ , and  $p_{jk} \in \{-1, 1\}$  denotes the excitatory ( $p_{jk} = 1$ ) or inhibitory ( $p_{jk} = -1$ ) response of the  $k$ th dendrite of  $M_j$  to the received input.

It follows from the formulation  $L(i) \subseteq \{0, 1\}$  that the  $i$ th neuron  $N_i$  can have at most two synapses on a given dendrite  $k$ . Also, if the value  $\ell = 1$ , then the input  $(x_i + w_{ijk}^1)$  is excitatory, and inhibitory for  $\ell = 0$  since in this case we have  $(x_i + w_{ijk}^0)$ .

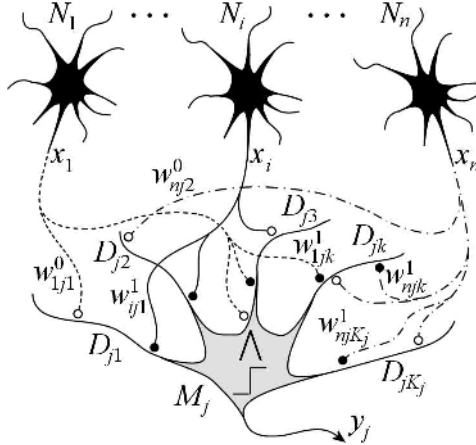


**Fig. 3.** Morphological perceptron with dendritic structure. Terminations of excitatory and inhibitory fibers are marked with  $\bullet$  and  $\circ$ , respectively. Symbol  $D_{jk}$  denotes dendrite  $k$  of  $M_j$  and  $K_j$  its number of dendrites. Neuron  $N_i$  can synapse  $D_{jk}$  with excitatory or inhibitory fibers, e.g. weights  $w_{1jk}^1$  and  $w_{nj2}^0$  respectively denote excitatory and inhibitory fibers from  $N_i$  to  $D_{jk}$  and from  $N_n$  to  $D_{j2}$

The value  $\tau_k^j(\mathbf{x})$  is passed to the cell body and the state of  $M_j$  is a function of the input received from all its dendrites. The total value received by  $M_j$  is given by

$$\tau^j(\mathbf{x}) = p_j \bigwedge_{k=1}^{K_j} \tau_k^j(\mathbf{x}) , \quad (2)$$

where  $K_j$  denotes the total number of dendrites of  $M_j$  and  $p_j = \pm 1$  denotes the response of the cell body to the received dendritic input. Here again,  $p_j = 1$  means that the input is accepted, while  $p_j = -1$  means that the cell rejects the received input. The next state of  $M_j$  is then determined by an activation function  $f$ , namely  $y_j = f(\tau^j(\mathbf{x}))$ . In this exposition we restrict our discussion to the hard-limiter

$$f(\tau^j(\mathbf{x})) = \begin{cases} 1 & \text{if } \tau^j(\mathbf{x}) \geq 0 \\ 0 & \text{if } \tau^j(\mathbf{x}) < 0 \end{cases} \quad (3)$$

unless otherwise stated. The total computation of  $M_j$  is, therefore, given by

$$y_j(\mathbf{x}) = f \left[ p_j \bigwedge_{k=1}^{K_j} \left( p_{jk} \bigwedge_{i \in I(k)} \bigwedge_{\ell \in L(i)} (-1)^{1-\ell} x_i + w_{ijk}^\ell \right) \right] . \quad (4)$$

Figure 3 provides a graphical representation of this model.

A *single layer morphological perceptron* (SLMP) is a special case of this model. Here the neurons  $N_1, \dots, N_n$  would denote the input neurons and the neurons  $M_1, \dots, M_m$  the output neurons. For SLMPs we allow  $\mathbf{x} = (x_1, \dots, x_n) \in \mathbb{R}^n$ . That is, the value  $x_i$  of the  $i$ th input neuron  $N_i$  need not be binary.

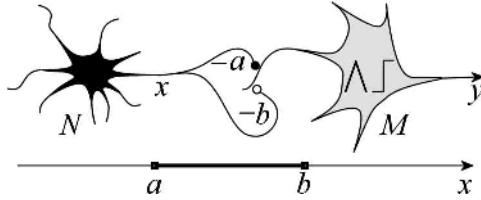


**Fig. 4.** The output neuron  $M$  will fire ( $y = 1$ ) for input values from the interval  $[a, b]$ ; if  $x \in \mathbb{R} \setminus [a, b]$ , then  $y = 0$

### 3 Examples

Having defined the computational model of dendritic processes and SLMPs, it will be instructive to provide a few examples in order to illustrate the computational capabilities of the proposed model.

*Example 1.* The simplest case occurs when the SLMP consists of just one input neuron  $N$ , and one output neuron  $M$  with a single dendrite having an excitatory ( $p_{jk} = 1$ ) response to the received input. Here the notation can be simplified by discarding subscripts  $i$ ,  $j$  and  $k$  (as being all 1). Figure 4 illustrates such an SLMP. If the response of the cell body  $p = 1$ , then by (1) and (2) we have  $\tau(x) = (x - a) \wedge (x - b)$ , and  $\tau(x) \geq 0 \iff x \geq a$  and  $x \leq b$ . Hence, the output neuron  $M$  will fire ( $y = f(\tau(x)) = 1$ ) when  $x \in [a, b]$ .

*Example 2.* The SLMP depicted in Fig. 5 also consists of one input neuron and one output neuron, but this time the output neuron has three dendrites,  $D_1$ ,  $D_2$  and  $D_3$ . The corresponding network parameters are given in Table 1. For algebraic consistency as well as numerical computation when using (1) and (4), *unused* terminal fibers with a hypothetical excitatory or inhibitory input will be assigned a weight of  $+\infty$  or  $-\infty$ , respectively. If  $a < b < c < d$ , by substituting the values of the synaptic weights in (1) and (2), we obtain  $\tau(x) = [(x - a)] \wedge [(x - a) \wedge (x - b)] \wedge [(x - c) \wedge (x - d)]$ . The output neuron  $M$  will fire when  $\tau(x) \geq 0 \iff x \in \{a\} \cup [b, c] \cup [d, \infty)$ , as depicted on the axis at the bottom of Fig. 5.

*Example 3.* An SLMP with two input neurons,  $N_1$  and  $N_2$ , and two output neurons,  $M_1$  and  $M_2$ , can be used to solve the XOR problem, formulated as a two-class problem. Figure 6 illustrates such an SLMP. If  $\mathbf{y} = (y_1, y_2)$ , where  $y_j$  denotes the output signal of neuron  $M_j$  ( $j = 1, 2$ ), then the desired network output is:

$$\mathbf{y} = \begin{cases} (1, 0) & \text{if } \mathbf{x} \in C_1 \\ (0, 1) & \text{if } \mathbf{x} \in C_2 \\ (0, 0) & \text{if } \mathbf{x} \in \mathbb{R}^2 \setminus (C_1 \cup C_2) \end{cases} . \quad (5)$$

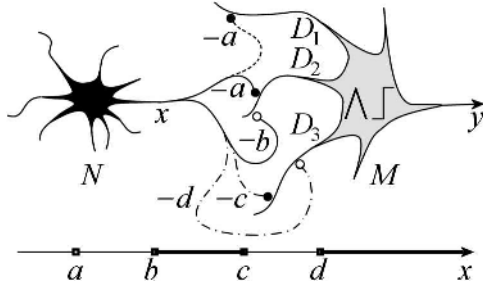


**Fig. 5.** The output neuron  $M$  will fire ( $y = 1$ ) for input values from the set  $X = \{a\} \cup [b, c] \cup [d, \infty)$ ; if  $x \in \mathbb{R} \setminus X$ , then  $y = 0$

**Table 1.** Weights and Synaptic Responses, Ex. 2

	$D_k$	$w_{1k}^1$	$w_{1k}^0$	$p_k$
$D_1$	$a$	$\infty$	$+1$	
$D_2$	$a$	$b$	$1$	
$D_3$	$c$	$d$	$1$	

As in classical perceptron theory, solving this problem requires two output neurons. However, in contrast to the classical model, no hidden layer is necessary for the morphological perceptron to solve the problem.

In this case,  $\mathbf{y} = f(\tau^1(\mathbf{x}), f(\tau^2(\mathbf{x})))$ , where  $\tau^j(\mathbf{x}) = \bigwedge_{k=1}^{K_j} \tau_k^j(\mathbf{x})$ , denotes the computation performed by  $M_j$ , and  $K_j$  denotes the number of dendrites of  $M_j$ . The values of the axonal branch weights  $w_{ijk}^\ell$  and output responses  $p_{jk}$  are specified in Table 2.

## 4 Computational Capability of an SLMP

Analogous to the classical single layer perceptron (SLP) with one output neuron, a single layer morphological perceptron (SLMP) with one output neuron also consists of a finite number of input neurons that are connected via axonal fibers to the output neuron. However, in contrast to an SLP, the output neuron of an SLMP has a dendritic structure and performs the lattice computation embodied by (4). Figure 3 provides a pictorial representation of a general SLMP with a single output neuron. As the examples of the preceding section illustrate, the computational capability of an SLMP is vastly different from that of an SLP as well as that of classical perceptrons in general. No hidden layers were necessary to solve the XOR problem or to specify the points of the non-convex region of Fig. 7. Observing differences by examples, however, does not provide answer as

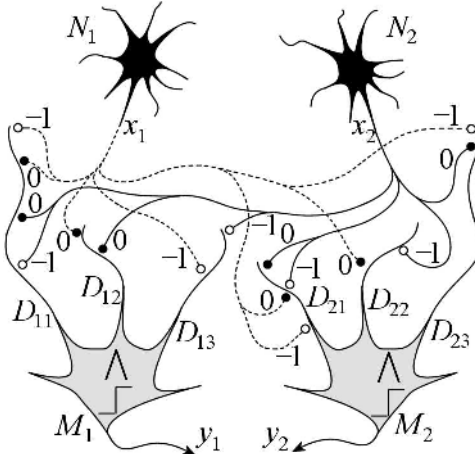


**Fig. 6.** SLMP that solves the two-class XOR problem for points from the domain  $\mathbf{x} = (x_1, x_2) \in \mathbb{R}^2$

**Table 2.** Two-Class XOR Network Parameters, Ex. 3

$D_{jk}$	$w_{1jk}^1$	$w_{1jk}^0$	$w_{2jk}^1$	$w_{2jk}^0$	$p_{jk}$
$D_{11}$	0	1	0	1	+1
$D_{12}$	0	$\infty$	0	$\infty$	1
$D_{13}$	$+\infty$	1	$+\infty$	1	1
$D_{21}$	0	1	0	1	+1
$D_{22}$	0	$\infty$	$+\infty$	1	1
$D_{23}$	$+\infty$	1	0	$\infty$	1

to the specific computational capabilities of an SLMP with one output neuron. Such an answer is given by the following two theorems.

**Theorem 1.** If  $X \subset \mathbb{R}^n$  is compact and  $\varepsilon > 0$ , then there exists a single layer morphological perceptron that assigns every point of  $X$  to class  $C_1$  and every point  $\mathbf{x} \in \mathbb{R}^n$  to class  $C_0$  whenever  $d(\mathbf{x}, X) > \varepsilon$ .

The expression  $d(\mathbf{x}, X)$  in Theorem 1 refers to the distance of the point  $\mathbf{x} \in \mathbb{R}^n$  to the set  $X$ . Figure 7 illustrates this concept. All points of  $X$  will be classified as belonging to class  $C_1$  and all points outside the *banded* region of thickness  $\varepsilon$  will be classified as belonging to class  $C_0$ . Points within the banded region may be misclassified. As a consequence, any compact configuration, whether it is convex or non-convex, connected or not connected, contains a finite or infinite

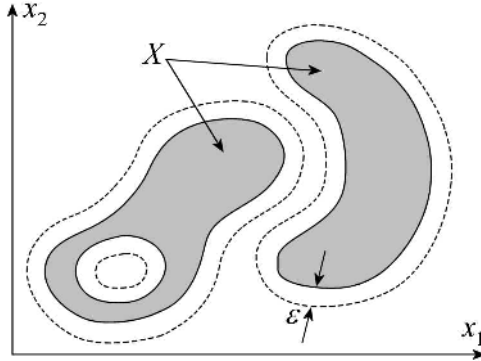


**Fig. 7.** The compact region  $X$  (shaded) and the banded region of thickness  $\varepsilon$  (dashed)

number of points, can be approximated to any desired degree of accuracy  $\varepsilon > 0$  by an SLMP with one output neuron.

The proof of Theorem 1 requires tools from elementary point set topology and is given in [23]. Although the proof is an existence proof, part of it is constructive and provides the basic idea for our training algorithms.

Theorem 2 is a generalization of Theorem 1 to multiple sets. Suppose  $X_1, X_2, \dots, X_m$  denotes a collection of disjoint compact subsets of  $\mathbb{R}^n$ . The goal is to classify,  $\forall j = 1, \dots, m$ , every point of  $X_j$  as a point belonging to class  $C_j$  and not belonging to class  $C_i$  whenever  $i \neq j$ . For each  $p \in \{1, \dots, m\}$ , define  $Y_p = \bigcup_{j=1, j \neq p}^m X_j$ . Since each  $Y_p$  is compact and  $Y_p \cap X_p = \emptyset$ ,  $\varepsilon_p = d(X_p, Y_p) > 0$   $\forall p = 1, \dots, m$ . Let  $\varepsilon_0 = \frac{1}{2} \min\{\varepsilon_1, \dots, \varepsilon_p\}$ .

**Theorem 2.** *If  $\{X_1, X_2, \dots, X_m\}$  is a collection of disjoint subsets of  $\mathbb{R}^n$  and  $\varepsilon$  a positive number with  $\varepsilon < \varepsilon_0$ , then there exists a single layer morphological perceptron that assigns each point  $\mathbf{x} \in \mathbb{R}^n$  to class  $C_j$  whenever  $\mathbf{x} \in X_j$  and  $j \in \{1, \dots, m\}$ , and to class  $C_0 = \neg \bigcup_{j=1}^m C_j$  whenever  $d(\mathbf{x}, X_i) > \varepsilon$ ,  $\forall i = 1, \dots, m$ . Furthermore, no point  $\mathbf{x} \in \mathbb{R}^n$  is assigned to more than one class.*

Figure 8 illustrates the conclusion of Theorem 2 for the case  $m = 3$ . The proof of this theorem is somewhat lengthy and because of page limitation could not be included. The proof is given in [24]. Based on the proofs of these two theorems, we constructed training algorithms for SLMPs [23, 24]. During the learning phase, the output neurons grow new dendrites and input neurons expand their axonal branches to terminate on the new dendrites. The algorithms always converge and have rapid convergence rate when compared to backpropagation learning in traditional perceptrons.

These training algorithms are similar in that they all dynamically grow dendrites and axonal fibers during the learning phase, which will use the patterns of the training set in just one iteration (one *epoch*). The algorithms differ in the strategy of partitioning the pattern space, by either growing a class region by merging smaller hyper-boxes, or reducing an initial large box through elimination

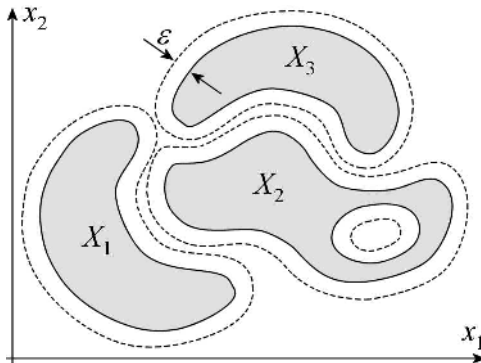


**Fig. 8.** The compact region  $X$  (shaded) and the banded region of thickness  $\varepsilon$  (dashed)

of foreign patterns and smaller regions that enclose them. Also, as a consequence of the aforementioned theorems on which the algorithms are based, the trained SLMPs will always correctly recognize 100% of the patterns in the training set. The next examples illustrate the performance of these training algorithms for some well-known problems.

*Example 4.* A nontrivial benchmark for testing the performance of a training algorithm is the well known problem of the *two intertwined spirals* [25]. For our tests, we used two *Archimedean* spirals defined by the complex expression  $z_c(\theta) = x_c(\theta) + i\alpha^{-1}y_c(\theta) = (-1)^{c\rho\theta}e^{i\theta}$ , where  $i = \sqrt{-1}$ ,  $c \in \{0, 1\}$  denotes the spiral class label,  $\theta$  is the angle in radians,  $\alpha > 0$  denotes the aspect ratio between the  $x_c$  and  $y_c$  coordinates, and  $\rho > 0$  is a constant that controls the spread of the spiral turns.

This problem was used to test the performance of one SLMP training algorithm that we developed, which is tailored to handle data sets where the patterns are points on a curve in 2-D space. The data set consists of 192 patterns, 96 on each spiral, 75% of which were used for training and 25% for test, selected at random from the entire set. During a typical training session, the algorithm grew 163 dendrites (161 excitatory and 2 inhibitory). Recognition of the test patterns was 100% correct. The class  $C_1$  region learned by the SLMP is illustrated in Fig. 9. In the figure, each small rectangle represents an elementary area recognized by an individual dendrite. The solid-line rectangles correspond to excitatory dendrites; regions of inhibitory dendrites are drawn with dashed lines. The learned class  $C_1$  region is the union of the solid-line rectangles minus the dashed-line rectangles.

*Example 5.* Another data set we used is the one considered in [26] to test their simulation of a radial basis function network. The data set consists of two non-linearly separable classes of 10 patterns each. This pattern set was used as input by two other training algorithms that we developed. The former algorithm uses region merging, but assumes no a priori distribution of the patterns as did the

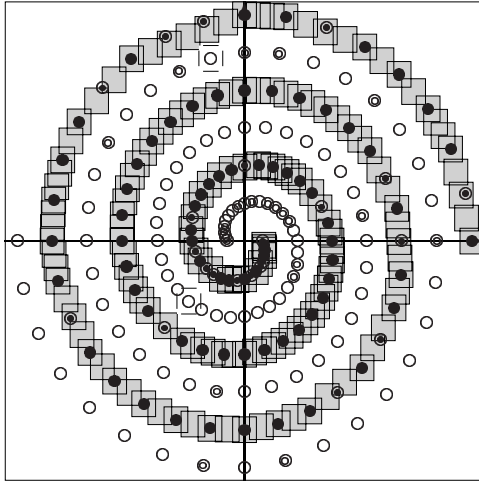


**Fig. 9.** The two-spirals problem. Each spiral consists of 96 patterns, 75% of which were used for training. Class  $C_1$  patterns are marked with filled circles (training) and circled dots (test); class  $C_2$  patterns with empty circles (training) and double circles (test). The shaded area is the learned class  $C_1$  region; recognition is 100% correct

method mentioned in Example 4. The latter algorithm uses region elimination, i.e. it starts training by drawing an enclosing large hyper-box and proceeds by eliminating smaller regions around patterns that do not belong to the class corresponding to the enclosing hyper-box. The results of the two training algorithms are illustrated in Fig. 10 and 11, respectively. In both cases, all patterns were used for both training and test, and classification was 100% correct, as expected.

For comparison, Fig. 12 depicts the results after training a classical MLP on the same data set. The dotted lines represent the decision boundaries learned after 2000 epochs by a two-layer MLP with 13 nodes in the hidden layer using backpropagation as training algorithm. Figure 12 shows that the separation surfaces learned by the MLP are open, in contrast to the separation surfaces of SLMPs, which are guaranteed to result closed. Furthermore, convergence of the MLP is much slower than the SLMP's counterpart, even for this small data set of 20 patterns.

## 5 Remarks on Fuzzy Computing and Inhibitory Neurons

In our SLMP model the values of the output neurons are always crisp, i.e. having either value 1 or 0. In many application domains it is often desirable to have fuzzy valued outputs in order to describe such terms as very tall, tall, fairly tall, somewhat tall, and not tall at all. Obviously, the boundaries between these concepts cannot be exactly quantified. In particular, we would like to have output values  $y_j(\mathbf{x})$  such that  $0 \leq y_j(\mathbf{x}) \leq 1$ , where  $y_j(\mathbf{x}) = 1$  if  $\mathbf{x}$  is a clear member

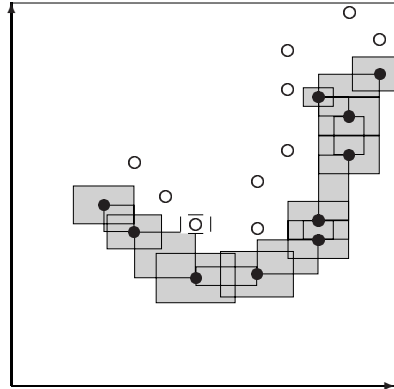


**Fig. 10.** The shaded area is the class  $C_1$  region learned by the merging version of the SLMP training algorithm applied to this two nonlinearly separable classes problem. Patterns of the two classes are marked with  $\bullet$  and  $\circ$ , respectively. The algorithms grows 20 dendrites (19 excitatory and 1 inhibitory, dashed); recognition is 100% correct

of class  $C_j$  and  $y_j(\mathbf{x}) = 0$  whenever  $\mathbf{x}$  has no relation to class  $C_j$ . However, we would like to say that  $\mathbf{x}$  is close to full membership of class  $C_j$  the closer the value of  $y_j(\mathbf{x})$  is to value 1. To illustrate how the SLMP can be extended to produce fuzzy outputs, we reconsider Example 1 of Section 3.

Suppose we would like to have every point in the interval  $[a, b] \subset \mathbb{IR}$  to be classified as belonging to class  $C_1$  and every point outside the interval  $[a - \alpha, b + \alpha]$  as having no relation to class  $C_1$ , where  $\alpha > 0$  is a specified fuzzy boundary parameter. For a point  $x \in [a - \alpha, a]$  or  $x \in [b, b + \alpha]$  we would like  $y(x)$  to be close to 1 when  $x$  is close to  $a$  or  $b$ , and  $y(x)$  close to 0 whenever  $x$  is close to  $a - \alpha$  or  $b + \alpha$ . In this case we simply convert the input  $x \in \mathbb{IR}$  to a new input format  $\frac{x}{\alpha}$ . If  $w_1^0 = b$  and  $w_1^1 = a$  denote the weights found either by inspection or the aforementioned algorithms for input  $x$ , then set  $v_1^0 = \frac{w_1^0}{\alpha} - 1$  and  $v_1^1 = \frac{w_1^1}{\alpha} + 1$  for the weights of the new input  $\frac{x}{\alpha}$  and use the ramp activation function

$$f(z) = \begin{cases} 1 & \text{if } z \geq 1 \\ z & \text{if } 0 \leq z \leq 1 \\ 0 & \text{if } z \leq 0 \end{cases}. \quad (6)$$

Computing  $\tau\left(\frac{x}{\alpha}\right)$  we obtain  $\tau\left(\frac{x}{\alpha}\right) = \frac{x}{\alpha} + v_1^1 \wedge \frac{x}{\alpha} + v_1^0 = [\frac{1}{\alpha}(x - a) + 1] \wedge [\frac{1}{\alpha}(x - b) + 1]$ . Thus,

$$f\left[\tau\left(\frac{x}{\alpha}\right)\right] = \begin{cases} 1 & \text{if } x \in [a, b] \\ 0 & \text{if } \tau\left(\frac{x}{\alpha}\right) < 1 \text{ if } x \notin [a, b] \\ 0 & \text{if } x \notin [a - \alpha, b + \alpha] \end{cases}. \quad (7)$$

The Equation (7) is illustrated in Fig. 13 and the network in Fig. 14. By choosing fuzzy factors  $\alpha_i$  for each  $x_i$ , it is intuitively clear how this example generalizes to pattern vectors  $\mathbf{x} = (x_1, \dots, x_n) \in \mathbb{IR}^n$ .

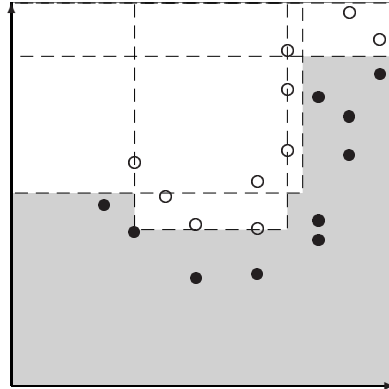


**Fig. 11.** The same problem as in Fig. 10, this time solved using the elimination version of the SLMP training algorithm. Only 4 dendrites of the class  $C_1$  output neuron are sufficient to partition the pattern space similarly to the partitioning learned by a 13-hidden unit MLP, but with closed surfaces. Recognition is again 100% correct

One assumption made in our model is that a neuron  $N_i$  can provide *both* excitatory as well as inhibitory input to a neuron  $M_j$ . This assumption has no foundation in biology. In real neural networks, a neuron can send only excitatory or only inhibitory signals to other neurons. Neurons that act as inhibitors on other neurons are called *inhibitory neurons*. It is interesting to observe that all the examples given in this exposition can be expressed in terms of networks consisting entirely of excitatory and inhibitory neurons. As an illustration, let us again consider Example 1 of Section 3. In this case there are several ways of adding an inhibitory neuron. For example, we can add an inhibitory neuron  $N_2$  so that we now have two input neurons  $N_1$  and  $N_2$ , one sending only excitatory and the other only inhibitory inputs to the output neuron  $M$ , as shown in Fig. 15(a). In this case the axonal weights of the excitatory and inhibitory neuron are  $w_1^1 = a$  and  $w_1^0 = b$ , respectively. Obviously,  $\tau(x) = (x - a) \wedge (x - b) \geq 0 \iff a \leq x \leq b$  and, therefore, the output of  $M$  is 1 if and only if  $x \in [a, b]$ . The downside of this approach is that the network topology has become a bit more complex in that we are now dealing with two input neurons. If only one input neuron is desired, then  $N_2$  can be *partially hidden* as illustrated in Fig. 15(b). In this case,  $N_1$  sends excitatory signals to  $M$  and  $N_2$ , and  $N_2$  sends inhibitory signals to  $M$ . Since  $N_2$  is not an input neuron, its states are binary, the activation function for  $N_2$  is a hard limiter of form

$$g(z) = \begin{cases} 1 & \text{if } z > 0 \\ 0 & \text{if } z \leq 0 \end{cases} \quad (8)$$

and its axonal weight is  $w_2^0 = .5$ . The weights of the input neuron's dendritic fibers are  $w_{12}^1 = a$  and  $w_{21}^1 = b$ , which terminate on the single dendrites of  $N_2$  and  $M$ , respectively. If  $\tau(x)$  and  $\tau^2(x)$  denote the total received inputs of  $M$  and  $N_2$ , then  $M$  fires if and only if  $\tau(x) = (x - a) \wedge [g(\tau^2(x)) - 0.5] \geq 0$ . Thus,

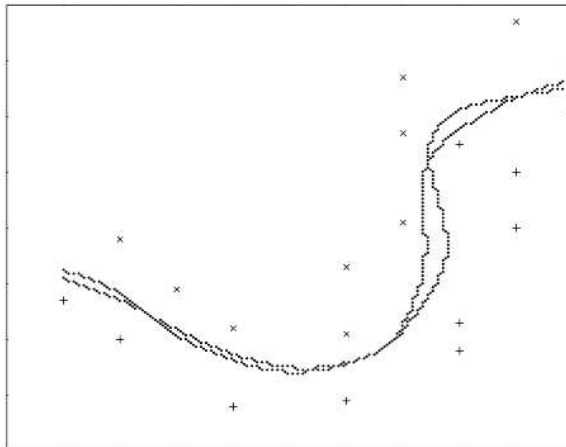


**Fig. 12.** Decision boundaries learned by a two-layer perceptron with 13 nodes in the hidden layer, using backpropagation. The thin space between the boundaries represents a region of uncertainty. Note that the separation surfaces are open, and compare with the regions learned by an SLMP in Fig. 10 and 11

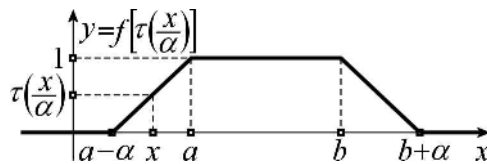


**Fig. 13.** Illustration of computing fuzzy output values

the output of  $M$  has value 1 if and only if  $a \leq x \leq b$ . Although this network also solves the problem of having only excitatory and inhibitory neurons, it is again more complex than the two-neuron model of Example 1. Even considering more complex pattern recognition problems, we have seen no *mathematical advantage* thus far in using inhibitory neurons. This does not imply that future research will not discover more powerful neural networks with dendritic structures consisting of only excitatory and inhibitory neurons. This facet of our investigations remains an active area of research.

## 6 Conclusions

We presented a new paradigm for neural computation that is based on lattice algebra and takes into account synaptic responses as well as computations in dendrites. The training algorithms that we developed grow new axonal fibers as well as dendritic structures during the learning phase. These facets of our model are more in agreement with current understanding of cerebral neural networks than current fashionable ANNs. The theorems that we established as

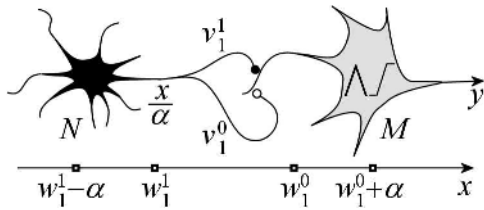


**Fig. 14.** The modified network of Example 1

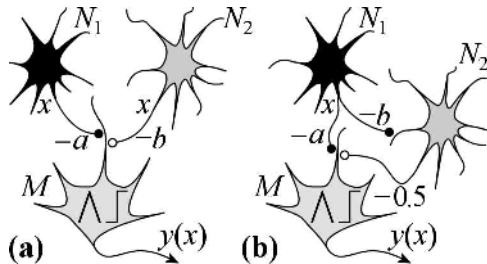


**Fig. 15.** Examples of two different SLMPs using only excitatory and inhibitory neurons. In (a) two input neurons are required, while in (b) a semi-hidden neuron is required

well as the examples presented in this paper make it obvious that an SLMP with just one output neuron is far more powerful as a pattern recognizer than the traditional single layer perceptron with one output neuron or a perceptron with one output neuron and one hidden layer. In fact, our training algorithms always draw a closed surface around the training set, thus preventing the problems of traditional perceptrons discussed in the Introduction.

We also indicated how our model can be generalized to include fuzzy computation. This remains an area of further research and applications. Additionally, we discussed the problem of employing only excitatory and inhibitory neurons in our model. As mentioned, this remains an active area of research and we hope that other researchers will join us in further exploration of these problems in order to bring ANNs into closer relationship with biological neural networks.

## References

1. Eccles, J.C.: *The Understanding of the Brain*. McGraw-Hill, New York (1977)
2. Koch, C., Segev, I. (eds.): *Methods in Neuronal Modeling: From Synapses to Networks*. MIT Press, Boston (1989)
3. Segev, I.: Dendritic Processing. In: Arbib, M. (ed.): *The Handbook of Brain Theory and Neural Networks*. MIT Press, Boston (1998) 282–289
4. Arbib, M.A. (ed.): *The Handbook of Brain Theory and Neural Networks*. MIT Press, Boston (1998)

5. Holmes, W.R., Rall, W.: Electronic Models of Neuron Dendrites and Single Neuron Computation. In: McKenna, T., Davis, J., Zornetzer, S.F. (eds.): *Single Neuron Computation*. Academic Press, San Diego (1992) 7–25
6. McKenna, T., Davis, J., Zornetzer, S.F. (eds.): *Single Neuron Computation*. Academic Press, San Diego (1992)
7. Mel, B.W.: Synaptic Integration in Excitable Dendritic Trees. *J. of Neurophysiology* **70** (1993) 1086–1101
8. Rall, W., Segev, I.: Functional Possibilities for Synapses on Dendrites and Dendritic Spines. In: Edelman, G.M., Gall, E.E., Cowan, W.M. (eds.): *Synaptic Function*. Wiley, New York (1987) 605–636
9. Shepherd, G.M.: Canonical Neurons and their Computational Organization. In: McKenna, T., Davis, J., Zornetzer, S.F. (eds.): *Single Neuron Computation*. Academic Press, San Diego (1992) 27–55
10. Gori, M., Scarselli, F.: Are Multilayer Perceptrons Adequate for Pattern Recognition and Verification? *IEEE Trans. on Pattern Analysis and Machine Intelligence* **20**(11) (1998) 1121–1132
11. Davidson, J.L.: Simulated Annealing and Morphological Neural Networks. In: *Image Algebra and Morphological Image Processing III. Proc. SPIE* **1769**, San Diego, CA (July 1992) 119–127
12. Davidson, J.L., Hummer, F.: Morphology Neural Networks: An Introduction with Applications. *IEEE Systems and Signal Processing* **12**(2) (1993) 177–210
13. Davidson, J.L., Srivastava, R.: Fuzzy Image Algebra Neural Network for Template Identification. Second Annual Midwest Electro-Technology Conference. Ames, IA (April 1993) 68–71
14. Davidson, J.L., Talukder, A.: Template Identification Using Simulated Annealing in Morphology Neural Networks. Second Annual Midwest Electro-Technology Conference. Ames, IA (April 1993) 64–67
15. Ritter, G.X., Sussner, P.: Associative Memories Based on Lattice Algebra. *IEEE Inter. Conf. Systems, Man, and Cybernetics*. Orlando, FL (October 1997) 3570–3575
16. Ritter, G.X., Sussner, P., Diaz de Leon, J.L.: Morphological Associative Memories. *IEEE Trans. on Neural Networks* **9**(2) (March 1998) 281–293
17. Ritter, G.X., Diaz de Leon, J.L., Sussner, P.: Morphological Bidirectional Associative Memories. *Neural Networks* **12** (March 1999) 851–867
18. Ritter, G.X., Urcid, G., Iancu, L.: Reconstruction of Noisy Patterns Using Morphological Associative Memories. *J. of Mathematical Imaging and Vision* **19**(5) (2003) 95–111
19. Suarez-Araujo, C.P., Ritter, G.X.: Morphological Neural Networks and Image Algebra in Artificial Perception Systems. In: *Image Algebra and Morphological Image Processing III. Proc. SPIE* **1769**, San Diego, CA (July 1992) 128–142
20. Sussner, P.: Observations on Morphological Associative Memories and the Kernel Method. *Neurocomputing* **31**, Elsevier (2000) 167–183
21. Won, Y., Gader, P.D.: Morphological Shared Weight Neural Network for Pattern Classification and Automatic Target Detection. *Proc. 1995 IEEE International Conference on Neural Networks*, Perth, Western Australia (November 1995)
22. Won, Y., Gader, P.D., Coffield, P.: Morphological Shared-Weight Networks with Applications to Automatic Target Recognition. *IEEE Trans. on Neural Networks* **8**(5) (1997) 1195–1203
23. Ritter, G.X., Urcid, G.: Lattice Algebra Approach to Single Neuron Computation. *IEEE Trans. on Neural Networks* **14**(2) (March 2003) 282–295

24. Ritter, G.X., Iancu, L.: Morphological Perceptrons. Preprint submitted to IEEE Trans. on Neural Networks.
25. Lang, K.J., Witbrock, M.J.: Learning to Tell Two Spirals Apart. In: Touretzky, D., Hinton, G., Sejnowski, T. (eds.): Proc. of the 1988 Connectionist Model Summer School. Morgan Kaufmann, San Mateo, CA (1988) 52–59
26. Wasnikar, V.A., Kulkarni, A.D.: Data Mining with Radial Basis Functions. In: Dagli, C.H., et al. (eds.): Intelligent Engineering Systems Through Artificial Neural Networks. ASME Press, New York (2000)

# Robot Vision for Autonomous Object Learning and Tracking

Alberto Sanfeliu

Institut de Robòtica i Informàtica Industrial

Universitat Politècnica de Catalunya (UPC)

sanfeliu@iri.upc.es

<http://www-iri.upc.es/groups/lrobots>

**Abstract.** In this paper we present a summary of some of the research that we are developing in the Institute of Robotics of the CSIC-UPC, in the field of Learning and Robot Vision for autonomous mobile robots. We describe the problems that we have found and some solutions that have been applied in two issues: tracking objects and learning and recognition of 3D objects in robotic environments. We will explain some of the results accomplished.

## 1 Introduction

Computer vision in autonomous mobile robotics is a very well known topic that is being treated by many research groups [1]. However, the use of perception techniques to automatically learn and recognize the environment and the objects located on it is probably not so well known. One part of our research has concentrated in the development of techniques to capture and process the information that surrounds a robot, taking into account that this information can be captured by diverse perception sensors (colour video cameras, stereo vision, laser telemeter, ultrasonic sensors, etc.) and the sensors related to robot movement (odometers).

We have focused our research in the development of “robust” techniques that must be as much as possible, “invariant” to illumination, colour, surface reflectance, sensor uncertainty, dead reckoning and dynamic environments. However, this wish is not always possible. We also orient our research to develop techniques to learn the perceptive world, in order to create a data base that can be used later on, by robots.

In this paper we describe our research in two topics in the field: adaptive learning and tracking of moving objects; and learning and recognition of 3D objects of the environment. Although these topics lead to different techniques and methodologies, they share the same perception information formats, colour images and depth maps.

However, we also use other kind of perception information formats which are captured by means of stereo vision, laser telemeter, ultrasonic and odometer sensors. The diverse information captured by these sensors is combined to obtain redundancy in order to improve the robustness of the techniques.

Before explaining the methods, we will start describing the typical “problems” that we find in the perception of a dynamic environment where the robot or the objects are moving.

## 2 Common Problems on the Acquisition of Perception Information Based on Colour Images and Depth Maps

Colour represents a visual feature commonly used for object detection and tracking systems, especially in the field of human-computer interaction. When the environment is relatively simple, with controlled lighting conditions and an uncluttered background, colour can be considered a robust cue. The problem appears when we are dealing with scenes with varying illumination conditions and varying camera position and confusing background.

The colour of an object surface can be modified by several circumstances, which limits the applicability of the use of colour images in robot vision. The following issues modify the colour perception of an object surface:

- the type of the illumination source, the illumination orientation, the number and distribution of the sources of illumination,
- the surface reflectance and the surface orientation,
- the texture of the surface,
- and the shadows produced by other objects or by the own concavities of the object.

Some of these problems can be diminished in static scenes, by controlling the illumination (for example, for indoor robot environments, the type and position of the illumination), the object surfaces (for example, by choosing objects with Labertian surfaces) or the type of objects (for example, by using convex objects).

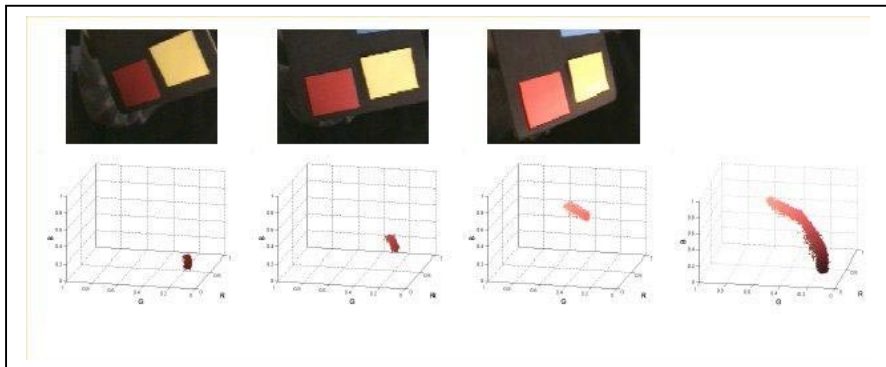


**Fig. 1.** Typical reflectance problems of a colour (red) planar surface: (a) a sequence of a red planar surface; (b) RGB map of the colour distribution of the sequence of the planar surface.

However, although we can impose some of these constraints in indoor environments, still many of the aforementioned drawbacks persist, due to the relative position and orientation of the robot sensors, the illumination devices and the scene objects. This relative position not only involves the passive sensor (colour camera), but also the illumination sources, for example, the robot can interfere with the illumination of an object surface by means of its shadow cast or a new “virtual” illumination source appears due to the reflection of another surface. A typical example of the last case is the reflectance of the “ground”.

Other typical problems are due to the camera sensor, for example, the optical aberration and geometrical deformation, the separation of the channel colour bands, the colour sensibility, the sensor sensibility to the illumination, the problems associated with the shutter speed or the resolution of the camera.



**Fig. 2.** Some problems with the reflectance of the ground

With respect to the capture of depth information, we have also other drawbacks. In the case of a laser telemeter, the sensor drawbacks are due to the features of laser source, the resolution or the speed of depth acquisition and processing, or the problems related to partial surface occlusion. If the depth sensors (for example, stereo vision or laser telemeter) are in the mobile robot, then other problems come around. For example, the relative position and orientation of the sensors with respect to the scene, because of the “skew” of the elevation, pitch or roll of cameras and laser telemeter with respect to ground.

Additionally to the abovementioned problems, we always find that in robot perception, the uncertainty is an important issue that must be taken into account when discerning from sensory data the objects and the limits of the robot environment. This perception uncertainty must be incorporated in the models for robot navigation, object tracking, object recognition and landmark identification.

### 3 Developing “Robust Techniques” for Object and Face Tracking

Object and face tracking are two typical problems in robot vision which have been studied using different types of sensors and techniques [2, 3]. One of the most used sensors is the colour video camera, since it provides enough information to follow an object and avoid uncertainties. However, in a real unconstrained environment, the varying illumination conditions, camera position and background create important problems to the robot tracker. Different approaches have been presented to solve these problems in robot tracking, but still this is an open problem from the point of view of robustness.

The important challenge in colour tracking is the ability to accommodate to the variations of the illumination and the environment, that is, the tracker must modify its parameters depending on the circumstances. However, the use of independent adaptive techniques, many times, is not enough to cope with the problem, since the adaptation only takes into account one of the potential variations, for example the colour reflectance, however the variations are usually multivariate. For this reason, we have studied solutions that combine different techniques to take into account the multivariable effect.

One of our first approaches combines information of colour changes and depth for face tracking in real time [4]. The purpose is to follow a face or an object that has colour and depth continuity avoiding the loss of them due to the presence of similar colour in the background. The technique fuses colour adaptation and stereo vision, in such a way, that the tracked objects only is analysed in a surface with similar depth information. The technique uses an ellipse to model the face of a person similar to the work of Birchfield [5] and adaptive colour models, for example [21]. The face is adapted by means of intensity gradients and colour histograms, and the stereo vision information dynamically adapts the size of the tracked elliptical face. The system uses the Kalman filter to predict the new position of the cameras and robot, and it runs at 30 Hz, that is, in real time.

A second approach, [6] tries to solve two important problems in object tracking: the change of the colour and the confusing background. As it was mentioned before, the colour of an object surface changes with the orientation of the surface (in principle only the intensity, but due to the illumination conditions and surface reflectance, the colour can also change). Moreover, if the background is confusing, then the tracking of an object surface becomes very difficult. In order to solve these two problems, we propose a solution based on fusing colour adaptation with shape adaptation. We have developed a method that, by using the CONDENSATION technique [7], combines the use of colour histograms adaptation with snake shape adaptation [8]. The algorithm formulates multiple hypotheses about the estimate of the colour distribution in the RGB space, and validates them taking into account the contour shape of the object. This combination produces a very robust technique whose results can be seen in Fig. 4. The technique is described in detail in [6].

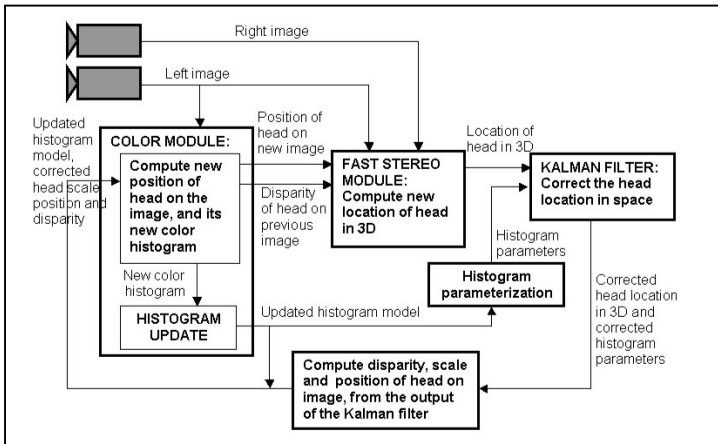


**Fig. 3.** The tracking vision system



**Fig. 4.** Four experiments: (1) tracking of circles that change the colour; (2) tracking an object surface with different orientations and illumination; (3) tracking an insect in real environment; (4) tracking a snail in real environment

#### 4 Learning and Identifying of Objects in Mobile Robotic Environments

The process of learning and identifying new 3D objects in robot environments has been treated using different methodologies, for example [9][20], however these techniques only work for very constrained environments. Unfortunately, many of the

proposed methods fail in real unstructured environments, due to problems of illumination, shadows, object and camera position, or confusing background.

In order to overcome some of these problems we are designing our methods taken into account the following criteria:

- the perception features must be, as much as possible, robust and relative invariant to changes of the environment,
- the representation models must be flexible and must include the statistical variations of the structure and of the perception features that are intrinsic in the learning process,
- the recognition, or matching, process must be robust against local variations and have to take into account the problems derived of partial occlusion.
- in the recognition process, the matching must be guided to reduce the number of potential model candidates.

The first criteria is one of the most difficult to solve, since the perception features depend too much of uncontrolled environment conditions. For these reason we have selected as basic perception features, the surface colour and surface shape. The first one can be obtained from colour images and the second one from depth sensors (for example, stereo vision and laser telemeter). The invariance of surface colour is a difficult task, but we are diminishing its influence by using colour constancy methods and statistical information of the feature variations. However, colour constancy algorithms are not yet given us the results that we expect, although our new developments are promising [22]. In the other hand, the surface shape obtained from the depth sensors is a robust feature.

One of the preliminary works to obtain robust results was the fusion of colour segmentation and depth, to improve the segmentation results. The method [23] processes independently colour segmentation and depth map, and then combines both outcomes. The idea of the method is to balance the over-segmentation and under-segmentation, by joining or splitting the singular areas. Fig. 5 shows the results of this method in a colour scene.

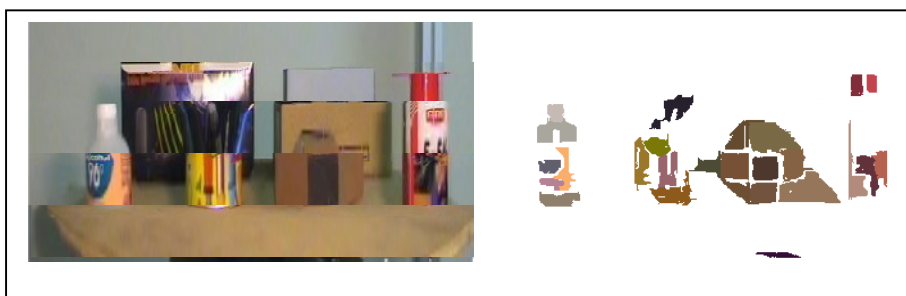


**Fig. 5.** Fusion of colour segmentation and depth map to segment a colour scene

In the rest of this section, we will describe the solutions adopted for representation models, the recognition and the learning processes. The basic representation models that we are using are structural representations, chain of symbols and graphs. In the first case we use cocircuits (of the matroid theory) and in the last case, we use random graphs which combine structural information with statistical information of the attributes of the nodes and arcs. In this way, we have a representation model that can be learned directly from the colour images taken into account the potential variations of the perception features.

Our research group has developed several methods to learn and recognise 3D objects described by multiple views in a scene. These methods have been oriented in two directions: a first one, whose goal is to reduce the number of candidates in object recognition by an indexing technique in 3D object hypothesis generation from single views; and a second one, whose goal is to identify the input object with respect to the model candidates by looking for the minimum measure distance between the object and the model candidates. The first direction allows the reduction of the number of potential model candidates to a few ones, which can be done very fast. The second direction allows to identify the best candidate.

#### 4.1 Indexing Views of 3D Objects

In the first group of techniques, the idea is to represent a 3D object view by means of topological properties of the regions of the segmented image and then to create a table with each of the topological representations of the object. Then the identification process is based on indexing the input representation of one scene view to the table of the topological representations of the 3D object views.

A topological representation is created using the oriented matroid theory by means of encoding incidence relations and relative position of the elements of the segmented image, and by giving local and global topological information about their spatial distribution. The result is a set of cocircuits [10] of sign combinations that relate segmented regions with respect to the convex hull of two selected regions of the scene. The details of this process are explained in [11, 12]. The set of cocircuits obtained is projective invariant, which is an important feature for the representation of the model objects. Fig. 6 shows the segmentation and process indexing of one object and Table 1 shows the resulting indexes of the object.

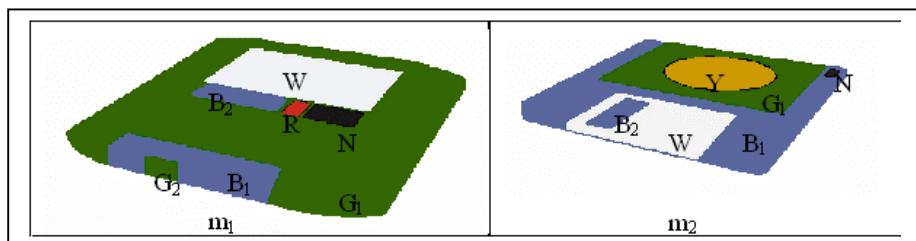


**Fig. 6.** Segmentation and process indexing of two objects

The result of the process indexing looks as follows:

**Table 1.** Index result of the process indexing of the images of Fig. 6. The first column is the baseline area from where the segmented regions are related. 0 means the region is inside the baseline area; - the region is one the left side; + the region is on the right side; and \* means the region does not exist in the segmented image.

	<b>W</b>	<b>R</b>	<b>Y</b>	<b>G<sub>1</sub></b>	<b>G<sub>2</sub></b>	<b>B<sub>1</sub></b>	<b>B<sub>2</sub></b>	<b>N</b>	<b>Object</b>
WR	0	0	*	0	0	0	-	+	m <sub>1</sub>
WY	0	*	0	0	*	0	0	-	m <sub>2</sub>
WG <sub>1</sub>	0	*	*	0	*	*	*	*	m <sub>1</sub>
WG <sub>1</sub>	0	*	0	0	*	0	0	0	m <sub>2</sub>
WG <sub>2</sub>	0	0	*	0	0	+	0	0	m <sub>1</sub>
WB <sub>1</sub>	0	0	*	0	0	0	0	0	m <sub>1</sub>
WB <sub>1</sub>	0	0	*	+	+	+	0	+	m <sub>2</sub>
WB <sub>2</sub>	0	0	*	+	+	+	0	+	m <sub>1</sub>
WN	0	0	*	-	-	-	-	0	m <sub>1</sub>
WN	0	*	+	+	*	0	0	0	m <sub>2</sub>
RG <sub>1</sub>	*	0	*	0	*	*	*	*	m <sub>1</sub>
...	...	...	...	...	...	...	...	...	
B <sub>2</sub> N	+	0	*	-	-	-	0	0	m <sub>1</sub>
B <sub>2</sub> N	-	*	+	+	*	+	0	0	m <sub>2</sub>

## 4.2 Learning and Recognising 3D Objects Represented by Multiple Views

In the second group, the idea is to represent 3D object views by means of graphs and then to obtain the model as the synthesis from the graphs that represent the views of a 3D object. Once the model has been learned, the recognition process is based on applying a distance measure among the input graph (the graph that encodes the 3D view of a scene object) and the object models. The input graph is assigned to the model graph with the minimum distance measure value. Fig. 7 shows the process of learning (synthesis of the object graph views) and recognition.

Object views are often represented by graphs, and one of the most robust representations is based on attributed graphs. When a synthesis of these attributed graphs is required to learn a complete object through its views, then a good model representation are the Random Graphs. The generalization of these graphs is denominated General Random Graphs (GRG) which has theoretically, great representation power, but they need a lot of space to keep up with the associated data. We have defined several simplifications to the GRG to reduce the space and also to diminish the time matching complexity to compare among graphs. Wong and You [13] proposed the First-Order Random Graphs (FORGS) with strong simplifications of the GRG, specifically they introduce three assumptions about the probabilistic independence between vertices and arcs which restrict too much the applicability of these graphs to object recognition. Later, our group introduced a new class of graphs called Function-Described Graphs (FDG) [14][15] to overcome some of the problems of the FORG. The FDG also considers some independence assumptions, but some useful 2° order functions are included to constrain the generalisation of the structure.

Specifically an FDG includes the antagonism, occurrence and existence relations which apply to pairs of vertices and arcs. Finally, we have expanded this representation, [17][18] by means of Second-Order Random Graphs (SORG), which keep more structural and semantic information than FORGs and FDGs. These last types of representation have led to the development of synthesis techniques for model object generation (by means of 3D object views) and graph matching techniques for graph identification.

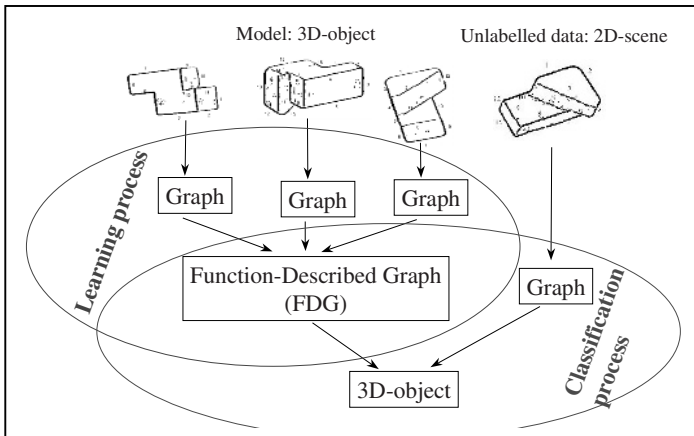


**Fig. 7.** Learning and classification processes in the classifiers that use only one structural representation per model

We show in this article, one example of unsupervised learning and recognition of 3D objects represented by multiple views. The set of objects was extracted from the database COIL-100 from Columbia University. We did the study with 100 isolated objects, where each one is represented by 72 views (one view each 5 degrees). The test set was composed by 36 views per object (taken at the angles 0, 10, 20 and so on), whereas the reference set was composed by the 36 remaining views (taken at the angles 5, 15, 25 and so on).

The learning process was as follows: (1) perform colour segmentation in each individual object view image; (2) create an adjacency graph for each one of the segmented regions of each object view; (3) transform the adjacency graph in an attributed graph (AG) using the hue feature as the attribute for each node graph; (4) synthesize a group of 35 object views in a FORG, FDG and SORG using the algorithms described in [16][19] (we use groupings of varying number of graphs to represent an object in order to evaluate the results, concretely we used 3, 4, 6 and 9 random graphs for each 3D object). The recognition process follows a similar procedure, but instead of synthesizing the graphs a measure distance between them was applied to evaluate to which 3D object the input graph belonged.

Fig. 8 shows 20 objects at angle 100 and their segmented images with the adjacency graphs. FORGs, FDGs and SORGs were synthesised automatically using the AGs in

the reference set that represent the same object. The method of incremental synthesis, in which the FDGs are updated while new AGs are sequentially presented, was applied. We made 6 different experiments in which the number of random graphs, FORGs, FDGs and SORGs, that represents each 3D-object varied. If the 3D-object was represented by only one random graph, the 36 AGs from the reference set that represent the 3D-object were used to synthesise the random graph. If it was represented by 2 random graphs, the 18 first and consecutive AGs from the reference set were used to synthesise one of the random graphs and the other 18 AGs were used to synthesise the other random graph. A similar method was used for the other experiments with 3, 4, 6 and 9 random graph per 3D-object. Note that if 4 random graphs are used, then each random graph represents 90 degrees of the 3D object.

The best result appears when the SORG and FDG representations were used, although the best is the SORG representation. Fig. 9 shows the ratio of recognition success of the 100 objects using different object representation and distance measures. This figure also shows the result of describing individually each object view by means of an AG and then comparing each input AG against the rest of the prototype AG.



**Fig. 8.** Some objects at angle 100 and the segmented images with the AGs

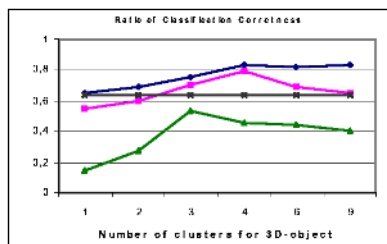


**Fig. 9.** Ratio of recognition correctness of the 100 objects using SORG, FDG, FORG and AG-AG. SORG:  $\diamond$ ; FDG:  $\blacksquare$ ; FORG:  $\blacktriangle$ ; AG-AG:  $\times$

## 5 Conclusions

Robot vision methods require close attention to two important issues. First the real time issue: the methods must have adaptable mechanisms to overcome the variance in the sensing of the basic perception features and they must be robust. Another desirable feature in robot vision is that the objects, map, motion and control models must be learned on line. Not in only in one path, but in successive robot motions. In this article we have presented some of the methods, in tracking and object learning that we are developing following these ideas. We have also applied the same ideas for map building.

## References

- [1] G.N. DeSouza and A.C. Kak: Vision for mobile robot navigation, a survey. *IEEE Trans. on Pattern Analysis and Machine Intelligence*, Vol. 24, No. 2, Feb. 2002.
- [2] B. Thomas, Moeslund and E. Granum: A Survey of Computer Vision-Based Human Motion Capture. *Computer Vision and Image Understanding: CVIU*, vol.81(3), pp.231–268, 2001.
- [3] D.A. Forsyth and J. Ponce: *Computer Vision: A Modern Approach- Tracking* (Chapt. 19). Prentice Hall. 1st edition ,2002.
- [4] F. Moreno, A. Tarrida, Juan Andrade-Cetto and A. Sanfeliu: 3D real-time head tracking fusing color histograms and stereovision. *Proceedings of the 16th International Conference on Pattern Recognition*, Quebec, August 12–15.
- [5] S. Birchfield: Elliptical head tracking using intensity gradient and colour histograms. *Intl. Conference in Computer Vision and Pattern Recognition*, pp. 232–237, 1998.
- [6] F. Moreno, J. Andrade-Cetto and A. Sanfeliu: Fusion of color and shape for object tracking under varying illumination. *Pattern Recognition and Image Analysis*, Lecture Notes in Computer Science 2652, Springer-Verlag, pp. 580–588, 2003.
- [7] M. Isard and A. Blake: Condensation-conditional density propagation for visual tracking. *Int. J. Computer Vision*, 28(1), pp.5–28, 1998.
- [8] M. Kass, A. Witkin and D. Terzopoulos: Snakes: active contour models. *Int. J. Computer Vision*. 1(4), pp. 228–233, 1987.
- [9] C. Chen and A. Kak: Robot vision system for recognizing objects in low-order polynomial time. *IEEE Trans. On System, Man and Cybernetics*, 18(6), pp. 1535–1536, Nov. 1989.
- [10] A. Björner, M.L. Vergnas, B. Sturmfels, N. White, G.M.: Oriented matroids. Volume 43 of *Encyclopedia of Mathematics and its Applications*. Cambridge University Press, 1993.
- [11] E. Staffetti, A. Grau, F. Serratosa, A. Sanfeliu: Oriented matroids for 3-D object views representation and indexing. *Pattern Recognition and Image Analysis*, First Iberian Conference; IbPRIA 2003. Lecture Notes in Computer Science, LNCS 2652, Springer Verlag, Mallorca, 4–6 June. 2003
- [12] E. Staffetti, A. Grau, F. Serratosa and A. Sanfeliu: Shape representation and indexing based on region connection calculus and oriented matroid theory. In *Discrete Geometry for Computer Imagery*, Lecture Notes in Computer Science, Springer-Verlag, Napolis, 2003.
- [13] A.K.C. Wong and M. You: Entropy and distance of random graphs with application to structural pattern recognition. *IEEE Trans. On Pattern Analysis and Machine Intelligence*, Vol. 7, pp. 599–609, 1985.

- [14] A. Sanfeliu, R. Alquezar, J. Andrade, J. Climent, F. Serratosa and J. Verges: Graph-based representations and techniques for image processing and image analysis. *Pattern Recognition*, Vol. 35, pp. 639–650, 2002.
- [15] F. Serratosa, R. Alquezar and A. Sanfeliu: Function-described graphs for modelling objects represented by sets of attributed graphs. *Pattern Recognition*, Vol. 36, pp. 781–798, 2003.
- [16] F. Serratosa, R. Alquezar and A. Sanfeliu: Synthesis of function-described graphs and clustering of attributed graphs. *Int. J. Pattern Recognition*, 16(6), pp. 621–655, 2002.
- [17] F. Serratosa, R. Alquezar and A. Sanfeliu: Estimating the joint probability distribution of random graphs vértices and arc by means of 2º order random graphs. *SSPR'2002*, Lecture Notes in Computer Science, LNCS 2396, pp. 252–262, 2002.
- [18] A. Sanfeliu and F. Serratosa: Learning and recognising 3D models represented by múltiple views by means of methods based on random graphs. *IEEE Int. Conference on Image Processing*, Barcelona 2003 (ICIP 2003), Sept. 2003.
- [19] A. Sanfeliu, F. Serratosa and R. Alquezar: Second-order graphs for modelling sets of attributed graphs and their application to object learning and recognition. *Int. J. Pattern Recognition* (in press).
- [20] H. Murase y S.K. Nayar. Visual learning and recognition of 3D objects from appearance. *International Journal of Comp. Vision*, 14(1): 5–24, 1995.
- [21] J. Vergés-Lalhi, A. Tarrida and A. Sanfeliu: New approaches for colour histogram adaptation in face tracking tasks. *Proceedings of the 16th International Conference on Pattern Recognition*, Quebec, August 12–15, 2002.
- [22] J. Vergés-LLahí, A. Sanfeliu: Colour constancy algorithm based on object function minimization. *Iberian Conference on Pattern Recognition and Image Analysis (IbPRIA)*, Puerto Andrax, Mallorca, 4–6 June. Lecture Notes in Computer Science. 2003.
- [23] J. Andrade and A. Sanfeliu: Integration of perceptual grouping and depth. *Proceedings of the 15th International Conference on Pattern Recognition*, Barcelona, September 3–7, IEEE Computer Society, Vol. 1, pp. 295–298, 2000.

# Graduated Scale Inspection Using Computer Vision

Benjamín Valera, Sergio Padilla, Gabriel Chávez, and Victor García Garduño

Centro de Ciencias Aplicadas y Desarrollo Tecnológico, UNAM, Ciudad Universitaria,  
04510 D.F., México  
metro@aleph.cinstrum.unam.mx

**Abstract.** A method for graduated scale inspection using computer vision is proposed. We deal mainly with the lens distortion problem in the image acquire device due to its influence in the uncertainty of the graduated scale inspection process. This paper presents an algorithm for image correction by means of camera calibration and distortion compensation. The camera calibration method provides the ideal undistorted coordinates of the system using as input distorted images of a 2D calibration pattern. The distortion compensation stage is implemented using the ideal undistorted coordinates as an unwarped mesh. Then distortion compensation can be applied to any image acquired with the system, improving the inspection procedure. Test results using real data are presented. Also, we describe the image feature extraction approach used in order to automate the process.

## 1 Introduction

There is an important effort to take advantage of computer vision systems in the dimensional metrology field [1]. Computer vision hardware and software have been used to improve calibration, measurement or inspection process. However, main problems arise when high accuracy is needed in order to accomplish with high-quality uncertainty levels. This is the case in the graduated scale inspection process, where the uncertainty source comes from lens distortion in the image intensifier device coupled to the image acquisition system. Consequently, lens distortion must be taken into account in measurements or inspections outcomes.

The graduated scale inspection process consists of a comparison approach between the scale under inspection and a length standard, as Fig.1 shows.

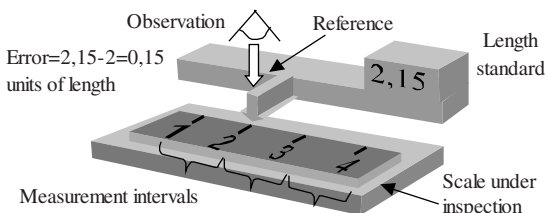


**Fig. 1.** Scale graduated inspection. A typical scale is compared against a length standard.

In Fig. 1 the reference cursor on the length standard is placed mechanically against a measurement interval on the scale under inspection. The user does this through an observation device. For this example the measurement error is calculated as the difference in the length standard, 2,15, and the scale under inspection, 2,0, resulting in an error of 0,15 units of length. In our practical implementation of the layout in Fig. 1, we use an optical encoder as the length standard, a multimedia camera with microscope as the observation device and a mechanical artifact that supports the whole arrangement in concordance with international recommendations [4]. Then the accuracy of the inspection resides in the exactness of the positioning of the cursor over the printed graduation in the scale. Two factors have influence in the positioning: the mechanical device and the good judgment of the user that is controlling the inspection through the observation device. We pay attention in the second factor; supplying undistorted images to the user, thus improving the visual inspection.

This paper then deals with image distortion correction for the particular case of graduated scale inspection using the layout described. In particular, the distortion generated by the combination of the camera and microscope lenses, provides deformations that greatly fails with the classical distortion models described in the literature [6]. Instead, we adopt a mesh unwarping approach in which the whole image is subdividing and a local correction is applied to each independent region. The camera calibration procedure [2] provides a reference unwarped mesh, which takes as input real distorted images of a 2D grid pattern and a least squares approach leads to a “straight lines in the scene should be straight in the image” sense. Furthermore, image feature extraction is used in order to achieve a reliability system and automation.

The paper is organized as follows. Section 2 describes the camera calibration method by using real distorted images of a 2D calibration pattern. A warped mesh is obtained by means of image feature extraction and it is used by the least squares approach to derive the unwarped mesh. Section 3 presents the distortion compensation algorithm. The algorithm takes both warped and unwarped meshes to reproduce unwarped images. The performance of our method is demonstrated in section 4 by the results of applying distortion compensation to real images of graduated scales. Section 5 gives concluding remarks and future work.

## 2 Camera Calibration Method

In the camera calibration procedure, we use an approach similar to the pinhole camera model [5]. In the model presented in this paper there are two main differences. The first is that the scene is magnified and not inverted compared to the pinhole camera [2]. In the second, the short field-of-view of the acquisition system imposes planar scenes with no depth. Then a 2D calibration pattern is used and the depth remains as a free parameter. The calibration model is shown in Fig. 2. In this figure, the calibration pattern is placed in the target plane,  $T$ , and the image is formed in the image plane,  $I$ . The model is completed with the focal plane,  $F$ , which contains de focal point. Then, a feature in the calibration pattern,  $M$ , is projected to the image plane,  $m$ . Focal and image planes are separated  $f$  units and target and image plane are at  $d$  units of length. The image plane has two components: distorted and undistorted, both related by a distortion model. In order to perform image-processing tasks, image coordinates are

stored and managed in row-column computer arrays. The distortion produces warped and unwarped computer arrays. The parallel depth alignment ( $Z$  axis) between the target and image planes is achieved by focusing.

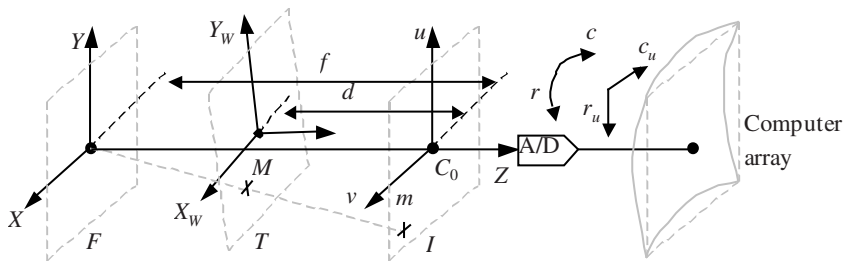


**Fig. 2.** Camera model. A geometrical model relates global coordinate to array coordinates.

The main idea of calibration is to obtain a set of unwarped features starting from a set of warped features. As we will show, features are line crossings in the image formed by the calibration target. To achieve automation, the procedure is performed in two stages: feature extraction and distortion estimation.

## 2.1 Feature Extraction

Feature extraction is performed with some modifications as described in [2]. The procedure starts with an original image of a  $0,5 \times 0,5$  mm calibration grid (Fig. 3(a)). Then, a gray scale closing filter extracts the background. The subtraction between the original image and its background followed by thresholding yields to a simplified image. Horizontal and vertical line extraction is applied to the binary image by convolving with horizontal and vertical structural elements. The feature image in Fig. 3(b) is obtained by computing the center of gravity of the horizontal and vertical intersection. Each center of gravity conforms the starting point in the search of a finest subpixel feature extraction.

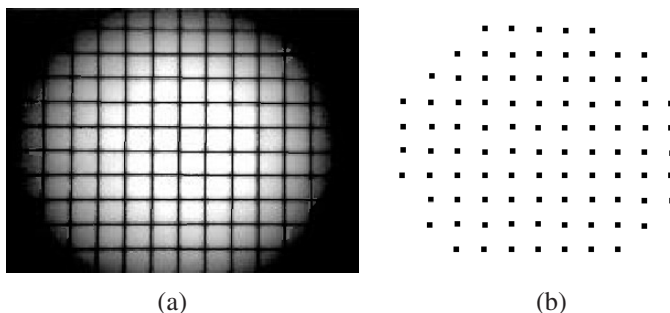


**Fig. 3.** Image pre-processing using morphological.

The crossing points of the vertical and horizontal lines are extracted with subpixel accuracy through a method based on the starting point and the analysis of a squared pattern around it, similar to the one proposed in [3]. This method avoids the iterative minimization procedure described in [2] and constitutes a closed form solution in order to gather computation speed without a loss of exactness. The main idea surrounding the algorithm is to fit lines to image data and then found the intersection point. Two lines are needed for subpixel feature extraction: horizontal and vertical. The lines are defined by analyzing the original grayscale image along a squared pattern centered at starting points. The Fig. 4 shows a detail of the sampled squared pattern around the starting point. The gray level profile of the pattern defines eight border points marked as circles signs in Fig. 4(a). The border points are arranged in horizontal and vertical pairs to find their midpoints. Then the four midpoints, marked as triangles signs in Fig. 4(a), define the two lines. Simple mathematics is used to locate the intersection point with subpixel accuracy marked with a star sign. The Fig. 4(b) shows a typical gray level profile of the squared pattern. The first order derivative of the profile is computed. Then, the local maxima of derivative is detected and grouped into pairs to conform the border points. Since the original image is on a discrete domain, the gray level intensity is computed using bilinear interpolation.

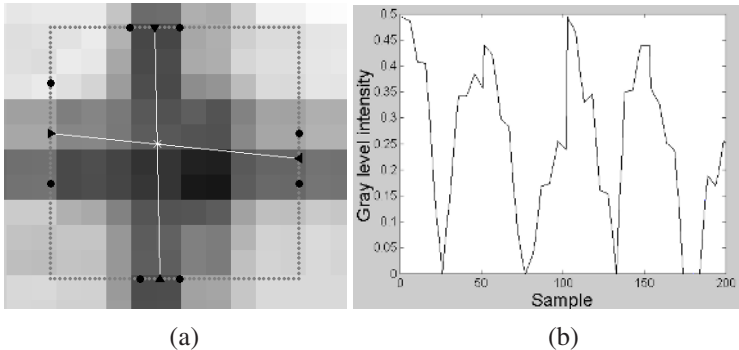


**Fig. 4.** Squared pattern of the original grayscale image and its samples.

Then the whole image is processed using the method described in order to extract the  $N$  entire feature points. The Fig. 5(a) shows the extracted points overlying the original image. Additional processing is required to correlate warped feature points,  $(r_i, c_i)$ , against their global position defined in the grid pattern,  $(X_{wi}, Y_{wi})$ , where  $i=1, \dots, N$  points. First, horizontal and vertical images are labeling with a consecutive number starting from one. Then, 2D global positions are assigned to feature points by searching its position in both labels image. The  $X_{wi}$  and  $Y_{wi}$  coordinates are calculated through multiplying the size of the grid and the label number. Fig. 5(b) shows the 2D world coordinate assignment.

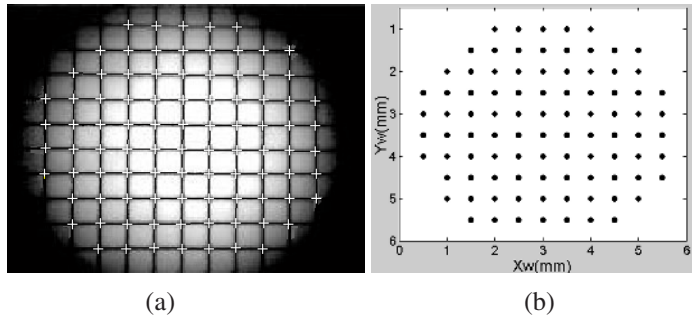


**Fig. 5.** Feature points with subpixel accuracy and their correlation with 2D global positions.

## 2.2 Distortion Estimation

Distortion estimation is performed by first generating an unwarped set of points from the extracted warped features, their correlation with 2D global positions and the camera calibration model. In the camera calibration model, the main idea is to obtain a set of parameters that relates world positions,  $(X_{wi}, Y_{wi})$  to unwarped computer array,  $(r_{ui}, c_{ui})$ . Following the procedure described in [2] this relation is

$$\begin{bmatrix} c_u \\ r_u \end{bmatrix} = \begin{bmatrix} a_u & -a_v & t_u \\ a_v & a_u & t_v \end{bmatrix} \begin{bmatrix} X_w \\ Y_w \\ 1 \end{bmatrix} \quad (1)$$

where

$$a_u = s \cos \theta \quad a_v = s \sin \theta \quad t_u = st_x + c_0 \quad t_v = st_y + r_0 \quad s = \frac{f s_u}{Z_w + f - d} = \frac{f s_v}{Z_w + f - d}$$

and  $t_x$ ,  $t_y$  are translation in  $X$  and  $Y$ ,  $\theta$  is the rotation in the  $Z$  direction,  $(r_o, c_o)$  is the pixel position of the origin  $C_o$ , and  $s_u = s_v$  is the aspect factor of the ccd camera.

Then the distortion estimation is derived as the relationship between unwarped,  $(r_{ui}, c_{ui})$ , and warped,  $(r_i, c_i)$  computer arrays. The equation (1) should fit a set of  $N$  observations  $(c_i, r_i), (X_{wi}, Y_{wi})$   $i=1, \dots, N$  to the model in the equation with adjustable parameters  $\rho = (a_x, a_y, t_x, t_y)$ . Therefore,  $\rho$  should minimize the following error

$$\gamma(\mathbf{p}) = \frac{1}{N} \sum_{i=1}^N \left[ (c_i - c_{ui})^2 + (r_i - r_{ui})^2 \right] \quad (2)$$

Substituting equation (1) into (2) and taken into account that at the minimum the partial derivatives of  $\gamma$  with respect to  $\rho$  vanish, we obtain the following

$$\begin{bmatrix} C & 0 & A & B \\ 0 & C & -B & A \\ A & -B & 1 & 0 \\ B & A & 0 & 1 \end{bmatrix} \begin{bmatrix} a_u \\ a_v \\ t_u \\ t_v \end{bmatrix} = \begin{bmatrix} D_1 \\ D_2 \\ C_0 \\ R_c \end{bmatrix} \quad (3)$$

The equation (3) can be resolved for  $\rho$  taken as input data 2D global positions ( $X_{wi}$ ,  $Y_{wi}$ ) and their correlated projections into the image plane ( $c_i$ ,  $r_i$ ), since

$$\begin{aligned} A &= \frac{1}{N} \sum_{i=1}^N X_{wi} & B &= \frac{1}{N} \sum_{i=1}^N Y_{wi} & C &= \frac{1}{N} \sum_{i=1}^N (X_{wi}^2 + Y_{wi}^2) \\ R_c &= \frac{1}{N} \sum_{i=1}^N r_i & C_0 &= \frac{1}{N} \sum_{i=1}^N c_i & D_1 &= \frac{1}{N} \sum_{i=1}^N (c_i X_{wi} + r_i Y_{wi}) & D_2 &= \frac{1}{N} \sum_{i=1}^N (r_i X_{wi} - c_i Y_{wi}) \end{aligned}$$

Then, equation (1) can be used to generate an unwarped grid using the warped features and their correlation with 2D global positions (Fig. 6).

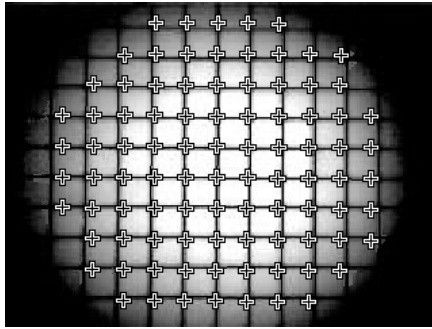


**Fig. 6.** Unwarped grid overlying the original warped image.

### 3 Distortion Compensation Algorithm

We test with the following well-known model of distortion

$$r_u = r + \delta_r(r, c) \quad c_u = c + \delta_c(r, c)$$

where  $r_u$  and  $c_u$  are the ideal unwarped coordinates,  $r$  and  $c$  are the corresponding warped coordinates and  $\delta_r(r, c)$  and  $\delta_c(r, c)$  are bi-variable polynomials of  $n$  degree. The bi-variable polynomial method fails in representing the real system distortion. This is due to the fact that local distortions are not in agreement with the proposed model. In general, cheap lenses, like the one used in this vision system, presents a substantial amount of local distortion. Therefore, to increase the accuracy in the distortion compensation stage, we introduce a region-based approach similar to the mesh-warping algorithm used in image morphing [7]. This algorithm requires both source and destination meshes to perform bilinear transformations between regions

inside the mesh. As a first step and referring to the Fig. 7(a), a uniform auxiliary mesh (circle sign) is placed on top the non-uniform mesh (dot sign) obtained in the feature extraction stage. In this sense, there are defined quadrilateral regions and the features that do not define quadrilaterals are discarded. Quadrilateral regions are marked with the triangle sign, which is enclosed by only four feature points marked with both circle and dot signs. Then, warped quadrilateral sub-regions are transformed to the corresponding quadrilateral unwarped sub-region as shown in Fig. 7(b), according with the following backward transformation formula

$$r = a_0 + a_1 r_u + a_2 c_u + a_3 r_u c_u \quad c = b_0 + b_1 r_u + b_2 c_u + b_3 r_u c_u \quad (4)$$

where parameters  $a$  and  $b$  are defined by the knowledge of the eight vertex points as follows

$$\begin{bmatrix} r_0 \\ r_1 \\ r_2 \\ r_3 \end{bmatrix} = \begin{bmatrix} 1 & r_{u0} & c_{u0} & r_{u0}c_{u0} \\ 1 & r_{u1} & c_{u1} & r_{u1}c_{u1} \\ 1 & r_{u2} & c_{u2} & r_{u2}c_{u2} \\ 1 & r_{u3} & c_{u3} & r_{u3}c_{u3} \end{bmatrix} \begin{bmatrix} a_0 \\ a_1 \\ a_2 \\ a_3 \end{bmatrix} \quad \begin{bmatrix} c_0 \\ c_1 \\ c_2 \\ c_3 \end{bmatrix} = \begin{bmatrix} 1 & r_{u0} & c_{u0} & r_{u0}c_{u0} \\ 1 & r_{u1} & c_{u1} & r_{u1}c_{u1} \\ 1 & r_{u2} & c_{u2} & r_{u2}c_{u2} \\ 1 & r_{u3} & c_{u3} & r_{u3}c_{u3} \end{bmatrix} \begin{bmatrix} b_0 \\ b_1 \\ b_2 \\ b_3 \end{bmatrix}$$

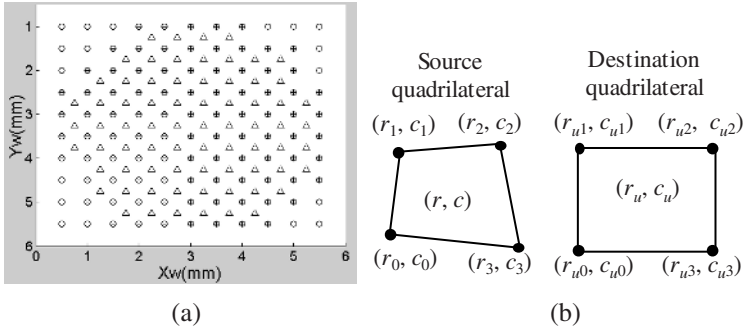


**Fig. 7.** Region-based approach for distortion compensation.

Finally, applying the backward transformation in (4) to the whole original image, we obtain the unwarped image shown in Fig 8(a). Once the camera is calibrated using the procedure described here, the visual inspection of a graduated scale can be improved with the backward transformation as shown in Fig 8(b).

## 4 Results

In order to obtain quantitative results, we perform two experiments to proof the “straight lines in the scene should be straight in the image” sense. In the first experiment, we fit the unwarped feature points to straight lines and the squared sum of the residuals is compared against the one obtained with warped features. The

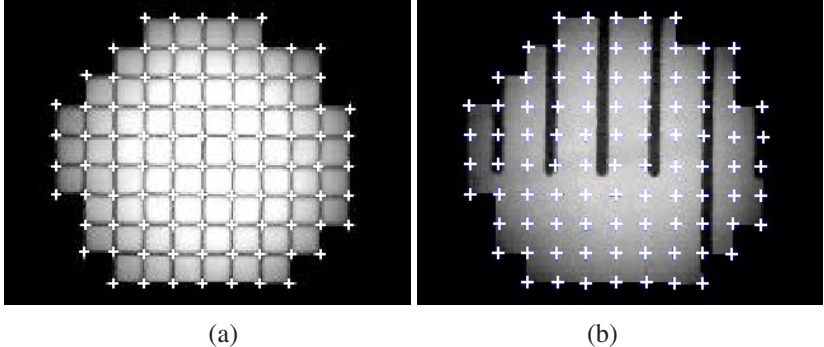


**Fig. 8.** Distortion compensation using the region-based approach described.

squared sum of residuals for the warped grid is 19,4188 (pixels) against  $1,4086 \times 10^{-15}$  for the unwarped one. In the second experiment we test the uniformity in distance between vertical and horizontal lines in the warped and unwarped images of the calibration grid. We obtained a uniform distance between lines of 23,2 pixels for the unwarped case against the non-uniform distance of 21,6 to 25 pixels for the warped case. Then, in our mind, the two experiments are indicatives of the main idea shaped to project the scene without distortion. Further results of automated feature extraction, camera calibration and distortion compensation procedures were presented all along the paper.

## 5 Conclusions and Future Work

A computer vision system for graduated scale inspection was presented. The main problem faced up was the optical distortion in the acquisition hardware. The generation of a reference unwarped set of features was done using camera calibration tools. Then the algorithm generates nearly ideal images by the distortion compensation method. Also, feature extraction and image processing achieved the automation of the process. The results indicate us the reliability of the approach in the “straight lines in the scene should be straight in the image” sense. For metrological purposes, the accuracy of the system was tested qualitatively and quantitatively by the development of two experiments.

In the future, additionally image processing can be done in order to complete the automation of the measurement process and avoid the human intervention. In our idea, the layout presented in the Fig. 1 will suffer of few changes. First, the length standard will be precisely placed in a known position. Then, the vision system will assign a measurement to the observation process. Then, the main problem is concerned with the human knowledge that is used in a measurement with graduated scales.

**Acknowledgments.** This work has been financially supported by DGAPA-UNAM. The authors of this paper are indebt to the grant No IN111001 from PAPIIT.

## References

1. Aguilar, J. J., Torres, F. and Lope, M. A.: Stereo Vision for 3D Measurement: Accuracy Analysis, Calibration and Industrial Applications. *Measurement* **18** 4 (1996) 193–200.
2. Cañero, C., Vilariño, F., Mauri, J. and Radeva, P.: Predictive (un)distortion model and 3D Reconstruction by Biplane Snakes. *IEEE Transactions on Medical Imaging* **21** 9 (2002) 1188–1201.
3. Harris, K., Efstratiadis, S. N., Maglaveras, N., Gourassas, J., Pappas, C. and Louridas, G.: Coronary Arterial Tree Extraction based on Artery Tracking and Mathematical Morphology. *Computers in Cardiology* (1988) 769–772.
4. International Recommendation No. 35: Material Measures of length for General Use. OIML (1985) 22.
5. Tsai, R. Y.: A Versatile Camera Calibration Technique for High-Accuracy 3D Machine Vision Metrology Using Off-the-Shelf TV Cameras and Lenses. *IEEE Journal of Robotics and Automation* **3** 4 (1987) 323–344.
6. Weng, J., Cohen, P. and Herniou, M.: Camera Calibration with Distortion Models and Accuracy Evaluation. *IEEE Transactions on Pattern Analysis and Machine Intelligence* **14** 10 (1992) 965–980.
7. Woldberg, G.: *Digital Image Warping*. Wiley (2002) 340.

# Vision System for Subpixel Laser Stripe Profile Extraction with Real Time Operation

Ulises Martínez, Benjamin Valera, José Sánchez, and Victor García

Centro de Ciencias Aplicadas y Desarrollo Tecnológico, UNAM, Ciudad Universitaria,  
04510 D.F., México  
metro@aleph.cinstrum.unam.mx

**Abstract.** Computer vision systems are playing an important role in 3D measurement for industrial applications. Real time image processing algorithms are useful in order to achieve reliability in feature extraction from the global environment starting from planar images. For example, in a *structured light* vision system is essential to extract the pattern that a laser source is shaping with the objects under inspection. In this sense, this work describes a single strip image extraction algorithm that could be used as an analysis tool in those structured light systems. The experimental setup is implemented using the following equipment: A PC equipped with a frame grabber, a high-resolution CCD camera, a laser stripe projector and specific software developed using Visual C++6. The system accomplishes with real time operation and high subpixel accuracy.

## 1 Introduction

Recently, in our dimensional metrology laboratory, have been developed measurement techniques using computer vision with real time operation for industrial applications. Computer vision efforts are directed to reduce costs and operative time in the industrial field [1]. Additionally, measurement vision systems offer the great advantage of measuring without mechanical contact. However, vision systems still lack of high accuracy due to some restrictions in the image formation process. On the other hand, our aim to develop a measuring vision system is based on the utilization of auxiliary techniques that contributes with the high accuracy purpose. For example, the mechanical arrangement in the computer vision layout can be tested with higher accuracy standards, like coordinates measuring and form scan machines. Moreover, the accuracy in a measurement vision system is not only limited by the resolution of the acquisition devices; the planar image, highlighted by a structured light source, is improved and reduces some limitations in the image formation process. Also, the structured light contributes to simplification of the image management for feature extraction [2].

It is well known that computer vision techniques take advantage of subpixel feature extraction [6]. In particular, a structured light system needs to extract the strip image that is formed by the intersection of a laser stripe projector with the object under inspection. Then, relevant extracted features can be reconstructed in a 3D environment using the triangulation principle together with the camera and laser

source calibration. Therefore, it is possible to perform 3D measurements using monocular vision [5].

This paper deals with the sub pixel laser stripe profile extraction in planar images incoming from a structured light system for metrological purposes. The aim is to create a real time operation system to be operated as a high accuracy measurement instrument. The relevance of our work is the development of a practical implementation, this is to apply a feature extraction algorithm to create a useful tool with industrial application. The organization of this paper is as follows: Section 2 presents the computer vision system principle for dimensional measurements. A review of an algorithm for laser stripe profile extraction is presented in section 3. We give emphasis to in a closed form solution that meets accuracy and committed processing time. Section 4 describes hardware and software platform supporting our implementation. Section 5 presents some results of applying three-dimensional reconstruction to the feature extraction process. Finally, our work is summarized in section 6.

## 2 Measurement Principle Using Structured Light

Our scheme for the dimensional measurement using computer vision is based on the well-known triangulation principle and the layout in Fig. 1(a). The hardware was selected in order to gain high accuracy at low cost. The laser stripe projector generates a sharp light pattern that intersects with the 3D object under inspection. Then the pattern is digitized with a CCD camera and a frame grabber attached to a computer. The resulting planar image contains simplified information about the object, useful for 3D reconstruction purposes. It is possible to demonstrate that a 3D reconstruction process of the 2D stripe pattern can be done by means of camera and laser plane calibration, as Fig. 1(b) shows.

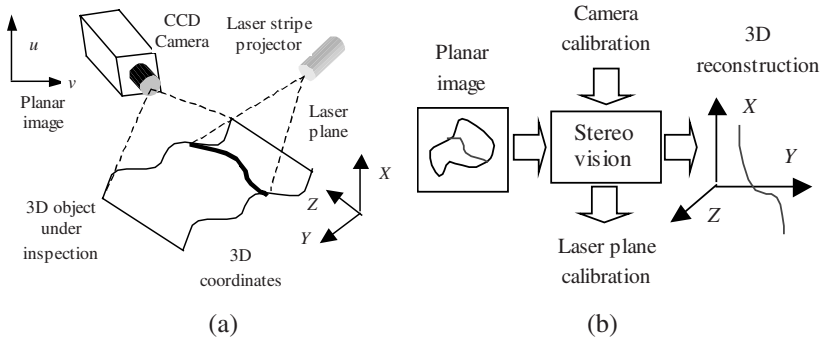


**Fig. 1.** Dimensional measurement using computer vision.

The layout of Fig. 1 involves the following main tasks:

1. Camera calibration. Implies to find the mathematical model that relates 3D global coordinates with its planar projection [7, 8].

2. Laser plane calibration. It consists in finding the mathematical expression of the laser plane.
3. Stripe image processing. The main idea is to extract the spine of the stripe image with subpixel accuracy.
4. Reconstruction. This is the aim of the measurement instrument and takes as inputs the calibration process and the stripe image to generate 3D positions.

In this paper we focus mainly in the stripe image processing stage, due to its importance in the measurement process and its relevance in the automation of the procedure.

### 3 Stripe Image Processing

The aim of the algorithm described in this section is to extract the spine of the stripe image accomplishing with subpixel accuracy. The physical situation presented in Fig. 1 imposes planar stripe images, which pattern approximates a Gaussian distribution. Then, the feature extraction process provides a reduced set of descriptor parameters and also contributes with the improvement in the reconstruction. The algorithm is divided in two main stages: Image simplification in order to isolate the stripe profile and subpixel feature extraction in order to obtain accurately the set of parameters conforming the spine.

#### 3.1 Image Simplification

The Fig. 2 shows typical planar images generated by the proposed layout in Fig 1. The Fig. 2(a) shows the scene with no light from the laser stripe projector when it is turned off. In the Fig. 2(b), the laser plane intersects the scene when the projector is turned on. The Fig. 3(c) shows the absolute value of the difference between figures 2(a) and 2(b), isolating in this way the profile of the object under inspection. The laser projector is turned on and off by simple electronics and control software.

#### 3.2 Subpixel Feature Extraction

In this stage [4], the image in Fig. 2(c)  $I(u, v)$  is processed by establishing initial conditions for a center of the stripe  $\mathbf{p}_i(p_{xi}, p_{yi})$  together with a line width  $w_i$  and a line direction  $\mathbf{d}_i(d_{xi}, d_{yi})$ . The initial center of the stripe is obtained using a scan procedure from top to bottom and left to right in image coordinates. The extracted information conforms a line element  $\mathbf{e}_i(\mathbf{p}_i, w_i, \mathbf{d}_i)$ , as shown in fig 3(a). Then, starting from the initial conditions, the subsequent line elements are generated in the following way. The next line element  $\mathbf{e}_i(\mathbf{p}_i, w_i, \mathbf{d}_i)$  is estimated by forming a circular pattern  $t(\mathbf{p}_i, r)$  with center in  $\mathbf{p}_i$  and radius  $r_i=0.6w_i$ . The pattern is used as reference trajectory in finding the borders of the stripe  $\mathbf{b}_1 \mathbf{b}_2$ , as shown in Fig. 3(b). The position, direction and width of the next element line are given by

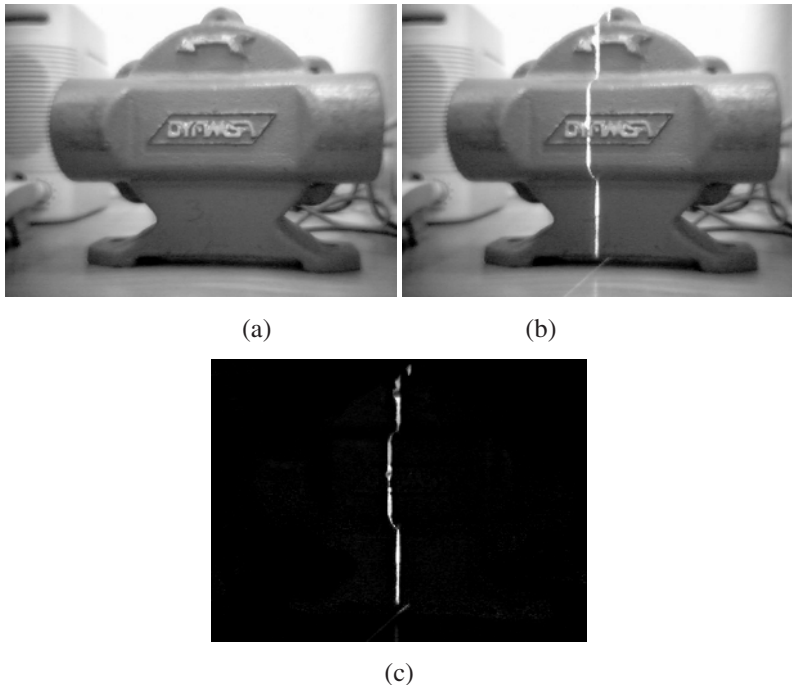


**Fig. 2.** Planar projections of the measurement system by vision

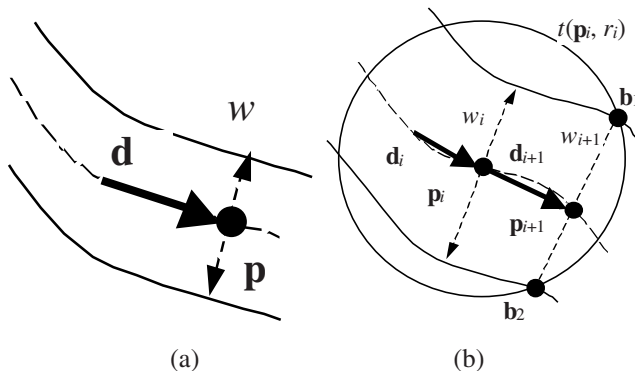


**Fig. 3.** Line elements of a gray scale image.

$$\mathbf{p}_{i+1} = \frac{\mathbf{b}_1 + \mathbf{b}_2}{2} \quad \mathbf{d}_{i+1} = \mathbf{p}_{i+1} - \mathbf{p}_i \quad w_{i+1} = \|\mathbf{b}_1 - \mathbf{b}_2\|$$

The border points  $\mathbf{b}_1$  and  $\mathbf{b}_2$  are detected by analyzing the gray level intensity of the circular pattern  $t$ . The circular pattern is a set of  $\lfloor 2\pi r \rfloor$  samples taken over the perimeter of the circumference with center  $\mathbf{p}_i$  and radius  $r$ , in other words,  $t(\mathbf{p}, r) = (c_0, c_1, \dots, c_{\lfloor 2\pi r \rfloor})$ , where

$$c_i = I(px + |\mathbf{p}| \cos(i\delta\theta), py + |\mathbf{p}| \sin(i\delta\theta))$$

for  $i=1, 2, \dots, \lfloor 2\pi r \rfloor - 1$  and  $\delta\theta = 2\pi/\lfloor 2\pi r \rfloor$ . Due to discrete nature of the gray scale image  $I$ , the samples  $c_i$  are computed using bilinear interpolation. Then, the first derivative of  $t(\mathbf{p}, r)$ ,  $dt(\mathbf{p}, r)$ , is computed using finite differences. The local maximum of the magnitude  $|dt(\mathbf{p}, r)|$  is detected and grouped in to pairs by means of the sign in  $dt(\mathbf{p}, r)$ . Given a pair of border points, it is reported a line element only if the magnitude of  $|dt(\mathbf{p}, r)|$  in the border points is larger than a threshold. On the opposite way, it begins a new scan procedure. In our practical implementation, we use only one half of the circular pattern, as Fig. 4(a) shows in a zoomed detail. The gray level of the pattern is shown in Fig. 4(b). The Fig. 5(a) shows the whole spine extraction of a stripe image and the Fig. 5(b) presents a detail.

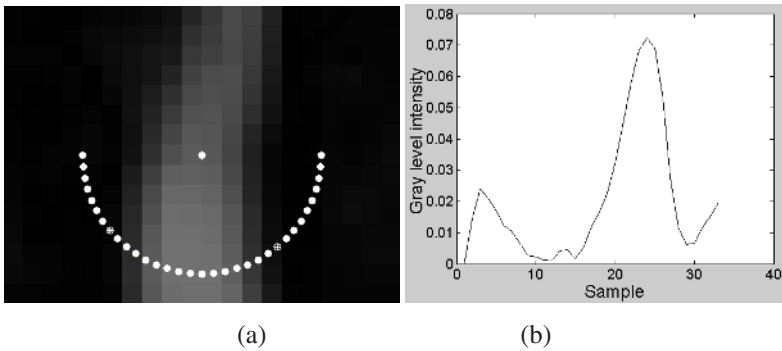


**Fig. 4.** Circular pattern

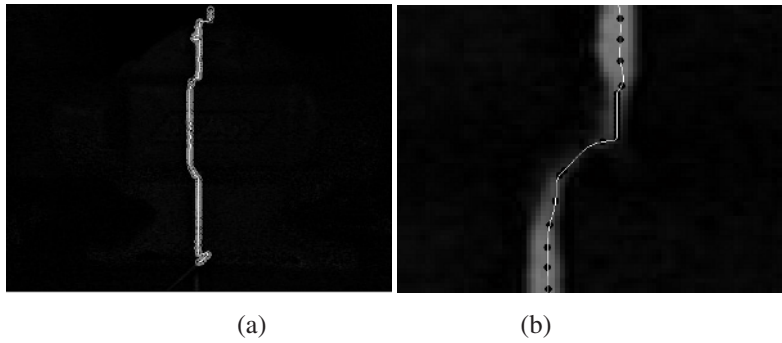


**Fig. 5.** Spine extraction with subpixel accuracy.

## 4 Hardware and Software Platform

The layout of the computer vision system for dimensional measurement using computer vision is presented in Fig. 6(a). In this figure, a PC equipped with a DT3155

frame grabber [3] acquires 640X480X8 planar images incoming from a high resolution CCD camera. In order to achieve real time process, the algorithm described in the previous section was written in Visual C++ 6.0. The user interface is shown in Fig. 6(b).

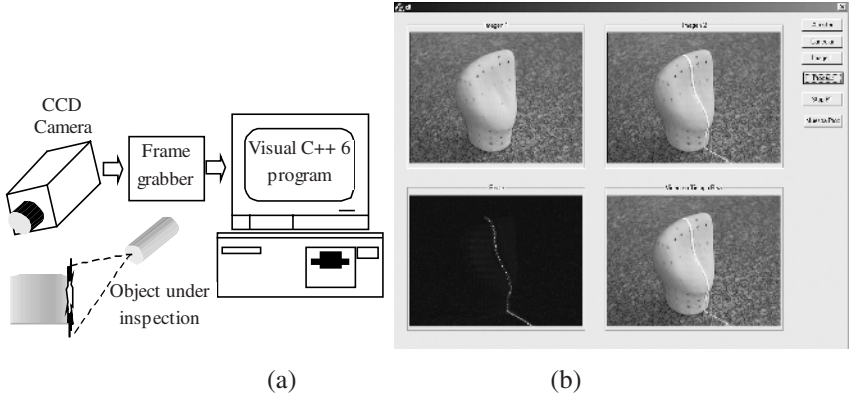


**Fig. 6.** Hardware and software platform for dimensional measurement using computer vision.

## 5 Experimental Results

Some experimental results can be reported with the 3D reconstruction of the spine extracted from the stripe image. The experimental arrangement, Fig. 7, is supported by a coordinate measuring machine with the purpose of system calibration. After laser plane and camera calibration, the reconstruction is implemented with a similar approach as described in [5]. In our test setup, the object under inspection is a scaled model of a tooth. It is easy to prove that the reconstruction problem can be stated as follows.

$$\begin{bmatrix} r_7 \frac{X_u}{f} - r_1 & r_8 \frac{X_u}{f} - r_2 & r_9 \frac{X_u}{f} - r_3 \\ r_7 \frac{Y_u}{f} - r_4 & r_8 \frac{Y_u}{f} - r_5 & r_9 \frac{Y_u}{f} - r_6 \\ A & B & C \end{bmatrix} \begin{bmatrix} T_x - T_z \frac{X_u}{f} \\ T_y - T_z \frac{Y_u}{f} \\ -D \end{bmatrix} = \begin{bmatrix} x_w \\ y_w \\ z_w \end{bmatrix} \quad (1)$$

and

$$X_d = \frac{dp_x}{sx} (X_f - c_x) \quad Y_d = dp_y (Y_f - c_y)$$

$$X_u = X_d \left[ 1 + k(X_d^2 + Y_d^2) \right] \quad Y_u = Y_d \left[ 1 + k(X_d^2 + Y_d^2) \right]$$

where  $\{r_i, T_x, T_y, T_z, f, dp_x, dp_y, k, c_x, c_y\}$  are camera calibration parameters,  $\{A, B, C, D\}$  are laser plane calibration parameters,  $(X_f, Y_f)$  are coordinates in the digitized image,  $(X_d, Y_d)$  are image distorted coordinates,  $(X_u, Y_u)$  are image undistorted

coordinates and  $(x_w, y_w, z_w)$  are the 3D reconstructed coordinates of the 2D feature  $(X_f, Y_f)$ . Then, using simple matrix algebra, the 3D coordinates can be computed from equation (1). Applying equation (1) to the extracted spine, the 3D plot of Fig. 8 is obtained. Comparing the measurement outcomes using the computer vision system described here against the one performed with coordinate measuring machine, we compute an RMS reconstruction error of 0.08mm in a 100X100X100mm measurement volume.



**Fig. 7.** Experimental setup.

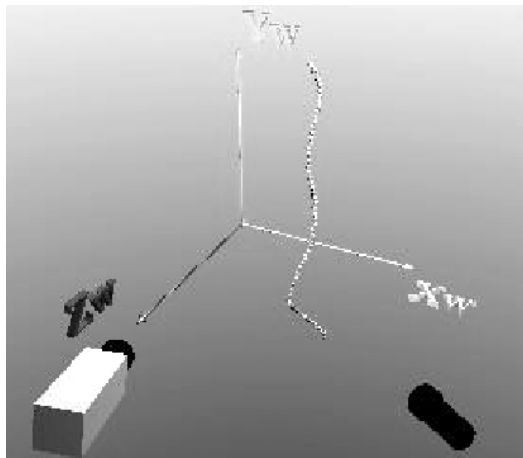


**Fig. 8.** Plot of a 3D reconstruction.

## 6 Conclusions and Future Work

A vision system for subpixel laser profile extraction was presented. The system accomplishes with high accuracy in both, image processing and 3D reconstruction. An algorithm for feature extraction with real time operation was tested in an

experimental setup. The geometric oriented approach of the image processing algorithm contributes to an easy implementation using Visual C++. For this reason we discard the use of third party software for image or mathematical processing; our developed software was implemented using basic development tools. The results oriented our future work in the following directions.

1. The development of an electro-mechanical device in order to scan the whole geometry of 3D work pieces. In our concept, a rotary support with angular position feedback is needed to perform a complete measurement process.
2. The incorporation of 3D graphics in the user interface. We are planning the development of real time render in the user interface using, for example, OpenGL.
3. The calibration improvement. We are planning to build a rotary support and calibrate it with the use of higher accuracy standards, like coordinate measuring and form scan machines.

**Acknowledgments.** This work has been financially supported by DGAPA-UNAM. The authors of this paper are indebt to the grant No IN111001 from PAPIIT.

## References

1. Aguilar, J., Torres, F., Lope, M.A.: Stereo Vision for 3D Measurement: Accuracy Analysis, Calibration and Industrial Applications. *Measurement* **18** 4 (1996) 193–200.
2. Chi, L.-C., Chih, L.-Y.: A new approach to high precision 3-D measuring system. *Image and Vision Computing* 17 (1999) 805–814.
3. Data Translation: SDK DT-Active Open Layers User's Manual. Data Translation, USA (1999).
4. Harris, K., Efstratiadis, S.N., Maglaveras, N., Gourassas, J., Pappas, C., Louridas, G.: Coronary Arterial Tree Extraction based on Artery Tracking and Mathematical Morphology. *Computers in Cardiology* 25 (1998) 769–772.
5. Izquierdo, M.A.G., Sánchez, M.T., Ibáñez, A., Ullate, L.G.: Sub-pixel measurement of 3D surfaces by laser scanning. *Sensors and Actuators* **76** (1999) 1–8.
6. Steger, C.: Subpixel-Precise Extraction of Lines and Edges. *International Archives of Photogrammetry and Remote Sensing* **XXXIII** (2000) 141–156.
7. Tsai, R.Y.: A Versatile Camera Calibration Technique for High-Accuracy 3D Machine Vision Metrology Using Off-the-Shelf TV Cameras and Lenses. *IEEE Journal of Robotics and Automation* **3** 4 (1987) 323–344.
8. Weng, J., Cohen, P. and Herniou, M.: Camera Calibration with Distortion Models and Accuracy Evaluation. *IEEE Transactions on Pattern Analysis and Machine Intelligence* **14** 10 (1992) 965–980.

# Multi-channel Reconstruction of Video Sequences from Low-Resolution and Compressed Observations

Luis D. Alvarez<sup>1</sup>, Rafael Molina<sup>1</sup>, and Aggelos K. Katsaggelos<sup>2</sup>

<sup>1</sup> Departamento de Ciencias de la Computación e Inteligencia Artificial,  
University of Granada, 18071 Granada, Spain  
`{ldac, rms}@decsai.ugr.es`

`http://decsai.ugr.es/{~ldac, ~rms}/`

<sup>2</sup> Department of Electrical and Computer Engineering,  
Northwestern University, Evanston, IL 60208, USA  
`{aggk}@ece.nwu.edu`

`http://www.ece.northwestern.edu/~aggk/`

**Abstract.** A framework for recovering high-resolution video sequences from sub-sampled and compressed observations is presented. Compression schemes that describe a video sequence through a combination of motion vectors and transform coefficients, e.g. the MPEG and ITU family of standards, are the focus of this paper. A multichannel Bayesian approach is used to incorporate both the motion vectors and transform coefficients in it. Results show a discernable improvement in resolution in the whole sequence, as compared to standard interpolation methods.

## 1 Introduction

High-frequency information is often discarded during the acquisition and processing of an image. This data reduction begins at the image sensor, where the original scene is spatially sampled during acquisition, and continues through subsequent sampling, filtering or quantization procedures. Recovering the high-frequency information is possible though, as multiple low-resolution observations may provide additional information about the high-frequency data. This information is introduced through sub-pixel displacements in the sampling grid, which allows for the recovery of resolution.

Although work has been devoted to the problem of reconstruction of one high resolution image from a sequence of low resolution ones (see for instance [1-5] and [6] for a review), not much work has been reported on the problem of increasing the resolution of a whole image sequence simultaneously (see however [7-9]).

In this paper we present a new method to obtain a whole high resolution sequence from a set of low resolution observations. The method will use the relationship between the high resolution images in the sequences and also the process to obtain the low resolution compressed ones from their corresponding high resolution images.

The rest of this paper is organized as follows: In section 2, we formulate the problem within the Bayesian framework, define the acquisition system to be considered and the prior information we are going to use on the high resolution image

sequence. In section 3, we introduce an iterative algorithm for estimating the high-resolution sequence. In section 4, we present results from the proposed procedure. Conclusions are presented in section 5.

## 2 System Model

When images from a single camera are captured at closely spaced time instances, then it is reasonable to assume that the content of the frames is similar. That is, we can say that

$$f_l(x, y) = f_k(x + d_{l,k}^x(x, y), y + d_{l,k}^y(x, y)) + n_{l,k}(x, y), \quad (1)$$

where  $f_l(x, y)$  and  $f_k(x, y)$  are the gray level values at spatial location  $(x, y)$  in the high-resolution images at times  $l$  and  $k$ , respectively,  $d_{l,k}^x(x, y)$  and  $d_{l,k}^y(x, y)$  comprise the displacement that relates the pixel at time  $k$  to the pixel at time  $l$ , and  $n_{l,k}(x, y)$  is an additive noise process that accounts for any image locations that are poorly described by the displacement model.

The expression in (1) can be rewritten in a matrix-vector form as

$$\mathbf{f}_l = C(\mathbf{d}_{l,k})\mathbf{f}_k + \mathbf{n}_{l,k}, \quad (2)$$

where  $\mathbf{f}_l$  and  $\mathbf{f}_k$  are formed by lexicographically ordering each image into an one-dimensional vector,  $C(\mathbf{d}_{l,k})$  is the two-dimensional matrix that describes the displacement across the entire frame,  $\mathbf{d}_{l,k}$  is the column vector defined by lexicographically ordering the values  $(d_{l,k}^x(x, y), d_{l,k}^y(x, y))$  and  $\mathbf{n}_{l,k}$  is the noise process.

When the images are  $PM \times PN$  arrays, then  $\mathbf{f}_l$ ,  $\mathbf{f}_k$ ,  $\mathbf{d}_{l,k}$  and  $\mathbf{n}_{l,k}$  are column vectors with length  $PMPN$  and  $C(\mathbf{d}_{l,k})$  has dimension  $PMPNxPMPN$ .

The conversion of a high-resolution frame to its low-resolution and compressed observation is expressed as

$$\mathbf{y}_k = T_{DCT}^{-1} Q \left[ T_{DCT} \left( \mathbf{A} \mathbf{H} \mathbf{f}_k - \sum_{\forall i} C(\mathbf{v}_{k,i}) \mathbf{y}_i \right) \right] + \sum_{\forall i} C(\mathbf{v}_{k,i}) \mathbf{y}_i, \quad (3)$$

where  $\mathbf{y}_k$  is a vector that contains the compressed low-resolution images with dimension  $MN \times I$ ,  $\mathbf{f}_k$  is the high-resolution data,  $\mathbf{v}_{k,i}$  is the motion vector transmitted by the encoder that signals the prediction of frame  $k$  from previously compressed frame  $i$ ,  $C(\mathbf{v}_{k,i})$  represents the prediction process with a matrix (for images said to be “intra-coded”, the prediction from all frames is zero),  $\mathbf{A}$  is an  $MN \times PMPN$  matrix that sub-samples the high-resolution image,  $\mathbf{H}$  is an  $PMPN \times PMPN$  matrix that filters the high-resolution image,  $T_{DCT}$  and  $T_{DCT}^I$  are the forward and inverse DCT calculations, and  $Q$  represents the quantization procedure.

Let  $\mathbf{F}$  be the vector  $(\mathbf{f}_1^T, \mathbf{f}_2^T, \dots, \mathbf{f}_k^T, \dots, \mathbf{f}_L^T)^T$  that contains all the high-resolution frames and let  $\mathbf{Y}$  be the vector that contains all the low-resolution frames  $(\mathbf{y}_1^T, \mathbf{y}_2^T, \dots, \mathbf{y}_k^T, \dots, \mathbf{y}_L^T)^T$ . We propose to follow a maximum *a posteriori* (MAP)

estimation approach in recovering the high resolution information from the low resolution compressed observations. Towards this task, we will use the following approximation for the conditional distribution of the observed low resolution images given the high resolution sequence

$$p(\mathbf{Y} | \mathbf{F}) = p(\mathbf{y}_1, \dots, \mathbf{y}_L | \mathbf{f}_1, \dots, \mathbf{f}_L) = \prod_i p(\mathbf{y}_i | \mathbf{f}_i), \quad (4)$$

where

$$p(\mathbf{y}_i | \mathbf{f}_i) \propto \exp\left\{-\lambda_4 \|\mathbf{y}_i - \mathbf{A}\mathbf{H}\mathbf{f}_i\|^2\right\}. \quad (5)$$

This conditional distribution enforces similarity between the compressed low resolution image and its high resolution image (through a process of blurring and downsampling, represented by  $\mathbf{H}$  and  $\mathbf{A}$  respectively). With  $\lambda_4$  we control this resemblance.

In this paper we assume that the high resolution motion vectors  $\mathbf{d}_{l,k}$  have been previously estimated (see [6] for different approaches to perform this task).

In the literature about motion estimation there are methods based on optical flow (see [10] and [11]), block matching [12], and feature matching. Simoncelli in [13] uses the optical flow equation but also adds an uncertainty model to solve the extended aperture problem and a Gaussian pyramid to deal with big displacements. Another interesting method was proposed by Irani and Peleg (see [14]) using an object based approach. The motion parameters and the location of the objects (it is supposed that there are several moving objects in the image sequence) are computed sequentially taking into account only one object at a time by using segmentation. A Gaussian pyramid from coarse to finer resolution is also used to avoid problems with the displacements.

In our implementation the motion field has been computed, for all the compressed low resolution frames, mapping the previous frame into the current one, and then interpolating the resulting low resolution motion field to obtain the high resolution motion field. Better motion field estimation procedures, which probably would provide better reconstruction results, are currently under study.

From equation (2) ,assuming smoothness within the high resolution images and trying to remove the blocking artifacts in the low resolution uncompressed images, we use the following prior model to describe the relationship between the high resolution images:

$$p(\mathbf{f}_1, \dots, \mathbf{f}_L) \propto \exp\left\{-\lambda_1 \sum_{i=2}^L \|\mathbf{f}_{i-1} - C(\mathbf{d}_{i-1,i}) \mathbf{f}_i\|^2 - \lambda_2 \sum_{i=1}^L \|\mathbf{Q}_1 \mathbf{f}_i\|^2 - \lambda_3 \sum_{i=1}^L \|\mathbf{Q}_2 \mathbf{A} \mathbf{H} \mathbf{f}_i\|^2\right\}. \quad (6)$$

In the first term of the above prior distribution we are including the quality in the prediction (if the prediction of our frame  $\mathbf{f}_i$  from the previous one is a good prediction, this term will be small). The second and third terms represent smoothness constraints, where  $\mathbf{Q}_1$  represents a linear high-pass operation,  $\mathbf{Q}_2$  represents a linear high-pass operation across block boundaries, and  $\lambda_2$  and  $\lambda_3$  control the influence of the two norms. By increasing the value of  $\lambda_2$ , the density describes a smoother image frame, while increasing the value of  $\lambda_3$  results in a frame with smooth block boundaries.

After having defined the prior and degradation models, several points are worth mentioning. First, note that the degradation process (see equations (4) and (5)) relate each low resolution observation to its corresponding high resolution one and so no

prediction of high resolution images is included in it. Due to this fact, this model is different from the one currently used in most high resolution methods (see Segall et al. [6] for a review). Note also that the prior model is responsible for relating the high resolution images and so a change in a high resolution image will enforce (through the prior model) changes in the other high resolution images. Finally, note that, although it is also possible to include prior models over the high-resolution motion vectors, in this work we assume that they have been estimated previously to the reconstruction process, see however [15–16] for the simultaneous estimation of high-resolution motion and images. Work on prior motion models which are consistent over time will be reported elsewhere.

### 3 Problem Formulation and Proposed Algorithm

The maximum *a posteriori* (MAP) estimate provides the necessary framework for recovering high-resolution information from a sequence of compressed observations. Following the Bayesian paradigm the MAP high resolution sequence reconstruction satisfies

$$\hat{\mathbf{F}} = \arg \max_{\mathbf{F}} \{p(\mathbf{F})p(\mathbf{Y}|\mathbf{F})\}. \quad (7)$$

Applying logarithms to equation (7) we find that the high resolution image sequence estimate  $\hat{\mathbf{F}}$  satisfies

$$\begin{aligned} \hat{\mathbf{F}} = \arg \min_{\mathbf{F}} & \left\{ \lambda_1 \sum_{i=2}^L \|\mathbf{f}_{i-1} - C(\mathbf{d}_{i-1,i})\mathbf{f}_i\|^2 + \lambda_2 \sum_{i=1}^L \|\mathbf{Q}_1 \mathbf{f}_i\|^2 + \lambda_3 \sum_{i=1}^L \|\mathbf{Q}_2 \mathbf{A} \mathbf{H} \mathbf{f}_i\|^2 + \right. \\ & \left. + \lambda_4 \sum_{i=1}^L \|\mathbf{y}_i - \mathbf{A} \mathbf{H} \mathbf{f}_i\|^2 \right\} \end{aligned} \quad (8)$$

In order to find the MAP we propose the following iterative procedure. Let  $\mathbf{F}^0$  be an initial estimate of the high resolution sequence. Then given the sequence  $(\mathbf{f}_1^n)^T, (\mathbf{f}_2^n)^T, \dots, (\mathbf{f}_k^n)^T, \dots, (\mathbf{f}_L^n)^T$  we obtain, for  $l=1, \dots, L$  the high resolution image  $\mathbf{f}_l^{n+1}$  at step  $n+1$  by using the following equation

$$\begin{aligned} \mathbf{f}_l^{n+1} = & \mathbf{f}_l^n - \alpha_{f_l} \left\{ \lambda_1 C^T (\mathbf{d}_{l-1,l}) [\mathbf{f}_{l-1}^{n+1} - C(\mathbf{d}_{l-1,l}) \mathbf{f}_l^n] + \lambda_1 [\mathbf{f}_l^n - C(\mathbf{d}_{l,l+1}) \mathbf{f}_{l+1}^n] + \right. \\ & \left. + \lambda_2 \mathbf{Q}_1^T \mathbf{Q}_1 \mathbf{f}_l^n + \lambda_3 \mathbf{H}^T \mathbf{A}^T \mathbf{Q}_2^T \mathbf{Q}_2 \mathbf{A} \mathbf{H} \mathbf{f}_l^n - \lambda_4 \mathbf{H}^T \mathbf{A}^T (\mathbf{y}_l - \mathbf{A} \mathbf{H} \mathbf{f}_l^n) \right\} \end{aligned} \quad (9)$$

The relaxation parameter  $\alpha_{f_l}$  determines convergence as well as the rate of convergence of the iteration. It is important to note that for the first and last frames in the sequence,  $\mathbf{f}_1$  and  $\mathbf{f}_L$  respectively, the frames  $\mathbf{f}_0$  and  $\mathbf{f}_{L+1}$  do not exist and so the above equation has to be adapted by removing the presence of  $\mathbf{f}_0$  and  $\mathbf{f}_{L+1}$  respectively.

### 4 Experimental Results

The performance of the algorithm is illustrated by processing frames from the *Mobile* sequence. Each original image is 704x576 pixels and it is decimated by a factor of

two in each dimension, cropped to a size of  $176 \times 144$  pixels and compressed with an *MPEG-4* encoder operating at  $1024Kbps$ . Three frames from the compressed bit-stream are then sequentially provided to the proposed algorithm,  $\mathbf{Q}_1$  is a  $3 \times 3$  discrete Laplacian,  $\mathbf{Q}_2$  is a difference operation across the horizontal and vertical block boundaries, and the model parameters were experimentally chosen to be  $\lambda_1=100$ ,  $\lambda_2=0.01$ ,  $\lambda_3=0.002$ ,  $\lambda_4=1$ , and  $\alpha_{fl}=0.125$ . The algorithm is terminated when

$$\left\| \hat{\mathbf{F}}_{k+1} - \hat{\mathbf{F}}_k \right\|^2 / \left\| \hat{\mathbf{F}}_k \right\|^2 < 1 \times 10^{-7}. \quad (10)$$

The performance of the algorithm is defined in terms of the improvement in signal-to-noise ratio, defined by

$$ISNR = 10 \log_{10} \left( \frac{\|\mathbf{F} - \bar{\mathbf{Y}}\|^2}{\|\mathbf{F} - \hat{\mathbf{F}}\|^2} \right), \quad (11)$$

where  $\bar{\mathbf{Y}}$  is the zero-order hold of image  $\mathbf{Y}$ . A representative algorithm result is presented in the Figs. 1-4. The original image is shown in Fig. 1, the compressed observation after bi-linear interpolation in Fig. 2, and the image provided by the proposed algorithm is depicted in Fig. 3. Fig. 4 zooms a part of the image obtained by bi-linear interpolation (Fig. 4a) and our proposed method (Fig. 4b). The sign “Maree” unreadable in the image shown in Fig. 4a whereas is almost readable in Fig. 4b. The smoothness constraint also performs well, as can be observed in the left area of the images. The corresponding ISNR values for Fig. 2 and 3 are 30.4123dB and 31.1606dB, respectively. These figures, as well as the visual inspection, demonstrate the improvement obtained by the proposed algorithm. Figure 5 plots the value of the stopping criterium of the algorithm (see equation (10)) as a function of the number of iteration  $k$ , demonstrating the convergence of the algorithm.



**Fig. 1.** Cropped part of the original image from the sequence before decimation and compression. The proposed method’s aim is to estimate all these images at the same time.



**Fig. 2.** Decoded observations after bi-linear interpolation. The compression artifacts are easily noticeable.



**Fig. 3.** Image obtained by the proposed method. The comparison should be established between this figure and Fig. 2.



**Fig. 4. a)** Decoded image after bi-linear interpolation. **b)** The improvement achieved by the method. The sign "Maree" unreadable in the image a) whereas is almost readable in b). The smoothness constraint works well, as can be observed in the left area of the images.

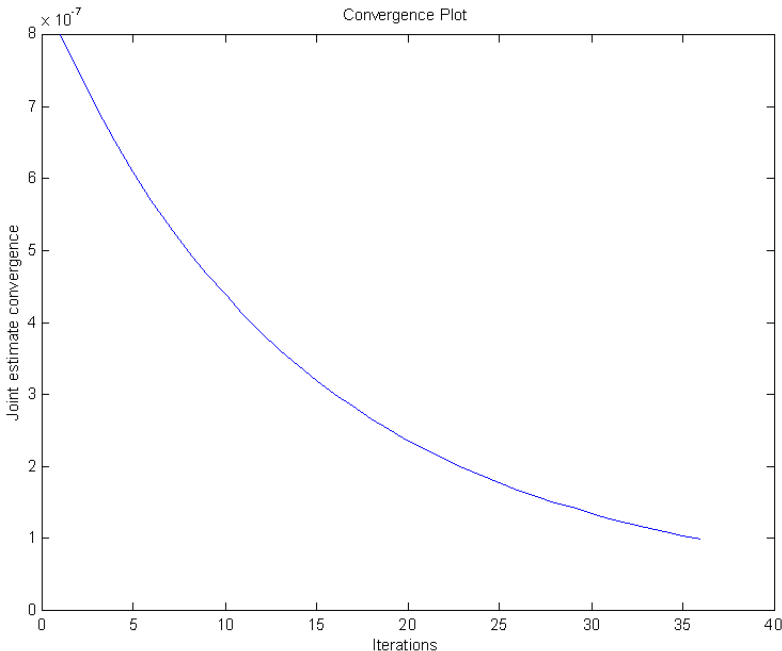


**Fig. 5.** Convergence plot of the iterative procedure. The implemented method guarantees convergence.

## 5 Conclusions

In this paper we have proposed a new iterative procedure to estimate a high resolution video sequence from low resolution observations. The method uses fidelity to the low resolution data and smoothness constraints whithin and between the high resolution images to estimate the sequence. Incorporating temporal coherence of the high resolution motion vectors as well as the development of a parallel implementation of the algorithm are currently under study. The proposed method has been experimentally validated.

## References

1. Chen, D., Schultz, R.R.: Extraction of High-Resolution Still from MPEG Sequences. Proceedings of the IEEE ICIP, Chicago, IL, (1998) 465–469
2. Altunbasak, Y., Patti, A.J., Mersereau, R.M.: Super-resolution still and video reconstruction from mpeg-coded video. IEEE Transactions on Circuits and Systems for Video Technology, vol. 12 (2002) 217–226

3. Segall, C.A., Molina, R., Katsaggelos, A.K., Mateos, J.: Bayesian High-Resolution Reconstruction of Low-Resolution and Compressed Video. Proceedings of the IEEE ICIP, vol 2, Thessaloniki, Greece (2001) 21–25
4. Segall, C. A., Katsaggelos, A. K., Molina, R., Mateos, J.: Super-Resolution from Compressed Video. In: Chaudhuri, S.: Super-Resolution Imaging, Kluwer Academic Publishers (2001) 211–242
5. Gunturk, B.K., Altunbasak, Y., Mersereau, R.M.: Multiframe Resolution-Enhancement Methods for Compressed Video. IEEE Signal Processing Letters, vol. 9 (2002) 170–174
6. Segall, C. A., Molina, R., Katsaggelos, A. K.: High Resolution Images from a Sequence of Low Resolution and Compressed Observations: A Review. IEEE Signal Processing Magazine, vol. 20, no. 3 (2003) 37–48
7. Choi, M. C., Yang, Y., Galatsanos, N. P.: Multichannel Regularized Recovery of Compressed Video Sequences. IEEE Trans. on Circuits and Systems II, vol. 48 (2001) 376–387
8. Elad, M., Feuer, A.: Super-Resolution Reconstruction of Image Sequences. IEEE Transactions on Pattern Analysis and Machine Intelligence, vol 21 (1999) 817–834
9. Elad, M., Feuer, A.: Super-Resolution Restoration of an Image Sequence: Adaptive Filtering Approach. IEEE Transactions on Image Processing, vol 8 (1999) 387–395
10. Horn, B. K. P., Schunk, B. G.: Determining Optical Flow. Artificial Intelligence, vol. 17 (1981) 185–203
11. Lucas, B. D., Kanade, T.: An Iterative Image Registration Technique with an Application to Stereo Vision. Proceedings of Imaging Understanding Workshop (1981) 121–130
12. Trucco, E., Verri, A.: Introductory Techniques for 3-D Computer Vision. Prentice Hall (1998)
13. Simoncelli, E. P.: Bayesian Multi-Scale Differential Optical Flow: In: Jähne, B., Haussecker, H., Geissler, P.: Handbook of Computer Vision and Applications, Academic Press, vol. 2 (1999) 97–402
14. Irani, M., Rousso, B., Peleg, S.: Computing Occluding and Transparent Motions. Int. J. Computer Vision, vol. 12, no. 1 (1994) 5–16
15. Hardie, R. C., Barnard, K. J., Armstrong, E. E.: Joint MAP Registration and High-Resolution Image Estimation Using a Sequence of Undersampled Images. IEEE Transactions on Image Processing, vol. 6, no. 12 (1997) 1621–1633
16. Hardie, R. C., Barnard, K. J., Bognar, J. G., Armstrong, E. E., Watson, E. A.: High-Resolution Image Reconstruction from a Sequence of Rotated and Translated Frames and its Application to an Infrared Imaging System. Optical Engineering, vol. 37, no. 1 (1998) 247–260

# 3D Rigid Facial Motion Estimation from Disparity Maps

N. Pérez de la Blanca<sup>1</sup>, J.M. Fuertes<sup>2</sup>, and M. Lucena<sup>2</sup>

<sup>1</sup>Department of Computer Science and Artificial Intelligence  
ETSII. University of Granada, 18071 Granada, Spain  
[nicolas@ugr.es](mailto:nicolas@ugr.es)

<sup>2</sup>Departamento de Informática. Escuela Politécnica Superior. Universidad de Jaén  
Avenida de Madrid 35, 23071 Jaén .Spain  
[{jmf, mlucena}@ujaen.es](mailto:{jmf, mlucena}@ujaen.es)

**Abstract.** This paper proposes an approach to estimate 3D rigid facial motions through a stereo image sequence. The approach uses a disparity space as the main space in order to represent all the 3D information. A robust algorithm based on the RANSAC approach is used to estimate the rigid motions through the image sequence. The disparity map is shown to be a robust feature against local motions of the surface and is therefore a very good alternative to the traditional use of the set of interest points.

## 1 Introduction

To date, many efforts have been made to study the problem of camera motion from features extracted from monocular or stereo images [6,9,13]. The main approach estimates the motion by establishing correspondences between interest points on each image. There are two main shortcomings of such an approach: firstly, it requires the set of interest points on each image to lie on static 3D surfaces of the scene; and secondly, the surfaces of the scene must be textured enough to allow interest points to be estimated. When we approach the problem of estimating 3D rigid facial motions from images, we find that the problem of estimating the rigid motion of a 3D surface with many instantaneous local deformations is usually due to local facial motions [1,5,8]. Furthermore, it is well known that the surface of the face is not textured enough. Therefore, alternatives to the traditional use of the set of interest points must be considered. In this paper, a homography between disparity spaces is used to estimate 3D rigid motions. Dense disparity maps are used as a feature from which the homography parameters can be estimated.

Since we are interested in studying 3D object motions near the camera, we use the general perspective camera model in order to analyze our images. An important instance of this situation appears in 3D videoconferencing systems, where the 3D shape of the head and face of each participant must be refreshed in each instant of time, and the usual short distance between cameras and surfaces introduces strong perspective effects [12].

In Section 2, we introduce the geometrical concepts of the disparity space. In Section 3, we study the rigid motion estimation in the disparity space. In Section 4, disparity map estimation is discussed. In Section 5, experiments carried out on image data are shown. Finally, in Section 6, discussions and conclusions are presented.

## 2 Stereo Images

Let us consider a calibrated rectified stereo rig, *i.e.* the epipolar lines are parallel to the  $x$ -axis. There is no loss of generality since it is possible to rectify the images of a stereo rig once the epipolar geometry is known [6]. We also assume that both cameras of the rectified stereo rig have internal parameters which are similar and known.

Stereo reconstruction has been studied for years, and is now a standard topic in computer vision. Let us consider a rectified image pair, and let  $(x,y)$  and  $(x',y')$  be two corresponding points in that image pair. Since the corresponding points must lie on the epipolar line, the relation between the two points is

$$\begin{aligned} x' &= x - d \\ y' &= y \end{aligned} \quad (1)$$

where  $d$  is defined as the disparity of the point  $(x,y)$ . From rectified stereo images, we can define representation spaces based on the projected coordinates that are equivalent to a 3D reconstruction of the points up to a homography of the 3D space [4]. These spaces are known as *disparity spaces*. The equations relating the 3D coordinates  $(X,Y,Z)$  with the disparity coordinates in the case of oriented and rectified cameras are [13]:

$$\begin{pmatrix} X \\ Y \\ Z \end{pmatrix} = \frac{B}{\bar{x} - \bar{x}'} \begin{pmatrix} \bar{x} \\ \bar{y} \\ 1 \end{pmatrix} \quad \bar{x} = \frac{x - x_0}{\alpha}, \quad \bar{y} = \frac{y - y_0}{\alpha}, \quad \bar{x}' = \frac{x' - x'_0}{\alpha'} \quad (2)$$

where  $x_0, y_0, x'_0$  are the principal point coordinates of the left and right image, respectively,  $\alpha$  and  $\alpha'$  are the focal distance of the left and right cameras, respectively and  $B$  is the baseline of the stereo rig. All image coordinates are expressed in terms of pixels.

In this paper, we use the disparity space defined by the triple  $(x,y,d)$ . From expression (2), taking  $\alpha=\alpha'$ , the homographic relationship between the 3D coordinates of a point  $X=(X,Y,Z)^T$  and its associated disparity vector  $(\bar{x}, \bar{y}, d)^T$  can be expressed as

$$\begin{pmatrix} \bar{x} \\ \bar{y} \\ d \\ 1 \end{pmatrix} = \begin{bmatrix} \alpha & 0 & 0 & 0 \\ 0 & \alpha & 0 & 0 \\ 0 & 0 & 0 & \alpha B \\ 0 & 0 & 1 & 0 \end{bmatrix} \begin{pmatrix} X \\ Y \\ Z \\ 1 \end{pmatrix} \quad (3)$$

or in a shorter way as

$$\begin{pmatrix} \tau \\ 1 \end{pmatrix} \cong \mathbf{H}_B \begin{pmatrix} \mathbf{X} \\ 1 \end{pmatrix} \quad , \quad \tau = (\bar{x}, \bar{y}, d)^T \quad (4)$$

From equation (3), it is clear that in the case of non-calibrated cameras each pair of rectified stereo images provides us with the reconstruction of the surface being imaged up to projectivity. From the intrinsic parameters of the stereo rig, the projective reconstruction can be upgraded to metric.

### 3 Rigid Motions in the Disparity Space

Let us apply a rigid motion on the 3D data. If  $\mathbf{X}$  and  $\mathbf{X}'$  represent the 3D coordinates of a point before and after the motion, then

$$\begin{pmatrix} \mathbf{X}' \\ 1 \end{pmatrix} = \begin{pmatrix} \mathbf{R} & \mathbf{T} \\ \mathbf{0}^T & 1 \end{pmatrix} \begin{pmatrix} \mathbf{X} \\ 1 \end{pmatrix} \quad (5)$$

From expressions (4) and (5) we obtain

$$\lambda \begin{pmatrix} \tau' \\ 1 \end{pmatrix} = \mathbf{H}_B \begin{pmatrix} \mathbf{R} & \mathbf{T} \\ \mathbf{0}^T & 1 \end{pmatrix} \mathbf{H}_B^{-1} \begin{pmatrix} \tau \\ 1 \end{pmatrix} = \Gamma \begin{pmatrix} \tau \\ 1 \end{pmatrix} \quad (6)$$

Equation (6) describes the 3D homography  $\Gamma$  relating the disparity homogeneous coordinates of a point before and after the motion.

#### 3.1 Noise on the Data

An important feature of the disparity space is that the noise associated to the data vectors  $(\bar{x}, \bar{y}, d)^T$  under some assumptions can be considered isotropic and homogeneous. The  $\bar{x}, \bar{y}$  disparity coordinates are affected by the noise produced by the discretization effect and without additional information can be assumed equal for all pixels. The noise on  $d$  is associated to the change in the gray level of the pixels in the stereo matching process and could be estimated from this process. We can therefore assume, that the noises associated to  $\bar{x}, \bar{y}$  and  $d$  are independent. If we assume that the variance of  $d$  is of the same magnitude as the variance of the discretization error, the covariance matrix of the noise on each point of our disparity space is  $\Omega = \sigma^2 \mathbf{I}_{3 \times 3}$ . In our case, apart from the above measurement errors, we also assume that in our scene there are points in motion. All the correspondences associated with these moving points are therefore potentially erroneous. In order to select point correspondences which are unaffected by the moving points, we use the RANSAC algorithm to select the subset of point correspondences that are free of this contamination.

### 3.2 Rigid Motion Estimation

Let  $(\tau_i, \tau'_i)$  be a set of point correspondences. The problem of estimating the rigid motion parameters  $(\mathbf{R}, \mathbf{T})$  from the set of points  $(\tau_i, \tau'_i)$  amounts to minimizing the error

$$E^2 = \sum_i d(\tau'_i, \Gamma \tau_i)^2, \quad d(\tau'_i, \Gamma \tau_i)^2 = (\tau'_i - \tau'^{\Gamma}_i)^T \Omega^{-1} (\tau'_i - \tau'^{\Gamma}_i) \quad (7)$$

where  $\tau'^{\Gamma}_i = (\tau'_{i1}/\tau'_{i4} \quad \tau'_{i2}/\tau'_{i4} \quad \tau'_{i3}/\tau'_{i4})$  is the estimated Euclidean coordinate vector for  $\tau'_i$  from (6), and  $\Omega$  is the covariance matrix of the disparity vectors. Here we assume an i.i.d noise model. Equation (6) shows that this error function is not linear in the parameters for  $(\mathbf{R}, \mathbf{T})$ , so a non-linear method has been used to estimate the vector of six unknowns by parameterizing the rigid motion. Here we are interested in the case of small rotations (< 5 degree), so the rotation matrix can be expressed as  $\mathbf{R} = \mathbf{I} + [\omega]_x$ , where  $\mathbf{I}$  is the identity matrix and  $[\omega]_x$  represents the skew-symmetric matrix associated to the vector  $\omega$ . In order to estimate the solution vector  $(\omega, \mathbf{T})^T$  a quasi-linear iterative algorithm has been used on the normalized image coordinated [3]. An initial solution for the vector  $(\omega, \mathbf{T})^T$  can be calculated from equation (6), solving the linear system that appears by considering the equations associated to Euclidean coordinates of all the points  $\tau$  and  $\tau'$  and assuming all  $\lambda=1$ . In the next iteration we recalculate the value of  $\lambda$  from the above solution and again solve equation (6) for a new solution. We iterate until convergence of the vector  $(\omega, \mathbf{T})^T$ . In our experience, three or four iterations are enough.

Nevertheless, the presence of outliers in the correspondences between the disparity maps degrades the estimation considerably. In order to circumvent this problem a RANSAC based algorithm is proposed in Table 1. This algorithm makes a robust iterative linear estimation as a first approach, but because of the noise in the disparity estimation, a non-linear optimization step from the pixel color values is necessary.

## 4 Disparity Map Estimation

In this paper two different dense disparity maps are used. Firstly, we estimate the disparity map for each stereo image, and from this we estimate a region of interest by applying a binary thresholding operator on it. Secondly, we estimate the dense motion vector map associated to every two consecutive left and right images, respectively. In this case we assume that the region of interest is the region of moving pixels nearest the camera.

**Table 1.**

```

Iterative robust algorithmI. To estimate and normalize the set of
disparity vectors
II. Repeat N iterations
    To choose n>=2 disparity vectors randomly
    i. For each vector calculate  $\lambda_i$ ,  $A_i$  and  $b_{iii}$ . Solve  $\lambda A = b$  for
    X
    iii. Count the number of inliers.III. To take the solution
with higher number of inliers as the best linear solution.
IV. To minimize the pixel color differences between images by
applying the Levenberg-Mardquart algorithm from the linear
solution.

```

Figure 1 shows how we estimate our region of interest on each stereo image. In short, we segment the subset of moving points of the scene to a distance of the camera, which is less than a fixed threshold. In our case, the planar motion is calculated in pixel units. In order to remove isolated small regions we apply a size filter. All the pictures shown correspond to the left image of the stereo pair.

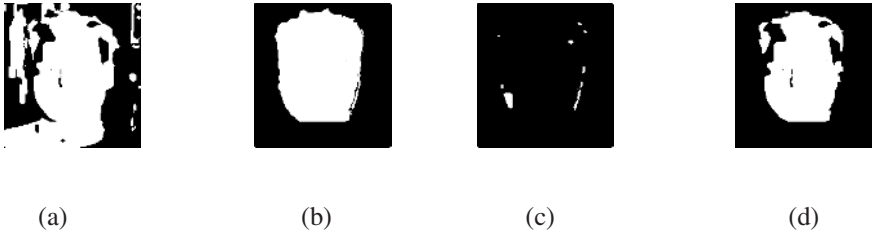


**Fig. 1.** This example corresponds to rotation left-right of the head. Picture (a) represents the estimated stereo disparity map, picture (b) represents the x-motion dense map, picture (c) represents the y-motion dense map, and picture (d) represents the result of the union of picture (b) and picture (c) intersection with picture (a).

Dense disparity maps from two images is a very active field of research [10]. Very recently, new energy minimization algorithms based on cut graphs was proposed [2][7]. These algorithms achieved a very good compromise between temporal efficiency and accuracy of the estimation [7]. Since the implementation of these algorithms only depends on a free parameter,  $\lambda > 0$ , associated to the scale of the estimation [10], very different estimations can be achieved by varying the  $\lambda$  value. Low values of  $\lambda$  provide us with more accurate estimations but a larger number of points will be undefined. A scale combination scheme therefore provides us with a better estimation. In our case, four different scales ( $\lambda = 3, 5, 10, 30$ ) have been considered in order to estimate the disparity maps. The combination scheme defined the disparity value on each pixel as the value of the lowest scale in which the disparity is defined. For motion estimation only the lowest scale has been used, since the other

scales do not contribute much information. In order to obtain as accurate a segmentation as possible, there has been some loss in computational efficiency.

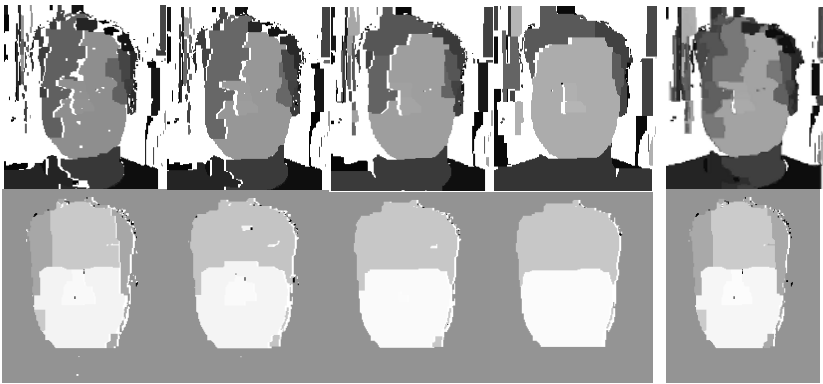


**Fig. 2.** The first four columns of each row show the stereo disparity map from a stereo image, and the x-motion estimation from two consecutive stereo images, respectively, for different  $\lambda$  values. The last column shows the resulting estimation from combining the different scales. All these images correspond to the left image of the stereo pair.

The first row of Figure 2 shows the stereo disparity map estimation from a stereo image for different values of  $\lambda$  joined to the final estimation obtained by combining the different scales. The second row shows the x-motion map estimation from two consecutive stereo images. It is possible to appreciate how the use of multiple scales does not greatly improve the first scale estimation in the case of motion estimation. However, the combination of different scales proves to be very useful when the stereo disparity map is estimated.

## 5 Experimental Results

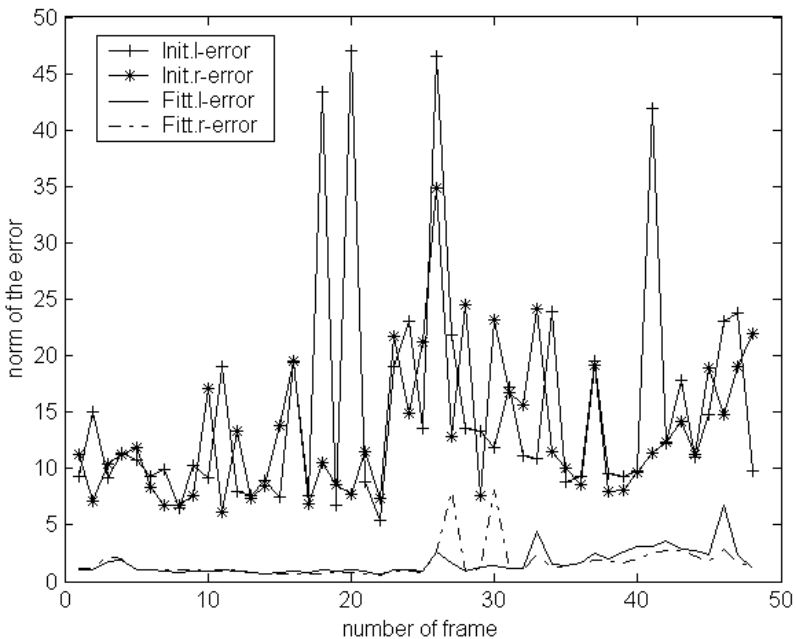
Experiments to estimate 3D rigid facial motion have been carried out from different stereo image sequences captured by a Pointgrey stereo camera (Bumblebee) watching an actor moving his face freely. A fixed window inside the captured images fixed the sub-images of interest. Our algorithm was applied to the image sequence defined by the sub-images. The proposed algorithm was applied on every two consecutive stereo images in the sequence. In order to assess the goodness of the estimation process we synthesized a new sequence of images by interpolating from the estimated motions and the original sequence.

Figure 3 shows six sampled images to a distance of ten samples, each, of a stereo sequence of our examples. It can be seen how the strength and unpredictability of local facial motions makes it difficult to use interest points in the estimation process. Figure 4 shows how accurate the estimated motion for a particular sequence is. We

compare the norm of the difference between two consecutive images, with the norm of the residual calculated by the difference between an original image and its corresponding synthetic. The large decrease of the norm of the difference image from the first case to the second case, shows that the estimated motion is right and precise enough. We should point out that it is difficult to visualize the accuracy of the parameter estimation from this type of graph, but we prefer this type because it is much more difficult to appreciate small residual motions by comparing eye static pictures.



**Fig. 3.** These pictures show local motions present in a standard stereo sequence.



**Fig. 4.** This figure shows four graphs each of which is the norm of the gray level difference pixel-by-pixel from two images. The graphs Init.l-error and Init.r-error represent the case in which the images are two original consecutive right images and left images, respectively, of the sequence. The graphs Fitt.l.error and Fitt.r.error represent the case in which the two images are the original and synthesized one, using the proposed algorithm, for the right and left images, respectively.

## 6 Discussion and Conclusions

In this paper a new approach to estimate the 3D rigid motion of a deformable surface is proposed. The algorithm we propose is accurate and fast enough since no more than 3-4 linear iterations plus 2 non-linear iterations are needed for convergence. The use of stereo images allows us to estimate the motion without the need for external information. This result will allow us to use this approach to remove the rigid motion component from the disparity vector to estimate local deformations. Of course, in this latter case and for large image sequences, the accumulated error might get very large. In order to avoid this situation, the present accuracy of the estimated motion based on two images must be improved. An alternative in order to improve estimation would be the joint use of all images in a bundle algorithm, but this approach is inapplicable in time efficiency demanding applications

**Acknowledgments.** This work, has been financed by Grant IT-2001-3316 from the Spanish Ministry of Science and Technology.

## References

1. Basile, B., and Blake, A.: Separability of pose and expression in facial tracking and animation. In Proc. Int. Conf. Computer Vision. 1998.
2. Boykov,Y.,Veksler,O.,and Zabih,R.,: Fast approximate energy minimization via grpah cuts, IEEE Trans. PAMI vol-23,11,1222–1239,2001.
3. Demirdjian, D., and Darell, T.: Motion estimation from disparity images, In Proc. ICCV01, Vancouver Canada,,2001, vol-II, 628–635.
4. Devernay, F. and Faugeras, O.: From projective to Euclidean reconstruction. In Proceedings Computer Vision and Pattern Recognition,264–269,1996.
5. Fua, P.: Regularized bundle-adjustment to models heads from image sequences without calibration data, International Journal of Computer Vision, 38(2), 2000.
6. Hartley, R. and Zisserman, A.,: Multiple View geometry in computer vision. CUP, 2002
7. Kolmogorov,V., and Zabih, R.,: Visual correspondences with occlusions using graph cuts, In ECCV'02, Lecture Notes in Computer Science 2352, 82–96,2002
8. Lanitis, A., Taylor, C.J., Cootes, T.F. and Ahmed, T.: Automatic interpretation of human faces and hand gestures using flexible models. In International Workshop on Automatic Face-and-Gesture Recognition, 1995.
9. Pollefeys, M., Van Gool, L., Zisserman, A., and Fitzgibbon, A: 3D Structure from images – SMILE 2000, Lecture Notes in Computer Science 2018, Springer, 2000.
10. Scharstein,D., and Szeliski,R.,: A Taxonomy and evaluation of dense two-frame stereo correspondence algorithms, IJCV, 47(1):7–42, 2002..
11. Tarel, J.P.: Global 3D Planar Reconstruction with Uncalibrated Cameras, A Rectified Stereo Geometry, Machine Graphics & Vision Journal, vol-6, 4, 1997, 393–418.
12. Valente.S. and Dugelay, J.L.: A visual analysis/synthesis feedback loop for accurate face tracking, Signal Processing Image Communications, 16, 2001, 585–608.
13. Zhang,Z., Faugeras,O.: 3D Dynamic Scene Analysis,: A stereo based approach. Springer series in Information Science, 27, Springer-Verlag, 1992.

# Robust Techniques in Least Squares-Based Motion Estimation Problems\*

Raúl Montoliu and Filiberto Pla

Dept. Lenguajes y Sistemas Informáticos, Jaume I University  
Campus Riu Sec s/n 12071 Castellón, Spain  
 [{montoliu,pla}@uji.es](mailto:{montoliu,pla}@uji.es), <http://www.vision.uji.es>

**Abstract.** In the literature of computer vision and image processing, motion estimation and image registration problems are usually formulated as parametric fitting problems. Least Squares techniques have been extensively used to solve them, since they provide an elegant, fast and accurate way of finding the best parameters that fit the data. Nevertheless, it is well known that least squares estimators are vulnerable to the presence of outliers. Robust techniques have been developed in order to cope with the presence of them in the data set. In this paper some of the most popular robust techniques for motion estimation problems are reviewed and compared. Experiments with synthetic image sequences have been done in order to test the accuracy and the robustness of the methods studied.

## 1 Introduction

Motion estimation and image registration are important problems in computer vision, and much effort has been paid to solve them. Video compression, video processing, image mosaicing, video surveillance, robot navigation, medical imaging, traffic monitoring, . . . , are only some of the many applications where motion estimation and image registration techniques can be applied. In the literature of computer vision and image processing there are different approaches to motion estimation, nevertheless, there are still challenging open problems to make solutions faster, more robust and accurate, or more general.

The motion estimation problem can be formulated in many different ways. A well known way of solving it, is to approach it as a parametric fitting problem, where the parameters to be fitted are the motion parameters. Least squares provides a well-known way for parameter estimation. In general problems, least squares methods are based on finding the values for the parameters  $\chi$  that best fit a model to a set  $S$  of  $r$  data measurements, i.e. minimizing an objective function  $O$  over a set  $S$  of  $r$  observations vectors,  $S = \{L_1, \dots, L_r\}$ .

$$O = \sum_{L_i \in S} (F_i(\chi, L_i))^2, \quad (1)$$

---

\* This work has been partially supported by project CTIDIB/2002/333 from the *Conselleria de Educació Cultura i Ciència*, Generalitat Valenciana

where  $\chi = (\chi^1, \dots, \chi^p)$  is a vector of  $p$  parameters and  $L_i$  is a vector of  $n$  observations  $L_i = (L_i^1, \dots, L_i^n)$ ,  $i = 1, \dots, r$ .

Least squares estimators assume that the noise corrupting the data is of zero mean and implicitly assume that the entire set of data can be interpreted by only one parameter vector of a given model. It is well known that least squares estimators are vulnerable to the violation of these assumptions. Robust techniques have been developed in order to cope with the presence of outliers in the data set.

One of the oldest robust method used in image analysis and computer vision is the **Hough transform**. The Hough transform is robust to outliers and it can be used to detect multiples models, but it attempts to solve a continuous problem with a discrete method and consequently it can not produce accurate results. In addition, this algorithm needs high computational effort when the number of parameters is elevate, as in the case of using an affine model in motion estimation problems.

Another popular robust technique is the **Least Median of Squares** (LMedS) method, which must yield the smallest value for the median of squares residuals computed for the entire data set. The use of the median ensures that the estimates is very robust to outliers. The main drawback is that LMedS does not have a closed form solution. There are methods that can obtain an approximate solution, but they need high computational effort. Therefore, the computational complexity of LMedS algorithms does not allow them to be used in global motion estimation problems. Nevertheless they can be used to obtain an initial estimate of the parameters of the dominant motion (see [1]).

The **Regression Diagnostics** or **outlier rejection** method [5] tries to iteratively detect possibly wrong data and reject them through analysis of the globally fitted model. This method has three steps: determine an initial fit to the whole set of data, using a ordinary least squares estimator; reject all data whose residuals exceed a threshold; determine a new fit with the remaining data set, and repeat. The success of this method clearly depends on the quality of the initial fit. Many improvements can be added to this method. For instance, estimate the initial fit using robust statistics [3] or add an additional step that collect inliers between the outliers previously rejected [4].

**Robust statistics**, also called **M-Estimators**, is one of the most popular robust techniques. M-Estimators try to reduce the effect of outliers by repacting the square residuals in Equation 1 by a kernel function  $\rho$ , as follows:

$$O = \sum_{L_i \in S} \rho(\epsilon_i), \quad (2)$$

where  $\rho(\epsilon_i)$  is a symmetric, positive-definite function with a unique minimum at zero and  $\epsilon_i = F_i(\chi, L_i)$ . If  $\rho(\epsilon_i) = \epsilon_i^2$ , it is the least square estimator. To analyze the behavior of an estimator, the Hampel influence function  $\psi(\epsilon) = \frac{\partial \rho(\epsilon)}{\partial \epsilon}$  can be used. For least squares estimator  $\psi(\epsilon) = 2\epsilon$ , i.e. the influence of the outliers increases linearity and without bound. For a comprehensible study of the performance of M-Estimators see [8]. In order to solve the robust estimation

problem an iterative reweighted least squares (IRLS) technique is used. The idea of the IRLS is to assign weights  $w_i$  to the residuals at each observation  $L_i$ , where the weights control the influence of the observations in the global estimation. High weights are assigned to “good” data and lower heights to outlying data. The M-Estimator problem is converted into a equivalent weighted least squares problem as follows:

$$\sum_{L_i \in S} \rho(\epsilon_i) = \sum_{L_i \in S} w_i \epsilon_i^2. \quad (3)$$

To minimize we derivate both sides and set them equal to zero, then the following expression is obtained for each  $w_i$ :

$$w_i = \frac{\psi(\epsilon_i)}{\epsilon_i}. \quad (4)$$

**Gradient weighted least squares** (GWLS) [8] techniques can be also used in order to achieve robustness to outliers. GWLS technique divides the original function by its gradient with respect to the observation in order to obtain a constant variance function. The solution of the GWLS problem can be also obtained using a IRLS technique replacing the weight function by:

$$w_i = \frac{1}{\sum_{j=1..n} \left( \frac{\partial F}{\partial (L_j^i)} \right)^2}. \quad (5)$$

In real motion estimation problems many of the previous robust techniques can be combined in order to deal with their problems. For instance, in [3] robust statistics, Hough transform and outlier rejection techniques are combined; in [1] LMedS and outlier rejection techniques are combined.

In this paper, four robust motion estimation algorithms are compared, three of them use a linear least squares estimator in order to estimate the motion parameters, and each of them make use of a different robust technique in order to cope with outliers: M-Estimators, Gradient Weighted and Outlier Rejection. These algorithms are explained in the Section 2.1. The last algorithm uses a non-linear least squares estimator and a gradient weighted-based technique to cope with outliers. It is explained in the Subsection 2.2. Experiments with synthetic image sequences have been done in order to show the performance of the algorithms explained. They are shown in the Section 3.

## 2 Robust Motion Estimation Algorithms

In motion estimation problems, the objective function  $O$  is based on the assumption that the grey level of all the pixels of a region  $R$  remains constant between two consecutive images in a sequence (Brightness Constancy Assumption). Using the BCA the objective function is expressed as follows:

$$O_{BCA} = \sum_{(x_i, y_i) \in R} (I_1(x'_i, y'_i) - I_2(x_i, y_i))^2, \quad (6)$$

where  $I_1(x'_i, y'_i)$  is the grey level of the first image in the sequence at the transformed point  $x'_i, y'_i$ , and  $I_2(x_i, y_i)$  are the grey level of the second image in the sequence at point  $x_i, y_i$ . Here, for each point  $i$  ( $i = 1 \dots r$ , with  $r$  being the number of pixels) the vector of observations  $L_i$  has three elements ( $n = 3$ ),  $L_i = (x_i, y_i, I_2(x_i, y_i))$ . The vector of parameters  $\chi$  depends on the motion model used.

The BCA can not be directly used using an ordinary least squares (OLS) technique since it is not linear. The well-known solution to this problem derives the optic flow equation as the function to be minimized. Using the optic flow equation the objective function is expressed as follows:

$$O_{OF} = \sum_{x_i, y_i \in R} (I_t + u_x I_x + u_y I_y)^2, \quad (7)$$

where  $I_x, I_y$  and  $I_t$  are the spatial and temporal derivates of the sequence.

Nevertheless, it is possible to directly use the BCA using a non-linear least squares-based estimator. Generalized least-squares methods (GLS) [4] are an interesting approach to extend the applicability of least-squares techniques (e.g., to non-linear problems). GLS techniques can be successfully applied in motion estimation related problems [6,7].

## 2.1 OLS-Based Robust Motion Estimation Algorithms

**Motion Estimation.** The solution of the motion estimation problem using an ordinary least squares method uses Taylor series expansion that produces the well known optic flow equation. The solution of  $O_{OF}$  (Equation 7) is now obtained setting to zero the derivates with respect to each of the parameters of the motion model, and solving the resulting system of equations. The solution is obtained by solving the overdetermined linear equation system  $A\chi = d$  using the closed solution  $\chi = (A^t A)^{-1} A^t d$ , where for affine motion  $\chi$  is  $\chi = (a_1, b_1, c_1, a_2, b_2, c_2)$ , and  $A$  ( $r \times 6$ ) and  $d$  ( $r \times 1$ ) are expressed as follows:

$$\begin{aligned} A &= (A_1, A_2, \dots, A_r)^T & d &= (d_1, d_2, \dots, d_r)^T \\ A_i &= (xI_x, yI_x, I_x, xI_y, yI_y, I_y)_{(1 \times 6)} & d_i &= (xI_x + yI_y - I_t)_{(1 \times 1)} \end{aligned} \quad (8)$$

The OLS-based motion estimation is accurate only when the frame-to-frame displacements due to the motion are a fraction of pixel. The accuracy of the estimation can be improved using an iterative alignment procedure and a multi-resolution pyramid, see [2] for details. We will refer to this algorithm as *Hierarchical and Incremental Ordinary Least Squares* (HIOLS). In order to cope with outliers a IRLS-based technique is used. For the sake of clarity, the IRLS process is described in 4 steps:

1. Create a diagonal matrix of weights  $W$  with dimensions  $r \times r$ . Each  $w_i$  measures the influence of the observation  $L_i$  in the global estimation. Set all  $w_i = 1$ .

2. Estimate the motion parameters using the equation:  $\chi = (A^T W A)^{-1} A^T W d$ .
3. Improve the weights using the parameters previously estimated.
4. Repeat until some termination condition is met.

This process is integrated in the HIOLS algorithm improving the weights after each parameter estimation is performed. Three robust techniques are studied: M-Estimators (R-HIOLS algorithm), Gradient Weighted-based (GW-HIOLS) and Outlier Rejection (OR-HIOLS).

*R-HIOLS.* The weights are calculated using the Huber M-Estimator as follows:

$$w_i = \begin{cases} 1.0 & \text{if } |\epsilon_i| \leq k \\ \frac{k}{|\epsilon_i|} & \text{if } |\epsilon_i| > k \end{cases} \quad (9)$$

*GW-HIOLS.* The weights are calculated using the Equation 5.

*OR-HIOLS.* In the outlier rejection technique the outliers do not have influence in the estimation of the parameters. Now, the weight are set to 1 for inliers and to 0 for outliers. The threshold is calculated using a scale measure  $s(\chi)$  based on the median of the residual as follows:

$$s(\chi) = 1.4826 * \text{median}(|\epsilon_i - \text{median}(\epsilon_i)|). \quad (10)$$

The scale estimated is used to reject outliers.  $w_i = 0$  if  $\epsilon_i > s(\chi)$ , i.e. the observation  $i$  is considered as outlier. On the other hand, it is considered as inlier and  $w_i = 1$ . Other similar scale measures can be used ([1], [4]).

## 2.2 Generalized Least Squares

The Generalized Least Squares (GLS) algorithm is based on minimizing an objective function  $O$  (see Equation 1) over a set  $S$  of  $r$  observation vectors,  $S = \{L_1, \dots, L_r\}$ . In general, this equation can be non-linear, but it can be linearized using the Taylor expansion and neglecting higher order terms. This implies that an iterative solution has to be found. At each iteration, the algorithm estimates  $\Delta\chi$ , that improves the parameters as follows:  $\chi_{t+1} = \chi_t + \Delta\chi$ . The increment  $\Delta\chi$  is calculated (see [4]) using the following expressions:

$$\begin{aligned} \Delta\chi &= (A^T (BB^T)^{-1} A)^{-1} A^T (BB^T)^{-1} W & w_i &= -F_i(\chi_t, L_i) \\ B_i &= \left( \frac{\partial F_i(\chi_t, L_i)}{\partial L_i^1}, \dots, \frac{\partial F_i(\chi_t, L_i)}{\partial L_i^n} \right)_{(1 \times n)} & A_i &= \left( \frac{\partial F_i(\chi_t, L_i)}{\partial \chi^1}, \dots, \frac{\partial F_i(\chi_t, L_i)}{\partial \chi^p} \right)_{(1 \times p)} \\ B &= \begin{pmatrix} B_1 & 0 & 0 & 0 \\ 0 & B_2 & 0 & 0 \\ \vdots & \vdots & \ddots & \vdots \\ 0 & 0 & 0 & B_r \end{pmatrix}_{(r \times (r \times n))} & A &= \begin{pmatrix} A_1 \\ A_2 \\ \vdots \\ A_r \end{pmatrix}_{(r \times p)} & W &= \begin{pmatrix} w_1 \\ w_2 \\ \vdots \\ w_r \end{pmatrix}_{(r \times 1)} \end{aligned} \quad (11)$$

In our motion estimation problems the objective function is  $O_{BCA}$  (see Equation 6). Here, for each point  $i$  ( $i = 1 \dots r$ , with  $r$  being the number of pixels) the vector of observation  $L_i = (x_i, y_i, I_2(x_i, y_i))$  has three elements ( $n = 3$ ): column, row and grey level of second image at these coordinates. The affine motion model is used in this work, which is able to cope with translations, scaling, rotation and shear of images and it is defined with a vector of  $\chi = (a_1, b_1, c_1, a_2, b_2, c_2)$ , ( $p = 6$ ). Therefore,  $B_i$ ,  $A_i$  and  $w_i$  are expressed as follows:

$$\begin{aligned} B_i &= (a_1 I_x^1 + a_2 I_y^1 - I_x^2, b_1 I_x^1 + b_2 I_y^1 - I_y^2, -1.0)_{(1 \times 3)} \\ A_i &= (x_i I_x^1, y_i I_x^1, I_x^1, x_i I_y^1, y_i I_y^1, I_y^1)_{(1 \times 6)} \quad w_i = -(I_1(x'_i, y'_i) - I_2(x_i, y_i)) \end{aligned} \quad (12)$$

where  $I_x^1$ ,  $I_y^1$ , are the gradient of first image at the pixel  $(x'_i, y'_i)$  in  $x$  and  $y$  direction, and  $I_x^2$ ,  $I_y^2$ , are the gradient of second image at the pixel  $(x_i, y_i)$  in  $x$  and  $y$  direction.

Similarly to OLS estimator, a multi-resolution pyramid is used in order to cope with large motion, but the iterative nature of the GLS estimator makes unnecessary the use of the alignment process of the HIOLS algorithm. We name this algorithm: *Hierarchical Generalized Least Squares* (HGLS) (see [7] for details). The robustness of the algorithm is obtained through the matrix  $B^T B$  which can be viewed as a matrix of weights. Clearly the HGLS algorithm uses a gradient weighted-based technique in order to cope with outliers.

### 3 Experimental Work

In order to test the accuracy and robustness of the proposed methods two synthetic experiments have been carried out. In the first experiment, 100 transformed images have been created using random values of the affine parameters between the limits:  $a_1, b_2 \in [0.85, 1.15]$ ,  $a_2, b_1 \in [0.0, 0.15]$  and  $c_1, c_2 \in [-10.0, 10.0]$ . The reference image and an example of a transformed image are showed in Figure 1(a, b). Table 1 shows the averages of the differences between the real values and the estimated values for the affine parameters, for each method.

**Table 1.** Error in the estimation of the motion parameters for the first experiment.

Algorithm	$a_1$	$b_1$	$c_1$	$a_2$	$b_2$	$c_2$
R-HIOLS	9.7E-07	1.3E-06	0.0001	9.8E-07	9.1E-07	0.0011
GW-HIOLS	2.8E-06	2.2E-06	0.0003	1.6E-06	2.8E-06	0.0003
OR-HIOLS	0.0002	0.0001	0.0043	4.4E-06	6.0E-06	0.0013
HGLS	2.8E-05	3.9E-05	0.0052	7.9E-05	6.4E-05	0.0103

The second experiment have been done in order to test the robustness of the algorithms. For this purpose, a patch of  $150 \times 150$  pixels is added to the reference image and a patch of  $100 \times 100$  pixels is added to the transformed

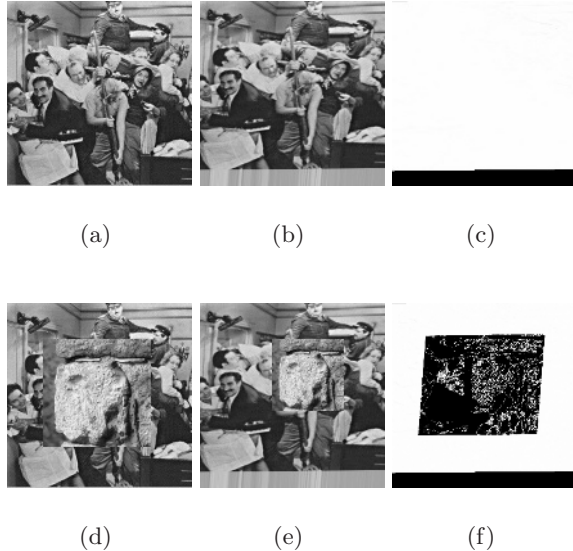


**Fig. 1.** Test image sequences: 1<sup>st</sup> column, reference images, 2<sup>nd</sup> column, transformed ones. 3<sup>rd</sup> column, likelihood images: dark grey values for low likelihood, i.e. outliers

images. The patch undergoes a different motion than of the background. The reference image and an example of a transformed image are showed in Figure 1(d, e). The averages of the differences between the real values of the background and the estimated values are shown in Table 2. All the methods accurately extract the motion of the background, i.e. the pixels belonging to the patch are considered as outliers, and therefore, they have not influenced the estimation of motion of the background.

**Table 2.** Error in the estimation of the motion parameters for the second experiment.

Algorithm	$a_1$	$b_1$	$c_1$	$a_2$	$b_2$	$c_2$
R-HIOLS	1.8E-06	2.5E-06	0.0003	2.8E-06	1.2E-06	0.0003
GW-HIOLS	7.5E-05	4.8E-05	0.0069	1.4E-05	2.9E-05	0.0057
OR-HIOLS	0.0002	0.0001	0.0167	7.8E-05	6.5E-05	0.0079
HGLS	5.6E-05	5.1E-05	0.0065	6.7E-05	7.7E-05	0.0096

The results obtained for the experiments show that all methods obtain accurate estimation of the motion parameters of the dominant motion present in the sequence, even in the case of high number of outliers as in the second experiments. No significant differences among the methods can be found. However, the results show the benefits of using a HGLS technique since it can obtain estimates as accurate as the other methods and it is more general and simpler,

mainly due to the fact that it does not need the alignment process, which can introduce unexpected errors and can increase the processing time, specially in the case of large images.

In order to illustrate how the outliers have been correctly rejected, a likelihood image have been created. For each pixel, the likelihood measure  $L(\chi, p_i) = e^{-0.5 * \frac{\epsilon_i^2}{\sigma^2}}$  (see [3]) of the pixel  $p_i$  belonging to the model estimated with parameters  $\chi$  is calculated. Light grey values are used to represent high values of  $L(\chi, p_i)$  in the likelihood image. On the other hand, dark grey values are used for low values of  $L(\chi, p_i)$ , i.e. for outliers. Figures 1(c,f) show an example of the likelihood image for the samples of the experiments. They have been created using the HGLS algorithm, but similar results would be obtained using the other algorithms. They show how the outliers have been correctly detected and rejected.

## 4 Conclusions

In this paper, four robust least squared-based motion estimation techniques have been explained, implemented and compared. They use M-Estimators, gradient weighted and outliers rejection techniques in order to achieve robustness in the estimation of the motion parameters.

The performance of the four algorithms have been tested using synthetic image sequences with the presence of outliers. The four methods obtain accurate estimations of the dominant motion, even in the case of an elevate number of outliers. No significant differences among the methods were found. However, the results show the benefits of using a HGLS technique since it can yield estimates as accurate as the other methods while it is more general and simpler, mainly due to the fact that it does not need the alignment process which can introduce unexpected errors and can increment the processing time, specially in the case of large images.

## References

1. Alireza Bad-Hadiashar and David Suter. Robust optic flow computation. *International Journal on Computer Vision*, 29(1):59–77, 1998.
2. J.R. Bergen, P.J. Burt, R. Hingorani, and S. Peleg. A three-frame algorithm for estimating two-component image motion. *PAMI*, 14(9):886–896, September 1992.
3. M. Bober and J. V. Kittler. Estimation of complex multimodal motion: An approach based on robust statistics and hough transform. *IVC*, 12(10):661–668, December 1994.
4. G. Danuser and M. Stricker. Parametric model-fitting: From inlier characterization to outlier detection. *PAMI*, 20(3):263–280, March 1998.
5. M. Irani, B. Rousso, and S. Peleg. Computing occluding and transparent motion. *IJVC*, 12(1):5–16, February 1994.
6. R. Montoliu and F. Pla. Multiple parametric motion model estimation and segmentation. In *ICIP01, 2001 International Conference on Image Processing*, volume II, pages 933–936, October 2001.

7. R. Montoliu, V.J. Traver, and F. Pla. Log-polar mapping in generalized least-squares motion estimation. In *Proceedings of 2002 IASTED International Conference on Visualization, Imaging, and Image Processing (VIIP'2002)*, pages 656–661, September 2002.
8. Z. Zhang. Parameter-estimation techniques: A tutorial with application to conic fitting. *Image and Vision Computing*, 15(1):59–76, 1997.

# Inexact Graph Matching for Facial Feature Segmentation and Recognition in Video Sequences: Results on Face Tracking

Ana Beatriz V. Graciano<sup>1</sup>, Roberto M. Cesar Jr.<sup>1</sup>, and Isabelle Bloch<sup>2</sup>

<sup>1</sup> Department of Computer Science, IME, University of São Paulo. São Paulo, Brazil.  
cesar,abvg}@ime.usp.br

<sup>2</sup> Signal and Image Processing Department, CNRS UMR 5141 LTCI, École Nationale Supérieure des Télécommunications. Paris, France.  
Isabelle.Bloch@enst.fr

**Abstract.** This paper presents a method for the segmentation and recognition of facial features and face tracking in digital video sequences based on inexact graph matching. It extends a previous approach proposed for static images to video sequences by incorporating the temporal aspect that is inherent to such sequences. Facial features are represented by *attributed relational graphs*, in which vertices correspond to different feature regions and edges to relations between them. A reference model is used and the search for an optimal homomorphism between its corresponding graph and that of the current frame leads to the recognition.

## 1 Introduction

This paper deals with segmentation and recognition of facial features in digital video sequences through the use of an inexact graph matching technique. The proposed technique constitutes a first approach to the generalization of the methodology developed in [3,4] for facial feature segmentation and recognition in static images.

This extension is motivated by the fact that the subject of face analysis and recognition arises in various computer vision applications involving human activity recognition, such as affective computing, surveillance, teleconferencing and multimedia databases. Since many of these involve video sequence processing, it is also interesting to incorporate the notion of *motion-based recognition* [8] in the methodology.

The main idea is to model the target facial features in a given face through an *attributed relational graph* (ARG), a structure in which vertices represent the facial features and their attributes, while edges represent spatial relations among them. The model image is manually segmented into the facial features of interest and relations are computed to derive a model ARG. In each input image where recognition has to be performed, i.e. each frame, its gradient is extracted and a watershed algorithm is applied to it. Then, an input ARG is obtained from the resulting oversegmented image as for the model. The recognition step relies on an

inexact graph matching procedure that finds a suitable homomorphism between the graph obtained from the model and the one obtained from the image.

The technique of inexact graph matching has been extensively studied in several different domains [2,9,10], such as pattern recognition, computer vision, cybernetics, among others. This approach is justified here due to the difficulty in finding an isomorphism between the model image graph and the input image one: since the latter represents an oversegmented image, it is not possible to expect a bijective correspondence between both structures.

It is worth noting that the term facial feature recognition used hereby means that each facial feature of interest will be located and classified as such. Therefore, it is not related to the recognition performed as a means of matching a face against a known database of faces for instance (no face recognition is performed). Based on [3] where the static methodology is introduced and on [4] where the optimization of the graph matching process is addressed using several methods, the main contribution of the present work is to develop a methodology that can be applied to video sequences, i.e. incorporating the temporal dimension.

This paper is organized as follows. Section 2 explains how a face is modeled as an attributed relational graph. Section 3 explains the inexact graph matching step of the methodology. Section 4 shows how the tracking process is performed throughout the video frames. Section 5 presents some obtained results and conclusions.

## 2 Face Representation

*Attributed Relational Graphs.* In this work, a directed graph will be denoted by  $\tilde{G} = (N, E)$ , where  $N$  represents the set of vertices of  $\tilde{G}$  and  $E \subseteq N \times N$  the set of edges. Two vertices  $a, b$  of  $N$  are said to be adjacent if  $(a, b) \in E$ . When each vertex of  $\tilde{G}$  is adjacent to all others, then  $\tilde{G}$  is said to be complete. Furthermore,  $|N|$  denotes the number of vertices in  $G$ , while  $|E|$  denotes its number of edges.

An *attributed relational graph* (also referred to as ARG) is a graph in which attribute vectors are assigned to vertices and to edges. Formally, we define an ARG as  $G = (N, E, \mu, \nu)$ , where  $N$  represents the set of vertices of  $G$  and  $E \subseteq N \times N$  the set of edges. Furthermore,  $\mu : N \rightarrow L_N$  assigns an attribute vector to each vertex of  $G$ , while  $\nu : E \rightarrow L_E$  assigns an attribute vector to each edge in  $G$ .

The structure of a face can be thought of as being a collection of features (e.g: lips, eyebrows, nostrils, chin) which are somehow related in terms of their relative positions on the face. In the proposed model, facial feature regions are represented by vertices in a graph, while relations between them are represented by edges. The attribute vectors  $\mu$  and  $\nu$  may also be called object and relational attributes, respectively. The former refers to connected regions in the image and the latter to the spatial arrangement of the regions.

*Attributes.* The object and relational attributes convey the knowledge about faces to the ARG structure. The attributes which have been considered in this

work are the same as in [3]. Let us consider an ARG  $G = (N, E, \mu, \nu)$  and any two vertices  $a, b$  in  $N$ .

**The object attribute**  $\mu(a)$  is defined as:

$$\mu(a) = (g(a), w(a), l(a)). \quad (1)$$

The term  $g(a)$  corresponds to the average gray-level of the image region associated to vertex  $a$ , whereas  $w(a)$  is a coefficient obtained from the application of a Morlet wavelet. Both  $g(a)$  and  $w(a)$  are normalized between 0 and 1 with respect to the maximum possible grey-level. Finally,  $l(a)$  is a region label.

**The relational attribute**  $\nu(a, b)$ , for  $a, b$  in  $E$ , is defined as:

$$\nu(a, b) = (\vec{v}, \text{sym}(a, b)). \quad (2)$$

The first attribute is the vector  $\vec{v} = (p_b - p_a)/2d_{max}$ , where  $d_{max}$  is the maximum distance between any two points of the input graph, while  $p_a$  and  $p_b$  denote the centroids of the image regions to which vertices  $a$  and  $b$  correspond. The term  $\text{sym}(a, b)$  denotes a reflectional symmetry calculated as described in [1].

*The Face Model.* A face model image is used as a reference to recognize facial features of interest. This image can be for instance the first frame of a given video sequence. It is manually segmented into facial feature regions of interest and the landmark of each region is calculated. Then, the corresponding ARG is derived.

The model graph should contain vertices associated to each target facial feature region (e.g. lips, iris, eyebrows, skin). However, if a single feature presents considerable variability within its domain, it might need to be subdivided into smaller sub-regions, so that the averages considered when calculating both vertex and edge attributes can be more representative.

### 3 The Facial Feature Recognition Process

*Graph Homomorphism.* Consider two ARGs  $G_1 = (N_1, E_1, \mu_1, \nu_1)$  derived from the image and  $G_2 = (N_2, E_2, \mu_2, \nu_2)$  derived from the model. They will be called *input* and *model* graphs respectively. Also, subscripts will be used to refer to vertices and edges in each graph, e.g.  $a_1 \in N_1$  is a vertex in  $G_1$ ,  $(a_2, b_2) \in E_2$  is an edge in  $G_2$ . It is also important to notice that, since  $G_1$  results from an oversegmented image,  $|N_1|$  is much greater than  $|N_2|$  in general.

An *association graph*  $\tilde{G}_A$  between  $G_1$  and  $G_2$  is defined as the complete graph  $\tilde{G}_A = (N_A, E_A)$ , where  $N_A = N_1 \times N_2$  and  $E_A = E_1 \times E_2$ .

A graph homomorphism  $h$  between  $G_1$  and  $G_2$  is a mapping  $h: N_1 \rightarrow N_2$  such that  $\forall a_1 \in N_1, \forall b_1 \in N_1, (a_1, b_1) \in E_1 \Rightarrow (h(a_1), h(b_1)) \in E_2$ . This definition assumes that all vertices in  $G_1$  should be mapped to  $G_2$ .

Finding a homomorphism between  $G_1$  and  $G_2$  is essential to the face feature recognition process. Since  $|N_1|$  is greater than  $|N_2|$ , a suitable homomorphism between the input and model graphs should map distinct vertices of  $G_1$  into a

single vertex of  $G_2$ , which corresponds to merging coherent sub-regions in the input oversegmented image.

As proposed in [3], a solution for finding a homomorphism between  $G_1$  and  $G_2$  may be defined as a complete sub-graph  $\tilde{G}_S = (N_S, E_S)$  from the association graph  $\tilde{G}_A$ , in which  $N_S = \{(a_1, a_2), a_1 \in N_1, a_2 \in N_2\}$  such that  $\forall a_1 \in N_1, \exists a_2 \in N_2, (a_1, a_2) \in E_S$ , and  $\forall (a_1, a_2) \in E_S, \forall (a_1', a_2') \in E_S, a_1 = a_1' \Rightarrow a_2 = a_2'$ , assuring that each vertex from the input graph corresponds to exactly one vertex of the model graph and  $|N_S| = |N_1|$ . It should be clear that such a solution only considers the structures of  $G_1$  and  $G_2$ , and that it gives rise to many possible homomorphisms between both graphs.

*Objective Function.* In order to evaluate the quality and suitability of a given homomorphism between the input and model graphs, an objective function must be defined. It should consider not only the structure of the graphs, but also the attributes of the facial features and their relations. In this paper, the assessment of a certain homomorphism is accomplished through the minimization of the following function:

$$f(\tilde{G}_S) = \frac{\alpha}{|N_S|} \sum_{(a_1, a_2) \in N_S} c_N(a_1, a_2) + \frac{(1 - \alpha)}{|E_S|} \sum_{e \in E_S} c_E(e) \quad (3)$$

where  $c_N$  and  $c_E$  are dissimilarity measures given as follows:

$$c_N(a_1, a_2) = \begin{cases} \gamma_N |g_1(a_1) - g_2(a_2)| + (1 - \gamma_N) |w_1(a_1) - w_2(a_2)|, \\ \text{if } l(a_1) = l(a_2) \\ \infty, \text{ otherwise} \end{cases} \quad (4)$$

$$c_E(e) = \gamma_E \phi_v + (1 - \gamma_E) \phi_{sym} \quad (5)$$

and  $\phi_v$  and  $\phi_{sym}$  are defined as

$$\phi_v = \gamma_v \|\vec{v}_1\| - \|\vec{v}_2\| + (1 - \gamma_v) \frac{|\cos \theta - 1|}{2} \quad (6)$$

$$\phi_{sym} = |sym(a_1, b_1) - sym(a_2, b_2)| .$$

In this case,  $\cos \theta = \frac{\vec{v}_1 \cdot \vec{v}_2}{\|\vec{v}_1\| \|\vec{v}_2\|}$  and the values  $\gamma_N$ ,  $\gamma_E$  and  $\gamma_v$  are weighting parameters.

*Performing Inexact Graph Matching.* Many approaches have been explored for optimizing inexact graph matching for pattern recognition purposes, such as those mentioned in [3], [7] and [10].

In this work, the matching is achieved through the use of a tree search algorithm. Other possible alternatives include genetic and estimation of distribution algorithms [3].

In general terms, the tree-search optimization algorithm builds a search-tree where each vertex represents a pair of vertices  $(k, l)$ ,  $k \in N_1$  and  $l \in N_2$ . The root vertex is labelled  $(0, 0)$  and it is expanded in  $|N_2|$  sons labelled  $(1, l)$ ,  $l = 1 \dots |N_2|$ . At each step  $k$  of the algorithm, the son which minimizes the objective function, say  $(k, l_{min})$  is chosen and therefore expanded in  $|N_2|$  sons  $(k+1, i)$ ,  $i = 1 \dots |N_2|$ . The process is repeated until a vertex  $(|N_1|, l)$  is reached, which guarantees that all vertices of  $G_1$  have been assigned to a vertex of  $G_2$ , thus establishing a homomorphism between the input and model graphs.

## 4 The Tracking Process

In this section, we aim at generalizing the previous approach to video sequences. Since digital video is composed of a sequence of images which change over time, it is needed to incorporate in the methodology this temporal aspect and transitions between images, reflecting facial feature changes throughout the video (e.g. a progressive smile or a blink). In this section, we present our first approach towards reflecting such changes in the facial features.

*General Scheme.* The overall sequence of steps performed in order to segment and recognize the facial features of interest in a generic frame of the input video sequence is illustrated in Figure 1.

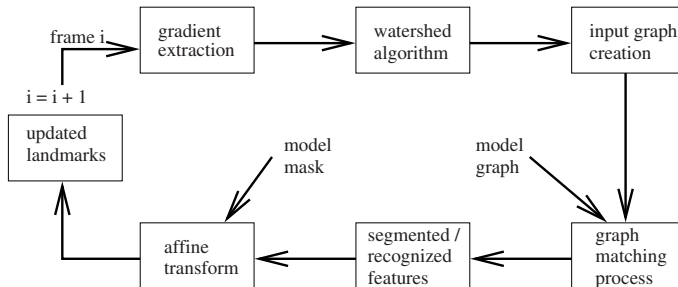


**Fig. 1.** Overview of the tracking process.

Initially, approximative landmarks of the target facial features are located in the first frame for future constraint on the region in which the oversegmentation will be performed. They are obtained through the use of the Gabor Wavelet Network (GWN) [6]. Then the previous algorithm for static images is applied in the regions of the face around the landmarks.

One of the main contributions in the methodology is related to updating the landmarks which will be used in the subsequent frame in the video sequence, thus avoiding the need for a global face tracking procedure (i.e. GWN in our specific case) in addition to the graph matching. If the same landmarks were applied to all frames, the matching and recognition results would possibly not be satisfactory,

since the features in each frame usually have considerable differences in terms of their positions.

*Landmark Updating.* The GWN technique could be applied to each frame of the sequence in order to update the landmarks. However, it would be interesting to make use of the information obtained directly from the graph methodology and the model image. To accomplish this, an *affine transformation* is applied in order to map the model image to the frame under consideration based on the recognized facial features, allowing the landmark updating.

For the first frame, the model landmarks, which have been obtained as explained in Sect. 2, are also used as landmarks for that frame. For the subsequent frames, once the recognition procedure is finished, the centroids of the facial features of interest are calculated. Also, the centroids of the pre-defined regions in the model are calculated. Then, the affine transformation that best maps the model set of centroids to that of the considered frame is estimated and applied through the following formula [5]:

$$\vec{q} = \alpha(A\vec{s} + \vec{b}) \quad (7)$$

where  $A$  corresponds to a  $2 \times 2$  non-singular matrix representing the sought transformation,  $\alpha$  is any scalar value, and  $\vec{q}$ ,  $\vec{s}$  are the centroid-coordinate vectors for the frame and model respectively.

This affine transformation allows us not only to update the input face landmarks to be applied to the following frame in the process, but also to project the model image onto the segmented and recognized target frame, conveying a visual assessment of the matching process.

*Possible Extensions.* Although this change in the methodology already makes it more robust for the application in video sequences, our ongoing research aims at making better use of the possibly redundant information present in distinct frames.

One possible approach is to insert *temporal edges* to the set  $E$  of an ARG  $G$ . These edges would represent the transitions and relations among vertices of consecutive frames in the sequence. Through this, it would be possible to recalculate both vertex and edge attributes and a model image could be no longer needed for the recognition. Also, features which were not present in the first frame could be added to the recognition process on-the-fly.

Furthermore, the results obtained in the graph matching procedure for, say, frame  $i$  could be reused as the initial solution for the matching step in frame  $i+1$ , thus reducing the tree expansion and taking into account the smooth changes presented in frame transitions. This generalization belongs to our ongoing research.

## 5 Results and Conclusion

In this section we show some of the first results obtained from the application of the new steps introduced in the previous section. For the tests, different video

sequences were considered, such as sequences of male and female faces with static or changing background. All sequences presented considerable changes in the face (e.g. smiles, head movement, blinking) throughout time.

Figure 2 depicts the results obtained for the frame-to-frame projection of the model-mask onto the corresponding target frames. The video sequence was composed of 96 color frames of size  $512 \times 512$  which have been converted to grey-level images for the purpose of the algorithm. As it can be seen, the model mask is successfully matched up to the face, thus allowing it to be tracked along the video sequence. The facial features defined by the mask are approximately matched up to their correspondents in the image, though some mismatched regions (mouth in the last image) may be noted due to the global nature of the affine transform and to differences in the facial expressions among the frames.

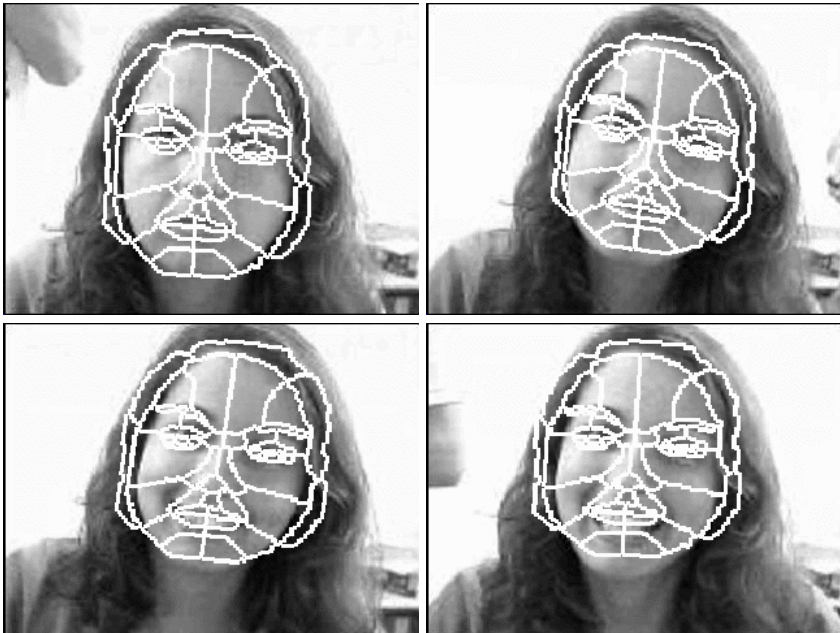


**Fig. 2.** Model masks superimposed on successive target frames using the recognized facial features.

In terms of the results obtained by the advances proposed in this paper, i.e., the landmark updating and its assessment through the projection of the model mask onto the input face, it can be seen that the mask projection follows the head movements in a plausible manner. Also, most facial features which may be of interest are correctly tracked (e.g.: eyebrows, nostrils, nose, lips), showing that the recognition process and the landmark updating can be effective and provide encouraging results.

Nevertheless, certain refinements in the technique are still called for, especially when a considerable sudden change is present between frames, or when unknown facial features, i.e. those which were not present in the model, appear throughout the sequence. In such cases, the unknown facial features will be necessarily mapped to one of the classified facial features, which might lead to results such as the one seen in the frames of Figure 2 where a smile occurs.

Thus, in this paper we have proposed a first approach towards the generalization of the methodology presented in [3]. The first results have shown that it is possible to reflect the changes in facial features in each frame that occurs throughout time using appropriate affine transformations. Although the introduced steps have provided encouraging results, the other possibilities mentioned in Sect. 4 are being considered in our ongoing work.

**Acknowledgments.** This work was partially funded by a CAPES/COFECUB grant. A. Graciano is grateful to CNPq (132562/2003-0). R. Cesar is grateful to FAPESP (99/12765-2) and to CNPq (300722/98-2).

## References

- [1] O. Colliot, A.V. Tuzikov, R.M. Cesar Jr., and I. Bloch. Approximate reflectional symmetries of fuzzy objects with an application in model-based object recognition. *Fuzzy Sets and Systems*, 2003. In Press.
- [2] D. Fontaine and N. Ramaux. An approach by graphs for the recognition of temporal scenarios. *IEEE Transactions on Systems, Man, and Cybernetics - Part B: Cybernetics*, 28(3):387–403, June 1998.
- [3] R.M. Cesar Jr., E. Bengoetxea, and I. Bloch. Inexact graph matching using stochastic optimization techniques for facial feature recognition. In *16th International Conference on Pattern Recognition*, volume 2, pages 465–468, August 2002.
- [4] R.M. Cesar Jr. and I. Bloch. First results on facial feature segmentation and recognition using graph homomorphisms. In *Proc. VI Simpósio Ibero-Americano de Reconhecimento de Padrões*, pages 95–99, Florianópolis, Brazil, 2001.
- [5] R.M. Cesar Jr. and L. da F. Costa. *Shape Analysis and Classification – Theory and Practice*. CRC Press, 1 edition, 2001.
- [6] V. Kruger and G. Sommer. Affine real-time face tracking using a wavelet network. In *Proc. of ICVV'99 Workshop Recognition, Analysis, and Tracking of Faces and Gestures in Real-Time Systems*, pages 141–148, Corfu, Greece, 1999.
- [7] A. Perchant and I. Bloch. Fuzzy morphisms between graphs. *Fuzzy Sets and Systems*, 128(2):149–168, 2002.
- [8] M. Shah and R. Jain, editors. *Motion-Based Recognition*. Computational Imaging and Vision. Kluwer Academic Publishers, 1997.
- [9] L.B. Shams, M.J. Brady, and S. Schaal. Graph matching vs mutual information maximization for object detection. *Neural Networks*, 14:345–354, 2001.
- [10] R.C. Wilson and E.R. Hancock. A Bayesian compatibility model for graph matching. *Pattern Recognition Letters*, 17(3):263–276, 1996.

# Crater Marking and Classification Using Computer Vision

Alejandro Flores-Méndez

LIDETEA, Universidad la Salle  
México, D.F. México  
[aflores@ci.ulsa.mx](mailto:aflores@ci.ulsa.mx)

**Abstract.** In the last three years NASA and some other Space Agencies have drawn some interest to date Mars surface, mainly because the relationship between its geological age and the probable presence of water beneath it. One way to do this is by classifying craters on the surface attending to their degree of erosion. The naïve way to solve this problem would let a group of experts analyze the images of the surface and let them mark and classify the craters. Unfortunately, this solution is unfeasible because the number of images is huge in comparison with the human resources any group can afford. Different solutions have been tried [1], [2] over this period of time. This paper offers an autonomous *Computer Vision System* to detect the craters, and classify them.

## 1 Introduction

In the past three years a number of studies under the supervision of NASA and some other Research Institutes and Space Agencies have been done to date the geological age of some celestial bodies. An important number of works over this issue center on Mars surface, mainly because of the relationship between its relative geological age and the probable presence of water beneath the surface.

One way to assign a planet or a moon its relative geological age is by dating craters on it. The first naïve approach one might think to solve this problem would dedicate a group of experts analyze a series of images from Mars surface and let them classify the craters that appear on them. Nevertheless there are not enough human resources available to dedicate a team to do this. In order to solve this problem, a number of different solutions have been studied. One project, under the name of *clickworkers*, proposed by NASA investigators [1] put a group of grayscale images from the NASA database of Viking Orbiter Mission to Mars on the Internet (for a further look see <http://clickworkers.arc.nasa.gov/top>). The project let anyone who was willing to help, after doing a very basic instruction, signal the position (mark) and classify craters within a series of images that are presented to the collaborator, who received the title of *clickworker*. The system presents every image it has, not to one, but to many clickworkers who give their opinion about the position and class the craters have. The system collects these opinions and obtains the consensus of them. Finally it *colors* a map of Mars based on these information. Some of the results obtained from the clickworkers project (CP) were quite similar when compared with the solutions of the

experts. The problem with this project is that it still depends on the human factor. Some projects have tried to automate this labor, being one example the work done by Negrete [2]. On his work, Negrete gave an autonomous system based basically on the Hough Transform to detect and mark craters over an image, and after that, the system used ontologies to classify the craters that were detected. Sadly, this investigation was not able to detect more than 60% of the craters. The purpose of this paper is to offer yet another computer vision system [3] for the marking and classification of the craters using a number of different image processing techniques [4] and some others, like Fuzzy Logic [5]. A scheme of the proposed system is presented in the following figure.

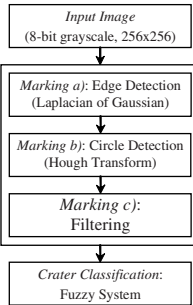


**Fig. 1.** Scheme of the system proposed for crater marking and classification

A detailed explanation of the system and the results obtained from it are presented in the following sections.

## 2 Computer Vision System

The system proposed here is very simple, and it was intended to be this way, since the algorithm should be as fast as possible so it can manipulate a large volume of data. That is why a number of processes like equalization of the image, mathematical morphology and clustering among others are omitted at this point. In spite of the system's simplicity, the results obtained were in general satisfactory. Moreover, some techniques were ruled out because the system was not truly enhanced when these were added. For example, equalization was omitted because the images captured by the satellite are almost equalized. Nevertheless, when this is not the case, the classification system absorbed most of these differences. In the following subsections a deeper description of the marking and classification subsystems will be presented.

### 2.1 Crater Marking Subsystem

Marking of the crater is a three step process (see Fig. 1). First, we must obtain the borders of the image. A number of different techniques are available for this matter. An analysis of the nature of the images suggested that the Laplacian of the Gaussian Method (LOG) is a good choice in this case. Some other methods were tried, among

them, Sobel (which is suggested by Negrete in his work [2]), but our experiments favored LOG in most of the cases. The better results for LOG were attained when using a threshold of 0.006 and a neighborhood of 2. These borders were feed as an input to the Hough Transform [6] to detect the circles (craters) on the image.

**Hough Transform.** As already has been stated, the Hough Transform (HT) is used to obtain the probable locations of the craters. The general case of the HT was developed to detect lines, but the generalization of the Transform to detect some other geometric bodies is straightforward in many cases. An example of the pseudocode<sup>1</sup> for the HT that detects the circles within an image, given the set of coordinates of the borders, a radio  $r$ , and the number of samples to be taken over the perimeter of a circle would be as follows:

```
HT_circles (borders, r, sample_rate)
initialize (acum)
for i ← 1 to length [borders]
    (x, y) ← borders [i]
    angle = 0;
    repeat
        angle = angle + sample_rate
        a ← round (x - r * cos (angle))
        b ← round (y - r * sin (angle))
        acum [a, b] = acum [a, b] + 1
    until angle > 2π
return acum
```

Nevertheless, a number of problems arise when the HT is used for detection of a geometrical shape such as incomplete borders or deformed shapes. For the project, both things must be accounted for. One way to deal with the geometric body deformations is by using a variation of the HT called sliding window (HTSW). The HTSW uses a neighborhood around the point being analyzed, which enhances the local maxima stored in the accumulator. For the experiments an  $n$  by  $n$  neighborhood was selected with the evaluated point as its center. The value of  $n$  was obtained as a function of the radio ( $r$ ) through the following expression:

$$n = \begin{cases} 2 & 15 \leq r \\ 1 & r < 15 \end{cases}. \quad (1)$$

To solve the problem of incomplete borders, the system takes into account a threshold value  $0 < \theta \leq 1$  which measures the percentage needed to detect a crater. The best results were obtained for  $\theta = 0.3$ . The marking process using a biased HTSW system is exemplified in the following figure.

---

<sup>1</sup> The pseudocode follows the conventions proposed on Cormen's book [7]

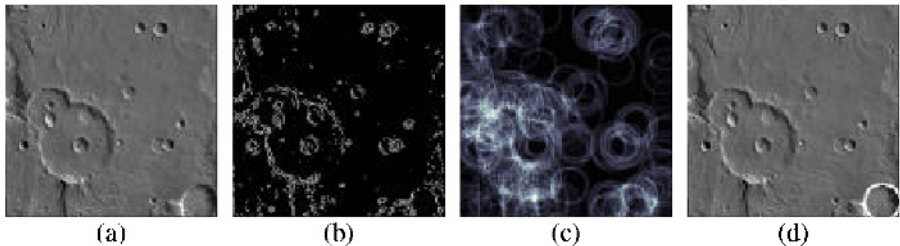


**Fig. 2.** The marking process takes an image of Mars surface (a) obtains its borders with the LOG (b) and then uses this borders for the HTSW (c) to detect craters of a particular radio (d)

**Filtering.** Once a crater has been marked, the borders associated with this crater are deleted (since two different craters will have their own rims). By eliminating these borders, not only the process is accelerated, but this also reduces the number of false detections. After deletion is done there are still two problems that the system handles. The first problem was that some craters were detected because the region selected was not a crater, but the borders from a group of different geological accidents. To avoid this, the system sums the borders in that area. If the number of borders not used in the detection of the crater is greater than a threshold, the detected crater is discarded, unless there is clear evidence of the presence of the crater (the accumulator shows that at least 80% of the elements were accounted). An example of how deletion and filtering contributed in the detection process is presented in the following figure.

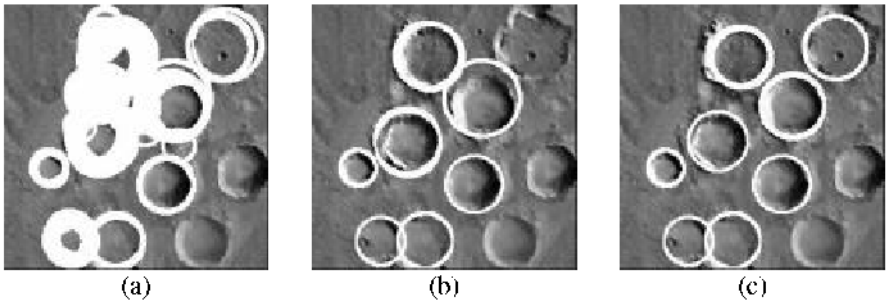


**Fig. 3.** Series of images showing the craters detected with the HTSW (a), detection using deletion of the borders used (b) and detection with deletion and filtering (c)

## 2.2 Crater Classification Subsystem

The crater classification, as stated in the CP proposes that there are three basic categories called *fresh*, *degraded* and *ghost* related with crater aging. Depending on the aging, each crater will have a number of features that can be looked upon. The definition given by CP states that "...a fresh crater displays a sharp rim, distinctive ejecta blanket, and well-preserved interior features (if any). In a degraded crater the surrounding ejecta blanket is gone, interior features are largely or totally obliterated

and the rim is rounded or removed. Finally, the ghost craters are faintly visible through overlying deposits". The next figure shows an example of these classes.

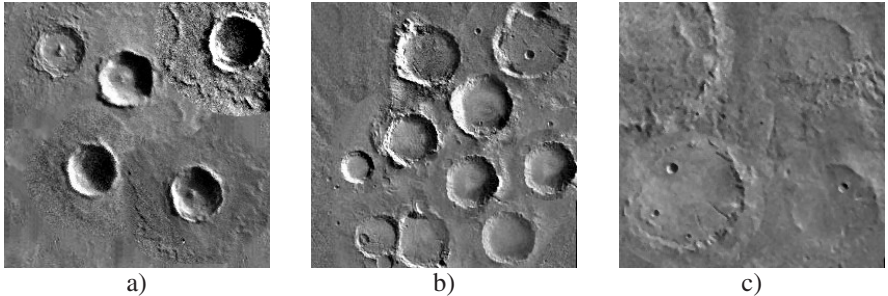


**Fig. 4.** The basic classification proposed by the CP states that there are three categories based on crater aging. The craters could be fresh (a), degraded (b) and ghost (c)

A common problem with automated classification arises when the rules that define a category are ambiguous or there is some level of "spatial vagueness". On these cases a different approach like a fuzzy logic system is needed. Fuzzy systems have been applied for a number of different problems of classification such as medical applications [8], soil classification [9], fish grading [10], etc. For the crater classification process, a number of problems are inherited from the ambiguity and vagueness of the definitions, and because of this, the use of a fuzzy system was considered. The system proposed in fact is a supervised fuzzy system.

**Fuzzy System.** In the preceding lines, the reader learned that crater classification is related with a number of features to be looked upon the image. Nevertheless, for an untrained eye, trying to determine how recent the crater is might be equivalent to simply say how deep the crater is. Luckily this very simple feature proved to be enough for the vast majority of the cases. A simple observation related with this feature (how deep a crater is) is that the number of bright pixels for a fresh crater (Fig. 5(b)) is considerably larger than the same number for a ghost crater (Fig. 5(d)). Another way to say this is that the distribution of the graylevels for a fresh crater tends to be uniform while Normal distribution is better suited for ghost craters.

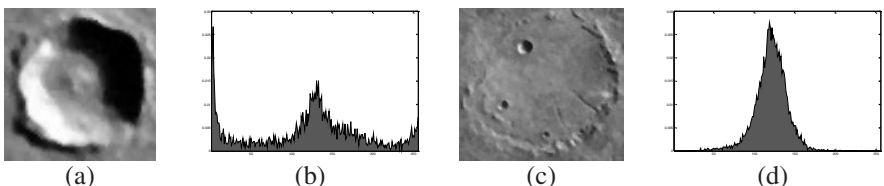


**Fig. 5.** Histograms (b), (d) of a fresh (a) and a phantom crater (c)

The fuzzy system proposed here, will use as inputs the maximum over the first and the second quartiles ( $\max Q_1$ ,  $\max Q_2$ ) of the histogram of the square region containing a crater detected from the marking process. For simplicity, the fuzzy input

variables will be labeled after the values they receive, *i.e.*  $\max Q_1$ ,  $\max Q_2$ . Each of these fuzzy inputs will have three different sets called *small*, *medium* and *large*; which were determined experimentally. As output, a single variable is used. This variable receives the name of *category* and it contains three fuzzy sets (also determined experimentally) called *fresh*, *degraded* and *ghost*. The sets of the input variables are trapezoidal, while the sets for the classes are triangular as can be seen in Fig. 6. The inputs variables are related with the category simply by an AND operator as reflected in the following table.

**Table 1.** AND Relationship between fuzzy input variables  $\max Q_1$  and  $\max Q_2$  and the fuzzy output variable *category* for the classification system

$\max Q_2$	<i>small</i>	<i>medium</i>	<i>large</i>
$\max Q_1$			
<i>small</i>	<i>degraded</i>	<i>ghost</i>	<i>ghost</i>
<i>medium</i>	<i>degraded</i>	<i>degraded</i>	<i>degraded</i>
<i>large</i>	<i>fresh</i>	<i>fresh</i>	<i>degraded</i>

For the defuzzification, the mean of maximum method was selected. The combination of this method together with the type of sets choose for the classes allowed to determine, by using a simple hard limiter nonlinear function, in which category the crater was. As an example, the following figure shows the results of the fuzzy system when it was feed with the pairs (0.0267,0.0124) and (0.0009,0.0276). These pairs represent the input  $(\max Q_1, \max Q_2)$  for the craters in Fig. 5(a) and (c).

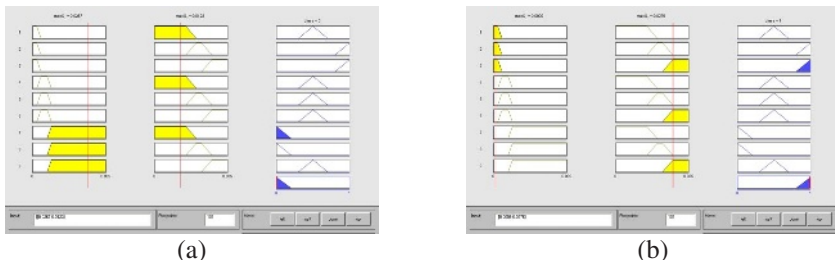


**Fig. 6.** When the system was feed with the inputs for the craters shown in Fig. 5(a) (a) and the ghost crater shown in Fig. 5(c) (b), it correctly classified the craters

The results obtained by this system correctly classified more than 90% of the craters marked.

### 3 Results

To determine the factors used for every part of the system a number of experiments were conducted over a set of 100 grayscale images of 256 x 256 pixels containing little less than 300 craters. The experiments were carried out to obtain first the

parameters related with the marking process. After the best set of parameters was determined from these results the performance of the classifier was obtained.

### 3.1 Experiments for the Marking

For the marking process, a group of 30 images containing approximately 100 craters were used. A number of border techniques were tested. In combination with the border techniques, different approaches were tested as the HT, HTSW, HTSW with border deletion (HTSW/D) and HTSW with deletion and filtering (HTSW/DF). The following table (Table 2) contains the results for some schemes that were studied. The first number of the combination refers to the percentage of craters detected, while the second number refers to the percentage of the false detections. For example, when the HTSW with Deletion and Filtering (HTSW/DF) was selected to detect craters with a threshold  $\theta = 0.3$  using the Sobel Technique with a threshold of 0.06, 53.12% of the craters were detected, but 23.52% of the crater detections were false. In some cases, the number of false detections for a particular combination was above 50%. When this is the case, the data from the experiments is not presented in the table.

**Table 2.** Statistics obtained from some of the different combinations tried for crater marking

Canny 0.175, 0.05	Sobel 0.05	Sobel 0.06	LOG 0.0055	LOG 0.006	LOG 0.0065
HTSW/DF		65.62%		81.25%	66.67%
$\theta = 0.25$		41.83%		43.48%	42.11%
HTSW/DF	47.75%	53.12%	68.75%	71.88%	65.63%
$\theta = 0.3$	46.14%	23.52%	42.42%	22.58%	19.23%
HTSW/DF	37.50%	21.50%	48.48%	46.87%	43.75%
$\theta = 0.35$	38.09%	31.17%	11.76%	22.22%	14.29%
					40.62%
					4.17%

It is important to point out that the output for the HT and HTSW in general detected more than 50% of false detections. From the results presented in the table, it can be said that the best ratio between true and false recognition was obtained for the HTSW/DF when the threshold was set at 30% and the LOG Method was chosen for the borders with a threshold of 0.006.

### 3.2 Results for the Classification

For the classification process we let the best system (HTSW/DF and LOG with proper parameters) mark the craters of 100 images which contain little less than 300 craters. After marking was done 200 images containing craters (no false detection was selected) were manually classified using the CP criteria. The classification subsystem was feed with the images previously selected and its results were compared with the ones manually obtained. The results generated in this way agreed in 91.5% of the cases.

## 4 Conclusions and Further Work

The time used by the system to mark and classify the craters (less than 5 seconds per image in average using a Pentium 4, 2 GHz, 512 MB RAM computer) makes it possible to think that this process can be used in practice. Nevertheless, if the process is to be useful, the marking subsystem needs to be further developed to obtain at least an 85% of recognition while the false recognition is kept below 7%. There are some signals from some research lines being studied at this moment that both percentages can be achieved, but further work will be needed. Sadly, recognition close to 100% has already been discarded, because the recognition of some “hard to identify” craters (usually phantom craters) implies almost certainly an increment in the number of false recognitions. For the fine tuning of the detection, is probable that Mathematical Morphology will be helpful. Still, more experiments in this sense are to be accomplished.

On the other hand, the classification subsystem proved not only to be a good classifier but also it was very robust because it was capable of correctly classify craters even when the area contained only partially the crater, the area was bigger than the one from the crater or the area contained some other elements besides the crater. The success of this part of the system, in my opinion, resides mainly on the selection of the histogram based feature, and because of this, some other techniques different from fuzzy logic might be used with this feature as its input to classify the craters. Still, I do not believe that great improvements can be done in this line since the classification remain being a subjective process, and that's why some results in this area might vary but not meaningfully.

## References

1. Kanefsky, B., Barlow, N. G., Gulick, V. C.: “Can distributed volunteers accomplish massive data analysis task?”, *Lunar and Planetary Science XXXII*, paper 1272 (2001).
2. Negrete, V.: Crater Image Classification using Classical Methods and Ontologies, M. Sc. Thesis, University of Houston (2002).
3. Parker, J. R.: *Algorithms for Image Processing and Computer Vision*, John Wiley & Sons (1996).
4. Gonzalez, R. C., Woods, R. E.: *Digital Image Processing*, Addison-Wesley Pub Co., 2nd edition (2002).
5. Zadeh, L A.: A theory of approximate reasoning. *Machine Intelligence 9*, ed. J. Hayes. D. Michie, L. I. Mikulich, 149–194. New York, Halstead Press. (1979).
6. Sonka M., Hlavac V., Boyle R.: *Image Processing, Analysis and Machine Vision*, Chapman and Hall Computing, London, (1993).
7. Cormen T. H. (ed.): *Introduction to Algorithms*, 2nd. Edition, MIT Press, (2001).
8. Belacel, N., Boulassel, M. R.: Multicriteria Fuzzy Classification Procedure PROCFTN: Methodology and Medical Application, *Fuzzy Sets and Systems* (2003) in press.
9. McBratney, A. B., deGruijter, J. J.: A continuum approach to soil classification by modified fuzzy k-means with extragrades. *Journal of Soil Science* 43: 159–75, (1992).
10. Hu, B. G., Gosine, R. G., Cao, L. X., de Silva, C. W.: *IEEE Trans. on Fuzzy Systems*, Vol.6, No.1, February (1998).

# Using Optical Flow for Tracking

M. Lucena<sup>1</sup>, J.M. Fuertes<sup>1</sup>, and N. Perez de la Blanca<sup>2</sup>

<sup>1</sup> Departamento de Informatica, Escuela Politecnica Superior, Universidad de Jaen,  
Avda de Madrid 35, 23071 Jaen, Spain  
[{mlucena,jmf}@ujaen.es](mailto:{mlucena,jmf}@ujaen.es)

<sup>2</sup> Departamento de Ciencias de la Computacion e Inteligencia Artificial,  
ETSII. Universidad de Granada  
C/ Periodista Daniel Saucedo Aranda s/n,  
18071 Granada, Spain  
[nicolas@ugr.es](mailto:nicolas@ugr.es)

**Abstract.** We present two observation models based on optical flow information to track objects using particle filter algorithms. Although, in principle, the optical flow information enables us to know the displacement of the objects present in a scene, it cannot be used directly to displace a model since flow estimation techniques lack the necessary precision. We will define instead two observation models for using into probabilistic tracking algorithms: the first uses an optical flow estimation computed previously, and the second is based directly on correlation techniques over two consecutive frames.

## 1 Probabilistic Tracking

The probabilistic models applied to tracking [1,2,3] enable us to estimate the *a posteriori* probability distribution of the set of valid configurations for the object to be tracked, represented by a vector  $\mathbf{X}$ , from the set of measurements  $\mathbf{Z}$  taken from the images of the sequence,  $p(\mathbf{X}|\mathbf{Z})$ . The estimation in the previous instant is combined with a dynamical model giving rise to the *a priori* distribution in the current instant,  $p(\mathbf{X})$ . The relation between these distributions is given by Bayes' Theorem:

$$p(\mathbf{X}|\mathbf{Z}) \propto p(\mathbf{X}) \cdot p(\mathbf{Z}|\mathbf{X})$$

The distribution  $p(\mathbf{Z}|\mathbf{X})$ , known as the *observation model*, represents the probability of the measurements  $\mathbf{Z}$  appearing in the images, assuming that a specific configuration of the model in the current instant is known.

In this paper, two optical flow based observation models are defined. The first one uses as evidence an existing estimation of the optical flow of the sequence, and the second one is based on correlation techniques.

## 2 Optical Flow Estimation

The most well-known hypothesis for calculating the optical flow [4] assumes that the intensity structures found in the image, on a local level, remain approximately constant over time, at least during small intervals of time.

There is no algorithm for estimating the optical flow field which is clearly superior to the others. Each may have small advantages over the others in particular situations, but in general it may be said that from a practical point of view all are equivalent [5,6]. In this paper, we have preferred to use the algorithm in [7], for the following reasons:

- It does not impose restrictions on the sequence to be analyzed.
- It provides a dense estimation of the optical flow.
- It is designed to preserve discontinuities in the flow, which is necessary for the observation model proposed in this section to behave appropriately.

## 3 The Dynamical Model

Other authors have successfully used characteristics such as the gradient [8] or intensity distributions [3] for tracking tasks. The dynamical model of the object will provide an *a priori* distribution on all the possible configurations in the instant  $t_k$ ,  $p(\mathbf{X}(t_k))$ , from the estimated distributions in the previous instants of time. In this paper, a second-order dynamical model has been used in which the two previous states of the object model are considered, and this is equivalent to taking a first-order dynamical model with a state vector for the instant  $t_k$  of the form [8]

$$\mathcal{X}_{t_k} = [\mathbf{X}_{t_{k-1}} \ \mathbf{X}_{t_k}]^T$$

The integration of the *a priori* distribution  $p(\mathbf{X})$  with the set  $\mathbf{Z}$  of the evidences present in each image, in order to obtain the *a posteriori* distribution  $p(\mathbf{X}|\mathbf{Z})$ , is obtained with Bayes' Theorem. This fusion of information can be performed, if the distributions are Gaussian, using Kalman's Filter [1]. However, in general, the distributions involved in the process are normally not Gaussian and multimodal [2]. Sampling methods for modeling this type of distribution [9] have shown themselves to be extremely useful, and *particle filter* algorithms [10, 11, 3] based on sets of weighted random samples, enable their propagation to be performed effectively.

## 4 Observation Models

If there is a good optical flow measurement and the object is perfectly localized, it is possible to *slide* the points of the model in accordance with the flow vectors, thereby obtaining a good estimate of its position for the following frame. Unfortunately, the small errors in the flow will mount up with each frame, so that the model gradually separates from the real object, until it loses it completely.

Nevertheless, it may be supposed that the object to be tracked will move in an environment that has other displacements, and therefore it may be assumed that there will be discontinuities in the optical flow on its contour –or at least part of it. The observation model will be defined in such a way that it not only helps the flow inside the object to concur with the displacement implied by the value of  $\mathcal{X}$ , but also so that discontinuities in the optical flow appear in the contour of the model.

#### 4.1 Observation Model Based on Optical Flow

Let us suppose that we have an estimation of the flow field  $\mathbf{v}$  for the image  $I$  in the instant  $t_k$ . The following error function may be defined, with  $S \subseteq I$  being an area inside the image:

$$Z_S(\mathbf{v}; \mathbf{d}) = \sum_{(x,y) \in S} W(x,y) \|\mathbf{v}(x,y) - \mathbf{d}(x,y)\|^2 \quad (1)$$

where  $W(x,y)$  is a weight function and  $\mathbf{d}(x,y)$  is given by the state vector  $\mathcal{X}$ , relating the point on the model in the instant  $t_{k-1}$  with the same point in the instant  $t_k$ . This measurement will always be non-negative and will only be equal to zero when the flow vectors are perfectly adjusted to the displacement predicted by the model.

Let us now consider a point  $\mathbf{x} = (x,y)$  of the image belonging to the outline of the model in the instant  $t_k$ . This point will be given by the expression

$$\mathbf{x} = f(\mathbf{X}_{t_k}; \mathbf{m})$$

where  $\mathbf{X}_{t_k}$  defines the specific configuration of the object model, and  $\mathbf{m}$  is the parameter vector which associates each point within the model with a point on the image plane. The displacement vector can be calculated for the same point on the model between two consecutive instants of time as

$$\mathbf{d}(\mathcal{X}_{t_k}, \mathbf{m}) = f(\mathbf{X}_{t_k}; \mathbf{m}) - f(\mathbf{X}_{t_{k-1}}; \mathbf{m}) \quad (2)$$

Considering  $S$  as a 2D region centered at  $f(\mathbf{X}_{t_{k-1}}; \mathbf{m})$ , the measurement (1) would be:

$$Z_S(\mathcal{X}_{t_k}, \mathbf{m}) = \sum_{(x,y) \in S} W(x,y) \|\mathbf{v}(x,y) - \mathbf{d}(\mathcal{X}_{t_k}, \mathbf{m})\|^2 \quad (3)$$

The flow field is expected to present discontinuities on the boundaries of the moving objects –otherwise, it would be impossible to locate the object only from the flow vectors–, which is why if we subdivide  $S$  into two areas  $S_i$  and  $S_e$ , corresponding respectively to the parts of  $S$  interior and exterior of the object contour. If the model's prediction is good enough, the adjustment must be much better in  $S_i$  than in  $S_e$ , so that the point in question may be considered to

be placed on the contour. In order to detect that, we compute  $Z_{S_i}(\mathcal{X}_{t_k}, \mathbf{m})$ ,  $Z_{S_e}(\mathcal{X}_{t_k}, \mathbf{m})$ , and the following measurement:

$$Z(\mathcal{X}_{t_k}, \mathbf{m}) = \frac{Z_{S_e}(\mathcal{X}_{t_k}, \mathbf{m})}{Z_{S_e}(\mathcal{X}_{t_k}, \mathbf{m}) + Z_{S_i}(\mathcal{X}_{t_k}, \mathbf{m})} \quad (4)$$

The value of  $Z(\mathcal{X}_{t_k}, \mathbf{m})$  satisfies the following properties:

- $0 \leq Z(\mathcal{X}_{t_k}, \mathbf{m}) \leq 1$
- If  $Z_{S_e}(\mathcal{X}_{t_k}, \mathbf{m}) \gg Z_{S_i}(\mathcal{X}_{t_k}, \mathbf{m})$ , then  $Z(\mathcal{X}_{t_k}, \mathbf{m}) \rightarrow 1$ , which indicates that the adjustment is much better in  $S_i$  than in  $S_e$ , and therefore the point must be situated exactly in a flow discontinuity, in which the inner area coincides with the displacement predicted by the model.
- If  $Z_{S_e}(\mathcal{X}_{t_k}, \mathbf{m}) \ll Z_{S_i}(\mathcal{X}_{t_k}, \mathbf{m})$ , then  $Z(\mathcal{X}_{t_k}, \mathbf{m}) \rightarrow 0$ . The adjustment is worse in the inner area than it is in the outer area, and therefore the estimated flow does not match the model's prediction.
- If  $Z_{S_e}(\mathcal{X}_{t_k}, \mathbf{m}) = Z_{S_i}(\mathcal{X}_{t_k}, \mathbf{m})$ , then the adjustment is the same in the inner area as it is in the outer area, and therefore the flow adequately matches the displacement predicted by the model, but it is impossible to guarantee that it is situated on a flow discontinuity –nor, therefore, on the contour of the object. In this case,  $Z(\mathcal{X}_{t_k}, \mathbf{m}) = 1/2$ .

Assuming that the values of  $Z_{S_e}$  and  $Z_{S_i}$  are bounded, it may be assumed that the probability of a point on the image corresponding to the point on the outline of the model given by the vectors  $\mathcal{X}_{t_k}$  and  $\mathbf{m}$  is proportional to  $Z(\mathcal{X}_{t_k}, \mathbf{m})$ :

$$p(\mathbf{Z}|\mathcal{X}_{t_k}, \mathbf{m}_i) \propto Z(\mathcal{X}_{t_k}, \mathbf{m}_i) \quad (5)$$

Finally, assuming statistical independence, we may obtain the expression for the observation model based on optical flow vectors, as the product of the values obtained for each individual point on the contour:

$$p(\mathbf{Z}|\mathcal{X}_{t_k}) \propto \prod_i Z(\mathcal{X}_{t_k}, \mathbf{m}_i) \quad (6)$$

with  $\mathbf{m}_i$  being the vector which identifies the  $i$ -nth point on the contour of the model.

When it comes to partitioning the neighborhood  $S$  corresponding to a point  $\mathbf{x}$  of the contour of the model into two halves, one ( $S_i$ ) inside and the other ( $S_e$ ) outside the model, respectively, a good approximation consists in using the tangent to the contour in  $\mathbf{x}$  as the dividing line between  $S_i$  and  $S_e$ .

The difficulty in determining a dense flow [12] has led us to establish that those points with a more reliable flow measurement are of more use when calculating the internal and external values for the measurement  $Z$  –expression (1). This is easily achieved by calculating the value of  $W(x, y)$  in this expression from any of these *reliability* measurements of the calculated flow. In the experiments carried out for this paper, the magnitude of the intensity gradient has been used,

$$W(x, y) = \|\nabla I(x, y)\|$$

## 4.2 Observation Model Based on Similarity Measures

In the model defined in this section, in order to estimate the observation probability of each point of the contour, similarity measurements shall be used. If the prediction which the model makes is good and the intensity maps corresponding to the neighborhood of each point are superimposed, the inner part of the model must fit better than the outer part.

Let  $\mathbf{x} = f(\mathbf{X}_{t_k}; \mathbf{m})$  be a point belonging to the model contour at the instant  $t_k$ , let  $S$  be a neighborhood of  $\mathbf{x}$  subdivided in turn into  $S_i$  and  $S_e$ , let  $\mathbf{d}(\mathcal{X}_{t_k}, \mathbf{m})$  be calculated from expression (2), and let  $I^{(k-1)}$  and  $I^{(k)}$  be images corresponding to the instants of time  $t_{k-1}$  and  $t_k$ . The quadratic errors are therefore calculated in the following way:

$$\begin{aligned} Z_{S_i}(\mathbf{X}_{t_k}, \mathbf{m}) &= \sum_{S_i} W(\mathbf{x}) \left( I^{(k-1)}(\mathbf{x}) - I^{(k)}(\mathbf{x} - \mathbf{d}(\mathcal{X}_{t_k}, \mathbf{m})) \right)^2 \\ Z_{S_e}(\mathbf{X}_{t_k}, \mathbf{m}) &= \sum_{S_e} W(\mathbf{x}) \left( I^{(k-1)}(\mathbf{x}) - I^{(k)}(\mathbf{x} - \mathbf{d}(\mathcal{X}_{t_k}, \mathbf{m})) \right)^2 \end{aligned} \quad (7)$$

where  $W(\mathbf{x})$  is a weighting function. Two non negative magnitudes are obtained, that may be combined using expression (4), in order to obtain a value of  $Z(\mathcal{X}_{t_k}, \mathbf{m})$ . Since the magnitudes  $Z_{S_i}$  and  $Z_{S_e}$  are restricted,  $Z(\mathcal{X}_{t_k}, \mathbf{m})$  may be considered to be proportional to the observation density  $p(\mathbf{Z}|\mathcal{X})$ , and therefore we again have:

$$p(\mathbf{Z}|\mathcal{X}_{t_k}, \mathbf{m}_i) \propto Z(\mathcal{X}_{t_k}, \mathbf{m}_i) \quad (8)$$

Supposing the measurements on each point are statistically independent, we can use the expression (6) to compute the final observation probability.

## 5 Experiments

The observation models proposed have been incorporated into the CONDENSATION algorithm [8], and its performance has been compared with that of the observation model based on normals as proposed in [8]. Two image sequences are used, lasting 10 seconds, with 25 frames per second,  $320 \times 240$  pixels, 8 bits per band and pixel, corresponding to the movement of a hand over an uniform and non uniform background.

### 5.1 Tracking an Object over an Uniform Background

For modelling the hand, a contour model based on a closed spline with 10 control points and a Euclidean similarity deformation space were used.

For the observation model based on contour normals, 20 normals were sketched for each sample. The observation model was applied with parameters  $\alpha = 0.025$  and  $\sigma = 3$ , incorporated into the CONDENSATION algorithm with 200 samples. The initialization was carried out manually, indicating the position

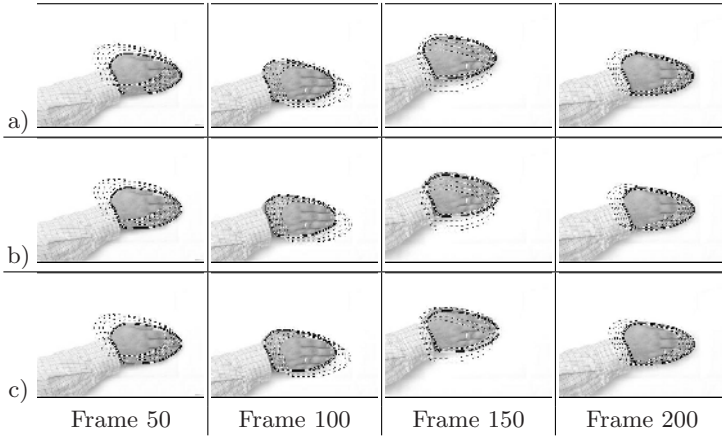


**Fig. 1.** a) Results obtained with the observation model for the contour normals. b) Results obtained with the observation model based on optical flow. c) Results obtained with the observation model based on similarity measures. The distribution average appears in solid line in the current frame, and the averages in some previous frames appear in dashed line.

of the object in the first frame. Figure 1.a shows the weighted average of the distribution obtained.

For our first observation model, the algorithm of [7] was used on the images to obtain an optical flow map between each two consecutive frames. The size of the area centered on each point was  $5 \times 5$  pixels. As a reliability measure  $W(x, y)$  when it comes to weighting the quadratic differences in expression (3), the magnitude of the intensity gradient  $\nabla I$  was used on each point.

The CONDENSATION algorithm was applied in exactly the same conditions as for the previous model, obtaining the results showed in figure 1.b.

In order to apply the observation model based on similarity measures, the same conditions were used as in previous experiments (200 samples and 20 points along the contour, considering a neighborhood of  $5 \times 5$  pixels for each point). The result obtained is illustrated in Figure 1.c.

## 5.2 Tracking an Object over a Non Uniform Background

In order to use the observation model based on contour normals, 18 normals were sketched to each contour, and the same technique was used to detect the boundaries as the one used in the previous series of experiments, with a slightly lower threshold (0.04). The number of samples is still 200, and the parameters for the observation model in this case were  $\sigma = 3$  and  $\alpha = 0.055$ . The results can be seen in Figure 2.a.

For the observation models based on optical flow, the algorithm in [7] was used once again, areas of  $5 \times 5$  pixels, and  $W(x, y) = \|\nabla I\|$ . With the same

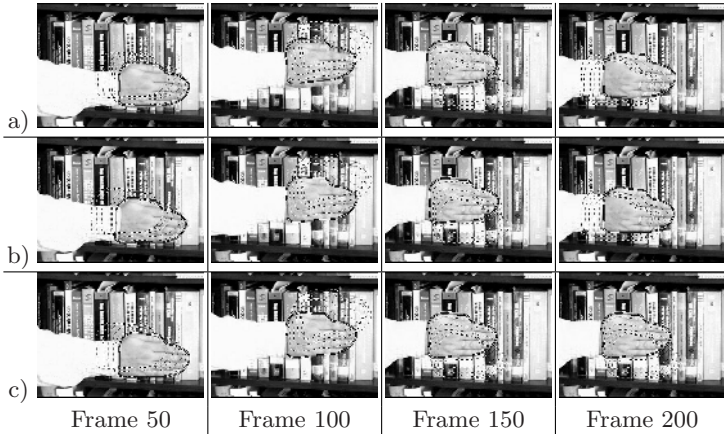


**Fig. 2.** a) Results obtained with the observation model for the contour normals. b) Results obtained with the observation model based on optical flow. c) Results obtained with the observation model based on similarity measures. The distribution average appears in solid line in the current frame, and the averages in some previous frames appear in dashed line.

number of samples as in the previous experiment (200), and the same 18 points on the contour, the results (Figure 2.b) are clearly better for this observation model.

For the observation model based on similarity measures, neighborhoods of  $5 \times 5$  pixels and 200 samples for the CONDENSATION algorithm were also used. The results obtained are shown in Figure 2.c.

## 6 Discussion and Conclusions

The experimental results obtained by the two proposed observation models on the sequence with an uniform background are satisfactory, although at one moment the distribution average strays slightly below and to the right of the hand, covering its shadow. This is due to the fact that, since there is no texture on the background, the shadow appears as a small grey patch which moves around with the hand, which is why the flow boundary can be placed on the contour of the hand-shadow set.

In the second sequence, there were significant differences in the results obtained in the tracking according to which observation model was used. With the observation model for the contour normals, as there are many edges on the background, samples emerge with a significant likelihood value, although they are not placed on the object. Consequently, the distribution average strays from the real position of the object in some frames, although at no time does it lose it completely.

With the two new observation models, it can be seen how the model never loses the object, and that it is not affected by the presence of clutter outside the real object, since the only discontinuities in the flow map will be given by the contour of the hand.

As can be seen, in a non uniform background, the observation models proposed here perform better than the model based on contour normals. In a uniform background, the absence of texture means that the model based on normals behaves better. This suggests that the proposed model and the contour normals model can be considered, in some way, complementary.

**Acknowledgement.** This work has been financed by the grant TIC-2001-3316 of the Spanish Minister of Science and Technology.

## References

1. R.E. Kalman, "A new approach to linear filtering and prediction problems," *Transactions of the ASME-Journal of Basic Engineering*, vol. 82, no. Series D, pp. 35–45, 1960.
2. J. Deutscher, A. Blake, B. North, and B. Basclle, "Tracking through singularities and discontinuities by random sampling," in *Proceedings of International Conference on Computer Vision*, 1999, vol. 2, pp. 1144–1149.
3. J. Sullivan, A. Blake, M. Isard, and J. MacCormick, "Bayesian object localisation in images," *International Journal of Computer Vision*, vol. 44, no. 2, pp. 111–135, 2001.
4. Berthold K. P. Horn and Brian G. Schunck, "Determining optical flow.," *Artificial Intelligence*, vol. 17, no. 1–3, pp. 185–203, 1981.
5. E. H. Adelson and J. R. Bergen, "The extraction of spatiotemporal energy in human and machine vision," in *Proceedings of IEEE Workshop on Visual Motion*, Los Alamitos, CA, 1986, pp. 151–156, IEEE Computer Society Press.
6. B. McCane, K. Novins, D. Crannitch, and B. Galvin, "On benchmarking optical flow," *Computer Vision and Image Understanding*, vol. 84, pp. 126–143, 2001.
7. M. Proesmans, L. Van Gool, E. Pauwels, and A. Oosterlinck, "Determination of optical flow and its discontinuities using non-linear diffusion," in *Proceedings of 3rd European Conference on Computer Vision*, 1994, vol. 2, pp. 295–304.
8. A. Blake and M. Isard, *Active Contours*, Springer, 1998.
9. A. Gelfand and A. Smith, "Sampling-based approaches to computing marginal densities," *Journal of the American Statistical Association*, vol. 85, no. 410, pp. 398–409, 1990.
10. M. Isard and A. Blake, "Contour tracking by stochastic propagation of conditional density," in *Proceedings of European Conference on Computer Vision*, Cambridge, UK, 1996, pp. 343–356.
11. J. Deutscher, A. Blake, and I. Reid, "Articulated body motion capture by annealed particle filtering," in *Proceedings of IEEE Conference on Computer Vision and Pattern Recognition (CVPR)*, 2000.
12. J. L. Barron, David J. Fleet, and S. S. Beauchemin, "Performance of optical flow techniques.," *International Journal of Computer Vision*, vol. 12, no. 1, pp. 43–77, 1994.

# Another Paradigm for the Solution of the Correspondence Problem in Motion Analysis

Ayoub Al-Hamadi, Robert Niese, and Bernd Michaelis

Institute for Electronics, Signal Processing and Communications (IESK)  
Otto-von-Guericke-University Magdeburg  
D-39016 Magdeburg, P.O. Box 4210 Germany  
[ayoub@iesk.et.uni-magdeburg.de](mailto:ayoub@iesk.et.uni-magdeburg.de)

**Abstract.** This paper demonstrates a technique of analysing the following three problems: automatic extraction of moving objects, suppression of the remaining errors and solution of the correspondence problem for the video sequences motion analysis. Here we use a new *paradigm* for solving the correspondence problem and then determination of a motion trajectory based on a trisectional structure. I.e., firstly it distinguishes between real world objects, secondly extracts image features like Motion Blobs and colour-Patches and thirdly abstracts objects like Meta-Objects that shall denote real world objects. The efficiency of the suggested technique for determination of motion trajectory of moving objects will be demonstrated in this paper on the basis of analysis of strongly disturbed real image sequences.

## 1 Introduction

Video object segmentation is required by numerous applications ranging from high-level computer vision tasks [1], traffic monitoring [2] to second-generation video coding [3]. The suggested technique pursues the target of segmentation of each moving object automatically and furthermore the determination of the motion trajectory of these moving objects making use of a multi feature correlation, MFC. Our approach differs from the other methods of the motion analysis (*blockmatching*, BM [4], *optical flow* [5], *feature-based methods* [6,7] and *deformable model-based method* [8]) due to the fact that on one hand object-adapted regions will be applied but not fixed block and on the other hand the colour information is evaluated. Another significant difference of the proposed work as compared to the work reported by other researchers, is that instead of image-primitives (e.g. *edges and corners*) the *hierarchical features extracted* from the moving image regions for the solution of the corresponding problem in image sequences. This is because of the fact that the image primitives occur in a large number and generally they don't have good characteristics for the removal of ambiguities. In fact, a complete search is impossible for primitive-oriented concepts in the contemplated image. In contrast, our method will allow the extraction for the solution of the corresponding problem in image sequences in such a way that only moving regions are extracted. This procedure facilitates the reduction of image data and also allows robust determination of motion information.

## 2 Tracking Paradigm

In image processing the question of “*what is an object or a car*” is of a philosophical nature. One can try to find objects by searching for them with pre-defined model-patterns that requires previous knowledge. Naturally, no clear set of models are available that can cover the whole spectrum of vehicles. Therefore the proposed method goes in a different way.

In this paper, since the real time processing and robustness by the segmentation of moving object is essential for the video surveillance and tracking analysis, hence a modified difference-image-based (MDI) approach is used for segmentation of moving objects. The whole procedure allows extraction of arbitrary objects automatically. After extracting regions of motion, there are always some residual errors in general, which are normally eliminated via morphological and the separation algorithm. Thereby a *robust* segmentation of moving image regions is reached despite the change of lighting condition that occurs often in the real environment. The resulting image regions present the object candidates that are used for further tracking analysis. Here the tracking **paradigm** can be defined as “the *Motion Blobs* (MB) and *colour patches* (colour-structure code, CSC) representing two *feature-levels* in a tracking hierarchy” (Fig. 1). Basically, these features describe the noticeable motion in an image pair of two consecutive images. To find and track objects in a longer image sequence an abstraction level is introduced. In this level a set of so-called *Meta-Objects* (MO) are suggested to denote real world objects. MOs are specified by a set of CSC-Patches. Now, the task to track MO splits into two parts. The first to do is a correlation at the feature level, i.e. a correlation of MO and CSC-Patches in image pairs. The second part is a correlation at the *abstraction level*, i.e. the assignment of the correlated CSC-Patches to the right MO. Generally the paradigm uses a trisection, i.e. it distinguishes between firstly the *real world* objects, secondly the image features like MB and CSC-Patches and thirdly the abstract objects like Meta-Objects that shall denote real world objects. The *relationship* between *feature* and *abstraction level* will be elucidated in detail after the introduction of the MB and CSC-Patch correlation.

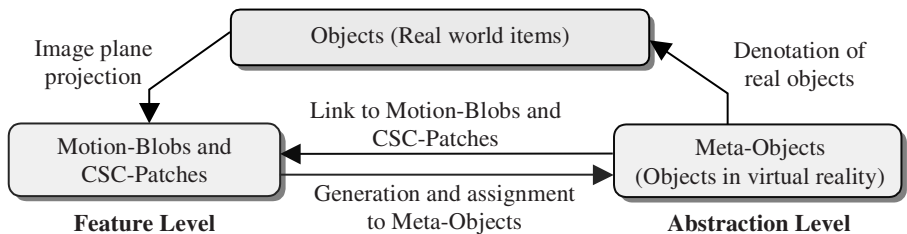


**Fig. 1.** The suggested technique for the automatic detection and tracking analysis

### 2.1 Automatic Segmentation of the Moving Objects

Compared with the motion-field-based methods [4] for segmenting moving objects, a **difference image** (DI) scheme represents a simple way to detect the moving objects in

a scene. This is because a difference image is produced quickly by simple subtractions. Here it is to be emphasised that the transition borders between regions (*i.e.* *discontinuity*) will not be cleaned up by this approach. This is because some parts of the stationary background is detected as a moving region (Fig. 2  $D_{t=1}$ ). The cause is attributed to the fact that the background is *changed* behind the moving object and it is *detected* in the resulting  $D_{t=1}$ -difference image as movement. A consequence of that is that the moving image regions will merge by this background. In extreme cases the stationary background will be detected as a moving region. This problem is represented in here as a motivation for a *modified approach* for segmentation of the moving objects. The principle for this **modified difference image-based** (MDI) approach is based simply on the fact that the resulting difference image will be received only if the extracted moving regions from two consecutive DIs are *multiplied* (Fig. 2). This operation takes place in accordance with Eq. 1. Thus zero crossings will appear in the DI image, however, an accurate position of the moving objects (middle image) at the time  $t$  is

$$Mdi(x, y, t) = DI_{t-\delta_t, t}(x, y) \cdot DI_{t, t+\delta_t}(x, y) \quad (1)$$

In general, a MDI approach has two good advantages. The first one is that motion regions on the multiplication level keeps the shape of the moving object at a time ' $t$ '. Regions on a normal DI do not express the shape of the object because it is a mixture of the object shape on the image plane at time ' $t-1$ ' and that at time ' $t$ '. The other advantage is that it is easy to detect whether the current frame contains motion information or not. If motion regions on a MDI approach are small or do not exist, it indicates that the moving object stands still and there is no need to estimate the pose in that frame. It should be recognised from Fig. 2 that the MDI approach, a substantial problem isn't solved yet. If one pixel of a moving object has coincidentally the same grey value as the stationary background or if these pixels do not have a texture foreground at this position, then the change of the intensity value will not be detected in the difference image, although the object moved there. These pixels are missing in the difference image, so that the resulting moving regions are occupied with holes as a result of this step. **The goal** of the following *pre-processing* algorithm is the suppression of the remaining errors (*holes, outliers or fusion of regions*) by the segmentation. The holes are, therefore, filled up first via morphologic operations. A suitable structural element must be defined by the application of morphologic operations. The optimal size of the structural element is reached through the following steps: (1) *Closing-Dilation* with a larger square structural element, in order to interconnect ranges with much movement (2) *Closing-Erosion* with a small structural element, in order to separate closer objects. Subsequently, a separation algorithm is applied for the separation of merged image regions (*Removal of thin background connection between objects*). The separation happens, if two peripheral points have an Euclidean distance  $d$  to each other, which is below a threshold value  $d_{min}$  and thereto a minimum number exists between the two points of  $n$  peripheral points. This algorithm is used further for the *smoothing* of the contour-region, then outliers will be *removed* simply and quickly from the previously segmented regions (Fig. 2). The resulting image is binary only after execution of the multiplication operation and not before. Thereby the weak

edges, which move fast or the strong edges, which move slowly, are considered. The generation of the motion mask can be accomplished, by setting these regions with a threshold value. After the moving image regions are extracted, the motion parameters for each moving region will be determined. This happens in the next step of the suggested technique.

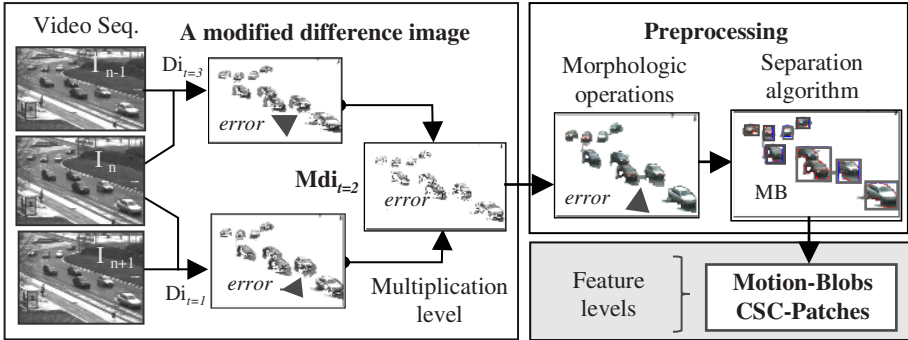


**Fig. 2.** The *segmentation* of moving objects making use of the MDI approach and pre-processing with morphological and separation operators

## 2.2 Generation of Motion Blobs and CSC-Patches (Feature Level)

In the next step object candidates and their corresponding motion trajectories will be determined. This will be based on the analysis of all previously found regions of Motion-Blobs (MB). For this task it becomes necessary to do a further segmentation of the MB. There are several algorithms, which are potentially more suitable for this purpose. The algorithm which combines most of the features required is the Colour-Structure-Code (CSC). It produces a stable real-time capable for segmentations and ease of control. The CSC is an advanced region growing approach that combines the pros of fast local region growing algorithms and the robustness of global methods [7,9]. In a region growing approach usually small segments are built first, which grow bottom-up in a second step of the procedure. That means the initial segments are merged with other segments that fulfils a similarity criterion. Common problems in region growing approaches are *transitive errors*, which emerge from local similarities. Through successive local similarities, distant pixels with different colours may fall into the same segment. Also the segmentation result depends on the order of all merging steps. The CSC avoids both disadvantages through the hierarchical hexagonal topology. It assumes colour images that have all pixels arranged in a hexagonal structure. This can easily be simulated for conventional orthogonal images. In a hexagonal structure each pixel has six equidistant neighbours. Each second pixel per row and each second pixel per column represent the central pixel of a so-called “*island of level 0*”, which consists of exactly this central pixel and six neighbours. Also, all pixels but the central pixels belong to exactly two islands of level 0. In general, each fourth island of level  $i$  represents the centre of an island of level  $i+1$ , which itself consists of seven islands of level  $i$ . The CSC algorithm takes advantage of the numerous overlap-

ping islands. In the *initial* stage, a colour segmentation is conducted for each island of level 0, resulting in segments of at least two pixels size. During the iterative process segments are merged or split, depending on a colour similarity criterion. The parameter to control the similarity is the Euclidean distance between two colours in an arbitrary colour-space [7,9].

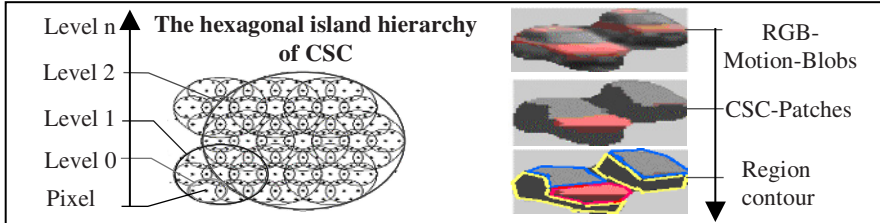


**Fig. 3.** The principle of the colour feature extraction of the motion region using CSC

The real-time capable CSC approach gives superior results in the quality of segmentation and computing time in comparison to other approaches like the top-down Split-and-Merge or Recursive-Histogram-Splitting algorithm [10]. Thus, the CSC is an adequate method to further subdivide a motion region. The search for the correspondences between subdivided motion regions in subsequent images takes place in the next section.

### 2.2.1 Tracking Analysis

To find and track objects in a longer image sequence an abstraction level is introduced. In this level the so-called *Meta-Objects* (MOs) are suggested to denote real world objects. MOs are specified by a set of CSC-Patches. Now, the task to track MO splits into two parts (Fig. 4). The first to do is a correlation at the feature level, i.e. a correlation of MO and CSC-Patches in image pairs. The second part is a correlation at the *abstraction level*, i.e. the assignment of correlated CSC-Patches to the right MO. The relationship between feature and abstraction level will be explained in detail after the introduction of the MB and CSC-Patch correlation.

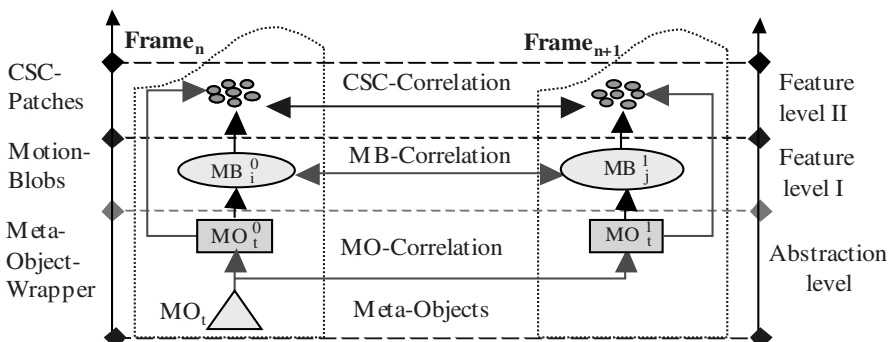


**Fig. 4.** Relationship of the different correlation levels

### 2.2.1.1 Motion-Blob Correlation

The MB correlation (MBC) is the basis for a subsequent CSC-Patch correlation, which itself is the basis for the MO correlation. The MBC is founded on the assumption of real world objects, which are the reason for any MB can only cover a limited distance between two frames. The MBC is manifold, the simplest case is a 1:1 assignment when one MB in the image  $i$  is assigned to another one in image  $i+1$ . In general, an arbitrary  $\mathbf{m} : \mathbf{n}$  assignment is possible, where many MB are simultaneously split and merged. The following section will describe the algorithm for the automatic assignment of Motion-Blobs between two frames. In the initial situation there is a MB-set  $S_0$  of frame  $i$  and another set  $S_1$  of frame  $i+1$ . Task of the algorithm is to entirely partition  $S_0 = \{b_0, b_1, b_2, \dots, b_n\}$  and  $S_1 = \{b'_0, b'_1, b'_2, \dots, b'_m\}$ , additionally each subset  $U_0_i \subseteq S_0$  shall be assigned to another subset  $U_1_j \subseteq S_1$ . The assignment is based on spatial vicinity and a similarity measure for the area covered by  $U_0_i$  and  $U_1_j$ . To exactly characterize the relation between  $U_0_i$  and  $U_1_j$  a definition by cases becomes necessary. The different cases (Fig. 5) are the following:

- {(a) 0 : 1 – emerge; (b) 1 : 0 – vanish; (c) 1 : 1 – simple movement; (d) 1 : n – split; (e) n : 1 – merge; (f) 2 : 2 – simultaneous split and merge of 2 blobs; (g) n : m – simultaneous split and merge of  $n$  blobs at a time}.

Case (a) eventuates for any MB  $b_{1,i}$  of  $S_1$  that has not been correlated in the algorithms main loop. The knowledge of the present case of the assignment is of great help to afterwards realize the Meta-Object correlation. This will be the point when actual objects are located inside of a MB.

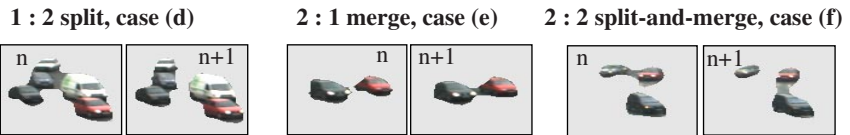


**Fig. 5.** Examples MB-Correlation Cases

### 2.2.1.2 CSC-Patch-Correlation

Once all MB are correlated, the second feature level can be processed. This task is performed for each correlated MB-Set-Pair, i.e. all related CSC-Patches will be correlated themselves on the basis of different matching criteria. The matching process is realized through a combination of *four separately weighted correlation tables* that achieves a high accuracy at a low computational expense. The matching is done between two CSC-Patch-Sets  $M_0$  and  $M_1$  that belong to previously correlated Motion-Blobs. Matching criteria of CSC-Patches within the MB are (1) *relative location*, (2) *Inter-frame-distance*, (3) *colour value* and (4) *size*.

Each correlation value is computed separately, assessed with respect to reliability and combined to a single overall similarity measure. When the similarity table is filled, those CSC-Patches of  $M_0$  and  $M_1$  that have the highest correlation value  $V$ , which is at least as high as a minimal similarity threshold value  $V_{min}$ , becomes mutually linked. All four similarity measures are weighted and combined to a single correlation table, which is used to a set of finally assigned CSC-Patches of the successive

frames. In evaluation of the table, each CSC-Patch  $p_{0_i}$ , will be linked to exactly one CSC-Patch  $p_{1_j}$  if there is a correlation value  $V$  that is maximal for the respective pair. Additionally  $V$  needs to be as least as high as a minimal threshold  $V_{min}$ . However, there may occur cases of *equivocation* when the table is not of quadratic format and several patches  $p_{0_i}$  become linked to one patch  $p_{1_j}$ . To resolve that problem patches are redistributed to their counterparts with the next best correlation value.

### 2.2.1.3 Correlation in the Abstraction Level Assignment of Meta-objects

After accomplishing the correlation in the feature level, i.e. the correlation in the last pair of blob frames, which resulted in the inter-frame assignment of MB and CSC-Patches, now the assignment of Meta-Objects can be conducted. In contrast to the prior correlation, which is always regarded as only two different frames, this step considers a longer history that is related to the Meta-Objects. So-called Meta-Object-Wrapper (MOW) are used to “wrap” the MO specific information of a certain frame pair. The Fig. 4 presents a general overview about the connection of the different correlation levels. As shown in Fig. 4, the abstraction level is connected to the feature level via MOW, which has access to Motion-Blobs as well as to CSC-Patches that are specific for a particular MO. Meta-Objects are “kept alive” from frame to frame with the help of their MOW. To initialise this process, we must specify how a MO can initially be generated. By definition, in the initial stage of the tracking system each MB shall be one MO. This is a very unlikely assumption, but in the course of time it is approximated to best fit the actual case.

## 3 Results

We want to *briefly* demonstrate the analysis of a real image sequence, which is overlaid by image-specific disturbances (*brightness change, shadow and small partial occlusion*). There, the results of segmentation of moving objects is represented by means of the suggested technique as motion trajectory (Fig. 6). It is to be recognized that during the evaluation, the segmentation of moving objects and the determination of motion trajectory is reliable. A *robust* segmentation of the moving MB objects was reached by means of applying the suggested technique.

In Fig. 6 the resulting movement vectors in form of motion trajectory (Fig. 6) and a tracking contour (MB) are represented. When using the conventional procedure the contour no longer describes the actual object position due to the shadow of that object. Whereas the suggested technique pursues the possible regarded image region over the entire image sequence, because the object regions are stable due to the saturated colours of moving regions.

## 4 Summary and Conclusion

A robust algorithm has been developed for automatic segmentation of moving objects and robust tracking under the influence of disturbed image situations. The robustness is reached by the use of a MDI approach for extracting moving objects. The solution

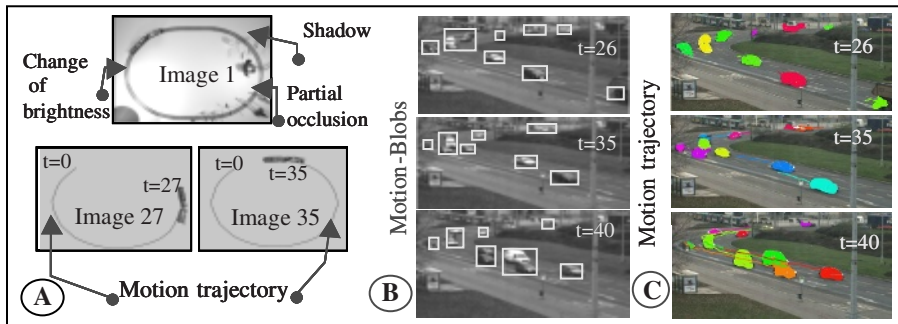


**Fig. 6.** The analysis for moving objects in real video sequence with the suggested technique. Part A presents the analysis under the influence of brightness change, shadow and small partial occlusion. Part B shows the results of the motion segmentation (MB) in the first feature level for a sequence. In C, the analyses in the second level are presented.

of the correspondence problem in the tracking has taken place in the next stage of the algorithm via *hierarchy feature correlation* from moving image regions between consecutive images. The matching process is realized through the combination of four separately weighted correlation tables that achieve a high accuracy at lower computational expenses. Each correlation value is computed separately, assessed with respect to the reliability and combined to a single overall similarity measure. By the suggested technique, reliable results are achieved despite overlaid by image-specific disturbances (*brightness change, shadow and small partial occlusion*). Further reached improvement is the invariant with object enlargement, object miniaturisation or object rotation.

**Acknowledgements.** This work was supported by LSA/ Germany grant (FKZ: 3133A/0089B).

## References

1. Ullman S.: High-Level Vision: Object Recognition and Visual Cognition, MIT Press, Cambridge, MA, 1996 Torres.
2. Badenas J.; Sanchitz J.M. and Pla F.: Using Temporal Integration for Tracking Regions in Traffic Monitoring Sequences; 15<sup>th</sup> ICPR; Barcelona 2000; Sept; Vol. III; pp.1137–1140.
3. Torres L.; Delp E.J.: New trends in image and video compression, in X European Signal Processing Conference, Tampere, Finland, September 4–8, 2000.
4. Al-Hamadi, A.; Michaelis, B.: Intensity-based method for tracking f objects in colour video sequences under the influence of non-cooperative situations; IASTED; SPPRA, Crete, Greece, June 25–28., 2002; pp. 62–67 [ISBN:88986-338-5].
5. Klette, R.; Koschan A.; Schluens K.: Computer Vision; Vieweg T.; [ISBN 3-528-06625-3]
6. Deriche R. and Faugeras O.: Tracking line segments. Image and Vision Computing; 8(4): 261–270,1990.

7. Rehrmann V.: Object-oriented Motion Estimation in colour image sequences; in Proc. Of the 5<sup>th</sup> European conference on computer vision; Springer-Verlag, June-1998. Freiburg.
8. Blake A., Curwen R. and Zisserman A: A framework for spatio-temporal control in the tracking of visual contours; International Journal of CV; 11(2):127–145; 1993.
9. Priese L.; Rehrmann V.: On hierarchical colour segmentation and applications; in proceedings of the computer vision and pattern recognition; pp. 633-634, IEEE computer society press, June 1993, New York city.
10. Lutz Priese: Vergleich von Farbsegmentierungstechniken, Labor fuer Bilderkennung Universitaet Koblenz, [www.uni-koblenz.de/~lb](http://www.uni-koblenz.de/~lb).
11. Kim c.; Hwang J.N.; A fast and robust moving object segmentation in video sequences; IEEE International Conference on Image Processing; Kobe Japan;1999, pp. 131–134.

# Improvement of the Fail-Safe Characteristics in Motion Analysis Using Adaptive Technique

Ayoub Al-Hamadi, Ruediger Mecke, and Bernd Michaelis

Institute for Electronics, Signal Processing and Communications (IESK)  
Otto-von-Guericke-University Magdeburg  
D-39016 Magdeburg, P.O. Box 4210 Germany  
[ayoub@iesk.et.uni-magdeburg.de](mailto:ayoub@iesk.et.uni-magdeburg.de)

**Abstract.** In this paper, we propose an adaptive technique for the automatic extraction and tracking of moving objects in video sequences that works robustly under the influence of image-specific disturbances (e.g. brightness variations, shadow and partial occlusion). For this technique, we apply the colour information, a neural recognition system and a recursive filtering algorithm to the improvement of the matching quality when disturbances occur. This suggested intensity-based technique is adaptive and robust compared to the conventional intensity-based methods.

## 1 Introduction

The extraction of moving objects and subsequent recognition of their trajectories (tracking) in video sequences is of increasing importance for many applications. Examples are video surveillance, motion estimation and human computer interaction. Generally, the motion or tracking methods can be divided into four groups: A) Three-dimensional-based methods [1]. B) Feature-based methods [2,3]. C) Deformable model-based methods [4] and D) Intensity-based methods [5]. Usually these conventional intensity-based methods of the motion analysis (e.g. *Blockmatching* or *optical flow*) don't operate reliably by the influence of *image-specific* disturbances such as *brightness variations, shadow, small grey tone gradients and partial occlusion*.

Our technique is an intensity-based method which can take advantage of characteristics found in colour scenes. The developed technique here pursues the objective of automatic segmentation of each moving object and furthermore the determination of the motion trajectory of these moving objects. For initial object selection, the motion vector field (full search Blockmatching BM) is used. Thereby moving blocks can be extracted. For the following tracking analysis the blocks with similarity motion parameters (*if they fulfill a homogeneity criterion*) will be combined to object candidates, which are transformed into adaptive colour space. This adaptive colour space is generated as a function of image content. By this adaptive colour space, we'll achieve an optimal channel reduction, separation the luminance and chrominance information on the one hand and on a high dynamic gain the other. The calculation of the colour components is obtained via the **Karhunen Loéve Transformation** (KLT) [6,7]. This method

provides the optimal subspace which minimizes the mean-square-error between the given set of vectors and their projections on the subspace. The resulting image regions present the object candidates that are used for the solution of the correspondence problem in video sequences.

Next to the successful tracking of the extracted moving regions in the video sequences a **multi matching** method ( $M^3$ ) is applied. This differs from the simple **Blockmatching** (BM) by the fact that in our approach object-adapted regions (*extracted from the initial step*) will be used for further tracking in the sequences instead of fixed blocks. Thus problems of fixed block (e.g. aperture problem) are eliminated. This is because the object-adapted regions contain the energetic features (e.g. edge, corner etc.) which are used for the improvement of fail safe characteristics by the motion analysis. Another advantage of our approach is the extension of the sample matching on  $M^3$  (*due to colour components*) to obtain reliable results. This is because the colour components of the adaptive colour space are invariant by the modification of the intensity value due to overlay of *shadow* or *brightness fluctuations*. For further improvement regarding the partial *occlusion* the prehistory is evaluated by means of a *recursive filtering algorithm* [8,9]. In general, this paper consists of two main parts: the first section describes the adaptive technique. The second section presents some experimental results of this technique.

## 2 Adaptive Technique for Motion Analysis

The suggested technique is described by two processing levels (Fig. 1), whereby the first level deals with the segmentation of the moving objects and analysis of the colour information. The second level of this system is specified by the  $M^3$ , a neural recognition system and a recursive modified algorithm for the estimation of the displacement vectors under the influence of image-specific disturbance (*partial occlusion*).

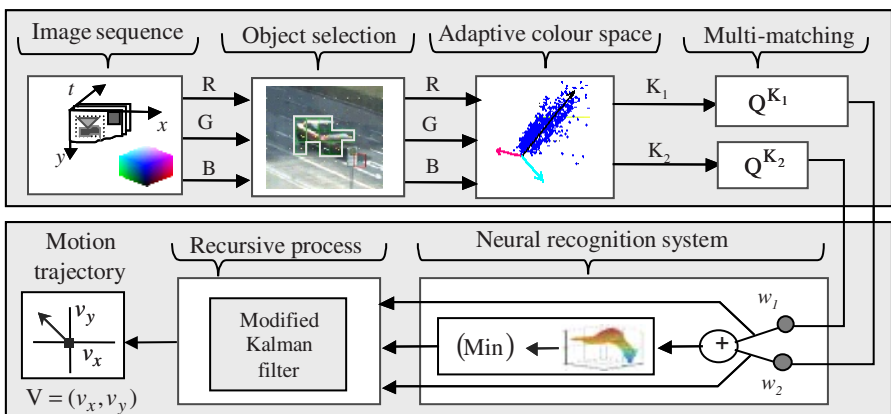


**Fig. 1.** The simplified suggested adaptive technique for the automatic detection and tracking analysis of objects in colour video sequences

## 2.1 Segmentation of Objects Using Motion Field

In the motion analysis, it is desirable to apply automatic techniques for the selection of moving objects from image sequences. In this work we use a motion vector field (*full search BM*) for automated initial object selection in the RGB image sequence. One receives a displacement vector, which describes the determined motion of the represented image region as a result of the BM for each reference block. The calculation of the displacement vectors takes place via a Q-criterion (e.g. **mean absolute difference MAD**). Due to the small implementation expenditure the criterion of the MAD was used. More specifically, denoting  $I(s,k)$  the intensity values of the reference image at pixel  $s$  and time  $k$ , and  $R$  the search region, the displacements vector  $v = (v_x, v_y)$  is obtained by *minimizing* MAD over the search region.  $M$  and  $N$  (Eq. 1) are the dimensions of the reference block.

$$\text{MAD}(v) = (M \cdot N)^{-1} \cdot \sum_{s \in R} |I(s, k) - I(s - v, k - \Delta k)| \quad (1)$$

The resulting vector field of the individual blocks of the overall view can be analysed as blocks, in which blocks with identical (*length, direction and neighbourhood*) displacement vectors are combined into an object. These blocks establish the *object candidates* (cluster). The blocks outside of this cluster are analysed as outliers or other objects because the displacement vectors don't belong to this cluster (*different direction*). Increasing the accuracy of the exact object delimitation can only be achieved by extending this segmenting procedure hierarchy. For the following *tracking analysis*, the selected object candidates are transformed into an adaptive colour space, so that a good result is achieved under the influence of *disturbances* (e.g. *brightness variations, shadow and small grey tone gradients*) in the sequence.

## 2.2 The Adaptive $K_1 K_2 K_3$ - Colour Space

Good properties for a colour space with respect to tracking are among others illumination invariance and separability. The colour of the object then remains constant and distinct which makes tracking and detection easier and more reliable. A further demand would be the increase of the dynamic gain. To obtain optimal channel reduction and a high dynamic gain, we use an adaptive colour space after the segmentation of the moving region for the fulfilment of this demand. In the following linear transformation, the components  $K_i$  in the adaptive  $K_1 K_2 K_3$ - colour space for a pixel in the RGB colour space are obtained as:

$$[K_1 \ K_2 \ K_3]^T = [Q_{ij}] [R \ G \ B]^T \quad (2)$$

For the generation of the transformation matrix  $Q_{ij}$  we use the KLT [6], in which the components  $K_i$  are aligned in the direction of the largest variances to obtain the largest possible contrast. The first component  $K_1$  contains the brightness information. A larger dynamic gain is obtained by this component, compared with the conventional average value-based brightness  $H$  [7]. The other components  $K_2$  and  $K_3$  represent the chromi-

nance information, which one uses for the suppression of the influence by *shadow* and *brightness variations*. This is obtained, since this channel occurs as *difference relation*. This behaviour corresponds to the visual colour perception in such a way that by the variation of the saturation or the brightness of a region the hue remains approx. constant. For the description of the variance of each component (*part variance*), a quality measure (Eq. 3) is defined as control criterion for the data in the respective channel. While the quality measure  $E_i$  indicates the preservation of the part variance in the respective channel, the  $E_3$  describes the variance removed by the component  $K_3$ . The evaluation of the real image scenes shows that the value of the quality measure of  $E_3$  is approx. above 98%. This is because grey tones and little saturated colours predominantly occur in the real scenes. Therefore the component  $K_3$  will be removed by the tracking analysis of objects without significant information loss.

$$E_i = \lambda_i \cdot \left( \sum_{i=1}^{n=3} \lambda_i \right)^{-1} \quad \text{and} \quad E_3 = \frac{\lambda_1 + \lambda_2}{\lambda_1 + \lambda_2 + \lambda_3} \quad (3)$$

### 2.3 The Motion Analysis

Next to the successful tracking of the extracted moving regions in the video sequences a **multi matching method** ( $M^3$ ) will be used for the determination of the displacement vectors. In this concept, the improvement of the tracking quality during the correspondence determination in image sequences is clearly reached by the fact that on the one hand side *object-adapted* image regions are utilized, and on the other *colour information* is evaluated for the improvement of fail safe characteristics. In order to exploit the characteristic of the individual channels optimally (table 1), it is necessary to summarise the channel-specific Q-criterion (e.g. MAD) for a combined total criterion ( $MAD_{KIK_2}$ , Eq. 4).

**Table 1.** The characteristics of MAD-criterion under the influence of disturbances

	Small grey tone gradients	Shadow and brightness fluctuation	Partial occlusion	Another disturbance
$MAD_{K_1}$	<i>reliable</i>	<i>unreliable</i>	<i>unreliable</i>	<i>reliable</i>
$MAD_{K_2}$	<i>reliable</i>	<i>reliable</i>	<i>unreliable</i>	<i>unreliable</i>
$MAD_{KIK_2}$	<i>reliable</i>	<i>reliable</i>	<i>unreliable</i>	<i>reliable</i>

From this the respective displacement vector is calculated. For this purpose a priority of the MAD criterion is suggested according to its reliability.

$$MAD_{K_1 K_2}(V)^t = (w_1^t + w_2^t)^{-1} \cdot \{ w_1^t \cdot MAD_{K_1}(V)^t + w_2^t \cdot MAD_{K_2}(V)^t \} \quad (4)$$

$K_1, K_2$  : Channels of the adaptive colour space.

$$w_i^t : \text{weight factor at time } t. \quad 0 < w_i \leq 1; \text{ Whereby } w_i = \begin{cases} 0.4 \leq w_i \leq 1 & \text{reliable} \\ \text{else} & 0 \text{ unreliable} \end{cases}$$

Inappropriate weighting factors will be determined in this equation by means of an artificial neural recognition system. This motivates the next part of the paper.

### 2.3.1 Artificial Neural Recognition System

The fundamental idea of generating the total criterion (Eq. 4) is based on the fact that the neural network supplies an output activation that weights the Q- criterion. Using these weighting factors  $w_i$  the two channel-specific Q-criteria are summed up. As a result, the influence of *shadow* or *lighting changes* could be reduced considerably by using the total criterion (Eq. 4). This means good results for the determination of displacement vectors can be obtained. For the determination of the weights factors (Eq. 4), a three-layer feed-forward network topology of a Multi-Layer Perception (MLP) is applied.

The feature vector (*learning data*) for the MLP is gained by an individual MAD criterion (*absolute features*) and/or from *two* consecutive MAD criteria (*difference features*). Such difference features are e.g. the change of the *minimum value*, the change of the MAD *margin values*, the change of the *average value* and of the *surrounding region values* of the MAD function. Thus, a better description of the image interference is obtained by combination the *difference* and *absolute* features. With the weighting factors ( $w_i$ ) the reliability of the MAD criteria is not only evaluated under the influence of shadow or lighting changes, a partial *occlusion* can also be detected. This can take place, if the weighting factors  $w_1$  and  $w_2$  of the two components under-run a threshold (*approx. zero*) at the same time. Then a partial occlusion occurs as disturbance in the sequence. In this case the computed motion vector is unreliable. To solve this problem, a *recursive algorithm* is used. This will be clarified in the following section.

### 2.3.2 A Modification of the Kalman Filter

Own experiments on real-world *greyscales* images have shown that measuring values (motion vectors) calculated by this procedure are corrupted by noise. Especially, if there are applications with high requirements regarding the quality of motion vectors, it is necessary to minimize the influence of noise. A recursive filtering algorithm (Kalman filter (KF) [7,8]) is used for this task. The position of the minimum of the Q-criterion (*motion vector*) is the input of the filter.

Besides the capability of the filter to reduce the influence of noise, there are some other *important* advantages. For instance the inclusion of the internal system model makes it possible to *predict* the motion vector at the next time step. This can be used effectively to reduce the *search area* in the matching algorithm. However, in case of problematic image situations (e.g. *partial occlusion* of the tracked image region), outliers in the calculated motion vectors cause false estimates of the KF.

In order to cope with this problem, a modification of the conventional KF has been proposed by [10]. This modified KF is used in the proposed technique. It estimates the quality of the respective motion vector based on the weighting factors  $w_1$  and  $w_2$  (Fig. 1). That means that the incoming (false) motion vectors are weighted less than before and the KF uses its internal model for the estimation increasingly. As a result, the influence of the *partial occlusions* of the tracked image region on the KF estimates is reduced considerably.

### 3 Results of the Analysis

In the following sequence we demonstrate the suitability and capability of the proposed technique by the motion analysis. The object of interest is overlaid by *shadow* in image<sub>k=5</sub> and *lighting modifications* in image<sub>k=10</sub> in this sequence. These influences lead to clear modifications of the intensity values (e.g. *darkening Fig. 2 A*). In the *first step* the object is selected using the motion vector field. The resulting vector field is evaluated by the combination of blocks with identical displacement vectors to one object candidate. These blocks establish the object candidates, which are transformed afterwards into the adaptive colour space for the improvement of fail-safe characteristics (*suppression of the influence of shadow and lighting modifications*). For the object-adapted image region according to Fig. 2 (image<sub>k=4</sub>), the calculated components K<sub>i</sub> are forwarded to the second processing level of the technique. There, the motion analysis of the image region takes place via M<sup>3</sup>. This also guarantees the determination of reliable motion vectors in extreme cases, if the real image objects are overlaid by disturbances. Generally, the M<sup>3</sup> operates like the BM and shows good results, since the block dimension is adapted to the object boundaries and *two channels* of the adaptive colour space for the computation of the Q-criterion (MAD) are used. Here the MAD function will be calculated according to Eq. 4 for all discrete displacement vectors  $v_x$  and  $v_y$  in the channels (K<sub>1</sub> and K<sub>2</sub>). For this overlay of shadow in image<sub>k=5</sub>, deformations and several minima occur in the Q-criterion. This occurs in the light-intensity-dependent component (K<sub>1</sub>) (Fig. 2 C) as well as in the total Q-criterion, if the matching is accomplished by using the image contents in the *RGB colour space* or in *Greyscale* image sequences. These incorrect results in the determination of the displacement vectors lead to the fact that the treated image region leaves the originally pursued region (Fig. 2 E) and the motion trajectory doesn't describe the actual position of the object. In contrast to it the Q-criterion of the component K<sub>2</sub> allow an error free motion estimation due to good minimum development (Fig. 2 C). For the automatic weighting of the channel-specific MAD (Eq. 4), a neural recognition system is used to suspend the faulty MAD function.

The training data for the neural network are formed from a quantity of feature vectors from the MAD function, which are in this case generated from the test sequence which contains sufficiently significant image interferences. Here the unreliable channel-specific MAD<sub>K1</sub> of the component (K<sub>1</sub>) is suppressed. In opposite to MAD<sub>K1</sub> the reliable similarity criterion (MAD<sub>K2</sub>) contributes to a high weight in the total criterion (Fig. 2 C). This can be demonstrated clearly via the MLP. When analysing the calculated MAD<sub>K1</sub> functions, the MLP<sub>K1</sub> supplies an output activation of zero ( $w_1=0$ ) at the time<sub>k=5</sub> (Fig. 2 D). The other MLP<sub>K2</sub> of systems evaluates the MAD<sub>K2</sub> of the K<sub>2</sub> component as reliable at the same time<sub>k=5</sub> ( $w_2=0.9$ ). The total criterion allows an error free motion estimation (*motion trajectory* Fig. 2 E) due to a good minimum. The total criterion ensures improved results compared to the conventional procedures in the motion analysis (Fig. 2 E). If the moving object is not occluded in one frame and its match is partially occluded in the following frame, then the displacement vectors estimated for this object region may have some error caused by the changed shape of the

region due to the partial occlusion. In this case the weighting factors  $w_1$  and  $w_2$  of the two components under-run a threshold (*approx. zero*) at the same time.

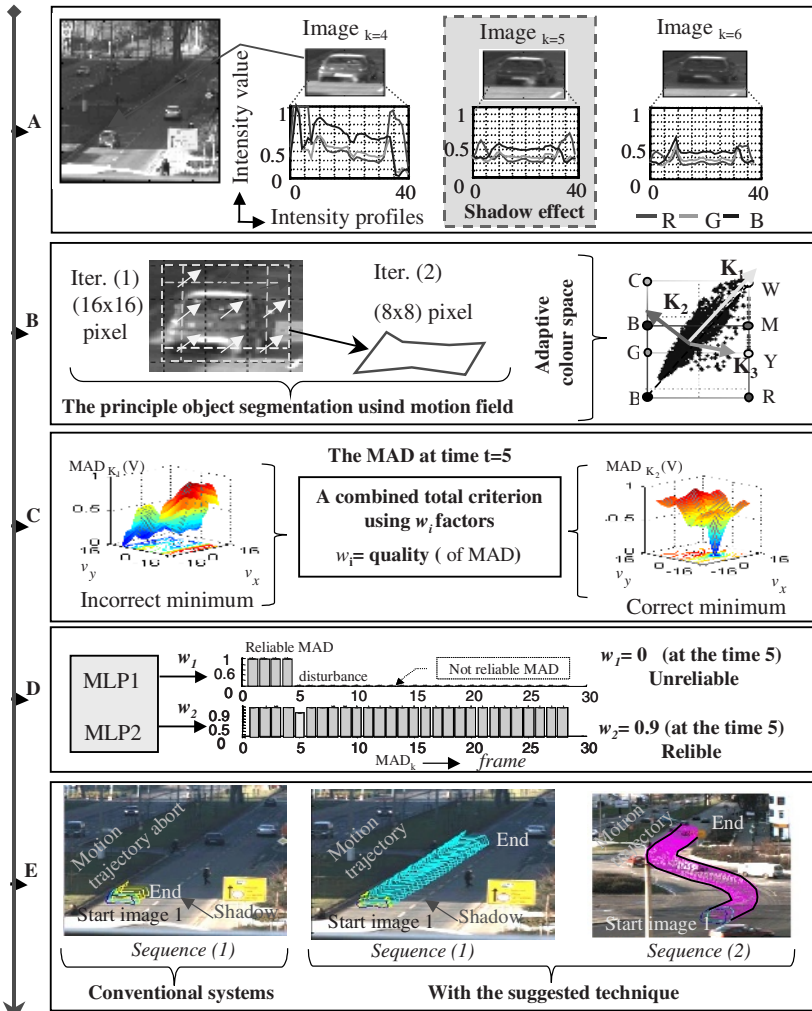


**Fig. 2.** The analysis of the image sequence under the influence of the shadow effect in the image  $Image_{k=5}$  and lighting modifications in image  $Image_{k=10}$ . The calculated MAD functions for the object of interest is shown in C. The weight  $w_i$  shows that the  $MAD_{K_1}$  criterion starting at the time  $k=5$  can't be evaluated anymore (D). The MLP1 supplies an output activation  $w_1$  of zero. In opposite to it MLP2 evaluates  $MAD_{K_2}$  as reliable. In E) The results of the tracking analysis for an image region in a video sequence with conventional methods and with the suggested system structure (b). The right image shows the analysis for another sequence with the influence of disturbances (shadow).

For the solution of this problem those displacement vectors are used as input data for a recursive process of estimation, which additionally include the temporal '*prehistory*' of the motion in the analysis. This procedure generates a *back-up* trajectory, which is valid within a limited area in case of failure of the measuring information by occlusion. For the solution of this problem those displacement vectors are used as input data for a recursive process of estimation, which additionally include the temporal '*prehistory*' of the motion in the analysis. This procedure generates a *back-up* trajectory, which is valid within a limited area in case of failure of the measuring information by occlusion.

## 4 Summary and Conclusion

In this paper, a technique was suggested for the motion estimation of objects in video sequences. For an automatic object selection, a motion vector field was used. Because the BM for the displacement calculation under the influence of disturbance situations is quite sensitive, the use of an adaptive colour space during the tracking of the objects was suggested. For a successful tracking of the extracted moving regions in the video sequences, a  $M^3$  was used. The channel-specific criteria are combined to a total criterion according to their reliability, which show more *exact* and durable results compared to conventional procedures, in particular to problematic measuring situations by adaptive priority of the proportions. In the suggested technique, a modified recursive filtering algorithm was applied for the reduction of the influence of *partial occlusions* on the tracked image region. By the suggested technique, reliable results are achieved despite the influence of disturbance situations.

**Acknowledgements.** This work was supported by LSA/Germany grant (FKZ: 3133A/0089B).

## References

1. Frank T., Haag M., Kollnig H. and Nagel H.: Tracking of occluded vehicles in traffic scenes. 7<sup>th</sup> European Conference on Computer Vision, pages 485-494, Cambridge, April 1996, Springer-Verlag.
2. Deriche R. and Faugeras O.: Tracking line segments. IVC; 8(4):261–270,1990
3. Rehrmann V.: Object-oriented Motion Estimation in colour image sequences; in Proc. Of the 5<sup>th</sup> European conference on computer vision; Springer-Verlag, June-1998. Freiburg.
4. Blake A., Curwen R. and Zisserman A: A framework for spatio-temporal control in the tracking of visual contours; Inter. Journal of Computer Vision; 11(2):127–145; 1993.
5. Badenas J.; Sanchitz J.M. and Pla F.: Using Temporal Integration for Tracking Regions in Traffic Monitoring Sequences; 15<sup>th</sup> International Conference on Pattern Recognition; Barcelona 2000; Sept; III; pp.1137–1140.
6. Devaux J.C.; Gouton P.; Truchetet F.: A erial colour image segmentation by Karhunen-Loeve Transform ; ICPR 2000 ; Barcelona 2000 ; Volume 1 ; pp. 309–312.

7. Al-Hamadi A.; Michaelis B.: Fulfilment of the demand for robustness and flexibility in the motion analysis systems by adaptive colour space transformation; CGIV'2002; April, 2002; Poitiers; France; pp.540–545.
8. Sorenson, H. W.: Kalman Filtering: Theory and Application. IEEE Press, ISBN 0-87942-191-6, 1985.
9. Maybeck, P S.: Stochastic Models, Estimation and Control. Acad. Press Inc., 1–3, 1982.
10. Mecke, R.; Al-Hamadi , A.; Michaelis, B.: A Robust Method for Block-Based Motion Estimation in RGB-Image Sequences. 14<sup>th</sup> ICPR 1998, Brisbane, Australien, pp. 663–667.

# Spatially Adaptive Algorithm for Impulse Noise Removal from Color Images

Vitaly Kober<sup>1</sup>, Mikhail Mozerov<sup>2</sup>, and Josué Álvarez-Borrego<sup>3</sup>

<sup>1</sup>Department of Computer Sciences, Division of Applied Physics  
CICESE, Ensenada, B.C. 22860, Mexico,  
[vkober@cicese.mx](mailto:vkober@cicese.mx)

<sup>2</sup>Laboratory of Digital Optics, Institute for Information Transmission Problems  
Bolshoi Karetnii 19, 101447 Moscow, Russia  
[mozer@iitp.ru](mailto:mozer@iitp.ru)

<sup>3</sup>Optics Department, Division of Applied Physics  
CICESE, Ensenada, B.C. 22860, Mexico  
[josue@cicese.mx](mailto:josue@cicese.mx)

**Abstract.** An effective method for removal impulse noise in corrupted color images is proposed. The method consists of two steps. Outliers are first detected using spatial relationships between the color image components. Then the detected noise pixels are replaced with the output of the vector median filter over a local spatially connected area excluding the outliers, while noise-free pixels are left unaltered. Simulation results in a test color image show a superior performance of the proposed filtering algorithm comparing with the conventional vector median filter. The comparisons are made using a mean square error, a mean absolute error, and a subjective human visual error criteria.

## 1 Introduction

Color images are often corrupted by impulse noise due to a noise sensor or channel transmission errors. The major objective of impulse noise removal is to suppress the noise while preserving the image details. Color images can be considered as two-dimensional three channel signals. So, monochrome image processing techniques such as median and, in general, order statistics filters [1-4] demonstrating good ability in the removal of impulse noise can be applied to each color component plane. However, such component-wise noise removal does not give desirable results because the output values may be with possible chromaticity shifts. Therefore, it is desirable to employ the dependence between the color components. Recently an effective nonlinear vector filter called as vector median filter (VMF) [5] was proposed. The VMF and its variants [6] represent ones of the most popular approaches for noise removal in color images. However, because these approaches are typically implemented uniformly across a color image, they also tend to modify pixels that are undisturbed by noise. Moreover, they are prone to edge jitter when the percentage of

impulse noise is large. Consequently, the effective removal of impulses is often at the expense of blurred and distorted features. Recently nonlinear filters for monochrome images with a signal-dependent shape of the moving window have been proposed [7]. In this paper, we utilize the approach for suppressing the impulse noise in highly corrupted color images. First outliers are detected using spatial relationships between the color components. Then the detected noise pixels are replaced with the output of the VMF computed over a local spatially connected area excluding the outliers from the area. In the case of independent channel impulse noise, the proposed detector greatly reduces the miss probability of impulse noise. The performance of the proposed filter is compared with that of the conventional VMF algorithm.

The presentation is organized as follows. In Section 2, we present a novel efficient algorithm for detection of noise impulses. A modified vector median filter using the proposed detector is also described. In Section 3, with the help of computer simulation we test the performance of the conventional and proposed filter. Section 4 summarizes our conclusions.

## 2 Spatially Adaptive Algorithm for Detection and Removal Impulse Noise

In impulse noise models, corrupted pixels are often replaced with values near to the maximum and minimum of the dynamic range of a signal. In our experiments, we consider a similar model in which a noisy pixel can take a random value either from sub-ranges of the maximum or the minimum values with a given probability. The distribution of impulse noise in the sub-ranges can be arbitrary. To detect impulse noise in a color image, we use the concept of a spatially connected neighborhood. An underlying assumption is as follows: image pixels geometrically close to each other belong to the same structure or detail. The spatially connected neighborhood is defined as a subset of pixels  $\{v_{n,m}\}$  of a moving window, which are spatially connected with the central pixel of the window, and whose values deviate from the value of the central pixel  $v_{k,l}$  at most predetermined quantities  $-\varepsilon_v$  and  $+\varepsilon_v$  [7]:

$$CEV(v_{k,l}) = CON \left( \{v_{n,m} : v_{k,l} - \varepsilon_v \leq v_{n,m} \leq v_{k,l} + \varepsilon_v\} \right). \quad (1)$$

The size and shape of a spatially connected neighborhood are dependent on characteristics of image data and on parameters, which define measures of homogeneity of pixel sets. So the spatially connected neighborhood is a spatially connected region constructed for each pixel, and it consists of all the spatially connected pixels, which satisfy a property of similarity with the central pixel.

The vector median filter replaces the color vector of each pixel by the vector median value. However, the VMF is often implemented uniformly across a color image. This leads to undesired smoothing of image details, which are uncorrupted by impulse noise. Therefore, the quality of the filtering depends on an impulse noise detector. The detector must decrease the probabilities of impulse noise miss and false detection.

In other words, it should detect as much as possible noisy pixels, while the false detection should be as less as possible to preserve image details. We propose to detect outliers with the help of spatial relations between the color components. We assume that a spatially connected region corrupted with impulse noise is relatively small comparing to details of the image. Therefore, the impulsive noise can be detected by checking the size of its region. If the size is less than a given threshold value, say  $M$ , impulse noise is detected. Obviously, such a detector omits impulses with the size greater than  $M$ . The probability of occurrence of a four-connected noise cluster of the size  $M$  in a moving window can be computed using the addition formula of probabilities. The noise cluster occurs simultaneously with one of the mutually exclusive events  $H_1, \dots, H_N$ . Here  $H_k$  is the event denoting that there is a noise cluster of the size exactly  $M$  noise impulses surrounded by uncorrupted image pixels. The probability of occurrence of a noise cluster of the size  $M$  at a given image pixel is given as

$$\Pr(M) = \sum_{k=1}^N \Pr(H_k), \quad (2)$$

where the probability of the event  $H_k$  is  $\Pr(H_k) = P^M (1 - P)^{E_k(M)}$ ,  $E_k(M)$  is the number of surrounded uncorrupted image pixels. Taking into account that some of the probabilities  $\Pr(H_k)$  are equal, the Eq.(2) is computationally simplified to

$$\Pr(M) = P^M \sum_{k=1}^{K(M)} C_k(M) (1 - P)^{E_k(M)}, \quad (3)$$

where  $K(M)$ ,  $C_k(M)$ ,  $E_k(M)$  are coefficients determined from the geometry (binary region of support) of the cluster of noise.

**Table 1.** Coefficients for calculating the probability of impulsive clusters

Size of cluster $M$	$K(M)$	$k$	$C_k(M)$	$E_k(M)$
1	1	1	1	4
2	1	1	4	6
3	2	1	12	7
		2	6	8
4	3	1	36	8
		2	32	9
		3	8	10
5	5	1	5	8
		2	100	9
		3	140	10
		4	60	11
		5	10	12

For a given image pixel,  $K(M)$  is the number of groups, each of them contains  $C_k(M)$  events  $H_k$  with the equal probabilities  $\Pr(H_k)$ ,  $k=1, \dots, K(M)$ . For example, the number of groups with  $M=2$  is  $K(2)=1$ , and the number of surrounding four-connected

uncorrupted pixels is  $E_I(M)=6$ . The number of the events is  $C_I(M)=4$  (four possible variants of the noise cluster on the grid including the given pixel). With the help of Table 1 and Eq. (3), the probability of occurrence of a four-connected impulse noise cluster of the size  $M$  can be easily calculated. Table 2 presents the probability of occurrence of impulse cluster of size  $M$  versus the probability of impulse noise on a rectangular grid. We see that when the probability of impulse noise is high, the occurrence of impulse cluster is very likely.

**Table 2.** The probability of occurrence of impulse clusters of the size  $M$  versus the probability  $P$  of impulse noise.

M	Probability of impulse noise		
	P=0.01	P=0.1	P=0.2
0	0.99	0.9	0.8
1	5.6x10 <sup>-3</sup>	6.5x10 <sup>-2</sup>	8.2x10 <sup>-2</sup>
2	3.7x10 <sup>-4</sup>	2.1x10 <sup>-2</sup>	4.2x10 <sup>-2</sup>
3	1.7x10 <sup>-5</sup>	8.3x10 <sup>-3</sup>	2.8x10 <sup>-2</sup>
4	7x10 <sup>-7</sup>	3x10 <sup>-3</sup>	1.8x10 <sup>-2</sup>
5	2.8x10 <sup>-8</sup>	1.1x10 <sup>-3</sup>	1.1x10 <sup>-2</sup>

Here we provided the coefficients for  $M \leq 5$ . In a similar manner, the coefficients for greater sizes of noise clusters can be calculated.

Suppose that impulsive noise is independent in  $L$  signal channels. The probability of occurrence of a noise cluster of the size  $M$  at a given image pixel can be written as

$$\Pr(M) = (P^L)^M \sum_{k=1}^{K(M)} C_k(M) (1-P^L)^{E_k(M)}, \quad (4)$$

For a color image ( $L=3$ ), the probability of impulse noise with  $M=1$  and  $P=0.1$  becomes 0.000996 (compare to 0.065 for  $L=1$ ). We see that the probability of multichannel impulse noise greatly decreases when the number of channels increases. The algorithm of impulse noise detection in a color image is given as follows. First, we construct spatially connected neighborhoods in the RGB channels, independently. The parameters spatially connected neighborhoods in the channels are chosen on the base either a priori or measured information about the spread of the signal to be preserved.

Let ICON and UCON be two sets obtained as intersection and union of the regions of supports of the spatially connected channel neighborhoods  $\text{CON}_R$ ,  $\text{CON}_G$ ,  $\text{CON}_B$ , respectively. If the number of elements in ICON is small, then at least in one channel there exists impulse noise. If the size of UCON is large, then a detected impulse is probably in one channel. If the both sets are small, impulse noise is in three channels. However, the probability of this event is very small. Finally, for the moving window of  $3 \times 3$  pixels we use the following threshold values for the sets: if the size of ICON  $\leq 1$  and UCON  $\leq 1$ , the central pixel is corrupted in three channels; if the size of ICON  $\leq 2$  and the difference between two sizes  $\geq 3$ , then the central pixel is corrupted in one

or two channels; if the size of ICON $\geq 2$  and the difference $\leq 2$ , the central pixel is not corrupted and there is a high local signal variation in the channels.

Finally, the detected impulse noise is replaced with the output of the VMF computed over a local spatially connected area excluding the outliers. The conventional VMF is defined as follows. For a set of  $N$  vectors in the RGB color space  $S \in (\mathbf{x}_1, \mathbf{x}_2, \dots, \mathbf{x}_N)$ ,  $\mathbf{x}_n = (R_n, G_n, B_n)$  with a vector norm  $\|\mathbf{x}\|_L$ , the vector median filter is given by

$$\mathbf{x}_{VM} = (R_{VM}, G_{VM}, B_{VM}), \mathbf{x}_{VM} \in S, \quad (5)$$

with

$$\sum_{n=1}^N \|\mathbf{x}_{VM} - \mathbf{x}_n\|_L \leq \sum_{n=1}^N \|\mathbf{x}_a - \mathbf{x}_n\|_L, \quad \forall \mathbf{x}_a \in S.$$

This operation selects such a vector in the moving window, which minimizes the sum of the distances to the other  $N-1$  vectors regarding the L-norm. We suggest to find the median value among the vectors belonging only to the set of spatially connected neighborhoods with the region of support UCON excluding corrupted pixels. However, if the size of UCON is small, for noise filtering a small region surrounding UCON is used. The proposed algorithm is extension of the algorithm [7] to color images, and it can be written as

$$\hat{v}_{n,m} = \begin{cases} v_{n,m}, & \text{if } SIZE(ICON) \geq Th\_ICON \\ VMF(v_{n,m} \setminus UCON) - v_{n,m} \{ICON\} & \text{if } SIZE(UCON) \geq Th\_UCON, \\ VMF(v_{n,m} \setminus UCON) - v_{n,m} \{UCON\} & \text{otherwise} \end{cases} \quad (6)$$

where  $Th\_ICON$  and  $Th\_UCON$  are threshold values of outlier detection for the sets ICON and UCON, respectively; " $-$ " denotes the set difference operationvvvv;  $v_{n,m} \{S\}$  is the subset of pixels of the moving window with the region of support S;  $\overline{UCON}$  is a small region surrounding UCON. The algorithm starts from the first line of Eq. (6).

### 3 Computer Experiments

Signal processing of a color image degraded due to impulse noise is of interest in a variety of tasks. Computer experiments are carried out to illustrate and compare the performance of conventional and proposed algorithms. We are interested in answering how well, relative to the other filters, does each perform in terms of noise removal and preservation of fine structures. However, it is difficult to define an error criterion to accurately quantify image distortion. In this paper, we will base our comparisons on the mean square error (MSE), the mean absolute error (MAE), and a subjective visual criterion. The empirical normalized mean square error is given by

$$MSE = \frac{\sum_{n=1}^N \sum_{m=1}^M \sum_{k=1}^3 |v_{n,m,k} - \hat{v}_{n,m,k}|^2}{\sum_{n=1}^N \sum_{m=1}^M \sum_{k=1}^3 v_{n,m,k}^2}, \quad (7)$$

where  $\{v_{n,m,k}\}$  and  $\{\hat{v}_{n,m,k}\}$  are the original image and its estimate (filtered image), respectively. In our simulations,  $N=320$ ,  $M=200$  (320x200 image resolution), and each pixel has 256 levels of quantization. The empirical normalized mean absolute error is defined as:

$$MAE = \frac{\sum_{n=1}^N \sum_{m=1}^M \sum_{k=1}^3 |v_{n,m,k} - \hat{v}_{n,m,k}|}{\sum_{n=1}^N \sum_{m=1}^M \sum_{k=1}^3 |v_{n,m,k}|}. \quad (8)$$

The use of these error measures allows us to compare the performance of each filter. Fig. 1(a) shows a test color image degraded due to impulse noise. The probability of independent noise impulse occurrence is 0.07 in each color channel. This means that the total noise probability is  $P_{RGB}=1-(1-P)^3=1-0.93^3\approx 0.2$ . In computer simulation, the values of impulses were set to 0-15 or 240-255 with equal probability. Table 3 shows the errors under the MSE and MAE criteria for the VMF and the proposed filter. The size of the moving window is 3x3. The value  $\varepsilon_v$  to construct spatially connected channel neighborhoods is equal to 10. The threshold values are taken as  $Th\_ICON=1$  and  $Th\_UCON=4$ . The first two rows in the table show the errors after filtering of the original image without noise. We see that in this case the conventional VMF has a worse performance comparing with the proposed algorithm. Fig 1 (b, c) show the filtered images obtained from the noise image in Fig. 1 (a) with the conventional VMF and the proposed filter, respectively. The proposed filter using the spatial pixel connectivity has a strong ability in impulse noise suppression and a very good preservation of fine structures and details. The visual comparison of the filtered images in Fig. 1 (b) and 1 (c) shows that the filtered image with the VMF is much smoother than the output image after filtering with proposed method.

**Table 3.** Impulse noise suppression with different filters

Type of Filters	Measured Errors	
	MSE	MAE
VMF 3x3 (WN)	0.0173	0.0802
Proposed algorithm (WN)	0.0014	0.0056
Noisy image	0.0897	0.1338
VMF 3x3	0.0197	0.0887
Proposed algorithm	0.0087	0.0319



**Fig. 1.** (a) Noisy color image



**Fig. 1.** (b) Filtered image by VMF



**Fig. 1.** (c) Filtered image by the proposed algorithm

## 4 Conclusion

In this paper, we have presented a new algorithm for detection and suppression of impulse noise in color images. The filter utilizes an explicit use of spatial relations between color image elements. When the input color image is degraded due impulse noise, extensive testing has shown that the proposed spatially adaptive vector median filter outperforms the conventional vector median filter in terms of the mean square error, the mean absolute error, and a subjective visual criterion.

**Acknowledgment.** This work was supported by the grant 36077-A from CONACYT.

## References

1. Arce G.R., Gallagher N.C., and Nodes T., Median filters: Theory and applications, in Advances in Computer Vision and Image Processing, Huang, T., Ed. Greenwich, CT: JAI (1986).
2. Pitas I. and Venetsanopoulos A.N., Nonlinear digital filters. Principles and applications, Kluwer Academic Publishers, Boston (1990).
3. Tsekridou S., Kotropoulos C., Pitas I., Adaptive order statistic filters for the removal of noise from corrupted images, Optical Engineering, Vol. 37, (1998), 2798–2815.
4. Abreu E., Lingstone M., Mitra S.K., and Arakawa K., A new efficient approach for the removal of impulse noise from highly corrupted images, IEEE Trans. on Image Processing, Vol. 2, No. 6, (1993), 1012–1025.
5. Astola J., Haahtisto P., and Neuvo Y., Vector median filter," Processing of the IEEE, Vol. 78, (1990), 678–689.
6. Vardavoulia M.I., Andreadis I., Tsalides Ph., A new vector median filter for colour image processing, Pattern Recognition Letters, Vol. 22, (2001), 675–689.
7. Kober V., Mozerov M., Alvarez-Borrego J., Nonlinear filters with spatially connected neighborhoods, Optical Engineering, Vol. 40, No. 6, (2001), 971–983.

# Improving Phase-Congruency Based Feature Detection through Automatic Scale-Selection

Veit U.B. Schenk<sup>1,2</sup> and Michael Brady<sup>2</sup>

<sup>1</sup> Laboratory of Computational Engineering, Helsinki University of Technology, P.O. Box 9203,  
FIN-02015 HUT, Finland, vubs@robots.ox.ac.uk

<sup>2</sup> Robotics Research Group, Dept. of Engineering Science, Ewert House, Oxford, OX2 7SG UK

**Abstract.** In this paper we present a novel method for computing phase-congruency by automatically selecting the range of scales over which a locally one-dimensional feature exists. Our method is based on the use of local energy computed in a multi-resolution steerable filter framework. We observe the behaviour of phase over scale to determine both the type of the underlying features and the optimal range of scales over which they exist. This additional information can be used to provide a more complete description of image-features which can be utilized in a variety of applications that require high-quality low-level descriptors. We apply our algorithm to both synthetic and real images.

**Keywords:** Phase-congruency, local energy feature-detection, scale-detection, steerable filters

## 1 Introduction

Phase congruency [7] is a very appealing concept for general feature detection because it permits feature detection independent of the actual feature type, i.e. rather than being optimized to detect edges or ridges or valleys it can be used to detect almost any type of feature in a unified framework. The underlying principle is that phase is constant or *congruent* over all scales at the location of what the human visual system would perceive as a locally one-dimensional feature, such as an edge, a ridge or a valley (as opposed to two-dimensional features, e.g. junctions) [6]. An advantage of phase-congruency is that the type of feature can be classified using the phase-value at which congruency occurs. Furthermore, the degree to which phases are congruent can readily be computed as a ratio of some ‘ideal’ value and the actual phase-values leading to a measure that is contrast and brightness independent. There are interesting parallels between the concept of phase-congruency and Lindeberg’s [5] concept of the *scale-space edge*, which is defined as a connected set of points in scale-space: features are found where a certain measure persists over a consecutive range of scales. The method presented in this paper identifies locations in image signals at which phase takes on a small set of fixed values over a range of subsequent scales.

The use of phase is particularly appealing for a number of reasons: it has been demonstrated experimentally [8] that most of the information in a signal is stored in the phase, rather than the amplitude: the phase effectively encodes the ‘location’ at which

the individual sinusoid contribute to the overall signal. Furthermore, phase is stable not only under translation but also geometric deformations and contrast variations [1].

One of the great advantages of the use of phase is that the exact position of a feature can be determined easily to sub-pixel accuracy [3] without the need for explicit sub-pixel feature detection.

Morrone and Owens [7] show that for a one-dimensional signal  $I(x)$  which has the short-term Fourier Transform expansion:

$$I(x) = \sum_{n>0} A_n \cos(n\omega x + \phi_n) = \sum_{n>0} A_n \cos(\phi_n(x)) \quad (1)$$

where  $A_n, \phi_n$  are respectively the  $n^{th}$  components of amplitude and phase at position  $x$ , all phase-components  $\phi_n(x)$  are (near) identical at the location  $x$  of a feature.

Phase congruency can be shown to be directly related to local energy [10] which in the one-dimensional case is defined as

$$LE_{1D} = \sqrt{I^2 + H^2} \quad (2)$$

where  $I$  is the input signal and  $H$  its Hilbert transform.

In practice, phase-congruency is obtained by computing local energy at a number of scales and integrating the resulting coefficients appropriately. Kovesi [4] presents the first such computationally efficient implementation of phase-congruency. He defines a phase congruency measure  $PC(x)$  at signal location  $x$  as:

$$PC(x) = \max_{\bar{\phi}} \frac{\sum_{n>0} A_n \cos(\phi_n(x) - \bar{\phi}(x))}{\sum_{n>0} A_n} = \frac{LE}{\sum_{n>0} A_n} \quad (3)$$

The value of  $\bar{\phi}(x)$  that maximizes (3) is the amplitude weighted mean local phase-angle. It can be shown that the numerator  $LE$  in the above expression is the local energy of the signal [10];  $PC$  is consequently the (local) maximum of the amplitude-weighted sum of the phases (computed over a range of scales) normalized by the amplitude sum. Kovesi extends the concept to two dimensional signals and addresses issues such as noise or advanced phase-congruency based operators for symmetry and asymmetry. Although  $PC$  gives good results for a wide range of synthetic and natural images and produces feature maps that compare favourably with e.g. a Canny edge detector [4], there are a number of drawbacks which are related to one major oversight: the fact that local energy is proportional to phase-congruency (see (3)) is only valid for isolated features and is no longer valid as soon as the spatial extent of the filter used overlaps neighbouring features in the input signal. This is illustrated in Fig. 1 which shows in (A) a signal consisting of a square wave with decreasing frequency (from left to right). Subfigure (B) is the energy amplitude scaleogram (computed using (2) over a range of centre frequencies  $\lambda = 0.1 : 0.65$ .) The corresponding phaseogram is shown in Subfig. (C). A number of observations are immediately obvious:

- The range of scales over which edges have significant energy is much larger than the rather small range of scales over which ridges and valleys respond.

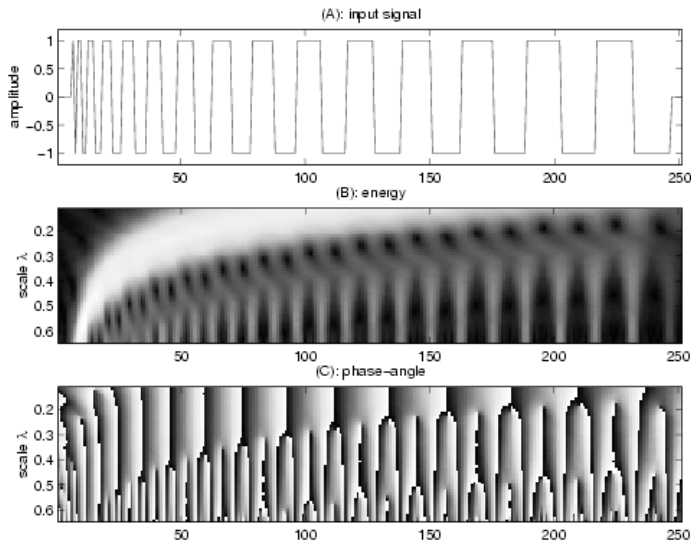


**Fig. 1.** Locality of energy response: the energy distribution over scale depends not only on the underlying feature, but also its neighbourhood. See text for details.

- There is interference as filters overlap neighbouring features leading to the cancellation of responses which in (B) correspond to the ‘black holes’ along the centre of the scaleogram (or alternatively, the regions in (C) where two columns of constant phase merge). In these regions phase is unstable and must not be used for further processing [3].
- A second form of interference occurs towards the low-frequencies (small  $\lambda$ ): responses due to combinations (rather than isolated) of neighbouring features add up to high energy amplitudes as shown by the broad high intensity curve in the scaleogram. The response is high even in between what we would regard as a feature and therefore must be excluded from further processing.

Since  $PC$  is computed over *all* scales, rather than the appropriate range of scales and – as illustrated above – strong features (edges) dominate neighbourhoods,  $PC$  responds predominantly to edges and isolated very thin lines and produces spurious responses in areas with high energy which is due to interference of low-frequency responses. This is illustrated in Fig. 2 and Fig. 3. The left of Fig. 2 shows a synthetic image with a variety of structures including ridges, valleys and edges over a wide range of orientations, scales and with different amounts of smoothing.

The raw  $PC$  output is shown on the right in Fig. 2. There are high responses near most of the edges apart from the rather smooth edges in the lower left quadrant. The responses at the edges are also significantly stronger than those corresponding to the ridges and valleys in between these edges. As a result, the post-processed version shown in Fig. 3 marks as interesting features only edges and is rather unsuccessful at identifying the smoothed features in the lower left quadrant. The method proposed in this paper

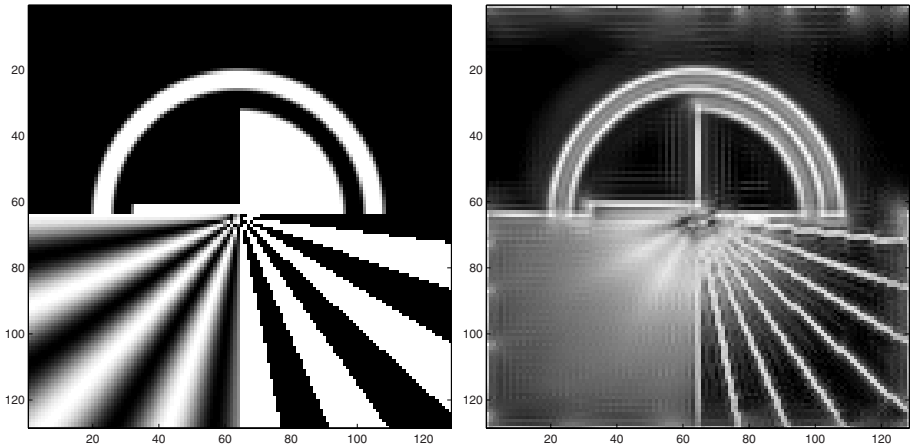


**Fig. 2.** Left: Synthetic signal with variety of locally one-dimensional features (edges, ridges, valleys). Right: corresponding *PC* map. Note the strong responses at edges, almost uniform response in bottom-left quadrant and weak responses at ridges/valleys.

identifies a wider range of geometric features than just edges and provides a better response to heavily smoothed features, as in the lower left quadrant of the image, thus taking advantage of local energy's inherent ability to respond to *any* type of locally one-dimensional feature equally well.

## 2 Methodology

Our approach is based on the use of local energy for feature detection. At each location in the image, we compute an energy response, which can be used to obtain an energy-amplitude and a phase-angle  $\phi$ . Since we are interested in the energy response and phase-angle at each image feature independent of its orientation, we interpolate the exact response at the orientation  $\theta_l$  of each image-point through the use of steerable filters [2]. We define  $\theta_l$  to be *perpendicular* to the locally one-dimensional feature, i.e. along the orientation of maximum variation. Only regions of the image with high local energy will be selected for further processing. Since the post-processing stages involve tracking phase  $\phi$  over multiple scales, the signal is decomposed at multiple resolutions.

### 2.1 Decomposition and Orientation Computation

Local energy is computed using quadrature pairs of odd-symmetric and even-symmetric bandpass filters. We decompose the image using a steerable filter bank at  $N_o = 4$  odd-symmetric and  $N_e = 5$  even-symmetric orientations  $\theta_o$  and  $\theta_e$  distributed evenly over the half-circle of orientations  $0..\pi$  (i.e.  $\theta_o = \frac{\pi}{4}[0, 1, 2, 3]$  and  $\theta_e = \frac{\pi}{5}[0, \dots, 4]$ ) and  $S = 15$  closely spaced scales (spacing of 0.2 octaves for filters with 1-octave bandwidth) in order to approximate a continuous decomposition (in scale). In the following, where

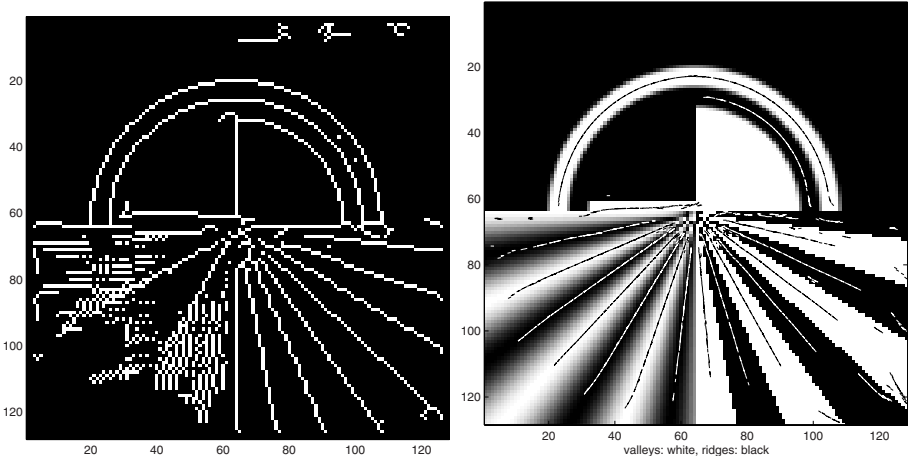


**Fig. 3.** Left:  $PC$  map after postprocessing (non-maximum suppression and hysteresis thresholding). Note the noisy response in bottom left quadrant. Furthermore, only edges are detected. Right:  $LE$ : Ridge (black) and valley (white) feature points overlaid onto original image. See text for more details

appropriate, the scale index  $s$  is omitted to improve legibility. The polar-separable filters are constructed in the Fourier domain with a cosine raised to the power 2 on a log-scale as the radial component and a quadrature pair of filters for the angular component which has a  $\cos^3$  and  $|\cos^3|$  cross-section for the odd/even-symmetric filter-parts respectively [9].

The image is convolved with the resulting filterbank by multiplying the Fourier Transform of the image with the individual filters and inverse Fourier transforming. The resulting subbands are kept at full resolution, i.e. no pyramid scheme is used, which facilitates the tracking of phase through scale. The 2D extension of (2) is

$$LE_n = \sqrt{O_n^2 + E_n^2} \quad (4)$$

where  $O_n, E_n$  are the  $n^{th}$  odd/even-symmetric responses for each of the  $N_o$  orientations. Since  $N_o \neq N_e$  and the odd-symmetric and even-symmetric filters consequently are not aligned, they need to be aligned prior to computing  $LE$ . This is achieved by steering the even-symmetric filters to the orientations  $\theta_o$ .

**Orientation Computation.** At each point and for every scale local orientation  $\theta_l$  is found as

$$\theta_l = \frac{1}{2} \arctan(imag(\bar{V})/real(\bar{V})) \quad (5)$$

where  $\bar{V} = \sum_{n=0}^{N_o-1} \exp(i2n\pi/N_o) |LE_n|$  is the amplitude weighted sum of oriented unit length vectors aligned with  $\theta_o$ .

At each point and scale  $S$ , the  $N_o$  subband coefficients are steered to  $\theta_l$ . The result of this operation is a cuboid of  $S$  steered energy response-maps.

## 2.2 Tracking Phase over Scale

The basic idea for determining the correct range of scales over which to compute phase-congruency is to track the precise, i.e. sub-pixel contours of phase over scale and to label a location in the image as ‘interesting’ if phase is congruent over a minimum number of scales. The candidate points are obtained using the Matlab function `contourc` on each response map of the cuboid using the appropriate phase-angles for positive/negative edges and ridges and valleys.

In order to avoid having to exhaustively search the entire image, we use hysteresis thresholding of local energy amplitude to reduce the number of candidate points.

For each of the (equally spaced along a phase-contour) candidate points  $p$ , we iterate through all scales  $\lambda$ . If  $p$  has correspondences with the same phase-value in a minimum number  $l_{min}$  of subsequent scales, then  $p$  is marked as a feature point for that particular phase-value. The start and end-scales  $\lambda_b$  and  $\lambda_e$  of where phase is congruent are recorded. All points in the chain from  $\lambda_b$  to  $\lambda_e$  are removed from the set of candidate points, i.e. they will not be considered at subsequent stages. Correspondence is established if the contours at subsequent scales are no further apart (measured as the distance between two parallel contours) than a specified fraction  $d_{max}$  of pixels. The subpixel location of  $p$  is recorded as the mean of all points in the chain.

Through extensive experimentation on a large set of images we found that the values  $d_{max}=0.3$  pixels and  $l_{min}=4$  scales give excellent results for a wide range of images. The choice of  $d_{max}$  is not critical, values between  $0.2 \leq d_{max} \leq 0.5$  give acceptable results. The choice of  $l_{min}$  directly affects

- 1) the sensitivity to the degree of smoothing a feature has undergone: strong smoothing leads to responses with a small frequency spread, i.e. there are only significant responses over a (very) small range of scales. Values of  $l_{min} \gg 4$  therefore eliminate strongly smoothed features and favour sharp transitions. Since edges exist over a wider range of scales than lines, too large a value for  $l_{min}$  would therefore favour edges over lines.
- 2) How features in closely packed neighbourhoods are treated: as the filter-size increases, the filters quickly start to overlap multiple features, leading to interference in responses. As a result, stability in phase over scale is only guaranteed over a small range of scales. If  $l_{min}$  is too large, regions with densely packed features are eliminated. Note that  $l_{min}=4$  is a value we obtained empirically for a decomposition over  $S=15$  scales with a corresponding step-size of 0.2 octaves.  $l_{min}=4$  therefore implies that a feature needs to exist over just under one octave.

The method is stable with respect to the thresholds, small changes lead to gradual changes in the output, rather than catastrophic failure.

## 3 Results

The methods described in the previous sections were applied to a number of synthetic and real images with varying noise and contrast levels and different densities of features. The results of  $LE$  are displayed as follows: since the location of the feature-point is computed at subpixel accuracy, the resulting points are displayed as short lines perpendicular to  $\theta_l$ , i.e. parallel to the orientation of the locally one-dimensional feature.

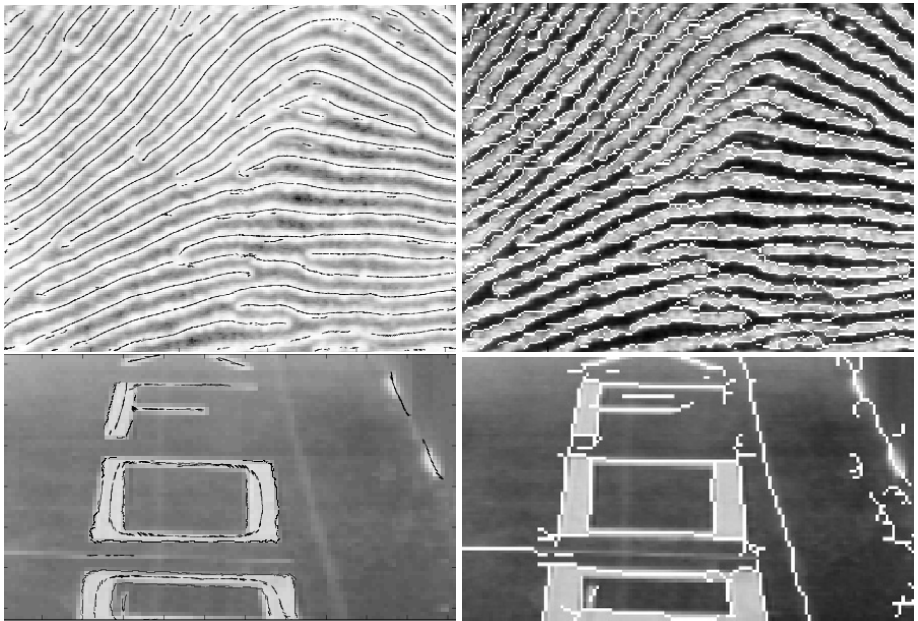


**Fig. 4.** Top: Fingerprint. Bottom: Writing on floor. See text for details

The right of Fig. 3 shows the ridges and valleys found in the synthetic signal of Fig. 2 overlaid in black and white respectively. For clarity the edges were not marked. Note that we have found and marked a range of features which were completely missed by *PC* as shown on the left in Fig. 3. In particular, we have found the relevant ridges and valleys independently of their actual width not only in the regions with sharp transitions, but also in the smoothed region of the image. It is clear that broad ridges and valleys towards the edge of the image are not marked, this is due to the fact that the filters used were not large enough to respond to features of this size. As expected, the edges of these features are detected however. This example also illustrates one of the problems of the method: very fine lines or edges in neighbourhoods with closely spaced features are not detected reliably as shown e.g. in the centre of the image. At these locations, phase is only valid over a very limited range of scales, due to interference from neighbouring features. This is however a property of phase-congruency per se, rather than the fault of *LE*.

In the two images at the top of Fig. 4 the ridges found in an image of a fingerprint are highlighted. The left image shows the output of the *LE* method (for clarity, the edges and valleys were not marked). Despite the noise-levels and variation in width, the exact centres of the ridges have been marked correctly. This means, not only can we detect the ridges, but we can also describe it in terms of width, orientation etc. The right image shows the output of *PC*. As with the other examples, the edges dominate most other features. Additionally, because the features are relatively closely spaced, there is significant interference between neighbouring features, leading to a high level of spurious, noisy responses.

The two images at the bottom of Fig. 4 shows the image of a piece of writing on a floor. Note how the width of the letters gets narrower towards the top of the image (rear of the scene). On the left we see the result of  $LE$ . Despite this considerable variation in width of the lines, all letters were detected correctly. Note however, that the faint lines on the floor have not been marked. This is due to the use of the global hysteresis thresholds  $[0.15, 0.30]$  of the maximum energy amplitude. Since local energy is computed at a local level as the name implies, a future improvement would be to use hysteresis thresholding based on a local rather than a global threshold. The image on the right shows the output of hysteresis thresholded  $PC$ . Once again, where lines are broad enough to have distinct edges, the edges dominate the broad lines.

## 4 Discussion and Conclusions

We have introduced a novel method  $LE$  for computing phase-congruency over the *appropriate* range of scales, rather than averaging over *all* scales. The features obtained using  $LE$  are a great improvement over existing phase-congruency implementations and a further step towards a truly general feature detector.

The correct range of scales can be used to further describe a feature and the position of a feature is computed to subpixel precision. We have demonstrated the usefulness of the new method using both synthetic as well as real images.

## References

1. D. J. Fleet and A. D. Jepson. Stability of phase information. *IEEE Transactions on Pattern Analysis and Machine Intelligence*, 15(12):1253–1268, 1993.
2. William T. Freeman and Edward H. Adelson. The design and use of steerable filters. *IEEE Transactions on Pattern Analysis and Machine Intelligence*, 13(9):891–906, September 1991.
3. A.D. Jepson and D.J. Fleet. Phase singularities in scale-space. *Image and Vision Computing*, 9(5):338–343, 1991.
4. Peter Kovesi. Image features from phase congruency. *Videre: A Journal of Computer Vision Research*, 1(3), 1999.
5. Tony Lindeberg. Edge detection and ridge detection with automatic scale selection. *International Journal of Computer Vision*, 30(2):117–154, 1998.
6. M. Morrone and D. Burr. Feature detection in human vision: a phase dependent energy model. *Proc. Royal Soc. London Bulletin*, pages 221–245, 1988.
7. M. C. Morrone and R. A. Owens. Feature detection from local energy. *Pattern Recognition Letters*, 6:303–313, 1987.
8. A.V. Oppenheim and J.S. Lim. The importance of phase in signals. *Proc. of IEEE 69*, pages 529–541, 1981.
9. Veit U B Schenk. *Visual Identification of Fine Surface Incisions*. PhD thesis, University of Oxford, Dept. of Engineering Science, March 2001.
10. S. Venkatesh and R.A. Owens. On the classification of image features. *Pattern Recognition Letters*, 11:339–349, 1990.

# Robust Estimation of Roughness Parameter in SAR Amplitude Images

Héctor Allende and Luis Pizarro

Departamento de Informática, Universidad Técnica Federico Santa María,  
Casilla 110-V, Valparaíso, Chile  
[{hallende, lpizarro}@inf.utfsm.cl](mailto:{hallende, lpizarro}@inf.utfsm.cl)

**Abstract.** The precise knowledge of the statistical properties of synthetic aperture radar (SAR) data plays a central role in image processing and understanding. These properties can be used for discriminating types of land uses and to develop specialized filters for speckle noise reduction, among other applications. In this work we assume the distribution  $\mathcal{G}_A^0$  as the universal model for multilook amplitude SAR images under the multiplicative model. We study some important properties of this distribution and some classical estimators for its parameters, such as Maximum Likelihood (ML) estimators, but they can be highly influenced by small percentages of ‘outliers’, i.e., observations that do not fully obey the basic assumptions. Hence, it is important to find Robust Estimators. One of the best known classes of robust techniques is that of M estimators, which are an extension of the ML estimation method. We compare those estimation procedures by means of a Monte Carlo experiment.

**Keywords:** Robust Estimation, SAR Images, Speckle Noise, Monte Carlo.

## 1 Introduction

Last decade was marked by the affirmation of SAR images as a tool for earth monitoring. Several studies were made confirming their relevance, where image processing techniques were developed especially devoted to them. Most of the SAR image processing techniques are based on statistical properties of the SAR data, those properties might be used for the development of tools for SAR image processing and analysis, for instance, filters to reduce speckle noise, as well as classification and segmentation algorithms.

There are many statistical models for synthetic aperture radar (SAR) images, among them, the multiplicative model is based on the assumption that the observed random field  $Z$  is the result of the product of two independent and unobserved random fields:  $X$  and  $Y$ . The random field  $X$  models the terrain backscatter and thus depends only on the type of area each pixel belongs to. The random field  $Y$  takes into account that SAR images are the result of a coherent imaging system that produces the well known phenomenon called speckle

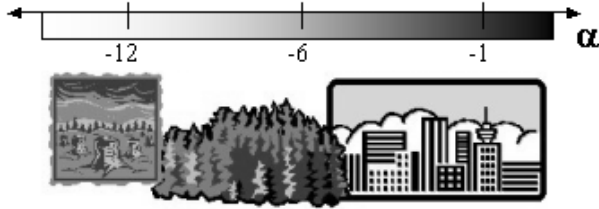


**Fig. 1.** Meaning of the  $\alpha$  parameter of the  $\mathcal{G}_A^0$  distribution in SAR images.

noise and are generated by performing an average of  $L$  independent image looks in order to reduce the speckle effect. This is assuming that  $X$  and  $Y$  are both weak stationary stochastic processes. The last fact is based on the assumption that the speckle noise corresponding to cells of different resolution is generated by the interaction of many independent dispersion points. Speckle refers to a noise-like characteristic produced by coherent systems, including sonar, laser, ultrasound and synthetic aperture radars. It is evident as a random structure of picture elements caused by the interference of electromagnetic waves scattered from surfaces or objects.

There are various ways of modelling the random fields  $X$  and  $Y$ . Classically, both the speckle noise  $Y$  and the backscatter  $X$  have been modelled with a  $\Gamma^{1/2}$  distribution [TCG82]. This parametrization makes the return  $Z$  obey the  $K_A$  distribution. The  $K_A$  distribution fails to model many situations where the return is extremely heterogeneous, besides being computationally cumbersome.

On the other hand, in [FMYS97] was proposed the  $\Gamma^{-1/2}$  distribution to model the amplitude backscatter  $X$ . This new model, when used along with the classical one for the speckle noise yields a new distribution for the return, called  $\mathcal{G}_A^0$ . The advantage of the  $\mathcal{G}_A^0$  distribution over the classical  $K_A$  distribution is that it models very well extremely heterogeneous areas like cities, as well as moderately heterogeneous areas like forests and homogeneous areas like crops.

The  $\mathcal{G}_A^0$  distribution is characterized by as many parameters as the  $K_A$  distribution: the number of looks ( $L$ ), a scale parameter ( $\gamma$ ) and a roughness parameter ( $\alpha$ ). Besides the advantages, this  $\mathcal{G}_A^0$  distribution proposal has the same nice interpretational properties than the  $K_A$  distribution has, see [FMYS97]. The parameter  $\gamma$  is a scale parameter and is related to the relative power between reflected and incident signals. The parameter  $\alpha$  is of particular interest in many applications, since it is directly related to the roughness of the target. The figure 1 shows how the  $\alpha$  parameter can be used to make inferences about the type of land seen from a particular SAR image.

The figure 2 is representative of the typical complexity of real SAR images, where we can distinguish several types of roughnesses or textures. This work discusses the problem of estimating the parameters of the  $\mathcal{G}_A^0$  distribution for the case of single looks that arises in image processing and analysis with large and small samples. Two typical estimation situations arise in image processing



**Fig. 2.** SAR Image of a Chilean copper mine.

and analysis, namely large and small samples, being the latter considered in this work. Statistical inference with small samples is subjected to many problems, mainly bias, large variance and sensitivity to deviations from the hypothesized model. The last issue is also a problem when dealing with large samples.

Robustness is a desirable property for estimators, since it allows their use even in situations where the quality of the input data is below the level accepted by standards [HRRS86]. Most image processing and analysis procedures, like classification, restoration, segmentation, use field data. A situation where this occurs is when ground controls points (GCP) appear in the SAR image, which are essential for data calibration. These points produce a return higher than the rest of the image, for this reason they are called corner reflectors. If the data from a corner reflector is included in the SAR image, the estimation procedure is non-robust, and the results may be completely unreliable.

In Section 2 a brief explanation of the  $\mathcal{G}_A^0$  distribution is presented together with the classical maximum likelihood estimators of its parameters. Section 3 presents the robust M-estimators, which are capable to deal with non perfect data. In section 4 estimation procedures are compared by means of a Monte Carlo study.

## 2 The $\mathcal{G}_A^0$ Distribution

The general (multilook) form of the density, which characterizes the  $\mathcal{G}_A^0(\alpha, \gamma, L)$  distribution is given in [FMY97] as

$$f(z) = \frac{2L^L \Gamma(L - \alpha)}{\gamma^\alpha \Gamma(L) \Gamma(-\alpha)} \frac{z^{2L-1}}{(\gamma + Lz^2)^{L-\alpha}}, \quad z > 0, \quad (1)$$

where  $\alpha < 0$  is referred to as the roughness parameter,  $\gamma > 0$  is a scale parameter and  $L \geq 1$  is the number of looks. The number of looks is controlled in the early generation steps of the image, and is known beforehand or it is estimated using extended homogeneous targets. This parameter remains constant over all the image. This law was originally devised to describe extremely heterogeneous clutter, and lately proposed and assessed as an universal model for speckled imagery in [MFJB01]. Improved estimation using bootstrap for the parameters  $\alpha$  and  $\gamma$  of this distribution is presented in [CFS02], while the robustness for the  $L = 1$  case is studied in [BLF02] using M-estimators.

The single look case is of particular interest, and it will be considered here, since it describes the noisiest images. The distribution of interest is, then, characterized by the density

$$f(z; (\alpha, \gamma)) = -\frac{2\alpha}{\gamma^\alpha} \frac{z}{(\gamma + z^2)^{1-\alpha}} = -\frac{2\alpha z}{\gamma(1 + z^2/\gamma)^{1-\alpha}}, \quad z > 0, \quad (2)$$

with  $-\alpha, \gamma > 0$ . This distribution will be denoted  $\mathcal{G}_A^0(\alpha, \gamma)$ , whose cumulative distribution function is given by

$$F(z; (\alpha, \gamma)) = 1 - (1 + z^2/\gamma)^\alpha. \quad (3)$$

Several parameter estimation techniques are available, being the most remarkable ones those based on sample moments and maximum likelihood. The  $k$ -th order moment of the  $\mathcal{G}_A^0(\alpha, \gamma)$  distribution is given by

$$E(z^k) = \begin{cases} \gamma^{k/2} \frac{k\Gamma(k/2)\Gamma(-\alpha-k/2)}{2\Gamma(-\alpha)} & \text{if } -\alpha > k/2 \\ \infty & \text{otherwise.} \end{cases} \quad (4)$$

The maximum likelihood estimator of  $\theta = (\alpha, \gamma)$ , based on the observations  $z_1, z_2, \dots, z_N$ , is defined as the value  $\hat{\theta}_{ML}$  which maximizes  $\prod_{i=1}^N f_\theta(z_i)$ , or equivalently as the value  $\hat{\theta}_{ML}$  which minimizes  $-\sum_{i=1}^N \ln f_\theta(z_i)$ . Equating to zero the derivates of this function, we get

$$\sum_{i=1}^N s(z_i; \theta) = 0, \quad (5)$$

where  $s(z; \theta) = (s_1(z; \theta), s_2(z; \theta))^T = \left( \frac{\partial}{\partial \theta} \ln f_\theta(z), \frac{\partial}{\partial \theta_2} \ln f_\theta(z) \right)^T$  denotes the vector of likelihood scores. Explicitly, the score functions are:

$$\begin{cases} s_1(z; \theta) = \frac{1}{\alpha} + \ln \left( 1 + \frac{z^2}{\gamma} \right), \\ s_2(z; \theta) = \frac{-\alpha}{\gamma} - \frac{1-\alpha}{\gamma-z^2}. \end{cases} \quad (6)$$

From equations (5) and (6), following [MFJB01], we derive, for the single look case, the ML-estimator  $\hat{\theta}_{ML} = (\hat{\alpha}_{ML}, \hat{\gamma}_{ML})$  as:

$$\begin{cases} \hat{\alpha}_{ML} = -\left(\frac{1}{N} \sum_{i=1}^N \ln \left(1 + \frac{z_i^2}{\hat{\gamma}_{ML}}\right)\right), \\ \hat{\gamma}_{ML} = \left[\left(1 + \frac{1}{N} \sum_{i=1}^N \ln \left(1 + \frac{z_i^2}{\hat{\gamma}_{ML}}\right)\right) \frac{1}{N} \sum_{i=1}^N \left(\hat{\gamma}_{ML} + z_i^2\right)^{-1}\right]^{-1}. \end{cases} \quad (7)$$

### 3 Robust Estimators

As previously seen, the parameter  $\alpha$  of the  $\mathcal{G}_A^0$  distribution is defined for negative values. For near zero values of  $\alpha$ , the sampled area presents very heterogeneous gray values, as is the case of urban areas. As we move to less heterogeneous areas like forests, the value  $\alpha$  diminishes, reaching its lowest values for homogeneous areas like crops. This is the reason why this parameter is regarded as a roughness or texture parameter (recall figure 1).

Corner reflectors can be considered as additive outliers in SAR imagery, as physical equipment in the sensed area that return most of the power they receive. The image in these areas is dominated by the biggest possible values admitted by the storage characteristics, and their effect is typically limited to a few pixels. Corner reflectors are either placed on purpose, for image calibration, or due to man-made objects, such as highly reflective urban areas, or the result of double-bounce reflection [OQ98].

In the reality, it is necessary to use procedures that behave fairly well under deviations from the assumed model, these procedures are called robust. One of the best known classes of robust estimators are M-estimators, which are a generalization of the ML-estimators [AGV01]. In this work, we use them to estimate the parameters of the  $\mathcal{G}_A^0$  distribution. These estimators, based on a sample  $z_1, z_2, \dots, z_N$ , are defined as the solution  $\hat{\theta}_M$  of the estimation equation

$$\sum_{i=1}^N \psi(z_i; \theta) = 0. \quad (8)$$

Equation (8) is a generalization of the maximum likelihood equation (5).  $\psi$  is a composition of functions of the score function (6) and the Huber's function given by  $\psi_b(y) = \min\{b, \max\{y, -b\}\}$ , where  $b$  is called tuning parameter. The importance of the  $\psi$  functions is that they truncate the score of the influential observations in the likelihood equation. Many theoretical results concerning the asymptotic and the robustness properties of M-estimators are available in the literature [AGV01], [BLF02], [RV02]. On the other hand, it is possible consider M-estimators with asymmetrical influence functions [AFGP03], which depend on underlying distributions.

With the purpose of obtain unbiased and optimal estimators, we redefine the M-estimator  $\hat{\theta}_M$  as a solution of the equation

$$\sum_{i=1}^N \psi[s(z_i; \theta) - c] = 0, \quad (9)$$

where the Fisher consistency is accomplished by means of the  $c$  function, which is defined implicitly as

$$\int_{-\infty}^{\infty} \psi[s(z_i; \theta) - c] dF_{\theta}(z) = 0. \quad (10)$$

The rule for determining the tuning parameter  $b$ , is to require the asymptotic relative efficiency of the M-estimator, with respect to the ML-estimator in the model without outliers, ranges from 90% to 95% [MR96].

## 4 Simulation Study

A Monte-Carlo study is performed in order to assess the behavior of the robust M-estimator with respect to ML-estimator. It is considered that each sample is contaminated by a fraction  $\epsilon$  of outliers of magnitude  $v$ . Hence, a sample  $z_1, z_2, \dots, z_N$  obey the following data contamination model:

$$F(z; (\alpha, \gamma); \epsilon; v) = (1 - \epsilon) F(z; (\alpha, \gamma)) + \epsilon \delta_v(z), \quad (11)$$

where  $\delta_v(z) = 1_{[v; +\infty)}(z)$  with  $v$  a very large value as compared to most of the sample data, which is chosen as a factor of the sample mean.

A numerical comparison is made over  $R = 1000$  different samples generated by means of (11). Using (4), the parameter  $\gamma$  depends on a given value for  $\alpha$  through  $E(Z) = 1$ . The methodology used to compute the estimates was that described in [MR96].

Tables 1 and 2 show, for both the ML-estimator and the M-estimator, for several values of the roughness parameter  $\alpha = \{-1, -6, -10\}$ , the sample mean and the mean square error, defined as  $E[\hat{\alpha}] = R^{-1} \sum_{i=1}^R \hat{\alpha}_i$  and  $mse[\hat{\alpha}] = E[\hat{\alpha} - \alpha]^2$  respectively, where  $\alpha$  is the true value of the parameter and  $\hat{\alpha}$  is its estimator. The simulation study considers the estimates in several situations, varying the sample size  $N = \{9, 25, 49, 81\}$  and the contamination level  $\epsilon = \{0\%, 1\%, 5\%, 10\%\}$ . Also, the outliers were considered as a factor of the sample mean of  $v = 15$ .

The results in the tables show that both ML and M estimators exhibit almost the same behavior when the sample is exempt of contamination. Besides, when the sample size grows both methods show better estimates. Nevertheless, when the percentage of outliers increases, the ML-estimators lose accuracy faster than M-estimators. Summarizing, M-estimators show either equal or better performance than ML-estimators in all cases.

## 5 Conclusions

In this paper different estimators were used to estimate the roughness parameter  $\alpha$  of the  $\mathcal{G}_A^0$  distribution for the single look case. In a Monte-Carlo study, classical ML-estimators were compared with robust M-estimators, where the latter were better performance than the former in all considered situations, as varying the sample size and varying the contamination level.

**Table 1.** Numerical comparison of the mean between ML and M estimators, for varying  $\alpha$ , sample size and contamination level  $\epsilon$ , with  $v = 15$ .

$\epsilon$	$N$	$\alpha = -1$		$\alpha = -6$		$\alpha = -10$	
		$E[\hat{\alpha}_{ML}]$	$E[\hat{\alpha}_M]$	$E[\hat{\alpha}_{ML}]$	$E[\hat{\alpha}_M]$	$E[\hat{\alpha}_{ML}]$	$E[\hat{\alpha}_M]$
0%	9	-1.162	-1.140	-6.508	-6.507	-9.997	-9.997
	25	-1.048	-1.041	-6.265	-6.264	-10.295	-10.295
	49	-1.013	-1.004	-6.114	-6.114	-10.175	-10.175
	81	-1.014	-1.012	-6.060	-6.060	-10.123	-10.123
1%	9	-0.682	-0.920	-1.818	-2.801	-2.298	-3.343
	25	-0.837	-0.943	-3.245	-4.355	-4.432	-5.957
	49	-0.894	-0.957	-4.042	-4.937	-5.961	-7.379
	81	-0.922	-0.967	-4.464	-5.190	-6.808	-8.036
5%	9	-0.668	-0.909	-1.691	-2.592	-2.130	-3.080
	25	-0.767	-0.900	-2.701	-3.787	-3.695	-5.080
	49	-0.796	-0.905	-3.112	-4.146	-4.286	-5.700
	81	-0.802	-0.908	-3.156	-4.183	-4.346	-5.771
10%	9	-0.638	-0.886	-1.553	-2.365	-1.957	-2.798
	25	-0.701	-0.861	-2.147	-3.111	-2.835	-3.975
	49	-0.681	-0.830	-2.136	-3.110	-2.877	-4.066
	81	-0.666	-0.814	-2.068	-3.052	-2.752	-3.941

**Table 2.** Numerical comparison of the mean square error between ML and M estimators, for varying  $\alpha$ , sample size and contamination level  $\epsilon$ , with  $v = 15$ .

$\epsilon$	$N$	$\alpha = -1$		$\alpha = -6$		$\alpha = -10$	
		$mse[\hat{\alpha}_{ML}]$	$mse[\hat{\alpha}_M]$	$mse[\hat{\alpha}_{ML}]$	$mse[\hat{\alpha}_M]$	$mse[\hat{\alpha}_{ML}]$	$mse[\hat{\alpha}_M]$
0%	9	0.218	0.218	5.316	5.320	6.036	6.036
	25	0.046	0.052	1.647	1.647	3.636	3.636
	49	0.021	0.024	0.782	0.782	2.189	2.189
	81	0.014	0.016	0.444	0.444	1.415	1.415
1%	9	0.114	0.078	17.546	10.494	59.377	44.509
	25	0.045	0.042	7.815	3.225	31.439	17.195
	49	0.026	0.024	4.219	1.637	17.194	8.014
	81	0.016	0.014	2.777	1.051	11.325	4.962
5%	9	0.124	0.072	18.690	12.054	62.132	48.426
	25	0.074	0.045	11.444	5.793	40.882	26.000
	49	0.058	0.031	9.027	4.165	34.517	20.700
	81	0.050	0.022	8.690	3.835	33.603	19.612
10%	9	0.148	0.078	19.958	13.810	64.993	52.696
	25	0.110	0.052	15.480	9.404	52.624	38.525
	49	0.114	0.047	15.378	8.976	51.837	36.880
	81	0.120	0.046	15.725	9.086	53.149	37.672

As concluding remarks, one could say that the  $\mathcal{G}_A^0$  distribution is a quite good model for SAR data, whose parameters have relevant and immediate physical interpretation. Estimators of these parameters can be used in various ways, for

instance, as classification and segmentations tools of SAR images or development of digital filters, among others.

In future works, a simultaneous estimation of the  $\alpha$  and  $\gamma$  parameters will be considered. Also, M-estimators will be studied for the multilook case.

**Acknowledgements.** This work has been supported in part by the Fondecyt Grant 1010101, and in part by Universidad Técnica Federico Santa María DGIP Grant 240224. The authors are thankful to anonymous reviewers for the valuable comments and suggestions.

## References

- [AFGP03] Allende, H., Frery, Alejandro C., Galbiati, J., Pizarro, L.: M-Estimators with Asymmetric Influence Functions: the  $\mathcal{G}_A^0$  Distribution Case. Technical Report 2003/5, Departamento de Informática, Universidad Técnica Federico Santa María. Submitted to Computational Statistics and Data Analysis.
- [AGV01] Allende, H., Galbiati, J., Vallejos, R.: Robust image modelling on image processing. *Pattern Recognition Letters*, **22** (2001) 1219–1231.
- [BLF02] Bustos, O. H., Lucini, M. M., Frery, A. C.: M-estimators of roughness and scale for  $\mathcal{G}_A^0$ -modelled SAR imagery. *EURASIP Journal on Applied Signal Processing*, **1** (2002), 105–114.
- [CFS02] Cribari-Neto, F., Frery, A. C., Silva, M. F.: Improved estimation of clutter properties in speckled imagery. *Computational Statistics and Data Analysis*, **40** (4) (2002) 801–824.
- [FMYS97] Frery, A. C., Müller, H. J., Yanasse, C. C. F., Sant’Anna, S. J. S.: A model for extremely heterogeneous clutter. *IEEE Transactions on Geoscience and Remote Sensing*, **35**(3) (1997) 648–659.
- [HRRS86] Hampel, F., Ronchetti, E., Rousseeuw, P., Stahel, W.: *Robust Statistics*. Wiley, New York (1986)
- [MFJB01] Mejail, M. E., Frery, A. C., Jacobo-Berlles, J., Bustos, O.H.: Approximation of distributions for SAR images: proposal, evaluation and practical consequences. *Latin American Applied Research*, **31** (2001) 83–92.
- [MR96] Marazzi, A., Ruffieux, C.: Implementing M-estimators for the gamma distribution. In *Robust Statistics, Data Analysis and Computer Intensive Methods* (R. Helmut, ed.). Lecture Notes in Statistics **109** (1996). Springer-Verlag, Berlin.
- [OQ98] Oliver, C., Quegan, S.: *Understanding Synthetic Aperture Radar Images*. Artech House, London (1998)
- [RV02] Rousseeuw, P. J., Verboven, S.: Robust estimation in very small samples. *Computational Statistics and Data Analysis*, **40** (4) (2002) 741–758.
- [TCG82] Tur, M., Chin, K.C., Goodman, J.W.: When is the speckle noise multiplicative? *Applied Optics*, **21** (1982) 1157–1159.

# Two New Scale-Adapted Texture Descriptors for Image Segmentation

Miguel Angel Lozano and Francisco Escolano

Robot Vision Group

Departamento de Ciencia de la Computación e Inteligencia Artificial

Universidad de Alicante, Spain

{malozano, sco}@dccia.ua.es

<http://www.rvg.ua.es>

**Abstract.** In texture segmentation it is key to develop descriptors which provide acceptable results without a significant increment of their temporal complexity. In this contribution, we propose two probabilistic texture descriptors: polarity and texture contrast. These descriptors are related to the entropy of both the local distributions of gradient orientation and magnitude. As such descriptors are scale-dependent, we propose a simple method for selecting the optimal scale. Using the features at their optimal scale, we test the performance of these measures with an adaptive version of the ACM clustering method, in which adaptation relies on the Kolmogorov-Smirnov test. Our results with only these two descriptors are very promising.

## 1 Introduction

In the past, there have been many approaches to texture description: Gabor filters [6], quadrature filters [7], co-occurrence matrices [8], wavelets [9], second-order eigenstructure [10], and so on. As texture is not a pointwise feature but relies on a local neighborhood, there are two key problems to consider: (i) Find a good descriptor, like the ones listed above, and (ii) determine the optimal size of the neighborhood where such a descriptor is computed. In this paper, we address these two questions starting by revising two measures, polarity and texture contrast, which rely on the second-order eigenstructure. Later, we redefine such measures in terms of entropy and propose a way of automatically selecting the optimal scale of the measures. Finally, we test these measures in segmentation.

The polarity  $P_\sigma$  at a given pixel is defined in [1] as a measure of the extent to which the gradient vectors  $\nabla I$  in a certain neighborhood defined by the scale  $\sigma$  all point in the same direction:

$$P_\sigma = \frac{|E_+ - E_-|}{E_+ + E_-}, \quad (1)$$

where  $E_+$  and  $E_-$  are defined as follows

$$E_+ = \sum_{x,y} G_\sigma(x,y)[\nabla I \cdot \hat{n}]_+ \quad (2)$$

and

$$E_- = \sum_{x,y} G_\sigma(x,y) [\nabla I \cdot \hat{n}]_- , \quad (3)$$

where  $G_\sigma(\cdot)$  is a Gaussian smoothing kernel with variance  $\sigma^2$ ,  $[.]_+$  and  $[.]_-$  are the rectified positive and negative parts of their arguments, and  $\hat{n}$  is a unit vector perpendicular to  $\phi$ , the dominant direction in the neighborhood, which in turn is the argument of the principal eigenvector of the second-moment matrix

$$M_\sigma = \sum_{x,y} G_\sigma(x,y) (\nabla I) (\nabla I)^T . \quad (4)$$

Consequently,  $E_+$  and  $E_-$  measure, respectively, how many gradient vectors in the window defined by  $G_\sigma(\cdot)$  are in the positive side and negative side of  $\phi$ , and  $P_\sigma \in [0, 1]$ , will be close to zero when  $E_+ \approx E_-$ , that is, when we have a flow pattern; and it will be close to the unit for instance when  $E_- \approx 0$  and  $E_+ \neq 0$ , that is, when we have an edge.

## 2 Entropy-Related Measures

### 2.1 Probabilistic Polarity

As the underlying idea of polarity is to vanish as many different orientations appear in the neighborhood, we propose an alternative definition of polarity which does not rely on the eigenstructure of the local gradient, but on the structure of the distribution of local gradient orientations. Thus, the probability  $p_\sigma(z)$  of a given orientation  $z \in [0, 2\pi)$  at scale  $\sigma$  is defined by

$$p_\sigma(z) = \frac{\sum_{x,y} \delta(z - \theta(x,y)) W(x,y)}{\sum_w \{ \sum_{x,y} \delta(w - \theta(x,y)) W(x,y) \}} , \quad (5)$$

where

$$W(x,y) = G_\sigma(x,y) \|\nabla I\| , \theta(x,y) = \arctan I_y/I_x ,$$

that is, the weight of a given pixel in the neighborhood and the local orientation of its gradient, respectively. After quantizing the interval  $[0, 2\pi)$  into  $N$  bins of size  $\Delta = 2\pi/N$ , we define the empirical probability  $h_\sigma(k)$ , with  $k = 0, 1, \dots, N-1$ , which accumulates all probabilities  $p_\sigma(z) \in [k\Delta, (k+1)\Delta)$ . Using the latter  $N$ -component histogram, the entropy of the distribution is approximated by

$$H_\sigma = \sum_{k=0}^{N-1} h_\sigma(k) \log h_\sigma(k) . \quad (6)$$

In principle, the inverse entropy  $1 - H_\sigma$  is a good measure of polarity because it tends to the unit when all gradient vectors in the neighborhood have a similar orientation (minimal entropy, corresponding to a peaked distribution) and it vanishes when many different orientations appear (maximal entropy, corresponding to a uniform distribution). However, the inverse entropy decays too

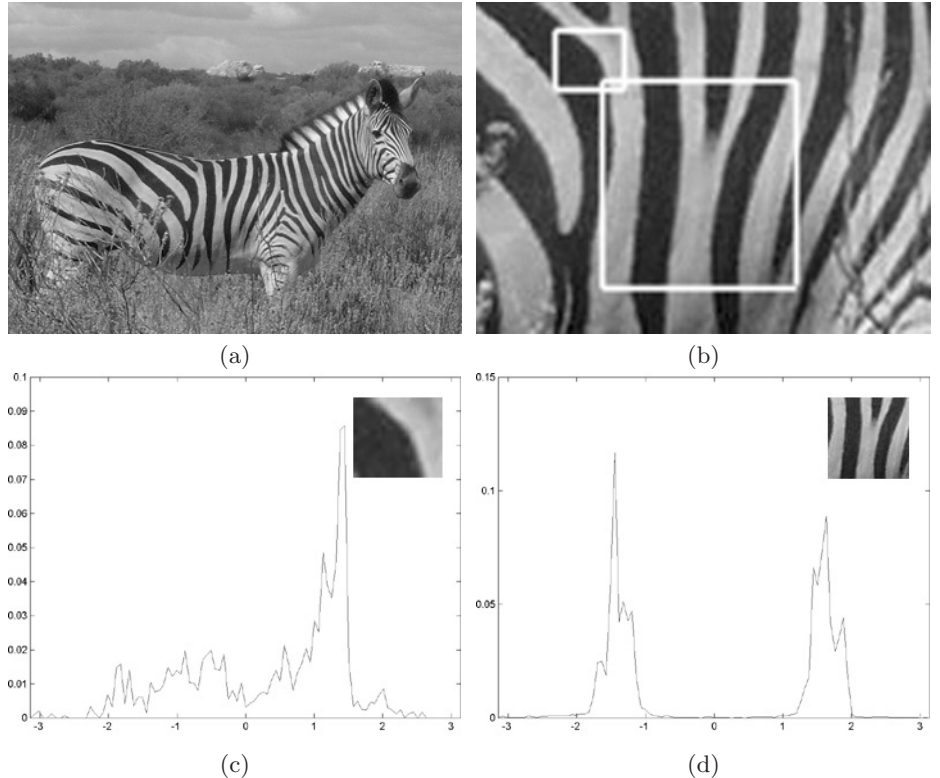


**Fig. 1.** (a) Input image (b) Zoom showing both a polarized and a de-polarized zone (c) Histogram of the polarized zone:  $1 - H_\sigma = 0.2568$ ,  $P_\sigma = 0.2568$  (d) Histogram of the de-polarized zone:  $1 - H_\sigma = 0.3722$ ,  $P_\sigma = 0.0079$

slowly as the neighborhood is de-polarized. Particularly, a distribution with two closer peaks (or one wider peak) and one with the same peaks but distant, have similar entropies. Consequently, the latter measure captures the number of peaks but not their separation, and such a separation, in addition to the appearance of new peaks, occurs when we progressively de-polarize a texture edge while incrementing the size of its neighborhood. For instance, Fig. 1 polarity vanishes when two significant peaks appear in a de-polarized zone, whereas inverse entropy even gets incremented in the same zone.

In order to capture peak separation we re-define polarity in terms of the expression

$$P_\sigma = 1 - \sum_{k=0}^{N-1} h_\sigma(k) \sum_{r=-\lfloor N/2 \rfloor}^{\lfloor (N-1)/2 \rfloor} g(r) h_\sigma([k+r]_N), \quad (7)$$

where each component  $h_\sigma(k)$  is no longer weighted by its logarithm but by the result of convolving it with a kernel  $g(.)$  defined in such a way that we ensure that  $P_\sigma \in [0, 1]$ . For a linear choice we have that

$$g(r) = ar = \frac{n}{\sum_{i=-\lfloor N/2 \rfloor}^{\lfloor (N-1)/2 \rfloor} |i|} r. \quad (8)$$

We also assume a cyclic histogram, because the orientation domain is also cyclic, where  $[k+r]_N \in \{0, 1, \dots, N-1\}$  refers to  $(k+r) \bmod N$ .

## 2.2 Probabilistic Texture Contrast

Another texture feature is texture contrast. In [1] it is defined by  $2\sqrt{\lambda_1 + \lambda_2}$ , where  $\lambda_1$  and  $\lambda_2$  are the two eigenvalues of the second-moment matrix  $M_\sigma$ . Following the probabilistic rationale above, and in order to define texture contrast we consider the local intensity probabilities

$$q_\sigma(z) = \frac{\sum_{x,y} \delta(z - I(x,y)) G_\sigma(x,y)}{\sum_w \{\sum_{x,y} \delta(w - I(x,y)) G_\sigma(x,y)\}}, \quad (9)$$

and proceed to quantize the normalized range of intensities  $[0, 1]$  yielding the  $M$ -component histogram  $c_\sigma(i)$ ,  $i = 0, 1, \dots, M-1$ , which accumulates the probabilities  $q_\sigma(z)$ . Texture contrast must be close to the unit when we have two peaks at maximal distance, must vanish when the intensity distribution is peaked. Again, we find that the entropy is not a proper choice and we replace it by

$$C_\sigma = \sum_{i=0}^{M-1} c_\sigma(i) \sum_{j=0}^{M-1} d(|i-j|) c_\sigma(j), \quad (10)$$

where  $d(\cdot)$  is defined in such a way that  $C_\sigma \in [0, 1]$ . For the simple linear case, we have that  $d(r) = 2r/(N-1)$ . With the latter definition we consider peak separation through a weighted correlation.

## 3 Scale Selection

As the probabilistic measures defined above depend on the scale, we are interested in a method for selecting them optimal scale for both of them. Few previous work has been done in this area [2]. However we follow the approach described in [1] and scale selection relies on polarity analysis. We will consider a sequence of scales  $\{\sigma_k\}$ , with  $k = 0, 1, 2, \dots, S$  and we will start by computing the polarity at the lower scale  $P_{\sigma_0}$  and assuming that the tentative optimal scale is  $\sigma_0$ . Thereafter, we will test whether an increment of scale is acceptable.

An increment of scale will always contribute either to de-polarize the pixel, or to leave its polarity unchanged. Consequently, given  $P_{\sigma_k}$ , and assuming that the temporary optimal scale is  $\sigma_k$ , we compute  $P_{\sigma_{k+1}}$ , and test whether the decrement  $P_{\sigma_k} - P_{\sigma_{k-1}} = \nabla P_{\sigma_k} \leq 0$  is *low enough*. If  $\nabla P_{\sigma_{k+1}} < \nu \nabla P_{\sigma_k}$ , with  $\nu \in [0, 1]$  then we will accept  $\sigma_{k+1}$  as a new temporary optimal scale because such scale de-polarizes the pixel significantly. Otherwise, we will assume that the optimal scale  $\sigma^* = \sigma_k$ . The coefficient  $\nu$  modulates the decrement needed to

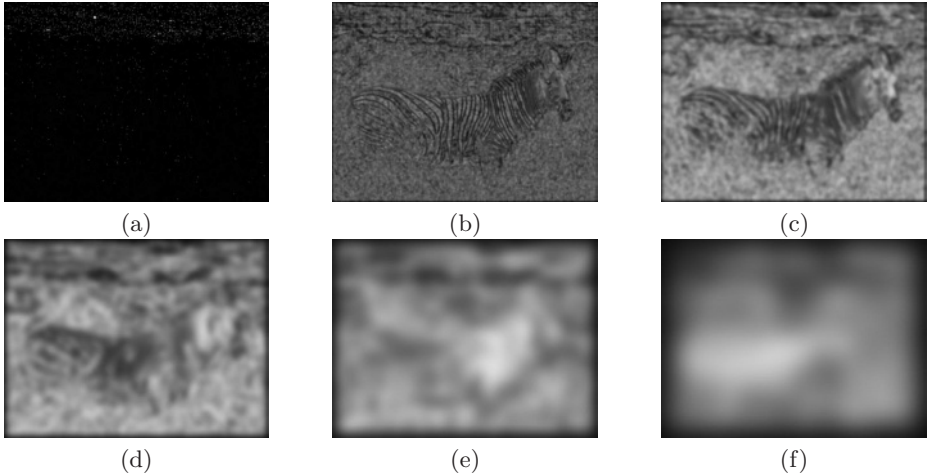


**Fig. 2.** Polarity at different scales. (a)  $\sigma = 0.25$  (b)  $\sigma = 0.5$  (c)  $\sigma = 1.0$  (d)  $\sigma = 2.0$  (e)  $\sigma = 4.0$  (f)  $\sigma = 8.0$

increment the scale: When  $\nu \rightarrow 0$  we will change easily of scale, whereas with  $\nu \rightarrow 1$  we will be more restrictive.

In our experiments we have the set of scales  $\{0.25, 0.5, 1.0, 2.0, 4.0, 8.0\}$  and we have set  $\nu = 0.5$ , that is, we set  $S = 6$ . In Fig. 2, we show the polarity at those scales, and in Fig. 3 we show some results of optimal scale selection: Optimal-scale image, with dark greys corresponding to low scales and light greys corresponding to high scales, polarity image at the optimal scale (each pixel with its optimal polarity  $P_{\sigma^*}$ ), and texture-contrast image at the optimal scale (each pixel with its optimal texture contrast  $P_{\sigma^*}$ ). Low polarity appears in light grey and high polarity appears in dark grey. On the other hand, low texture contrast appears in dark grey and high contrast appears in light grey.

## 4 Adaptive Segmentation

### 4.1 EM Algorithm for Asymmetric Clustering

Given  $N$  image blocks  $x_1, \dots, x_N$ , each one having associated  $M$  possible features  $y_1, \dots, y_M$ , the Asymmetric Clustering Model (ACM) maximizes the log-likelihood

$$L(I, q) = - \sum_{i=1}^N \sum_{\alpha=1}^K I_{i\alpha} KL(p_{j|i}, q_{j|\alpha}) , \quad (11)$$

where:  $p_{j|i}$  encodes the individual histogram, that is, the empirical probability of observing each feature  $y_j$  given  $x_i$ ;  $q_{j|\alpha}$  is the prototypical histogram associated to one of the  $K$  classes  $c_\alpha$ ;  $KL(., .)$  is the symmetric Kullback-Leibler divergence; and  $I_{i\alpha} \in \{0, 1\}$  are class-membership variables.

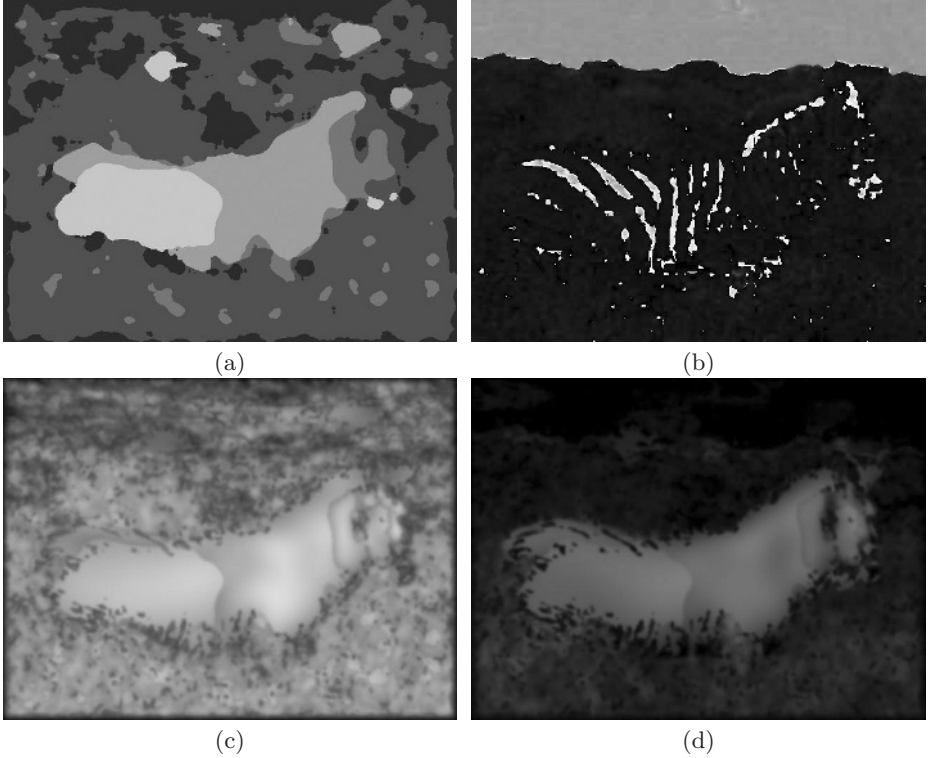


**Fig. 3.** Texture features. (a) Optimal-scale image (b) Hue component (c)  $P_{\sigma^*}$  image (d)  $C_{\sigma^*}$  image

The following EM algorithm was proposed in [3][5]. The E-step consists of estimating the expected membership variables  $\hat{I}_{i\alpha} \in [0, 1]$  given the current estimation of the prototypical histogram  $q_{j|\alpha}$ :

$$\hat{I}_{i\alpha}^{t+1} = \frac{\hat{\rho}_\alpha^t \exp\{-KL(p_{j|i}, \hat{q}_{i|\alpha})/T\}}{\sum_{\beta=1}^K \hat{\rho}_\beta^t \exp\{-KL(p_{j|i}, \hat{q}_{i|\beta})/T\}}, \quad (12)$$

where

$$\hat{\rho}_\alpha^t = \frac{1}{N} \sum_{i=1}^N \hat{I}_{i\alpha}^t,$$

that is, the probability of assigning any block  $x_i$  to class  $c_\alpha$  at iteration  $t$ , and  $T$  the temperature, a control parameter which is reduced at each iteration.

In the M-step, given the expected membership variables  $\hat{I}_{i\alpha}^{t+1}$ , the prototypical histograms are re-estimated as follows:

$$\hat{q}_{j|\alpha}^{t+1} = \sum_{i=1}^N \pi_{i\alpha} p_{j|i}, \text{ where } \pi_{i\alpha} = \frac{\hat{I}_{i\alpha}^t}{\sum_{k=1}^N \hat{I}_{k\alpha}^t}, \quad (13)$$

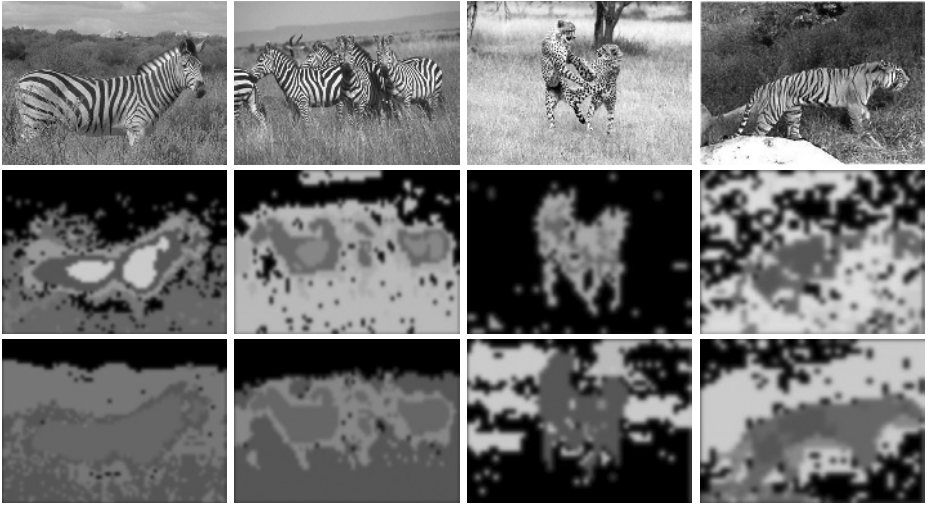


**Fig. 4.** Segmentation results. Top: Input images; Middle: Only texture features; Bottom: Including color features.

that is, the prototype consists of the linear combination of all individuals  $p_{j|i}$  weighted by the  $\pi_{i\alpha}$ .

In a previous work we have introduced an adaptation mechanism for ACM [4] where we start with a high number of classes and class-fusion relies on considering whether the dispersion of the resulting class is lower than the sum of the dispersion of the two fusing classes. Herein we propose a method relying on the Kolmogorov-Smirnov test. As in our early work, we assume that the iterative process is divided in epochs, and our adaptation mechanism consists of starting by a high number of classes  $K_{max}$  and then reducing such a number, if proceeds, at the end of each epoch. At that moment we consider all the  $K(K - 1)/2$  pairs of prototypes, where  $K$  is the current number of classes. For all these pairs we compute the Kolmogorov-Smirnov statistic with  $\alpha = 0.05$ , resulting from comparing their histograms, and then we select the pair  $\hat{q}_{j|\alpha}$  and  $\hat{q}_{j|\beta}$  with the lower statistic. If with such a statistic, the test does not succeed (both histograms are not different enough) we decide to fuse their classes.

Then, we compute the fused prototype  $\hat{q}_{j|\gamma}$  by applying Equation 13 and considering that  $I_{i\gamma} = I_{i\alpha} + I_{i\beta}$ , that is

$$\hat{q}_{j|\gamma} = \sum_{i=1}^N \pi_{i\gamma} p_{j|i} . \quad (14)$$

And then a new epoch starts, and proceeds until convergence is declared.

## 4.2 Segmentation Results

Dividing our input color images in blocks of  $8 \times 8$  pixels, we consider a histogram of 16 components both for polarity, texture contrast and hue component, and thus number of features is 32 when only texture is considered, and 48 when color is included. In Fig. 4 we compare the segmentation results obtained with and without color information, and assuming  $K_{max} = 10$ . In many cases texture features are enough for yielding acceptable segmentations, although color features usually improve the quality of the results.

## 5 Conclusion

In this paper we have proposed two entropy-related texture features, obtained through automatic scale selection. In order to demonstrate their utility in segmentation we have used them in an adaptive version of the ACM clustering model, and the obtained results were promising.

## References

1. Carson, C., Belongie, S., Greenspan, H., Malik, J. : Blobworld: Image segmentation using Expectation-Maximization and its application to image querying. *IEEE Trans. on Pattern Analysis and Machine Intelligence* (2002)
2. Gårding, J., Lindeberg, T.: Direct Computation of Shape Cues Using Scale-Adapted Spatial Derivative Operators. *International Journal of Computer Vision*, Vol 17, N 2 (1996) 163–191.
3. Hofmann, T., Puzicha, J.: Statistical Models for Co-occurrence Data. MIT AI-Memo 1625 Cambridge, MA (1998)
4. Lozano, M.A., Escolano, F.: Recognizing Indoor Images with Unsupervised Segmentation and Graph Matching. In: Garijo, F.J., Riquelme, J.C., Toro, M.(eds.): *Advances in Artificial Intelligence – Iberamia 2002. Lecture Notes on Artificial Intelligence*, Vol. 2527. Springer-Verlag, Berlin Heidelberg New York (2002) 933–942.
5. Puzicha, J.: Histogram Clustering for Unsupervised Segmentation and Image Retrieval. *Pattern Recognition Letters*, 20, (1999) 899–909.
6. A. Jain and F. Farrokhina. Unsupervised texture segmentation using gabor filters. *Pattern Recognition* 23, pp. 1167–1186, 1991.
7. H. Knutsson and G. Granlund. Texture analysis using two-dimensional quadrature filters. In *IEEE Computer Society Workshop on Computer Architecture for Pattern Analysis and Image Database Management*, pages 206–213, 1983.
8. Gotlieb C.C., Kreyszig. Texture descriptors based on cooccurrence matrices. *Comp. Vision, Graph. and Image Proc.* 51: 70–86, 1990.
9. Unser M., Texture Classification and Segmentation Using Wavelet Frames. *IEEE Trans. Image Processing*, 4, 11, 1549–1560, 1995.
10. N. Sochen, R. Kimmel and R. Malladi. A General Framework for Low Level Vision. *IEEE Trans on Image Processing*, Vol. 7, No. 3, pp. 310–318, 1998.

# Topological Query in Image Databases

Mihaela Scuturici, Jérémie Clech, and Djamel A. Zighed

Laboratoire ERIC – Université Lumière Lyon2

5, avenue Pierre Mendès-France – 69676 Bron cedex – France

{mscuturi, jcglech}@eric.univ-lyon2.fr; zighed@univ-lyon2.fr

**Abstract.** In this paper we propose a topological<sup>1</sup> model for image database query using neighborhood graphs. A related neighborhood graph is built from automatically extracted low-level features, which represent images as points of  $\mathbb{R}^p$  space. Graph exploration correspond to database browsing, the neighbors of a node represent similar images. In order to perform query by example, we define a topological query model. The query image is inserted in the graph by locally updating the neighborhood graph. The topology of an image database is more informative than a similarity measure usually applied in content based image retrieval, as proved by our experiments.

## 1 Introduction

The information retrieval in image databases is still a challenge due to the fact that frequently the users seek semantically similar images while an image database provides similarity only at low level, by using characteristics computed from pixel values. Visual information retrieval implies the use of an index. There are two approaches to image indexing [9]: visual content based and annotation based. Visual content indexing supposes that the visual information of each image (given by pixel values) is resumed to a feature vector containing low-level features (color histogram, textural features, form features). Consequently, the query process is reduced to neighbors research inside the representation space [1]. A similarity measure is defined to identify the neighborhood. In this context, the query will start with a sample image. Annotation based indexing suppose that each image is annotated by using a keyword, a label, more generically a text. Each image is described by keywords, expressing the image semantic. The user searching an image having a certain semantic can express his request as a list of keywords. A similarity measure can also be useful to identify a set of images expressing the query semantic.

In this paper we are interested in the concept of “neighbor – neighborhood” of an image in an image database. Most of the search algorithms in image databases pro-

<sup>1</sup> The word “topology” denotes here the relationships between elements linked together in a system. It is not used neither in terms of mathematical study of the geometric properties of figures that are independent of size or shape and are preserved through deformations, twisting and stretching, nor in terms of family of subsets (family of all open subsets of a mathematical set, including the set itself and the empty set, which is closed under set union and finite intersection) [12].

pose to seek the  $k$  nearest neighbors (kNN) [7] of an image by using a similarity measure [12]. For instance, the QBIC system [3], in its implementation for the Hermitage Museum<sup>2</sup> always returns 12 nearest neighbors of the sketch presented by the user as query in the color search or layer search engine. In some situations, as illustrated in the section 2, the kNN algorithm produces surprising results compared to user expectations. In section 3, we introduce a more appropriate neighborhood representation model: the topological neighborhood. Section 4 describes the topological query model. We will discuss its advantages and its limitations. In section 5 we present experimental results on an image database where the two query methods (kNN and topological neighborhood) are compared on the basis of recall and precision indicators. Concluding remarks and future works are presented in section 6.

## 2 Anomalies and Assumptions of the kNN

In the context of navigation in an image database, the system is typically driven by the user. Then, it would be more convenient for him that the system follows the human cognitive model. Since the user expects to see together sets of similar images, the system must guarantee a stability of those sets and we assume that the symmetry is one of the required conditions. Unfortunately, in some situations the kNN model does not verify this condition. We will illustrate this by an example based on a 2NN algorithm. Given the 6 images in Figure 1, their distance matrix, based on L1 color feature (sum of image pixel values) is computed in Table 1.a.

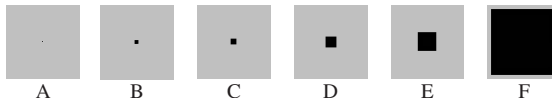


**Fig. 1.** Images list for 2NN example

**Table 1.** The distance matrix (a), the two nearest neighbors in the case of 2NN algorithm (b) and the geometrical neighbors (c). On each row, the black cells indicate the elements (columns) neighbors of the row element

Distance	A	B	C	D	E	F	
A	-						
B	0.01	-					
C	0.03	0.02	-				
D	0.09	0.08	0.06	-			
E	0.20	0.19	0.16	0.11	-		
F	0.58	0.57	0.55	0.50	0.40	-	

2 Nearest Neighbors	A	B	C	D	E	F	
A							
B							
C							
D							
E							
F							

Topological Neighbors	A	B	C	D	E	F	
A							
B							
C							
D							
E							
F							

(a)

(b)

(c)

The user runs a query giving the image D as request. The system returns the images B and C (Table 1.b). Then, the user expects to find D at least when he runs the query with the image C as request. However, the system returns A and B. These query results are then surprising and even doubtful for the user. The property of non-symmetry of the kNN have been underlined several times, but seldom criticized as leading to cognitively erroneous results.

<sup>2</sup> <http://www.hermitagemuseum.org/cgi-bin/db2www/qbicSearch.mac/qbic?selLang=English>

To avoid kNN to produce this adverse effect, the points have to be relatively uniformly distributed on the representation space. This assumption seems too strong for us and difficult to keep. We can manage this limitation by using the topological models which are symmetric (Table 1 c).

### 3 Topological Models

We consider a dataset  $\Omega$  composed by  $n$  images. Each image is represented as a  $p$  dimensional numerical feature vector  $X(i) = (X_1(i), X_2(i), \dots, X_j(i), \dots, X_p(i)) \in \mathbb{R}^p$ .

Therefore each image is a point in  $\mathbb{R}^p$  space. A distance measure can be computed for each couple of images, for instance Euclidian or Cosine distance.

The *topology* of a dataset defines how data points are connected to one another. Topology can be represented by a graph, where data points  $X_j$  for  $j \in [1, \dots, p]$  represent nodes and the neighborhood relationships denote edges connecting nodes.

Each image is represented as a node in a neighborhood graph. The neighbors of a node represent similar images. Two points (images) are neighbors and connected by an edge if they verify a specific binary relationship. Many models may be used: Delaunay triangulation, relative neighborhood graph, Gabriel graph or minimum spanning tree. We choose the relative neighborhood graph representation for the image database for the reasons presented below. The binary relationship defined by each graph is symmetric. For more details about all the graph models and their properties see [8].

**Relative Neighborhood Graph** is a related graph where two points  $\alpha$  and  $\beta$  are neighbors if they verify the following property: the lune, corresponding to the dashed area in Figure 2, must be empty. Two points  $\alpha$  and  $\beta$  are connected by an edge if the following equation is verified:

$$d(\alpha, \beta) \leq \text{Max}(d(\alpha, \gamma), d(\beta, \gamma)), \forall \gamma \in \Omega \setminus \{\alpha, \beta\} \quad (1)$$

where  $d(a, b)$  is a distance between  $a, b \in \Omega$  in  $\mathbb{R}^p$ .

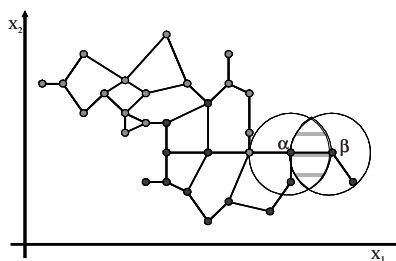


**Fig. 2.** Example of a Relative Neighborhood Graph in  $\mathbb{R}^2$

### 3.1 Topological Neighborhood

Content based image retrieval is based on similarity measures. In this context, image retrieval requires an understanding of the notion of image *neighborhood*. The neighborhood is generally defined as the set of all points belonging to a given set whose distances from a given point are less than a given positive number. In order to decide which points are neighbors, the *geometrical neighborhood* or the *topological neighborhood* have to be examined. A geometrical neighborhood includes all the points within a certain distance from the sample point. kNN algorithm uses the geometrical neighborhood. A topological neighborhood contains all the points within a certain number of edges from the desired sample point. Two points are linked by an edge only if they satisfy the criteria presented before and does not necessarily involves a minimal distance.

### 3.2 Choice of the Topological Neighborhood

All neighborhood graphs model the similarity between images represented as points in  $\mathbb{R}^p$  space. The relative neighborhood graph is a superset of minimal spanning tree and a subset of Delaunay triangulation [11]. We preferred the relative neighborhood graph because the definition of minimal spanning tree and for Delaunay triangulation is a global one. Therefore, each time we add a new image on the database, or we present a new image in order to perform similar image retrieval, the entire graph needs to be recalculated. Relative neighborhood graph and Gabriel graph are equivalent, they both have local definitions and we can easily insert new points in the graph, without redefining it. The Gabriel graph has more edges than relative neighborhood graph but in practice the computing time is equivalent. In our tests we used the relative neighborhood graph.

The related neighborhood graph is built in  $\mathbb{R}^p$  space. For  $p \geq 3$  the visual representation can be projected into the  $\mathbb{R}^2$  space using, for example, the principal components analysis or phylogenetic trees [5]. This representation is an alternative to Kohonen maps [6]. It can also be directly built from a given plane, like the first factorial plane if this one preserves the major part of information.

## 4 Topological Query

Given a query image  $I$ , and an image database, the user wants to find a set of similar images. When applying  $k$ NN algorithm,  $k$  images are returned, closest in distance with the query image  $I$ . Setting the value of  $k$  represents another drawback of the kNN approach, in addition to the non-symmetry. Each image has a variable number of neighbors, therefore we can distinguish two situations: either to *limit* the returned results at  $k$  items if the query image has more than  $k$  neighbors in the target database or to *force* the system to return  $k$  images if the query image has less than  $k$  neighbors in the target database.

Table 2 shows the distance matrix for eight images (presented in Figure 3) belonging to three semantic categories (“plants”, “fountain” and “mountain”). If we use a query

image similar to A (“plants”), intuitively the system should return A, B and C. If we set the value of  $k$  to 2, we will obtain only two results, say A and B. Another query has to be performed to obtain the C image, even if it is very similar with the two others. On the other hand, if  $k$  value is set to 3 and the query image is similar to D (“fountain”), the system will return D, E and also another image whose distance is closest from the query image. The distance matrix in our example shows H as the second nearest neighbor of the D image, therefore the user will obtain a “mountain” picture, visually not similar with the query image representing a fountain.

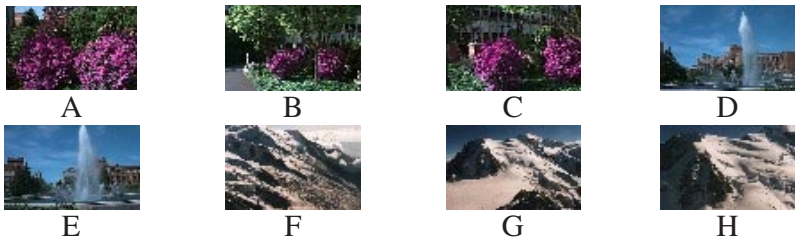


**Fig. 3.** Image list for three semantic categories: plants (A, B and C), fountain (D and E) and mountain (F, G and H)

**Table 2.** Distance matrix using the Euclidean distance and 15 color and textural features projected on the two first principal components

Distance	A	B	C	D	E	F	G	H
A	-							
B	2.35	-						
C	2.09	0.50	-					
D	15.44	13.91	14.42	-				
E	14.73	13.32	13.82	1.11	-			
F	8.54	9.11	9.39	11.95	10.88	-		
G	10.44	10.36	10.75	9.19	8.08	3.10	-	
H	10.59	10.19	10.62	7.80	6.71	4.25	1.41	-

The neighborhood graph we propose is build as in Figure 4-a by using color and textural features of images.

A visual exploration of the neighborhood graph shows that in this example the three clusters correspond to semantic classes. Distances between nodes in the neighborhood graph are a good representation of the visual similarity between images.

When a query image I is presented to the system, the following algorithm is applied:

1. Calculate the  $p$  low-level features corresponding to the representation space  $\mathbb{R}^p$ ;
2. Calculate the distances<sup>3</sup> between the new point and all the existing points;
3. Insert the new point in the neighborhood graph by verifying the criteria specified in section 3.

The advantages of this method are: first, the neighborhood graph is locally updated, it is not entirely rebuilt. Second, the user can browse the neighborhood graph and parse all the neighbors of the query image. The number of neighbors is not fixed as in the

<sup>3</sup> We considered the Cosine distance, but other distances may be used as well.

case of kNN algorithm where exactly  $k$  points are returned as query result. Third, the neighborhood relationship defined by RNG is symmetrical and more appropriated for the browsing process, as shown in section 2.

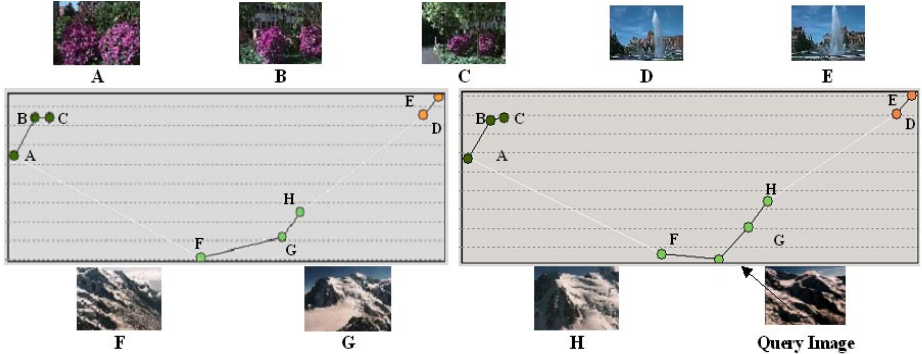


**Fig. 4.** The relative neighborhood graph. The nodes have different colors representing semantic categories. On left (4-a), without the Query Image ; included on right (4-b)

Figure 4-b presents an example of topological query. The new image is inserted in the neighborhood graph and the user can browse all of its neighbors. A new mountain image is used as query image (it does not belong to the database, but very similar with the other mountain images in the image database).

## 5 Experimentation

In our experiments we used a set of 259 images divided between six main categories, extracted from the Ground Truth Database<sup>4</sup> (University of Washington). We used predefined image categories as semantic information. We considered the following categories: “Arboregreens”, “Australia”, “Cherries”, “SwissMountains”, “Greenlake” and “SpringFlowers”. We used two categories of features automatically extracted from images: color features (normalized L1 and L2, predominant color) and textural features (the 14 features defined by Haralick in [4]). The numerical features may represent the whole image or objects inside the image. The features we used here are all global features. In a future work we will perform image segmentation and also use shape features on segmented regions.

### 5.1 Comparison Protocol

For a given representation space, we compare the coherence of a neighborhood in a related neighborhood graph (RNG) with the coherence of  $k$  nearest neighbors (kNN) of an image. To evaluate this coherence, RNG and kNN are compared in a classification context. Classification performances are usually measured in the term of the

<sup>4</sup> <http://www.cs.washington.edu/research/imagedatabase>

classic information retrieval notions of recall and precision [10]. Test images are spread over six semantic categories used to compute recall and precision. We specify that the relative neighborhood graph is built from low-level features only.

The recall and precision are defined as follows:

$$\text{recall} = \frac{\text{number of categories found and correct}}{\text{total number of categories correct}} \quad \text{precision} = \frac{\text{number of categories found and correct}}{\text{total number of categories found}}$$

We evaluate the capabilities of the graph used as a classifier, in order to find the category of the query image. To do that, the query image is inserted in the graph structure and the category is decided by its neighbor votes inversely weighted by the length of the edges. The length of the edges represent the distance between two linked nodes. Even if the nodes are neighbors in terms of distances, in RNG two nodes are linked by an edge if they verify the condition (1) presented in section 3. For the kNN classifiers, the category is decided by the votes of  $k$  nearest neighbors of the unknown image, inversely weighted by the distance. In our tests we have used the Cosine distance since it is scale invariant and then does not require to normalize the data. The number of neighbors ( $k$ ) for kNN vary from 1 to 5 and classifier results are compared after a 10 folds cross validation.

## 5.2 Results and Discussion

The Figure 5 shows the results obtained from our experiments. We observe that RNG outperforms the different kNN models. For kNN we have performed tests up to 30 neighbors ( $k=30$ ). Our results show that the success rate, the precision and recall in the case of RNG are superior of the best kNN results, obtained for 4NN. We can explain the better results for RNG by examining the category prediction process. In the case of kNN, exactly  $k$  neighbors will vote the query image category. In the case of RNG, the number of neighbors is adaptative according to the topology.

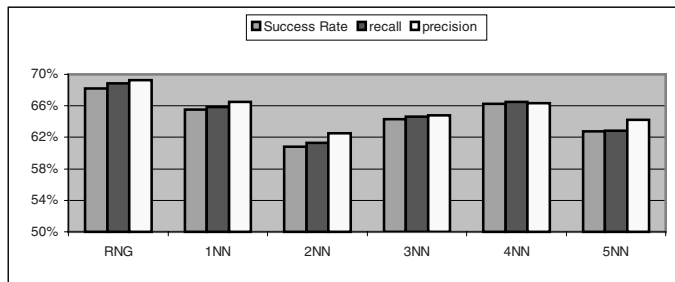


**Fig. 5.** Relative Neighbor Graph versus k-Nearest Neighbor ( $k$  varies from 1 to 5)

## 6 Conclusions and Future Work

Search algorithms in image databases usually return  $k$  nearest neighbors (kNN) of an image according to a similarity measure. This approach presents some anomalies and is based on assumptions that are not always satisfied. We have examined the causes of

these anomalies and we have concluded that image query models have to exploit topological properties rather than the similarity degree. The knowledge inside an image database lies on the topological structure of a set of points (images) rather than on the distance between them. We have proposed a topological representation method based on neighborhood graphs built on automatically extracted image features. On the other side, MPEG 7 standard is set up gradually and query models could be built on MPEG 7 descriptors of multimedia data. Automatic extraction of semantic descriptors of audio-visual content still remains a problem, as well as their pertinent exploitation. The topological model proposed in this paper offers an exploratory analysis of MPEG 7 descriptors and also allow to use these descriptors in a query process. In a future work we will use MPEG 7 files as data source for our topological model. We also work on a faster retrieval algorithm using related neighborhood graphs.

## References

1. P. Aigrain, H. Zhang, and D. Petkovic. “Content-based representation and retrieval of visual media: A state-of-the-art review”. In *Multimedia tools and applications*, vol. 3, pp. 179–202. Kluwer Academic Publishers, 1996.
2. J.-P. Barthélémy & A. Guénoche, *Trees and proximity representations*, New York : John Wiley & Sons, 1991.
3. C. Faloutsos, R. Barber, M. Flickner, J. Hafner, W. Niblack, D. Petkovic, and W. Equitz. “Efficient and Effective Querying by Image Content”. *Journal of Intelligent Information Systems*, vol. 3, no. 3, pp. 231–262, 1994.
4. Haralick, R. M. Shanmugan, K., Dinstein, I. *Texture features for image classification*. IEEE Transactions Systems, Man and Cybernetics, Novembre 1973, vol. 3, pp.610–621.
5. D.M. Hillis, M.W. Allard and M.M. Miyamoto. *Analysis of DNA sequence data: phylogenetic inference*. *Methods Enzymol* 1993;224:456–87.
6. T. Kohonen, *Self-Organizing Maps*. Berlin/Heidelberg, Springer, 1995, vol. 30.
7. T.M. Mitchell, *Machine Learning*. Computer Science, New York, 1997.
8. F. Preparata, M. I. Shamos. “Computational Geometry. An introduction”. Springer-Verlag, New-York, 1985.
9. Y. Rui, T.S. Huang and S-F. Chang. “Image retrieval: current techniques, promising directions and open issues”. *Journal of Visual Communication and Image Representation*, Vol. 10, no. 4, pp. 39–62, April 1999.
10. J.R. Smith. “Image retrieval evaluation”. In *IEEE Workshop on Content-based Access of Image and Video Libraries (CBAIVL'98)*, pp. 112–113, June 1998.
11. G.T. Toussaint. “The Relative Neighborhood Graph of a Finite Planar Set”. *Pattern Recognition*, 12(4), pp. 261–268, 1980.
12. R.C. Veltkamp and M. Tanase. “Content-based image retrieval systems : A survey.” Technical report UU-CS-2000-34, Department of Computing Science, Utrecht University, October 2000.
13. E. Weisstein. “The CRC Concise Encyclopedia of Mathematics”. CRC Press, 1998.

# Reconstructing 3D Objects from Silhouettes with Unknown Viewpoints: The Case of Planar Orthographic Views

Andrea Bottino<sup>1</sup>, Luc Jaulin<sup>2</sup>, and Aldo Laurentini<sup>1</sup>

<sup>1</sup>Dipartimento di Automatica ed Informatica, Politecnico di Torino,  
Corso Duca degli Abruzzi, 24 – 10129 Torino, Italy  
`{andrea.bottino,aldo.laurentini}@polito.it`

<sup>2</sup>LISA  
Avenue Notre Dame du Lac, 62, 49 000 Angers, France  
`jaulin@univ-angers.fr`

**Abstract.** 3D shapes can be reconstructed from 2D silhouettes by back-projecting them from the corresponding viewpoints and intersecting the resulting solid cones. This requires knowing the position of the viewpoints with respect to the object. But what can we say when this information is not available? This paper provides a first insight into the problem, introducing the problem of understanding 3D shapes from silhouettes when the relative positions of the viewpoints are unknown. In particular, the case of orthographic silhouettes with viewing directions parallel to the same plane is thoroughly discussed. Also we introduce sets of inequalities, which describe all the possible solution sets and show how to calculate the feasible solution space of each set.

## 1 Introduction

A central problem in computer vision is understanding the shape of 3D objects from various image features. Many algorithms are based on occluding contours or silhouettes. The main approach is volumetric, and consists in building the volume  $\mathbf{R}$  shared by the regions  $C_i$  (see Fig. 1) obtained by back-projecting each silhouette  $S_i$  from the corresponding viewpoint. This simple reconstruction technique is called *Volume Intersection* (VI) (see [1], [4], [8], [9], [10]). It requires the 3D positions of silhouettes and viewpoints. However, in several practical situations this information is not available and therefore VI cannot be performed. Even if this simple reconstruction technique is not possible, we would like to get the best of the available information.

Before entering the problem, we briefly review some definitions relevant to our problem. First, the concept of *visual hull* of an object [6], which is the object that can be obtained by VI using all the viewpoints that belong to a viewing region completely enclosing the original object without entering its convex hull. It is also the largest object that produces the same silhouettes as the given object. A point of the surface of the reconstructed object  $\mathbf{R}$  is an *hard point* [6] if it belongs to any object that produces the same silhouettes from the same viewpoints. The concept of hard point allows

stating a necessary condition for the reconstruction to be optimal, and is at the basis of interactive VI algorithms [3].

In the following, for brevity, we will use the expression “set of silhouettes” to specify a set of silhouettes together with the position of the corresponding viewpoint with respect to each silhouette. These data, allow constructing a solid cone for each silhouette, but not positioning the cones in the 3D space. To understand how the 3D shape is related to such a set of silhouettes, two main questions can be considered. The first question is: given a set of silhouettes, does an object exist able to produce them? We will call *compatible* a set of silhouettes if the same object can generate them. An object able to produce a compatible set of silhouettes will be said to be compatible with the set. The second question is the main practical issue: how can we find one or more compatible objects given a compatible set of silhouettes, as that produced by a real object? We will present a set of results that provide a first insight into the problem.

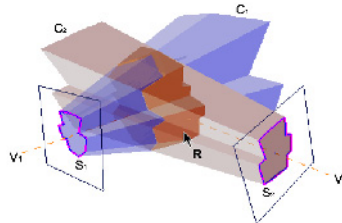


**Fig. 1.** The volume intersection technique

## 2 Compatibility of Orthographic Silhouettes of 3D Objects

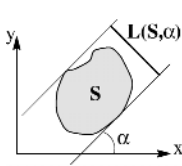
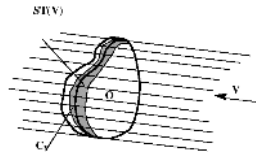
In the rest of this paper we will restrict ourselves to consider simply connected 3D objects and their orthographic projections. This approximates the practical case of objects small with respect to their distance from the camera. The reader is referred to [12] for a proof of the statements of this section.

First, we will investigate the compatibility of two silhouettes. Let  $S$  be a 2D orthographic silhouette of a 3D object. Let us project orthographically  $S$  along a direction in the plane of  $S$ . The 1D silhouette obtained depends on the angle  $\alpha$  that the chosen direction makes with the  $x$  axis of a coordinate system fixed with respect to  $S$  (Fig. 2). Let  $L(S, \alpha)$  be the length of the 1D silhouette of  $S$ . The following statement holds.

*Proposition 1. A necessary and sufficient condition for two orthographic silhouettes  $S_1$  and  $S_2$  to be compatible is that two angles  $\alpha_1$  and  $\alpha_2$  exist such that  $L(S_1, \alpha_1) = L(S_2, \alpha_2)$ .*

What happens when we have to deal with more silhouettes? That is, how can we find if three or more silhouettes are compatible? Clearly, we have that:

*Proposition 2. A necessary condition for a set of silhouettes to be compatible is that all pairs of silhouettes of the set are compatible.*

**Fig. 2.** The 1D silhouette  $L(S, \alpha)$ **Fig. 3.** The strip  $ST(V)$  and the curve  $C_v$ 

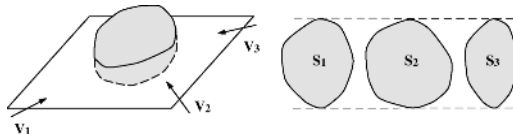
However, in general, to be compatible in pairs is not sufficient for a set of silhouettes to be compatible (see [12]). A necessary and sufficient condition for the compatibility of more than two silhouettes can be found considering a property of the reconstructed object **R**. Let us consider one of the silhouettes involved in the process, the corresponding viewing direction **V** and the cylinder circumscribed to the object **O** made of lines parallel to this direction (Fig. 3). Each line of this cylindrical surface must share with the surface of **O** at least one point. These points form a curve  $C_v$ . This curve belongs to an annular surface, a strip  $ST(V)$  of variable width, which is what is left of the original circumscribed cylinder after the various intersections. During the reconstruction process, this annular strip cannot be interrupted; at most it can reduce to a curve with zero width. In this case, the curve consists of hard points. Therefore we can formulate the following condition for the VI algorithm to be feasible:

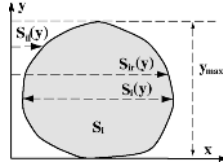
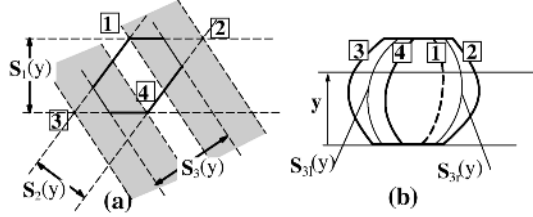
*Proposition 3. A necessary and sufficient condition for a set of silhouettes to be compatible is that it be possible to find viewpoints such that no annular strip of the reconstructed object is interrupted.*

In the next sections this condition will be used for constructing algorithms both for verifying the compatibility of a set of silhouettes and reconstructing compatible 3D objects.

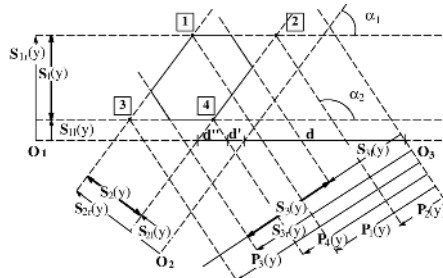
### 3 Silhouettes with Viewing Directions Parallel to a Plane

In this section we deal with a particular case of the general problem, where all viewing directions are parallel to the same plane (Fig. 4). Clearly, all silhouettes have the same height and the same plane must support all cylinders obtained by back-projection.

**Fig. 4.** Viewing directions parallel to the same plane

**Fig. 5.** Notations used for a silhouette.**Fig. 6.** (a) A case where  $S_3(y)$  is compatible with  $S_1(y)$  and  $S_2(y)$  in a horizontal plane. (b) The condition for the compatibility of the whole silhouettes.

We consider first the compatibility of three silhouettes  $S_1$ ,  $S_2$  and  $S_3$ . Each planar silhouette  $S_i$  is defined, for  $0 \leq y \leq y_{\max}$  by two curves  $S_{il}(y)$  and  $S_{ir}(y)$  (see Fig. 5). For simplicity, let us consider mono-valued functions. Also let  $S_i(y) = S_{ir}(y) - S_{il}(y)$ . Let us consider a horizontal plane corresponding to a value of  $y$  between 0 and  $y_{\max}$ , and its intersection with the three cylinders obtained by back-projecting the silhouettes. Let us consider in this plane the arrangement of the 2D silhouettes  $S_1(y)$ ,  $S_2(y)$ ,  $S_3(y)$  and of the viewpoints  $V_1, V_2, V_3$  shown in Fig. 6(a). It is not difficult to see that proposition 3 requires that the two lines projecting the endpoints of  $S_3(y)$  along the direction  $V_3$  must lie inside the two areas highlighted in Fig. 6(a). For the whole silhouettes to be compatible, this must hold for all  $y$ . For the reconstruction to be possible,  $S_3(y)$  must lie between the two leftmost curves, in this case the projections of the vertices **3** and **4**, and  $S_3(y)$  must lie between the two rightmost curves, the projections of the vertices **1** and **2**.

**Fig. 7.** The intersections in a horizontal plane

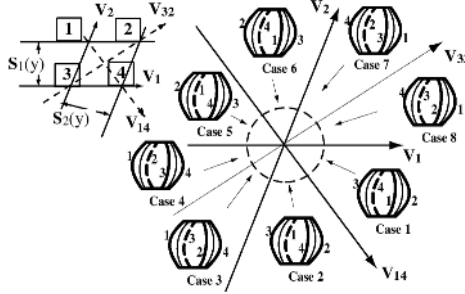


**Fig. 8.** The eight intersection cases

To derive the set of inequalities that define for this case feasible intersection parameters, let us inspect in more detail the intersection in a horizontal plane (Fig. 7). Let  $O_1, O_2, O_3$  be the intersections of the axes  $y$  of the coordinate system of each silhouette with this plane. Intersecting  $S_1(y)$  and  $S_2(y)$  requires to fix an angle, let it be  $\alpha_1$ . Intersecting also  $S_3(y)$  requires choosing two more parameters: the angle  $\alpha_2$  and a distance, let it be  $d$  (see Fig. 8).  $d$  is the distance between two points lying on the line projecting  $O_1$  along the direction  $V_1$ . The first is the intersection of this line with the line projecting  $O_2$  along  $V_2$ , and the second is the intersection with the line projecting  $O_3$  along  $V_3$ . Thus, to find feasible solutions we must search the 3-dimensional space  $[\alpha_1, \alpha_2, d]$ . Let  $P_1(y), P_2(y), P_3(y)$  and  $P_4(y)$  be the distances from  $O_3$  of the orthographic projections of the vertices of the parallelogram onto the line supporting  $S_3(y)$ . The compatibility condition for the three silhouettes is expressed by the following inequalities:

$$\begin{aligned} S_{3r}(y) &\geq P_4(y), \quad S_{3r}(y) \leq P_3(y), \quad S_{3l}(y) \geq P_2(y) \\ S_{3l}(y) &\leq P_1(y), \quad P_4(y) \geq P_1(y) \end{aligned} \quad (1)$$

In (1), the purpose of the fifth inequality is to characterize the case just analysed, let it be Case 1. Seven other cases, determined by the direction of  $V_3$  with respect to  $V_1, V_2$ , and the directions of the diagonals  $V_{14}$  and  $V_{32}$  of the parallelogram, are possible, each producing different sets of inequalities (see Fig. 8). For each case, a possible orthographic projection onto the plane of  $S_3$  of the edges of the object produced by the first intersection is shown with thick lines. The boundaries of  $S_3$  are the thin lines.

#### Four Silhouettes

Let us consider Case 1 and add a fourth silhouette  $S_4$ . In each horizontal plane  $S_1(y), S_2(y)$  and  $S_3(y)$  produce a polygon with six vertices and three pairs of parallel edges (Fig. 9). The new intersection is defined by two more parameters, the angle  $\alpha_3$  between  $V_1$  and  $V_4$  and the distance  $d_3$ , measured, as  $d$ , along the line that projects  $O_1$  from  $V_1$ . Satisfying the condition of Proposition 3 requires, in each horizontal plane, to cut away two opposite vertices, without eliminating completely the edges that meet at these vertices. By orthographically projecting the six vertices onto the plane of  $S_4$  we obtain six curves. For the new intersection to be feasible, the boundaries  $S_{4l}(y)$  and  $S_{4r}(y)$  of  $S_4$  must lie in the areas bounded by the two leftmost and the two rightmost curves respectively.

Various sets of inequalities result, depending on the direction of  $V_4$ . First, let us distinguish two cases (case **(a)** and **(b)** in the left of Fig. 9) related to the directions which determines the leftmost and rightmost vertices (**5** and **7** for case **(a)** and **7** and **5** for **(b)**). In each case we have four sub-cases for the leftmost and rightmost strips where  $S_{4l}$  and  $S_{4r}$  must lie (see right part of Fig. 9). The inequalities corresponding to each sub-case are easily written. For instance, for the sub-case **a<sub>1</sub>** it is:

$$P_5(y) \leq S_{3l}(y) \quad S_{3l}(y) \leq P_4(y)$$

$$P_1(y) \leq S_{3r}(y) \quad S_{3r}(y) \leq P_7(y)$$

$$P_4(y) \leq P_6(y) \quad P_8(y) \leq P_1(y)$$

where  $P_i(y)$  are the projections of the points  $i(y)$  onto the plane of  $S_4$ . As before, the last two inequalities guarantee that the inner boundaries of these areas are actually  $P_6$  and  $P_8$ .

Summarizing, each set of inequalities that defines feasible intersection parameters for four silhouettes contains 11 inequalities (the five inequalities related to the first three silhouettes and six new inequalities also referring to  $S_4$ ). As for the number of sets of inequalities, we have 8 cases for three silhouettes, 3 pairs of opposite vertices and 8 cases for each pair, and thus 192 sets each containing 11 inequalities.

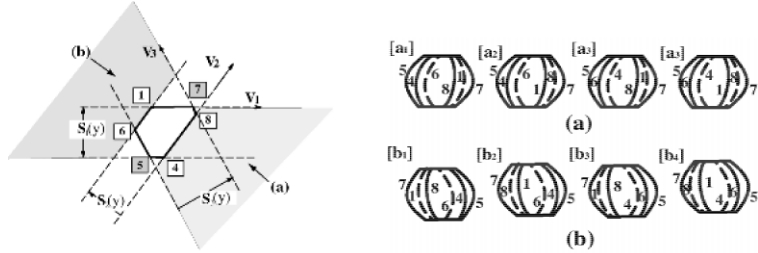


**Fig. 9.** Cases (a) and (b) and the 8 sub-cases

#### Five or More Silhouettes

The previous discussion about the fourth silhouette does hold for any further silhouette. In fact, we must always cut a pair of opposite vertices without deleting completely the edges converging at these edges. It follows that each new silhouette adds two parameters, seven inequalities for each case. Thus, for  $n$  silhouettes, the number of parameters is  $2n-3$ , and the number of inequalities  $6(n-3)+5$  ( $n \geq 3$ ). Each new silhouette adds 8 sub-cases for each pair of opposite vertices. For the  $n$ -th silhouette, the pair of vertices are  $n-1$ . Let  $N_c(n)$  be the number of sets of inequalities for  $n$  silhouettes. For  $n > 3$  it is:  $N_c(n) = 8(n-1)N_c(n-1)$ . Therefore we must face an exponential growth of the number of cases.

## 4 Writing the Sets of Inequalities

The inequalities discussed in the previous section allow to answer, in a particular case, both question raised in the introduction: finding objects compatible with a set of compatible silhouettes, and understanding if an (artificial) set of silhouettes is

compatible. We have developed an algorithm for automatically writing the sets of inequalities, which works on the following basis. In this section we will renumber the silhouette starting from  $S_0$ , and not  $S_1$ , in order to handle easily the indices of the. The axes of the reference system are aligned with the axis of the projection of  $S_0$  on the plane. Let's assume, without loss of generality, that  $V_0$  is parallel to the  $y$  axis of the reference system and the line supporting  $S_0$  is parallel to the  $x$  axis. The origin of the reference system corresponds with the intersection of the projections of  $\mathbf{O}_0$  along  $V_0$  and  $\mathbf{O}_1$  along  $V_1$  on the plane. The position of the  $i^{\text{th}}$  silhouette is determined by two parameters,  $d_i$  and  $\alpha_i$ , where  $d_i$  is the distance between the projection onto the  $y$  axis of the  $i^{\text{th}}$  origin  $\mathbf{O}_i$  along  $V_i$  and the origin (hence  $d_0=d_1=0$ ), and  $\alpha_i$  is the angle between  $V_i$  and  $V_0$  ( $\alpha_0=0$ ). We assume that the angle is positive if  $V_0 \times V_i$  has the same verse of  $x \times y$ ; it also follows that  $V_i = (\sin(\alpha_i), -\cos(\alpha_i))$ . Let  $C_j$  be the vertices of the polygon resulting from intersecting  $S_0$  and  $S_1$ . The equations of the first 4 vertices (Fig. 10) are:

$$C_1 = (S_{0l}, S_{0l} / \sin(\alpha_1) - S_{0l} / \tan(\alpha_1)), \quad C_2 = (S_{0r}, S_{0r} / \sin(\alpha_1) - S_{0r} / \tan(\alpha_1))$$

$$C_3 = (S_{1r}, S_{1r} / \sin(\alpha_1) - S_{1r} / \tan(\alpha_1)), \quad C_4 = (S_{0l}, S_{1r} / \sin(\alpha_1) - S_{0l} / \tan(\alpha_1))$$

The sets of inequalities previously introduced can be written in terms of the distances from the origin along the  $y$  axis of the projections of the vertices of the parallelogram and of  $S_{il}$  and  $S_{ir}$  along the viewing direction of the  $i^{\text{th}}$  silhouette. For each projection, the lines passing through the vertices of the polygons have equations  $C_j + V_i t$  and their intersections ( $P_{ij}$ ) with the  $y$  axis of the reference system are given by  $P_{ij} = c_{yi} + c_{xi} / \tan(\alpha_i)$ . Now, let  $d_{il}$ ,  $d_{ir}$  be the projections on the  $y$  axis of  $S_{il}$  and  $S_{ir}$ . It follows that:

$$d_{il} = d_i + S_{il}(y) / \sin(\alpha_i), \quad d_{ir} = d_i + S_{ir}(y) / \sin(\alpha_i)$$

Projecting the vertices and  $S_i$  onto the  $y$  axis, the verse of the inequalities also depends on the value of the angle between the current viewing direction and  $V_0$ . For instance, in the example shown in Fig. 11, we have:

$$P_{21} \leq d_{2l} \leq P_{22} \leq P_{24} \leq d_{2r} \leq P_{23}, \quad 0 < \alpha_2 < \pi$$

$$P_{21} \geq d_{2l} \geq P_{22} \geq P_{24} \geq d_{2r} \geq P_{23}, \quad \pi < \alpha_2 < 2\pi$$

In order to be able to write the inequalities in an automatic way, the general form of the inequalities can be rewritten multiplying each term by  $\sin(\alpha_2)$ . In the previous example, the set of inequalities become:

$$\begin{cases} P_{21}\sin(\alpha_2) \leq d_{2l}\sin(\alpha_2) \\ d_{2l}\sin(\alpha_2) \leq P_{22}\sin(\alpha_2) \end{cases} \quad \text{or} \quad \begin{cases} \sin(\alpha_2)(P_{21} - d_{2l}) \leq 0 \\ \sin(\alpha_2)(d_{2l} - P_{22}) \leq 0 \end{cases}$$

$$\begin{cases} P_{22}\sin(\alpha_2) \leq P_{24}\sin(\alpha_2) \\ P_{24}\sin(\alpha_2) \leq d_{2r}\sin(\alpha_2) \\ d_{2r}\sin(\alpha_2) \leq P_{23}\sin(\alpha_2) \end{cases} \quad \begin{cases} \sin(\alpha_2)(P_{22} - P_{24}) \leq 0 \\ \sin(\alpha_2)(P_{24} - d_{2r}) \leq 0 \\ \sin(\alpha_2)(d_{2r} - P_{23}) \leq 0 \end{cases}$$

In general, each term of the inequalities will be multiplied by  $\sin(\alpha_i)$ .

Each new vertex  $C_j$ ,  $j > 4$ , is the intersection of the line every edge lies on and the specific projection line relative to  $V_i$ . All these lines are projection lines, and can be written as:

$$D_{il} + V_i r \quad \text{or} \quad D_{ir} + V_i r, \quad \text{where:}$$

$$D_{il} = (S_{0l}, 0), i = 0; (0, d_{il}), i > 0 \quad D_{ir} = (S_{0r}, 0), i = 0; (0, d_{ir}), i > 0$$

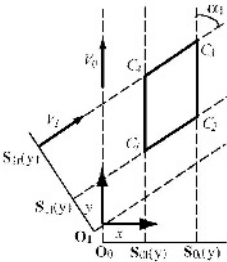


Fig. 10.

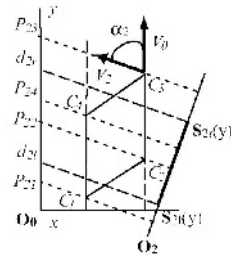


Fig. 11.

## 5 Solving the Inequalities

A set inversion technique ([7]) has been applied for finding the feasible solution set  $\mathbf{S}$  of the set of non-linear inequalities that characterizes each sub-case. This technique performs a paving the parameter space with boxes. If the current box  $[\mathbf{p}]$  is proved to be inside  $\mathbf{S}$ , then the box is kept as part of the solution space. If it is proved to have an empty intersection with  $\mathbf{S}$  then it is discarded. Otherwise,  $[\mathbf{p}]$  is bisected except if its width is smaller than a defined threshold. The dimensionality of the initial box is equal to the number of variables involved in the set of inequalities. To prove that a given box  $[\mathbf{p}]$  is inside  $\mathbf{S}$ , interval computation ([13]) has been used. The technique illustrated is used to find feasible parameter sets for one value of  $y$  between 0 and  $y_{\max}$ . Each feasible parameter set corresponds to a group of inequalities that can take place for the same object. If one of the parameter sets is empty, the corresponding group of inequalities can be discarded. Otherwise, we could perform an incremental computation, adding each time (or subtracting) a small  $\Delta y$ , related to the shape of the silhouettes, to the previous  $y$  or, in the case of polygonal silhouettes, taking as  $y + \Delta y$  the height of the next horizontal strip. For each group of inequalities, the new feasible parameter set at  $y + \Delta y$  must be a subset of the set at  $y$ . The cases are arranged in a tree, whose depth is the number of silhouettes. Instead of considering all the leaves at the lower level of the tree, that is all the intersections with all the silhouettes, we start the computation at higher level. If an inequality group has an empty feasible parameter set, the child cases can be discarded. Also, the initial feasible parameter set for each child is derived from the one evaluated for the father and it is not taken as the whole initial box.

In order to assess the validity of the approach described, we have experimented the algorithms in a virtual environment. An orthogonal camera rotating on a plane around the object has been used to create silhouettes of synthetic objects. The paving technique introduced has been used to find feasible parameter sets satisfying the inequality sets. For each point of the solution, a compatible object can be reconstructed using VI. We have experimented the approach with different minimal paving resolution and different number of silhouettes. Given the three silhouettes  $S_0$ ,  $S_1$  and  $S_2$  of Fig. 10 as input, several different compatible objects, each one reconstructed from one of the eight different feasible sets, can be seen in Fig. 13. Other examples can be seen in Fig. 12 and Fig. 13. Finally, in Fig. 14, the expanded

tree of the sub cases generated by four silhouettes of the chamfer box of Fig. 13 can be seen. The dark nodes correspond to the open nodes.

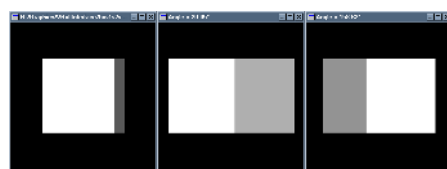


**Fig. 10.** The silhouettes S0, S1 and S2

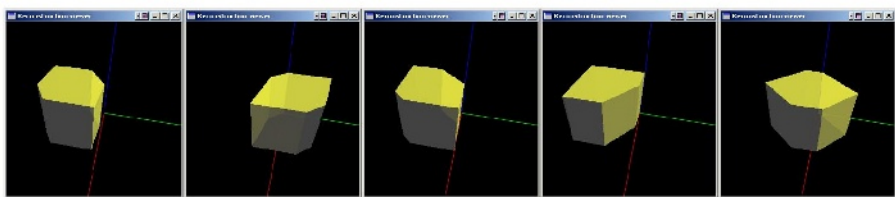


**Fig. 11.** Objects compatible with the silhouettes of Fig. 10

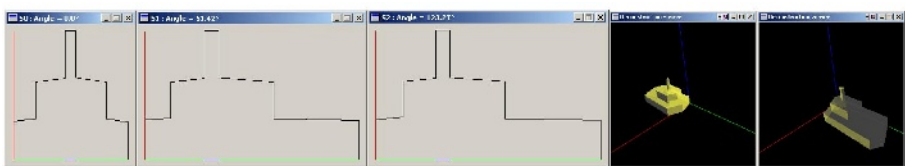


**Fig. 12.** A boat



**Fig. 13.** A chamfer box

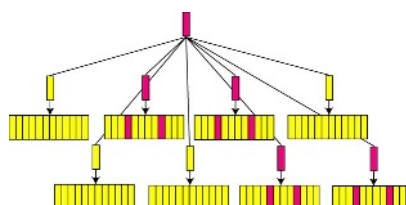


**Fig. 14.** Solution tree

## 6 Conclusions

We have introduced and explored the problem of understanding the shape of 3D objects from silhouettes when the relative position of the viewpoints is not known, which happens in several practical cases. We have presented a necessary and sufficient condition for a set of orthographic silhouettes to be compatible. This condition has been applied to the particular case of orthographic projections with viewing directions parallel to a plane. For this case, we have been able to work out sets of inequalities, involving the volume intersection parameters, which allow computing feasible solution sets. An algorithm for automatically writing the inequalities has been developed, and a technique involving the paving of the parameter space has been introduce to evaluate, if they exist, feasible parameter sets satisfying the inequalities.

Several problems are open. Among them, the case of orthographic projection with unrestricted viewing directions, and the case of perspective projections. We will also study and discuss thoroughly the case of generic silhouettes, which are not simply connected objects or having their boundaries defined by mono-valued functions. Another question is worth considering. Except for special cases, we expect that infinite compatible objects exist, specified by a region in the space of the intersection parameters. Simple ways for describing the shape of the compatible objects seem desirable.

## References

- [1] N. Ahuja and J. Veenstra: Generating octrees from object silhouettes in orthographic views, *IEEE Trans. on PAMI*, Vol.11,pp.137–149,1989
- [2] K. Astrom and F. Kahl: Motion estimation in image sequences using the deformation of apparent contours, *IEEE Trans. on PAMI*, Vol. 21, No.2, pp.114–126, 1999
- [3] Bottino, L. Cavallero, A.Laurentini, “Interactive reconstruction of 3D objects from silhouettes,” *Proc. WSCG’2001*, Vol.II, pp. 230–236, Plzen, February 5–9, 2001
- [4] E. Boyer and M. O. Berger,” 3D Surface Reconstruction Using Occluding Contours,” *Int’l. J. of Computer Vision*, vol.22, no.3, pp. 219–233, 1997
- [5] R. Cipolla and A. Blake,”Surface Shape from the Deformation of Apparent Contours,”*Int’l. J. of Computer Vision*, vol.9, no.2, pp. 83–112, 1992
- [6] A.Laurentini : How far 3-D shapes can be understood from 2-D silhouettes,” *IEEE Trans. on PAMI*, Vol.17, No.2, pp.188–195, 1995
- [7] L.Jaulin and E.Walter: Guaranteed nonlinear set estimation via interval analysis, *Bounding Approaches to System Identification*, edited by M.Milanese et al, Plenum Press, New York, pp.363–381, 1996
- [8] W. Matusik, et al.: Image based visual hulls, *Proc. ACM Siggraph 2000*,pp.369-374
- [9] Noborio et al.:Construction of the octree approximating three-dimensional objects by using multiple views, *IEEE Trans. on PAMI*, Vol.10, pp.769–782,1988
- [10] M.Potemesil: Generating octree models of 3D objects from their silhouettes in a sequence of images, *Comput.Vision Graphics Image Process.*,Vol.40,pp.1–29,1987
- [11] J. Y. Zheng: Acquiring 3D models from sequences of contours, *IEEE Trans. on PAMI*, Vol. 16, no.2, pp.163–178,1994
- [12] A.Bottino, A.Laurentini, Shape-from-silhouettes with unknown relative position of the viewpoints: investigating a new problem, Proc. SPPRA, 2002
- [13] R.E. Moore, Methods and Applications of Interval Analysis, Proc. SIAM, 1979

# Enforcing a Shape Correspondence between Two Views of a 3D Non-rigid Object

M. Benjamin Dias and Bernard F. Buxton

Department of Computer Science, University College London,

Gower Street, London, WC1E 6BT, UK

B.Dias@cs.ucl.ac.uk, <http://www.cs.ucl.ac.uk/staff/B.Dias/>

**Abstract.** We have developed an algorithm capable of enforcing a shape correspondence between two views of the same object in different shape-states. This algorithm, together with several other significant updates, has helped improve the performance of the Integrated Shape and Pose Model (ISPM) described in [1] by a factor of 10. The ISPM utilizes two flexible basis views to integrate the linear combination of views technique with a coupled-view Flexible Shape Model (FSM) [2]. As a proof-of-principle we have evaluated the performance of the improved ISPM in comparison to that of its predecessor [1] and of the conventional FSM [3], via two different databases. The results show that, unlike the FSM, the current ISPM is view-invariant and that, on average, it out-performs the FSM. It also out-performs the initial ISPM described in [1].

## 1 Introduction and Background

Machine vision systems that utilize two or more two-dimensional (2D) images to represent three-dimensional (3D) objects have recently become quite popular because they are sufficient for many purposes, while computationally being relatively easy to build. In particular, not building an explicit 3D model means that we can avoid poorly conditioned 3D reconstruction steps and can, therefore for example, generate virtual images with less noise [4]. There is also some evidence to suggest that such view-based representations are used by the human visual system [5]. Ullman and Basri [6] developed the view-based approach, also known as the Linear Combination of Views (LCV) technique, though only for representing rigid objects. In the LCV technique, any image of a 3D object is represented as a linear combination of at least “ $1\frac{1}{2}$ ” other images of the same object. Ullman and Basri [6] used line-drawings, whilst others have taken this concept further to the combination of real images [7,8] but using an over-complete approach so that the basis views may be treated symmetrically. We reformulated the over-complete LCV approach [1], via the Centred Affine Trifocal Tensor (CATT) [4], introducing the required constraints [9].

Thus far, however, the LCV technique has only been used to represent rigid 3D objects. We have taken this approach even further to model non-rigid 3D objects. For this we integrate an LCV model with a Coupled-View Flexible Shape Model (CVFSM) [2], via two flexible basis views, to form the Integrated

Shape and Pose Model (ISPM), which was first introduced in [1]. In order to generate such a model we need: (i) a technique for mapping the intrinsic shape from any given image, simultaneously to two (or more) preselected views and, (ii) a technique for ensuring the two mapped shapes correspond to the same 3D shape (as though they were images captured simultaneously from different views). Given two such techniques, we could train a CVFSM on almost any given set of images, by first transferring the intrinsic shape from each given image to two preselected views providing the required corresponding pairs of images [2]. Once we have two such flexible basis views, we can synthesize, via the CVFSM, an image of the object in any view by, for example, the LCV technique.

The first of the above mentioned techniques, (i), which we refer to as a 2D Pose Alignment, was first described in [1]. However, since we were missing technique (ii) for ensuring the two mapped shapes correspond to the same 3D shape, the success of the ISPM described in [1], though encouraging, was limited. We have now developed the second technique, (ii), which is explained in Sect. 3 of this paper. It has, along with several other new steps, described in Sect. 2.2, helped improve the performance of the ISPM by an order of magnitude.

## 2 An Implicit (2D) Pose Alignment via the CATT

Here we assume, for the moment, that we are given two images of the mean shape as seen from two preselected views (the basis views) i.e. we have two sets of corresponding landmark points,  $\bar{\mathbf{X}}'$  &  $\bar{\mathbf{X}}''$ , respectively from two images of the same shape (the mean shape) as seen from the two basis views. Let's also use two sets of corresponding landmark points  $\mathbf{X}'_i$  &  $\mathbf{X}''_i$  to represent the images, as seen from the two basis views, of the shape in a given image,  $i$  say, represented by the landmark points  $\mathbf{X}_i$  (i.e.  $\mathbf{X}_i$ ,  $\mathbf{X}'_i$  &  $\mathbf{X}''_i$  have the same shape). The aim of the 2D (implicit) Pose Alignment (2D-PA) process is then to recover  $\mathbf{X}'_i$  &  $\mathbf{X}''_i$  given  $\mathbf{X}_i$ ,  $\bar{\mathbf{X}}'$  &  $\bar{\mathbf{X}}''$ .

### 2.1 The Subset of Stable Points

Before we begin the 2D-PA process, we first select a subset of at least 4 non-co-planar landmark points that can be considered as forming a rigid sub-object. For this we employ a RANSAC algorithm [10] to select a subset of  $p$  ( $\geq 4$ ) landmark points that best conforms to the constraints of multi-view geometry for a rigid object by minimizing

$$e^2 = \sum_i e^2(i) , \quad \text{where for each } \mathbf{X}_i \quad e^2(i) = \|\mathbf{T}(i)\mathbf{Y}(i)\|^2 , \quad (1)$$

$\mathbf{T}(i)$  is the CATT matrix [1] and  $\mathbf{Y}(i) = (\mathbf{X}_i^T, \bar{\mathbf{X}}''^T, \bar{\mathbf{X}}'^T)^T$ . Here, in each case, each image is represented in the  $\mathbf{X}_i$ ,  $\bar{\mathbf{X}}'$  &  $\bar{\mathbf{X}}''$ , only by the subset of  $p$  landmark points being considered. In our experiments we used a subset of 6 stable points (i.e.  $p = 6$ ) and manually checked that the selected points were not co-planar. If

the selected subset were co-planar, then we continued to check the subset that provides the next smallest value for  $e^2$  until we found a non-co-planar one.

## 2.2 The 2D Pose Alignment (2D-PA) Process

Given the stable points, we begin the 2D-PA process, as in [1], by computing the best approximation to the CATT [4] corresponding to  $\mathbf{X}_i$ ,  $\overline{\mathbf{X}}'$  &  $\overline{\mathbf{X}}''$  by computing the  $\mathbf{T}(i)$  that minimizes  $e^2(i)$ . However, we now use only the subset of stable points for this, which provides a more accurate estimate of the CATT than reported in [1] and makes the process a lot faster. We then use the computed CATT and *all* the landmark points (not just the stable points) to generate the least squares estimate of  $\overline{\mathbf{X}}_i$ , the mean shape in the view of the given image  $\mathbf{X}_i$ . Next, we compute the *in-view* shape difference,  $\Delta\mathbf{X}_i = \mathbf{X}_i - \overline{\mathbf{X}}_i$ , which is then added to  $\overline{\mathbf{X}}'$  &  $\overline{\mathbf{X}}''$ , to generate our first estimates of  $\mathbf{X}'_i$  &  $\mathbf{X}''_i$ :

$$\mathbf{X}'_i(\text{temp}) = \overline{\mathbf{X}}' + \Delta\mathbf{X}_i \quad \& \quad \mathbf{X}''_i(\text{temp}) = \overline{\mathbf{X}}'' + \Delta\mathbf{X}_i . \quad (2)$$

Since  $\Delta\mathbf{X}_i$  is a shape difference in the view  $\mathbf{X}_i$ , applying it to the basis views will not, in general, lead to a valid result, since  $\mathbf{X}'_i(\text{temp})$  &  $\mathbf{X}''_i(\text{temp})$  will not, in general, conform to the constraints of multi-view geometry. However, in each case it provides a better estimate of the landmarks of the pose aligned image than the means  $\overline{\mathbf{X}}'$  &  $\overline{\mathbf{X}}''$ . We continue by extracting, from the CATT, the two fundamental matrices that link  $\mathbf{X}_i$  to each of the basis views via *Algorithm 14.1, on page 366* of [11]. We then use the fundamental matrices to compute the equations of the epipolar lines in each of the  $\mathbf{X}'_i(\text{temp})$  &  $\mathbf{X}''_i(\text{temp})$  corresponding to each landmark point in the given image  $\mathbf{X}_i$ . Next, we move each landmark point in each of  $\mathbf{X}'_i(\text{temp})$  &  $\mathbf{X}''_i(\text{temp})$  to the nearest point on the corresponding epipolar line to generate  $\widetilde{\mathbf{X}}'_i$  &  $\widetilde{\mathbf{X}}''_i$ , which are updated estimates of  $\mathbf{X}'_i$  &  $\mathbf{X}''_i$ . This step ensures that  $\widetilde{\mathbf{X}}'_i$  &  $\widetilde{\mathbf{X}}''_i$  conform to the multi-view geometry. We then align  $\widetilde{\mathbf{X}}'_i$  to  $\overline{\mathbf{X}}'$  &  $\widetilde{\mathbf{X}}''_i$  to  $\overline{\mathbf{X}}''$ , as in [1], via a further affine transformation applied to the landmark points of each image. This is done in order to determine all the degrees of freedom in the alignment process. However, now we do not stop at this point, but complete the alignment by enforcing a shape correspondence between the two sets of pose-aligned points  $\widetilde{\mathbf{X}}'_i$  &  $\widetilde{\mathbf{X}}''_i$ , as described in Sect. 3.

## 3 Enforcing a Shape Correspondence between Views

Suppose now that we are using the 2D-PA algorithm to align points in an image  $\mathbf{X}_i$  to the points,  $\overline{\mathbf{X}}'$  &  $\overline{\mathbf{X}}''$ , in two given mean basis views. The 2D-PA algorithm would generate two sets of points  $\widetilde{\mathbf{X}}'_i$  &  $\widetilde{\mathbf{X}}''_i$  as explained in Sect. 2.2 above, which are aligned as well as possible. Since  $\widetilde{\mathbf{X}}'_i$  &  $\widetilde{\mathbf{X}}''_i$  may not have the same shape, in order to complete the alignment, we need to update the shapes represented by each of them until they can be considered as simultaneous images of the same

3D object (i.e. we need to enforce shape correspondence between  $\widetilde{\mathbf{X}}'_i$  &  $\widetilde{\mathbf{X}}''_i$ ). Thus, our aim, here, is to recover  $\mathbf{X}'_i$  &  $\mathbf{X}''_i$ , given  $\overline{\mathbf{X}}'$ ,  $\overline{\mathbf{X}}''$ ,  $\widetilde{\mathbf{X}}'_i$  &  $\widetilde{\mathbf{X}}''_i$ .

We begin by setting  $\widetilde{\mathbf{X}}'_i$  &  $\widetilde{\mathbf{X}}''_i$  as our first estimates of  $\mathbf{X}'_i$  &  $\mathbf{X}''_i$ , respectively. Next, we use *Algorithm 13.1, on page 340* of [11], to compute the maximum likelihood estimate of the (affine) fundamental matrix that maps  $\mathbf{X}'_i$  to  $\overline{\mathbf{X}}''$ . Here again we use only the stable points in order to compute an estimate of the fundamental matrix, since a rigid-object is assumed in the algorithm used. We then use the fundamental matrix and *all* the landmark points (not just the stable points) to map the shape of  $\mathbf{X}'_i$  to  $\overline{\mathbf{X}}''$  and generate  $\hat{\mathbf{X}}'_i$ . This shape transfer is achieved, as explained in the 2D-PA process, by moving each landmark point to the nearest point along the corresponding epipolar line (see Sect. 2.2).  $\hat{\mathbf{X}}'_i$  corresponds to an image of the shape represented by points  $\mathbf{X}'_i$  as seen from the view of  $\overline{\mathbf{X}}''$ . We do the same for the pair of images  $\mathbf{X}''_i$  &  $\overline{\mathbf{X}}'$  to generate  $\hat{\mathbf{X}}''_i$  and update our estimates of  $\mathbf{X}'_i$  &  $\mathbf{X}''_i$  as follows:

$$\mathbf{X}'_i \rightarrow \frac{1}{2}(\mathbf{X}'_i + \hat{\mathbf{X}}'_i) \quad \& \quad \mathbf{X}''_i \rightarrow \frac{1}{2}(\mathbf{X}''_i + \hat{\mathbf{X}}''_i) . \quad (3)$$

We then iterate, using our current estimates of  $\mathbf{X}'_i$  &  $\mathbf{X}''_i$ , to re-compute  $\hat{\mathbf{X}}''_i$  &  $\hat{\mathbf{X}}'_i$  and using  $\hat{\mathbf{X}}''_i$  &  $\hat{\mathbf{X}}'_i$  to update our estimates of  $\mathbf{X}'_i$  &  $\mathbf{X}''_i$  via (3). We continue iterating until the difference between consecutive estimates of  $\mathbf{X}'_i$  &  $\mathbf{X}''_i$  is smaller than some tolerance.

### 3.1 The Initial Reference Images

At this point we recall that in order to begin the 2D-PA algorithm, we require landmark points,  $\overline{\mathbf{X}}'$  &  $\overline{\mathbf{X}}''$ , in the two mean basis views. Thus, initially, we generate all the distinct combinations of landmark points from image pairs in the training set. We consider each pair of images, enforce a shape correspondence between them (as explained next), and compute the error  $e^2$  defined in (1) corresponding to the selected pair. We then select the two images that produce the minimum value for  $e^2$ . The two images (with the shape correspondence enforced) thus selected, are then used as the initial reference images  $\mathbf{X}_{r1}$  &  $\mathbf{X}_{r2}$  in the Extended Procrustes Alignment (EPA) algorithm [1] to compute the points in the mean basis views. The EPA algorithm begins by considering  $\mathbf{X}_{r1}$  &  $\mathbf{X}_{r2}$  as the first estimates of  $\overline{\mathbf{X}}'$  &  $\overline{\mathbf{X}}''$ . Then we iterate, aligning points in all the training images (via the 2D-PA process) to the current estimates of  $\overline{\mathbf{X}}'$  &  $\overline{\mathbf{X}}''$  and re-computing  $\overline{\mathbf{X}}'$  &  $\overline{\mathbf{X}}''$  from the aligned sets of images, until convergence. Thus, until  $\overline{\mathbf{X}}'$  &  $\overline{\mathbf{X}}''$  are computed, we use their current estimates instead.

During the process of selecting the two initial reference images for the EPA algorithm (see Sect. 3.1), however, we only have two sets of points that correspond to  $\widetilde{\mathbf{X}}'_i$  &  $\widetilde{\mathbf{X}}''_i$ , since  $\overline{\mathbf{X}}'$  &  $\overline{\mathbf{X}}''$  have not yet been computed. Therefore, in order to enforce a shape correspondence between these two sets of points, in each iteration we use the current estimates of  $\mathbf{X}'_i$  &  $\mathbf{X}''_i$  in place of  $\overline{\mathbf{X}}'$  &  $\overline{\mathbf{X}}''$ .

## 4 The Integrated Shape and Pose Model (ISPM)

The ISPM, first introduced in [1], utilizes landmark points representing two flexible basis views to integrate the LCV technique with a CVFSM [2]. To build an ISPM, from (almost) any given set of images, we first select two reference images that define the basis views (see Sect. 3.1) and use the EPA algorithm [1] to simultaneously compute the points representing the two mean basis views and align all the training images to them (via the 2D-PA algorithm). This results, for each training image, in two corresponding sets of landmark points that represent simultaneous images of the object of interest taken from the two selected basis views while the object changes only its shape. Thus, we can then build two FSMs to model the intrinsic shape variation present in these two sets of landmark points and use the correspondence to build a hierarchical CVFSM. The parameters of the CVFSM (the shape parameters) enable us simultaneously to change the shape of the object in the two basis view images in a corresponding manner. Given the points representing the two basis views of the object with a particular shape, we may use the reformulated LCV technique [1] to synthesize that shape as seen from any desired view point via an appropriate CATT [4]. The elements of the CATT are the pose parameters. To use the ISPM, given the landmark points in a new image of the object, we first align them, via the 2D-PA algorithm, to the points representing the mean basis views. This provides: (i) the CATT that defines the pose of the object in the image (i.e. the pose parameters) and, (ii) the input set of landmark points to each of the two individual FSMs. The parameters of the individual FSMs then provide the input to the CVFSM, from which we extract the shape parameters in the usual way [2,3].

## 5 Evaluation

As a proof-of-principle the updated version of the ISPM detailed in this paper was evaluated in comparison to its predecessor [1] and a conventional Flexible Shape Model (FSM) as built by Cootes et al. [3]. The evaluation was carried out on landmark points selected from both real and synthetic image data. For the real images, we used landmark points manually selected from the same data as in [1], with five expressions (Neutral, Angry, Happy, Sad & Surprised) sampled at 13 different poses ( $\sim 5^\circ$  intervals from  $\sim -30^\circ$  to  $\sim +30^\circ$  where  $0^\circ$  corresponds to the frontal view) giving 65 sets of points in total. For the synthetic data, we utilized the 3D head model of Loizides et al. [12] to generate images of a face. A subset of the 3D model points was manually selected as landmarks. The error-free locations of these landmark points in the corresponding synthetic images, and the images themselves were computed via an affine projection matrix. Four expressions (Fear, Happiness, Sadness & Neutral) were sampled at 11 different poses (at  $5^\circ$  intervals from  $-25^\circ$  to  $+25^\circ$ ) to generate 44 sets of points in total. In both cases (real and synthetic), rotations were performed only about the vertical axis. Owing to the space limit here, we refer the reader to [13] for a complete description of the databases. Some example images and the landmark points used in each case are shown in Fig. 1.

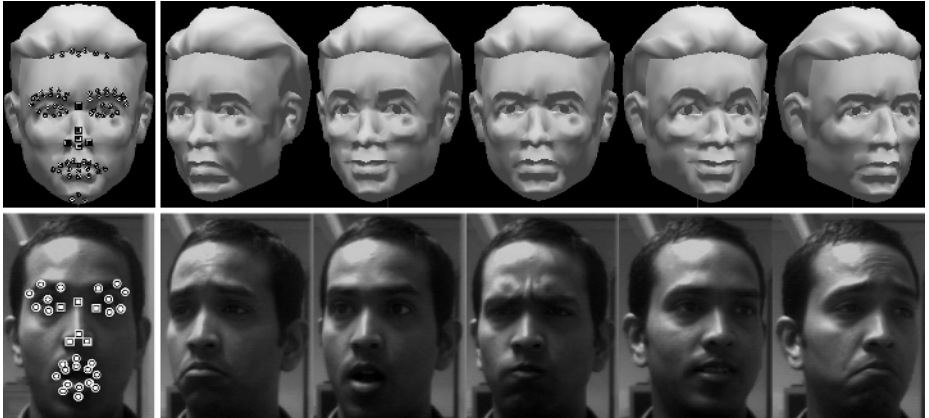


**Fig. 1.** Some examples of the real (bottom) and synthetic (top) images used in the evaluation. The subset of stable points (squares) and the other landmark points (circles) used in each case are shown in the leftmost images.

We evaluated the performance of each model (i.e. of the FSM, the initial ISPM [1] and the current ISPM described in this paper) by its ability to reconstruct the point configuration in a given image. For this we used each model to extract its own representation of a given image and use this representation to reconstruct the points representing the original image. The reconstruction error was then computed to be the root mean square error between the positions of the landmark points in the original image and the points reconstructed by the model. We represent this error as a percentage of the scale of the original image in order to make it scale invariant. The reconstruction errors were also averaged over expression, providing an error measure as a function of pose and independent of expression.

We performed cross-validation [14] and leave-one-out experiments on the two data sets in order to determine the accuracy of each model. The results of the leave-one-out experiments are shown in Fig. 2. The cross-validation experiments produced similar results. The graphs in Fig. 2 clearly show that the FSM is dependent on pose whereas the current ISPM isn't. Furthermore, in all experiments, on average the current ISPM out-performed the FSM. The minimum error of the initial ISPM was, however, much larger (always  $> 1.0\%$ ) and is therefore not shown in the graphs in Fig. 2. Thus, although the initial ISPM was pose-invariant, it wasn't able to rival the FSM in terms of accuracy as the current ISPM does. Since similar results were generated on the real and synthetic databases, which were completely different in size, shape, number of landmark points and noise level, we are confident they reflect the performance of the models of interest and not some peculiarity of a particular database.

We also evaluated the performance of our algorithm that enforces a shape correspondence between two views (see Sect. 3) by computing the Pearson Cor-

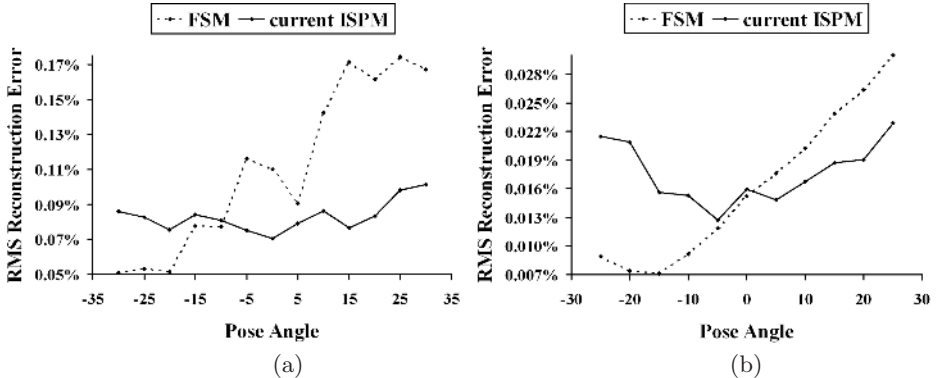


**Fig. 2.** The reconstruction errors from the leave-one-out experiments on the (a) real & (b) synthetic data for the FSM (dotted line) and the current ISPM (solid line).

relation Coefficient (PCC) between the eigenvectors, eigenvalues and the scatter matrices of the two individual FSMs that were built from the pose-aligned images. We use the absolute value of the PCC which is, by definition, between 0 (no apparent correlation) and 1 (highly correlated). In all experiments the PCC values for the current ISPM were above 0.9, which shows that a shape correspondence was successfully enforced. Except for the PCC values for the eigenvalues (0.9) and of the first eigenvector (0.8), all the other PCC values for the initial ISPM were below 0.7. Since space is limited here, we refer the reader to [13] for more details on our results.

## 6 Conclusions and Future Work

We have developed an algorithm capable of enforcing a shape correspondence between two views of the same 3D non-rigid object in different shape-states. We have used this algorithm, along with many other significant updates, to improve the version of the Integrated Shape and Pose Model (ISPM) described in [1] by a factor of 10. As a proof-of-principle we have evaluated the performance of the improved ISPM in comparison to that of its predecessor [1] and of the conventional FSM [3], on two different databases via cross-validation and leave-one-out experiments. The results show that, unlike the FSM, the current ISPM is view-invariant since we separate the extrinsic (pose) variations from the intrinsic (shape) variations. Furthermore, on average the current ISPM described in this paper out-performs the FSM, while also completely out-classing the initial ISPM. The algorithm that enforces a shape correspondence between two views was also evaluated and shown to be successful. We anticipate that the ISPM will be useful in a variety of applications including calculation of head pose and view-invariant expression recognition. The approach may also be of relevance to theories of human vision.

**Acknowledgements.** We thank Andreas Loizides for providing the 3D model used in [12]. We also thank Matthew Trotter for his helpful comments and suggestions on evaluating our model. Benjamin Dias is funded by an *ORS award*<sup>1</sup>, by financial support from *Unilever Research Colworth*<sup>2</sup> and by a *UCL Graduate Open Scholarship*.

## References

1. Dias, M.B., Buxton, B.F.: Integrated shape and pose modelling. In: Proc. BMVC. Volume 2. (2002) 827–836
2. Cootes, T.F., Wheeler, G.V., Walker, K.N., Taylor, C.J.: Coupled-view active appearance models. In: Proc. BMVC. Volume 1. (2000) 52–61
3. Cootes, T.F., Taylor, C.J., Cooper, D.H., Graham, J.: A trainable method of parametric shape description. In: Image and Vision Computing. Volume 10. (1992) 289–294
4. Bretzner, L., Lindeberg, T.: Use your hands as a 3-d mouse, or, relative orientation from extended sequences of sparse point and line correspondences using the affine trifocal tensor. In: Proc. 5<sup>th</sup> ECCV, LNCS. Volume 1406., Springer Verlag, Berlin (1998) 141–157
5. Tarr, M.J., Williams, P., Hayward, W.G., Gauthier, I.: Three-dimensional object recognition is viewpoint dependent. In: Nature Neuroscience. Volume 1. (1998) 275–277
6. Ullman, S., Basri, R.: Recognition by linear combinations of models. In: IEEE Transactions on PAMI. Volume 13. (1991) 992–1006
7. Pollard, S., Pilu, M., Hayes, S., Lorusso, A.: View synthesis by trinocular edge matching and transfer. In: Proc. BMVC. Volume 2. (1998) 770–779
8. Koufakis, I., Buxton, B.F.: Very low bit-rate face video compression using linear combination of 2d face views and principal component analysis. Image and Vision Computing **17** (1998) 1031–1051
9. Thórhallsson, T., Murray, D.W.: The tensors of three affine views. In: Proc. International Conference on Computer Vision and Pattern Recognition. Volume 1. (1999) 450–456
10. Fischler, M.A., Bolles, R.C.: Random sample consensus: A paradigm for model fitting with applications to image analysis and automated cartography. In: Communications of the ACM. Volume 24. (1981) 381–395
11. Hartley, R., Zisserman, A.: Multiple View Geometry In Computer Vision. Cambridge University Press, ISBN 0-521-62304-9 (2000)
12. Loizides, A., Slater, M., Langdon, W.B.: Measuring facial emotional expressions using genetic programming. In: Soft Computing and Industry Recent Applications. (2001) 545–554
13. Dias, M.B., Buxton, B.F.: Advances in integrated shape and pose modelling. Technical Report RN/03/10, University College London (UCL), Department of Computer Science (2003)
14. Kohavi, R.: A study of cross-validation and bootstrap for accuracy estimation and model selection. In: Proc. IJCAI. (1995)

---

<sup>1</sup> Granted by the CVCP, Woburn House, London WC1H 9HQ, UK.

<sup>2</sup> Colworth House, Sharnbrook, Bedford MK44 1LQ, UK.

# A Colour Constancy Algorithm Based on the Histogram of Feasible Colour Mappings<sup>\*</sup>

Jaume Vergés-Llahí and Alberto Sanfeliu

Institut de Robòtica i Informàtica Industrial  
Technological Park of Barcelona, U Building  
Llorens i Artigas 4-6, 08028 Barcelona, Catalonia.  
[{jverges, asanfeliu}@iri.upc.es](mailto:{jverges, asanfeliu}@iri.upc.es)

**Abstract.** Colour is an important cue in many applications in machine vision and image processing. Nevertheless, colour greatly depends upon illumination changes. Colour constancy goal is to keep colour images stable. This paper's contribution to colour constancy lies in estimating both the set and the likelihood of feasible colour mappings. Then, the most likely mapping is selected and the image is rendered as it would be seen under a canonical illuminant. This approach is helpful in tasks where light can be neither controlled nor easily measured since it only makes use of image data, avoiding a common drawback in other colour constancy algorithms. Finally, we check its performance using several sets of images of objects under quite different illuminants and the results are compared to those obtained if the true illuminant colour were known.

**Keywords:** Colour, colour mappings, colour change, colour constancy, colour histograms.

## 1 Introduction

In a number of applications from machine vision tasks such as object recognition, image indexing and retrieval, to digital photography or new multimedia applications, it is important that the recorded colours remain constant under changes in the scene illumination. Hence, a preliminary step when using colour must be to remove the distracting effect of the illumination change. This problem is usually referred to in the literature as *colour constancy*, i.e., the stability of surface colour appearance under varying illumination conditions. Part of the difficulty is that this problem is entangled with other confounding phenomena such as the shape of objects, viewing and illumination geometry, besides the changes in the illuminant spectral power distribution and the reflectance properties of the imaged objects.

A general approach to colour constancy is to recover a *descriptor* for each different surface in a scene as it would be seen by a camera under a canonical illuminant. This is similar to pose the problem as that of recovering an estimate

---

\* Partially funded by a grant of the Gov. of Catalonia and the CICyT DPI2001-2223.

of the colour of the scene illumination from an image taken under an unknown illumination, since it is relatively straightforward to map image colours back to illuminant independent descriptors [1].

Therefore, *finding a mapping between colours or the colour of the scene illuminant are equivalent problems*. This path has been traced by a great amount of algorithms, being those related to the *gamut-mapping* the most successful [2, 3,4,5].

Lately, the trend has slightly changed to make a guess on the illumination, as in *colour-by-correlation* [1] or *colour-voting* [6], rather than attempting to recover only one single estimate of the illuminant. A measure of the *likelihood* that each of a set of feasible illuminants was the scene illuminant is set out instead, which is afterwards used to select the corresponding mapping to render the image back into the canonical illuminant.

## 2 Discussion

These approaches have two common drawbacks. First, as a rule, all of them rely on the fact that the set of all possible colours seen under a canonical illuminant is, somehow, known and available. That is, we must know *a priori* how any possible surface will appear in an image.

The collection of gamut-mapping algorithms uses them to constrain the set of feasible mappings, while the colour-by-correlation algorithm builds the correlation matrix up with them, which in addition implies that this set of colours must be known for each single illumination taken into account.

Secondly, in gamut-mapping algorithms the set of realizable illuminants also needs to be known *a priori* to restrict the feasible transformations. Besides, while this set is a *convex hull* in the gamut-mapping family, it is a finite set in the colour-by-correlation algorithm not covering any intermediate illuminant.

In short, before any of the previous colour constancy algorithms can even be set to work, a pretty big chunk of *a priori* knowledge about reflectances and lights is needed, which reduces the scope of those methods. We point out this lack in two basic tasks where a mechanism of colour constancy is required [7], namely, *colour indexing* and *colour-based object recognition*. In both cases, it may be very difficult or simply impossible to have an *a priori* realistic database of surface and illuminant colours. Image indexing may be using images of unknown origin such as Internet while recognition may be part of a higher task where light conditions are uncontrollable or unknown.

Thus, this paper suggests a less information-dependent colour constancy algorithm which just relies on pixels and is capable of rendering images from an unknown illumination back into a task-dependent canonic illuminant. We only require that the set of images to transform shows similar scenes without caring about the number of imaged objects since no segmentation is carried out.

### 3 Diagonal Model and Chromaticity Coordinates

First of all, the problem of modelling the colour change must be considered. If referred to the literature, from Forsyth [2] to Finlayson et al. [3,1], the algorithms with best performance are based on a *diagonal model*, i.e., colours recorded under one illuminant can be mapped onto those under a different illuminant by applying *individual scaling factors* to each coordinate. Forsyth's gamut-mapping algorithm used 3D diagonal matrices to transform *RGB* sensor responses:

$$(R', G', B')^t = \begin{bmatrix} \alpha & 0 & 0 \\ 0 & \beta & 0 \\ 0 & 0 & \gamma \end{bmatrix} \cdot (R, G, B)^t \quad (1)$$

That algorithm worked well only on a restricted set of images which included flat, matte, uniformly illuminated scenes. To alleviate problems found in images with *specularities* or *shape* information and to reduce the computational burden, Finlayson [3] discarded intensity information by just working in a 2D chromaticity space usually referred to as *perspective colour coordinates*:

$$(r, g) = \left( \frac{R}{B}, \frac{G}{B} \right) \quad (2)$$

Therefore, the diagonal matrix of Eq. (1) expressed in perspective coordinates changes into the following relation:

$$(r', g')^t = \begin{bmatrix} \frac{\alpha}{\gamma} & 0 \\ 0 & \frac{\beta}{\gamma} \end{bmatrix} \cdot (r, g)^t = \begin{bmatrix} \tilde{\alpha} & 0 \\ 0 & \tilde{\beta} \end{bmatrix} \cdot (r, g)^t \quad (3)$$

Later, Finlayson and Hordley proved in [8] that there is no further advantage in using 3D algorithms because the set of feasible mappings after being projected into 2D is the same as the set computed by 2D algorithms. Hence, both chromaticity coordinates in Eq. (2) and 2D diagonal mappings in Eq. (3) will be used throughout this paper.

### 4 Measuring the Performance of Colour Constancy

The performance of a colour constancy algorithm is usually measured as the error of the illuminant estimates or the RMS error between the transformed and canonic images, which is useless if the point of view changes or objects move.

As reported in [9,7], colour histograms are an alternative way to globally represent and compare images. Thus, the *Swain&Ballard* intersection-measurement in [9] computes the *resemblance*<sup>1</sup> between two histograms  $\mathcal{H}$  and  $\mathcal{T}$ :

$$\cap(\mathcal{H}, \mathcal{T}) = \sum_k \min \{H_k, T_k\} \in [0, 1] \quad (4)$$

---

<sup>1</sup> A distance measure can be similarly defined as  $Dist(\mathcal{H}, \mathcal{T}) = 1 - \cap(\mathcal{H}, \mathcal{T}) \in [0, 1]$ .

The advantages of this measure are that it is very fast to compute if compared to other matching functions [10], and more importantly, if histograms are sparse and colours equally probable, this is a robust way of comparing images [9,10].

Since both colour indexing and colour-based object recognition using the *Swain&Ballard* measure fail miserably when scene light differs from that used in creating the database of model images [7], we suggest Eq. (4) as a mean of both computing the *performance* of a colour constancy algorithm and also that of *measuring* the suitability of a particular colour mapping if one histogram corresponds to a transformed image and the other to the canonic one.

## 5 Colour Constancy Algorithm

We suggest an algorithm to estimate the *set* and *likelihood* of feasible colour mappings from image pixels. This set is analogous to the set of possible mappings in [2,3,8], but here the likelihood of each mapping is computed, as in [1].

The algorithm supposes we have images of similar scenes under different illuminants and that we want to render them as seen under a canonic illuminant<sup>2</sup>. The number of objects in the scene does not matter since we do not segment the image and only the pixels are used to find a colour mapping as those of Eq. (3).

More precisely, let  $I^a$  and  $I^b$  be two colour images of nearly the same scene taken under *different* and *unknown* illuminants. We take  $I^b$  as the *canonic* and our goal is to find a colour transformation  $\mathcal{T} \in \mathbf{T}$  which maps the colour of the pixels of image  $I^a$  as close as possible onto those of image  $I^b$ .  $\mathbf{T}$  is the set of *feasible colour mappings*. We note the *transformed* image as  $\mathcal{T}(I)$ , which is formed by applying  $\mathcal{T}$  to every pixel in  $I$ .

The main idea of this algorithm is to estimate the *likelihood*  $\mathcal{L}(\mathcal{T} | I^a, I^b)$  of every feasible mapping  $\mathcal{T} \in \mathbf{T}$  just from pixel data of images  $I^a$  and  $I^b$ . Afterwards, we will select the most likely transformation  $\mathcal{T}_0$ :

$$\text{find } \mathcal{T}_0 = \underset{\mathcal{T} \in \mathbf{T}}{\operatorname{argmax}} \{ \mathcal{L}(\mathcal{T} | I^a, I^b) \} \quad (5)$$

According to Eq. (3),  $\mathcal{T} = \operatorname{diag}(\tilde{\alpha}, \tilde{\beta})$ , where  $\tilde{\alpha}, \tilde{\beta} \in [\frac{1}{255}, 255]$ . Therefore, for every pair of chromaticities  $(r^a, g^a) \in I^a$  and  $(r^b, g^b) \in I^b$  it is possible to compute the transformation relating them as the quotient:

$$(\tilde{\alpha}, \tilde{\beta}) = \left( \frac{r^b}{r^a}, \frac{g^b}{g^a} \right) \quad (6)$$

Extending these quotients to all the pixels in  $I^a$  and  $I^b$ , the set of all the feasible transformations can be computed as  $\mathbf{T} = \{(r_i^b/r_j^a, g_i^b/g_j^a) \mid (r_j^a, g_j^a) \in I^a \text{ and } (r_i^b, g_i^b) \in I^b\}$ , where  $j, i = 1, \dots, N$  correspond to the  $j^{\text{th}}$  and  $i^{\text{th}}$  pixels of images  $I^a$  and  $I^b$ , respectively.  $N$  is the total number of pixels of an image.  $\mathbf{T}$

---

<sup>2</sup> What is *canonic* is a convenience, so any illuminant could be the canonic one.

could be further constrained if any extra knowledge about surface or illuminant colour were available.

Whether this is the case or not, the key idea is that *the more proper a mapping is, the more occurrences must exist in  $\mathbf{T}$* . Once the set  $\mathbf{T}$  and its histogram  $\mathcal{H}(\mathbf{T})$  are obtained, the probability of a certain  $\mathcal{T} \in \mathbf{T}$ ,  $Pr(\mathcal{T} | I^a, I^b)$ , can be estimated as the relative frequency of the bin corresponding to  $\mathcal{T}$  from the histogram  $\mathcal{H}(\mathbf{T})$ . This way, a likelihood function depending of  $\mathcal{T}$  could be defined as:

$$\mathcal{L}(\mathcal{T} | I^a, I^b) = \log(Pr(\mathcal{T} | I^a, I^b)), \quad \mathcal{T} \in \mathbf{T} \quad (7)$$

where, according to Eq. (5) and (7), the most likely mapping  $\mathcal{T}_0$  would correspond to the bin of highest relative frequency in  $\mathcal{H}(\mathbf{T})$ , fulfilling the idea that *the most appropriate mapping must have the most occurrences*.

Unfortunately, the previous approach needs a large number of computations – $O(N^2)$ – to build the set  $\mathbf{T}$  and resources to store it. To alleviate those computations, a far better approach is the use of image histograms rather than pixels.

It is possible to construct the histogram of mappings  $\mathcal{H}(\mathbf{T})$  and to estimate the probability  $Pr(\mathcal{T} | I^a, I^b)$  by means of the chromaticity histograms  $H^a = \mathcal{H}(I^a)$  and  $H^b = \mathcal{H}(I^b)$  of images  $I^a$  and  $I^b$ , respectively. The relative frequency of each bin in  $\mathcal{H}(\mathbf{T})$  is the summation of the frequencies of each pair of chromaticities giving rise to a certain mapping  $\mathcal{T}$  by means of Eq. (6):

$$Pr(\mathcal{T} | I^a, I^b) = \sum_{\mathcal{T} \cap \mathbf{T}} Pr\left(\left(\frac{r^b}{r^a}, \frac{g^b}{g^a}\right) | I^a, I^b\right), \quad \mathcal{T} \in \mathbf{T} \quad (8)$$

where  $\mathcal{T} \cap \mathbf{T} = \{(r^a, g^a) \in I^a \text{ and } (r^b, g^b) \in I^b \mid \mathcal{T} = \left(\frac{r^b}{r^a}, \frac{g^b}{g^a}\right)\}$ . The probability of every element of  $\mathcal{T} \cap \mathbf{T}$  is:

$$Pr\left(\left(\frac{r^b}{r^a}, \frac{g^b}{g^a}\right) | I^a, I^b\right) = Pr((r^a, g^a) | I^a) \cdot Pr((r^b, g^b) | I^b) \quad (9)$$

where  $Pr((r^a, g^a) | I^a)$  and  $Pr((r^b, g^b) | I^b)$  are the relative frequencies of chromaticities  $(r^a, g^a) \in H^a$  and  $(r^b, g^b) \in H^b$ , respectively.

This procedure greatly reduces the number of computations to less than  $O(M^2)$ , where  $M$  is the number of bins in a histogram, since only non-zero bins are taken into account and  $M \ll N$ , considering that  $M \sim O(10^3)$  and  $N \sim O(10^5)$ . We average the set of mappings falling into a bin to get a better estimate of the mapping corresponding to that bin. The number of histogram bins affects the precision of the mapping estimate only if it is too low.

In practice, some spurious peaks may appear due to the accumulation of noisy or to redundant mappings which might mislead the algorithm. Hence, the intersection-measure of Eq. (4) is used to evaluate the performance of each particular mapping since it globally measures the colour resemblance between two images. The better a mapping is, the higher the histogram intersection is.

Therefore, to improve the chances of obtaining a more precise estimate, we newly define the likelihood function combining both Eq. (4) and Eq. (8) as:

$$\mathcal{L}(\mathcal{T} | I^a, I^b) = \log(\cap(\mathcal{T}(H^a), H^b) \cdot Pr(\mathcal{T} | I^a, I^b)), \quad \mathcal{T} \in \mathbf{T} \quad (10)$$

where  $\mathcal{T}(H) = \mathcal{T}(\mathcal{H}(I))$  is the transformation of a histogram  $\mathcal{H}(I)$  by  $\mathcal{T}$ , which is not as straightforward as mapping an image  $I$  since the discrete nature of histograms and the absence of *one-to-one* correspondence among histogram bins generally produce gaps and bin overlays.

To avoid gaps, the procedure begins from the bins in  $\mathcal{T}(H)$  and computes their corresponding bin in  $H$  using the inverse  $\mathcal{T}^{-1}$ . Bin overlays mean that some bins may have been repeatedly counted. Hence,  $\mathcal{T}(H)$  must be normalised.

Furthermore, the previous likelihood function is only computed on a limited set of mappings to reduce the computational burden. Only those of higher probability  $Pr(\mathcal{T} | I^a, I^b)$  are checked by Eq. (4) to be a good mapping. Finally, the most likely transformation  $\mathcal{T}_0$  is selected, as stated in Eq. (5).

## 6 Results

In this section, we perform the previous algorithm in a set of 220 images coming from 20 different colourful objects taken under 11 different illuminants<sup>3</sup>. We show the set of objects in Fig. 1. We have chosen this image database to benchmark the algorithm since it presents a wide range of both real objects and lights.

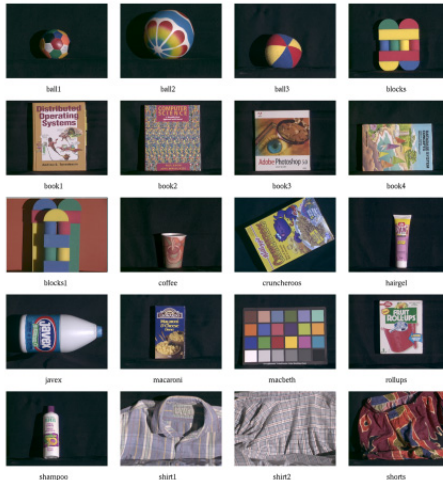


**Fig. 1.** Set of objects.

The experiment consists, for each object, in taking in turn each illuminant as the canonic while computing colour mappings from the rest of illuminants onto the canonic. We measure the performance of each computed mapping by

<sup>3</sup> These sets belong to the public database of the *Computational Vision Lab* at the *Simon Fraser University* located at URL: <http://www.cs.sfu.ca/~colour/>.

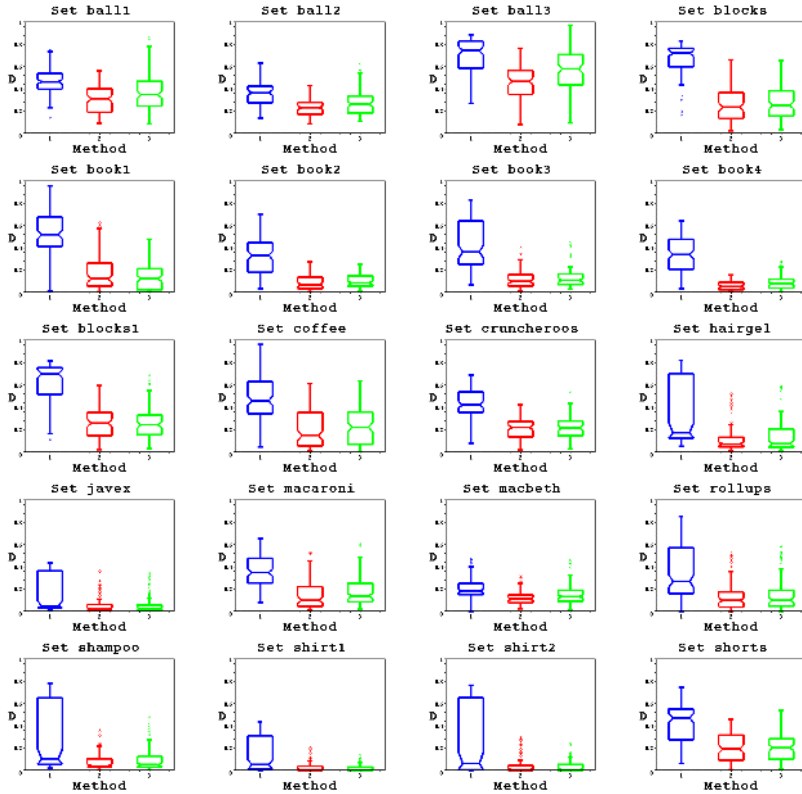


**Fig. 2.** Boxplots of the results per object set and method.

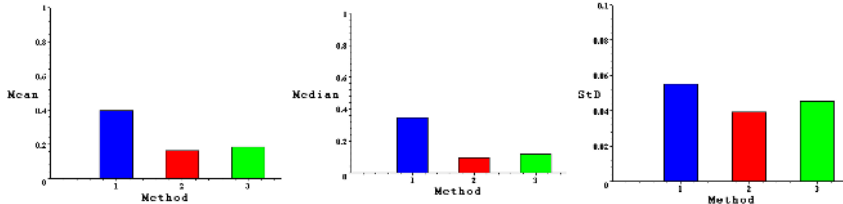


**Fig. 3.** Mean, median and standard deviation of the results per method.

comparing the chromaticity histogram of the transformed image with that of the canonic by means of the *distance* between histograms defined using the Eq. (4).

To compare the results with a *ground truth*, we directly calculate the colour transformation out of the *real illuminant colour*. That is, if two illuminants  $E^a$  and  $E^b$  have colours  $(R^a, G^a, B^a)$  and  $(R^b, G^b, B^b)$ , respectively, then the change from  $E^a$  onto  $E^b$  is  $(\alpha_0, \beta_0) = (r^b/r^a, g^b/g^a)$ , where  $(r^a, g^a)$  and  $(r^b, g^b)$  are the illuminant chromaticities, according to Eq. (2). This information was measured at the same time as the image database using a diffuse white surface at the scene

[4,5]. The mappings computed in this way are the limit of performance of any colour constancy algorithm using Eq. (3) to model the colour change.

In Fig. 2, for each object, we plot the histogram distances into three sets. In *blue* –(1)–, when no colour correction is carried out. These of using the real illuminant colour in *red* –(2)– and those of our algorithm in *green* –(3)–. Each set is depicted as a *boxplot*, where the three quartiles form the box with a notch at the median, and the maximum and the minimum are the extrema of the bars. It can be appreciated in all the sets that there has been a reduction in the colour difference with regard to not doing any colour correction –blue sets–. And more importantly, the performance of the algorithm is close to that of the mappings computed from the real illuminant colour –red sets–.

**Table 1.** Global results per method.

Method	Blue (1)	Red (2)	Green (3)
Mean	0.398	0.166	0.186
Median	0.346	0.097	0.118
St. Dev.	0.055	0.040	0.046

To globally describe the performance, we put together the former results and compute the mean, the median and the standard deviation for each category, as can be seen in Table 1 and Fig. 3. Thus, we can state that globally the colour difference has decreased from 0.394 to 0.186, a percentage reduction of 56.6%. Secondly, these values are close to those obtained when using the true illuminant colour, i.e., a distance of 0.166 and a percentage reduction of 60.6%.

## 7 Conclusions

The present paper shows a procedure based on image raw data that, in a framework where the colour change is modelled as a 2D diagonal matrix, finds a colour mapping so that the image colours can be rendered as seen under a canonic illumination reducing their dependence on the light conditions. The performance of the algorithm was checked with a wide range of real images of objects under different illuminants. The results show its performance is comparable to the case of knowing the real illuminant colour. Finally, we can state our algorithm improves colour images since stabilises pixel colours in front of illuminant changes.

## References

1. Finlayson, G., Hordley, S., Hubel, P.: Colour by correlation: A simple, unifying framework for colour constancy. *IEEE Trans. on Pattern Analysis and Machine Intelligence* **23** (2001) 1209–1221

2. Forsyth, D.: A novel algorithm for color constancy. *Int. Journal of Computer Vision* **5** (1990) 5–36
3. Finlayson, G.: Color in perspective. *IEEE Trans. on Pattern Analysis and Machine Intelligence* **18** (1996) 1034–1038
4. Barnard, K., Cardei, V., Funt, B.: A comparison of computational colour constancy algorithms: Part one: Methodology and experiments with synthesized data. *IEEE Trans. on Image Processing* **11** (2002) 972–983
5. Barnard, K., Martin, L., Coath, A., Funt, B.: A comparison of computational colour constancy algorithms: Part two: Experiments with image data. *IEEE Trans. on Image Processing* **11** (2002) 985–996
6. Sapiro, G.: Color and illuminant voting. *IEEE Trans. on Pattern Analysis and Machine Intelligence* **21** (1999) 1210–1215
7. Funt, B., Barnard, K., Martin, L.: Is colour constancy good enough? In: Proc. 5th European Conference Computer Vision. (1998) 445–459
8. Finlayson, G., Hordley, S.: Improving gamut mapping color constancy. *IEEE Trans. on Image Processing* **9** (2000) 1774–1783
9. Swain, M., Ballard, D.: Indexing via color histograms. In: Proc. Int. Conf. on Computer Vision. (1990) 390–393
10. Schiele, B., Crowley, J.: Object recognition using multidimensional receptive field histograms. In: Proc. Int. European Conf. on Computer Vision. (1996) 610–619

# Reconstruction of Surfaces from Cross Sections Using Skeleton Information

Joaquín Pina Amargós<sup>1</sup> and René Alquézar Mancho<sup>2</sup>

<sup>1</sup> Centro de Estudios de Ingeniería y Sistemas (CEIS), Polytechnic Institute “José A Echeverría” (CUJAE), Havana, Cuba  
jpina@ceis.cujae.edu.cu

<sup>2</sup> Departament de Llenguatges i Sistemes Informàtics (LSI), Universitat Politècnica de Catalunya (UPC), Barcelona, Spain  
alquezar@lsi.upc.es

**Abstract.** Surface reconstruction from parallel cross sections is an important problem in medical imaging and other object-modeling applications. Shape and topological differences between object contours in adjacent sections cause severe difficulties in the reconstruction process. A way to approach this problem is using the skeleton to create intermediate sections that represent the place where the ramifications occur. Several authors have proposed previously the use of some type of skeleton to face the problem, but in an intuitive way and without giving a basis that guarantees a complete and correct use. In this paper, the foundations of the use of the skeleton to reconstruct a surface from cross sections are expounded. Some results of an algorithm that is based on these foundations and has been recently proposed by the authors are shown that illustrate the excellent performance of the method in especially difficult cases not solved previously.

## 1 Introduction

The problem of reconstructing the surface of a solid object from a series of parallel planar cross sections (referred hereinafter simply as sections) has captured the attention in the Computer Graphics and Vision literature during the past three decades (see [1,6,9,10,11,13]). This important problem is found, for instance, in the processing of medical images that represent cross sections of the human body interior and are obtained through non-invasive methods like Computerized Tomography (CT) and Magnetic Resonance. Other applications are the non-destructive digitization of three-dimensional (3D) objects from their slices and the reconstruction of 3D models of the terrain from topographic elevation contours.

In general, the data consist of a series of sections that are separated to a constant distance. Each one of them is formed by a set of closed contours that define the boundary of the material of interest to be modeled. The problem resides in finding a set of planar closed convex polygons (usually triangles) that connect the vertices of the contours, so that the surface of a geometrically complete object (see definition in [3]) is built. As the sections are consecutive, the problem can be reduced to that of

finding the set of polygons that join the contour vertices corresponding to each pair of adjacent sections.

Until the beginnings of the eighties, the methods proposed to solve the problem forced the connection of each vertex of a section with some vertices of the adjacent sections. However, as a certain distance separates the sections, the information of the places where the ramifications occur in the surface of interest is often missing. This causes differences in shape (Fig. 1a) and in the number of contours (Fig. 1d) between adjacent sections. In these cases, the restriction aforementioned does not only make impossible the treatment of the ramifications (Fig. 1d), but rather it causes a not very real tiling, even producing unavoidable interceptions between the triangles that are formed (Fig. 1b).

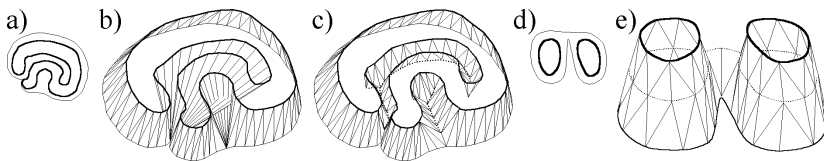


**Fig. 1.** Adjacent sections with shape differences. a), b) y c) are modified from [1]

A way to approach this problem is creating intermediate sections that represent the place where the ramifications occur (*dotted line* in Figs. 1c, e). To this end, several authors [1,6,8,9,10] have proposed previously the use of a skeleton, but in an intuitive way and without giving a basis that guarantees a complete and correct use.

The previous related works that approach the problem using some type of skeleton are commented in the next section. The relationships between the concepts of image, skeleton and section are studied in Sections 3 and 4, and they constitute the foundations of the use of the skeleton to reconstruct a surface from cross sections. Finally, some results of an algorithm recently proposed by the authors which is based on these foundations [11] are shown that illustrate the excellent performance of the method.

## 2 Overview of Previous Related Work

Sloan and Hrechanyk [13] were the first ones to suggest the creation of artificial intermediate sections between adjacent sections in the cases where these sections are very different. Then the tiling between this artificial section and each one of the two that originated it could be made using any of the proposed methods. In this way, the model would better fit the reality, representing the place where the ramification occurs in the intermediate section.

However, it is not until the work of Levin [8] where the first method is proposed that builds a set of intermediate contours between contours of adjacent original sections in order to solve the ramification and tiling problems. The Levin's method is based on calculating the *distance field* for each point of each section. This value is the signed distance between the analyzed point and its nearest contour. In terms of distance fields, contours can be regarded as isocurves with an isovalue of zero. The value

is positive or negative depending on whether the point is inside or outside the contour, respectively. The distance fields of the intermediate section are obtained by adding, for each point, the values of the corresponding distance fields in the original contiguous sections. The main limitation of this method is the very large number of triangles that the obtained surface presents.

The polygonal form of skeleton called *medial axis* is used for the first time in Meyers' doctoral thesis [9]. However, it is not inserted between adjacent sections, but used to obtain information about the relationships of vicinity among the regions where ramifications occur. The form of skeleton used was called *shaved medial axis* (SMA) (Fig. 1d) and the possible types of connections among its loops helped to classify the ramifications. The method does not work correctly in the cases of ramifications from many-to-many contours. In addition, the projections on a same plane of the contours related with the ramification can intercept each other.

Bajaj *et al.* [1] detected the parts of contours with very different shape and applied a method similar to the one used by Geiger [4] to tile them. This method requires the *edge Voronoi diagram* (EVD), but due to the difficulty in implementing a numerically stable algorithm, Bajaj *et al.* proposed to find a rough medial axis using an iterative decomposition of the polygon, in which cutting edges are added until all polygons are convex. The authors did not specify how to implement this decomposition.

Oliva *et al.* [10] used a new type of skeleton called *angular bisector network* (ABN) that was calculated as an approximation to the EVD. Each segment of the analyzed contours was associated with a cell of the ABN. The cells that guarantee a certain level of proximity can be triangulated in a straightforward way. Otherwise, an intermediate contour is inserted that consists of the common border between cells corresponding to contour segments in different sections. This procedure can be repeated recursively until all the cells are triangulated.

In a recent work, Klein *et al.* [6] presented an algorithm that combines the approach proposed by Levin and the recursive triangulation proposed by Oliva *et al.* Instead of the complex calculation of the ABN, Klein *et al.* computed discrete distance fields to define intermediate contours and the needed correspondences. The main advantage of the method proposed is the use of the *z-buffer* of standard graphics hardware to obtain the medial axis that separates the projections of the analyzed contours and the proximity correspondences between the vertices of the medial axis and those of the analyzed contours. All the examples shown by Klein *et al.* were artificial and none of them included holes.

### 3 Relationship between Image and Skeleton

#### 3.1 Definitions

An *image* can be defined as a function  $f: N \times N \rightarrow G$  where  $f(x, y)$  is the illumination of a pixel with spatial coordinates  $(x, y)$  belonging to the set  $N$  of natural numbers and  $G$  is the set of positive integer numbers representing their illumination. In this work, *binary images* will be used, where the two values represent the background and the object (*white* and *black pixels* in Fig. 2a, respectively).

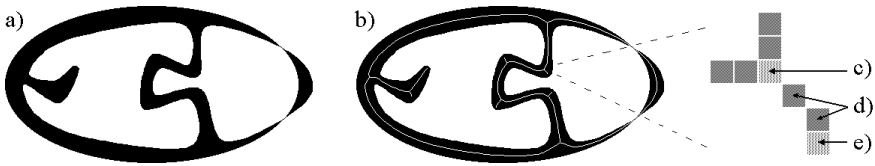


**Fig. 2.** Binary image (a), skeleton over it drawn in white (b) and pixel connectivity (c-e)

The skeleton or medial axis can be defined, in a general way, as a set of connected lines or curves that are equidistant with respect to the borders or limits of a figure [12]. If the figure is represented by a binary image, the skeleton is its narrowest representation (Fig. 2b). A specific definition is: the *skeleton*  $E(I)$  of an image  $I$  is a set of points  $p$  located inside the boundary of  $I$  such that there exists, for each one of them, at least two points belonging to the boundary that are separated at a minimum distance from it (and, therefore,  $p$  is halfway).

The process for which the skeleton of an image is obtained is denominated *skeletonization*. Most of the skeletonization algorithms erode the borders of the binary image repeatedly until narrow lines or simple pixels remain. This erosion process is also known as *thinning*. Taking into account the comparative analysis of twenty thinning algorithms carried out in [7], we selected, among the algorithms that preserve connectivity, the Suzuki-Abe algorithm [14] to be used in this work, due to its high speed, simplicity and demonstrated success, even in recent works [5].

### 3.2 Connectivity of Skeleton Vertices

By definition of skeleton, the connectivity of each one of its points  $p_i$  is determined by the number of pixels that belong to the boundary of  $I$  and are at a minimum distance from  $p_i$ . This means that the connectivity of the  $E(I)$  pixels is determined by the shape of the original image boundary. When the shape is similar along a certain trajectory what is obtained is just a path for this trajectory. For example, the skeleton of an image that represents a hand-written letter is an approximation of the way that the pencil tip goes through when drawing it.

Thus, each pixel of  $E(I)$  can be classified according to its connectivity. A *terminal pixel* has connectivity one and is caused by the presence of a local maximum in the  $I$  boundary. A terminal pixel appears at the end of a segment where a protuberance or local convex shape occurs in  $I$  (Fig. 2e). An *intermediate pixel* has connectivity two and is obtained when the  $I$  boundary presents a similar shape in both sides of the line that goes approximately through the pixel and its two adjacent pixels (Fig. 2d). Lastly, a *branch pixel* has connectivity greater than two and is caused by a ramification involving two or more trajectories. A branch pixel appears in the place where the shape of  $I$  ramifies (Fig. 2c). Terminal and branch pixels will be called *extreme pixels*.

Analyzing the existent connections among the different skeleton pixels, a skeleton can be considered as a set of extreme pixels that are connected to each other through zero or more intermediate pixels. A group of intermediate pixels that connect a pair of extreme pixels will be called a *rail* of the skeleton. Note that a rail is equidistant from two portions of the image boundary that present a similar shape along it.

## 4 Relationship between Skeleton and Section

The problem of surface reconstruction from sections consists of obtaining a surface that connects the vertices of the contours that belong to each pair of adjacent sections. A supposition that covers most of the real cases is that the projection of this surface, on an intermediate plane parallel to the original sections, should be in the region that separates the material of interest of each pair of adjacent sections. The strange cases not covered by this supposition have not been dealt with by any of the consulted authors. Nevertheless, some results on these strange cases are included in Section 5.

### 4.1 Construction of the Skeleton from Adjacent Sections

When projecting the regions occupied by the material of interest of the adjacent sections on a parallel plane (Fig. 3b), the region not common to both regions is the one that separates the material of interest of these sections (Fig. 3c).

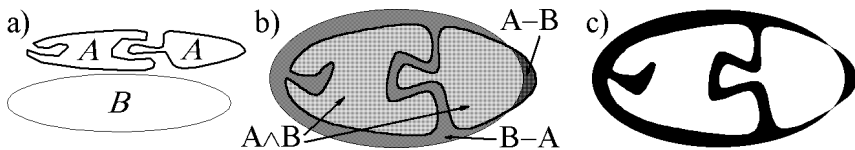


**Fig. 3.** Region that separates the material of interest in adjacent sections

This action can be expressed using logical operations on binary images. Each section is represented as a binary image where the region that occupies the material of interest has been determined. The image  $I$  that separates the material of interest of two adjacent sections is the result of the binary operation XOR ( $\vee$  exclusive) on the corresponding two images. In this way, the only pixels in  $I$  that are drawn are those that belong to the region of the material of interest in only one of the analyzed sections. After this operation, it is necessary to include the pixels that form the boundary of each one of the contours involved in order to be able to include in the skeleton the pixels where the contours of the adjacent sections intercept (if any). To obtain the skeleton it would remain to apply some skeletonization technique (commented in 3.1) to the image  $I$ , whose result would be similar to the one shown in Fig. 2b.

### 4.2 Significance of the Skeleton

As has been discussed in 3.2 the connectivity of the  $E(I)$  pixels is determined by the shape of the boundary that the image  $I$  represents. However, as has been defined in 4.1, the boundary of  $I$  is formed by the contours of the contiguous sections. Therefore, the shape of the analyzed contours determines the connectivity of the pixels of the resulting skeleton  $E(I)$ . The analysis that follows is very similar to the one discussed in 3.2, but taking into account that the shape of the image  $I$  is conditioned locally by the separation of the near contours in the adjacent sections.

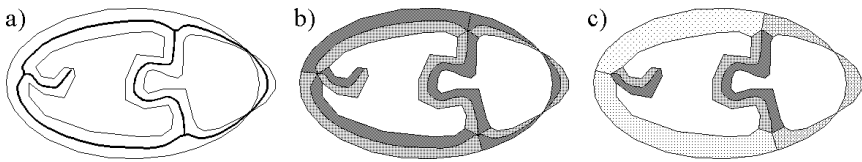


**Fig. 4.** Formation and fusion of ribbons

As has been explained in 3.2, a rail separates equidistantly two portions of the image boundary that present a similar shape along it. By construction of  $E(I)$ , these portions of the  $I$  boundary correspond to the projections of portions of the contours that belong to the analyzed adjacent sections. It is deduced then that a rail of  $E(I)$ , built according to 4.1, is halfway the projections of two nearby contour portions ( $PC_{Ca}$ ,  $PC_{Cb}$ ) with similar shape located in the contours  $C_a$  and  $C_b$ , respectively. If  $PC_{Ca}$  and  $PC_{Cb}$  belong to the same section, then the rail will represent the place where the necessary ramification occurs, so that these portions will be connected to each other at an intermediate height of the analyzed sections.

In this way, we arrive to the basic structure of the reconstruction called *ribbon*, which is composed by a rail  $L$  and a contour portion  $PC$ , such that they are close to each other and keep some shape similarity. The proximity relationship implies that there is no other rail or contour portion between  $L$  and  $PC$ . We can take advantage of these ribbon properties to reconstruct the surface that the ribbon forms using some simple and quick algorithm [2]. Notice that, due to the skeleton construction, each rail has two associated ribbons, one for each one of its sides.

During the reconstruction process, the endpoints of each contour portion should be included so that the union of the contour portions associated with each rail of the skeleton yields the original contours (Fig. 4b). In this way, the reconstruction of the surface between two adjacent sections is reduced to the union of the reconstruction of all the ribbons that form it.

The large number of generated triangles is one of the drawbacks of some of the consulted methods that use the skeleton in the surface reconstruction process. In order to reduce the number of triangles, the ribbons that share a common rail and connect contour portions located in different sections can be fused together (Fig. 4c).

## 5 Results and Discussion

We have recently proposed a surface reconstruction method which implements all the ideas presented in the two previous sections [11]. Fig. 5 displays some results on synthetic and real examples that are discussed below. See [11] for more details.

The example shown along this work (Fig. 5a) contains two adjacent sections that not only have a different number of contours, but also a very marked difference in their shapes. The result on this example is shown in Figs. 5a and 5b. Another example refers to the existence of holes in some of the sections, and the corresponding result is shown in Figs. 5c and 5d. Finally, Figs. 5e-5i display the results on an example that has not been solved by any method of the consulted literature. It is a surface portion

that twists abruptly among the sections, causing its projection to be found inside the region belonging to the material of interest in both sections.

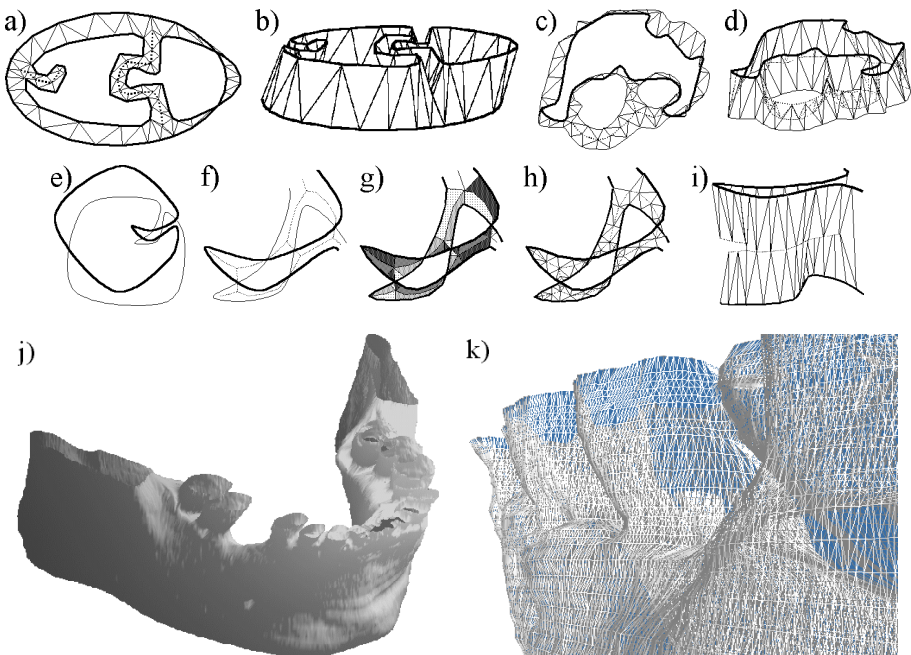


**Fig. 5.** Tiling result (*a, c, h*) and 3D view (*b, d, i, j, k*) of some reconstruction examples

In all synthetic cases it can be observed that the reconstructed surface is closed and does not intercept itself. The place where the ramifications occur is inserted in an intermediate height of the original sections and shown in the figures as dotted lines.

The results of the proposed algorithm are also shown in the reconstruction of a human jaw from real TC images (Figs. 5j, 5k), where the correct reconstruction of ramifications is observed in the base of the teeth.

## 6 Conclusions

In this paper, the foundations of the use of the skeleton to reconstruct a surface from cross sections have been explained and illustrated.

After a review of the previously reported works that have used some type of skeleton to solve the surface reconstruction problem, it was concluded that all of them made an intuitive use of the skeleton and there was a lack of a basis that guaranteed a complete and correct use of the skeleton information.

We have argued that there exists a close relationship between the contours of two adjacent sections and the rails of the skeleton built from the region that separates the material of interest in both sections. By skeleton construction, each rail separates equidistantly the projections of two nearby contour portions with similar shape. This

property can be used to reconstruct in an easy way the region, denominated ribbon, which is between the rail and one of the related contour portions. If both contour portions belong to the same section, then the rail can be used to represent the place where the ramification occurs in an intermediate height to the original sections. Otherwise, there is no ramification and, to reduce the number of triangles in the resulting surface, the rail may be discarded by fusing the adjacent ribbons that share it. The final surface reconstruction reduces to the union of the reconstruction of all the formed ribbons.

Some results of a surface reconstruction algorithm recently proposed by the authors have been shown. This algorithm [11] is based on the ideas presented here to give solution to the investigation problem. The examples displayed here have included difficult cases, even one not solved by the consulted literature. In all cases, a topologically correct surface is obtained. Moreover, all the cases are treated in a unified way, independently of whether the number of contours in the adjacent sections is the same or not, or whether the shapes of the involved contours are similar or not. Hence, a great deal of generality is achieved in the proposed solution.

## References

1. Bajaj, C.L., Coyle, E.J., Lin, K.N.: Arbitrary topology shape reconstruction from planar cross sections. *Graphical Models and Image Processing*. 58 (1996) 524–543
2. Christiansen, H.N., Sederberg, T.W.: Conversion of contour line definitions into polygonal element mosaics, *Computer Graphics*. 13 (1978) 187–192
3. Foley, J.D., Van Dam, A., Feinier, S.K., Hughes, J.F.: *Computer Graphics: Principles and Practice*. Second Edition in C. Addison Wesley (1996)
4. Geiger, B.: Tree-dimensional modeling of human organs and its applications to diagnosis and surgical planning. Technical report, 2105, INRIA, France (1993)
5. Kégl, B., Krzyzak, A.: Piecewise linear skeletonization using principal curves. *IEEE Transactions on Pattern Analysis and Machine Intelligence*. 24(1) (2002) 59–74
6. Klein, R., Schilling, A., Straßen, W.: Reconstruction and simplification of surface from contours. *Graphical Models*. 62(6) (2000) 429–443
7. Lee, S.W., Lam, L., Suen, C.: A systematic evaluation of skeletonization algorithms. *Int. J. of Pattern Recognition and Artificial Intelligence*. 7(5) (1993) 1203–1225
8. Levin, D.: Multidimensional reconstruction by set-valued approximation. *IMA J. Numerical Analysis*. (6) (1986) 173–184
9. Meyers, D.: Reconstruction of surfaces from planar contours. Doctoral dissertation. University of Washington (1994)
10. Oliva, J.M., Perrin, M., Coquillart, S.: 3D reconstruction of complex polyhedral shapes from contours using a simplified generalized Voronoi diagram. *Comp. Graphics Forum*, 15(3) (1996) C397–C408
11. Pina, J., Alquézar, R.: Results of a new method for surface reconstruction from tomographic images. In Proc., V Cong. Soc. Cub. de Bioingeniería, T0090, Havana, Cuba (2003)
12. Ritter, G.X., Wilson, J.N.: *Handbook of Computer Vision Algorithms in Image Algebra*. Second Edition. CRC Press (2001)
13. Sloan, K.R., Hrechanyk, L.M.: Surface reconstruction from sparse data. In Proc., IEEE Conf. on Patt. Recog. and Image Processing, Dallas (1981) 45–48
14. Suzuki, S., Abe, K.: Sequential thinning of binary pictures using distance transformation. In Proceedings of the 8th Int. Conf. on Patt. Recog. (1986) 289–292

# Extension of a New Method for Surface Reconstruction from Cross Sections

Joaquín Pina Amargós<sup>1</sup> and René Alquézar Mancho<sup>2</sup>

<sup>1</sup> Centro de Estudios de Ingeniería de Sistemas (CEIS), Polytechnic Institute “José A Echeverría” (CUJAE), Havana, Cuba  
jpina@ceis.cujae.edu.cu

<sup>2</sup> Departament de Llenguatges i Sistemes Informàtics (LSI), Universitat Politècnica de Catalunya (UPC), Barcelona, Spain  
alquezar@lsi.upc.es

**Abstract.** The principal steps of a new method to solve the problem of surface reconstruction from parallel cross sections are presented in this paper. This method constitutes the extension of one previously proposed by the authors using the skeleton to solve the investigation problem. The method guarantees the correct topology of the surface without altering the original contours. Some results are shown that illustrate the excellent performance of the method in particular difficult cases not solved previously. All the cases analyzed are manipulated in the same way. In real cases, the global time complexity improves the quadratic time of the quickest consulted methods.

## 1 Introduction

The problem of reconstructing the surface of a solid object from a series of parallel planar cross sections has been treated by the specialized literature in the last three decades [3,5,8,9,14]. A cross-section is formed by a set of closed contours defining the boundary of the material of interest to be reconstructed. As a distance separates the sections, information is often lost of the places where the ramifications occur in the surface of interest. This causes a shape difference and a different number of contours in adjacent sections (Fig. 1). A way to approach this problem is creating intermediate sections representing the place where the ramifications occur [8-10].

In this work, two verification criteria are taken into account. These criteria have been used by many authors (e.g. [1,3,9,10,14]): 1) The proposed solution should obtain a topologically correct surface (in general, closed and not intersected with itself) and 2) A resample of the same surface, in the place occupied by the original sections, should produce the original data.

The authors of the present work previously proposed a new method [10] to solve the branching problem. The method is based on the skeletonization technique to create new contours, corresponding to an artificial intermediate slice that models the level where branching occurs. This method makes a successful treatment of several ramifications cases without violating the verification criteria. However, it neither deals with the cases of local protuberances not present in the adjacent section (Fig. 1a)

nor the cases of multiple ramification where more than a contour of a section should connect with more than a contour of the adjacent section (Fig. 1b).

Only few of the consulted works ([1,8]) solve the “many to many” ramification case (Fig. 1b) and none has reported the solution to the case in which surface portions twist (Fig. 1c).

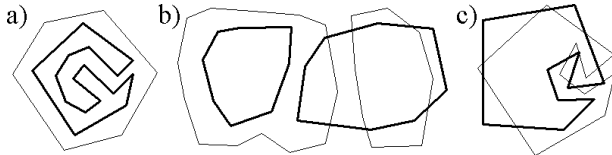


**Fig. 1.** Top view of several difficult cases

In this work a new method constituting an extension of [10] is proposed to offer an efficient and automatic solution to the investigation problem. The method reconstructs a topologically correct surface without modifying the data of the original sections.

Below, in Section 2, the main steps of the method are described. Their complexity is analyzed in Section 3. Finally, in Section 4, some results are shown in different complicated examples.

## 2 Proposed Method

For each original section, the initial data are a set of closed contours that define the boundary of the material of interest to be reconstructed. The proposed method consists of applying five steps to each pair of adjacent sections. The pseudocode of the main subroutine would be:

```

SUBROUTINE Reconstruction of model
  FOR EACH section  $S_i$  of model
    Detect correspondences between  $S_i$  and  $S_{i+1}$ 
    FOR EACH corresponding contours set
      Construct skeleton image
      Obtain skeleton graph
      Form ribbons
      Tile ribbons
    END FOR EACH
  END FOR EACH
END SUBROUTINE

```

The first step determines the correspondences existing among the contours of the sections analyzed. In this work, an overlapping method was used. This method establishes that two contours should be connected by a surface if the projections of the material of interest they wrap up overlap to a certain threshold. All the projections are made on a plane parallel to the original sections (usually the XY). The following steps are explained below and, by way of example, their results are shown in Fig. 2.

## 2.1 Skeleton Image Construction

The second step uses the same projection information than the previous step to build an image  $I$  representing the area that separates the material of interest of the analyzed contours (Fig. 2b). Then a thinning algorithm is applied, similar to the one used in [6], to obtain the skeleton  $E(I)$  (shown as thick lines in Fig. 2c). Optionally, the short hair can be eliminated (Fig. 2d). For more details concerning this step, [10] should be consulted. The skeleton built in this way offers very valuable information to reconstruct in a correct and quick way the surface that connects the corresponding contours [12].

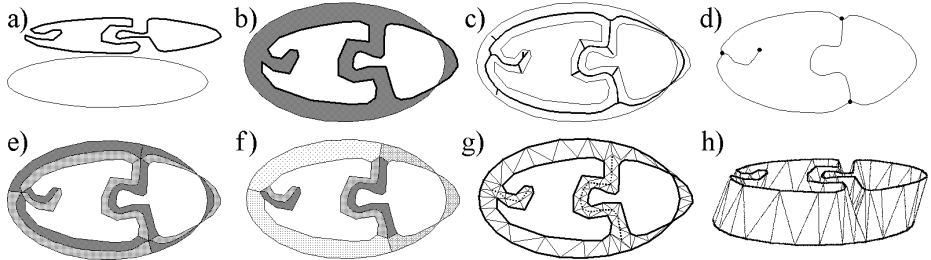


**Fig. 2.** Steps of the proposed method

## 2.2 Skeleton Graph Obtaining

Each black pixel of the skeleton image  $E(I)$ , built in the previous section, is included in the skeleton graph  $G$ . Structurally,  $G$  is formed by a list of nodes or extreme vertices  $VE$  (thick dots in Fig. 2d) and a list of arcs or rails  $L$  (lines in Fig. 2d). Each node  $VE$  contains its coordinates  $(x, y)$  and an ordered circular list of its connections  $N$ . Each connection  $N$  contains a rail  $L$  and the pixel of  $L$  to which  $VE$  is connected, called neighboring vertex  $VV$ . For convenience, the order of the connections follows the distribution of the neighboring vertices  $VV$  counterclockwise around  $VE$ . Each rail of  $G$  contains two extreme vertices and a list of the intermediate pixels that form the rail.

## 2.3 Formation and Fusion of Ribbons

In this step, the close relationship that exists between the image and its skeleton is used to simplify the final tiling, dividing the area to be reconstructed into parts called *ribbons* (Fig. 2e). Each ribbon is composed by a rail  $L$  of  $G$  and a portion  $PC$  of one of the contours analyzed.  $L$  and  $PC$  are near and bear similar shape so that there is no other rail or contour portion inside the ribbon conformed. The foundation of this decomposition is discussed in [12].

As a result of the previous steps, the rails  $L$  and extreme vertices  $VE$  of  $G$  are available. To form the ribbons we need to determine the portions  $PC$  of the original contours. During the reconstruction process, the endpoints of each contour portion should

be linked so that the union of the contour portions associated with each rail of the skeleton produces the original contours (Fig. 2e). Hence, in the union, these extreme vertices of portions are the only repeated points. In this way, the surface reconstruction between two adjacent sections is reduced to the union of all the ribbon reconstruction. The pseudo-code of an algorithm that guarantees the correct and quick selection of the contour portions to form the ribbons is presented below.

SUBROUTINE Form ribbons

```

(a) Initialize contours and extreme vertices connections as
    unmarked

FOR EACH branch vertex  $VE_i$ 
    FOR EACH connection  $N_j$  of  $VE_i$ 
        IF  $N_j$  IS unmarked
            (b) Find unmarked contour  $C$  and the nearest vertex  $V_{ini}$ 
                that would be connected to  $VE_i$  between  $N_j$  and  $N_{j+1}$ 
            (c) Choose connection  $N_{ini}$  that follows the direction of
                contour  $C$  FROM  $V_{ini}, N_j, N_{j+1}, VE_i$ 
            (d) Form contour ribbons FROM  $C, V_{ini}, VE_i, N_{ini}$ 
            (e) Mark the contour  $C$ 
        END IF
    END FOR EACH
END FOR EACH
END SUBROUTINE

```

The first step (a) is responsible for labeling all contours and rails (connections between extreme vertices) as unmarked. In step (b), the vertex  $V_{ini}$  of an unmarked original contour  $C$  that is met at the minimal distance from  $VE$ , but on the right side of the lines  $(VE, VV_{j+1})$ ,  $(VV_j, VE)$ , is found (Fig. 3a). In step (c), the connection whose  $VV$  is located on the same side as  $V_{ini+1}$  regarding the line  $(VE, V_{ini})$  is selected (Fig. 3b). This ensures that, when forming the ribbons related to the contour  $C$ , the path followed in the rails has the same direction as  $C$ . In step (d), the call to the subroutine that forms the ribbons related to  $C$  is made. Its pseudo-code is given next:

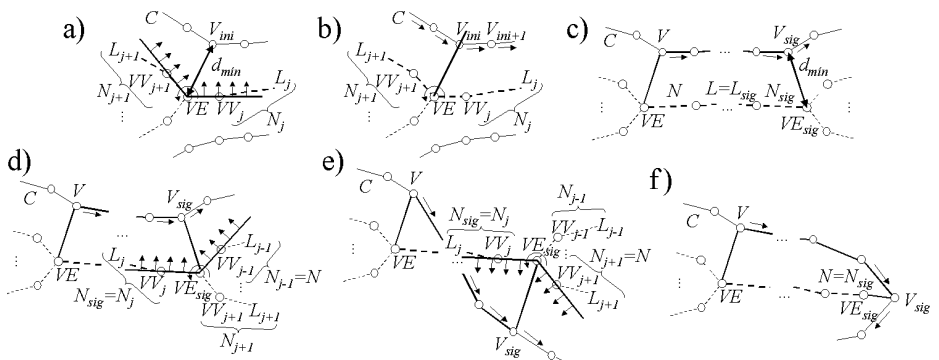


**Fig. 3.** Principal steps of the formation of ribbons

```

SUBROUTINE Form contour ribbons REQUIRE contour C, initial
vertex Vini, extreme vertex VEini, initial connection Nini
  SET V EQUAL TO Vini
  SET VE EQUAL TO VEini
  SET N EQUAL TO Nini
  REPEAT
    (f) Determine next extreme vertex VFsig and next connection
        Nsig FROM VE, N
    (g) Find the nearest vertex Vsig in contour C that would be
        connected to VEsig FROM V
    (h) Insert ribbon V, Vsig, VE, VEsig
    (i) Mark the connections N and Nsig
    (j) Determine initial connection N of the next ribbon
        FROM Vsig, VEsig, Nsig
  SET VE EQUAL TO VEsig
  SET V EQUAL TO Vsig
UNTIL (V EQUAL AS Vini) AND (VE EQUAL AS VEini)
END SUBROUTINE

```

After having executed the steps (f)-(i), that are self-explained, it is necessary to determine the initial connection  $N$  of the next ribbon. The three possible situations for step (j) to be executed are shown in the Fig. 3d-e-f. If  $VE_{sig}$  is terminal, then  $N = N_{sig}$  (Fig. 3f). If  $VE_{sig}$  is branch and  $V_{sig}$  is on the right side of the straight lines ( $VE_{sig}, VV_j$ ), ( $VV_{j-1}, VE_{sig}$ ), then  $N = N_{j-1}$  (Fig. 3d). Otherwise, the rail and the contour get crossed an odd number of times and then  $N = N_{j+1}$  (Fig. 3e).

Optionally, to simplify the result, the adjacent ribbons whose borders belong to contours of different sections may be fused. In this way, only the skeleton vertices that are involved in ramifications remain (Fig. 2f).

## 2.4 Tiling of Ribbons

As described in [12], a ribbon is composed by a rail  $L$  and a contour portion  $PC$  that keep to each other proximity and shape similarity. This property can be exploited to tile the surface it forms using some simple and quick algorithm [5]. In addition, the first verification criterion mentioned in Section 1 can always be satisfied.

Finally, in the fifth step of the main procedure, the tiling of each ribbon is performed and the final surface is obtained as their union (Fig. 2g-h). The height of the skeleton vertices is intermediate to the analyzed sections, which guarantees the second verification criterion.

## 3 Complexity Analysis

The overall complexity of the proposed method is  $O(n \cdot m)$ , where  $n$  is the number of vertices and  $m$  is the number of contours in the analyzed adjacent sections.

For the calculation of the complexity of the first step, it is taken for granted that the number of pixels to process is proportional to  $n$ . Both the construction of the skeleton image and the extraction of its skeleton graph can be performed in linear time  $O(n)$ .

The graphics of Fig. 4 show the results of the execution times of these steps in a real example composed by 151 sections, 449 contours and 91941 vertices. Their tendencies (*thick lines*) confirm the indicated linear time complexities.

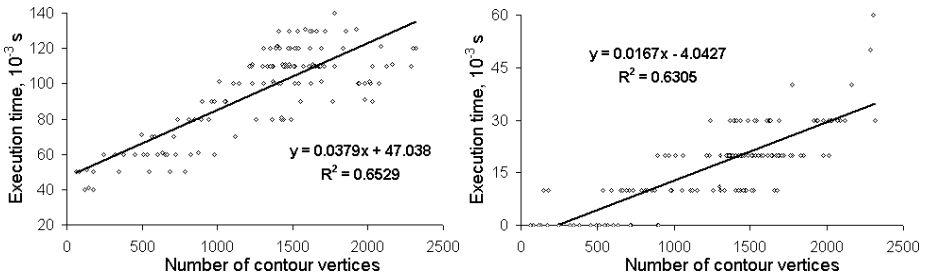


**Fig. 4.** Results of tests for construction of skeleton image (*left*) and graph (*right*) from different contours (Running in PC with Intel Pentium® processor at 736 MHz and RAM of 128 Mbyte)

The complexity of the fourth step is dominated by the initial search of the contour and nearest vertex. This step is run as many times as contours there exist in the analyzed sections. As in each call to this step, the vertices belonging to the already marked contours are not treated, its complexity is  $O(n \cdot m)$ . This is obtained from:

$$T = O\left(\sum_{i=0}^{m-1} \left( n - \frac{i \cdot n}{m} \right)\right). \quad (1)$$

A very quick algorithm is used for the ribbon reconstruction (fifth step), which presents a linear complexity  $O(n)$  [5].

## 4 Results and Discussion

Next, some results of the application of the proposed method are shown in different synthetic examples. For more details [11] should be consulted.

In a case of two contours with very different shape, similar to Fig. 1a, the results of surface reconstruction using three classical methods (greedy, optimization and contour composition; similar to [5,7,13], respectively) are shown in Fig. 5a-c, whereas the result of the proposed method is displayed in Fig. 5d. In the Figs. 5e-i, different ramification examples (without holes in the sections) are shown where a contour ramifies in two (5e-g) and three (5h-i) contours; Figs. 5g and 5i contain the results of our method. Another example refers to the existence of holes in some of the sections (Fig. 5k-l). A barely treated case in the consulted literature occurs when several contours of a section should be connected to several contours of the contiguous section; the results of our method on two such examples (the latter also with a hole) can be appreciated in the Figs. 5j, 5m. A case not approached by the consulted literature is shown in Fig. 6 in which a part of the surface twists abruptly between the sections.

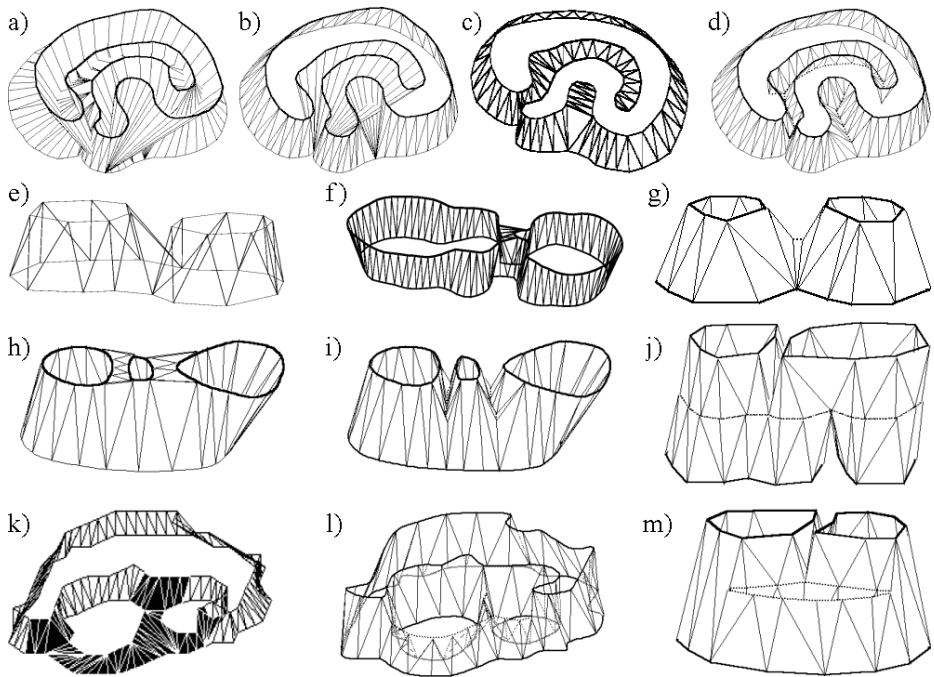


**Fig. 5.** 3D view of some reconstruction examples. a), b) are taken from [1]; c), f) from [13]; e) is taken from [4] and h), k) from [2]. d), g), i), j), l) and m) are results of the proposed method

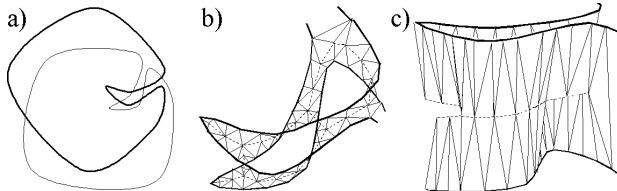


**Fig. 6.** Contours (a), detail of tiling (b) and 3D view (c) of a very difficult example

All the analyzed cases show the quality of the results not only from the aesthetic point of view, but also in the satisfaction of the verification criteria enunciated in Section 1. The rails related to the ramification are inserted at an intermediate height of the original sections (*dotted-lines* in Figs. 5, 6).

## 5 Conclusions

The main steps of a new method to reconstruct a surface from a set of cross-sections have been described. This method constitutes the extension of one previously pro-

posed by the authors using the skeleton to solve the investigation problem [10].

The proposed method always reconstructs the surface of the whole projected area separating the material of interest between each pair of adjacent sections. It guarantees the correct topology of the reconstructed surface, because the new vertices, that model the places where the contours ramify, are inserted at an intermediate height of the adjacent sections without altering the original contours.

The method is general, simple and quick. It permits to manipulate in a same way all the cases reported in the literature and, even, one not tried by other authors. Its overall complexity is  $O(n \cdot m)$ , where  $n$  is the number of vertices and  $m$  is the number of contours in the analyzed adjacent sections. This improves the complexity  $O(n^2)$  of the quickest consulted methods.

Some application results have been shown in different examples that, regardless of their high degree of complexity, illustrate the excellent performance of the method.

## References

1. Bajaj, C.L., Coyle, E.J., Lin, K.N.: Arbitrary topology shape reconstruction from planar cross sections. *Graphical Models and Image Processing*. 58 (1996) 524–543
2. Barequet, G., Sharir, M.: Piecewise-linear interpolation between polygonal slices. *Computer Vision and Image Understanding*. 63(2) (1996) 251–272
3. Barequet, G., Shapiro, D., Tal, A.: Multilevel sensitive reconstruction of polyhedral surfaces from parallel slices. *The Visual Computer*. 16(2) (2000) 116–133
4. Boissonnat, J.D.: Shape reconstruction from planar cross sections. *Computer Vision, Graphics and Image Processing*. 44 (1988) 1–29
5. Christiansen, H.N., Sederberg, T.W.: Conversion of contour line definitions into polygonal element mosaics, *Computer Graphics*. 13 (1978) 187–192
6. Kégl, B., Krzyzak, A.: Piecewise linear skeletonization using principal curves. *IEEE Transactions on Pattern Analysis and Machine Intelligence*. 24(1) (2002) 59–74
7. Keppel, E.: Approximating complex surfaces by triangulation of contour lines. *IBM Journal of Research and Development*. 19 (1975) 2–11
8. Klein, R., Schilling, A., Straßen, W.: Reconstruction and simplification of surface from contours. *Graphical Models*. 62(6) (2000) 429–443
9. Oliva, J.M., Perrin, M., Coquillart, S.: 3D reconstruction of complex polyhedral shapes from contours using a simplified generalized Voronoi diagram. *Comp. Graphics Forum*, 15(3) (1996) C397–C408
10. Pina, J., Alquézar, R.: A new method to solve the branching problem in surfaces of three-dimensional models reconstructed from parallel cross sections. *Revista Cubana de Investigación Operacional*, Universidad de La Habana, Cuba (to appear)
11. Pina, J., Alquézar, R.: Results of a new method for surface reconstruction from tomographic images. In Proc., V Cong. Soc. Cub. Bioingeniería, T0090, Havana, Cuba (2003)
12. Pina, J., Alquézar, R.: Reconstruction of surfaces from cross sections using skeleton information. In Proc. 8th Iberoamerican Congress on Pattern Recognition, Havana, Cuba (2003)
13. Sederberg, T.W., Klimaszewski, K.S., Hong, M.: Triangulation of branching contours using area minimization. *Int. J. of Computational Geometry & App.*, 8(4) (1998) 389–406
14. Surazhsky, T., Surazhsky, V., Barequet, G., Tal, A.: Blending polygonal shapes with different topologies. *Computers & Graphics*, 25 (2001) 29–39

# Imposing Integrability in Geometric Shape-from-Shading

Mario Castelán\* and Edwin R. Hancock

Dept. of Computer Science, University of York, York YO10 5DD, United Kingdom  
`{mario,erh}@cs.york.ac.uk`

**Abstract.** This paper describes a Fourier domain algorithm for surface height recovery using shape from shading. The algorithm constrains surface normals to fall on an irradiance cone. The axis of the cone points in the light source direction. The opening angle of the cone varies with iteration number, and is such that the surface normal minimizes brightness error and satisfies the integrability constraint. The results show that the method recovers needle maps that are both smooth and integrable, with improved surface stability.

## 1 Introduction

Shape-from-shading (SFS) is a problem in computer vision which has been an active topic of research for some three decades. The process was identified by Marr[10] as a key process in the computation of the 2.5D sketch, and was studied in depth by Horn[5]. The topic has also been the focus of recent research in the psychophysics literature [9][2][3]. Stated more formally, the SFS problem can be regarded as that of calculating the set of partial derivatives  $(Z_x, Z_y)$  corresponding to a surface  $Z = Z(x, y)$ , where  $Z$  is simply an intensity image.<sup>1</sup> In brief, we need to solve the image irradiance equation,  $E(x, y) = R(p(x, y), q(x, y), s)$ , where  $E$  is the intensity value of the pixel with position  $(x, y)$ ,  $R$  is a function referred to as *the reflectance map*[6], that maps the surface gradients  $p = \frac{\partial Z(x, y)}{\partial x}$  and  $q = \frac{\partial Z(x, y)}{\partial y}$  to an intensity value and  $s$  is the light source direction. If the surface normal at the location  $(x, y)$  is  $n = (p, q, -1)$  then under Lambertian reflectance model, the image irradiance equation becomes  $E(x, y) = n \cdot s$ .

Unfortunately, the image irradiance equation is underconstrained, and the family of surface normals fall on a reflectance cone whose apex angle  $\alpha$  is equal to  $\cos^{-1} E(x, y)$ , and whose axis points in the light source direction  $s$ . Several constraints have been used to overcome the underconstrained nature of the Lambertian shape-from-shading problem. However, their main drawback is that they have a tendency to oversmooth the recovered surface slopes and result in poor

\* Supported by National Council of Science and Technology (CONACYT), Mexico, under grant No. 141485.

<sup>1</sup> More than one image can be used, but this is an extension of SFS referred to as photometric stereo.

data-closeness. The net result is a loss of fine surface detail. For a complete survey of most SFS methods, see [16].

In a recent paper Worthington and Hancock [14] have demonstrated how these problems may be overcome by constraining the surface normals to lie on the reflectance cone and allowing them to rotate about the light source direction subject to curvature consistency constraints. Unfortunately, the needle maps delivered by the method are not guaranteed to satisfy the integrability constraint, which means that the recovered partial derivatives are not independent on the path of integration (i.e. the height function may not be recoverable). Besides, these needle maps also suffer the drawback of high dependency on the image intensities, making the method prone to noisy data such as specularities, roughness and overshadowed areas.

There are a number of ways in which a surface may be recovered from a field of surface normals [7,8]. One approach is to use trigonometry to increment the height function along a path or a front [1,12]. However, one of the most elegant approaches is that described by Frankot and Chellappa [4] which shows how the surface may be reconstructed subject to integrability constraints by performing a Fourier analysis of the field of surface normals.

The aim in this paper is to develop a shape-from-shading scheme that can be used to recover integrable needle maps subject to hard constraints on Lambertian reflectance as well as relaxing the image intensity dependance driven by such constraints. In order to demonstrate how the two techniques can be combined, in subsequent sections we will briefly explain the geometric approach developed by Worthington and Hancock[14] for solving SFS, as well as the algorithm proposed by Frankot and Chellapa [4] for enforcing integrability in SFS.

## 2 Geometric Approach for SFS

Worthington and Hancock [14] have developed an SFS method in which the image irradiance equation is treated as a hard constraint by constraining the recovered surface normals to lie on the reflectance cone. Suppose that  $\hat{N}_k$  is a smoothed<sup>2</sup> surface normals at step  $k$  of the algorithm, then the update equation for the surface normal directions is

$$\hat{N}_{k+1} = \Theta \hat{N}_k \quad (1)$$

where  $\Theta$  is a rotation matrix computed from the apex angle  $\alpha$  and the angle between the current smoothed estimate of the surface normal direction  $\hat{N}_k$  and the light source direction. To restore the surface normal to the irradiance cone, it must be rotated by an angle

$$\theta = \cos^{-1}(E) - \cos^{-1} \left( \frac{\hat{N}_k \cdot s}{\|\hat{N}_k\| \cdot \|s\|} \right) \quad (2)$$

---

<sup>2</sup> For further details about the suggested method for smoothing the normal field, see [13]

about the axis  $(u, v, w)^T = \tilde{N}_k \times s$ . Hence, the rotation matrix is

$$\Theta = \begin{pmatrix} c + u^2 c' & -ws + uvc' & vs + uw c' \\ ws + uvc' & c + v^2 c' & -us + vwc' \\ -vs + uw c' & us + vwc' & c + w^2 c' \end{pmatrix} \quad (3)$$

where  $c = \cos(\theta), c' = 1 - c$  and  $s = \sin(\theta)$ .

The needle maps delivered by this geometric framework have proved to be useful in experiments for topography-based object recognition [15].

### 3 Integrability in SFS

The integrability condition in SFS ensures that the recovered surface satisfies the following condition on the partial derivatives of the height function:  $Z_{xy} = Z_{yx}$ . This condition can also be regarded as a smoothness constraint, since the partial derivatives of the surface need to be continuous in order that they can be integrable or independent on the path of integration. In [4] Frankot and Chellappa proposed a method to project a gradient field to the nearest integrable solution. They suggested to use a set of integrable basis functions to represent the surface slopes so as to minimize the distance between an ideally integrable gradient field and a non integrable one.

Following [4], if the surface  $Z$  is given by

$$\tilde{Z}(x, y) = \sum_{\omega \in \Omega} \tilde{C}(\omega) \phi(x, y, \omega) \quad (4)$$

where  $\omega$  is a two dimensional index belonging to a domain  $\Omega$ , and  $\phi(x, y, \omega)$  is a set of basis functions which are not necessarily mutually orthogonal, the partial derivatives of  $\tilde{Z}$  can also be expressed in terms of this set of basis functions using the formulae

$$\tilde{Z}_x(x, y) = \sum_{\omega \in \Omega} \tilde{C}(\omega) \phi_x(x, y, \omega) \quad \text{and} \quad \tilde{Z}_y(x, y) = \sum_{\omega \in \Omega} \tilde{C}(\omega) \phi_y(x, y, \omega) \quad (5)$$

Given that  $\phi_x(x, y, \omega)$  and  $\phi_y(x, y, \omega)$  are integrable, then so are the mixed partial derivatives of  $\tilde{Z}(x, y)$ .

In the same way, the possibly non integrable gradient field (which, indeed, is the only information we have) can be represented as

$$\hat{Z}_x(x, y) = \sum_{\omega \in \Omega} \hat{C}_1(\omega) \phi_x(x, y, \omega) \quad \text{and} \quad \hat{Z}_y(x, y) = \sum_{\omega \in \Omega} \hat{C}_2(\omega) \phi_y(x, y, \omega) \quad (6)$$

Note that, as  $\hat{C}_1 \neq \hat{C}_2$ , then  $\hat{Z}_{xy} \neq \hat{Z}_{yx}$ .

The goal then is to find the set of coefficients that minimize the quantity

$$d\left\{(\hat{Z}_x, \hat{Z}_y), (\tilde{Z}_x, \tilde{Z}_y)\right\} = \int \int \left\| \tilde{Z}_x - \hat{Z}_x \right\|^2 + \left\| \tilde{Z}_y - \hat{Z}_y \right\|^2 dxdy \quad (7)$$

As Frankot and Chellappa proved, the set of coefficients  $\tilde{C}(\omega)$  minimizing the distance given by the above equation is

$$\tilde{C}(\omega) = \frac{P_x(\omega)\hat{C}_1(\omega) + P_y(\omega)\hat{C}_2(\omega)}{P_x(\omega) + P_y(\omega)}, \quad (8)$$

where  $P_x(\omega)$  and  $P_y(\omega)$  are  $\int \int \|\phi_x(x, y, \omega)\|^2 dx dy$  and  $\int \int \|\phi_y(x, y, \omega)\|^2 dx dy$  respectively.

If  $\phi(x, y, \omega)$  is assumed to be the set of Fourier basis functions  $\exp(j\omega_x x + j\omega_y y)$ , with  $\Omega = (2\pi n, 2\pi m)$ , where  $n \in \{0, 1, \dots, N-1\}$  and  $m \in \{0, 1, \dots, M-1\}$  for an  $N \times M$  image, then  $P_x = \omega_x^2$ ,  $P_y = \omega_y^2$ ,  $\hat{C}_1(\omega) = \hat{C}_x(\omega)/j\omega_x$ , and  $\hat{C}_2(\omega) = \hat{C}_y(\omega)/j\omega_y$ . Therefore, (8) is represented in the Fourier domain by

$$\tilde{C}(\omega) = \frac{-j\omega_x \hat{C}_x(\omega) - j\omega_y \hat{C}_y(\omega)}{\omega_x^2 + \omega_y^2}. \quad (9)$$

In this manner, by projecting the set of coefficients  $\tilde{C}(\omega)$  back to the spatial domain, a height map corresponding to the nearest integrable surface  $\tilde{Z}(x, y)$  can be obtained from the input gradient field.

## 4 Introducing the Integrability Condition in the Geometric Approach for SFS

The idea underpinning this paper is to calculate the nearest integrable surface and obtain the apex angle of the Lambertian cone on this surface after each iteration. The algorithm can be summarized as follows:

1. Calculate an initial estimate of surface normals  $N = (N_x, N_y, N_z)$ .
2. Smooth  $N$  to obtain  $\hat{N}$ .
3. Obtain the nearest integrable surface  $\tilde{Z}$  by solving (9) using the smoothed surface normal field  $\hat{N}$ .
4. Get the apex angle  $\alpha$  of the Lambertian cone using the values of  $\tilde{Z}$ , that is to say,  $\alpha = \cos^{-1}(\tilde{Z})$ .
5. Calculate  $\hat{\hat{N}}$ , by rotating  $\hat{N}$ , using (1).
6. Make  $N = \hat{\hat{N}}$  and return to step 2. Repeat until a desired number of iterations has been reached.

We should note that in this method the rotation matrix does not remain static through the iterative process, since the changes in  $\alpha$  depend on the recovered surface after each iteration. It is also important to remark that due to the projection of the surface normals to the reflectance cone after each iteration, the z-component  $\hat{\hat{N}}_z$  of the normal  $\hat{\hat{N}}$  will always correspond to the calculated height surface of the final gradient field when using the Frankot and Chellappa height recovery method. By contrast, in the method of Worthington and Hancock the z-component  $N_z$  will always be the normalised input intensity image. Therefore, besides calculating surface gradients, the new algorithm also calculates height information.

## 5 Experiments

The algorithm was tested on synthetic as well as real images. The evaluation criteria was based on the absolute height difference and degree of gradient consistency (i.e. the percentage of pixels of every image whose differences  $Z_{xy} - Z_{yx}$  are less than or equal to a certain threshold<sup>3</sup>). In our experiments we have compared the results obtained with the geometric approach of Worthington and Hancock, and the new integrable-geometric approach.

Three synthetic images were tested<sup>4</sup>. Forty real world images (fifteen of these with corresponding height data, taken from the range database in [17], and the rest taken from [11] and from [16]) were also used for tests<sup>5</sup>.

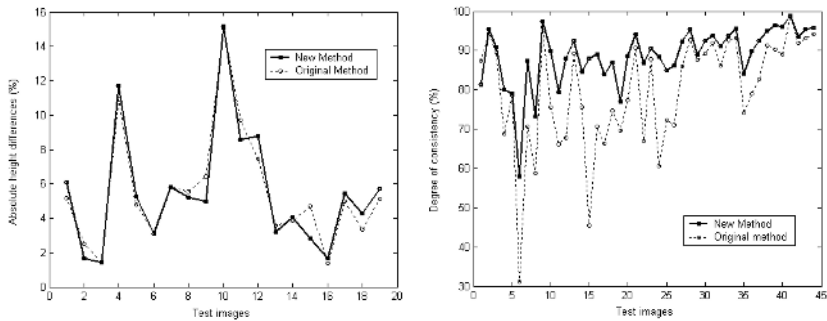


**Fig. 1.** Left: plot of the absolute height differences for synthetic and range images. Right: plot of the gradient consistency degree tests.

Figure 1 (left) shows the results for the absolute height differences. The original approach is represented by the dotted line, while the new one is represented by the solid line. The plot reveals that there seems to be no bias for favoring each method, and that the height difference between them is not significant.

The results of the experiments for degree of gradient consistency are summarized in Figure 1 (right). The figure shows that the combined algorithm (solid line) gives more consistent results than the original one (dotted line), as the percentage of gradient consistency is greater for the new approach. This suggests that the new method is enforcing integrability in the original method.

In a further analysis of the results, Figure 2 shows a 3D plot of the recovered heights for each method. The first column corresponds to the input image, the second column is a plot of the range data of each image given as a base for comparison, the third column represents the recovered height map for the new method and the fourth column shows the height maps for the original method.

<sup>3</sup> For all the experiments this threshold was set to 0.1.

<sup>4</sup> These images were also used in [16].

<sup>5</sup> For all the tests, the light source direction was assumed to be [0,0,1].

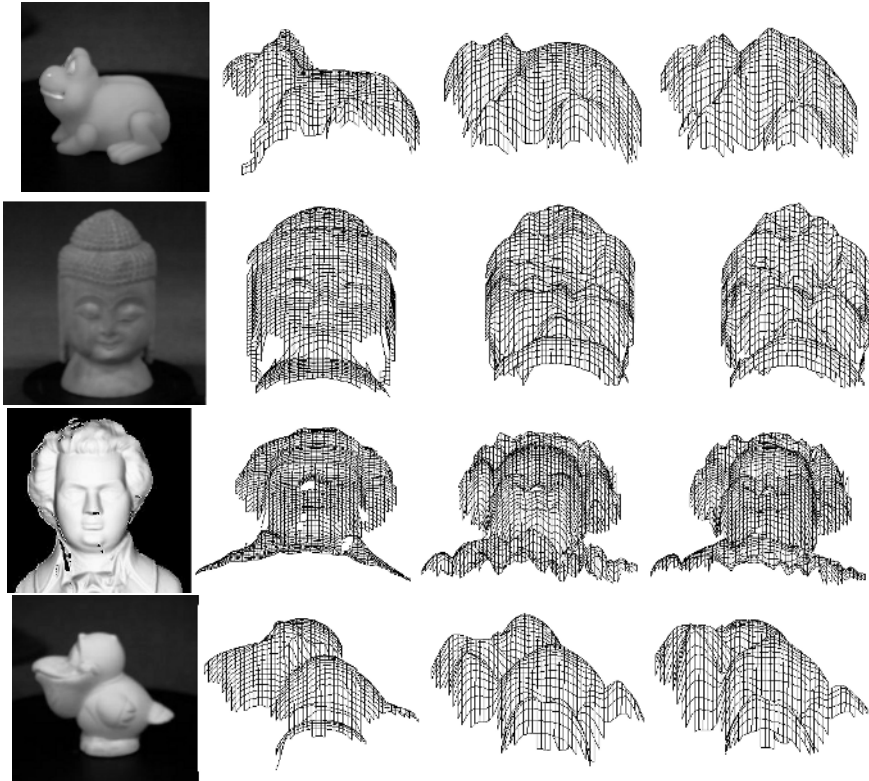


**Fig. 2.** Recovered height surface for range images. From left to right: intensity image, range data, recovered surface for the combined algorithm, recovered surface for the original algorithm.

We can observe that the new algorithm seems to stabilize the surface, avoiding some of the sudden changes present in the recovered surface for the original method. Specifically, in the cases of the frog and the pelican, the recovered surface appears to be smoother, with none of the spurious peaks in the height map which result from the use of the original method. Also, the height plots of Budda and Mozart show a more stable surface than those produced by the original method.

Figure 3 shows the recovered needle maps for each method. A visual examination of the results suggests that the new method delivers needle maps that are both smoother and contain more fine topographic detail than original method. This effect is more evident in the cases of the frog and Budda.

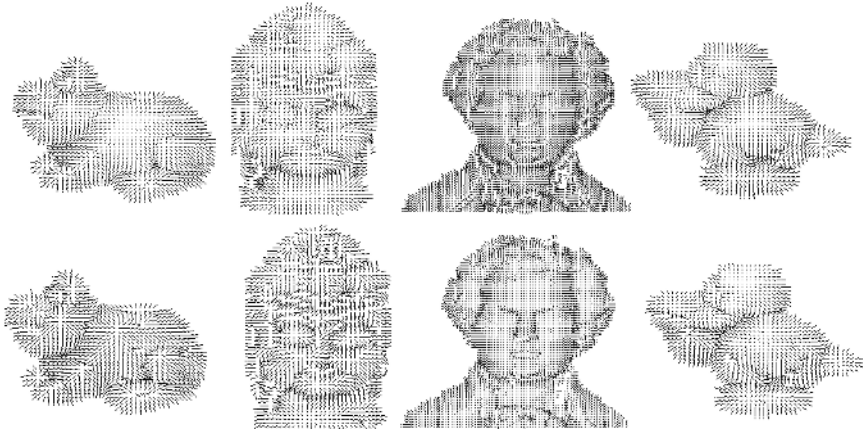


**Fig. 3.** Recovered needle maps for each method. Top row: combined algorithm. Bottom row: original algorithm.

## 6 Conclusions

In this paper we have demonstrated how to impose integrability constraints on the geometric approach for SFS suggested by Worthington and Hancock. We follow Frankot and Chellappa and impose the constraints in the Fourier domain. Experiments reveal that the resulting method exhibits improved robustness and gradient consistency. However, although the height difference statistics do not reveal any systematic improvement in algorithm performance, both the recovered height surfaces and the needle maps delivered by the new algorithm appear to be better behaved and also preserve fine surface detail. It is important to comment that in this new method the calculation of surface orientations is less constrained by the irradiances of the image, as the rotation matrix changes through the iterative process. This is a way of relaxing the original method's problem of hard constraints on data-closeness with the image irradiance equation. Our future plans include using alternative basis functions and in particular the discrete cosine transform, as well as comparing the output needle maps for local integration tests.

## References

1. A.G. Bors, E.R. Hancock, R.C. Wilson. Terrain Analysis Using Radar Shape-from-Shading. *IEEE Trans, on Pattern Analysis and Machine Intelligence*, 25(5), 2003.
2. R.G.F. Erens, A.M.L. Kappers and J.J. Koenderink. Perception of Local Shape from Shading. *Perception and Psychophysics*, 54(2):145–156, 1993.
3. R.G.F. Erens, A.M.L. Kappers and J.J. Koenderink. Estimating Local Shape from Shading in the Presence of Global Shading. *Perception and Psychophysics*, 54(3):334–342, 1993.

4. R.T. Frankot and R. Chellappa. A Method for Enforcing Integrability in Shape from Shading Algorithms. *IEEE Trans. Pattern Analysis and Machine Intelligence*, 10(4):438–451, 1988.
5. B.K.P. Horn and M.J. Brooks Shape from Shading. *MIT Press, Cambridge, MA*, 1989.
6. B.K.P. Horn. Understanding Image Intensities. *Artificial Intelligence*, 8:201–231, 1977.
7. R. Klette and K. Schluns, Height Data from Gradient Fields. *Proc. Machine Vision Applications, Architectures and Systems Integration*. 5:204–215, 1996.
8. R. Klette, K. Schluns, and A. Koschan. Computer Vision: Three-dimensional Data From Images. *Springer-Verlag Singapore*, 1998.
9. J.J. Koenderink, A.J. Van Doorn and A.M.L. Kappers. Surface Perception in Pictures. *Perception and Psychophysics*, 52(5):487–496, 1992.
10. D. Marr. Vision. *W.H. Freeman & Co., San Francisco*, 1982.
11. S.A. Nene, S.K. Nayar, and H. Murase. Columbia Object Image Library: COIL-100. Technical Report CUCS-006-96, Department of Computer Science, Columbia University, February 1996.
12. A. Robles-Kelly and E.R. Hancock. A Graph-Spectral Method for Surface Height Recovery from Needle-maps. *Proceedings of the IEEE Conference on Computer Vision and Pattern Recognition, IEEE Computer Society*, 2001.
13. P.L. Worthington and E.R. Hancock. Needle Map Recovery Using Robust Regularizers. *Image and Vision Computing*, 17(8):545–559, 1998.
14. P.L. Worthington and E.R. Hancock. New Constraints on Data-closeness and Needle Map Consistency for Shape-from-shading. *IEEE Trans. on Pattern Analysis and Machine Intelligence*, 21(12):1250–1267, 1999.
15. P.L. Worthington and E.R. Hancock. Object Recognition Using Shape-from-Shading. *IEEE Trans. on Pattern Analysis and Machine Intelligence*, 23(5):535–542, 2001.
16. R. Zhang, P.S. Tsai, J.E. Cryer and M. Shah. Shape from Shading: A Survey. *IEEE Trans. on Pattern Analysis and Machine Intelligence*, 21(8):690–706, 1999.
17. Signal Analysis and Machine Perception Laboratory, Department of Electrical Engineering, The Ohio State University,  
<http://sampl.eng.ohio-state.edu/> sampl/data/3DDB/RID/index.htm

# Correcting Radial Lens Distortion Using Image and Point Correspondences

Leonardo Romero and Felix Calderon

UMSNH, Morelia, Mich., 52000, Mexico  
`{lromero,calderon}@zeus.umich.mx`

**Abstract.** This paper describes two new methods for lens distortion calibration using image and point correspondences. Images (or feature points) captured by a camera are undistorted and projected into a calibration pattern image. Both methods apply the Gauss–Newton–Levenberg–Marquardt non–linear optimization technique to match, in one case, the camera image and the pattern image, and in the other case, selected point correspondences from the camera image to the pattern image. One way to automatically find good point correspondences is presented. Experimental results compare the performance of both methods and show better results using point to point correspondences.

## 1 Introduction

Most algorithms in 3-D Computer Vision rely on the pinhole camera model because of its simplicity, whereas video optics, especially wide–angle lens, generate a lot of non–linear distortion. In some applications, for instance in stereo vision systems, this distortion can be critical.

Camera calibration consists of finding the mapping between the 3-D space and the camera plane. This mapping can be separated in two different transformations: first, the relation between the origin of 3-D space and the camera coordinate system, which forms the external calibration parameters (3-D rotation and translation), and second the mapping between 3-D points in space and 2-D points on the camera plane in the camera coordinate system, which form the internal calibration parameters [1].

This paper introduces two new methods to find the internal calibration parameters of a camera, specifically those parameters related with the radial distortion due to wide–angle lens.

The first method works with two images, one from the camera and one from a calibration pattern (without distortion) and it is based on a non–linear optimization method to match both images. The search is guided by analytical derivatives with respect to a set of calibration parameters. The image from the calibration pattern can be a scanned image, an image taken by a high quality digital camera (without lens distortion), or even the binary image of the pattern (which printed becomes the pattern).

The second method works with point correspondences from the camera image to the pattern image, and apply a similar procedure to the first method to

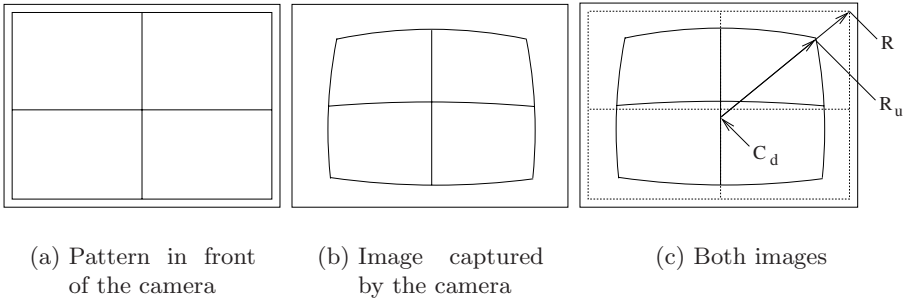


**Fig. 1.** The distortion process due to lens

find the best set of parameters. The set of point correspondences are computed automatically, taking advantage of results of the first method.

The rest of this paper is organized as follows. Sections 2 and 3 describe the distortion and projective model that we are using. Sections 4 and 5 present the methods to match images and to match pairs of points, respectively. Experimental results are shown in Section 6. A brief comparison of previous calibration methods with our methods are in section 7. Finally, some conclusions are given in Section 8.

## 2 The Distortion Model

The distortion process is illustrated in Figure 1. Figure 1 (b) shows an image taken from the camera when the pattern shown in Figure 1 (a) is in front of the camera. Note the effect of lens, the image is distorted, specially in those parts far way from the center of the image. Figure 1 (c) shows the radial distortion in detail, supposing that the center of distortion is the point  $c_d$  with coordinates  $(c_x, c_y)$ . Undistorted pixel at position  $R$  with coordinates  $(x, y)$  points to pixel  $R_u$  with coordinates  $(x_u, y_u)$ .

Let  $I_d$  be the distorted image captured by the camera and  $I_u$  the undistorted image associated to  $I_d$ . The relationship between both images is modeled by:

$$I_u(\theta^d, x, y) = I_d(x_u(\theta^d, x, y), y_u(\theta^d, x, y)), \quad \theta^d = (k_1, k_2, c_x, c_y, s_x) \quad (1)$$

$$x_u = c_x + \frac{x - c_x}{s_x} (1 + k_1 r^2 + k_2 r^4), \quad y_u = c_y + (y - c_y) (1 + k_1 r^2 + k_2 r^4)$$

$$r = \sqrt{\left(\frac{x - c_x}{s_x}\right)^2 + (y - c_y)^2}$$

Where  $\theta^d$  are internal calibration parameters of the camera. Parameters  $k_1$  and  $k_2$  define how strong is the radial distortion with distortion center  $(c_x, c_y)$ . Parameter  $s_x$  is the aspect ratio of pixels ( $s_x = 1$  means square pixels).

### 3 The Projection Model

Figure 1 shows an ideal case, where the plane of the pattern is parallel to the camera plane and center of the pattern coincides with the optical axis of the camera. Using homogeneous coordinates, the class of 2-D planar projective transformations between the camera plane and the pattern plane is given by [5]  $[x', y', w']^t = M[x, y, w]^t$ , where matrix  $M$  has eight independent parameters,

$$M = \begin{bmatrix} m_0 & m_1 & m_2 \\ m_3 & m_4 & m_5 \\ m_6 & m_7 & 1 \end{bmatrix}$$

Plane and homogeneous coordinates are related by  $(x_{p1} = x/w, y_{p1} = y/w)$  for one plane and  $(x_{p2} = x'/w', y_{p2} = y'/w')$  for the other plane. Let  $I_p$  be the projection from the camera plane (with the undistorted image  $I_u$ ), to the pattern plane. The new image is given by:

$$\begin{aligned} I_p(\theta^p, x, y) &= I_d(x_p(\theta^p, x_u, y_u), y_p(\theta^p, x_u, y_u)) \\ \theta^p &= (m_0, m_1, m_2, m_3, m_4, m_5, m_6, m_7) \\ x_p &= \frac{m_0 x_u + m_1 y_u + m_2}{m_6 x_u + m_7 y_u + 1}, & y_p &= \frac{m_3 x_u + m_4 y_u + m_5}{m_6 x_u + m_7 y_u + 1} \end{aligned} \quad (2)$$

### 4 The Image Registration Method

The goal is to find a set of parameters  $\theta^d$  and  $\theta^p$  so the projected image,  $I_p$ , match the image,  $I_r$ , of the calibration pattern put in front of the camera.

We formulate the goal of internal calibration as to find a set of parameters  $\theta = (m_0, m_1, m_2, m_3, m_4, m_5, m_6, m_7, k_1, k_2, c_x, c_y, s_x)$  such the sum,  $E_t$ , of square differences between pixels of  $I_p$  and  $I_r$ , is a minimum.

$$\theta = \operatorname{argmin} E_t(I_p(\theta), I_r) = \operatorname{argmin} \sum_{\forall(x,y) \in I_r} (I_p(\theta, x, y) - I_r(x, y))^2 \quad (3)$$

#### 4.1 Non-linear Optimization

The Gauss-Newton-Levenberg-Marquard method (GNLM) [3] is a non-linear iterative technique specifically designated for minimizing functions which has the form of sum of square functions, like  $E_t$ . At each iteration, the increment of parameters,  $\delta\theta$ , is computed solving the following linear matrix equation:

$$\begin{aligned} A \delta\theta &= B \\ A &= [J^t J + \lambda I], B = -J^t e \end{aligned} \quad (4)$$

If there is  $p$  pixels in images and  $q$  parameters in  $\theta$ ,  $A$  is a matrix of dimension  $q \times q$ . Matrix  $J$ , of dimension  $p \times q$ , is the Jacobian of  $e$ .  $I$  is the identity matrix,  $e$  is the vector of all differences of pixels between both images and has dimension  $q \times 1$ , so  $B$  has dimension  $q \times 1$ .  $\lambda$  is a parameter which is allowed to vary at each

iteration. After a little algebra, the elements of  $A$  and  $B$  are computed using the following formulas,

$$a_{i,j} = \sum_{k=1}^p \frac{\partial e_k}{\partial \theta_i} \frac{\partial e_k}{\partial \theta_j}, \quad b_i = - \sum_{k=1}^p \frac{\partial e_k}{\partial \theta_i} e_k, \quad e_k = I_p(\theta, x_k, y_k) - I_r(x_k, y_k) \quad (5)$$

Applying the chain rule to compute the partial derivatives and considering eq. 2, we get,

$$\frac{\partial e_k}{\partial \theta_i} = \frac{\partial I_p(\theta, x = x_k, y = y_k)}{\partial \theta_i} = \frac{\partial I_p(x_p, y_p)}{\partial x_p} \frac{\partial x_p}{\partial \theta_i} + \frac{\partial I_p(x_p, y_p)}{\partial y_p} \frac{\partial y_p}{\partial \theta_i} \quad (6)$$

In order to simplify the notation, we use  $x_p$  instead of  $x_{pk}$  and  $y_p$  instead of  $y_{pk}$ .  $\frac{\partial I_d(x_p, y_p)}{\partial x_p}$  and  $\frac{\partial I_d(x_p, y_p)}{\partial y_p}$  are the partial derivatives of the image  $I_p$  in the  $x$  and  $y$  directions.  $\frac{\partial x_p}{\partial \theta_i}$  and  $\frac{\partial y_p}{\partial \theta_i}$  for  $(\theta_0, \dots, \theta_7)$  can be derived from eq. 2,

$$\begin{aligned} \frac{\partial x_p}{\partial m_0} &= \frac{x_u}{D} & \frac{\partial y_p}{\partial m_0} &= 0 \\ \frac{\partial x_p}{\partial m_1} &= \frac{y_u}{D} & \frac{\partial y_p}{\partial m_1} &= 0 \\ \frac{\partial x_p}{\partial m_2} &= \frac{1}{D} & \frac{\partial y_p}{\partial m_2} &= 0 \\ \frac{\partial x_p}{\partial m_3} &= 0 & \frac{\partial y_p}{\partial m_3} &= \frac{x_u}{D} \\ \frac{\partial x_p}{\partial m_4} &= 0 & \frac{\partial y_p}{\partial m_4} &= \frac{y_u}{D} \\ \frac{\partial x_p}{\partial m_5} &= 0 & \frac{\partial y_p}{\partial m_5} &= \frac{1}{D} \\ \frac{\partial x_p}{\partial m_6} &= \frac{-x_u x_p}{D} & \frac{\partial y_p}{\partial m_6} &= \frac{-x_u y_p}{D} \\ \frac{\partial x_p}{\partial m_7} &= \frac{-y_u x_p}{D} & \frac{\partial y_p}{\partial m_7} &= \frac{-y_u y_p}{D} \end{aligned} \quad (7)$$

Where  $D = m_6 x_u + m_7 y_u + 1$ . Partial derivatives of distortion parameters are derived from eq. 1 and two more applications of the chain rule,

$$\frac{\partial x_p}{\partial \theta_i} = \frac{\partial x_p}{\partial x_u} \frac{\partial x_u}{\partial \theta_i} + \frac{\partial x_p}{\partial y_u} \frac{\partial y_u}{\partial \theta_i}, \quad \frac{\partial y_p}{\partial \theta_i} = \frac{\partial y_p}{\partial x_u} \frac{\partial x_u}{\partial \theta_i} + \frac{\partial y_p}{\partial y_u} \frac{\partial y_u}{\partial \theta_i} \quad (8)$$

$$\begin{aligned} \frac{\partial x_p}{\partial x_u} &= (Dm_0 - (m_0 x_u + m_1 * y_u + m_2) m_6) / D^2, & \frac{\partial x_p}{\partial y_u} &= (Dm_1 - (m_0 x_u + m_1 * y_u + m_2) m_7) / D^2 \\ \frac{\partial y_p}{\partial x_u} &= (Dm_3 - (m_3 x_u + m_4 * y_u + m_5) m_6) / D^2, & \frac{\partial y_p}{\partial y_u} &= (Dm_4 - (m_3 x_u + m_4 * y_u + m_5) m_7) / D^2 \end{aligned} \quad (9)$$

Finally, the last set of formulas presented in [6],

$$\begin{aligned} \frac{\partial x_u}{\partial k_1} &= r^2(x - c_x) / s_x \\ \frac{\partial y_u}{\partial k_1} &= r^2(y - c_y) \\ \frac{\partial x_u}{\partial k_2} &= r^4(x - c_x) / s_x \\ \frac{\partial y_u}{\partial k_2} &= r^4(y - c_y) \\ \frac{\partial x_u}{\partial c_x} &= 1 - (1/s_x)(1 + k_1 r^2 + k_2 r^4) - 2(k_1 + 2k_2 r^2)(x - c_x)^2 / (s_x^3) \\ \frac{\partial y_u}{\partial c_x} &= -2(k_1 + 2k_2 r^2)(x - c_x)(y - c_y) / s_x^2 \\ \frac{\partial x_u}{\partial c_y} &= -2(k_1 + 2k_2 r^2)(x - c_x)(y - c_y) / s_x \\ \frac{\partial y_u}{\partial c_y} &= 1 - (1 + k_1 r^2 + k_2 r^4) - 2(y - c_y)^2(k_1 + 2k_2 r^2) \\ \frac{\partial x_u}{\partial s_x} &= -(x - c_x)(1 + k_1 r^2 + k_2 r^4) / s_x^2 - 2(k_1 + 2k_2 r^2)(x - c_x)^3 / s_x^4 \\ \frac{\partial y_u}{\partial s_x} &= -2(y - c_y)(k_1 + 2k_2 r^2)(x - c_x)^2 / s_x^3 \end{aligned} \quad (10)$$

where  $r$  was defined previously in eq. 1.

## 4.2 The Calibration Process

The calibration process starts with one image from the camera,  $I_d$ , another image from the calibration pattern,  $I_r$ , and initial values for parameters  $\theta$ . The GNLM algorithm is as follows:

1. Compute the total error,  $E_t(I_p(\theta), I_r)$  (eq. 3).
2. Pick a modest value for  $\lambda$ , say  $\lambda = 0.001$ .
3. Compute the image  $I_p$  (eq. 1, 2) applying bilinear interpolation to improve the quality of the image.
4. Solve the linear system of equations (4), and calculate  $E_t(I_p(\theta + \delta\theta), I_r)$ .
5. if  $E_t(I_p(\theta + \delta\theta), I_r) > E_t(I_p(\theta), I_r)$ , increase  $\lambda$  by a factor of 10, and go the previous step. If  $\lambda$  grows very large, it means that there is no way to improve the solution  $\theta$ .
6. if  $E_t(I_p(\theta + \delta\theta), I_r) < E_t(I_p(\theta), I_r)$ , decrease  $\lambda$  by a factor of 10, replace  $\theta$  by  $\theta + \delta\theta$ , and go to the first step.

When  $\lambda = 0$ , the GNLM method is a Gauss–Newton method, and when  $\lambda$  tends to infinity,  $\delta\theta$  turns to so called steepest descent direction and the size  $\delta\theta$  tends to zero.

## 5 The Point Correspondences Method

This method tries to improve the calibration results using the approach described in previous section. When the calibration ends, the undistorted and projected image,  $I_p$ , is very similar to the pattern image,  $I_r$ . The idea is to extract points of both images associated to distinctive features. In our experiments we use corners as features because they are detected easily with subpixel precision.

The first step is to detect features in  $I_r$  and then search its correspondence in  $I_p$ . This search is limited to a small area because  $I_r$  and  $I_p$  are very similar. Let  $n$  be the number of features,  $(x_{rk}, y_{rk})$  be the coordinates of a feature in  $I_r$  and  $(x_k, y_k)$  be its correspondence in  $I_p$ . From  $(x_k, y_k)$  and using eq. 1 and 2 we can get the coordinates  $(x_{pk}, y_{pk})$  of the feature in the camera image ( $I_d$ ). These calculations are denoted as follows,  $x_{pk} = f_x^{pd}(\theta, x = x_k, y = y_k)$ ,  $y_{pk} = f_y^{pd}(\theta, x = x_k, y = y_k)$  and  $(x_{pk}, y_{pk}) = f^{pd}(\theta, x = x_k, y = y_k)$ . So we have a set of pairs of points  $P = \{<(x_{r1}, y_{r1}), (x_{p1}, y_{p1})>, \dots, <(x_{rn}, y_{rn}), (x_{pn}, y_{pn})>\}$ .

We formulate the goal of the calibration as to find a set of parameters  $\theta$  such the sum,  $D_t$ , of square *distances* between points  $f^{pd}(\theta, x_{rk}, y_{rk})$  and  $(x_{pk}, y_{pk})$ , is a minimum,

$$\begin{aligned} \theta &= \operatorname{argmin} D_t(\theta, P) \\ &= \operatorname{argmin} \sum_{k=1}^n (f_x^{pd}(\theta, x_{rk}, y_{rk}) - x_{pk})^2 + (f_y^{pd}(\theta, x_{rk}, y_{rk}) - y_{pk})^2 \end{aligned} \quad (11)$$

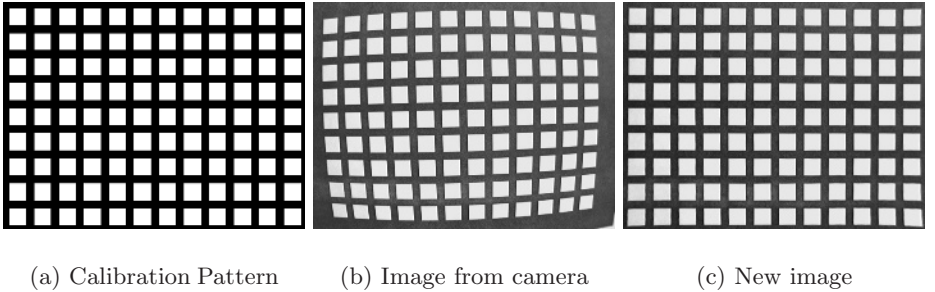


**Fig. 2.** The calibration process

### 5.1 Non-linear Optimization

We use again the GNLM method to minimize  $D_t$ , but this time, the elements of matrix  $A$  and matrix  $B$  in eq. 4 are given by,

$$\begin{aligned} a_{i,j} &= \sum_{k=1}^n \left( \frac{\partial x_{pk}}{\partial \theta_i} \frac{\partial x_{pk}}{\partial \theta_j} + \frac{\partial y_{pk}}{\partial \theta_i} \frac{\partial y_{pk}}{\partial \theta_j} \right), \quad b_i = -\sum_{k=1}^n \left( \frac{\partial x_{pk}}{\partial \theta_i} d_{xk} + \frac{\partial y_{pk}}{\partial \theta_i} d_{yk} \right) \\ d_{xk} &= f_x^{pd}(\theta, x_{rk}, y_{rk}) - x_{pk}, \quad d_{yk} = f_y^{pd}(\theta, x_{rk}, y_{rk}) - y_{pk} \end{aligned} \quad (12)$$

## 6 Experimental Results

We test two Fire-i400 firewire industrial color camera from Unibrain with 4.00mm C-mount lens. These cameras acquire 30fps with resolution of  $640 \times 480$  pixels.

The pattern calibration (image  $I_r$ ), showed in Figure 2(a), was made using the program xfig under Linux. The image taken by the camera is shown in Figure 2(b). The corrected and projected image, using the image registration method, is shown in Figure 2(c). The GNLM process required 17 iterations and 57 seconds (using a PC Pentium IV, 1.8Ghz). We apply derivatives of Gaussians with  $\sigma = 1$  pixels, initial values of  $\theta^d = (0, 0, 240, 320, 1)$  and  $\theta^p = (1, 0, 0, 0, 1, 0, 0, 0)$ . At the end of the calibration process, the total error,  $E_t$ , between the projected image  $I_p(\theta)$  and  $I_r$  (Figures 2(a) and (c)), was 14,820. This result is very good.

Corners of Figure 2(c) are easily detected applying two derivative filters. We apply a derivative of Gaussian ( $\sigma = 2$  pixels) in one direction and then another in the other direction (see Figure 3). Pixels around corners have higher (or lower) values in Figure 3 (b). Corners are calculated, with subpixel precision, as the *center of mass* of pixels around the corners.

The point correspondences method required 39 iterations and less than 5 seconds. This time,  $E_t$  was 14,165, a slightly better result than with the other method. The difference is more evident from the sum of square distances,  $D_t$ . When using the image registration method we got  $D_t = 518$ , and  $D_t = 131$  for

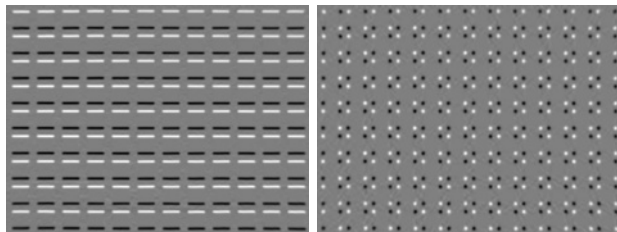


**Fig. 3.** Detecting corners

the point correspondences method, a significant reduction. This difference also can be observed calculating the maximum individual distance between points ( $d_i = \sqrt{d_{xi}^2 + d_{yi}^2}$ ). Using this criteria, the image registration method got  $d_i^{max} = 1.84$  pixels and the point correspondences method  $d_i^{max} = 1.25$  pixels.

Finally, Figure 4 shows an application of the parameters obtained with the second method,  $\theta^d = (-7.86 \times 10^{-7}, 6.43 \times 10^{-13}, 217.75, 310.68, 1.00)$ . Images were expanded from  $640 \times 480$  pixels to  $800 \times 600$ , to see the complete expansion.

## 7 Related Works

There are two kinds of calibration methods. The first kind is the one that uses a calibration pattern or grid with features whose world coordinates are known. The second family of methods is those that use geometric invariants of the image features like parallel lines, spheres, circles, etc. [2].

The Methods described in this paper are in the first family of methods. The image registration method uses all points or pixels of the image as features, instead of the set of point correspondences of the second method. The correspondence with reference points are given implicitly in the pattern image (for



**Fig. 4.** Original and corrected images

the first method) or computed automatically (for the second method). Other methods require a human operator (with a lot of patience) to find such correspondences [6].

This method is an improved version of the method proposed by Tamaki et al. [6] and the differences between both approaches are:

- We take into account exact derivatives of  $x_p$  and  $y_p$  with respect to  $\theta^p$  (eq. 7). Tamaki uses an approximation that is valid only when  $x_u$  and  $x_p$  (and  $y_u$  and  $y_p$ ) are very similar. This approximation makes the method not very robust. Convergence problems arise when parameters  $\theta$  are not so closed to the right ones. Tamaki's method for the same images shown in Figure 2 gave us  $E_t = 15310$ , a slightly greater value than our method.
- We optimize the whole set of parameters  $\theta$  using the GNLM method. Tamaki apply twice the Gauss–Newton method, one for  $\theta^d$  and other for  $\theta^p$ .
- We use a direct registration (from the camera image towards the pattern image), while Tamaki uses inverse registration (from the pattern image to the camera image).

## 8 Conclusions

We have described two calibration methods based on the Gauss–Newton–Levenberg–Marquardt non–linear optimization method using analytical derivatives. Other approaches compute numerical derivatives (e.g. [1,2,4]), so we have faster calculations and better convergence properties.

The first method is an image registration method, which is an improved version of a previous one [6]. The second method takes advantages of results from the first method to solve the correspondence problem between features of the camera image and the pattern image. Also takes advantage of detecting features (corners) with subpixel precision. This combination gives better calibration results than with the image registration method.

## References

1. F. Devernay and O.D. Faugeras. Automatic calibration and removal of distortion from scenes of structured environments. *SPIE*, 2567:62–72, July 1995.
2. F. Devernay and O.D. Faugeras. Straight lines have to be straight. *MVA*, 13(1):14–24, 2001.
3. W. Press, B. Flannery, S. Teukolsky, and Vetterling W. *Numerical recipes, the art of scientific computing*. Cambridge University Press, 1986.
4. G. P. Stein. Lens distortion calibration using point correspondences. In *Proc. Conference on Computer Vision and Pattern Recognition (CVPR '97)*, June 1997.
5. R. Szeliski. Video mosaic for virtual environments. *IEICE Computer Graphics and Applications*, 16(2):22–30, March 1996.
6. T. Tamaki, T. Yamamura, and N. Ohnish. A method for compensation of image distortion with image registration technique. *IEICE Trans. Inf. and Sys.*, E84-D(8):990–998, August 2001.

# Characterization of Surfaces with Sonars Using Time of Flight and Triangulation

Carlos Albores and José Luis Gordillo

Intelligent Systems Center, ITESM Campus Monterrey  
Ave. Eugenio Garza Sada 2501 Sur, C. P. 64849  
Monterrey, Nuevo León, México, Tel. (+52)(81)83284379  
[calbores@cia.mty.itesm.mx](mailto:calbores@cia.mty.itesm.mx), [JLGordillo@itesm.mx](mailto:JLGordillo@itesm.mx)

**Abstract.** This paper presents a simple and original method that uses a configuration of only two sonars to measure and characterize surfaces. The method uses simultaneously the Time Of Flight (TOF) technique and basic triangulation, and characterizes the obtained sonar data into corners, edges and planes, along with non-classified points. The characterization is based on a simple trigonometric evaluation. A commutation system with two sonars that use a configuration with a transmitter and two receivers was built to verify the proposed methodology. Experiments and satisfactory results are also presented.

## 1 Introduction

Sonars are ultrasonic devices widely used in autonomous vehicles and robot navigation [1,2]. These sensors provide a cheap option to measure distances and to detect obstacles. The most common strategy used by sonars to obtain measurements is called Time Of Flight (TOF), which consists of sending an ultrasonic pulse and measuring the elapsed time until the echo returns after hitting an object. Although TOF measurement in several cases is simple and precise, its interpretation is difficult and tends to provide incorrect appreciations. An example of the results obtained by a sequence of readings with a rotating system of sonars (rotational scan) is shown in Figure 1, with the real environment superimposed. The modelling of a certain environment with only a set of straight and well-defined lines is difficult because some surfaces cannot be clearly detected. This fact provoked the abandonment of sonars as a sole medium of navigation [3]. In spite of this, some variants of the original TOF technique have recently proved to be useful in environment mapping and characterization. These variants are characterized by increasing the number of receiving sonars for each sonar emission. This approach obtains quite reliable measurements, thus better representations of the studied environment [4,5]. These works have been developed testing different quantities of receiving sonars (2 to 4) by one transmitting sonar. The transducers used as transmitters are activated one by one, but never at the same time. These methods are based on information redundancy obtained after activating all the transmitting sonars [6]. All of these investigations use more than two sonars. In addition, a system capable of distinguishing objects with

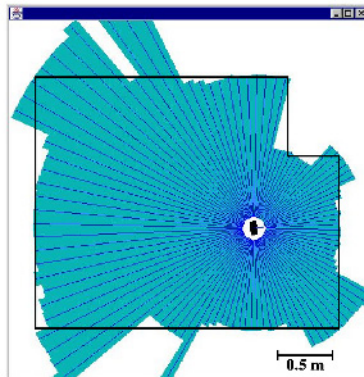


**Fig. 1.** Scan of a sonar, the real environment is superimposed for comparison.

a minimum of two transmitters and two receivers has been described [7]. This configuration uses three sonars: a sonar used exclusively as transmitter, another used exclusively as receiver, whereas the third one has a transmitter/receiver function. In all the previous methods, the characterization is based on complex probabilistic estimation.

This article describes a simple and cheap method for characterizing indoor environments. It consists of using two sonars simultaneously under a one transmitter and two receivers configuration, in such a manner that complementary TOF values are obtained. Using triangulation, these values allow us to classify the measurements in concave corners, edges, planes and non-classified points. The sonar configuration is similar to the used in [8], however, in our research, both sonars alternate the transmitting role. Thus, in this investigation the structures of interest were mainly polygonal indoor environments with right angles.

The proposed method is optimal in the sense that, in order to achieve triangulation, the minimum number of required sonars are used. At the same time, the characterization is based on a very simple trigonometric evaluation, whose equations are also provided in this paper.

Furthermore, a very cheap system of sonars was built to verify the method. The system only uses two Polaroid® 6500 modules to sense the environment.

This paper is organized as follows: Section 2 analyses the configuration with one transmitter and two receivers. In Section 3 some experiments and their results are shown. Finally, Section 4 presents the conclusions of this work.

## 2 A Commutated Transmitter with Two Receivers

The signal emitted by the sonars could behave in two different ways. If the dimension of the surfaces that produce echo is larger than the wavelength of the sonar, the signal will be reflected. Otherwise, the signal will be diffracted. The reflecting surfaces return the signal based on the law of reflection, causing

a specular reflection. Planes and corners are in this category. In contrast, the diffracting surfaces return the signal in all directions in a similar way to diffuse reflection, decreasing the echo signal very fast. In this category the edges are included.

Figure 2(a) describes the configuration used in this research. The commutating sonars ( $T_1$  and  $T_2$ ) are separated by a distance  $b$ . First, sonar  $T_1$  transmits and both sonars ( $T_1$  and  $T_2$ ) receive the signal, obtaining two measurements ( $r_{11}$  and  $r_{12}$ ). Afterwards, sonar  $T_2$  transmits and its signal is received by both sonars, obtaining other two measurements ( $r_{21}$  and  $r_{22}$ ).  $r_{ij}$  is the distance obtained when sonar  $T_i$  transmits and sonar  $T_j$  receives. Therefore, the proposed plan of a transmitter and two receivers obtains four measurements to calculate the distance between the object and the sonars, which helps to classify the objects into concave or convex, as corners and edges, respectively.

Next, measurements in different surfaces are analyzed, in the following order: plane, corner and edge. To distinguish between these types of surfaces the relationship:  $r_{12} + r_{21} - (r_{11} + r_{22})$  is analyzed and corresponds to the sum of the crossed distances (different transmitter than receiver) minus the direct distances (same transmitter and receiver). Moreover, in each case it will be derived the distance  $a$  which is the length from the center of the arrangement of sonars to the analyzed point, and the angle  $\phi$  which is the angle between  $a$  and  $b$ 's perpendicular line. These two variables represent the most accurate measurements that can be obtained for both distance and angle. This is shown in Figure 2(a). A more detailed description of the obtained equations is found in [9].

To validate these calculations, we assume that  $r_{12} = r_{21}$ , which establishes that, in an environment that does not change in time, and in which each sonar is found inside the other's range; the crossed distances (different transmitter than receiver) should be the same.

Finally, note that the sonars reflections are used in the plane and corner analysis [7] to make them easier.

Analyses of the three cases (*plane, corner and edge*) are presented in the next subsections.

## 2.1 Plane

In Figure 2(a) the reflections of the sonars are shown. Distances  $r_{ij}$  represent the distance obtained from the sonar  $T_i$  to sonar  $T_j$  reflection ( $T'_j$ ); for example,  $r_{11}$  goes from  $T_1$  to  $T'_1$ .

Along with these distances, Figure 2(a) shows the following variables:

- $b$ : distance of  $T_1$  to  $T_2$ .  $b = |\mathbf{b}|$ , where  $\mathbf{b} = \overline{T_2 T_1}$ .
- $a$ : distance between the medium point of  $\mathbf{b}$  and the plane.  $a = |\mathbf{a}|$ , where  $\mathbf{a}$  is the vector that goes from  $\mathbf{b}$ 's medium point to the plane.
- $r_{ij}$ : distance from  $T_i$  to  $T'_j$ .  $r_{ij} = |\mathbf{r}_{ij}|$ , where  $\mathbf{r}_{ij} = \overline{T_i T'_j}$ .
- $\alpha_1$ : angle from  $\mathbf{b}$ 's perpendicular to  $\mathbf{r}_{11}$ .
- $\alpha_2$ : angle from  $\mathbf{b}$ 's perpendicular to  $\mathbf{r}_{12}$ .
- $\beta$ : angle from  $\mathbf{r}_{11}$  to  $\mathbf{r}_{12}$ .

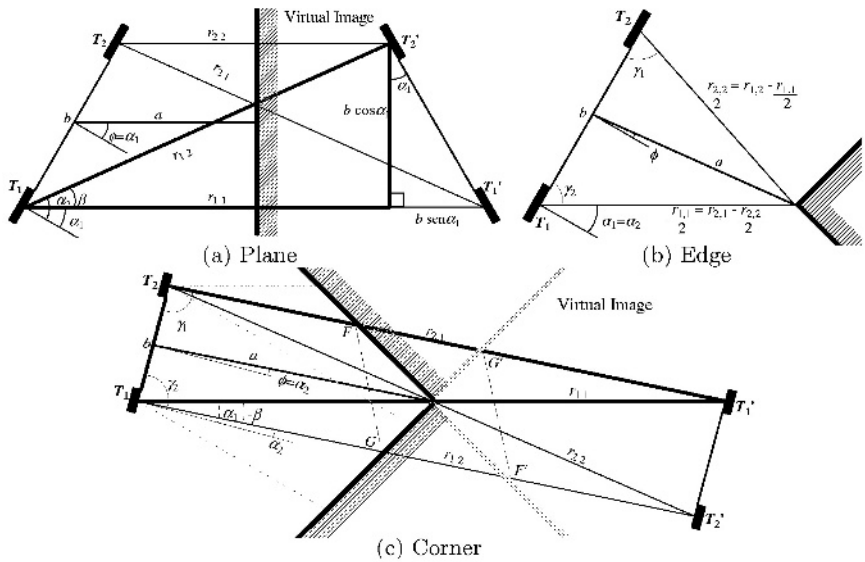


**Fig. 2.** Plane, Corner and Edge analysis. In (a) and (c) it is illustrated the reflection of both sonars over the wall ( $T'_1$  and  $T'_2$ ). Besides, the four distances  $r$  are observed in all three cases.(based on [6]).

$\phi$ : angle from **b**'s perpendicular to **a**.

From these values we will deduce  $a$ ,  $\phi$ , and the behavior of  $r_{12} + r_{21} - (r_{11} + r_{22})$ .

According to Figure 2(a):

$$r_{11} + r_{22} = 4a, \quad (1)$$

from the triangle conformed by  $r_{12}$  and  $b \cos \alpha_1$  it can be demonstrated that its base is equal to  $2a$ . Now, to determine the difference between  $r_{12} + r_{21} - (r_{11} + r_{22})$ , first  $r_{11}$  is derived,

$$r_{11} = b \sin \alpha_1 + 2a, \quad (2)$$

of the right triangle is obtained:

$$r_{12} = r_{21} = \sqrt{4a^2 + b^2 \cos^2 \alpha_1}, \quad (3)$$

adding the crossed distances, considering  $a \gg b$ , and rearranging some terms,

$$r_{12} + r_{21} = 2\sqrt{4a^2 + b^2 \cos^2 \alpha_1} \approx 4a \left( 1 + \frac{b^2 \cos^2 \alpha_1}{8a^2} \right), \quad (4)$$

then, the relationship of the crossed and direct distances is obtained

$$r_{12} + r_{21} - (r_{11} + r_{22}) \approx \frac{b^2 \cos^2 \alpha_1}{2a}. \quad (5)$$

Finally,  $\phi$  is obtained easily, since is equal to angle  $\alpha_1$ ,

$$\alpha_1 = \arcsin \left( \frac{r_{11} - r_{22}}{2b} \right). \quad (6)$$

As it is clearly observed in equation (5), the result is always positive and varies according to  $a$  and  $\alpha_1$ , since  $b$  remains constant once it is defined.

## 2.2 Corner

Figure 2(c) describes the corner analysis. It is worth to mention that the analysis is valid only if the corner's angle is  $90^\circ$ . In Figure 2 a reflection is made, similar to the one performed for the plane, adding or modifying the following variables:

$a$ : distance between the center of  $b$  and the corner's vertex. This definition changes in regard to the presented one in the previous section

$\gamma_1$ : angle from  $\mathbf{b}$  to  $\mathbf{r}_{2\ 1}$

$\gamma_2$ : angle from  $\mathbf{r}_{1\ 2}$  to  $-\mathbf{b}$

As the previous case, we will obtain  $a$ ,  $\phi$  and  $r_{1\ 2} + r_{2\ 1} - (r_{1\ 1} + r_{2\ 2})$ .  $a$  is defined as,

$$r_{1\ 2} + r_{2\ 1} = 4a \quad (7)$$

$$r_{1\ 2} = r_{2\ 1} = 2a \quad (8)$$

of the triangle formed by  $b$ ,  $r_{1\ 1}$  and  $r_{2\ 1}$ , and making use of the cosines law,

$$r_{1\ 1} = \sqrt{r_{2\ 1}^2 + b^2 - 2r_{2\ 1}b \cos \gamma_1} \quad (9)$$

from the Figure 2(c)  $\gamma_1 = \frac{\pi}{2} + \alpha_2$  is obtained. Using a variable change in (9) and the following identities:  $\cos(\frac{\pi}{2} + \alpha) = -\sin \alpha$  and  $r_{2\ 1} = 2a$ ,

$$r_{1\ 1} = \sqrt{r_{2\ 1}^2 + b^2 - 2r_{2\ 1}b \cos\left(\frac{\pi}{2} + \alpha_2\right)} \approx +\frac{b^2}{4a} + b \sin \alpha_2. \quad (10)$$

It also can be shown that:

$$r_{2\ 2} \approx 2a + \frac{b^2}{4a} - b \sin \alpha_2 \quad (11)$$

using equation (11) in  $r_{1\ 2} + r_{2\ 1} - (r_{1\ 1} + r_{2\ 2})$ ,

$$4a - \left(2a + \frac{b^2}{4a} + b \sin \alpha_2\right) - \left(2a + \frac{b^2}{4a} - b \sin \alpha_2\right) \approx -\frac{b^2}{2a}. \quad (12)$$

In agreement with equation (12), the result for the corners is always negative, varying according to  $a$ . Finally, in the Figure 2 is observed that  $\phi = \alpha_2$ . It is not possible to get a general equation for corners whose angle is different from  $90^\circ$  using the described analysis, because in those cases the relation  $|\overline{GF}| = |\overline{GF'}| = |\overline{G'F}| = |\overline{G'F'}|$  is no longer true and it is not valid to use the sonars reflection.

## 2.3 Edge

The edge analysis will be based on Figure 2(b). In this case, it is not possible to use the reflection of the sonars or virtual image, because the distances are not conserved when the reflection is done. Due to the lack of virtual image, the distances observed in Figure 2(b) only represent half of the measurements  $r_{1\ 1}$  and  $r_{2\ 2}$ .

For the convex corners case, it can be shown that  $r_{1\ 2} + r_{2\ 1} - (r_{1\ 1} + r_{2\ 2}) = 0$ , this is because

$$r_{1\ 2} = r_{2\ 1} = \frac{r_{1\ 1}}{2} + \frac{r_{2\ 2}}{2}. \quad (13)$$

Then  $a$  is obtained using the sinus law with the triangle formed by  $\frac{r_{22}}{2}$ ,  $\frac{b}{2}$  and  $a$ , deriving

$$a = \sqrt{\left(\frac{r_{22}}{2}\right)^2 + \left(\frac{b}{2}\right)^2 - \frac{r_{22}b}{2} \cos \gamma_1}. \quad (14)$$

Finally,  $\phi$  is obtained,

$$\phi = \frac{\pi}{2} - \cos^{-1} \left( \frac{\left(\frac{b}{2}\right)^2 + a^2 - \left(\frac{r_{22}}{2}\right)^2}{ab} \right). \quad (15)$$

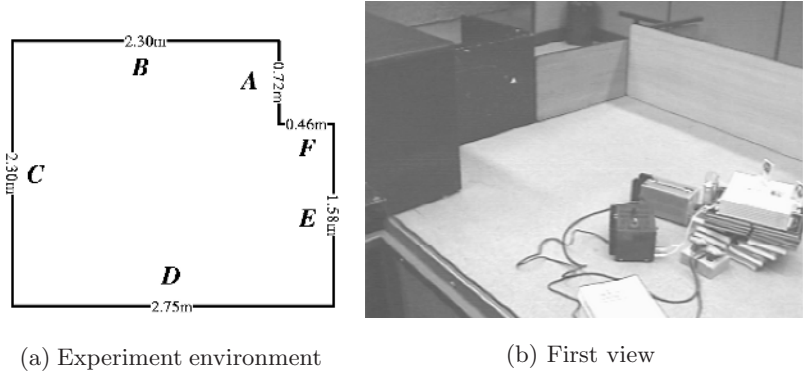


**Fig. 3.** Experiment environment and different views of the designed environment and the experimental setup. In (a) each capital letter represents a line in the environment.

### 3 System Implementation and Experiments

To verify the theory described in this article a system with an arrangement of two sonars mounted on a rotating mechanism (see Figure 3) was built and a graphic interface was developed in JAVA to visualize, store and analyze the collected data. The system is composed of two Polaroid 6500 modules to control the sonar transducers.

The experimental environment is similar to that of an indoor robot. Views of the environment and its dimensions are illustrated in Figure 3.

The environment was built having in mind following considerations: First, The environment was built using a proper material to reflect adequately the sonar signal. Tables and desks of wood were used for this purpose. Besides, the surfaces should be flat and without holes.

The first experimental step consists in scanning the environment to obtain the readings. The system delays around two minutes to obtain a scan, and it senses 100 points in one scan (400  $r$  distances). Then, the information is processed and its characterization is obtained. Examples of the results of this process are shown

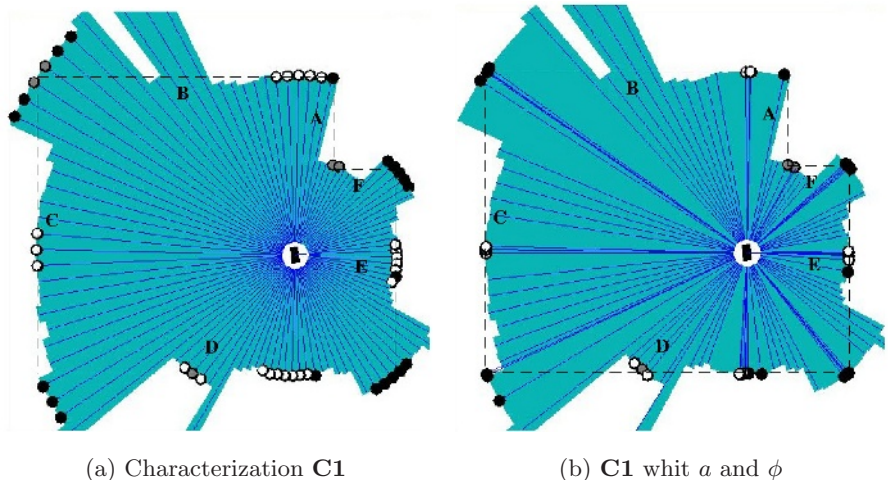


**Fig. 4.** Scan characterizations from a given position. The points are characterized as follows: corners, black circles; planes, white and edges, gray. In (b) distance  $a$  and angle  $\phi$  mentioned in the text are shown and represented by the lines that come out of the center of the figure. Non-classified points were assigned an omission value of  $\phi = 0$  and don't have a circle to represent them. Real environment is shown in dashed lines.

in Figures 4(a) and 4(b). The circles are points that the system recognizes as corners, planes or edges. It is observed in the Figures that it is difficult to detect the edges correctly. The dashed line in these Figures represents the real environment.

In contrast, it is observed in the Figures that not all the scan readings are classified as corners, edges, or planes. These are the non-classified points, due to:

1. The condition that the crossed distances must be equal ( $r_{12} = r_{21}$ ) is not satisfied, probably because one sonar signal is not detected by the other (receiver).
  2. One of the sonars or both are unable to detect the surfaces to be measured.
  3. The sum of the crossed distances minus the sum of the direct distances does not correspond to any of the three cases afore mentioned.

As it is shown in Figure 4, the system has a detection level of more than 80% in corners and planes (in readings that should be characterized as such entities), but only reaches a level of 40% in edges, since they are very difficult to measure due to the diffraction of the echo. It is worth to mention that when a reading is considered as not classified, the system uses for analysis the smallest of the four  $r$  obtained in that point.

Note that Figure 4(a) show groups of readings mainly in the corners and planes of the real environment. In Figure 4(b) angle  $\phi$  is used, and it is observed

how the characterized points converge in the corners and planes of the real environment.

This technique has advantages upon similar vision techniques, i.e. structured light or stereoscopic vision, mainly in the price and amount of information that is needed to process.

## 4 Conclusions

This investigation proposes a method that utilizes two sonars for the measurement and characterization of surfaces. The method is based on the combination of the TOF technique and triangulation, which applies basic trigonometry calculations to differentiate among corners, edges and planes.

The experiments were performed in an environment built up with tables and desks in order to validate and evaluate the behavior of the implemented System.

The System recognized corners and planes correctly, but edges were more difficult.

The system proved to be reliable and efficient . In addition, the system is very cheap, no expensive hardware is required.

The system could be improved, specially in regards to noise problems with sonars, characterization of discontinued segments and verification of erroneous segments generated by data segmentation.

Finally, based on the obtained results we conclude that the proposed method is reliable when used in environments complying with the requisites afore mentioned. In addition, this research leaves a solid base for future jobs that require sonar systems. For example, the system can be included in robots and autonomous vehicles that require a more precise, cheap and reliable environment modelling for a better navigation.

## References

1. Leonard, J., Durrant-Whyte, H.: Simultaneous map building and localization for an autonomous mobile robot. In: IEEE International Workshop on Intelligent Robots and Systems. Volume 3. (1991) 1442–1447
2. Jensfelt, P. and Austin, D.W.O.A.M.: Feature based condensation for mobile robot localization. In: IEEE International Conference on Robotics and Automation. Volume 3. (2000) 2531–2537
3. Kuc, R.: A spatial sample criterion for sonar obstacle detection. IEEE Transactions on Pattern Analysis and Machine Intelligence **12** (1990) 686–690
4. Arikan, O., Barshan, B.: A comparison of two methods for fusing information from a linear array of sonar sensors for obstacle localization. In: International Conference on Intelligent Robots and Systems. Volume 2. (1995) 536–541
5. Hong, M.L., Kleeman, L.: A low sample rate 3D sonar sensor for mobile robots. In: IEEE International Conference on Robotics and Automation. Volume 3. (1995) 3015–3020

6. Barshan, B., Kuc, R.: Differentiating sonar reflections from corners and planes by employing an intelligent sensor. *IEEE Transactions on Pattern Analysis and Machine Intelligence* **12** (1990) 560–569
7. Kleeman, L., Kuc, R.: Mobile robot sonar for target localization and clasification. *The International Journal of Robotics Research* **14** (1995) 295–318
8. Manyika, J., Durrant-Whyte, H.: A tracking sonar sensor for vehicle guidance. In: IEEE. Volume 3. (1993) 424–429
9. Albores, C.: Sistema de sonares para la localización y caracterización de superficies 2-D usando tiempo de vuelo y triangulación. Master's thesis, Instituto Tecnológico y de Estudios Superiores de Monterrey, Campus Monterrey (2001) in spanish.

# Non-speech Sound Feature Extraction Based on Model Identification for Robot Navigation

Yolanda Bolea<sup>1</sup>, Antoni Grau<sup>1</sup>, and Alberto Sanfeliu<sup>2</sup>

<sup>1</sup>Automatic Control Dept, Technical University of Catalonia UPC,

<sup>2</sup>Robotics Institute, IRI/CSIC, UPC

08028-Barcelona, Spain

{yolanda.bolea;antonи.grau}@upc.es, sanfeliu@iri.upc.es

**Abstract.** Non-speech audio gives important information from the environment that can be used in robot navigation altogether with other sensor information. In this article we propose a new methodology to study non-speech audio signals with pattern recognition techniques in order to help a mobile robot to self-localize in space domain. The feature space will be built with the more relevant coefficients of signal identification after a wavelet transformation preprocessing step given the non-stationary property of this kind of signals.

## 1 Introduction

Sound offers advantages for information systems in delivery of alerts, duration information, encoding of rapidly incoming information, representing position in 3-D space around the person and her localization. Hearing is one of human beings most important senses. After vision, it is the sense most used to gather information about our environment. Despite this, little research has been done into the use of sound by a computer to study its environment. The research that has been done focuses mainly on speech recognition [1], [2], while research into other types of sound recognition has being neglected. In robotics, non-speech audio has been ignored in front of artificial vision, laser beams and mechanical wave sensors beyond the audible spectrum. But the study and modeling of non-speech audio can help greatly to robot navigation and localization in the space domain. The existing research in non-speech sound is incipient and focuses on signal processing techniques for feature extraction with the use of neural networks as a classification technique [3], [4]. In this article a new technique based on pattern recognition techniques in order to locate a robot in the space domain by non-speech audio signals is proposed. The feature space will be built with the coefficients of model identification of audio signals. Due to their non-stationary property wavelet decomposition is needed as a preprocessing step. We also propose a technique (transform function) to convert the samples in the feature space into the space domain, based in the sound derivative partial equation described in [1]. In section 2 the feature selection and feature vector are described as soon as the procedure to obtain the transform function. In section 3 we present an experiment in order to test the proposed algorithms and techniques.

## 2 Non-speech Audio Feature Extraction Approach for Localization in Space Domain

In this section we propose a new localization in space domain approach from non-speech audio signals that will be applied on a robot in an industrial environment, the approach follows the next steps: 1) measurement and data preprocessing. 2) MAX models signals identification by the wavelet transform; 3) feature selection, feature extraction and its correspondence with the space domain. Non-speech audio signal generated by any audio source (industrial machinery, appliances, etc.) is continuous by its nature. Preliminary, non-speech signal preprocessing includes sampling the analog audio signal with a specific frequency and to convert it into a discrete set of samples. Sampling interval should be chosen in such a way that essential information be preserved. In this case, due to the audio signal form we have followed the same criteria as [5] in order to choose the sampling frequency because its similarity to speech signals.

### 2.1 Model Identification by the Wavelet Transform and Feature Selection

Non-speech audio signal have the property of non-stationary signal in the same way that many real signals encountered in speech processing, image processing, ECG analysis, communications, control and seismology. To represent the behavior of a stationary process is common the use of models (AR, ARX, ARMA, ARMAX, OE, etc.) obtained from the experimental identification [6]. The coefficient estimation can be done with different criteria: LSE, MLE, among others. But in the case of non-stationary signals the classical identification theory and its results are not suitable. Many authors have proposed different approaches to modeling this kind of non-stationary signals, that can be classified: i) assuming that a non stationary process is locally stationary in a finite time interval so that various recursive estimation techniques (RLS, PLR, RIV, etc.) can be applied [6]; ii) a state space modeling and a Kalman filtering; iii) expanding each time-varying parameter coefficients onto a set of basis sequences [7]; and iv) nonparametric approaches for non-stationary spectrum estimation such a local evolving spectrum, STFT and WVD are also developed to characterize non-stationary signals [8].

To overcome the drawbacks of the identification algorithms, wavelets could be considered for time varying model identification. The distinct feature of a wavelet is its multiresolution characteristic that is very suitable for non-stationary signal processing [9]. Wavelet transform can decompose  $L^2(R)$  space to a linear combination of a set of orthogonal subspace adaptively which divide the whole frequency bands into a series of subbands from high to low frequency, representing the multiresolution characteristics of the original signal.

As non-speech audio signals are non-stationary and have very complex waveforms because of the composition of various frequency components, a signal transformation is performed. The idea of signal transformation is to separate the incoming signal into frequency bands. This task may be solved with the use of filter bank or wavelet transform, as psychoacoustics has associated human hearing to non-uniform critic bands. These bands can be realized roughly as a four-level dyadic tree. For sampling at 8kHz

the frequencies of the dyadic tree are 0-250Hz, 250-500Hz, 500-1000Hz, 1000-2000Hz, 1000-2000Hz and 2000-4000Hz. Each input signal are decomposed in 4 levels, that is, the audio signal  $S_i = A4_i + D4_i + D3_i + D2_i + D1_i$ , where  $A4_i$  is the approximation of the original  $S_i$  signal and  $Dj_i$  ( $j=1,4$ ) are the detail signals for  $S_i$ .

The wavelet transform have been done with the Daubechies wavelet, because it captures very well the characteristics and information of the non-speech audio signals. This set of wavelets has been extensively used since its coefficients capture the maximum amount of the signal energy [9].

A MAX model (Moving Averaging Exogenous) represents the sampled signals in different points of the space domain because the signals are correlated. We use the closest signal to the audio source as signal input for the model. Only the model coefficients need to be stored to compare and to discriminate the different audio signals. This would not happen if the signal were represented by a AR model because the coefficients depend on the signal itself and, with a different signal in every point in the space domain, these coefficients would not be significative enough to discriminate the audio signals. When the model identification is obtained by wavelets transform, the coefficients that do not give information enough for the model are ignored. The eigenvalues of the covariance matrix are analyzed and we reject those coefficients that do not have discriminatory power. For the estimation of each signal the approximation signal and its significative details are used following the next process: i) model structure selection; ii) model parameters calibration with a estimation model (the LSE method can be used for its simplicity and, furthermore a good identified model coefficients convergence is assured); iii) validation of the model.

Let us consider the following TV-MAX model and be  $S_i = y(n)$ ,

$$y(n) = \sum_{k=0}^q b(n;k)u(n-k) + \sum_{k=0}^r c(n;k)e(n-k) \quad (1)$$

where  $y(n)$  is the system output,  $u(n)$  is the observable input, which is assumed as the closest signal to the audio source, and  $e(n)$  is a noise signal. The second term is necessary whenever the measurement noise is colored and needs further modeling. In discrete time, wavelet expansions are computed through filter banks. Now we expand the coefficients  $b(n;k)$  and  $c(n;k)$  onto a wavelet basis,

$$y(n) = T_1(n) + T_2(n) \quad \text{where} \quad (2)$$

$$T_1(n) = \sum_{k=0}^q \sum_m \zeta_{Jmax,m}^{(b_k)} \left[ \tilde{h}_0^{(Jmax)}(n - 2^{Jmax}m)u(n-k) \right] + \sum_{k=0}^q \sum_{j=Jmin}^{Jmax} \xi_{j,m}^{(b_k)} \left[ \tilde{h}_1^{(j)}(n - 2^j m)u(n-k) \right] \quad (3)$$

$$T_2(n) = \sum_{k=0}^r \sum_m \zeta_{Jmax,m}^{(c_k)} \left[ \tilde{h}_0^{(Jmax)}(n - 2^{Jmax}m)e(n-k) \right] + \sum_{k=0}^r \sum_{j=Jmin}^{Jmax} \xi_{j,m}^{(c_k)} \left[ \tilde{h}_1^{(j)}(n - 2^j m)e(n-k) \right] \quad (4)$$

Let  $h_0(n)$  and  $h_1(n)$ , be a dyadic Perfect Reconstruction Filter Bank (PRFB).

Then, for a fixed  $k$ , the wavelet coefficients, corresponding to the low-resolution and the detail signal of  $b(n;k)$ , are given by

$$\zeta_{l,m}^{(b_k)} = \sum_l h_0(l)b(2m-l;k) \quad \text{and} \quad (5)$$

$$\xi_{l,m}^{(b_k)} = \sum_l h_l(l) b(2m-l;k) \quad (6)$$

respectively. Therefore the signal  $b(n;k)$  can be reconstructed from  $\zeta_{l,m}^{(b_k)}$  and  $\xi_{l,m}^{(b_k)}$  by the synthesis equation,

$$b(n;k) = \sum_m \zeta_{l,m}^{(b_k)} \tilde{h}_0(n-2m) + \sum_m \xi_{l,m}^{(b_k)} \tilde{h}_1(n-2m) \quad (7)$$

where  $\tilde{h}_l(n) = h_l(-n)$ ,  $l=1,2$ . See reference [9] for further details. In order to obtain the  $c(n;k)$  coefficients we follow the same procedure.

## 2.2 Feature Extraction and Spatial Recognition

The coefficients for the different models will be used as the feature vector, which can be defined as  $X_S$ , where

$$X_S = (b_1, b_2, \dots, {}^{q+1}, \dots, c_1, c_2, \dots, {}^{r+1}, \dots) \quad (8)$$

where  $q+1$  and  $r+1$  are the amount of **b** and **c** coefficients respectively. From every input signal a new feature vector is obtained representing a new point in the  $(q+r+2)$ -dimensional feature space,  $fs$ . For feature selection, it is not necessary to apply any statistical test to verify that each component of the vector has enough discriminatory power because this step has been already done in the wavelet transform preprocessing.

This feature space will be used to classify the different audio signals entering the system. For these reason we need some labeled samples with their precise position in the space domain. (In the following section an specific experiment is shown). When an unlabeled sample enters the feature space, the minimum distance to a labeled sample is computed and this measure of distance will be used to estimate the distance to the same sample in the space domain. For this reason we need a transformation function which converts the distance in the feature space in the distance in the space domain,  $f_T : \Re \rightarrow \Re$ , ( $f_T : ((q+r+2)\text{-D } fs) \rightarrow (2\text{-D x-y space domain})$ ), note that the distance is an scalar value, independently of the dimension of the space where it has been computed.

The Euclidean distance is used, and the distance between to samples  $S_i$  and  $S_j$  in the feature space is defined as

$$d_{fs}(S_i, S_j) = \sqrt{\sum_{k=0}^q (b_{kS_i} - b_{kS_j})^2 + \sum_{k=0}^r (c_{kS_i} - c_{kS_j})^2} \quad (9)$$

where  $b_{kS_i}$  and  $c_{kS_i}$  are the **b** and **c** coefficients, respectively, of the wavelet transform for the  $S_i$  signal. It is not necessary to normalize the coefficients before the distance calculation because they are already normalized intrinsically by the wavelet transformation.

This distance computation between the unlabeled sample and labeled samples is repeated for the three closest samples to the unlabeled one. Applying then the transformation function  $f_T$  three distances in the x-y domain are obtained. These distances indicate where the unlabeled sample is located. Now, with a simple process of geometry, the position of the unlabeled sample can be estimated. The intersection of the three

circles, ideally yields a unique point, corresponding to the position of the unlabeled sample. In the practice, the three circles intersection yields an area proportional to the error of the whole system. The position of the sample is approximated by the centroid of this area.

$$f_T : d_{fs}(S_i, S_k) \rightarrow d_{xy}(S_i, S_k) = r_i; f_T : d_{fs}(S_j, S_k) \rightarrow d_{xy}(S_j, S_k) = r_j; f_T : d_{fs}(S_p, S_k) \rightarrow d_{xy}(S_p, S_k) = r_p$$

where  $S_i$ ,  $S_j$  and  $S_p$  are three labeled samples and  $r_i$ ,  $r_j$  and  $r_p$  are the distances in the space domain to the unlabeled sample  $S_k$ . The distance is understood as a radius because the angle is unknown.

Because there exist the same relative distances between signals with different models, and with the knowledge that the greater the distortion the farther the signal is from the audio source, we choose those correspondences ( $d_{xy}, d_{fs}$ ) between the samples that are closest to the audio source equidistant in the  $d_{xy}$  axis. These points will serve to estimate a curve of  $n$ -order, that is, the transformation function  $f_T$ . Normally this function is a polynomial of 4<sup>th</sup> order and there are several solutions for a unique distance in the feature space, that is, it yields different distances in the x-y space domain. We solve this drawback adding a new variable: previous position of the robot. If we have an approximate position of the robot, its speed and the computation time between feature extraction samples, we will have a coarse approximation of the new robot position, coarse enough to discriminate among the solutions of the 4<sup>th</sup>-order polynomial. In the experiments section a waveform for the  $f_T$  function can be seen, and it follows the model from the sound derivative partial equation proposed in [1].

In the figure 1 the localization system can be shown, including the wavelet transformation block, the modeling blocks, the feature space and the spatial recognition block which has as input the environment of the robot and the function  $f_T$ .

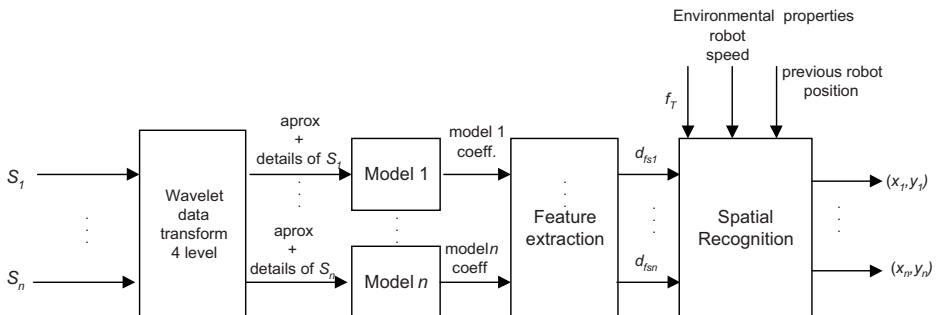


**Fig. 1.** Localization system in space domain from non-speech audio signals.

### 3 Experimental Results

In order to prepare a setting as real as possible, we have used a workshop with a CNC milling machine as non-speech audio source. The room has a dimension of 7 meters by 10 meters and we obtain 9 labeled samples (from  $S_1$  to  $S_9$ ), acquired at regular positions, covering all the representative workshop surface. With the dimensions of the room, these 9 samples are enough because there is not a significative variance when oversampling. In figure 3 (right) the arrangement of the labeled samples can be observed. The robot [10] enters the room, describes a predefined trajectory and gets off. In its trajectory the robot picks four unlabeled samples (audio signals) that will be used as data test for our algorithms ( $S_{10}$ ,  $S_{11}$ ,  $S_{12}$  and  $S_{13}$ ). The sample frequency is 8kHz and a capacitive microphone is used.

First, in order to obtain the 9 models coefficients corresponding to the 9 labeled non-stationary audio signals, these signals are decomposed by the wavelet transform in 4 levels, with one approximation signal and 4 detail signals, figure 2. For the whole samples, the relevance of every signal is analyzed. We observe the more significative decomposition to formulate the prediction model, that is, those details containing the more energy of the signal. With the approximation ( $A4_i$ ) and the detail signal of 4<sup>th</sup> level ( $D4_i$ ) is enough to represent the original signal, because the mean and deviation for the  $D3_i$ ,  $D2_i$  and  $D1_i$  detail signals are two orders of magnitude below  $A4_i$  and  $D4_i$ . Figure 2 (up right) shows the difference between the original signal and the estimated signal with  $A4_i$  and  $D4_i$ . Practically there is no error when overlapped. In this experiment we have chosen the Daubechies 45 wavelet transform because it yields good results, after testing different Daubechies wavelets.

After a initial step for selecting the model structure, it is determined that the order of the model has to be 20 (10 for the  $A4_i$  and 10 for  $D4_i$  coefficients), and a MAX model has been selected, for the reasons explained above. When those 9 models are calibrated, they are validated with the error criteria of FPE (Function Prediction Error) and MSE (Mean Square Error), yielding values about  $10^{-6}$  and 5% respectively using 5000 data for identification and 1000 for validation. Besides, for the whole estimated models the residuals autocorrelation and cross-correlation between the inputs and residuals are uncorrelated, indicating the goodness of the models.

These coefficients form the feature space, where the relative distances among all the samples are calculated and related in the way explained in section 2 in order to obtain the transform function  $f_T$ . With these relations, the curve appearing in figure 3 (left) is obtained, under the minimum square error criteria, approximated by a 4<sup>th</sup>-order polynomial with the following expression:

$$f_T = d_{fs} = -9.65e(-10)d_{xy}^4 + 1.61e(-5)d_{xy}^3 - 8.49e(-2)d_{xy}^2 + 144.89d_{xy} + 107.84 \quad (10)$$

which is related with the solution of the sound equation in [1] with a physical meaning.

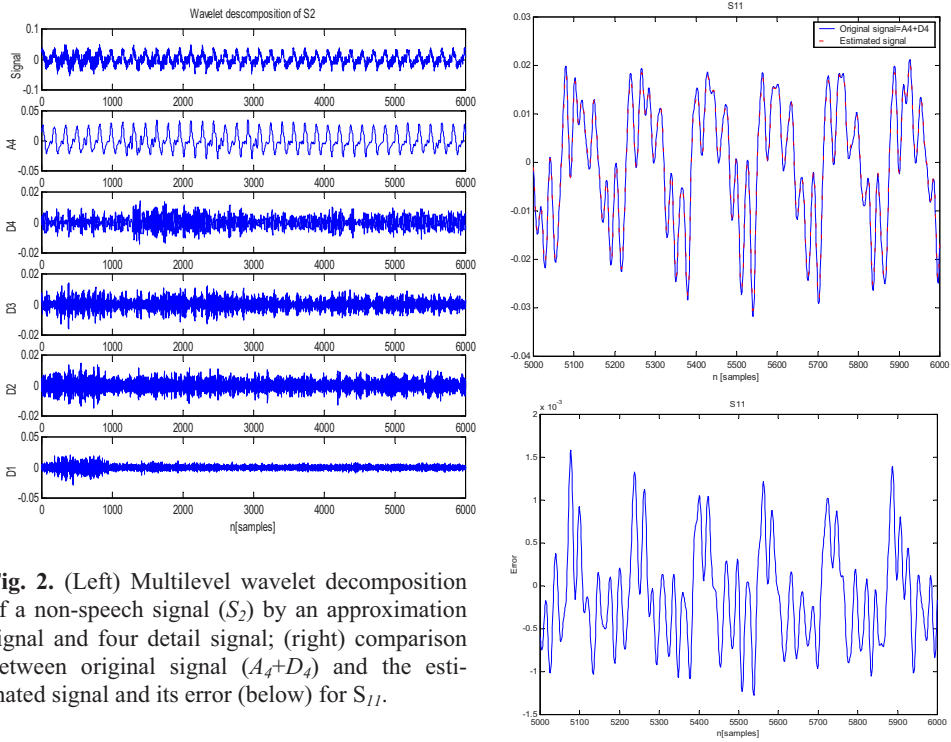


**Fig. 2.** (Left) Multilevel wavelet decomposition of a non-speech signal ( $S_2$ ) by an approximation signal and four detail signal; (right) comparison between original signal ( $A_4+D_4$ ) and the estimated signal and its error (below) for  $S_{11}$ .

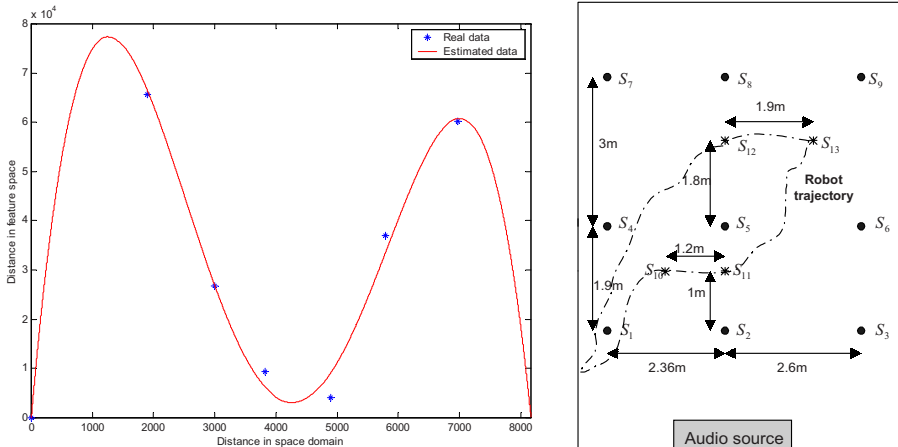


**Fig. 3.** (Left) Transform function  $f_T$ ; (right) robot environment: labeled audio signals and actual robot trajectory with unlabeled signals ( $S_{10}, S_{11}, S_{12}, S_{13}$ ).

With the transform function  $f_T$  we proceed to find the three minimum distances in the feature space to each unlabeled sample respect the labeled ones, that is, for audio

signals  $S_{I0}$ ,  $S_{I1}$ ,  $S_{I2}$  and  $S_{I3}$ , respect  $S_I$ , ...,  $S_9$ . We obtain four solutions for each signal because each distance in the feature space crosses four times the  $f_T$  curve. In order to discard the false solutions we use the previous position information of the robot, that is the  $(x_i, y_i)_{\text{prev}}$  point. We also know the robot speed ( $v = 15\text{cm/sec}$ ) and the computation time between each new position given by the system, which is close to 3 sec. If we consider the movement of the robot at constant speed, the new position will be  $(x_i, y_i)_{\text{prev}} \pm (450, 450)\text{mm}$ . With this information we choose the solution that best fits with the crossing circles solution. In table 1, the recognition rate for each estimated position in space domain are presented, in any case there is an error bigger than the 15%, and in one case the error is under the 0.5%.

**Table 1.** Rate of spatial recognition results for unlabeled samples respect their actual position.

Original signal	$S_{I0}$		$S_{I1}$		$S_{I2}$		$S_{I3}$	
Cartesian coord.	$x_{I0}$	$y_{I0}$	$x_{I1}$	$y_{I1}$	$x_{I2}$	$y_{I2}$	$x_{I3}$	$y_{I3}$
Recognition rate (%)	90.4	85	97.98	87.69	89.18	99.58	88.35	94.42

## 4 Conclusions

With the methodology presented in this article we have achieved some interesting results that encourage the authors to keep on walking in this research field. The introduction of more than one audio source is also a new challenge. The experimental results show a narrow correspondence with the sound physical model and this demonstrates a high reliability of the proposed methodology.

## References

- [1] Rabenstein, R., Trautmann, L.: Digital Sound Synthesis by Physical Modeling. *Symposium on Image and Signal Processing an Analysis* (ISPA'01), 2001.
- [2] Y. Zhong et al, “Binary Quantization of Feature Vectors for Robust Text-Independent Speaker Identification”, *IEEE Trans on Speech and Audio Proc*, vol. 7, no 1, Jan. 1999.
- [3] Spevak, C. & Polfreman, R. (2001). Distance measures for sound similarity based on auditory representations and dynamic time warping. In: *Proceedings of the International Symposium on Systematic and Comparative Musicology*, pp. 165-170. Jyväskylä, Finland, 2001.
- [4] Tzanetakis, G. & Cook, P. (2000). *MARSYAS: A framework for audio analysis*. Organised Sound 4(3), Cambridge University Press.
- [5] Bielińska, E.: *Speaker identification*. Artificial Intelligence Methods, AI-METH 2002.
- [6] Ljung, L.: *System identification: Theory for the user*. Prentice-Hall, 1987.
- [7] Charbonnier, R., Barlaud, M., Alengrin, G., Menez, J.: Results on AR-modeling of non-stationary signals. *IEEE Trans. Signal Processing* 12 (2) (1987) 143-151.
- [8] Kayhan, A.S., Ei-Jaroudi, A., Chaparro, L.F.: Evolutionary periodogram for nonstationary signals. *IEEE Trans. Signal Process.* 42(6) (1994) 1527-1536.
- [9] Tsatsanis, M.K., Giannakis, G.B.: Time-varying system identification and model validation using wavelets. *IEEE Trans. Signal Process.* 41(12) (1993) 3512-3523.
- [10] Sanfeliu, A. et al.: MARCO: A mobile robot with learning capabilities to perceive and interact with its environment”, *IX Symposium on Pattern Recognition and Image Processing*, (SNRFAI'01), pp. 219-224, Castellón, Spain, 2001.

# Enhancement of Noisy Speech Using Sliding Discrete Cosine Transform

Vitaly Kober

Department of Computer Sciences, Division of Applied Physics  
CICESE, Ensenada, B.C. 22860, Mexico  
[vkober@cicese.mx](mailto:vkober@cicese.mx)

**Abstract.** Denoising of speech signals using a sliding discrete cosine transforms (DCT) is proposed. A minimum mean-square error (MMSE) estimator in the domain of a sliding DCT is derived. In order to provide speech processing in real time, a fast recursive algorithm for computing the sliding DCT is presented. The algorithm is based on a recursive relationship between three subsequent local DCT spectra. Extensive testing has shown that background noise in actual environment such as the helicopter cockpit can be made imperceptible by proper choice of suppression parameters.

## 1 Introduction

Processing of speech degraded due to additive background noise is of interest in a variety of tasks. For example, many speech transmission and coding systems, whose design is predicated on a relatively noise-free environment, degrade quickly in quality and performance in the presence of background noise. Thus, there is a considerable interest in and application for the development of such systems, which compensate for the presence of noise. In many cases, intelligibility is affected by background noise so that a principal objective of a speech processing system may be to improve intelligibility. Numerous systems have been proposed to remove or reduce background noise [1-8]. These systems provide an apparent improvement in signal-to-noise ratio, but intelligibility is in fact reduced. In this paper, an approach to speech denoising on the base of a sliding DCT is used.

In many filtering and spectral analysis applications, the signals such as speech have inherently infinite length. Moreover, since the signal properties (amplitudes, frequencies, and phases) usually change with time, a single orthogonal transform is not sufficient to describe such signals. As a result, the concept of short-time signal processing with filtering in the domain of an orthogonal transform can be used [9]. The short-time orthogonal transform of a signal  $x_k$  is defined as

$$X_s^k = \sum_{n=-\infty}^{\infty} x_{k+n} w_n \psi(n, s), \quad (1)$$

where  $w_n$  is a window sequence,  $\psi(n, s)$  represents the basis functions of an orthogonal transform. Equation (1) can be interpreted as the orthogonal transform of  $x_{k+n}$  as

viewed through the window  $w_n$ .  $X_s^k$  displays the orthogonal transform characteristics of the signal around time  $k$ . Note that while increased window length and resolution are typically beneficial in the spectral analysis of stationary data, for time-varying data it is preferable to keep the window length sufficiently short so that the signal is approximately stationary over the window duration.

We assume that the window has finite length around  $n=0$ , and it is unity for all  $n \in [-N_1, N_2]$ . Here  $N_1$  and  $N_2$  are integer values. This leads to signal processing in a sliding window [10]. In other words, local filters in the domain of an orthogonal transform at each position of a moving window modify the orthogonal transform coefficients of a signal to obtain only an estimate of the pixel  $x_k$  of the window. The choice of orthogonal transform for sliding signal processing depends on many factors. The DCT is one the most appropriate transform with respect to the accuracy of power spectrum estimation from the observed data that is required for local filtering, the filter design, and computational complexity of the filter implementation. For example, linear filtering in the domain of DCT followed by inverse transforming is superior to that of the discrete Fourier transform (DFT) because a DCT can be considered as the DFT of a signal evenly extended outside its edges. This consequently attenuates boundary (temporal aliasing) effects caused by circular convolution that are typical for linear filtering in the domain of DFT. In the case of DFT, speech frames are usually windowed to avoid temporal aliasing and to ensure a smooth transition of filters in successive frames. For the filtering in the domain of DCT, the windowing operation can be skipped. In such a manner the computational complexity can be further reduced.

The presentation is organized as follows. In Section 2, we present computationally efficient algorithm for computing the sliding DCTs. In Section 3, an explicit filter formula minimizing the MMSE defined in the domain of the sliding DCT is derived. We also test the filter performance in actual environment such as the helicopter cockpit. Section 4 summarizes our conclusions.

## 2 Fast Algorithm for Computing the Sliding DCT

The discrete cosine transform is widely used in many signal processing applications such as adaptive filtering, video signal processing, feature extraction, and data compression. This is because the DCT performs close to the optimum Karhunen-Loeve transform for the first-order Markov stationary data, when the correlation coefficient is near 0.9 [11]. Four types of DCTs were classified [12]. The DCT discussed in the paper is referred to the type-II. The kernel of the DCT is defined for the order  $N$  as

$$DCT = \left\{ k_s \cos\left(\pi \frac{s(n+1/2)}{N}\right) \right\}, \quad (2)$$

where  $n, s=0, 1, \dots, N-1; k_s = \begin{cases} 1/\sqrt{2} & \text{if } s=0, \\ 1 & \text{otherwise.} \end{cases}$ . For clarity, the normalization factor  $\sqrt{2/N}$  for the forward transform is neglected until the inverse transform. The sliding cosine transform (SCT) is defined as

$$X_s^k = \sum_{n=-N_1}^{N_2} x_{k+n} \cos\left(\pi \frac{(n+N_1+1/2)s}{N}\right), \quad (3)$$

where  $N=N_1+N_2+1$ ,  $\{X_s^k; s=0, 1, \dots, N-1\}$  are the transform coefficients around time  $k$ . The coefficients of the DCT can be obtained as  $\{C_0^k = X_0^k / \sqrt{2}; C_s^k = X_s^k, s=1, \dots, N-1\}$ . We now derive fast algorithm for the SCT on the base of a recursive relationship between three subsequent local DCT spectra [13]. The local DCT spectra at the window positions  $k-1$  and  $k+1$  are given by

$$X_s^{k-1} = \sum_{n=-N_1-1}^{N_2-1} x_{k+n} \cos\left(\pi \frac{(n+N_1+1/2)s}{N} + \frac{\pi s}{N}\right), \quad (4)$$

$$X_s^{k+1} = \sum_{n=-N_1+1}^{N_2+1} x_{k+n} \cos\left(\pi \frac{(n+N_1+1/2)s}{N} - \frac{\pi s}{N}\right). \quad (5)$$

Using properties of the cosine function and equations (4) and (5), we can write

$$\begin{aligned} X_s^{k+1} = & 2X_s^k \cos\left(\frac{\pi s}{N}\right) - X_s^{k-1} + \cos\left(\frac{\pi s}{2N}\right) \\ & \left( x_{k-N_1-1} - x_{k-N_1} + (-1)^s (x_{k+N_2+1} - x_{k+N_2}) \right). \end{aligned} \quad (6)$$

We see that the computation of the DCT at the window position  $k+1$  involves values of the input sequence  $x_k$  as well as the DCT coefficients computed in two previous positions of the moving window. The number of arithmetic operations required for computing the sliding discrete cosine transform at a given window position is evaluated as follows: the SCT for the order  $N$  with  $N=N_1+N_2+1$  requires  $2(N-1)$  multiplication operations and  $2N+5$  addition operations; the DCT requires one extra operation of multiplication. Table 1 lists numerical results of computational complexity for the proposed algorithm and known fast DCT algorithms. Note that fast DCT algorithms require the length of a moving window to be of a power of 2,  $N=2^M$ . In contrast, the length of a moving window for the proposed algorithm is an arbitrary integer value determined by the characteristics of the signal to be processed.

We see that the proposed algorithm yields essentially better results when the length of the window increases.

**Table 1.** Number of multiplications and additions for computing the sliding DCT

M	Fast DCT[14, 15]		Proposed algorithm	
	Mult.	Add.	Mult.	Add.
16	33	81	30	37
32	81	209	62	69
64	193	513	126	133
128	449	1217	254	261
256	1025	2817	510	517

The inverse algorithms for the sliding DCT can be written as follows.

$$x_k = \frac{1}{N} \left( 2 \sum_{s=1}^{N-1} X_s^k \cos\left(\pi \frac{(N_1 + 1/2)s}{N}\right) + X_0^k \right), \quad (7)$$

where  $N=N_1+N_2+1$ . The computational complexity is  $N$  multiplication operations and  $N$  addition operations. If  $x_k$  is the central pixel of the window, that is,  $N_1=N_2$  and  $N=2N_1+1$ , then the inverse transform is simplified to

$$x_k = \frac{1}{N} \left( 2 \sum_{s=1}^{N_1} (-1)^s X_{2s}^k + X_0^k \right). \quad (8)$$

We note that in the computation only the spectral coefficients with even indices are involved. The computation requires one multiplication operation and  $N_1+1$  addition operations.

### 3 Denoising of Speech Signals in the Sliding DCT Domain

The objective of this section is to develop a noise suppression technique on the base of the sliding DCT, and to test the algorithm performance in actual noise environment. We design locally adaptive filters to enhance noisy speech. Assume that a clean speech signal  $\{a_k\}$  is degraded by zero-mean additive noise  $\{v_k\}$

$$x_k = a_k + v_k, \quad (9)$$

where  $\{x_k\}$  is a noisy speech sequence.

Let  $\{X_s^k, A_s^k, V_s^k, \hat{A}_s^k; s=0, 1, \dots, N-1\}$  be the DCT transform coefficients around time  $k$  of noisy speech, clean speech, noise, and filtered signal, respectively. Here  $N=2N_1+1$  is the length of the DCT. Note that  $N_1$  is an arbitrary integer value, which is determined by pitch period of speech. One can be chosen to be approximately as the maximum expected pitch period for adequate frequency resolution.

Various criteria can be exploited for the filter design. In the following analysis we use the criterion of the MMSE around time  $k$  which is defined in the domain of DCT, taking into account (8), as follows:

$$MMSE_k = E \left\langle \sum_{t=0}^{N_1} \alpha_t^2 [A_{2t}^k - \hat{A}_{2t}^k]^2 \right\rangle, \quad (10)$$

where  $E \langle \cdot \rangle$  denotes the expected value.

As we mentioned above, the length of the window is chosen in such a way that noise can be considered as stationary in the window. Let  $P_t^k = E \langle |V_t^k|^2 \rangle$  denote the power spectrum of noise in the domain of DCT. Suppose that  $\hat{A}_t^k = X_t^k H_t^k$ , here  $H_t^k$  is the filter to be designed around time  $k$ . By minimizing  $MMSE_k$  with respect to  $H_t^k$ , we arrive to a version of the Wiener filter in the domain of DCT:

$$H_t^k = \frac{|X_t^k|^2 - P_t^k}{|X_t^k|^2} = 1 - \frac{P_t^k}{|X_t^k|^2}. \quad (11)$$

The MMSE estimation of the processed speech in the domain of the sliding DCT is given by

$$\hat{A}_t^k = \begin{cases} \left( 1 - \frac{P_t^k}{|X_t^k|^2} \right) X_t^k, & \text{if } |X_t^k|^2 > P_t^k \\ 0, & \text{otherwise} \end{cases}. \quad (12)$$

The obtained filter can be considered as a spectral subtraction method in the domain of sliding DCT. In general, spectral subtraction methods [1], while reducing the wide-band noise, introduce a new “musical” noise due to the presence of remaining spectral peaks. To attenuate the “musical” noise, one can suggest oversubtraction of the power spectrum of noise by introducing a nonzero power spectrum bias. Finally, the MMSE estimation of the processed speech in the domain of the sliding DCT can be written as follows:

$$\hat{A}_t^k = \begin{cases} \left( 1 - \frac{P_t^k}{|X_t^k|^2} \right) X_t^k, & \text{if } |X_t^k|^2 > P_t^k + B^k \\ 0, & \text{otherwise} \end{cases}, \quad (13)$$

where  $B^k$  is a speech-dependent bias value.

The filtered speech signal can be obtained with use of (8). It also follows from (8) that in the estimation only the spectral coefficients with even indices are involved.

A test speech signal recorded in helicopter environment is presented in Fig.1. The data was sampled at 16.00kHz. In our tests the window length of 761 samples is used. The sliding squared DCT coefficients averaged over all positions of the running window for noisy speech is presented in Fig. 2. The power spectrum of noise is obtained by actual measurement from background noise in intervals where speech is not presented. It is shown in Fig. 3. We see the difference in spectral distributions of the speech and the helicopter noise, which will help us to suppress the helicopter noise.

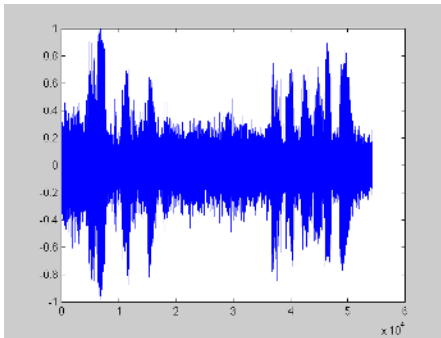


**Fig. 1.** Time waveform of helicopter speech

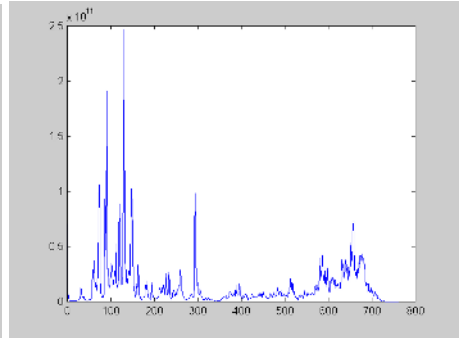


**Fig. 2.** Average squared DCT magnitude of noisy speech

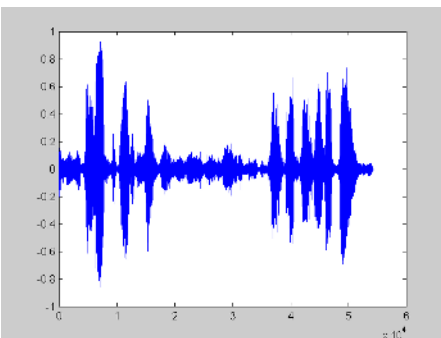


**Fig. 4.** Enhanced speech signal

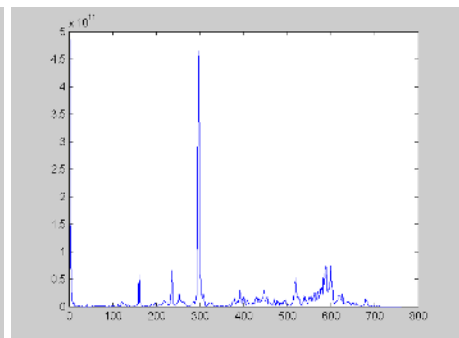


**Fig. 3.** Average squared DCT magnitude of noise

The result of filtering by using the proposed filter is shown in Fig. 4. It is clearly that the system is capable of significant noise reduction. Numerous formal subjective tests are shown that the helicopter noise can be made imperceptible by proper choice of the filter parameters in (13).

In this section we derived a filter for noise suppression on assumption that speech is always was presented in the measured data. However, if a given frame of data consists of noise alone, then obviously a better suppression filter can be used [5, 6]. In general, an optimal algorithm should include a detector of voiced and unvoiced speech signals. After detecting, different strategies of processing should be applied to voiced and unvoiced speech signals.

## 4 Conclusions

In this paper, we have presented a new technique for enhancing speech degraded by additive noise. The technique utilizes the sliding DCT. A MMSE estimator in the domain of the sliding DCT has been derived. In order to provide speech processing in real time, a fast recursive algorithm for computing the sliding DCT has been suggested. The algorithm requires essentially less operations of multiplication and addition comparing with known fast DCT algorithms. Extensive testing has shown that background noise such as in the helicopter cockpit can be significantly reduced by proper choice of suppression parameters.

**Acknowledgment.** This work was supported by the grant 36077-A from CONACYT

## References

1. Boll S.F., Suppression of acoustic noise in speech using spectral subtraction, *IEEE Trans. Acoust. Speech Signal Process.*, Vol. ASSP-27, (1979) 113–120.
2. Lim J.S. and Oppenheim A.V., Enhancement and bandwidth compression of noisy speech, *Proc. IEEE*, Vol. 67, (1979) 1586–1604.
3. McAulay R.J., Malpass M.L., Speech enhancement using a soft-decision noise suppression filter, *IEEE Trans. Acoust. Speech Signal Process.*, Vol. ASSP-28, (1980) 137–145.
4. Ephraim Y. and Malah D., Speech enhancement using a minimum mean-square error short-time spectral amplitude estimator, *IEEE Trans. Acoust. Speech Signal Process.*, Vol. ASSP-32, No. 6, (1984) 1109–1121.
5. Ahmed M.S., Comparison of noisy speech enhancement algorithms in terms of LPC perturbation, *IEEE Trans. Acoust. Speech Signal Process.*, Vol. 37, No. 1, (1989) 121–125.
6. Chen Y.M. and O'Shaughnessy D., Speech enhancement based conceptually on auditory evidence, *IEEE Trans. Signal Process.*, Vol. 39, No. 9, (1991) 1943–1953.
7. Ephraim Y., A Bayesian estimation approach for speech enhancement using hidden Markov models, *IEEE Trans. Signal Process.*, Vol. 40, (1992) 725–735.
8. Hu H.T., Robust linear prediction of speech signals based on orthogonal framework, *Electronics Letters*, Vol. 34, No 14, (1998) 1385–1386.
9. Oppenheim A.V., Shafer R.W., *Discrete-time signal processing*, Prentice Hall, Englewood Cliffs, NJ (1989).
10. Vitkus R.Y., and Yaroslavsky L.P., Recursive algorithms for local adaptive linear filtration, in: *Mathematical Research.*, Eds.: Yaroslavsky L.P., Rosenfeld A., and Wilhelm W., Academy Verlag, Berlin, (1987) 34–39.
11. Jain A.K., A sinusoidal family of unitary transforms, *IEEE Trans. Pattern Anal. Machine Intell.*, Vol. PAMI-1, No 4, (1979) 356–365.
12. Wang Z., Fast algorithms for the discrete W transform and for the discrete Fourier transform, *IEEE Trans. Acoust. Speech Signal Process.*, Vol. ASSP-32, No 4, (1984) 803–816.
13. Kober V. and Cristobal G., Fast recursive algorithms for short-time discrete cosine transform, *Electronics Letters*, Vol. 35, No 15, (1999) 1236–1238.
14. Hou H.S. , A fast recursive algorithm for computing the discrete cosine transform, *IEEE Trans. Acoust. Speech Signal Process.*, Vol. ASSP-35, No 10, (1987) 1455–1461.
15. Britanak V, On the discrete cosine computation, *Signal Process.*, Vol. 40, No 2-3, (1994) 183–194.

# Integrating High and Low Smoothed LMs in a CSR System\*

Amparo Varona and Ines Torres

Departamento de Electricidad y Electrónica. Facultad de Ciencias. UPV/EHU.

Apartado 644. 48080 Bilbao. SPAIN.

{amparo, manes}@we.lc.ehu.es

**Abstract.** In Continuous Speech Recognition (CSR) systems, acoustic and Language Models (LM) must be integrated. To get optimum CSR performances, it is well-known that heuristic factors must be optimised. Due to its great effect on final CSR performances, the exponential scaling factor applied to LM probabilities is the most important. LM probabilities are obtained after applying a smoothing technique. The use of the scaling factor implies a redistribution of the smoothed LM probabilities, i.e., a new smoothing is obtained. In this work, the relationship between the amount of smoothing of LMs and the new smoothing achieved by the scaling factor is studied. High and low smoothed LMs, using well-known discounting techniques, were integrated into the CSR system. The experimental evaluation was carried out on two Spanish speech application tasks with very different levels of difficulty. The strong relationship observed between the two redistributions of the LM probabilities was independent of the task. When the adequate value of the scaling factor was applied, not very different optimum CSR performances were obtained in spite of the great differences between perplexity values.

## 1 Introduction

In Continuous Speech Recognition (CSR) systems a Language Model (LM) is required to represent the syntactic constraints of the language. But there are a high number of sequences of words that do not appear in training and could appear in tests. Thus, a certain mass of probability must be subtracted from the seen combinations and redistributed among the unseen ones, i.e., a smoothing technique must be applied [1] [2].

The test set perplexity is typically used to evaluate the quality of the LM [1] [2]. Perplexity can be interpreted as the (geometric) average branching factor of the language according to the model. It is a function of both the language and the model. It is supposed that the “best” models get the “lowest” Word Error Rates (WER) of the CSR system. But there are plenty of counterexamples in literature [3]. The ability of the test set perplexity to predict the real behavior of a

---

\* This work has been partially supported by the Spanish CICYT under grant TIC2002-04103-C03-02 and by the Basque Country University under grant (9/UPV 00224.310-13566/2001)

smoothing technique when working in a CSR system could be questioned because it does not take into account the relationship with acoustic models. Several attempts have been made to devise metrics that are better correlated with the application error rate than perplexity [4]. But for now perplexity remains the main metric for practical language model construction [3]. In fact, the quality of the model must ultimately be measured by its effect on the specific application for which it was designed, namely by its effect on the system error rate. However, error rates are typically non-linear and poorly understood functions of language models [3]. In this work we try to clarify how the smoothing technique applied to the LM works in the CSR system and to show its real impact on final system error rates.

Integration of language and acoustic models is invariably based on the well-known Bayes' rule. However, it is well known that the best performance of a CSR system is obtained when LM probabilities in the Bayes' rule are modified by introducing an exponential scaling factor [5] [6]. This factor can be understood as a new redistribution of the smoothed LM probabilities. As a consequence, LMs are smoothed twice: first by means of the smoothing technique and then by the exponential scaling parameter. The aim of this work is to establish a relationship between the amount of smoothing given by the smoothing technique and the amount of smoothing achieved by the exponential scaling factor (see Section 2).

Thus, different amounts of smoothing need to be applied to LMs. Two different well-established smoothing techniques leading to high and low-smoothed LM respectively, have therefore been evaluated (see Section 3). The relationship between the amount of smoothing given by the smoothing technique and the amount of smoothing achieved by the exponential scaling factor is studied in terms of both classical test set perplexity and CSR performance. CSR performance was evaluated in terms of both, the obtained WER and involved computational cost (see Section 4). Experimental evaluation was carried out over two Spanish databases of very different difficulty recorded by two consortia of Spanish research groups to work in understanding and dialogue systems respectively. Finally, some concluding remarks are given in Section 5.

## 2 Introducing the LM in the CSR System

Within a CSR system there are several heuristic parameters that must be adjusted to obtain optimum performances, such as the beam-search factor to reduce the computational cost, etc. But, the most important, due to its great effect on final CSR performance, may be the exponential scaling factor  $\alpha$  applied over LM probabilities in Bayes' rule [5]. In Bayes' rule, the recognizer must find the word sequence  $\hat{\Omega}$  that satisfies:

$$\hat{\Omega} = \arg \max_{\Omega} P(\Omega)^\alpha P(A/\Omega) \quad (1)$$

where  $P(\Omega)$  is the probability that the word sequence  $\Omega \equiv \omega_1 \omega_2 \dots \omega_{|\Omega|}$  from some previously established finite vocabulary  $\Sigma = \{\omega_j\}$ ,  $j = 1 \dots |\Sigma|$ , will be

uttered and  $P(A/\Omega)$  is the probability of the sequence of acoustic observations  $A = a_1a_2...a_{|A|}$  for a given sequence of words  $\Omega$ . Probabilities  $P(A/\Omega)$  are represented by acoustic models, usually Hidden Markov Models (HMM). The *a priori* probabilities  $P(\Omega)$  are given by the LM.

From a theoretical point of view, the scaling parameter  $\alpha$  is needed because acoustic and LM probability distributions are not real but approximations [5]. The two probability distributions are estimated independently using different stochastic models that represent different knowledge sources. Moreover, the parameters of the acoustic and language models are estimated on the basis of speech and text data corpora, respectively. Each corpora was designed with different purposes, and they have therefore different vocabulary, size, complexity, etc. Thus, a balance parameter  $\alpha$  needs to be applied to lessen these effects and then obtain good system performances.

In practice, acoustic and LM have very different ranges of values. The accumulated probabilities at the end of each partial sequence of words  $\Omega$  in the Viterbi trellis is a combination of acoustic  $P(A/\Omega)$  and language  $P(\Omega)$  probabilities. Acoustic probabilities are usually smaller than language probabilities and are applied many more times. The gap among accumulated probabilities is therefore usually bigger than the gap among LM probabilities. The immediate consequence is that LM probabilities are irrelevant in most situations for deciding the best path to choice<sup>1</sup>[7]. However, when LM probabilities are raised to a power  $\alpha > 1$ :  $(P(\Omega))^{\alpha}$ , all of them are attenuated, but this attenuation is higher for lower probability values. A bigger gap is therefore obtained between high and low probabilities and then LM probabilities are now more relevant to decide the next word combination. There is a maximum value of  $\alpha$  from which LM probabilities are overvalued.

It is important to notice that the smoothing technique clearly defines the LM probability distributions and thus, the “*a priori*” gap among probabilities. So that, the relationship between the smoothing technique and the exponential scaling factor applied over LM probabilities must be established.

### 3 High and Low Smoothed LMs

The purpose of this work was not to achieve an exhaustive comparison of smoothing techniques like others authors did [1] [2]. The main goal was to observe the relationship between the amount of smoothing given by the smoothing technique and the amount of smoothing achieved by the scaling exponential factor. Thus, two well-known back-off smoothing techniques [8] involving very different amount of discounting have been chosen. Witten-Bell (WBd) and Add-One (AOd) discounting have been used to obtain high and low smoothed LMs respectively. In high-smoothed LMs the probability reserved by the smoothing technique for the unseen events is bigger than in low-smoothed LM. As a consequence the gap be-

---

<sup>1</sup> This phenomenon is also related to the problem of the negligible impact that transition probabilities have in acoustic models.

tween LM probabilities in high-smoothed LMs is smaller than in low-smoothed models.

The amount of discounting performed by Witten-Bell and Add-one techniques does not need to be adjusted by any additional parameter, like in other well-known techniques, such as Kneser-Ney, linear, etc [1] [2]. In both cases the amount of discounting is fixed and fully defined by the technique.

If  $h = (\omega_{i-(n-1)}^{i-1})$  is a history representing a sequence of  $n - 1$  words,  $N(w_i/h)$  is the number of times that word  $w_i$  appears after history  $h$ ,  $N(h) = \sum_{\substack{\forall \omega / \\ N(\omega_i/h) \neq 0}} N(\omega_i/h)$  and  $\beta(w_i/h^*)$  is the probability distribution of a more general

model ( $h^*$  represents a history of words of length less than  $h$ ), the smoothed LM probability  $P(w_i/h)$  is calculated as:

$$P(w_i/h) = \begin{cases} (1 - \lambda) \frac{N(w_i/h)}{N(h)} & N(w_i/h) \neq 0 \\ \left( \sum_{\substack{\forall w_j / \\ N(w_j/h) \neq 0}} \lambda \frac{N(w_j/h)}{N(h)} \right) \frac{\beta(w_i/h^*)}{\sum_{\substack{\forall w_j / \\ N(w_j/h) = 0}} \beta(w_j/h^*)} & N(w_i/h) = 0 \end{cases} \quad (2)$$

$(1 - \lambda)$  represents the discount factor, that is, the amount of probability to be subtracted and then redistributed among unseen events. The discount factor  $(1-\lambda)$  can have very different formulations [1] [2]. In fact, we have given adequate values to  $(1-\lambda)$  to obtain high and low-smoothed LMs using Witten-Bell and Add-One discounting respectively. Those discounting are fully explained in the following paragraphs.

#### *High-Smoothing: Witten-Bell Discounting:*

In Witten-Bell, the discount  $(1 - \lambda)$  depends fundamentally on the number of different events  $T$  following the history  $h$ . That is:

$$1 - \lambda = \frac{N(h)}{N(h) + T} \quad (3)$$

It is widely used since it leads to low text set perplexities when compared to other classical back-off methods [1]. However, a dependence was found [2] between perplexity and the size of the training of the LMs when Witten-Bell discounting was used.

In this case a quite important mass of probability is assigned to unseen events (high-smoothing) and the gap between seen and unseen probabilities is reduced. Combinations of words unseen in training can have a relative high probability in test.

#### *Low-Smoothing: Add-One Discounting:*

This is a very simple discounting method, adding one to all the counts. It was calculated as:

$$1 - \lambda = \frac{N(h)}{N(h) + 1} \quad (4)$$

This method does not usually perform well and thus is not commonly used by itself. Usually it is applied as part of more complicate methods <sup>2</sup> [1].

Since  $1 \leq T$ , using add-one discounting a smaller mass of probability is re-distributed among unseen events (low-smoothing) than using Witten-Bell discounting. The gap among LM probabilities is therefore bigger using Add-One discounting.

### 3.1 LM Evaluation in Perplexity

Topics related to the obtaining of LMs, such as smoothing techniques, are usually evaluated in terms of perplexity. The test set Perplexity (PP) is based on the mean log probability that a LM assigns to a test set  $\omega_1^L$  of size L. It is thus based exclusively on the probability of words which actually occur in the test as follows:

$$PP = P(\omega_1^L)^{-1/L} = e^{-\frac{1}{L} \sum_{i=1}^L \log(P(\omega_i / \omega_1^{i-1}))} \quad (5)$$

The test set perplexity measures the branching factor associated to a task, which depends on the number of different words in the text. Low perplexity values are obtained when high probabilities are assigned to the test set events by the LM being evaluated. When the test set includes a high number of unseen combinations of  $n$  words, the probability  $P(\omega_i / \omega_1^{i-1})$  mainly depends on the smoothing technique. In such a case,  $P(\omega_i / \omega_1^{i-1})$  is lower for low-smoothed LMs and, as a consequence bad Perplexity values will be obtained. Thus, high-smoothed techniques lead to good perplexity values when evaluated over test-set including a high number of unseen events. However, this good LM behavior is not always confirmed by the CSR system performance which also includes the acoustic models [4].

## 4 Experimental Evaluation

In this section the relationship between the two redistributions of the LM probabilities, i.e., the application of the smoothing technique and the scaling factor, is experimentally established. The experimental evaluation was carried out with two Spanish databases of very different levels of difficulty: Bdgeo and Info\_Tren.

Bdgeo is a task-oriented Spanish speech corpus [9] consisting of 82000 words and a vocabulary of 1208 words. This corpus represents a set of queries to a Spanish geography database. This is a specific task designed to test integrated systems (acoustic, syntactic and semantic modelling) in automatic speech understanding. The training corpus consisted of 9150 sentences. The test set consisted of 600 sentences. Recording was carried out by 12 speakers in laboratory environments at 16Kz.

---

<sup>2</sup> This technique is applied in Katz's discounting when all events at one state  $q$  are seen more than  $r$  times [1]

Info\_Tren database has recently been recorded as part of a project to develop a dialogue system. Info\_tren is a very difficult task of spontaneous Spanish speech dialogues with a vocabulary of around 2000 words plus 15 different acoustic types of disfluencies such as noises, filled pauses, lengthenings, etc. [10]. The task consisted of 227 Spanish dialogues on train information. They were recorded at 8KHz across telephone lines, applying the well known Wizard of Oz mechanism. The training corpus consisted of 191 dialogues uttered by 63 different speakers (1349 user turns resulting in 16500 words plus 5000 disfluencies). The test set consisted of 36 dialogues corresponding to 12 different speakers (308 user turns including 4000 words plus around 500 disfluencies). Info\_tren is the first spontaneous dialog database recorded by Castilian Spanish speakers.

High and low-smoothed n-gram LMs with  $n = 2 \dots 4$  were obtained, using Witten-Bell (WBd) and Add-One (AOd) discounting respectively. Table 1 shows the perplexity (PP) results obtained. LMs associated to the Info\_Tren database included the disfluencies as part of the vocabulary and there was a quite considerable mismatching between training and test [10]. As a consequence, the Perplexity values associated with this task are quite high.

For both tasks, the best (lowest) PP values were obtained using high-smoothed LMs (WBd). Nevertheless, differences among high and low-smoothed models behavior were more important for Info\_Tren task. In this task the number of word sequences appearing in the test set but not appearing in the training set is higher than in Bdgeo task. Higher PP values are obtained using low-smoothed LMs, since they assign lower backoff probabilities than high-smoothed LMs to those sequences. For the Bdgeo task, the best PP values were obtained with 4-grams using both high and low-smoothed LMs. However, for the Info\_Tren task the best PP results were reached with 3-grams (trigrams) by high-smoothed LMs and with 2-grams (bigrams) by low-smoothed LM were used.

The LMs in Table 1 were integrated into a Spanish CSR system. Uttered sentences were decoded by the time-synchronous Viterbi algorithm with a fixed beam-search to reduce the computational cost. A chain of Hidden Markov models were used to represent the acoustic model of the word phonetic chain. Different exponential scaling parameters on LM probabilities were applied ( $\alpha=1 \dots 7$ ). Table 2 shows the CSR performances obtained: the Word Error Rate (WER) and the Average number of Active Nodes (AAN) (including both acoustic and LM nodes) needed to decode a sentence. Optimum performances are emphasised and underlined.

When no scaling factor was applied ( $\alpha = 1$ ) low-smoothed LMs got better performances for both databases. As mentioned above, low-smoothed LMs lead to a bigger gap among LM probabilities than high-smoothed models. Thus, LM probabilities are more significant in the Viterbi trellis and, as a consequence, WER are lower than the obtained when using high-smoothed LMs. Computational cost (ANN) is also lower for low-smoothed LMs because, for a fixed beam-search factor, when differences among probabilities are increased, the number of paths to keep in the lattice are reduced.

**Table 1.** Perplexity (PP) evaluation of n-grams LMs with  $n = 1 \dots 4$  for Bdgeo and Info\_Tren tasks. Witten-Bell (WBd), Add-One (AOd) discounting were evaluated.

n	Bdgeo				Info_Tren			
	high smoothing		low smoothing		high smoothing		low smoothing	
	WBd	AOd	WBd	AOd	WBd	AOd	WBd	AOd
2	13.1		13.89		36.84		57.22	
3	7.53		8.30		34.88		69.87	
4	7.17		7.72		36.37		77.33	

**Table 2.** %WER evaluation of n-grams LMs of Table 1 with  $n = 2 \dots 4$  for Bdgeo and Info\_Tren tasks. Witten-Bell (WBd), Add-One (AOd) discounting were evaluated.

n	$\alpha$	Bdgeo				Info_Tren			
		high smoothing		low smoothing		high smoothing		low smoothing	
		WBd	AOd	WER	AAN	WBd	AOd	WER	AAN
n=2	1	41.62	3964	33.29	2209	61.69	3260	56.75	2610
	2	25.80	2588	21.60	1207	50.23	2594	47.15	1827
	3	20.22	1508	17.33	684	43.83	1912	42.13	1199
	4	16.99	764	<b>14.98</b>	<b>416</b>	41.08	1291	<b>39.89</b>	<b>760</b>
	5	<b>15.80</b>	<b>380</b>	15.20	258	<b>39.60</b>	<b>799</b>	40.75	484
	6	15.95	218	15.93	173	40.32	467	42.30	335
	7	17.01	143	18.14	126	41.75	294	43.92	245
n=3	1	38,85	5189	28,3	2935	58,69	6400	55,60	5172
	2	21,86	2984	16,49	1325	48,72	4668	45,21	3233
	3	15,35	1529	12,5	633	42,14	3172	41,50	1876
	4	11,74	702	<b>10,98</b>	<b>339</b>	38,72	1978	<b>39,36</b>	<b>1060</b>
	5	<b>10,82</b>	<b>328</b>	11,04	193	<b>38,01</b>	<b>1135</b>	40,24	610
	6	10,85	179	13,08	123	38,41	631	43,13	386
	7	13,04	114	15,67	88	41,58	378	47,41	269
n=4	1	38.50	5374	28.59	3058	58.80	6480	55.20	5380
	2	21.86	3053	16.03	1356	48.90	4720	45.00	3410
	3	14.44	1544	11.91	640	42.25	3286	41.04	2237
	4	10.92	704	10.89	339	38.83	2229	<b>39.10</b>	<b>1250</b>
	5	10.24	328	<b>10.67</b>	<b>190</b>	<b>37.84</b>	<b>1269</b>	41.24	708
	6	<b>10.22</b>	<b>177</b>	13.44	120	38.63	702	43.70	436
	7	12.48	113	16.46	85	42.31	415	48.26	296

As it was mentioned in Section 2, the gap among LM probabilities is bigger for low-smoothed LMs than for high-smoothed ones. The scaling factor  $\alpha$  increases this gap. As a consequence, low-smoothed LMs need lower values of  $\alpha$  to get the best CSR performance (see Section 2). In any case, differences between optimum system WER obtained by low and high-smoothing techniques are not very significant.

For Bdgeo task, the best performances were obtained using 4-grams as it was predicted by perplexity. However, for Info\_Tren task, optimum performances were also obtained with 4-grams for both low and high smoothed LM in spite of the perplexity predictions. In fact, for Info\_Tren task, perplexity increases strongly with  $n$ , specially using low-smoothed LMs, but WER decreases with  $n$ . The results obtained corroborate that PP is not the most adequate measurement of the smoothing technique.

It has been experimentally established that there is a strong dependence between the smoothing technique and the value of the scaling parameter  $\alpha$  needed

to get the best performance of the system (which in many cases is perplexity independent).

## 5 Concluding Remarks

When smoothed LMs are integrated into the CSR system there are several heuristic parameters that must be taken into account. Due to its great effect on final CSR performances, the exponential scaling factor applied to LM probabilities is one of the most important. This factor increases the gap between LM probabilities to make them more competitive with acoustic probabilities in the Viterbi trellis. In this work, the relationship between the smoothing technique and the scaling factor is established. Low and high smoothed LMs have been evaluated in two Spanish tasks of very different difficulty. Similar optimum CSR performances could be obtained applying the adequate value of the scaling factor in each case. Low-smoothed LM reach their optimum CSR performances with lower values of the scaling factor than high smoothed LMs because they have an “*a priori*” bigger gap among LM probabilities. Experiments showed that an increase of the test set perplexity of a LM does not always mean degradation in the model performance, which depends fundamentally on empirical factors.

## References

1. Ney, H., Martin, S., Wessel, F.: Statistical Language Modeling using leaving-one-out. In Young, S., ed.: LM. Kluwer Academic Publishers (1997) 174–207
2. Chen, F.S., Goodman, J.: An empirical study of smoothing techniques for language modeling. Computer, Speech and Language **13** (1999) 359–394
3. Rosenfeld, R.: Two decades of statistical language modeling: Where do we go from here (2000)
4. Clarkson, P., Robinson, R.: Improved language modelling through better language model evaluation measures. Computer, Speech and Language **15** (2001) 39–53
5. Jelinek, F.: Five speculations (and a divertimento) on the themes of h. bourlard, h. hermansky and n. morgan. Speech Communication **18** (1996) 242–246
6. Klakow, D., Peters, J.: Testing the correlation of word error rate and perplexity. Speech Communication **38** (2002) 19–28
7. Varona, A., Torres, I.: Back-Off smoothing evaluation over syntactic language models. In: Proc. of European Conference on Speech Technology. Volume **3**. (2001) 2135–2138
8. Torres, I., Varona, A.: k-tss language models in a Speech recognition Systems. Computer, Speech and Language **15** (2001) 127–149
9. Díaz, J., Rubio, A., Peinado, A., Segarra, E., Prieto, N., F.Casacuberta: Albayzin: a task-oriented spanish Speech Corpus. In: First Int. Conf. on language resources and evaluation. Volume **11**. (1998) 497–501
10. Rodríguez, L., Torres, I., Varona, A.: Evaluation of sublexical and lexical models of acoustic disfluencies for spontaneous Speech recognition in spanish. In: Proc. of European Conference on Speech Technology. Volume **3**. (2001) 1665–1668

# Selection of Lexical Units for Continuous Speech Recognition of Basque

K. López de Ipiña<sup>1</sup>, M. Graña<sup>2</sup>, N. Ezeiza<sup>3</sup>, M. Hernández<sup>2</sup>, E. Zulueta<sup>1</sup>, A. Ezeiza<sup>3</sup>, and C. Tovar<sup>1</sup>

<sup>1</sup>Sistemen Ingeniaritz eta Automatika Saila Gasteiz.  
{isplopek, iepzugee}@vc.ehu.es

<sup>2</sup>Konputazio Zientziak eta Adimen Artifiziala Saila, Donostia. ccpgrrom@si.ehu.es

<sup>3</sup>IXA group, Donostia. aitzol@si.ehu.es  
University of the Basque Country

**Abstract.** The selection of appropriate Lexical Units (LUs) is an important issue in the development of Continuous Speech Recognition (CSR) systems. Words have been used classically as the recognition unit in most of them. However, proposals of non-word units are beginning to arise. Basque is an agglutinative language with some structure inside words, for which non-word morpheme like units could be an appropriate choice. In this work a statistical analysis of units obtained after morphological segmentation has been carried out. This analysis shows a potential gain of confusion rates in CSR systems, due to the growth of the set of acoustically similar and short morphemes. Thus, several proposals of Lexical Units are analysed to deal with the problem. Measures of Phonetic Perplexity and Speech Recognition rates have been computed using different sets of units and, based on these measures, a set of alternative non-word units have been selected.

**Keywords:** Lexical Units, CSR, aglutinative languages.

## 1 Introduction

This paper presents an approach to the selection of Lexical Units (LUs) for Continuous Speech Recognition (CSR) of Basque. This language presents a wide dialectal distribution, being 8 the main dialectal variants. This dialectal diversity involves differences at phonetic, phonologic and morphological levels. Moreover, it is relevant the existence of the unified Basque, a standardisation of the language created with the aim of overcoming dialectal differences. Nowadays, a significant amount of speakers and most of mass media uses this standard. Thus, in this work the unified Basque is the main reference.

The development of a CSR system for a language involves the selection of a set of suitable LUs. These LUs are used not only in Language Modelling, but also to define the dictionaries where the acoustic-phonetic models can be integrated. Classically, words have been used as LUs in most of the CSR systems. However, some recent proposals point out non-word units as alternative LUs for some languages. In fact for

languages whose words are not clearly delimited inside sentences such as Japanese [1], or with words with some structure within them such as Finish, German, Basque etc., these alternative units seem to be more accurate. There have been several proposals for alternative LUs, such as morphemes [1], automatically selected non-word units [2], etc. Thus, taking into account the morphological structure of Basque, the use of morphemes seems to be an appropriate approach.

**Table 1.** Main characteristics of the textual databases

	STBASQUE	NEWSPAPER	BCNEWS
<b>Text amount</b>	<b>1,6M</b>	<b>1,3M</b>	<b>2,5M</b>
<b>Number of words</b>	197,589	166,972	210,221
<b>Number of pseudo-morphemes</b>	346,232	304,767	372,126
<b>Number of sentences</b>	15,384	13,572	19,230
<b>Vocabulary size in words</b>	50,121	38,696	58,085
<b>Vocabulary size in pseudo-morphemes</b>	20,117	15,302	23,983

The following section describes the main morphological features of the language and details the statistical analysis of morphemes using three different textual samples. Section 3 presents the experiments and the evaluation criteria that have been used. Finally, conclusions are summarised in section 4.

## 2 Morphological Features of Basque

Basque is an aglutinative language with a special morpho-syntactic structure inside the words [3][4] that may lead to intractable vocabularies of words for a CSR when the size of task is large. A first approach to the problem is to use morphemes instead of words in the system in order to define the system vocabulary [4]. This approach has been evaluated over three textual samples analysing both the coverage and the Out of Vocabulary rate, when we use words and pseudo-morphemes obtained by the automatic morphological segmentation tool AHOZATI [5]. Table 1 shows the main features of the three textual samples relating to size, number of words and pseudo-morphemes and vocabulary size, both in words and pseudo-morphemes for each database. The first important outcome of our analysis is that the vocabulary size of pseudo-morphemes is reduced about 60% (Fig. 1) in all cases relative to the vocabulary size of words. Regarding the unit size, Fig. 2 shows the plot of Relative Frequency of Occurrence (RFO) of the pseudo-morphemes and words versus their length in characters over the textual sample STDBASQUE. Although only 10% of the pseudo-morphemes in the vocabulary have less than 4 characters, such small morphemes have an Accumulated Frequency of about 40% in the databases [5] (the Accumulated Frequency is calculated as the sum of the individual pseudo-morphemes RFO).

To check the validity of the unit inventory, units having less than 4 characters and having plosives at their boundaries were selected from the texts. They represent some 25% of the total. This high number of small and acoustically difficult recognition

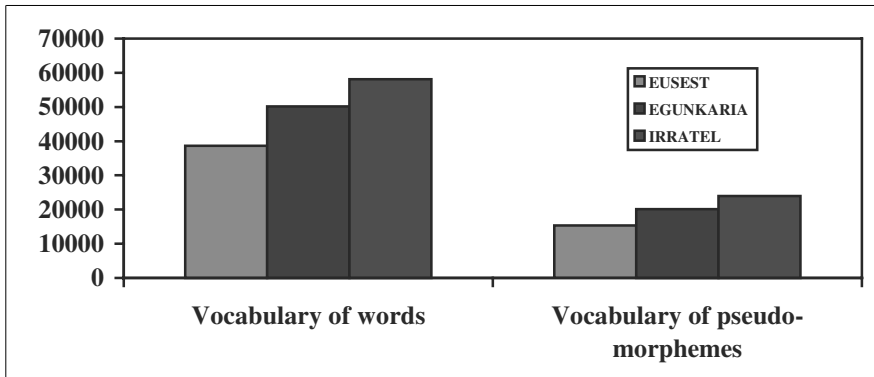


**Fig. 1.** Vocabulary size of the words and pseudo-morphemes

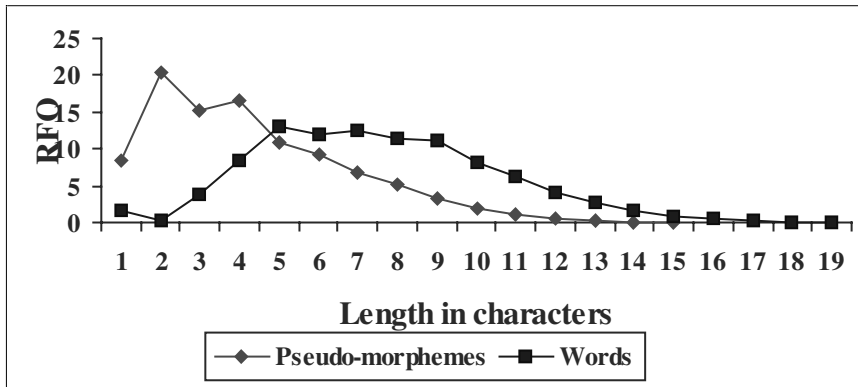


**Fig. 2.** Relative Frequency of Occurrence (RFO) of the words and pseudo-morphemes in relation to their length in characters (STDBASQUE sample)

units could lead to an increase of the acoustic confusion, and could also generate a high number of insertions (Fig. 3 over the textual sample EGUNKARIA).

Finally, Fig. 4 shows the analysis of coverage and Out of Vocabulary rate over the textual sample BCNEWS. When pseudo-morphemes are used, the coverage in texts is better and complete coverage is easily achieved. OOV rate is higher in this sample.

### 3 Experimentation

#### 3.1 Description of the Tasks

Appropriate tasks with controlled vocabularies are required to test LM and/or LUs. Two tasks have been created [4] for this purpose:

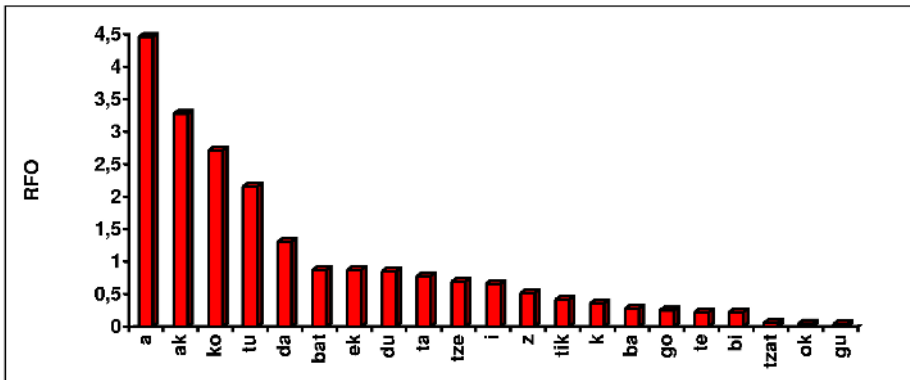


Fig. 3. Relative Frequency of Occurrence (RFO) of small and acoustically difficult recognition units (EGUNKARIA sample)

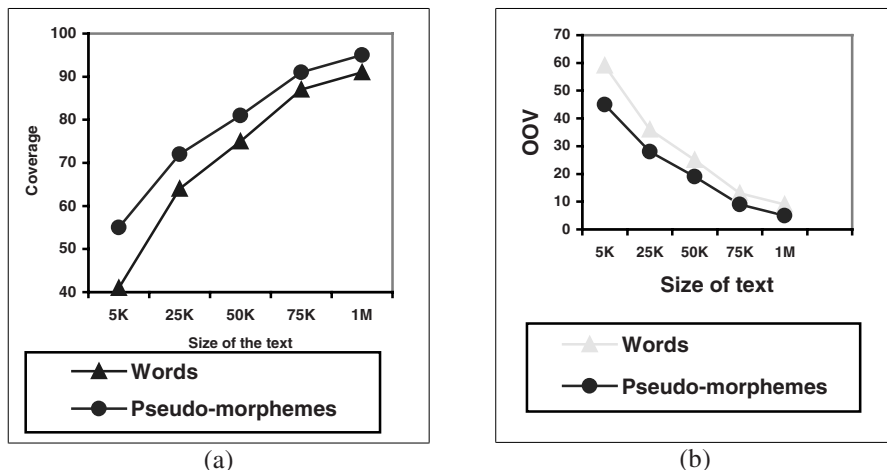


Fig. 4. Coverage (a) and OOV rate (b) for the textual sample BCNEWS

- a) Miniature Language Acquisition (MLA) task is the language used by a computer system to give examples of pictures paired with true statements about those pictures. The task in Basque has 15,000 sentences with about 150,000 words, being 47 the vocabulary size. It has very low perplexity and very restrictive vocabulary size. It was created for preliminary experiments of CSR.
- b) Basic Vocabulary of Basque (BVB) is a task based on beginner's level of Basque. The task consists of 5,000 sentences with about 30,000 words, being 3,500 the vocabulary size. Most of the features of the language described in section 2 are present in this task. It has a high perplexity comparing to MLA task and, it was created to measure the precision of the system when a larger scale task is used.

Both tasks were automatic morphologically segmented into pseudo-morphemes by AHOZATI. The MLA task reduces its vocabulary size to 35 pseudo-morphemes and, BVB task to 1,900. Finally, a segmentation in N-WORDS was obtained resulting in,

40 and 2500 different vocabulary units for MLA and BVB tasks respectively. The sentences of MLA task were divided into 14,500 sentences for training and 500 for test and, the sentences of BVB task into 4,000 for training and 500 for test. 20 speakers, 10 males and 10 females, recorded both tasks, obtaining 400 sentences for MLA and 800 sentences for BVB. In the speech recognition experiments a subset of BVB (MBVB) was used. The subset has a vocabulary size of 550 for WORDS, 400 for PS-MORPHS and 500 for N-WORDS.

### 3.2 Evaluation Criteria

- a) A perplexity function to evaluate the influence of the LUs in the LM. The classical perplexity function used to evaluate LMs might not be valid in this case. This function depends on the units used to compose sentences. Therefore, the evaluation must be based on an invariant unit, such as it is the phoneme. Thus, Phonetic Perplexity will be used to validate LUs. This perplexity is expressed as in [6]:

$$PP = 2^{\left[ \frac{-1}{F} \sum_{i=1}^N \log_2 \text{Prob}(W_i|M) \right]} = P^{K/F} \quad (1)$$

Where PP is the Phonetic Perplexity function, P is the perplexity and F and K are the number of phonemes and units composing the sentences, respectively. The CMU-Cambridge Toolkit [6] has been used to calculate both PP and P for different N-gram lengths.

- b) Speech Recognition experiments without LM have been carried out to evaluate both the influence of acoustic confusion of LUs and the insertion of short LUs. Moreover, Recognition Rates for LUs (LURR) have been analysed using the raw stream of LUs (LURR-NA) and also the stream of words after the alignment of the non-words LUs (LURR-A) to words using simple information about the set of words. A set of 28 Contextual Independent Sublexical units modelled by Discrete HMMs with four codebooks will be used as acoustic models.
- c) The computational cost of the experiments is also tested. We evaluate the Computational Time (CT) (the performance in msec. Real time operative corresponding to 10 msec) and the Time Weighted LURR (T-LURR).

### 3.3 Preliminary Experiment

The previously analysed morphological features of the language make difficult the selection of appropriate LUs for CSR. Furthermore, evaluating the statistical measures of morphemes, it can be observed that the performance of the Acoustic Phonetic Decoding system could potentially be worse due to several factors. On the one hand, acoustically similar morphemes could lead to increase acoustic confusion. On the other hand, the amount of short units could also increase the amount of insertions [5].

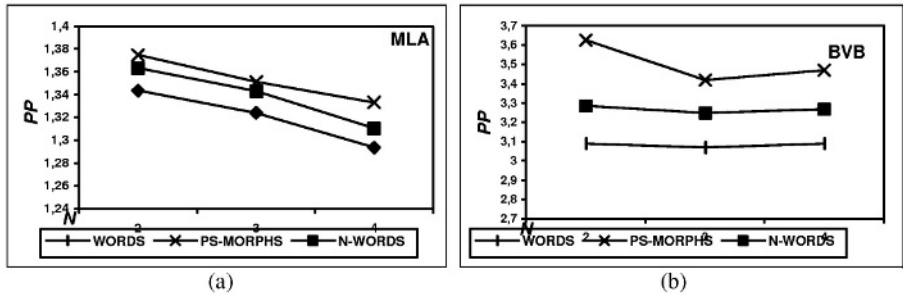


**Fig. 5.** Measurements of Phonetic Perplexity for MLA (a) and BVB (b) tasks

**Table 2.** Recognition rates (LURR) using the three sets of lexical units, WORDS, N-WORDS and PS-MORPHS

	<b>MLA</b>				<b>MBVB</b>					
	LURR- NA	LURR- A	LURR- BIGR	CT	T- LURR	LURR- NA	LURR- A	LURR- BIGR	CT	T- LURR
<b>WORDS</b>	80,61	80,61	91,34	6	13,4	43,71	43,71	48,44	33	1,46
<b>N-WORDS</b>	74,84	76,30	88,82	5	14,96	30,09	32,60	42,07	28	1,50
<b>PS-MORPHS</b>	60,29	63,80	82,38	3	20,09	28,98	29,09	39,85	25	1,59

Three sets of LUs are used in the experiments [4]:

1. **WORDS:** words are our baseline LU set.
2. **PS-MORPHS:** these pseudo-morpheme units are morphemes automatically obtained and slightly transformed for Speech Recognition by ad-hoc rules [5].
3. **N-WORDS:** An alternative proposal. Pseudo-morphemes of length lower than 3 characters with a high level of confusion are merged with adjacent units [5]. This proposal reduces the vocabulary size about 25% with respect to WORDS.

### 3.4 Experimental Results

Experiments with WORDS and PS-MORPHS sets were carried out to analyse the influence of the morphological structure in the recognition of the LUs. Measures of PP were computed for different values of N. Fig. 5 shows lower PP of WORDS with respect to PS-MORPHS in both tasks. The results of the speech recognition experiments also show better performance for WORDS than for PS-MORPHS in both tasks (table 2) This is due to the frequent confusion and the high amount of insertion in the case of the shortest pseudo-morphemes. Consequently, the alignment improves the results and reduces the insertion of short LUs. However, WORDS still obtained better results than PS-MORPHS. With regard to the CT and T-LURR the advantage is for PS-MORPHS. Regarding BVB task, it can be observed that the overall results are worst than in MLA (table 2), but it must be taken into account that the perplexity of the task is considerably higher [4]. The results show that PS-MORPHS has worst result of recognition but better results with regard to the computational cost.

The experiments using the new LUs N-WORDS show that PP is lower than the one for PS-MORPHS (Fig. 5) and closer to the perplexity measure for WORDS. Table 2 indicates also that N-WORDS outperforms PS-MORPHS for MLA and MBVB tasks with or without alignment. Moreover the recognition rate of N-WORDS is closer to the rate for WORDS in both tasks. N-WORDS shows in table 2 the best balance of LURR and computational cost (CT and T-LURR).

Finally, table 2 shows the performance of the system with a bigram Language Model. The introduction of a Language Model improves all the results, but the increase in performance is more significant for non-word LUs.

## 4 Concluding Remarks

This work deals with the selection of appropriate LUs for Basque language. Since Basque is an agglutinative language, non-word units could be an adequate choice for LUs. First, morphemes and words have been tested, including a statistical analysis of morphemes in Basque. This analysis shows a large amount of short and acoustically similar morphemes, leading to a bad performance of the CSR system. Measures of phonetic perplexity, computational cost and speech recognition experiments have been completed to validate both proposals. Although word model obtains the best results, it becomes intractable for medium-large dictionaries. Thus, a new set of non-word units has been created based on morphemes. This proposal shows an appropriate performance of the system and reduces the problems raised by morphemes. In future works the obtained sets of LUs will be evaluated in a LVCSR system.

**Acknowledgements.** The authors would like to thank all the volunteer speakers that has collaborated recording the databases. We thank also all people have collaborated in the development of this work: Euskaldunon Egunkaria, UZEI [7], EITB [8] and the University of the Basque Country (this work has been partially supported by the University of the Basque Country, under project (UPV00147.345-E-14895/2002).

## References

- [1] Otsuki K. et al. "*Japanese large-vocabulary continuous-speech recognition using a newspaper corpus and broadcast news*", Speech Communication. Vol 28, pp 155–166, 1999.
- [2] Peñagarikano M. et al. "*Using non-word Lexical Units in Automatic Speech Understanding*", Proceedings of IEEE, ICASSP99, Phoenix, Arizona.
- [3] Alegria I. et al. "*Automatic morphological analysis of Basque*", Literary & Linguistic Computing Vol,11, No, 4, 193–203, Oxford University Press, 1996.
- [4] Lopez de Ipiña K. et al. "*First Selection of Lexical Units for Continuous Speech Recognition of Basque*", Proceedings of ICSLP. Beijing 2000, Vol II, pg. 531–535.
- [5] Lopez de Ipina K., N. Ezeiza, G. Bordel. & M. Graña. "Automatic Morphological Segmentation for Speech Processing in Basque" Proceeding of IEEE TTS Workshop. Santa Monica USA. 2002.
- [6] P.R. Clarkson and R. Rosenfeld. Statistical Language Modelling Using the CMU-Cambridge Toolkit From Proceedings ESCA Eurospeech 1997.
- [7] <http://www.uzei.com>
- [8] <http://www.eitb.com>

# Creating a Mexican Spanish Version of the CMU Sphinx-III Speech Recognition System

Armando Varela<sup>1</sup>, Heriberto Cuayáhuitl<sup>1</sup>, and Juan Arturo Nolazco-Flores<sup>2</sup>

<sup>1</sup> Universidad Autónoma de Tlaxcala,  
Department of Engineering and Technology,  
Intelligent Systems Research Group,  
Apartado Postal #140, 90300 Apizaco, Tlaxcala, Mexico.

{avarela, hcuayahu}@ingenieria.uatx.mx

<http://orion.ingenieria.uatx.mx:8080/si/si.jsp>

<sup>2</sup> Instituto Tecnológico de Estudios Superiores de Monterrey,  
Sucursal de Correos “J”, 64849, Monterrey, Nuevo Leon, Mexico.  
jnolazco@itesm.mx

**Abstract.** In this paper we present the creation of a Mexican Spanish version of the CMU Sphinx-III speech recognition system. We trained acoustic and N-gram language models with a phonetic set of 23 phonemes. Our speech data for training and testing was collected from an auto-attendant system under telephone environments. We present experiments with different language models. Our best result scored an overall error rate of 6.32%. Using this version is now possible to develop speech applications for Spanish speaking communities. This version of the CMU Sphinx system is freely available for non-commercial use under request.

## 1 Introduction

Today, building a new robust Automatic Speech Recognition (ASR) system is a task of many years of effort. In the Autonomous University of Tlaxcala - Mexico, we have two goals in the ASR field: Do research for generating a robust speech recognizer, and build speech applications for automating services. In order to achieve our goals in a short time, we had to take a baseline work. We found that the CMU (Carnegie Mellon University) Sphinx speech recognition system is freely available and currently is one of the most robust speech recognizers in English. The CMU Sphinx system enables research groups with modest budgets to quickly begin conducting research and developing applications. This arrangement is particularly pertinent in Latin America, where the financial support and experience otherwise necessary to support such research is not readily available. In the past, few research efforts have been done for Spanish and these includes work from CMU in broadcast news transcription [1, 2], where basically acoustic and language models have been trained. Our motivations for developing this work are due to the fact that many applications require a speech recognizer for Spanish, and because Spoken Dialogue Systems (SDS) require a robust speech recognizer were reconfiguration and retraining is necessary.

In this research, we have generated a lexicon and trained acoustic and language models with Mexican Spanish speech data for the CMU Sphinx speech recognition system. Our experiments are based on data collected from an auto-attendant application (CONMAT) deployed in Mexico [3], with a vocabulary of 2,288 entries from names of people and places inside a university, including synonyms. Our speech data used for training and testing was filtered avoiding noisy utterances. Results are given in terms of the well known evaluation metric: Word Error Rate (WER). In the remainder of the paper we first provide an overview of the system in section 2. In section 3 we describe the components of the Sphinx system and how these were trained. In Section 4 we present experimental results. Finally, in section 5 we provide our conclusions and future directions.

## 2 System Overview

The Carnegie Mellon University Sphinx-III system is a frame-based, HMM-based, speaker-independent, continuous speech recognition system, capable of handling large vocabularies (see Fig. 1). The word modeling is performed based on subword units, in terms of which all the words in the dictionary are transcribed. Each subword unit considered in its immediate context (triphone) is modeled by 5-state left-to-right HMM model. Data is shared across states of different triphones. These groups of HMM states sharing distributions between its member states are called senones [4].

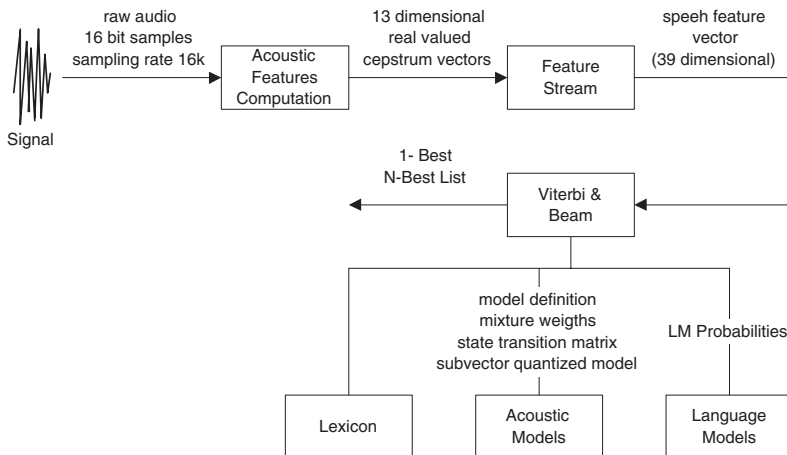


**Fig. 1.** Architecture of the CMU Sphinx-III speech recognition system. The lexical or pronunciation model contains pronunciations for all the words of interest to the decoder. Acoustic models are based on statistical Hidden Markov models (HMMs). Sphinx-III uses a conventional backoff bigram or trigram language model. The result is a recognition hypothesis with a word lattice representing an N-best list.

The feature vector computation is a two-stage process. In the first stage, an off-line front-end module is first responsible for processing the raw audio sample stream into a cepstral stream. The input is windowed, resulting in frames of duration 25.625 ms. The output is a stream of 13-dimensional real-valued cepstrum vectors. The frames overlap, thus resulting in a rate of 100 vectors/sec. In the second stage, the stream of cepstrum vectors is converted into a feature stream. This process consists of a Cepstrum Mean-Normalization (CMN) and Automatic Gain Control (AGC) step. The final speech feature vector is created by typically augmenting the cepstrum vector (after CMN and AGC) with one or more time derivatives. The feature vector in each frame is computed by concatenating first and second derivatives to the cepstrum vector, giving a 39-dimensional vector.

### 3 System Components

#### 3.1 Lexicon

The lexicon development process consisted of defining a phonetic set and generating the word pronunciations for training acoustic and language models.

**Table 1.** ASCII Phonetic Symbols for Mexican Spanish.

Manner	Label	Example	Worldbet Word
Plosives	p	<b>punto</b>	p u n t o
	b	<b>baños</b>	b a ñ o s
	t	<b>tino</b>	t i n o
	d	<b>donde</b>	d o n d e
	k	<b>casa</b>	k a s a
	g	<b>ganga</b>	g a n g a
Fricatives	f	<b>falda</b>	f a l d a
	s	<b>mismo</b>	m i s m o
	x	<b>jamas</b>	x a m a s
Affricates	tS	<b>chato</b>	tS a t o
Nasals	m	<b>mano</b>	m a n o
	n	<b>nada</b>	n a d a
Semivowels	ñ	<b>baño</b>	b a ñ o
	l	<b>lado</b>	l a d o
	L	<b>pollo</b>	p o L o
	r(	<b>pero</b>	p e r( o
	r	<b>perro</b>	p e r o
Vowels	w	<b>hueso</b>	w e s o
	i	<b>piso</b>	p i s o
	e	<b>mesa</b>	m e s a
	a	<b>caso</b>	k a s o
	o	<b>modo</b>	m o d o
	u	<b>cura</b>	k u r( a

Our approach for modeling Mexican Spanish phonetic sounds in the CMU Sphinx-III speech recognition system consisted of an adapted version from the WORLDBET Castilian Spanish phonetic set [5], which resulted in 23 phonemes listed in Table 1. The adaptation consisted in a manual comparison of spectrograms from words including a common phoneme; we found common sounds which we merged in our final list of phonemes. The following are the modifications made to the Castilian Spanish sounds set for generating a Mexican Spanish version:

- Fricative /s/ as in “kasa” and fricative /z/ as in “mizmo” merged into /s/,
- Plosive /b/ as in “baños” and fricative /V/ as in “aVa” merged into /b/,
- Plosive /d/ as in “donde” and fricative /D/ as in “deDo” merged into /d/,
- Plosive /g/ as in “ganga” and fricative /G/ as in “lago” merged into /g/,
- Semi-vowels /j/ as in “majo” and /L/ as in “poLo”, and affricate /dZ/ as in “dZugo” merged into /L/,
- Nasal /n/ as in “nada” and nasal /N/ as in “baNko” merged into /n/,
- Fricative /T/ as in “luTes” was deleted due to the fact that this sound does not exist in Mexican Spanish.

The vocabulary size has 2,288 words, which is based on names of people and places inside a university, including synonyms. The automatic generation of pronunciations was performed using a simple list of rules and exceptions. The rules determine the mapping of clusters of letters into phonemes and the exceptions list covers some words with irregular pronunciations. A Finite State Machine (FSM) was used to develop the pronunciations from the word list.

### 3.2 Acoustic Models

For training acoustic models is necessary a set of feature files computed from the audio training data, one each for every recording in the training corpus. Each recording is transformed into a sequence of feature vectors consisting of the Mel-Frequency Cepstral Coefficients (MFCCs). The training of acoustic models is based on utterances without noise. This training was performed using 3,375 utterances of speech data from an auto-attendant system, which context is names of people and places inside a university.

The training process (see Fig. 2) consists of the following steps: Obtain a corpus of training data and for each utterance, convert the audio data to a stream of feature vectors, convert the text into a sequence of linear triphone HMMs using the pronunciation lexicon, and find the best state sequence or state alignment through the sentence HMM for the corresponding feature vector sequence. For each senone, gather all the frames in the training corpus that mapped to that senone in the above step and build a suitable statistical model for the corresponding collection of feature vectors. The circularity in this training process is resolved using the iterative Baum-Welch or forward-backward training algorithm. Due to the fact that continuous density acoustic models are computationally expensive, a model is built by sub-vector quantizing the acoustic model densities (sub-vector quantizing was turned off in our work).

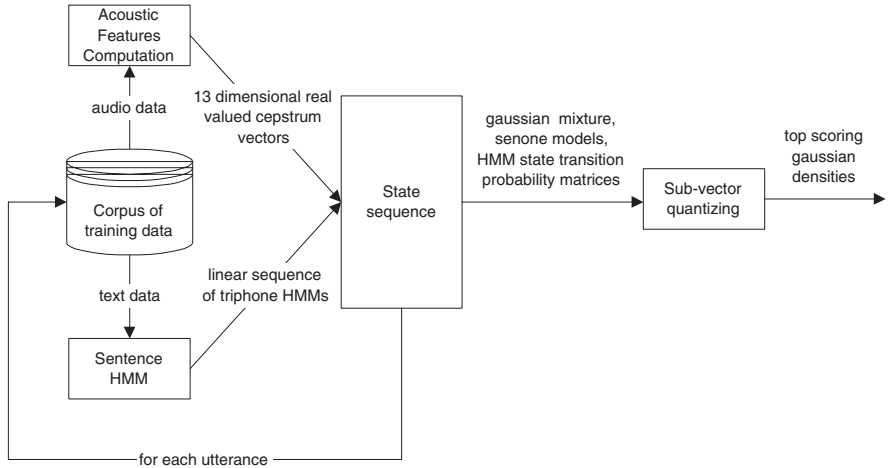


**Fig. 2.** A block schematic diagram for training acoustic models.

### 3.3 Language Models

The main Language Model (LM) used by the Sphinx decoder is a conventional bigram or trigram backoff language model. Our LMs were constructed from the 2,288 word dictionary using the CMU-Cambridge statistical language model toolkit version 2.0 [6], see Fig. 3. The training data consisted of 3,375 transcribed utterances of speech data from an auto-attendant system. We trained bigrams and trigrams with four discounting strategies: Good Turing, Absolute, Linear, and Witten Bell. The LM probability of an entire sentence is the product of the individual word probabilities. The output from the CMU-Cambridge toolkit is an ASCII text file, and because this file can be very slow to load into memory, the LM must be compiled into a binary form. The decoder uses a disk-based LM strategy to read the binary into memory. Although the CMU-sphinx recognizer is capable for handling out-of-vocabulary speech, we did not set any filler models. Finally, the recognizer needs to exponentiate the LM probability using a language weight before combining the result with the acoustical likelihood.

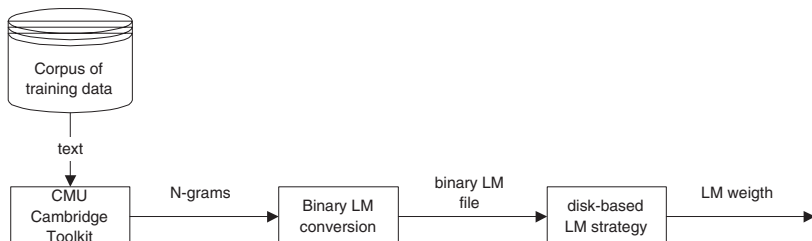


**Fig. 3.** A block schematic diagram for training language models.

## 4 Experimental Results

### 4.1 Experimental Setup

We performed two experiments for evaluating the performance of the CMU Sphinx system trained with Mexican speech data (872 utterances) in the context of an auto-attendant application: the first experiment considered names of people and places as independent words (i.e. any combination of first names and last names was allowed), the second experiment considered names of people and places as only one word. Each experiment was evaluated with two different LMs.

### 4.2 Evaluation Criteria

The evaluation of each experiment was made according to recognition accuracy and computed using the WER (Word Error Rate) metric defined by the equation 1, which align a recognized word string against the correct word string and compute the number of substitutions (S), deletions (D), and insertions (I) from the number of words in the correct sentence (N).

$$WER = (S + D + I) / N * 100\%. \quad (1)$$

### 4.3 Results

Recognition results for each decoding stage for the CMU with Sphinx Mexican Spanish test data are shown in Tables 2 and 3. In table 2 (experiment 1), we can observe that the use of Good Turing discount strategy is not convenient, and the use of different n-grams does not make much difference, perhaps bigger training and test sets would yield significant differences. In the mean time, for this experiment the best option is bigrams with Witten Bell discounting strategy, but we observed problems with this approach due that this experiment can yield incorrect hypothesis, i.e. nonexistent names of people and places. Thus, another solution was necessary to solve this problem. In table 3 (experiment 2), we observe that due to the conditions of the experiment, would yield no further significant improvements with different n-grams. Despite of this, the best gains are shown in trigrams with Witten Bell discounting strategy.

**Table 2.** Word error rate in the test set after decoding from the experiment 1, which considered names of people and places as independent words.

Discounting Strategy	Bigrams	Trigrams
Good Turing	12.95	12.88
Absolute	7.82	7.63
Linear	7.94	8.07
Witten Bell	7.63	7.75

**Table 3.** Word error rate in the test set after decoding from the experiment 2, which considered names of people and places as only one word.

Discounting Strategy	Bigrams	Trigrams
Good Turing	6.88	6.44
Absolute	6.38	6.38
Linear	6.50	6.57
Witten Bell	6.38	6.32

## 5 Conclusions and Future Work

We described the training and evaluation processes of the CMU Sphinx-III speech recognition system for Mexican Spanish. We performed two experiments in which we grouped differently the word dictionary entries. Our best results of this development considered dictionary entries as only one word for avoiding nonexistent names of people and places inside a university. Through a simple lexicon and set of acoustic and language models, we demonstrated an accurate recognizer which scored an overall error rate of 6.32% on in-vocabulary speech data. We achieved the goal of this work from which now we have a baseline product for performing research in speech recognition, which is an important component of spoken language systems. Also, with this work we can start development of speech applications with the advantage that we can retrain and adapt the recognizer according to our needs. This work was motivated due to the fact that people around the world need to develop applications involving speech recognition for Spanish speaking communities. Therefore, the resulted lexicon, acoustic and language models are freely available for non-commercial purposes under request.

An immediate future work is to provide a bridge for invoking the recognizer and see it as a black box, perhaps we can build a dll file or we can provide something similar as SAPI. This is indispensable for programmers who need to develop speech applications from different programming environments. Another important future direction and due that this development considers only in-vocabulary speech, we plan to retrain the recognizer considering Out-Of-Vocabulary (OOV) speech, measuring computational overhead. This is due to the fact that OOV speech is an important factor in spoken dialogue systems and degrades significantly the performance in such systems [7]. Also, we plan to train Sphinx in different domains, as well as optimize configuration parameters. Finally, we plan to train Sphinx release 4 which was implemented in Java, and make a comparison between Sphinx III and Sphinx 4 in Spanish domains. All this work would be performed considering a bigger corpus.

**Acknowledgements.** This research was possible due to the availability of the CMU Sphinx speech recognizer. We want to thank to the people involved in the

development of the CMU Sphinx-III and of course the formers of the recognizer [8]. Also, we want to thank Ben Serridge for his writing revision on this paper.

## References

1. J. M. Huerta, E. Thayer, M. Ravishankar, and R. M. Stern: The Development of the 1997 CMU Spanish Broadcast News Transcription System. Proc. of the DARPA Broadcast News Transcription and Understanding Workshop, Lansdowne, Virginia, Feb 1998.
2. J. M. Huerta, S. J. Chen, and R. M. Stern: The 1998 Carnegie Mellon University Sphinx-III Spanish Broadcast News Transcription System. In the proceedings of the DARPA Broadcast News Transcription and Understanding Workshop, Herndon, Virginia, Mar 1999.
3. Cuayáhuitl, H. and Serridge, B.: Out-Of-Vocabulary Word Modeling and Rejection for Spanish Keyword Spotting Systems. Lecture Notes in Computer Science, Vol, 2313. Berlin Heidelberg New York (2002) 158–167.
4. Hwang, M-Y: Subphonetic Acoustic Modeling for Speaker-Independent Continuous Speech Recognition. Ph.D. thesis, Carnegie Mellon University, 1993.
5. Hieronymus L., J.: ASCII Phonetic Symbols for World's Languages: worldbet. Technical report, Bell Labs, 1993.
6. P. Clarkson, and R. Rosenfeld.: Statistical Language Modeling Using the CMU-Cambridge Toolkit. In the proceedings of Eurospeech, Rodhes, Greece, 1997, 2707–2710.
7. Farfán, F., Cuayáhuitl H., and Portilla, A.: Evaluating Dialogue Strategies in a Spoken Dialogue System for Email. In the proceedings of the IASTED Artificial Intelligence and Applications, ACTA Press, Manalmádena, Spain, Sep 2003.
8. CMU Robust Speech Group, Carnegie Mellon University.  
<http://www.cs.cmu.edu/afs/cs/user/robust/www/>

# Decision Tree-Based Context Dependent Sublexical Units for Continuous Speech Recognition of Basque

K. López de Ipiña<sup>1</sup>, M. Graña<sup>2</sup>, N. Ezeiza<sup>3</sup>, M. Hernández<sup>2</sup>, E. Zulueta<sup>1</sup>, and A. Ezeiza<sup>3</sup>

<sup>1</sup>Sistemen Ingeniaritza eta Automatika Saila Gasteiz.  
{isplopek, iepzugee}@vc.ehu.es

<sup>2</sup>Konputazio Zientziak eta Adimen Artifiziala Saila, Donostia.  
{ccpgrrrom, ccphegom}@si.ehu.es

<sup>3</sup>IXA group, Donostia. {aitzol, nerea}@si.ehu.es  
University of the Basque Country

**Abstract.** This paper presents a new methodology, based on the classical decision trees, to get a suitable set of context dependent sublexical units for Basque Continuous Speech Recognition (CSR). The original method proposed by Bahl [1] was applied as the benchmark. Then two new features were added: a data massaging to emphasise the data and a fast and efficient Growing and Pruning algorithm for DT construction. In addition, the use of the new context dependent units to build word models was addressed. The benchmark Bahl approach gave recognition rates clearly outperforming those of context independent phone-like units. Finally the new methodology improves over the benchmark DT approach.

**Keywords:** Sublexical Units, Decision Trees, Growing and Pruning Algorithm

## 1 Introduction

The choice of a suitable set of sublexical units is one of the most important issues in the development of a Continuous Speech Recognition (CSR) system. As shown in the literature, authors have proposed a wide range of them: diphones, triphones and other context dependent units, transitional units or demiphones. Such a variety of approaches aim at the accurate model of the influence of contexts in the realisation of Phone Like Context Independent Sublexical Units (PL-CI-SLUs). System efficiency can exploit the benefits of context modelling by using context dependent sublexical units to generate lexical baseforms, taking into account not only intraword but also between-word contexts, as we will see.

Decision Trees (DT) are one of the most common approaches to the problem of selecting a suitable set of context dependent sublexical units (DT-CD-SLUs) for speech recognition [1][2][3].

DT combine the advantages of applying some phonetic knowledge about how contexts affect the articulation of speech and a strictly quantitative validation procedure based on the likelihood of speech samples with regard to some probabilistic models.

In this work DT have been used to model both intraword and between-word context dependencies. Starting from the classical scheme [1], some attempts have been made in order to improve the accuracy and the discriminative power of the models. An alternative methodology, the fast and efficient Growing and Pruning algorithm [4], has also been applied to build the decision trees.

The paper is organised as follows. Section 2 reviews the basic DT methodology, describing more carefully those points where major changes have been introduced. Section 3 presents the alternative DT methodology, based on the Growing and Pruning algorithm and on the data massaging. In section 4, the issue of between-word context modelling is discussed and some solutions are proposed. Finally, in Section 5 DT-based Context Dependent and Semicontextual Units (DT-CD-SLUs and DT-SC-SLUs) are applied to a Basque CSR task, and experimental results are discussed. Conclusions are summarised in section 6.

## 2 The Baseline Methodology

Firstly, automatic segmentation of the training corpus was carried out to get the set of samples corresponding to each of the PL-CI-PLUs, each sample consisting of a string of labels, obtained by vector quantization of the acoustic observation vectors. In fact, four different strings of labels were used simultaneously, each corresponding to a different acoustic observation VQ codebook. Each DT, associated to a given PL-CI-SLUs, was built as follows. All the samples corresponding to that PL-CI-SLUs were assigned to the root node.

Then a set of binary questions, manually established by an expert phonetician, related to one or more left and right contexts, were made to classify the samples. Any given question  $Q$  divided the set of samples  $Y$  into two subsets,  $Y_l$  and  $Y_r$ . The resulting subsets were evaluated according to a quality measure, a *Goodness of Split* (GOS) function, reflecting how much the likelihood of the samples increased with the split. Heuristic thresholds were applied to discard those questions yielding low likelihoods (GOS threshold) or unbalanced splits (trainability threshold). Among the remaining questions, the one giving the highest quality was chosen, thus appearing two new –left and right- nodes, being the samples partitioned according to the answer (YES/NO) to that question. This procedure was iterated until no question exceeded the quality thresholds.

Following the classical scheme, a simple histogram was used to model acoustic events, each component of the histogram being modelled as a Poisson distribution. In fact, the model consisted of four different histograms, whose likelihoods were

multiplied to yield the combined likelihood. To evaluate the quality of the splits the classical GOS function was applied:

$$GOS = \log \left\{ \frac{P(Y_l|M_l) \cdot P(Y_r|M_r)}{P(Y|M)} \right\}$$

where  $Y_l$  and  $Y_r$  stand for the sets of samples resulting of the split of set  $Y$  that were used to train models  $M_l$ ,  $M_r$  and  $M$  respectively;  $P(Y|M)$  is the joint likelihood of a set of samples  $Y$  with regard to a previously trained model  $M$ . This  $GOS$  function measures the likelihood improvement resulting from the split –i.e. from the question  $Q$ .

### 3 Methodological Improvements

As said above, DTs were grown until any of the stopping criteria verified. Two thresholds were used, the first one establishing a minimum GOS value, the second one giving the minimum number of training samples. After some preliminary experimentation, adequate values were heuristically fixed for these thresholds. This is a very simple but inconvenient way to stop the growing procedure, because thresholds must be fixed for each training database.

An alternative methodology was designed to overcome this problem, based on the fast and efficient Growing and Pruning (G&P) algorithm [4].

The G&P algorithm divides the set of training samples corresponding to a given PL-CI-SLUs into two independent subsets. The tree is iteratively grown with one of the subsets, and pruned with the other, interchanging the roles of the two subsets in successive iterations. The growing procedure was identical to that described in section 2, but removing the  $GOS$  threshold. A minimum number of training samples was required for a node to be valid. As a second step, once a big DT was built, the pruning procedure applied a misclassification measure to discard leaf nodes below a given threshold. It can be shown that the algorithm converges after a few steps [4]. Among the DT building methods, G&P provides a good balance between classification accuracy and computational cost, compared to other methods like CART [5]. Note, however, that we use an alternative to the classic G&P. A new threshold must be still heuristically fixed to control the size of the sample sets associated to the leaf nodes, because a minimum number of samples is necessary for the acoustic models to be trainable.

Preprocessing the data (data massaging) may improve the performance of DT when databases are small. In this work we have computed the square to each histogram element to emphasise it, obtaining a better discrimination.

**Table 1.** Recognition rates for various methodologies of selection of the sets of sublexical units in a speaker independent acoustic-phonetic decoding task in Basque

Type of units	Context window size	G&P	Preprocessing	#Units	% REC
<b>CI-PLU</b>	-	-	-	28	64.01
<b>DT-std1</b>	1	-	Standard	256	71.10
<b>DT-std2</b>	1	-	Standard	217	71.45
<b>DT-g&amp;p1</b>	1	G&P	Standard	220	71.32
<b>DT-g&amp;p2</b>	2	G&P	Standard	234	70.99
<b>DT-g&amp;p-mass</b>	1	G&P	Data-massaging	215	<b>71.52</b>

## 4 The Word Models

The construction of word models can take a great advantage of the DT-CD-SLUs. In the linear lexicon framework applied in this work, a more consistent word model results from the concatenation of this kind of units. Intraword contexts are handled in a straightforward manner, because left and right contexts are known and DT-CD-SLUs guarantee a full coverage of such contexts. A challenging problem arises when considering between-word contexts, i.e. the definition of border units, because outer contexts are not known, and a lack of coverage is found for these situations. Which contexts should be considered outside the edges of words? A *brute force* approach would expand these border units with all the context dependent units fitting the inner context. This leads to an intractable combinatorial problem when dealing with a large search automaton. Usually, this problem is solved either by simply using context independent units, or by explicitly training border units [1] [2] [3] [6].

Two different approaches to represent inter word context dependencies were considered and tested in this work. DT-CD-SLUs introduced in previous section were used inside the words in any case.

- a) PL-CI-SLUs were used at word boundaries. As mentioned above, this approach involves a low computational cost but does not consider many acoustic influences of neighbouring phones.
- b) Decision Tree based Semicontextual sublexical (DT-SC-SLUs) units. Specific decision tree-based context dependent units were used at word boundaries [7]. These sets of units were specifically obtained to be insideword context dependent and outsideword context independent. These units were obtained using binary questions about either the left context or the right context. This set was used to transcribe the last phone of each word. This procedure agrees with the classical decision tree methodology used to get context dependent units. Thus, full coverage of inner contexts is guaranteed while keeping outside context independence. On the other

hand, the size of the lexicon as well as the computational cost of the search did not increase.

## 5 Experimental Evaluation

The corpus used to obtain all the DT-CD-SLUs previously presented was composed of 10000 sentences, phonetically balanced and uttered by 40 speakers, involving around 200000 phones. These samples were then used to train the acoustic model of each DT-derived context dependent unit. Discrete HMMs with four observation codebooks were used as acoustic models in these experiments.

A task has been created for this purpose. The Miniature Language Acquisition (MLA) [8] in Basque has 15,000 sentences with about 150,000 words, being 47 the vocabulary size. It has very low perplexity and very restrictive vocabulary size. It was created for preliminary experiments of CSR. Then, the task underwent an automatic morphological segmentation and we created two sets of lexical units as alternative to the words. We considered these new lexical units because Basque is an aglutinative language [9]. Thus, MLA task reduces the vocabulary size to 35 pseudo-morphemes (PS-MORPHS). Finally, N-WORDS acoustically more robust units [9] were obtained resulting in, 40. The sentences of MLA task were divided into 14,500 sentences for training and 500 for test. 20 speakers, 10 males and 10 females, recorded the task, obtaining 400 sentences.

### 5.1 Acoustic-Phonetic Decoding Experiments

Two groups of sublexical units were used in these experiments:

- The first and simplest one consisted of 24 PL-CI-SLU and it was used as a reference set.
- The second group of sublexical units was the DT-CD-SLUs set obtained through the methodology described in Section 2. Both the standard approach -with and without the new features described above- and the G&P approach, were used to generate the corresponding DT-CD-SLUs. The standard approach, using a set of phonetic questions about left and one right contexts and two different thresholds controlling the size of the training sets, was applied to get the sets **DT-stdN**. The standard approach, but replacing the standard data by the massaging data defined in section 3, was used to obtain the set **DT-mass**. Finally, the G&P approach was applied to obtain the sets **DT-g&p**. Results are shown in table 1.

From these results we conclude that DT-CD-SLUs outperform the reference sets CI-PLU and Freq-CDU. The two new features added to the standard DT methodology improve the performance. In fact, the best result (71.52%) obtained for **DT-g&p-mass**, integrate two methods only slightly better than the obtained for **DT-std1** (71.45%) but improve the result obtained for G&P in [7] for Spanish. The G&P

methodology performed faster than the standard. Most times the procedure did converge in two steps, each step involving half the samples of the standard methodology, thus providing considerable timesavings.

**Table 2.** Word recognition rates in a Basque CSR task (MLA), without language model, for various sets of sublexical units and three different approaches to the definition of border units by using three different sets of lexical units: WORDS, PS-MORPHS and N-WORDS

units used at word boundaries						
	WORDS		PS-MORPHS		N-WORDS	
	PL-CI-SLU	DT-SC-SLU	PL-CI-SLU	DT-SC-SLU	PL-CI-SLU	DT-SC-SLU
<b>CI-PLU</b>	80.61	-	-	-	-	-
<b>DT-std1</b>	86.73	87.68	84.03	83.68	69.20	72.13
<b>DT-g&amp;p2</b>	86.20	87.41	83.12	83.44	69.54	72.52
<b>DT-g&amp;p-mass</b>	86.43	<b>90.75</b>	83.96	<b>84.19</b>	69.68	<b>73.33</b>

## 5.2 Lexical Unit-Level Experiments

This second series of experiments was aimed to evaluate the proposed DT-CD-SLUs when used to build word models. Different lexicon transcriptions were applied according to the approach used to model word boundaries (section 4), while keeping DT-CD-SLUs inside words: PL-CD-SLUs and DT-SC-SLUs.

The experiments have been carried out without grammar and in the case of morphemes and N-WORDS the output was aligned to words to compare the results appropriately. Experimental results are shown in table 2. DT-CD-SLUs outperformed the reference sets PL-CI-SLUs in all cases. As expected, the use of DT-SD-SLUs at word boundaries led to the best results, establishing an upper bound to the benefits attainable by using context dependent sublexical units to build word models. This reveals the contribution of modelling between-word context to the speech recognition, and suggests further work in that line.

**DT-g&p-mass** gave the best recognition rates, being the best choice when handling isolated lexical units both with PL-CI-SLUs (86,43% for words, 83,96 for N-WORDS and 69,68 for PS-MORPHS) or DT-SC-SLUs SLUs (90,75% for words, 84,19 for N-WORDS and 73,33 for PS-MORPHS). Finally, the G&P methodology has a performance similar to standard methodology, with a very low computational cost.

## 6 Concluding Remarks

The classical decision tree classification methodology was improved to obtain a suitable set of context dependent sublexical units for Basque CSR tasks. A data massing methodology was used to emphasising differences among the samples. An alternative methodology, based on the fast and efficient G&P algorithm, was also proposed. Various sets of DT-based context dependent sublexical units were tested in a first series of speaker independent acoustic-phonetic decoding experiments, where our methodology outperforms the classical one proposed by Bahl. Two different strategies to handle border units in the construction of word models were described and tested in a second series of experiments. Results showed the potential contribution of modelling between-word contexts to speech recognition, and suggest further work in that line.

**Acknowledgements.** The authors would like to thank all the volunteer speakers that has collaborated recording the databases. We thank also all people have collaborated in the development of this work. This work has been partially supported by the University of the Basque Country, under project UPV00147.345-E-14895/2002.

## References

- [1] Bahl R.L., V.P. de Souza, P.S. Gopalakrishnan, D. Nahamoo and M.A. Picheny. "*Decision Trees for Phonological Rules in Continuos Speech Recognition*", Proc. IEEE ICASSP-94, pp. 533–536.
- [2] Kuhn R., A. Lazarides and Y. Normandin. "*Improving Decision Trees for Phonetic Modelling*". Proc. IEEE ICASSP-95, pp. 552–555.
- [3] Odell J. "*The Use of Context in Large Vocabulary Speech Recognition*". Ph. Thesis. Cambridge University. March 1995.
- [4] Gelfand S.B., C.S. Ravishankar and E.J. Delp. "*An Iterative Growing and Pruning Algorithm for Classification Tree Design*". IEEE Trans. on PAMI, Vol. 13, No. 2, pp. 163–174. 1991.
- [5] Breiman L., J.H. Friedman, R.A. Olshen and C.J. Stone. "*Classification and Regression Trees*". Wadsworth & Brooks, 1984.
- [6] Young S.J., J. Odell and P. Woodland. "*Tree-Based State Tying for High Accuracy Acoustic Modelling*". ARPA Workshop on Human Language Technology, pp. 286–291, March 1994.
- [7] López de Ipiña K., A. Varona, I. Torres and L. J. Rodríguez, "*Decision Trees for Inter-Word Context Dependencies in Spanish Continuous Speech Recognition Tasks*". EURO-SPEECH99. Budapest.
- [8] Feldman J.A., A. Lakoff, A. Stolcke and S.H. Weber, "*Miniature language Acquisition: a touch-stone for cognitive science*". Technical Report, Tr-90-009. ICSI, Berkeley, California. April 1990.
- [9] Lopez de Ipiña K., I. Torres, L. Oñederra, M. Hernandez, M. Peñagarikano, N. Ezeiza, A. Varona and L.J. Rodríguez. "*First Selection of Lexical Units for Continuos Speech Recognition of Basque*", Proceedings of ICSLP. Beijing 2000, vol II, pg. 531–535

# Uniclass and Multiclass Connectionist Classification of Dialogue Acts\*

María José Castro<sup>1</sup>, David Vilar<sup>1</sup>, Emilio Sanchis<sup>1</sup>, and Pablo Aibar<sup>2</sup>

<sup>1</sup> Departament de Sistemes Informàtics i Computació  
Universitat Politècnica de València. Camí de Vera s/n, 46022 València, Spain

<sup>2</sup> Departament de Llenguatges i Sistemes Informàtics  
Universitat Jaume I de Castelló. E-12071 Castelló, Spain  
`{mcastro,dvilar,esanchis}@dsic.upv.es aibar@lsi.uji.es`

**Abstract.** Classification problems are traditionally focused on uniclass samples, that is, each sample of the training and test sets has one unique label, which is the target of the classification. In many real life applications, however, this is only a rough simplification and one must consider some techniques for the more general multiclass classification problem, where each sample can have more than one label, as it happens in our task. In the understanding module of a domain-specific dialogue system for answering telephone queries about train information in Spanish which we are developing, a user turn can belong to more than one type of frame. In this paper, we discuss general approaches to the multiclass classification problem and show how these techniques can be applied by using connectionist classifiers. Experimentation with the data of the dialogue system shows the inherent difficulty of the problem and the effectiveness of the different methods are compared.

## 1 Introduction

In many real pattern recognition tasks, it is convenient to perform a previous classification of the objects in order to treat them in a specific way. For instance, if language models can be learnt for specific sub-domains of a task, better performance can be achieved in an automatic speech recognition/understanding system. The aim of this work is to propose some classification techniques in order to improve the understanding process of a dialogue system.

The task of our dialogue system consists of answering telephone queries about train timetables, prices and services for long distance trains in Spanish. The understanding module gets the output of the speech recognizer (sequences of words) as input and supplies its output to the dialogue manager. The semantic representation is strongly related to the dialogue management. In our approach, the dialogue behavior is represented by means of a stochastic network of dialogue acts. Each dialogue act has three levels of information: the first level represents the general purpose of the turn, the second level represents the type of semantic

---

\* This work has been partially supported by the Spanish CICYT under contracts TIC2000-0664-C02-01 and TIC2002-04103-C03-03.

message (the frame or frames), and the third level takes into account the data supplied in the turn.

We focus our attention on the process of classification the user turn in terms of the second level of the dialogue act, that is, the identification of the frame or frames. This classification will help us to determine the data supplied in the sentence in a later process, where depending on the output of the classifier, one or more specific understanding models are applied. Our previous work on this same topic can be found in [1, 2].

Dealing with this frame detection problem, we encountered the problem of the multiclass classification as a natural issue in our system. A user can ask in the same utterance about timetables and prices of a train, for example, and these are two of the categories we have defined. This poses an interesting problem, as most of the classification problems and solutions up to now have focused exclusively on the uniclass classification problem, and few have dealt with this kind of generalization.

## 2 The Uniclass Classification Problem

Uniclass classification problems involve finding a definition for an unknown function  $k^*(\mathbf{x})$  whose range is a discrete set containing  $|\mathcal{C}|$  values (i.e.,  $|\mathcal{C}|$  “classes” of the set of classes  $\mathcal{C} = \{c^{(1)}, c^{(2)}, \dots, c^{(|\mathcal{C}|)}\}$ ). The definition is acquired by studying collections of training samples of the form

$$\{(\mathbf{x}_n, c_n)\}_{n=1}^N, \quad c_n \in \mathcal{C}, \quad (1)$$

where  $\mathbf{x}_n$  is the  $n$ -th sample and  $c_n$  is its corresponding class label.

For example, in handwritten digit recognition, the function  $k^*$  maps each handwritten digit to one of  $|\mathcal{C}| = 10$  classes. The Bayes decision rule for minimizing the probability of error is to assign the class with maximum a posteriori probability to the sample  $\mathbf{x}$ :

$$k^*(\mathbf{x}) = \operatorname{argmax}_{k \in \mathcal{C}} \Pr(k|\mathbf{x}). \quad (2)$$

**Uniclass Classification using Neural Networks.** Multilayer perceptrons (MLPs) are the most common artificial neural networks used for classification. For this purpose, the number of output units is defined as the number of classes,  $|\mathcal{C}|$ , and the input layer must hold the input samples. Each unit in the (first) hidden layer forms a hyperplane in the pattern space; boundaries between classes can be approximated by hyperplanes. If a sigmoid activation function is used, MLPs can form smooth decision boundaries which are suitable to perform classification tasks [3].

For uniclass samples, the activation level of an output unit can be interpreted as an approximation of the a posteriori probability that the input sample belongs to the corresponding class. Therefore, given an input sample  $\mathbf{x}$ , the trained MLP computes  $g_k(\mathbf{x}, \omega)$  (the  $k$ -th output of the MLP with parameters  $\omega$  given the input sample  $\mathbf{x}$ ) which is an approximation of the a posteriori probability

$\Pr(k|\mathbf{x})$ . Thus, for MLP classifiers we can use the uniclass classification rule as in equation (2):

$$k^*(\mathbf{x}) = \operatorname{argmax}_{k \in \mathcal{C}} \Pr(k|\mathbf{x}) \approx \operatorname{argmax}_{k \in \mathcal{C}} g_k(\mathbf{x}, \omega). \quad (3)$$

### 3 The Multiclass Classification Problem

In contrast to the uniclass classification problem, in other real-world learning tasks the unknown function  $k^*$  can take more than one value from the set of classes  $\mathcal{C}$ . For example, in many important document classification tasks, documents may each be associated with multiple class labels [4, 5]. A similar example is found in our classification problem of dialogue acts: a user turn can be labeled with more than one frame label. In this case, the training set is composed of pairs of the form<sup>3</sup>

$$\{(\mathbf{x}_n, C_n)\}_{n=1}^N, \quad C_n \subseteq \mathcal{C}. \quad (4)$$

There are two common approaches to this problem of classification of objects associated with multiple class labels.<sup>4</sup> The first is to use specialized solutions like the accumulated posterior probability approach described in the next section. The second is to build a binary classifier for each class as explained afterwards.

#### 3.1 Accumulated Posterior Probability

In a traditional (uniclass) classification system, given an estimation of the a posteriori probabilities  $\Pr(k|\mathbf{x})$ , we can think of a classification as “better estimated” if the probability of the destination class is above some threshold (i.e., the classification of a sample  $\mathbf{x}$  as belonging to class  $k$  is better estimated if  $\Pr(k|\mathbf{x}) = 0.9$  than if it is only 0.4). A generalization of this principle can be applied to the multiclass approximation problem.

We can consider that we have correctly classified a sample only if the *sum* of the a posteriori probabilities of the assigned classes is above some threshold  $\mathcal{T}$ . Let us define this concept more formally. Suppose we have an ordering (permutation)  $(k^{(1)}, k^{(2)}, \dots, k^{(|\mathcal{C}|)})$  of the set  $\mathcal{C}$  for a sample  $\mathbf{x}$ , such that

$$\Pr(k^{(i)}|\mathbf{x}) \geq \Pr(k^{(i+1)}|\mathbf{x}) \quad \forall 1 \leq i < |\mathcal{C}|. \quad (5)$$

We define the “accumulated posterior probability” for the sample  $\mathbf{x}$  as

$$\Pr_{\mathbf{x}}(j) = \sum_{i=1}^j \Pr(k^{(i)}|\mathbf{x}) \quad 1 \leq j \leq |\mathcal{C}|. \quad (6)$$

---

<sup>3</sup> The uniclass classification problem is a special case in which  $|C_n| = 1$  for all samples.

<sup>4</sup> In certain practical situations, the amount of possible multiclass labels is limited due to the nature of the task. For instance, if we know that the only possible appearing multiple labels can be  $\{c^{(i)}, c^{(j)}\}$  and  $\{c^{(i)}, c^{(k)}\}$  we do not need to consider all the possible combinations of the initial labels. In such situations we can handle this task as an uniclass classification problem with the extended set of labels  $\hat{\mathcal{C}}$  defined as a subset of  $\mathcal{P}(\mathcal{C})$ .

Using the above equation, we classify the sample  $\mathbf{x}$  in  $n$  classes, being  $n$  the smallest number such that

$$\Pr_{\mathbf{x}}(n) \geq \mathcal{T}, \quad (7)$$

where the threshold  $\mathcal{T}$  must also be learnt automatically in the training process. The set of classification labels for the sample  $\mathbf{x}$  is simply

$$K^*(\mathbf{x}) = \{k^{(1)}, \dots, k^{(n)}\}. \quad (8)$$

**Accumulated Probability using MLPs.** We can apply this approach using neural networks by modifying slightly equation (7). As the output of the output layer is an *approximation* of the a posteriori probabilities, it is possible that the sum exceeds the value of 1, so a more suitable estimation would be<sup>5</sup>

$$|1 - \Pr_{\mathbf{x}}(n)| \leq \mathcal{S}, \quad (9)$$

where the accumulated posterior probabilities  $\Pr_{\mathbf{x}}(j)$  are computed as in equation (6) by approximating the posterior probabilities with an MLP of  $|\mathcal{C}|$  outputs

$$\Pr_{\mathbf{x}}(j) = \sum_{i=1}^j \Pr(k^{(i)} | \mathbf{x}) \approx \sum_{i=1}^j g_i(\mathbf{x}, \omega) \quad 1 \leq j \leq |\mathcal{C}|. \quad (10)$$

The outputs  $g_i(\mathbf{x}, \omega)$  of the trained MLP are also ordered according (5). During the training phase, the desired outputs for the sample  $\mathbf{x}$  are the “true” posterior probabilities of each class.<sup>6</sup>

### 3.2 Binary Classifiers

Another possibility is to treat each class as a separate binary classification problem (as in [6–8]). Each such problem answers the question, whether a sample should be assigned to a particular class or not.

For  $C \subseteq \mathcal{C}$ , let us define  $C[c]$  for  $c \in \mathcal{C}$  to be:

$$C[c] = \begin{cases} \text{true,} & \text{if } c \in C; \\ \text{false,} & \text{if } c \notin C. \end{cases} \quad (11)$$

A natural reduction of the multiclass classification problem is to map each multiclass sample  $(\mathbf{x}, C)$  to  $|\mathcal{C}|$  binary-labeled samples of the form  $((\mathbf{x}, c), C[c])$  for all  $c \in \mathcal{C}$ ; that is, each sample is formally a pair,  $(\mathbf{x}, c)$ , and the associated binary label,  $C[c]$ . In other words, we can think of each observed class set  $C$  as specifying  $|\mathcal{C}|$  binary labels (depending on whether a class  $c$  is or not included in  $C$ ), and we can then apply uniclass classification to this new problem. For

<sup>5</sup> Note the different interpretation of the threshold value in equations (7) and (9). In the first one,  $\mathcal{T}$  represents the probability mass that we must have for correctly classifying a sample, whereas in the second one  $\mathcal{S}$  is a measure of the distance to the “ideal” classification with a posteriori probability value of 1.

<sup>6</sup> Nevertheless, a simplification is assumed: as the true posterior probabilities usually cannot be known, we consider all the classes of a training sample equally probable.

instance, if a given training pair  $(\mathbf{x}, C)$  is labeled with the classes  $c^{(i)}$  and  $c^{(j)}$ ,  $(\mathbf{x}, \{c^{(i)}, c^{(j)}\})$ , then  $|\mathcal{C}|$  binary-labeled samples are defined as  $(\langle \mathbf{x}, c^{(i)} \rangle, \text{true})$ ,  $(\langle \mathbf{x}, c^{(j)} \rangle, \text{true})$  and  $(\langle \mathbf{x}, c \rangle, \text{false})$  for the rest of classes  $c \in \mathcal{C}$ .

Then a set of binary classifiers is trained, one for each class. The  $i$ th classifier is trained to discriminate between the  $i$ th class and the rest of the classes and the resulting classification rule is

$$K^*(\mathbf{x}) = \{k \in \mathcal{C} \mid \Pr(k|\mathbf{x}) \geq T\}, \quad (12)$$

being  $T$  a threshold which must also be learnt.

**Binary Classification Using MLPs.** Let  $(\omega_1, \dots, \omega_{|\mathcal{C}|})$  be the MLP classifiers trained as in the uniclass case. Furthermore, let  $g(\mathbf{x}, \omega_i)$  be the output of the  $i$ th MLP classifier when given an input sample  $\mathbf{x}$ . New samples are classified by setting the predicted class or classes to be the index of the classifiers attaining the highest posterior probability,

$$K^*(\mathbf{x}) = \{k \in \mathcal{C} \mid \Pr(k|\mathbf{x}) \geq T\} \approx \{k \in \mathcal{C} \mid g(\mathbf{x}, \omega_k) \geq T\}. \quad (13)$$

An alternative approach is to assign a binary string of length  $|\mathcal{C}|$  to each class  $c \in \mathcal{C}$  or set of classes  $C \subseteq \mathcal{C}$ . During training for a pattern from classes  $c^{(i)}$  and  $c^{(j)}$ , for example, the desired outputs of these binary functions are specified by the corresponding units for classes  $i$  and  $j$ . With MLPs, these binary functions can be implemented by the  $|\mathcal{C}|$  output units of a single network.

In this case, the multiclass classification rule is redefined as: an input sample  $\mathbf{x}$  can be classified in the classes  $K^*(\mathbf{x})$  with a posteriori probability above a threshold  $T$ :

$$K^*(\mathbf{x}) = \{k \in \mathcal{C} \mid \Pr(k|\mathbf{x}) \geq T\} \approx \{k \in \mathcal{C} \mid g_k(\mathbf{x}, \omega) \geq T\}, \quad (14)$$

being  $g_k(\mathbf{x}, \omega)$  the  $k$ -th output of an MLP classifier with parameters  $\omega$  given the input sample  $\mathbf{x}$ .

## 4 The Dialogue Task

The final objective of our dialogue system is to build a prototype for information retrieval by telephone for Spanish nation-wide trains [9]. Queries are restricted to timetables, prices and services for long distance trains. A total of 215 dialogues were acquired using the Wizard of Oz technique. From these dialogues, a total of 1 440 user turns (14 923 words with a lexicon of 637 words) were obtained. The average length of a user turn is 10.27 words. All the utterances we used for our experiments were transcribed by humans from the actual spoken responses.

The turns of the dialogue were labelled in terms of three levels [10]. An example is given in Figure 1. We focus our attention on the most frequent second level labels, which are Affirmation, Departure\_time, New\_data, Price, Closing, Return\_departure\_time, Rejection, Arrival\_time, Train\_type, Confirmation. Note that each user turn can be labeled with more than one frame label<sup>7</sup> (as in the example).

---

<sup>7</sup> In related works of dialogue act classification [11], a hand-segmentation of the user turns was needed in order to have sentence-level units (utterances) which corre-

<b>Original sentence</b>	Hello, good morning. I would like to know the price and timetables of a train from Barcelona to La Coruña for the 22nd of December, please.
<b>1st level (speech act)</b>	Question
<b>2nd level (frames)</b>	Price, Departure_time
<b>3rd level (cases)</b>	Price (Origin: barcelona, Destination: la_coruña, Departure_time: 12/22/2003) Departure_time (Origin: barcelona, Destination: la_coruña, Departure_time: 12/22/2003)

**Fig. 1.** Example of the three-level labeling for a multiclass user turn. Only the English translation of the original sentence is given.

For classification and understanding purposes, we are concerned with the semantics of the words present in the user turn of a dialogue, but not with the morphological forms of the words themselves. Thus, in order to reduce the size of the input lexicon, we decided to use categories and lemmas. In this way, we reduced the size of the lexicon from 637 to 311 words. Then, we discarded those words with a frequency lower than five, obtaining a lexicon of 120 words.

We think that for this task the sequential structure of the sentence is not fundamental to classifying the type of frame.<sup>8</sup> For that reason, the words of the preprocessed sentence were all encoded with a local coding: a 120-dimensional bit-vector, one position for each word of the lexicon. When the word appears in the sentence, its corresponding unit is set to 1, otherwise, its unit is set to 0.

#### 4.1 Codification of the Frame Classes

For the uniclass problem we used the usual “1-of- $|C|$ ” coding, the desired output for each training sample is set to 1 for the one frame class that is correct and 0 for the remainder. The codification in the multiclass problem is different for each approach:

**Binary classification with  $|C|$  MLPs.** The target of the training sample is 1 if the sample belongs to the class of the MLP classifier, and 0 if not.

**Binary classification with one MLP.** The target of the training sample is coded with a  $|C|$ -dimensional vector: the desired outputs for each training sample  $(x_n, C_n)$  are set to 1 for those (one or more) frame classes that are correct and 0 for the remainder.

**Accumulated posterior probability.** The target of the training sample is coded with a  $|C|$ -dimensional vector: the desired outputs for each training sample  $(x_n, C_n)$  are set to  $1/|C_n|$  for those (one or more) frame classes that are correct and 0 for the remainder.

---

sponded to a unique dialogue act. The relation between user turns and utterances was also not one-to-one: a single user turn can contain multiple utterances, and utterances can span more than one turn. After the hand-segmentation process, each utterance unit was identified with a single dialogue act label.

<sup>8</sup> Nevertheless, the sequential structure of the sentence is essential in order to segment the user turn into slots to have a real understanding of it.

## 5 Experiments

The dataset is composed of 1 338 user turns after discarding the sentences labeled with the less-frequent frame classes. We have decided to split the corpus in two datasets, the first one containing only the uniclass turns (867 samples) and the complete one, which comprises uniclass and multiclass turns (1 338 samples). For each type of experiment, the dataset was randomly split (but we guarantee that each frame class is represented in the training and test set) so that about 80% of the user turns are used for training and the rest for testing.

### 5.1 Training the Neural Networks

With any neural network algorithm, several parameters must be chosen by the user. For the MLPs, we must select the network topology and their initialization, the training algorithm and their parameters and the stopping criteria [3, 12, 13]. We selected all the parameters to optimize performance on a validation set: the training set is subdivided into a subtraining set and a validation set (20% of the training data). While training on the subtraining set, we observed generalization performance on the validation set (measured as the mean square error) to determine the optimal setting of configuration and the best point at which to stop training. The thresholds  $S$  and  $T$  of the different multiclass classification rules were also learnt in the training process: we performed classification with the optimal configuration of MLP on the patterns of the validation set, proving several values of the thresholds and keeping the best one.

### 5.2 UC and MC Experiments

Table 1 shows the selected topology and the classification rate for each of the experiments. For the UC experiment, we used only the uniclass user turns (867 samples). For the MC experiments, we consider a sample as correctly classified if the set of the original frame classes is detected. That is, if a user turn is labeled with two frame classes, only and exactly those classes should be detected.

In the Accumulated Probability case, when applying classification rule (9) with a threshold  $S$  close to 0, that is, when the accumulated probability is close to 1, the error rate was very poor, misclassifying (nearly) all the multiclass samples. By analyzing the MLP outputs, we observed that when one or more classes are detected, each of the corresponding output values are close to one. Therefore, the MLP with a sigmoid activation function is unable to learn the true probability distribution across the whole set of classes. Due to this fact, we decided to apply the classification rule given in equation (14).

## 6 Discussion and Conclusions

This work is an attempt to show the differences between uniclass and multiclass classification problems applied to detecting dialogue acts in a dialogue system. We experimentally compare three connectionist approaches to this end: using accumulated posterior probability, binary multiple classifiers and one extended

**Table 1.** Classification error rates for the UC and MC experiments.

Experiment	Topology	Total	Uniclass	Multiclass
UC experiment	120-64-64-10	9.14	9.14	—
<b>MC experiments</b>				
Binary classifiers with $ \mathcal{C} $ MLPs	120-8-1	17.91	13.71	25.80
Binary classifiers with 1 MLP	120-32-32-10	11.19	7.43	18.28
Accumulated Probability	120-32-16-10	14.55	8.57	25.81

binary classifier. The results clearly shows that: firstly, multiclass classification is much harder than uniclass classification and, secondly, the best performance is obtained using one extended binary classifier.

On the other hand, the results obtained for classifying dialogue acts also show that using a connectionist approach is effective for classifying the user turn according to the type of frames. This automatic process will be helpful to the understanding module of the dialogue system: firstly, the user turn, in terms of natural language, is classified into a frame class or several frame classes; secondly, a specific understanding model for each type of frame is used to segment and fill the cases of each frame.

## References

1. M. J. Castro and E. Sanchis. A Simple Connectionist Approach to Language Understanding in a Dialogue System. In *Advances in Artificial Intelligence*, pages 664-673. Springer-Verlag, 2002.
2. E. Sanchis and M. J. Castro. Dialogue Act Connectionist Detection in a Spoken Dialogue System. In *Soft Computing Systems. Design, Management and Applications*, pages 644-651. IOS Press, 2002.
3. D. E. Rumelhart, G. E. Hinton, and R. J. Williams. *PDP: Computational models of cognition and perception, I*, pages 319-362. MIT Press, 1986.
4. A. K. McCallum. Multi-Label Text Classification with a Mixture Model Trained by EM. In *Proc. NIPS'99*, 1999.
5. R. E. Schapire and Y. Singer. Boostexter: A boosting-based system for text categorization. *Machine Learning*, 39(2/3):135-168, 2000.
6. Y. Yang. An evaluation of statistical approaches to text categorization. *Information Retrieval*, 1(1/2):69-90, 1999.
7. T. Joachims. Text categorization with Support Vector Machines: Learning with many relevant features. In *Proc. ECML'98*, pages 137-142. Springer Verlag, 1998.
8. K. Nigam et al. Text classification from labeled and unlabeled documents using EM. *Machine Learning*, 39(2/3):103-134, 2000.
9. A. Bonafonte et al. Desarrollo de un sistema de diálogo oral en dominios restringidos. In *Primeras Jornadas de Tecnología del Habla*, Sevilla (Spain), 2000.
10. C. Martínez et al. A Labelling Proposal to Annotate Dialogues. In *Proc. LREC 2002*, vol. V, pages 1577-1582, Las Palmas de Gran Canaria (Spain), 2002.
11. A. Stolcke et al. Dialogue Act Modeling for Automatic Tagging and Recognition of Conversational Speech. *Computational Linguistics*, 26(3):339-373, 2000.
12. A. Zell et al. *SNNS: Stuttgart Neural Network Simulator. User Manual, Version 4.2*. Univ. of Stuttgart, Germany, 1998.
13. C. M. Bishop. *Neural networks for pattern recognition*. Oxford Univ. Press, 1995.

# A Technique for Extraction of Diagnostic Data from Cytological Specimens\*

Igor Gurevich, Andrey Khilkov, and Dmitry Murashov

Scientific Council “Cybernetics” of the Russian Academy of Sciences. 40, Vavilov street,  
Moscow, GSP-1, 119991, Russian Federation  
igourevi@ccas.ru, dmmur@rbcmail.ru

**Abstract.** In this paper, a possibility of developing a new criterion for diagnostics of hematopoietic tumors, such as chronic B-cell lymphatic leukemia, transformation of chronic B-cell lymphatic leukemia into lymphosarcoma, and primary B-cell lymphosarcoma, from images of cell nuclei of lymphatic nodes is considered. A method for image analysis of lymphatic node specimens is developed on the basis of the scale space approach. A diagnostically important criterion is defined as a total amount of points of spatial intensity extrema in the families of blurred images generated by the given image of a cell nucleus. The procedure for calculating criterion values is presented.

## 1 Introduction

A large quantity of research in image processing and analysis are directed at the development of medical diagnostics. Recently appeared a new perspective trend concerned with the development of diagnostic techniques for automated analysis of morphology of blood cells and hematopoietic organs using analysis of microscopic images. In this paper, a relatively small sample of images is used for obtaining the criterion for diagnostics of hematopoietic tumors, such as chronic B-cell lymphatic leukemia, its transformation to lymphosarcoma, and primary B-cell lymphosarcoma (according to the classification of A. Vorob'ev and M. Brilliant [5]).

Experts in hematology have found out, that specimen cell nuclei of a tissue of lymphatic nodes taken from patients with the malignant tumor diagnose are larger than those taken from patients with the non-malignant tumor diagnose. Thus, an obvious diagnostic criterion is the area of cell nucleus. But this criterion is unsuitable for more accurate diagnostics: it is impossible to distinguish such diseases as transformation of chronic lymphoid leukemia and lymphosarcoma.

The procedure of searching for a diagnostic criterion includes the following steps: the experts indicate the diagnostically important cell nuclei in the images of lymphatic node specimens of three groups of patients having the diagnosed diseases. These images are considered as an input information. Next, the developed method of specimen

---

\* This work was partly supported by the Russian Foundation for Basic Research (grants NN 01-07-90016, 01-07-90017, 03-07-90406).

image analysis is used for calculating qualitative characteristics (features) from the indicated nuclei. The obtained values are analyzed, and this gives an opportunity to formulate a criterion for making diagnostic decisions. The proposed method for specimen image analysis is based on the known scale space approach [1,3,4].

## 2 Properties of Cell Images and Requirements to the Method

The image of a lymphatic node specimen is a color image taken by a camera and enlarged by a microscope (24 bits per pixel). The size of the image is 1536x1024 pixels covering a site of 60—100 microns in diameter. The resolution is 0,06 microns per pixel. The analyzed objects are the fragments of the gray-scale specimen images containing cell nuclei. These images are characterized by inhomogeneous coloring and by the presence of dark spots and bright areas representing their internal structure.

For a diagnostics, experts pay a special attention to the cells of two classes: mature cells, with the mature structure of chromatin, (see Fig. 1) and sarcoma cells, with the immature structure of chromatin, (see Fig. 2) [5-7]. In the first case (chronic lymphatic leukemia), with few exceptions, the image contains only mature cells. In the case of sarcoma transformation of the chronic lymphatic leukemia, the specimen contains both mature and immature (sarcoma) cells. In the case of primary lymphatic sarcoma, the sarcoma cells prevail in the image.

It is necessary to take into account such specific properties of cell images as low dye quality, instability of specimen characteristics, non-uniformity of specimen light exposure during microscoping, presence of damaged and unsuitable for analysis cells. Mature chromatin is homogeneous with light furrows. Immature chromatin can have a filamentous structure of different patterns, a fibrous, or a granular structure [7]. The analysis of cell nucleus images should yield quantitative characteristics that capture the structure and pattern of chromatin.

In view of the specific properties of cell images listed above, the following requirements to the method are formulated: (a) suitability for selection of features for classification of cell images; (b) resistance to noise caused by image acquisition process and specimen quality; (c) resistance to errors and noise of image processing algorithms; (d) correspondence of classification results to expert estimations.

The quantitative analysis cytological and tissue specimen images is based on the evaluation of shape, intensity, and textural features. In practice, the great attention is paid to automated analysis of chromatin arrangement in the cell nuclei. It has been proven in many studies that chromatin distribution corresponds to the state of malignancy. Two basic approaches to analysis of a chromatin constitution are known [9]. Within the first, structural, the chromatin distribution is considered as a local arrangement of rather small objects of varying intensity. The intensity features of dark and bright particles are evaluated. This approach is substantially heuristic. The second approach, textural, is based on the statistical characteristics of chromatin arrangement and related to analysis of the regularities of chromatin structure. Applied in practice methods for textural analysis use grey level dependency matrices [8], co-occurrence, run-length features, rice-field operators, and watersheds (topological methods) [10],



**Fig. 1.** Grayscale images of mature cell tumor

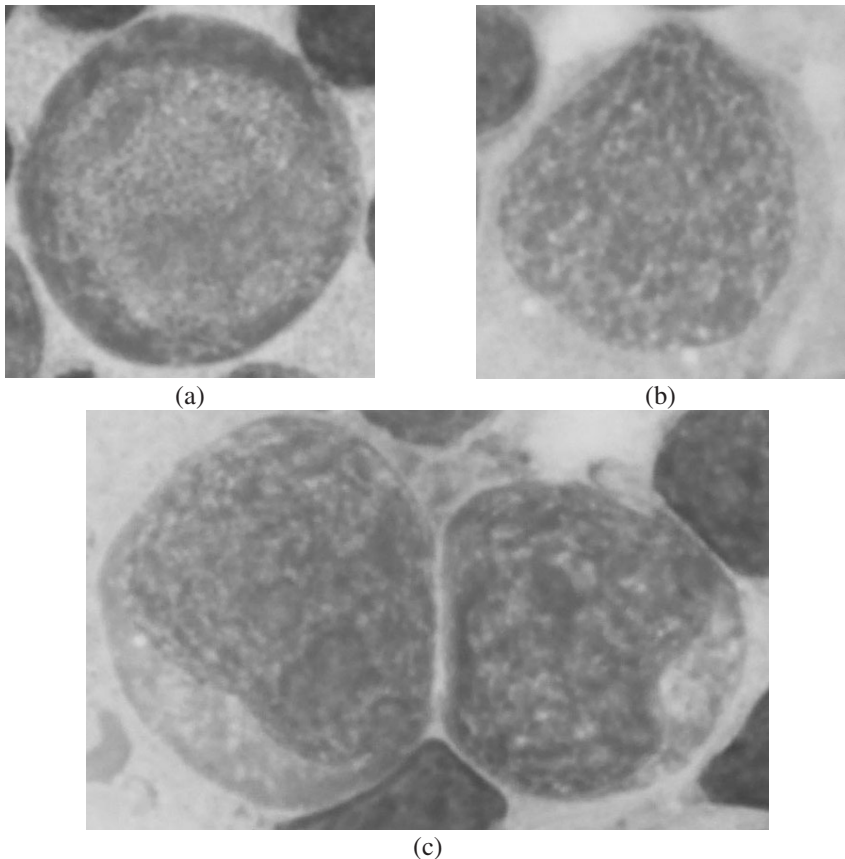


**Fig. 2.** Grayscale images of sarcoma cells of lymphatic nodes: filamentous structure of chromatin (a); granular (b); fibrous (c)

heterogeneity, clumpiness, margination, and radius of particles [12] (the Mayall/Young features), invariant features (polynomial invariants).

The main disadvantage of known textural methods [9] is their sensitivity parameters and conditions of image acquisition, to properties of researched preparations, and also to precision of microscope focusing.

Below, we consider a method for analysis of cell nucleus images that was used for searching for a diagnostic criterion. The proposed method combines features of both approaches: on the one hand the intensity features of the chromatin particles are analyzed, and on the other hand, the diagnostic criterion is formulated in terms of the simple quantitative characteristics, describing the chromatin structure of cell nuclei – the amount of intensity extrema in the families of blurred cell nuclei images. This feature is related to the amount of chromatin particles and characterizes the state of malignancy.

### 3 Method for Analysis of Nuclei Images

Among contemporary approaches to image analysis the approach of Gaussian scale space entirely meets the listed above requirements [1,3,4]. The scale space technique provides properties of invariance with respect to shift, rotation, scaling, and linear transformations of intensity. It decreases the sensitivity of the analysis to microscope focusing. The concept of the scale space gives the natural way to represent an input image  $L(x)$  ( $L(x)$  is the intensity function of spatial coordinates) at finite resolution by convolving it with a Gaussian kernel  $G(x,t)$  of various widths, thus obtaining a smoothed image at a scale determined by the width  $\sigma = \sqrt{2t}$  ( $t$  – is a scale parameter).  $L(x,t)$  satisfies the heat equation. The heat equation generates a family of blurred images [3]. As  $t$  increasing the blur effect grows, and fine details of the image are lost. The properties of constructed scale space reflect properties of the initial image. Scale space properties are explored by using localization of its critical points.

The proposed method for cytological specimen analysis consists in construction of a family of blurred images (scale space) for various  $t$  and selection of diagnostic criterion using localization of scale space critical points. Critical points reflect the internal structure of the objects in the image, and exploration of the entire family of derived images allows one to analyze both fine details and large structural elements.

#### 3.1 Main Objectives of the Proposed Method

Taking into account the concept of scale space approach, the following problems should be solved during cell image analysis and selection of diagnostic criterion: (a) construction of the one-parameter family of derived images  $L(x;t)$  (a scale space) from initial image  $L(x)$  for different diseases; (b) extraction of critical points in scale space images; (c) analysis of spatial critical points distribution for different groups of patients for diagnostic criterion selection; (d) calculation of diagnostic criterion values.

#### 3.2 Construction of a Family of Blurred Images

For construction of a family of blurred images, it is necessary to determine the range and the step of scale parameter  $t$ . The computational experiments have shown that the analysis of critical points in image family is expedient for the values of scale parame-

ter in the range of  $8 \leq t \leq 60$ . The step value of a scale parameter should be taken in the range of  $0.005 \leq \Delta t \leq 0.032$ . As a result, the families of blurred images corresponding to the scale spaces of malignant and non-malignant cell nuclei images were constructed.

### 3.3 Localization of Spatial Critical Points

According to the scale space approach, the derived families of images were explored for detection of critical points.

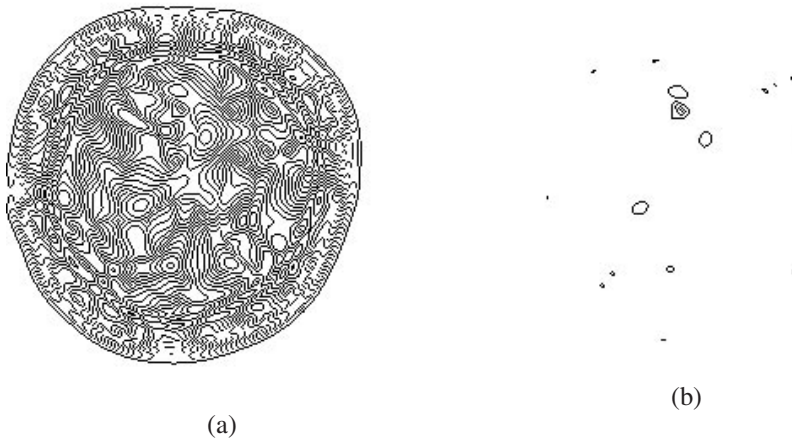


**Fig. 3.** Spatial gradients ( $L_{x_1}(x;t)$  OR  $L_{x_2}(x;t)$ ) at  $t = 32$  (a) and extracted closed curves around extrema in a single scale-space image (b) (negative images)

For localization of critical points within proposed method, the topological properties of iso-intensity manifolds in the neighborhoods of critical points [1] are used. The algorithm for selection of closed loops (curves of a nonzero gradient values, bounding iso-intensity curves around points of extremum) is applied. A special procedure that includes the standard image processing operations was developed. It consists in the following steps:

1. The following operations are carried out for each image in the family: (a) logical summation of images  $L_{x_1}(x;t)$  and  $L_{x_2}(x;t)$ ; (b) thresholding of the resulting image; (c) removing of the “rubbish”; (d) overlaying of a nucleus mask to restrict the area of interest and remove the residual noise at the peripheries of a nucleus.
2. All scale space images processed at Step 1 are overlaid (logical OR).
3. The morphological operations are applied in order to fill regions bounded by closed curves of nonzero gradient and to remove residual rubbish.
4. The coordinates of the geometrical centers of the filled regions (the neighborhoods of extrema) are found.
5. The total amount of the centers of the filled regions is calculated.

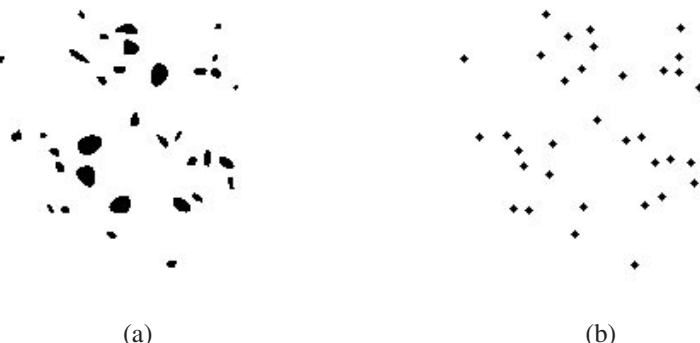


**Fig. 4.** Neighborhoods of scale space spatial extrema (a), centers of extrema neighborhoods (b)

In Figs. 3, 4, the steps of extrema localization are illustrated. In Fig. 3 (a), the logical “OR” of spatial gradient images at  $t=32$  is presented. In Fig. 3 (b), one can see the extracted closed curves around extrema at  $t=32$ . In Fig. 4 (a), the neighborhoods of extrema for the whole family of scale space images are filled with black and, in Fig. 4 (b), the centers of colored areas are presented.

### 3.4 Selection of Diagnostic Criterion

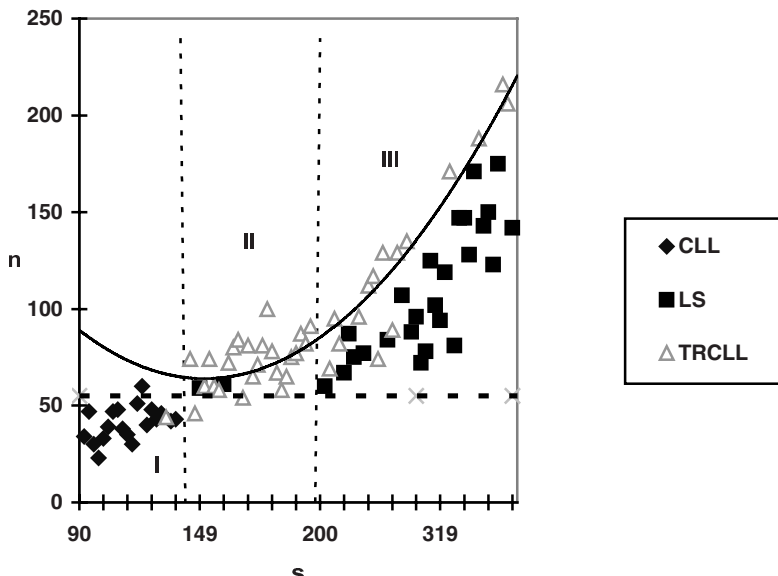
The developed procedure was applied to the analysis of scale spaces, generated by images of lymphatic node specimens for diagnoses of malignant (primary B-cell lymphosarcoma and transformation of chronic B-cell lymphocytic leukemia) and non-malignant (chronic B-cell lymphocytic leukemia) tumours. 86 images of cell nuclei from 25 patients were analyzed. Families of blurred images for scale parameter in the range of  $12.5 \leq t \leq 50$  were generated and explored. In Table 1 the statistical characteristics of amount of spatial extrema for various diagnoses are given.

Using the results of experiments, the chart displaying the characteristics of cell nuclei images, such as total amount of spatial extrema  $n$  and the area of a nucleus  $s$ , was created (see Fig. 4). The chart area (see Fig. 4) includes three significant parts: (I) the area, located to the left of value  $s = 137$  and below  $n = 60$ ; (II) the area, where  $137 < s < 200$  and  $n > 60$ ; (III) the area to the right of value  $s = 200$ .

The first area mainly contains the points corresponding to the diagnose of chronic lymphocytic leukemia (CLL). In the second area, the transformation of chronic lymphocytic leukemia (TRCLL) is dominating. The third area contains transformation of chronic lymphocytic leukemia as well as lymphosarcoma (LS). For classification of cell nuclei located in area (III), it is possible to construct a separating functions. The spread of points in Fig. 4 in the region (III) is caused by the different types of structure and pattern of chromatin of the malignant cell nuclei (see Fig. 2). Therefore, the more accurate classification requires analysis of critical points for different types of chromatin structure.

**Table 1.** Range of spatial extrema total amount for specimen images corresponding to various diagnoses

Diagnose	Min	Max
Chronic lymphocytic leukemia	23	60
Transformation of chronic lymphocytic leukemia	44	216
Lymphosarcoma	59	175
Transformation of chronic lymphocytic leukemia and lymphosarcoma	44	216

**Fig. 5.** Distribution of cell nuclei in coordinates “nucleus area”, “amount of extrema” (s,n)”

The results presented in Fig. 4 and in Table 1 allow us to conclude that the total amount of spatial extrema in cell nuclei images may be used as a diagnostic criterion. A special technique for calculation of the diagnostic criterion value is developed and implemented in the “Black Square” software system [2].

#### 4 Conclusions and Directions of Further Research

We considered a possibility of developing a new criterion for diagnostics of hematopoietic tumors from the images of cell nuclei of lymphatic nodes. The results are as follows.

1. The method for analysis of the images of lymphatic node specimens is developed.
2. A diagnostically important criterion is obtained; it is defined as a total amount of spatial extrema in scale space generated by the image of a cell nucleus.

3. The technique for calculating the diagnostic criterion value is developed and integrated in the “Black Square” [2] system library.

The further research will be aimed at (a) increasing the precision of critical points localization, (b) selecting of diagnostic criteria based on the analysis of all types of critical points, and their evolution at the increasing scale parameter; (c) augmenting the sample of cell images. At the final stage of research, the decision rules for making diagnostic decisions will be formulated.

**Acknowledgements.** We are grateful to Prof. I.A. Vorob’ev, Dr. D.V. Kharazishvili, and their colleagues in the Hematological Center of the Russian Academy of Medical Sciences for providing a material for this work and for their professional advices.

## References

1. Florack, L.M.J., Kuijper, A.: The topological structure of scale-space images. *Journal of Mathematical Imaging and Vision*, Vol. 12, N1 (2000) 65–80
2. Gurevich, I.B., Khilkov, A.V., Murashov, D.M., Smetanin, Yu.G., Zhuravlev, Yu.I.: Black Square Version 1.0: Programm Development System for Automation of Scientific Research and Education. *Pattern Recognition and Image Analysis: Advances in Mathematical Theory and Applications*, Vol. 9, N4 (1999) 609–634
3. Koenderink, J.J.: The structure of images. *Biol. Cybern.*, Vol.50. (1984) 363–370
4. Lindeberg, T.: Scale-space Theory in Computer Vision. *The Kluwer International Series in Engineering and Computer Science*. Kluwer Academic Publishers (1994)
5. Vorob’ev A.I., ed. *Atlas “Tumors of lymphatic system”*, Hematological Scientific Center of the Russian Academy of Medical Sciences (2001)
6. Vorob’ev A.I., Vorob’ev I.A., Kharazishvili D.V., et.al. Recognition of lymphatic tumours of a mediastinum. *Problems of a tuberculosis*, 2 (2001) 21–25
7. Kharazishvili D.V., “Morphometrical analysis of intracellular neoplasms of lymphatic system”, Hematological Scientific Center of the Russian Academy of Medical Sciences, Ph.D. thesis, (2001)
8. Weyn B., Van de Wouwer G., Koprowski M., Van Daele A., Dhaene K., Scheunders P., Jacob W., and Van marck E. Value of morphometry, texture analysis, densitometry and histometry in the differential diagnosis and prognosis of malignant mesothelioma, *Journal of Pathology*, 189 (1999) 581–589
9. K. Rodenacker, and E. Bengtsen. A feature set for cytometry on digitized microscopic images. *Anal Cell Pathol*, 25(1) (2003)1–36
10. K. Rodenacker. Applications of topology for evaluating pictorial structures. In Reinhard Klette and Walter G. Kropatsch, editors, *Theoretical Foundations of Computer Vision*, Akademie-Verlag, Berlin, (1993) 35–46
11. Rodenacker. Quantitative microscope image analysis for improved diagnosis and prognosis of tumours in pathology. In Creaso Info Medical Imaging, Vol. 22 (1995)
12. I.T. Young, P. Verbeek and B.H. Mayall, Characterization of chromatin distribution in cell nuclei, *Cytometry* 7(5) (1986) 467–474

# Segmentation and Morphometry of Histological Sections Using Deformable Models: A New Tool for Evaluating Testicular Histopathology

Miguel A. Guevara<sup>1</sup>, Augusto Silva<sup>2</sup>, Helena Oliveira<sup>3</sup>, Maria de Lourdes Pereira<sup>3</sup>, and Fernando Morgado<sup>3</sup>

<sup>1</sup> Computer Sciences Faculty, University of Ciego de Avila, Ciego de Avila 69450, Cuba  
[mguevara1@yahoo.com](mailto:mguevara1@yahoo.com)

<sup>2</sup> IEETA, University of Aveiro, 3810 -193 Aveiro, Portugal  
[asilva@ieeta.pt](mailto:asilva@ieeta.pt)

<sup>3</sup> Biology Department, University of Aveiro, 3810 – Aveiro, Portugal  
[{holiveira, lpereira, fmorgado}@bio.ua.pt](mailto:{holiveira, lpereira, fmorgado}@bio.ua.pt)

**Abstract.** This paper presents a tool that uses image segmentation and morphometric methods to evaluate testicular toxicity through the analysis of histological sections of mice testis. The tool is based on deformable models (Snakes) and includes several adaptations to solve important difficulties of histological sections imaging, mainly the low contrast edges between the boundary tissue of seminiferous tubules and the interstitial tissue. The method is designed to produce accurate segmentation and to keep track of tubular identities on images under study. The extracted data can be used straightforwardly to compute quantitative parameters characterizing tubular morphology. The method was validated on a realistic data set and the results were compared with those obtained with traditional techniques. The application of this new technique facilitates measurements allowing assessing a higher number of tubules in a fastest and accurate way.

## 1 Introduction

Histopathology is considered the most sensitive endpoint for evaluating testicular toxicology. One of histopathological signs of testicular toxicology is tubular contraction or dilation. Tubular contraction occurs as a result of reduction of fluid secretion and consequently reduction in the overall diameter of the seminiferous tubule. Chlordane is one of the substances that induce a reduction in the diameter of seminiferous tubules [1]. Tubular dilation, with the dilation of tubular lumen may also occur as a result of the increase of the fluid volume in the lumen, or as a consequence of obstruction of fluid flow. For example carbendazim causes obstruction of the ductular system that result in a severe and diffuse dilation of the seminiferous tubules [2]. The dilation of the tubular lumen may be a diffuse change and may not be obvious by microscopic observation [3], so quantitative analysis measuring tubule diameters or tubule area may be a sensitive way to detect tubule dilation.

In this paper, we present a new technique, motivated by the desire to study histological testicular sections for evaluating testicular toxicology. Our method is

based on deformable models (snakes) and includes several adaptations to solve important difficulties posed by histological section imaging, mainly the low contrast edges between the boundary tissue of seminiferous tubules and the interstitial tissue. First a median filter and morphological operations are applied to enhance the image contrast and differentiation of objects (seminiferous tubules) from background. Second a local edge detector is applied to obtain an approximation to objects contours. Segmentation is completed using an adapted variant of a gradient vector flow (GVF) model [4], [5]. A smoothed instance of the final contour is then obtained through spline approximation based on the detected edge points. Morphometric parameters such as area, diameter and others are then easily computed. Our method was validated on a realistic data set and the results compared with those obtained with traditional techniques.

In section 2, we describe preprocessing steps designed to enhance the detection of seminiferous tubules, where we introduce a new local edge detector based on the use of local average of differences between pixels and the median of neighborhood pixels. Section 3 recalls the original snake model [6], as well as a useful and popular extension, the GVF model [4], [5], and discusses their applicability to our data. Computation of features and measurements such as diameters and area are described in section 4. In section 5, we show results of our method and briefly present an algorithm prototype to study tubular testicular sections. Section 6 concludes with a short summary of our work.

## 2 Preprocessing

In this study male mice were used. After sacrifice, the left testes were removed for histological studies. Small pieces of testis tissue were fixed in Bouin's fluid, dehydrated and embedded in paraffin wax. Transverse tissue sections with 5 microns thick were made in a microtome (Leitz model 1512) and stained with haematoxylin and eosin (H&E). Images were acquired with the Leica IM 100 Image Manager software. The hardware used to capture the images was composed by a Leica DC 200 camera attached to a Leitz Laborlux K microscope. However, our prototype accepts as input any true color image in jpg or bmp format. The difficulty in detecting tubular testicular sections stems for the fact that they can not be distinguished only based on their gray level or gradient values, or using a simple combination of smoothing and edge detector filters. To address these problems we attempted with a combination of noise suppression filter like average and median filter, with different mask sizes and histogram thresholding, followed by binarization and edge tracking [7]. Experiments were also carried out with edge maps detectors [8]. However, these methods fail frequently where tubular sections are out the focal plane or due to background contamination. We propose a new approach that is a combination of median filtering, morphological processing and a new developed edge detector to produce an edge map to be processed by the GVF Snake [4], [5].

## 2.1 Initial Image Preparation

The presence of noise in images represents an irrecoverable loss of information. The median type filters are widely used for noise suppression in early stages of a vision system [9], due to the following properties:

- They preserve the ramp edges and boundaries of the objects,
- They suppress impulses of short duration without significantly modifying others components, and,
- They may be implemented easily and fast.

The steps followed in the initial image preparation were: convert the input image I (a true color image) first to a 256 gray level image and then build the median image M , applying the median filter with a mask of size  $5 \times 5$ .

## 2.2 Morphological Operations

Mathematical morphology is a novel geometry-based technique for image processing and analysis, originally developed to process binary images, based on the use of simple concepts from set theory and geometry such as set inclusion, intersection, union, complementation, and translation [10]. This resulted in a collection of tools, called morphological operators, which are eminently suited for the analysis of shape and structure in binary images [11]. The most well-known of these operators are erosion and dilation. Soon mathematical morphology was extended to grey-scale images. To extend binary morphology to grey-scale images different approaches have been proposed. Our work relied on the threshold set approach, in which a grey-scale image is decomposed in terms of its threshold (or level) sets. To each of these sets one can apply a binary operator, after which the resulting sets can be used to synthesize a transformed gray scale image [11].

A morphological operator when applied to a binary image may be regarded as a binary convolution where the convolution kernel is usually defined within a small mask. This kernel is better known as the operator structuring element, and its size and shape determines the outcome of the operation. Morphological operations apply structuring elements to an input image, creating an output image of the same size. Therefore the choice of size and shape of the structuring element be a major design issue in our image preprocessing strategy.

**Image Enhancement.** Images under study contain many seminiferous tubules of different sizes that may be touching each other. Due to this, to increase the potential for future object discrimination we use a suitable combination of the top-hat and bottom-hat operations. The top-hat transform is defined as the difference between the original image and its opening. The opening of an image is the collection of foreground parts of an image that fits a particular structuring element. The bottom-hat transform is defined as the difference between the closing of the original image and the original image. The closing of an image is the collection of background parts of an image that fit a particular structuring element. We evaluated structuring elements of different shapes and sizes, obtaining the best results with the octagonal structuring element. A flat octagonal structuring element was created computing the radius of the minimum horizontal diameter in the smallest seminiferous tubule of the image under study. Figure 1b show results obtained after to enhance image.

The mathematical formulation used to enhance  $M$  was:

$$E = A - B \text{ where } E \text{ is the enhanced image}$$

$$A = M + T$$

$$B = \varphi(M) - M \text{ bottom-hat of } M$$

$$\varphi(M) = M \bullet K = [(M \oplus K) \diamond K] \text{ close } M \text{ with the structuring element } K$$

$$T = M - \gamma(M) \text{ top-hat of } M$$

$$\gamma(M) = M \circ K = [(M \ominus K) \oplus K] \text{ open } M \text{ with the structuring element } K$$

$M$  Median image

$K$  Structuring element

$\ominus$  erode operator

$\oplus$  dilate operator

**Objects Differentiation.** The image complement in combination with the flood-fill were the operations used for object (seminiferous tubules) differentiation (Fig. 1c). Image complement consists in subtracting each image pixel value from the maximum gray level pixel value supported by the image (in our case 255). Image flood-fill fills holes in the input image. A hole is a set of background pixels that cannot be reached by filling in the background from the edge of the image, in our case, a hole is an area of dark pixels surrounded by lighter pixels.

The mathematical formulation to achieve objects differentiation (image  $X$ ) was the following:

$$X = [ff(K^C)]^F \text{ where } ff \text{ is the flood - fill operation}$$

$$K^C \text{ image complement of } K ; \quad K = E - E^C \text{ where } E \text{ is the enhanced image} .$$

### 2.3 Edge Detection

Edge detection is a critical step, since edge information is major driving factor in subsequent “snake” performance. As we mentioned before in the initial part of this section different techniques were tested such as a combination of noise suppression by average and median filtering, with different masks and histogram thresholding, followed by binarization and edge tracking [7]. We also tried with edge maps detectors [8], but these methods fail frequently where tubular sections are out the focal plane or due to background contamination. However we found that applying a local median average to images has achieved a more suitable answer to distinguish boundary pixels between objects and background pixels. With a  $3 \times 3$  mask size this new filter is a powerful edge detector, which produces a fine edge map contour (Fig. 1d).

The mathematical formulation of our edge detector is the following:

$X$  input image

$\omega$   $N \times N$  windows center on pixel  $(i_0, j_0)$

$$M = \frac{N-1}{2}$$

$\varpi$  median of  $\omega$

$E_{map}$  ouput image

$$E_{map}(i, j) = \frac{1}{(2M+1)^2} \sum_{(k,l) \in [-M,M]} |X(i_0+k, j_0+l) - \varpi|$$

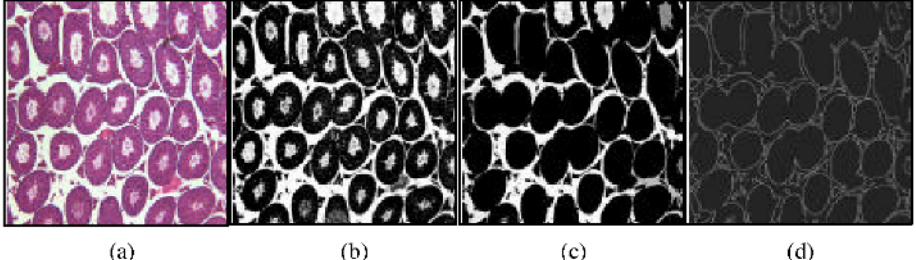


**Fig. 1.** (a) Original image. (b) Enhanced image. (c) Tubules differentiation. (d) Local median average.

### 3 Deformable Models

Mathematical foundations of deformable models represent the confluence of geometry, physics, and approximation theory. Geometry is used to represent object shape, physics inflict constraints on how the shape may vary over space and time, and optimal approximation theory make available the formal underpinnings of mechanisms for fitting the models to measured data. Deformable curve, surface, and solid models gained popularity after they were proposed by Terzopoulos for use in computer vision [12] and computer graphics [13] in the mid 1980's. Terzopoulos introduced the theory of continuous (multidimensional) deformable models in a Lagrangian dynamics setting, based on deformation energies in the form of (controlled continuity) generalized splines. The deformable model that has attracted the most attention to date is popularly known as "snakes" [6]. Snakes are planar deformable contours that are useful in several image analysis tasks. They are often used to approximate the locations and shapes of object boundaries in images based on the reasonable assumption that boundaries are piecewise continuous or smooth.

One of the more successful implementation of parametric active contours is the gradient vector flow (GVF) field approach proposed by Xu and Prince [4], [5]. The active contour that uses the GVF field as its external force is called a GVF snake. The GVF field points toward the object boundaries when is very near to the boundary, but varies smoothly over homogeneous image regions, extending to image border. The main advantages of the GVF field over the original snake model are that it can capture a snake from a long range – from either side of the object boundary – and can force it into concave regions. However, although the GVF model was proven to be superior capturing a snake from a long range from either side of the object boundary, it did not solve the difficulties posed by background contamination and the lost of contrast between seminiferous tubules edges. Therefore, our work was focused to develop a specific approach to enhance contrasts and to improve the edge map of images under study. These processes were described in details in the preprocessing section. We use

the GVF snake model [4], [5] to complete the segmentation process, which can be summarized as follows: for each edge map ( $E_{map}$ ) we computed the GVF field (Fig. 2a). Then in a semiautomatic way are defined polygons. This procedure is carrying out first selecting manually a few edge points from seminiferous tubules. After initial snakes (Fig. 2a) are produced through spline approximation based on the selected polygons. Finally the GVF snake deformation is performed for producing an array of edge point  $\varsigma$  (final snakes) with a more accurate segmentation results (Fig. 2b). We used the following parameters values in the snake deformation process: elasticity (0.05), rigidity (0.0), viscosity (1), external force weight (0.6) and pressure force weight (0).

## 4 Features

Morphometric features express the overall size and shape of objects. For these features only the object mask  $O$  and its border  $\varsigma$  are needed, not the actual gray scale image [14]. In our case the shape and size were decisive to discriminate seminiferous tubules, allowing to analysis their dilation and contraction on images under study. Traditional methods only take in consideration the smallest horizontal diameter to differentiate tubules. Our proposal introduces the computation of minimum and maximum diameters and area. We use as input the final snake deformation  $\varsigma$  (see section 3), which (as was described before) is the array of edge points of seminiferous tubules detected.

Mathematical formulation and computational sequence of measurements is the following:

$O$  object pixels (seminiferous tubule)

$\varsigma \subset O$  set of edge pixels, contour of  $O$  (final snake deformation points)

$P_\varsigma \in \varsigma$  edge point

$A = |O|$  area = number of elements of  $O$

$$ci = \frac{1}{A} \sum_{(i,j) \in p \in O} i \quad i\text{-coordinate of centroid}$$

$$cj = \frac{1}{A} \sum_{(i,j) \in p \in O} j \quad j\text{-coordinate of centroid}$$

$C$  centroid point with coordinates  $(ci, cj)$

$d(p1, p2)$  = euclidian distance between  $p1$  and  $p2$

$rad = \min(d(C, P_\varsigma))$  minimum radius

$P_{\varsigma\_diam}(0) = P_\varsigma$  with  $rad \cap P_\varsigma \neq \emptyset$  initial minimum diameter point

$RAD = \max(d(C, P_\varsigma))$  maximum radius

$P_{\varsigma\_DIAM}(0) = P_\varsigma$  with  $RAD \cap P_\varsigma \neq \emptyset$  initial maximum diameter point

$$P_{diam} = P_{\varsigma\_diam}(0) + 2 * rad$$

$$P_{\varsigma\_diam}(1) = P_{\varsigma} \longrightarrow \min(d(P_{diam}, P_{\varsigma})) \text{ final minimum diameter point}$$

$$diam = d(P_{\varsigma\_diam}(1), P_{\varsigma\_diam}(0)) \text{ minimum diameter}$$

$$P_{DIAM} = P_{\varsigma\_RAD}(0) + 2 * RAD$$

$$P_{\varsigma\_DIAM}(1) = P_{\varsigma} \longrightarrow \min(d(P_{DIAM}, P_{\varsigma})) \text{ final maximum diameter point}$$

$$DIAM = d(P_{\varsigma\_DIAM}(1), P_{\varsigma\_DIAM}(0)) \text{ maximum diameter}$$

Finally calculations include an average of area, minimum and maximum diameters of the seminiferous tubules set processed on the image under study (see figure 2c).

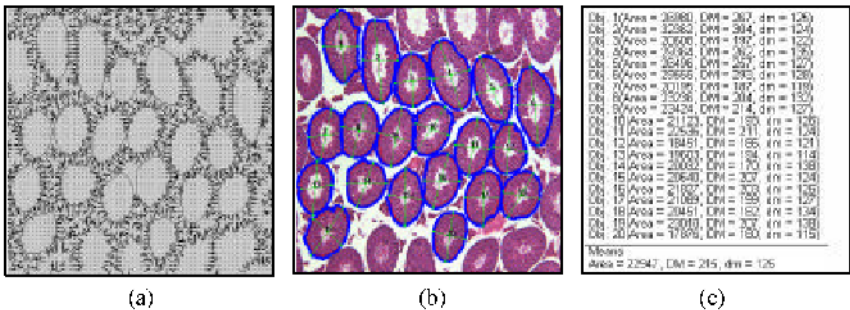


**Fig. 2.** (a) GVF and initial snakes (b) Final snake deformation. (c) Micron's measures of each object (seminiferous tubules): area, maximum diameter (DM) and minimum diameter (dm), and the averages of area, maximum diameter and minimum diameter.

## 5 Results

The practical implementation of our technique for evaluating testicular toxicity in histological sections images can be summarized as follows: for each image, we first construct the edge map ( $E_{map}$ ), based on procedures described in section 2. Then the GVF field is computed. After in a semiautomatic way polygons are defined base on manual selection of few edge points from seminiferous tubules. The initial snakes then are produced (Fig. 2a) through spline approximation based on the selected polygons. Finally, snake deformation is performed to produce an array of edge point  $\varsigma$  (final snakes) with more precise segmentation results (Fig. 2b).

The traditional method for measuring seminiferous tubule diameter is based on measurement of the minimum diameter. However, it is difficult, if not impossible, for the human eye to distinguish which is the minimum diameter, so an approximation must be made. This approximation may lead to a lost of accuracy, mainly in the toxicology studies, because if we can not be sure that we are measuring the same feature it's difficult to compare between different treatments. Our new method allows numerating the tubules measured and provides a range of parameters related to the tubule (e.g. area, minimum and maximum diameter). By the end, we know exactly

which tubules were measured and the characteristics of each one. By other hand, applying the traditional method, we cannot mark the tubules that are being measured, so the same tubule can be measured twice, and we can not be absolutely sure that the measurement is being made by the minimum diameter.

## 6 Conclusions

We presented a semiautomatic method to segment and to measure histological testicular sections, which in a first step is the result of a correct combination of statistical and morphological operations. Hereafter based on the detected edges the segmentation process is completed using a parametric deformable model. Our technique allows a suitable segmentation of seminiferous tubules in histological section. The ability of our method was demonstrated on an experimental representative data set. This approach will be successful to study quantitatively histological sections of different specimens and can be extended easily to other fields of study such as cell counting and somatic embryos classification among others. Compared with traditional methods, our method computes two new measures: the maximum diameter and the area, and it facilitate measurements, assessing a higher number of tubules in a fastest and reproducible way and minimizing the typical errors.

**Acknowledgment.** The authors wish to thank to Research Institute of University of Aveiro Project CTS 2002/22 for financial support.

## References

1. Al-Omar M.A., Abbas A.K., Al-Obaidy S.A.: Combined Effect of Exposure to Lead and Chlordane on the Testicular Tissues of Swiss Mice. *Toxicology Letters* 115(1) (2000) 1–8.
2. Hess R.A. and Nakai M.: Histopathology of the male reproductive system induced by the fungicide benomyl. *Histology and Histopathology* 15: (2000) 207–2024.
3. Creasy D.M.: Pathogenesis of male reproductive toxicity. *Toxicologic Pathology* 29: (2001) 64–76
4. Xu, C. and Prince, J.L.: Gradient Vector Flow. A New External Force for Snakes. *Proc. IEEE Conf. on Comp. Vis. Patt. Recog. (CVPR)*, Los Alamitos: Comp. Soc. Press. (1997) 66–71.
5. Xu, C. and Prince, J.L.: Snakes, shapes, and gradient vector flow. *IEEE Trans. Image Processing*, Vol. 7 (1998) 359–369.
6. Kass, M., Witkin, A. and Terzopoulos, D.: Snakes: Active contour models. *International Journal of Computer Vision* 1(4) (1988) 321–331.
7. Guevara, M. A., Rodríguez R.: Knowledge-based vision techniques to classify sugarcane somatic embryos. *Proceedings 13<sup>th</sup> ISPE/IEEE International Conference on CAD/CAM, Robotic and Factories of the Future (CARS & FOF'97)*. (1997) 388–396.
8. Canny J.F.: A computational approach to edge detection. *IEEE Trans. Pattern Anal. Machine Intell.* Vol. PAMI-8, (1986) 679–678.
9. Zheng, J., Valavanis, K., and Gauch.: Noise removal from color images, *Journal of Intelligent and Robotic Systems*, Kluwer Academic Publisher 7: (1993) 257–285.
10. Serra, J.: *Image Analysis and Mathematical Morphology*. Academic Press, London (1982).
11. Soille, P. *Morphological Image Analysis*. Springer-Verlag, Berlin (1999).

12. Terzopoulos, D., Witkin, A. and Kass, M.: Constraints on deformable models: Recovering 3D shape and nonrigid motion. *Artificial Intelligence* 36(1): (1988) 91–123.
13. Terzopoulos, D. and Fleischer, K.: Deformable models. *The Visual Computer* 4(6): (1988) 306–331.
14. Rodenacker K., Bengtsson E.: A feature set for cytometry on digitized microscopic images. *Analytical Cellular Pathology* IOS Press, Vol. 25 (2003). 1–36.

# Robust Markers for Blood Vessels Segmentation: A New Algorithm

Roberto Rodríguez, Teresa E. Alarcón, and Oriana Pacheco

Institute of Cybernetics, Mathematics and Physics (ICIMAF)  
Digital Signal Processing Group  
Calle 15 No. 551 e/ C y D CP 10400, La Habana, CUBA  
[rrm@icmf.inf.cu](mailto:rrm@icmf.inf.cu), [tere@icmf.inf.cu](mailto:tere@icmf.inf.cu)

**Abstract.** In this paper, we present a new algorithm to obtain robust markers for blood vessels segmentation in malignant tumors. We propose a two-stage segmentation strategy which involves: 1) extracting an approximate region containing blood vessels and part of the background, and 2) segmenting blood vessels from the background within this region. The approach was effectively very useful in blood vessels segmentation and its validity was tested by using the watershed method. The proposed segmentation technique is tested on manual segmentation. It is demonstrated by extensive experimentation, by using real images, that the proposed strategy was suitable for our application.

## 1 Introduction

Information contained within sampled medical image data sets is essential to several clinical tasks. Advances in technology allowed clinician not only the visualization, but also the identification of different objects. A major hurdle in the effective use of this technology is the image segmentation, where pixels are grouped into regions based in image features [1].

In the study of the angiogenesis process, the pathologists analyse all information related with blood vessels by using a microscope [2–4]. This work is very tedious and time consuming and obviously, the automation of this analysis is highly desirable. In such a sense, an useful task for digital images processing should be the segmentation of blood vessels.

Segmentation and contour extraction are key points of image analysis. Many segmentation methods have been proposed for medical image data [5–7]. Unfortunately, segmentation using traditional low level image processing techniques, such as thresholding, gradient, and other classical operations, requires a considerable amount of interactive guidance in order to get satisfactory results. Automating these model free approaches is difficult because of shape complexity, shadows, and variability within and across individual objects. Furthermore, noise and other image artifacts can cause incorrect regions or boundary discontinuities in objects recovered from these methods.

The watersheds is a powerful segmentation tool developed in mathematical morphology [8, 9]. However, the correct way to use watersheds for grayscale image segmentation consists in first detecting markers of the objects to be extracted. The design of robust marker detection techniques involves the use of knowledge specific of images under study. Not only object markers, but also background markers need to be extracted.

The goal of this paper is to present a new algorithm to obtain robust markers for blood vessels segmentation in malignant tumors. The validity of our strategy was tested by using the watersheds method, where, according to criterion of physicians, blood vessels were contoured well.

This paper is organized as follows: In Section II is outlined the theoretical aspects. In section III, we give the features of the studied images. In section IV, we present the steps to obtain markers, we also discuss an algorithm. Finally, we describe our conclusions in Section V.

## 2 Theoretical Aspects

This section presents the most important theoretical aspects.

### 2.1 Pre-processing

With the goal of diminishing the noise in the original images we used the Gauss filter, where we carried out the process of Gaussian smoothing with  $\sigma = 3$  and a 3x3 window size. We carried out also the morphological opening. In this work, we used a structuring element type rhombus of 3x3 size.

### 2.2 Watershed Segmentation

Let us consider a two-dimensional grayscale picture  $F$  whose definition domain is denoted  $D_F \subset \mathbb{Z}^2$ .  $F$  is supposed to take discrete (gray) values in a given range  $[0, L]$ ,  $L$  being an arbitrary positive integer. In the following, we consider grayscale images as numerical functions or as topographic relief.

**Definition 1** (Regional Minimum).

A regional minimum  $M$  at altitude  $h$  of grayscale image  $F$  is a connected component  $C$  of  $T_h(F)$  such that  $C \cap T_{h-1}(F) = \emptyset$ ,  $T_h(F)$  being a threshold of  $F$  at level  $h$ .

**Definition 2** (Watershed by Immersion).

We can figure that we have pierced holes in each regional minimum of  $F$ , this picture being regarded as a topographic surface. We then slowly immerse this surface into a lake. Starting from the minimum of lowest altitude, the water will progressively fill up the different catchment basins of  $F$ . Now, at each pixel where the water coming from two different minimum would merge, we build a dam (see Fig. 1). At the end of this immersion procedure, each minimum is completely surrounded by dams, which delimit its associated catchment basin. The whole set of dams which has been built thus provides a tessellation of  $F$  in its different catchment basins. These dams correspond to the watershed of  $F$ , that is, these represent the edges of objects.

## 3 Features of the Studied Images

The studied images were of arteries, which had atherosclerotic lesions and these were obtained from different parts of the human body, from more than 80 autopsies. In Figure 2 can be seen typical image, which were captured via MADIP system with a resolution of 512x512x8 bit/pixels [10].

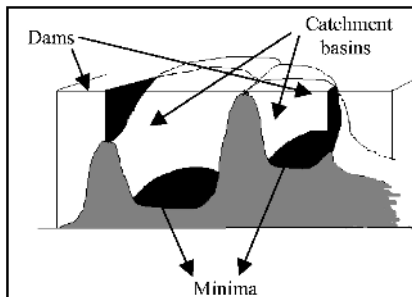


**Fig. 1.** Building dams at the places where the water coming from two different minimum would merge.

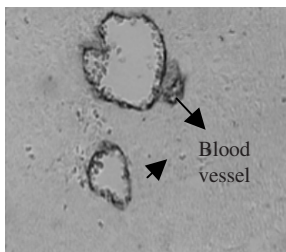


**Fig. 2.** These images represent the angiogenesis process. Blood vessels are marked with arrows.

There are several notable characteristics of this image, which are common to typical images that we encounter in the tissues of biopsies:

1. High local variation of intensity is observed both, within blood vessels (BV) and the background. However, the local variation of intensities is higher within BV than in background regions.
2. It is common of these images the diversity in shape and size of BV.

## 4 Experimental Results: Discussion

### 4.1 Obtaining the Region of Interest

The next stage of the strategy is to segment the approximate region, that is, a region which contains the blood vessel and its neighboring background. The exact shape and size of this region are not important, and hence the region is referred to as an approximate region. A measure of local variation of intensity is provided by the variance of the gray level intensity. The result of applying this procedure is shown in Figure 3.

Figure 3 shows that the high variance corresponds to blood vessels while that the low variance belongs to background. We verified in what we did that for large window sizes the results were poor. On the one hand, it was obtained a higher homogeneity of the region, and on the other hand blood vessels were notably fattened.

We obtained the region of interest by applying a global threshold to the local variation of intensity. Figure 4 shows the obtained result of this segmentation process.

Then, we introduced the following algorithm to obtain robust markers for blood vessels segmentation in malignant tumors.



**Fig. 3.** Obtaining a region of interest. The variance map was obtained with 5x5 window size.

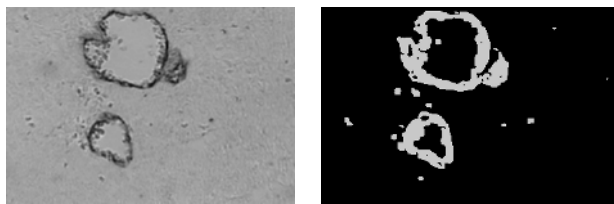


**Fig. 4.** (a) Original image. (b) Regions of interest.

## 4.2 Algorithm to Obtain Robust Markers

The steps of the algorithm are described below.

1. Obtain the regions of interest. Let IREZI be the resulting image.
2. Label the resulting image of the step 1. Then, to create an auxiliary image, let IA1 be. All pixels of this image are put in zero. Scan IREZI at iterative way, then in this image all the background is labeled with value equal to 1.
3. With the goal of finding connected components (BV), scan IREZI again from the top to the bottom and from the left to the right. If there is a pixel, which belongs to a connected component and in IA1 this pixel has value zero, then other iterative method begins to work. This new iterative method marks with a determined value within IA1 all pixels belonging to a connected component. In addition, pixels within IREZI are marked also with a value, which identifies the connected component to which they belong. This action is carried out in the whole image. As this step is finished, in the IREZI image all the connected components were filled and in IA1 all the connected components were labeled.
4. Create other auxiliary image (let IA2 be) with the same values of the IA1 image. Create also an array, which controls if a connected component was reduced. In the IA2 image is where in each step the reduction of the connected components are obtained, the final result in the IA1 image is represented.
5. Scan the labeled image (IA1). When a pixel is found, which belongs to a connected component, via other iterative method the same is reduced and in the IA2 image all the frontiers of the connected component are marked. If some pixel within the connected component is yet, which is no frontier, then in IA2 and IA1 the frontiers are eliminated and this function begins again until that all points are frontiers. In this case, the obtained result (reduction) is taken as the mark. In the

array (see step 4) is indicated that the labeled component with this value was processed and it is begun to look for other component.

6. Finish when the IA1 image is completely scanned. When this step is concluded, in the IA1 image all marks of BV are. These marks are collocated in the IREZI image, where the connected components of the IREZI image after the step two were filled. The IREZI image is the resulting image.

Figure 5 shows the obtained results of applying this algorithm. In Figure 5(b) can be seen that the mark is unique to each of blood vessels, which is always within them. Figure 6 depicts all steps of the proposed strategy to obtain robust markers in blood vessel images.

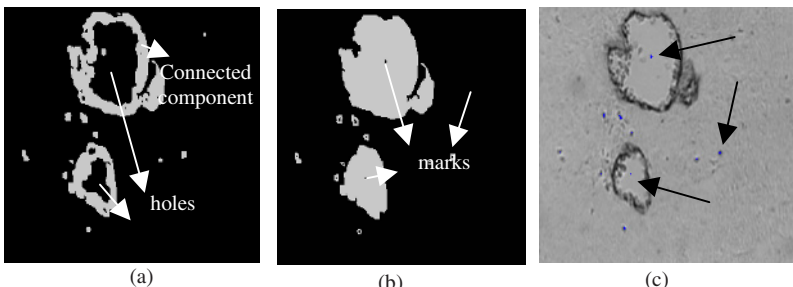


**Fig. 5.** (a) Image with regions of interest. The arrows indicate the connected components and the holes within them. (b) Image with the connected components filled, the interior hole is the obtained mark (c) Superimposed original image on the obtained marks, which some are indicated with arrows.

#### 4.3 Application of the Obtained Strategy in the Watershed Segmentation

There are many applications in digital image processing where is very important to eliminate the minima not wished and consider only the necessary minima (see section 2). In the following, we propose a way to detect these necessary minima:

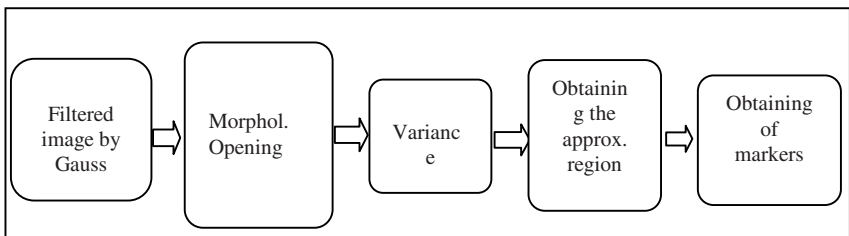


**Fig. 6.** Steps to obtain markers in angiogenesis images

- (a) Carry out a reconstruction by geodesic dilations with a rhombus of size 5x5 (in pixels) as structuring element and with constant  $h = 30$  [8].
- (b) Carry out a morphological gradient to the resulting image of the reconstruction.
- (c) Define via a horizontal profile from the gradient image the pixels belonging to background and those belonging to blood vessels. Of this way are obtained two thresholds. Then, carrying out a thresholding, in which we assigned a value to blood vessels and other to background.

The obtained result of applying the steps (a), (b) and (c) is pictured in Figure 7. In many practical cases the watershed segmentation produces an over-segmentation if one does not obtain robust markers. In fact, when transformation is directly applied to the gradient image is produced an over-segmentation due to existing noise in the original image. Figure 8 shows this effect.

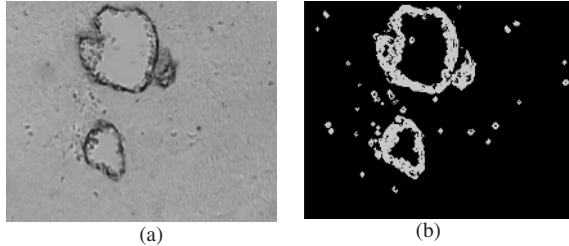


**Fig. 7.** (a) Original image. (b) Resulting image.

Figure 8 (b) shows the poor result when are not obtained good markers. It is evident as the edges are not correctly defined. However, in Figure 9, we show the obtained result of applying our strategy.

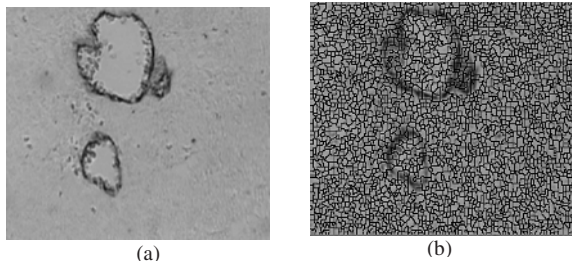


**Fig. 8.** (a) Original image. (b) Watershed segmentation. It is evident the over-segmentation.

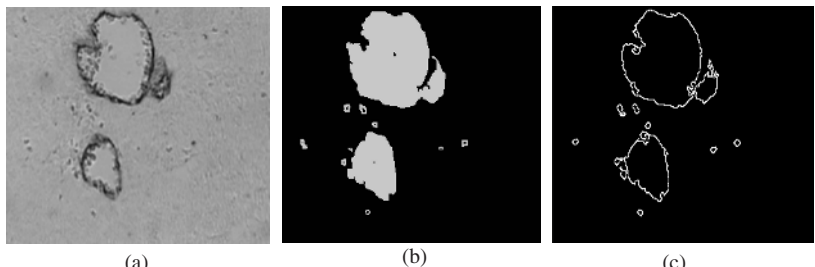


**Fig. 9.** (a) Original image. (b) Image of marks. (c) Watershed segmentation. It is evident the quality of the obtained result.

As can be seen in Figure 9 (c) the edges of blood vessels were correctly defined. In order to verify the good performance of our strategy, we superimposed the contours on the original image. This result can be observed in Figure 10. It is evident that were obtained the exact edges of blood vessels. In addition, the obtained edges were continuos, which is very important for this application. With the classical methods is not possible to obtain continuos edges.

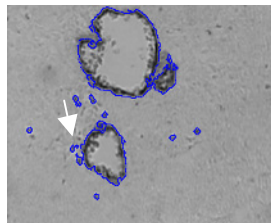


**Fig. 10.** Contours superimposed on the original image.

## 5 Conclusions

In this work, we presented a new strategy to obtain robust markers for blood vessel segmentation via watershed method. A such a sense, we introduced a new algorithm, which identifies correctly blood vessels and eliminate considerably all spurious information. In order to obtain such goal, we carried out a study of the region of interest. We demonstrated by extensive experimentation, by using real images data, that the proposed strategy was fast and robust for the images which were considered.

## References

1. R. González and R. E. Woods, *Digital Image Processing*, Addison-Wesley Publishing Company, Inc., Reading, Massachusetts, E. U. A, 1992.
2. Boschner, B. H., Cote, R. J., Weidner, N., Groschen, S., Chen, S. C., Skinner, D. G., Nichols, P. W., “Angiogenesis in bladder cancer: relationship between microvessel density and tumor prognosis”, *J. Natl. Cancer Inst.*, 87: 21, no.1, 1603–1612, 1995.
3. Díaz-Flores, L., Gutiérrez, R., Varela, H., “Angiogenesis: an update”, *Histol Histopath* 9: 807–843, 1992.
4. Weidner N., Carroll, P. R., Flax, J., Blumenfeld, W., Folkman, J., “Tumor angiogenesis correlates with metastasis in invasive prostate carcinoma”, *American Journal of Pathology*, vol. 143, no.2, 1993.
5. W. Kenong, D. Gauthier and M. D. Levine, “Live Cell Image Segmentation”, *IEEE Transactions on Biomedical Engineering*, vol.42, no. 1, enero 1995.
6. J. Sijbers, P. Scheunders, M. Verhoye, A. Van der Linden, D. Van Dyck, E. Raman, “Watershed-based segmentation of 3D MR data for volume quantization”, *Magnetic Resonance Imaging*, vol. 15, no. 6, pp 679–688, 1997.
7. C. Chin-Hsing, J. Lee, J. Wang and C. W. Mao, “Color image segmentation for bladder cancer diagnosis”, *Mathl. Comput. Modeling*, vol. 27, no. 2, pp. 103–120, 1998.
8. Vincent, L.: “Morphological grayscale reconstruction in Image Analysis: Applications and Efficient Algorithms”. *IEEE Transactions on Image Processing*, vol.2, pp. 176–201, April, 1993.
9. Vicent, L and Soille, P.: “Watersheds in digital spaces: An efficient algorithm based on immersion simulations”, *IEEE Transact. Pattern Anal. Machine Intell.*, 13:583–593; 1991.
10. R. Rodríguez, T. E. Alarcón and L. Sánchez: “MADIP: Morphometrical Analysis by Digital Image Processing”, *Proceedings of the IX Spanish Symposium on Pattern Recognition and Image Analysis*, Vol. I, pp. 291–298, ISBN 84-8021-349-3, 2001, Spain.

# **Discriminative Power of Lymphoid Cell Features: Factor Analysis Approach<sup>1</sup>**

Igor Gurevich<sup>1</sup>, Dmitry Harazishvili<sup>2</sup>, Irina Jernova<sup>1</sup>,  
Alexey Nefyodov<sup>1</sup>, Anastasia Trykova<sup>1</sup>, and Ivan Vorobjev<sup>2</sup>

<sup>1</sup> Scientific Council "Cybernetics" of the Russian Academy of Sciences  
40, Vavilov str., 119991 Moscow, GSP-1, Russian Federation  
[igourevi@ccas.ru](mailto:igourevi@ccas.ru)

<sup>2</sup> Hematological Scientific Center of the Russian Academy of Medical Sciences  
4a, Novyi Zykorskii pr., 125167 Moscow, Russian Federation  
[ivorobjev@mail.ru](mailto:ivorobjev@mail.ru)

**Abstract.** The new results of the research in the field of automation of hematopoietic tumor diagnostics by analysis of the images of cytological specimens are presented. Factor analysis of numerical diagnostically important features used for the description of lymphoma cell nucleus was carried out in order to evaluate the significance of the features and to reduce the considered feature space. The following results were obtained: a) the proposed features were classified; b) the feature set composed of 47 elements was reduced to 8 informative factors; c) the extracted factors allowed to distinguish some groups of patients. This implies that received factors have substantial medical meaning. The results presented in the paper confirm the advisability of involving factor analysis in the automated system for morphological analysis of the cytological specimens in order to create a complex model of phenomenon investigated.

## **1 Introduction**

In this paper, we describe new results of the research into automation of hematopoietic tumors diagnostics on the base of analysis of the images of cytological specimens. This work has been conducted since 2000 by the researchers of the Scientific Council "Cybernetics" of the Russian Academy of Sciences together with the researchers of the Hematological Scientific Center of the Russian Academy of Medical Sciences [1]. The necessary condition of such automation is the development of information technology for morphological analysis of the lymphoid cell nuclei of patients with hematopoietic tumors, which could be implemented in corresponding software system for automated diagnostics. The paper is devoted to the investigation of the numerical features used for the description of lymphoma cell nucleus by means of factor analysis. The method of factor analysis, which allows reducing and structur-

---

<sup>1</sup> This work was partly supported by the Russian Foundation for Basic Research (grant No. 01-07-90016, and 03-07-90406) and by Federal Target-Oriented Program "Research and Development in the Priority Directions of Science and Technology" in 2002-2006 (project No. 37.0011.11.0016).

ing the initial data, proved to be efficient for the problem of morphological analysis of lymphocyte nucleus.

The paper is organized as follows. Section 2 contains a brief description of the developed information technology for the morphological analysis of the cytological specimens. Section 3 contains information about the initial data for factor analysis and about methods used for factor analysis. The results of factor analysis and some conclusions are presented in section 4. Note that the developed technology is described entirely in [4].

## 2 The Main Stages of the Morphological Analysis of the Blood Cells

The developed information technology for the morphological analysis of the cytological specimens includes the following stages of data preparation and analysis:

1. Creation of a database containing images of specimens of lymphatic tissues with isolated lymphocyte nuclei for patients with different lymphoid tumors.
2. Normalization of the images in order to compensate for different illumination conditions and different colors of stain used for the specimens.
3. Choice of features which capture morphological characteristics of lymphocytes nuclei useful for lymphoma diagnostics.
4. Calculation of values, statistical and qualitative analysis of the chosen features for the set of available nuclei.
5. Selection of features for generating feature descriptions of lymphoma cell nuclei.
6. Cluster analysis of the nuclei by using different subsets of the generated set of features.
7. Qualitative and quantitative analysis of the obtained clusters.
8. Formation of a new feature space for description of the patients:
  - the ‘large’ clusters of the cell nuclei are selected;
  - the new features are relational numbers of patient’s nuclei that belong to the selected clusters.
9. Diagnosing the patients by the use of efficient recognition algorithms (for example, recognition algorithms based on estimate calculation [5]) applied to the feature descriptions developed in p.9.

### 2.1 General Characteristic of the Source Data

A base of photomicrographic images of lymphatic tissue imprints was created to select and describe diagnostically important features of lymphocyte nuclei images. The base contains 1585 photos of specimens of 36 patients. We choose 25 cases of aggressive lymphoid tumors (de novo large and mixed cell lymphomas (L) and transformed chronic lymphocytic leukemia (TCLL)) and 10 cases of indolent chronic lymphocytic leukemia (CLL). In one case the reactive lymphoid hyperplasia was diagnosed.

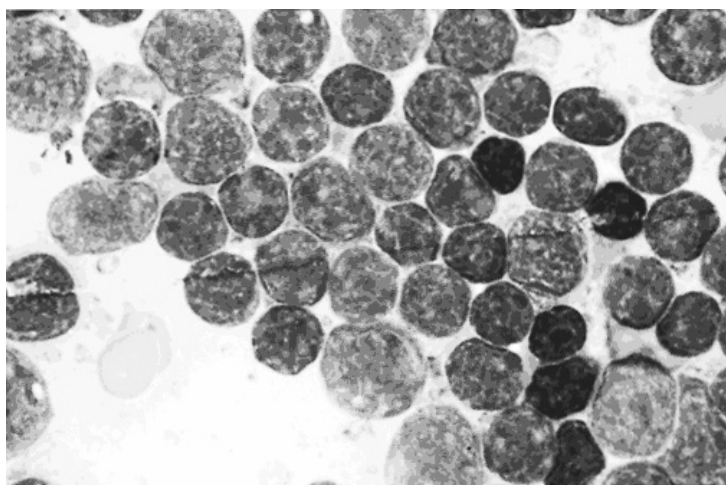


**Fig. 1.** Monochrome photomicrographic image of the footprint of lymphatic gland. Objective  $\times 100$ .

The photos of specimens were collected and stored as the RGB-images in 24-bit TIFF format. Figure 1 shows monochrome picture of the slide of lymphatic gland. On the original RGB-images 4327 nuclei of lymphocytic cells important for diagnostics were indicated by experts. These nuclei were further segmented and analyzed.

## 2.2 Selection and Extraction of Features for Lymphocyte Nuclei Description

The principal property of the proposed technology is the generation of lymphocyte nuclei description by the features chosen and calculated from the images of specimens by the methods of image processing and analysis, and also by the methods of mathematical morphology and Fourier analysis.

During the morphological analysis of lymphocyte nuclei, hematologists use the following characteristics.

1. Nuclei size and density of different lymphoid cells in the specimen (presence of cells with nucleus larger than in most cells).
2. Nuclear form (round, oval, folded), presence of invaginations.
3. Textural features of chromatin (dispersed or condensed pattern; if dispersed – visual diameter of chromatin fibrils).
4. Presence or absence of nucleoli; if present – their number, size, form and location in nuclei (central or peripheral).

We provided formal equivalents of some of the above characteristics. They can be translated into geometrical and textural features of cell nuclei. Thus, the following 47 features were chosen to describe nuclei morphology:

- 1) an area of nucleus in pixels;
- 2) four statistical features calculated on nucleus brightness histogram (average, dispersion, 3<sup>rd</sup> and 4<sup>th</sup> central moments);

- 3) 16 granulometric features of nucleus;
- 4) 26 features calculated on the Fourier spectrum of nucleus.

### **2.3 Cluster Analysis of the Nuclei**

To preprocess the images of the specimens and to calculate the nuclei' features, a program was developed which uses the libraries of the “Black Square” software system [3]. After calculation of the features, their statistical and qualitative analysis was carried out. Conducted analysis allowed us to select several groups of features, which further yielded diagnostically-perspective taxonomies.

The main results of the lymphocytic cells investigations are based on their cluster analysis using developed feature space and its subspaces with the help of FOREL algorithm [2].

A number of sets of clusters were received by using different sets of features and different values of parameter of FOREL algorithm. Obtained sets of clusters were evaluated using various criteria (e.g., the number and the size of clusters in each set, the character of nuclei distribution in large clusters, etc.). Several “interesting” sets of clusters were selected which have good formal characteristics of their clusters and are promising for interpretation by hematologists.

The obtained results showed that:

- 1) the set of diagnostically important nuclei of the patients with considered lymphoid tumors is substantially heterogeneous since different clusters in it were clearly identified;
- 2) clusterization of the lymphocytic nuclei using developed feature set is important from the medical standpoint;
- 3) formal nucleus characterization by the developed feature set corresponds well with its qualitative morphological description and serves as a basis for development the automated software systems of morphological analysis of the blood cells and diagnosis of hemoblastoses;
- 4) the suggested technology provides transition from the diagnostic analysis of lymphocytes nuclei to diagnosing patients with hematopoietic tumors by the use of pattern recognition techniques.

### **3 Factor Analysis of the Features of Lymphocyte Nuclei**

As it is known, factor analysis allows one to estimate the dimensionality of a set of observed variables and to determine the structure of interconnections between these variables. Factor analysis can be used to replace a large set of observed variables with a smaller set of new hypothetical variables called factors. These factors are treated as principal variables that truly describe investigated phenomenon.

The initial data were represented as a table with the rows corresponding to the nuclei' feature descriptions. Factor analysis was conducted on the whole of given nucleus, on different combinations of nucleus taken from patients with different forms

of hemoblastoses (L, CLL and TCLL), and on 5 large clusters, extracted in the set of nucleus by means of taxonomy method.

The tables of nucleus feature descriptions were normalized by columns by the rule

$$z_{ij} = \frac{y_{ij} - \bar{y}_j}{s_j}, \quad (1)$$

where  $z_{ij}$ ,  $y_{ij}$  are the normalized and primary values of the  $j$ th feature of the  $i$ th nucleus,  $s_j$  is a standard deviation of the  $j$ th feature,  $\bar{y}_j$  is an average value of the  $j$ th feature. As a result of such transformation the features' variances became unit. Then, the correlations of the features were calculated in each group of nuclei. Factor analysis was applied to the corresponding reduced correlation matrices with the communities on the principal diagonal. In some cases iterative procedure was applied for evaluation of communities, or squared coefficient of multiple correlation of features with the other ones was considered. The extraction of the factors was realized by means of 3 methods, namely by means of principal-factor method, centroid method and maximum-likelihood method. The quantity of the factors was determined as a result of combining the Kaiser criterion and the scree-test. The varimax-rotate strategy was applied with the purpose of obtaining the contansive interpretation of factors.

It is known that factor problem has an ambiguous solution depending on restrictions imposed on (the choice of factorial method). But considering that a single simple factor explanation lay in the very data, different methods should yield nearly the same mappings, and it signifies that it is possible to establish a certain correspondence between factors from different solutions. Thus, next stage of analysis was the search of correspondences between factor mappings received with the help of 3 different methods. Then average factor loadings of each feature under 3 methods were calculated, and factors were ranked by a maximal percent of variance explained by them.

The conducted factor analysis allowed classifying different numerical features according to the cross correlation in independent groups, defining dominant factors. As a matter of fact each new factor proved to be a linear combination of several initial features, signed with high loadings (exceeding 0,7) for this factor (the most informative features). The additional analysis revealed that a choice of the value 0,7 as a threshold was advisable as long as the combination of features with high loadings did not vary significantly under decrease of this value.

## 4 The Results of Factor Analysis

The results of factor analysis are presented in Table 1. The factor mappings received on the different groups of cell nucleus are presented in the columns of Table 1, and the factors of the same significance level are presented in the rows. The increase of row number corresponds to a reduction of statistical significance of the factor, which is determined in turn by decrease of the variance of this factor. Thus, we come to the following conclusions:

1. The initial set of features (47 elements) breaks at the average into 8 significant groups – factors. There are some cases where 3 factors of the greatest information

density (which explain the largest part of the total variance of the features) combine into a single factor (general distribution of features by factors) in the group of patients with T CLL diagnosis and in the first cluster; and into 2 factors as well – in the groups of patients with CLL and L diagnosis. Due to mentioned above the quantity of important factors varies. The increase of the quantity of factors on the samples of nucleus of the smaller size may be explained by the following rule: if the dimensionality of the considered sample decreases until a certain moment the accuracy of its description with the help of the greater number of factors increases.

2. The factor mappings explain at the average 75% of the total variance of the features.
3. The analysis conducted allows establishing the following classification of the features.
  - a. The main factors include nearly all texture features, the feature with the number 1 (an area of nucleus in pixels) and 3 granulometric features with the numbers 14, 15, 16 (the general number of light grains in nuclei, the number of grains with typical size and with minimal size respectively). The features included in the main factors are of the greatest importance for hematopoietic tumors diagnostics and these very features should be considered in the first place.
  - b. The second dominant factor includes the statistical features with the numbers 3, 4, 5 – variance, 3<sup>rd</sup> and 4<sup>th</sup> central moments calculated on nucleus brightness histogram respectively.
  - c. The features with the numbers 6, 7 (average and variance calculated on nucleus size histogram respectively) fall into the same factor with a minor statistical significance as a rule.
  - d. Granulometric features with the numbers 10, 18 (the number of grains with sizes corresponding to local maxima and local minima of the constructed functions) occur together as well.

The coefficients of cross correlation of the features are high enough in each factor.

4. It appeared that there are features that are inessential (have minor factor loadings) in all kinds of analysis, so these features bring in a little of new information. All these variables belong to the class of granulometric features of the nuclei and have the numbers 8, 9 - 3<sup>rd</sup> and 4<sup>th</sup> central moments calculated on nucleus brightness histogram, 11, 12, 13 – typical, minimal and maximal size of light grains in the nuclei respectively. The features with the numbers 9, 11, 12, and 13 have minor pair correlations with the other parameters stably ( $<0,7$ ).
5. The clusters and groups of patients are distinguished by the factors. It is important to note that some groups of nucleus contain features which don't occur in the set of the other groups.

		Groups of patients							Cluster ID			
All patients		CLL diagnosis	TCLL diagnosis	L diagnosis	1	3	4	11	13			
1	1	0,8684	2 0,9405	22 0,95088	22 0,918	1 0,807	30 0,879	2 0,871	30 0,779	2 0,7973		
	14	0,8364	31 0,9184	23 0,94704	23 0,842	15 0,774	33 0,923	30 0,871	33 0,935	4 -0,768		
	15	0,8665	33 0,7420	24 0,86301	26 0,91	16 0,778	38 0,917	31 0,839	38 0,838	22 -0,921		
	16	0,8624	39 0,7405	25 0,70666	27 0,823	22 0,965	39 0,91	32 0,839	39 0,931	23 0,8467		
	20	0,8102	41 0,7415	26 0,95364	29 0,903	23 0,96	41 0,923	33 0,836	41 0,933	24 0,9189		
	22	0,8010	43 0,8112	27 0,87856	34 0,912	24 0,951		38 0,878		25 0,9561		
	23	0,8263	44 0,8922	28 -0,7286	35 0,702	25 0,96		39 0,843		31 0,7416		
	24	0,8169	46 0,8086	29 0,95396	37 0,903	26 0,942		41 0,836		43 0,7505		
	25	0,7102	47 0,8884	30 0,91999	42 0,875	29 0,961		43 0,802		44 0,7263		
	26	0,7453		31 0,8554	45 0,875	30 0,962		44 0,822		46 0,7475		
	29	0,8183		32 0,90004		31 0,908		46 0,801		47 0,7083		
	30	0,8299		33 0,88044		32 0,908		47 0,828				
	31	0,8536		34 0,95437		33 0,921						
	32	0,8266		35 0,86902		34 0,942						
	33	0,8771		37 0,95392		35 0,874						
	34	0,7439		38 0,9215		37 0,961						
	35	0,7808		39 0,88239		38 0,962						
	37	0,8184		40 0,75237		39 0,929						
	38	0,8370		41 0,87916		40 0,861						
	39	0,8848		42 0,93716		41 0,923						
	40	0,8188		43 0,82977		42 0,937						
	41	0,8782		44 0,77761		43 0,941						
	42	0,8088		45 0,93711		44 0,88						
	43	0,8864		46 0,82985		45 0,937						
	44	0,8846		47 0,78202		46 0,94						
	45	0,8086				47 0,886						
	46	0,8860										
	47	0,8793										
2	27	0,6304	22 0,82808	1 0,71857	2 0,749	2 0,535	22 -0,944	22 -0,762	22 -0,928	33 0,9615		
			23 0,96263	14 0,70185	31 0,799		24 0,943	24 0,762	24 0,922	39 0,9635		
			24 0,84334	15 0,7106	32 0,73		25 0,936		25 0,899	41 0,9585		
			25 0,96846		33 0,714							
			29 0,96126		41 0,714							
			30 0,74572		43 0,711							
			37 0,95388		44 0,811							
			38 0,7392		46 0,71							
					47 0,816							
3	3	-0,7199	3 0,80844	3 0,7074	1 0,777	3 -0,72	1 0,828	26 -0,837	26 -0,902	28 -0,943		
	4	-0,6700	4 0,77032		14 0,703	4 -0,736	15 0,798	34 -0,833	34 -0,902	32 0,7686		
	5	-0,8217	5 0,88762			5 -0,842	16 0,794			36 -0,945		
			15 0,70442				26 -0,903			40 0,7416		
							34 -0,903					
4	2	0,6069	27 -0,8944	2 0,77808	6 0,897	6 0,71	3 -0,864	3 0,832	15 0,839	15 0,8988		
	6	0,8133	28 0,88313			7 0,838	5 -0,849	4 0,781	16 0,841	16 0,8955		
			32 -0,7118				5 0,88					
5	10	-0,8827	10 0,91554	6 -0,8389	3 0,888							
	18	-0,7255	18 0,86401		5 0,914							
6			6 0,84595	10 0,90486	10 -0,887		6 0,829	6 0,786	6 0,697	26 0,9271		
			7 0,69465	18 0,82595	18 -0,801			7 0,864	7 0,812	34 0,9147		
7			26 0,78856		25 0,716		42 0,947	42 -0,888	3 0,884	7 0,8834		
			34 0,78194				45 0,948	45 -0,885	5 0,825			
8			12 0,55118		19 -0,688					42 -0,886	42 -0,968	
					21 -0,667					45 -0,885	45 -0,972	
9			42 0,87081							29 -0,637	29 0,4215	
			45 0,87081							37 0,633	37 -0,403	
10											3 0,7141	

**Table 1.** The results of factor analysis of the features for different groups of the nuclei. First column contains factor numbers, in the rest of columns first number is the feature number while the second number is the value of the respective factor loading.

## 5 Conclusion

The method of factor analysis, which allows reducing and structuring the initial data, proved to be efficient conformably to the problem of morphological analysis of lymphocyte nucleus. It confirmed that the proposed feature space, reflecting morphological characteristics of lymphocyte nucleus used in diagnostics, has a sufficiently simple factor structure. The main goals of factor analysis were achieved, since we succeeded in reducing the feature set composed of 47 elements at least to 8 informative factors and in making a classification of the features proposed. The important result is that the extracted factors allow to distinguish some groups of patients. This implies that received factors have diagnostic medical meaning. The results presented above are the prerequisites for involving factor analysis in the automated system for morphological analysis of the cytological specimens in order to create a complex model of phenomenon investigated.

In future we intend to carry out the factor analysis on the other samples of patients in supplemented feature space for the purpose of conformation of existence of extracted factors, and to exploit new methods of factor analysis as well.

## References

- Churakova, J.V., Gurevich, I.B., Hilkov, A.V., Jernova, I.A., Kharazishvili, D.V., Nefyodov, A.V., Sheval, E.V.: Selection of Diagnostically Valuable Features for Morphological Analysis of Blood Cells. *Pattern Recognition and Image Analysis: Advances in Mathematical Theory and Applications*. **2** (2003) 382 –383
- Elkina, V.N., Zagoruiko, N.G.: Some Classification Algorithms Developed at Novosibirsk. In: Simon, J.C. (ed.): *Intelligence Artificielle, Reconnaissance des Formes. R.A.I.R.O. Informatique/Computer Science*. **1** (1978) 37–46
- Gurevich, I.B., Khilkov, A.V., Murashov, D.M., et al.: Black Square Version 1.0: Programm Development System for Automation of Scientific Research and Education. *Pattern Recognition and Image Analysis: Advances in Mathematical Theory and Applications*. **4** (1999) 609–634
- Gurevich, I.B., Harazishvili, D.V., Jernova, I.A., Nefyodov, A.V., Vorobjev, I.A.: Information Technology for the Morphological Analysis of the Lymphoid Cell Nuclei. *Proceedings of the 13th Scandinavian Conference on Image Analysis (SCIA 2003)*, Sweden, June 29 - July 2, Springer, (2003) 541-548
- Zhuravlev, Yu.I., Gurevitch, I.B.: Pattern Recognition and Image Recognition. *Pattern Recognition and Image Analysis: Advances in Mathematical Theory and Applications in the USSR*. **2** (1991) 149–181

# Retinal Angiography Based Authentication

C. Mariño<sup>1</sup>, M.G. Penedo<sup>1</sup>, M.J. Carreira<sup>2</sup>, and F. González<sup>3</sup>

<sup>1</sup> Dep.Computación,Universidade da Coruña,

15781 A Coruña, [castormp@fi.udc.es](mailto:castormp@fi.udc.es), [cipenedo@dc.fi.udc.es](mailto:cipenedo@dc.fi.udc.es)

<sup>2</sup> Dep.Electrónica e Computación, Fac.Física de Santiago de Compostela,

15782 Santiago de Compostela, [mjose@dec.usc.es](mailto:mjose@dec.usc.es)

<sup>3</sup> Dep.Fisiología, Servicio de Oftalmología,

Centro Hospitalario Universitario de Santiago,

15782 Santiago de Compostela, [fspaco@usc.es](mailto:fspaco@usc.es)

**Abstract.** Traditional authentication (identity verification) systems, employed to gain access to a private area in a building or to data stored in a computer, are based on something the user *has* (an authentication card, a magnetic key) or something the user *knows* (a password, an identification code). But emerging technologies allow for more reliable and comfortable for the user, authentication methods, most of them based in biometric parameters. Much work could be found in literature about biometric based authentication, using parameters like iris, voice, finger-print, face characteristics, and others. In this work a novel authentication method is presented, and first results obtained are shown. The biometric parameter employed for the authentication is the retinal vessel tree, acquired through a retinal angiography. It has already been asserted by expert clinicians that the configuration of the retinal vessels is unique for each individual and that it does not vary in his life, so it is a very well suited identification characteristic. Before the verification process can be executed, a registration step is needed to align both the reference image and the picture to be verified. A fast and reliable registration method is used to perform that step, so that the whole authentication process takes very little time.

## 1 Introduction

Reliable authentication of people has long been an interesting goal, becoming more important as the need of security grows, so that access to a reliable personal identification infrastructure is an essential tool in many situations (airport security controls, all kinds of password-based access controls, ...). Conventional methods of identification based on possession of ID cards or exclusive knowledge are not altogether reliable. ID cards can be lost, forged or misplaced; passwords can be forgotten or compromised. A solution to that problems has been found in the biometric based authentication technologies. A biometric system is a pattern recognition system that establishes the authenticity of a specific physiological or behavioral characteristic possessed by a user. Identification can be in the form of verification, authenticating a claimed identity, or recognition, determining the

identity of a person from a database of known persons (determining who a person is without knowledge of his/her name).

Many authentication technologies can be found in the literature, with some of them already implemented in commercial authentication packages [1]. Other methods are the fingerprint authentication [2][3] (perhaps the oldest of all the biometric techniques), hand geometry [4], face recognition [5] or speech recognition [6]. It also has been shown that for a more reliable system, combination of two or more of those techniques could be good choice [7].

But today the most of the efforts in authentication systems tend to develop more secure environments, where it is harder, or ideally, impossible, to create a copy of the properties used by the system do discriminate between authorized individuals and unauthorized ones, so that an impostor could be accepted by the biometric system as a true sample.

In that sense, the system proposed here employs for authentication biometric parameter the blood vessel pattern in the retina of the eye: it is a unique pattern in each individual, it is almost impossible to forge that pattern in a false individual. Of course, the pattern is the same since the person is born until she dies, at least it appears a pathology in the eye. In <http://www.eye-dentify.com> a commercial authentication system is available, where characteristic points extracted from the vessels are used to measure the similarity between images. Here a novel authentication method based in the whole retinal vessel pattern of the eye is presented, and first results obtained with that technique are shown. In the first section, a brief outline about image registration is presented, because of the necessity of a prior alignment of the images to be compared. Second section describes the system developed in our laboratory to test the accuracy of our method, and in the third section an experiment run in collaboration with the University Hospital of Santiago and results obtained are shown. Finally conclusions and future lines are included as a closing section.

## 2 Methodology

### 2.1 Image Registration

In many cases it is almost impossible to acquire the biometric parameter in the same conditions than the stored template used for the authentication, so that a first step of normalization of both parameters (the acquired and the reference one) is needed in order to make the system reliable enough, avoiding the rejection of legitimate users by changes due to illumination, translations or rotations in the image. The main drawback of retinal angiographies is the different position of the vessels used in the authentication, because it is very difficult that the user place the eye in the same position in different acquisitions, so that an alignment is necessary prior to the authentication. To perform that alignment, an image registration algorithm is employed.

Image registration consists in estimating the transformation  $\hat{T}$  (we will only consider affine transformations) that aligns two images so that the points in one

image can be related to points in the other. To determine the optimal transformation an iterative process is performed so that a similarity measure is optimized.

There is a lot of image registration methods (see [8][9] for complete surveys about them). The registration method developed for the alignment of the images employed in the authentication process have been widely described in [10][11], but for the sake of convenience a brief outline will be included in the following subsection.

**Creaseness based registration method.** Vessels can be thought as creases (ridges or valleys) when images are seen as landscapes. Amongst the many definitions of crease, the one based on level set extrinsic curvature (LSEC) has useful invariance properties. Given a function  $L : \mathcal{R}^d \rightarrow \mathcal{R}$ , the level set for a constant  $l$  consists of the set of points  $\{\mathbf{x} | L(\mathbf{x}) = l\}$ . For 2D images,  $L$  can be considered as a topographic relief or landscape and the level sets are its level curves. Negative minima of the level curve curvature  $\kappa$ , level by level, form valley curves, and positive maxima ridge curves.

$$\kappa = (2L_x L_y L_{xy} - L_y^2 L_{xx} - L_x^2 L_{yy})(L_x^2 + L_y^2)^{-\frac{3}{2}} \quad (1)$$

However, the usual discretization of LSEC is ill-defined in a number of cases, giving rise to unexpected discontinuities at the center of elongated objects. Instead, we have employed the *MLSEC – ST* operator, as defined in [12]. This alternative definition is based on the divergence of the normalized vector field  $\bar{\mathbf{w}}$ :

$$\kappa = -\text{div}(\bar{\mathbf{w}}) \quad (2)$$

Although equations (1) and (2) are equivalent in the continuous domain, in the discrete domain, when the derivatives are approximated by finite centered differences of the Gaussian-smoothed image, equation (2) provides much better results.

After the extraction of the vessel landmarks (see figure 1 (c) and (d)), the straightest approach is to perform an iterative optimization of some alignment function: one image is taken as reference, while the other is iteratively transformed until the function attains a hopefully global maximum. As the optimization function, Downhill Simplex Iterative algorithm was selected, as implemented in [13], and for alignment, the linear correlation function.

But this straight approach works only for almost-aligned and identical content images; the common case is that the optimization gets trapped in a local maximum. Therefore, some sort of exhaustive search for most promising seeds must be performed before the Simplex search starts. An efficient way to do it is in the Fourier domain, employing a well known property which relates a multiplication in this domain to the values of linear correlation. Furthermore, in order to overcome the time bottleneck that this computation demands, we build a pyramid for each image, where each level is a sampled version of a local maximum of the previous level. The exhaustive search is computed only at the top (smaller) image, which greatly reduces the computation time. The method is more widely described in [14][10].

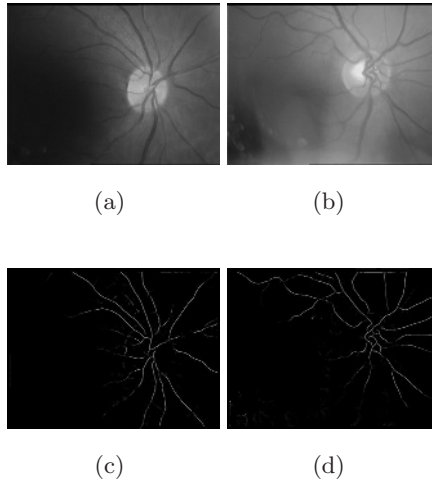


**Fig. 1.** Two examples of retinal angiographies, where variation between individuals can be seen. Images in (c) and (d) depict the extracted vessels of (a) and (b) respectively.

## 2.2 Retinal Based Authentication

Once the registration process has been performed and images are aligned, extracted registered creases images are utilized to obtain a similarity measure between them. So, if two images belong to the same person, aligned creases images will be more similar than images from different persons, although the registration process is successfully performed. The measure employed must be robust against changes in image amplitude such as those caused by changing lighting conditions, and also against the number of points obtained in the creases extraction process. Such conditions are fulfilled by the Normalized Cross-Correlation coefficient (*NCC*), that is defined as [15]:

$$\gamma = \frac{\sum_{x,y} [f(x,y) - \bar{f}][t(x,y) - \bar{t}]}{\left\{ \sum_{x,y} [f(x,y) - \bar{f}]^2 \sum_{x,y} [t(x,y) - \bar{t}]^2 \right\}^{0.5}} \quad (3)$$

where  $\bar{t}$  is the mean of the registered image, and  $\bar{f}$  is the mean of the image. It must be noted that although the sums are over all of the images, only the overlapping areas of them are not null (as depicted in Figure 2, where the original and the registered images are shown).

Once calculated the normalized correlation coefficient  $\gamma$ , a confidence measure must be determined to know if two images belong to the same person. To avoid false acceptance cases caused by errors in the acquisition, where only small creases could be extracted, an acquired image is considered valid for the authentication algorithm if the number of points in the creases is above a minimum

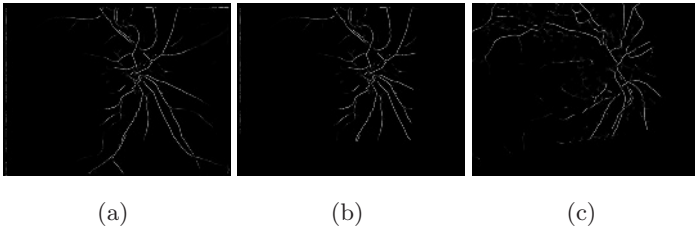


**Fig. 2.** (a) Original with no overlapping area creases image, (b) cropped original with only the overlapping area creases image and (c) registered creases image. Only overlapping area of the images are not null

number of points. That threshold is obtained by the application of the Tchebycheff theorem [16]: if the number of points in the creases  $N_c$  fulfills that  $N_c > 3\sigma$ , where  $\sigma$  is the mean number of points in the creases of a set of well acquired images, then the image will be considered as valid image for the system, but if  $N_c < 3\sigma$  then the image will be rejected by the system.

### 3 Method Validation and Results

Images employed in our experiments were acquired in a period of 15 months and in different centers of the University Hospital of Santiago de Compostela (CHUS), although all of them with the same camera, a Cannon CR6-45NM Non-Mydriatic Retinal Camera, with a resolution of  $768 \times 584$  pixels. Although originally they were color images, a conversion to gray-level images was performed prior to the storage in the database, since color does not provide any useful information.

First experimental results showed that the value of the  $NCC$  of the images belonging to the same individual, although acquired in different times, is always above the value 0.6. In that first experiments, a set of 4 images from 5 different persons (20 images) were evaluated by the system.

To test the reliability of our system, a bigger blind experiment was designed in collaboration with the CHUS: a set of 119 retinal angiographies was introduced in the system. In the benchmark two kind of images could be found: the more of the images (110) belonged to different individuals, and a reduced number of them (6 from 3 individuals, 2 of each) were images from the same persons taken in different times. The system should be able to find the images in the benchmark which pertain to the same persons.

In the test, the  $NCC$  of the cartesian product of the set of 116 images was calculated (three images were eliminated from the total of 119 because they presented very poor contrast, so creases were too small and were refused by the system as described above). The value of the  $NCC$  of the rest of images was normalized to the interval  $[0, 1]$ , as can be seen in the figure 3. It is clear that the values of the diagonal of that image are all 1, since it belongs to the

correlation of the images with themselves. The other values belong to the other two categories: values bigger than 0.6 are obtained correlating images pertaining to the same person but acquired in different moments, and the rest of the values, which are all of them under the peak value 0.35 corresponds to the value of the *NCC* of images of different individuals. That way, to verify the identity of an individual, the system only has to search in the set of stored templates, and if the value of the *NCC* is below a confidence level for all the correlation values, the person will not gain permission to get into the protected area or to read the information.

The confidence level represents a very important parameter in the system, since a too low level would lead the system to accept even false individuals, but a too high level would reject legitim individuals. Figure 4 shows the percentages of false rejection and false acceptance cases. It can be clearly seen in that figure that until the threshold value is 0.60, true positive cases percentage is 1, meaning that no true positive is rejected. From that point until the threshold is 1 the acceptance cases are just the values from the *NCC* of each image with itself, which is always 1.0. In the opposite side, when the threshold goes down, false negative cases does not appear until its value is 0.35, growing exponentially from that point. From this values, when the threshold value is in the range from 0.35 to 0.60 the successful percentage of the system is 100%.

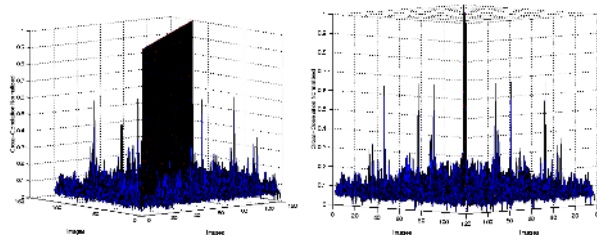


**Fig. 3.** Two views of a graph representing the values of the correlation obtained in the experiment with 119 images. Main diagonal is always 1, since it corresponds to *NCC* of each image with itself, and the other peaks with value 0.6 correspond to the correlation of images from the same person taken in different moments.

All the conclusions exposed in this work were tested by the expert clinicians of the CHUS, since they knew before the experiment was performed, which images belonged to the same individuals, and which were not, concluding that results were right, and that matching images were effectively taken from the same patients, and that did not exist false rejections, so the system got, for this first tests, a 100% of success.

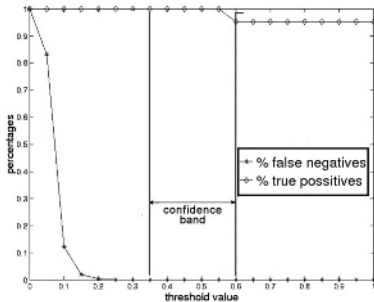


**Fig. 4.** Percentages of false acceptance and false rejections when the threshold level is varied.

## 4 Conclusions and Future Lines

A novel authentication method has been presented here. The authentication procedure employs the retinal vessel tree as the biometric parameter, with a prior registration stage needed to align the template image and the acquired image. To measure the similarity between the images, Normalized Cross Correlation of the aligned creases extracted from the images is used. The technique has been extensively tested, with a test that involved 14.161 cases, giving very good results. It must be noted that the registration method employed here is coherent [17], since the result obtained from the registration of image  $I_1$  registered against  $I_2$  is the same than the result obtained using  $I_2$  as the reference image (figure 3). From that experiment, it can be assessed that  $NCC$  could be used as a robust measure of the similarity of the images, with values over 0.6 for the 127 cases of images from the same person, and values under 0.35 for the 14034 images which belong to different individuals. Moreover, an analysis of the behavior of the system when the acceptance threshold is varied is presented, so that it can be seen that a wide band of 0.35 in the  $NCC$  appears between the acceptance area and the rejection area. The mean time taken to perform each image authentication is 0.3 seconds, 0.26 seconds for the registration and 0.04 seconds to perform the computation of the  $NCC$  value, so that the method is very well-fitted to be employed in a real authentication system.

Future research will include the development of a hardware system based on the technique presented here which will improve performance until almost real time authentication.

**Acknowledgements.** This paper has been partly funded by the Xunta de Galicia through the grant contract PGIDT01PXI10502PR.

## References

1. J.G. Daugman. Biometric personal identification system based on iris analysis. United States Patent No.5,291,560, 1994.
2. Federal Bureau of Investigation. The science of fingerprints: Classifications and uses. Technical report, U.S.Government Printing Office, Washington D.C., 1984.
3. A. Jain, L. Hong, S. Pankanti, and R. Bolle. An identity authentication system using fingerprints. *Proceedings of the IEEE*, 85(9), September 1997.
4. R. Zunkel. Hand geometry based verification. In *BIOMETRICS:Personal Identification in Networked Society*. Kluwert Academic Publishers, 1999.
5. W. Zhao, R. Chellappa, A. Rosenfeld, and P. Phillips. Face recognition: A literature survey. Technical report, National Institute of Standards and Technology, 2000.
6. J.Bigün, C.Chollet, and G.Borgefors, editors. *Proceedings of the 1st.International Conference on Audio- and Video-Based Biometric Person Authentication*, Crans-Montana,Switzerland, March 1997.
7. Patrick Verlinde, Gerard Chollet, and Marc Achery. Multi-modal identity verification using expert fusion. *Information Fusion*, 1(1):17–33, 2000.
8. L.G. Brown. A survey of image registration techniques. *ACM Computer Surveys*, 24(4):325–376, 1992.
9. J.B.A. Maintz and M.A. Viergever. A survey of medical image registration. *Medical Image Analysis*, 2(1):1–36, 1998.
10. D. Lloret, C. Mariño, J. Serrat, A.M. López, and J.J. Villanueva. Landmark-based registration of full slo video sequences. In *Proceedings of the IX Spanish Symposium on Pattern Recognition and Image Analysis*, volume I, pages 189–194, 2001.
11. C. Mariño, M. Penas, M.G. Penedo, D. Lloret, and M.J Carreira. Integration of mutual information and creaseness based methods for the automatic registration of slo sequences. In *Proceedings of the SIARP'2001, VI Simpósio Ibero-Americano de Reconhecimento de Padrões*, volume I, 2001.
12. A. López, D. Lloret, J. Serrat, and J.J. Villanueva. Multilocal creasness based on the level set extrinsic curvature. *Computer Vision and Image Understanding*, 77:111–144, 2000.
13. W. Press, S. Teukolsky, W. Vetterling, and B. Flannery. *Numerical Recipes in C*. Cambridge University Press, 2 edition, 1992.
14. D. Lloret, A. López, J. Serrat, and J.J. Villanueva. Creaseness-based CT and MR registration: comparison with the mutual information method. *Journal of Electronic Imaging*, 8(3):255–262, July 1999.
15. J.P.Lewis. Fast template matching. *Vision Interface*, pages 120–123, 1995.
16. S. Ehrenfeld and S.B. Littauer. *Introduction to Statistical Method*, page 132. McGraw-Hill, 1964.
17. G.E.Christensen and H.J.Johnson. Consistent image registration. *IEEE Trans. on Medical Imaging*, 20(7):568–582, July 2001.

# Suboptimal Classifier for Dysarthria Assessment

Eduardo Castillo Guerra<sup>1</sup> and Dennis F. Lovely<sup>2</sup>

<sup>1</sup>Centre for Studies on Electronics and Information Technologies, Central University "Marta Abreu" of Las Villas, Carr. Camajuaní Km 5½, Santa Clara, VC, Cuba, 50100  
ecastillo@fie.uclv.edu.cu

<sup>2</sup> Department of Electrical Engineering, University of New Brunswick, Fredericton, NB,  
E3B5A3, Canada.  
lovely@unb.ca

**Abstract.** This work is focused on the design and evaluation of a suboptimal classifier for dysarthria assessment. The classification relied on self organizing maps to discriminate 8 types of dysarthria and a normal group. The classification technique provided an excellent accuracy for assessment and enabled clinicians with a powerful relevance analysis of the input features. This technique also allows a bi-dimensional map that shows the spatial distribution of the data revealing important information about the different dysarthric groups.

## 1 Introduction

Dysarthria is a collective name given to a group of neurological diseases that are originated by lesions in the peripheral or central nervous system. The location of the lesions determines the perturbation induced on the speech signal. Therefore, there is a relationship between the speech perturbations observed and the type of dysarthria.

The assessment of dysarthria is often performed based on features extracted from recorded speech which reflect the perturbation patterns described by the different types. The goal for dysarthria assessment is to obtain high sensitivity in the discrimination process while allowing clinicians to perform backward analysis of the feature contribution to the final decision of the classifier. This analysis is necessary to establish a correlation between the most prominent features in each dysarthric group and the neurological damage.

The main limitations encountered in dysarthria assessment can be defines as: the unavailability of objective measures that describe efficiently the speech perturbations, the lack of a gold standard to compare different techniques developed and the few databases available for research. The first limitation mentioned is currently being studied exhaustively where new digital signal processing algorithms are being developed to describe more accurately those perturbations used as clues for assessment [1], [2], [3], [4], [5], [6]. The second limitation is still an unsolved problem in the research community due to the existence of different severity levels of the speech perturbation, the disagreement among researchers about the best set of features to use in the assess-

ment and the interrelation between perturbations. However, steps have been given toward this limitation with the workshop on acoustic voice analysis [6]. The last limitation is a critical problem due to the difficulty of recording large population of subjects with these diseases. New pathological speech databases are now available for research but are not focused only on dysarthric patients, therefore, they provide limited information [7]. As a consequence of these limitations, the development of efficient classification techniques for this application is highly desirable and necessary.

## 2 Experiences in Dysarthria Assessment

Several protocols have been used for dysarthria assessment considering a variety of descriptive features. The diagnosis of the dysarthria has been traditionally performed by the differential diagnosis of dysarthria [8]. This diagnosis method relies on perceptual judgments (PJ) of the pathological speech as the main descriptors. The authors defined 38 features or dimensions that describe more efficiently the speech perturbations. The judgments are grouped into clusters according to the speech mechanism affected and the combination of the clusters exhibited determines the type of dysarthria. The decision is based on minimal distance between the clusters manifested and the combination of clusters that characterize each type of dysarthria.

A survey performed regarding the use of this assessment method showed that more than 60% of clinicians in North America use this system in their clinical practice. However, there are limitations reported for this method in the effectiveness to assess subjects with mixed dysarthrias [9]. The PJ can also be imprecise and inconsistent when certain speech features are analyzed, particularly when they are performed by clinicians which come from different schools and have different reference points. This way of judging often leads to low reliability and repeatability of the process of describing the speech perturbations, causing low assessment rates and difficulties standardizing the results of the research in this area.

Other assessment methods, summarized in [10], describe similar protocols based on linear analyses of different sets of features. The definition of the descriptive features is also different but provides information of similar speech perturbations. Most of these protocols rely also on perceptual judgments of speech and suffer from similar limitations as the traditional method. Some assessment protocols reported perform the discrimination between classes using linear discriminant analysis (LDA). This approach provides better performance than the traditional clustering method. However, the relevancy analysis of the input feature has been found imprecise [3].

More recent studies reported by Callan et al. 1999 [11], implemented the assessment of few dysarthric groups using a small set of objective measures and self-organizing maps (SOM). Despite the small number of subject and groups of dysarthrias assessed the study revealed the effectiveness of the method and opened new options in the assessment of dysarthria.

Nowadays, the trend in dysarthria assessment is the use of different tools to provide objective measures of the speech perturbations and implement non-linear classification techniques to differentiate the different groups [5]. This approach could lead to better and

more consistent judgments. However, the backward analysis on the decision of the classification is an important requirement that the classification method has to meet to provide a global picture these diseases.

### 3 Self-Organizing Maps

A self-organizing map is an unsupervised neural network that learns to recognize regularities and correlations in its input data and adapts future responses according to that input. This network (see block diagram in Fig. 1.) not only learns to recognize groups of similar input vectors but also neighboring neurons learn to recognize neighboring sections of the input space. Therefore, the SOM learns both the distribution and topology of the input vectors on which they are trained.

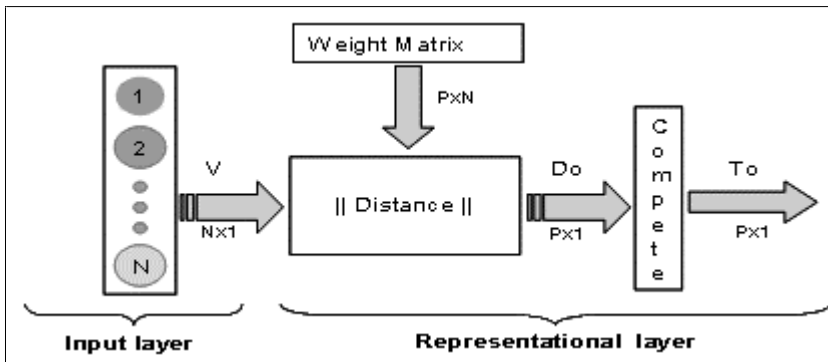


**Fig. 1.** Diagram of a self-organizing map Network

SOMs are made up of an input layer that interfaces with the multidimensional features and a representational layer. This second layer is a two-dimensional array of nodes which has a weight matrix associated. A distance box is used to estimate the negative distance between the input vectors ( $V$ ) and the weight matrix. This estimates the neuron that more likely represents the characteristics of the input case (winning neuron). The competitive level produces a one for the output element corresponding to the winning neuron while all other elements are set to zero. However, neurons close to the winning neuron are updated along with the winning neuron using the Kohonen learning rule [12] expressed as:

$$m_i(t+1) = m_i(t) + \alpha(t)[x(t) - m_i(t)] \quad (1)$$

where  $m_i$  is the connection weights of node  $i$  for time step  $t$ ,  $x(t)$  is the input vector for time step  $t$ , and  $\alpha(t)$  is learning rate for time step  $t$ .

The characteristics described previously allow this type of network not only to learn the distribution of the input vector but also to gain information regarding the neighborhood. The way that neighbors' neurons are updated depends on the topology selected, which can vary between rectangular, hexagonal or random. The weight values are determined

by an unsupervised learning algorithm that offers the advantage that a gold standard target is not required.

Iteratively, the network learns the distribution of the input vector while the data are presented and the weighted connection of the representational layer is corrected. Each winning neuron is obtained through a process of determining which of the nodes in the representational layer is closer to the input vector, according to the distance criteria [12].

### 3.1 Design of the Classifier

A SOM network designed for this type of application requires two layers, an input layer and the representational layer (Fig. 1). The input layer contains 20 inputs neurons corresponding to the 20 observations obtained from perceptual and acoustic analysis<sup>1</sup>, described more precisely in [3]. The representational layer consisted of a 9-by-9-node layer with a hexagonal lattice configuration. A bubble neighborhood function type was used in the training phase as recommended by Kohonen (1995) [12]. This bubble function is reported to provide a configuration that can show better visual information in the map.

Fifteen SOMs were trained using different initial random weights and the configuration that provided the lowest overall quantization error was selected for further studies. The SOMs were trained in two steps as recommended by Kohonen (1995), the ordering phase and the convergence phase. The ordering phase refers to the task of ordering the reference vectors. In this phase, the neighborhood radius is close to the diameter of the map and is decreased during the training. The learning rate is large and decreases toward zero as the network is trained. The initial radius used in the network was 9 with a learning factor of 0.09 and 2000 iterations. This phase established a gross association between the nodes and the input vectors.

The convergence phase is the step in which the reference vector on each node converges to an ‘optimal’ location. The radius and the learning rate are usually smaller in this phase while the number of iterations is usually larger than in the ordering phase. The radius used in this phase of the design decreased from 1 to 0 with a learning rate of 0.008 decreasing to 0 as well. The number of iterations in this phase was 52000 to allow time for the convergence to the optimal position. This phase allows a fine tuning between the vectors and the nodes. The SOM\_PAK software [13] was used for both phases of the training.

### 3.2 Evaluation of the Performance of the Classifier

The performance of the classifier was evaluated using a set of 127 subjects from 9 target classes (AD: Ataxic dysarthria, ALS: Amyotrophic Lateral Sclerosis, FD: Flaccid dysarthria, HC: Chorea, HD: Dystonia, OVT: Organic Voice Tremor, HP: Parkin-

---

<sup>1</sup> Observations: Pitch level, pitch break, tremor, excess of loudness variation, harsh voice, breathy voice, voice stoppages, audible inspirations, speech rate, short phrases, short rushes of speech, monoloudness, hypernasality, reduced stress, variable rate, prolonged intervals, inappropriate silences, excess or equal stress, articulatory breakdowns and distorted vowels.

son's disease, SD: Spastic dysarthria and NS: Control Group). A cross-validation technique was used to prevent an overly optimistic classification rate. This technique works by omitting one subject's data, then retraining the neural network using the remaining data and finally classifying the omitted observation. In this way, more data samples participate in the network training and a more realistic performance measure is obtained. The main disadvantage of this method is that a set of networks is obtained from the training process. However, the network that provided the lowest overall quantization error was kept as the most representative network. The distribution of the vectors across the SOM map for this network is shown in Fig. 2.

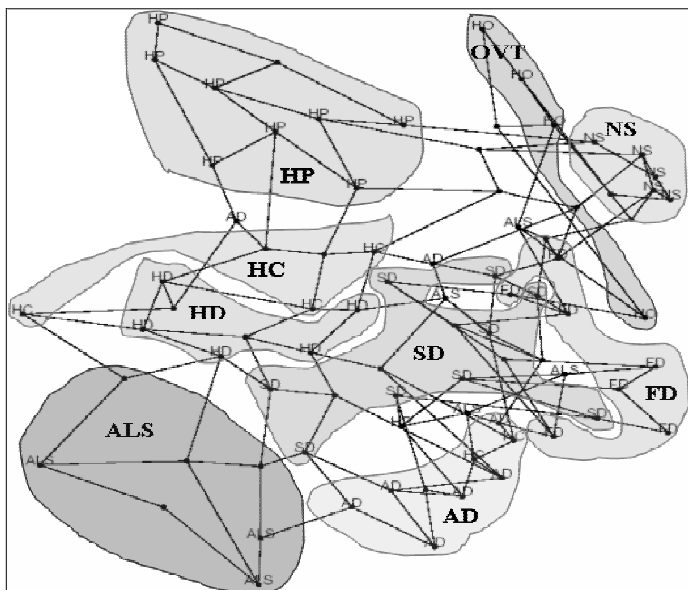


**Fig. 2.** Distribution of the classified groups across the SOM. The dots represent the nodes of the 9x9 map implemented and the lines represent the Euclidean distances between each node. The colored areas enclose the most probable neurons for each group

It is observed that the SOM performed a good separation between the different groups. The shaded areas represent the zones in which a larger number of nodes of each class tends to concentrate. The normal group is the most concentrated in its area with HP, AD, HD, and OVT having very well defined areas. As expected, the HC group is observed close to HD since both are hyperkinetic dysarthrias sharing common typical dimensions. Similarly, the area of the groups FD and SD are overlapped due to both share many similar dimensions. It is noticeable that there are some ALS neurons in between the area defined for FD and SD. This is explained from the clinical view point based on the fact that ALS is a mixed dysarthria made of a combination of FD and SD.

The confusion matrix observed in Table 1 shows the performance of the classification technique. The lowest classification rates are observed for HD and HC groups due to the great overlap among its speech deviations. It is observed that although ALS class was the most scattered across the map, its percent of correct classification (PCC) was not the worst. The quantization error of each sample of the dataset with respect to the selected map was 1.916 for the network that performed worst.

**Table 1.** Confusion matrix of SOM classifier after cross-validating the dataset

<i>Group</i>	<i>True Groups</i>								
	AD	ALS	FD	HC	HD	OVT	HP	NS	SD
AD	11	0	0	1	1	0	1	0	0
ALS	0	10	1	2	1	0	0	0	0
FD	2	0	12	0	1	1	0	0	0
HC	0	0	0	8	0	1	0	0	0
HD	0	0	0	2	10	0	0	0	0
HO	0	1	0	0	0	11	0	0	0
HP	0	0	0	0	0	0	15	0	0
NS	0	0	0	0	0	0	0	19	0
SD	0	2	0	0	1	0	0	0	13
Total	13	13	13	13	14	13	16	19	13
Correct	11	10	12	8	10	11	15	19	13
PCC	0.846	0.769	0.923	0.615	0.714	0.846	0.938	1.00	1.00
N total=127	N Correct=109				Proportion Correct=0.8583				

The total PCC obtained with the SOM method is 0.86, which outperformed the results obtained with the traditional method (0.66) and the LDA method (0.81). The difference in performance between the SOM and the LDA methods is not very significant since some of the input features were measures made of linear combination of different objective algorithms [3]. However, the SOM provided a more reliable relevancy analysis of the input features and provided the bi-dimensional map.

#### 4 Relevance Analysis of the Dataset Features

The contribution of the dimensions to the differentiation of the dysarthric groups can be explained with the use of SOM networks. This has been the main drawback of many non-linear analyses, such as those performed with some types of ANN, in which the relevancy of the observations is not properly understood. The SOM emerged from a vector quantization algorithm that places a number of reference codebooks into a high dimensional input data space which is an organized approximation of the dataset structure. The self-organizing algorithm that shapes this structure can be analyzed as a non-linear regression of the reference vectors through the data points [12]. Therefore, the node's weight vectors corresponding to each group can provide information on the relevance

vancy of the input dimensions to the group. Each neuron will have a set of weights characterizing each target group with a weight associated with each dimension.

Based on the previous explanation, the neurons closer to the centroid of each group will have weights associated with similar characteristics to the mean values of each group. The magnitude and sign of these weights will provide a clinically valuable relevance indicator.

Table 2 shows an example of the most relevant dimensions obtained for the classification of the FD group. The most clinically relevant dimensions found with the traditional and lineal discriminant analyses are also shown for comparison.

**Table 2.** Relevance analysis for the traditional method of dysarthria assessment (PA), linear discriminant analysis and self-organizing map. '\*' indicates coincidence in all studies

Analysis	ORDER												
	1	2	3	4	5	6	7	8	9	10	11	12	13
PA	HN	IC	M	AI	SP	ML	BV	NE	HV	R	-	-	-
LDA	HN	DV	RS	ML	IS	IAB	SP	EES	VR	ELV	VST	R	AI
SOM	HN*	SP	BV	R*	AI*	ML*	PI	PB	HV	EES	-	-	-

The analysis shows, in agreement with the other methods, the dimension hypernasality as the most prominent feature in this group. This is in correspondence with reported studies based on physiological analysis of this type of disease [10]. Short phases (SP), breathy voice (BV), rate (R), audible inspirations (AI), monoloudness (ML), harsh voices (HV), prolonged intervals and excess of loudness variations are speech features also typical in this Dysarthric group. This analysis shows the dimension PB as relevant although it was not found relevant in the previous studies. However, PB is often heard in subjects with FD (i.e. Darley, Aronson & Brown listened PB in 5 of their 30 FD subjects [14]).

The other methods, especially the LDA method, show features that are not commonly seen in this type of disease such as irregular articulatory breakdown (IAB), variable rate (VR) and imprecise consonant (IC). These methods also partially disagree with other physiological studies with respect to the relevancy order [10]. Similar relevancy analyses can be implemented on the rest of the dysarthric groups. In all cases the SOM method performed better than the others method studied demonstrating the feasibility of this technique to perform the relevancy analysis of the input features.

## 5 Conclusions

The results of the classification process reveal the convenience of using SOM for the assessment of dysarthria. A comparison with the implementation of the traditional and LDA classification methods shows that the SOM classifier outperformed the other two methods nearly by 5% and 20% respectively. The SOM also learned the topology of the data, producing a bidimensional map that provides more complete information

about the different dysarthric groups. The map obtained for the dysarthric database can provide information no only about the type of disease or the contribution of the observation, but also about the evolution of the subjects after treatment. This is always an issue in providing objective testimonies of the disease progress.

The SOM technique also bestows a more accurate relevancy analysis than the other methods studied acting as a non-linear regression algorithm. The relevancy analysis implemented in the form explained in Section 4 is simpler and easier to understand than other methods reviewed. This is important to ensure that a system based on this technique is used in regular practice by speech language pathologists. An assessment tool implemented with this classification technique can also avoid exposure to radiation or high magnetic fields in analysis commonly performed on subjects with these diseases.

## References

1. Michaelis, D., Strube, H.W.: Empirical study to test the independence of different acoustic voice parameters on a large voice database. *Eurospeech proceedings*. Vol. 3. (1995) 1891–1894
2. Michaelis, D., Gramss, T. & Strube H.W.: Glottal to noise excitation ratio – A new measure for describe pathological voices. *Acust. Acta Acust.* Vol. 83 (1997) 700–706
3. Castillo-Guerra E.: A modern approach to dysarthria classification. Ph.D. Thesis at University of New Brunswick. Canada (2002)
4. Klatt D.H., Klatt L.C.: Analysis, synthesis and perception of voice quality variations among female and male talkers. *J. Acous. Soc. Am.* Vol. 87. No. 2. (1990)
5. Kent, R.D., Weismar, G., Kent, J.F., Houry, K.V., Duffy J.R.: Acoustic studies of dysarthric speech: Methods, progress, and potential. *J. Comm. Disord.* Vol. 32. (1999) 141–186
6. Titze, I.R.: Recommendation on acoustic voice analysis, summary statement. Workshop on Acoustic Voice Analysis. Denver. Colorado (1994)
7. Kay Elemetrics Corp.: Disordered speech database. Massachusetts Eye and Ear Infirmary. Voice and Speech Lab. Boston. M.A. Ver. 1.03 (1994)
8. Darley F.L., Aronson A.E., Brown J.R.: Differential diagnostic patterns of dysarthrias. *J. Speech Hear. Res.* Vol. 12. (1969a) 462–496
9. Simmons K.C., Mayo R.: The use of the Mayo Clinic system for differential diagnosis of dysarthria. *J. Comm. Disord.* Vol. 30 (1997) 117–132
10. Murdoch B.E., Chenery H.J.: Dysarthria, a physiological approach to assessment and treatment. Singular Publishing Group Inc., Aug (1997)
11. Callan, E.D., Roy N., Tasko S.M.: Self organized maps for the classification of normal and disordered female voices. *J. Speech Hear. Res.* Vol. 42 (1999) 355–366
12. Kohonen, T.: Self-organized maps. Berlin Springer (1995) 77–127
13. Kohonen, T. , Hynninen, J., Kangas J., Laaksonen, J.: SOM\_PAK: The Self-Organizing Map Program Package. Technical Report A31. Helsinki University of Technology. Laboratory of Computer and Information Science. FIN-02150 Espoo. Finland (1996)
14. Darley, F.L., Aronson, A.E., Brown, J.R.: Differential diagnostic patterns of dysarthria. *J. Speech Hear. Res.* Vol. 12 (1969a) 246–249

# Approximate Nearest Neighbour Search with the Fukunaga and Narendra Algorithm and Its Application to Chromosome Classification

Francisco Moreno-Seco, Luisa Micó, and Jose Oncina\*

Dept. Lenguajes y Sistemas Informáticos  
Universidad de Alicante, E-03071 Alicante, Spain,  
`{paco,mico,oncina}@dlsi.ua.es`

**Abstract.** The nearest neighbour (NN) rule is widely used in pattern recognition tasks due to its simplicity and its good behaviour. Many fast NN search algorithms have been developed during last years. However, in some classification tasks an exact NN search is too slow, and a way to quicken the search is required. To face these tasks it is possible to use approximate NN search, which usually increases error rates but highly reduces search time.

In this work we propose using approximate NN search with an algorithm suitable for general metric spaces, the Fukunaga and Narendra algorithm, and its application to chromosome recognition. Also, to compensate the increasing in error rates that approximate search produces, we propose to use a recently proposed framework to classify using  $k$  neighbours that are not always the  $k$  nearest neighbours. This framework improves NN classification rates without extra time cost.

**Keywords:** Approximate Nearest Neighbour, Pattern Recognition, Chromosome Recognition.

## 1 Introduction

The nearest neighbour (NN) rule classifies an unknown sample into the class of its nearest neighbour according to some similarity measure (a *distance*). Despite its simplicity, classification accuracy is usually enough for many tasks. However, some tasks may require finding the  $k$  nearest neighbours in order to improve classification rates, thus the NN rule has been generalized to the  $k$ -NN rule [3]. Many classification tasks represent data as vectors and use one of the Minkowsky metrics as the distance, usually the  $L_2$  (Euclidean distance). However, there are other tasks where a vector representation is not suitable, and thus other distance measures are used: string distance, tree distance, etc.

Although heavily used in pattern recognition, the NN rules have been also of interest for other fields such as data mining and information retrieval, which usually involves searching in very large databases and facing with high dimensional

---

\* The authors wish to thank the Spanish CICYT for partial support of this work through project TIC2000-1703-CO3-02.

data. Whenever the classification task requires large training sets or expensive distance measures, the simple exhaustive search for the NN becomes unpractical. To overcome some of these problems, a large number of fast NN search algorithms [5,4,13,11,2,10] have been developed; most of them have been easily extended to find the  $k$ -NN. However, the requirement of finding exactly the  $k$ -NN involves higher computing effort (dependent on the value of  $k$ ).

For some tasks finding exactly the NN (even using a fast NN search algorithm) may become too slow; some approximate NN search algorithms [1] have been proposed to face these tasks, yielding slightly worse classification rates but obtaining much lower classification times.

Recently [9], a framework for approximate  $k$ -NN classification based on approximation-elimination fast NN search algorithms has been proposed. The main idea in that work is to modify a NN search algorithm keeping a sorted array with the prototypes whose distance to the sample has been computed during the search (the *selected* prototypes), and classify the sample by voting among the nearest  $k$  prototypes found while searching for the NN, including the NN itself. Those prototypes are called the  $k$  nearest selected prototypes ( $k$ -NSN).

In this work we have applied the ideas from [1] to the Fukunaga and Narendra algorithm, which has been implemented using a priority queue to allow approximate search. Then, to improve classification rates we propose to use either the  $k$ -NSN classification scheme or the  $k$ -NN scheme; while the first improves classification rates without increasing classification times, the latter obtains better classification rates than  $k$ -NSN but at an extra time cost that depends on the value of  $k$ .

## 2 The Fukunaga and Narendra Algorithm Implemented Using a Priority Queue

The algorithm from Fukunaga and Narendra [5] is a classic NN search algorithm. In the preprocessing phase, a tree is built from the training set, using some hierarchical clustering algorithm. In [5] the  $k$ -means algorithm is suggested for clustering the set at each level in the tree, and due to this suggestion the Fukunaga and Narendra algorithm is often considered suitable only for Euclidean spaces. However, if a more general clustering algorithm is used instead, the search algorithm is suitable for any metric space.

In the tree, each non-leaf node  $p$  contains a representative  $M_p$  of a set of prototypes  $S_p$ , a radius  $R_p$  (the maximum of the distances between  $M_p$  and all the other prototypes in  $S_p$ ), and  $l$  children. Leaf nodes contain only a representative  $M_p$  and the set of prototypes  $S_p$ . The search phase traverses the tree using a branch and bound scheme. At each node, the distances from the representatives of its children to the sample are computed and stored. Given a child  $p$ , the pruning condition is:

$$d_{nn} + R_p < d(x, M_p) \quad (1)$$

where  $x$  is the sample and  $d_{nn}$  is the distance to the nearest neighbour found so far. For all non-pruned nodes, the search continues, starting with the nearest child. When the node  $p$  is a leaf, all the prototypes stored in the node are tested: if they can not be the nearest neighbour, they are pruned; otherwise, its distance to the sample is computed and the nearest neighbour is updated if necessary. Given a leaf node  $p$ , the pruning condition for a prototype  $x_i \in S_p$  is:

$$d_{nn} + d(x_i, M_p) < d(x, M_p) \quad (2)$$

Please note that  $d(x, M_p)$  has been previously computed, and  $d(x_i, M_p)$  is computed and stored during the building of the tree, so this condition does not involve new distance computations.

The original formulation of the Fukunaga and Narendra algorithm [5] is usually reformulated in a more intuitive recursive way, but in this work we have implemented it using a priority queue that allows for approximate search: after computing all the distances to the children, all non-pruned nodes are stored in a priority queue (similar to the one used in [1]), using  $d(x, M_p) - R_p$  as the key for the queue (see equation 1). Then, the closest element from the queue is extracted and compared (again) with  $d_{nn}$ ; if the current node key is greater than  $d_{nn}$ , the search is finished as all the nodes in the queue are farther from the sample than the current nearest neighbour (see figure 1 for details).

The Fukunaga and Narendra algorithm can be extended to find exactly the  $k$ -NN with a couple of simple modifications: first, let  $d_{nn}$  be the distance to the  $k$ th NN instead of the distance to the NN. Second, each time a distance is computed, store it in a sorted array of the  $k$ -NN distances (if possible). As the value of  $d_{nn}$  in the pruning condition changes, the time expended by the algorithm to find exactly the  $k$ -NN increases in a quantity that depends on the value of  $k$ .

### 3 Approximate Search and Classification

The condition labelled as (a) in the figure 1 is the condition to finish the search: if the nearest (to the sample) element in the queue has a key  $m$  that is greater than the current distance to the nearest neighbour  $d_{nn}$ , then the nodes in the queue (including the one who has just been extracted) can not contain the nearest neighbour and the search may be finished.

Applying a technique similar to that in the work by S. Arya and D.M. Mount [1], the condition (a) in figure 1 may be transformed into:

$$\text{if } (1 + \epsilon)m > d_{nn} \quad \text{or} \dots \quad (3)$$

This new condition (with  $\epsilon > 0$ , obviously) allows to finish the search when the current nearest neighbour is not too far from the nearest neighbour. Using this new condition, the search will become faster, but the classification rate will become slightly worse. As it may be expected, the faster the search, the worse the classification rate will be, thus the choice of the value for  $\epsilon$  should be a trade-off between classification time and accuracy.

```

function pqsearch
  input       $t$  (tree)
               $x$  (unknown sample)
  output      $nn \in P$  ( $x$ 's nearest neighbour in  $P$ )
begin
  insertPQ( $t, 0$ )                                //insert the root of the tree in the queue
  endsearch := false ;  $B := \infty$ 
  while not endsearch do
     $(t, m) := \text{extractMinPQ}()$            //extract node  $t$  with minimum key  $m$ 
    (a)   if  $m > d_{nn}$  or emptyPQ() then
      endsearch := true
    else
      for all  $p = \text{Child}(t)$  do
        let  $M_p$  be the representative of  $p$ , and  $R_p$  the radius of  $p$ 
         $d_p := d(x, M_p)$ 
        if  $d_p < d_{nn}$  then                         // Updating nearest neighbour
           $d_{nn} := d_p$  ;  $nn := p$ 
        endif
        if  $d_p \leq d_{nn} + R_p$  then                  // non-pruned child
          if Leaf( $p$ ) then
            for all prototype  $x_i \in S_p$  do
              if  $d_p \leq d(x_i, M_p) + d_{nn}$  then
                 $d_{x_i} := d(x, x_i)$ 
                if  $d_{x_i} < d_{nn}$  then // Updating nearest neighbour
                   $d_{nn} := d_{x_i}$  ;  $nn := x_i$ 
                endif
              endif
            endfor
          else
            insertPQ( $p, d_p - R_p$ )
          endif
        endif
      endfor
    endif
  endwhile
end pqsearch

```

**Fig. 1.** Fukunaga and Narendra algorithm using a priority queue

On the other hand, classification rates may be improved using more than just the nearest neighbour found in the search. If we use the  $k$ -NN, the search will become slower, so we need a way to improve classification without increasing classification time. In [9] it is showed that storing the closest  $k$  prototypes whose distance to the sample is computed during a (non-approximate) NN search (the  $k$  nearest *selected* neighbours, the  $k$ -NSN), and classifying the sample by voting among these prototypes improves significantly classification rates, yielding rates

similar to those of a  $k$ -NN classifier with the classification time of a NN classifier (finding exactly the  $k$ -NN requires an extra overhead).

In this work we present some preliminary results of the application to the Fukunaga and Narendra algorithm of a combination of the two ideas above: approximate search using  $\epsilon$  to improve speed, and approximate  $k$ -NN classification (that is,  $k$ -NSN classification) in order to improve classification rates (approximate NN search usually produces higher error rates). Two main changes have been made to the Fukunaga and Narendra's algorithm: the use of a priority queue in the search to allow approximate NN search, and storing the  $k$  nearest prototypes visited during the search (the so called  $k$ -NSN), in order to classify the sample by voting among them.

## 4 Experiments

We have developed a set of experiments with a chromosome database [8,7,6] that contains 4400 samples coded as strings. We have chosen to use the Levenshtein distance [12] to measure the distance between two chromosomes in this task. The database has been divided into two sets of 2200 samples each, and two experiments have been performed using one of them for training and the other one for test. The tree has been chosen to be a binary tree containing only one prototype at each leaf, and the  $k$ -medians algorithm has been used to recursively partition the training set to build the tree.

The experiments were repeated for several values of  $\epsilon$  and, in order to test the effect of using more than just one neighbour to classify, the  $k$ -NSN and  $k$ -NN schemes were used for classification; the values of  $k$  ranged from 1 to 15. Figure 2 shows the evolution of both error rate and classification time of a 1-NN search for increasing values of  $\epsilon$  (1-NSN and 1-NN results are the same by definition). The results for  $k = 15$  are plotted in figure 3, which shows as a reference the 1-NN error rate and classification time.

As the figures 2 and 3 show, the choice of a value for  $\epsilon$  depends on the amount of allowable error increase, or on the amount of speed increase required. Also, using more than just one neighbour to classify improves error rates, thus allowing a higher value for  $\epsilon$ . If classification time is critical for the task, then the best choice seems to be the  $k$ -NSN, which requires no extra time over a  $k = 1$  search and improves NN classification rates. However, using  $k$ -NN produces lower error rates but with a certain time overhead. For the classification task presented in this work, the overhead is low due mainly to the low value of  $k$ ; higher values of  $k$  have been tested but did not yield better classification results.

## 5 Conclusions and Future Work

We have combined two techniques to speed up the classification time and to improve classification rates, and we have tested that combination on a classic and widely known fast NN search algorithm, the Fukunaga and Narendra algorithm. The results show that the classification process using approximate search

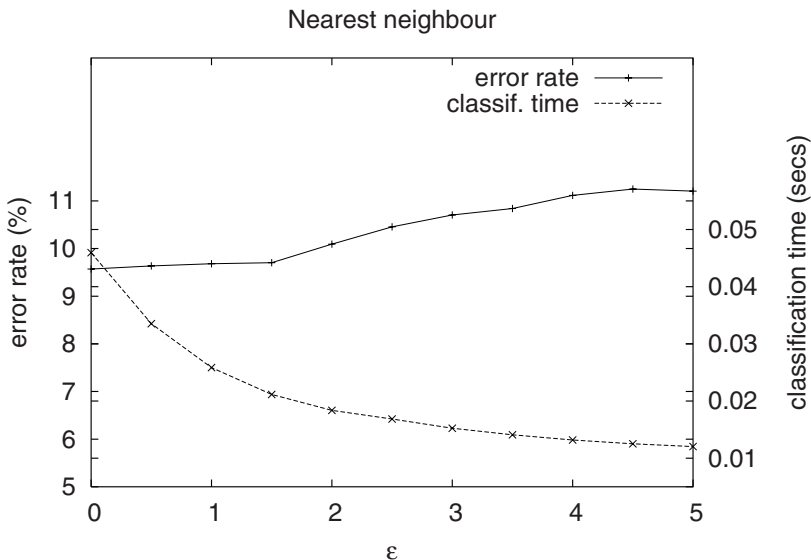


**Fig. 2.** Error rates and classification times for several values of  $\epsilon$ , for a 1-NN search.

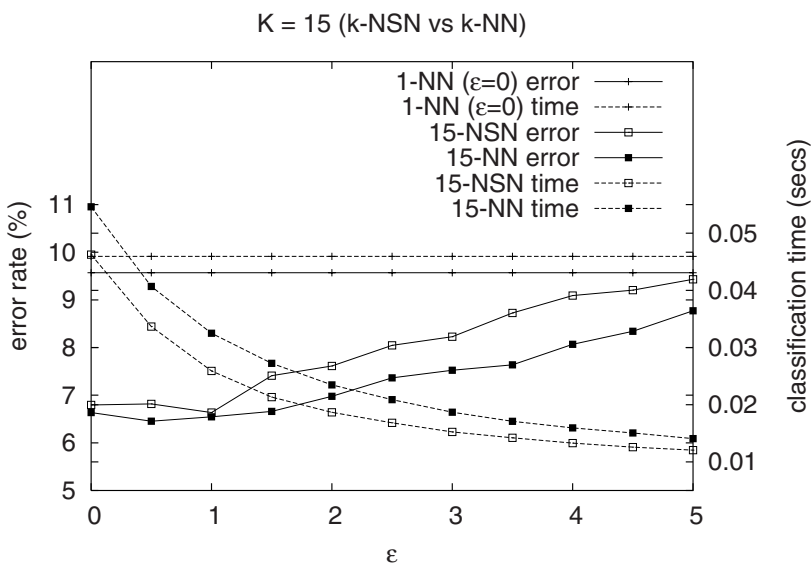


**Fig. 3.** Comparison of error rates and classification times for several values of  $\epsilon$ , for  $k = 15$ .

(with  $\epsilon > 0$ ) is considerably faster, about four times faster for the chromosomes database. Also, the classification rates obtained may be improved using either  $k$ -NSN or  $k$ -NN classification schemes, which yield to rates always better than those of a non-approximate NN classifier, even with high values for  $\epsilon$ .

As for the future we plan to apply the same techniques to tree-based NN search algorithms other than Fukunaga and Narendra's. We will also study the relation between the value of  $\epsilon$  and the classification time and accuracy, using also other databases, either synthetic or real.

**Acknowledgments.** The authors wish to thank Alfons Juan for providing us with the chromosomes database.

## References

1. Arya, S., Mount, D.M., Netanyahu, N.S., Silverman, R., Wu, A.: An optimal algorithm for approximate nearest neighbor searching. *Journal of the ACM* (1998) **45** 891–923
2. Brin, S.: Near Neighbor Search in Large Metric Spaces. *Proceedings of the 21<sup>st</sup> VLDB Conference* (1995) 574–584
3. Duda, R., Hart, P.: *Pattern Classification and Scene Analysis*. Wiley (1973)
4. Friedman, J.H., Bentley, J.L., Finkel, R.A.: An algorithm for finding best matches in logarithmic expected time. *ACM Transactions on Mathematical Software* (1977) **3** 209–226
5. Fukunaga, K., Narendra, M.: A branch and bound algorithm for computing  $k$ -nearest neighbors. *IEEE Trans. Computing* (1975) **24** 750–753
6. Granum, E., Thomason, M.G.: Automatically inferred Markov network models for classification of chromosomal band pattern structures. *Cytometry* (1990) **11** 26–39
7. Granum, E., Thomason, M.G., Gregor, J.: On the use of automatically inferred Markov networks for chromosome analysis. In *Automation of Cytogenetics*, C. Lundsteen and J. Piper, eds., Springer-Verlag (1989) 233–251
8. Lundsteen, C., Phillip, J., Granum, E.: Quantitative analysis of 6985 digitized trypsin G-banded human metaphase chromosomes. *Clinical Genetics* (1980) **18** 355–370
9. Moreno-Seco, F., Micó, L., Oncina, J.: Extending fast nearest neighbour search algorithms for approximate  $k$ -NN classification. *Pattern Recognition and Image Analysis. Lecture Notes in Computer Science*, F.J. Perales et al (Eds.) vol. 2652, Springer-Verlag (2003) 589–597
10. Nene, S., Nayar, S.: A Simple Algorithm for Nearest Neighbor Search in High Dimensions. *IEEE Transactions on Pattern Analysis and Machine Intelligence* (1997) **19**(9) 989–1003
11. Vidal, E.: New formulation and improvements of the Nearest-Neighbour Approximating and Eliminating Search Algorithm (AESA). *Pattern Recognition Letters* (1994) **15** 1–7
12. Wagner, R.A., Fischer, M.J.: The String-to-String Correction Problem. *Journal of the Association for Computing Machinery* (1974) **21**(1) 168–173
13. Yianilos, P.N.: Data Structures and Algorithms for Nearest Neighbor Search in General Metric Spaces. *ACM-SIAM Symposium on Discrete Algorithms* (1993) 311–321

# Characterization of Viability of Seeds by Using Dynamic Speckles and Difference Histograms

Margarita Fernández<sup>1</sup>, Adriana Mavilio<sup>1</sup>, Héctor Rabal<sup>2</sup>, and Marcelo Trivi<sup>2</sup>

<sup>1</sup> Instituto Superior Politécnico “José A. Echeverría”, Dpto. de Física, Facultad de Ingeniería Eléctrica, Calle 114 s/n, Apartado 6028, Marianao 15, La Habana, Cuba.

[mflimia@electrica.cujae.edu.cu](mailto:mflimia@electrica.cujae.edu.cu), [adriana@electrica.cujae.edu.cu](mailto:adriana@electrica.cujae.edu.cu)

<sup>2</sup> Centro de Investigaciones Ópticas (CIC-CONICET) and UID Optimo, Dpto. Fisicomatemáticas, Facultad de Ingeniería, Universidad Nacional de La Plata , Casilla de Correo 124, 1900 La Plata, Argentina  
[hrabal@volta.ing.unlp.edu.ar](mailto:hrabal@volta.ing.unlp.edu.ar) , [marcelot@ciop.unlp.edu.ar](mailto:marcelot@ciop.unlp.edu.ar)

**Abstract.** We propose the use of Difference Histogram method for classification of soya seed speckle images. The time history speckle patterns (THSP), obtained from the dynamic speckle patterns of the seeds were processed for texture classification based on seed vigor and viability. In this work, bean seeds were analyzed with different humidity levels, ie. at 15, 25, 35 and 45 minutes since the sample was taken out from the humid germination paper and submitted to the imaging process, with the aim of determining the influence of this temporal parameter in the classification result (dead or alive). The whole set of seeds was previously analyzed and classified in viable (alive) or not viable (dead) by experts in the matter by applying a traditional method. According to the obtained results the proposed method revealed to be appropriate for the task of classification of seeds. In the case of the highest humidity level the disagreement between our method and the conventional one was the greatest. It should be said that in this case the analyzed images were noisier.

## 1 Introduction

Dynamic speckle is a related phenomenon occurring when laser light is scattered by objects showing some type of activity [1]. This is the case of many biologic samples as seeds [2], fruits, etc., and some non biologic ones as corrosion phenomena and drying of paints [3].

In the activity images [3], corresponding to dynamic speckles, the size, shapes and spatial distribution of the areas of same gray tones, change with time. Characterization of seed quality can be done by taking into account vigor and viability of seeds through textural analysis of the *time history of speckle patterns (THSP)*, obtained from the dynamic speckles [4]. In the THSP images, the rows represent different points on the object and the columns their intensity state in every sampled instant. The activity of the sample appears as intensity changes in the horizontal direction. So, when a phenomenon shows low activity (dead seeds), time variations of

the speckle pattern are slow and the THSP shows elongated shapes. When the phenomenon is very active (alive seeds), the THSP resembles an ordinary granulated speckle diagram. Consequently, textural features provide information that allows the quantitative characterization of the seed state.

Many methods for texture analysis have been reported [5-8], such as statistical and spectral ones using digital filtering [9-11]. We propose a methodology based on the Histogram Difference Method developed by Unser in 1986 [7] to characterize texture of the THSP images. The images were analyzed through the Unser discrimination function which was computed by using the elements of the difference histogram [7] as texture features. This is the histogram of the image obtained by subtracting a shifted image from the original image.

In this work, bean seeds were analyzed with different humidity levels, ie. at 15, 25, 35 and 45 minutes since the sample was taken out from the humid germination paper and submitted to the imaging process. It was done in order to study the influence of this temporal parameter in the classification process (dead or alive). The whole set of seeds was previously analyzed and classified in viable or not by experts in the matter by applying a traditional method.

A similar procedure could be used to classify other kinds of images, corresponding to a dynamic speckle processes.

## 2 Time-History Images of Dynamic Speckle Patterns (HTSP)

In the optical experiment, dynamic speckle patterns corresponding to different seeds were registered. The samples were illuminated with an expanded and attenuated 10 mW He-Ne laser. The speckle images were then registered by a CCD camera, digitized to 8 bits by a frame grabber and stored in the memory of a personal computer.

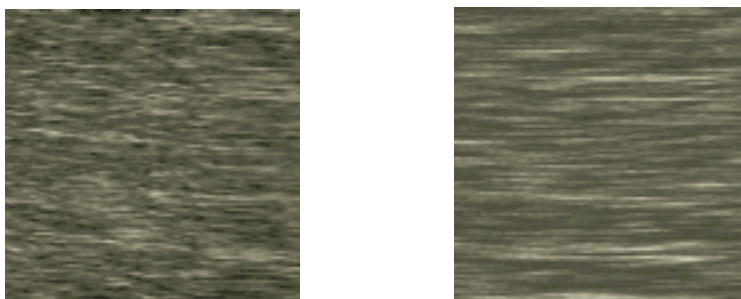


**Fig. 1.** (a) Dynamic speckles corresponding to a seed "alive" (b) Dynamic speckles corresponding to a seed "dead"

To recorded the time evolution of a speckle pattern we used the Oulamara et al. method [4]. It is, for every state of the phenomenon being assessed, 512 successive images were registered of the dynamical speckle pattern and a certain column was selected in each of them. With the selected column, a new  $512 \times 512$  pixel<sup>2</sup> composite

image was then constructed. In this image, named the time history of the speckle pattern (THSP), the rows represent different points on the object and the columns their intensity state in every sampled instant.

The activity of the sample appears as intensity changes in the horizontal direction. So, when a phenomenon shows low activity (died seeds), time variations of the speckle pattern are slow and the THSP shows elongated shape. When the phenomenon is very active (alive seeds), the THSP resembles an ordinary (spatial) speckle pattern as shown in Fig. 1.

### 3 Difference Histogram Method

The difference histogram of the image  $Y[i,j]$  is the histogram of the auxiliary image, that is obtained by subtracting the original image of its replica, with a relative displacement of  $[d_1, d_2]$  among them.

$$Y_{d_1, d_2}^{(d)}[i, j] = Y[i + d_1, j + d_2] - Y[i, j] \quad (1)$$

The classification method is completed by applying the decision Bayesian rule and by assuming a multinomial distribution law for the histograms values  $x = \{x_1, x_N\}$  [7].

The image whose histogram is  $x$ , belongs to the class "i" if:

$$U_i(x) = \min \{U_j(x)\}, j = 1, \dots, k \quad (2)$$

where:

$$U_j(x) = -\sum_{i=1}^N x_i \log [P_{j,i}] \quad (3)$$

where  $P_{j,i}$  is the probability that the HD takes the value  $x_i$  for the class " $j$ ". These values are obtained from the HD patterns, which are representative of the  $k$  classes.

In this experiment we have only one class: "dead", and for this reason it was necessary to use the parameter  $U_j$  not to discriminate between some classes but to define a discrimination threshold between "dead" and "not dead" or "alive" textures.

## 4 Classification Procedure. Results

Four groups of THSP images of seeds, corresponding to different levels of humidity were conformed. From each humidity group of 54 samples, a THSP image was picked up as the most representative of the “dead” state, according to its textural characteristics. This image texture was considered as the pattern corresponding to the “dead” class.

It was selected an subset of 10 THSP images textures with heterogeneous character (five of them corresponding to seeds qualified as “alive” and the other five as “dead” by a conventional method). The values of the Unser discrimination function related to the corresponding pattern were computed for this subset. These values were used to define a discrimination threshold between “alive” and “dead” textures for each humidity group. The heterogeneous character of the sample subset contributes to fit the threshold in a more precise way.

For classification process, the value of the discrimination function of each sample was compared to the threshold in order to classify the seeds in viable and not viable. The results were compared with those obtained by the conventional method.

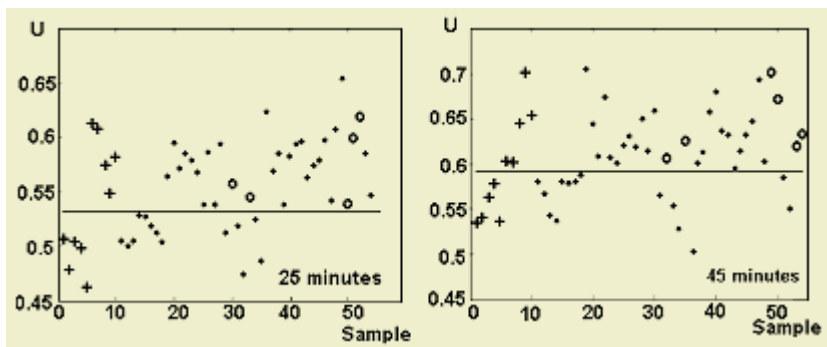


**Fig. 2.** The figure 2 shows the classification results for two levels of humidity. The value of the discrimination function  $U_j$  related to the pattern is plotted for each THSP image.

The straight line represents the threshold value of the discrimination function. For our method all results located under this line belong to the “dead” or non viable class. The crosses correspond to the sample subset that was considered to define the threshold value. The asterisks correspond to coincident classifications according to both methods: this method and the conventional one, and the circles correspond to non-coincident classifications.

The percent of coincident classifications was 85%, 91%, 92% and 90% for times of drying of 15, 25, 35 and 45 minutes respectively.

## 5 Conclusions

According to the obtained results the proposed method revealed to be appropriate for the task of classification of seeds. In the case of the highest humidity level the disagreement between our method and the conventional one was the greatest. It should be said that in this case the analyzed images were noisier.

The characterization process of seeds done in this work, by using dynamic speckles and image processing, constitutes a less subjective method than the traditional ones and allows the automation of the process, increasing its efficiency.

The proposed method could be applied, not only to classification of seeds but also to any other phenomenon where the mean speckle lifetime be a significant measure of some type of sample activity, making possible the characterization of the temporary evolution of the phenomena.

## References

- 1 Dainty, J.C. (ed.) : *Laser speckle and related phenomena*, Springer-Verlag, Berlin (1975).
- 3 Braga R. Et al.: *Proc. SPIE* 4419, Tandil, Argentina (2001) 34-37.
- 2 Fernández, M.,Mavilio, A.,Rabal, H., Trivi,M.: *Proc. SPIE* 4419, Tandil, Argentina (2001) 178-181.
- 4 G. Oulamara et al.: *Journal of Modern Optics*, Vol.36(1989), 165-179.
- 5 Haralick R. M.: *Proc. IEEE.*, Vol. 67, No. 5(1979) p. 786.
- 6 Haralick R. M.: *IEEE Trans. Syst., Man, Cybern.*, Vol. SMC-3, No. 6(1973), p. 610.
- 7 Unser M.: *IEEE Trans. Pattern Anal. Mach. Intell.*, Vol 8, No.1 (1986).p 118,
- 8 Tejera, M., Mavilio, A., Fernández, M.: Dimensiones Promediadas como descriptores de la textura. *Mem. Foro Iberoam. Trat. Dig. Imag.*, Valencia, España, Oct. (1996 ).
- 9 Weldon T. P. y Higgins W. E. :*Proc. ICIP-94*, Austin, ,Texas, T-II(1994), p 620.
- 10 Palisson P.: *Proc. ICIP-94*, Austin, ,Texas, T-II, (1994) p 625.
- 11 Chang T., and Kuo,C.C.J.: *Proc. Int. Conf. Acoust. Speech, Signal Proc*, Vol. 3, (1992) pp. 661-664.

# An Adaptive Enhancer with Modified Signal Averaging Scheme to Detect Ventricular Late Potentials

Alberto Taboada-Crispí<sup>1</sup>, Juan V. Lorenzo-Ginori<sup>1</sup>, and Dennis F. Lovely<sup>2</sup>

<sup>1</sup> Center for Studies on Electronics and Information Technologies, Universidad Central de Las Villas, Carretera a Camajuaní, km 5 ½, Santa Clara, VC, CP 54830, Cuba  
Alberto.Taboada@unb.ca, juanl@fie.uclv.edu.cu  
<http://www.fie.uclv.edu.cu>

<sup>2</sup> Electrical and Computer Engineering Department, University of New Brunswick, P.O. Box 4400, 15 Dineen drive, D41, Head Hall, Fredericton, NB, E3B 5A3, Canada  
lovely@unb.ca

**Abstract.** Ventricular late potential detection can be used as a non-invasive diagnostic tool, but traditional detection techniques need around 300 heartbeats and fail to obtain the beat-to-beat information. This paper combines a modified signal averaging and an adaptive enhancer to deal with non-stationary environments and get beat-to-beat information from as little as 60 beats. In the ventricular late potential region of the recovered signal, discernible patterns indicate the presence or not of such waveforms. A maximum absolute value “averaging” can emphasize the boundaries of the QRS complex even further to successfully detect ventricular late potentials.

## 1 Introduction

Ventricular late potentials (VLPs) are low-amplitude, wideband-frequency waveforms that appear, in the last portion of the QRS complex or beginning of the ST segment, in the high-resolution electrocardiogram (see top plot in Fig. 1) of patients with some life-threatening cardiac diseases. Consequently, the detection of ventricular late potentials can be used as a non-invasive diagnostic marker. However, their detection constitutes a challenge because ventricular late potentials are masked by the other components of the electrocardiogram (ECG) and noise and interference, both in time and frequency domains.

The most commonly used noise reduction strategy for ventricular late potential detection is the coherent averaging [1]. This needs around 300 heartbeats and may introduce a severe low pass filtering effect due to misalignments, not to mention that the beat-to-beat information is completely lost. A modified signal averaging technique [6] [7], which is a combination of mean and median filtering, outperforms the previous way, although the problem of destruction of beat-to-beat information remains.

The standard time-domain analysis employs a high-pass filter to enhance the ventricular late potentials, while attenuating the other components of the ECG and the noise and interference. To avoid ringing and to ensure that the onset and offset of the filtered QRS coincide with those in the original signal, a bi-directional four-pole But-

terworth high-pass recursive digital filtering is used [4]. This filter, however, cannot be applied in a single direction. In addition, it introduces distortion within the QRS complex. Recently, a finite impulse response filter design based on a parallel combination of all-pass and binomial low-pass filters have been proposed to overcome these problems [6] [7].

A novel adaptive enhancer with modified signal averaging and maximum absolute value “averaging” was designed to obtain certain beat-to-beat information and to emphasize the boundaries of the QRS complex. This facilitates the recognition of patterns in the ventricular late potential (VLP) region, differentiating VLP and non-VLP subjects for diagnosis purposes. The new algorithm can handle certain non-stationary environments and provide beat-to-beat information.

## 2 Adaptive Enhancer Plus Modified Signal Averaging for Beat-to-Beat Ventricular Late Potential Detection

An alternative time domain analysis strategy for beat-to-beat ventricular late potential detection, based on adaptive line enhancing (ALE) plus modified signal averaging (MSA), was designed here. For ventricular late potential detection, ALE alone may not be good enough [3]. However, combining ALE and MSA, good results have been obtained with less than 64 beats, even for extreme noisy conditions [5]. Here, the initial ALE plus MSA prototype was analyzed and improved.

### 2.1 Initial Adaptive Line Enhancing Plus Modified Signal Averaging Prototype

Adaptive line enhancing followed by modified signal averaging was proposed for ventricular late potential detection in [5]. Using this approach, it was concluded that the acquisition time can be reduced five-fold to approximately one minute, while maintaining standards in noise reduction for ventricular late potential analysis. However, in a more complete evaluation, increasing the number of real signals, some limitations of this prototype system became apparent.

For some real high-resolution electrocardiographic signals, the system caused troublesome ringing inside the QRS due to instabilities. The concatenation of consecutive windowed heartbeats may introduce discontinuities on the adaptive line enhancing input, due to different levels of the PR and ST segments in the vicinity of the QRS complex. These discontinuities may cause instability in the algorithm, introducing ringing on the output signal. In addition, the same effect may appear associated to the abrupt transitions of the QRS. Consequently, a new adaptive enhancer was devised in an attempt to overcome these limitations.

### 2.2 New Adaptive Enhancer with Modified Signal Averaging

Fig. 1 shows the new adaptive enhancer with modified signal averaging. The original high-resolution electrocardiographic signal (top plot in Fig. 1) was high-pass filtered

(second plot on Fig. 1). This allows a better performance of the adaptive algorithms by diminishing the dynamic range of the input signals, attenuating the drift within the isoelectric segments and enhancing the signal-to-noise ratio in general. In addition, the baseline wandering almost disappears and the filtered segments PR and ST become leveled, avoiding any sharp transition in the further concatenation process.

An enhanced version of the double-level QRS detector algorithm [6] was used to detect  $N$  fiducial marks (vertical lines in Fig. 1). Then, the filtered signal was windowed around the marks (100 ms to the left and 156 ms to the right). This can yield a  $256N$ -element vector, by concatenation, and an  $N$ -by-256 matrix,  $x$ , where every row represents a windowed heartbeat, to perform the modified signal averaging [7].

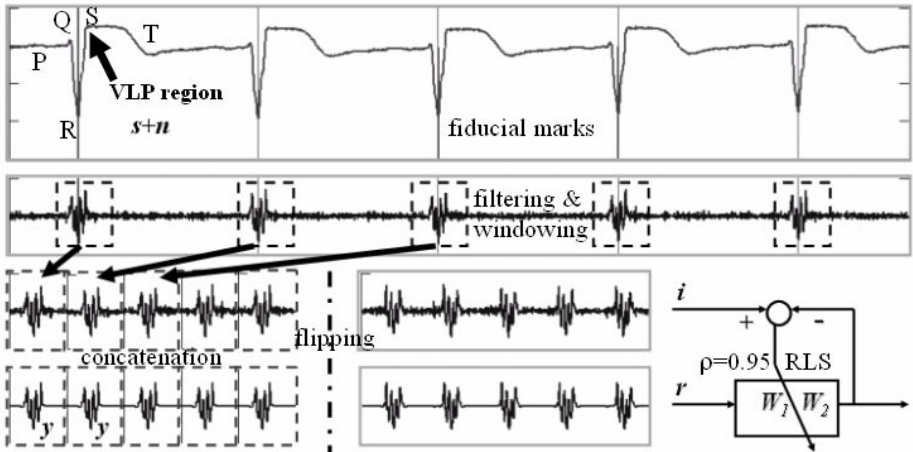


**Fig. 1.** New adaptive enhancer with modified signal averaging

In the new enhancer, the modified signal averaging [7] was computed to obtain a good quality reference for the adapter enhancer, by repeating  $N$  times its output vector  $y$ . The main mission of the new enhancer was not to enhance the signal but to track small changes, otherwise lost in the averaging process. This gives certain information on the ventricular late potential beat-to-beat variability that can help in the diagnosis.

Given the matrix  $x$ , a matrix  $m$  (of size  $(2d+1)$ -by-256) is obtained by appending to it  $d$  delayed versions of  $x$  (each one-column delayed with respect to the previous one) and  $d$  advanced versions of  $x$  (each one-column advanced with respect to the previous one). Then, the modified signal averaging obtains the output  $y$  as

$$y[j] = \frac{\sum_{k=1}^{(2d+1)N} w_{k,j} m_{k,j}}{\sum_{k=1}^{(2d+1)N} w_{k,j}}, \quad (1)$$

where  $w_{k,j}$  is the  $k$ -th element (row) of the  $j$ -th column of the weighting matrix  $w$  with similar size as  $m$ , and  $d = 7$ . The elements of the weighting matrix can be 0 or 1, de-

pending on the median of every column in matrix  $x$  ( $\text{med}(x_j)$ ) and the standard deviation of the background noise ( $\sigma_{iso}$ ),

$$w_{k,j} = \begin{cases} 1 & \text{if } |m_{k,j} - \text{med}(x_j)| \leq 2\sigma_{iso} \\ 0 & \text{otherwise} \end{cases}. \quad (2)$$

Due to the steep transition between the large QRS complex and low level ventricular late potentials, it was “conjectured” that filtering from the end of the data toward the beginning would give better results. Consequently, a time reversed or “flipped” filtering scheme was adopted.

A flipping operation yields the main input ( $i$ ) and the reference ( $r$ ) for the adaptive enhancer. By flipping the concatenated-vectors over, the high-resolution electrocardiogram sequence is processed in the backward direction. This processing from left to right achieved better stability (less ringing and distortion), and good tracking of the ventricular late potential changes.

A second-order RLS adaptive scheme, with a forgetting factor of 0.95, was used to “enhance” the signal  $i$  with the reference  $r$ . The adaptive enhancer here does not reduce noise in the isoelectric segment compared to the reference  $r$ , but it detects certain changes in the ventricular late potential segment. It should be mentioned, to be precise, that the system cannot follow every change in  $i$  because of the limitations of the reference  $r$ , but it gives a good idea of the variability.

The RLS algorithm allows a fast adaptation to any variation in the signal. By using a forgetting factor  $\rho$  of 0.95, the data in the distant past are forgotten [2] and the enhancer can cope with a certain degree of non-stationarity. A filter of order two was found as a good compromise to provide an acceptable frequency separation (long enough), with a quick convergence and low computational load (short enough). It was found that the algorithm converged during the first windowed heartbeat. This enhancer can track not only amplitude variations, but also displacement or phase variations.

The vector at the output of the adaptive system has to be flipped to recover the normal forward direction. This recovered vector can be written as an  $N$ -by-256 matrix,  $o_2$ , by taking every heartbeat as a different row. Finally,  $o_2$  can be used to obtain an “averaged” vector  $o_3$  by means of a maximum absolute value (MAV) operation. To avoid the influence of outliers, the samples of every column of  $o_2$  were sorted and the 5% on the top and the 5% on the bottom were trimmed out before applying the MAV. The MAV operation selects, from every column of the matrix  $o_2$  after trimming, the sample whose absolute value is maximum to obtain the vector  $o_3$ .

### 3 Adaptive Enhancer Evaluation

The adaptive enhancer implemented here includes two features that have to be tested. This scheme provides a matrix (output  $o_2$ ) including certain beat-to-beat information and, at the same time, yields an “averaged” vector (output  $o_3$ ) that can be used for an overall detection of the ventricular late potential, equivalent to the standard method.

To evaluate the algorithms in very realistic scenarios, a high resolution electrocardiographic (HRECG) database was created. This database includes the HRECG signal

from 59 post-myocardial infarction patients and 63 healthy volunteers with no evidence of cardiovascular disease. 5-minute records of the bipolar X, Y, and Z leads from each subject were simultaneously collected at a sample frequency of 1 kHz [6]. Furthermore, simulations of the HRECG signal, ventricular late potentials (fixed-VLP and variable-VLP) and noise were designed to evaluate these algorithms in a more controlled environment [6]. More than a thousand combinations were used for testing.

The quality of a particular segment of the HRECG signal can be expressed in terms of several parameters. Some of the most important parameters used here to qualify a recovered sequence are the variance of noise  $\sigma_\theta^2$ , which represents the noise power, the bias  $b_\theta$ , and the signal-to-noise ratio SNR [6].

### 3.1 Beat-to-Beat Information

Fig. 2 shows an example of how the novel adaptive enhancer plus modified signal averaging recovers the high-resolution electrocardiographic signal from a noisy environment. The 60-heartbeat records shown in the figure were previously high pass filtered and windowed around the fiducial marks (-100ms/+156ms), to confine the 3-D plots. The time axis was reversed to see the ventricular late potential region (around 150 - 200ms).

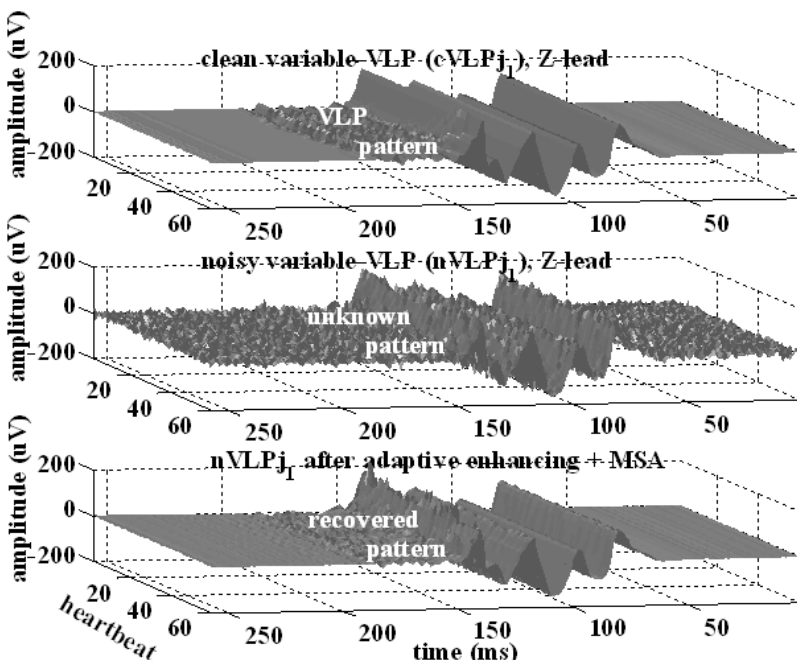


**Fig. 2.** Example of the performance of the adaptive enhancer with a noisy variable-VLP record

The plot on the top shows a clean record with variable ventricular late potentials ( $cVLPj_1$ ). Observe, however, that there is not a recognizable pattern in the region of

interest (VLP region, around 150 - 200ms) in the noisy signal  $nVLPj_1$  (central plot). The plot on the bottom represents the recovered signal by using the adaptive enhancer plus modified signal averaging (output  $o_2$  explained above). In the recovered signal, there is some distortion close to the steepest regions due to the adaptive algorithm. This distortion avoids following the exact ventricular late potential beat-to-beat structure, which is the main limitation of the adaptive scheme. However, the bottom plot in Fig. 2 clearly shows the pattern of variable ventricular late potentials, which can be distinguished even in a beat-to-beat basis.

As expected, the performance of the algorithm is better for lower levels of noise. It is important to note that, for the same level of noise, the algorithm performs better with non-VLP and fixed-VLP than with the variable-VLP records, although some distortion may be present close to the peaks. Fig. 3 shows an example of that performance with a non-VLP noisy record. Observe the contrast between the enhanced signals (those at the bottom) in the Fig. 2 (variable-VLP) and Fig. 3 (non-VLP).

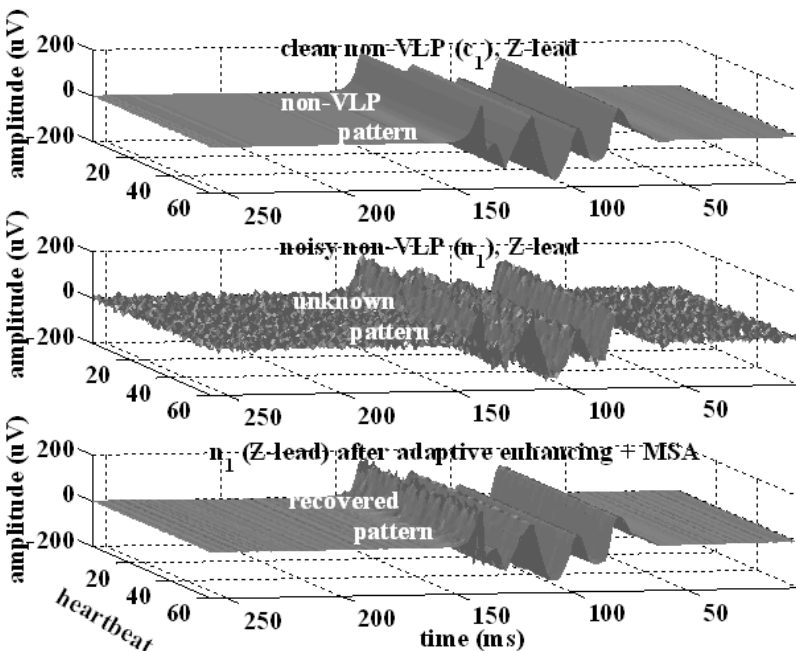


**Fig. 3.** Example of the performance of the adaptive enhancer with a noisy non-VLP record

### 3.2 Overall Detection of Ventricular Late Potential

The rationale for the maximum absolute value at the end of the enhancing scheme was that the new modified signal averaging, used to generate the reference  $i$  for the adaptive enhancer, worked well in the isoelectric (PR and ST) segments, providing good recovery of that part of the signal, but tended to attenuate the peaks. In the adaptation process, the higher instability is around those peaks because of the worse match between the main input  $i$  and the reference input  $r$ , and because of the adaptation process

itself. The maximum absolute value block does not affect much the isoelectric segment, but it “catches” the peaks (including those in the ventricular late potential region) that are lost otherwise in the averaging process. In this case, the “averaged” vector  $o_3$  does not exhibit better noise reduction in the isoelectric segment than  $y$ , but a higher difference between the ventricular late potential and the isoelectric regions, more evident in the presence of variable ventricular late potentials.

Fig. 4 shows the absolute value of the “averaged” 60-heartbeat filtered signal by using the standard method and the adaptive enhancer plus maximum absolute value, i.e. output  $o_3$ , compared to the first filtered heartbeat of the ideally clean signal. It can be noticed that the standard averaging method works acceptably well in the isoelectric segments, but attenuates considerably the variable ventricular late potentials (VLP region), making difficult to distinguish the end of the QRS (offset). However, the adaptive enhancing plus maximum absolute value, although introduces some distortion, intensifies the differences between the isoelectric segment and the ventricular late potential region, making easier the recognition of the offset.

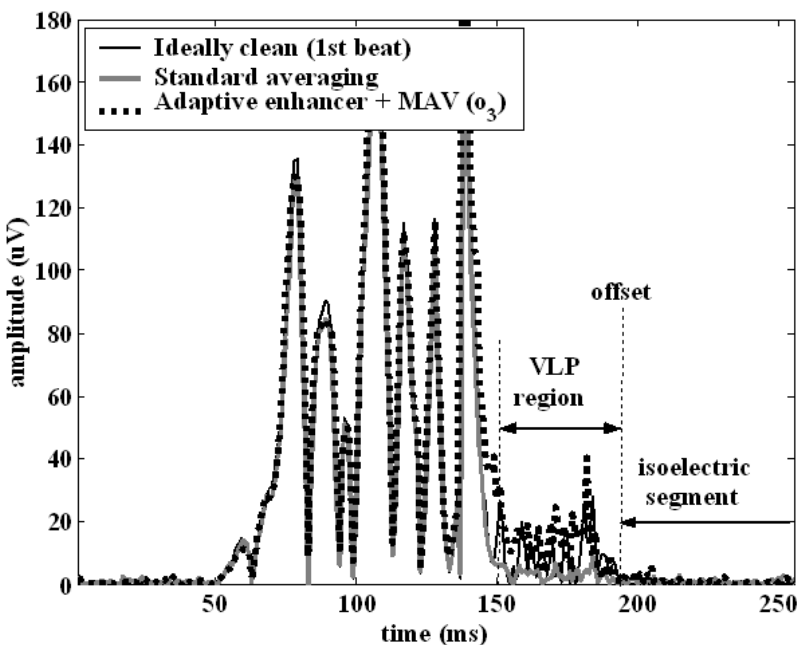


**Fig. 4.** Absolute value of the “averaged” filtered signals compared to one ideally clean beat

When the ventricular late potentials are fixed (beat-to-beat repeatable), the distortion introduced by the algorithm can be discarded. For these cases, the offset is again easily distinguishable, providing a good discrimination between the VLP and the non-VLP subjects.

A detailed study with 1min test records, showed a perfect classification for the enhancing plus maximum absolute value scheme by using the duration of the QRS as a discriminant feature.

In the previous sections, a limited set of representative figures illustrate the results of the more exhaustive evaluation. However, it was verified qualitative (simple inspection) and quantitatively (computing  $\sigma_\theta^2$ ,  $b_\theta$ , and SNR) that the algorithms here presented consistently outperform those reported in [1] and [5].

## 4 Conclusions

The number of heartbeats needed for the processing algorithms here designed was decreased to less than 60 (i.e. approximately 5 times less than for the standards.) By reducing the acquisition time, the high-resolution electrocardiographic signal is less likely to exhibit non-stationary behavior; nevertheless, the algorithms implemented here have certain capability to handle non-stationary data (forgetting factor < 1 and modified signal averaging which rejects outliers). The new adaptive enhancer plus modified signal averaging provides beat-to-beat information, and different patterns are associated to the VLP region for VLP and non-VLP subjects.

Although some other tests have to be performed before definitively introducing these algorithms to the clinic application, the results so far show a great improvement in the sensitivity and specificity. The processing techniques assessed, outperformed the classical time-domain analysis method. Improved processing algorithms to detect and analyze ventricular late potentials allow for better diagnosis capabilities. Therefore, the results of this work can have a direct impact on the lives of many individuals.

## References

1. Breithardt, G., Cain, M.E., El-Sherif, N., Flowers, N., Hombach, V., Janse, M., Simson, M.B., Steinbeck, G.: Standards for Analysis of Ventricular Late Potentials Using High Resolution or Signal-Averaged Electrocardiography. *Eur. Heart J.*, Vol. 12, No. 4 (1991) 473–480
2. Haykin, S.: *Adaptive Filter Theory*. Prentice Hall, New Jersey (1996)
3. Mitchell, R.H.: Evaluation of Adaptive Line Enhancement for Beat-to-Beat Detection of Ventricular Late Potentials. *Electronics Letters*, Vol. 35, No. 13 (1999) 1037–1038
4. Simson, M.B.: Use of Signals in the Terminal QRS Complex to Identify Patients with Ventricular Tachycardia after Myocardial Infarction. *Circulation*, Vol. 64, No. 2 (1981) 235–241
5. Taboada-Crispí, A., Lorenzo-Ginori, J.V., Lovely, D.F.: Adaptive Line Enhancing plus Modified Signal Averaging for Ventricular Late Potential Detection. *Electronics Letters*, Vol. 35, No. 16 (1999) 1293–1295
6. Taboada-Crispí, A.: Improving Ventricular Late Potential Detection Effectiveness, PhD Thesis, Dept. of Electrical and Computer Engineering, University of New Brunswick (2002)
7. Taboada-Crispí, A., Lorenzo-Ginori, J.V., Mendoza-Reyes, M.A., Lovely, D.F.: Modified Signal Averaging Scheme to Detect Ventricular Late Potentials, in Proc. Informática2003, Havana (2003)

# A Study on the Recognition of Patterns of Infant Cry for the Identification of Deafness in Just Born Babies with Neural Networks

José Orozco-García and Carlos A. Reyes-García

Instituto Nacional de Astrofísica Óptica y Electrónica (INAOE)

Luis Enrique Erro # 1,  
Tonantzintla, Puebla, México,  
[jose@ccc.inaoep.mx](mailto:jose@ccc.inaoep.mx), [kargaxxi@inaoep.mx](mailto:kargaxxi@inaoep.mx)

**Abstract.** In this paper we present the methodologies and experiments followed for the implementation of a system used for the automatic recognition and classification of patterns of infant cry. We show the different stages through which the system is trained to identify normal and hypo acoustic (deaf) cry. The cry patterns are represented by acoustic features obtained by the Mel-Frequency Cepstrum and Lineal Prediction Coding techniques. For the classification we used a feed-forward neural network. Results from the different methodologies and experiments are shown, as well as the best results obtained up to the moment, which are up to 96.9% of accuracy.

## 1 Introduction

The infant crying is a communication way, although more limited, it is similar to adult's speech. Through crying, the baby shows his or her physical and psychological state. Based on human and animal studies, it is known that the cry is related to the neuropsychological status of the infant [1]. According to the specialists, the crying wave carries useful information, as to determine the physical and psychological state of the baby, as well as to detect possible physical pathologies, from very early stages. In previous works on the acoustical analysis of baby crying, it has been shown that there exist significant differences among the several types of crying, like healthy, pain and pathological infant cry. Using classification methodologies based on Self-Organizing Maps, Cano [2] attempted to classify cry units from normal and pathological infants. In another study, Petroni used Neural Networks [3] to differentiate between pain and no-pain crying. Previously, in the seminal work done by Wasz-Hockert spectral analysis was used to identify several types of crying [4]. In a recent investigation, Taco Ekkel [5] attempted to expand a set of useful sound characteristics, and find a robust way of classifying these features. The goal of Ekkel was to classify neonate crying sound into categories called normal or abnormal (hypoxia). However, up to this moment, there is not a concrete and effective automatic technique, on baby crying, useful for clinical and diagnosis purposes.

## 2 Infant Cry

Crying is the only communication mean that the baby has in the first months of life, before the use of signs or words. The Crying wave is generated in the Central Nervous System, that's why the cry is thought to reflect the neuropsychological integrity of the infant, and may be useful in the early detection of the infants at risk for adverse developmental outcome. In this work, two kinds of crying are considered: normal and pathological (hypo acoustical) crying. The Automatic Infant Cry Recognition process (Fig. 1) is basically a problem of pattern processing. The goal is to take the crying wave as the input pattern, and finally obtain the type of cry or pathology detected in the baby. First, we have to take a sample set, apply acoustical analysis and principal component analysis to get a reduced vector, which is used to train the recognizer. Second, we take a test sample set, and also apply acoustical analysis and principal component analysis to reduce the vector's dimension. Then the reduced unknown vector is passed by the pattern classifier, which, at the end, classifies the crying sample.

In the acoustical analysis, the crying signal is analyzed to extract the more important features in time domain. Some of the more usual simple techniques for signal processing are: Linear Prediction Coding, Cepstral Coefficients, Pitch, Intensity, among others. The extracted features from each sample are kept in a vector, and each vector represents a pattern.

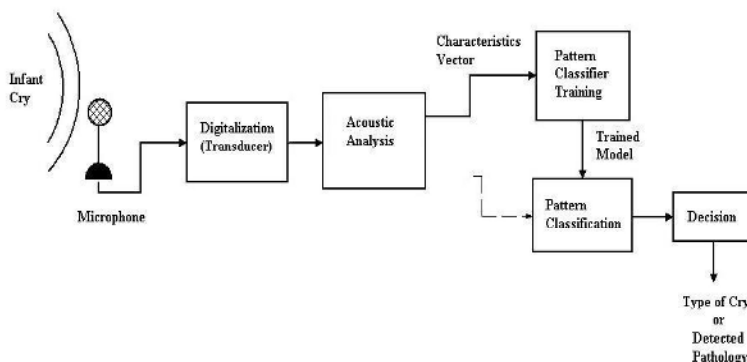


**Fig. 1.** Automatic Infant Cry Recognition Process

Infant cry shows significant differences between the several kinds of crying, which can be perceptually distinguished by a trained person. The general acoustical features for normal crying show, raising-falling pitch pattern, ascending-descending melody, high intensity as shown in Fig. 2. Pathological crying (Fig. 3) shows acoustical characteristics like: intensity lower than normal, rapid pitch shifts, generally glottal plosives, weak phonations and silences during the crying.

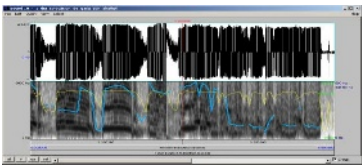


**Fig. 2.** Waveform and spectrogram of normal crying

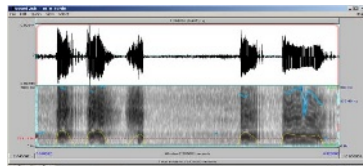


**Fig. 3.** Waveform and spectrogram of pathological crying

### 3 Mel Frequency Cepstral Coefficients

The digitized sound signal contains irrelevant information and requires large amounts of storage space. To simplify the subsequent processing of the signal, useful features must be extracted and the data compressed. The power spectrum of the speech signal is the most often used method of encoding. Mel Frequency Cepstral coefficients (MFCCs) [6] are used to encode the speech signal. Cepstral analysis calculates the inverse Fourier transform of the logarithm of the power spectrum of the speech signal. For each utterance, the Cepstral coefficients are calculated for all samples with successive frames. The energy values in 20 overlapping Mel spaced frequency bands are calculated. This results in each frame being represented by 16 and 21 MFCCs.

### 4 Linear Prediction Coefficients

The objective of the application of these techniques is to describe the signal in terms of its fundamental components. Linear Prediction (LP) analysis has been one of the time domain analysis techniques more used during the last years. LP analysis attempts to predict "as well as possible" a speech sample through a linear combination of several previous signal samples. Thus, the spectral envelope can be efficiently represented by a small number of parameters, in this cases LP coefficients. As the order of the LP model increases, more details of the power spectrum of the signal can be approximated.

### 5 Neural Networks

Neural Networks are one of the more used methodologies for classification and patterns recognition. Among the more utilized neural network models, there are the feed-forward networks which use some version of the back-propagation training method. In general, a neural network is a set of nodes and a set of links. The nodes correspond to neurons and the links represent the connections and the data flow among neurons. Connections are quantified by weights, which are dynamically adjusted during train-

ing. The required training can be done through the back-propagation technique. During training (or learning), a set of training instances is given. Each training instance is typically described by a feature vector (called an input vector). It should be associated with a desired output (a concept, a class), which is encoded as another vector, called the desired output vector. In our study, several methods were tested to train the feed-forward neural networks.

### 5.1 Training with Scaled Conjugate Gradient Method

After analyzing the performance of the algorithms [13], we chose the one with high classification accuracy and low training time. Under these conditions we selected SCG to continue with our experiments. From an optimization point of view, learning in a neural network is equivalent to minimizing a global error function, which is a multivariate function that depends on the weights in the network. Many of the training algorithms are based on the gradient descent algorithm. SCG belongs to the class of Conjugate Gradient Methods, which show super-linear convergence on most problems. By using a step size scaling mechanism SCG avoids a time consuming line-search per learning iteration, which makes the algorithm faster than other second order algorithms. And also we got better results than when using other training methods and neural networks tested, as standard back-propagation and cascade neural network.

## 6 Training Process and Experimentation

We made two kinds of experiments, one with Linear Prediction Coefficients (LPCs) and the other with Mel-Frequency Cepstral Coefficients (MFCCs). The selection of samples for training and testing was done at random. Training stops when the maximum number of epochs is reached, or when the maximum quantity of time has been exceeded, or when the performance error has been minimized. To be sure the performance is at an acceptable level, in terms of accuracy and efficiency, we used the 10-fold cross validation technique [10]. The sample set was randomly divided into 10 disjoint subsets, each time leaving one subset out for testing and the others for training. After each training and testing process, the classification scores were collected, and a new complete process started. In this way, we performed 10 different classification cycles, until all data subsets were used once for testing. All the experiments are done without ever using the same training data for testing. Once the 10 experiments were done, the overall scores were calculated from the average of all the individual ones. For the MFCCs and LPCs analysis, the samples were segmented in windows of 50 ms and 100 ms for different experiments. We extracted 16 and 21 MFCCs per window. Depending on coefficients number and window length, we got different parameters number for each sample. For example, with 16 coefficients for a window length of 50ms for a one second sample, the features vector contains 320 parameters, corresponding to 320 data inputs to the neural network. In this situation, the dimension of the input vector is large, but the components of the vectors are highly correlated

(redundant). It is useful in this situation to reduce the dimension of the input vectors. An effective procedure for performing this operation is the Principal Component Analysis (PCA). After several tests, we got good results with 50 parameters by each vector or pattern [13].

## 7 Data Set

A set of 116 samples have been directly recorded from 53 babies by pediatricians, with digital ICD-67 Sony digital recorders, and then sampled at 8000 Hertz. The same pediatricians, at the end of each recorded sample, do the labeling. The collection of pathological samples is done by a group of doctors specialized in communication disorders, from babies already diagnosed as deaf by them. The babies selected for recording are from just born up to 6 month old, regardless of gender. The corpus collection is still in its initial stage, and will continue for a while. 116 crying records, from both categories, were segmented in signals of one second length. 1036 segmented samples were obtained, 157 of them belong to normal cry, and 879 to pathological cry. For the reported experiment, we took the same number of samples for each class, 157.

## 8 System Implementation

For the acoustic processing of the cry waves, we used Praat 4.0.2 [11] to obtain the LPCs and MFCCs. To perform pattern recognition, a 50 input nodes – 15 hidden layer nodes – 2 output nodes, feed-forward network was developed for training and testing with LPC and MFCC samples. The number of nodes in the hidden layer was heuristically established. The implementation of the neural network and the training methods were done with the Neural Networks Tool Box of Matlab 6.0.0.88 [12]. The same Matlab version was used to implement the PCA algorithm.

## 9 Experimental Results

To establish the adequate number of principal components, we made an analysis on the information each number preserves. The Fig. 4 shows the preserved information by principal components from 1 to 928. For example, the 10 first components keep 90.89%, while the 30 first components keep 93.08% from the original features. The original LPC features vector was reduced to different number of principal components. Their performance was evaluated by measuring the precision of the classifier with vectors containing between 10 to 110 principal components (Fig. 5). As can be observed, up to 50 components, the recognition accuracy increases as the number of principal components also increases. From 50 components on, the precision slightly

decreases (Fig. 5). Based on this analysis we selected 50 to be the size of the input vector.

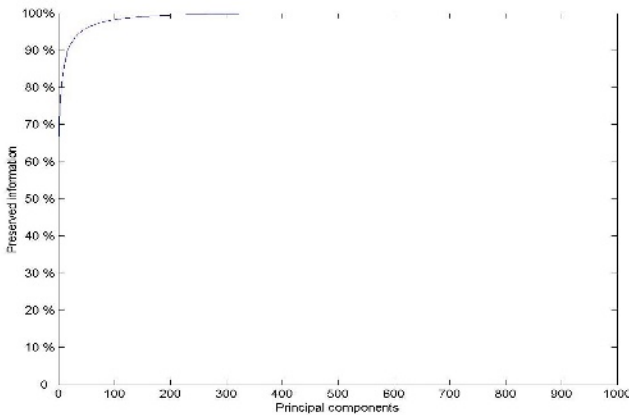


**Fig. 4.** Preserved information to different number of principal components

We did not analyze more than 110 components because our goal was to reduce the original features vector to a manageable size. These results were obtained with the SCG network configured by 50, 15 and 2 nodes, in the input, hidden, and output layers, respectively.

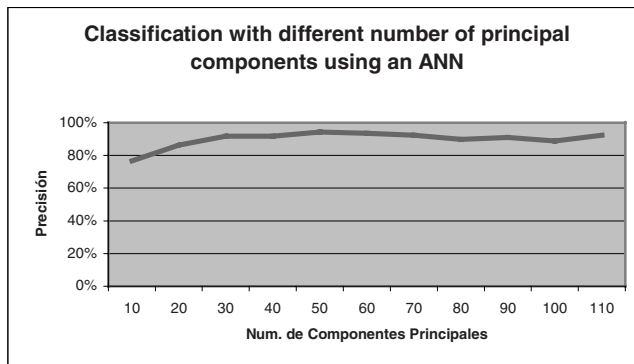


**Fig. 5.** Accuracy achieved by using different number of principal components.

## 9.1 Training and Classification Results

The neural networks were trained to classify the cries into normal and pathological classes. For training with 10-fold cross validation technique, the sample set is divided into 10 subsets, 4 groups with 32 samples and 6 groups with 31 samples. Each time

leaving one set for testing and the remaining for training. This process is repeated until all sets have been used once for testing. The classification accuracy was calculated by taking the number of correctly classified samples by the network, and divided by the total number of samples into the test data set. Some of the best results obtained for both types of features, LPC and MFCC are shown in the following confusion matrices in Table 1 and Table 2 respectively. In both cases, the results were produced by the net from a 50 principal components input vector. The reduced vectors come from the original feature vectors, which are one second length samples divided in 21 coefficients per 100 ms window. Table 1 shows the results obtained with LPC features, and Table 2 shows the corresponding to the MFCC features.

**Table 1.** Infant Cry classification for LP Coefficients

Type of Cry	# of Samples	Confusion Matrix		Classification
		Normal	Deaf	
Normal	157	<b>150</b>	7	
Deaf	157	11	<b>146</b>	
<b>Total</b>	314			<b>94.3 %</b>

**Table 2.** Infant Cry classification for MFC Coefficients.

Type of Cry	# of Samples	Confusion Matrix		Classification
		Normal	Deaf	
Normal	157	<b>149</b>	8	
Deaf	157	2	<b>155</b>	
<b>Total</b>	314			<b>96.80 %</b>

## 10 Conclusion and Future Work

This work has shown that the results obtained when using the MFCCs features are better than LPCs features in the test. Besides observing the neural network's performance, we have gathered useful acoustical information on the infant cry. We hope this information could be helpful to pediatricians and doctors in general. As can be noticed ,in the confusion matrices, still many samples from one class can be confused as belonging to the other. We are working to explain why that happens, in order to avoid the problem and to improve the classification accuracy. At this moment we are starting new experiments to also identify asphyxia in new born babies, by their crying. As

future work we consider to collect enough samples to train the classifiers appropriately and to have some other classes to classify. We still intent to experiment with mixed features, as well as with hybrid intelligent classification models. Moreover, we will intent to identify the degree of deafness.

**Acknowledgment.** This work is part of a project that is being financed by CONACYT (37914-A number). We like to thank Dr. Edgar M. Garcia-Tamayo and Dr. Emilio Arch-Tirado for their invaluable collaboration in helping us to collect the cry samples.

## References

- [1] Bosma, J. F., Truby, H. M., & Antolop, W. *Cry Motions of the Newborn Infant*. Acta Paediatrica Scandinavica (Suppl.), 163, 61–92. 1965.
- [2] Sergio D. Cano, Daniel I. Escobedo y Eddy Coello, *El Uso de los Mapas Auto-Organizados de Kohonen en la Clasificación de Unidades de Llanto Infantil*, Grupo de Procesamiento de Voz, 1er Taller AIRENE, Universidad Católica del Norte, Chile, 1999, pp 24–29.
- [3] Marco Petroni, Alfred S. Malowany, C. Celeste Johnston, Bonnie J. Stevens. *Identification of pain from infant cry vocalizations using artificial neural networks (ANNs)*, The International Society for Optical Engineering. Volume 2492. Part two of two. Paper #: 2492-79. 1995. pp.729–738.
- [4] O. Wasz-Hockert, J. Lind, V. Vuorenkoski, T. Partanen y E. Valanne, *El Llanto en el Lactante y su Significación Diagnóstica*, Científico-Médica, Barcelona, 1970.
- [5] Ekkel, T. “Neural Network-Based Classification of Cries from Infants Suffering from Hypoxia-Related CNS Damage”, Master Thesis. University of Twente, 2002. The Netherlands.
- [6] Huang, X., Acero, A., Hon, H. “Spoken Language Processing: A Guide to Theory, Algorithm, and System Development”, Prentice-Hall, Inc., USA, 2001.
- [7] Markel, John D., Gray, Augustine H., *Linear prediction of speech*. New York: Springer-Verlag, 1976.
- [8] LiMin Fu, *Neural Networks in Computer Intelligence*, Ed-McGraw-Hill Inc., 1994.
- [9] Moller, A Scaled Conjugate Gradient Algorithm for Fast Supervised Learning, *Neural Networks*, 6 (4), 1993, 525–533.
- [10] Haykin, Simon S. *Neural Networks: A Comprehensive Foundation*. New York: Macmillan College Publishing Company, Inc., 1994.
- [11] Boersma, P., Weenink, D. Praat v. 4.0.8. *A system for doing phonetics by computer*. Institute of Phonetic Sciences of the University of Amsterdam. February, 2002.
- [12] Manual *Neural Network Toolbox*, Matlab V.6.0.8, Development by MathWorks, Inc.
- [13] Orozco-García, J., Reyes-García, C. A. “Acoustic Features Analysis for Recognition of Normal and Hypoacoustic Infant Cry Based on Neural Networks”, in Lecture Notes in Computer Science 2687: IWANN 03, Artificial Neural Nets Problem Solving Methods, Springer, Berlin, pp. 615–622, ISBN 3-540-40211, ISSN 0302-9743.

# **Patients Classification by Risk Using Cluster Analysis and Genetic Algorithms\***

Max Chacón and Oreste Luci

Informatic Engineering Department, University of Santiago de Chile,

Av. Ecuador 3659, PO Box 10233, Santiago, Chile.

{mchacon, oluci}@diinf.usach.cl

**Abstract.** Knowing a patient's risk at the moment of admission to a medical unit is important for both clinical and administrative decision making: it is fundamental to carry out a health technology assessment. In this paper, we propose a non-supervised learning method based on cluster analysis and genetic algorithms to classify patients according to their admission risk. This proposal includes an innovative way to incorporate the information contained in the diagnostic hypotheses into the classification system. To assess this method, we used retrospective data of 294 patients (50 dead) admitted to two Adult Intensive Care Units (ICU) in the city of Santiago, Chile. An area calculation under the ROC curve was used to verify the accuracy of this classification. The results show that, with the proposed methodology, it is possible to obtain an ROC curve with a 0.946 area, whereas with the APACHE II system it is possible to obtain only a 0.786 area.

## **1 Introduction**

In order to determine the admission risk, it is necessary to know the patient's condition at the moment he or she is admitted to a medical unit. This condition represents very valuable information to make clinical decisions such as the admission of the patient to an Intensive Care Unit (ICU) and helps decide the distribution of resources within the unit [1–2]. Besides, it is crucial to carry out a health technology assessment [3]. The problem that exists when determining the admission risk is that, after making the preliminary assessment, the patient is treated, thus modifying his initial condition. A true quantification of this risk could be achieved by assessing the results of the natural evolution of the illness without applying medical technologies, which would be an ethical impossibility.

In medicine, the traditional way to deal with this problem has been the creation of physiological indexes intended to determine the seriousness of the patient's condition at the moment of admission, such as: Simplified Acute Physiology Score (SAPS) [4] or Acute Physiology and Chronic Health Evaluation (APACHE [5]). Among the main disadvantages of these indexes, we may quote the lack of an adequate characterization of the medical information at the moment of admittance, such as a quantification of comorbidities [6], the linear characteristics of the composition of these indexes and the lack

\* This study has been supported by FONDECYT (Chile) project No. 1990920 and DICYT-USACH No. 02-0219-01CHP.

of precision to determine each individual patient's risk. This last point makes possible that these indexes permit to carry out global comparisons between units (they offer accurate risk values on the average) but they are not of great help to assess technologies within a medical unit.

At present, there exists a number of publications that intend to forecast the outcome of medical procedures. To this effect they have applied different Data Mining methods such as: Logistic Regression, Cluster Analysis, Neural Networks and Bayesian Networks [2,7-9]. Especially, the work carried out by Peña-Rojas and Sipper [8] contains an extensive revision of genetic algorithm applications in various fields of medicine. Of the aforementioned works, the one that is closest to admission risk estimate is the one published by Dubowski et al [7], which analyses the outcome considering the deaths that take place during admittance to the hospital. In spite of the fact that the prediction of the outcome is useful when making some decisions - such as the admission of patients- these predictions do not represent the condition of the patient at the moment of admission and the use of these results to make a technological assessment in health is questionable since it includes the utilization of the same technology it intends to assess [10].

This work's proposal is based on two fundamental points: the first one consists of using a group of variables similar to those used in physiological indexes, such as APACHE [5]. It uses an original way of quantifying diagnostic hypotheses (including comorbidities) as a way to incorporate the medical knowledge that exists at the moment of admission. The second point consists of using a non-supervised learning method, which takes as a basis the clustering of *k-means*, together with a strong search method like the *genetic algorithms*. This type of learning allows the formation of groups of patients, based exclusively on the information we have about each patient at the moment of admission. Later on we use the information contained in the outcome of the interventions, just to assign risk to each group. It is always possible to do this when accepting the hypothesis that interventions tend to modify the patient's state positively. In this way, the groups that show a greater number of patients who did not survive, in spite of the treatment, represent the groups of higher initial risk. Thus it will be possible, later on, to classify a new patient depending exclusively on the conditions presented at the moment of admission.

In order to assess the proposed methodology, we have used the information taken from 294 medical records of patients who were admitted in two Intensive Care Units (ICU) for adults. These were classified in accordance with afore described methodology. The results were compared using the classification that resulted from applying the APACHE II [11] index by means of ROC [12] curves.

## 2 Data Collection and Pre-processing

The data were obtained from the Intensive Care Units (ICU) of two public hospitals of the city of Santiago, Chile. A total of 294 medical records of adult patients were collected. 50 out of the 294 correspond to patients who died during their stay at ICU. Table 1 shows a list of the variables that were taken at the moment of admission or during the first 12 hours of hospitalization.

The discreet or binary variables, such as infection upon admission, can be represented directly, but the variables used to represent physiological acuteness require a monotonous

severity scale in order to be used efficiently with the clustering method. These variables do not have a monotonous behavior with respect to seriousness. For example, in its original form, temperature has a normal severity range located at the middle of the scale, but both hypothermia and fever produce an increase in the patient's severity condition. To capture the severity increase in only one direction, we resort to the code used by the APACHE system, which uses discrete ranges between zero and four. In this way, severity always increases from zero value, which is considered normal. To encode age we also use the five ranges defined in the APACHE system.

The method used to quantify the information contained in the diagnostic hypotheses was the knowledge of intensivists with the double purpose of enriching the information contained in the diagnoses and carrying out a quantification that may reflect severity. The procedure included four steps: First, the 780 diagnoses (each patient considers the principal diagnosis and co-morbid states up to a maximum of eight) were split into 17 groups that represent physiological systems and morbid groups (Table 2).

**Table 1.** List of input variables for the grouping method.

Variable	Units
Age *	In years
Sex	Binary
Glasgow Coma Scale	0 - 10
Admittance Infection	Binary
Admittance with Respiratory	Binary
Cardio arrest	
Pre-Admittance Surgery	Binary
Temperature* (axilar)	°C
Mean arterial pressure *	mmHg
Heart rate *	Breaths per min
Respiratory rate *	Breaths per min
PaO <sub>2</sub> -AO <sub>2</sub> * (Arterial Oxygen Pressure Difference)	mmHg
pH* (Arterial)	pH (Arterial)
Serum Sodium * (Sodium ion in the blood)	Meq/l
Serum Potassium * (Potassium ion in the blood)	Meq/l
Serum Creatinin* (It measures renal function)	mg/dl
Hematocrit * (It measures globular mass)	%
White Blood Count *	Cel /cm <sup>3</sup>
Neoplasia Presence	Binary
Multiorganic Failure	Binary

\* Variables were codified according to APACHE index.

**Table 2.** Quantification of the Diagnostic Hypothesis

Physiological System or Morbid Group
Neurological
Respiratory
Cardiovascular
Renal
Metabolic
Digestive
Endocrine
Immunologic
Obstetric-Gynecologist
Osteomyoarticular
Psychiatric
Uro-gynecological
Transplant
Otorhinological
Hematological
Dermatologic

Then, the specialists classified each diagnosis in three different categories: *chronic*, *acute* and *hyperacute* (except in the cases of trauma, that are all *acute* or *hyperacute*). A third step considered that in each physiological or morbid group there may exist more than one of these categories or there may exist a combination of these, for instance two *chronic* and one *hyperacute* diagnoses. With these combinations, a classification system

was created that had an associate increasing severity order according to the combination of *chronic*, *acute* and *hyperacute* in each patient. Finally, an algorithm was used to assign severity condition values to each one of the 17 groups for each patient, according to the combination of existing diagnoses.

### 3 K-Means and Genetic Algorithms

The combination proposed for the clustering rescues the main strengths of the traditional clustering methods, especially those of the *k-means* [13] and *Genetic Algorithms (GA)* [14]. From the *k-means*, we can save the simplicity in the representation for cluster creation, which has an influence in the capacity to look for different alternatives at the same time, thus increasing the solution space and its capacity to avoid being trapped in local minimals. From a general perspective, the first problem to be solved is to determine the optimum number of clusters. We based the solution to this problem on a measure of quality for the clustering. The existing literature on cluster analyses shows that one of the most efficient measurements to determine the quality of the clustering is that of Calinski-Harabasz [15]. We leave as a parameter the cluster range. Clustering is started with the largest number of clusters. After that, the quality of the clustering is measured and then the closest clusters are identified and merged. This process continues until the lower bound of the selected clusters interval is reached. Finally, the number of clusters that present the highest value for the Calinski-Harabasz measurement is selected.

For the particular case of admission risk, the selection of the clusters ranking made by the user becomes easy since a large number of clusters (over 10) does not contribute any significant advantages in the final classification and it is difficult to make a later identification of the risk of each cluster by means of the assignation of the death rate that is obtained from the results of the medical interventions.

#### 3.1 Representation and Initialisation

One of the crucial aspects in the application of *GA* and meta-heuristic methods in general is the nature of each particular problem. In the case of *GA*, the problem is to determine which elements of the problem will be represented in each individual's chromosome. After assessing different proposals found in the existing literature for the application of *GA* to clustering [16–17], we chose to represent – in each chromosome – the set of centroids calculated in each iteration. In this way, the *GA* will be responsible for running the solution space in a higher hierarchical level and the method component, corresponding to the *k-means*, will be responsible for forming new cluster, assigning the individuals to the nearest centroid.

A random cluster creation was used for the initialization process, making sure that all clusters will have at least one individual. Later on, their centroids, which are used to create chromosomes, were calculated. This initialization process is done for all the individuals of the population.

### 3.2 Selection, Crossing, and Mutation

The selection was made using the *proportional or roulette method* [17], which is the method that is most commonly used when designing GA. To assign each cluster (or chromosome) its area in the roulette, the measurement of clustering quality called *sum of squares* [17] was used. The proportional method allows to choose, with higher probability, those individuals that have been better evaluated, but it does not discard those who have low qualification. Pairs of chromosomes are gathered for the crossover, the same individual may be selected more than once in subsequent crossovers. In this stage all that matters is to verify that the selected pairs correspond to different chromosomes.

To carry out the crossing, it is necessary to obtain the pair of individuals from the selection stage and to consult the crossing probability, which was previously assigned as an initial parameter of the program. If the indication is no-crossing, the selected chromosomes are copied to the new generation. On the contrary, if the indication is crossing, the crossing operator is applied and the offspring are assigned in the new population. The crossing operator works taking a random number of centroids from both parents in order to transmit them to the offspring. The total number of centroids must correspond to the number of clusters that are being looked for at that stage.

The representation of centroids that have been chosen facilitates this crossing operation because, in order to guarantee the creation of valid individuals it is only necessary to make sure that there are not repeated centroids. In case of repetition, a new centroid is chosen. Besides the aforementioned this representation does not require to manipulate the individual data for the crossing. It only requires to assign data to the nearest centroid and then recalculate the centroids to form the new generation.

The experimental tests showed that the centroid recalculation is a fundamental stage of this method because it improves substantially the results and the speed with which they are obtained. This recalculation may be interpreted as a local optimization that improves the quality of individuals before they are passed on to the next generation. To carry out mutation, we must consider the mutation probability that is established as an initial parameter of the program. In this way the values of a centroid that is chosen at random are aleatorily altered. When modifying some of the centroid's values, this moves through the solutions giving the opportunity of the production of new genetic material.

## 4 Results

The procedure followed for the cluster formation is centred in the adjustment of parameters to obtain the maximum values in the Calinski-Harabasz quality scale. After trying different parameter combinations, the quality measure reached a maximum of 48.4799 when forming four groups with a population of 20 individuals and crossing and mutation probabilities of 0.75 and 0.05 respectively.

Once the clusters have been formed, the problem is to create an ordinal risk scale for the groups. To this effect, in each group the proportion of dead and survivors was identified (death rate). If we accept that the use of technology avoids death, it is possible to affirm that the groups with the highest death rate correspond to the groups that presented a higher admission risk.

Figure 1 shows the groups in decreasing order according to the risk, with the dead number in each group. It is interesting to mention that when the number of groups increases or diminishes not only does the value of the quality measurement of the clustering decreases but also the difficulty to differentiate the risk based on death proportions increases.

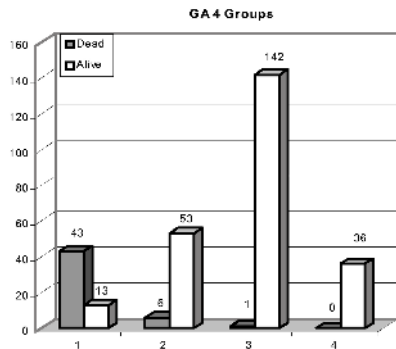


**Fig. 1.** Grouping obtained by the Genetic Algorithm (GA) for 4 groups. CH=48,4799.

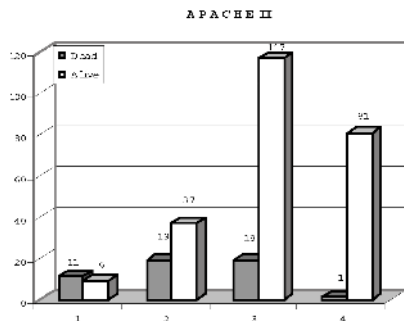


**Fig. 2.** Distribution of the dead in the groups formed by APACHE II.

It is important to assess what has been achieved with the clustering. To this effect we can resort to the APACHE method, which is the most commonly used method to determine risk at the moment of admission to the ICU. In the specific case of the units that have been mentioned, all the variables that conform the APACHE II index are registered. Using these variables it is possible to estimate the risk of each patient, using a logistic transformation that assigns a probability to the weighed score obtained from the APACHE II variables.

To make an equivalent comparison we formed four groups, gathering the individual risks in a decreasing order. Figure 2 shows the clustering made according to APACHE II index, indicating the number of dead and survivors in each cluster.

It is also interesting to compare the efficiency of the proposed GA method in relation to other traditional clustering methods. To carry out this comparison, a clustering was made using the k-means method assigning risk in the same manner as in the case of GA.

The presentation of results based on histograms is useful to identify the group risk, but does not offer an objective comparative parameter between the different methods. Given the fact that the comparison is based on the classification between dead and survivors, it is possible to measure the sensitivity and specificity to detect death as if each method were a binary death rate classifier, with the discrimination threshold taken from each of the generated clusters. Each binary classification generates a point (sensitivity, specificity). Using these, it is possible to draw an ROC curve and, in this way, the area below the ROC curve will be an objective comparative parameter. Figure 3 shows the ROC curves that measure the advantage of the death classification of APACHE II index (area equals

0.786); the k-means method (with a 0.888 area) and the proposed method that uses *GA* (with a 0.946 area).

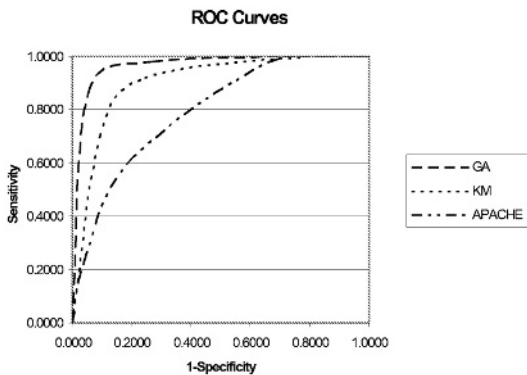


Fig. 3. ROC curves for GA, K-Means and APACHE.

As mentioned in the introduction, an important point in this design is the incorporation of information that contains the diagnosis hypotheses and therefore it would be interesting to assess the contribution of this information. In order to carry out this assessment, the 17 variables that represented the diagnosis hypotheses were withdrawn and the proposed method was applied again. The area below the ROC curve gave a 0.824 value.

## 5 Discussion

The histogram that appears in Figure 2 (APACHE II) shows the groups in a decreasing order according to their seriousness. However, in spite of this, the dead shows a more homogeneous distribution among the groups than the proposed model (Figure 1). This proves the difficulty that is found with the APACHE system to classify the patients' individual risks correctly (despite the fact that in this case the patients are grouped together). For this reason the APACHE system has been criticized because, although everybody recognizes its effectiveness to determine the number of patients that may die in a unit, it fails in the individual classification [18–19]. This limits its field to comparative studies between units and it does not offer guarantees when it is necessary to know the admission risk of a specific patient. But this is exactly what is needed to carry out an effectiveness analysis of the technologies that are used in a unit.

A more precise quantification of the differences between the *GA* grouping method and the APACHE system can be made comparing the ROC curve areas. Knowing that the perfect discriminator has an area that is equal to that of the unit, the *GA* grouping reaches 0.946, exceeding the ROC curve area reached by the APACHE II system by 0.161.

The influence of incorporating the *GA* to the method can be assessed when comparing the classification obtained through *GA* with the *k-means* classification. In this case we can see that the *GA* classification surpasses the curve obtained by *k-means* by 0.058. This is an indication that the sole idea of using simple grouping method produces an increase of 0.103 in the ROC curve area with respect to the classification obtained by the APACHE II system (36% of the gain is attributed to the *GA* and the remaining 64% corresponds to the grouping in an isolated way).

The experiment of deleting the variables that quantify diagnosis hypotheses shows that the inclusion of this information produces a decrease of 0.122 of the area, which corresponds to 75.8% of the gain obtained with the total of the variables proposed with respect to APACHE II.

From this analysis we can infer that the basic idea of using a non-supervised method such as clustering produces improvement with respect to the standard risk evaluation systems in medicine. But the highest values are achieved when we incorporate adequately the information contained in the diagnosis hypotheses and the use of *GA* to achieve a better clustering of patients by the risk.

## 6 Conclusions

Starting from the idea of using clustering analysis to build classifiers that may allow to classify patients according to their admission risk, this paper includes the diagnosis hypothesis quantification and the *GA* as the two main pillars that proved fundamental to achieve the results shown here.

We must point out the simplicity and capacity to be reproduced offered by diagnosis quantification, provided that we can count on the specialists to carry out the diagnosis classification. The main problem with this classification is the splitting of diagnoses into two degrees of acuteness: acute and hyperacute. This problem can be overcome through consensus meetings with groups of specialists.

From the application of *GA* to the clustering analysis, it is worth pointing out the simplicity of the representation and the crossing stage since the traditional applications for this problem present complex crossing operators [16–17], with high probability to create crippled descendants and loss of genetic material along the generations. The use of centroids in the chromosome formation allows to preserve more adequately the ancestors' best genetic material, circumscribing the random component exclusively to mutation.

A second stage in this research would be to increase the number of patients, trying to include all the existing pathologies in one ICU; to implement a classification system to carry out a prospective study that classifies the patients at the moment of admission and, later on, to assess the results achieved in the unit operation.

The extension of this method to other complex treatment systems such as Neonatal Intensive Care Units, Coronary Units or Multiple Trauma Units offers great possibilities since in these cases the pathologies are sometimes more restricted and it is possible to state the quantification of the diagnosis hypotheses even more accurately. But certainly the richest field for its application are the studies on Technology Assessment in

Health Care, where the admission risk assessment is fundamental to achieve technology effectiveness.

## References

1. L.I. Iezzoni: An introduction to risk adjustment. *Am J Med Qual* 11 (1996) p. 8–11.
2. N. Marvin, M. Bower, J.E. Rowe, and AI Group, De Montfort University, Milton Keynes, UK,: An evolutionary approach to constructing prognostic models. *Artif Intell Med*, 15 (1999) 155–65.
3. R.W. Evans,: Health care technology and the inevitability of resource allocation and rationing decisions. *JAMA* 249 (1983) 2047–2053.
4. J.R. Le Gall, S. Lemeshow and F. Saulnier,: new simplified acute physiology score (SAPS II) based on a European/North American multicenter study. *JAMA* 270 (1993) 2957–63.
5. W.A. Knaus, J.E. Zimmerman, D.P. Wagner, E.A. Draper and D.E. Lawrence,: APACHE-acute physiology and chronic health evaluation: a physiologically based classification system. *Crit Care Med* 9 (1981) 591–7.
6. M. Shwartz, L.I. Iezzoni, M.A. Moskowitz, A.S. Ash and E. Sawitz,: The importance of comorbidities in explaining differences in patient costs. *Med Care* 34 (1996) 767–82.
7. R. Dybowski, P. Weller, R. Chang and V. Gant: Prediction of outcome in critically ill patients using artificial neural network synthesised by genetic algorithm. *Lancet* 347 (1996) 1146–50.
8. C.A. Peña-Reyes and M. Sipper,: Evolutionary computation in medicine: an overview. *Artif Intell Med* 19 (2000) 1–23.
9. B. Sierra and P. Larranaga,: Predicting survival in malignant skin melanoma using bayesian networks automatically induced by genetic algorithms. An empirical comparison between different approaches. *Artif Intell Med* 14 (1998) 215–30.
10. J.D. Horbar, L. Onstad and E. Wright,: Predicting mortality risk for infants weighting 501–1500 grams at birth: A National Institute of Health Neonatal Research Network report. *Crit Care Med* 21 (1993) 12–8.
11. W.A. Knaus, E.A. Draper, D.P. Wagner and J.E. Zimmerman,: APACHE II: a severity of disease classification system. *Crit Care Med* 13 (1985) 818–29.
12. M.C. Weinstein and H.V. Fineberg, Clinical Decision Analysis, W.B. Saunders Company, Philadelphia, (1980).
13. M. Aldenderfer and R. Blashfield, Cluster Analysis, Sage University Paper, California (1984).
14. D.E. Goldberg, Genetic Algorithms in Search, Optimization Machine Learning, Addison-Wesley, Reading (1989).
15. T. Calinski and J. Harabasz, A Dendrite Method For Cluster Analysis. *Communications in Statistics* 3 (1974) 1–27.
16. H. Ding, A.A. El-Keib and R.E. Smith, Optimal Clustering of Power Networks Using Genetic Algorithms, TVGA Report No. 92001, University of Alabama, Tuscaloosa, AL (1992).
17. E. Falkenauer, Genetic Algorithms and Grouping Problems, John Wiley & Sons (1999).
18. R.B. Becker and J.E. Zimmerman,: ICU scoring systems allow prediction of patient outcomes and comparison of ICU performance. *Crit Care Clin* 12 (1996) 503–14.
19. G. Thibault, Prognosis and clinical predictive models for critically ill patients, Brockton-West Roxbury Veterans Affairs Medical Center, West Roxbury, Massachusetts, (2000).

# Mathematical Morphology on MRI for the Determination of Iberian Ham Fat Content

Andrés Caro<sup>1</sup>, Marisa Durán<sup>1</sup>, Pablo G. Rodríguez<sup>1</sup>, Teresa Antequera<sup>2</sup>,  
and Ramón Palacios<sup>3</sup>

<sup>1</sup> Dpto. Informática, Escuela Politécnica, Univ. Extremadura, 10071 Cáceres  
[andresc@unex.es](mailto:andresc@unex.es), [mlduran@unex.es](mailto:mlduran@unex.es), [pablogr@unex.es](mailto:pablogr@unex.es)  
<http://webepcc.unex.es/pablogr/jamon.html>

<sup>2</sup> Tecnología de los Alimentos, Facultad de Veterinaria, Univ. Extremadura, 10071 Cáceres  
[tantero@unex.es](mailto:tantero@unex.es)

<sup>3</sup> Servicio de Radiodiagnóstico, Hospital Universitario Infanta Cristina, Badajoz

**Abstract.** Intermuscular Fat Content and its distribution during the ripening process of the Iberian ham is a relevant task from the point of view of technological interest. This paper attempts to study the Iberian ham during the ripening process with images obtained from a MRI (*Magnetic Resonance Imaging*) device using Pattern Recognition and Image Analysis algorithms, in particular Mathematical Morphology techniques. The main advantage of this method is the non-destructive nature. A concrete algorithm is proposed, which is based on the Watershed transformation. In addition, the results are compared with the Otsu thresholding algorithm. The decreases of the total volume in the ripening process are shown. Also the decrease of the meat percentage and intermuscular fat content are calculated. As a conclusion, the viability of these techniques is proved for the possible future utilization in the meat industries to discover new characteristics in the ripening process.

## 1 Introduction

Image classification by segmentation is a very important aspect of the Computer Vision techniques. It is being applied in the field of Food Technology to determine some features of this kind of images, as for example the quantification and distribution of intermuscular fat content in the Iberian ham. In our study, these results will be computed attempting to improve the industrial process, since fat content and its distribution influences water loss and salt diffusion during the ripening process [1].

Iberian ham images have been processed in this research in order to find out some characteristics and reach conclusions about this excellent product. The Iberian pig is a native animal bred from the south-western area of Spain, and dry-cured ham from Iberian pig is a meat product with a high sensorial quality and first-rate consumer acceptance in our country. The ripening of Iberian ham is a long process (normally 18-24 months). Physical-chemical and sensorial methods are required to evaluate the different parameters in relation with quality, being generally tedious, destructive and

expensive [1]. Traditionally, the maturation time is fixed, when the weight loss of the ham is approximately 30% [2]. So, other methodologies have long been awaited by the Iberian ham industries.

The use of image processing to analyze Iberian products is quite recent. Some researches have processed flat images taken by a CCD camera from Iberian ham slices for different purposes [3, 4, 5]. They estimated some parameters in Iberian ham like intramuscular fat content [5] and marbling [3] or classified various types of raw Iberian ham [4]. The obtained results were very encouraging and suggestive to its application for the systematic inspection of Iberian products. However, although Computer Vision is essentially a non-destroying technique, ham pieces must be destroyed to obtain images using these techniques.

MRI (Magnetic Resonance Imaging) offers great capabilities to non-invasively look inside the bodies. It is widely used in medical diagnosis and surgery. It provides multiple planes (digital images) of the body or piece. Its application to the Food Technology is still recent and it is confined for researching purposes. Cernadas et al. [6, 7, 8] analyze MRI images of raw and cured Iberian loin to classify genetic varieties of Iberian pigs and to predict the intramuscular fat content [9]. The results are promising to its application to ham [10]. The loin is a uniform and simple muscle, and this is a very important advantage, comparing with the great number and complex distribution of muscles of the ham, being this one a significant drawback.

The image segmentation can be realized via the Mathematical Morphology methods. These techniques detect object structures or forms in images. A special method of segmentation is the Watershed Transformation, which is based on Mathematical Morphology [11, 12, 13]. In our paper, the Watershed Segmentation will be applied to characterize the quantification and distribution of the fat content in Iberian hams. The results of this last technique will be tested by a well-known segmentation method based on Otsu thresholding [14]. A comparative study between these two techniques is realized to analyze three regions in images (background, intermuscular fat content and meat).

This method is applied over a database of specific MR images from Food Technology, particularly Iberian ham images obtained at three different maturation stages (raw, semi-cured and dry-cured Iberian ham). Mathematical Morphology is used to achieve the quantification and distribution of intermuscular fat content in the total Iberian ham, studying its volume changes during the ripening process of the Iberian ham. The verification of the presented approach is shown examining these changes, and the obtained practical results may allow us to optimize time, temperature and salt content during ripening of Iberian ham.

## 2 Data Set

The presented research is based on MRI sequences of Iberian ham images. Its application to Food Technology is still recent and it is confined for researching purposes. Four Iberian hams have been scanned, in three stages during their ripening time. The images have been acquired using an MRI scan facilitated by the "Infanta Cristina"

Hospital in Badajoz (Spain). The MRI volume data set is obtained from sequences of T1 images with a FOV (field-of view) of 120x85 mm and a slice thickness of 2 mm, i.e. a voxel resolution of 0.23x0.20x2 mm. The total number of images in the obtained database is 252.

### 3 Classification Methods

Watershed transformation is used to classify different tissues in images of Iberian hams (based on regions), in comparison with thresholding segmentation Otsu method (based on pixels).

#### 3.1 Thresolding: Otsu Method

Otsu method is a widely used thresholding segmentation technique, which can be employed for classification of tissues. Concretely, Otsu and multi-level Otsu methods minimize the weighted sum of group variances: let  $\sigma_w^2$ ,  $\sigma_B^2$  and  $\sigma_T^2$  be the within-class, between-class variance, and the total variance, respectively [14]. An optimal threshold, t, can be determined by maximizing one of the following criterion functions with respect to t:

$$\lambda = \frac{\sigma_B^2}{\sigma_w^2} \quad \eta = \frac{\sigma_B^2}{\sigma_T^2} \quad \kappa = \frac{\sigma_T^2}{\sigma_w^2}$$

The Otsu segmentation method in Iberian ham for intramuscular fat content has been perfectly evaluated, in comparison with the chemical analyses that are realized habitually on this kind of meat [15].

#### 3.2 Mathematical Morphology: Watershed Segmentation

The Watershed transformation segments images into watershed regions [10]. Considering the gray scale image as a surface, each local minimum can be thought of as the point to which *water* falling on the surrounding drainage regions (figure 1).

Noise and small unimportant fluctuations in the original image can produce spurious minima, which leads to *oversegmentation*. Smoothing the original image is an approach to overcoming this problem.

We have used the Watershed Transformation to classify three different regions in Iberian ham images from MRI (background, meat and fat).

Figure 2 shows images from the proposed algorithm. Different regions can be appreciated in the Watershed images, and the classification in three categories.

The algorithm works over our database with original images (figure 2.A shows one these images). This image is filtered by a Morphological Closing algorithm, using

as structural element a disk with a radio of 5 pixels (figure 2.B). A median filter is used with a window size of 5x5 pixels. Next step consists on using a *Sobel* operator in order to detect boundaries, in which Watershed regions could be placed. The output image is converted to a binary image (bilevel image) and a median filter is applied again. All these steps (median filter, *Sobel* operator, binarization and median filter again) are necessary to avoid the *oversegmentation* of the regions with the Watershed Transformation.

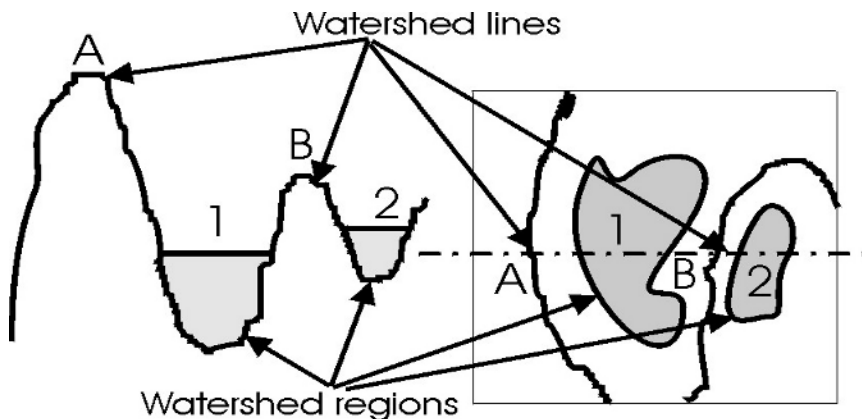


**Fig. 1.** Intuitive definition of the Watershed Transformation (Watershed regions: 1 and 2; Watershed lines: A and B).

When the image is correctly pre-processed the Watershed Transformation is applied, obtaining different interesting images. One of them is the figure 2.C, which shows Watershed regions. They are classified with the average gray level of the same regions over the original image. Another interesting image is the figure 2.D, with the original image mixed with the Watershed regions. Figure 2.E illustrates the final multi-level Otsu classification in three gray levels. Finally, the figure 2.F is the classification of the Watershed regions. They have been obtained by the proposed algorithm, which can be easily compared in the original image (2.A) and in the Otsu classification (2.E). The numerical results as well as the comparison of both methods are shown in the following sections.

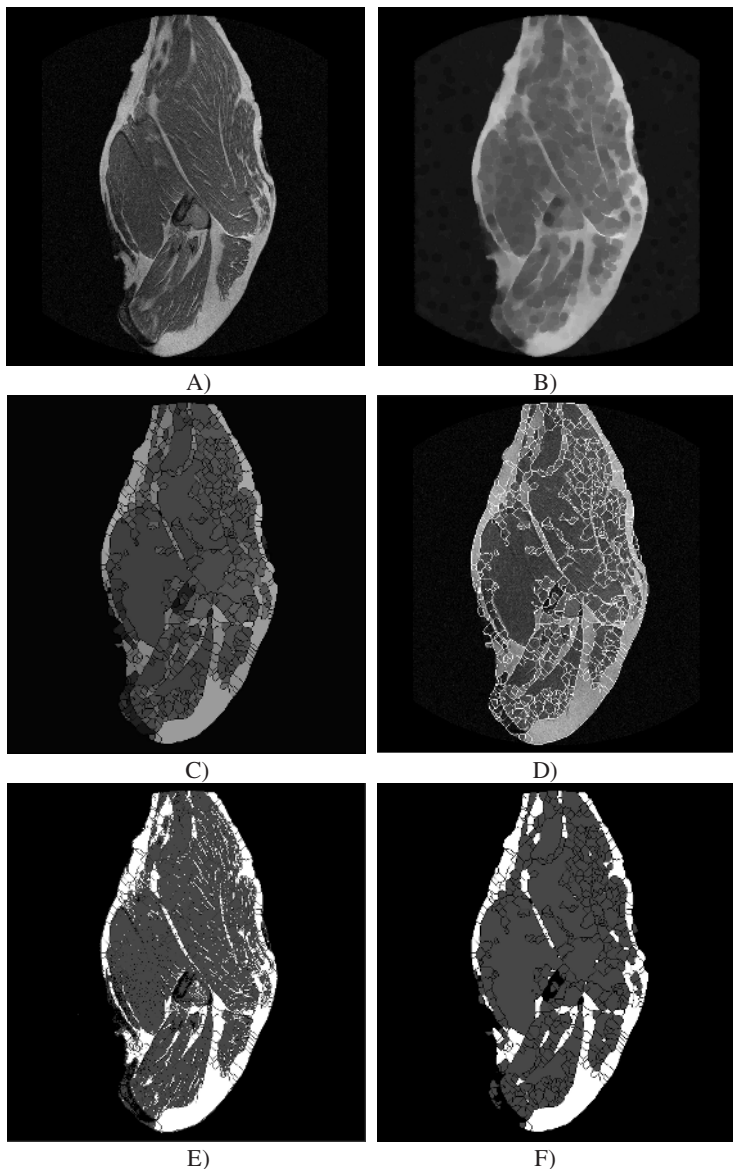


**Fig. 2.** Example images. A) Original image. B) Morphological closing. C) Watershed regions with the average of gray levels for each area. D) Binarization of the image with the watershed regions. E) Classification in three regions by thresholding with the Otsu method. F) Classification in three regions by the Watershed transformation.

## 4 Results

Four bar charts show the obtained results with the two tested algorithms. Three stages have been considered (MR images acquired) in the ripening process: raw, semi-dry and dry-cured ham.

The total volume decrease in the ripening process of the Iberian ham can be observed in the figure 3. The total absolute reduction is shown in figure 3.A, with the average of the four considered hams of this study. The comparative studies between both techniques (Watershed and Otsu) are quite similar. For example, the first bar of the graph shows values near 80.000 pixels in both cases. The percentage reduction has been 15-20% in average, from the initial to the final stage (figure 3.B).

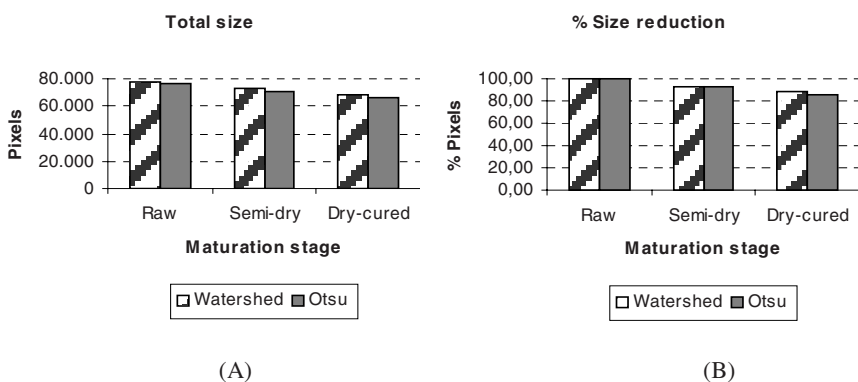


**Fig. 3.** Total size reduction, in absolute (A) and relative (B) values.

Figure 4 shows the percentage size of the fat (4.A) and meat (4.B) content as an average of the four hams (relative quantity in relation to the number of pixels in the ham area). The results are similar in the Watershed and Otsu segmentation as well.

In addition, as it was waited, the total size of the ham decreases; however, the relative quantity of fat content keeps more or less constant.

## 5 Discussion and Conclusions

The results obtained using both computer vision techniques are quite similar to the quantities calculated by the Food Technology specialists. They have estimated the total weight decrease at 30% in the Iberian ham during the same time. The proposed algorithm obtains a reduction of the ham size of about 15-20% approximately, in all the processed images. Therefore, a relationship between the ham weight decrease (30%) and total volume reduction (15%) could be established for the maturation time, as a first approximation. This size reduction could be caused by the loss of water dur-

ing the maturation process. Optimal ripening time could not be the same for different Iberian pig hams. By studying the percentage rate of volume during the process, it could be possible to predict the optimal ripening moment.

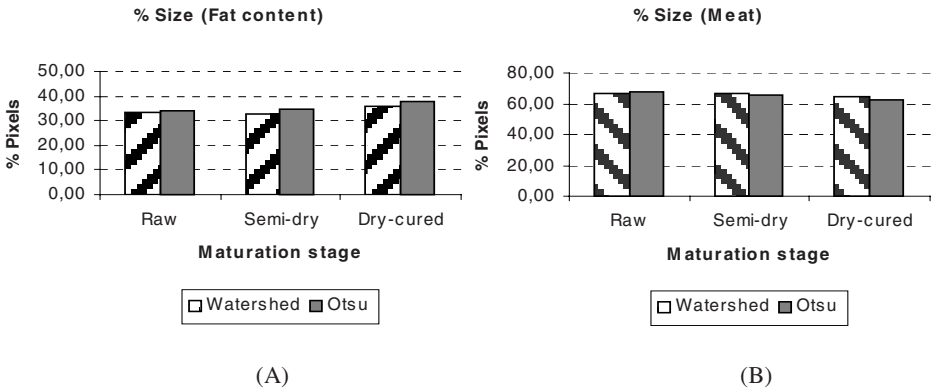


**Fig. 4.** Fat (A) and meat content (B), in percentage over the ham volume.

Discussing about both techniques, Otsu method could be considered a good way to evaluate the fat level, but it does not offer information about the distribution of fat, i.e. it is only a good quantification method. The classification process is realized pixel by pixel. Wrong pixel classifications could be achieved, for example when noisy pixels appears on the image.

On the other hand, Watershed transform classifies full regions into the selected class. This method catalogs the whole region (all the pixels of the watershed region) into the adequate category. Therefore, not only quantitative information is achieved by this method, but also its distribution inside of the image, which is quite important too.

The main aim of this paper is the quantification and distribution of the intermuscular and subcutaneous fat content. The selected method to this classification is Watershed Transformation, due to the fact that it not only computes the quantity of fat, but in addition the regions of fat content are perfectly located.

**Acknowledgments.** The authors are grateful to the Denominación de Origen “Dehesa de Extremadura” and the Hermanos Alonso Roa company from Villar del Rey (Badajoz). In addition, we wish to express our gratitude to the Department of Systèmes Logiques et Numériques in the University Libre de Bruxelles (Belgium). This work has been supported by Junta de Extremadura (Local Government), under the IPR98A03P and the 2PR01C025 projects.

## References

1. Antequera, T., López-Bote, C.J., Córdoba, J.J., García, C., Asensio, M.A., Ventanas, J. and Díaz, Y., "Lipid oxidative changes in the processing of Iberian pig hams", *Fod. Chem.*, 54, 105, 1992.
2. Cava, R. and Ventanas, J., "Dinámica y control del proceso de secado del jamón ibérico en condiciones naturales y cámaras climatizadas", *Tecnología del jamón ibérico*, Ed. Mundiprensa, 260–274, 2001.
3. Cernadas, E., Durán, M.L., Antequera, T., "Recognizing Marbling in Dry-Cured Iberian Ham by Multiscale Analysis". *Pattern Recognition Letters*, 23, pp.1311–1321, 2002.
4. Durán, M. L., Cernadas, E., Caro, A., Antequera, T., "Clasificación de distintos tipos de jamón ibérico utilizando Análisis de Texturas", *Revista Elec. Visión por Comp.*, N° 5, 2001.
5. Durán, M. L., Caro, A., Cernadas, E., Plaza, A., Petrón, M. J., "A fuzzy schema to evaluate fat content in iberian pig meat images", *Ibero-American Symp. Patt. Recog.*, 207–216, 2000.
6. Cernadas, E., Durán, M.L., Rodríguez, P.G., Caro, A., Muriel, E. and Palacios, R., "Estimating intramuscular fat content of cured Iberian loin using statistical analysis of its magnetic resonance images", *12<sup>th</sup> Portuguese Conference on Pattern Recognition*, 2002.
7. Cernadas, E., Plaza, A., Rodríguez, P.G., Durán, M.L., Hernández, J., Antequera, T., Gallardo, R. y Villa, D., "Estimation of Dry-Cured Iberian Ham Quality Using Magnetic Resonance Imaging", *5<sup>th</sup> Int. Conf. Applic. Mag. Resonance in Food Science*, pp.46–47, 2000.
8. Cernadas, E., Antequera, T., Rodríguez, P.G., Durán, M.L., Gallardo, R. y Villa, D., "Magnetic Resonance Imaging to Classify Loin from Iberian Pigs", *Mag. Resonance in Food Science*, pp. 239–254. Ed. The Royal Society of Chemistry, 2001.
9. Antequera, T., Muriel, E., Rodríguez, P.G., Cernadas, E., Ruiz J., "Magnetic Resonance Imaging as a Predictive Tool for Sensing Characteristic and Intramuscular Fat Content of Dry-Cured Loin". *Int. Journal of Science and Food and Agric.*, Vol.83, pp. 268–274, 2003.
10. Caro, A., Rodríguez, P.G., Cernadas, E., Antequera, T., "Disminución volumétrica del jamón ibérico durante su maduración analizando imágenes de Resonancia Magnética mediante Contornos Activos", *Revista "Información Tecnológica"* Vol. 13 N° 3, pp. 175–180, 2002.
11. Beucher, S. and Meyer, F., "The Morphological Approach to Segmentation: The Watershed Transformation", *Math. Morphology in Image Processing*, pp. 433–482, E.R. Dougherty, ed., New York, Basel, Hong Kong: Marcel Dekker, 1993.
12. Serra, J. "Image Analysis and Mathematical Morphology", Academic Press, New York. 1982
13. Caro, A., Rodríguez, P.G., Ávila, M., Rodríguez, F., Rodríguez, F.J., "Active Contours Using Watershed Segmentation", *9<sup>th</sup> Int. Workshop on Systems, Signal and Image Processing*, pp. 340-345, Manchester (UK), 7–8 November 2002.
14. Otsu, N., "A Threshold Selection Method from Gray-Level Histograms", *IEEE Trans. Systems, Man, and Cybernetics*, Vol. SMC-9, No. 1, Jan 1979.
15. Durán, M.L., Cernadas, E., Plaza, A., Sánchez, J.M., Rodríguez, F., Petrón, M.J., "Could Machine Vision Replace Chemical Procedure to Evaluate Fat Content in Iberian Pig Meat? An Experimental Study", *3<sup>rd</sup> Int. Conf. on Computer Vision, Pattern Recognition, and Image Processing*, pp. 256–259, Atlantic City, New Jersey (USA), 2000.

# Automatic Dark Fibres Detection in Wool Tops

Juan Bazerque, Julio Ciambelli, Santiago Lafon, and Gregory Randall

Instituto de Ingeniería Eléctrica  
Facultad de Ingeniería  
Universidad de la República  
`randall@fing.edu.uy`

**Abstract.** Is proposed a method for the automatic detection of dark fibres in wool tops based on image processing. A software which implements this method was developed, composed by five modules: KL projection, light correction, Gabor filtering, segmentation and morphology. The digital image are taken by a camera placed in a balanced illumination system. The method was calibrated and tested on 170 images marked by experts from Secretariado Uruguayo de la Lana.

**Keywords:** Dark Fibres Detection, Wool Industry, Balanced Illumination, Light Correction, Gabor Filtering

## 1 Introduction

### 1.1 Context

One of the problems of the wool industry is the presence of impurities in its raw material. One kind of this impurities are dark fibres coming from urine stain, black spots or other animal defects. These fibres remind coloured after the dying process, and appears as not desired dark lines, when tops destination is soft colour tissue production. Wool depreciates 15% [1] if it contains more than a specified number of dark fibres (DF) per Kg. The wool is collected from the sheep by shear, the fleece is then washed and combed. At this level the product is called wool top and is the input for the spinning industry.

In order to improve wool quality, is necessary to control the DF number as early as possible in the industrial process, but the difficulty of the problem is lower at the end of the industrial chain because the fibres are clean and parallelized. It exists a standardized method to manually count the DF per Kg on the top [2], in use at the Secretariado Uruguayo de la Lana (SUL).

In this article is presented an automatic solution for the counting module of DF in wool tops, integrating image processing techniques and the associated acquisition system.

### 1.2 Specification and Image Data Bases

Wool fibres are categorized by its coloration level in a 0 to 8 scale. The CSIRO standard [2] [3] defines as dark fibre those with level greater than 4 with the additional condition of being longer than 10mm [2].

Fibres diameter are between 20 and  $30\mu m$ . Working with a 1536x2048 resolution camera, a 18x24mm field of view was selected. A collection of 170 images of this size was acquired combining Merino and Corriedale races top samples. A SUL expert indicates the presence of DF in the images and gives its position and colour level. The data base formed by this images was divided in two groups, the A base, with 70 images for the system calibration and the B base reserved to validation. A new partition was made in de A base to form the sub-bases A1 and A2 with 20 and 50 images respectively.

### 1.3 Balanced Illumination System

To acquire the images the digital camera was placed on a controllable illumination system. The wool sample is placed between upper and below light sources. The light intensity is balanced to cancel white fibres shadows, vanish the background and enhance the presence of the DF [3][4]. Figure 1 shows the effect of this system comparing the same image acquired with wrong and balanced illumination.

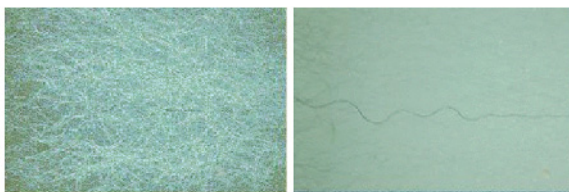


**Fig. 1.** Balanced illumination effect

## 2 Processes and Algorithms

### 2.1 Noise Reduction

The image is filtered by a median filter in order to reduce the image noise preserving borders [5].

### 2.2 Projection

The source image obtained from the balanced illumination system is RGB. To keep the software module compatible to a system implemented with an available high resolution B&W industrial camera, a projection was done at this point. In order to preserve as much DF information as possible in this process, a direction that statistically approximates the direction of the Karhunen Loeuve transform primary component was selected.

After finding this direction for the set of images in base A1, no relevant variation in its coordinates were found for other images. Therefore a statistically mean direction obtained in a training period was used to project the other images. This approximated direction was called AKL .

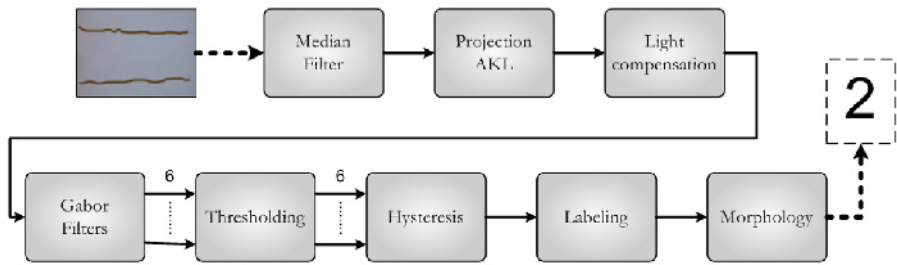


**Fig. 2.** Blocks diagram

### 2.3 Non Uniform Illumination Compensation

It was observed a non uniform illumination in the acquired images. The centre of the images are more illuminated than the border. Its effect is shown on figure 3 as at the surface representation.

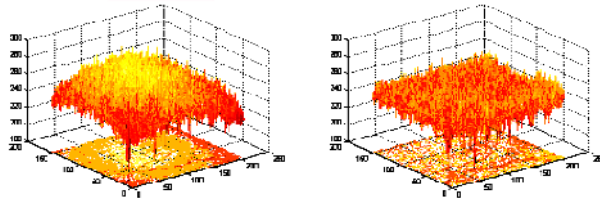


**Fig. 3.** Left: Surface representation of the acquired image. Right: image after non uniform illumination correction

To solve this problem a compensation step was introduced. A multiplicative model ( $\mathcal{I}(x, y) = \mathcal{P}(x, y)\mathcal{F}(x, y)$ ) was supposed, where  $\mathcal{I}$  is the original image,  $\mathcal{F}$  represents the uniformly illuminated image and  $\mathcal{P}$  is a parabolic surface with the maximum near the image centre. In order to estimate  $\mathcal{P}$ , a mean squares method is used with samples of  $\mathcal{I}$  as input data. Knowing  $\mathcal{I}$  and  $\mathcal{P}$ , it is possible to correct the acquired image using the multiplicative model.

### 2.4 Gabor Filters

The aim of this process is to extract from the image as much information as possible about DF presence. Gabor Filters [6] are used in order to enhance the dark fibres in a textured white background. The bank of filters are tuned for a maximum response in presence of the outlying fibre depending on its direction and diameter.

Impulse response of this filters are deduced by scale transformation and rotations from the Gabor function (1) formed by a complex exponential modulated by a gaussian.

$$f(x, y) = \frac{1}{2\pi\sigma_x\sigma_y} e^{-\frac{1}{2}\left(\frac{x^2}{\sigma_x^2} + \frac{y^2}{\sigma_y^2}\right)} e^{2\pi j f_h x} \quad (1)$$

The basic frequency of the filters are represented by  $f_h$ . The impulse response of the Gabor filters are given by

$$f_{pq}(x, y) = \alpha^{-p} f(x', y') \quad (2)$$

$$x' = \alpha^{-p} (x \cos(\theta_q) + y \sin(\theta_q)) \quad y' = \alpha^{-p} (-x \sin(\theta_q) + y \cos(\theta_q))$$

Where  $\alpha^{-p}$  is the scale factor and  $\theta_q$  the selected direction. Each filter acts as a directive bandpass filter with parameters p and q.

To design the filters, 3 central frequencies and 2 directions (vertical and horizontal) was chosen. The highest frequency was placed in  $f_h = 1/8$ . Following [7], with  $S = 3$  and  $L = 4$ , were calculated the remaining filter parameters  $\alpha$ ,  $\sigma_x$ ,  $\sigma_y$  and the lower and medium frequencies  $f_l$  and  $f_m$ , getting the following parameters:

$$\alpha = 2 \quad \sigma_x = 4.497 \quad \sigma_y = 1.038 \quad f_m = \frac{1}{16} \quad f_l = \frac{1}{32}$$

To evaluate the filter orientations, the formula  $\theta_q = \frac{\pi(q-1)}{L}$  was used, with  $q = 1 \dots 4$ .

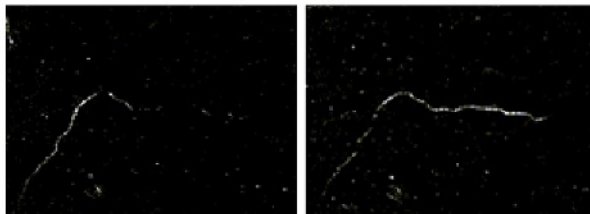


**Fig. 4.** Behaviour of two filters at the same frequency but in vertical and horizontal directions.

A FIR implementation was used for the filter realization. The used kernels are elongated, with axis size calculated in order to let place two times the Gaussian deviations in each direction.

The convolution kernel is applied to a subset of the input image formed by bidirectional subsampling in a 4 to 1 ratio.

Notice that the Gabor filtering separates the clusters corresponding to DF and background on the histogram of the image. Figure 5 shows the histogram of the expert marked pixels on the image before and after the Gabor filtering with an horizontal kernel.

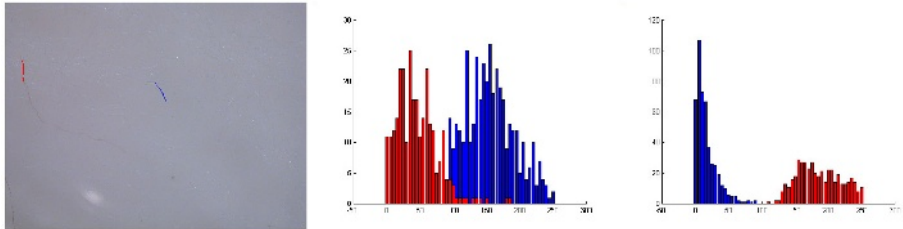


**Fig. 5.** Histogram of the expert marked pixels on the image before (left) and after (right) the Gabor filtering with an horizontal kernel.

## 2.5 Thresholding

The Gabor filter step generates 6 images: 2 orthogonal directions and 3 frequency bands. Each one is thresholded using a linear model in order to binarize the images after the Gabor filtering.

$$u_i = a_i \mu_i + b_i \sigma_i + c_i \quad i = 1 \dots 6 \quad (3)$$

The parameters of the linear model are estimated in a learning process using the A1 image set. On this set an expert marked, for each Gabor filter response, a set of pixels corresponding to DF and another similar sized set for the background cluster. These sets carry the necessary information to estimate an optimal threshold for these responses, as explained in next section.

Parameters  $a$ ,  $b$  and  $c$  of equation 3, are adjusted by a least squared method using the optimal thresholds estimated with the A1 data set.

**Optimal threshold.** Let be  $\mathbf{J}$  a statistical error cost function formed by prior cluster probabilities  $\mathcal{P}_F$  and  $\mathcal{P}_B$  (DF and background respectively), the classification error probabilities  $\alpha$  (classify a DF pixel as background) and  $\beta$  (classify a background pixel as DF), and the assigned error costs ( $\mathcal{C}(\alpha)$  and  $\mathcal{C}(\beta)$ ):

$$\mathbf{J} = \mathcal{P}_1 \mathcal{C}(\alpha) \alpha + \mathcal{P}_2 \mathcal{C}(\beta) \beta \quad (4)$$

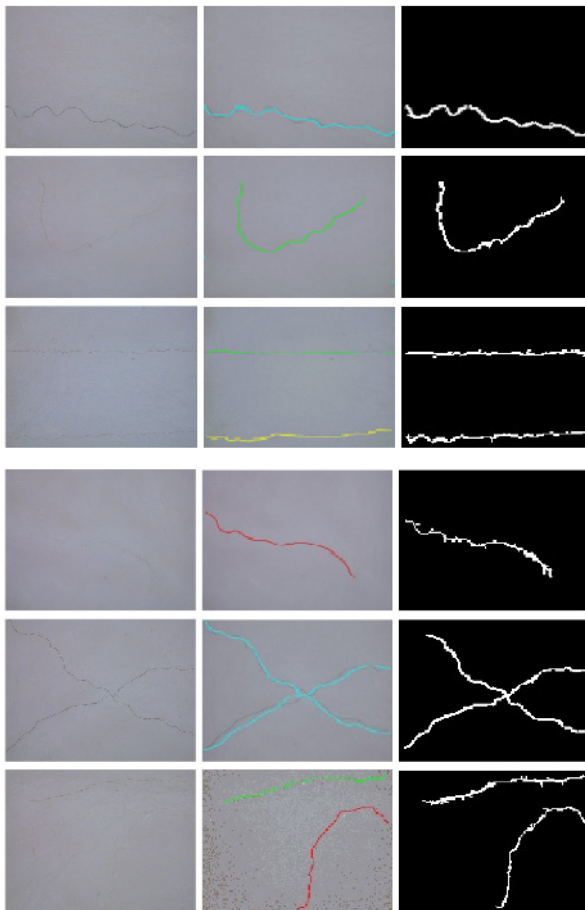
The optimal threshold will be the minimum of  $\mathbf{J}$  function. A Gaussian model for clusters distribution has been used.

The minimum of  $\mathbf{J}$  function solves the next equation

$$(\sigma_F^2 - \sigma_B^2)x^2 + 2(\sigma_B^2 \mu_F - \sigma_F^2 \mu_B)x + \mu_B^2 \sigma_F^2 - \mu_F^2 \sigma_B^2 - 2(\sigma_F \sigma_B)^2 \ln\left(\frac{\sigma_F}{\sigma_B}\right) = 0 \quad (5)$$

being  $\lambda = \frac{\mathcal{P}_B \mathcal{C}(\beta)}{\mathcal{P}_F \mathcal{C}(\alpha)}$ .

Once the Gaussian parameters  $\mu_F$ ,  $\mu_B$ ,  $\sigma_F$  and  $\sigma_B$  are extracted from the training test, optimal threshold is deduced from the equation 5. Changing the  $\lambda$  parameter allows the system to varies its sensibility, penalizing false positives or false negatives.

**Fig. 6.**

## 2.6 Dark Fibres Segmentation

Next step is to combine the 6 binarized images produced by the Gabor filter and threshold steps, into one binary output image with DF pixels marked.

First, the 6 binarized images are added pixel a pixel. On that new image, a directive hysteresis was used in order to select the pixels belonging to DF.

Directional thresholding hysteresis is done using two thresholds  $T_{high}$  and  $T_{low}$ . Pixels with values surpassing the  $T_{high}$  are settled as DF starting points. A convenient direction is browsed for each starting point, and a walking process start adding pixels in this direction as the  $T_{low}$  test is passed.

At each step, the process allows direction to vary  $30^\circ$  and if this test is not passed another intent is accomplished doubling the walking step.

Thresholds was settled to  $T_{high} = 5$  and  $T_{low} = [0.5, 3]$  according to the system sensitivity chosen.

## 2.7 Morphologic Operations

A labelling process [5] have been done on the resulting image, marking the regions which are associated to DF. The local and global angles, and the diameter are calculated for each region. This parameters are used to perform morphologic operations [13] to join regions belonging to the same dark fibres, and to eliminate small noisy regions.

## 3 Results

The image set B, formed by 100 images, were marked by an expert using the standardized manual procedure and processed by the automatic system. According to the SUL expert 87 of these 100 images has at least one DF. The total number of DF in the set is 118.

Table 1 presents the automatic success rates, categorized in fibres coloration levels, as the comparison between expert sentences and system sentences, applying to the same image. This table contains rates obtained placing  $\lambda = 2$  and  $T_{low} = 1.5$ .

**Table 1.**

fibre kind	fibres detected by expert	system success	success rate	95% confidence interval
5	16	15	94%	(77%, 100%)
6	29	26	90%	(76%, 98%)
7	42	42	100%	(98%, 100%)
8	31	31	100%	(97%, 100%)

Added to the previous table, the system made two false negatives in the 100 images set.

Figure 6 illustrates some results. The first column shows the image after the non uniform illumination step. For each image, the second column shows the DF marked by the expert. The DF colour category is detailed in a colour scale as follows: red: 5, yellow: 6, green: 7 and cyan: 8. The third column shows the dark fibres detected by the automatic system.

## References

1. Kremer, R.: *Personal communication* Facultad de Veterinaria, Universidad de la Repùblica.
2. Foulds, R.A., Wong, P., Andrews, M.W.: *Dark fibres and their economic importance* Wool technology and Sheep Breeding, Vol XXXII, N°11, 91–100

3. *Wool Contamination: Detection of dark fibre contamination on Merino wool* Fact\_sheet\_018, July 2001. Queensland Department of Primary Industries; Queensland, Australia.
4. IWTO(E)-13-88 *Counting of Coloured Fibres in Tops by the Balanced Illumination Method*. International Wool Textile Organization, London, U.K.
5. González, R.C., Woods, R.E.: *Tratamiento Digital de Imágenes*. Addison-Wesley, 1992.
6. Mallat, S.: *A Wavelet Tour of Signal Processing*, Academic Press, 1998
7. Kumar, A., Pang,G.K.H.: *Defect Detection in Textured Materials Using Gabor Filters*, IEEE Transactions on Industry Applications Vol 38, N°.2, March/April 2002.
8. Kittler, J.; *Pattern Recognition*, University of Surrey, Spring semester 1999.
9. DeHoff, R.: *The Essential Guide to Digital Video Capture*, Imagenation Corporation.
10. West, P.: *A Roadmap for Building a Machine Vision System*, Automated Vision Systems, Inc.
11. Delfosse, P., Galère, H., Grignet, J., Lemaire, P., Lkèonard, J., Longrèe, M., Muller, J., Paquet, V.: *Maesurement of Cleanliness in Combed Wool by Artificial Vision and Image Processing* The 9<sup>th</sup> International Wool Textile Reserch Conference, Vol 4, 97–105, June/July 1995.
12. Russ, J.C.: *The Image Processing Handbook* CRC Press Second Edition, 1994.
13. Coster, M.,Chermant, J.L.: *Precis d'Analyse d'Images* Presses Du CNRS, 1989.

# Musical Style Identification Using Grammatical Inference: The Encoding Problem\*

Pedro P. Cruz-Alcázar<sup>1</sup>, Enrique Vidal-Ruiz<sup>2</sup>, and Juan C. Pérez-Cortés<sup>1</sup>

<sup>1</sup> Departamento de Informática de Sistemas y Computadores  
Universidad Politécnica de Valencia  
Valencia, Spain  
[{ppcruz,jcperez}@disca.upv.es](mailto:{ppcruz,jcperez}@disca.upv.es)

<sup>2</sup> Departamento de Sistemas Informáticos y Computación  
Universidad Politécnica de Valencia  
Valencia, Spain  
[evidal@dsic.upv.es](mailto:evidal@dsic.upv.es)

**Abstract.** A Musical Style Identification model based on Grammatical Inference (GI) is presented. Under this model, regular grammars are used for modeling Musical Style. Style Classification can be used to implement or improve content based retrieval in multimedia databases, musicology or music education. In this work, several GI Techniques are used to learn, from examples of melodies, a stochastic grammar for each of three different musical styles. Then, each of the learned grammars provides a confidence value of a composition belonging to that grammar, which can be used to classify test melodies. A very important issue in this case is the use of a proper music coding scheme, so different coding schemes are presented and compared, achieving a 3 % classification error rate.

## 1 Introduction

Grammatical Inference (GI) aims at learning models of languages from examples of sentences of these languages. Sentences can be any structured composition of primitive elements or symbols, though the most common type of composition is the concatenation. From this point of view, GI find applications in all those many areas in which the objects or processes of interest can be adequately represented as strings of symbols. Perhaps the most conventional application areas are Syntactic Pattern Recognition (SPR) and Language Modeling. But there are many other areas in which GI can lead to interesting applications. One of these areas is Musical Style Identification (MSI). Here, the very notion of language explicitly holds, where primitive symbols or “notes” are adequate descriptions of the acoustic space, and the concatenation of these symbols leads to strings that represent musical sentences. By adequately concatenating symbols of a given musical system, a musical event emerges. However, not any possible concatenation can be considered a “proper” event. Certain rules dictate what can or can not be considered an appropriate concatenation, leading to the concept of

---

\* This work has been partially supported by CYCIT Project TIC2000-1703-C03-01 “TAR”.

*musical style.* Main features of a musical style are rhythm and melody, which are directly related with the rules used to concatenate duration and pitch of sounds, respectively.

The interest in modeling musical style resides in the use of these models to generate (Automatic Composition) and classify music by style (MSI), which are our areas of interest. The MSI area is being recently explored, mostly in the field of multimedia databases, trying to improve content based retrieval in multimedia databases, allowing indexing by musical style in addition to other suitable indexes. But other applications can be musicology (finding authors for anonymous pieces) or music education. Some AI techniques that have been employed are Hidden Markov Models [11], Self-Organising Maps [12] and Neural Networks [17]. This paper is focused in our MSI work [4] [5] that have been extended by adding new coding schemes for music.

## 2 Grammatical Inference

In this section we first quickly review the field of GI and later we will explain briefly the techniques used in our study. *Grammatical Inference* is a well established discipline originated by the work of Gold about “*Language Identification in the Limit*” [8]. Perhaps the most traditional applicative field of GI has been Syntactic Pattern Recognition; but there are many other potential applications. In general, GI aims of finding the rules of a grammar  $G$ , which describes an unknown language, by means of a positive sample set  $R_+ \subseteq \{ \alpha \mid \alpha \in L(G) \}$  and a negative sample set (of samples that should be rejected)  $R_- \subseteq \{ \beta \mid \beta \in \Sigma^* - L(G) \}$ . A more limited framework, but more usual in practice, is the use of only positive samples. The main problem lies in finding a more “*abstract*” or general grammar  $G'$  so that  $R_+ \subset L(G')$  and  $L(G') - R_+$  (the extra-language) contains only strings with “*similar features*” to the strings from  $R_+$ . A grammar  $G$  is said to be *identified in the limit* [8] if, for sufficiently large sample sets,  $L(G')=L(G)$ . Grammars and Formal Languages can be seen from a probabilistic viewpoint too, in which different rules have different probability of being used in the derivation of strings. The corresponding extension of GI is called *Stochastic Grammatical Inference* and this is the way of work of all the techniques used in our study. Next, we concisely explain three of the techniques used in our study to infer the grammars employed for *composing* and *identifying* musical styles. Other techniques employed with less success are Regular Positive Negative Inference (RPNI) [10] and a State Merging Technique based on probabilistic criteria called ALERGIA [3]. These techniques are fairly well known in the GI community and have been proven useful in other fields.

The Error-Correcting Grammatical Inference (ECGI) technique is a GI heuristic that was explicitly designed to capture relevant regularities of concatenation and length exhibited by substructures of unidimensional patterns. It was proposed in [14] and relies on error-correcting parsing to build up a stochastic regular grammar through a single incremental pass over a positive training set. This is achieved through a Viterbi-like, error-correcting parsing procedure [6] which also yields the corresponding optimal sequence of both non-error and error rules used in the parse.

Similarly, the parsing results are also used to update frequency counts from which probabilities of both non-error and error rules are estimated. One of the most used models in Natural Language Processing are N-Grams (a class of Markov models) [9]. An N-Gram is a sequence of symbols of length N. The first N-1 of these are the context. The size of N can in theory be anything from 1 upwards. However, certain values are better than others at capturing the characteristics of the language. The larger the value of N, the more context is captured. Though it would seem useful to have a great N, it is not a case of the larger the better. As N grows, it captures more context. Eventually the sequences learned become not just characteristic of the corpus, but the exact sequences in the corpus. The parameter estimation method can be consulted in [9]. In our study, modeling with N-Grams is performed using the CMU-Cambridge Statistical Language Modeling Toolkit (SLM-Toolkit) [13]. The k-TSI technique infers *k-Testable Languages in the Strict Sense* (k-TSSL) in the limit. It has been demonstrated that they are equivalent to N-Grams with N=k [15]. The main difference between them is that it is generally assumed that an N-Gram embodies the (N-i)-Grams [i=1..N], while a k-TSSL model consists only in the model of order k. The inference of k-TSSLs was discussed in [7] where the k-TSI technique was proposed.

As each inferred automaton or N-Gram model represents a musical style, “recognizing” the style of a test melody consists in finding the automaton which best recognizes this melody. This can be best achieved by using an algorithm that performs stochastic Error-Correcting Syntactic Analysis through an extension of the Viterbi algorithm [6]. The probabilities of error rules (Insertion / Deletion / Substitution) can be estimated from data [1]. The Analysis Algorithm returns the probability that the analyzed melody is (error-correcting) generated by the automaton. By analyzing the same melody with different automata, we classified it as belonging to the musical style (language) represented by the automaton that gave the largest probability.

### 3 How to Code Music for Syntactic Pattern Recognition

GI, as a Syntactic Pattern Recognition (SPR) technique, works with symbol strings. Even though only duration and pitch of sounds (as main features of music) are used in this work, the way they are represented implies the inclusion of more or less musical information. The amount and/or meaning of this musical information can be key in for the success in Musical Style Recognition (MSI). So, we have to deal with the selection of pitch and duration representations and the coding into symbol strings. Many efforts have been done within the Computer Music research community in musical representation systems and it is not clear that one system is always better than the others [2] [16] [18], being very dependant on the application and the recognition paradigm. In next subsections, we present the pitch and duration representations that, in our opinion, are more suitable for a SPR technique as GI, as well as some encoding examples into symbol strings. Brief comments will be done for every representation, according to its performance for MSI and Automatic Composition (AC) with GI.

### 3.1 Pitch Representation

**Absolute.** Pitch is most often represented either by the traditional pitch naming system (e.g. F#4-G#4-A4) or as absolute pitch (e.g. in MIDI: 66, 68, 69). It is the same representation as in musical scores, but may be insufficient for applications in tonal music. The main problem is that transpositions are not accounted for (e.g. repeating the same pitch motive transposed in different samples or within the same one).

**Relative.** A solution for the transposition problem is the use of the *relative pitch* between notes. That is, the *interval* (number of semitones) between two notes. There exists a somewhat ‘peculiar’ relationship between pitch strings and pitch interval strings. If one pitch interval in a string of pitch intervals is altered then *all* the succeeding notes are altered (transposed) [2]. So a change in a string of pitches and in a string of pitch intervals is not exactly the same thing. This effect appeared in our AC experiments [4].

**Melodic Contour.** Pitch interval encodings readily lend themselves to the construction of a number of more abstract representations of musical strings such as *contour strings*. Intervals can be categorised in a number of classes according to the signs of intervals. Instead of taking the absolute or relative pitch, it is coded if the next pitch goes “up” (U), “down” (D) or it is “equal” (E) to the last one. So, melodic contour can be represented as a string from the alphabet {U, D, E}, leading to a very small alphabet which provides less musical information than previous representations.

**Relative to Tonal Centre.** This coding scheme arose along with our experiments in AC [5] in order to correct the *relative* representation ‘peculiar’ effect mentioned before. Pitch is coded as the distance to the *tonal centre* or *tonic* in semitones. It includes more musical information than the others, as it allows characterizing relationships between pitches and *tonality*.

### 3.2 Duration Representation

In terms of the rhythmic component of musical strings, almost the same representations as pitch ones can be applied. It should be noted, however, that the problems that arise with pitch representations (highlighted in the previous section) apply also for duration representations.

**Absolute.** It is a direct translation of the representation used in musical scores (e.g. whole note, half note, quarter note, and so on). It is the most commonly applied in musical string processing algorithms [2] and, to this end, is the only one we have tested.

**Relative.** It is well known that listeners usually remember a rhythmic pattern as a relative sequence of durations that is independent of an absolute tempo. So, with *absolute* duration encoding, the same rhythmic pattern written with two different *metrics* will be considered as two different patterns. Representing rhythm as *duration ratios* can overcome augmentations or diminutions of a rhythmic pattern (Fig. 1).

**Rhythmic Contour.** Like melodic contour, durations can be coded in terms of *contour* strings. Instead of taking the absolute or relative duration, it is coded if the next duration is “shorter” (S), “longer” (L) or “equal” (E).

	♩ ♪ ♪ ♩		♩ ♪ ♪ ♩
dur.	12 2 2 8		6 1 1 4
ratios	<u>1/6</u> 1 4		<u>1/6</u> 1 4

**Fig. 1.** Two rhythmic patterns that match at the level of duration ratios are in fact the same

### 3.3 Musical String Representation

Notes can be coded as one symbol (what we call *not-splitted* encodings), or with two symbols (what we call  *splitted* encodings). In the beginning of our study, only *not-splitted* encodings were used, but we realized that these coding schemes could be establishing a relationship between the pitch and length stronger than the one generally existing in music. Therefore,  *splitted* encodings were introduced as a modification from previous ones, just separating with a space character the pitch and duration symbols (Fig. 2), obtaining better results in MSI (see section 5).

Combining pitch and duration representations exposed in the previous subsections, 12 *not-splitted* encodings can be defined. *Splitting* them, other 12 arise and, if pitches and durations are used stand-alone, 7 more emerge. As a result, we have 31 different coding schemes that can be tested. For naming conventions, the format “pitch representation name - duration representation name” is used (Fig. 2). The “ *splitted*” term is not used with *not-splitted* encodings. To this end, 13 coding schemes have been tested and results are presented in next section. In order to obtain the *musical string*, for these coding schemes, we have used numbers for pitch representations (except for *contour* representation) and letters for duration representation (only *absolute* representation has been tested). Thus, musical strings are easier to understand, as can be seen in Fig. 2.

Absolute-Absolute:  
22c 26c 24c 24c 24n 0c 24c 27c 24c 26c 27c 24c 22c 26c 22c 24c 26c 24n  
Relative-Absolute:  
Sc 4c -2c 0c 0n 99c 0c 3c -3c 2c 1c -3c -2c 4c -4c 2c 2c -2n  
Splitted Contour-Absolute:  
S c U c D c E c E n R c E c U c D c U c D c D c U c D c U c D n

**Fig. 2.** A Gregorian style score coded with different representations

## 4 Experiments

We chose 3 occidental musical styles from different epochs and we took 100 sample melodies from each one. These samples were 10 to 40 seconds long. The first style was *Gregorian Chant*. As a second style, we used passages from the sacred music of *J. S. Bach*. The third style consisted of passages from *Scott Joplin's Ragtimes*. Experiments in Style Identification were performed using ECGI, k-TSI, N-Grams and other GI techniques (mentioned in section 3). Three automata (one per style) are inferred with each GI technique, trying different values of  $k$  (with k-TSI) and  $N$  (with N-Grams). Test melodies are analyzed to see which of the learned automaton can generate them with the greatest probability. Given the small size of the available corpus, 10-fold *Cross-Validation* was used to measure the identification accuracy of the different techniques and coding schemes. *Average Classifying Error* in identification for each style was obtained and the best results are presented here.

### 4.1 Results

For the sake of conciseness, results will be summarized in Table 1, which shows the best *Average Classifying Error* for each GI technique with some of the tested encodings. Due to N-Gram's results, the *stand-alone* and *tonal centre* encodings have only been tested with them. Results are worst than the obtained with the other coding schemes, being the best one a 6.66 % classifying error when using *tonal centre* pitch representation.

**Table 1.** Classifying Error in Musical Style Identification experiments with the different GI techniques and coding schemes employed

	ECGI	K-TSI	N-GRAM
<i>Absolute-Absolute</i>	34.33 %	10 %	4.66 %
<i>Relative-Absolute</i>	13.66 %	8.66 %	<b>4.33 %</b>
<i>Contour-Absolute</i>	8.66 %	7 %	5.33 %
<i>Tonal Centre-Absolute</i>			5.33 %
<i>Splitted Absolute-Absolute</i>	9.66 %	5.66 %	3.33 %
<i>Splitted Relative-Absolute</i>	<b>7.66 %</b>	<b>5 %</b>	<b>3 %</b>
<i>Splitted Contour-Absolute</i>	10 %	5.66 %	5.33 %
<i>Splitted Tonal Centre-Absolute</i>			4.66 %

### 4.2 Discussion

Analyzing these results by GI techniques, the best of them is clearly the N-Gram technique. A 3% error in Style Identification is obtained, comparing with a 5% using k-TSI and a 7.66 % using ECGI techniques. Although comparisons with the success rates of other style identification models is not very meaningful unless the same datasets are used, if we look to other similar studies [11] [12] [17], these average rates of success can be considered as quite good. It is worth noting that GI techniques tend

to need a larger quantity of training samples to get good results. So, it is expected that our results will be improved if the amount of training samples is increased. The advantage of the N-Gram technique, over k-TSI and ECGI, relays on using the *Back-off smoothing* procedure within the analysis algorithm [9]. It is well known in the Pattern Recognition community that N-Gram inference with back-off smoothing outperforms many other Syntactic Pattern Recognition techniques and, in our study, this has been a fact.

Although the GI technique used for modeling musical style is very important, as seen before, our study has shown that the musical string representation is determinant in the results. It is clear that with the *relative* pitch representation are obtained the best results, consequently, it is expected that *relative* duration representation will be a good option to try in the future, specially  *splitted relative-relative* encoding. The *stand-alone* encodings results are bad, showing the necessity of more musical information within the coding scheme. Thus, we do not consider the future use of the remainder (*relative* duration and *contour* duration). Although with *tonal centre* representation, Automatic Composition results were improved, in MSI it has been very different. It can be due to this approach does not accounts for transpositions of a pattern within the same piece. An important fact is that *contour* pitch encodings, specially the  *splitted* one, have not achieved as good results as the others. It is due to the small size of the alphabet (symbols) for these coding schemes (e.g. only 9 symbols for Gregorian style in the splitted encoding).

Another conclusion of the study is that  *splitted* encodings are clearly better than joined pitch and duration representations. As a result of this discussion, for future studies, we can discard *contour* and *stand-alone* representations, remaining 6 combinations with *relative* duration representations to be tested. Of them, the  *splitted* encodings are expected to be the best.

## 5 Conclusions and Future Works

A Musical Style Identification (MSI) model based on Grammatical Inference is presented. Different coding schemes for music have been proposed and compared according to their suitability for working with Syntactic Pattern Recognition techniques and the results obtained in our experiments. Result from this work shows the need of proper music coding schemes, being the most important the use of two separated symbols (pitch and duration) for the encoding of each musical note. The best results in MSI have been obtained with the N-Gram technique, achieving a 3 % classifying error. Several lines of study can be followed to attempt improving results. First, the amount of data used so far is insufficient and better performance is expected by increasing the number of training samples. From the coding schemes presented in this work there are still 6 to be tested. Of course, other coding schemes must be explored, as trees or strings labelled with information about modulations or harmony. Once these tasks are dealt with, we could employ entire musical pieces as samples, and not just small fragments as was done in this study.

## References

1. Amengual, J.C.; Vidal, E. 1996. Two Different Approaches for Cost-efficient Viterbi Parsing with Error Correction. Advances in Structural and Syntactic Pattern Recognition, pp. 30-39. P. Perner, P. Wang and A. Rosenfeld (eds.). LNCS 1121. Springer-Verlag.
2. Cambouropoulos, E. et al. 2001. Pattern Processing in Melodic Sequences. Computers and the Humanities 35(1):9–21
3. Carrasco, R.C.; Oncina, J. 1994. Learning Stochastic Regular Grammars by means of a State Merging Method. “Grammatical Inference and Applications”. Carrasco, R.C.; Oncina, J. eds. Springer-Verlag, (Lecture notes in Artificial Intelligence (862)).
4. Cruz, P.; Vidal, E. 1998. Learning Regular Grammars to Model Musical Style: Comparing Different Coding Schemes. Proceedings of the 4<sup>th</sup> International Colloquium on Grammatical Inference ICGI-98, Vasant Honavar, Giora Slutzki (Eds.) Lecture Notes in Artificial Intelligence 1433, Subseries of Lecture Notes in Computer Science.
5. Cruz, P.; Vidal, E. 2003. Modeling Musical Style Using Grammatical Inference Techniques: a Tool for Classifying and Generating Melodies. Proceedings of the 3<sup>rd</sup> International Conference on Web Delivering of Music (WEDELMUSIC 2003), Leeds, UK. To appear in September 2003. IEEE Computer Society.
6. Forney, G. D. 1973. The Viterbi algorithm. IEEE Proc. 3, pp. 268–278.
7. García, P.; Vidal, E. 1990. Inference of K-Testable Languages In the Strict Sense and Application to Syntactic Pattern Recognition. IEEE Trans. on PAMI, 12, 9, pp. 920–925.
8. Gold, E. M. 1967. Language Identification in the Limit. Inf. and Control, Vol. 10, pp. 447–474.
9. Jelinek, F. 1998. Statistical Methods for Speech Recognition. MIT Press.
10. Oncina, J.; García, P. “Inferring regular languages in polynomial update time. Pattern Recognition and Image Analysis”. N. Pérez de la Blanca, A. Sanfeliú and E. Vidal eds. World Scientific, 1992.
11. Pollastri, E.; Simoncelli, G. 2001. Classification of Melodies by Composer with Hidden Markov Models. Proceedings of the First International Conference on WEB Delivering of Music WEDELMUSIC’01. IEEE Computer Press, pp. 88–95.
12. Ponce de León, P. J.; Iñesta, J. M. 2002. Musical Style Identification Using Self-Organising Maps. Proceedings of the Second International Conference on WEB Delivering of Music WEDELMUSIC’02. IEEE Computer Press, pp. 82–92.
13. Rosenfeld, R.; Clarkson, P. 1997. Statistical Language Modeling using the CMU-Cambridge Toolkit. Proceedings of the Eurospeech’97. Volume 5, pages 2707–2710.
14. Rulot, H.; Vidal, E. 1987. Modelling (sub)string-length based constraints through a Grammatical Inference method. NATO ASI Series, Vol. F30 Pattern Recognition Theory and Applications, pp. 451–459. Springer-Verlag.
15. Segarra, E. 1993. Una Aproximación Inductiva a la Comprensión del Discurso Continuo. PhD diss. Facultad de Informática. Universidad Politécnica de Valencia.
16. Selfridge-Field, E. 1998. Representing Musical Information for Retrieval. Invited talk, Association for Computing Machinery: SIGIR: Exploratory Workshop on Music Information Retrieval, Berkeley, CA; 19 August 1998.
17. Soltau, H. et al. 1998. Recognition of Music Types. Proceedings of the International Conference on Acoustics, Speech and Signal Processing ICASSP 98, pp. 1137–1140. Seattle, Washington.
18. Wiggins, G. et al. 1993. A Framework for the Evaluation of Music Representation Systems. Computer Music Journal 17(3):31–42

# New Distance Measures Applied to Marble Classification

J. Caldas Pinto, J.M. Sousa, and H. Alexandre

Technical University of Lisbon, Instituto Superior Técnico  
Dept. of Mechanical Engineering, GCAR/IDMEC  
1049-001 Lisbon, Portugal  
[{jcpinto,j.sousa}@dem.ist.utl.pt](mailto:{jcpinto,j.sousa}@dem.ist.utl.pt)

**Abstract.** Automatic marble classification based on their visual appearance is an important industrial issue, but due to the presence of randomly distributed high number of different colors and its subjective evaluation by human experts, the problem remains unsolved. In this paper, several new measures based on similarity tables built by human experts are introduced. They are used to improve the behavior of some clustering algorithms and to quantitatively characterize the results, increasing the correspondence of the measures to the visual appearance of the results. The obtained results show the effectiveness of the proposed methods.

## 1 Introduction

Ornamental stones are quantitatively characterized by properties such as geological-petrographical and mineralogical composition, or mechanical strength. However, the properties of such products differ not only in terms of type, but also in terms of origin, and their variability can also be significant within the same deposit or quarry. Though useful, these methods do not fully solve the problem of classifying a product whose end-use makes appearance so critically important. Appearance is conditioned not only by the kind of stone, but it also depends on the subjective evaluation of “beauty”. Traditionally, the selection process is based on human visual inspection, given a subjective characterization of the materials’ appearance, instead of an objective, reliable measurement of the visual properties, such as color, texture, shape and dimensions of their components. Yet, quality control is essential to keep marble industries competitive: shipments of finished products (e.g. slabs) must be of uniform quality, and the price demanded for a product, particularly a new one, must somehow be justified. Thus, it is very important to have a tool for the objective characterization of appearance.

In this paper, we are concerned with marble classification. Several clustering techniques for this purpose are presented and discussed. In order to support these algorithms and to better emulate results obtained by human experts, several new distances and measures are proposed. Hence, we introduce a so-called *Weighted Manhattan* (WM) distance, whose weights are determined by a genetic algorithm, which optimizes a distance between marbles based on a similarity table built by human experts. This distance is used to automatically cluster the marbles. The clustering techniques obtain the clusters based on a set of features. These features are derived by a quadtree based segmentation analysis of marble images, as previously presented and discussed in [6,7]. The clustering results are evaluated by the proposed new error measures, which are motivated by

the fact that standard error measures do not satisfactorily agree with the classification results obtained by visual inspection of human experts. The proposed measures are the *similarity table* and the *similarity score*, which are based on expert evaluations.

This paper is organized as follows. In Section 2 the distance measures are presented, and the weighted Manhattan distance, the similarity error and the similarity score, which are all proposed in this paper, are described. Section 3 presents a short description of the clustering algorithms used in this paper, namely, simulated annealing, fuzzy c-means, neural networks, and Takagi-Sugeno fuzzy models optimized by genetic algorithms. The application to real marbles data is discussed in Section 4. This section presents the results demonstrating the validity of the approaches introduced in this paper. Section 5 concludes the paper, giving guidelines for future developments in this important area.

## 2 Distance Measures

The evaluation of the obtained results can be a significant problem in situations where the visual appearance dictates the qualitative results. Sometimes results are visually very good but this fact is not revealed using standard error measures. On the other hand, a team of experts can build a so-called *similarity table* where, for each marble, those that could be considered very similar in appearance, from the available collection, are indicated. In the application in this paper, this number varies from 2 up to 10 marbles with an average of 4. The marbles considered to be similar to a given marble are called *neighbors*. The table containing the marbles that are similar to a given example is called the *complete similarity* (CS) table. From this table another was derived, with a maximum number of 4 neighbors, and where a weight  $\omega$  reflecting the number of votes received from the experts was added to each neighbor. This table is named *weighted similarity* (WS) table.

### 2.1 Weighted Manhattan Distance

The weighted similarity table can be used to develop a new distance measure, the so-called *Weighted Manhattan* distance, which can find correct neighbors for new marbles in a simple way. The WM distance between the points  $x_m$  and  $x_n$  is given by:

$$d_w = \sum_{i=1}^N \alpha_i |x_{m_i} - x_{n_i}|^{\beta_i}, \quad (1)$$

where  $i = 1, \dots, N$  are the coordinates of the space (features) with dimension  $N$ . The weights  $\alpha_i$  and  $\beta_i$  are determined by optimizing the cost function

$$J^{(k)} = \sum_{i=1}^{N_d} \sum_{v=1}^{n_{\max}} \omega_{iv} S(n_{iv} - n_{iv}^{(k)}) \quad (2)$$

where  $k$  is the iteration of an optimization algorithm,  $N_d$  is the total number of data points,  $n_{\max}$  is the maximum number of neighbors defined for each data point,  $n_{iv}$  is the  $v$  neighbor of data point  $i$ ,  $n_{iv}^{(k)}$  is the  $v$  neighbor defined at step  $k$ , and  $\omega_{iv}$  is the

weight, defined by the experts, associated to the  $v$  neighbor of data point  $i$ . The function  $S$  is simply given by

$$S(n_{iv} - n_{iv}^{(k)}) = \begin{cases} 0, & \text{if } n_{iv} \neq n_{iv}^{(k)} \\ 1, & \text{otherwise} \end{cases} \quad (3)$$

Note that in this paper the data points are marbles,  $N_d$  is equal to 112, and  $n_{\max}$  was settled to 4. A standard genetic algorithm based on real code [5] was used to optimize the weights  $\alpha_i$  and  $\beta_i$  in (1). Due to lack of space, we do not present the genetic algorithm parameterization in this paper.

## 2.2 Similarity Error and Similarity Score

This paper intends to cluster a given collection of marbles from a set of features, in order to be able to classify these marbles. Besides the visual appearance of the results, which is in general very good, it is important to evaluate quantitatively the classification results in order to compare different algorithms. However, the most common error measures based on the differences between the original marble classification and the attributed one are not consistent with the visual quality of the clusters. This is mainly due to the difficulty of experts in attributing a certain class to a given marble. Most marbles could be classified in a different, although similar, way. Based on the importance of the visual appearance, the CS table can be used to evaluate the clustering algorithms. Therefore, this paper introduces two new measures, which are called *similarity score* and *similarity error*, respectively.

Let  $V_{x_i}$  be the set of neighbors of the marble  $x_i$  and  $C_j$  be the cluster  $j$  with  $n_j$  elements. A score for the cluster  $C_j$  can be defined as

$$SC_j = \sum_{i=1}^{n_j} \#(V_{x_i} \cap C_j). \quad (4)$$

The global score of a given clustering algorithm for the total number of clusters  $n_c$  is given by:

$$SC = \sum_{j=1}^{n_c} SC_j \quad (5)$$

On the other hand, a marble is wrongly integrated in a cluster if there are no marbles of its neighborhood in that cluster. So a *similarity error* measure can be defined as follows:

$$SE_j = \sum_{i=1}^{n_j} f(V_{x_i} \cap C_j), \quad (6)$$

where

$$f(V_{x_i} \cap C_j) = \begin{cases} 1, & \text{if } V_{x_i} \cap C_j = \emptyset \\ 0, & \text{otherwise} \end{cases} \quad (7)$$

And the global error of a given clustering algorithm for the total number of clusters  $n_c$  is given by:

$$SE = \sum_{j=1}^{n_c} SE_j \quad (8)$$

This measure can be normalized in order to facilitate the comparisons. The normalization is given by:

$$se = \frac{SE}{N_d} \quad (9)$$

The similarity score  $SC$  and the similarity error  $SE$  are related but not dual, as it will be clear in the results presented in Section 4.2.

### 3 Clustering Algorithms

This paper uses both supervised and unsupervised clustering methods. The unsupervised methods do not use the training set classification to derive the proper clusters. This type of algorithms has a cost function that must be optimized. The classification of a given data point (marble) is achieved through the distance of its features to the respective clusters. This paper uses two types of unsupervised clustering algorithms: simulated annealing and fuzzy c-means. In the supervised methods, the classification given in the training set is used to derive the clusters. Thus, the classification is achieved through the simulation of the derived model, where the inputs are the marbles to be classified. The supervised methods applied in this paper are neural networks, and fuzzy models optimized by a genetic algorithm.

Let  $\{\mathbf{x}_1, \dots, \mathbf{x}_{N_d}\}$  be a set of  $N_d$  data objects where each object is an instance represented by the vector  $\mathbf{x}_i \in \mathbb{R}^N$ , which is described by a set of  $N$  features. The set of data objects can then be represented as a  $N_d \times N$  data matrix  $\mathbf{X}$ . The clustering algorithms used in this paper determine a partition of  $\mathbf{X}$  into  $C$  clusters.

#### 3.1 Simulated Annealing

This optimization algorithm simulates the annealing process, by reproducing the crystallization process of particles. These particles move during the solidification process, which occurs when the temperature decrease. In the final stage, the system reaches the minimal energy configuration [8]. The process starts at an initial temperature, which should consider the number of changes that increases the system energy, in order to allow the system to escape from local minima. This algorithm defines the proportion for acceptable changes that increases the system's energy. The cost function is represented by the Euclidean, Manhattan, or weighted Manhattan distances between the data points and the cluster centers. This cost function indicates if the system is converging or not to a lower energy state. The number of iterations to accomplish at each temperature is proportional to the number of elements. This parameter is proportional to the dimension of the data set  $N_d$ . The temperature  $T$  must decrease between the several energy levels. For consecutive levels, the temperature decrement is given by

$$T^{(k+1)} = d \cdot T^{(k)} \quad (10)$$

The *stop criterion* can be given by a predetermined number of temperature decreases or when after some consecutive temperature decreases the final cost does not change.

### 3.2 Fuzzy C-Means

Considering the set of data objects  $\mathbf{X}$ , the fuzzy c-means algorithm determine a fuzzy partition of  $\mathbf{X}$  into  $C$  clusters by computing a  $N_d \times C$  partition matrix  $\mathbf{U}$  and the  $C$ -tuple of corresponding cluster prototypes [2]:

$$\mathbf{V} = [\mathbf{v}_1, \dots, \mathbf{v}_C]. \quad (11)$$

Most often, the cluster prototypes are points in the cluster space, i.e.  $\mathbf{v}_i \in \mathbb{R}^N$ . The elements  $u_{ik} \in [0, 1]$  of  $\mathbf{U}$  represent the membership of data object  $\mathbf{x}_k$  in cluster  $i$ . This paper uses the standard fuzzy c-means algorithm, as described in [2,1]. Note however, that two distance measures are used; the Euclidean and the WM distances.

### 3.3 Neural Networks

Neural networks have been largely used as input-output mapping for different applications including modeling, control and classification [4]. The main characteristics of a neural network are its parallel distributed structure and its ability to learn, which produces reasonable outputs for inputs not encountered during training. Moreover, the structure can be chosen to be simple enough to compute the output(s) from the given input(s) in very low computational time.

The neural network used in this paper has hidden-layers with hyperbolic tangent activation functions and a linear output layer. The network must have few neurons in the hidden-layers, and is trained using the resilient backpropagation algorithm [3].

### 3.4 Fuzzy Models

Fuzzy models have gained in popularity in various fields such as control engineering, decision making, classification and data mining [10]. One of the important advantages of fuzzy models is that they combine numerical accuracy with transparency in the form of rules. Hence, fuzzy models take an intermediate place between numerical and symbolic models. A method that has been extensively used for obtaining fuzzy models is fuzzy clustering. Several fuzzy modeling approaches to classification based on fuzzy clustering, have been compared in [11]. From the ones compared the optimization of Takagi-Sugeno fuzzy models using a genetic algorithm (GA) as described in [9] proved to be the best, and as so, this algorithm is applied in this paper.

## 4 Application: Marble Classification

### 4.1 Parameters of the Algorithms

The clustering algorithms are tested for two situations: clustering veins for the color with more elements, where the training set has 29 marbles and the test set 14 marbles, and clustering colors, where the training set has 69 marbles and the test set 43 marbles.

First, simulated annealing and fuzzy c-means was applied using the Euclidian distance and the weighted similarity distance. These classifiers used 6 and 3 clusters to

classify marbles color and marbles veins, respectively. In the SA algorithm, the acceptable change used to compute the initial temperature is 0.3, the constant used to compute the number of iterations to accomplish in each temperature is set to 5, the parameter  $d$  in (10) is equal to 0.9; and finally 100 temperature decreases are allowed.

In the feedforward neural networks, the parameters are derived experimentally in order to obtain good classification results. In this paper, three hidden layers with 9, 12 and 9 neurons showed to derive the best classification results. The number of epochs is set to 100, in order to avoid overfitting.

The Takagi–Sugeno fuzzy models returns as output a real number, which must be transformed to a given class  $c_k$ . As so, the output of the model  $y$  is set to a class as follows:

$$c_k = \text{round}(y). \quad (12)$$

The classification value  $c_k$  corresponds to the set  $c_k \in \{1, 2, 3\}$  for the case of the veins, and to the set  $c_k \in \{1, 2, 3, 4, 5, 6\}$  when the colors are classified.

## 4.2 Results

Table 1 presents the comparison of the results obtained for vein classification. The error measures are the the following:  $e$  – mean classification error,  $SC$  – global score of clusters as defined in (5) and  $se$  – normalized similarity error, as defined in (9). The clustering algorithms in Table 1 are the simulated annealing (SA), the simulated annealing using the WM distance (SAw), the fuzzy c-means (FC), the fuzzy c-means using the WM distance (FCw), neural networks (NN) and the fuzzy model optimized by genetic algorithms (FGA). Table 2 presents the comparison of the results obtained for color classification. The notation used in Table 1 stands also for Table 2.

**Table 1.** Comparison of the results obtained for vein clustering.

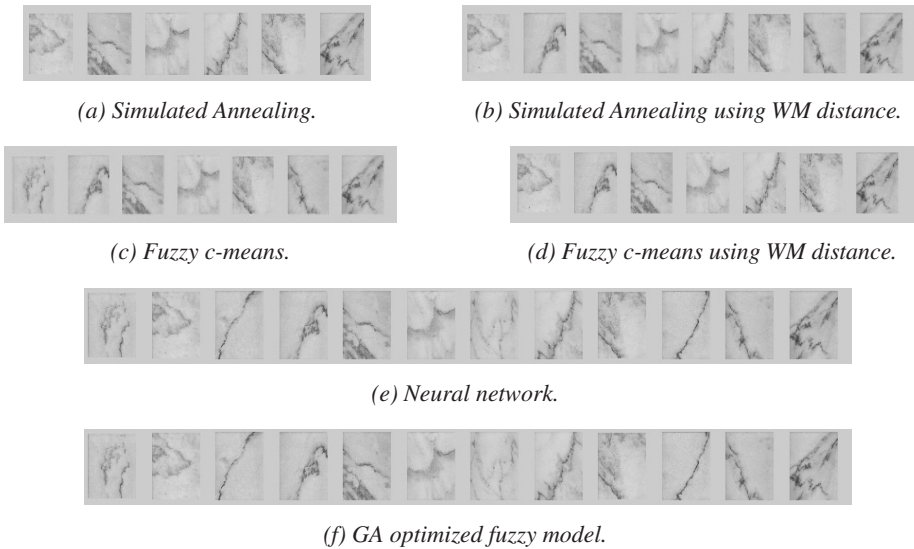
	$e$		$se$		$SC$	
	train data	test data	train data	test data	train data	test data
SA	0.41	0.42	0.00	0.14	90	23
SAw	0.38	0.50	0.03	0.00	112	23
FC	0.41	0.36	0.03	0.29	89	21
FCw	0.38	0.50	0.03	0.00	112	23
NN	0.10	0.21	0.03	0.14	130	22
FGA	0.10	0.50	0.03	0.07	130	19

In both tables it is clear that the results of the unsupervised methods are not so good as the ones using the supervised methods, especially when evaluated with traditional measures. However, the measures  $se$  and  $SC$  proposed in this paper allow to conclude that in general the WM distance improved the performance of the unsupervised algorithms. Thus, the apparent big differences between supervised and unsupervised algorithms are less evident with the introduced measures  $SC$  and  $se$ . These results are confirmed by

**Table 2.** Comparison of the results obtained for color clustering.

	<i>e</i>		<i>se</i>		<i>SC</i>	
	train data	test data	train data	test data	train data	test data
SA	0.48	0.67	0.06	0.14	195	93
SAw	0.46	0.53	0.03	0.16	240	87
FC	0.45	0.63	0.06	0.12	197	69
FCw	0.48	0.60	0.06	0.14	234	92
NN	0.13	0.26	0.09	0.07	254	81
FGA	0.10	0.44	0.01	0.16	268	52

visualizing the marbles. Due to the lack of space, we present only the visual results of one clustered region in the vein clustering presented in Table 2. The marble classification is presented in Figure 1.

**Fig. 1.** Example of marbles veins clusters: results for one region in the training set.

## 5 Conclusions

This paper deals with the problem of clustering natural surfaces based on their visual appearance (marble classification in this case). Standard classification error measures do not satisfactorily correspond to the classification results obtained by visual inspection of

human experts. Therefore, new measures are proposed in this paper, namely a *similarity table* and a *similarity score*, which are both based on expert evaluations. Further, we also introduced the so-called weighted Manhattan distance, which is based on a weighted expert table, and tuned through the use of genetic algorithms. This distance was applied to simulated annealing and fuzzy c-means clustering, and in general it improved the clustering results. Two supervised techniques were also tested, neural networks and a fuzzy model optimized by genetic algorithms. All the tested algorithms have shown that the set of features used to describe the marbles are quite adequate for clustering based on visual appearance.

Future work includes further studies in the weighted Manhattan distance, further evaluation and possible improvements of the introduced new measures, and finally a possible combination of clustering techniques to obtain a reliable marble classification system.

**Acknowledgements.** This research is partially supported by the “Programa de Financiamento Plurianual de Unidades de I&D (POCTI), do Quadro Comunitário de Apoio III”, and by the FCT project POCTI/2057/1995 - CVAM, 2nd phase, Ministério do Ensino Superior, da Ciência e Tecnologia, Portugal.

## References

1. R. Babuška. *Fuzzy Modeling for Control*. Kluwer Academic Publishers, Boston, 1998.
2. J. C. Bezdek. *Pattern Recognition with Fuzzy Objective Function*. Plenum Press, New York, 1981.
3. C. Bishop. *Neural Networks for Pattern Recognition*. Oxford University Press, New York, 1995.
4. S. Haykin. *Neural Networks: A Comprehensive Foundation*. Prentice-Hall, Upper Saddle River, NJ, second edition, 1999.
5. Z. Michalewicz. *Genetic Algorithms + Data Structures = Evolution Programs*. Springer, Berlin, third, revised and extended edition, 1999.
6. J. C. Pinto, A. Marcolino, and M. Ramalho. Clustering algorithm for colour segmentation. In *Proc. of V Ibero-American Symposium On Pattern Recognition, SIARP'2000*, pages 611–617, Lisbon, Portugal, September 2000.
7. J. C. Pinto and J. Sousa. Comparison of fuzzy clustering and quadtree methods applied to color segmentation. In *Proceedings of 12th Portuguese Conference on Pattern Recognition, RecPad'2002*, pages Session: Pattern Recognition, pp. 1–4, Aveiro, Portugal, June 2002.
8. P. Salamon, P. Sibani, and R. Frost. *Fact, Conjectures, and Improvements for Simulated Annealing*. SIAM, Philadelphia, USA, 2002.
9. M. Setnes and H. Roubos. GA-fuzzy modeling and classification: complexity and performance. *IEEE Transactions on Fuzzy Systems*, 8(5):516–524, October 2000.
10. J. Sousa and U. Kaymak. *Fuzzy Decision Making in Modeling and Control*. World Scientific Pub. Co., Singapore, 2002.
11. J. M. Sousa, U. Kaymak, and S. Madeira. A comparative study of fuzzy target selection methods in direct marketing. In *Proceedings of 2002 IEEE World Congress on Computational Intelligence, WCCI'2002, FUZZ-IEEE'2002*, pages Paper 1251, pp. 1–6, Hawaii, USA, May 2002.

# Online Handwritten Signature Verification Using Hidden Markov Models

Juan J. Igarza, Iñaki Goirizelaia, Koldo Espinosa, Inmaculada Hernández, Raúl Méndez,  
and Jon Sánchez

Department of Electronics and Telecommunications.

University of the Basque Country

Alameda Urquijo, s/n

48013 Bilbao, Spain

{jtpigugj, jtpgoori, jtpesacj}@bi.ehu.es  
{inma, raul, ion}@bips00.bi.ehu.es

**Abstract.** Most people are used to signing documents and because of this, it is a trusted and natural method for user identity verification, reducing the cost of password maintenance and decreasing the risk of eBusiness fraud. In the proposed system, identity is securely verified and an authentic electronic signature is created using biometric dynamic signature verification. Shape, speed, stroke order, off-tablet motion, pen pressure and timing information are captured and analyzed during the real-time act of signing the handwritten signature. The captured values are unique to an individual and virtually impossible to duplicate. This paper presents a research of various HMM based techniques for signature verification. Different topologies are compared in order to obtain an optimized high performance signature verification system and signal normalization pre-processing makes the system robust with respect to writer variability.

## 1 Introduction

Day by day, natural and secure access to interconnected systems is becoming more and more important. It is also necessary verifying people identity in a fast, easy to use and user-friendly way.

Traditionally, during the process of identification and controlling the access to systems or applications, we used objects, e.g. keys or smart cards, or we used knowledge based systems like PINs, or passwords. However, objects may be lost and knowledge may be forgotten and both may be stolen or copied.

Biometrics [1] relies on several personal and unique body features (e.g. fingerprints, iris or the retina) and individual behavior features (e.g. the way of speaking, writing, signing or walking). Those individual features, either physical or behavioral, allow identifying each individual univocally offering a solution for the conventional security problem. Because of this, biometric solutions are considered one of the most

trusted and natural ways of identifying a person and controlling access to systems and applications.

Normally, most citizens are not confident on biometric identification systems based on body features like fingerprints, iris or retina, because they feel these systems to be related to criminals and police issues. However, those features related to our behavior are accepted even though they are much less precise.

Research groups of four Spanish universities joined in the research project [2] called “*Aplicación de la Identificación de Personas mediante Multimodalidad Biométrica en Entornos de Seguridad y Acceso Natural a Servicios de Información*”. The first result from this project was the creation of a Multimodal Biometric Database [3] (fingerprints, signatures and voice) which is the starting point for the rest of the research of each participating group. This paper is a result of the subsequent research on handwritten signature using that database.

Section 2 is an introduction to signature verification, section 3 is dedicated to the description of the system, section 4 to the produced results and finally, in section 5 the conclusions are explained.

## 2 Signature Verification

Handwritten signature is commonly used and accepted as a way to verify people's identity; we usually sign documents to verify their contents or to authenticate financial transactions. Signature verification usually consists just of an “eye inspection” as if we compared two photographs, but this is not an efficient method against impostors and many times there is no verification process at all.

The automation of the verification process tries to improve the current situation and eliminate the eBusiness fraud. Automatic signature verification is divided into two main areas, depending on the way the data are acquired: In *off-line* signature verification, the signature is available in a handwritten document which is scanned to obtain the digital representation of the image. On the other hand, in *on-line* signature verification specific hardware is used (digitizing tablets) to register pen movements on the paper during the act of signing.

Off-line verification is used with signatures from past documents, not acquired in a digital format, and only the shape of the signature remains important. However, in on-line verification, we also use dynamic information of the signature, such as pen pressure or inclination, apart from the 2D spatial representation. The presence of the individual at the time of the digital capture is also required.

### 3 System Description

#### 3.1 Online Signature Acquisition Module

Our system uses a graphics tablet from Wacom as capturing device. More precisely it is the Intuos A6 model with USB interface. This tablet provides 100 samples per second containing values for pressure and the four degrees of freedom: X and Y coordinates, pen azimuth and inclination for every sample.

Strokes with no pressure, also known as *pen-ups*, are also sampled, and because of this the system is able to know the trajectory with ink and inkless, which means that we have extra information, making the system more robust.

The signature information, once digitized, is stored in a file as a matrix, and afterwards it may be used to create a new input in the database or as a test signature for the verification process.



**Fig. 1.** The digitized signature consists of a sequence of sample points along the signature, captured with a frequency fixed by the acquisition device. Its length is directly proportional to the time of signing, in this example 9.4s. *Pen-up* symbols occur during the time in black.

#### 3.2 Online Signature Database

The system uses a database, in which each individual has 25 true signatures. At the same time, each individual makes 5 forgeries of every of his/her 5 immediately previous entries in the database. This means that for every individual we have 25 true signatures and 25 forgeries made by 5 different people.

Data from 150 individuals were used in the research presented in this paper, i.e. 3.750 files of true signatures and the same number of forgeries.

The forgeries in the database are *skilled forgeries*, as the impostor tries several times to imitate the true user's signature before the forgery is acquired and finally stored in the database. Trying to improve the quality of the forgeries we encouraged the participants to do their best offering them a prize.

### 3.3 Signature Preprocessing

Every time we sign, we do it in a different way. Because of this, some factors like speed variation, different sizes or rotations or different places within the tablet have to be taken into account in order to get a representation of the signature independent from these factors.

The preprocessing module makes a time normalization so that the resulting signatures have the same length or number of samples. To do this, a process of interpolation or extrapolation is done depending on the number of samples of the original signature. This normalization is user-defined as the user can decide to keep the original size.

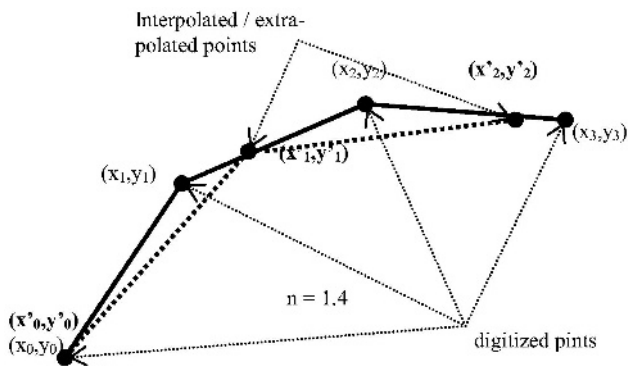


**Fig. 2.** Time normalization algorithm. In the example,  $n = 1.4$  represents the ratio between the original size of the signature (420 samples) and the normalized one (300 points). The acquired points are represented as  $(x_j, y_j)$ , with  $j$  from 0 to 420, and the normalized points are  $(x'_i, y'_i)$ , with  $i$  from 0 to 300.

Coordinates after normalization are calculated following this algorithm:

$$(x'_i, y'_i) = (a * x_j + b * x_{j+1}, a * y_j + b * y_{j+1}) \quad (1)$$

$$\text{with: } \begin{cases} j = \text{floor}(i * n) \\ b = (i * n) - j \\ a = 1 - b \end{cases}$$

Yang, Widjaja and Pradsad's method [4] consists of an algorithm that eliminates size variability (X-Y coordinates) and rotations with respect to the tablet. These authors use the absolute value of the angle corresponding to the segment that ties two consecutive normalized points, using the formula below:

$$\phi(k) = \arctan \left[ \frac{\sum_{l=i+1}^{i+n} s_l^{(k)} \sin \theta_l^{(k)}}{\sum_{l=i+1}^{i+n} s_l^{(k)} \cos \theta_l^{(k)}} \right] \quad (2)$$

with  $\theta_l^{(k)} = \theta_l^{(k)} - \theta_1$ , where  $\theta_1$  is the absolute angle of the first segment and  $s_l^{(k)}$  is the length of the segment between two consecutive points. This formula normalizes the signature and subtracts the absolute value of the first segment at the same time.

To improve the computational efficiency of this algorithm we propose some modifications to the Yang's original formula, adapting it to the algorithm represented in the figure 2. Developing  $\sin(\theta_l^{(k)} - \theta_1)$  and  $\cos(\theta_l^{(k)} - \theta_1)$  trigonometric expressions and as  $\Delta y_l^{(k)} = s_l^{(k)} \sin \theta_l^{(k)}$  and  $\Delta x_l^{(k)} = s_l^{(k)} \cos \theta_l^{(k)}$ , Yang, Widjaja and Prasad's formula (2) takes this new appearance:

$$\phi(k) = \arctan \left[ \frac{(y_{i+n}^{(k)} - y_i^{(k)}) \cos \theta_1 - (x_{i+n}^{(k)} - x_i^{(k)}) \sin \theta_1}{(x_{i+n}^{(k)} - x_i^{(k)}) \cos \theta_1 + (y_{i+n}^{(k)} - y_i^{(k)}) \sin \theta_1} \right] \quad (3)$$

Although this formula seems much more complex, it is more efficient, as  $\cos \theta_1$  and  $\sin \theta_1$  are only computed once, because they are constant values for all the samples along the signature. Besides, if we apply this algorithm to the normalized length the final result is as follows:

$$\phi(i) = \arctan \left[ \frac{(y'_{i+1} - y'_i) \cos \theta_1 - (x'_{i+1} - x'_i) \sin \theta_1}{(x'_{i+1} - x'_i) \cos \theta_1 + (y'_{i+1} - y'_i) \sin \theta_1} \right] \quad (4)$$

### 3.4 Model Training

Training a verification system consists of generating a model of the item that we want to verify using a set of observations of it. Models are initialized using the first 5 original signatures of each signer and reestimated using 4 more signatures. Afterwards they are stored in a database.

The set of observations used to generate the model must show the natural variation of the user's signature and the efficiency of these systems depends strongly on how representative these observations are of the user's signature during the creation of the database.

### 3.5 Verification and Threshold Selection

To verify whether the signer is a true user or an impostor we calculate the similarity between its signature and the trained model. Then we compare this value to the threshold selected to determine if we accept the signature or we reject it.

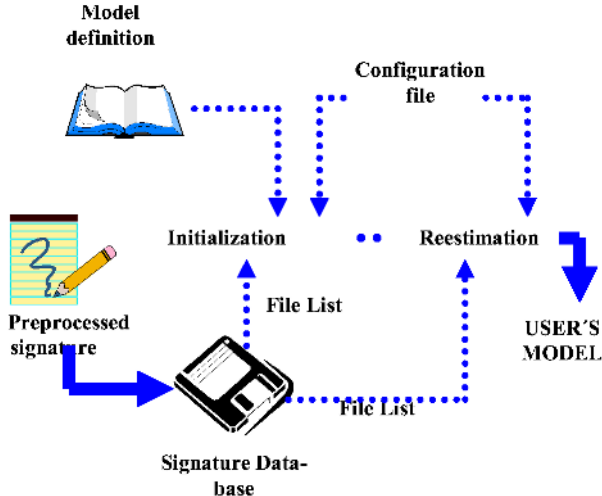


**Fig. 3.** Initialization and reestimation process of user's model.

Defining this threshold, we have to take into account the security level we need for our application, this is, if we need a low FAR (*False Acceptance Rate*) or a low FRR (*False Reject Rate*) as reducing one of this values means increasing the other. Normally, a security system should guarantee a FAR close to zero, but this means a higher FRR, because they are inversely proportional.

To check how accurate this algorithm is, we studied the DET plots (*Detection Error Tradeoff*) for all the users, defining the minimum cost point as follows:

$$DCF = C_{miss} * P_{miss} | True * P_{true} + C_{fa} * P_{fa} | False * P_{false} \quad (5)$$

where  $C_{miss}$  and  $P_{miss}$  are respectively the cost and probability of a false reject,  $C_{fa}$  and  $P_{fa}$  the cost and probability of a false acceptance,  $P_{true}$  is the a priori probability of the target and  $P_{false}$  is  $1 - P_{true}$ . This function will be evaluated for every point along the DET plot, finding the point where the function takes the minimum value. This point defines the threshold for which the accuracy of the algorithm is optimum. Another reference point is the EER point (*Equal Error Rate*) where FAR and FRR are the same.

These plots have been calculated using the free software of NIST [5]. These programs dynamically change the reject threshold and calculate the FAR and the FRR for different situations. The more collaborative the user is the lower FRR we'll get. His/her DET plot will be closer to the axis and the EER will be lower too.

## 4 Developed Models

In our first models, signatures were described using the directional normalized angle along the trajectory of the signature (equation (4)). An important part of this study was the definition of the number of states, the number of symbols, the transition matrix, and the initial probability of the distribution of the states, i.e. the topology of the models.

We made some tests to determine which topology of the HMMs [6] showed the best efficiency, these tests were made with signatures normalized to 300 samples and quantified with 32 symbols. We verified that 6-state L-R (*left-right*) models were more efficient than other L-R models. The worst results were obtained using ergodic or generalized models, those in which transitions between all the states are allowed.

Having defined the architecture of our models, we tested the application's accuracy for different normalized lengths. We normalized all the signatures to 100, 200, 300, 400, 500, 600 samples and also we used non-normalized signatures (keeping their original size) and found that the algorithm was more accurate using values between 300 and 500. These values are clearly related to the average signatures duration of about 3 seconds.

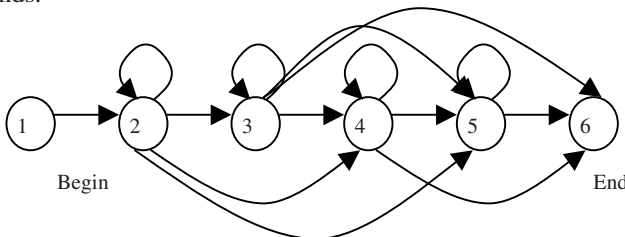


**Fig. 4.** 6-state HMM L-R topology

### 4.1 Verification Results

We studied the performance of the system working in verification mode, i.e. validating a person's identity comparing the captured signature with the individual's template, which is stored in the system database. Table 1 shows the initial results.

**Table 1.** Initial results using Yang, Widjaja and Prasad's preprocessing, which only includes angles. Although the FAR is close to 0, the false reject rate is nearly 50%, which means that an average user should sign twice to gain access to the system.

	<b>FAR</b>	<b>FRR</b>	<b>EER</b>
Mean value	0,295%	48,21%	17,565%

To set the optimum working point, we calculated the minimum cost point with NIST functions, favoring a very low FAR weighted 10 to 1, at expense of a high FRR.

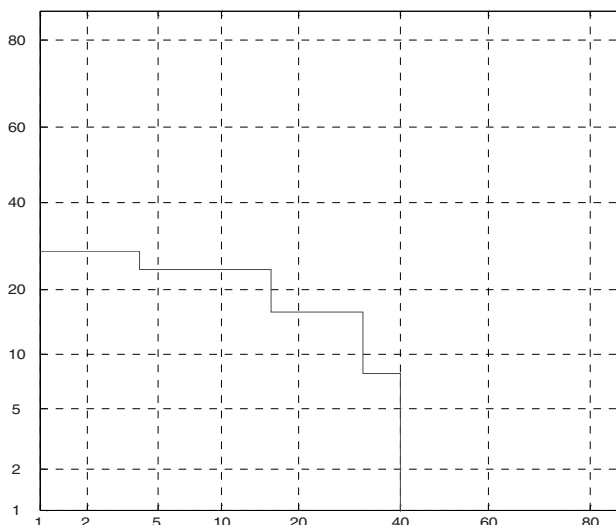


**Fig. 5.** DET (Detection Error Tradeoff) plot for user No.208, with FAR and FRR as X and Y axis. EER is quite similar to the mean value shown in table 1 and FRR is slightly better.

In the next tests we eliminated the first angle subtraction proposed by Yang, Widjaja and Prasad because we believe that the database creation methodology (users signed inside a grid) made it unnecessary. The new results showed that the EER was halved by eliminating this subtraction, implying that it introduced a noise harmful to the verification process. Finally, our system was trained including pressure, azimuth and inclination.

**Table 2.** Results with the new preprocessing method including angles, pressure, azimuth and inclination

	<b>FAR</b>	<b>FRR</b>	<b>EER</b>
Mean value	0,00%	31,52%	9,253%

Introducing these additional parameters results in a remarkable improvement of the algorithm efficiency.

## 5 Conclusions

The first angle subtraction proposed by Yang, Widjaja and Prasad is unnecessary in our system because users sign all inside a grid and it introduces a noise harmful to the verification process. For a system in which users are not asked to sign inside a grid, we propose to subtract the angle of the principal axis of inertia of the signature, as it is a more stable value than the first angle.

Adding additional parameters such as speed, acceleration, mass center, inertia axis, linear and circular segments length [7], curvature radii, etc. would result in a large EER improvement of the system, satisfying commercial requirements.

Multimodal fusion of several biometric methods (fingerprints, voice, signature, etc.) is another way to improve the efficiency of the verification. In the same way, we could talk about intramodal fusion, combining several verification methods based on the same biometric feature. Fusion of on-line and off-line signature methods can make the system more robust and efficient.

## References

1. S. Prabhakar, S. Pankanti, A. Jain "Biometric Recognition: Security and Privacy concerns" IEEE Security and Privacy. March/April 2003. pp. 33–42
2. Site of the Project TIC2000-1669-C04-03 [Online] <http://www.infor.uva.es/biometria>
3. J. Ortega, D. Simón, M. Faúndez, V. Espinosa, I. Hernández, J.J. Igarza, C. Vivaracho, Q.I. Moro. "MCYT: A Multimodal Biometric Database" COST275-The Advent of Biometrics on the Internet. Rome, 2002. pp. 123–126
4. L. Yang, B.K. Widjaja, R. Prasad. "Application of Hidden Markov Models for Signature Verification". Pattern Recognition, 28(2). 1995. pp. 161–170
5. National Institute of Standards and Technology. [Online] Available <http://www.nist.gov>
6. L.R. Rabiner, B.H. Juang "An Introduction to Hidden Markov Models", IEEE ASSP Magazine, January 1986. pp. 4–16
7. I. Goericelaya, J.J. Igarza, J.J. Uncilla, F. Pérez, J. Romo, K. Espinosa "Modelización de Contornos Mediante la Búsqueda de Segmentos Lineales y Circulares en Imágenes de Nivel de Gris" XII Simposium Nacional de la Unión Científica Internacional de Radio, Bilbao September 97. pp 1203–1206

# Fast Handwritten Recognition Using Continuous Distance Transformation

Joaquim Arlandis and Juan-Carlos Perez-Cortes

Universitat Politècnica de València, Camí de Vera s/n 46022 València, Spain  
`{jarlandi,jcperez}@disca.upv.es`

**Abstract.** The Continuous Distance Transformation (CDT) used in conjunction with a  $k$ -NN classifier has been shown to provide good results in the task of handwriting recognition [1]. Unfortunately, efficient techniques such as  $kd$ -tree search methods cannot be directly used in the case of certain dissimilarity measures like the CDT-based distance functions. In order to avoid exhaustive search, a simple methodology which combines  $kd$ -trees for fast search and Continuous Distance Transformation for fine classification, is presented. The experimental results obtained show that the recognition rates achieved have no significant differences with those found using an exhaustive CDT-based classification, with a very important temporal cost reduction.

## 1 Introduction

Statistical non-parametric methods, such as  $k$ -nearest neighbor classifiers ( $k$ -NN) provide very good results on many pattern recognition tasks (e.g.[11, 4]). One of the basic requirements for these methods to obtain good performances, however, is the use of a very large database of labeled prototypes. In some tasks, like handwritten character recognition, collecting a large number of examples is not as hard as in other applications, but searching through the whole database to find the nearest objects to a test image is time-consuming, and has to be done for every character in a document. This has been a recurring argument against the use of  $k$ -NN classifiers for this task, since a character recognizer is supposed to carry out many classifications per second on a moderately powerful machine to be useful and competitive. On other hand, the use of complex distances, aggravates the problem of the speed in the classification phase, where a distance computation for each test character to every prototype in the training set must be done.

In order to avoid searching over the whole training set,  $kd$ -tree data structures can be used. A  $kd$ -tree is a binary tree which allows fast and approximate search in large databases, providing results very similar to exhaustive search. Unfortunately, only certain metrics, including  $L$ -norms, can be naturally used as a distance function by traditional  $kd$ -tree search algorithms.

In this work, the problem of the computational complexity reduction associated to a  $k$ -NN classifier using complex distance functions has been approached

in a simple way: find a number  $k'$  of nearest neighbors using a fast approximate  $kd$ -tree search in a first feature space and, then, use a more complex or qualified dissimilarity measure applying exhaustive  $k$  nearest neighbors search to the subset of  $k'$  neighbors selected by the  $kd$ -tree. This results in a huge reduction on the the number of heavy computations needed to be performed. CDT-based features and distance functions have been selected in this paper because of the good results reported in previous works [1] for the particular task of handwriting recognition.

## 2 The Continuous Distance Transformation

Obtaining feature maps from images, where the distance relationships among their pixels are taken into account is the goal of a well-known technique usually referred to as *Distance Transformation* or DT [10]. The Distance Transformation is traditionally defined as an operation that transforms a binary image consisting of feature and non-feature pixels into a distance map, where all non-feature pixels have a value corresponding to the distance (any suitable distance function on the plane) to the nearest feature pixel [6]. Unfortunately, binarization is a necessary step in order to compute the classical Distance Transforms from continuous-valued images, causing a loss of information.

Recently, a generalization of the DT, the Continuous Distance Transformation (CDT), has been presented as a technique to compute distance maps from continuous-valued images [2]. Applicable to gray-level images, the CDT technique avoids binarization process and make use of the whole information content of the original range of representation,

Taking the definition of Distance Transformation as a basis, an item  $(i, j)$  of a “Distance Map to the Nearest White Pixel” holds the distance from pixel  $(i, j)$  on the image to the nearest white pixel. Note that this value can be interpreted as the number of fringes expanded from  $(i, j)$  until the first fringe holding a white pixel is reached, where a “fringe” is defined as the set of pixels that are at the same distance of  $(i, j)$ .

A parallelism between a distance map of binary images and one whose pixel values are defined in the gray-scale domain [0..MaxBright] implies the replacement of the “white pixel” concept by the “maximum bright value” and actions as “find the nearest white pixel” by “accumulate a maximum bright value on an expanding neighborhood”. Moreover, the value of an item on the continuous distance map is a function of the pixel value itself, as well as, of the number of fringes expanded until an accumulated bright value reaches a threshold according to a certain criteria of bright value accumulation, which is applied to the pixels belonging to each fringe analyzed. Then, the concept of “distance to the nearest white pixel” is substituted by the concept of “distance from a pixel to the limit of their minimum area of brightness saturation”.

Two types of CDT-based maps can be defined: Continuous Distance Map to Direct Scale Saturation or  $\Theta^D$  and, Continuous Distance Map to Reverse Scale Saturation or  $\Theta^R$  depending on if a maximum value of bright intensity or

a maximum value of reverse bright intensity is accumulated, respectively. Both maps provide distinct information about a point and its surrounding area. In [2], detailed descriptions of these concepts are presented. Given an image, either a  $\Theta^D$  map or a  $\Theta^R$  map are more or less descriptive depending on its brightness distribution. The cost of a CDT map computation is in  $\Omega(m^2 \times n^2)$  for an image of  $n \times m$  pixels, but, in practice, it is much lower.

Several distance and dissimilarity measures based on the Continuous Distance Transformation can be used to take advantage of the full possibilities of the representation obtained. These measures are collected in three generic, families including several distance functions each [2]:

- Continuous Fringe Distance measures including Fringe Distance using  $\Theta^D$  maps (FDD), Fringe Distance using  $\Theta^R$  maps (FDR) and Symmetrical Fringe Distance (SFD) which uses both  $\Theta^R$  and  $\Theta^D$  maps.
- Continuous Pixel Distance measures or  $PDL_p$ , which use the  $L$ -norm metric in its computation along with  $\Theta^R$  and  $\Theta^D$  maps<sup>1</sup>.
- $L$ -norm between CDT maps. Three sub-families can be computed depending on the CDT maps taken: the  $L_p D$  metrics if the  $L$ -norm of  $\Theta^D$  maps is computed; the  $L_p R$  metrics if the  $\Theta^R$  maps are used instead; and the  $L_p DR$  metrics if both maps are employed.

### 3 Fast Approximate Search of $k$ Nearest Neighbors Using $kd$ -Trees

The nearest neighbor search problem can be formulated in several distinct domains: from Euclidean vector spaces to (pseudo)metric spaces. Most algorithms intended for vector spaces are directly based on the construction of a data structure known as  $kd$ -tree [7, 5].

A  $kd$ -tree is a binary tree where each node represents a region in a  $k$ -dimensional space. Each internal node also contains a hyper-plane (a linear subspace of dimension  $k - 1$ ) dividing the region into two disjoint sub-regions, each inherited by one of its children. Most of the trees used in the context of our problem divide the regions according to the points that lay in them.

In many cases, an absolute guarantee of finding the real nearest neighbor of the test point is not necessary. In this sense, a number of algorithms of approximate nearest neighbor search have been proposed [3, 8].

In a  $kd$ -tree, the search of the nearest neighbor of a test point is performed starting from the root, which represents the whole space, and choosing at each node the sub-tree that represents the region of the space containing the test point. When a leaf is reached, an exhaustive search of the  $b$  prototypes residing in the associated region is performed. Unfortunately, the process is not complete at this point, since it is possible that among the regions defined by the initial partition, the one containing the test point be not the one containing the nearest prototype. It is easy to determine if this can happen in a given configuration,

---

<sup>1</sup> In previous works, this family of measures was named  $GPD_p$ .

in which case the algorithm backtracks as many times as necessary until all the regions that can hold a prototype nearer to the test point have been checked.

If a guaranteed exact solution is not needed, the backtracking process can be aborted as soon as a certain criterion is met by the current best solution. In [3], the concept of  $(1 + \epsilon)$ -approximate nearest neighbor query is introduced, along with a new data structure, the BBD-tree. A point  $p$  is a  $(1 + \epsilon)$ -approximate nearest neighbor of  $q$  if the distance from  $p$  to  $q$  is less than  $1 + \epsilon$  times the distance from  $p$  to its nearest neighbor.

## 4 Combining *kd*-Trees and the Continuous Distance Transformation

A simple methodology combining *kd*-trees and Continuous Distance Transformation for handwriting recognition is proposed. In a first step, fast search using *kd*-trees is applied to a test observation in order to get a number  $k'$  of nearest prototypes. Secondly, an exhaustive search of the  $k$  nearest neighbors,  $k < k'$ , among the  $k'$  pre-selected prototypes using specific features and distance functions is carried out to assess better performances.

For handwritten character classification we tested CDT-based distance functions due to its good results reported in previous works [1]. The computational cost of this combined methodology is significantly lower than that of exhaustive search over the whole training set. The computational cost of the method will depend on  $k'$ , the number of neighbors pre-selected, because it will determine the number of computations of the second step.

## 5 Experiments

The main goal of the experiments was to show if the proposed technique performs similarly to exhaustive search method in the task of handwritten character recognition, and quantify the computation time improvements obtained.

In this context, several configurations of the classification parameters can be identified. In order to analyze the behavior of the system in each of those possible settings, three experimental phases were planned: *a*) Selection of the features to use in the *kd*-tree pre-classifier; *b*) Test of the performance of different CDT variations and *c*) test for different values of  $k$  and  $k'$ .

### 5.1 Datasets, Preprocess, and Algorithms

The well-known NIST Special Database 3 (SD3) contains a large number of isolated handwritten characters: lower-case, upper-case letters, and digits. In this work, the 44951 upper-case letters from the SD3 were chosen for the experiments. The characters are stored as  $128 \times 128$  binary pixels images, segmented and labeled by hand. The database was split into two sets used for error estimation: the first 39941 upper-case letters for training, and the last 5009 for test. No writer appeared in both sets.

**Table 1.** Results of phase *a*). Error rates of the three methods using different feature maps, for  $k'=100$ ,  $k=4$ , PDL<sub>3</sub> distance function, and  $\epsilon=1.5$ .

Method \ Map	Image	$\Theta^D$	$\Theta^R$
<i>kd</i> -tree	6.05	8.66	4.99
<i>kd</i> -tree & CDT	3.87	4.07	3.85
Exhaustive CDT		3.85	

To obtain a usable representation of the images in a lower dimensional space, common resampling and normalizing procedures were applied. These techniques generate gray-level images that keep most of the original information. Thus, the character images were sub-sampled from  $128 \times 128$  binary pixels into  $28 \times 28$  gray value by first computing the minimum inclusion box of each character, keeping the original aspect ratio, and then accumulating into each of the  $28 \times 28$  divisions the area occupied by black pixels to obtain a continuous value between 0 and 1.

The Continuous Distance Transformation was applied to the subsampled images, obtaining the CDT maps. Some parameters that have influence in this process have been fixed to present comparative results: the maximum number of fringe expansions was set to 3; the fringe value function chosen was “the maximum pixel value on the fringe”; and, the  $L_\infty$ , or chessboard distance, was the metric on the plane used for computing the pixels belonging to each fringe<sup>2</sup>.

In order to make use of the *kd*-tree, Principal Component Analysis (PCA) was performed on the representations to reduce its dimensionality to 40 [9]. The approximate nearest neighbor algorithm used was based on [3].

## 5.2 Phase *a*)

In the first phase, the main goal was to compare performances using the following three classification methodologies: 1) Approximate  $k$ -NN search using *kd*-trees with  $k=4$ ; 2) Approximate  $k'$  nearest neighbors search using *kd*-trees with  $k'=100$  followed by exhaustive  $k$  nearest neighbors search with  $k=4$  using a CDT-based measure over the 100 pre-selected neighbors; and 3) Exhaustive  $k$  nearest neighbors using a CDT-based measure with  $k=4$  over the whole of the training set. In the *kd*-tree classifier, the image, and the  $\Theta^D$  and  $\Theta^R$  maps were tested as feature vectors.

The approximation parameter  $\epsilon$  used for approximate search in *kd*-trees was 1.5. It has been shown that this value reduces the computation time without affecting recognition rates in other related experimental contexts [9]. A common dissimilarity measure, PDL<sub>3</sub>, was chosen for tests which involve CDT evaluations. The results are shown in Table 1 as error rates at zero rejection.

Notice the excellent error rate of 4.99% obtained from the *kd*-tree technique using the  $\Theta^R$  map as features, and the 3.85% error rate obtained from our

---

<sup>2</sup> Some tools and functions in ANSI-C related to the Continuous Distance Transformation can be found at <http://tafetan.disca.upv.es/sw/cdt>

**Table 2.** Results of phase *b*). Error rates for CDT-based measures using the combined methodology for (if applied),  $k'=100$ ,  $k=4$ , and  $\epsilon=1.5$ . The  $kd$ -tree features were the  $\Theta^R$  map.

Distance \ p	1	2	3	4	5	6	7	8	9	10	11	12
$L_p D$	9.42	8.64	8.48	9.00	9.32							
$L_p R$	5.77	4.83	4.51	4.39	4.29	4.11	4.19	4.23	4.31	4.39		
$L_p DR$	6.19	4.97	4.39	4.23	4.07	4.19	4.13	4.01	4.05	4.17	4.15	4.09
FDD						7.77						
FDR							4.83					
SFD							8.80					
$PDL_p$	5.39	4.13	3.85	3.81	3.73	3.75	3.89	3.85	3.77	3.91		

combined methodology. Both rates improve significantly the error rate obtained from  $kd$ -trees when it uses images map as features.

### 5.3 Phase *b*)

According to the results of the previous phase, the combined  $kd$ -tree and CDT methodology was chosen to be analyzed in more detail. Thus, in order to get the best CDT-based measures using our methodology in the task of handwriting recognition, tests over all CDT families of measures were done. For those measures having a  $p$  potency (related to the  $L$ -norm of the CDT maps), a range of values of  $p$  between 1 and 12 were tested. For the Fringe Distance measure family, the three existing functions were used. The results presented in Table 2 show that the Pixel Distance family gives the best performance with very low error rates, followed by the  $L_p DR$  and  $L_p R$  metrics.

### 5.4 Phase *c*)

This phase is intended to analyze the combined  $kd$ -tree and CDT system performance in function of the number of pre-selected nearest neighbors  $k'$ . Several tests using  $PDL_5$  distance function for an exhaustive search through a number of pre-selected prototypes between 25 and 500 were performed. For each  $k'$  value tested, error rates for several  $k$  values between 1 and 7 are provided too. The results are shown in Figure 1.

For a given value of  $k$ , the performance of the combined method approaches the exhaustive CDT rates as  $k'$  increases. In practice, for a moderately large  $k'$  the system performs as the exhaustive search. In the context of the experiments presented, good results are achieved from around 75 neighbors. Nevertheless, this is expected to be a function of the size of the training set, growing as the size of the training set increases.

The recognition times per character (in a Pentium III, 800 MHz.) for the three methodologies presented were: 3.17 ms. using the  $kd$ -tree search, 7.78 ms. using  $kd$ -trees and CDT with  $k'=100$ , and, 287.5 ms. using exhaustive CDT

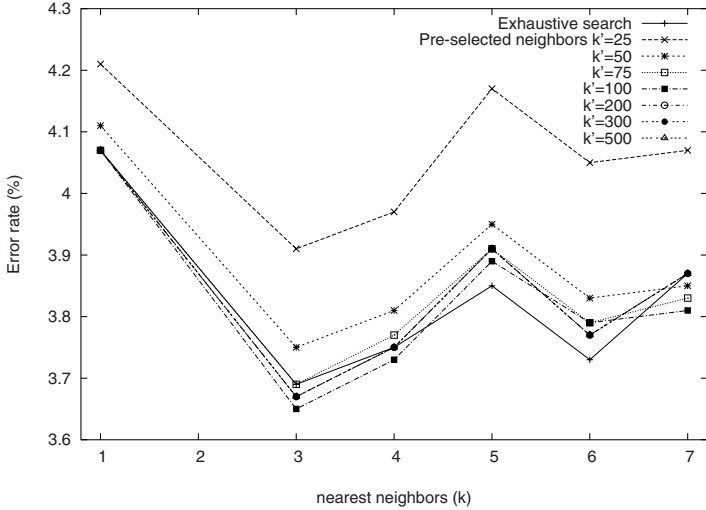


**Fig. 1.** Results of phase *c*). For values of  $k' \geq 75$ , no difference with exhaustive search is found.

**Table 3.** Error rates of the three methods for  $k'=100$ ,  $k=3$ , and  $\epsilon=1.5$ .

Method \ Distance	$L_6R$	$L_9DR$	FDR	$PDL_5$
Exhaustive CDT	4.17	3.93	5.05	3.69 (287 ms/char)
$kd$ -tree ( $\Theta^R$ ) & CDT	4.17	3.93	5.01	3.65 (7.78 ms/char)
$kd$ -tree (image)			6.05 (3.69 ms/char)	
$kd$ -tree ( $\Theta^R$ )			4.99 (3.17 ms/char)	

search. Further, the computation times for different values of  $k'$  in the combined methodology were directly proportional to the  $k'$  value used, and perfectly competitive in a real application.

## 5.5 Summary

In Table 3, a summary of results is shown. Error rates are presented for the best measure from each CDT-based family, obtained in phase *b*) - $PDL_5$ ,  $L_9DR$ ,  $L_6R$  and FDR, excluding the  $L_pD$  distances- using a  $k$  value of 3 (the best one from phase *c*), and a value of  $k' = 100$ . Results for the  $kd$ -tree technique using image and  $\Theta^R$  features are also shown. A significant reduction of 1.06% can be achieved using the  $\Theta^R$  map as input features to the  $kd$ -tree instead of directly the image features (PCA to 40-D is always applied as the last feature extraction step). The error reduction reaches 2.4% when the combined methodology is applied using the Pixel distance with  $p=5$ .

As shown in Figure 1, values of  $k'$  lower than 100 can be used when a higher recognition speed is needed, at the expense of a small increase of the error rate.

## 6 Conclusions

A combined methodology using *kd*-trees and the Continuous Distance Transformation is presented. In a first step, fast search using *kd*-trees is applied to each observation in order to get a selected number of nearest prototypes. Then, exhaustive search among the pre-selected prototypes using more complex measures, such as the CDT-based ones, is carried out to refine the result. The error rates obtained are equivalent to those from exhaustive search on the whole training set. The execution times reported are an order of magnitude lower than those of exhaustive search and only moderately higher than those of approximate *kd*-tree search methods, with a significantly lower error rates that clearly compensate for this small cost increase in most cases.

## References

- [1] Arlandis, J., Perez-Cortes, J.C., Llobet, R.: Handwritten Character Recognition Using Continuous Distance Transformation. Proceedings of the 15th. International Conference on Pattern Recognition **1** (2000) 940–943
- [2] Arlandis, J., Perez-Cortes, J.C.: The Continuous Distance Transformation: A Generalization of the Distance Transformation for Continuous-valued Images. Pattern Recognition and Applications **56** (2000) 89–98
- [3] Arya, S., Mount, D.M., Netanyahu, N.S., Silverman, R., Wu, A.: An optimal algorithm for approximate nearest neighbor searching. Journal of the ACM **45** (1998) 891–923
- [4] Beis, J.S., Lowe, D.G.: Indexing without Invariants in 3D Object Recognition. IEEE Trans. on PAMI **21(10)** (1999) 1000–1015
- [5] Bentley, J.L., Weide, B.W., Yao, A.C.: Optimal Expected Time Algorithms for Closest Point Problems. CM Trans. Math. Software **6** (563–580)
- [6] Borgefors, C.: A New Distance Transformation Approximating the Euclidean Distance. Proceedings of the 8th. International Conference on Pattern Recognition **1** (1986) 336–338
- [7] Friedman, J.H., Bentley, J.L., Finkel, R.A.: An algorithm finding best matches in logarithmic expected time. ACM Trans. Math. Software **3** (209–226)
- [8] Perez, J.C., Vidal, E.: An Approximate Nearest Neighbours Search Algorithm Based on the Extended General Spacefilling Curves Heuristic. Lecture Notes in Artificial Intelligence **1451** (1998) 697–706
- [9] Perez-Cortes, J.C., Arlandis, J., Llobet, R.: Fast and Accurate Handwritten Character Recognition using Approximate Nearest Neighbours Search on Large Databases. Lecture Notes in Artificial Intelligence **1876** (2000) 767–776
- [10] Rosenfeld, A., Pfaltz, J.L.: Sequential Operations in Digital Picture Processing. Journal of the ACM **13(4)** (1966) 471–494
- [11] Tomasi, C., Manduchi, R.: Stereo Matching as a Nearest-Neighbor Problem. IEEE Trans. on PAMI **20(3)** (1998) 333–340

# Stroke Boundary Analysis for Identification of Drawing Tools

Paul Kammerer, Georg Langs, Robert Sablatnig, and Ernestine Zolda

PRIP - Vienna University of Technology,  
Favoritenstrasse 9/183/2, A-1040 Vienna, AUSTRIA  
[{paul, lang, sab, zolda}@prip.tuwien.ac.at](mailto:{paul, lang, sab, zolda}@prip.tuwien.ac.at)  
<http://www.prip.tuwien.ac.at/Research/Cassandra>

**Abstract.** An algorithm for the automatic identification of drawing tools based on the appearance of the stroke boundary is presented. The purpose of this stroke analysis is the determination of drawing tools in underdrawings - the basic concept of an artist - in ancient panel paintings. This information allows significant support for a systematic stylistic approach in the analysis of paintings. Up to now the identification of drawing tools is performed by an expert visually. Our tool will support the expert to investigate larger numbers of underdrawings, provides objective and reproducible information and simplifies comparison of different underdrawings. Stroke analysis in paintings is related to the extraction and recognition of handwritings, therefore similar techniques to stroke analysis are used. Following the segmentation, the approximation of the stroke boundary is done by active contours with different parameters. Deviations between a rigid and elastic “snake” are used as descriptive features for differentiation between drawing tools. Results of the algorithm are presented for sets of three different types of strokes.

## 1 Introduction

Computer aided analysis is an important tool for the examination of works of art [1]. Within an interdisciplinary project between the fields art history and image analysis we are developing a system to investigate infrared images (infrared reflectograms [2]) of medieval and Renaissance panel paintings with methods of digital image processing and analysis. In conservation and art history three prominent questions are of particular interest. The first question deals with the development of underdrawings and their relations to other drawings and between underdrawing and the covering painting. Secondly, art historians and restorers are interested in the style of the underdrawing, and questions whether the underdrawing is sketchy, freehand or a copy from a template. Finally an important question is, what kind of materials and drawing tools are used in an underdrawing [3].

This paper will contribute to answering the third question and addresses the automatic identification of drawing tools used in the underdrawing of medieval paintings. This is a first step towards a subsequent stylistic analysis of underdrawings and a classification of painters. We present a method that analyzes the

visual appearance of the stroke boundary. Up to now appearance based analysis of drawing tools is made only visually by experts. A problem of visual analysis is, that it is often not possible to inspect a large amount of drawings as a whole and in detail and therefore the analysis usually is reduced to selected objects and to certain regions of a painting. The restricted human optical retentiveness further complicates the comparison of different underdrawings concerning drawing tools, drawing materials, and stroke characteristics. Automatic analysis tools will objectify the analysis. They will speed up the recognition process, will provide objective and reproducible data and support the experts in studying underdrawings.

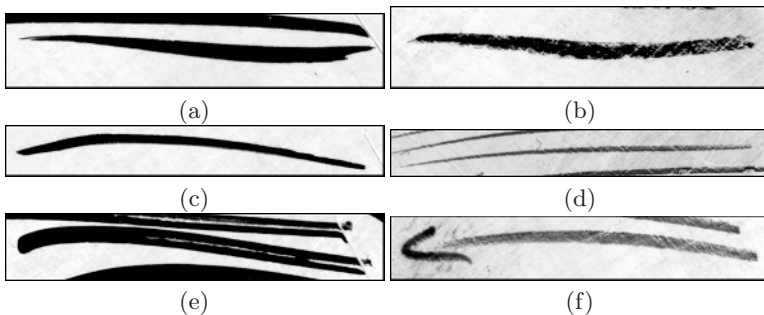


**Fig. 1.** Stroke details showing tools using fluid materials on the left, brush (a), quill (c), reed pen (e) and dry material tools on the right, black chalk (b), silver point (d) and graphite (f).

The paper is organized as follows. In Section 2 an overview about the characteristics of drawing tools and materials used in medieval underdrawings is given. The analysis process, like the standard approach, is split into a segmentation step, a refinement step and a feature extraction step which are described in Section 3. Section 4 will present and discuss the results obtained with our method. Whereas Section 5 will give a brief overview about work in progress and on future work.

## 2 Characterizing Drawing Tools / Materials

Drawing tools, used in medieval panel paintings can be categorized into two different types, into those that are fluid and into a group consisting of dry drawing material [3]. In Figure 1 six examples of a stroke for both of the groups are depicted. Three strokes represent the class of drawing tools using fluid materials (a,c,e) and three strokes represent dry materials (b,d,f). These examples have been taken from a panel prepared for our experiments by a restorer.

Our analysis approach is based on the observation that prominent characteristics of drawn strokes are variations of shape and variations of the intensity in the drawing direction. Table 1 gives an overview about the characteristics of the

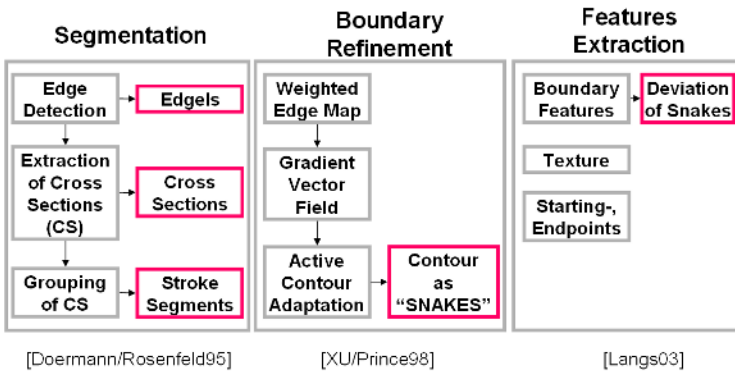


**Fig. 2.** Schematic diagram of our approach

two groups of drawing tools. The first characteristic we analyzed is the boundary of a stroke. It can be observed, that there are variations in smoothness depending on the drawing tool used. While strokes applied with a pen or brush using a fluid medium show a smoother boundary, the boundary of strokes applied with a dry material, e.g. black chalk or graphite is less smooth. This observation is used in the method presented in the next section.

**Table 1.** Characteristics of different drawing tools and materials

Tools/Materials	Characteristics
<b>fluid materials</b>	<b>fluid lines</b>
- paint or ink applied by pen or brush	<ul style="list-style-type: none"> <li>- <b>continuous and smooth</b></li> <li>- vary in width and density</li> <li>- pooling of paint at the edges</li> <li>- droplet at the end</li> <li>- different endings (brush/pen)</li> </ul>
<b>dry materials</b>	<b>dry lines</b>
- charcoal - chalks - metal points - graphite	<ul style="list-style-type: none"> <li>- less <b>continuous and smooth</b></li> <li>- less variation in width</li> <li>- more granular</li> </ul>

### 3 Stroke Segmentation and Feature Extraction

Stroke segmentation in paintings is related to the extraction and recognition of handwritings [4]. Letters and words in Western languages and symbols or signs in Chinese or Japanese languages are built of manually drawn strokes or lines. Many approaches start with thresholding and thinning methods. While these methods are fast and save resources, valuable information for a more detailed analysis

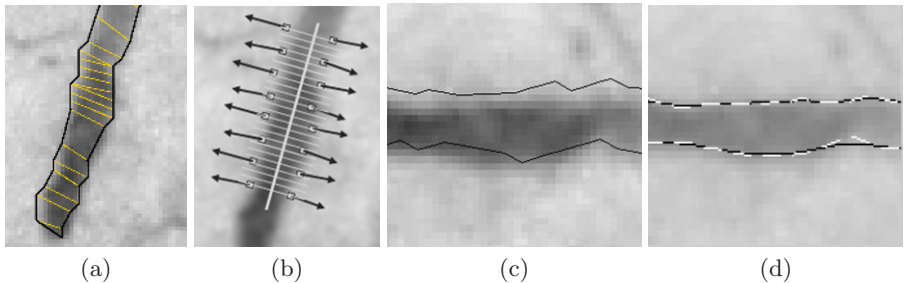


**Fig. 3.** Segmentation and Refinement (a) cross sections and polygonal boundary (b) edgels with axis and gray value profiles (c) initial “top” and “bottom” boundary boundary (d) converged “rigid” (black) and “non-rigid” snakes (white-dashed)

of strokes requires an approach that also incorporates boundary information [5]. We used Doermann’s segmentation algorithm in the Segmentation part of our approach, since it provides both, the boundary of a stroke and intensity profiles, which will be used to characterize strokes. Figure 2 gives an overview of our approach consisting of three basic steps, segmentation, boundary refinement and feature extraction.

**Segmentation.** In the Step I, first edgels located at the stroke contour are detected by a Canny edge detector. Second, cross sections (perpendicular to the stroke boundary) are built as the connection form pairs of opposite edgels. To form a cross section the gradient vectors have to point to opposite directions. Finally, neighbored cross sections are linked into groups and represent a stroke segment. Figure 3(a) shows the cross sections grouped into one stroke segment and the polygonal boundary. For further algorithmic details of we refer to [1].

**Boundary refinement.** In Step II the approximation of the stroke boundary by a closed polygon is refined by “snakes”, a method based on active contours [6]. After determining the principal component of the edgel distribution of a stroke segment, the contour is split into two sides (“top” and “bottom” boundary) that are treated separately. A set of gray value profiles, perpendicular to the axis, represent the domain for the snake algorithm. Figure 3(b) shows the equidistant profiles in the original image, and rearranged as an image (c). The snake moves through this domain to minimize an energy functional determined by inner parameters controlling rigidity and tension of the snake and an external energy influenced by a gradient vector flow in order to provide accurate and fast convergence to boundary concavities.

**Feature extraction.** Contour estimates with different levels of elasticity provide descriptive information by means of deviation against each other. We used two succeeding snakes. The first rigid snake was initialized on the coarse contour estimate. The second, more elastic snake proceeds from this position. MEAN of the deviation and standard deviation (SDV) of the deviation between the two snakes are used as descriptive features. For more details please refer to [7].

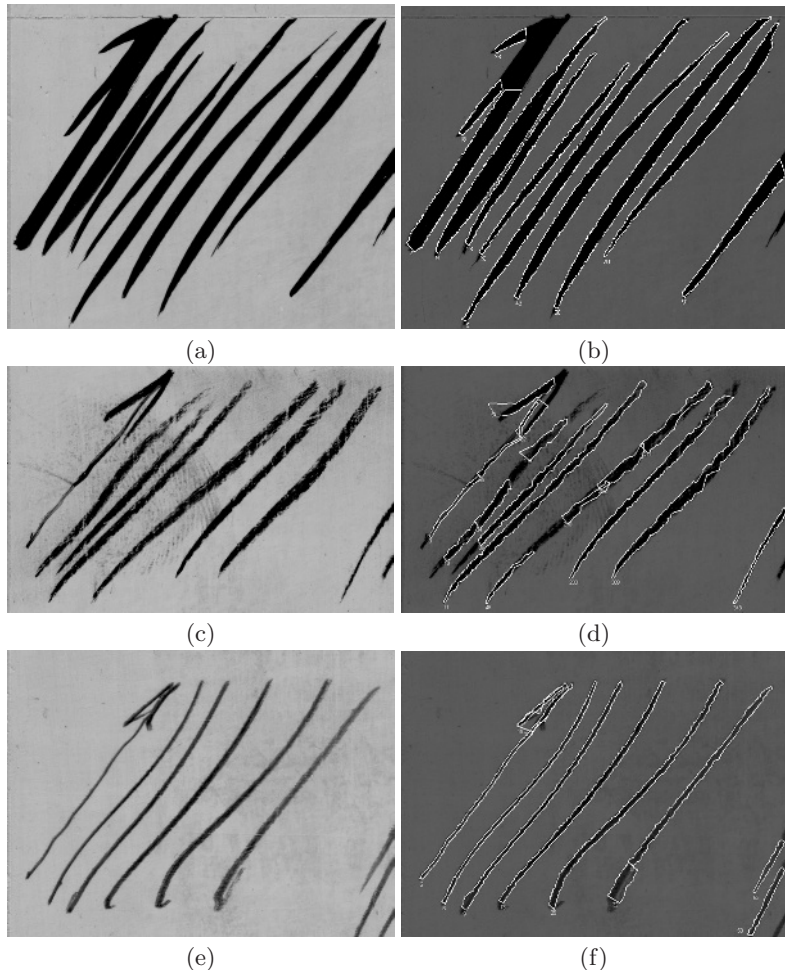


**Fig. 4.** The left column shows details from the test panel with strokes used in our experiments: brush strokes (873x729 pixel) (a), chalk strokes (992x631 pixel)(c) and graphite strokes (989x729) pixel)(e). The right column shows the detected boundaries of the segmentation step (the original images are displayed darker for better illustration of the boundaries

#### 4 Experimental Results and Discussion

In our experiments we studied the differences of three types of drawing tools – brush, chalk and graphite. Test panels (21cm x 30cm) containing sets of the mentioned strokes have been prepared by a restorer. The test panels were digitized using a flat-bed scanner with an optical resolution of 1200 dpi. Details from images, as depicted in Figure 4 have been cropped manually. Figure 4 (a) shows a series of brush strokes, (c) chalk strokes and (e) graphite strokes, all applied in bottom up direction.

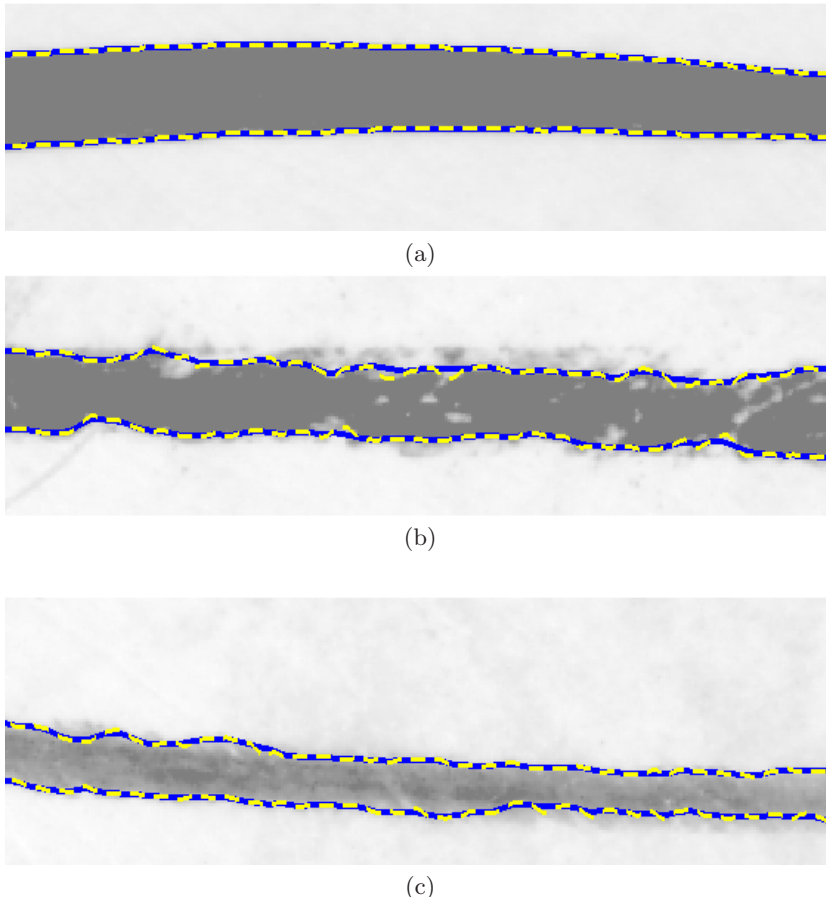


**Fig. 5.** Details from the test panel showing stroke used in our experiments and the overlay of the snakes: brush strokes (a), chalk strokes (b) and graphite strokes (c).

The result of the segmentation step is illustrated in Figure 4 (b),(d) and (f) respectively. The boundary of the stroke segments, that consist of at least 20 cross sections are depicted. The segmentation algorithm works well for most of the brush strokes and graphite strokes. Problems arise e.g. at left stroke in Figure 4(a), which is not segmented completely, since the stroke width parameter was set to narrow. The segmentation algorithm, still has problems with overlapping strokes like the “arrow top ” in the left most stroke of Figure 4(f) and (d). Problems occur with the chalk strokes in Figure 4(d) which are segmented into many small segments due to the inhomogeneity of the strokes. This necessitates a further processing step, that will be handled together with the overlapping problem.

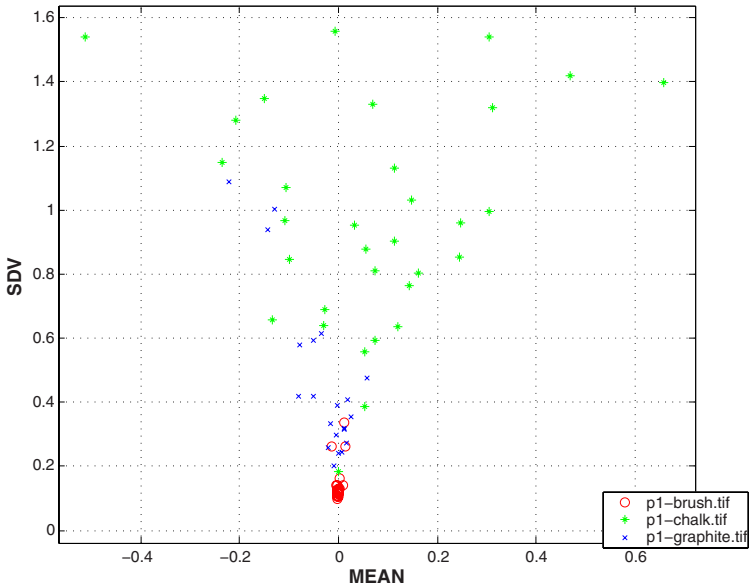


**Fig. 6.** Standard deviation (SDV) and MEAN of the snake deviations. The deviations are measured on the “top” and “bottom” boundary of the individual brush, chalk and graphite strokes.

For the refinement and feature extraction step, the stroke segments shown are used. First, the refinement step is initialized by the boundary of the segmentation step. The refinement algorithm, i.e. the adaptation of the two snakes with different rigidity, is applied separately to the “top” and “bottom” boundary of a stroke. Figure 5(a,b,c) shows three exemplary strokes together with an overlay of the more elastic (dotted bright line) and more rigid snake (underlying black line). It can be observed that the deviation of the rigid and elastic snake is smaller from the brush stroke than those from the black chalk and graphite strokes.

To show the differences calculated, the SDV- and MEAN-values of the deviations of the two snakes, i.e. two values, one for the “top” and one for the “bottom” boundary, are plotted in the diagram of Figure 6. The MEAN values of the brush strokes (denoted as circles) are concentrated near zero, while there is a higher variation of the MEAN graphite strokes (denoted as “x”) and brush strokes (denoted as stars). Similarly, the standard deviation SDV of brush strokes is below 0.2 for all but two of the stroke borders. The SDV values for chalk and graphite is between 0.2 and 1.6 in our samples. So using the SDV feature will allow to distinguish between brush, i.e. a fluid drawing tool, and graphite and chalk respectively as dry drawing tools. Using a combination of SDV and MEAN the data of our samples can be used do differentiate between graphite and chalk, since most of the chalk values are positioned right and above the graphite values.

Still, these results are preliminary and experiments with more samples are necessary. Furthermore the reliability of this differentiation can be improved if a set of strokes is considered. As can be observed in underdrawings, certain regions of a drawing, a couple of strokes is applied with the same drawing tool, e.g. as hatches or cross hatches.

## 5 Conclusion and Outlook

The boundary analysis algorithm presented in this paper successfully detects and refines the boundary of strokes and extracts features that allow to differentiate between dry and fluid drawing tools. The first results showed, that the visual appearance of the boundary of a stroke can be used for discrimination. Still, further experiments with more samples are necessary to prove our method. The next steps will also incorporate additional features, like the texture of the different types of strokes, to get a measure for granularity of a stroke. Further we have noticed, that, in some cases, there is a difference between the “top” and “bottom” boundary of a stroke in dry drawing tools. This observation has to be proofed and evaluated. As reported, some problems occur in the segmentation step, if the strokes are interrupted. So one of our goals is to improve the robustness of the segmentation step and to extend the approach to segment overlapping and crossing stroke formations as e.g. reported in [8].

## References

1. P. Kammerer, G. Langs, R. Sablatnig, and E. Zolda. Stroke segmentation in infrared reflectograms. In *Image Analysis*, volume LNCS2749, pages 1138–1145, 2003.
2. J.R.J. Van Asperen de Boer. *Infrared Reflectography. - A Contribution to the Examination of Earlier European Paintings*. PhD thesis, Univ. Amsterdam, 1970.
3. D. Bomford, editor. *Art in the Making, Underdrawings in Renaissance Paintings*. National Gallery, London, 2002.
4. R. Plamondon and S.N. Srihari. On-line and off-line handwriting recognition: A comprehensive survey. *Trans. on Pattern Analysis and Machine Intelligence*, 22(1):63–84, 2000.
5. D.S. Doermann and A. Rosenfeld. Recovery of temporal information from static images of handwriting. *International Journal of Computer Vision*, 52(1-2):143–164, 1994.
6. Chenyang Xu and Jerry L. Prince. Snakes, shapes and gradient vector flow. *IEEE Transactions on image Processing*, 7(3):359–369, March 1998.
7. G. Langs, H. Bischof, and P.L. Peloschek. Automatic quantification of destructive changes caused by rheumatoid arthritis. Technical Report 79, Vienna University of Technology, Pattern Recognition and Image Processing Group, 2003.
8. E. L'Homer. Extraction of strokes in handwritten characters. *Pattern Recognition*, 33(7):1147–1160, 1999.

# Solving the Global Localization Problem for Indoor Mobile Robots

Leonardo Romero<sup>1</sup>, Eduardo Morales<sup>2</sup>, and Enrique Sucar<sup>2</sup>

<sup>1</sup> UMSNH, Morelia, Mich., 52000, Mexico, lromero@zeus.umich.mx

<sup>2</sup> ITESM Campus Cuernavaca, Mor., 62589, Mexico  
{emorales,esucar}@itesm.mx

**Abstract.** Global localization is the problem of determining the position of a robot under global uncertainty. This problem can be divided in two phases: 1) from the sensor data (or *sensor view*), determine clusters of hypotheses where the robot can be; and 2) devise a strategy by which the robot can correctly eliminate all but the right location. In the second phase, previous approaches consider an ideal robot, a robot with a perfect odometer, to predict robot movements. This paper introduces a non deterministic prediction approach based on a Markov localization that include an uncertainty model for the movements of the robot. The non deterministic model can help to solve situations where a deterministic or ideal model fails. Hypotheses are clustered and a greedy search algorithm determines the robot movements to reduce the number of clusters of hypotheses. This approach is tested using a simulated mobile robot with promising results.

## 1 Introduction

Global localization is the problem of determining the location of the robot under global uncertainty. This problem arises, for example, when a robot uses a map that has been generated in a previous run, and it is not informed about its initial location within the map.

The global localization problem can be seen as consisting of two phases: hypothesis generation and hypothesis elimination [4]. The first phase is to determine the set of *hypothetical locations*  $H$  that are consistent with the sensing data obtained by the robot at its initial location. The second phase is to determine, in the case that  $H$  contains two or more hypotheses, which one is the true location of the robot, eliminating the incorrect hypotheses. Ideally, the robot should travel the minimum distance necessary to determine its exact location.

This paper presents an approach to solve the global localization problem in a known indoor environment modeled by an occupancy grid map, a two dimensional map where the environment is divided in square regions or cells of the same size. This approach is an improved version of the global localization approach given in [10]. We use a Markov localization (see [7,10]) in both phases, to represent and update the set  $H$  of hypotheses, and predict movements of the robot in order to eliminate hypotheses. The main contribution of this paper is to predict

movements using a *Markov localization that includes an uncertainty model for the movements of the robot*. Previous approaches [8,5,10] only consider a deterministic or ideal model for the robot (a robot with a perfect odometer) during the prediction process.

The rest of this paper is organized as follows. Section 2 describes relevant issues of our approach to generate hypotheses [10]. Section 3 presents the framework of Markov localization. Section 4 explains our approach to eliminate hypotheses. Experimental results using a mobile robot simulator are shown in Section 5. We choose a simulator because it is easy to create complex environments, with many similar places, to test the robustness of our approach. Finally, some conclusions are given in Section 6.

## 2 Hypotheses Generation

In this section a simple occupancy grid map is used as an example to show the ideas behind the proposed approach. Figure 1 (a) shows this simple map built using a mobile robot simulator. Figure 1 (b) shows a local map view, extracted from the map for the position of the robot shown in (a), considering that the robot direction is aligned with a global fixed direction (pointing downwards in this case). Figure 1 (c) shows the sensor view (generated by the simulator) considering that the robot is aligned with the global direction. Both views have an angular resolution of 0.5 degrees, a common value found in laser range sensors, and include the robot position for reference as a black cell. Perceptual limitations are taken into account setting a maximum range of 3 meters. The problem consist in estimating the set  $H$  of possible locations that have local map views consistent with the sensor view.

### 2.1 Polar Correlation

To have a simple model of robot motion and hence a small state space in the Markov localization, we assume that the robot should be in one of 8 possible directions ( $\theta_i = 45 * i$  degrees,  $i = 0,..7$ ), with respect to the global fixed direction, one for each adjacent cell. A polar correlation, using a sum of absolute

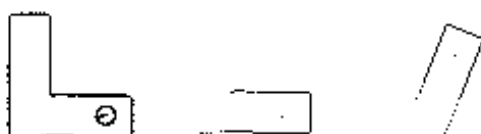


**Fig. 1.** A simple environment. From left to right: (a) Occupancy grid map. (b) Local map view computed from the map and the robot location showed in (a). (c) Actual sensor view

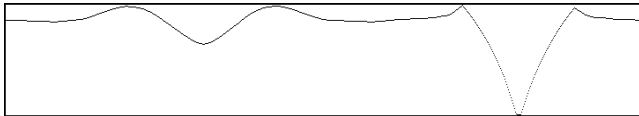


**Fig. 2.** Correlation results. Angular displacements are from 0 (left) to 359.5 degrees (right)

differences, can be used to find the match between a local map view and the sensor view. Figure 2 shows the correlation results for all the possible angular displacements of the sensor view against the local map view shown in Figure 1. From the minimum difference an angular displacement can be computed to align the robot with one of the directions  $\theta_i$ . Obviously, the right angular displacement should be indicated considering the most probable position of the robot. In the case of Figure 2 the angular displacement corresponds to  $-21$  degrees, and the best estimated direction is  $270$  degrees. As the Markov localization needs a probabilistic value  $p(s|l)$  of perceiving a sensor view  $s$  given that the robot is at location  $l = (< x, y >, \theta_i)$ , a difference value  $d(s, v(l))$  can be computed from the correlation results between the sensor view  $s$  and the local map view at the cell  $< x, y >$ , denoted by  $v(l)$ , and then a probabilistic value can be obtained from  $d(s, v(l))$ . We compute  $d(s, v(l))$  as the minimum difference (in the correlation results) for an angular interval with center at  $\theta_i$ . The desired probability is computed by  $p(s|l) = e^{-\alpha d(s, v(l))}$  where  $\alpha$  is a positive real number.

Given that this procedure is expensive, the next section shows a fast way to find a small set of candidate cells to apply this procedure, instead of all the free cells in the map.

## 2.2 Roadmap

Following the ideas described in [9], the set of possible cells where the robot is allowed to move, tries to keep a fixed distance  $k$  to obstacles. Figure 3 (a) shows the full set of free cells where the robot can be as white pixels, while Figure 3 (b) shows the cells that form the roadmap. There is a significant reduction in the number of cells. To get a robust procedure, our approach considers a *thick roadmap* (see Fig. 3 (c)) which include the cells in the neighborhood of the *thin roadmap* (see Fig. 3 (b)). The idea is to use the thin roadmap to predict movements of the robot (in the case of more than one group of hypotheses) and to use the thick roadmap to restrict the possible locations where the robot can be. The following section describes the process to update the probability of hypotheses after the robot senses or moves.

## 3 Markov Localization

Following [5], the key idea of Markov localization is to compute a probability distribution over all possible locations in the environment.  $p(L_t = l)$  denotes the

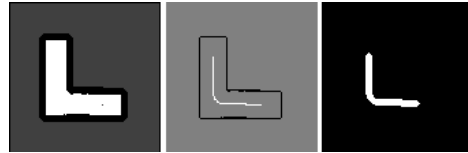


**Fig. 3.** A roadmap. From left to right: (a) Full set of free cells. (b) Thin roadmap for  $k = 1$  m. (c) Thick roadmap

probability of finding the robot at location  $l$  at time  $t$ . Here,  $l$  is a location in  $x - y - \theta_i$  space where  $x$  and  $y$  are Cartesian coordinates of cells and  $\theta_i$  is a valid orientation.  $p(L_0)$  reflects the initial state of knowledge and it is uniformly distributed to reflect the global uncertainty.  $p(L_t)$  is updated whenever:

1. *The robot moves.* Robot motion is modeled by a conditional probability, denoted by  $p_a(l|l')$ .  $p_a(l|l')$  denotes the probability that motion action  $a$ , when executed at  $l'$ , carries the robot to  $l$ .  $p_a(l|l')$  is used to update the belief upon robot motion:

$$p(L_{t+1} = l) \leftarrow \frac{\sum_{l'} p_a(l|l') p(L_t = l)}{p(s)} \quad (1)$$

Here  $p(s)$  is a normalizer that ensures that  $p(L_{t+1})$  sums up to 1 over all  $l$ . An example of  $p_a(l|l')$  is shown in Figure 4, considering that the robot moves forward in the thick roadmap, and the orientation of the robot is aligned to one of the possible 8 directions  $\theta_i$ . Circles denote grid cells and the most probable transition in Figure 4 is labeled with 4/10.

2. The robot senses. When sensing  $s$ ,

$$p(L_{t+1} = l) \leftarrow \frac{p(s|l)p(L_t = l)}{p(s)} \quad (2)$$

Here  $p(s|l)$  is the probability of perceiving  $s$  at location  $l$ . In order to get an efficient procedure to update the probability distribution, cells with probability below some threshold  $u$  are set to zero.

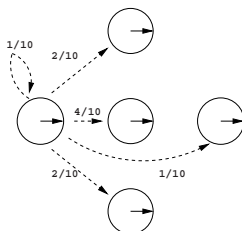


**Fig. 4.** Robot motion for one direction

## 4 Hypothesis Elimination

Locations,  $l$ , with  $p(L_t = l) \geq u$  are clustered into  $n$  clusters or groups according to their location  $l$  using AutoClass [3], a Bayesian clustering technique.

The idea to eliminate hypotheses is to move the robot through the thin roadmap trying to reduce the number of clusters.

To get an efficient procedure, our approach considers that the mobile robot is at the most probable location and then considers all the cells of the thin roadmap as valid movements for the robot. If we assign to locations of the thin roadmap the number of possible groups of hypotheses, a good movement to eliminate hypotheses is to direct the robot toward the nearest cell with less than  $n$  groups. Let this cell be called the *goal* cell.

To compute the similarity between local map view associated to two cells of the thin roadmap we introduce a *similarity matrix*. Let  $c_i$ , ( $i = 1, \dots, m$ ) denote the  $m$  cells of the thin roadmap, and  $\text{sim}(c_i, c_j)$  be the similarity between the local map views associated to cells  $c_i$  and  $c_j$ . A similarity measure  $\text{sim}$  can be computed using the correlation technique previously presented,

$$\text{sim}(c_i, c_j) = \max_{i=0, \dots, 7} \{P(s = v(c_i) | l = (c_j, \theta_i))\} \quad (3)$$

$\text{sim}(c_i, c_j)$  for all  $i, j = 1, \dots, m$  form a *similarity matrix*  $\mathbf{S}$  that can be computed from the map and the roadmap, before the localization process starts.

If there are more than one group of hypotheses, we can predict a robot movement in two different ways: 1) using an ideal model for the robot movements and 2) using a model that include uncertainty. Let these types of prediction be called deterministic and non deterministic prediction respectively.

In both cases we use a Markov localization representation  $p'(L)$ , to track groups of hypotheses under the possible set of *virtual* movements of the robot; and  $p(L)$  to represent the set of hypotheses of the location of the robot, given the set of *real* movements. When a prediction process starts,  $p'(L)$  and  $p(L)$  are the same. Once a goal cell in  $p'(L)$  is computed, assuming that the robot location is given by the most probable hypothesis, the robot can move towards the goal cell, updating  $p(L)$ . The prediction process is repeated if there are more than one group of hypotheses, until there is only one group.

### 4.1 Deterministic Prediction

If the movements of the robot are considered deterministic or ideal, they can be represented like a rotation followed by a translation [5]. Let  $c_b$  be the most probable location where the robot can be. After a given *virtual movement*  $v$  from  $c_b$  to a cell  $c_i$  of the thin roadmap, the transformation given by  $v$  can be applied to all locations of the probability distribution. Let  $c_j$  be the new position for one hypothesis, after transformation  $v$ . After this virtual movement, a *virtual sensing* is applied. Here we use the similarity matrix to estimate  $p(s|l)$ , assuming that the robot is at location  $l = < c_j, \theta_j >$ , and that  $s$  corresponds to the local map view from cell  $c_i$  (the most probable):

$$P(s|l)) = \begin{cases} sim(c_i, c_j') & \text{if } c_j \in \text{ thick roadmap} \\ 0 & \text{otherwise} \end{cases} \quad (4)$$

where  $c_j'$  is the cell of the thin roadmap closest to  $c_j$ .

## 4.2 Non Deterministic Prediction

An improvement over the deterministic prediction is to include an uncertainty model for the virtual movements of the robot (e.g. the model illustrated in Figure 4). A virtual movement from a cell  $c_b$  to  $c_i$  (as in the deterministic prediction) is split in a sequence of  $<(m_1, s_1), (m_2, s_2)\dots>$ , where  $m_i$  indicates a motion step to an adjacent cell, and  $s_i$  is a sensing step. In other words, instead of considering only a target cell where the robot can be, there will be a set of cells (limited by the trimming process after the sensing step). The sensing step is the same as in the deterministic prediction.

Considering that the thin roadmap is usually of one or two cells wide, results from an adjacent cell can be used to compute further results, giving a fast algorithm. In the implementation we use a breadth first search over the thin roadmap.

## 5 Experimental Results

This section presents preliminary results obtained using a mobile robot simulator. The robot simulates sonars and a low cost laser range sensor, implemented with a laser line generator and a camera. The laser sensor gives good measurements within a range of 3 m. The simulated robot has an uniform random error on displacements of  $\pm 10\%$  and  $\pm 5\%$  on rotations. We present two experiments to test the deterministic and non deterministic prediction for two complex environments.

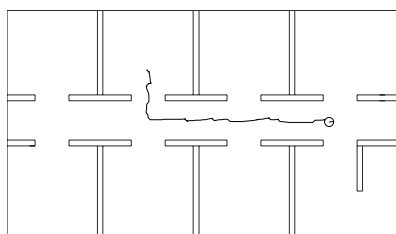


**Fig. 5.** A complex environment

Figure 5 shows a complex simulated environment of  $17.5 \times 10 \text{ m}$ . At the beginning there were 6 groups of hypotheses, one per room except in the two

rightmost rooms. After moving through 5 cells (of  $10 \times 10\text{ cm}$ ) towards the predicted goal cell, a sensing step is inserted and the prediction process is repeated until there is only a group of hypotheses. At the end of the path followed by the robot, there is only a group of hypotheses, the right one. In this case, both types of predictions, deterministic and non deterministic, solved the localization problem and lead to similar paths.

Figure 6 shows another simulated environment of  $12 \times 15.5\text{ m}$  where the corridor on the left is slightly longer than corridor on the right. At the beginning there were 2 groups of hypotheses,  $C_0$  and  $C_1$ . The deterministic prediction computes a goal cell  $P_d$  near the intersection of corridors, while the non deterministic prediction indicates a cell  $P_{nd}$  in the bottom part of the roadmap. In this case, the non deterministic prediction solves the localization problem and the deterministic prediction fails. The deterministic prediction is faster (2 seconds versus 6 seconds on a PC Pentium III 733Mhz) but it fails to solve the global localization problem.

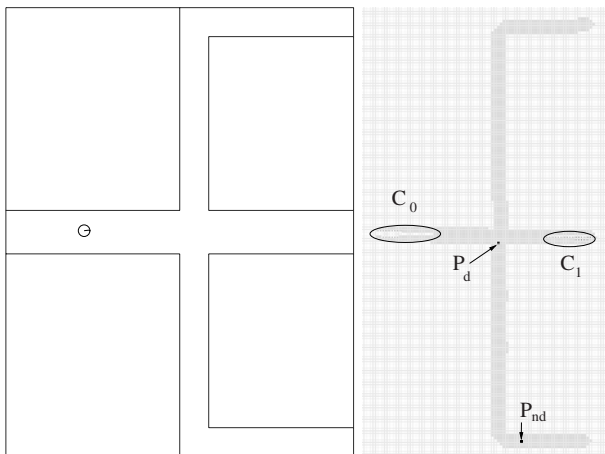


**Fig. 6.** (left) The simulator. (right) Roadmap with clusters  $C_0$  and  $C_1$  and results from the deterministic ( $P_d$ ) and non deterministic prediction ( $P_{nd}$ )

## 6 Conclusions

A robust approach to solve the global localization problem in indoor environments has been presented. It can be seen as the application of two Markov localization representations: one to track probable locations of the robot; an another to predict movements of the robot when there is more than one group of hypotheses. The second Markov representation can use a deterministic or a non deterministic model for the movements of the robot. As the experiments confirm, a non deterministic prediction is more robust than a deterministic one, specially

when the odometer of the robot or its sensors are not very accurate, or there are long corridors in the environment. In these cases the non deterministic prediction (using a model for the uncertainty of the robot), succeeds while a determinist prediction (modeled by a single rotation followed by a translation) can fail.

In the future, we plan to test this approach using real robots and environments with long corridors and similar places.

## References

1. J. Borenstein, B. Everett, and L. Feng. *Navigating Mobile Robots: Systems and Techniques*. A.K. Peter, Ltd., Wellesley, MA, 1996.
2. J.A. Castellanos and J. D. Tardos. *Mobile robot localization and map building: a multisensor fusion approach*. Kluwer Academic Publishers, 1999.
3. P. Cheeseman and J Stutz. Bayesian classification (autoclass): Theory and results. In U.-M. Fayyad, G. Piatetsky-Shapiro, P. Smyth, and R. Uthurusamy, editors, *Advances in Knowledge Discovery and Data Mining*. AAAI Press/MIT Press, 1996.
4. G. Dudek, K. Romanik, and S. Whitesides. Localizing a robot with minimum travel. *SIAM J. Comput.*, 27(2):583–604, 1998.
5. D. Fox and W. Burgard. Active markov localization for mobile robots. *Robotics and Autonomous Systems*, 1998.
6. L. Guibas, R. Motwani, and P. Raghavan. The robot localization problem. In K. Goldberg, D. Halperin, and J. C. Latombe, editors, *Algorithmic Foundations of Robotics*. A. K. Peters, 1995.
7. J.-S. Gutmann, W. Burgard, D. Fox, and K. Konolige. An experimental comparison of localization methods. In *Proc. International Conference on Intelligent Robots and Systems (IROS'98)*, 1998.
8. L. P. Kaelbling, A. R. Cassandra, and J. A. Kurien. Acting under uncertainty: Discrete Bayesian models for mobile-robot navigation. In *Proceedings of the IEEE/RSJ International Conference on Intelligent Robots and Systems*, 1996.
9. L. Romero, E. Morales, and E. Sucar. A robust exploration and navigation approach for indoor mobile robots merging local and global strategies. In M. C. Monard and J.S. Sichman, editors, *Advances in Artificial Intelligence, LNAI 1952*. Springer, 2000.
10. L. Romero, E. Morales, and E. Sucar. A hybrid approach to solve the global localization problem for indoor mobile robots considering sensor's perceptual limitations. In *Proc. International Joint Conference on Artificial Intelligence (IJCAI)*, Seattle, WA, 2001.
11. R. Simmons and S. Koenig. Probabilistic robot navigation in partially observable environments. In *Proc. International Joint Conference on Artificial Intelligence*, 1995.
12. S. Thrun. Learning maps for indoor mobile robot navigation. *Artificial Intelligence*, 99(1):21–71, 1998.
13. S. Thrun, A. Bucken, W. Burgar, et al. Map learning and high-speed navigation in rhino. In D. Kortenkamp, R. P. Bonasso, and R. Murphy, editors, *Artificial Intelligence and Mobile Robots*. AAAI Press/The MIT Press, 1998.
14. G. Weib, C. Wetzler, and E. Puttkamer. Keeping track of position and orientation of moving indoor systems by correlation of range-finder scans. In *Intelligent Robots and Systems*, 1994.

# Restricted Decontamination for the Imbalanced Training Sample Problem<sup>\*</sup>

R. Barandela<sup>1,2</sup>, E. Rangel<sup>1</sup>, J.S. Sánchez<sup>3</sup>, and F.J. Ferri<sup>4</sup>

<sup>1</sup> Lab for Pattern Recognition, Inst. Tecnológico de Toluca  
52140 Metepec, México [rbarandela@hotmail.com](mailto:rbarandela@hotmail.com)

<sup>2</sup> Instituto de Geografía Tropical, La Habana, Cuba

<sup>3</sup> Dept. Llenguatges i Sistemes Informàtics, U. Jaume I, 12071 Castelló, Spain

<sup>4</sup> Dept. Informàtica. Universitat de València. 46100 Burjassot, Spain

**Abstract.** The problem of imbalanced training data in supervised methods is currently receiving growing attention. Imbalanced data means that one class is much more represented than the others in the training sample. It has been observed that this situation, which arises in several practical domains, may produce an important deterioration of the classification accuracy, in particular with patterns belonging to the less represented classes. In the present paper, we report experimental results that point at the convenience of correctly downsizing the majority class while simultaneously increasing the size of the minority one in order to balance both classes. This is obtained by applying a modification of the previously proposed Decontamination methodology. Combination of this proposal with the employment of a weighted distance function is also explored.

## 1 Introduction

Design of supervised pattern recognition methods is usually based on a training sample (TS): a collection of examples previously analyzed by a human expert. Performance of the resulting classification system depends on the quantity and the quality of the information contained in the TS. Recently, concern has arisen about the complications produced by imbalance in the TS. A TS is said to be imbalanced when one of the classes (the minority one) is heavily under-represented in comparison to the other (the majority) class. For simplicity, and consistently with the common practice [7,13], we consider here only two-class problems. It has been observed that imbalanced training samples may cause a significant deterioration in the performance attainable by standard supervised methods. High imbalance occurs in real-world domains where the decision system is aimed to detect a rare but important case, such as fraudulent telephone calls [9], oil spills in satellite images of the sea surface [12], an infrequent disease [17], or text categorization [14].

\* Work partially supported by grants 32016-A (Mexican CONACyT), 744.99-P (Mexican Cosnet), TIC2000-1703-C03-03 (Spanish CICYT) and P1-1B2002-07 (Fundació Caixa Castelló-Bancaixa).

Most of the attempts for dealing with this problem can be categorized as [7]:

- a) Over-sampling the minority class to match the size of the other class [5].
- b) Downsizing the majority class so as to match the size of the other class [13].
- c) Internally biasing the discrimination based process so as to compensate for the class imbalance [8,12].

As pointed out by many authors, overall accuracy is not the best criterion to assess the classifier's performance in imbalanced domains. For instance, consider a practical application where only 2% of the patterns belong to the minority class. In such a situation, labeling all new patterns as members of the majority class would give an accuracy of 98%. Obviously, this kind of system would be useless. Consequently, other criteria have been proposed. One of the most widely accepted criterion is the geometric mean,  $g = (a^+ \cdot a^-)^{1/2}$ , where  $a^+$  is the accuracy on cases from the minority class and  $a^-$  is the accuracy on cases from the majority one [13]. This measure tries to maximize the accuracy on each of the two classes while keeping these accuracies balanced.

In an earlier study [4], we provide preliminary results of several techniques addressing the class imbalance problem. In such a work, we focused on under-sampling the majority class and also on internally biasing the discrimination process, as well as on a combination of both approaches. In the present paper, we introduce a new proposal for balancing the TS through reduction of the majority class size and, at the same time, an increase in the amount of prototypes in the minority class. To this aim, we employ a modification of the Decontamination methodology [2] that will be referred to as Restricted Decontamination. We also explore the convenience of using this technique in combination with a weighted distance measure aimed at biasing the classification procedure. These ideas are evaluated over four real datasets using the Nearest Neighbor (NN) rule for classification and the geometric mean as the performance measure.

The NN rule is one of the oldest and better-known algorithms for performing supervised nonparametric classification. The entire TS is stored in the computer memory. To classify a new pattern, its distance to each one of the stored training patterns is computed. The new pattern is then assigned to the class represented by its nearest neighboring training pattern. Performance of NN rule, as with any nonparametric method, is extremely sensitive to incorrectness or imperfections in the TS. Nevertheless, the NN rule is very popular because of its characteristics: a) conceptual simplicity, b) easy implementation, c) known error rate bounds, and d) potentiality to compete favorably in accuracy with other classification methods in real data applications.

## 2 Related Works

The two basic methods for resampling the TS cause the class distribution to become more balanced. Nevertheless, both strategies have shown important drawbacks. Under-sampling may throw out potentially useful data, while over-sampling increases the TS size and hence the time to train a classifier. In the

last years, research has focused on improving these basic methods. Kubat and Matwin [13] proposed an under-sampling technique that is aimed at removing those majority prototypes that are “redundant” or that “border” the minority instances. They assume that these bordering cases are noisy examples. However, they do not use any of the well-known techniques for cleaning the TS.

Chawla et al. [5] proposed a technique for over-sampling the minority class. Instead of merely replicating prototypes of the minority class, they form new minority “synthetic” instances. This is done by taking each minority class instance and creating synthetic instances along the line segments joining any/all of the  $k$  minority class nearest neighbors.

Barandela et al. [3] explore the convenience of designing a multiple classification system for working in imbalanced situations. Instead of using a single classifier, an ensemble is implemented. The idea is to train each one of the individual components of the ensemble with a balanced TS. In order to achieve this, each individual component of the ensemble is trained with a subset of the TS. As many subsets of the TS as required to get balanced subsets are generated. The number of subsets is determined by the difference between the amount of prototypes from the majority class and that of the minority class.

Pazzani et al. [15] take a slightly different approach when learning from an imbalanced TS by assigning different weights to prototypes of the different classes. On the other hand, Ezawa et al. [8] bias the classifier in favor of certain feature relationships. Kubat et al. [12] use some counter-examples to bias the recognition process.

### 3 Proposed Strategies

In several practical applications, class identification of prototypes is a difficult and costly task. There is another source of distortion in the training data: prototypes with errors in some attribute values and instances that are atypical or exceptional. Generalization accuracy of the supervised method may be degraded by the presence of incorrectness or imperfections in the TS. Particularly sensitive to these facts are nonparametric classifiers whose training is not based upon any assumption about probability density functions. This explains the emphasis given to the evaluation of procedures used to collect and to clean the TS.

In a previous work [2], a methodology for correcting a TS while employing nonparametric classifiers has been presented. The Decontamination procedure can be regarded as a cleaning process removing some elements of the TS and correcting the label of several others while retaining them. Experimental results with both simulated and real datasets have shown that the Decontamination methodology allows to cope with all types of imperfections (mislabeled, noisy, atypical or exceptional) in the TS, improving the classifier’s performance and lowering its computational burden. The Decontamination methodology is based on two previously published editing techniques.

### 3.1 Basic Editing Techniques

Editing techniques are mainly aimed at improving the performance of the NN rule by filtering the training prototypes. As a byproduct, they also obtain a decrease in the TS size and, consequently, a reduction of the computational cost of the classification method. The first work of editing corresponds to Wilson [16] and several others have followed.

**Wilson's Editing procedure.** This technique consists of applying the  $k$ -NN ( $k > 1$ ) classifier to estimate the class label of every prototype in the TS. Those instances whose class label does not agree with the class associated to the majority of the  $k$  neighbors are discarded. The procedure is:

1. Let  $S = X$  ( $X$  is the original TS and  $S$  will be the edited TS)
2. For each  $x$  in  $X$  do:
  - a) Find the  $k$  nearest neighbors of  $x$  in  $X - \{x\}$
  - b) Discard  $x$  from  $S$  if its label disagrees with the class associated with the largest number of the  $k$  neighbors.

**Generalized Editing (GE: Koplowitz and Brown [11]).** This is a modification of the Wilson's algorithm. Out of concern with the possibility of too many prototypes being removed from the TS because of Wilson's editing procedure, this approach consists of removing some suspicious prototypes and to change the class labels of some other instances. Accordingly, it can be regarded as a technique for modifying the structure of the TS (through re-labeling of some prototypes and not only for eliminating atypical instances). In GE, two parameters have to be defined:  $k$  and  $k'$  in such a way that  $(k + 1)/2 \leq k' \leq k$ . This editing algorithm can be written as follows:

1. Let  $S = X$  ( $X$  is the original training set and  $S$  will be the processed TS)
2. For each  $x$  in  $X$  do:
  - a) Find the  $k$  nearest neighbors of  $x$  in  $X - \{x\}$ .
  - b) If a class has at least  $k'$  representatives among those  $k$  neighbors, then label  $x$  according to that class (independently of its original class label). Otherwise, discard it from  $S$ .

### 3.2 The Decontamination Methodology in Brief

The Decontamination methodology involves several applications of the GE technique, followed by the employment, also repeatedly, of the Wilson's Editing algorithm. Repetition in the application of each one of these techniques stops if one of the following criteria is fulfilled:

1. Stability in the structure of the TS has been reached (no more removals and no more re-labeling).
2. Estimate of the misclassification rate (leave-one-out method; see [10]) has begun to increase.

3. One class has resulted emptied (all its representatives in the TS have been removed or transferred to another class) or has resulted with too few prototypes (less than five training instances for each attribute).

### 3.3 Proposed Modification of the Decontamination Methodology

In the present paper, we present a modification of the Decontamination methodology: the Restricted Decontamination. In this restricted way, the Decontamination process is applied only to the majority class. That is, changes of label or removal from the TS affect only to those prototypes representing the majority class. In this way, a decrease in the amount of prototypes of the majority class is obtained. At the same time, some prototypes, originally in the majority class, are incorporated (by changing their labels) to the minority class, increasing the size of this latter class.

In the present work, Restricted Decontamination is employed for the first time for handling imbalance. This restricted procedure was initially designed to handle situations when information about the particular application area could imply existence of contamination in only some of the classes [1]. The source for this information could be given by some characteristics of the process used to collect the TS or by the intrinsic nature of the problem at hand.

### 3.4 The Weighted Distance Function

As a technique for internally biasing the discrimination procedure, we have experimented with a modification of the Euclidean metric that can be regarded as a weighted distance function [4]. With this modification, when classification of a new pattern  $y$  is attempted, and in the search through the TS of its nearest neighbor, the following quantity must be computed for each training instance  $x$ :

$$d_W(y, x) = (n_i/n)^{1/m} d_E(y, x)$$

where  $i$  refers to the class of instance  $x$ ,  $n_i$  is the number of training patterns from this class,  $n$  is the TS size,  $m$  is the dimensionality of the feature space and  $d_E(\cdot)$  is the Euclidean metric.

The idea behind this distance proposal is to compensate for the imbalance in the TS without actually altering the imbalance. Weights are assigned, unlike in the usual weighted  $k$ -NN rule proposals, to the respective classes and not to the individual prototypes. In that way, since the weighting factor is greater for the majority class than for the minority one, distance values to training instances of the minority class are much more reduced than the distance values to the training examples of the majority class. This produces a tendency for the new patterns to find their nearest neighbor among the cases of the minority class, increasing the accuracy in that class.

**Table 1.** Characterization of the datasets employed in the experiments

Datasets	Attributes	Training Sample		Test Sample	
		class 1	class 2	class 1	class 2
Phoneme	5	1268	3054	318	764
Satimage	36	500	4647	126	1162
Glass	9	24	150	5	35
Vehicle	18	170	508	42	126

## 4 Experimental Results

The Restricted Decontamination proposal, and its combination with the weighted distance in the classification stage, are assessed through experiments carried out with four real datasets taken from the UCI Database Repository [6]. In each dataset, five-fold cross validation was employed (80% for the TS and 20% for a test set). Results to be presented hereafter represent the averaged values of the five replications. To facilitate comparison with other published results [13], in the Glass set the problem was transformed for discriminating class 7 against all the other classes, and in the Vehicle dataset the task is to classify class 1 against all the others. Satimage dataset was also mapped to configure a two-class case, the training patterns of classes 1, 2, 3, 5, and 6 were joined to form a unique class and the original class 4 was left as the minority one. These modified datasets are described in Table 1. As can be seen, now class 2 is the majority class and class 1 is the minority one.

The results are shown in Table 2. The average  $g$  values obtained when classifying with the original TSs, and with these TSs after we have processed them with the idea of Kubat and Matwin [13], are also included for comparison purposes. For a better illustration, results produced by the usual Decontamination procedure [2] are reported too. The Restricted Decontamination proposed here yields an improvement in performance (as measured by the  $g$  criterion), in comparison to all the other methods. This improvement is more remarkable when the weighted distance is employed for classifying new patterns. It is also important to note that the results from the procedure of Kubat and Matwin are excelled in all datasets. The usual Decontamination methodology has been shown to produce important benefits [2] when considering the general accuracy, but it is not convenient in those cases when imbalance in the TS is present.

**Table 2.** Averaged mean values (and standard deviations) of the  $g$  criterion

Procedure	Phoneme	Satimage	Glass	Vehicle
Original TS	73.8	70.9	86.7	56.0
Decontamination & Euclidean classif.	69.6	67.3	84.6	46.8
<b>Restricted Decontam. &amp; Euclidean classif.</b>	<b>73.8</b>	<b>75.4</b>	<b>86.2</b>	<b>66.4</b>
Decontamination & Weighted classif	73.6	68.9	84.6	49.7
<b>Restricted Decontam. &amp; Weighted classif.</b>	<b>74.6</b>	<b>77.4</b>	<b>87.9</b>	<b>66.3</b>
Kubat and Matwin	68.3	72.9	79.0	65.4

The effects of the Restricted Decontamination can be better analyzed by considering the balance obtained in the TS after its application (see Table 3). Results in this table indicate a decrease in the size of the majority class (number 2), while the minority class (number 1) size is increased. On the other hand, the usual Decontamination procedure deteriorates the imbalance in the TS, when compared with the original TS. The proposal of Kubat and Matwin, by aggressively under-sampling the majority class, produces an imbalance in the other direction, very remarkable in Phoneme and Glass datasets.

**Table 3.** Percentage of patterns in each class

Procedure	Phoneme		Satimage		Glass		Vehicle	
	class 1	class 2						
Original TS	29.34	70.66	9.71	90.29	13.79	86.21	25.07	74.93
Decontamination	25.68	74.32	10.04	89.96	11.68	88.32	15.24	84.76
<b>Restricted Decont.</b>	<b>35.04</b>	<b>64.98</b>	<b>15.09</b>	<b>84.91</b>	<b>15.06</b>	<b>84.94</b>	<b>43.97</b>	<b>56.03</b>
Kubat and Matwin	85.76	14.24	52.40	47.60	75.00	25.00	57.75	42.25

## 5 Concluding Remarks

In many real-world applications, supervised pattern recognition methods have to cope with highly imbalanced TSs. Traditional learning systems such as the NN rule can be misled when applied to such practical problems. This effect can become moderate by using a procedure that allows to under-sample the majority class while over-sampling the minority class. In this direction, a new approach has been proposed in this paper. The Restricted Decontamination has been shown to improve the balance in the TS. Classification with the weighted distance, after preprocessing the TS with the Restricted Decontamination has produced important progress in the resulting g value, when compared with the original TS. These results have also excelled those obtained by the proposal of Kubat and Matwin. This can be explained because the proposal of Kubat and Matwin is based upon techniques for eliminating redundant instances and not for cleaning the TS from noisy or atypical prototypes.

Benefits of the proposal are shown even in the Glass dataset. This dataset suffers not only of the imbalance problem, but also the minority class is too small. Adequacy of the TS size must be measured by considering the number of prototypes in the smaller class and not in the whole TS. For the minority class in Glass dataset, the size/dimensionality ratio is very low: only 2.7 instances for each attribute. Restricted Decontamination and weighted distance have been able to handle this critical situation.

A more extensive research is currently being conducted to explore all the issues linked to the imbalanced TSs. At present, we are studying the convenience of applying genetic algorithms to reach a better balance among classes. We are also experimenting in situations with more than two classes, as well as doing

some research about the convenience of using these procedures to obtain a better performance with other classifiers, such as the neural networks models.

## References

1. R. Barandela. *The Nearest Neighbor rule: an empirical study of its methodological aspects*. PhD thesis, Univ. Berlin, 1987.
2. R. Barandela, E. Gasca, and R. Alejo. Correcting the training data. In D. Chen and X. Cheng, editors, *Pattern Recognition and String Matching*. Kluwer, The Netherlands, 2003.
3. R. Barandela, J. S. Sánchez, and R. M. Valdovinos. New applications of ensembles of classifiers. *Pattern Analysis and Applications*, to appear, 2003.
4. R. Barandela, J.S. Sánchez, V. García, and E. Rangel. Strategies for learning in class imbalance problems. *Pattern Recognition*, 36:849–851, 2003.
5. N. V. Chawla, K. W. Bowyer, L. O. Hall, and W. P. Kegelmeyer. SMOTE: synthetic minority over-sampling technique. *Journal of Artificial Intelligence Research*, 16:321–357, 2000.
6. Merz C.J. and P. M. Murphy. Uci repository of machine learning databases. Technical report, University of California at Irvine, Department of Information and Computer Science, 1998.
7. T. Eavis and N. Japkowicz. A recognition-based alternative to discrimination-based multi-layer perceptrons. In *Workshop on Learning from Imbalanced Data Sets*. TR WS-00-05, AAAI Press, 2000.
8. K.J. Ezawa, M. Singh, and S.W. Norton. Learning goal oriented bayesian networks for telecommunications management. In *Proc. 13th Int. Conf. on Machine Learning*, pages 139–147, 1996.
9. T. Fawcett and F. Provost. Adaptive fraud detection. *Data Mining and Knowledge Discovery*, 1:291–316, 1996.
10. D. J. Hand. *Construction and assessment of classification rules*. John Wiley and Sons, Chichester, 1997.
11. J. Koplowitz and T. A. Brown. On the relation of performance to editing in nearest neighbor rules. In *Proceedings of the 4th International Joint Conference on Pattern Recognition*, 1978.
12. M. Kubat, R. Holte, and S. Matwin. Detection of oil-spills in radar images of sea surface. *Machine Learning*, 30:195–215, 1998.
13. M. Kubat and S. Matwin. Addressing the curse of imbalanced training sets: One-sided selection. In *Proceedings of the 14th International Conference on Machine Learning*, pages 179–186, 1997.
14. D. Mladenic and M. Grobelnik. Feature selection for unbalanced class distribution and naive bayes. In *Proc. 16th Int. Conf. on Machine Learning*, pages 258–267, 1999.
15. M. Pazzani, C. Merz, P. Murphy, K. Ali, T. Hume, and C. Brunk. Reducing misclassification costs. In *Proc 11th Int. Conf. on Machine Learning*, pages 217–225, 1994.
16. D. L. Wilson. Asymptotic properties of nearest neighbor rules using edited data. 2(3):408–421, 1972.
17. K. Woods, C. Doss, K.W. Bowyer, J. Solka, C. Priebe, and W.P. Kegelmeyer. Comparative evaluation of pattern recognition techniques for detection of microcalcifications in mammography. *International Journal of Pattern Recognition and Artificial Intelligence*, 7:1417–1436, 1993.

# An Entropy Maximization Approach to Optimal Model Selection in Gaussian Mixtures

Antonio Peñalver, Juan M. Sáez, and Francisco Escolano

Robot Vision Group

Departamento de Ciencia de la Computación e Inteligencia Artificial

Universidad de Alicante, Spain

{apenalver, jmsaez, sco}@dccia.ua.es

<http://rvg.ua.es>

**Abstract.** In this paper we address the problem of estimating the parameters of a Gaussian mixture model. Although the EM (Expectation-Maximization) algorithm yields the maximum-likelihood solution it has many problems: (i) it requires a careful initialization of the parameters; (ii) the optimal number of kernels in the mixture may be unknown beforehand. We propose a criterion based on the entropy of the pdf (probability density function) associated to each kernel to measure the quality of a given mixture model, and a modification of the classical EM algorithm to find the optimal number of kernels in the mixture. We test this method with synthetic and real data and compare the results with those obtained with the classical EM with a fixed number of kernels.

## 1 Introduction

Gaussian mixture models, have been widely used in the field of statistical pattern recognition. One of the most common methods for fitting mixtures to data is the EM algorithm [4]. However, this algorithm is prone to initialization errors and, in these conditions, it may converge to local maxima of the log-likelihood function. In addition, the algorithm requires that the number of elements (kernels) in the mixture is known beforehand. For a given number of kernels, the EM algorithm yields a maximum-likelihood solution but this does not ensure that pdf of the data (multi-dimensional patterns) is properly estimated. A maximum-likelihood criterion with respect to the number of kernels is not useful because it tends to use a kernel to describe each pattern.

The so called model-selection problem has been addressed in many ways. Some approaches start with a few number of kernels and add new kernels when necessary. For instance, in [14], the kurtosis is used as a measure of non-Gaussianity yielding a test for splitting a kernel in one-dimensional data. In [15] this method is extended to the multi-dimensional case. This approach has same drawbacks, because kurtosis can be very sensitive to outliers. In [16] it is proposed a greedy method, which performs a global search in combination with another local search whenever a new kernel is added.

Other model-selection methods start with a high number of kernels and proceed to fuse them. In [5][6], the EM algorithm is initialized with many kernels randomly placed and then the Minimum-description length principle [9] is applied to iteratively remove some of the kernels until the optimal number of them is found. In [11], the proposed algorithm is allowed both to split and fuse kernels. Kernel fusion arises when many patterns have the same posterior probability and splitting is driven by the Kullback-Leibler divergence between a component density and empirical density in the neighborhood of the component. In this approach, the number of components remains unchanged.

In this paper we propose a method that starting with few kernels, typically one, find the maximum-likelihood solution. Then it tests whether the underlying pdf of each kernel is Gaussian and otherwise it replaces that kernel with two kernels adequately separated from each other. In order to detect non-Gaussianity we compare the entropy of the underlying pdf with the theoretical entropy of a Gaussian. After two new kernels are introduced, our method performs several steps of partial EM in order to obtain a new maximum-likelihood solution.

## 2 Gaussian-Mixture Models

A d-dimensional random variable  $\mathbf{y}$  follows a finite-mixture distribution when its pdf  $p(\mathbf{y}|\Theta)$  can be described by a weighted sum of known pdf's named kernels. When all these kernels are Gaussian, the mixture is named in the same way:

$$p(\mathbf{y}|\Theta) = \sum_{i=1}^K \pi_i p(\mathbf{y}|\Theta_i), \text{ where } 0 \leq \pi_i \leq 1, \quad i = 1, \dots, K, \quad \text{and} \quad \sum_{i=1}^K \pi_i = 1, \quad (1)$$

being  $K$  the number of kernels,  $\pi_1, \dots, \pi_k$  the a priori probabilities of each kernel, and  $\Theta_i$  the parameters describing the kernel. In Gaussian mixtures,  $\Theta_i = \{\mu_i, \Sigma_i\}$ , that is, the average vector and the covariance matrix.

The set of parameters of a given mixture is  $\Theta \equiv \{\Theta_1, \dots, \Theta_k, \pi_1, \dots, \pi_k\}$ . Obtaining the optimal set of parameters  $\Theta^*$  is usually posed in terms of maximizing the log-likelihood of the pdf to be estimated:

$$\ell(Y|\Theta) = \log p(Y|\Theta) = \log \prod_{n=1}^N p(y_n|\Theta) = \sum_{n=1}^N \log \sum_{k=1}^K \pi_k p(y_k|\Theta_k). \quad (2)$$

$$\Theta^* = \arg \max_{\Theta} \ell(\Theta). \quad (3)$$

where  $Y = \{y_1, \dots, y_N\}$  is a set of  $N$  i.i.d. samples of the variable  $Y$ .

### 2.1 EM Algorithm

The EM (Expectation-Maximization) algorithm [4] is an iterative procedure that allows us to find maximum-likelihood solutions to problems involving *hidden variables*. The EM algorithm generates a sequence of estimations of parameters

$\{\Theta^*(t), t = 1, 2, \dots\}$  by alternating an expectation step and the maximization step until convergence. In the case of mixtures [8], the hidden variable can be regarded as the kernel each data has been sampled from. The E-step estimates the posterior probability that the data  $\mathbf{y}_n$  was sampled with the kernel  $k$ :

$$p(k|\mathbf{y}_n) = \pi_k p(\mathbf{y}^{(n)}|k) / \sum_{j=1}^K \pi_j p(\mathbf{y}^{(n)}|k) \quad (4)$$

In M-step, the new parameters  $\Theta^*(t+1)$  are given by:

$$\pi_k = \frac{1}{N} \sum_{n=1}^N p(k|\mathbf{y}_n), \quad \mu_k = \frac{\sum_{n=1}^N p(k|\mathbf{y}_n) \mathbf{y}_n}{\sum_{n=1}^N p(k|\mathbf{y}_n)} \text{ and } \mu_k = \frac{\sum_{n=1}^N p(k|\mathbf{y}_n) \mathbf{y}_n}{\sum_{n=1}^N p(k|\mathbf{y}_n)}. \quad (5)$$

A detailed description of this classic algorithm is given in [8]. Here we focus on the fact that if  $K$  is unknown beforehand it cannot be estimated through maximizing the log-likelihood because  $\ell(\Theta)$  grows with  $K$ . Fig. 1 shows the effect of using only a kernel, in classical EM algorithm with fixed number of kernels, to describe two Gaussian distributions: density is underestimated giving a poor description of the data. In the next section we describe the use of entropy to test whether a given kernel properly describes the underlying data.

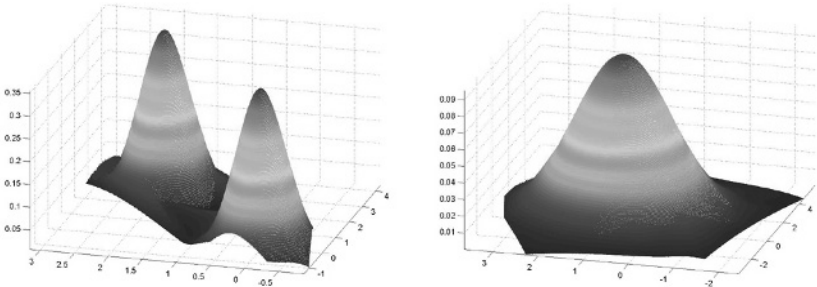


**Fig. 1.** Classic EM algorithm, fits erroneously data of a bimodal distribution (with averages  $\mu_1 = [0, 0]$  y  $\mu_2 = [3, 2]$ ) (left) to a Gaussian with  $\mu = [1.5, 1]$  (right).

### 3 Entropy Estimation

Entropy is a basic concept in information theory. The entropy of a given variable  $Y$  can be interpreted in terms of information, randomness, dispersion, and so on [3][10]. For a discrete variable we have:

$$H(Y) = -E_y[\log(P(Y))] = -\sum_{i=1}^N P(Y = y_i) \log p(Y = y_i). \quad (6)$$

where  $y_1, \dots, y_N$  is the set of values of variable  $Y$ . A fundamental result of information theory is that Gaussian variables have the maximum entropy among all

the variables with equal variance. Consequently the entropy of the underlying distribution of a kernel should reach a maximum when such a distribution is Gaussian. This theoretical maximum entropy is given by:

$$H(Y) = \frac{1}{2} \log[(2\pi e)^d |\Sigma|]. \quad (7)$$

Then, in order to decide whether a given kernel is truly Gaussian or must be replaced by two other kernels, we compare the estimated entropy of the underlying data with the entropy of a Gaussian. However, one of the main problems of this approach is that we must estimate, in principle, the pdf given a few samples [12][13][17].

### 3.1 Entropy Estimation with Parzen's Windows

The Parzen's windows approach [7] is a non-parametric method for estimating pdf's for a finite set of patterns. The general form of these pdf's using a Gaussian kernel and assuming diagonal covariance matrix  $\psi = \text{Diag}(\sigma_1^2, \dots, \sigma_{N_a}^2)$  is:

$$P^*(Y, a) \equiv \frac{1}{N_a} \sum_{y_a \in a} \frac{1}{\prod_{i=1}^d \sigma_i (2\pi)^{d/2}} \prod_{j=1}^d \exp \left\{ -\frac{1}{2} \left( \frac{y^j - y_a^j}{\sigma_j} \right)^2 \right\}, \quad (8)$$

where  $a$  is a sample of the variable  $Y$ ,  $N_a$  is the size of the sample,  $y^j$  represents the  $j$ -th component of  $y$  and  $y_a^j$  represents the  $j$ -th component of kernel  $y_a$ . In [12] it is proposed a method for adjusting the widths of the kernels using maximum likelihood. Given the definition of entropy in Equation 6, we have:

$$H_b(Y) \equiv -E_b[\log(P(Y))] = -\frac{1}{N_b} \sum_{y_b \in b} \log(P(y_b)) = -\frac{1}{N_b} \log(\ell(b)), \quad (9)$$

where  $\ell(b)$  is the likelihood of the data. As maximizing likelihood is equivalent to minimize entropy, this approach consists of estimating the derivative of entropy with respect to the widths of the kernels, and performs a gradient descent towards the optimal widths:

$$\frac{\partial}{\partial \sigma_d} H^*(Y) = \frac{1}{N_b} \sum_{y_b \in b} \sum_{y_a \in a} \frac{K_\psi(y_b - y_a)}{\sum_{y_a \in a} K_\psi(y_b - y_a)} \left( \frac{1}{\sigma_d} \right) \left( \frac{[y_b - y_a]_d^2}{\sigma_d^2} - 1 \right), \quad (10)$$

being  $\sigma_d$  the standard deviation in each dimension.

Given the optimal widths of the kernel, the entropy is estimated by

$$H^*(Y) = \frac{1}{N_b} \sum_{y_b \in b} \log \left( \frac{1}{N_a} \sum_{y_a \in a} K_\psi(y_b - y_a) \right), \quad (11)$$

In Fig. 2 we show the entropy estimation obtained for a sample of a 2D Gaussian variable with a diagonal covariance matrix with  $\sigma_1^2 = 0.36$  and  $\sigma_2^2 = 0.09$ , for different widths. The approximation of the maximum entropy defined in Equation 7 is 1.12307. From the shape of this function, it can be deduced that the optimal widths lay in a wide interval and consequently their choice is not so critical.

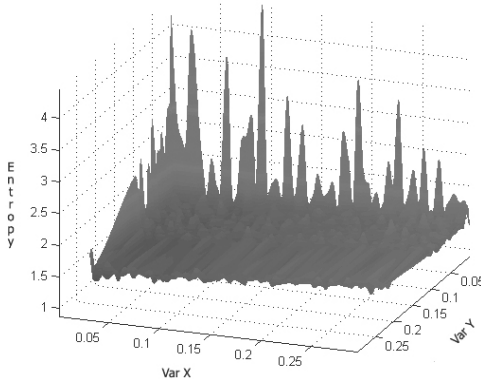


**Fig. 2.** Representing entropy as a function of the widths of the Parzen's kernels.

## 4 Optimal Model Selection with Maximum Entropy

### 4.1 Proposed Method

Comparing the estimations given for Equations 7 and 11, we have a way of quantifying the degree of Gaussianity of a given kernel. Given a set of kernels for the mixture (initially one kernel) we evaluate the real global entropy  $H(y)$  and the theoretical maximum entropy  $H_{max}(y)$  of the mixture by considering the individual pairs of entropies for each kernel, and the prior probabilities:

$$H(Y) = \sum_{k=1}^K \pi_k H_k(Y) \text{ and } H_{max}(Y) = \sum_{k=1}^K \pi_k H_{max_k}(Y). \quad (12)$$

If the ratio  $H(y)/H_{max}(y)$  is above a given threshold (typically 0.95) we consider that all kernels are well fitted. Otherwise, we select the kernel with the lowest individual ratio and it is replaced by two other kernels that are conveniently placed. Then, a new EM starts.

As the estimation of the entropy of a kernel requires two data sets, we select those whose distance to the average  $\mu_k$  is between the limits of a Gaussian:  $-3\sqrt{\lambda_i^k} \leq b_i \leq 3\sqrt{\lambda_i^k}$ , with  $b = P_t^T(\mu_k - y)$ .  $\lambda_i^k$ , with  $i = 1, 2..d$ , are the eigenvectors associated to the kernel, and  $b$  is the projection of a data  $y$  on the eigenspace spanned by the eigenvectors of the covariance matrix collected in  $P_k$ .

### 4.2 Introducing a New Kernel

A low  $H(y)/H_{max}(y)$  local ratio indicates that multimodality arises and thus the kernel must be replaced by two other kernels. Applying PCA (Principal Component Analysis) to the original kernel we find that the main eigenvector

indicates the direction of maximum variability and we can put the two new kernels along the opposite senses of this direction (Fig. 3). Being  $k$  the kernel with low Gaussianity, after splitting it, the two new kernels  $k_1$  and  $k_2$  with parameters  $\Theta_{k_1} = (\mu_{k_1}, \Sigma_{k_1})$  and  $\Theta_{k_2} = (\mu_{k_2}, \Sigma_{k_2})$  have the following initial averages  $\mu_{k_1} = \mu_k + \sqrt{\lambda_k} \mathbf{V}$  and  $\mu_{k_2} = \mu_k - \sqrt{\lambda_k} \mathbf{V}$ , with  $\lambda_k$  the principal eigenvalue for kernel  $k$  and  $\mathbf{V}$  its associated normalized eigenvector. Furthermore, the width of the two

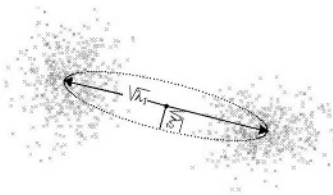


**Fig. 3.** The direction of maximum variability is associated to the eigenvector with highest eigenvalue autovector  $\lambda_1$

new kernel is divided by two. If  $\lambda'_k$  is the main eigenvalue in both kernels, then  $\sqrt{\lambda'_k} = \frac{\sqrt{\lambda_k}}{2}$ , consequently,  $\Sigma_{k_1} = \Sigma_{k_2} = \frac{1}{4} \Sigma_k$ . Finally, the new priors should also verify  $\sum_{k=1}^K \pi_k = 1$ , so we initialize them with  $\pi_{k_1} = \pi_{k_2} = \frac{1}{2} \pi_k$ . The proposed algorithm is described in Fig. 4.

**Initialization:** Start with a unique kernel.  $K = 1$ .  $\Theta_1 = \{\mu_1, \Sigma_1\}$  with random values.

**Repeat:** Main loop

**Repeat:** E, M Steps

        Estimate log-likelihood in iteration  $i$ :  $\ell_i$

**Until:**  $|\ell_i - \ell_{i-1}| < \text{CONVERGENCE\_THRESHOLD}$

    Evaluate  $H(Y)$  and  $H_{max}(Y)$  globally

**If**  $(H(Y)/H_{max} < \text{ENTROPY\_THRESHOLD})$

        Select kernel  $k$  with the lowest ratio and decompose into  $k_1$  and  $k_2$

**Initialize** parameters  $\Theta_{k_1}$  and  $\Theta_{k_2}$

        Initialize new averages:  $\mu_{k_1} = \mu_k + \sqrt{\lambda_k} \mathbf{V}$ ,  $\mu_{k_2} = \mu_k - \sqrt{\lambda_k} \mathbf{V}$

        Initialize new covariance matrices:  $\Sigma_{k_1} = \Sigma_{k_2} = \frac{1}{4} \Sigma_k$

        Set new a priori probabilities:  $\pi_{k_1} = \pi_{k_2} = \frac{1}{2} \pi_k$

**Else**

        Final = True

**Until:** Final = True

**Fig. 4.** Our maximum-entropy algorithm

### 4.3 Validation of the Method

In order to test our approach we have performed several experiments with synthetic and real data. In the first one we have generated 2500 samples from 5 bi-dimensional Gaussians with prior probabilities  $\pi_k = 0.2 \forall k$ . Their averages are:  $\mu_1 = [-1, -1]^T$ ,  $\mu_2 = [6, 3]^T$ ,  $\mu_3 = [3, 6]^T$ ,  $\mu_4 = [2, 2]^T$ ,  $\mu_5 = [0, 0]^T$  and their covariance matrices are

$$\Sigma_1 = \Sigma_5 = \begin{bmatrix} 0.20 & 0.00 \\ 0.00 & 0.30 \end{bmatrix}, \Sigma_2 = \begin{bmatrix} 0.60 & 0.15 \\ 0.15 & 0.60 \end{bmatrix}, \Sigma_3 = \begin{bmatrix} 0.40 & 0.00 \\ 0.00 & 0.25 \end{bmatrix}, \Sigma_4 = \begin{bmatrix} 0.60 & 0.00 \\ 0.00 & 0.30 \end{bmatrix}.$$

We have used a Gaussianity threshold of 0.95, and a convergence threshold of 0.001 for the EM algorithm. In order to evaluate the robustness of the proposed algorithm, several outliers were added to the data set. The sample size for estimating entropy through Parzen has been 75. We have found that despite this small size, entropy estimation is good enough. Our algorithm converges after 30 iterations finding correctly the number of kernels. In Fig. 5 we show the evolution of the algorithm. We have also applied the classical EM with 5 kernels. We

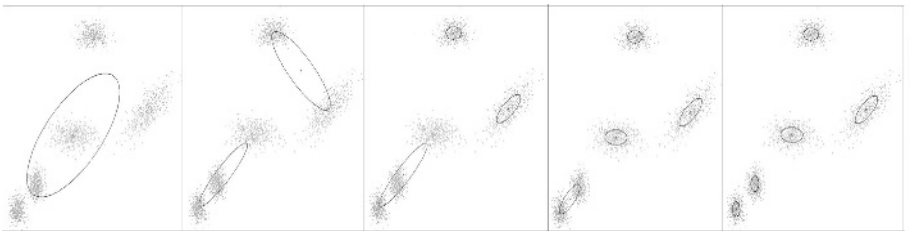


**Fig. 5.** Evolution of our algorithm from one initial kernel to 5 real kernels.

have performed 20 experiments with the latter data but randomly placing the kernels in each one. In 18 of the 20 experiments the classical EM finds a local maxima. The averaged number of iterations needed was 95 (being 250 the maximum and 23 the minimum). Then, only in two cases the classical EM found the global maxima using 21 and 31 iterations respectively. Thus, our approach addresses two basic problems of the classical EM: the initialization and the model selection.

Finally, we have applied the proposed method to the well known *Iris* [2] data set, that contains 3 classes of 50 (4-dimensional) instances referred to a type of iris plant: *Versicolor*, *Virginica* and *Setosa*. Because the problem is 4-dimensional, 50 samples are insufficient to construct the pdf using Parzen. In order to test our method, we have generated 300 training samples from the averages and covariances of the original classes and we have checked the performance in a classification problem with the original 150 samples. Starting with  $K = 1$ , the method correctly selected  $K = 3$ . Then, a maximum a posteriori classifier was built, with classification performance of 98% (only three *Versicolor* were classified like *Virginica*).

## 5 Conclusions and Future Work

In this paper we have presented a method for finding the optimal number of kernels in a Gaussian mixture based on maximum entropy. We start the algorithm with only one kernel and then we decide to split it on the basis of the entropy of the underlying pdf. The algorithm converges in few iterations and is suitable for density estimation and classification problems. We are currently validating this algorithm in real image classification problems and also exploring new methods of estimating entropy directly, bypassing the estimation of the pdf.

## References

1. Bishop, C.: Neural Networks for Pattern Recognition. Oxford Univ. Press (1995).
2. Blake, C.L, Merz, C.J.:UCI repository of machine learning databases. University of California, Irvine, Dept. of Information and Computer Sciences (1998).
3. Cover, T, Thomas, J: Elements of Information Theory. J. Wiley and Sons (1991).
4. Dempster, A, Laird, N, Rubin, D.: Maximum Likelihood estimation from incomplete data via the EM Algorithm. Journal of The Royal Statistical Society B, vol. 39 pp. 1-38 (1977).
5. Figueiredo, M.A.T, Leitao, J.M.N, Jain, A.K.: On Fitting Mixture Models. In: Hancock, E.R., Pelillo, M. (eds.): Energy Minimization Methods in Computer Vision and Pattern Recognition. Lecture Notes in Computer Science, Vol. 1654. Springer-Verlag, Berlin Heidelberg New York (1999) 54-69.
6. Figueiredo, J.M.N, Jain, A.K.: Unsupervised Selection and Estimation of Finite Mixture Models. In Proceedings of the International Conference on Pattern Recognition. ICPR2000 (Barcelona), 2000.
7. Parzen, E. On estimation of a probability density function and mode. Annals of Mathematical Statistics, 33:1065-1076, 1962.
8. Redner, R.A, Walker, H.F.: Mixture Densities, Maximum Likelihood, and the EM Algorithm. SIAM Review, 26(2):195-239, (1984).
9. Rissanen, J.: Stochastic Complexity in Statistical Inquiry. World Scientific, (1989).
10. Shannon, C.: A Mathematical Theory of Communication. The Bell System Technical Journal, Vol. 27, 379-423, 623-656, (1948).
11. Ueda, N, Nakano, R, Ghahramani, Z., G. E. Hinton: SMEM Algorithm for Mixture Models. Neural Computation, 12:2109-2128, (2000).
12. Viola, P, Wells III, W. M.: Alignment by Maximization of Mutual Information. In 5th Intern. Conf. on Computer Vision, pages 16-23, Cambridge, MA. IEEE. (1995).
13. Viola, P, Schraudolph, N.N, Sejnowski, T.J.: Empirical Entropy Manipulation for Real-World Problems. Adv. in Neural Infor. Proces. Systems 8, MIT Press (1996).
14. Vlassis, N, Likas, A.: A Kurtosis-Based Dynamic Approach to Gaussian Mixture Modeling. IEEE Trans. Systems, Man, and Cybernetics, 29(4):393-399 (1999).
15. Vlassis, N, Likas, A, Krose, B.: A Multivariate Kurtosis-Based Dynamic Approach to Gaussian Mixture Modeling. Intelligent Autonomous Systems Tech. Report (2000).
16. Vlassis, N, Likas, A.: A Greedy EM Algorithm for Gaussian Mixture Learning. Neural Processing Letters. To appear.
17. Wolpert, D, Wolf, D.: Estimating Function of Probability Distribution from a Finite Set of Samples. Physical Review E, Volume 52, No 6 (1995).

# Gaussian Mixture Models for Supervised Classification of Remote Sensing Multispectral Images

Ana Claudia Oliveira de Melo<sup>1</sup>, Ronei Marcos de Moraes<sup>1</sup>, and  
Liliane dos Santos Machado<sup>2</sup>

<sup>1</sup> UFPB – Federal University of Paraíba - Department of Statistics,  
Cidade Universitária s/n, 58051-900, João Pessoa, PB, Brazil,  
[{anaclaudia, ronei}@de.ufpb.br](mailto:{anaclaudia, ronei}@de.ufpb.br)  
<http://www.de.ufpb.br/>

<sup>2</sup> UFPB – Federal University of Paraíba - Department of Computer Sciences,  
Cidade Universitária s/n, 58051-900, João Pessoa, PB, Brazil  
[liliane@di.ufpb.br](mailto:liliane@di.ufpb.br)  
<http://www.di.ufpb.br/>

**Abstract.** This paper proposes the use of Gaussian Mixture Models as a supervised classifier for remote sensing multispectral images. The main advantage of this approach is provide more adequate adjust to several statistical distributions, including non-symmetrical statistical distributions. We present some results of this method application over a real image of an area of Tapajós River in Brazil and the results are analysed according to a reference image. We perform also a comparison with Maximum Likelihood classifier. The Gaussian Mixture classifier obtained best adjust about image data and best classification performance too.

## 1 Introduction

Several times, researchers in image processing justify the use of Gaussian approach due to the data volume. In the practice of image classification, this approach should not be applied without verify the Gaussian distribution hypothesis. It implicates in a low percentage of correct classification, as example, when the Maximum Likelihood classifier is utilized. To minimize this effect, several approaches was experimented, using: fuzzy membership functions [1], multiple classifiers [2], Neural Networks [3], expert systems [4], etc.

The Gaussian Mixture Models (GMM), in theory, can be applied to modeling a large number of statistical distributions, including non-symmetrical distributions. These models have been used to data classification [5] and speech and speaker recognition [6]. In image processing applications, researchers commonly use the unsupervised version of mixture models [7], [8].

In this paper, we proposed the utilization of ellipsoidal GMM [9] as a supervised classifier for remote multispectral sensing images. We applied this method in a real image of an area of Tapajós River in Brazil and compare the results with a Maximum Likelihood classifier.

## 2 Theoretical Aspects

In this section, we present the Gaussian Mixture Models method for image classification. The clusters associated to the mixture components are ellipsoidal, centered at the means  $\mu_k$  and variances matrix  $\Sigma_k$  determine their geometric characteristics of the ellipses. Parameter estimation equations for classes models are presented first. After, the GMM method for classification is then described as a maximum likelihood classifier [6].

### 2.1 Gaussian Mixture Models (GMM)

Let  $X = \{x_1, x_2, \dots, x_T\}$  be a set of  $T$  vectors, extracted from attribute space, obtained from the samples areas of the image. These information can be extracted at  $T$  different spectral bands of the image. Since the distribution of these vectors is unknown, it is approximately modeled by a mixture of Gaussian densities as the weighted sum of  $c$  component densities, given by the equation

$$p(x_t|\lambda) = \sum_{i=1}^c w_i N(x_t, \mu_i, \Sigma_i), \quad t = 1, \dots, T \quad (1)$$

where  $\lambda$  denotes a prototype consisting of a set of model parameters  $\lambda = \{w_i, \mu_i, \Sigma_i\}$ ,  $w_i, i = 1, \dots, c$  are the mixture weights and  $N(x_t, \mu_i, \Sigma_i)$ , are the  $T$ -variate Gaussian component densities with mean vectors  $\mu_i$  and covariance matrices  $\Sigma_i$ :

$$N(x_t, \mu_i, \Sigma_i) = \frac{\exp\left\{-\frac{1}{2}(x_t - \mu_i)' \Sigma_i^{-1} (x_t - \mu_i)\right\}}{(2\pi)^{d/2} |\Sigma_i|^{1/2}}. \quad (2)$$

To train the GMM, these parameters are estimated such that they best match the distribution of the samples from the image. The maximum likelihood estimation is widely used as a training method. For a sequence of sample vectors  $X$  for a  $\lambda$ , the likelihood of the GMM is done by:

$$p(X|\lambda) = \prod_{t=1}^T p(x_t|\lambda). \quad (3)$$

The aim of maximum likelihood estimation is to find a new parameter model  $\bar{\lambda}$  such that  $p(X|\bar{\lambda}) \geq p(X|\lambda)$ . Since the expression in (3) is a nonlinear function of parameters in  $\lambda$ , its direct maximisation is not possible. However, these parameters can be obtained iteratively using the Expectation-Maximisation algorithm[10]. In this algorithm, we use an auxiliary function  $Q$  done by:

$$Q(\lambda, \bar{\lambda}) = \sum_{t=1}^T \sum_{i=1}^c p(i|x_t, \lambda) \log [\bar{w}_i N(x_t, \bar{\mu}_i, \bar{\Sigma}_i)] \quad (4)$$

where  $p(i|x_t, \lambda)$  is the a *posteriori* probability for each mixture component of image class  $i$ ,  $i = 1, \dots, c$  and satisfies

$$p(i|x_t, \lambda) = \frac{w_i N(x_t, \mu_i, \Sigma_i)}{\sum_{k=1}^c w_k N(x_t, \mu_k, \Sigma_k)}. \quad (5)$$

The Expectation-Maximisation algorithm is such that if  $Q(\lambda, \bar{\lambda}) \geq Q(\lambda, \lambda)$  then  $p(X|\bar{\lambda}) \geq p(X|\lambda)$ [13]. Setting derivatives of the  $Q$  function with respect to  $\bar{\lambda}$  to zero, we found the following reestimation formulas:

$$\bar{w}_i = \frac{1}{T} \sum_{t=1}^T p(i|x_t, \lambda), \quad (6)$$

$$\bar{\mu}_i = \frac{\sum_{t=1}^T p(i|x_t, \lambda) x_t}{\sum_{t=1}^T p(i|x_t, \lambda)}, \quad (7)$$

$$\bar{\Sigma}_i = \frac{\sum_{t=1}^T p(i|x_t, \lambda) (x_t - \mu_i) (x_t - \mu_i)' }{\sum_{t=1}^T p(i|x_t, \lambda)}. \quad (8)$$

The algorithm for training the GMM is described as follows:

1. Generate the a *posteriori* probability  $p(i|x_t, \lambda)$  at random satisfying (5);
2. Compute the mixture weight, the mean vector, and the covariance matrix following (6), (7) and (8);
3. Update the a posteriori probability  $p(i|x_t, \lambda)$  according to (5) and compute the  $Q$  function using (4);
4. Stop if the increase in the value of the  $Q$  function at the current iteration relative to the value of the  $Q$  function at the previous iteration is below a chosen threshold, otherwise go to step 2.

**The GMM classification.** To provide GMM classification, we need several classes of image  $\lambda$ . So, let  $\lambda_k$ ,  $k = 1, \dots, N$ , denote models of  $N$  possible classes of image. Given a feature vector sequence  $X$ , a classifier is designed to classify  $X$  into  $N$  classes of image by using  $N$  discriminant functions  $g_k(X)$ , computing the similarities between the unknown  $X$  and each class of image  $\lambda_k$  and selecting the class of image  $\lambda_{k^*}$  if

$$k^* = \arg \max_{1 \leq k \leq N} g_k(X) \quad (9)$$

In the minimum-error-rate classifier, the discriminant function is the a *posteriori* probability:

$$g_k(X) = p(\lambda_k|X). \quad (10)$$

We can use the Bayes' rule

$$p(\lambda_k|X) = \frac{p(\lambda_k)p(X|\lambda_k)}{p(X)} \quad (11)$$

and we can assume equal likelihood of all performances, i.e.,  $p(\lambda_k) = 1/N$ . Since  $p(X)$  is the same for all performance models, the discriminant function in (10) is equivalent to the following[14]:

$$g_k(X) = p(X|\lambda_k) \quad (12)$$

Finally, using the log-likelihood, the decision rule used for class of performance identification is:

*Select performance model  $k^*$  if*

$$k^* = \arg \max_{1 \leq k \leq N} \sum_{t=1}^T \log p(x_t|\lambda_k) \quad (13)$$

where  $p(x_t|\lambda_k)$  is given by (1) for each  $k$ ,  $k = 1, \dots, N$ .

## 2.2 The Bayesian Information Criterion

Several information criteria are presented in literature as Bayesian Information Criterion (BIC) [9] and Akaike Information Criterion (AIC) [11]. However, Bieracki and Govaert [12] concluded that BIC has a better performance than others to choose a good mixture model after the comparison of some information criteria.

The Bayesian Information Criterion (BIC) was proposed by Schwartz [9] to evaluate the quality of estimations. This criterion compares models with different parameters or different number of components. Formaly, let a data set  $X$  and a model  $m$ ,  $p(X|\lambda_m)$ ,  $m = 1, 2, \dots$  with  $c$  components,  $c = 1, 2, \dots$ , the BIC for this model is done by:

$$BIC(m, c) = -2\log[p(X|\lambda_m)] + \nu_{m,c} \ln(T) \quad (14)$$

where  $p(X|\lambda_m)$  is done by (3),  $\nu_{m,c}$  is the number of independent parameters to be estimated in the model  $m$  with  $c$  components and  $T$  is the number of components in vector  $X$ .

The best model to represent the data set  $X$  is the model  $m^*$  that

$$m^* = \arg \max_m BIC(m, c) \quad (15)$$

## 3 A Case Study

To test the classifier proposed in Sect. 2.2, we performed a case study with a real image of Brazilian state of Pará at Tapajós River. The image was obtained from the number 4 spectral sensor of Landsat satellite. The image was composed by three classes: Tapajós River (class 1), Contact Areas (class 2) and Human Occupation Areas (class 3).

To evaluate the quality of estimations, we use Bayesian Information Criterion (BIC) [9], which compares models with different parameters or different number

of components. This criteria points to the best model. So, according to the BIC, the classes 1 and 3 were modeled using two components ( $K = 2$ ), because those original data distributions were not Gaussian distributions, and the class 2 was modeled using one component. The Fig. 1 shows all the models.

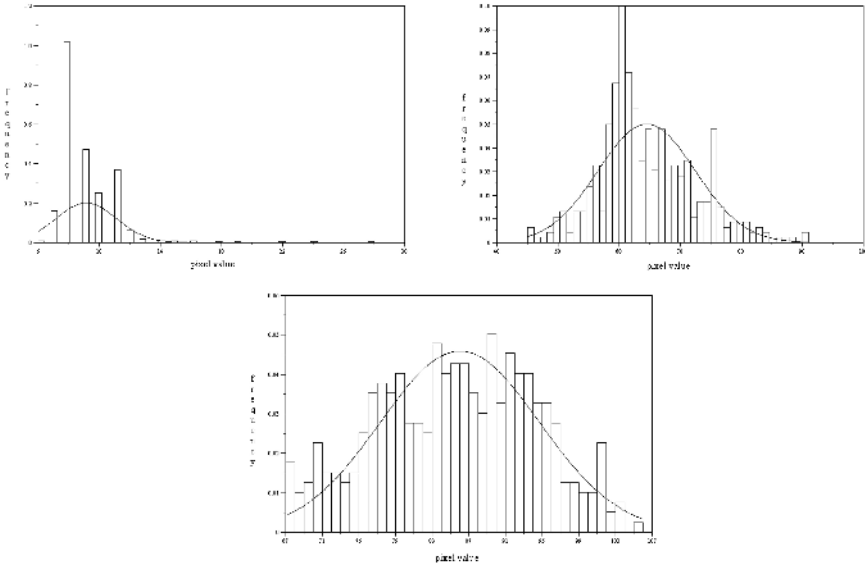


**Fig. 1.** Gaussian Mixture Models for classes 1, 2 and 3. Class 1 (a) was modeled using  $K = 2$ , class 2 (b) was modeled using  $K = 1$  and Class 3 (c) was modeled using  $K = 2$ .

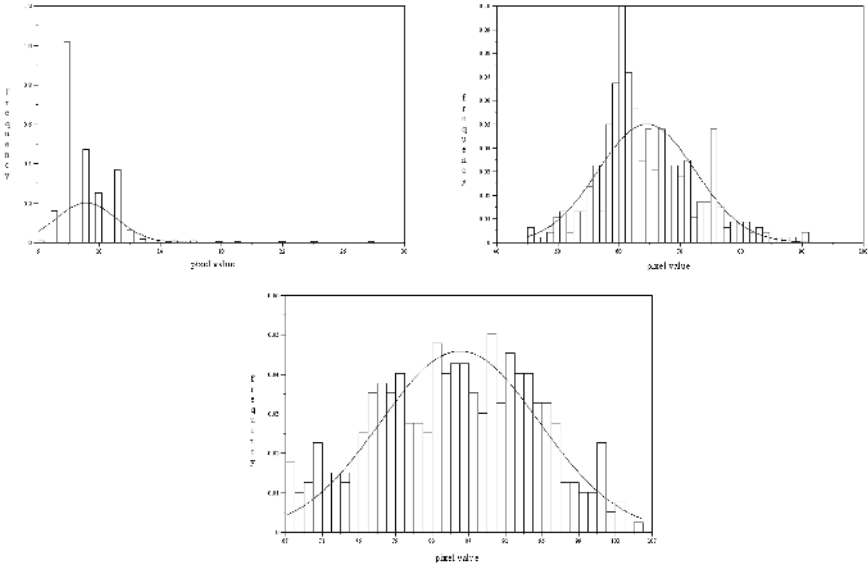
A statistical comparison between classification and a reference map of the same area was performed using Kappa coefficient. The Kappa result was 90.6793% with variance  $9.5815 \times 10^{-5}$ . The same coefficient for each class results were: 99.6929% for class 1, 84.5049% for class 2 and 86.7262% for class 3. The percentuals of correct classification for each class were respectively: 99.8134%, 89.3032% and 90.6801%. The main misclassification occurred with classes 2 and 3. In fact, there is an overlapping of those classes distributions. The Table 1 shows the matrix classification used for calculations we presented above.

We can note, in Table 1, that only one pixel of class 1 was classified as class 2, 46 pixels of class 2 were classified as class 3 and 37 pixels of class 3 were classified as class 2. The cause of these facts is the overlapping of classes 2 and 3 distributions.

Thus, the classification can be considered satisfactory in statistical terms, even if we consider the overlapping of class 2 and class 3 distributions. It is important to note that these results were obtained using only one original spectral band.

**Table 1.** Matrix classification for GMM classifier using a reference map.

Classes	class 1	class 2	class 3
class 1	535	1	0
class 2	0	384	46
class 3	0	37	360

**Fig. 2.** Maximum Likelihood Models for classes 1 (a), 2 (b) and 3 (c). All classes were modeled as a Gaussian distribution.

#### 4 Comparison with a Maximum Likelihood Classifier

To compare performances between GMM classifier with another classifier, we performed a classification using a Maximum Likelihood classifier. Using the same reference map, the statistical Kappa coefficient for Maximum Likelihood classification was 89.2355 with variance  $1.09389 \times 10^{-4}$ . The same coefficient for each class results were: 99.0809% for class 1, 84.2878% for class 2 and 82.9756% for class 3. The percentuals of correct classification for each class were respectively: 99.4403%, 89.3032% and 87.9093%. Again, the overlapping of 2 and 3 classes distributions was responsible for misclassification. The Table 2 shows the matrix classification used for calculations we presented above.

We can note, in Table 2, that 3 pixels of class 1 was classified as class 2, 46 pixels of class 2 were classified as class 3 and 48 pixels of class 3 were classified as class 2. Besides the overlapping of 2 and 3 classes distributions, we can observe that Maximum Likelihood has obtained satisfactory results too. However, it is

**Table 2.** Matrix classification for Maximum Likelihood classifier using a reference map.

Classes	class 1	class 2	class 3
class 1	533	3	0
class 2	0	384	46
class 3	0	48	349

important to note that all results are not better than GMM classifier. The Fig. 2 shows all the models.

## 5 Conclusions and Future Works

In this paper, we proposed the use of Gaussian Mixture Models for supervised image classification. We obtained results of a real data classification using an area of Tapajós River in Brazil. We did a comparison of this classifier with the Maximum Likelihood classifier.

The Gaussian Mixture Models classifier is adequate to classify images which classes can not be adjusted by Gaussian distributions. These models provide more adequate adjust to several distributions with lower variance. This property in particular is welcome in image classification for reduce misclassification, but these properties are already used in others applications, as data analysis and speech and speaker recognition.

We presented an application using only one original spectral image. In this application we observed better statistical results of GMM classifier. It is important to note that classes 1 and 3 do not have Gaussian distribution as showed in the Fig. 1 and Fig. 2. This fact is relevant to explain the inferior performance of Maximum Likelihood classifier, mainly to classify the class 3.

As future works we intend to do a performance statistical comparison with others statistical classifiers.

## References

1. Kent, J. T.; Mardia, K. V. Spatial classification using fuzzy membership models. *IEEE Trans. on Patt. Anal. and Mach. Intel.* **10** (1988) 659–671
2. Ho, T. K.; Hull, J. J.; Srihari, S. N.; Decision combination in multiple classifier systems. *IEEE Trans. on Patt. Anal. and Mach. Intel.* **16** (1994) 66–75
3. Simpson, P. K. *Artificial Neural Systems*. Pergamon Press, New York (1990)
4. Moraes, R. M.; Sandri, S. A.; Banon, G. J. F. Expert Systems Architecture for Image Classification Using Mathematical Morphology Operators. *Information Science* **142** (2002) 7–21
5. Yang, M. H., Ahuja, N. Gaussian Mixture Model for Human Skin Color and Its Application in Image and Video Databases, Proc. of the SPIE, vol. 3656: Conf. on Storage and Retrieval for Image and Video Databases, San Jose (1999) 458–466

6. Tran, D., Pham, T., Wagner, M., Speaker recognition using Gaussian mixture models and relaxation labeling. in Proceedings of the 3rd World Multiconference on Systemetics, Cybernetics and Informatics/ The 5th Int. Conf. Information Systems Analysis and Synthesis (SCI/ISAS99), USA **6** (1999) 383–389
7. H. Caillol, W. Pieczynski and A. Hillon, Estimation of fuzzy Gaussian mixture and unsupervised statistical image segmentation, IEEE Trans. on Image Proces. **6** (1977) 425–440
8. W. Pieczynski, J. Bouvrais, and C. Michel, Estimation of generalized mixture in the case of correlated sensors, IEEE Trans. on Image Proces., **9**,(2000) 308–311
9. G. Schwartz, Estimating the Dimension of a Model. The Ann. of Stat. **6** (1978) 461–464
10. A.P. Dempster, N.M. Laird and D.B. Rubin, Maximum Likelihood from Incomplete Data via the EM Algorithm. J.R.Stat.Soc. B, **39** (1977) 1–38
11. Akaike, H. A new look at the statistical identification model. IEEE Trans. on Automatic Control, **19** (1974) 716–723.
12. Biernacki, C. and Govaert, G. Choosing models in model-based clustering and discriminant analysis. Technical Report INRIA no. 3509, (1998).
13. Rabiner, L. R., A Tutorial on Hidden Markov Models and Selected Application in Speech Recognition. Proceedings of the IEEE, **77** (1989)
14. Johnson, R. A. and Wichern, D. W., Applied Multivariate Statistical Analysis. Prentice Hall (1998)

# Fast Multistage Algorithm for K-NN Classifiers

I. Soraluze, C. Rodriguez, F. Boto, and A. Cortes

Computer Architecture and Technology Department, Computer Science Faculty, UPV/EHU,  
Aptdo. 649, 20080 San Sebastian, Spain  
acrneura@si.ehu.es

**Abstract.** In this paper we present a way to reduce the computational cost of k-NN classifiers without losing classification power. Hierarchical or multistage classifiers have been built with this purpose. These classifiers are designed putting incrementally trained classifiers into a hierarchy and using rejection techniques in all the levels of the hierarchy apart from the last. Results are presented for different benchmark data sets: some standard data sets taken from the UCI Repository and the Statlog Project, and NIST Special Databases (digits and upper-case and lower-case letters). In all the cases a computational cost reduction is obtained maintaining the recognition rate of the best individual classifier obtained.

## 1 Introduction

Pattern classification based on the  $k$ -nearest-neighbors ( $k$ -NN) [1], [2] approach has been proven to perform well in pattern classification on many domains. It is well known that the main drawback of this kind of classifier in practice is the computational cost demand. In order to find the  $k$  nearest patterns, a dissimilarity measure between the test sample and a large number of samples in the training set is computed making this approach very computational. One method for solving this problem is to reduce the large data set to a small and representative one using condensing algorithms [4]. The objective of selecting a subset of the original training data is the computational efficiency in the classification phase, or/and making the resulting classification and generalization more reliable. Other kinds of methods try to reduce the data set by generating artificial prototypes summarizing representative characteristics of similar instances [10]. In many works has been proven that hierarchical systems are good too to reduce the computational cost in classifiers with a large data set. Besides, in recent years there is an increasing interest in schemes that combine multiple classifiers [5].

In this paper, multistage classifiers based on  $k$ -NN classifiers are proposed for the reduction of the computational cost. The multistage classifiers are built with  $l$  levels of individual  $k$ -NN classifiers trained incrementally and using rejection techniques in the levels. Each of the individual classifiers is built with different characteristics and the computational cost of classifying a pattern is proportional to the level where the pattern has been recognized. When a pattern has not enough classification certainty in

a level of the hierarchy goes to the next level where a more complex classifier will try to classify it. A lot of the patterns are classified in the lowest levels of the hierarchy, where the computational cost is low because the simplest classifiers have been put there.

We have used different benchmark data sets to validate our system. Three data sets have been selected from the UCI Repository and the Statlog project [6]. The results obtained with these data sets are put together with previously obtained results with characters of the NIST Special Databases [12]: digits, upper-case and lower-case letters.

The paper has the following structure. In Section 2 a formal description of the multistage system is presented. In Section 3 we describe the particular classifiers used and the experimental results obtained. Finally in section 4 the conclusions are presented.

## 2 Formal Description of the System

We are going to give now some definitions and the notation used throughout the paper. After that the algorithms used in the training and recognition process to build the multistage system are presented.

A pattern is represented by  $x_i$  and is identified by the orderly pair  $(r_i, c_i)$ , where  $r_i = (r_{i,1}, r_{i,2}, \dots, r_{i,d})$  are the  $d$  feature values that represent the pattern  $x_i$  and  $c_i$  is the class label assigned to the pattern.

The Training Set formed for all the training patterns,  $TS$ , is defined by  $TS = \{x_i \mid x_i = (r_i, c_i)\}$  and the Reduced Set,  $RS$ , is a subset of  $TS$ , obtained with a learning or training algorithm.

The following operators will appear in next sections:

- $C(x_i) = c_i$  is the class of the pattern  $x_i$ .
- $d(x_i, x_j) = |r_i - r_j|$  is the Euclidean distance between two feature vectors  $(r_i, r_j)$  associated to the patterns  $x_i$  and  $x_j$  respectively.
- $D(x) = \min(d(x, x_j)) \forall x_j \in RS \wedge C(x_j) = C(x)$  are the nearest patterns to  $x$  belonging to the same class.
- $\neg D(x) = \min(d(x, x_j)) \forall x_j \in RS \wedge C(x_j) \neq C(x)$  are the nearest patterns to  $x$  belonging to a different class.  $\neg D(x) = \infty \mid C(x_j) = C(x) \forall x_j \in RS$
- $NN_k(x, S) = (x_1, x_2, \dots, x_k) \mid x_i \in S \quad 1 \leq i \leq k$  is the distance-ordered set of the  $k$ -nearest patterns to  $x$  in the set  $S$ .

### 2.1 Classic Training Algorithm (TA)

The training algorithm shown in Fig.1 generates a reduced data set  $RS$  taking the training set  $TS$ . Two rules, specified as (1) and (2) in the figure, have been applied to obtain the reduced set. The reduction obtained depends on the parameter  $tt$  (*training*

*threshold*). The threshold can take values between 0 and infinite. If the threshold takes value 0 the maximum reduction is obtained and this algorithm becomes into Hart's algorithm [4]. If the value assigned to this parameter is infinite, there is no reduction and  $RS$  and  $TS$  are the same data set.

$Initializations$ $RS = \emptyset$ $training = true$ $while(training)$ $training = false$ $\forall x_i \in TS$ $(1) : if (C(x_i) \neq C(NN_1(x_i, RS)))$ $RS = RS \cup x_i$ $training = true$ $else$ $(2) : if \left( \frac{-D(x_i) - D(x_i)}{D(x_i)} < tt \right)$ $RS = RS \cup x_i$ $training = true$ $end \forall$ $end while$
--

**Fig. 1.** Training Algorithm (TA)

$Initializations$ $IRS_i = IRS_{i-1}$ with $IRS_0 = \emptyset$ $training = true$ $while(training)$ $training = false$ $\forall x_j \in ITS_i$ $(1) : if (C(x_j) \neq C(NN_1(x_j, IRS_i)))$ $IRS_i = IRS_i \cup x_j$ $training = true$ $else$ $(2) : if \left( \frac{-D(x_j) - D(x_j)}{D(x_j)} < tt_i \right)$ $IRS_i = IRS_i \cup x_j$ $training = true$ $end \forall$ $end while$
--

**Fig. 2.** Incremental Training Algorithm (ITA)

## 2.2 Incremental Training Algorithm (ITA)

The different classifiers used to build a hierarchy have been trained using an incremental training algorithm, which is a modification of the algorithm shown in previous section. The training set  $TS$  is divided in  $s$  subsets:

$$TS = \bigcup_{i=1}^s TS_i \quad TS_i \cap TS_j = \emptyset \quad \forall i, j | i \neq j. \quad (1)$$

The incremental training set  $i$ ,  $ITS_i$ , is defined as following:

$$ITS_i = \bigcup_{j=1}^i TS_j \quad |ITS_i = ITS_{i-1} \cup TS_i \text{ with } ITS_0 = \emptyset. \quad (2)$$

The cardinal of  $ITS_i$  follows a exponential and uniform distribution.

The *Incremental Training Algorithm (ITA)*, creates an incremental reduced set,  $IRS_i$ , taking the incremental training set,  $ITS_i$ , and the incremental reduced set  $i-1$ ,  $IRS_{i-1}$ , by applying the same two rules shown previously in Fig. 1. The incremental algorithm is shown in Fig. 2.

Having used this algorithm, we can use the following property in the recognition process:

$$\forall i > 0 \quad IRS_{i-1} \subseteq IRS_i \text{ with } IRS_0 = \emptyset. \quad (3)$$

The incremental training algorithm reduces the computational cost of the training process because the training starts from an already built classifier and only some new patterns are learnt to create the new classifier.

### 2.3 Multistage Recognition Algorithm (*MRA*)

The multistage classification process is obtained using classifiers trained in an incremental way and putting them into a hierarchy ordered according to the number of patterns they have. Having a pattern  $x$ , we will define a confidence value,  $CV_{i,k_i}$ , used to decide if the pattern  $x$  has enough classification certainty to be classified in the level  $i$  of the hierarchy (this rule is known as  $k,l$ -Nearest Neighbor [1]). The expression can be seen in Equation 4.

$$CV_{i,k_i}(x) = \frac{\max(CPC_{c,k_i})}{k_i}. \quad (4)$$

$k_i$  is the number of nearest neighbors taken in level  $i$  and  $CPC_{c,k_i}$  determines how many of these patterns belong to class  $c$ . The expression is shown in Equation 5.

$$CPC_{c,k}(x) = \left| \{x_j \mid C(x_j) = c \wedge x_j \in NN_k(x, IRS_i)\} \right|. \quad (5)$$

The multistage recognition algorithm is shown in Fig. 3. This recurrent algorithm starts with the call  $MRA(x, 1)$  and represents the classification process of a pattern  $x$  of the test set. This algorithm reduces the computational cost in the classification process, because the discriminating capacity of the hierarchical classifier is adapted to the recognition difficulty of each pattern.

```

MRA(x, i)
{
  if (i = max_level) return  $WR_{i,k}(x)$ ;
  else
    if ( $CV_{i,k_i}(x) > rt_i$ ) return  $c$ 
    else return ( $MRA(x, i+1)$ );
}
max_level is the number of levels
rt_i is the rejection threshold associated to the level i.

```

**Fig. 3.** Multistage Recognition Algorithm

When the pattern reaches to the last level of the hierarchy we use the Weighted rule  $WR_{i,k}(x)$  [1] modified (Equation 6) to classify it.

$$WR_{i,k}(x) = \max_c(D_{c,k}(x)) \quad (6)$$

with  $D_{c,k}(x) = \sum_{j=1}^k d(x_j, x_k)^2 \mid x_j, x_k \in NN_k(x, IRS_i) \wedge C(x_j) = c$ .

## 2.4 Multistage Recognition Algorithm with Active Memory (*MRAMA*)

In order to reduce the computational cost of the previous algorithm, a modification has been introduced. This new algorithm keeps memory about what happened in the previous levels [3] of the hierarchy and uses it when a pattern is going to be classified in a later level. This is a memory-based method or a method with “*active memory*”. Particularly, the information known about the previous levels is the set of classes found among the  $k$  nearest patterns of that level, referred as  $CS_{i,k}$ . The expression for this set is in Equation 7.

$$CS_{i,k_i}(x) = \left\{ C(x_j) \mid x_j \in NN_{k_i}(x, IRS_i) \wedge C(x_j) \in CS_{i-1,k_{i-1}}(x) \right\} \forall i > 0 \quad (7)$$

where  $CS_{0,k_0}$  contains all the possible classes.

The description of the new algorithm is shown in Fig. 4. The algorithm starts with the call  $MRAMA(x, 1, CS_{0,k_0})$ . The only difference between the expressions  $MAWR_{i,k}(x)$  and  $MACV_{i,k}(x)$  and the presented in previous section  $WR_{i,k}(x)$  and  $CV_{i,k}(x)$  is that in the new expressions the  $k_i$  patterns are searched only among the patterns of the classes in the set  $CS_{i,k}$ , which reduces the cost.

```

MRAMA(x, i, CSi-1,ki-1)
{
    if (i = max_level) return MAWRi,k(x);
    else
        if (MACVi,ki(x) > rti) return c
        else return (MRAMA(x, i+1, CSi,ki));
}
max_level is the number of levels
rti is the rejection threshold associated to the level i.

```

**Fig. 4.** Multistage Recognition Algorithm with Active Memory

The computational cost associated to recognize a pattern  $x$  in the level  $i$  using this algorithm and incremental training is defined with the following expression:

$$RCC_i(x) = RCC_{i-1}(x) + \left| \left\{ x_j \mid x_j \in \{IRS_i - IRS_{i-1}\} \wedge C(x_j) \in CS_{i-1,k_{i-1}}(x) \right\} \right| \quad (8)$$

$$\forall i > 1 \wedge RCC_1(x) = |IRS_1|.$$

The average computational cost of the hierarchical or multistage classifier with  $L$  levels taking a test pattern set  $X$  is defined in Equation 9

$$RCC(X) = \frac{1}{|X|} \sum_{j=1}^{|X|} RCC_{L_{x_j}}(x_j) \quad (9)$$

Where  $L_{x_j}$  is the level where the pattern  $x_j$  has been recognized.

### 3 Experimental Results

The experimentation has been carried out with different data sets: Statlog LandSat Satellite (Satimage), Statlog Shuttle (Shuttle) and UCI Letter Recognition database (Letter), taken from the UCI Repository and the Statlog project. Table 1 presents the characteristics of these benchmark data sets.

**Table 1.** Benchmark data sets used

	TS	Test Set	Classes	Features
Shuttle	43,500	14,500	7	9
Letters	15,600	4,400	26	16
Satimage	4,435	2,000	7	36

The first experimentation has been carried out for individual classifiers using the training algorithm *TA* and the  $WR_{i,k}(x)$  rule. Different *training thresholds* and *TS* sizes have been proven in order to find the classifier with best recognition rate. For Satimage data sets have been defined 3 *TS* of 1,200, 2,400 and 4435 patterns respectively. For Shuttle data sets 5 *TS* have been used with 2,100, 4,200, 8,400, 16,800 and 43,500 patterns. Finally for Letter data set 4 *TS* have been defined with 2,600, 5,200, 10,400 and 15,600 patterns. For all the data set a bigger *TS* contains the patterns of the smaller ones. We can see in Table 2 the best results obtained for these three data sets and the characteristics of the classifiers that provide these results. The recognition rate achieved is similar to the presented by other authors [7], [11]. Together with the results of these three benchmarks, the results previously obtained with characters of NIST Special Databases, digits [8] and letters [9] are presented. We can see that the best results for all the data sets are obtained with a reduced set of the bigger *TS* used. Selecting some patterns a computational cost reduction is obtained.

**Table 2.** Results obtained with individual classifiers

	TS	RS	Recognition	tt	[7]	[11]
NIST, digits	160,000	23,493	99.50	0.5%		
NIST, upper-case	60,194	24,348	95.44	0.5%		
NIST, lower-case	49,842	24,503	88.34	0.5%		
Shuttle	43,500	567	99.88	0.75%	99.86	99.94
Letters	15,600	8,406	95.73	0.75%	96.6	68.30
Satimage	4,435	1,924	91.15	0.25%	90.15	86.25

The best recognition rate presented can be obtained with less computational cost if we use the multistage classifiers with incremental training and active memory. We have built hierarchies with different number of levels for each data set depending on the number of training subsets we have. The *TS* subsets created for each data set have been trained incrementally now, using the previous trained subset as described in the section 2.2 and put into a hierarchy ordered by the number of patterns they have. The *tt* used to obtain *IRS* has been 0 except for the last *IRS*. The last *TS* (the one with more patterns) has been trained using the value 0 for the *tt*, and using the *tt* which provides

the best recognition rate. The incremental training helps to reduce the computational cost in the recognition process because in each level of the hierarchy only the new patterns of the classifier need to be checked.

These classifiers have been put into a hierarchy and applying the algorithm presented in section 2.4 and important computational cost reduction has been obtained maintaining the hit rate presented before (The computational cost is calculated with the expression in Equation 8, and compared with the computational cost of the individual classifier in the last level, which gives the same recognition rate). These results are shown in Table 3. In this case too, results obtained with NIST Databases are presented in order to make a comparison.

**Table 3.** Results obtained with multistage and incremental classifiers

	Levels	Recognition	Computational cost / Speed-up
NIST digits	12	99.48	957.69 / 167
NIST upper-case	12	95.44	744.23 / 80.88
NIST lower-case	12	88.12	1145 / 43.53
Shuttle	6	99.88	329 / 132.2
Letters	5	95.54	4070 / 3.82
Satimage	2	91.5	1093 / 4.05

We can observe that although there is always a computational cost reduction (speed-up) applying the hierarchical recognition algorithm, when the data set contains few patterns the reduction is not very high. In problems with large *TS* or in easy problems, the computational cost reduction is higher.

Besides, for the Satimage data set we have selected a classifier of two levels although we primarily took a classifier with 4 levels as described before. The first two classifiers in this case had very few patterns so they rejected all the patterns and selected a class set not correct that increment the error rate in the next levels. For this reason these first classifiers have been removed from the hierarchy, building a hierarchy of only 2 levels.

## 4 Conclusions

It is well known that *k*-NN classifier provides good recognition results on pattern recognition systems of different domains. In this paper we have presented a multistage incremental algorithm that reduces the computational cost associated to *k*-NN classifiers, solving one of the most important problems of these algorithms.

The multistage classifier is built with different *k*-NN classifiers (with different number of patterns used in the classification) trained in an incremental way. The discriminating capacity of the classifiers is adapted to the classification needs of each pattern in the classification process; the easiest patterns are classified in the first levels of the hierarchy, with low computational cost. Only the most difficult patterns reach the last level of the hierarchy where the classifiers with more patterns have been put.

The experimental results have been presented for different benchmark data set. We have observed that although always a computational cost reduction is obtained main-

taining the recognition rate of the best classifiers, the speed-up is higher when large training sets are taken. The speed-up obtained with data sets as NIST digits databases where we have taken 160,000 patterns for training is of 167 times whereas the reduction for data sets as Satimage with 4435 training patterns is of 4.05 times. In all the cases a good recognition rate is maintained.

**Acknowledgments.** This work was supported in part by the Spanish Government (CICYT project number TIC2000-0389). We also want to thank the collaboration of the company ADHOC Synectic Systems, S.A.

## References

1. Dasarathy, B.V.: "Nearest Neighbor (NN) Norms: NN Pattern Classification Techniques". Ed: IEEE Computer Society Press (1991)
2. Devroye, L., Györfi, L. and Lugosi, G.: "A Probabilistic Theory of Pattern Recognition". Ed. Springer-Verlag, New York, (1996)
3. Giusti, N., Masulli, F., Sperduti, A.: "Theoretical and Experimental Analysis of a Two-Stage System for Classification". IEEE Trans. PAMI, Vol. 24 Nº 7 pp. 893–905 (2002)
4. Hart, P.E., "The Condensed Nearest Neighbour Rule". IEEE Transactions on Information Theory, Vol. 14, pp. 515–516, (1968)
5. Ho, T.K., Hull, J. J. and Srihari, S.N.: "Decision Combination in Multiple Classifier Systems". IEEE Trans. PAMI, Vol. 16 Nº 1 pp. 66–75 (1994)
6. Murphy, P.M. and Aha, D.W.: UCI Repository of Machine Learning databases. [<http://www.ics.uci.edu/~mlearn/MLRepository.html>]. Irvine, CA: University of California, Department of Information and Computer Science (1994)
7. Paredes, R., Vidal, E.: "A class-dependent weighted dissimilarity measure for nearest neighbor classification problems". Pattern Recognition Letters, Vol. 21 pp. 1027–1036 (2000)
8. Soraluze, I., Rodriguez, C., Boto, F., Perez, A.: "Multidimensional Multistage K-NN classifiers for handwritten digit recognition" Proceedings of eighth IWFHR, Niagara-on-the-lake (Ontario), Canada, pp 19–23 (2002)
9. Soraluze, I., Rodriguez, C., Boto, F., Perez, A.: "An Incremental and Hierarchical k-NN classifier for Handwritten characters" 16<sup>th</sup> International conference on Pattern Recognition Quebec, Canada (2002)
10. Vijaya Saradhi, V., Narasimha Murty, M.: "Bootstrapping for efficient handwritten digit recognition". Pattern recognition, Vol. 34 pp. 1047–1056 (2001)
11. Murthy, S.K. and Salzberg, S.: A system for the induction of oblique decision trees. Journal of Artificial Intelligence Research 2, 133 (1994)
12. Wilkinson, R.A., Geist, J., Janet, S., Groter, P., Burges, R., Creecy, R., Hammond, B., J. Hull, N. Larsen, T. Vogl and C. Wilson, *First Census Optical Character Recognition System Conference*. National Institute of Standards and Technology (NIST) 1992

# Some Improvements in Tree Based Nearest Neighbour Search Algorithms

Eva Gómez-Ballester, Luisa Micó, and Jose Oncina\*

Dept. Lenguajes y Sistemas Informáticos  
Universidad de Alicante, E-03071 Alicante, Spain,  
`{eva,mico,oncina}@dlsi.ua.es`

**Abstract.** Nearest neighbour search is one of the most simple and used technique in Pattern Recognition. In this paper we are interested on tree based algorithms that only make use of the metric properties of the space. One of the most known and refereed method in this class was proposed by Fukunaga and Narendra in the 70's.

This algorithm uses a tree that is traversed on search time and uses some elimination rules to avoid the full exploration of the tree.

This paper proposes two main contributions: two new ways for constructing the tree and two new elimination rules. As shown in the experiment section, both techniques reduce significantly the number of distance computations.

**Keywords:** Nearest Neighbour, Metric Spaces, Elimination rule, Pattern Recognition.

## 1 Introduction

Nearest neighbour search (NNS) is a simple technique very popular in problems related with classification. The NNS method consists on finding the nearest point from a prototype set to a given sample point using a distance function [3].

To avoid the exhaustive search many algorithms have been developed in the last thirty years [1]. One of the most popular and refereed algorithm was proposed by Fukunaga and Narendra [4].

This algorithm builds, on preprocess time, a tree that is traversed in search time using some elimination rules to avoid the exploration of some branches.

The algorithm does not make any assumption on the way the points are coded. It can be used in any metric space, that is, the distance function has to fulfil the following conditions:

- $d(x, y) \geq 0$  ( $= 0$  if  $x = y$ ).
- $d(x, y) = d(y, x)$  (symmetry).
- $d(x, z) \leq d(x, y) + d(y, z)$  (triangle inequality).

---

\* The authors thank the Spanish CICYT for partial support of this work through project TIC2000-1703-CO3-02.

Although some recently proposed algorithms are more efficient, the Fukunaga and Narendra algorithm is a basic reference in the literature and in the development of new rules to improve the main steps of the algorithm that can be easily extended to other tree based algorithms [9] [10] [2] [6] [7].

In this paper we propose two new ways of building the tree and two new elimination rules.

## 2 The Fukunaga and Narendra Algorithm

The Fukunaga and Narendra algorithm is a fast search method that use a hierarchical clustering to build a search tree where all the prototypes are stored. In particular, it uses a divisive strategy splitting the training data into  $l$  subsets. Moreover each subset is divided into  $l$  subsets again, and applying recursively this procedure a search tree is built. Fukunaga and Narendra proposed to use the  $c$ -means at each step. Each node  $p$  of the tree represents a group of samples, and is characterised by the following parameters:

- $S_p$  set of samples
- $N_p$  number of samples
- $M_p$  representative of  $S_p$
- $R_p = \max_{x_i \in S_p} d(x_i, M_p)$ , (the radius of the node)

When an unknown sample  $x$  is given, the nearest neighbour is found by searching in the tree by first-depth strategy. Among the nodes at the same level, the node with a smaller distance  $d(x, M_p)$  is searched earlier. Let  $n$  be the current nearest neighbour to  $x$  among the prototypes considered up to the moment, the following two rules permit to avoid the search in the subtree  $p$ :

**rule for internal nodes:** no  $y \in S_p$  can be the nearest neighbour to  $x$  if

$$d(x, n) + R_p < d(x, M_p)$$

**rule for leaf nodes:**  $y \in S_p$  cannot be the nearest neighbour to  $x$  if

$$d(x, n) + d(y, M_p) < d(x, M_p)$$

In this work only binary trees with one point on the leafs<sup>1</sup> are considered. On such case the second rule becomes a special case of the first one. This rule will be refereed as the Fukunaga and Narendra's rule (FNR).

## 3 The Searching Tree

Two approximations have been developed as alternative to the use of the well known  $c$ -means algorithm that was recursively used by Fukunaga in the construction of the tree structure.

The first clustering strategy is called *Most Separated Points* (MSP), and consists on:

---

<sup>1</sup> In the Fukunaga and Narendra algorithm, leaf nodes can have more than one point.

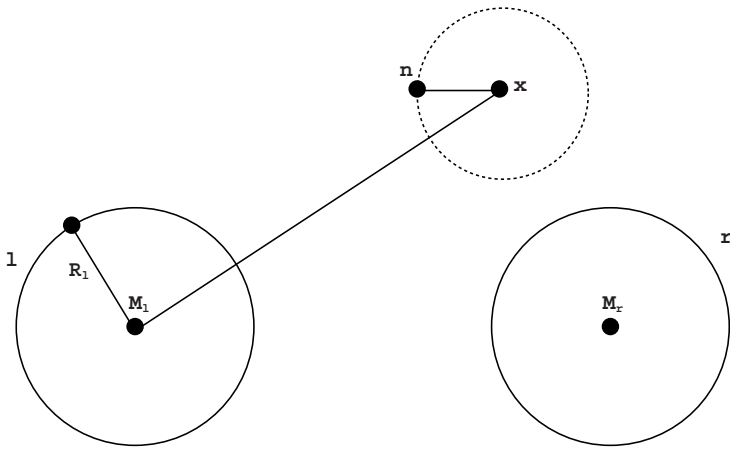


**Fig. 1.** Original elimination rule used in the algorithm of Fukunaga and Narendra (FNR).

- use as representative of the two children of each node the two more separated prototypes,
- classify the rest of the prototypes in the node of the nearest representative,
- recursively repeat the process until each final node has only a prototype, the representative.

The second clustering strategy is called *Most Separated Father Point* (MSFP)<sup>2</sup>, and consists on:

- randomly select a prototype as the representative of the root node,
- in the following level, use as representative of one of the nodes the representative of the father node. The representative of the sibling node is the farthest prototype among all the prototypes belonging to the father node.
- classify the rest of the prototypes in the node of the nearest representative,
- recursively repeat the process until each leaf node has only one point, the representative.

Of course, the second strategy is not as symmetric as the first one and it will produce deeper trees. On the other hand, this strategy permits to avoid the computation of some distances in the search procedure as one of the representatives is the same than the father, each time that it is necessary to expand a node, only one new distance computation is needed.

## 4 The New Rules

The elimination rules defined by Fukunaga and Narendra only make use of the information between the node to be prune and the hiperespherical surface cen-

<sup>2</sup> note that this tree can be built in  $O(n \log(n))$ , where  $n$  is the prototype set size

tried in the test sample with radius the distance to the nearest point considered up to the moment.

In the proposed new rules, to eliminate a node  $l$ , also information related with the sibling node  $r$  is used.

#### 4.1 The Sibling Based Rule (SBR)

A first proposal requires that each node  $r$  stores the distance between the representative of the node,  $M_r$ , and the nearest point,  $e_\ell$ , in  $S_\ell$ .

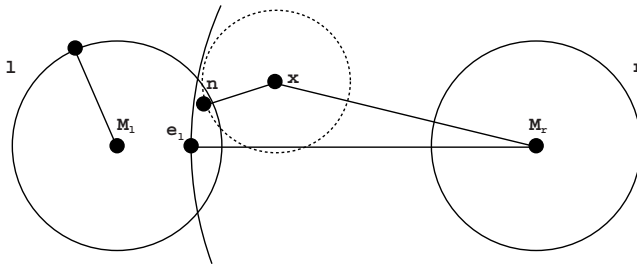


**Fig. 2.** Sibling based rule (SBR).

**Definition of SBR:** given a node  $r$ , a test sample  $x$ , an actual candidate to be the nearest neighbour  $n$ , and the nearest point to the representative of the sibling node  $\ell$ ,  $e_\ell$ , the node  $\ell$  can be prune if the following condition is fulfil:

$$d(M_r, e_\ell) > d(M_r, x) + d(x, n)$$

It is interesting to see that this rule don't need to know the distance between  $x$  and  $M_\ell$ . That will permit to avoid some distance computations in the search procedure<sup>3</sup>.

#### 4.2 Generalised Rule (GR)

This rule is an iterated combination of the FNR and the SBR. Let  $l$  be a node, to apply this rule, first a set of points  $\{l_i\}$  is defined in the following way:

$$\begin{aligned} G_1 &= S_\ell \\ \ell_i &= \operatorname{argmax}_{p \in G_i} d(p, M_\ell) \end{aligned}$$

<sup>3</sup> In the search procedure, each time a node expansion is needed, the distances between each representative of the children to the test sample is calculated. After that, the elimination rules are applied.

Now, as the new rule SBR don't use  $d(x, M_\ell)$ ,  $\ell$  can be eliminated before computation of  $d(x, M_\ell)$ .

$$G_{i+1} = \{p \in G_i : d(p, M_r) < d(\ell_i, M_r)\}$$

In preprocessing time, the distances  $d(M_r, \ell_i)$  are stored in each node  $\ell$ .

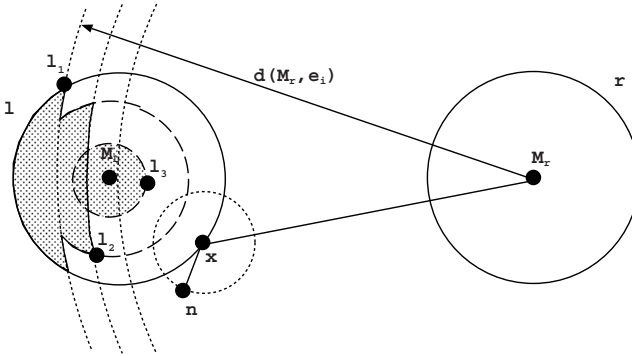


**Fig. 3.** Generalised rule (GR).

**Definition of GR:** given two sibling nodes  $l$  and  $r$ , a test sample  $x$ , an actual candidate to be the nearest neighbour  $n$ , and the list of point  $\ell_1, \ell_2, \dots, \ell_s$ , the node  $\ell$  can be prune if there is an integer  $i$  such that:

$$d(M_r, \ell_i) \geq d(M_r, x) + d(x, n) \quad (1)$$

$$d(M_\ell, \ell_{i+1}) \leq d(M_\ell, x) - d(x, n) \quad (2)$$

Cases  $i = 0$  and  $i = s$  are also included not considering equations (1) or (2) respectively. Note that condition (1) is equivalent to SBR rule when  $i = s$  and condition (2) is equivalent to FNR rule when  $i + 1 = 1$ .

## 5 Experiments

Some experiments with synthetic and real data were carried out to study the behaviour of the algorithm.

The prototypes in the synthetic experiment set were extracted from a 6-dimensional uniform distribution in the unit hypercube. The Euclidean distance was used.

All the experiments were repeated with 10 different sets of prototypes, 1000 samples were used as test.

A first set of experiments were carried out in order to study the behaviour of the algorithm when using  $c$ -means (the proposed by Fukunaga and Narendra), MSP and MSFP clustering algorithm to build the tree (fig. 4).

The experiments show that *c*-means and MSP have a very similar behaviour<sup>4</sup> and that MSFP is neatly superior. This is because the saving of one distance computation at each level compensates the fact that the trees are deepest.

A second set of synthetic experiments were carried out to show the behaviour of the algorithm when using the elimination rules FNR, FNR+SBR and GR using the MSFP clustering algorithm (see fig. 5).

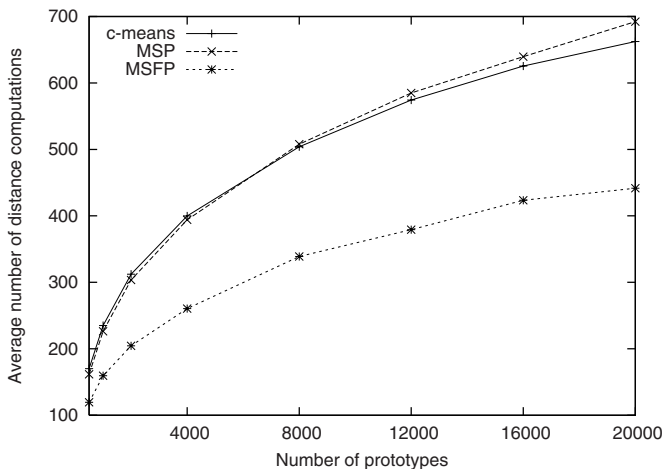


**Fig. 4.** Influence on the Fukunaga and Narendra algorithm when *c*-means, MSP and MSFP clustering algorithms are used in the tree building process with a 6-dimensional uniform distribution.

As was expected the addition of the SBR reduces slightly the number of distance computations but the GR<sup>5</sup> reduces it drastically.

Some experiments using real data have also been made. In particular, PHONEME database from the ROARS ESPRIT project [8] was used. The PHONEME database consists of 5404 5-dimension vectors from 2 classes. The set was divided in 5 subsets, using 4 sets as prototypes and 1 set as samples. A leaving one out technique was used.

The results plotted in figure 6 show the average number of distance computations as the size of the training set increases. All the combinations of the tree clustering algorithms and FNR and GR are shown. The behaviour using this data seems similar to the obtained results with artificial data, as figure illustrates.

<sup>4</sup> note that MSP is much faster than *c*-means

<sup>5</sup> note that the FNR and the SBR are special cases of the GR

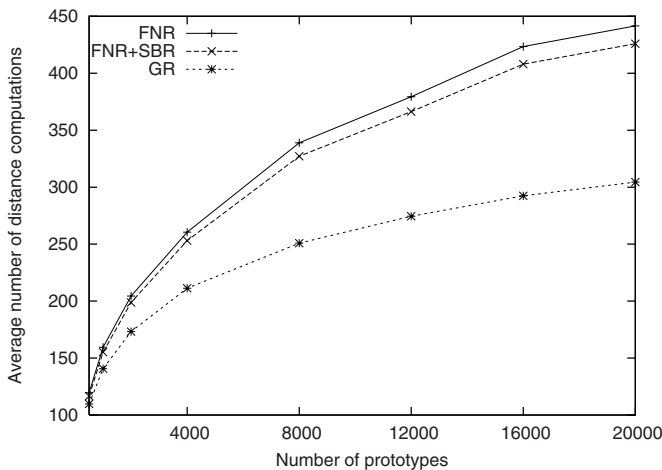


**Fig. 5.** Influence on the Fukunaga and Narendra algorithm when MSFP is used to build the tree and the rules FNR, FNR+SPR and GR are used in the search.

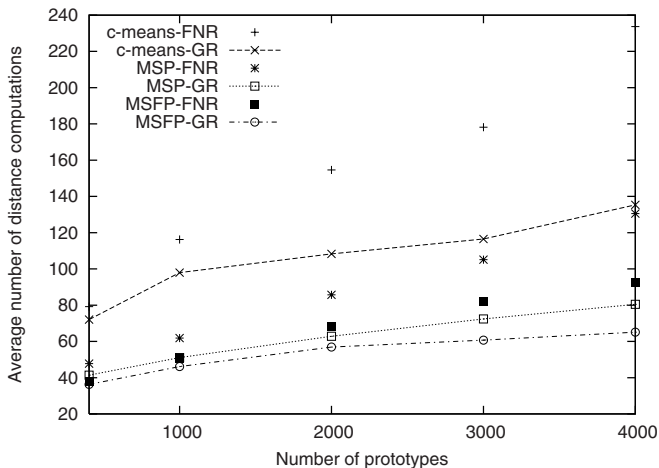


**Fig. 6.** Average number of distance computations by sample in relation to the size of the training set for the PHONEME database.

## 6 Conclusions

In this paper we have developed a series of improvements based on the algorithm proposed by Fukunaga and Narendra. These algorithm builds a tree in preprocess time to speed the nearest neighbour search.

On the one hand, two new methods to build the tree has been proposed. This tree is quicker to build and allows the search algorithm to find the nearest neighbour with less distance computations.

On the other hand, two new elimination rules are proposed to speed up the nearest neighbour search. The experiments suggest that high speed ups can be obtained.

In the future, we plan to apply these approximations to other nearest neighbour search algorithms based on a tree structure. We are also interested in testing these techniques in general metric spaces.

## References

1. Belur V. Dasarathy: Nearest Neighbour(NN) Norms: NN Pattern Classification Techniques. IEEE Computer Society Press (1991).
2. Chen, Y.S., Hung, Y.P., Fuh, C.S.: Fast Algorithm for Nearest Neighbour Search Based on a Lower Bound Tree. Proceedings of the 8th International Conference on Computer Vision, Vancouver, Canada, (2001), **1** 446–453
3. Duda, R., Hart, P.: Pattern Classification and Scene Analysis. Wiley (1973)
4. Fukunaga, K., Narendra, M.: A branch and bound algorithm for computing  $k$ -nearest neighbours. IEEE Trans. Computing (1975) **24** 750–753
5. Kalantari, I., McDonald, G.: A data structure and an algorithm for the nearest point problem. IEEE Trans. Software Engineering (1983) **9** 631–634
6. L. Miclet, M. Dabouz: Approximate fast nearest-neighbour recognition. Pattern Recognition Letters (1983) **12** 277–285.
7. Micó, L., Oncina, J., Carrasco, R.C.: A fast branch and bound nearest neighbour classifier in metric spaces. Pattern Recognition Letters (1996) **17** 731–739
8. Alinat, P.: Periodic progress report 4, ROARS project ESPRIT II – Number 5516. Thomson Technical Report TS ASM 93/S/EGS/NC/079 (1993)
9. S. Omachi, H. Aso: A fast algorithm for a k-NN classifier based on branch and bound method and computational quantity estimation. Systems and Computers in Japan, vol. 31, no 6, pp. 1–9 (2000).
10. Geofrey I. Webb: OPUS: An Efficient Admissible Algorithm for Unordered Search. Journal of Artificial Intelligence Research 3 (1995) 431–465.

# Impact of Mixed Metrics on Clustering\*

Karina Gibert and Ramon Nonell

Department of Statistics and Operation Research,  
Universitat Politècnica de Catalunya, C. Pau Gargallo 5, Barcelona 08028, SPAIN.  
[karina@eio.upc.es](mailto:karina@eio.upc.es)

**Abstract.** One of the features involved in clustering is the evaluation of distances between individuals. This paper is related with the use of mixed metrics for clustering messy data. Indeed, when facing complex real domains it becomes natural to deal simultaneously with numerical and symbolic attributes. This can be treated on different approaches. Here, the use of mixed metrics is followed.

In the paper, a family of mixed metrics introduced by Gibert is used with different parameters on an experimental data set, in order to assess the impact on final classes.

**Keywords:** clustering, metrics, qualitative and quantitative variables, messy data, ill-structured domains ...

## 1 Introduction

Clustering is one of the more used technique to separate data into groups. In fact, we agree with the idea that a number of real applications in *KDD* either require a clustering process or can be reduced to it [18]. Also, in apprehending the world, men constantly employ three methods of organization, which pervade all of their thinking: (*i*) the differentiation of experience into particular objects and their attributes; (*ii*) the distinction between whole objects and its parts and (*iii*) the formation and distinction of different classes of objects. That's why, several well known expert systems (MYCIN [23], ...) are actually classifiers.

However, when facing *ill-structured domains* as mental disorders, sea sponges, disabilities... clustering has to be done on heterogeneous data matrices. In this kind of domains (see [5], [6]), the consensus among experts is weak —and sometimes non-existent; when describing objects, quantitative and qualitative information coexists in what we call *non-homogeneous* data bases. Even more, the number of modalities of qualitative variables depends on the expertise of who is describing the objects: the more he knows about the domain, the greater is the number of modalities he uses.

In this work, mixed metrics introduced by Gibert in [4],[10] for measuring distances with messy data is used. This measure has been successfully implemented in a clustering system called **Klass** [5], [6] and applied to very different ill-structured domains [7], [9], [11], [12].

---

\* This research has been partially financed by the project *CICYT'2000*.

Main goal of this paper is to study the behavior of different metrics of Gibert's family (which also includes Ralambondrainy proposals as particular cases) on a set of experimental data that presents different structures, in order to study which parameters of Gibert's metrics perform better in clustering, according to the data structure. Formal approach to this problem requires a too complex theoretical development. That's why an experimental approach is presented here as a first step of the research. A similar experiment was also performed by Diday in [2], comparing the performance of two metrics [14] and [13] in clustering. Next step of this work is to make a global comparison.

This paper is organized as follows: after the general introduction, an overview of the possibilities of working with messy data is presented. Then, details on the indexed family of distances that combines qualitative and quantitative information introduced by Gibert is presented in 3, together with several proposals on the indexes values. In section 4 the experiment context is provided. Section 4.1 introduces the experimental data sets, while section 5 presents main results. Finally, the last section presents some conclusions and future work.

## 2 Clustering Heterogeneous Data Matrices

Management of non-homogeneous data matrices requires, indeed, special attention when classifying ill-structured domains. Standard clustering methods were originally conceived to deal with quantitative variables. Upon [1], data analysis with heterogeneous data bases may follow three main strategies:

*Variables partitioning.* It consists on partitioning the variables upon their type, then reducing the analysis to the dominant type (determined owing to the group with a greater number of variables, or the group containing the more relevant variables, or the background knowledge on the domain...).

For example, if dominant type is qualitative variables, then correspondence analysis could be used and later a clustering on the factorial components is possible [24], [17]. Since the classification is performed in a fictitious space, additional tools are required to enable the interpretation of the results.

This approach of course misses the information provided by the non dominant groups of variables. A natural extension is to perform independent analysis inside every type of variables. Problem, then, is later integration of results of parallel analysis to produce a consistent, coherent and unique final result. Even in this case, interactions between variables of different types (like cooking temperature and final color of a ceramic) cannot be analyzed under this approach.

*Variables converting.* It consists on converting all the variables to a unique type, trying to conserve as much original information as possible. First of all, final converting type has to be decided. Conversion is not a trivial process (every variable may be converted to a unique one, or split to a group of variables or several original variables will be grouped to a unique transformed one). In Statistics, traditionally, symbolic variables has been converted to a set of binary variables,

to generate the *complete incidence table*. Then, clustering using  $\chi^2$  metrics may be performed [3]. Dimensions of the complete incidence table implies a significant cost increase. In Artificial Intelligence, grouping of quantitative values into a qualitative one [22] is much more popular. This transformation implies a relevant loss of information as well as the introduction of some instability in the results, which depend on the defined grouping.

Many authors, among them [1], [16], discuss different strategies on this line, together with the associated problems of loss of relevant information or even making difficult final interpretation, since the transformed variables could be in a fictitious space. Also, in [5] it is shown how converting all the variables to qualitative ones introduces, almost always, a bias on the results, which can be sometimes even arbitrary.

*Compatibility measures.* It consists on the use of compatible measures which cover any combination of variable types, making an homogeneous treatment of all the variables. It can, for instance, be defined a non-senseless distance (or similarity) between individuals which uses different expressions for every variable type.

The idea is to allow clustering on a domain simultaneously described by qualitative and quantitative variables without transforming the variables themselves. Since in the core of the classification process distances between individuals have to be calculated, a function to do it with non homogeneous data has to be found. In the literature several proposals on this line can be found. Upon discussions on [4] and [5], this is the approach of this work. Main advantages of this approach are: respecting the original nature of data, there is not loss of information, it is not necessary to take previous arbitrary decisions which can bias results, it is possible to study all the variables together, it is possible to analyze interactions between variables of different types. Proposals on this line could be, chronologically: Gower 71 [14], Gowda & Diday 91 [13], Gibert 91 [4,8], Ichino & Yaguchi 94 [15], Ralambondrainy 95 [21], Ruiz-Schulcloper [19].

### 3 Gibert's Mixed Metrics

The input of a clustering algorithm is a data matrix with the values of  $K$  variables  $X_1 \dots X_K$  observed over a set  $\mathcal{I} = \{1, \dots, n\}$  of individuals. Variables are represented in columns while individuals in the rows of data matrix. The cells contain the value,  $x_{ik}$ , taken by individual  $i \in \mathcal{I}$  for variable  $X_k$ , ( $k = 1 : K$ ). In our context, heterogeneous data matrices are supposed, so let us name  $\zeta \in \{1 \dots K\}$  the indexes of numerical variables and  $Q = \{1 \dots K\} - \zeta$  the indexes of categorical variables, being  $n_\zeta = \text{card}(\zeta)$  and  $n_Q = \text{card}(Q)$ .

Mixed metrics introduced by Gibert in [4], [10] is defined, for clustering purposes as a family of metrics indexed by the pair  $(\alpha, \beta)$ :

$$\{d_{(\alpha, \beta)}^2(i, i')\}_{(\alpha, \beta) \in [0, 1] \times [0, 1]} \quad (1)$$

Being,  $d_{(\alpha,\beta)}^2(i, i') = \alpha d_\zeta^2(i, i') + \beta d_Q^2(i, i')$ ;  $(\alpha, \beta)$  indexes for weighting the influence of variables in  $\zeta$  versus those in  $Q$ ;  $d_\zeta^2(i, i')$  the normalized euclidian metrics calculated with variables in  $\zeta$  and  $d_Q^2(i, i')$  a rewriting of  $\chi^2$  metrics calculated with variables in  $Q$ , supporting symbolic representation:

$$d_\zeta^2(i, i') = \sum_{\forall k \in \zeta} \frac{(x_{ik} - x_{i'k})^2}{s_k^2} \quad ; \quad d_Q^2(i, i') = \frac{1}{n_Q^2} \sum_{\forall k \in Q} d_k^2(i, i') \quad (2)$$

where  $s_k^2 = var(X_k)$ . Referring to  $d_k^2(i, i')$ ,  $I^{k_j}$  is the number of observations equal to the  $j$ -th modality of  $X_k$  (namely  $c_j^k$ );  $I_{k^i} = card(\hat{i} : x_{ik} = x_{i'k})$ . An *extended value* appears for a class representative if  $X_k$  is not constant inside the class; it is represented as  $(f_i^{k_1}, f_i^{k_2}, \dots, f_i^{k_{n_k}})$  where  $f_i^{k_j}, j = 1, 2, \dots, n_k$ , is the proportion of objects of the class represented by  $i$  with  $x_{ik} = c_j^k$ , then

$$d_k^2(i, i') = \begin{cases} 0 & , \text{ if } x_{ik} = x_{i'k} \\ \frac{1}{I_{k^i}} + \frac{1}{I_{k^{i'}}} & , \text{ if } x_{ik} \neq x_{i'k} \\ \frac{(f_i^{k_s} - 1)^2}{I^{k_s}} + \sum_{j=1, j \neq s}^{n_k} \frac{(f_i^{k_j})^2}{I^{k_j}} & , \text{ if } x_{ik} = c_s^k \text{ and } i' \text{ extended on } X_k \\ \sum_{j=1}^{n_k} \frac{(f_i^{k_j} - f_{i'}^{k_j})^2}{I^{k_j}} & , \text{ for } i \text{ and } i' \text{ extended on } X_k \end{cases}$$

In [10] an heuristic criteria is used to propose proper values for index  $(\alpha, \beta)$ :

$$\alpha_0 = \frac{\alpha}{\alpha + \beta} \quad \& \quad \beta_0 = \frac{\beta}{\alpha + \beta} \quad ; \quad \alpha = \frac{n_\zeta}{d_{\zeta max^*}^2} \quad \& \quad \beta = \frac{n_Q}{d_{Q max^*}^2} \quad (3)$$

with  $d_{\zeta max^*}^2 = \max_{i, i'} \{d_\zeta^2(i, i')\}$  and  $d_{Q max}^2 = \max_{i, i'} \{d_Q^2(i, i')\}$ . This values<sup>1</sup> refers the two components of the distance to a common interval, in order to give equal influence in the determination of  $d_{(\alpha,\beta)}^2(i, i')$ ; the numerators give to each component a proportional weight to its presence in the objects description.

**Ralambondrainy proposal.** In [21], Ralambondrainy also proposes a metrics to work with heterogeneous data matrices; it is defined exactly as expression (1). In [20], two practical ways of standardization for calculating  $(\alpha, \beta)$  are presented:

- by the inertia:  $\pi_1 = \frac{1}{n_\zeta}$  ;  $\pi_2 = \frac{1}{\sum \{n_k - 1 : k \in Q\}}$
  - by the norm:  $\pi'_1 = \frac{1}{\sqrt{\sum \{\rho^2(X_k, X_{k'}) : k, k' \in \zeta\}}}$  ;  $\pi'_2 = \sqrt{\sum \{n_k - 1 : k \in Q\}}$ ,
- $\rho^2(X_k, X_{k'})$  correlation between  $X_k, X_{k'}$ ;  $n_k$  number of modalities of  $X_k$ .

Those proposals identify two elements of the Gibert family of mixed distances that will also be considered in this paper.

---

<sup>1</sup> Maximums can also be truncated to the 95% in order to acquire more robustness.

## 4 The Experiment

As said before the main goal of this paper is to analyze the behavior of different elements of Gibert's family in the clustering of different data sets. An experiment was designed according to that. For this work a single clustering algorithm will be considered: a hierarchical reciprocal neighbors algorithm using Ward criteria (see [24]). In future works other algorithms will also be taken into account. As a first approach, four elements of Gibert's family will be considered in the experiment:  $d_{(\alpha_0, \beta_0)}^2(i, i')$  as proposed by Gibert,  $d_{(\pi_1, \pi_2)}^2(i, i')$ ,  $d_{(\pi'_1, \pi'_2)}^2(i, i')$ , as proposed by Ralambondrainy, and  $d_{(0.5, 0.5)}^2(i, i')$  which represents a non-informed option with equal contribution to the distances of both components.

On the other hand, experimental data has to be simulated (see §4.1). Structure of data sets was decided on the basis of factors that can influence into the behavior of the metrics, regarding the clustering process: *distinguishability* of the classes is relevant (that's why some data sets will contain overlapping classes and others separated ones, variance of classes will also be considered); also, the *form* of the classes is important (recognition of convex or filiform classes will be tested); finally different *number of classes* will be tested.

For all the data sets, four clustering processes will be performed, one with every metrics indicated above. On the results of every clustering, relevant information will be codified in a new data matrix. A multivariate analysis will be done with it, to see relationships among different runs. It seems reasonable to determine good behavior on the basis of real data structure recognition, which is easy with simulated data, since real class of every object is a priori known.

### 4.1 The Simulated Data Set

The basis of experimental data is also following the guidelines presented in [2], where comparison of several hierarchical clustering methods is performed using several kinds of experimental data with different structures. Figure 1 shows the experimental data sets used in this work. It is obvious that it only shows the structure of the numerical part of data sets. Every data set contains also as many categorical variables as numerical, randomly generated with 3 modalities.

Some data sets correspond to the proposal presented in [2], others are specially introduced for our purposes. The basic structures from [2] are: *concentric classes* (fig. 1(d)), *chained classes* (fig. 1(f)), *mixture of convex and concentric classes* (fig. 1 (e)) and *filiform classes in 2D* (figure 1(g)), since it is known that certain clustering algorithms perform confusing recognition in this case. Regarding the discussion previously introduced, and making wider the scope of the analysis, other structures were added in the experiment: *uniform*, representing lack of structure (fig. 1(j)), *convex classes* (fig. 1(a,b,c)), which are supposed to be the easier to recognize; variability of the classes is increasing from (a) to (c) in such a way that distinguishability of classes decreases. Finally, *filiform classes in three dimensions* (see figure 1 (h)).

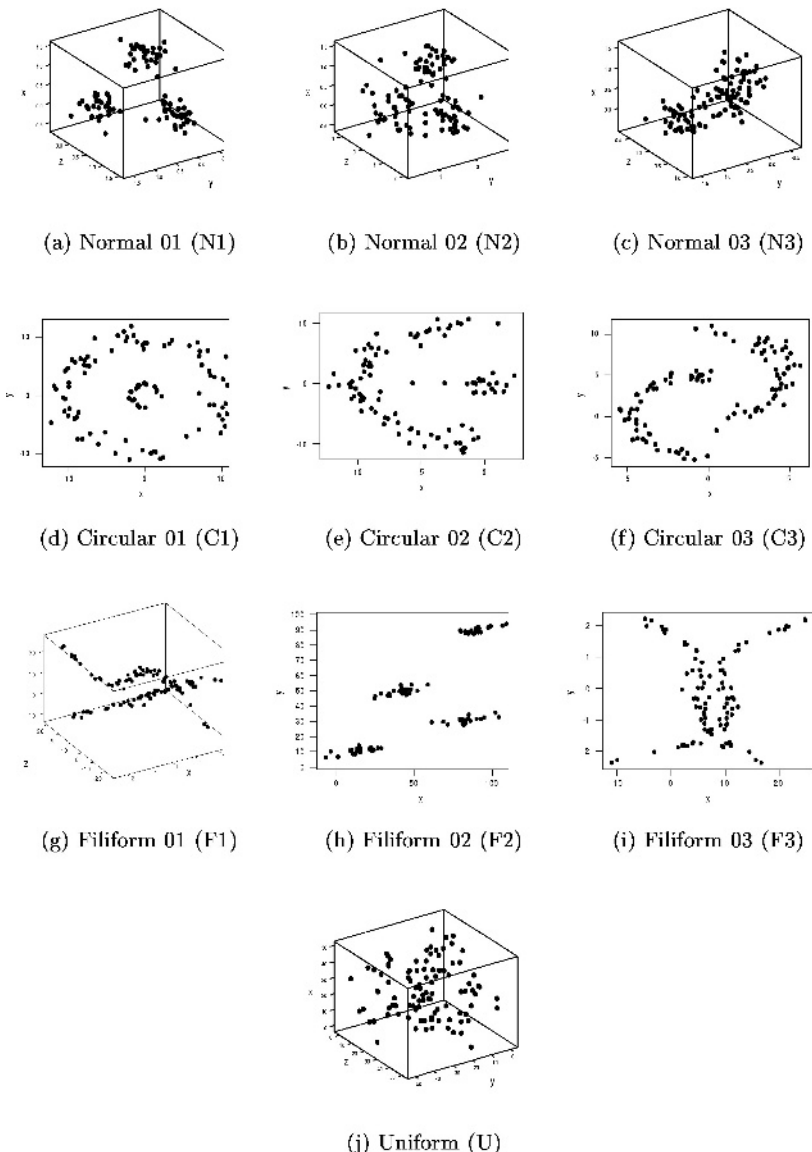


**Fig. 1.** Experimental data sets

## 5 Results

Every data set is clustered using the four metrics given in §4. Then some relevant information on the results (like number of resulting classes —which is an output in hierarchical clustering, size of every class, number of real classes, real classes form, etc) is used for a later Principal Components Analysis, in order to study

relationships among runs; tax of misclassification is used as a quality measure of runs (fig. 2 shows the projection of the runs on the first factorial plane).

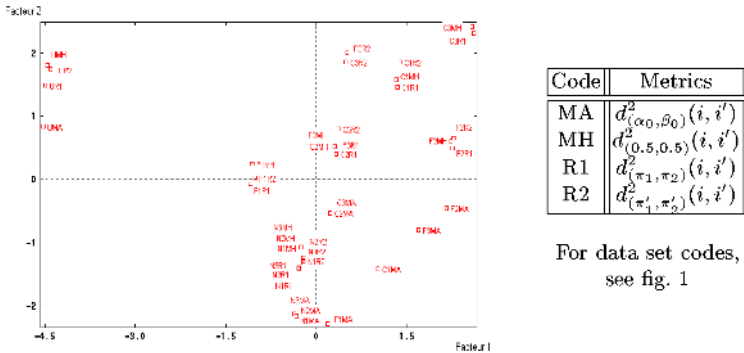


**Fig. 2.** First factorial plane with experimental run represented.

It seems that first axis is opposing less structured data sets (on the left hand side, like *uniform*) against more structured ones (on the right, *filiform 02* or *circular 03*). The more remarkable thing, regarding the second axis, is that given a data set, its four runs use to be vertically displayed in two subsets: on the lower side the clustering performed with Gibert proposal  $d_{(\alpha_0, \beta_0)}^2(i, i')$  (*-MA* in the figure), much more down than a second group, where the rest of runs appear in close neighborhood (except for *circular 02* and *filiform 03* for which runs with  $d_{(\pi'_1, \pi'_2)}^2(i, i')$  (*-R2* in the figure) are projected in intermediate positions). So, in general it can be said that the second axis is opposing Gibert proposal for  $(\alpha, \beta)$  to the other ones, which are difficult to distinguish.

## 6 Conclusions and Future Work

It has been seen that changing metrics produces real effects on the clustering results. It is then important to know when different metrics have better behaviour for recognizing real classes.

From the four studied elements of Gibert's family,  $d_{(\alpha_0, \beta_0)}^2(i, i')$  is the one which produces more different results on the used experimental data sets. It seems, from this work, that the other three possibilities do not produce great differences on the used clustering method. In addition, for case *filiform 03*,  $d_{(\alpha_0, \beta_0)}^2(i, i')$  is the only one that allows recognition of real classes.

Next step is to complete the experiment in order to check if this separate behavior of  $d_{(\alpha_0, \beta_0)}^2(i, i')$  is maintained, and if it is possible to obtain more knowledge on the other metrics; it will be interesting to work with different structures on the categorical part of data matrix, which was blocked for this work to uniform distribution. After that, comparison with results reported in [2] will also be done, as well as with other proposals from the literature, like Gower coefficient.

In the last step, including other clustering algorithms will enable study of more general properties of those metrics.

**Acknowledgements.** To Àngela Twose for his help on running experiments.

## References

1. Michel R. Anderberg. *Cluster Analysis for applications*. Academic Press, 1973.
2. E. Diday and J.V. Moreau. Learning hierarchical clustering from examples. In Rapport N 289 Centre de Rocquencourt, editor, *INRIA*, 1984.
3. W.R. et al. Dillon. *Multivariate analysis. Methods & applications*. Wiley, 1984.
4. K. Gibert. Klass. Estudi d'un sistema d'ajuda al tractament estadístic de grans bases de dades. Master's thesis, UPC, 1991.
5. K. Gibert. *L'ús de la Informació Simbòlica en l'Automatització del Tractament Estadístic de Dominis Poc Estructurats*. phd. thesis., UPC, Barcelona, Spain, 1994.
6. K. Gibert. The use of symbolic information in automation of statistical treatment for ill-structured domains. *AI Communications.*, 9(1):36–37, march 1996.
7. K. Gibert and R. et al. Annicchiarico. Kdd on functional disabilities using clustering based on rules on who-das ii. In *ITI 03.*, pages 181–186, Croatia, 2003.
8. K. Gibert and U. Cortés. KLASS: Una herramienta estadística para ... poco estructurados. *proc. IBERAMIA-92.*, pages 483–497, 1992. Noriega Eds. México.
9. K. Gibert and U. Cortés. Combining a knowledge-based system and a clustering method ... volume 89 of *LNS*, pages 351–360. Springer-Verlag, 1994.
10. K. Gibert and U. Cortés. Weighing quantitative and qualitative variables in clustering methods. *Mathware and Soft Computing*, 4(3):251–266, 1997.
11. K. Gibert and U. Cortés. Clustering based on rules and knowledge discovery in ill-structured domains. *Computación y Sistemas*. 1(4):213–227, 1998.
12. K. Gibert and Z. Sonicki. Classification Based on Rules and Thyroids Dysfunctions. *Applied Stochastic Models in Business and Industry*, 15(4):319–324, octuber 1999.
13. K. Chidananda Gowda and Diday E. *Symbolic clustering using a new similarity measure*. IEEE Tr SMC, Vol 22, No 2, March/April, 1991.
14. J.C. Gower. A General coefficient if similarity ... *Biometrics*, 27:857–874, 1971.
15. M. Ichino and H. Yaguchi. Generalized Minkowski Metrics for Mixed feature-type data analysis. *IEEE Tr SMC*, 22(2):146–153, 1994.
16. L. Kaufman and P.J. Rousseeuw. *Finding Groups in Data, an Introduction to Cluster Analysis*. John Wiley & Sons, London (England), 1990.
17. L. Lebart. *Traitemet statistique des données*. Dunod, Paris., 1990.
18. G. Nakhaeizadeh. Classification as a subtask of of Data Mining experiences form some industrial projects. In *IFCS*, volume 1, pages 17–20, Kobe, JAPAN, 1996.
19. J. R-Schlumper. Data analysis between sets of objects. In *ICSRIC'96*. 85-81, vIII.
20. H. Ralambondrainy. *A clustering method for nominal data and mixture ...* H.H.Bock, Elsevier Science Publishers, B.V. (North-Holland), 1988.
21. H. Ralambondrainy. *A conceptual version of the K-means algorithm*. Lifetime Learning Publications, Belmont, California, 1995.
22. M. Roux. Algorithmes de classification, 1985. Paris: Masson, Paris, France.
23. E. H. Shortlife. *MYCIN: A rule-based computer program for advising physicians regarding antimicrobial therapy selection*. PhD thesis, Standford.
24. M. Volle. Analyse des données, 1985. Ed. Economica, Paris, France.

# A Comparison between Two Fuzzy Clustering Algorithms for Mixed Features

Irene Olaya Ayaquica-Martínez and José F. Martínez-Trinidad

Instituto Nacional de Astrofísica, Óptica y Electrónica  
Luis Enrique Erro No. 1  
Santa María Tonantzintla, Pue. C.P. 72840, México  
{ayaquica, fmartine}@inaoep.mx

**Abstract** In this paper, a comparative analysis of the mixed-type variable fuzzy c-means (MVFCM) and the fuzzy c-means using dissimilarity functions (FCMD) algorithms is presented. Our analysis is focused in the dissimilarity function and the way of calculating the centers (or representative objects) in both algorithms.

## 1 Introduction

Restricted unsupervised classification (RUC) problems have been studied intensely in Statistical Pattern Recognition (Schalkoff, 1992). The fuzzy c-means algorithm is based on a metric over a n-dimensional space. It has shown its effectiveness in the solution for many unsupervised classification problems.

The fuzzy c-means algorithm starts with an initial partition then it tries all possible moving or swapping of data from one group to others iteratively to optimize the objective measurement function. The objects must be described in terms of features such that a metric can be applied to evaluate the distance. Nevertheless, the conditions in soft sciences as Medicine, Geology, Sociology, Marketing, etc., are quite different. In these sciences, the objects are described in terms of quantitative and qualitative features (mixed data). For example, if we look at geological data, features such as age, porosity, and permeability, are quantitative, while others such as rock types, crystalline structure and facies structure, are qualitative. Likewise, missing data is common in this kind of problems. In these circumstances, it is not possible measure the distance between objects; only the degree of similarity can be determined.

Nowadays, the mixed-type variable fuzzy c-means algorithm (MVFCM) of Yang et al. (2003) and the fuzzy c-means using dissimilarity functions (FCMD) of Ayaquica (2002) (see also Ayaquica and Martínez (2001)) are the most recent works that solve the RUC problem when mixed data appear.

In this paper, the mixed-type variable fuzzy c-means and the fuzzy c-means using dissimilarity functions algorithms are analyzed. In addition, a comparison between them is made.

## 2 Mixed-Type Variable Fuzzy C-Means Algorithm (MVFCM)

In this section, the mixed-type variable fuzzy c-means algorithm (MVFCM) of Yang et al. (2003) is presented. They proposed a dissimilarity function to handle symbolic and fuzzy features.

The dissimilarity function used to evaluate the dissimilarity between symbolic features is the function proposed by Gowda and Diday, with some modifications. According to Gowda and Diday, the symbolic features can be divided into quantitative and qualitative in which each feature can be defined by  $d_p(A_k, B_k)$  due to position  $p$ ,  $d_s(A_k, B_k)$  due to span  $s$  and  $d_c(A_k, B_k)$  due to content  $c$  (see Yang et al. (2003) for details).

$$a) \text{ Quantitative features } d(A_k, B_k) = d_p(A_k, B_k) + d_s(A_k, B_k) + d_c(A_k, B_k)$$

$$b) \text{ Qualitative features } d(A_k, B_k) = d_s(A_k, B_k) + d_c(A_k, B_k)$$

Let  $A = m(a_1, a_2, a_3, a_4)$  and  $B = m(b_1, b_2, b_3, b_4)$  be any two fuzzy numbers. The dissimilarity  $d_f(A, B)$  is defined as  $d_f^2(A, B) = \frac{1}{4} (g_-^2 + g_+^2 + (g_- - (a_3 - b_3))^2 + (g_+ + (a_4 - b_4))^2)$

where  $g_- = 2(a_1 - b_1) - (a_2 - b_2)$  and  $g_+ = 2(a_1 - b_1) + (a_2 - b_2)$ .

Then, the dissimilarity function for both symbolic and fuzzy features is

$$d^2(X_j, A) = \sum_{k \text{ of symbolic}} \left( \sum_p d^2(X_{jk}, A_{k'p|i}) \cdot e_{k'p|i} \right) + \sum_{fuzzy} d^2(X_{jk}, A_k) \quad (1)$$

Let  $\{X_1, \dots, X_n\}$  be a data set of mixed feature types. The MVFCM objective function is defined as  $J(\mu, e, a) = \sum_{i=1}^c \sum_{j=1}^n \mu_{ij}^m d^2(X_j, A_i)$ , where  $d^2(X_j, A_i)$  is (1).

The equation to evaluate the membership degree is

$$\mu_{ij} = \left( \sum_{q=1}^c \frac{(d^2(X_j, A_q))^{1/(m-1)}}{(d^2(X_j, A_q))^{1/(m-1)}} \right)^{-1} \quad i = 1, \dots, c, \quad j = 1, \dots, n \quad (2)$$

This algorithm evaluates two cluster centers, one for symbolic features as  $A_{ik'} = [A_{k'1|i}, e_{k'1|i}], \dots, [A_{k'p|i}, e_{k'p|i}]]$  where  $A_{k'p|i}$  is the  $p$ th event of symbolic feature  $k'$  in cluster  $i$  and  $e_{k'p|i}$  is the membership degree of association of the  $p$ th event  $A_{k'p|i}$  to the feature  $k'$  in the cluster  $i$ .

The equation for  $e_{k'p|i}$  is

$$e_{k'p|i} = \frac{\sum_{j=1}^n \mu_{ij}^m \cdot \theta}{\sum_{j=1}^n \mu_{ij}^m} \quad (3)$$

where  $\theta \in \{0,1\}$  and  $\theta = 1$  if the  $k$ th feature of the  $j$ th datum  $X_j$  consists of the  $p$ th event, otherwise  $\theta = 0$ . The membership of  $X_j$  in the cluster  $i$  is  $\mu_{ij} = \mu_i(X_j)$ .

For fuzzy features the center is calculated considering  $A_{ik}$  as the  $k$ th fuzzy feature of the  $i$ th cluster center with parametric form  $A_{ik} = m(a_{ik1}, a_{ik2}, a_{ik3}, a_{ik4})$  where

$$a_{ik1} = \frac{\sum_{j=1}^n \mu_{ij}^m (8x_{jk1} - x_{jk3} + x_{jk4} + a_{ik3} - a_{ik4})}{8 \sum_{j=1}^n \mu_{ij}^m}, \quad (4)$$

$$a_{ik2} = \frac{\sum_{j=1}^n \mu_{ij}^m (4x_{jk2} + x_{jk3} + x_{jk4} - a_{ik3} - a_{ik4})}{4 \sum_{j=1}^n \mu_{ij}^m},$$

$$a_{ik3} = \frac{\sum_{j=1}^n \mu_{ij}^m (-2x_{jk1} + x_{jk2} + x_{jk3} + 2a_{ik1} - a_{ik2})}{\sum_{j=1}^n \mu_{ij}^m},$$

$$a_{ik4} = \frac{\sum_{j=1}^n \mu_{ij}^m (2x_{jk1} + x_{jk2} + x_{jk4} - 2a_{ik1} - a_{ik2})}{\sum_{j=1}^n \mu_{ij}^m}$$

### *MVFCM Algorithm*

Step 1: Fix  $m$  and  $c$ . Give  $\varepsilon > 0$ . Initialize a fuzzy  $c$ -partition  $\mu^{(0)} = \{\mu_1^{(0)}, \dots, \mu_c^{(0)}\}$ . Set  $l=0$ .

Step 2: For symbolic feature  $k'$ , compute  $i^{\text{th}}$  cluster center

$A_{ik}^{(l)} = [A_{k'1|i}^{(l)}, e_{k'1|i}^{(l)}, \dots, A_{k'p|i}^{(l)}, e_{k'p|i}^{(l)}]$  using (3). For fuzzy feature  $k$ , compute  $i^{\text{th}}$  cluster center  $A_{ik}^{(l)} = (a_{ik1}^{(l)}, a_{ik2}^{(l)}, a_{ik3}^{(l)}, a_{ik4}^{(l)})$  using (4).

Step 3: Update  $\mu^{(l+1)}$  using (2)

Step 4: Compare  $\mu^{(l+1)}$  with  $\mu^{(l)}$  in a convenient matrix norm.

IF  $\|\mu^{(l+1)} - \mu^{(l)}\| < \varepsilon$ , THEN STOP

ELSE  $l = l+1$  and GOTO Step 2.

In this algorithm a dissimilarity function defined as the sum of the dissimilarity between symbolic features and the dissimilarity between fuzzy features is used to solve the mixed data problem. However, the dissimilarity for symbolic and fuzzy features is always computed using the expressions  $d_p$ ,  $d_s$ ,  $d_c$  and  $d_f$  respectively. In the practice, the manner for evaluating the similarity between feature values is not only in dependence of the nature of features. Also, the context or the problem must be considered. When  $d_p$ ,  $d_s$ ,  $d_c$  and  $d_f$  are used we are forcing to evaluate the dissimilarity always in the same form independently of the context or nature of the problem. A fixed function does not allow representing the criterion used by the specialist to compare these features in a determined context. Therefore if two features are of the same type, the manner of comparing them not necessarily must be the same.

In other hand, this algorithm evaluates two cluster centers, one for symbolic features and other one for fuzzy features. These cluster centers are fictitious elements, i.e. the cluster centers cannot be represented in the same space of the objects however they are used to classify the objects.

## **3 Fuzzy C-Means Algorithm Using Dissimilarity Functions (FCMD)**

In this section, the fuzzy c-means algorithm using dissimilarity functions (FCMD) of Ayaquica and Martínez (2001) is presented.

Let us consider a clustering problem where a data set of  $n$  objects  $\{O_1, O_2, \dots, O_n\}$  should be classified into  $c$  clusters. Each object is described by a set  $R = \{x_1, x_2, \dots, x_m\}$  of features. The features take values in a set of admissible values  $D_i$ ,  $x_i(O_j) \in D_i$ ,  $i=1, 2, \dots, m$ . We assume that in  $D_i$  there exists a symbol "?" to denote missing data.

Thus, the features can be of any nature (qualitative: Boolean, multi-valued, etc. or quantitative: integer, real) and incomplete descriptions of the objects can be considered.

For each feature a comparison criterion  $C_i : D_i \times D_i \rightarrow L_i$   $i=1,2,\dots,m$  is defined, where  $L_i$  is a totally ordered set. This function allows to evaluate the similarity between two values of a feature. In the practice, this function is defined in basis of the manner to compare or evaluate the similarity between two values of the feature. When features are numeric, it is usually used a norm or distance, but it cannot be the unique way to evaluate the similarity between values. Therefore, in the formulation proposed here, this function is a parameter that the user can define according to the problem.

Some examples of comparison criteria are:

$$1. C_s(x_s(O_i), x_s(O_j)) = \begin{cases} 0 & \text{if } x_s(O_i) = x_s(O_j) \vee x_s(O_i) = ? \vee x_s(O_j) = ? \\ 1 & \text{otherwise} \end{cases}$$

where  $x_s(O)$  is the value of the feature  $x_s$  in the object  $O$ ; 0 means that the values are coincident and 1 means that the values are different; “?” denote missing data. This is a Boolean comparison criterion.

$$2. C_s(x_s(O_i), x_s(O_j)) = \begin{cases} 0 & \text{if } x_s(O_i) = ? \vee x_s(O_j) = ? \\ 1 & \text{if } x_s(O_i), x_s(O_j) \in A_{s1} \\ 2 & \text{if } x_s(O_i), x_s(O_j) \in A_{s2} \\ \vdots & \\ k-1 & \text{if } x_s(O_i), x_s(O_j) \in A_{sk-1} \end{cases}$$

where  $A_{s1} \cup \dots \cup A_{sk-1} = D_s$ . This is a  $k$ -value comparison criterion.

$$3. C_s(x_s(O_i), x_s(O_j)) = |x_s(O_i) - x_s(O_j)| \text{ this is a comparison criterion that takes real values.}$$

In this way, it is not fixed a unique comparison criterion for all problems to solve, but fairly we give the liberty of using the comparison criterion, which more reflects the manner that the objects are compare in the practice. Note that the dissimilarity functions defined by Yang et al. (2003) for quantitative and qualitative features may be used too.

In addition, let  $\Psi : (D_1 \times \dots \times D_n)^2 \rightarrow [0,1]$  be a dissimilarity function. This function allows evaluating the dissimilarity between object descriptions. Thus, this function is given in dependence of comparison criteria.

Let

$$\Psi(O_i, O_j) = \sum_{x_s \in R} C_s(x_s(O_i), x_s(O_j)) / |R| \quad (5)$$

be the dissimilarity between the objects  $O_j$  and  $O_k$ . The value  $\Psi(O_j, O_k)$  satisfies the following three conditions:

1.  $\Psi(O_j, O_k) \in [0,1]$  *for*  $1 \leq j \leq n, 1 \leq k \leq n$
2.  $\Psi(O_j, O_j) = 0$  *for*  $1 \leq j \leq n$
3.  $\Psi(O_j, O_k) = \Psi(O_k, O_j)$  *for*  $1 \leq j \leq n, 1 \leq k \leq n$

Let  $u_{ik}$  the degree of membership of the object  $O_k$  in the cluster  $K_i$ , and let  $R^{c \times n}$  be the set of all real  $c \times n$  matrices. Any fuzzy  $c$ -partition of the data set is represented by a matrix  $U = [u_{ik}] \in R^{c \times n}$ . The fuzzy  $c$ -partition matrix  $U$  is determined from

minimization of the objective function given by  $J_m(U, \vartheta) = \sum_{k=1}^n \sum_{i=1}^c u_{ik} \Psi(O_k, O_i^*)$  where  $\vartheta$  is a set of representative objects, one for each  $K_i$ , and  $\Psi(O_k, O_i^*)$  is the dissimilarity between the object  $O_k$  and the representative object  $O_i^*$  of  $K_i$ . In the case of classical fuzzy c-means  $\vartheta$  are the centers for the clusters and  $\Psi$  is the Euclidean distance.

Since in our algorithm the objects descriptions are not only in terms of quantitative features the mean cannot be computed. Then instead of use a center (or centroid) for a cluster we will use an object in the sample as representative for this cluster. In order to determine a *representative object*  $O_i^*$  for the cluster  $K_i$ ,  $i=1,\dots,c$  we proceed as follows:

We consider the crisp subset  $K'_i$  of objects that have their maximum degree of membership in this cluster  $K_i$ . Then the representative object of cluster  $K_i$  is determined as the object  $O_i^*$  that satisfies

$$O_i^* = \min_{q \in K'_i} \left\{ \sum_{k=1}^r u_{ik} \Psi(O_k, O_q) \right\} \quad (6)$$

The object  $O_i^*$  may be not unique, then we take the first object found.

Note that our algorithm considers as representative object one object of the sample instead of one fictitious element as occurs in the MVFCM algorithm.

In order to determine the degree of membership of the object  $O_k$  to the cluster  $K_i$ , we define for each object  $O_k$  the sets  $I_k = \{i / 1 \leq i \leq c; \Psi(O_k, O_i^*) = 0\}$ . This set contains the indexes of the clusters such that the dissimilarity between the object to classify  $O_k$  and the representative objects  $O_i^*$ ,  $i=1,\dots,c$ , is zero. And  $\bar{I}_k = \{1,2,\dots,c\} - I_k$  in this set are those indexes of the clusters such that the dissimilarity between  $O_k$  and  $O_i^*$ ,  $i=1,\dots,c$ , is greater than zero.

Thus, the degree of membership of  $O_k$  to  $K_i$  is computed via (7a) or (7b).

$$I_k = \emptyset \Rightarrow u_{ik} = \frac{1}{\sum_{j=1}^c \left( \frac{\Psi(O_k, O_j^*)}{\Psi(O_k, O_i^*)} \right)^2} \quad (7a)$$

We can see that the degree of membership  $u_{ik}$  increases if simultaneously the dissimilarity between  $O_k$  and  $O_i^*$  for  $K_i$  decreases and the dissimilarity between  $O_k$  and  $O_j^*$  for  $K_j$ ,  $j=1,\dots,c$ , increases (and vice versa).

$$I_k \neq \emptyset \Rightarrow u_{ik} = 0 \quad \forall i \in \bar{I}_k \text{ and } \sum_{i \in I_k} u_{ik} = 1 \quad (7b)$$

The equation (7b) is the alternative form for  $O_k$  when  $\exists i \in I_k$  so that  $\Psi(O_k, O_i^*) = 0$ .

The membership of  $O_k$  to the clusters  $K_i$  ( $i \in I_k$ ) will be  $\frac{1}{|I_k|}$ , i.e., the degree of membership is distributed among the clusters  $K_i$ ,  $i \in I_k$ . In addition, for the clusters  $i \in \bar{I}_k$  we assign zero as degree of membership.

#### *FCMD Algorithm*

Step 1. Fix  $c$ ,  $2 \leq c \leq n$ .  $I = 0$

Step 2. Select  $c$  objects in the data as representative objects,  $\vartheta^{(l)}$ .

Step 3. Calculate the  $c$ -partition  $U^{(l)}$  using (7a) and (7b).

Step 4. Determine the representative objects for each fuzzy cluster using (6),  $\mathcal{S}^{(l+1)}$ .

Step 5. If  $\mathcal{S}^{(l)} = \mathcal{S}^{(l+1)}$  then STOP

Otherwise  $l=l+1$  and go to step 3.

An important point to highlight is that this algorithm has the flexibility that uses a dissimilarity function, which is defined in terms of comparison criteria. The comparison criteria allow expressing the way in which features values are compared depending of the problem context to solve.

This algorithm, unlike the MVFCM algorithm, evaluates a unique “cluster center” called the *representative object*, which is an object of the sample instead of one fictitious element as occurs in the MVFCM algorithm. It is more reasonable consider an object of the data set to classify as representative object instead of using an element that cannot be represented in the same space of the objects.

## 4 Analysis

In this section, the  $c$ -partitions generated by both algorithms are analyzed. The analysis is based on the manner to calculate the membership degrees and the way to calculate the cluster centers (representative objects).

In order to make the analysis, the data set shown in Table 1 was used. There are 10 brands of automobiles from four companies: Ford, Toyota, China-Motor and Yulon-Motor in Taiwan. In each brand, there are six feature components –company, exhaust, price, color, comfort and safety. In the color feature, the notations W=white, S=silver, D=dark, R=red, B=blue, G=green, P=purple, Gr=grey and Go=golden are used. The features: company, exhaust and color are symbolic, the feature price is real data and the features comfort and safety are fuzzy. The obtained results are shown in Table 2.

In this experimentation for FCMD  $\Psi$  was used as dissimilarity function and as comparison criteria the functions  $d(A_k, B_k)$  defined by Yang for quantitative and qualitative features were used. In other words, the same criteria for features were used in both algorithms.

The results shown in table 2 for MVFCM were taken from Yang et al. (2003).

**Table 1.** Data set of automobiles

No.	Brands	Company	Exhaust (L)	Price (NT\$10000)	Color	Comfort	Safetiness
1	Virage	China-Motor	1.8	63.9	W,S,D,R,B	[10,0,2,2]	[9,0,3,3]
2	New Lancer	China-Motor	1.8	51.9	W,S,D,R,G	[6,0,2,2]	[6,0,3,3]
3	Galant	China-Motor	2.0	71.8	W,S,R,G,P,Gr	[12,4,2,0]	[15,5,3,0]
4	Tierra Activa	Ford	1.6	46.9	W,S,D,R,G,Go	[6,0,2,2]	[6,0,3,3]
5	M2000	Ford	2.0	64.6	W,S,D,G,Go	[8,0,2,2]	[9,0,3,3]
6	Tercel	Toyota	1.5	45.8	W,S,R,G	[4,4,0,2]	[6,0,3,3]
7	Corolla	Toyota	1.8	74.3	W,S,D,R,G	[12,4,2,0]	[12,0,3,3]
8	Premio G2.0	Toyota	2.0	72.9	W,S,D,G	[10,0,2,2]	[15,5,3,0]
9	Cerfiro	Yulon-Motor	2.0	69.9	W,S,D	[8,0,2,2]	[12,0,3,3]
10	March	Yulon-Motor	1.3	39.9	W,R,G,P	[4,4,0,2]	[3,5,0,3]

As the dissimilarities matrices are symmetric then triangular matrices are shown in a unique matrix in the Table 3, where a) is calculated using the expression (1) and b) is calculated using the expression (5). The values in b) are values of  $\Psi$  normalized in [0,1].

**Table 2.** Clusters obtained with MVFCM and FCMD for mixed data.

Data	MVFCM		FCMD	
	$\mu_{1j}$	$\mu_{2j}$	$\mu_{1j}$	$\mu_{2j}$
1	<b>0.9633</b>	0.0367	<b>0.9215</b>	0.0785
2	<b>0.9633</b>	0.0367	0.0000	<b>1.0000</b>
3	<b>0.9951</b>	0.0049	<b>0.9959</b>	0.0041
4	0.0966	<b>0.9034</b>	0.0020	<b>0.9980</b>
5	<b>0.9951</b>	0.0049	<b>0.9561</b>	0.0439
6	0.0135	<b>0.9865</b>	0.0047	<b>0.9953</b>
7	<b>0.9633</b>	0.0367	<b>0.9959</b>	0.0041
8	<b>0.9951</b>	0.0049	<b>0.9978</b>	0.0022
9	<b>0.9951</b>	0.0049	<b>1.0000</b>	0.0000
10	0.0185	<b>0.9815</b>	0.0258	<b>0.9742</b>

**Table 3.** Dissimilarities matrices.

a)	0.0	0.0213	0.0132	0.0397	0.0006	0.0471	0.0156	0.0148	0.0062	0.0820
	676.1	0.0	0.0646	0.0031	0.0220	0.0055	0.0725	0.0677	0.0460	0.0205
	420.8	2046.0	0.0	0.0929	0.0133	0.1025	0.0023	0.0009	0.0041	0.1517
	1257.2	101.1	2943.3	0.0	0.0412	0.0009	0.1039	0.0974	0.0719	0.0085
	19.3	698.3	423.5	1305.5	0.0	0.0480	0.0152	0.0138	0.0047	0.0839
	1492.9	175.1	3248.4	31.0	1520.5	0.0	0.1142	0.1073	0.0801	0.0059
	494.7	2297.0	73.0	3293.1	482.5	3619.2	0.0	0.0025	0.0046	0.1666
	471.1	2145.9	31.2	3086.2	438.3	3400.0	79.7	0.0	0.0031	0.1582
	197.4	1457.4	131.8	2277.8	149.6	2538.1	147.8	99.8	0.0	0.1259
	2596.7	649.5	4807.1	269.3	2657.6	187.2	5277.9	5011.9	3987.4	0.0

b)

The fuzzy c-means algorithm has as main characteristic that builds clusters where objects with low dissimilarity obtain high membership degree into the same cluster while objects that are relatively distinct obtain high membership degree into different clusters.

The object 2 obtains high membership degree into the cluster 1, but it has low dissimilarity with objects having high membership degree to the cluster 2 (see Table 3), i.e. the description of the object 2 is more similar with the description of the objects 4, 6 and 10 (see Table 2). Therefore, the object 2 should have high membership degree to the cluster 2. So the MVFCM algorithm does not build clusters with the characteristic above mentioned. The membership degrees for MVFCM are calculated using the expression (2). This expression is in function of the dissimilarity between the object to be classified and the cluster centers. In the example, the object 2 obtains high membership to the cluster 1 because it is less dissimilar with the center of cluster 1 than the center of the cluster 2. So that the cluster centers play a determinant role in these dissimilarity values; therefore the obtained c-partitions depend of these centers.

The FCMD, unlike the MVFCM, builds clusters, which satisfy the characteristic above mentioned. So the object 2 obtains high membership degree to the cluster 2. The membership degrees for FCMD are evaluated using the expression (7a) and (7b). These expressions also are in function of the dissimilarity between the object to be classified and the representative objects. But in this case, the representative objects are objects in the sample. So, if two objects are low dissimilar with the representative object, then they must be low dissimilar between them. In this example, the object 2 is just the representative object of the cluster 2.

In addition, the objects 1, 2 and 7 obtain the same membership degree to the cluster 1, and then according to the fuzzy c-means algorithm classification strategy, the

descriptions of these objects must be similar or equal. However, the dissimilarities between the objects 1, 2 and 7 are very different; the dissimilarity between 1 and 2 is 676.1, the dissimilarity between 2 and 7 is 2297.0 and the dissimilarity between 1 and 7 is 494.7 (see Table 3). This shows that, the manner in which the cluster centers are calculated in the MVFCM algorithm determines that objects having low dissimilarity with the cluster center can be very dissimilar among them. In the case of FCMD algorithm, the object 2 has a high membership degree to the cluster 2 and the objects 1 and 7 both have different membership degree to the cluster 1 (see Table 2).

When objects have the same membership degree to a cluster for FCMD algorithm, for example, objects 3 and 7 in the cluster 1; the dissimilarity between them is 73.0357, very low (see Table 3). Again this situation occurs because the representative object is an object in the sample.

## 5 Conclusions

The FCMD algorithm allows using comparison criteria defined by the specialist according to the specific context of a practical problem. In addition, this algorithm evaluates “cluster centers” called representative objects, which are objects in the sample instead of a fictitious element as occurs in the MVFCM algorithm. Also, as we can observe in the definition of comparison criteria, the symbol “?” was introduced to denote missing data, then the FCMD algorithm allows working with databases that contain incomplete descriptions of objects.

We can observe that the MVFCM algorithm builds clusters containing objects which have high membership degree to a cluster but with low dissimilarity with objects belonging with high membership degree to other clusters. On the other hand, the FCMD algorithm builds clusters where the objects with high membership degree to a cluster have low dissimilarity among them.

Based on the analysis made we can say that the FCMD algorithm is a more flexible alternative in the solution of fuzzy unsupervised classification problems where mixed and missing data appear.

**Acknowledgement.** This work was financially supported by CONACyT (Mexico) through project J38707-A.

## References

1. Schalkoff R. J. (1992): Pattern Recognition: Statistical, Structural and Neural approaches, John Wiley & Sons, Inc. USA.
2. Yang M. S., Hwang P. Y. and Chen D. H. (2003): Fuzzy Clustering algorithms for mixed feature variables, *Fuzzy Sets and Systems*, in Press.
3. Ayaquica M. I. and Martínez T. J. F. (2001): Fuzzy c-means algorithm to analyze mixed data. VI Iberamerican Symp. on Pattern Recognition. Florianopolis, Brazil. pp. 27-33.
4. Ayaquica M. I. (2002): Fuzzy c-means algorithm using dissimilarity functions. Thesis to obtain the Master Degree. Center for Computing Research, IPN, Mexico. In Spanish.
5. Gowda K. C. and Diday E. (1991): Symbolic clustering using a new dissimilarity measure, *Pattern Recognition* 24 (6) pp. 567-578.

# Extended Star Clustering Algorithm

Reynaldo J. Gil-García<sup>1</sup>, José M. Badía-Contelles<sup>2</sup>, and Aurora Pons-Porrata<sup>1</sup>

<sup>1</sup> Universidad de Oriente, Santiago de Cuba, Cuba

{gil,aurora}@app.uo.edu.cu

<sup>2</sup> Universitat Jaume I, Castellón, Spain

badia@icc.uji.es

**Abstract.** In this paper we propose the extended star clustering algorithm and compare it with the original star clustering algorithm. We introduce a new concept of star and as a consequence, we obtain different star-shaped clusters. The evaluation experiments on TREC data, show that the proposed algorithm outperforms the original algorithm. Our algorithm is independent of the data order and obtains a smaller number of clusters.

## 1 Introduction

Clustering algorithms are widely used for document classification, clustering of genes and proteins with similar functions, event detection and tracking on a stream of news, image segmentation and so on. For a good overview see [1,2]. Given a collection of  $n$  objects characterized by  $m$  features, clustering algorithms try to construct partitions or covers of this collection. The similarity among the objects in the same cluster should be maximum, whereas the similarity among objects in different clusters should be minimum.

One of the most important problems in recent years is the enormous increase in the amount of unorganized data. Consider, for example, the web or the flow of news in newspapers. We need methods for organizing information in order to highlight the topic content of a collection, detect new topics and track them. The star clustering algorithm [3] was proposed for these tasks and three scalable extensions of this algorithm are presented in [4]. The star method outperforms existing clustering algorithms such as single link [5], average link [6] and k-means [7] in the organizing information task as it can be seen in [3]. However, the clusters obtained by this algorithm depend on the data order and it could obtain “illogical” clusters.

In this paper we propose a new clustering method that solves some of its drawbacks. We define a new concept of star and as a consequence, we obtain different star-shaped clusters. Both algorithms were compared using TREC data and the experiments show that our algorithm outperforms the original star clustering algorithm.

The rest of the paper is organized as follows. Section 2 describes the star clustering algorithm and shows its drawbacks. Section 3 describes the proposed algorithm and the experimental results are shown in Section 4. Finally, conclusions are presented in Section 5.

## 2 Star Clustering Algorithm

The star algorithm is different to the Scatter-Gather [8] and Charikar algorithm [9], because it does not impose a fixed number of clusters as a constraint on the solution. Besides, it guarantees a lower bound on the similarity between the objects in each cluster if the space of representation has metric properties. The clusters created by the algorithm can be overlapped. This is a desirable feature in the organization information problems, since documents can have multiple topics.

Two objects are  $\beta_0$ -similar if their similarity is greater or equal to  $\beta_0$ , where  $\beta_0$  is a user-defined parameter. We call  $\beta_0$ -similarity graph the undirected graph whose vertices are the objects to cluster and there is an edge from vertex  $o_i$  to vertex  $o_j$ , if  $o_j$  is  $\beta_0$ -similar to  $o_i$ . Finding the minimum vertex cover of a graph is a NP complete problem. This algorithm is based on a greedy cover of the  $\beta_0$ -similarity graph by star-shaped subgraphs. A star-shaped subgraph of  $l + 1$  vertices consists of a single *star* and  $l$  *satellite vertices*, where there exist edges between the star and each of the satellite vertices. The stars are the objects with highest connectivity. The isolated objects in the  $\beta_0$ -similarity graph are also stars. The algorithm guarantees a pairwise similarity of at least  $\beta_0$  between the star and each of the satellite vertices, but such similarity is not guaranteed between satellite vertices. Another characteristic of this algorithm is that two stars are never adjacent.

The star algorithm stores the neighbors of each object in the  $\beta_0$ -similarity graph. Each object is marked as star or as satellite. The main steps of the algorithm are shown in Algorithm 1.

---

**Algorithm 1** Star clustering algorithm.

---

```

Calculate all similarities between each pair of objects to
construct the  $\beta_0$ -similarity graph
Let  $N(o)$  be the neighbors of each object  $o$  in the  $\beta_0$ -similarity
graph
Let each object  $o$  initially be unmarked
Sort the objects by degree  $|N(o)|$ 
While an unmarked object exists:
    Take the highest degree unmarked object  $o$ 
    Mark  $o$  as star
    For  $o'$  in  $N(o)$ :
        Mark  $o'$  as satellite
    For each object  $o$  marked as star:
        Add a new cluster  $\{o\} \cup N(o)$ 

```

---

The complexity time of the algorithm is  $O(n^2m)$ , since it must calculate the similarities between all objects, each with  $m$  features.

The star clustering algorithm has some drawbacks. First, the obtained clusters depend on the order of the objects. If two or more neighbor objects with the same degree exist, only the first of them in the arrangement is a star. This problem is illustrated with the help of Figure 1, where the dark circles are the obtained stars and the clusters are outlined. In the figure on the left, the star algorithm takes first the object B, thus B is star and A, C are satellites. However, if object A (or C) is the first in the arrangement, the algorithm obtains the clusters shown in the figure on the right. As we can see, the obtained clusters are different.

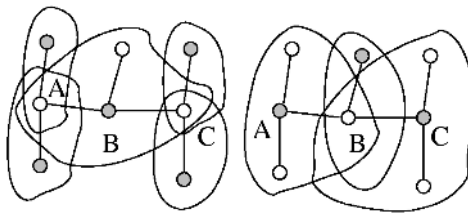


**Fig. 1.** Dependency of the data order.

The second main drawback of the star algorithm is that it can produce illogical clusters. Since two stars are never neighbors, the illogical clusters could be obtained. Figure 2 shows this problem. Object B should be a star and its neighbors with less degree should not be stars.

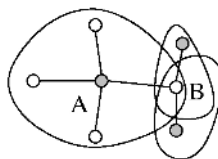


**Fig. 2.** Illogical clusters.

### 3 Extended Star Clustering Algorithm

In our algorithm we make two main changes with respect to the star clustering algorithm mentioned above. The complement degree of an object  $o$  is the degree of  $o$  taking into account its neighbors not included yet in any cluster, namely:

$$CD(o) = |N(o) \setminus Clu|$$

where  $Clu$  is the set of objects already clustered. As we can see, the complement degree of an object decreases during the clustering process as more objects are included in clusters.

Besides, an object  $o$  is considered a star if it has at least a neighbor  $o'$  with less or equal degree than  $o$  that satisfies one of the following conditions:

- $o'$  has not a star neighbor.
- The highest degree of the stars that are neighbors of  $o'$  is not greater than the degree of  $o$ .

It is worth mentioning that these conditions are necessary but not sufficient. That is, some objects that satisfy the previous conditions could not be selected as stars by the algorithm.

The main steps of our algorithm are shown in Algorithm 2.

### **Algorithm 2** Extended star clustering algorithm.

```

Calculate all similarities between each pair of objects to
construct the  $\beta_0$ -similarity graph
Let  $N(o)$  be the neighbors of each object  $o$  in the  $\beta_0$ -similarity
graph
For each isolated object  $o$  ( $|N(o)| = 0$ ):
    Create the singleton cluster  $\{o\}$ 
Let  $L$  be the set of non-isolated objects
Calculate the complement degree of each object in  $L$ 
While a non-clustered object exists: (*)
    Let  $M_0$  be the subset of objects of  $L$  with maximum
    complement degree
    Let  $M$  be the subset of objects of  $M_0$  with maximum degree
    For each object  $o$  in  $M$ :
        If  $o$  satisfies the condition to be a star, then
            If  $\{o\} \cup N(o)$  does not exist:
                Create a cluster  $\{o\} \cup N(o)$ 
        Delete the processed objects from  $L$  (**)
    Update the complement degree of the objects in  $L$ 

```

---

In the step (\*\*) we can delete from  $L$  the objects in  $M$  or all the objects already clustered. We named these variations the unrestricted and restricted versions of the algorithm. In the restricted version, only the objects not yet clustered, can be star. Each version has advantages and disadvantages. The unrestricted version has more possibilities to find the best stars. The restricted version is faster but can obtain illogical clusters.

The complexity time of the algorithm is  $O(n^2m)$  and is determined by its first step: the calculation of the similarities between objects. The complexity of the cycle (\*) is  $O(n^2)$ . In the worst case, this cycle is repeated  $\log_2 n$  times. The most expensive step in it, is the update of the complement degree of the objects, which is  $O(\frac{n^2}{\log_2 n})$  if we have a table containing the differences between all combination of blocks of bits with a size  $\log_2 n$ . This table is not needed if

$\log_2 n$  is less than or equal to the word of the computer processor, because in this case the difference operation between blocks of bits is  $O(1)$ .

The proposed algorithm creates overlapped clusters and guarantees a pairwise similarity  $\beta_0$  between the star and its neighbors. Unlike the original star clustering algorithm, the obtained clusters are independent of the data order. If two or more objects with the highest connectivity exist, our algorithm select as stars all of them. Besides, the selection of stars using the complement degree allows to cover quickly the data and it reduces the overlapping among the clusters.

The extended star clustering algorithm solves the problems of the original star clustering algorithm cited on section 2. An object is considered a star even if it has a star neighbor. Moreover, the second condition in the new star concept guarantees that if an object is a neighbor of two possible stars, both will be stars. Thus, it is independent of the order of objects.

Figure 3a) shows the stars obtained by our algorithm in the same case that in Figure 1.

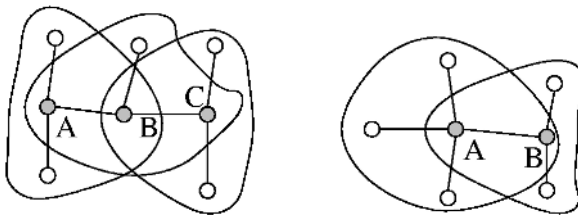


**Fig. 3.** Solutions: a) Order problem. b) Illogical clusters.

The unrestricted version of our algorithm does not form illogical clusters because it allows neighbor stars. Figure 3b) shows the stars obtained in the same case that in Figure 2 for the unrestricted version.

## 4 Experimental Results

In order to evaluate the performance of our algorithm, we compared it with the original star clustering algorithm. We used data (in Spanish) from the TREC-4 and TREC-5 conferences as our testing medium [11]. The TREC-4 collection contains a set of “El Norte” newspaper articles in 1994. This collection has 5828 articles classified in 50 topics. The TREC-5 consists of articles from AFP agency in 1994-1996 years, classified in 25 topics. We have only the data from 1994, for a total of 695 classified articles.

The documents are represented using the traditional vectorial model. The terms of documents represent the lemmas of the words appearing in the texts. Stop words, such as articles, prepositions and adverbs are disregarded from the

document vectors. Terms are statistically weighted using the normalized term frequency (TF). Moreover, we use the traditional cosine measure to compare the documents.

To evaluate the quality of our algorithm, we partitioned the “El Norte” collection in five sub-collections. Each sub-collection is composed of articles related to 10 distinct topics. So, if we add the AFP collection we have a total of 6 collections. The general characteristics of these collections are summarized in Table 1.

**Table 1.** Description of collections

Collection	# of documents	Topics	Collection	# of documents	Topics
eln-1	1534	SP1-SP10	eln-4	811	SP31-SP40
eln-2	1715	SP11-SP20	eln-5	829	SP41-SP50
eln-3	1732	SP21-SP30	afp	695	SP51-SP75

To evaluate the clustering results, we use the F1-measure [12]. This measure compares the system-generated clusters with the manually labeled topics. It is widely applied in Information Retrieval Systems, and it combines the precision and recall factors. The F1-measure of the cluster number  $j$  with respect to the topic number  $i$  can be evaluated as follows:

$$F1(i, j) = 2 \frac{n_{ij}}{n_i + n_j}$$

where  $n_{ij}$  is the number of common members in the topic  $i$  and the cluster  $j$ ,  $n_i$  is the cardinality of the topic  $i$ , and  $n_j$  is the cardinality of the cluster  $j$ .

To define a global measure, first each topic must be mapped to the cluster that produces the maximum F1-measure:

$$\sigma(i) = \max_j \{F1(i, j)\}$$

Hence, the overall F1-measure is calculated as follows:

$$F1 = \frac{1}{S} \sum_{i=1}^N n_i F1(i, \sigma(i)), \quad S = \sum_{i=1}^N n_i$$

where  $N$  is the number of topics.

In our experiments we compare the original star clustering algorithms with the unrestricted and restricted versions of the proposed algorithm. Table 2 shows the best F1-measure obtained by the algorithms for optimized values of  $\beta_0$  in the 6 collections. As we can see, both versions of our algorithm outperform the original star algorithm in all of these collections except in eln-5. Besides, in most collections our algorithm obtain less clusters than the original star algorithm.

This is another important result, because our algorithm achieves a greater precision.

If we compare the results obtained by the original star algorithm with the restricted version of our algorithm, we can see the effect of using the complement degree and the new star concept. The restricted version always has better or equal F1 values with smaller quantity of clusters. The unrestricted version outperforms the restricted one in three cases whereas it has smaller performance in one case. We can expect that the unrestricted version has the best performance in most cases, hence if the main goal is to obtain the best clusters, we recommend the unrestricted version of the algorithm. On the other hand, if we want to reduce the number of clusters or the execution time, we should use the restricted version of the algorithm.

**Table 2.** Experimental results

Algorithm	Original Star		Extended Star (restricted)		Extended Star (unrestricted)	
Collection	F1	# of clusters	F1	# of clusters	F1	# of clusters
afp	0.76	136	0.77	99	0.78	105
eln-1	0.61	139	0.63	59	0.63	81
eln-2	0.66	62	0.67	59	0.72	61
eln-3	0.53	109	0.53	52	0.59	67
eln-4	0.55	62	0.58	68	0.58	43
eln-5	0.74	57	0.74	48	0.72	59

## 5 Conclusions

In this paper we presented a new clustering algorithm, named the extended star clustering algorithm. We use the complement degree of an object and we define a new concept of star. As a consequence, we obtain different star-shaped clusters. Our algorithm solves the problems of dependency of data order and illogical clusters of the original star algorithm.

We compare the proposed algorithm with the original star algorithm in several collections of TREC data. Our algorithm obtains a better performance in these collections and produces less clusters.

The new algorithm can be used in tasks such as information organization, browsing, topic tracking and new topic detection. Besides, our algorithm can be useful in other areas of Pattern Recognition.

As a future work we will construct a parallel version of our algorithm to process very large data sets.

## References

1. Jain, A.K.; Murty, M.N. and Flynn, P.J.: Data Clustering: A Review. *ACM Computing Surveys*, Vol. 31, No. 3, September 1999.

2. Berkhin, P.: Survey of Clustering Data Mining Techniques, Technical Report, Accruve Software, 2002.
3. Aslam, J.; Pelekhop, K. and Rus, D.: Static and Dynamic Information Organization with Star Clusters. In *Proceedings of the 1998 Conference on Information Knowledge Management*, Baltimore, MD, 1998.
4. Aslam, J.; Pelekhop, K. and Rus, D.: Scalable Information Organization. In *Proceedings of RIAO*, 2000.
5. Croft, W. B.: Clustering large files of documents using the single-link method. *Journal of the American Society for Information Science*, pp. 189-195, November 1977.
6. Voorhees, E. M.: Implementing agglomerative hierarchical clustering algorithms for use in document retrieval. *Information Processing and Management*, 22:465—476, 1986.
7. Mc Queen, J.: Some methods for classification and analysis of multivariate observations. In *Proceedings of the Fifth Berkeley Symposium on Mathematical Statistics and Probability*, pp. 281–297, 1967.
8. Cutting, D.; Karger, D. and Pedersen, J.: Constant interaction-time Scatter/Gather browsing of very large document collections. In *Proceedings of the 16th SIGIR*, 1993.
9. Charikar, M.; Chekuri, C.; Feder, T. and Motwani, R.: Incremental clustering and dynamic information retrieval. In *Proceedings of the 29th Symposium on Theory of Computing*, 1997.
10. Cormer, T. H.; Leiserson, C. E.; Rivest, R. L. Introduction to Algorithms. McGraw-Hill, 1993.
11. <http://trec.nist.gov>
12. Larsen, B. and Aone, C.: Fast and Effective Text Mining Using Linear-time Document Clustering. In *KDD'99*, San Diego, California, pp. 16–22, 1999.

# Two New Metrics for Feature Selection in Pattern Recognition

Pedro Piñero<sup>1</sup>, Leticia Arco<sup>2</sup>, María M. García<sup>2</sup>, Yaile Caballero<sup>3</sup>,  
Raykenler Yzquierdo<sup>1</sup>, and Alfredo Morales<sup>1</sup>

<sup>1</sup>Bioinformatic Laboratory, University of the Informatics Sciences. La Habana, Cuba  
{ppp, ryzquierdo, amoraleso}@uci.cu

<sup>2</sup>Artificial Intelligence Laboratory, Central University of Las Villas. Santa Clara, Cuba.  
{leticiaaa, mmgarcia}@uclv.edu.cu

<sup>3</sup>Informatics Department, University of Camagüey. Camagüey, Cuba  
yaile@reduc.cmw.edu.cu

**Abstract.** The purpose of this paper is to discuss about feature selection methods. We present two common feature selection approaches: statistical methods and artificial intelligence approach. Statistical methods are exposed as antecedents of classification methods with specific techniques for choice of variables because we pretend to try the feature selection techniques in classification problems. We show the artificial intelligence approaches from different points of view. We also present the use of the information theory to build decision trees. Instead of using Quinlan's Gain we discuss others alternatives to build decision trees. We introduce two new feature selection measures: MLRelevance formula and the PRelevance. These criteria maximize the heterogeneity among elements that belong to different classes and the homogeneity among elements that belong to the same class. Finally, we compare different feature selection methods by means of the classification of two medical data sets.

## 1 Introduction

The Pattern Recognition is an interdisciplinary science, having strong connections with Mathematics, Engineering and Computer Sciences. The following problems can be solved by means of the pattern recognition techniques:

- search of effective object descriptions and
- classification problems.

In classification problems, the studied objects are described in terms of a set of features. Each feature ( $x_i$ ) has a set ( $M_i$ ) of acceptable values and a comparison criterion ( $\delta_i$ ) associated to it. Suppose that a given training sample, in a framework of a supervised classification problem, has a (training) matrix representation  $I_0(C_1, C_2, \dots, C_r)$ , that is, object descriptions ( $O_1, O_2, \dots, O_p$ ) are stored in a matrix with as many columns as features, as many rows as objects in the sample, and they are split in groups corresponding with their respective classes ( $C_1, C_2, \dots, C_r$ ). Likewise the succession  $I(O'_1, O'_2, \dots, O'_q)$  of standard descriptions of the objects ( $O'_1, O'_2, \dots,$ ,

$O'_q)$  such that  $O'_j \notin I_0(C_1, C_2, \dots, C_r)$  with  $1 < j < q$  is called control matrix. Usually the feature selection problem appear in the classification problems and in problems of search of effective object descriptions, as a necessary step to reduce the dimensions of the initial space of representation of objects and simplify the classification process complexity. The problem of the selection of features for the classification consists on finding an algorithm  $\zeta$  such that:

$$\text{First: } \zeta(K(x_1(O), x_2(O), \dots, x_n(O))) = K(x_{i_1}(O), x_{i_2}(O), \dots, x_{i_p}(O))$$

$\forall O \in I_0(C_1, C_2, \dots, C_r)$  where  $K$  is a classification criterion It means that the algorithm  $\zeta$  reduces the dimensions of the space without affecting the belonging of each object to its respective class. In other words, using the  $\zeta$  algorithm the belonging  $r$ -plus of the initial training matrix remains constant although the dimensions of the space are smaller than the initial dimensions.

Second: Given a classification algorithm  $A$  and a function  $\Phi$  that measures the quality of it.

$$\Phi[A(I_0(C_1, C_2, \dots, C_r), I(O'_1, O'_2, \dots, O'_q))] \leq \Phi[A(I_0(C_1, C_2, \dots, C_r), \zeta(I(O'_1, O'_2, \dots, O'_q)))]$$

For  $\zeta(I(O'_1, O'_2, \dots, O'_q))$  we denote the projection of the control matrix in a new space. This new space is obtained from applying  $\zeta$  to the initial space. Theoretically having more features should give us more discriminating power. However the real world provides us with many reasons why this is not generally the case [1] :

- First: the induction algorithm complexity grows dramatically with the number of features.
- Second: the irrelevant and redundant features also cause problems in the classification context as they may confuse the learning algorithm by helping to obscure the distributions of the small set of truly relevant features for the task at hand.

The analysis of the techniques and traditional criteria for feature selection will be exposed with details in other sections of this paper. The second section shows the most popular statistic and artificial intelligence techniques used to solve the feature selection problems. In the third section, we'll introduce two new criteria related with the relevance or the irrelevance of features, which are valid for any feature selection technique. Finally, we'll show comparison results of algorithms that use different criteria of feature selection.

## 2 Statistical, Artificial Intelligence and Logical Combinatorial Pattern Recognition Techniques for Feature Variable Selection

### 2.1 Statistic Techniques for Feature Variable Selection

The feature selection appears in the classical statistics, in relation with all the techniques of the multivariate analysis, from the most elementary techniques: the analysis of variance (ANOVA) and the regression. In fact, in the multiple lineal

regression theory some new feature selection procedures appear, influencing the ulterior development of the multivariate statistic. We talk about the step-to-step methods as a way to get the better equation of regression among all the possible, keeping in mind the correlation among variables. The procedures "step-to-step" are easily extended to the classification statistical techniques: the discrimination analysis, the logistic regression, the decision trees, etc. [2]

There isn't a strong criterion to divide the classification procedures in separate groups. In a way sense, they are always extensions of some statistical techniques such as: the discriminate analysis, the methods based on decision trees (CHAID technique: Chi-square Automatic Interaction Detector), the methods of estimating of densities (KNN:  $k$ -nearest neighbors), or the techniques of hierarchical group formations.

These four procedures (linear discrimination, decision-tree,  $k$ -nearest-neighbors and clustering) are prototypes for four kinds of classification procedures. Not surprisingly they have been refined and extended, but they still represent the major strands in current classification practice and research. Then, it may be a good criterion of classification. However, in [3], the authors preferred create groups of methods around the more traditional heading of classical statistics, modern statistical techniques, Machine Learning and neural networks.

## 2.2 Artificial Intelligence Techniques for Feature Variable Selection

There are a lot of applications of the heuristic search methods to solve the feature variable selection problems [4]. To characterize the feature selection algorithms four issues should be defined in [5].

Other approaches to solve the feature selection problems have as principal idea to apply a weighting function to features. The weighting schemes generally are easier to implement than the others machine learning methods. They are frequently more difficult to understand because usually work as a black box.

Perceptron is a well-known feature weighting method, which adds or eliminates weights on the linear threshold unit in response to errors that occurs during the classification process. Many learning algorithms such as: back-propagation algorithm and least-mean square algorithm have been well studied. The results of Perceptron-weighting techniques can be affected when the number of irrelevant features grows. To decrease the sensibility of the Perceptron algorithm the Winnow algorithm is proposed in [5].

Other approach to solve the problems related to the relevant features in classification problems is the filter methods [6]. This viewpoint divides the feature selection process and the induction process. These methods make a preprocessing of the training data and filter out the irrelevant features before the induction process occurs. The filter methods work independent of the induction methods. They can be used in combination with different induction methods. Besides, the filter methods evaluate each feature based on its correlation with set of classes choosing the suitable number of relevant features. Two of the most well known filter methods for feature selection are RELIEF [7] and FOCUS [8].

Other feature selection methodology, which has recently received much attention, is the wrapper model. This model searches through the space of feature subsets using the estimated accuracy from an induction algorithm as the measure of goodness for a particular feature subset [6]. Actually the wrapper methods are well known in statistic and pattern recognition. The principal notion in the wrapper methods is to determine the feature subset that allows us better estimations than separate measures. The major disadvantage of wrapper methods over filter methods is the high computational cost of them. The wrapper methods similar to the filter methods can be used in combination with different induction methods. In fact the OBLIVION [9] wrapper algorithm combines the wrapper notion with the nearest-neighbor method.

The embedded approaches to determine relevant features are popular methods too. A clearest example of feature selection methods embedded within a basic induction algorithm, are the “methods for inducing logical descriptions”. For these algorithms the space of hypotheses is described by the partial ordering and the algorithms use this ordering to organize their search for concept descriptions. The core of these algorithms is to add or remove features from the concept description in response to prediction errors on new instances. For example, recursive partitions methods for induction, such as Quinlan’s ID3 Quinlan [10], C4.5 [11] and CART [12] carry out a greedy search through the space of decision trees, at each node using an evaluation criterion to choose the feature having the best ability to discriminate among classes.

Information theory is one approach to solve the information uncertainty problems; however, it’s not a tool for manipulating uncertain knowledge. Instead, it’s a tool for measuring uncertainty. In information theory, uncertainty is measured by a quantity called “entropy”. It’s similar to, but not the same as, the concept of entropy in physics [13]. An example of the entropy computation is presented in the selection variable building decision trees. In fact, Quinlan propose the ID3 algorithm to induce classifications rules in form of decision tree [11, 14]. In recent years, Quinlan introduces the algorithms C4.5 [11, 14] and C5.0 [15]. These Quinlan’s algorithms improve the ID3 algorithm because they work with numeric and symbolic data and manipulate cases with missing values.

In the information theory approach many other measures have been proposed, for example, instead of using Quinlan’s Gain, Mántaras [16] propose two-feature selection measures based on a distance between partitions.

### **2.3 Logical Combinatorial Pattern Recognition and Testor Theory in the Feature Variable Selection**

Some problems related to the feature selection can be solved in the context of the testor theory. This is a branch of Mathematical Logic that began in the Soviet Union at the end of the 50’s. I. A. Chegus and S. V. Yablonskii [17] were the first researchers that developed this theory. Their works were motivated by the problem of fault detection in logical schemes, particularly applied to computer logical circuits.

In the middle of the 60’s, Y. I. Zhuravlev adapted the testor concept to pattern recognition [18].

Testor definition (Zhuravlev): If the complete set of features R allows us to distinguish between objects (rows of MI) from different classes, then R is a testor. Furthermore, any non-empty feature subset of R, that satisfies this property, is a testor. Others Testor's concepts, that improve the original Zhuravlev's concept are proposed in [19] [20]

### 3 Two New Alternative Criteria for Feature Variable Selection

In this section we propose two alternative criteria to choose the relevant features in classification problems. Some theoretical results obtained from the analysis of this measure of relevance are presented.

#### 3.1 The MLRelevance Criterion

Suppose a feature (A) with  $i = 1, 2, \dots, k$  acceptable values,  $S$  set of samples and  $S_i$  subset of  $S$  that contains the samples having the value  $i$  in the feature A. Then the expression  $|S_i|/|S|$  is the relative frequency of the value  $i$  in  $S$ .

Then Equation 1 shows a measure that determines the relevance of the feature A.

$$\text{MLRelevance measure} \quad R(A) = \sum_{i=1}^K \frac{|S_i|}{|S|} e^{(1-C_i)} \quad (1)$$

where  $R(A)$  is the relevance measure of the feature A on set  $S$ ,  $k$  is the number of different values for the feature A and  $C_i$  is the number of different classes presented in objects having the value  $i$  for the feature A.

Let us begin by saying some general aspects of our measure:

- its principal idea is to maximize the heterogeneity among elements that belong to different classes and the homogeneity among elements that belong to the same class and,
- $0 \leq R(A) \leq 1$  and  $\sum_{i=1}^K \frac{|S_i|}{|S|} = 1$ . Consequently, the feature that maximizes  $R(A)$  is better.
- The Equation 1 will always be defined for any set  $S$  that is a good property of this equation.

#### 3.2 The PRelevance Criterion

Another criterion is a lineal combination of the MLRelevance criterion and a heuristic. The core of this second metric deals with to determine the relevance of an attribute  $a$  as a lineal combination of the relevance of the isolated attribute " $a$ " and the relevance of the groups of attributes  $B$  such that  $a \in B$ .

### 3.2.1 Preliminary Concepts

The heuristic that we use in the *PRelevance* computation is based on the rough sets theory [21].

Lets the decision system  $W = (U, A \cup D)$ , and the sets  $B \subseteq A$  y  $S \subseteq U$ . We can approximate  $S$  using only the information contained in  $B$  by constructing the *B-lower* and the *B-upper* approximations of  $S$ , denoted  $(B_S)$  and  $(B^*)$  respectively. A rough set is any set  $S$ ,  $S \subseteq U$  defined from its *B-lower* and *B-upper* approximations [22].

We'll define indiscernibility, this is the fundamental notion in the rough sets theory. The objects that are characterized by the same information are indiscernible (similar) in the view of the information that is available.

**Definition 1 Indiscernibility:** To each set of the attribute  $B$  such that  $B \subseteq A$ , is associated an indiscernible binary relation denoted by  $I_B$ . This relation allows us to determine which objects are indiscernible from the others by the relation.  $I_B = \{(x,y) \in U \times U : f(x,a_i) = f(y,a_i) \text{ para todo } a_i \in B\}$ . If  $(x,y) \in I_B$  we said that the objects  $x$  and  $y$  were  $B$ - indiscernible.

The lower approximation of a set  $S$  respect to a set of attributes  $B$  is defined as the collection of objects which equivalences classes are contained completely in the set; whereas the upper approximation is defined as the collection of objects which equivalences classes are partially contained in the set. Formally,

$$B_S(S) = \{x \in U \mid B(x) \subseteq S\} \quad (2)$$

$$B^*(S) = \{x \in U \mid B(x) \cap S \neq \emptyset\} \quad (3)$$

Now, we can define the boundary region on  $S$  as:

$$BN_B(S) = B^*(S) - B_S(S) \quad (4)$$

If the set  $BN_B$  is empty then the set  $S$  is exact respect to the equivalence relation  $B$ . In any other case  $BN_B(X) \neq \emptyset$ , the set  $S$  is inexact, vague, rough; respect to  $B$ . Using the lower and upper approximations of a concept, three regions are defined:

I Positive region:  $POS(X) = B_S(X)$ .

II Boundary region:  $BN_B(X)$ .

III Negative region:  $NEG(X) = U - B^*(X)$

### 3.2.2 Dependences between Attributes

Intuitively, a set of decision attributes  $D$ , depends totally on a set of  $B$  attributes, denoted by  $B \Rightarrow D$ , if all the values of the  $D$  attributes are univocally determined by the values of the attribute in  $B$ .

In other words,  $D$  depends totally on  $B$ , if there is a functional dependency between the values of  $D$  and  $B$  [22].

**Definition 2: Dependency in  $k$  grade.**

It's said that  $D$  depends on  $B$  in a  $k$  grade ( $0 \leq k \leq l$ ), denoted by  $B \Rightarrow_k D$ , by the  $k$  value, and defined by the expression 5.

$$k = \frac{|POS_B(D)|}{|U|} \quad (5)$$

$$\text{Donde } POS_B(D) = \bigcup_{x \in U_D} B_*(X) \quad (6)$$

If  $k=1$  then it's said that D depends totally on B, while if  $k < 1$  it's said that D depends partially on B.

### 3.2.3 PRelevance Computation

From what it's been defined till now, so far the calculus of *PRelevance* with respect to an attribute “*a*” it's defined as *RP(a)* expression:

$$\text{PRelevance } RP(a) = R(a) + H(a) \quad (7)$$

Where *R(a)* is the function of the equation 1 and *H(a)* is calculated as it shown in the algorithm 1. The attribute that maximizes *RP(a)* is the most relevant attribute.

#### *Algorithm 1*

Step1: it is calculated the vector  $R(T) = (R(a_1), R(a_2), R(a_3), \dots, R(a_{r(a)}))$  with  $T \subseteq A$

Step2: It's determined the n best attributes, begin the best those which maximize  $R(a_i)$ . As a result of this step the vector,  $RA = (R(a_i), R(a_j), \dots, R(a_t))$  with  $n = |RA|$ , is obtained.

Step3: The n combinations are determined in p from the attributes selected in the step2. A vector of combinations is obtained:  $\text{Comb} = (\{a_i, a_j, a_k\}, \dots, \{a_i, a_l, a_p\})$

An example of it being,  $n = 4$  and  $p = 3$  and being the selected attributes in the step 2 ( $a_1, a_3, a_5, a_8$ ) the combination vector has

$$C_p^n = \frac{n!}{p!(n-p)!} = 4 \text{ components which would be } \text{Comb} = (\{a_1, a_3, a_5\}, \\ \{a_1, a_3, a_8\}, \{a_3, a_5, a_8\}, \{a_1, a_5, a_8\}).$$

Step 4: We calculated the independency grade of the classes with respect to each of the obtained combinations in the previous step. As a result of this step we obtain the vector of dependencies  $DEP = (k(\text{Comb}_1, d), k(\text{Comb}_2, d), \dots, k(\text{Comb}_r, d))$ .

Step 5: For each attribute “*a*” we calculate the value of *H(a)* following the equation 8:

$$H(a) = \sum_{\forall i / a \in \text{Comb}_i} k(\text{Comb}_i, d) \quad (8)$$

As it can be appreciated in the computation of *PRelevance* for an attribute, is very expensive and depends on ( $|A|$ ), ( $n$ ), ( $p$ ) and ( $|d|$ ). These parameters depend on the real problem that we can to solve. Also, if we want to use the *PRelevance* metric to build decision trees then the expensive procedure is repeated and the cost of our learning increases a lot. In order to reduce the learning duration we propose a *PRelevance*'s implementation using a parallel platform (MPI, PVM)

## 4 Comparisons between Different Feature Selection Methods

In this section we shall compare different feature selection methods using data of two medical domains. We use in our comparisons: the thyroid database provided by the

Garvan Institute of Medical Research, Sydney and the heart database assays from the European Statlog project, Dept. Statistics and Modeling Science, Strathclyde University in 1993. Both medical databases appear in UCI Repository of Machine Learning databases, University of California [23].

We compare the correctness percents of classification among systems C5.0 [15], KNN IB4 implementation [24], MLClassif (VCramer), MLClassif (Mantarás) and MLClassif (MLRelevance). We use the VCramer formula; this is a measure of interrelation between variables [25] [2]. The C5.0 system developed by Ross Quinlan creates a decision tree based on Quinlan's gain. The MLClassif system developed by our team creates partitions by recursive sorting of the training set. To rearrange each partition an appropriate feature is selected. To choose the most relevant feature in each moment we use: Mántaras's distance, the VCramer formula or the MLRelevance measure.

From each database we create randomly ten partition pairs (Table 1), having each partition pair 75% of elements for train and the rest for test. We execute the algorithms in each partition. The values that we show in the table 1 represent the percent of correct classification obtained from each algorithm in the partition.

To compare the algorithms results we applied the Kruskal-Wallis Test for each variable; we used the Monte Carlo method for computing the significance level and considered 99% as confidence interval for the significance.

The superscript letters used in tables 1 and 2 represent different sets. These sets were obtained from to apply the Kruskal-Wallis test. Values having the same superscript belong to the same set. It means that these values have not a significant difference.

To compare two algorithms we used the Mann-Whitney U test for each variable; we used the Monte-Carlo method for computing the significance level and considered 99% as confidence interval.

In thyroid significant differences are found regard train and test variables, however in heart only is found significant differences regards train variable. The Table 2 shows the algorithms grouping.

**Table 1.** Partition 1 experimental results

Partition 1, accuracy results	Thyroids database		Heart database	
	Train	Test	Train	Test
MLClassif (Vcramer)	30.12 <sup>a</sup>	33.38 <sup>a</sup>	89.16 <sup>b</sup>	88.06 <sup>a</sup>
MLClassif (Mantarás)	85.46 <sup>b</sup>	87.45 <sup>b</sup>	92.61 <sup>c</sup>	89.55 <sup>a</sup>
MLClassif (MLRelevance)	96.39 <sup>c</sup>	95.26 <sup>c</sup>	93.1 <sup>c</sup>	88.6 <sup>a</sup>
KNN IB4	87.4 <sup>b</sup>	83.9 <sup>b</sup>	71.8 <sup>a</sup>	88.1 <sup>a</sup>
C5.0	98.3 <sup>c</sup>	95.4 <sup>c</sup>	93.1 <sup>c</sup>	87.7 <sup>a</sup>

**Table 2.** Resulting groups from applying the statistic tests to the classification results

Group	Thyroids (Train and test)	Heart (Train)
1	C5.0 <sup>c</sup> , MLClassif (MLRelevance) <sup>c</sup>	C5.0 <sup>c</sup> , MLClassif (MLRelevance) <sup>c</sup> , MLClassif (Mántaras) <sup>c</sup>
2	KNN MLClassif (Mántaras) <sup>b</sup>	IB4 <sup>b</sup> , MLClassif (VCramer) <sup>b</sup>
3	MLClassif (VCramer) <sup>a</sup>	KNN IB4 <sup>a</sup>

As a conclusion of the above tables: the methods of group1, are better than the methods of group2, likewise the group2 methods are better than the group3 methods and the methods that belong to the same group don't have significant differences.

## 5 Conclusions

The purpose of this paper was to discuss about feature selection methods. We presented there common feature selection approaches: statistical methods, logical combinatorial pattern recognition approach and artificial intelligence approach. For each approach we discussed some methods and algorithms.

Statistical methods are presented as antecedents of the other methods with their specific techniques for choice and transformation variables. In the logical combinatorial pattern recognition we discuss the testor theory and its application to the classification and feature selection problems. Different artificial intelligence techniques are presented and its properties briefly discussed.

We introduce two new relevance criteria the *MLRelevance R(A)* and the *PRelevance RP(A)*.

These feature selection criteria maximizes the heterogeneity among elements that belong to different classes and the homogeneity among elements that belong to the same class. *R(A)* always will be defined for any set S,  $0 \leq R(A) \leq 1$  and is not sensitive to the number of features values. The *RP(A)* computation is very expensive and we propose a PRelevance's implementation using a parallel platform.

Finally we compare different features selection measures by means of two medical databases. We compare the measures: VCramer (statistic measure), C5.0 algorithm (Quinlan's gain), Mántaras and MLRelevance. We conclude: C5.0 and MLRelevance obtain the best results and VCramer obtains the worse results in Thyroid database; while in Heart database, C5.0, MLRelevance and Mántaras obtain the best results and KNN obtains the worse results.

## References

1. Koller, D. and S. Mehran, *Toward Optimal Feature Selection*. 1997, Computer Science Department Stanford University: Stanford.
2. Grau, R., *Estadística aplicada con ayuda de paquetes de software*. 1994, Editorial Universitaria: Jalisco México.
3. Michie D. Spiegelhalter J., T.C.C., *Machine Learning, Neural and Statistical Classification*. 1994: Springer.
4. Bello., R., *Métodos de Solución de Problemas para la Inteligencia Artificial*. 1998, Santa clara: Universidad Central de Las Villas.
5. Blum, A. and P. Langley, *Selection of relevant features and examples in machine learning*. Artificial Intelligence 97, 1997: p. 245–271.
6. John, G., R. Kohavi, and K. Pfleger. *Irrelevant features and the subset selection problems*. in *Proceedings 11th International conferences on Machine Learning*. 1994. New Brunswick, NJ.
7. Kira, K. and L.A. Rendell. *A practical approach to feature selection*. in *Proceedings 9th International Conference on Machine Learning*. 1992. Aberdeen, Scotland.
8. H. Almuallim, T.G.D. *Learning with many irrelevant features*. in *Proceedings of AAAI-92*. 1992: MIT Press.
9. Langley, P. and S. Sage. *Oblivious decision trees and abstract cases*. in *Working Notes of the AAAI-94, Workshop on Case Base Reasoning*. 1994. Seattle.
10. Quinlan, J.R., *Induction of Decision Trees*. Machine Learning, 1986: p. 81–106.
11. Quinlan, J.R., *Improved Use of Continuous Attributes in C4.5*. Research Journal of Artificial Intelligence, 1996. **4**: p. 77–90.
12. Breiman, L.F., J.H. Olshen, R.A. Stone, C.J. *Classification and Regression Trees*. Wadsworth Belmont, CA. 1984.
13. Brender, J. *Measuring quality of medical knowledge*. in *In Proceeding of the Twelfth International Congress of the European Federation for Medical Informatics*. 1994.
14. Quinlan, J., *C4.5: Programs for Machine Learning*. 1993, San Mateo: Morgan Kaufman.
15. Quinlan, J.R., *See5/C5.0*. 2002.,
16. Mántaras, R.L., *A Distance-Based Attribute Selection Measure for Decision Tree Induction*. Machine Learning, 1991.
17. Chegus, I. and S.Yablonskii, *K-Testor*. 1958, Moscow: Trudy Matematicheskava Instituta imeni V. A. Steklova LI. 270–360.
18. Zhuravlev, Y.I. and S.E. Tuliganov, *Measures to Determine the Importance of Objects in Complex Systems*. Vol. 12. 1972, Moscu. 170–184.
19. Aizenberg, N.N. and A.I. Tsipkin, *Prime Tests*. Vol. 4. 1971: Doklady Akademii Nauk. 801–802.
20. Ruiz-Shulcloper, J. and M.L. Cortés, *K-testores primos*. Revista Ciencias Técnicas Físicas y Matemáticas, 1991. 9: p. 17–55.
21. Pawlak, Z., *Rough Sets- Theoretical Aspects of Reasoning about Data*. 1991, Dordrecht: Kluwer Academic.
22. Komorowski, J., et al., *A Rough Set Perspective on Data and Knowledge*, in *The HandBook of DataMining and Knowledge Discovery*, W. Klosgen, Editor. 1999, Oxford University Press.
23. Blake, C.L. and C.J. Merz, *UCI Repository of Machine Learning databases*. 2003, University of California, Department of Information and Computer Science.
24. Aha, D.W., *Case-Based Learning Algorithm*. 1991.
25. Jabson, D., *Applied Multivariate Data Analysis*. Vol. 2 Categorical and Multivariate methods. 1992: Springer.

# Conditions of Generating Descriptive Image Algebras by a Set of Image Processing Operations\*

Igor B. Gurevich and Vera Yashina

Scientific Council "Cybernetics" of the Russian Academy of Sciences  
40, Vavilov str., 119991 Moscow GSP-1, Russian Federation  
[igourevi@ccas.ru](mailto:igourevi@ccas.ru), [werayashina@mail.ru](mailto:werayashina@mail.ru)

**Abstract.** It is outlined new results of investigations into development of mathematical tools for analysis and estimation of information represented by images. It continues research of a new class of image algebras (IA) – the Descriptive Image Algebras (DIA). Practical implementation of DIA in image analysis applications requires a study of a set of operations, leading or not leading to DIA construction, having or not having physical interpretation. Operations of the ring in these algebras are both standard algebraic operations and special operations of image processing and transformation. The problem of operations that can be used for construction of DIA and of how this possibility is connected with physical interpretation of corresponding algebra operations is still open. This problem is reduced to formulation of the conditions that should be satisfied by a set of operations for construction of the DIA. The first stage of its solution is the construction of the examples of the sets of operations (having physical meaning), leading or not leading to DIA construction. The basic results of the report are both the method of testing the specified conditions and the examples of sets with various elements and the operations introduced on them (both generating algebras and not).

## 1 Introduction

The new results of investigations in the field of the development of mathematical apparatus for analysis and evaluation of information represented in the form of images are described in this paper. These studies have been conducted in the recent years at the Scientific Council “Cybernetics”, Russian Academy of Sciences, and they are concerned with development and implementation of the Descriptive Approach to Image Analysis and Recognition [2]. A new class of image algebras (standard IA was described in [4], definition 1) is defined within this framework – Descriptive Image Algebras (DIA [3], definition 2). The main purpose of this investigation is construction of unifying theory that covers different transformations and operations of image analysis, processing and understanding. DIA generalizes some famous

---

\* This work was supported in part by the Russian Foundation for Basic Research (project nos. 01-07-90016 and 02-01-00182) and RAS (project no. 10002-251/P-16/097-025/310303-0 of the Complex Program of Scientific Research of the Presidium of RAS “Mathematical Modeling, Intellectual Systems, and Control of the Nonlinear Mechanical Systems”).

mathematical theory and the algebraic specificity of DIA is defined by the fact that the elements of the ring include both the models of images and the operations on images. This specific of DIA provides the effective synthesis and implementation of the basic procedures of formal image description, processing, analysis, and recognition. So the developed algebraic tools can help to solve many problems related to intellectual computer systems and to automatization of image-based decision making (i.e. design of systems for automated image processing and analysis, design of systems for automation of scientific research, high quality medical and technical diagnostics, ecological monitoring, remote sensing, non-destructive testing, quality control, etc). Useful practical implementation of new algebra is also development of language for comparison and standardization of different algorithms for image analysis, recognition and processing.

The practical implementation of DIA in image analysis applications requires research of the set of operations, leading or not leading to DIA construction, having or not having physical interpretation. Operations of the ring in these algebras can be both standard algebraic operations and special operations of image processing and transformation. The problem of operations that can be used for construction of DIA and of how this possibility is connected with physical interpretation of corresponding algebra operations is still open. Thus, the following problems appear: (a) to define the class of the allowable operations, having physical meaning; (b) to define the class of the allowable operations having no physical meaning; (c) to define the class of the operation (both having physical meaning and not), which do not lead to the construction of algebras. In the whole, this problem is reduced to formulation of the conditions that should be satisfied by a set of operations for DIA construction.

The first stage is the construction of the examples of the sets of operations (having physical meaning), which lead (or not) to DIA construction. The basic results of the paper are (a) 2 examples of the basic DIA having one ring with various elements and operations of a certain physical meaning: in the example 2 the elements of the ring are images; in the example 3 the elements of the ring are binary operation on images; (b) the example 4 where the constructed set of elements with operations introduced over it is an additive group.

The following lines of research dating back to 1970s—80s contributed to the development of DIA: (a) the Algebra of Zhuravlev (Yu.Zhuravlev and his scientific school [6]); (b) the Descriptive Approach for Image Analysis and Understanding (I.Gurevich [2]); (c) the General Pattern Theory developed by U.Grenander [1]; (d) the extended image algebra developed by G.Ritter [4].

## 2 Images and Operations on Images. The Main Conceptions and Definitions

### 2.1 Basic Definitions

*Definition 1:* Algebra over field A is called IA, if the elements of its ring are images (sets of points) and the values and properties associated with these images.

*Definition 2:* Algebra over field A is called DIA, if the elements of its ring are either the models of images (including images themselves and the values and properties associated with these images), or operations on images, or both the models and operations.

*Definition 3:* DIA is called a basic DIA, if its ring consists either of the image models or of the operations on images.

For generality of the results, during construction of examples we use the definition of an image (see *Definition 4*) and the operations on images, introduced by G. Ritter in [4].

*Definition 4:* Let F be a set of values and X be a set of points. An F-valued image on X is any element of  $F^X$  (i.e.,  $a: X \rightarrow F$ ):

$$I = \{(x, a(x)), x \in X, a(x) \in F\}.$$

### 2.2 Operations on Images ([4])

Let  $I_1 = \{(x, a(x)), x \in X\}$ ,  $I_2 = \{(x, b(x)), x \in X\}$  and let the following operations be defined on the set F: operations of addition, multiplication, finding the maximum and inverse operations of difference, division, finding the minimum, and the operation of raising to power ( $\forall a(x), b(x) \in F \exists! a(x)+b(x); \exists! a(x)*b(x); \exists! a(x) \vee b(x); \exists! a(x)-b(x); \exists! a(x) \wedge b(x);$  for  $b(x) \neq 0 \exists! a(x)/b(x);$  for  $a(x) > 0 \exists! a(x)^{b(x)}$ ).

The basic operations on images from  $F^X$  are the pointwise addition, multiplication, and finding the maximum respectively:

- (1)  $I_1 + I_2 = \{(x, c(x)), c(x) = a(x) + b(x), x \in X\};$
- (2)  $I_1 * I_2 = \{(x, c(x)), c(x) = a(x) * b(x), x \in X\};$
- (3)  $I_1 \vee I_2 = \{(x, c(x)), c(x) = a(x) \vee b(x), x \in X\}..$

The operations of difference, division, and finding the minimum are introduced as operations inverse to addition, multiplication, and finding the maximum respectively:

- (4)  $I_1 - I_2 = \{(x, c(x)), c(x) = a(x) - b(x), x \in X\};$
- (5)  $\frac{I_1}{I_2} = \{(x, c(x)), c(x) = \frac{a(x)}{b(x)}, b(x) \neq 0, c(x) = 0, b(x) = 0\};$
- (6)  $I_1 \wedge I_2 = \{(x, c(x)), c(x) = a(x) \wedge b(x), x \in X\}.$

Similarly, we may introduce other operations on images:

$$(7) \quad I_1^{12} = \{(x, c(x)), c(x) = a(x)^{b(x)}, \text{if } a(x) > 0, \text{otherwise } c(x) = 0, x \in X\}.$$

We may introduce unary operations: for example, multiplication by an element from the field of real numbers ( $\alpha \in \mathbb{R}$ ):  $\alpha I_1 = \{(x, c(x)), c(x) = \alpha a(x), x \in X\}$

### 3 Conditions of Membership in DIA-Class: Checking Satisfiability

#### 3.1 Examples of Sets of Operations Which Generate an Algebra

Various sets  $U$  with the operations of addition, multiplication and multiplication by the element from the field of real numbers introduced on them are considered.

1. The elements of the set  $U$ :
- 1.1 Images, defined on the set  $X$  with an arbitrary range of values  $F$  of the dimension equal to the dimension of the set  $X$ , i.e.  $X, F \subset R^n$ ;
- 1.2 Images, defined on the set  $X$  with the range of values  $X, X \subset R^n$ ;
- 1.3 Standard binary operations on images [4].
2. Operations on the set elements (2.1,2.2,2.3): addition; multiplication; multiplication by an element from the field of real numbers.
3. Physical meaning of the operations:
- 3.1. (a) addition – total brightness of two images; (b) multiplication – pointwise filter; (c) multiplication by an element from the field of real numbers – proportional increase or decrease in image brightness.
- 3.2. (a) addition – total brightness of two images; (b) multiplication – (b1) global (non-pointwise) filter; (b2) definition of one image on a set defined by the other image; (c) multiplication by an element from the field of real numbers – a proportional increase or decrease in image brightness.
- 3.3. ( ) addition –global filter: first two operations are applied to both images; then result images are added; (b) multiplication – global filter: the second operation is applied to both images; the first and the second operands of the first operation are the result of applying second operation; (c) multiplication by an element from the field of real numbers –multiplication of an image by an element from the field of real numbers (unary operation on the image – a standard operation of the multiplication of an image by an element of the field of real numbers [4]).

Below, we give the examples of the DIA, generated by the sets  $U$  with the specified characteristics (the types of set elements and operations together with their physical interpretation are specified in parentheses according to the list given above). Proof of DIA generation by the set  $U$  with the operations of addition, multiplication and multiplication by the element from the field of real numbers introduced on them is based on checking algebra properties. (definition of algebra is in [5]). Example 1 (1.1, 2.1, 3.1) is omitted due to space limitations.

#### **Example 2: (2.1, 2.2, 2.3).**

Suppose that:

- $R$  is a field of real numbers;
- $I = \{(x, f(x)), x \in X, f(x) \in X\} (X \subset R^n, n \in N)$ ;
- $I_1 = \{(x, a(x)), x \in X, a(x) \in X\}, I_2 = \{(x, b(x)), x \in X, b(x) \in X\}$ ;

- the operation of addition of two elements from  $X$  is introduced:  $i,j=1,2,\dots \forall a(x), b(x) \in X: \exists! a(x)+b(x) \in X$ ; this operation satisfies some conditions ( $\forall a(x), b(x), c(x) \in X$ ):
  - $a(x)+(b(x)+c(x)) = (a(x)+b(x))+c(x)$ ;
  - $a(x)+b(x) = b(x)+a(x)$ ;
  - $\forall a(x) \in X, \exists 0 \in X: a(x)+0=a(x)$ ;
  - $\forall a(x) \in X, \exists (-a(x)) \in X: a(x)+(-a(x))=0$ ;
- the operation of superposition of two elements from  $X$  is introduced:  $\forall a(x), b(x) \in X: \exists! a(b(x)) \in X$ ;
- the operation of multiplication by the element of the field  $R$  is introduced on the set  $X: \forall \alpha \in R, a(x) \in X: \exists! \alpha a(x) \in X$ ; this operation satisfies some conditions ( $\forall a(x), b(x), c(x) \in X, \forall \alpha, \beta \in R$ ):
  - $(\alpha a(x)+\beta b(x)) c(x) = \alpha a(x) c(x)+\beta b(x) c(x)$ ;
  - $\alpha(\beta a(x)) = \alpha\beta a(x)$ ;
  - $(\alpha + \beta)a(x) = \alpha a(x) + \beta a(x)$ ;
  - $\alpha(a(x)+b(x)) = \alpha a(x)+\alpha b(x)$ .

(So we can notice, that set  $X$  is vector field on field  $R$  (properties 2.1-2.4, 2.7, 2.8)).

Let us introduce

- operation of addition of two images  $I_1, I_2$ :  
 $I_1 + I_2 = \{(x, a(x) + b(x)), x \in X\}$ ;
- operation of multiplication of two images  $I_1, I_2$ :  
 $I_1 * I_2 = \{(x, a(b(x))), x \in X\}$  (this operation leaves us in the set  $X$ );
- operation of the multiplication of image  $I$  by an element of the field of the real number  $\alpha \in R$ :  
 $\alpha I = \{(x, \alpha f(x)), x \in X\}$ .

All properties of the ring, field, and vector space are satisfied, thus, the created construction is algebra.

### Example 3: (1.3, 2.3, 3.3).

Suppose that

- $R$  is a field of real numbers;
- the elements of a set  $U$  are the binary operations on images [4];
- $A, B, C, \dots$  are the images, transforming  $X$  into  $X, X \subset R^n$ ;
- operations on images are introduced [4];
- $r_1, r_2, \dots \in \{+, *, \vee, \wedge, -, \setminus, A^B\}$ , i.e.,  $r_1, r_2, \dots$  are the operations on two images;
- $r(A, B)$  is the image after applying the operation  $r$  on images  $A$  and  $B$ .

Let us introduce

- operation of addition of two operations  $r_1, r_2$ :  
 $(r_1 \oplus r_2)(A, B) = r_1(A, B) + r_2(A, B)$ ;
- operation of multiplication of two operations  $r_1, r_2$ :  
 $(r_1 \otimes r_2)(A, B) = r_1(r_2(A, B), r_2(A, B))$ ;
- operation of the multiplication of the operation  $r$  by an element of the field of the real number  $\alpha \in R: (\alpha r)(A, B) = \alpha r(A, B)$  (the right part means the multiplication of an image by the element of the field).

All properties of the ring, field, and vector space are satisfied, thus, the created construction is algebra.

### 3.2 Examples of Sets of the Operations Which Do Not Provide Generation of Algebra

Similarly to Section 3.1, various sets  $U$  are considered with operations of addition, multiplication, and multiplication by the element from the field of real numbers introduced on them.

1. The elements of the set  $U$ :

- 1.4 Images, defined on the set  $X$  with arbitrary range of values  $F$  of the dimension equal to the dimension of the set  $X$ , i.e.  $X, F \subset R^n$ ;
- 1.5 Images, defined on arbitrary set  $X_i$  with arbitrary range of values  $F_i$  of the dimension equal to the dimension of the set  $X_i$ , i.e.  $X_i, F_i \subset R^n$ ,  $i=1,2,\dots$

2. Operations on the elements of a set (2.4, 2.5): addition, multiplication, and multiplication by an element from the field of real numbers.

3. Physical meaning of the operations:

- 3.4 (a) addition – total brightness of two images; (b) multiplication – (b1) global (non-pointwise) filter; (b2) definition of one image on a set defined by the other image (in the case when this operation is not determined ( $F \not\subset X$ ), the value of the second operand is taken as a result of multiplication); (c) multiplication by an element from the field of real numbers – proportional increase or decrease in image brightness.
- 3.5 (a) addition – total brightness of two images on intersection of the sets on which these images are given; in the points of a set  $X$  where only one image is determined, it is considered as a result of the operation; (b) multiplication: (b1) global (non-pointwise) filter; in the points of a set  $X$ , where only one image is determined (first or second operands), the image (first or second operands, respectively) is considered as a result of the operation; (c) the multiplication by the element from the field of real numbers – proportional increase or decrease in image brightness.

Below, we give the examples of constructions, generated by the sets  $U$  with the specified characteristics (the types of set elements and operations together with their physical interpretation are specified in parentheses according to the list given above). These constructions are not algebras. Example (1.5, 2.5, 3.5) is omitted due to space limitations.

#### Example 4 (1.4, 2.4, 3.4)

Suppose that:

- $R$  is the field of real numbers;
- $I = \{(x, f(x)), x \in X, f(x) \in F\}$  ( $X, F \subset R^n$ ,  $n \in N$ );  $I_1 = \{(x, a(x)), x \in X, a(x) \in F_1\}$ ;  
 $I_2 = \{(x, b(x)), x \in X, b(x) \in F_2\}$ , where  $F_1$  and  $F_2$  are ranges of values of images  $I_1$  and  $I_2$ , respectively, on the set  $X$ ;

- the operation of addition of two elements from  $F_i, F_j \subset R^n$  is introduced:  $i, j = 1, 2, \dots$ ,  
 $\forall a(x) \in F_i, b(x) \in F_j; \exists! a(x) + b(x) \in F_k, i=1,2,\dots, F_k \subset R^n$ ; this operation satisfies some conditions ( $\forall a(x) \in F_i, b(x) \in F_j, c(x) \in F_y, i,j,y = 1,2,\dots$ ):  
 $a(x) + (b(x) + c(x)) = (a(x) + b(x)) + c(x);$   
 $a(x) + b(x) = b(x) + a(x);$   
 $\forall i: \forall a(x) \in F_i, \exists 0 \in F_i: a(x) + 0 = a(x);$   
 $\forall i: \forall a(x) \in F_i, \exists (-a(x)) \in F_i: a(x) + (-a(x)) = 0;$
- the operation of superposition of two elements from  $F_i, F_j$  is introduced:  $i, j = 1, 2, \dots$ ,  
 $\forall a(x) \in F_i, b(x) \in F_j$ , at the points, where  $b(x) \in X: \exists! a(b(x)) \in F_i$ ;
- the operation of multiplication by the element of the field  $R$  is introduced on the set  $F: \forall \alpha \in R, a(x) \in F: \exists! \alpha a(x) \in F$ ; this operation satisfies some conditions ( $\forall a(x) \in F_i, b(x) \in F_j, c(x) \in F_y, i,j,y=1,2,\dots, \forall \alpha, \beta \in R$ ):  
  - $(\alpha a(x) + \beta b(x))c(x) = \alpha a(x)c(x) + \beta b(x)c(x); \quad \alpha(\beta a(x)) = \alpha \beta a(x);$
  - $(\alpha + \beta)a(x) = \alpha a(x) + \beta a(x); \quad \alpha(a(x) + b(x)) = \alpha a(x) + \alpha b(x).$

Let us introduce:

- the operation of addition of two images  $I_1, I_2$ :  
 $I_1 + I_2 = \{(x, a(x) + b(x)), x \in X\};$
- the operation of multiplication of images  $I_1, I_2$ :

$$I_1 * I_2 = \begin{cases} (x, a(b(x))), b(x) \in X \\ (x, b(x)), b(x) \notin X \end{cases};$$

- the operation of multiplication of image  $I$  by an element of the field of real numbers  $\alpha \in R$ :  
 $\alpha I = \{(x, \alpha f(x)), x \in X\}.$

The created construction is not algebra - it is an additive group, because the associativity of multiplication operation is not satisfied and all properties of an additive group are satisfied (definition of group is in [5]).

## 4 Conclusion

The examples of sets with various elements and the operations introduced on them are considered both belonging to algebras and not. For constructing the examples, the standard operations on images are used to show that DIA covers mathematical constructions of the standard IA[4] which satisfies the conditions of algebra[5]. The examples mentioned in this paper are the first step in ordering the operations introduced on various sets, generating and not generating DIA. Further it is planned to precisely formulate necessary and sufficient conditions of DIA generation by the sets of considered type.

Our technique for formulating and checking the conditions for the set of operations that ensures the DIA construction is a basis for obtaining mathematically proven criterion for a choice of operations for producing efficient image analysis and recognition algorithmic schemes. This criterion is useful for practical implementation.

## References

1. Grenander, U.: General Pattern Theory. A Mathematical Study of Regular Structures, Oxford: Clarendon Press (1993)
2. Gurevich, I.B.: The Descriptive Framework for an Image Recognition Problem, Proc. of the 6<sup>th</sup> Scandinavian Conf. on Image Analysis, Oulu, Finland, Vol.1(Pattern Recognition Society of Finland) (1989) 220–227
3. Gurevich, I.B., Smetanin, Yu.G., Zhuravlev, Yu.I.: Descriptive Image Algebras: Determination of the Base Structures, Pattern Recognition and Image Analysis, Vol. 9, No.4 (1999) 635–647
4. Ritter, G.X., Wilson, J.N.: Handbook of Computer Vision Algorithms in Image Algebra, 2-d Edition. CRC Press Inc. (2001)
5. Van Der Waerden, B.L.: Algebra I,II, Springer-Verlag, Berlin Heidelberg New York (1971, 1967(in Russian))
6. Zhuravlev, Yu.I.: Correct Algebras Over Sets of Incorrect (Heuristic) Algorithms, Cybernetics (Kiev), N. 4. (1977) 14–21, N. 6. (1977) 21–27, N. 2. (1978) 35–42, (in Russian)

# Completeness Conditions of a Class of Pattern Recognition Algorithms Based on Image Equivalence\*

Igor B. Gurevich and Irina A. Jernova

Scientific Council “Cybernetics” of the Russian Academy of Sciences,  
40, Vavilov str., Moscow GSP-1, 119991 Russian Federation  
[igourevi@ccas.ru](mailto:igourevi@ccas.ru)

**Abstract.** The paper presents recent results in establishing existence conditions of a class of efficient algorithms for image recognition problem including the algorithm that correctly solves this problem. The proposed method for checking on satisfiability of these conditions is based on the new definition of image equivalence introduced for a special formulation of an image recognition problem. It is shown that the class of efficient algorithms based on estimate calculation contains the correct algorithm in its algebraic closure. The main result is an existence theorem. The obtained theoretical results will be applied to automation of lymphoid tumor diagnostics by the use of hematological specimens.

## 1 Introduction

During last several years in Scientific Council “Cybernetics” of the Russian Academy of Sciences the research was conducted in the field of development of mathematical techniques for image analysis and estimation. The theoretical base for this research is the Descriptive Theory of Image Analysis and Recognition [2-5,10,11]. This paper presents recent results in establishing existence conditions of a class of efficient algorithms for image recognition problem, including the algorithm, which solves this problem correctly. The proposed method for checking on satisfiability of these conditions is based on the new definition of image equivalence, introduced for the special formulation of an image recognition problem. It is shown that the class of efficient Algorithms Based on Estimate Calculation (AEC) [10,11] contains the correct algorithm in its algebraic closure. The main result is an existence theorem.

One of the issues of the day in the field of image recognition is the search of the algorithm, which correctly classifies an image by using its description. The approach to image recognition, developed by the authors, is a specialization of the algebraic approach to recognition and classification problems (Yu. Zhuravlev [10,11]). The main idea of this approach consists in the following. There are no accurate mathematical models for such poorly formalizable areas as geology, biology, medicine, and sociology. However, in many cases nonrigorous methods based on the

---

\* The paper was partly supported by the grants of the Russian Foundation for Basic Research nos. 01-07-90016, 02-01-00182 and Russian Academy of Sciences (project no. 2.14 of the Complex Program of Scientific Research of the Presidium of RAS “Mathematical Modeling and Intellectual Systems”).

heuristic considerations yield appreciable practical results. Therefore, it is enough to construct a family of such heuristic algorithms for solving appropriate problems, and then, to construct the algebraic closure of this family. The existence theorem is proved, which states that any problem from a set of problems concerning poorly formalized situations, is solvable in this algebraic closure [10].

An image recognition is a classical example of a problem with ill-formalized and partly contradictory information. This gives us good reasons to believe that the use of the algebraic approach to image recognition can lead to important results and, consequently, an “algebraization” of the field is the most promising way of development of desired mathematical techniques for image analysis and estimation.

Note, that the idea of creating the unified algebraic theory covering different approaches and procedures used in image and signal processing has a certain background beginning with the works of von Neumann and extended by S. Unger, U. Grenander, M. Duff, Yu. Zhuravlev, G. Matheron, G. Ritter, J. Serra, et al. [1,7-11]. Our research is carried out in the field of the Descriptive Approach to Image Analysis and Recognition, which differs from the studies in the field of algebra mentioned above, and is completely original.

Unfortunately, the algebraic approach developed by Yu. Zhuravlev cannot be applied directly to an image recognition problem. Mostly, it is due to the difficulty of an image as a recognition object and to considerable distinctions between the classical pattern recognition problem and the image recognition problem which consist in the following:

- a standard object in the classical pattern recognition theory is, as a rule, described by a set of features; whereas there is no such natural way for image description that does not lose an important information about image; common methods of image description are either too complicated and require much computational resources (e.g., raster representation of an image), or semantically primitive (set of features);
- a single object (a scene) can correspond to several images differing in brightness, contrast, scale, and observer's point of view; within the framework of a recognition problem, it means that different images of an object should be identically classified by the recognizing algorithm.

Thus, the problem of image equivalence provokes much interest, especially the use of this property in pattern recognition problem [3–5].

## 2 Image Equivalence

Image equivalence relation on the set of images may be introduced in different ways:

- a) we may consider equivalence as a closeness of image descriptions with respect to a metric in a metric space, for example, a metric in the Euclidean space  $E^n$ , where image is described by its  $n$ -dimensional feature vector;
- b) if the set of allowable image transformations is given in the image recognition problem (for example, image rotations by angle  $2\pi k/n$ ,  $k=0,1,\dots,n-1$ ), the two images are considered to be equivalent, if the first image is obtained from the second one by applying a certain transformation from the given set of allowable transformations.

In this work, we propose a definition of image equivalence, based on a special setup of an image recognition problem. Consider a set of allowable images, described by their  $n$ -dimensional feature vectors, and the recognizing algorithm  $A$ , which constructs  $l$ -dimensional information vector by using  $n$ -dimensional description vector. We remind, that information vector is a vector of object's membership of classes, where the values of vector components  $0, 1, \Delta$  mean “object does not belong to a class”, “object belongs to a class”, “algorithm fails to determine, whether object belongs to a class or not”, respectively [10].

**Definition 1.** Two images are *equivalent* with respect to a recognizing algorithm  $A$ , if their information vectors, obtained by the recognizing algorithm  $A$ , coincide.

A simple way of constructing an image equivalence class is introduced, based on this definition. The idea consists in applying a certain set of transforms to generating images.

Let a binary image  $I$  of a plane polygon be given. We call it *generating image*. Let the transforms of plane rotation group  $C_n$  be given as a set of transforms: each  $n$ -order group  $C_n$  consists of all rotations by angles  $2\pi k/n$ ,  $k=0, 1, \dots, n-1$ , around a fixed point, and it is essentially, that given transforms form a group. Applying each transform from  $C_n$  to generating image  $I$ , we obtain a set of images.

The equivalence of the obtained images is established by the identity of their information vectors. Here, it is reasonable to describe images by vectors of invariant features and the simplest way is to exploit the invariants with respect to the given group of transformations  $C_n$ . As a result, all images from the obtained set have the same feature vectors, and recognizing algorithm constructs the same information vectors for these images. Consequently, all obtained images are equivalent. It is essential that, in case when transformations form a group, mathematical methods are developed for constructing invariants with respect to this group of transforms [6].

### 3 Mathematical Formulation of a Recognition Problem

In order to prove the existence theorem for AEC that correctly solves the image recognition problem, it is necessary to introduce a new formulation of an image recognition problem, differing either from classical formulation [10,11], or from the formulation of the Descriptive Approach [2]. Let us have a look at these formulations.

#### 3.1 Classical Mathematical Formulation of Pattern Recognition Problem Z

$Z(I_0, S_1, \dots, S_q, P_1, \dots, P_l)$  is a pattern recognition problem, where  $I_0$  is allowable initial information,  $S_1, \dots, S_q$  is a set of allowable objects, described by feature vectors,  $K_1, \dots, K_l$  is a set of classes,  $P_1, \dots, P_l$  is a set of predicates on allowable objects,  $P_i = P_i(S)$ ,  $i=1, 2, \dots, l$ . The problem  $Z$  is to find the values of predicates  $P_1, \dots, P_l$ .

**Definition 2.** Algorithm is *correct* for a problem  $Z$  [10], if the following equation is satisfied:

$$A(I, S_1, \dots, S_q, P_1, \dots, P_l) = \left\| \alpha_{ij} \right\|_{q \times l}, \text{ where } \alpha_{ij} = P_j(S_i).$$

### 3.2 Mathematical Formulation of Image Recognition Problem $Z^l$

Taking into account the introduced notion of image equivalence an image recognition problem may be formulated in the following way:

$Z^l \left( \{I_i^{j_i}\}_{i=1,2,\dots,q}^{j_i=1,2,\dots,p_i}, \{M_i\}_{i=1,2,\dots,q}, \{K_t\}_{t=1,2,\dots,l}, \{P_t^{i,j_i}\}_{t=1,2,\dots,l}^{i=1,2,\dots,q; j_i=1,2,\dots,p_i} \right)$  is an image recognition problem  $Z^l$ , where  $\{I_i^{j_i}\}$  are images,  $i=1,2,\dots,q$ ,  $j_i$  is a number of an image within the  $i$ -th equivalence class,  $p_i$  is a quantity of images in the  $i$ -th equivalence class,  $j_i=1,2,\dots,p_i$ ;  $M_i = \{I_i^1, I_i^2, \dots, I_i^{p_i}\}$ ,  $i=1, 2, \dots, q$ , is an equivalence classes on the set  $\{I_i^{j_i}\}$ ;  $K_1, K_2, \dots, K_l$  are classes in the image recognition problem;  $P_t^{i,j_i} : "I_i^{j_i} \in K_t"$ ,  $t=1,2,\dots,l$ ,  $i=1,2,\dots,q$ ,  $j_i=1,2,\dots,p_i$ , are predicates. The problem  $Z^l$  is to find the values of predicates  $P_t^{i,j_i}$ .

### 3.3 Mathematical Formulation of Image Recognition Problem $Z^2$

The distinction between the problem  $Z^2$  and the problem  $Z^l$  is that each equivalence class is replaced by a single image, a representative of a class, with number  $n_i$ ,  $1 \leq n_i \leq p_i$ , where  $i$  is a number of an equivalence class. This replacement is realized with a help of a definition of an allowable transform.

**Definition 3.** An arbitrary transform  $f: \{I_i^j\} \rightarrow \{I_i^j\}$  is an allowable transform, if  $f(I_i^j)$  and  $I_i^j$  belong to the same equivalence class for each  $I_i^j$ .

$Z^2 \left( \{I_i^{n_i}\}_{i=1,2,\dots,q}^{n_i=1,2,\dots,q}, \{K_t\}_{t=1,2,\dots,l}, \{P_t^i\}_{t=1,2,\dots,l}^{i=1,2,\dots,q} \right)$  is an image recognition problem  $Z^2$ , where  $I_i^{n_i}$ ,  $i=1,2,\dots,q$  are images,  $I_i^{n_i} \in M_i$ ;  $K_1, K_2, \dots, K_l$  are classes in the image recognition problem;  $P_t^i : "I_i^{n_i} \in K_t"$ ,  $t=1,2,\dots,l$ ,  $i=1,2,\dots,q$ , are predicates. The problem  $Z^2$  is to find the values of predicates  $P_t^i$ .

## 4 Conditions of Completeness of the Class of Algorithms Based on Estimate Calculation for Image Recognition Problem

The main result of the paper is obtained for a class of efficient recognizing algorithms – AEC [10,11]. These algorithms are based on formalization of the idea of precedence or partial precedence: the “proximity” between parts of descriptions of the objects classified previously and object to be classified is analyzed. Suppose we have the standard descriptions of the objects  $\{\tilde{S}\}$ ,  $\tilde{S} \in K_j$  and  $\{S'\}$ ,  $S' \notin K_j$ , and the method of the “closeness” evaluating for parts of the description of  $S$  and the corresponding parts of descriptions of  $\{I(\tilde{S})\}, \{I(S')\}$ ;  $S$  is an object presented for recognition,  $j=1,2,\dots,l$ .

By evaluating the “proximity” between the parts of descriptions of  $\{I(\tilde{S})\}$  and  $\{I(S')\}$ , and between  $I(S)$  and  $I(S')$ , respectively, it is possible to evaluate a generalized “proximity” between  $S$  and the sets of objects  $\{\tilde{S}\}, \{S'\}$  (in the simplest case, the value of a generalized “proximity” is a sum of values of “proximity” between the parts of descriptions). Then, the total estimate for an object of a class is formed by the set of estimates, which is the value of object’s membership function of a class.

The existence theorem for AEC that solves recognition problem  $Z$  correctly is proved for the algebraic closure of the class of AEC.

**Theorem 1** [10]. Let the conditions of non-identity of descriptions of classes and of objects in pattern recognition problem  $Z$  with given vectors of features be satisfied. Then the algebraic closure of the class of AEC-algorithms is correct for  $Z$ .

Note, that the definition of image equivalence is not used in the classical formulation of a recognition problem, therefore, the Theorem 1 of a correct algorithm existence cannot be applied directly to an image recognition problem.

The distinction between the problem  $Z$  and the problem  $Z'$  is that, in the latter, the image equivalence classes are explicitly considered. In order to reduce the image recognition problem  $Z'$  to the standard recognition problem  $Z$ , it is necessary to proceed from classification of a group of objects to classification of a single object. The problem  $Z^2$ , differing from  $Z'$  by the presence of allowable transforms and by the lack of image equivalence classes, allows us to operate with a single image – a representative of a corresponding equivalence class – for each equivalence class under certain restrictions on the set of allowable transforms.

Direct generalization of Theorem 1 for the image recognition problem  $Z^2$  is Theorem 2.

**Theorem 2.** Let the allowable transforms  $\{f_1, f_2, \dots\}$  form a transitive group. Then, the image recognition problem  $Z'$  may be reduced to the problem  $Z^2$  and the algebraic closure of the class of AEC-algorithms is correct for  $Z^2$ .

Theorem 2 establishes the conditions of existence of a correct algorithm for image recognition problem and proves that such algorithm can be found in the algebraic closure of AEC-algorithms.

## 5 Conclusion

The task of searching for the correct algorithm for image recognition problem was investigated. The definition of image equivalence was introduced, and the formulation of image recognition problem was modified. It was proved that, under certain restrictions on the image transforms, an image recognition problem may be reduced; and the correct algorithm for the reduced problem can be found in the algebraic closure of AEC.

The future research will be devoted to detailed analysis of image equivalence and establishment of relationship between image equivalence and image invariance. The

obtained theoretical results will be applied to automation of lymphoid tumor diagnostics by using hematological specimens.

## References

1. Grenander, U.: General Pattern Theory. A Mathematical Study of Regular Structures, Oxford: Clarendon Press (1993)
2. Gurevich, I.B.: The Descriptive Framework for an Image Recognition Problem, Proc. of the 6<sup>th</sup> Scandinavian Conf. on Image Analysis, Oulu, Finland, Vol.1 (Pattern Recognition Society of Finland) (1989) 220–227
3. Gurevich, I.B., Jernova, I.A., Smetanin, Y.G.: A Method of Image Recognition Based on the Fusion of Reduced Invariant Representations: Mathematical Substantiation // Proceedings of the 16th International Conference on Pattern Recognition (ICPR2002), Quebec, Canada, August 11–15, 2002 [R.Kasturi, D.Laurendeau, C.Suen (Eds.)]: in 4 volumes. Vol.3 The Institute of Electrical and Electronics Engineers, Inc. (2002) 391–394
4. Gurevich, I.B., Smetanin, Y.G.: On the Equivalence of Images in Pattern Recognition Problems // Proceedings of the 12th Scandinavian Conference on Image Analysis, Bergen, June 11th – 14th, 2001. [Ed. I.Austvoll]. Norwegian Society for Image Processing and Pattern Recognition (2001) 679–685
5. Gurevich, I.B., Zhuravlev Y.I.: An Image Algebra Accepting Image Models and Image Transforms // Proceedings of the 7th International Workshop "Vision, Modeling, and Visualization 2002" (VMV2002), November 20–22, 2002, Erlangen, Germany [G.Greiner, H.Niemann, T.Ertl, B.Girod, H.-P.Seidel (Eds.)], IOS Press, B.V.Amsterdam, Infix, Akademische Verlagsgesellschaft, Aka GMBH, Berlin (2002) 21–26
6. Mundy, J.L., Zisserman, A.: Towards a New Framework for Vision, Geometric invariance in computer vision/ edited by J. Mundy, A. Zisserman. (1992) 1–39
7. Ritter, G.X., Wilson, J.N.: Handbook of Computer Vision Algorithms in Image Algebra, 2-d Edition. CRC Press Inc. (2001)
8. Serra, J.: Image Analysis and Mathematical Morphology. L., Academic Press (1982)
9. Sternberg, S.R.: Language and Architecture for Parallel Image Processing, Proceedings of the Conference on Pattern Recognition in Practice. Amsterdam (1980)
10. Zhuravlev, Yu.I.: An Algebraic Approach to Recognition or Classification Problems, Pattern Recognition and Image Analysis: Advances in Mathematical Theory and Applications, V. 8, No. 1 (1998) 59–100
11. Zhuravlev, Yu.I., Gurevitch, I.B.: Pattern Recognition and Image Recognition, Pattern Recognition and Image Analysis: Advances in Mathematical Theory and Applications in the USSR, V. 1, No. 2 (1991) 149–181

# Typical Segment Descriptors: A New Method for Shape Description and Identification

Nancy Aimé Alvarez-Roca<sup>1</sup>, José Ruiz-Shulcloper<sup>2</sup>, and Jose M. Sanchiz-Martí<sup>3</sup>

<sup>1</sup> Departamento de Ciencia de la Computación  
Universidad de Oriente, Santiago de Cuba, Cuba  
aime@csd.uo.edu.cu

<sup>2</sup> Laboratorio de Reconocimiento de Patrones,  
Instituto de Cibernética, Matemáticas y Física, La Habana, Cuba.  
recpat@cidet.icmf.inf.cu

<sup>3</sup> Departamento de Ingeniería y Ciencia de los Computadores,  
Universidad Jaume I, Castellón, Spain.  
sanchiz@uji.es

**Abstract.** In this paper we introduce a new method for recognizing and classifying images based on concepts derived from Logical Combinatorial Pattern Recognition (LCPR). The concept of Typical Segment Descriptor (TSD) is introduced, and algorithms are presented to compute TSDs sets from several chain code representations, like the Freeman chain code, the first differences chain code, and the vertex chain code. The typical segment descriptors of a shape are invariant to changes in the starting point, translations and rotations, and can be used for partial occlusion detection. We show several results of shape description problems pointing out the reduction in the length of the description achieved.

## 1 Introduction

Recognition of 2D objects is an important task useful in many machine vision applications and research areas such as robotics and computer vision [1, 2]. A 2D shape is a feature often used for its distinctive classification power. A shape is what remains of a region after disregarding its size, position and orientation in the plane [3]. Non-numeric shape description methods search representations (e.g. a chain code, a graph) of the original shape so that only important characteristics are preserved. Other shape description techniques generate numerical descriptors given as feature vectors. The required properties of a shape description scheme are invariance to translation, rotation and scaling. Shape matching or recognition refers to methods for comparing shapes. Usually, given a group of known objects, the identical or most similar objects in a scene must be found. There are many imaging applications where scene analysis can be reduced to the analysis of shapes [4], though effectively representing shapes remains one of the biggest hurdles to overcome in the field of automated recognition.

In this paper we introduce a new boundary-based method for recognizing and classifying images originated from concepts of Logical Combinatorial Pattern Recognition (LCPR). The concept of Typical Segment Descriptor (TSD) is introduced. Using a shape's Freeman chain code its TSDs are computed, so they inherit the data reduction property of this representation. An algorithm for computing the TSD set from closed shapes is given.

Conversion (mapping) of an analog image onto a discrete one (digitization) is based on several assumptions [5]. It is assumed that the acquisition of an image is done using a set of physical captors, which could be modeled by a set of subsets of the continuous plane. The simplest idea is to assume a discrete partition of the plane. If only partitions involving regular polygons are considered, the number of different partitions is reduced to three: triangles, squares, or hexagons. The selection of the type of partition determines differences in concepts like neighborhood, adjacency, and connectivity. In this work we assume that partition is in regular squares and the algorithms presented assume closed boundary shapes.

Recently, machine learning and symbolic processing tools have been extended to Image Processing problems. New image representation concepts have been developed [6, 7]. The new method presented here uses ideas from LCPR.

Chain codes are frequently used for image representation since they allow considerable data reduction. The first approach for representing digital curves was introduced by Freeman [8]. By means of this representation several properties of arbitrary planar curves can be determined: moments, inertial axes, etc. [9]. Curves are encoded as line segments that link points of a rectangular grid. These points are the grid points closer to the curve. This process is called *chain encoding*.

Many authors have used chain coding for shape representation [2, 10], a normalization of the code with respect to the starting point is achieved by using shape numbers [3]. In [11] contours of handwritten characters are chain coded and recognition cost and accuracy are reported.

A new chain code for shapes composed of regular cells is defined in [12]. It is called *Vertex Chain Code* (VCC), and is based on the number of cell vertices that are in touch with the bounding contour of the shape. Concepts of VCC are extended for representing 3D shapes in [13], producing a curve descriptor invariant to translation.

Concepts from LCPR are used for image identification in [14], where a method for solving supervised pattern recognition problems using binary descriptors is reported. A generalization can be achieved by transforming numerical descriptors into k-valued sets so that k-valued logic tools can be used.

If some features of an object take values that cannot be found in the descriptions of objects of the remaining classes, then such a sequence of values is called a *descriptor*. If a certain descriptor loses this property when a feature is not included, then it is called a *Non-Reducible Descriptor* (NRD) [15].

In [16] an algorithm (KORA) is reported to select the features that form a minimal descriptor of every object in a database of descriptors. It has been extended and used on non-image-like data [17, 18] and is used in [14] for recognition of objects in raw images. In this latter work the concept of sub-description of an object is transformed in a fragment of an image. Considering each image as a one-dimensional array a learning matrix is formed. Differences of corresponding pixels are used to conform a dissimilarity matrix. In this manner, the concept of feature is lost and the set of co-

lumns selected as descriptive attributes change if transformations such as rotations, translations or scaling are applied.

NRDs are reported as a concept for representing a minimal set of characteristics that can be used for object recognition, the TSD proposed here complies with the same objective but, instead of using the whole learning matrix, only the chain code is used. This paper is organized as follows: in Section 2 TSDs are defined and their main properties discussed. Section 3 presents results, and in Section 4 conclusions are drawn.

## 2 Typical Segment Descriptors

Suppose that a set of segmented binary 2D-images (shapes)  $X_1, X_2, \dots, X_n$  is known. For each shape, the chain code is computed based on  $\delta$ -connectivity,  $\delta=4,8$ . Each  $\delta$ -chain has a *first difference (derivative)*  $D(X_1), D(X_2), \dots, D(X_n)$  associated. The derivative of a shape is a sequence of codes representing changes of direction. The length of the derivative  $D(X)$  will be denoted  $|D(X)|$ . It is assumed that objects can be rotated in angles  $k * \frac{360}{\delta}$ , with  $k$  integer, without change in the derivative.

**Definition.** A sequence  $y_1y_2\dots y_p$  is a *p-segment* of a circular sequence of codes  $D(X)=x_1x_2\dots x_m$  if  $p \leq m$  and for some fixed  $j=1, \dots, m$  it is observed that  $y_t=x_{j+t}$  with  $t=1, \dots, p$ .  $p$  is the *length* of the *p-segment*. For example 222310 is a 6-segment of 112223100223312.

**Definition.** Given two segments  $\Theta$  and  $\Xi$  of length  $p$  and  $q$  respectively,  $\Theta$  is a *sub-segment* of  $\Xi$ , if  $p \leq q$ , and for a certain circular index rotation  $y_t=x_t$ ,  $t=1, \dots, p$ . It is easy to observe that  $\Phi=12112$  is a sub-segment of  $\Theta=112223100223312$ .

**Definition.** A *p-segment*  $\Theta$  of the derivative  $D(X)$  is a *segment descriptor* of image  $X$  with respect to image  $Y$ , if there does not exist a *p-segment*  $\Xi$  of  $D(Y)$  such that  $\Xi=\Theta$ . If, from  $\Theta$  it is not possible to eliminate either the first element or the last one while keeping the property of segment-descriptor, then  $\Theta$  is a *typical segment descriptor*. It will be denoted as  $tsd(X/Y)$  or simply  $tsd$ . A *tsd* of minimal length is called *minimal segment descriptor*. In general, it is not unique.

Figure 1 shows two shapes, the starting point from which their boundary was traversed, the path of their 4-chain codes which are given as shape numbers, and corresponding first differences.

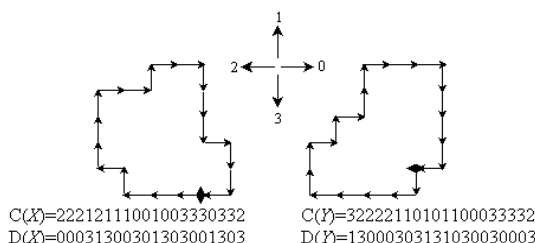


**Fig. 1.** Two shapes, their 4-chain codes (C) and first derivatives (D)

It can be verified that the  $\Theta=30300$  is a 5-segment descriptor of the shape  $X$  with respect to  $Y$ , while  $\Xi=3003$  is not.  $\Theta$  is not a typical segment-descriptor because 3030 (a subsegment) is a segment descriptor of  $X$  with respect to  $Y$ .

The previous definitions do not depend on the concept of the derivative. That is, they can be applied to chain codes or other representations directly.

The set of all typical segment descriptors of  $X$  with respect to  $Y$  will be denoted as  $TSD(X/Y)$ . A *tsd* can be present only in  $X_i$  (but not in  $X_j$  ( $i \neq j$ )), so it differentiates  $X_i$  with respect to the other shapes. The set of *tsds* that fulfill this quality will be denoted  $TSD(X_i)$ .

The properties of a shape's TSD set include:

**Property 1.** From the condition  $X_i \neq X_j$ ,  $i \neq j$ ,  $i, j = 1, \dots, n$ , it follows that each shape has at least one *typical segment descriptor*. This is obvious because in the worst case, for each  $X_i$ , a subchain of  $D(X_i)$  of length  $|D(X_i)|-1$  is a *tsd*.

**Property 2.** Different *tsds* have different discriminative power, since they can discriminate with respect to a different number of shapes. Based on this, a *weight*  $W(\Theta)$  can be associated with each *tsd*  $\Theta$ , being proportional to the number of discriminated shapes.

**Property 3.** Each *tsd*  $\Theta \in TSD(X/Y)$  is linked to a unique subsequence in its original chain code which corresponds to a differentiating characteristic of  $X$ . Therefore, two or more occurrences of  $\Theta$  inside  $TSD(X/Y)$  can be associated to the appearance of this characteristic with different or equal starting directions.

To highlight the differences between two occurrences of the same  $\Theta$  in  $TSD(X/Y)$ , we adopt the following conventions:

- $\Theta^0$  : the first code of the subsequence of  $X$  that originates  $\Theta$  is 0.
- $\Theta^1$  : the first code of the subsequence of  $X$  that originates  $\Theta$  is 1.
- ...
- $\Theta^{\delta-1}$  : the first code of the subsequence of  $X$  that originates  $\Theta$  is  $\delta-1$ .

Observe that, though a *tsd*  $\Theta$  can appear as  $\Theta^d$  ( $d \in \{0, 1, \dots, \delta-1\}$ ) in  $TSD(X/Y)$ , the same *tsd* can appear as  $\Theta^f$  ( $f \neq d$ ) in other object having the same shape. In Figure 1, 01 is a *tsd* of  $X$  with respect to  $Y$  and the subsequence 330 originates it. That means that the four subsequences: 001, 112, 223, and 330, never can be present in  $Y$ . Figure 2 shows a graphical representation of these subsequences.

Note that not necessarily all of these sequences are simultaneously present in the shape, but they can eventually appear depending on the shape pose. In Figure 1, 001 and 330 are present, but not 112 nor 223.

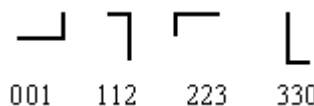


**Fig. 2.** Subsequences that can originate *tsd* 01 from  $TSD(X/Y)$

The following holds for the shapes in Figure 1:

$$\begin{aligned} TSD(X/Y) &= \{01^3, 01^0, 3030^1, 1303^3, 3030^0, 13003^1\} \\ TSD(Y/X) &= \{10^0, 131^0, 0303^2, 3031^2, 00300^0, 13000^2, 00030^2\} \end{aligned}$$

## 2.1 TSD Rotation Invariance

**Property 4.** Compatibility of  $TSD(X/Y)$ : Let  $TSD(X/Y) = \{\Theta_1^{d_1}, \Theta_2^{d_2}, \dots, \Theta_q^{d_q}\}$ ,  $d_i < \delta$ . For any rotation of  $X$  with magnitude  $\delta_j \in \{0, 1, \dots, \delta\}$ , all  $\Theta_i^{d_i}$  in  $D(X)$  are in the form  $\Theta_i^{d_i \oplus_{\delta} \delta_j}$  for  $i=1,\dots,q$ , where  $\oplus_{\delta}$  represents the sum mod  $\delta$ . This property states that each  $TSD(X/Y)$  has associated other  $\delta$ -1 sets that contain the results of rotating the original set, and that it is possible to predict in what form every *tsd* will appear in each set. So, if shape  $X$  is rotated by  $\delta_j$ , there will be a corresponding set  $TSD(X/Y)$  with a known form for every *tsd*.

**Definition.** *Compatibility* of  $X$  with respect to  $Y$ ,  $Comp(X/Y)$ , is the set of all possible  $n$ -tuples of  $d_j$  in all possible sets  $\{\Theta_1^{d_1}, \Theta_2^{d_2}, \dots, \Theta_q^{d_q}\}$ , these sets can be obtained by rotating the original. A similar definition could be formulated for  $TSD(X)$ . In Figure 1 it holds that the set of *tsds*  $\{1303^3, 3030^0, 13003^2\}$  is not a compatible set. However,  $\{1303^0, 3030^1, 13003^2\}$  is compatible.

## 2.2 Partial Occlusion Detection Using TSD

**Definition.** The number of occurrences of a *tsd*  $\Theta^d \in TSD(X/Y)$  is denoted the *frequency* of  $\Theta^d$ ,  $\alpha_d$ . The frequency of  $\Theta$  is a  $\delta$ -tuple,  $Freq(\Theta) = (\alpha_0, \alpha_1, \dots, \alpha_{\delta-1})$ .  $\sum_{i=0}^{\delta-1} \alpha_i$  is the *absolute frequency* of  $\Theta$  in  $TSD(X/Y)$  and will be denoted as  $\|\Theta\|$ .

Another important attribute is the relative order in which the *tsds* appears.  $\Theta$  is the *predecessor* of  $\Xi$  ( $\Theta = Pre(\Xi)$ ) if there is no other *tsd* in between. Then  $\Xi$  is the *successor* of  $\Theta$  ( $\Xi = Suc(\Theta)$ ). In Figure 1,  $3030^1$  is the predecessor of  $01^3$ .

**Definition.** A sequence of *tsd* in  $TSD(X/Y)$  is *connected* if they, all in sequence, form a subchain of the original chain code. The *connectivity* of  $X$ , denoted as  $Con(X)$ , is the set of all connected sequences in  $TSD(X/Y)$ . Each single *tsd* is a member of  $Con(X)$ . In Figure 1,  $3030^1, 01^3, 1303^3$  and  $3030^0$  are connected.

Note that attributes of each  $\Theta$  (*tsd* of  $X$ ) such  $\|\Theta\|$ ,  $Pre(\Theta)$ ,  $Suc(\Theta)$ , as well as features of  $X$  such  $Comp(X)$  and  $Con(X)$  can be used for detecting the presence of the shape in a scene, even in case of partial occlusion. If a *tsd* of the shape if not detected due to an occlusion, but some of its attributes are checked, as well as other properties of the shape, then some certainty about the presence of the shape could be calculated. This is subject of our current research.

## 2.3 An Algorithm for the Computation of $TSD(X/Y)$

In order to determine the set of all possible *tsds* of a shape with respect to other shapes,  $TSD(X/Y)$ , two situations can be considered: each shape constitutes a class; each class is formed by more than one shape. In this latter case, the procedure is the same but only segments from different classes have to be compared [17].

Let  $D(X)$  and  $D(Y)$  be two derivatives. Each p-segment of  $X$  is tested as being a *tsd*. The set of tested segments are denoted  $\text{Rev}(X)$ . The algorithm is:

**Step 1.** Let  $p = 1$ ,  $\text{TSD}(X/Y) = \emptyset$ ,  $\text{Rev}(X) = \emptyset$ .

**Step 2.** Let  $S_p$  be the next p-segment that can be extracted from  $D(X)$ , i.e., a p-segment formed from an incremental starting position in  $D(X)$ .

**Step 3.** If  $S_p \in \text{Rev}(X)$  go to step 9.

**Step 4.** If  $S_p \in \text{TSD}(X/Y)$  go to step 9.

**Step 5.** If some  $\Theta \in \text{TSD}(X/Y)$  is a subsegment of  $S_p$ , go to step 8.

**Step 6.** If there is in  $D(Y)$  a p-segment  $E_p$  such that  $E_p = S_p$  go to step 8.

**Step 7.** Add  $S_p$  to  $\text{TSD}(X/Y)$ , go to step 9.

**Step 8.** Add  $S_p$  to  $\text{Rev}(X)$ .

**Step 9.** If it is not possible to extract another p-segment from  $D(X)$ , make  $p=p+1$ .

**Step 10.** If  $p=|D(X)|$  end, else go to step 2.

The design of an algorithm for computation of the set  $\text{TSD}(X)$  is not complex. It is only necessary to find the intersection of all sets of *tsds* of  $X$  with respect to the other shapes. The identification of  $X$  in an image will be easy if the shapes are isolated in the scene, finding at least one *tsd* from this intersection is sufficient to verify that shape  $X$  appears in the scene.

Additional steps should be added if the intersection is empty. Several alternatives can be used in these circumstances. A simple choice is to build a set taking one *tsd* from each set of *tsds* of  $X$  with respect to the other shapes. In order to verify the presence of  $X$  in an image it will be necessary to find all the elements of the set created in this manner. In our experiments we build this set selecting *tsds* with bigger weights.

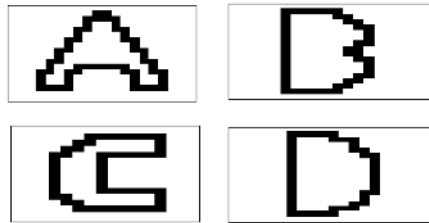


**Fig. 3.** Shape contours of letters A, B, C, D

### 3 Results

Figure 3 shows contours of some letters used in our experiments. *Tsds* that differentiate B from the remaining shapes were computed using the proposed algorithm. Results are shown in Table 1. Note that the sum of the lengths of *tsds* in  $\text{TSD}(B/X)$ , with  $X=\{A,C,D\}$ , is less than the length of C(B), so they describe shape B with respect to the others in a more compact form. Even in cases where the sum of *tsds* is

bigger than the length of C(B) it will not be necessary, in general, to compare the chain code or the derivatives with respect to all the *tsds*.

**Table 1.** Sets of typical segment descriptors of shape B with respect to the other shapes.

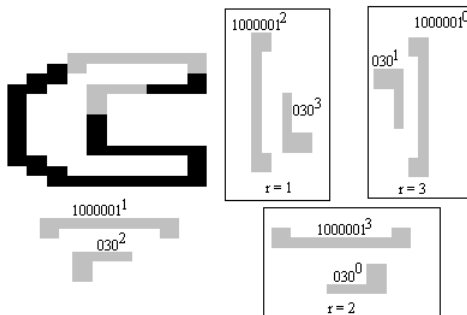
TSD(B/A):	$\{33^2, 1000^0, 0001^0, 1313^0, 3131^3, 00131^0, 13100^0, 00000^1, 310013^3\}$
TSD(B/C):	$\{33^2, 31001^3, 10013^0, 100001^1, 0001000^2, 0000000^1, 00000010^1\}$
TSD(B/D):	$\{33^2, 1313^0, 1001^0, 00131^0, 100001^1, 000010000^2\}$

Table 2 shows the sets of TSD( $X$ ),  $X=\{A,B,D\}$ . In case of C the intersection of its sets of tsds with respect to the others letters was empty, so we use the alternative described in 2.3. Figure 4 illustrates the set of *tsds* obtained for C and their compatibility with rotations in direction r.

**Table 2.** TSD sets calculated for A, B and D.

TSD(A/{B,C,D})	TSD(B/{A,C,D})	TSD(D/{A,B,C})
$\{11^1\}$	$\{33^2\}$	$\{01310^3\}$

Note that the presence of the shape can be verified finding only one *tsd*. This property is useful when the shapes are isolated in the scene. Other properties of the *tsds* can be used if noise or occlusions affect the boundary: their *absolute frequency*, order of appearance, *connectivity*, etc.



**Fig. 4.** TSD(C) elements and compatibility with rotations with magnitude r

## 4 Conclusions

A new method for description and identification of objects has been introduced. The concept of Typical Segment Descriptor is defined and its properties are enumerated.

The invariance of TSD to changes in starting point, translation, rotation and scaling, and its usefulness for partial occlusion detection are explained. The rotation applied to a known shape in the scene can be detected using the compatibility of the TSD.

Advantages of using TSD instead of chain codes are verified through examples with sensible reduction in the length of the description that will be used during identification.

Algorithms for the computation of the typical segment descriptors of one shape with respect to another, and to all shapes of a different class, are proposed. They can be used when the boundary is encoded using the Freeman's chain code or any other chain such as the Vertex chain code.

The efficiency of using the TSD approach for shape identification has been shown in synthetic scenes, obtaining encouraging results.

Suggestions for further work include to extend the use of typical segment descriptors to segmentation techniques, to study other properties that could be useful for detection of changes in scale.

## References

1. Sanchiz, J.M., Pla, F.: Feature Correspondence and Motion Recovery in Vehicle Planar Navigation. *Pattern Recognition* 32 (1999) 1961–1977
2. Agam, G., Dinstein, I.: Geometric Separation of Partially Overlapping Nonrigid Objects Applied to Automatic Chromosome Classification. *IEEE Trans. Pattern Analysis and Machine Intelligence* 19 (1997) 1212–1222
3. Bribeasca, E., Guzman, A.: How to describe Pure Form and How to Measure Differences in Shapes Using Shape Numbers. *Pattern Recognition* 12 (1980). 101–112
4. Pajares, G., de la Cruz, J.M.: Computer Vision, Digital Images and Applications. RA-MA, Madrid (2001)
5. Marchand-Maillet, S., Sharaiha, Y.M. : Binary Digital Image Processing: A Discrete Approach. Academic Press (2000)
6. Hatef, M., Kittler, J.: Combining Symbolic with Numeric Attributes in Multiclass Object Recognition Problems. Proceedings of the Second International Conference on Image Processing Vol. 3. Washington D.C (1995) 364–367
7. Hsu, J.C., Hwang, S.H.: A Machine Learning Approach for Acquiring Descriptive Classification Rules for Shape Contours. *Pattern Recognition* 30 (1997) 245–252
8. Freeman., H.: Techniques for the Digital Computer Analysis of Chain-encoded Arbitrary Plane Curves. *Proceedings of Nat. Electr. Conf.* 17 (1961) 421–432
9. Freeman., H.: Computer Processing of Line-drawing Images. *Computing Surveys* 6 (1974). 57–97
10. Loncaric, S.: A Survey of Shape Analysis Techniques. *Pattern Recognition* 31 (1998) 983–1001
11. Madhvanath, S., Kim, G., Govindaraju, V.: Chaincode Contour Processing for Handwritten Word Recognition. *IEEE Trans. Pattern Analysis and Machine Intelligence* 21 (1999) 928–932
12. Bribeasca, E.: A New Chain Code. *Pattern Recognition* 32 (1999) 235–251
13. Bribeasca, E.: A Chain Code for Representing 3D Curves. *Pattern Recognition* 33 (2000) 755–765
14. Valev, V.: A Method of Solving Pattern or Image Recognition Problems by Learning Boolean Formulas. *Proceedings of 11th International Conference on Pattern Recognition*. Vol 2. (1992) 359–362

15. Valev, V., Radeva, P.: Structural Pattern recognition by Non-Reducible Descriptors. Shape, Structure and Pattern Recognition. World Sci. Publ. (1995) 221–230
16. Djukova, E.V.: Pattern Recognition Algorithms of the Kora Type. Pattern Recognition, Classification, Forecasting – Mathematical Techniques and their Applications. 2 (1989) 99–125
17. Lazo, M., Douglas, M., Quintana, T.: Tests for classes: An application on character recognition, Proceedings of III Iberoamerican Workshop on Pattern Recognition (1998) 229–236
18. Pico, R., Almagro, G., Mena, J.: Logical Combinatorial Pattern Recognition application for classification of pathological mushrooms of sugar cane, Proceedings of III Iberoamerican Workshop on Pattern Recognition (1998) 279–292

# A New Approach That Selects a Single Hyperplane from the Optimal Pairwise Linear Classifier

Luis Rueda\*

School of Computer Science, University of Windsor,  
401 Sunset Avenue, Windsor, ON, Canada, N9B 3P4.  
lrueda@uwindsor.ca

**Abstract.** In this paper, we introduce a new approach to selecting the *best hyperplane classifier (BHC)* from the optimal pairwise linear classifier is given. We first propose a procedure for selecting the BHC, and analyze the conditions in which the BHC is selected. In one of the cases, it is formally shown that the BHC and *Fisher's classifier (FC)* are coincident. The empirical and graphical analysis on synthetic data and real-life datasets from the UCI machine learning repository, which involves the optimal quadratic classifier, the BHC, the optimal pairwise linear classifier, and FC.

## 1 Introduction

Linear classifiers have been extensively studied because of their classification speed and their simplicity in the implementation. We consider two classes,  $c_1$  and  $c_2$ , which are represented by two normally distributed  $d$ -dimensional random vectors,  $\mathbf{x}_1 \sim N(\boldsymbol{\mu}_1, \boldsymbol{\Sigma}_1)$  and  $\mathbf{x}_2 \sim N(\boldsymbol{\mu}_2, \boldsymbol{\Sigma}_2)$ . Thus, the statistical information about the classes is determined by the mean vectors,  $\boldsymbol{\mu}_1$  and  $\boldsymbol{\mu}_2$ , and the covariance matrices,  $\boldsymbol{\Sigma}_1$  and  $\boldsymbol{\Sigma}_2$ . We assume that these parameters are already known, or estimated by using a conventional estimation method, such as the *maximum likelihood estimate (MLE)*, the *Bayesian estimate* [4,14], etc. We also assume that the *a priori* probabilities of the two classes are equal. When dealing with two normally distributed random vectors, the general form of the optimal Bayesian classifier is quadratic. In special cases, the quadratic function can be factored as a product of two linear functions, as follows:

$$\frac{c_1}{c_2} g_1(\mathbf{x})g_2(\mathbf{x}) \leqslant 0, \quad (1)$$

where  $g_1(\mathbf{x}) = \mathbf{w}_1^t \mathbf{x} + w_1$  and  $g_2(\mathbf{x}) = \mathbf{w}_2^t \mathbf{x} + w_2$ .

This is possible when the necessary and sufficient conditions hold [11,12]. Although (1) is optimal, and it achieves high classification accuracy, it requires two linear algebraic operations to classify a single object. We will see later in this paper that using the best of these two hyperplanes leads to nearly optimal classification.

---

\* Member, IEEE. Partially supported by NSERC, the Natural Science and Engineering Research Council of Canada.

Various schemes that yield linear classifiers have been reported in the literature, including *Fisher's classifier* [4,6,13], the *perceptron algorithm* (the basis of the back propagation neural network learning algorithms) [9], *piecewise recognition models* [7], *random search optimization* [8], *removal classification structures* [1], *adaptive linear dimensionality reduction* [5] (which outperforms Fisher's classifier for some data sets), *linear constrained distance-based classifier analysis* [3] (an improvement to Fisher's approach designed for hyperspectral image classification), and *recursive Fisher's discriminant* [2].

Rueda and Oommen [11,12] have recently shown that the optimal classifier between two normally distributed classes can be linear even when the covariance matrices are not equal. They showed that although the optimal classifier for normally distributed random vectors is a second-degree polynomial, this polynomial degenerates to be either a single hyperplane or a pair of hyperplanes. In this paper, we introduce a novel approach to selecting the *best hyperplane classifier* (BHC) in the framework of optimal pairwise linear classifiers.

## 2 Optimal Pairwise Linear Classifiers

Let  $\mathbf{x}_1 \sim N(\boldsymbol{\mu}_1, \boldsymbol{\Sigma}_1)$  and  $\mathbf{x}_2 \sim N(\boldsymbol{\mu}_2, \boldsymbol{\Sigma}_2)$  be two normally distributed random vectors. The three cases and the conditions in which the optimal classifier is a pair of hyperplanes are listed below.

Case I: Suppose that<sup>1</sup>

$$\boldsymbol{\mu}_1 = -\boldsymbol{\mu}_2 = [\mu_1, \dots, \mu_d]^t, \boldsymbol{\Sigma}_1 = \mathbf{I}, \text{ and } \boldsymbol{\Sigma}_2 = \text{diag}(a_1^{-1}, \dots, a_d^{-1}). \quad (2)$$

The optimal classifier is a pair of hyperplanes if and only if any of the following conditions is satisfied.

- (i)  $0 < a_i < 1, a_j > 1, a_k = 1, \mu_k = 0$ , for all  $k = 1, \dots, d, i \neq j, k \neq i, k \neq j$ , with

$$a_i(1-a_j)\mu_i^2 + a_j(1-a_i)\mu_j^2 - \frac{1}{4}(a_ia_j - a_i - a_j + 1) \log(a_ia_j) = 0 .. \quad (3)$$

- (ii)  $a_i \neq 1, a_j = 1, \mu_j = 0$ , for all  $j \neq i ..$
- (iii)  $a_i = 1$ , for all  $i = 1, \dots, d ..$

When  $d = 2$ , and the parameters have the form of:

$$\boldsymbol{\mu}_1 = -\boldsymbol{\mu}_2 = [r, s]^t, \boldsymbol{\Sigma}_1 = \mathbf{I}, \boldsymbol{\Sigma}_2 = \text{diag}(a^{-1}, b^{-1}), \quad (4)$$

the condition of (4) is instead:

$$a(1-b)r^2 + b(1-a)s^2 - \frac{1}{4}(ab - a - b + 1) \log(ab) = 0, \quad (5)$$

---

<sup>1</sup> In this paper,  $\text{diag}(a_1, \dots, a_d)$  represents a  $d \times d$  diagonal matrix, whose diagonal elements are  $a_1, \dots, a_d$  respectively.

Case II: Suppose that

$$\boldsymbol{\mu}_1 = [\mu_1, \dots, \mu_i, \dots, \mu_j, \dots, \mu_d]^t,$$

$$\boldsymbol{\mu}_2 = [\mu_1, \dots, \mu_{i-1}, -\mu_i, \mu_{i+1}, \dots, \mu_{j-1}, -\mu_j, \mu_{j+1}, \dots, \mu_d]^t \quad (6)$$

$$\boldsymbol{\Sigma}_1 = \text{diag}(a_1^{-1}, \dots, a_i^{-1} \dots, a_j^{-1}, \dots, a_d^{-1}), \text{ and}$$

$$\boldsymbol{\Sigma}_2 = \text{diag}(a_1^{-1}, \dots, a_i^{-1} \dots, a_j^{-1}, \dots, a_d^{-1}).. \quad (7)$$

The optimal classifier is a pair of hyperplanes if and only if  $\mu_i^2 = \mu_j^2$ .

When  $d = 2$ , and the parameters are of the form:

$$\boldsymbol{\mu}_1 = -\boldsymbol{\mu}_2 = [r, s]^t, \boldsymbol{\Sigma}_1 = \text{diag}(a^{-1}, b^{-1}), \text{ and } \boldsymbol{\Sigma}_2 = \text{diag}(b^{-1}, a^{-1}), \quad (8)$$

the necessary and sufficient condition is  $r^2 = s^2$ .

Case III: Suppose that the covariance matrices have the form of (7), and  $\boldsymbol{\mu}_1 = \boldsymbol{\mu}_2$ . Then, the classifier is always a pair of hyperplanes.

### 3 Selecting the Best Hyperplane

First of all, we introduce the following definition, which will be fundamental in the criteria for selecting the BHC.

**Definition 1.** Let  $g(\mathbf{x})$  be the value resulting from classifying a vector  $\mathbf{x}$ . The sign of  $g(\mathbf{x})$ ,  $\text{sgn}(g, \mathbf{x})$ , is defined as follows:

$$\text{sgn}(g, \mathbf{x}) = \begin{cases} -1 & \text{if } g(\mathbf{x}) < 0 \\ 0 & \text{if } g(\mathbf{x}) = 0 \\ 1 & \text{if } g(\mathbf{x}) > 0 \end{cases} \quad (9)$$

In other words, a new sample falls in the “negative” side,  $\text{sgn}(g, \mathbf{x}) = -1$ , or in the “positive” side,  $\text{sgn}(g, \mathbf{x}) = 1$ . Ties are resolved arbitrarily, where we assign 0 to  $\text{sgn}(g, \mathbf{x})$ . The criteria for selecting the BHC is based on the result of classifying the two means, and uses Definition 1 to evaluate the sign resulting from the classification.

**Rule 1** Let  $\mathbf{x}_1 \sim N(\boldsymbol{\mu}_1, \boldsymbol{\Sigma}_1)$  and  $\mathbf{x}_2 \sim N(\boldsymbol{\mu}_2, \boldsymbol{\Sigma}_2)$  be two normally distributed random vectors, and  $g_1(\mathbf{x})g_2(\mathbf{x})$  be the optimal pairwise linear classifier. The BHC is selected as per the following rule.

Select:

- $g_1$ , if  $\text{sgn}(g_1, \boldsymbol{\mu}_1) \neq \text{sgn}(g_1, \boldsymbol{\mu}_2)$ ,
- $g_2$ , if  $\text{sgn}(g_2, \boldsymbol{\mu}_1) \neq \text{sgn}(g_2, \boldsymbol{\mu}_2)$ , or
- $g_1$  and  $g_2$ , if  $\text{sgn}(g_1, \boldsymbol{\mu}_1) = \text{sgn}(g_1, \boldsymbol{\mu}_2) = 0$ .

□

In other words, the BHC is the hyperplane that separates the space into two regions when the mean vectors are different. One region contains  $\boldsymbol{\mu}_1$  and the other contains  $\boldsymbol{\mu}_2$ . When the mean vectors are coincident, both  $g_1$  and  $g_2$  are the best classifiers, and hence both must be selected.

We now analyze the conditions for selecting the BHC for the case in which the covariance matrices are the identity and a diagonal matrix respectively (Case I). The formal proof of the result can be found in [10].

**Theorem 1.** Let  $\mathbf{x}_1 \sim N(\boldsymbol{\mu}_1, \boldsymbol{\Sigma}_1)$  and  $\mathbf{x}_2 \sim N(\boldsymbol{\mu}_2, \boldsymbol{\Sigma}_2)$  be two normally distributed random vectors, where the parameters have the form of (4), and

$$y_+ = \alpha(a-1)x + \alpha(a+1)r - \beta s, \text{ and} \quad (10)$$

$$y_- = \alpha(1-a)x - \alpha(a+1)r - \beta s, \quad (11)$$

be the linear functions (in their explicit form) composing the optimal pairwise linear classifier, where  $\alpha = \frac{\sqrt{\frac{1-b}{a-1}}}{b-1}$  and  $\beta = \frac{b+1}{b-1}$ .

The linear function  $g_1(\mathbf{x})$  is selected as per Rule 1, if:

$$\kappa \in (\frac{a}{b}r, r) \text{ when } g_1(\boldsymbol{\mu}_1) > 0 \text{ and } g_1(\boldsymbol{\mu}_2) < 0, \text{ or} \quad (12)$$

$$\kappa \in (r, \frac{a}{b}r) \text{ when } g_1(\boldsymbol{\mu}_1) < 0 \text{ and } g_1(\boldsymbol{\mu}_2) > 0, \quad (13)$$

$$\text{where } \kappa = s\sqrt{\frac{a-1}{1-b}}.$$

Conversely,  $g_2(\mathbf{x})$  is selected when  $\kappa$  is outside the intervals.

The extension of Theorem 1 to  $d$ -dimensional normally distributed random vectors, where  $d > 2$ , is straightforward. The conditions for which the BHC is selected are similar to those of the two-dimensional case. The formal proof for the result can be found in [10].

We now analyze another case (Case II) in which the mean vectors are in opposite directions and the diagonal covariance matrices have the two elements of their diagonal switched.

**Theorem 2.** Let  $\mathbf{x}_1 \sim N(\boldsymbol{\mu}_1, \boldsymbol{\Sigma}_1)$  and  $\mathbf{x}_2 \sim N(\boldsymbol{\mu}_2, \boldsymbol{\Sigma}_2)$  be two normally distributed random vectors whose parameters are of the form of (8). The BHC is always:

$$g_1(\mathbf{x}) = x + y = 0 \text{ if } r = s, \text{ and} \quad (14)$$

$$= x - y = 0 \text{ if } r = -s .. \quad (15)$$

The formal proof of this theorem can be found in [10]. The extension to  $d$ -dimensional normally distributed random vectors, where  $d > 2$ , can be derived by replicating the steps of the proof of Theorem 2, and substituting  $r$  and  $s$  for  $\mu_i$  and  $\mu_j$  respectively. The formalization of the result is stated and proved in [10].

We now show that for the case discussed above, i.e. when the two distributions have mean vectors of the form of (6), and covariance matrices of the form of (7), the BHC is identical to Fisher's classifier. In the theorem below [10], we show the result for  $d$ -dimensional normally distributed random vectors, where  $d \geq 2$ .

**Theorem 3.** Let  $\mathbf{x}_1 \sim N(\boldsymbol{\mu}_1, \boldsymbol{\Sigma}_1)$  and  $\mathbf{x}_2 \sim N(\boldsymbol{\mu}_2, \boldsymbol{\Sigma}_2)$  be two normally distributed random vectors whose mean vectors and covariance matrices have the form of (6) and (7) respectively. The BHC is identical to Fisher's classifier.

The third case that we consider is when we deal with two normally distributed random vectors whose covariance matrices have the form of (7), and their mean vectors are coincident. This case is the generalized Minsky's paradox for the perceptron. The result for two-dimensional normally distributed random vectors is stated as follows, and the proof is available in [10].

**Theorem 4.** Let  $\mathbf{x}_1 \sim N(\boldsymbol{\mu}_1, \boldsymbol{\Sigma}_1)$  and  $\mathbf{x}_2 \sim N(\boldsymbol{\mu}_2, \boldsymbol{\Sigma}_2)$  be two normally distributed random vectors whose covariance matrices have the form of (8), and whose mean vectors have the form  $\boldsymbol{\mu}_1 = \boldsymbol{\mu}_2$ . The BHC is composed of two linear functions:

$$g_1(\mathbf{x}) = -x - y + (r + s), \text{ and } g_2(\mathbf{x}) = x - y + (s - r) \dots \quad (16)$$

The generalization of the result above for  $d$ -dimensional normally distributed random vectors, where  $d > 2$ , follows the same steps of the proof of Theorem 4. The details of the proof are found in [10]. The result of Theorem 4 is quite useful in deciding which linear function should be selected as the BHC, a single hyperplane or the pair of hyperplane composing the optimal pairwise linear classifier. Indeed, the case in which the distributions have coincident means rarely occurs in real-life scenarios.

The extension of the BHC classifier for more than two classes is straightforward. It can be achieved by deriving the BHC for each pair of classes. Then, the classification is performed by using the Voronoi diagram constructed using all the “inter-class” BHC classifiers. How this framework works in real-life scenarios is a problem that we are currently investigating.

## 4 Classification Accuracy and Speed

In order to test the accuracy and speed of the BHC and other two linear classifiers, we have performed some simulations for the different cases discussed in Section 3. We chose the dimensions  $d = 2$  and  $d = 3$  and trained our classifier using 100 randomly generated training samples, each sample represented by a two or three dimensional vector. For each case, we considered two classes,  $c_1$  and  $c_2$ , which are represented by two normally distributed random vectors,  $\mathbf{x}_1 \sim N(\boldsymbol{\mu}_1, \mathbf{I})$  and  $\mathbf{x}_2 \sim N(\boldsymbol{\mu}_2, \boldsymbol{\Sigma}_2)$  respectively, where  $\mathbf{I}$  is the identity.

The first case that we analyze consists of two examples that instantiate two-dimensional normally distributed random vectors, 2DD-1 and 2DD-2, whose mean vectors and covariance matrices satisfy the conditions of (4). The parameters are  $\boldsymbol{\mu}_1 = -\boldsymbol{\mu}_2 \approx [0.747, 1.914]^t$ ,  $\boldsymbol{\Sigma}_2 \approx \text{diag}(0.438, 5.827)$ ,  $\boldsymbol{\mu}_1 = -\boldsymbol{\mu}_2 \approx [-1.322, -1.034]^t$ , and  $\boldsymbol{\Sigma}_2 \approx \text{diag}(2.126, 0.205)$  respectively.

The second case tested in our simulations is an example of two three-dimensional normally distributed random vectors, 3DD-1, whose covariance matrices and mean vectors, which satisfy the constraints of (2), are  $\boldsymbol{\mu}_1 = -\boldsymbol{\mu}_2 \approx [0.855, 1.776, 0]^t$  and  $\boldsymbol{\Sigma}_2 \approx \text{diag}(0.562, 3.842, 1)$ .

In each case, the OPLC was obtained using the methods described in [11,12]. The BHC was obtained by invoking Rule 1 introduced in Section 3, and Fisher’s classifier (FC) was obtained using the method described in [4].

To test the classifiers, we then generated ten sets each containing 100 random samples for each class using the original parameters. The results obtained after testing the three classifiers are shown in Table 1. The classification accuracy was computed as the average of the percentage of testing samples that were correctly classified for each of the ten data sets. Besides for each individual data set, the average between the classification accuracies for classes  $c_1$  and  $c_2$  was computed. The classification speed represents the average number of CPU seconds taken to classify 100 testing samples.

**Table 1.** Classification accuracy and speed obtained after testing three linear classifiers, OPLC, BHC and FC, on randomly generated data sets.

Example	OPLC		BHC		FC	
	Accuracy	Speed	Accuracy	Speed	Accuracy	Speed
2DD-1	92.15	4.48	91.85	1.75	91.15	1.80
2DD-2	96.20	4.38	96.15	1.73	95.15	1.79
3DD-1	93.40	4.57	93.30	2.11	92.35	1.82

For the first two examples, 2DD-1 and 2DD-2, the classification accuracy of the BHC is very close to that of the OPLC, and higher than that of FC. For the three-dimensional example, 3DD-1, we again observe the superiority of the BHC over FC. We also see that the BHC attains nearly optimal classification – just 0.1% less than the optimal classifier, OPLC. The BHC and FC are more than twice as fast as the OPLC, and both the BHC and FC achieve comparable speed rates. In Figure 1 the BHC, the OPLC, and the samples of one of the testing data sets for each class, are plotted. It is clearly seen that FC misclassified objects which are in a region where the samples are more likely to occur. Similar plots for the other two examples are available in [10].

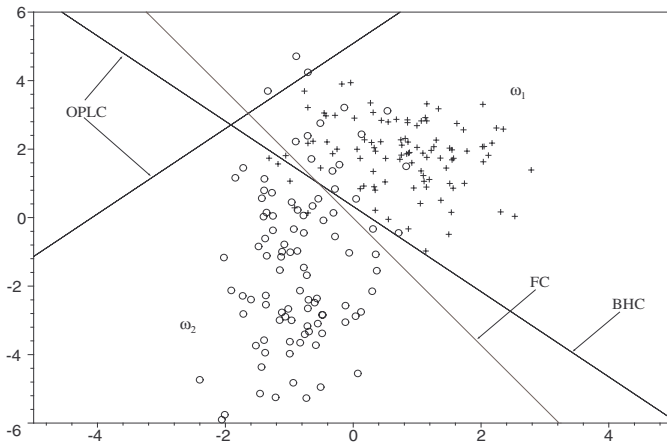


**Fig. 1.** Testing samples and the corresponding classifiers for two-dimensional normally distributed random vectors whose parameters are those of Example 2DD-1.

We also conducted experiments on real-life datasets. For the training and classification tasks we have composed 10 data subsets with all possible pairs of features obtained from the first five numeric features. For each of the pairs we composed the training set and the testing set by drawing samples without replacement from the original datasets.

The OQC and FC have been trained by invoking the traditional maximum likelihood method (MLE) [4,14]. The OPLC and the BHC have been trained by following the procedure described in [10], thus yielding the approximated pairwise linear classifier, and subsequently the best hyperplane, for each subset.

The classification of each object was performed using the classifiers mentioned above, and invoking a voting scheme, which assigns the class in which the sample yielded a positive result for the majority of voters. Ten voting rounds were invoked (one for each pair of features), and thus, the majority for class  $c_1$  was chosen to be *five* or more voters. From the WDBC dataset, we randomly selected, without replacement, 100 samples for training, and 100 samples for the testing phase for each class. The classification accuracy obtained from testing the OQC, the OPLC, the BHC and FC are shown in Table 2. The results on the table show that using the voting scheme, as expected, the OQC is more accurate than the other classifiers. We also observe that the OPLC and the BHC (both achieving the same classification accuracy) lead to higher classification accuracy than FC. When considering the pair-based classification, the averages on the fifth column show that the OQC was the most accurate classifier. In this scheme, the BHC outperformed the OPLC, and FC was the least accurate classifier. We also observe that on the WDBC, the OPLC and the BHC achieve nearly optimal classification. Similar results that show the efficiency of the BHC, and a graphical analysis on real-life date are available in [10].

**Table 2.** Classification accuracy obtained from testing the classifiers on the WDBC data set.

Classifier	Benign	Malignant	Avg.(voting)	Avg.(pair)
OQC	96.00	87.00	91.50	88.45
OPLC	95.00	86.00	90.50	87.85
BHC	95.00	86.00	90.50	88.05
FC	93.00	85.00	89.00	86.30

## 5 Conclusions

In this paper, we presented an approach that selects the best hyperplane classifier (BHC) from the optimal pairwise linear classifier (OPLC). We first introduced the criteria for selecting the BHC given the OPLC. We then formalized the conditions for selecting the BHC for three cases. In the second case (the most general scenario for multi-dimensional random vectors), we have shown that the BHC is identical to Fisher's classifier (FC).

The efficiency of the BHC, the OPLC and FC has been evaluated in terms of classification accuracy and speed. In terms of accuracy, we have shown that the BHC is nearly optimal, and in some cases, it achieves the same accuracy as FC. The empirical results on real-life datasets show that the OPLC and the BHC attained similar classification accuracy, and that the BHC is superior to FC in the WDBC datasets. The graphical analysis corroborates this relation.

The extension of the BHC for  $d$ -dimensional random vectors, where  $d > 2$ , is far from trivial, as it involves to derive an MLE method for the constrained pairwise linear classifier. How this MLE is designed, and how the corresponding BHC is derived is a problem that is currently being undertaken.

## References

1. M. Aladjem. Linear Discriminant Analysis for Two Classes Via Removal of Classification Structure. *IEEE Trans. on Pattern Analysis and Machine Intelligence*, 19(2):187–192, 1997.
2. T. Cooke. Two Variations on Fisher’s Linear Discriminant for Pattern Recognition. *IEEE Transactions on Pattern Analysis and Machine Intelligence*, 24(2):268–273, 2002.
3. Q. Du and C. Chang. A Linear Constrained Distance-based Discriminant Analysis for Hyperspectral Image Classification. *Pattern Recognition*, 34(2):361–373, 2001.
4. R. Duda, P. Hart, and D. Stork. *Pattern Classification*. John Wiley and Sons, Inc., New York, NY, 2nd edition, 2000.
5. R. Lotlikar and R. Kothari. Adaptive Linear Dimensionality Reduction for Classification. *Pattern Recognition*, 33(2):185–194, 2000.
6. W. Malina. On an Extended Fisher Criterion for Feature Selection. *IEEE Transactions on Pattern Analysis and Machine Intelligence*, 3:611–614, 1981.
7. A. Rao, D. Miller, K. Rose, , and A. Gersho. A Deterministic Annealing Approach for Parsimonious Design of Piecewise Regression Models. *IEEE Transactions on Pattern Analysis and Machine Intelligence*, 21(2):159–173, 1999.
8. S. Raudys. On Dimensionality, Sample Size, and Classification Error of Nonparametric Linear Classification. *IEEE Transactions on Pattern Analysis and Machine Intelligence*, 19(6):667–671, 1997.
9. S. Raudys. Evolution and Generalization of a Single Neurone: I. Single-layer Perception as Seven Statistical Classifiers. *Neural Networks*, 11(2):283–296, 1998.
10. L. Rueda. Selecting the Best Hyperplane in the Framework of Optimal Pairwise Linear Classifiers. Technical Report 02-009, School of Computer Science, University of Windsor, Windsor, Canada, 2002.
11. L. Rueda and B. J. Oommen. On Optimal Pairwise Linear Classifiers for Normal Distributions: The Two-Dimensional Case. *IEEE Transactions on Pattern Analysis and Machine Intelligence*, 24(2):274–280, February 2002.
12. L. Rueda and B. J. Oommen. On Optimal Pairwise Linear Classifiers for Normal Distributions: The  $d$ -Dimensional Case. *Pattern Recognition*, 36(1):13–23, January 2003.
13. R. Schalkoff. *Pattern Recognition: Statistical, Structural and Neural Approaches*. John Wiley and Sons, Inc., 1992.
14. A. Webb. *Statistical Pattern Recognition*. John Wiley & Sons, N.York, second edition, 2002.

# A Characterization of Discretized Polygonal Convex Regions by Discrete Moments

Joviša Žunić\*

Computer Science, Cardiff University, Queen's Buildings,  
Newport Road, Cardiff CF24 3XF, Wales, U.K.  
[J.Zunic@cs.cf.ac.uk](mailto:J.Zunic@cs.cf.ac.uk)

**Abstract.** For a given planar region  $P$  its discretization on a discrete planar point set  $\mathcal{S}$  consists of the points from  $\mathcal{S}$  which fall into  $P$ . If  $P$  is bounded with a convex polygon having  $n$  vertices and the number of points from  $P \cap \mathcal{S}$  is finite, the obtained discretization of  $P$  will be called *discrete convex  $n$ -gon*.

In this paper we show that discrete moments having the order up to  $n$  characterize uniquely the corresponding discrete convex  $n$ -gon if the discretizing set  $\mathcal{S}$  is fixed. In this way, as an example, the matching of discrete convex  $n$ -gons can be done by comparing  $\frac{1}{2} \cdot (n+1) \cdot (n+2)$  discrete moments what can be much efficient than the comparison “point-by-point” since a digital convex  $n$ -gon can consist of an arbitrary large number of points.

**Keywords:** Discrete shape, coding, moments, pattern matching.

## 1 Introduction

It is known for many years that the moments are good descriptors of real shapes ([4,8]). They are used in many computer vision, image processing, and pattern recognition tasks ([2,5]). For simple “continuous” shapes as they are lines, circles, ellipses,... a finite set of moments is sufficient for recovering the original shape – usually, it is enough to solve a system of equations. If we try to reconstruct regions bounded by convex polygons (triangles, quadrangles,...) the problem of reconstruction of the original shape from a set of moments becomes more complicated but still solvable. The complication comes from the fact that there are no suitable equations for the boundaries of such polygonal convex regions.

But, in computer applications of the “moment techniques” we manipulate mostly with discrete data – not with real objects described by their equations. In areas as they are pattern recognition, pattern classification, (digital) image analysis, e.t.c., real objects are replaced with their discretizations – i.e., they are represented by finite point sets which are obtained by some discretizing process. It implies that there are infinitely many real shapes with the same discretization.

---

\* The author is also with the Mathematical institute of Serbian Academy of Sciences and Arts, Belgrade.

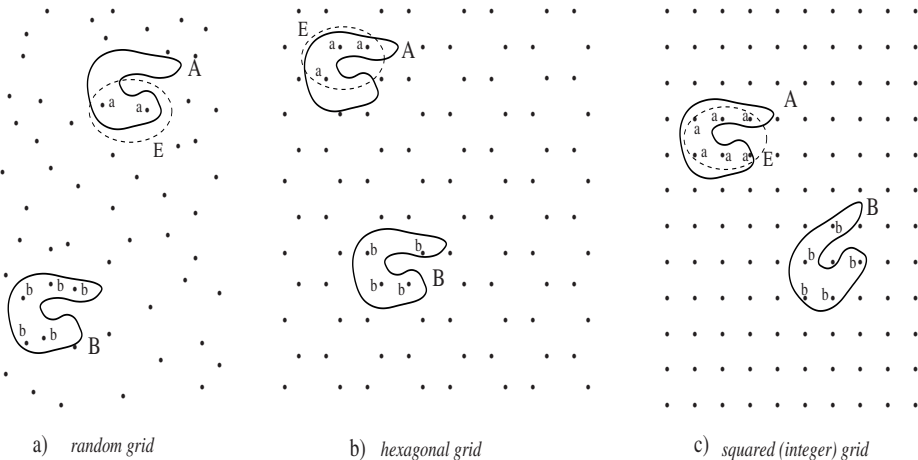


**Fig. 1.** Discretizations of isometric shapes  $A$  (points labeled by  $a$ ) and  $B$  (points labeled by  $b$ ) on three different discretizing sets are shown. In all presented cases, the discretizations of  $A$  and  $B$  are non-isometric, but discretizations of  $A$  coincide with the discretizations of a given ellipse  $E$ .

So, even if we know an equation of the real object (what usually does not happen in the mentioned research areas), it is not suitable to represent the discrete image of a given real object by the corresponded equation because it can be happened that the considered digital object has many different characterizations (see discretizations of the shape  $A$  from Fig. 1). More over, isometric planar regions may have non-isometric discretizations on the same discretizing set (see discretizations of the shapes  $A$  and  $B$  from Fig. 1) which also shows that the use of the “original objects” (sometimes called *preimages*) for a characterization of a given discrete object could be inappropriate.

Here, we prove that discrete moments having the order up to  $n$  are enough for a unique characterization of discrete convex  $n$ -gons presented on a fixed discrete set. In this way, as an example, a fast comparison between discrete convex  $n$ -gons is enabled. In case of a relatively small number of edges of digitized convex polygons with respect to the number of sample points the comparison of the corresponded discrete moments can be much faster than than the comparison “point-by-point”.

We conclude this introduction with the basic definitions and denotations.

By *discrete convex  $n$ -gon* we mean the discretization of a planar region which is bounded by a convex  $n$ -gon. Formally, a *discrete convex  $n$ -gon*  $\mathbf{D}(P)$ , (see Fig. 2) from a fixed discrete point set  $\mathcal{S}$  is defined as

$$\mathbf{D}(P) = \{(x, y) \mid (x, y) \in P \cap \mathcal{S}, \text{ the boundary of region } P \text{ is a convex } n\text{-gon}\}.$$

Throughout the paper, it will be assumed but not mentioned, any appearing discrete convex  $n$ -gons consists of a finite number of points. For an illustration,

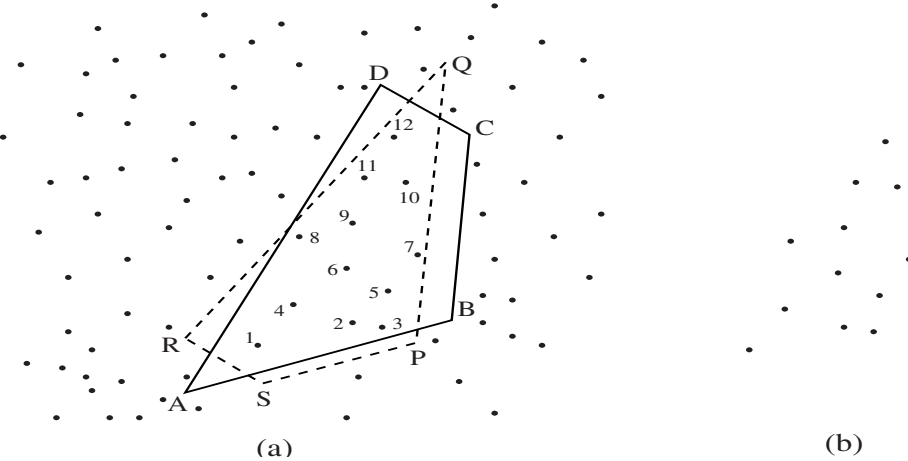


**Fig. 2.** (a) Discretizations of non isometric quadrangles  $ABCD$  and  $PQRS$  are identical and they consist of 12 numbered points. (b) During the discretization process the vertices  $A, B, C$ , and  $D$  (i.e.,  $P, Q, R$ , and  $S$ ) are usually unknown. We can only manipulate with the obtained discrete set (i.e., discrete 4-gon).

the discretizations on the set consisting of all points with the coordinates which are rational numbers (i.e.,  $\mathcal{S} = \mathbf{Q}^2$ ) are not considered.

Since the characterization of discrete convex  $n$ -gons described here is based on a suitable use of *discrete moments* we give a precise definition. The *discrete moment*  $\mu_{p,q}(X)$  of a finite number point set  $X$  is:

$$\mu_{p,q}(X) = \sum_{(x,y) \in X} x^p \cdot y^q.$$

The moment  $\mu_{p,q}(X)$  has the order  $p + q$ . In the rest of the paper it will be assumed (even not mentioned) that  $p$  and  $q$  are nonnegative integers. The set of nonnegative integers is denoted by  $\mathbf{N}_0$ .

Through the paper a *finite set* means a set consisting of a finite number of points. Also, a *unique characterization* and a *coding* will have the same meaning.

We shall say that a continuous function  $z = f(x, y)$  separates sets  $A$  and  $B$  if the sign of  $f(x, y)$  in the points from  $A$  differs from the sign of  $f(x, y)$  in the points from  $B$ . Precisely, it is

either  $A \subset \{(x, y) \mid f(x, y) > 0\}$  and  $B \subset \{(x, y) \mid f(x, y) < 0\}$ ,  
or  $A \subset \{(x, y) \mid f(x, y) < 0\}$  and  $B \subset \{(x, y) \mid f(x, y) > 0\}$ .

Some examples are given on Fig. 3.

## 2 Characterization of Discrete Convex $n$ -gons

In this section it will be shown that the discrete moments having order up to  $n$  match uniquely the discretized polygonal convex  $n$ -gon presented on a fixed set  $\mathcal{S}$ . We start with the following theorem.

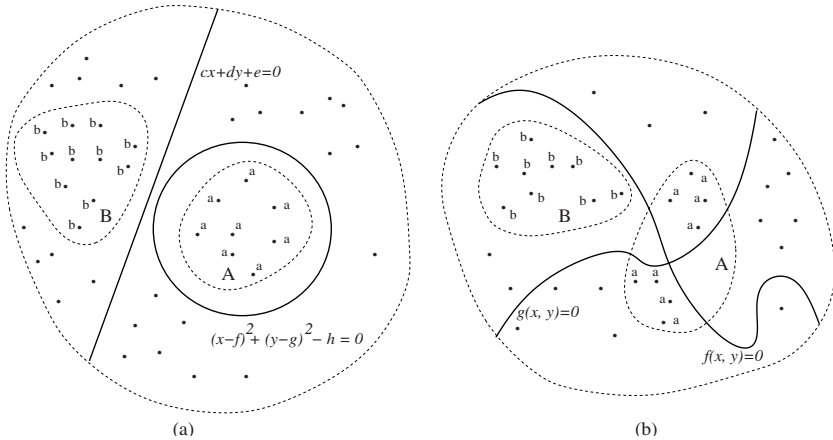


**Fig. 3.** (a)  $z = c \cdot x + d \cdot y + e$  separates discrete sets  $A$  (points labeled by  $a$ ) and  $B$  (points labeled by  $b$ ).  $z = (x - f)^2 + (y - g)^2 - h$  also separates  $A$  and  $B$ . But,  $z = (c \cdot x + d \cdot y + e) \cdot ((x - f)^2 + (y - g)^2 - h)$  does not separate  $A$  and  $B$ .  
(b)  $z = f(x, y)$  does not separate the sets  $A$  (points labeled by  $a$ ) and  $B$  (points labeled by  $b$ ).  $z = g(x, y)$  also does not separate  $A$  and  $B$ . But,  $z = f(x, y) \cdot g(x, y)$  separates  $A$  and  $B$ .

**Theorem 1.** Let  $A_1$  and  $A_2$  be two finite planar sets. If there exists a function of the form

$$f(x, y) = \sum_{p+q \leq k} \alpha_{p,q} \cdot x^p \cdot y^q, \quad \text{where } p, q \in \mathbf{N}_0 \quad (1)$$

which separates  $A_1 \setminus A_2$  and  $A_2 \setminus A_1$  then

$$\mu_{p,q}(A_1) = \mu_{p,q}(A_2) \quad \text{with } p, q \in \mathbf{N}_0 \quad \text{and } p + q \leq k$$

is equivalent to  $A_1 = A_2$ .

*Proof.* If  $A_1 = A_2$  then the corresponding discrete moments are equal obviously. It remains to prove that the equality of the corresponded moments of the order up to  $k$  preserves  $A_1 = A_2$ . We prove that  $A_1 \neq A_2$  and

$$\sum_{(x,y) \in A_1} x^p \cdot y^q = \mu_{p,q}(A_1) = \mu_{p,q}(A_2) = \sum_{(x,y) \in A_2} x^p \cdot y^q$$

(satisfied for all  $p, q \in \mathbf{N}_0$  with  $p + q \leq k$ ) lead to a contradiction. Since  $A_1 \neq A_2$  we can assume  $A_1 \setminus A_2 \neq \emptyset$  (else we can start with  $A_2 \setminus A_1 \neq \emptyset$ ). Further, because there exists a function  $f(x, y) = \sum_{p+q \leq k} \alpha_{p,q} \cdot x^p \cdot y^q$  which separates  $A_1 \setminus A_2$  and  $A_2 \setminus A_1$ , we can assume (for instance)  $f(x, y) > 0$  if  $(x, y) \in A_1 \setminus A_2$ , while  $(x, y) \in A_2 \setminus A_1$  implies  $f(x, y) < 0$ . Now, we are able to derive the contradiction  $0 < 0$  which finishes the proof.

$$0 < \sum_{(x,y) \in A_1 \setminus A_2} f(x, y) - \sum_{(x,y) \in A_2 \setminus A_1} f(x, y)$$

$$\begin{aligned}
&= \sum_{p+q \leq k} \left( \sum_{(x,y) \in A_1 \setminus A_2} \alpha_{p,q} \cdot x^p \cdot y^q + \sum_{(x,y) \in A_1 \cap A_2} \alpha_{p,q} \cdot x^p \cdot y^q \right) \\
&- \sum_{p+q \leq k} \left( \sum_{(x,y) \in A_2 \setminus A_1} \alpha_{p,q} \cdot x^p \cdot y^q + \sum_{(x,y) \in A_1 \cap A_2} \alpha_{p,q} \cdot x^p \cdot y^q \right) \\
&= \sum_{p+q \leq k} \left( \alpha_{p,q} \cdot \sum_{(x,y) \in A_1} x^p \cdot y^q - \alpha_{p,q} \cdot \sum_{(x,y) \in A_2} x^p \cdot y^q \right) = 0. \quad \blacksquare
\end{aligned}$$

Next, we prove the main result of the paper.

**Theorem 2.** Fix a discrete point set  $\mathcal{S}$ . Let given discrete convex  $n$ -gons  $\mathbf{D}(P)$ ,  $\mathbf{D}(P_1) \subset \mathcal{S}$ . Then

$$(\mu_{p,q}(\mathbf{D}(P)) = \mu_{p,q}(\mathbf{D}(P_1)) \text{ with } p+q \leq n, p, q \in \mathbf{N}_0) \implies \mathbf{D}(P) = \mathbf{D}(P_1).$$

*Proof.* Let  $\mathbf{D}(P)$  and  $\mathbf{D}(P_1)$  be different discrete convex  $n$ -gons. We will show that there always exists a separating function of the form (1) (with  $k \leq n$ ) which separates  $\mathbf{D}(P) \setminus \mathbf{D}(P_1)$  and  $\mathbf{D}(P_1) \setminus \mathbf{D}(P)$ . Then, the statement will follow directly from Theorem 1, specifying  $A_1 = \mathbf{D}(P)$  and  $A_2 = \mathbf{D}(P_1)$ .

Since  $\mathbf{D}(P) \neq \mathbf{D}(P_1)$  and  $\mu_{0,0}(\mathbf{D}(P)) = \mu_{0,0}(\mathbf{D}(P_1))$  are assumed, we have  $\mathbf{D}(P) \setminus \mathbf{D}(P_1) \neq \emptyset$  and  $\mathbf{D}(P_1) \setminus \mathbf{D}(P) \neq \emptyset$ .

For convenience and without loss of generality we can assume that  $P$  and  $P_1$  do not have common vertices and common edges, but also that there is no edge of  $P$  (i.e.,  $P_1$ ) which belongs to the boundary of  $P_1$  (i.e.,  $P$ ) – such an assumption is possible because  $\mathbf{D}(P)$  and  $\mathbf{D}(P_1)$  are finite number point sets.

Let we consider the set-intersection of  $P$  and  $P_1$  and let

$$\begin{aligned}
A_1, A_2, \dots, A_{i_1} &\equiv B_1, B_2, \dots, B_{j_1} \equiv \\
\equiv A_{i_1+1}, A_{i_1+2}, \dots, A_{i_2} &\equiv B_{j_1+1}, B_{j_1+2}, \dots, B_{j_2}, \\
&\dots \dots \\
A_{i_{k-1}+1}, A_{i_{k-1}+2}, \dots, A_{i_k} &\equiv B_{j_{k-1}+1}, B_{j_{k-1}+2}, \dots, B_{j_k} \equiv A_1
\end{aligned}$$

be the vertices of  $P \cap P_1$  listed in the counterclockwise order and denoted in such a way that the line segments

$$\begin{aligned}
&[A_1, A_2], \dots, [A_{i_1-1}, A_{i_1}], \\
&[A_{i_1+1}, A_{i_1+2}], \dots, [A_{i_2-1}, A_{i_2}], \\
&\dots \dots \dots, \\
&[A_{i_{k-1}+1}, A_{i_{k-1}+2}], \dots, [A_{i_k-1}, A_{i_k}]
\end{aligned}$$

belong to the boundary of  $P$ , while

$$\begin{aligned}
&[B_1, B_2], \dots, [B_{j_1-1}, B_{j_1}], \\
&[B_{j_1+1}, B_{j_1+2}], \dots, [B_{j_2-1}, B_{j_2}], \\
&\dots \dots \dots, \\
&[B_{j_{k-1}+1}, B_{j_{k-1}+2}], \dots, [B_{j_k-1}, B_{j_k}]
\end{aligned}$$

belong to the boundary of  $P_1$ . Further, let

- $\alpha_1 \cdot x + \beta_1 \cdot y - \gamma_1 = 0$  be the line  $l_1$  determined by  $A_1$  and  $A_{i_1}$ ;
- $\alpha_2 \cdot x + \beta_2 \cdot y - \gamma_2 = 0$  be the line  $l_2$  determined by  $A_{i_1+1}$  and  $A_{i_2}$ ;
- .....
- $\alpha_k \cdot x + \beta_k \cdot y - \gamma_k = 0$  be the line  $l_k$  determined by  $A_{i_{k-1}+1}$  and  $A_{i_k}$ .

Then we will show that the function

$$f(x, y) = \prod_{i=1}^k (\alpha_i \cdot x + \beta_i \cdot y - \gamma_i) \quad (2)$$

separates the set-differences  $\mathbf{D}(P) \setminus \mathbf{D}(P_1)$  and  $\mathbf{D}(P_1) \setminus \mathbf{D}(P)$ .

Namely, since the points

$$A_1, A_{i_1}, A_{i_1+1}, A_{i_2}, A_{i_{k-1}+1}, A_{i_k}$$

are successive intersection points of the boundaries of  $P$  and  $P_1$ , we have:

- i) for any  $i$  from  $\{1, 2, \dots, k\}$ , all points from  $\mathbf{D}(P) \setminus \mathbf{D}(P_1)$  belong to the same half-plane determined by the line  $l_i$  – consequently,  $f(x, y)$  in all points from  $\mathbf{D}(P_1) \setminus \mathbf{D}(P)$  takes the same sign;
- ii) for any point  $X$  from  $\mathbf{D}(P_1) \setminus \mathbf{D}(P)$  there is exactly one integer  $i$  from  $\{1, \dots, n\}$  such that  $l_i$  separates  $X$  from  $\mathbf{D}(P) \setminus \mathbf{D}(P_1)$ . In other words, the function  $f(x, y)$  takes the same sign in all points from  $\mathbf{D}(P_1) \setminus \mathbf{D}(P)$  and the sign differs from the sign taken in the points from  $\mathbf{D}(P) \setminus \mathbf{D}(P_1)$ .

The items i) and ii) imply that  $f(x, y)$  is a separating function for  $\mathbf{D}(P) \setminus \mathbf{D}(P_1)$  and  $\mathbf{D}(P_1) \setminus \mathbf{D}(P)$ .

Let us mention here that another separating function for the same set-differences is

$$\tilde{f}(x, y) = \prod_{i=1}^k (\tilde{\alpha}_i \cdot x + \tilde{\beta}_i \cdot y - \tilde{\gamma}_i) \quad (3)$$

where

- $\tilde{\alpha}_1 \cdot x + \tilde{\beta}_1 \cdot y - \tilde{\gamma}_1 = 0$  is the line  $\tilde{l}_1$  determined by  $B_1$  and  $B_{j_1}$ ;
- $\tilde{\alpha}_2 \cdot x + \tilde{\beta}_2 \cdot y - \tilde{\gamma}_2 = 0$  is the line  $\tilde{l}_2$  determined by  $B_{j_1+1}$  and  $B_{j_2}$ ;
- .....
- $\tilde{\alpha}_k \cdot x + \tilde{\beta}_k \cdot y - \tilde{\gamma}_k = 0$  is the line  $\tilde{l}_k$  determined by  $B_{j_{k-1}+1}$  and  $B_{j_k}$ .

Due to Theorem 1, the existence of a function of the form (1) which separates  $\mathbf{D}(P) \setminus \mathbf{D}(P_1)$  and  $\mathbf{D}(P_1) \setminus \mathbf{D}(P)$  (we can take either (2) or (3)) completes the proof.  $\blacksquare$

The previous proof is illustrated by Fig. 4. In the given example  $n = 7$ ,  $k = 3$ , and two separating functions are described in the capture of the figure.

### 3 Comments and Conclusion

In this paper we consider finite number point subsets of a fixed discrete point set  $\mathcal{S}$  which are occupied by planar regions whose boundaries are convex  $n$ -gons. Such sets are called discrete convex  $n$ -gons. Through the manuscript, there is no any assumption about the structure of  $\mathcal{S}$ . We derive a result which shows that there are no two different discrete convex  $n$ -gons whose corresponded discrete moments of the order up to  $n$  coincide. Or, more formally, the mapping

$$\mathbf{D}(P) \longrightarrow (\mu_{0,0}(\mathbf{D}(P)), \mu_{0,1}(\mathbf{D}(P)), \mu_{1,0}(\mathbf{D}(P)), \dots, \mu_{0,n}(\mathbf{D}(P)), \mu_{1,n-1}(\mathbf{D}(P)), \dots, \mu_{n,0}(\mathbf{D}(P)))$$

is one-to-one while  $\mathbf{D}(P)$  belongs to the set of digital convex  $n$ -gons.

A precise performance analysis could not be given since there are no assumption about the structure of  $\mathcal{S}$ . In any case, it can be said that the result enables the matching of discrete convex  $n$ -gons by comparing  $\frac{(n+1)\cdot(n+2)}{2}$  numbers (which are all discrete moments of the order up to  $n$ ) instead of the comparing “point-by-point”. Obviously, the comparison “point-by-point” can be very expensive

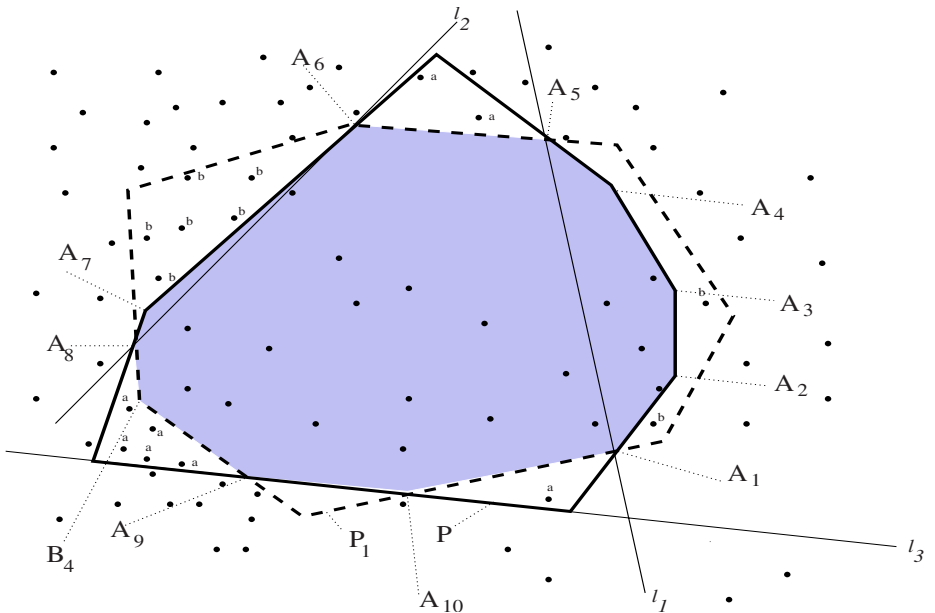


**Fig. 4.**  $f(x, y) = \prod_{i=1}^{i=3} (\alpha_{l_i} \cdot x + \beta_{l_i} \cdot y - \gamma_{l_i})$  is a separating function for  $\mathbf{D}(P) \setminus \mathbf{D}(P_1)$  (points labeled by  $a$ ), and  $\mathbf{D}(P_1) \setminus \mathbf{D}(P)$  (points labeled by  $b$ ).

In accordance with denotations from the proof of Theorem 2,  $B_1 \equiv A_5$ ,  $B_2 \equiv A_6$ ,  $B_3 \equiv A_8$ ,  $B_5 \equiv A_9$ ,  $B_6 \equiv A_{10}$ , and  $B_7 \equiv A_1$ . The function which is the product of the linear functions corresponded to lines determined by pairs of points  $(B_1, B_2)$ ,  $(B_3, B_5)$ , and  $(B_6, B_7)$  is also a function which separates  $\mathbf{D}(P) \setminus \mathbf{D}(P_1)$  and  $\mathbf{D}(P_1) \setminus \mathbf{D}(P)$ .

because the discrete convex  $n$ -gons may consist of an arbitrary large number of points. In areas of practical applications  $\mathcal{S}$  can correspond to the set of sensors or to the set of reference points whose choice depends of the nature of application.

Of course, more precise analysis can be done in the area of digital image analysis - i.e., if  $\mathcal{S}$  is an integer (squared) grid (it is planned as a future work). In the literature, the problems related to digital squares are already considered. In [3,9] the recognition problem is studied.

It is worth to mention that the representation (coding) problem for digital convex polygons from an integer grid can be solved by decomposing the boundary of the considered digital polygon onto digital straight line segments and, after that, to characterize (code) the obtained straight line segments. Both, efficient algorithms for the decomposition of digital curves into maximal straight line segments and efficient coding scheme for digital straight line segments already exist – see [6,10] and [1,7]. Let us notice, that the coding scheme presented here is expected to be more robust because it is not based on the boundary points only, as it would be in the case of the coding based on the boundary decomposition into digital straight line segments. Also, such a coding procedure could not be applied to discrete convex polygons from an arbitrary discretizing set.

## References

1. Dorst, L., Smeulders, A. W. M.: Discrete representation of straight lines. *IEEE Trans. Pattern Anal. Machine Intell.* **6** (1984) 450–463.
2. Duda, R. O., Hart, P. E.: *Pattern Classification and Scene Analysis*. Wiley, New York, USA, 1973.
3. Forchhammer, S., Kim, C. E.: Digital squares. *IEEE Trans. Pattern Anal. Machine Intell.* **22** (1988) 672–674.
4. Hu, M.: Visual pattern recognition by moment invariants, *IRE Trans. Inf. Theory* **8** (1962) 179–187.
5. Jain, R., Kasturi, R., Schunck, B. G.: *Machine Vision*. McGraw-Hill, New York, USA, 1995.
6. Lindenbaum, M., Bruckstein, A.: “On recursive,  $\mathcal{O}(N)$  partitioning of a digitized curve into digital straight segments,” *IEEE Trans. Pattern Anal. Machine Intell.* **15** (1993) 949–953.
7. Lindenbaum, M., Koplowitz, J.: A new parametrization of digital straight lines. *IEEE Trans. Pattern Anal. Machine Intell.* **13** (1991) 847–852.
8. Mamistvalov, A. G.:  $n$ -Dimensional moment invariants and conceptual mathematical theory of recognition  $n$ -dimensional solids. *IEEE Trans. Pattern Anal. Machine Intell.* **20** (1998) 819–831.
9. Nakamura, A., Aizawa, K.: Digital squares. *Computer Vision, Graphics Image Processing* **49** (1990) 357–368.
10. Smeulders, A. W. M., Dorst, L.: “Decomposition of discrete curves into piecewise straight segments in linear time,” in *Vision Geometry* (P. Bhattacharya, A. Rosenfeld, eds.), *American Mathematical Society, series Contemporary Mathematics*, **119** (1991) 169–195.

# Learning Probabilistic Context-Free Grammars from Treebanks

Jose L. Verdú-Mas, Jorge Calera-Rubio, and Rafael C. Carrasco \*

Departamento de Lenguajes y Sistemas Informáticos  
Universidad de Alicante, E-03071 Alicante, Spain.  
[{verdu,calera,carrasco}@dlsi.ua.es](mailto:{verdu,calera,carrasco}@dlsi.ua.es)

**Abstract.** This paper describes the application of a new model to learn probabilistic context-free grammars (PCFGs) from a tree bank corpus. The model estimates the probabilities according to a generalized  $k$ -gram scheme for trees. It allows for faster parsing, decreases considerably the perplexity of the test samples and tends to give more structured and refined parses. In addition, it also allows several smoothing techniques such as *backing-off* or *interpolation* that are used to avoid assigning zero probability to any sentence.

## 1 Introduction

Context-free grammars may be considered to be the customary way of representing syntactical structure in natural language sentences. In many natural-language processing applications, obtaining the correct syntactical structure for a sentence is an important intermediate step before assigning an interpretation to it. But ambiguous parses are very common in real natural-language sentences (e.g., those longer than 15 words). A set of rather radical hypotheses as to how humans select the best parse tree [1] propose that a great deal of syntactic disambiguation may actually occur without the use of any semantic information; that is, just by selecting a preferred parse tree. It may be argued that the preference of a parse tree with respect to another is largely due to the relative frequencies with which those choices have lead to a successful interpretation. This sets the ground for a family of techniques which use a probabilistic scoring of parses to the correct parse in each case.

Probabilistic scorings depend on parameters which are usually estimated from data, that is, from parsed text corpora such as the Penn Treebank [2]. The most straightforward approach is that of *treebank grammars*, [3]. Treebank grammars are probabilistic context-free grammars in which the probability that a particular nonterminal is expanded according to a given rule is estimated as the relative frequency of that expansion by simply counting the number of times it appears in a manually-parsed corpus. This is the simplest probabilistic scoring

\* The authors wish to thank the Generalitat Valenciana project CTIDIB/2002/173 and the Spanish CICYT project TIC2000-1599 for supporting this work.

scheme, and it is not without problems; we will show how a set of approximate models, which we will call *offspring-annotated* models, in which expansion probabilities are dependent on the future expansions of children, may be seen as a generalization of the classic  $k$ -gram models to the case of trees, and include treebank grammars as a special case; other models, such as Johnson's [4] *parent-annotated* models (or more generally, *ancestry annotated* models) and IBM history-based grammars [5, p. 423],[6] offer an alternate approach in which the probability of expansion of a given nonterminal is made dependent on the previous expansions. An interesting property of many of these models is that, even though they may be seen as context-dependent, they may still be easily rewritten as context-free models in terms of specialized versions of the original nonterminals.

The next section proposes our generalization of the classic  $k$ -gram models to the case of trees, which is shown to be equivalent to having a specialized context-free grammar. A simplification of this model, called the *child-annotated* model or  $k = 3$ , for short, is also presented in that section.

## 2 The Model

Let  $\Omega = \{\tau_1, \tau_2, \dots, \tau_{|\Omega|}\}$  be a treebank, that is, a sample of parse trees.

For all  $k > 0$  and for all trees  $\tau = \sigma(t_1 t_2 \dots t_m) \in \Omega$  we define the  $k$ -root of  $\tau$  as the tree

$$r_k(\sigma(t_1 \dots t_m)) = \begin{cases} \sigma & \text{if } k = 1 \\ \sigma(r_{k-1}(t_1) \dots r_{k-1}(t_m)) & \text{otherwise} \end{cases} \quad (1)$$

The sets  $f_k(t)$  of  $k$ -forks and  $s_k(t)$  of  $k$ -subtrees are defined for all  $k > 0$  as follows:

$$f_k(\sigma(t_1 \dots t_m)) = \cup_{j=1}^m f_k(t_j) \cup \begin{cases} \emptyset & \text{if } 1 + \text{depth}(\sigma(t_1 \dots t_m)) < k \\ r_k(\sigma(t_1 \dots t_m)) & \text{otherwise} \end{cases} \quad (2)$$

$$s_k(\sigma(t_1 \dots t_m)) = \cup_{j=1}^m s_k(t_j) \cup \begin{cases} \sigma(t_1 \dots t_m) & \text{if } 0 < \text{depth}(\sigma(t_1 \dots t_m)) < k \\ \emptyset & \text{otherwise} \end{cases} \quad (3)$$

where  $\text{depth}(t)$  denotes the depth of the tree  $t$  having in own that in a single node tree it is zero.

We define the treebank probabilistic  $k$  testable grammar  $G = (\mathcal{N}, \Sigma, \mathcal{S}, \mathcal{P})$  through:

- $\mathcal{N} = r_{k-1}(f_k(\Omega)) \cup s_{k-1}(\Omega) \cup \{\mathcal{S}\}$ ;
- $\Sigma$  is the set of labels in  $\Omega$ ;
- $\mathcal{S}$  is the start symbol;

- $\mathcal{P} = \{(r, p(r)) \mid r \in R \wedge p(r) \in [0, 1]\}$  where  $R \subset \mathcal{N} \times (\mathcal{N} \cup \Sigma)^+$  is a set of production rules (usually written as  $A \rightarrow \alpha$ , where  $A \in \mathcal{N}$  and  $\alpha \in (\mathcal{N} \cup \Sigma)^+$ ) and  $p(r)$  is the emission probability associated with the rule  $r$ . The set  $\mathcal{P}$  is built as follows:

- for every tree  $t \in r_k(\Omega)$  add to  $\mathcal{P}$  the rule  $S \rightarrow t$  with probability

$$p(S \rightarrow t) = \frac{\sum_{\tau \in \Omega} \delta_{t r_{k-1}(\tau)}}{|\Omega|} \quad (4)$$

where  $\delta_{a b} = 1$  if  $a = b$  and zero otherwise;

- for every tree  $\sigma(t_1 t_2 \dots t_m) \in f_k(\Omega)$  add to  $\mathcal{P}$  the rule  $r_{k-1}(\sigma(t_1 t_2 \dots t_m)) \rightarrow t_1 t_2 \dots t_m$  with probability

$$p(r_{k-1}(\sigma(t_1 t_2 \dots t_m)) \rightarrow t_1 t_2 \dots t_m) = \frac{\sum_{\tau \in \Omega} C(\sigma(t_1 t_2 \dots t_m), \tau)}{\sum_{\tau \in \Omega} C(r_{k-1}(\sigma(t_1 t_2 \dots t_m)), \tau)} \quad (5)$$

Here  $C(t, \tau)$  counts the number of times that the fork  $t$  appears in the tree  $\tau$ ;

- for every tree  $\sigma(t_1 t_2 \dots t_m) \in s_k(\Omega)$  add to  $\mathcal{P}$  the rule  $\sigma(t_1 t_2 \dots t_m) \rightarrow t_1 t_2 \dots t_m$  with probability

$$p(\sigma(t_1 t_2 \dots t_m) \rightarrow t_1 t_2 \dots t_m) = 1 \quad (6)$$

Defined in this way, these probabilities satisfy the normalization constraint

$$\text{for each } A \in \mathcal{N} : \sum_{\alpha: A \rightarrow \alpha \in \mathcal{P}} p(A \rightarrow \alpha) = 1 \quad (7)$$

and the consistency constraint. PCFGs estimated from treebanks using the relative frequency estimator always satisfy those constraints [7] [8].

Note that in this kind of models, the expansion probability for a given node is computed as a function of the subtree of depth  $k - 2$  that the node generates, i.e., every non-terminal symbol stores a subtree of depth  $k - 2$ . In the particular case  $k = 2$ , only the label of the node is taken into account (this is analogous to the standard bigram model for strings) and the model coincides with the simple rule-counting approach used in treebank grammars by Charniak [9].

However, in the case  $k = 3$ , we get a *child-annotated* model, that is, non-terminal symbols  $\sigma(\sigma_1 \sigma_2 \dots \sigma_m)$  are defined by:

- the node label  $\sigma$ ,
- the number  $m$  of descendants (if any) and
- the labels in the descendants  $\sigma_1, \sigma_2, \dots, \sigma_m$  (if any) and their ordering.

As an illustration, consider a very simple sample with only the tree in the figure 1. If we choose  $k = 2$ , then

- $r_1(S(NP VP)) = S$ ;

- $f_2(S(NP VP)) = \{S(NP VP), NP(N), VP(V NP), NP(NP PP), PP(P NP)\}$
- $s_1(S(NP VP)) = \emptyset$

and the CFG is

$$G^{[2]} = (\{S, NP, VP, PP\}, \{N, V, P\}, S, \mathcal{P}),$$

with  $\mathcal{P}$  containing the rules

$$\begin{aligned} S &\rightarrow NP VP \\ NP &\rightarrow NP PP \\ NP &\rightarrow N \\ VP &\rightarrow VP PP \\ VP &\rightarrow V NP \\ PP &\rightarrow P NP \end{aligned}$$

However, for  $k = 3$  we obtain

- $r_2(S(NP VP)) = S(NP VP)$
- $f_3(S(NP VP)) = \{S(NP(N) VP(V NP)), VP(V NP(NP PP)),$   
 $NP(NP(N) PP(P NP)), PP(P NP(N))\}$
- $s_2(S(NP VP)) = \{NP(N)\}$

and the CFG is

$$G^{[3]} = (\{S, S(NP VP), NP(N), VP(V NP), NP(NP PP), PP(P NP)\}, \{N, V, P\}, S, \mathcal{P}),$$

with  $\mathcal{P}$  containing the rules

$$\begin{aligned} S &\longrightarrow S(NP VP) \\ S(NP VP) &\longrightarrow NP(N) VP(V NP) \\ VP(V NP) &\longrightarrow V NP(NP PP) \\ NP(NP PP) &\longrightarrow NP(N) PP(P NP) \\ PP(P NP) &\longrightarrow P NP(N) \\ NP(N) &\longrightarrow N \end{aligned}$$

For comparison, if one uses a parent-annotated version of the grammar (following Johnson [4]), one gets the following rules<sup>1</sup> (where the superindex is the parent's label).

$$\begin{aligned} S &\longrightarrow {}^S NP {}^S VP \\ {}^S NP &\longrightarrow N \\ {}^S VP &\longrightarrow V {}^{VP} NP \\ {}^{VP} NP &\longrightarrow {}^{NP} NP {}^{NP} PP \\ {}^{NP} NP &\longrightarrow N \\ {}^{NP} PP &\longrightarrow P {}^{PP} NP \\ {}^{PP} NP &\longrightarrow N \end{aligned}$$

---

<sup>1</sup> As will be seen in section 3, parent-annotated grammars usually have *less* parameters than child-annotated grammars, contrary to what this example may suggest.

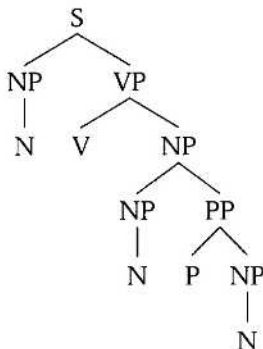


Fig. 1. A sample parse tree

### 3 Experiments

#### 3.1 General Conditions

We have performed a series of experiments to assess the structural disambiguation performance of offspring-annotated models as compared to standard treebank grammars, that is, to compare their relative ability for selecting the best parse tree. To better put these comparisons in context, we have also evaluated Johnson's [4] parent annotation scheme. To build training corpora and test sets of parse trees, we have used English parse trees from the Penn Treebank, release 3. In all experiments the training corpus, consisted of all of the trees (41,532) in sections 02 to 22 of the *Wall Street Journal* portion of Penn Treebank, modified as above. This gives a total number of more than 600,000 subtrees. The test set contained all sentences in section 23 having no more than 40 words.

A Chappelier and Rajman's [10] probabilistic extended Cocke-Younger-Kasami parsing algorithm (which constructs a table containing generalized items like those in Earley's [11] algorithm) was used to obtain the most likely parse for each sentence in the training set; this parse was compared to the corresponding gold-standard tree in the test set using the customary PARSEVAL evaluation metric [12, 5, p. 432] after deannotating the most likely tree delivered by the parser. PARSEVAL gives partial credit to incorrect parses by establishing the *labeled precision* ( $P$ ) and *labeled recall* ( $R$ ) measures.

#### 3.2 Structural Disambiguation Results

Here is a list of the models which were evaluated:

- A standard treebank grammar, with no annotation of node labels (NO or  $k = 2$ ), with probabilities for 15,140 rules.

- A child-annotated grammar (CHILD or  $k = 3$ ), with probabilities for 92,830 rules.
- A parent-annotated grammar (PARENT), with probabilities for 23,020 rules.
- A both parent- and child-annotated grammar (BOTH), with probabilities for 112,610 rules.

As expected, the number of rules obtained increases as more information is conveyed by the node label, although this increase is not extreme. On the other hand, as the generalization power decreases, some sentences in the test set become unparsable, that is, they cannot be generated by the grammar.

ANNOTATION	$R$	$P$	$f_{R=100\%}$	EXACT	PARED	$t$
NO ( $k = 2$ )	70.7%	76.1%	10.4%	10.0%	100%	57
CHILD ( $k = 3$ )	79.2%	74.2%	19.4%	13.6%	94.6%	9
PARENT	80.0%	81.9%	18.5%	16.3%	100%	340
BOTH	80.1%	75.6%	20.5%	14.7%	79.6%	75

**Table 1.** Parsing results with different annotation schemes: labelled recall  $R$ , labelled precision  $P$ , fraction of sentences with total labelled recall  $f_{R=100\%}$ , fraction of exact matches, fraction of sentences parsed by the annotated model, and average time per sentence in seconds.

The results in table 1 show that

- The parsing performance of parent-annotated and child-annotated PCFG is similar and better than those obtained with the standard treebank PCFG. The performance is measured both with the customary PARSEVAL metrics and by counting the number of maximum-likelihood trees that (a) match their counterparts in the treebank exactly, and (b) contain all of the constituents in their counterpart (100% labeled recall,  $f_{R=100\%}$ ). The fact that child-annotated grammars do not perform better than parent-annotated ones may be due to their larger number of parameters compared to parent-annotated PCFG. This makes it difficult to estimate them accurately from currently available treebanks (only about 6 subtrees per rule in the experiments).
- The average time to parse a sentence shows that child annotation leads to parsers that are much faster. This comes as no surprise because the number of possible parse trees considered is drastically reduced; this is, however, not the case with parent-annotated models.

It may be worth mentioning that parse trees produced by child-annotated models tend to be more structured and refined than parent-annotated and unannotated parses which tend to use rules that lead to flat trees.

On the other hand, child-annotated models, CHILD and BOTH, were unable to deliver a parse tree for all sentences in the test set (CHILD parses 94.6% of the sentences and BOTH, 79.6%). To be able to parse all sentences, those smoothed models, were evaluated:

- A linear interpolated model, M1, where the probability of a tree  $t$  is

$$p(t) = \lambda p_3(t) + (1 - \lambda)p_2(t) \quad (8)$$

here,  $p_3(t)$  and  $p_2(t)$  are the probabilities of the tree  $t$  in, respectively, the model  $k = 3$  and  $k = 2$ . The value of  $\lambda$  was 0.7 (selected to minimize the perplexity).

- A tree-level back-off, M2, where the highest order model such that the probability of the event is greater than zero is selected. Some care has to be taken in order to preserve normalization.
- A rule-level back-off model, M3 that builds a new PCFG from the rules of the tree- $k$ -grammar models and adding new rules which allow to switch among those models. In particular, the new PCFG consists of three different kinds of rules:
  1.  $k = 3$  rules with modified probability in order to preserve normalization,
  2. back-off rules that allow to switch to the lower model, and,
  3. modified  $k = 2$  rules to switch-back to the higher model.

The new grammar has 92,830  $k = 3$  rules, 15,140  $k = 2$  rules and 10,250 back-off rules.

MODEL	R	P	EXACT	PARSED	$t$
M1	80.2%	78.6%	17.4%	100%	57
M2	78.9%	74.2%	17.1%	100%	9.3
M3	82.4%	81.3%	17.5%	100%	68

Table 2. Parsing results with different smoothed models.

The results in table 2 show that:

- M2 is the fastest but its performance is worse than that of M1 and M3.
- M1 and M3 parse sentences at a comparable speed but recall and precision are better using M3.

Compared to un-smoothed models, smoothed ones:

- Cover the whole test set ( $k = 3$  did not).
- Parsed at reasonable speed (compared to PARENT).
- Achieved acceptable performance ( $k = 2$  did not).

## 4 Conclusion

We have introduced a new probabilistic context-free grammar model, *offspring-annotated* PCFG in which the grammar variables are specialized by annotating them with the subtree they generate up to a certain level. In particular, we have studied child-annotated models (one level) and have compared their parsing performance to that of unannotated PCFG and of parent-annotated PCFG [4]. Offspring-annotated models may be seen as a special case of a very general probabilistic state-based model, which in turn is based on probabilistic bottom-up tree automata. The experiments show that:

- The parsing performance of parent-annotated and the proposed child-annotated PCFG is similar.
- Parsers using child-annotated grammars are, however, much faster because the number of possible parse trees considered is drastically reduced; this is, however, not the case with parent-annotated models.
- Child-annotated grammars have a larger number of parameters than parent-annotated PCFG which may make it difficult to estimate them accurately from currently available treebanks.
- Child-annotated models tend to give very structured and refined parses instead of flat parses, a tendency not so strong for parent-annotated grammars.

## References

1. L. Frazier and K. Rayner. Making and correcting errors during sentence comprehension: Eye movements in the analysis of structurally ambiguous sentences. *Cognitive Psychology*, 14:178–210, 1982.
2. Mitchell P. Marcus, Beatrice Santorini, and Mary Ann Marcinkiewicz. Building a large annotated corpus of English: the Penn Treebank. *Computational Linguistics*, 19:313–330, 1993.
3. Eugene Charniak. Treebank grammars. In *Proceedings of the Thirteenth National Conference on Artificial Intelligence*, pages 1031–1036. AAAI Press/MIT Press, 1996.
4. Mark Johnson. PCFG models of linguistic tree representations. *Computational Linguistics*, 24(4):613–632, 1998.
5. Christopher D. Manning and Hinrich Schütze. *Foundations of Statistical Natural Language Processing*. MIT Press, 1999.
6. Ezra Black, Frederick Jelinek, John D. Lafferty, David M. Magerman, Robert L. Mercer, and Salim Roukos. Towards history-based grammars: Using richer models for probabilistic parsing. In *Proceedings of the DARPA Speech and Natural Language Workshop*, pages 31–37, 1992.
7. J.A. Sánchez and J.M. Benedí. Consistency of stochastic context-free grammars from probabilistic estimation based on growth transformations. *IEEE Transactions on Pattern Analysis and Machine Intelligence*, 19(9):1052–1055, 1997.
8. Zhiyi Chi and Stuart Geman. Estimation of probabilistic context-free grammars. *Computational Linguistics*, 24(2):299–305, 1998.
9. Eugene Charniak. Tree-bank grammars. In *Proceedings of the Thirteenth National Conference on Artificial Intelligence and the Eighth Innovative Applications of Artificial Intelligence Conference*, pages 1031–1036, Menlo Park, 1996. AAAI Press/MIT Press.
10. J.-C. Chappelier and M. Rajman. A generalized CYK algorithm for parsing stochastic CFG. In *Actes de TAPD'98*, pages 133–137, 1998.
11. J. Earley. An efficient context-free parsing algorithm. *Communications of the ACM*, 13(2):94–102, 1970.
12. Ezra Black, Steven Abney, Dan Flickinger, Claudia Gdaniec, Ralph Grishman, Philip Harrison, Donald Hindle, Robert Ingria, Frederick Jelinek, Judith Klavans, Mark Liberman, Mitch Marcus, Salim Roukos, Beatrice Santorini, and Tomek Strzalkowski. A procedure for quantitatively comparing the syntactic coverage of English grammars. In *Proc. Speech and Natural Language Workshop 1991*, pages 306–311, San Mateo, CA, 1991. Morgan Kauffmann.

# Simulated Annealing for Automated Definition of Fuzzy Sets in Human Central Nervous System Modeling

Francisco Mugica<sup>1</sup> and Angela Nebot<sup>2</sup>

<sup>1</sup> Instituto Latinoamericano de la Comunicación Educativa  
Calle del Puente, 45, Col.Ejidos de Huipulco, México D.F. 14380, México  
[fmugica@ilce.edu.mx](mailto:fmugica@ilce.edu.mx)

<sup>2</sup> Dept. Llenguatges i Sistemes Informàtics, Universitat Politècnica de Catalunya  
Jordi Girona Salgado, 1-3, Barcelona 08034, Spain  
[angela@lsi.upc.es](mailto:angela@lsi.upc.es)

**Abstract.** The main goal of this research is to study the usefulness of the Simulated Annealing (SA) approach, developed in the context of the Fuzzy Inductive Reasoning (FIR) methodology, for the automatic identification of fuzzy partitions in the human Central Nervous System (CNS) modeling problem. The SA algorithm can be viewed as a pre-process of the FIR methodology that allows the modeler to use it in a more efficient way. Two different SA algorithm cost functions have been studied and evaluated in this paper. The new approach is applied to obtain accurate models for the five controllers that compose the CNS. The results are compared and discussed with those obtained by other inductive methodologies for the same problem.

## 1 Introduction

The human central nervous system controls the hemodynamical system, by generating the regulating signals for the blood vessels and the heart. These signals are transmitted through bundles of sympathetic and parasympathetic nerves, producing stimuli in the corresponding organs and other body parts.

In this work, CNS controller models are identified for a specific patient by means of the Fuzzy Inductive Reasoning (FIR) methodology. FIR is a data driven methodology that uses fuzzy and pattern recognition techniques to infer system models and to predict its future behavior. It has the ability to describe systems that cannot easily be described by classical mathematics (e.g. linear regression, differential equations) i.e. systems for which the underlying physical laws are not well understood. The FIR methodology is composed of four main processes, namely: *fuzzification*, *qualitative model identification*, *fuzzy forecast* and *defuzzification*.

The first step of the FIR methodology is the *fuzzification* process, that converts quantitative data stemming from the system into fuzzy data. In this process the number of classes of each variable (i.e. the partition) needs to be provided.

In this paper an algorithm based on a simulated annealing technique/method, developed in the context of FIR, is used to automatically suggest a good partition of the system variables in an efficient way. The SA algorithm can be viewed as a pre-process of the FIR methodology that allows the modeler not to rely on heuristics for the definition of a system variable partition. Two SA algorithm cost functions are proposed in this research that make use of the qualitative model identification and the forecast processes of FIR methodology. A brief description of these processes are given next. The *qualitative model identification* process of the FIR methodology is the responsible to find causal and temporal relations between variables and therefore to obtain the best model that represents the system. A simplified diagram of the qualitative model identification process is presented in figure 1.

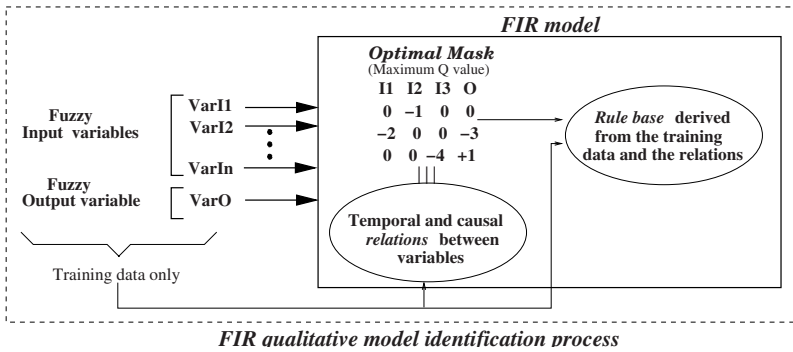


Fig. 1. Simplified diagram of the FIR qualitative model identification process

A FIR model is composed of a mask (model structure) and a pattern rule base. An example of a mask is presented in figure 1. Each negative element in the mask is called a m-input (mask input). It denotes a causal relation with the output, i.e. it influences the output up to a certain degree. The enumeration of the m-inputs is immaterial and has no relevance. The single positive value denotes the output. In position notation the mask of figure 1 can be written as (2, 5, 8, 11, 12), enumerating the mask cells from top to bottom and from left to right. The qualitative identification process evaluates all the possible masks and concludes which one has the highest prediction power by means of an entropy reduction measure, called the quality of the mask  $Q$ . The mask with the maximum  $Q$  value is the optimal mask. Starting from the fuzzified system data and using the optimal mask, the pattern rule base is then synthesized. Both, the pattern rule base and the mask constitute the FIR model. Once the pattern rule base and the optimal mask are available, system predictions can take place using FIR inference engine. This process is called *fuzzy forecast*. FIR inference engine is a specialization of the k-nearest neighbor rule, commonly used in the pattern recognition field. *Defuzzification* is the inverse process of fuzzification. It

allows to convert the qualitative predicted output into quantitative values that can then be used as inputs to an external quantitative model. For a deeper inside of the FIR methodology refer to [1].

## 2 Simulated Annealing for Identification of Fuzzy Partitions in FIR

Simulated annealing is a generalization of a Monte Carlo method and it is used to approximate the solution of large combinatorial optimization problems [4]. A simulated annealing algorithm consists of two loops. The outer-most loop sets the temperature and the inner-most loop runs a Metropolis Monte Carlo simulation at that temperature. The algorithm starts with an initial solution to the problem, which is also the best solution so far and a value for an initial high temperature. Each iteration consists of the random selection of a new solution (candidate solution) from the neighborhood of the current one. The cost function of the candidate solution is evaluated and the difference with respect to the cost function value of the current solution is computed. If this difference is negative the candidate solution is accepted. If the difference is positive the candidate solution is accepted with a probability based on the Boltzmann distribution. The accepted candidate solution becomes the current solution and if its cost function value is lower than the one of the best solution, this one is updated. If the candidate solution is rejected the current solution stays the same and it is used in the next iteration. The temperature is lowered in each iteration down to a *freezing* temperature where no further changes occur. A detailed description of the simulated annealing algorithm developed for the automatic identification of fuzzy partitions in the FIR methodology can be found in [2].

Two main aspects of the simulated annealing algorithm that need to be considered here are the *new solution generation mechanism* and the *cost function*. Both are highly important to achieve a good performance of the algorithm.

The *new solution generation mechanism* consists of two tasks. The first one is the generation of the initial partition at the beginning of the algorithm execution. The second one is the generation of a new solution (i.e. candidate solution) starting from the current solution, in each algorithm iteration. Two options have been studied in this paper to generate an initial partition: 3-classes partition and random partition. The first one sets all the variables to 3 classes. The second one performs a random generation of the number of classes for each system variable. In this research the number of classes allowed for each system variable is in the range [2 . . . 9].

The procedure to generate a new solution, i.e., the candidate solution, from the current one is to increment or decrement by one the number of classes associated to a certain system variable. The variable that is going to be modified is chosen randomly out of the vector of variables. The decision to increase or decrease the number of classes of this variable is also randomly taken.

Two different *cost functions* have been studied in this work: the quality of the optimal mask and the prediction error of the training data set.

As has been explained earlier, in the *qualitative model identification* process of the FIR methodology the optimal mask (i.e. the best model structure) is identified by means of a quality measure,  $Q$ . The quality of a mask is a value between 0 and 1, where 1 indicates the highest quality. Therefore, the first cost function proposed is  $1 - Q$ , due to the fact that the algorithm task should minimize the cost function.

The second cost function is defined as the prediction error of a portion of the training data set. The normalized mean square error in percentage (MSE), given in equation 1, is used for this purpose.

$$MSE = \frac{E[(y(t) - \hat{y}(t))^2]}{y_{\text{var}}} \cdot 100\% \quad (1)$$

$\hat{y}(t)$  is the predicted output,  $y(t)$  the system output and  $y_{\text{var}}$  denotes the variance of  $y(t)$ . The idea is to use part of the training data set to identify the model and the rest of the data set to evaluate the prediction performance of that model. The prediction error of the portion of the training data set not used in the model identification process is used as the cost function for the SA algorithm. The size of the portion of the training data set actually used for cost function evaluation purposes is defined with respect to the size of the whole training data set.

### 3 Central Nervous System Modeling

The central nervous system is composed of five controllers, namely, *heart rate* (HR), *peripheric resistance* (PR), *myocardiac contractility* (MC), *venous tone* (VT) and *coronary resistance* (CR). All the CNS controllers are SISO models driven by the same input variable, the *carotid sinus pressure* (CSP). The input and output signals of the CNS controllers were recorded with a sampling rate of 0.12 seconds from simulations of the purely differential equation model [3], obtaining 7279 data points. The model had been tuned to represent a specific patient suffering a coronary arterial obstruction, by making the four different physiological variables (right auricular pressure, aortic pressure, coronary blood flow, and heart rate) of the simulation model agree with the measurement data taken from the real patient. The five models obtained were validated by using them to forecast six data sets not employed in the training process. Each one of these six test data sets, with a size of about 600 data points each, contains signals representing specific morphologies, allowing the validation of the model for different system behaviors.

The main goal of this research is to study the usefulness of the SA approach as a pre-processing tool of the FIR methodology for the identification of good models for each of the five controllers. Let us explain the experimentation procedure for the coronary resistance controller. The same strategy has been used for the other four controllers. Their results are presented later.

As mentioned before, two cost functions were studied in this work. Table 1 shows the results obtained for the coronary resistance controller when  $1 - Q$  was used as cost function. Table 2 presents the results of the same controller when

**Table 1.** Partition results of the CR controller obtained using  $1 - Q$  as cost function

Ini.Part. CSP	Fin.Part. CSP	Opt.Mask CR	Q	$1 - Q$	$MSE_{test}$	#GS	Time
(3,3)	(9,3)	(1,4,6)	0.9787	0.0213	3.85%	35	2.98
(3,3)	(7,3)	(1,4,6)	0.9776	0.0224	4.76%	26	1.97
(3,3)	(8,3)	(1,4,6)	0.9776	0.0224	4.25%	37	2.56
(3,3)	(6,3)	(1,4,6)	0.9762	0.0238	1.75%	27	1.41
(3,3)	(5,3)	(1,4,6)	0.9749	0.0251	2.34%	24	1.69
(3,3)	(4,3)	(1,4,6)	0.9748	0.0252	1.33%	26	1.38
(8,8)	(9,3)	(1,4,6)	0.9787	0.0213	3.85%	33	6.17
(9,6)	(9,3)	(1,4,6)	0.9787	0.0213	3.85%	26	3.18
(7,2)	(9,3)	(1,4,6)	0.9787	0.0213	3.85%	35	2.38
(6,5)	(9,3)	(1,4,6)	0.9787	0.0213	3.85%	25	3.60
(5,5)	(9,3)	(1,4,6)	0.9787	0.0213	3.85%	35	3.24
(5,2)	(5,3)	(1,4,6)	0.9749	0.0251	2.34%	37	1.44
Optimal	Solution:	Opt.Mask=	(9,3);	Q=	0.9787;		

the cost function is defined as the prediction MSE of a portion of the training data set. In this application the last 25% of the training signal is used for cost function evaluation and only the first 75% of the signal is used to obtain the FIR models.

Both, the 3-classes and the random options have been evaluated as initial partitions. The upper rows of tables 1 and 2 show the results of the 3-classes initial partition, whereas the lower rows present the results of the random initial partition. For both options, 40 executions of the SA algorithm were performed. For an initial partition of 3 classes the SA algorithm suggested up to 6 different final partitions when  $1 - Q$  is used as cost function (see table 1) and 3 possible final partitions when the prediction error is used as cost function (see table 2). When the random initial partition is used, only 2 and 4 different final partitions are suggested by the SA algorithm for the  $1 - Q$  and prediction error cost functions, respectively.

The tables are organized as follows. The first column indicates the initial partition from which the SA algorithm starts the search. The second column presents the final partition suggested by the SA algorithm when the cooler temperature is reached (i.e. the algorithm stops). Note that the final partition is the input parameter to the *fuzzification* process of the FIR methodology. The third and fourth columns contain the optimal mask obtained by FIR for that specific partition (in position notation) and its associated quality, respectively. The fifth column corresponds to the cost function evaluation. Note that in table 1 the cost function is  $1 - Q$  and in table 2 the cost function is the prediction MSE of the last 25% data points of the training set. The next column shows the prediction error of the test data sets. As mentioned before, six test data sets of 600 data points each are available for each controller. The results presented in the tables are the mean value of the predictions errors obtained for these six test data sets. The seventh column indicates the total number of generated

**Table 2.** Partition results of the CR controller obtained using the prediction error of the last 25% of the training data set as cost function

Ini.Part. CSP	Fin.Part. CSP	Opt.Mask CR	Q	$MSE_{train}$	$MSE_{test}$	#GS	Time
(3,3)	(2,5)	(1,4,5,6)	0.9642	0.08%	0.15%	19	19.40
(3,3)	(3,4)	(4,5,6)	0.9638	0.12%	0.28%	32	38.39
(3,3)	(6,4)	(3,4,6)	0.9666	0.17%	0.42%	33	22.37
(4,4)	(2,5)	(1,4,5,6)	0.9642	0.08%	0.15%	24	17.51
(2,6)	(2,5)	(1,4,5,6)	0.9642	0.08%	0.15%	19	10.79
(3,5)	(3,4)	(4,5,6)	0.9638	0.12%	0.28%	23	12.31
(6,5)	(6,4)	(3,4,6)	0.9666	0.17%	0.42%	33	11.55
(5,4)	(6,4)	(3,4,6)	0.9666	0.17%	0.42%	30	16.28
(9,6)	(7,4)	(4,5,6)	0.9677	0.18%	0.41%	28	14.29
Optimal	Solution:	Opt.Mask=	(2,5);	$MSE_{train}= 0.08\%$			

solutions during the execution of the SA algorithm. The last column contain the CPU time (in seconds) used by the algorithm to find the final partition. Clearly, the biomedical application presented in this paper is not a large optimization problem, it is rather small due to the fact that only two variables are involved and a maximum of nine classes is allowed (in fact there are only eight, because class 1 is not used). Therefore, there exists 64 possible solutions and an exhaustive search can be performed easily. However, it is interesting to work with a real application that shows clearly the usefulness of the SA algorithm for the automated definition of fuzzy sets in the FIR methodology. Moreover, the FIR performance is considerably increased when the SA algorithm is used in the CNS application.

If we look closer to table 1 it is clear that the optimal solution that corresponds to the (9, 3) partition with a quality of 0.9787 is reached in both initial partition options. All the final partitions obtained when a (3, 3) initial partition is used have in common that a partition of 3 classes is always suggested for the output variable, whereas 4,5,6,7,8 or 9 classes are good partitions for the input variable. Notice that the qualities of all the suggested partitions are very close to the optimal one. With a random initial partition, only two final partitions are suggested by the SA algorithm, i.e. the optimal one (9, 3) and a suboptimal one (5, 3). The proportion shown in table 1, i.e. five times partition (9, 3) vs. one time partition (5, 3) is the relation encountered in the 40 runs of the algorithm.

**Table 3.** MSE prediction errors of the CNS controller models using NARMAX, TDNN and RNN methodologies (mean value of the 6 test data sets for each controller)

	HR	PR	MC	VT	CR
NARMAX	9.3%	18.5%	22.0%	22.0%	25.5%
TDNN	15.3%	33.7%	34.0%	34.0%	55.6%
RNN	18.3%	31.1%	35.1%	34.7%	57.1%

Table 2 shows the results of the same controller when the prediction error of part of the training data set has been used as a cost function for the SA algorithm. The function to be minimized now is the  $MSE_{train}$ . It is interesting to remark, that in this case, the mask is obtained using exclusively the first 75% data points of the training signal. Therefore, the data used for the cost function evaluation has not been seen for the model before. This is the reason why the best predictions obtained for the last 25% values of the training set do not correspond necessarily to the partitions with the associated optimal mask of highest quality. However, the quality of the optimal masks found for the suggested partitions are still high, i.e. 0.96. The optimal solution is the partition (2, 5) with a  $MSE_{train}$  of 0.08%, that is really very low. The SA algorithm is able to find the best final partition with both initial partition options, as happened also for the quality cost function. The (3, 4) and (6, 4) partitions with errors of 0.12% and 0.17%, respectively, are the best suboptimal solutions. Therefore, the SA algorithm obtains in fact the best three final partitions. Notice that although the number of generated solutions remains almost the same than table 1, the CPU time has considerably increased. This is due to the fact that the cost function evaluation is much more expensive computationally. Now, not only the qualitative model identification process of the FIR methodology is executed but also the fuzzy forecast process is.

**Table 4.** Partition results of the HR, PR, MC and VT controllers obtained using  $1 - Q$  cost function and prediction error of the last 25% of the training data set cost function

	HR			PR		
$1 - Q$	Fin.Part.	$1 - Q$	$MSE_{test}$	Fin.Part.	$1 - Q$	$MSE_{test}$
	(7,2)*	0.1674	13.43%	(8,7)*	0.1448	5.99 %
	(8,2)	0.1861	12.63%	(7,7)	0.1505	4.59 %
	(7,4)	0.2739	2.61 %	(5,7)	0.1564	3.15 %
$MSE_{train}$	Fin.Part.	$MSE_{train}$	$MSE_{test}$	Fin.Part.	$MSE_{train}$	$MSE_{test}$
	(3,7)*	0.89%	9.15%	(4,9)*	0.93%	2.28%
	(5,9)	1.01%	2.54%	(7,7)	1.08%	3.34%
	(6,7)	1.15%	13.39%	(2,6)	1.64%	3.77%
	MC			VT		
$1 - Q$	Fin.Part.	$1 - Q$	$MSE_{test}$	Fin.Part.	$1 - Q$	$MSE_{test}$
	(8,7)*	0.1866	11.88%	(8,7)*	0.1858	13.00%
	(7,7)	0.1950	42.45%	(7,7)	0.1952	41.88%
	(5,7)	0.2019	52.94%	(5,7)	0.2032	53.01%
$MSE_{train}$	Fin.Part.	$MSE_{train}$	$MSE_{test}$	Fin.Part.	$MSE_{train}$	$MSE_{test}$
	(4,9)*	0.60%	2.51%	(2,5)*	0.6117%	1.66%
	(2,5)	0.63%	2.74%	(2,8)	0.6359%	1.55%
	(3,9)	1.10%	3.87%	(3,7)	0.7855%	2.12%

It is interesting to analyze the  $MSE_{test}$  columns of both tables. As expected, the  $MSE_{train}$  cost function is able to obtain partitions with higher performance

on the prediction of the test data sets than the ones obtained by the  $1 - Q$  cost function. However, the results obtained in both cases are very good if compared with the ones obtained when other inductive methodologies are used. Table 3 contains the predictions achieved when NARMAX, time delay neural networks and recurrent neural networks are used for the same problem. The columns of the table specify the average prediction error of the 6 test sets for each controller. All methodologies used the same training and test data sets previously described.

The errors obtained for all the controllers using the SA approach hand in hand with the FIR methodology are much better than the ones obtained by the inductive methodologies presented in table 3. Moreover, the highest  $MSE_{test}$  of 4.76% obtained with the  $1 - Q$  cost function is half the value of the lower error obtained with these methodologies, i.e. 9.3%. Therefore, in this application, both cost functions can be considered good for the task at hand. The  $1 - Q$  cost function needs less time to be evaluated but the performance with respect to the test set prediction is lower. Contrarily, the  $MSE_{train}$  cost function is more expensive from the CPU time point of view but the performance is higher. The user should decide which cost function to use taking into account the size of the optimization problem and his/her own needs.

Table 4 contains the partition results of the other four CNS controllers. The random initial partition option has been used in all the executions. The SA algorithm has been executed 40 times for both cost functions for each controller. The final partition, the value of the cost function and the mean MSE of the 6 test data sets are presented for each controller and cost function. An \* means that that partition is the best possible one, and therefore it is the optimal solution. As can be seen in table 4 the optimal solution is reached for both cost functions in all partitions. The CPU time and number of generated solutions are equivalent to those of the CR controller in tables 1 and 2. It is interesting to analyze the  $MSE_{test}$  of the HR, PR, MC and Vt controllers. The errors of the test sets obtained when the  $MSE_{train}$  cost function is used are quite good for all controllers, and much better than the ones obtained using the inductive methodologies of table 3. However, this is not the case for all controllers when the  $1 - Q$  cost function is used. Notice that, although the SA algorithm finds both the best solution and good suboptimal solutions, the prediction errors of the test data sets obtained are of the same order of magnitude than the ones obtained by the NARMAX, time delay and recurrent neural networks, particularly for the MC and VT controllers. In this case, the quality measure used by the FIR methodology is not doing a good job. It can be interesting to study alternative quality measures for the task at hand.

## 4 Conclusions

In this paper the usefulness of a simulated annealing approach for the automated definition of fuzzy sets in the identification of human central nervous system FIR models has been shown. Two cost functions have been evaluated and compared from the perspective of their performance and computational time. The results

obtained in the CNS applications are much better than the ones obtained by other inductive methodologies such as NARMAX, time delay neural networks and recurrent neural networks.

**Acknowledgements.** The authors thank the valuable suggestions of F.E. Cellier of the University of Arizona, USA and P. Villar of the Universidad de Vigo, Spain. This research was supported by Spanish Consejo Interministerial de Ciencia y Tecnología (CICYT), under project DPI2002-03225.

## References

1. F. Cellier. Continuous System Modeling. Springer-Verlag, New York 1991.
2. A. Nebot. Automatic tuning of fuzzy partitions in inductive reasoning. In *Proceedings CIARP'03: 8th Iberoamerican Congress on Pattern Recognition*, Page 8, Havana, Cuba 26–29 November 2003. Under revision.
3. A. Nebot, F. Cellier, and M. Vallverdú. Mixed quantitative/qualitative modeling and Simulation of the cardiovascular system. *Computer Methods and Programs in Biomedicine* 55:127-155 1998.
4. C.D.G.J.S. Kirkpatrick and M. P. Vecchi. Optimization by simulated annealing. *Science*, 220:671–680, 1983.

# Automatic Tuning of Fuzzy Partitions in Inductive Reasoning

Angela Nebot

Departament de Llenguatges i Sistemes Informàtics  
Universitat Politècnica de Catalunya  
Jordi Girona Salgado, 1-3,  
Barcelona 08034, Spain  
[angela@lsi.upc.es](mailto:angela@lsi.upc.es)

**Abstract.** The aim of this research is to automatically tuning a good fuzzy partition, i.e. determine the number of classes of each system variable, in the context of the Fuzzy Inductive Reasoning (FIR) methodology. FIR is an inductive methodology for modelling and simulate those systems from which no previous structural knowledge is available. The first step of FIR methodology is the fuzzification process that converts quantitative variables into fuzzy qualitative variables. In this process it is necessary to define the number of classes into which each variable is going to be discretized. In this paper an algorithm based on simulated annealing is developed to suggest a good partition in an automatic way. The proposed algorithm is applied to an environmental system.

## 1 Introduction

The Fuzzy Inductive Reasoning (FIR) methodology emerged from the General Systems Problem Solving (GSPS) developed by Klir [1]. FIR is a data driven methodology based on systems behavior rather than structural knowledge. It is a very useful tool for modelling and simulate those systems from which no previous structural knowledge is available. FIR is composed of four main processes, namely: *fuzzification*, *qualitative model identification*, *fuzzy forecasting*, and *defuzzification*. Figure 1 describes the processes of FIR methodology.

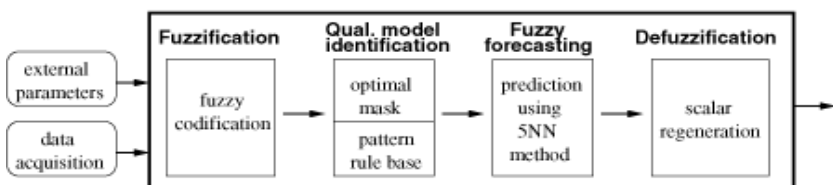


**Fig. 1.** FIR structure

The fuzzification process converts quantitative data stemming from the system into fuzzy data, i.e. qualitative triples. The first element of the triple is the

class value, the second element is the fuzzy membership value, and the third element is the side value. The side value indicates whether the quantitative value is to the left or to the right of the peak value of the associated membership function.

The model identification process is able to obtain good qualitative relations between the variables that compose the system, building a pattern rule base that guides the fuzzy forecasting process.

The fuzzy forecasting process predicts systems behavior. The FIR inference engine is a specialization of the  $k$ -nearest neighbor rule, commonly used in the pattern recognition field.

Defuzzification is the inverse process of fuzzification. It makes possible to convert the qualitative predicted output into a quantitative variable that can then be used as input to an external quantitative model. It has been shown in previous works that FIR methodology is a powerful tool for the identification and prediction of real systems, specially when poor or non structural knowledge is available [2,5]. For a deeper insight into FIR methodology the reader is referred to [4].

As can be seen in figure 1, for the fuzzification process of FIR methodology to start it is necessary to define some external parameters, i.e. the partition (number of classes of each system variable) and the landmarks (limits between classes). The default value for the number of classes' parameter for each system variable is three and the equal frequency partition (EFP) is used as the default method to obtain the landmarks of the classes. These default values have been used in different applications obtaining usually good results. However, experience has shown that in some them, i.e. biomedical and ecological, the determination of the partition parameter needed in the fuzzification step becomes relevant for the identification of a good model that captures systems behavior in an accurate way. The automatic determination of a good partition as a pre-process of FIR methodology is an interesting and useful alternative. To achieve this goal an algorithm base on simulated annealing is presented in this paper and used in an environmental application, i.e. prediction of ozone concentration in a specific area of Mexico city. The algorithm proposed is introduced in section 2. In section 3 the ozone application is addressed and the results obtained discussed. Finally, the conclusions of this research are given.

## 2 Simulated Annealing Algorithm

Simulated annealing is a generalization of a Monte Carlo method that was introduced by Metropolis et al. in 1953 [3]. This technique is used to approximate the solution of very large combinatorial optimization problems and is based on the manner in which liquids freeze in the process of annealing [7]. In an annealing process a melt, initially at high temperature and disordered, is slowly cooled so that the system at any temperature is approximately in thermodynamic equilibrium. Cooling proceeds until the final temperature is reached, that corresponds to the most stable (lowest energy) system state. If the initial temperature of the

system is too low or cooling is not done sufficiently slowly the system may be trapped in a local minimum energy state.

A simulated annealing algorithm consists of two nested loops. The outer-most loop sets the temperature and the inner-most loop runs a Metropolis Monte Carlo simulation at that temperature. The algorithm starts with an initial solution to the problem, which is also the best solution so far and a value for an initial high temperature. Each iteration consists of the random selection of a new solution (called candidate solution from now on) from the neighborhood of the current one. The cost function of the candidate solution is evaluated and the difference with respect to the cost function value of the current solution is computed ( $\delta$  in equation 1). If this difference is negative, i.e. the cost function value of the candidate solution is lower than the one of the current solution, the candidate solution is accepted. If the difference is positive the candidate solution is accepted with a probability based on the Boltzmann distribution (equation 1).

$$f_{Boltzmann}(\delta) = \exp(-\delta/k.T) \quad (1)$$

where  $T$  is the temperature value and  $k$  is the Boltzmann's constant. The accepted candidate solution becomes the current solution and if its cost function value is lower than the one of the best solution, this one is updated. If the candidate solution is rejected, i.e. the Boltzmann probability is less than the random number generated, the current solution stays the same and it is used in the next iteration. The temperature is lowered in each iteration down to a *frozenn* temperature where no further changes occur. The set of parameters that determine the temperature decrement is called the cooling schedule. This parameters are the initial temperature, the function that decrements the temperature between successive stages, the number of transitions needed to reach the quasi-equilibrium for each temperature value and the stop criterion.

The main aspects to be considered in a simulated annealing implementation are: 1) *solution configuration*, 2) *new solutions generation mechanism*, 3) *cost function* and 4) *cooling schedule*. These aspects, for the algorithm proposed in this paper, are explained in detail next while the algorithm is shown in figure 2.

### Solution Configuration

The solution should contain the number of classes for each variable. The configuration chosen is a vector with the same number of columns than the number of system variables, containing integers in the range  $[2 \cdots maxNC]$ .  $maxNC$  the maximum number of classes allowed.

### New Solutions Generation Mechanism

Two options can be used to generate the initial partition, i.e. current solution. The first one sets all the variables to 3 classes (default option in the current FIR implementation). The second one corresponds to a random generation of the number of classes for each system variable.

The procedure to generate a new solution, i.e. candidate solution, from the current one is to increment or decrement by one the number of classes associated to a certain system variable. The variable that is going to be modified is chosen randomly from the vector of variables. The decision to increase or decrease the

number of classes of this variable is also random. If the extremes are reached, i.e. 2 or  $maxNC$ , it is enforced to apply the increment and decrement operators, respectively.

### Cost Function

An important aspect in this research is to define an appropriate cost function for the evaluation of the partitions. To address this issue it is necessary to look closer to the qualitative model identification processe of FIR methodology.

In the process of modeling, it is desired to discover the causal and temporal relations between the inputs and the output of the system, that make the resulting state transition matrix as deterministic as possible. The more deterministic the state transition matrix is, the higher is the likelihood that the future system behavior will be predicted correctly. In FIR, the causal and temporal relations among the fuzzy qualitative variables are represented by a *mask* matrix. Equation 2 gives an example of a mask,

$$\begin{array}{c|cccc} t \setminus x & i_1 & i_2 & i_3 & O \\ \hline t - 2\delta t & 0 & 0 & 0 & -1 \\ t - \delta t & 0 & -2 & -3 & 0 \\ t & -4 & 0 & 0 & +1 \end{array} \quad (2)$$

where  $\delta t$  indicates the sampling period. A mask denotes a dynamic relationship among qualitative variables. The negative elements represents the causal relations between he inputs and the output (positive value in the mask). The sequence in which they are enumerated is immaterial. In position notation the mask of equation 2 can be written as (4, 6, 7, 9, 12), enumerating the mask from top to bottom and from left to write.

A *quality* value, based on an entropy reduction measure, is computed for each mask considered. In [4] the quality function is described in detail. The mask with highest quality is called the optimal mask. It is important to note that the optimality of the mask is evaluated with respect to the identification (training) data set. Therefore, the best mask is not, necessarily, the one that achieves the best forecast of the test data.

In this study the quality function that evaluates the information associated to the mask is used as the cost function. In that way, no prediction is needed in the partition evaluation process. Therefore, only the fuzzification and the model identification processes of FIR methodology (see figure 1) are executed to compute the cost function for a specific partition. This reduces considerably the execution time of the simulated annealing algorithm proposed.

### Cooling Schedule

Let us now take a look to all the parameters that conform the cooling schedule. The *initial temperature* depends on the initial solution generated and it is computed using equation 3,

$$T_0 = \frac{\mu}{-\ln(\Phi)} \cdot Cost(S_0) \quad (3)$$

where  $Cost(S_0)$  evaluates the cost function of the initial solution ( $S_0$ ) and  $\mu, \Phi \in [0, 1]$  and their values depend on the number of variables of the application as described in equation 4.

$$\mu = 0.3, \Phi = 0, 3 \text{ if } N \leq 3 \quad \mu = 0.1, \Phi = 0, 1 \text{ if } N > 3 \quad (4)$$

Equation 4 says that initially it is possible to accept solutions  $\mu$  per one worse than the initial solution with a probability  $\Phi$ .

Two different *cooling functions* are predominantly used, i.e. linear and proportional. In this work, the proportional cooling function proposed by Kirkpatrick [7] is used to decrement the temperature between successive stages. This function is presented in equation 5.

$$T_{k+1} = \alpha \cdot T_k \quad \text{with } \alpha = 0.9 \quad (5)$$

The *number of transitions* needed to reach the quasi-equilibrium for each temperature is defined by means of two values, the maximum number of transitions i.e. iterations in the inner loop and the maximum number of accepted solutions. The maximum number of iterations is set to  $N^3$  and the maximum number of accepted solutions is set to  $N^2$ , being  $N$  the number of system variables.

Three *stop criterions* have been used in this study. The simulation annealing algorithm stops when the number of iterations is greater than the maximum number of possible solutions ( $maxNC^N$ ), the last iteration has finished with no accepted solutions and/or  $N$  iterations have been completed without an enhancement of the global solution, i.e. the best solution is not changed during the last  $N$  iterations. It is important to remark here that if the algorithm stops due to the first criterion no advantage is obtained with respect to an exhaustive search. Moreover, the annealing algorithm does not guarantee that the optimal solution is found. The main algorithm is presented next.

```

function [BestSol] = Annealing (N,maxNC,data)
% A first solution (Current Solution) and an initial temperature (T) are
% generated. The evaluation of the cost function for the initial partition
% is also computed and stored in the CurrentSol structure
[CurrentSol,T] = GenerateCurrentSol(N,maxNC,data);

% The Current Solution is the Best Solution so far
BestSol = CurrentSol;

% The Current Solution is stored in the list of generated solutions
SolList = [CurrentSol];

% The total number of solutions generated is set to one
NumberSolutions = 1;

% Initialization of both the number of iterations without a global
% enhancement and the number of iterations without accepted solutions.
IterNoGlobalEnhance = 0;
IterNoAcceptedSol = 0; % boolean variable

% Loop that sets the temperature
while (NumberSolutions <= (maxNC^N)) & (IterNoGlobalEnhance < N)
    & (~IterNoAcceptedSol),

```

```

% Initialization of the boolean variable that establishes if a global
% enhancement has been produced, the number of accepted solutions and
% the number of iterations for the current temperature
GlobalEnhance = 0; % boolean variable
NumAcceptSol = 0;
NumIter = 0;

% Loop that runs the Metropolis Monte Carlo simulation
while (NumIter < N^3) & (NumAcceptSol < N^2),

    % The number of iterations is incremented
    NumIter = NumIter + 1;

    % The GenerateCandidateSol function generates the Candidate Solution.
    % If this solution is not in the list of generated solutions, evaluates
    % its cost function and includes both values in the solution list. If the
    % solution is already in the list (it has been generated one or more times
    % in the past), the cost function is available and it is not computed again.
    [CandidateSol,SolList] = GenerateCandidateSol(N,maxNC,CurrentSol,SolList,data);

    % The total number of solutions generated is incremented
    NumberSolutions = NumberSolutions + 1;

    % The difference between the cost function of the Candidate Solution and
    % the cost function of the Current Solution is stored in the Delta variable
    Delta = CandidateSol.cost - CurrentSol.cost;

    % Condition for the acceptance of the Candidate Solution
    if (rand(1) < exp(- Delta/T)) | (Delta < 0)

        % When accepted, the Candidate Solution becomes the Current Solution
        CurrentSol = CandidateSol;
        % The number of accepted solutions is incremented
        NumAcceptSol = NumAcceptSol + 1;
        % If the Current Solution has a lower cost function value than
        % the one of the Best Solution, this one is actualized
        if (CurrentSol.cost < BestSol.cost)
            BestSol = CurrentSol;
            GlobalEnhance = 1; % boolean variable
        end;
    end;
    % The temperature is decremented
    T = alpha*T;

    % The IterNoAcceptedSol and IterNoGlobalEnhance variables are actualized
    % once the quasi-equilibrium is reached for the current temperature
    IterNoAcceptedSol = (NumSolAcept == 0);
    if GlobalEnhance
        IterNoGlobalEnhance = 0;
    else IterNoGlobalEnhance = IterNoGlobalEnhance + 1;
    end;
end;
return

```

**Fig. 2.** Simulated Annealing algorithm for the automatic determination of fuzzy partitions in FIR methodology (Implemented in Matlab 6.5 language)

### 3 Ozone Concentration

The main air pollution problem that has been identified in Mexico city metropolitan area (MCMA) is the formation of photochemical smog, primarily ozone ( $O_3$ ). High levels of ozone causes eye irritation, respiratory disorders, crop damage and increased deterioration rate of material. In these circumstances, it is important and useful to provide early warnings of high levels of ozone concentration so that the authorities can react as fast as possible. Therefore, the construction of ozone models that capture the behavior of this gas in the atmosphere as precisely as possible is of interest not only for environmental scientists but also for government agencies. There are many different models available for local scale predictions of air quality and for ozone level forecasting. In recent years paradigms such as neural networks [8], decision trees or association rules [9] have been used for this purpose. In [6], FIR methodology has been used to model the ozone contaminant in the centre region of the Mexico city. Seven variables are involved in this study. The input variables are hour of day  $hd$  (from 0 to 23), day of week  $dw$  (from 1 to 7), wind speed  $ws$ , measured in meters per second (m/s), wind direction  $wd$ , measured in degrees (from  $0^\circ$  to  $359^\circ$ ), temperature  $t$ , measured in  $^\circ C$  and relative humidity  $hu$ , measured in percentage (from 0% to 100%). The ozone  $o3$  (measured in parts per million (PPM)), is the system's output variable. Ozone and weather data were available from January to May 2000 and contain missing values. The data of the first four months is used as identification data set, whereas the month of May is used as test data set. The mean square error in percentage (MSE) is used to determine the validity of each of the models.

In [6] three different partitions have been studied to find the model with the best prediction performance. The best optimal mask found, performing an exhaustive search, for the three partitions studied are presented in the first three rows of the table 1.

**Table 1.** Partitions results obtained by the previous work (first three rows) and the Simulated Annealing algorithm (last three rows)

Partition <i>hd dw ws wd t hu o3</i>	Optimal Mask	Quality	MSE test
(3, 3, 3, 3, 3, 3, 3)	(1,14,21)	0.595	52.08%
(5, 5, 4, 5, 4, 4, 4)	(4,14,17,21)	0.537	145.7%
(6, 6, 2, 3, 3, 4, 2)	(1,14,21)	0.738	39.36%
(3, 2, 6, 4, 6, 5, 2)	(1,14,17,21)	0.736	34.90%
(3, 3, 4, 2, 4, 2, 2)	(1,14,17,21)	0.763	38.33%
(3, 2, 5, 2, 3, 2, 2)	(1,14,17,21)	0.757	38.45%

In table 1, the first column contains the number of classes for each variable (partition). The second column describes the optimal mask associated to

that partition, in position notation. The third column contains the quality of the optimal mask, i.e. the cost function in the simulated annealing algorithm proposed. The last column contains de MSE prediction error of the test data set. The last 3 rows shows the partitions proposed by the simulated annealing algorithm when running it several times (more than 20). As can be observed from table 1 the partitions chosen by "hand" in the previous work have lower quality and performance than the partitions suggested by the simulated annealing algorithm. The partitions recommended by the SA algorithm have similar qualities and performances, and any of them can be used as a good partition parameter in the fuzzification process of FIR methodology. To chose a partition without previous criterion is a big risk that the modeler can avoid by using the SA algorithm presented. Clearly, the SA algorithm is a very useful tool that allows the modeler start using FIR in a more efficient way.

## 4 Conclusions

In this paper, a simulated annealing algorithm for the automatic tuning of fuzzy partitions in the context of the fuzzy inductive reasoning methodology has been presented. The SA algorithm suggests, for each variable, the number of classes to be discretized, basing its decision on the quality of the best mask associated to that partition. The use of the SA algorithm for the modeling of the ozone contaminant in Mexico city shows the potentiality of this approach.

**Acknowledgements.** The author thanks the suggestions of F.E. Cellier, F. Mugica and P. Villar during the development of this research. This research was supported by Spanish Consejo Interministerial de Ciencia y Tecnología (CICYT), under project DPI2002-03225.

## References

1. G. Klir. *Architecture of Systems Problem Solving*. Plenum Press, New York, 1985.
2. F. Mugica and F. Cellier. Automated synthesis of a fuzzy controller for cargo ship steering by means of qualitative simulation. In *Proc. ESM'94, European Simulation MultiConference*, pages 523–528, Barcelona, Spain, 1994.
3. M. R. N. Metropolis, A. Rosenbluth and E. T. A. Teller. Equation of state calculations by fast computing machines. *J. Chem. Phys.*, 21:1087–1092, 1953.
4. A. Nebot. *Qualitative Modeling and Simulation of Biomedical Systems Using Fuzzy Inductive Reasoning*. Ph.d. thesis, Dept. Llenguatges i Sistemes Informàtics. Universitat Politècnica de Catalunya, 1994.
5. A. Nebot, F. Cellier, and D. Linkens. Synthesis of an anaesthetic agent administration system using fuzzy inductive reasoning. *Artificial Intelligence in Medicine*, 8(3):147–166, 1996.
6. A. Nebot, F. Mugica, and P. Gómez. Long term prediction of maximum ozone concentration using fuzzy inductive reasoning. In *Proceedings EUNITE'01: European Symposium on Intelligent Technologies, Hybrid Systems and their implementation on Smart Adaptive Systems*, pages 91–101, Tenerife, Spain, 13–15 december 2001.

7. C. D. G. J. S. Kirkpatrick and M. P. Vecchi. Optimization by simulated annealing. *Science*, 220:671–680, 1983.
8. D. Wieland and W. Wotawa. Local maximum ozone concentration prediction using neural networks. In *Proceedings of the AAAI Workshop On Environmental Decision Support Systems and Artificial Intelligence*, pages 47–54, 1999.
9. F. Wotawa and G. Wotawa. From neural networks to qualitative knowledge in ozone forecasting. *AI Communications*, 14:23–33, 1993.

# Kernel Computation in Morphological Bidirectional Associative Memories

Gonzalo Urcid<sup>1,\*</sup>, Gerhard X. Ritter<sup>2</sup>, and Laurentiu Iancu<sup>2</sup>

<sup>1</sup> Optics Department, INAOE, Tonantzintla, Pue. 72000, Mexico  
[gurcid@inaoep.mx](mailto:gurcid@inaoep.mx)

<sup>2</sup> CISE Department, University of Florida, Gainesville, FL 32611–6120, USA  
[{ritter,liancu}@cise.ufl.edu](mailto:{ritter,liancu}@cise.ufl.edu)

**Abstract.** Morphological associative memories (MAMs) use a lattice algebra approach to store and recall pattern associations. The lattice matrix operations endow MAMs with properties that are completely different than those of traditional associative memory models. In the present paper, we focus our attention to morphological *bidirectional* associative memories (MBAMs) capable of storing and recalling *non-boolean* patterns degraded by random noise. The notions of morphological strong independence (MSI), minimal representations, and kernels are extended to provide the foundation of bidirectional recall when dealing with noisy inputs. For *arbitrary* pattern associations, we present a practical solution to compute kernels in MBAMs by induced MSI.

## 1 Introduction

The foundation of morphological associative memories was established in [9], where it was proved that morphological auto-associative memories have unlimited storage capacity and provide perfect recall for *noncorrupted boolean* inputs in comparison with traditional associative memories based on correlation encoding such as the classical Hopfield auto-associative memories [3,6]. Correlation encoding requires that the key vectors are orthogonal in order to exhibit perfect recall of the fundamental associations [1,4]. The morphological auto-associative memory does not restrict the domain of they key vectors in any way. Thus, as many associations as desired can be encoded into the memory; one step convergence and perfect recall of *boolean* noisy patterns using the idea of kernels were also settled [9]. Furthermore, the theoretical framework for morphological bidirectional associative memories, developed in [10], showed again, that for some *binary* pattern classes, MBAMs have large storage capacity and superior bidirectional recall than traditional BAM models [5] and also competitive with other feedforward BAM networks [15]. A characterization of kernel vectors for *binary patterns* that provided for a direct method for kernel computation as well as bounds for the allowable amount of corruption of the exemplar patterns that guarantee perfect recall appeared in [13]. An additional development that

---

\* Corresponding author. Fax: +52 (222) 247-2940; Tel.: +52 (222) 266-3100 Ext.8205

uses the notion of *dual kernels* to enhance the error correction capability of *binary* auto-associative morphological memories has been introduced in [14]. By redefining the notion of kernels, together with new concepts such as morphological strong independence and minimal representations of exemplar *non-boolean* patterns, MAMs were shown to be robust in the presence of noise [11,12].

Our work is organized as follows: Section 2 gives a brief background of lattice matrix operations for dealing with MAMs, and Section 3 provides an overview of the main results obtained from previous research on MAMs, where greyscale image pattern associations are used to illustrate their performance. Section 4 presents the known theoretical results related to MBAMs for *non-boolean* patterns including the kernel methodology for storing and recalling associations based on the notions of morphological strong independence (MSI) and minimal representations. Section 5 presents a new procedure for the computation of kernels by induced MSI. Finally, in Section 6 we give our conclusion to the research presented here.

## 2 Lattice Matrix Algebra

Lattice matrix operations are defined componentwise using the binary operations of the *bounded lattice-group* algebraic structure of  $\mathbb{IR}_{\pm\infty} = \mathbb{IR} \cup \{-\infty, +\infty\}$  [2,8]. The binary operators for the maximum or minimum of two numbers are denoted with the “join” and “meet” symbols employed in lattice theory, i.e.,  $x \vee y = \max(x, y)$  and  $x \wedge y = \min(x, y)$ . For example, the maximum of two matrices  $A, B$  of the same size  $m \times n$  is defined as  $(A \vee B)_{ij} = a_{ij} \vee b_{ij}$ , for all  $i = 1, \dots, m$  and  $j = 1, \dots, n$ . Inequalities between matrices are also verified elementwise, e. g.,  $A \leq B$  if and only if  $a_{ij} \leq b_{ij}$ . On the other hand, the *conjugate matrix*  $A^*$  is defined as  $-A^t$  where  $A^t$  denotes usual matrix transposition, or equivalently,  $(A^*)_{ij} = a_{ji}^*$ , hence  $(A \vee B)^* = A^* \wedge B^*$ . In addition, for appropriately sized matrices  $A, B$ , the  $ij$ th entry of the *max-sum* and the *min-sum* of  $A$  and  $B$ , is defined respectively, for all  $i = 1, \dots, m$  and  $j = 1, \dots, n$ , as follows

$$(A \boxminus B)_{ij} = \bigvee_{k=1}^p (a_{ik} + b_{kj}) \text{ and } (A \boxplus B)_{ij} = \bigwedge_{k=1}^p (a_{ik} + b_{kj}) , \quad (1)$$

where, e. g.,  $\bigwedge_{k=1}^p a_k$  is the minimum of the set of numbers  $\{a_1, \dots, a_p\}$ .

The relationship  $(A \boxminus B)^* = B^* \boxminus A^*$  holds for any  $A, B$ , and establishes the *duality* between both types of lattice matrix sums. Finally, the *morphological outer sum* of two vectors  $\mathbf{x} \in \mathbb{IR}^n$  and  $\mathbf{y} \in \mathbb{IR}^m$ , is given by the  $m \times n$  matrix (note that  $\mathbf{y} \oplus \mathbf{x}^t = \mathbf{y} \boxminus \mathbf{x}^t = \mathbf{y} \boxplus \mathbf{x}^t$ )

$$\mathbf{y} \oplus \mathbf{x}^t = \begin{pmatrix} y_1 + x_1 & \cdots & y_1 + x_n \\ \vdots & \ddots & \vdots \\ y_m + x_1 & \cdots & y_m + x_n \end{pmatrix} . \quad (2)$$

### 3 Morphological Associative Memories

For a given set of pattern associations  $\{(\mathbf{x}^\xi, \mathbf{y}^\xi) \in \mathbb{IR}^n \times \mathbb{IR}^m : \xi = 1, \dots, k\}$  we define a pair of associated pattern matrices  $(X, Y)$ , where  $X = (\mathbf{x}^1, \dots, \mathbf{x}^k)$  and  $Y = (\mathbf{y}^1, \dots, \mathbf{y}^k)$ . Thus,  $X$  is of dimension  $n \times k$  with  $i, j$ th entry  $x_i^j$  and  $Y$  is of dimension  $m \times k$  with  $i, j$ th entry  $y_i^j$ . To store  $k$  vector pairs  $(\mathbf{x}^1, \mathbf{y}^1), \dots, (\mathbf{x}^k, \mathbf{y}^k)$  in an  $m \times n$  MAM we use the morphological outer sum as follows [9]. The min-memory  $W_{XY}$  and the max-memory  $M_{XY}$ , that store a set of pattern associations  $(X, Y)$  are given, respectively, by the expressions

$$W_{XY} = Y \square X^* = \bigwedge_{\xi=1}^k [\mathbf{y}^\xi \oplus (-\mathbf{x}^\xi)^t] \text{ or } w_{ij} = \bigwedge_{\xi=1}^k (y_i^\xi - x_j^\xi) , \quad (3)$$

$$M_{XY} = Y \boxminus X^* = \bigvee_{\xi=1}^k [\mathbf{y}^\xi \oplus (-\mathbf{x}^\xi)^t] \text{ or } m_{ij} = \bigvee_{\xi=1}^k (y_i^\xi - x_j^\xi) . \quad (4)$$

We speak of a *hetero-associative* morphological memory (HMM) if  $X \neq Y$  and an *auto-associative* morphological memory (AMM) if  $X = Y$ . From (2), for each  $\xi$ ,  $\mathbf{y}^\xi \times (-\mathbf{x}^\xi)^t$  is a matrix  $A^\xi$  of size  $m \times n$  that memorizes the association pair  $(\mathbf{x}^\xi, \mathbf{y}^\xi)$ , hence  $W_{XY} = \bigwedge_{\xi=1}^k A^\xi$  and  $M_{XY} = \bigvee_{\xi=1}^k A^\xi$ , which suggests the given names. We use  $w_{ij}$  and  $m_{ij}$  as an alternative notation for the  $ij$ th entries of  $W_{XY}$  and  $M_{XY}$  if there is no confusion about which association is under discussion. Since,  $M_{YX}^* = (X \square Y^*)^* = Y \square X^* = W_{XY}$  and  $W_{YX}^* = (X \boxminus Y^*)^* = Y \boxminus X^* = M_{XY}$ , the retrieval of pattern  $\mathbf{y}^\xi$  from pattern  $\mathbf{x}^\xi$  can be expressed using the *direct* memory schemes (the vertical bar means “or”),

$$\mathbf{x}^\xi \rightarrow \{W_{XY} \mid M_{XY}\} \rightarrow \mathbf{y}^\xi , \quad (5)$$

where either one of  $W_{XY}$  or  $M_{XY}$  or their corresponding *duals* may be used. In a similar fashion,  $W_{YX} = M_{XY}^*$  and  $M_{YX} = W_{XY}^*$ , hence recalling the pattern  $\mathbf{x}^\xi$  from pattern  $\mathbf{y}^\xi$  can be realized using the *conjugate* or *reverse* memory schemes,

$$\mathbf{y}^\xi \rightarrow \{W_{YX} \mid M_{YX}\} \rightarrow \mathbf{x}^\xi . \quad (6)$$

The conditions of perfect recall for perfect input were established in [9] and we repeat them here for convenience. Specifically,  $W_{XY} \square X = Y$  or  $M_{XY} \boxminus X = Y$ , if and only if, for each row index  $i \in \{1, \dots, m\}$  and each pattern index  $\gamma \in \{1, \dots, k\}$ , there exists an index  $j \in \{1, \dots, n\}$  which depends on  $i, \gamma$ , such that

$$y_i^\gamma - x_j^\gamma = w_{ij} \text{ or } y_i^\gamma - x_j^\gamma = m_{ij} . \quad (7)$$

It is important to remark that, the conditions for perfect recall using MAMs may not be satisfied for arbitrary association pairs  $(X, Y)$ , with  $X \neq Y$ , that arise in most practical applications. However, even in the case that for each pattern  $\mathbf{x}^\gamma$  several row indexes do exist for which the expressions in (7) are not satisfied, the memories  $W_{XY}$  and  $M_{XY}$  still provide a storing mechanism

with *almost perfect recall*, in the sense of a suitable distance measure, between the *original* pattern  $\mathbf{y}_o^\xi$  and the *recalled* pattern  $\mathbf{y}_r^\xi$ . In particular, we use the normalized mean square error (NMSE), denoted by  $\varepsilon(\mathbf{y}_o^\xi, \mathbf{y}_r^\xi)$ , to quantify the difference between  $\mathbf{y}_o^\xi$  and  $\mathbf{y}_r^\xi$ , when recalling stored patterns by means of a specific hetero-associative memory scheme. The following example involving *non-boolean* patterns of high dimensionality illustrates our claim.

Consider the five pattern image associations  $(\mathbf{p}^1, \mathbf{q}^1), \dots, (\mathbf{p}^5, \mathbf{q}^5)$  shown in Fig. (1). Each individual pattern  $\mathbf{p}^\xi$  or  $\mathbf{q}^\xi$  is a  $50 \times 50$  pixels 256-gray scale image. For uncorrupted input, *almost* perfect recall is obtained if we use either of the memory schemes given by (5) or (6). Using the standard row-scan method, each pattern image, e.g.,  $\mathbf{p}^\xi$  can be converted into a pattern vector  $\mathbf{x}^\xi = (x_1^\xi, \dots, x_{2500}^\xi) \in \mathbb{R}^{2500}$  of  $X$  by defining,  $x_{50(r-1)+c}^\xi = p^\xi(r, c)$  for  $r, c = 1, \dots, 50$  (pattern vector  $\mathbf{q}^\xi$  is similarly defined for  $\mathbf{y}^\xi$  of  $Y$ ). Figure 2 shows the results when applying the memory scheme of (5) using the canonical memories  $W_{XY}$  and  $M_{XY}$ . A visual inspection does not reveal immediately the hidden differences that cause the recall to be non-perfect since  $\varepsilon(\mathbf{y}_o^\xi, \mathbf{y}_r^\xi) \approx 10^{-4}$  for  $\xi = 1, \dots, 5$ . Although, for a given arbitrary set  $(X, Y)$  of pattern associations, the HMMs,  $W_{XY}$  (or  $W_{YX}$ ) and  $M_{XY}$  (or  $M_{YX}$ ) are not necessarily perfect recall memories, they still can be applied successfully to deal with noisy inputs.



**Fig. 1.** The association  $(X, Y)$  that was used in constructing the memories  $W_{XY}$  and  $M_{XY}$  (of size  $2500 \times 2500$ ). First row: patterns of  $X$ ; second row: patterns of  $Y$

## 4 MBAMs and the Kernel Method

From [10], the conjugate morphological memories,  $M_{YX} = W_{XY}^*$  and  $W_{YX} = M_{XY}^*$ , also denoted by  $W^*$  and  $M^*$ , perform the feedback scheme for bidirectional recall in a MBAM. The basic association mechanisms for *perfect input* in the  $X$  to  $Y$  direction are given by the following one-step procedure without thresholding

$$\mathbf{x}^\xi \rightarrow \{W_{XY} | M_{XY}\} \rightarrow \mathbf{y}^\xi \rightarrow \{M_{YX} | W_{YX}\} \rightarrow \mathbf{x}^\xi . \quad (8)$$



**Fig. 2.** The first row displays the associated  $Y$  patterns as recalled by the memory  $W_{XY}$ ; the second row displays the associated  $Y$  patterns as recalled by the memory  $M_{XY}$

Again, conditions for *perfect recall* in MBAMs must satisfy relations similar to (7) (for MAMs) in both the forward and feedback paths for the memories involved. Even if perfect recall can not be accomplished, MBAMs allow for heavy overlap of features as was demonstrated in [10] using *boolean patterns*.

We now turn our attention to noisy patterns. Let  $I = \{1, \dots, n\}$ , a distorted version  $\tilde{\mathbf{x}}^\gamma$  of the pattern  $\mathbf{x}^\gamma$  has undergone an *erosive change* whenever  $\tilde{\mathbf{x}}^\gamma \leq \mathbf{x}^\gamma$  or equivalently if  $\forall i \in I, \tilde{x}_i^\gamma \leq x_i^\gamma$ . A *dilative change* occurs whenever  $\tilde{\mathbf{x}}^\gamma \geq \mathbf{x}^\gamma$  or equivalently if  $\forall i \in I, \tilde{x}_i^\gamma \geq x_i^\gamma$ . Let  $L, G \subset I$  be two non-empty disjoint sets of indexes; if  $\forall i \in L, \tilde{x}_i^\gamma < x_i^\gamma$  and  $\forall i \in G, \tilde{x}_i^\gamma > x_i^\gamma$ , then the distorted pattern  $\tilde{\mathbf{x}}^\gamma$  is said to contain *random noise*. In order to deal efficiently with corrupted versions of exemplar patterns, the kernel method has proven to be useful in the *binary* case for MAMs [9,13] and MBAMs [10]. Here, we will extend the kernel technique in MBAMs to store and recall *non-boolean* pattern associations.

The underlying idea of the kernel technique is to define a memory  $M$  which associates with each input pattern  $\mathbf{x}^\gamma$  an intermediate eroded pattern  $\mathbf{z}^\gamma$  called the *kernel pattern*. Another associative memory  $W$  is defined which associates each kernel pattern  $\mathbf{z}^\gamma$  with the desired output pattern  $\mathbf{y}^\gamma$ . In terms of min-max sums, one obtains the equation,  $W \boxtimes (M \boxtimes \mathbf{x}^\gamma) = \mathbf{y}^\gamma$ . The combination of the two morphological memories  $M$  and  $W$  is what motivated the following definitions and results (proved in [12]); for application purposes we assume that pattern features are *non-negative*, i.e.,  $x_i^\gamma \geq 0$  for all  $i, \gamma$ .

**Definition 4.1.** Let  $Z = (\mathbf{z}^1, \dots, \mathbf{z}^k)$  be an  $n \times k$  matrix. We say that  $Z$  is a *kernel* for  $(X, Y)$  with  $X \neq Y$ , if and only if  $Z \neq X$  and there exists a memory  $W$  such that  $W \boxtimes (M_Z \boxtimes \mathbf{x}^\gamma) = \mathbf{y}^\gamma$ .

**Definition 4.2.** A set of patterns  $Z \leq X$  is said to be a *minimal representation* of  $X$  if and only if for  $\gamma = 1, \dots, k$ ,  $\mathbf{z}^\gamma \wedge \mathbf{z}^\xi = \mathbf{0} \ \forall \xi \neq \gamma$ ,  $\mathbf{z}^\gamma$  contains at most one non-zero entry, and  $W_{ZX} \boxtimes \mathbf{z}^\gamma = \mathbf{x}^\gamma$ .

**Definition 4.3.** A set of pattern vectors  $X$  is said to be *morphologically strongly independent* (MSI) if and only if,  $\forall \xi \neq \gamma$ , the next two conditions are satisfied:

1.  $\forall \gamma \in \{1, \dots, k\}, \mathbf{x}^\gamma \not\leq \mathbf{x}^\xi,$
2.  $\forall \gamma \in \{1, \dots, k\}$ , there  $\exists j_\gamma \in \{1, \dots, n\}$  such that

$$x_i^\gamma - x_i^\xi \leq x_{j_\gamma}^\gamma - x_{j_\gamma}^\xi, \quad \forall i \in \{1, \dots, n\} . \quad (9)$$

**Theorem 4.1.** If  $X$  is morphologically strongly independent, then there exists a set of patterns  $Z \leq X$  with the property that for  $\gamma \in \{1, \dots, k\}$

1.  $\forall \xi \neq \gamma, \mathbf{z}^\gamma \wedge \mathbf{z}^\xi = \mathbf{0}$
2.  $\mathbf{z}^\gamma$  contains at most one non-zero entry, and
3.  $W_{XX} \boxtimes \mathbf{z}^\gamma = \mathbf{x}^\gamma$ .

**Corollary 4.1.** If  $X$  and  $Z$  are as in Theorem 4.1, then  $Z$  is a minimal representation of  $X$ .

**Corollary 4.2.** If  $X$  and  $Z$  are as in Theorem 4.1 and  $W_{XY}$  is a perfect associative recall memory, then  $Z$  is a kernel for  $(X, Y)$  with  $W = W_{XY} \boxtimes W_{XX}$ .

It is clear, from Corollary 4.2, that the recall mechanism in MBAMs is given by the following feed-forward network

$$\mathbf{x}^\xi \rightarrow M_{ZZ} \rightarrow W \rightarrow \mathbf{y}^\xi \rightarrow M_{VV} \rightarrow W' \rightarrow \mathbf{x}^\xi , \quad (10)$$

where,  $W = W_{XY} \boxtimes W_{XX}$ ,  $W' = W_{YX} \boxtimes W_{YY}$ , and  $V$  is a kernel for  $(Y, X)$ . The conditions that,  $W_{XX} \boxtimes \mathbf{z}^\gamma = \mathbf{x}^\gamma$  and  $W_{YY} \boxtimes \mathbf{v}^\gamma = \mathbf{y}^\gamma$  are crucial for the recall capability of the memory scheme of (10) when presented with noisy inputs. Given a pair of minimal representations  $Z, V$  which are also kernels, respectively, for  $(X, Y)$  and  $(Y, X)$ , and a noisy version  $(\tilde{\mathbf{x}}^\gamma, \tilde{\mathbf{y}}^\gamma)$  of the pattern association  $(\mathbf{x}^\gamma, \mathbf{y}^\gamma)$  having the property that  $(\mathbf{z}^\gamma, \mathbf{v}^\gamma) \leq (\tilde{\mathbf{x}}^\gamma, \tilde{\mathbf{y}}^\gamma)$  and  $(M_{ZZ} \boxtimes \tilde{\mathbf{x}}^\gamma, M_{VV} \boxtimes \tilde{\mathbf{y}}^\gamma) \leq (\mathbf{x}^\gamma, \mathbf{y}^\gamma)$ , then it must follow that

$$W_{XX} \boxtimes (M_{ZZ} \boxtimes \tilde{\mathbf{x}}^\gamma) = \mathbf{x}^\gamma \quad \text{and} \quad W_{YY} \boxtimes (M_{VV} \boxtimes \tilde{\mathbf{y}}^\gamma) = \mathbf{y}^\gamma . \quad (11)$$

Although the performance of the proposed feed-forward MBAM network when presented with noisy inputs can not be assured in a completely deterministic way, for any set  $(X, Y)$  of  $k$  associated patterns in  $\mathbb{R}^n \times \mathbb{R}^m$ , the expectation of recall capability is enhanced if  $\min(n, m) \gg 0$  and  $k \ll \min(n, m)$ .

## 5 Computation of Kernels

From a theoretical point of view, Theorem 4.1 and its corollaries provide the foundation for the kernel method when applied to *perfect inputs*. In addition, the combined memory scheme suggested by (10) together with the kernel association shown in (11) provide a useful mechanism for bidirectional pattern recall of *noisy inputs*. On the other hand, it is clear that the condition of morphological strong independence of the sets  $X$  and  $Y$  will be rarely satisfied in practical situations and seems to be very restrictive in its possible applications. A practical solution to this dilemma is given by the following procedure.

**Algorithm 5.1.** [MBAM kernels by induced MSI.]

STEP 1. Compute the global maximum  $U$ , and the global minimum  $L$  of the input set  $X$  that has  $k$  patterns of dimension  $n$ , i.e.,  $U = \max(X) = \bigvee_{i=1}^n \bigvee_{\xi=1}^k x_i^\xi$  and  $L = \min(X) = \bigwedge_{i=1}^n \bigwedge_{\xi=1}^k x_i^\xi$ .

STEP 2. Let  $I = \{1, \dots, n\}$ . For  $\xi = 1, \dots, k$ , compute an index  $i_\xi \in I$  where the first available maximum value occurs, i.e., let  $x_{i_\xi}^\xi = \bigvee_{i \in I} x_i^\xi$ ,  $I = I - \{i_\xi\}$ ,  $\xi = \xi + 1$ , and recompute  $x_{i_\xi}^\xi$  for the new pattern  $\mathbf{x}^\xi$ , hence  $\forall \gamma \neq \xi, i_\gamma \neq i_\xi$ .

STEP 3. Change the original pattern set  $X$ , at all positions  $i_\xi$  for  $\xi = 1, \dots, k$  with the  $U$  and  $L$  values determined in Step 1. Specifically, set  $x_{i_\gamma}^\xi = U$  if  $\gamma = \xi$  otherwise set it to  $L$ . It turns out, that the modified pattern set, denoted by  $\hat{X}$ , is a morphologically strongly independent set.

STEP 4. Apply to  $\hat{X}$  the kernel method and the morphological memory scheme as described in Section 4. The kernel  $Z$  of  $\hat{X}$  is readily obtained from Step 3, by defining for  $i = 1, \dots, n$  and  $\xi = 1, \dots, k$ ,  $z_i^\xi = U$  if  $i = i_\xi$  otherwise set it to 0.

STEP 5. Repeat STEPS 1–4 for set  $Y$  to find the kernel  $V$  of  $\hat{Y}$ . In this final step, a two way kernel  $(Z, V)$  has been determined for  $(X, Y)$ .

To complete the description of Algorithm 5.1, we next prove that set  $\hat{X}$  (similarly for  $\hat{Y}$ ) satisfies both conditions for MSI of Definition 4.3:

1.  $\forall \gamma \in \{1, \dots, k\}, x^\gamma \not\leq x^\xi$  for all  $\xi \neq \gamma$ ; that is, an index  $j_\gamma \in \{1, \dots, n\}$  exists such that  $x_{j_\gamma}^\gamma > x_{j_\gamma}^\xi$  for all  $\xi \neq \gamma$ . That this is true, follows immediately from the assignment made in STEP 3 by making the choice,  $j_\gamma = i_\gamma$ .
2.  $\forall \gamma \in \{1, \dots, k\}$ , there is an index  $j_\gamma \in \{1, \dots, n\}$  such that,  $\forall i \in \{1, \dots, n\}$ ,  $x_{j_\gamma}^\gamma - x_{j_\gamma}^\xi \geq x_i^\gamma - x_i^\xi$ ; take again,  $j_\gamma = i_\gamma$ , therefore  

$$U - L = \bigvee_{i=1}^n (x_i^\gamma - x_i^\xi) \geq x_i^\gamma - x_i^\xi \quad \square$$

Essentially, the kernel computation suggested in Algorithm 5.1, introduces an alternative MBAM scheme that substitutes (10), as follows,

$$\begin{aligned} \mathbf{x}^\xi &\rightarrow \hat{\mathbf{x}}^\xi \rightarrow M_{ZZ} \rightarrow W_{\hat{X}\hat{X}} \rightarrow W_{\hat{X}Y} \rightarrow \mathbf{y}^\xi \\ \mathbf{x}^\xi &\leftarrow W_{\hat{Y}X} \leftarrow W_{\hat{Y}\hat{Y}} \leftarrow M_{VV} \leftarrow \hat{\mathbf{y}}^\xi \leftarrow \mathbf{y}^\xi , \end{aligned} \tag{12}$$

where, the recollection mechanism is based on the modified pattern sets  $\hat{X}, \hat{Y}$  rather than the original  $X, Y$  sets. Observe that induced MSI introduces a negligible amount of deterministic “artificial noise” to the original patterns which does not affect the MBAM performance if  $\min(n, m) \gg 0$  and  $k \ll \min(n, m)$ .

## 6 Conclusion

Several key steps have been achieved for enhancing the recall capability as well as the error correction rate of morphological associative memories in the case of boolean patterns. However, the kernel technique in the non-boolean case has required more elaborate concepts to deal effectively with corrupted inputs. Morphological strong independence is a sufficient condition for building minimal representations and kernels; however, in most practical applications, the association pattern sets may not satisfy this requirement. Therefore, at the expense of reducing storage capacity, the induced MSI procedure presented here is useful for generating a two way kernel in a MBAM that is quite robust to random noise for *arbitrary* non-boolean associations.

## References

1. Chen H. et al.: Higher order correlation model for associative memories. Neural Networks for Computing, J. S. Denker, Ed. **151** (1986) AIP Proc.
2. Cuninghame-Green, R.: Minimax algebra. Lectures Notes in Economics and Mathematical Systems **166** (1979), New York, Springer.
3. Hopfield, J. J.: Neurons with graded response have collective computational properties like those of two state neurons. Proc. of the National Academy of Sciences **81** (1984) 3088–3092, U.S.A.
4. Kohonen, T.: Correlation matrix memory. IEEE Trans. Computers **C-21** (1972) 353–359.
5. Kosko, B.: Bidirectional associative memories. IEEE Trans. Systems, Man, and Cybernetics **18**(1)(1988) 49–60.
6. McEliece, R. et al.: The capacity of the Hopfield associative memory. Trans. Information Theory **1** (1987) 33–45.
7. Okajima, K., Tanaka, S., Fujiwara, S.: A heteroassociative memory with feedback connection. Proc. IEEE 1st Inter. Conf. Neural Networks **2** (1987) 711–718.
8. Ritter, G. X.: Image Algebra. Unpublished manuscript, available at <ftp://ftp.cise.ufl.edu/pub/scr/ia/documents> (1994) University of Florida, Gainesville, FL.
9. Ritter, G. X., Sussner, P., Diaz de Leon, J. L.: Morphological associative memories. IEEE Trans. Neural Networks **9**(2) (1998) 281–293.
10. Ritter, G. X., Diaz de Leon, J. L., Sussner, P.: Morphological bidirectional associative memories. Neural Networks **12**(6) (1999) 851–867.
11. Ritter, G. X., Urcid, G.: Minimal representations and morphological associative memories for pattern recall. Proc. 7th Iberoamerican Congress on Pattern Recognition (2002).
12. Ritter, G. X., Urcid, G., Iancu, L.: Reconstruction of noisy patterns using morphological associative memories. J. of Math. Imaging and Vision **19**(5) (2003) 95–111.
13. Sussner, P.: Observations on morphological associative memories and the kernel method. Neurocomputing **31** (2000) 167–183.
14. Sussner, P.: Binary autoassociative morphological memories based on the kernel and dual kernel methods. Int. Joint Conf. on Neural Networks (2003).
15. Wu, Y., Pados, D. A.: A feedforward bidirectional associative memory. IEEE Trans. Neural Networks **11**(4) (2000) 859–866.

# Improving Still Image Coding by an SOM-Controlled Associative Memory

Gerald Krell<sup>1</sup>, René Rebmann<sup>1</sup>, Udo Seiffert<sup>2</sup>, and Bernd Michaelis<sup>1</sup>

<sup>1</sup> Otto-von-Guericke University Magdeburg, Germany,  
krell@iesk.et.uni-magdeburg.de,  
<http://iesk.et.uni-magdeburg.de/~krell>

<sup>2</sup> Leibniz Institute of Plant Genetics and Crop Plant Research Gatersleben, Germany

**Abstract.** Archiving of image data often requires a suitable data reduction to minimise the memory requirements. However, these compression procedures entail compression artefacts, which make machine processing of the captured documents more difficult and reduce subjective image quality for the human viewer. A method is presented which can reduce the occurring compression artefacts. The corrected image yields as output of an auto-associative memory that is controlled by a Self-Organising Map (SOM).

## 1 Introduction

Standard image compression algorithms do not consider the image content for the selection of compression parameters. Often, the user has to do experiments with the compression parameters until his requirements are met. We propose a system for the correction of compression artefacts based on an associative memory that is improved by a Self-Organizing Map (SOM) controlling its parameters (Fig. 1).

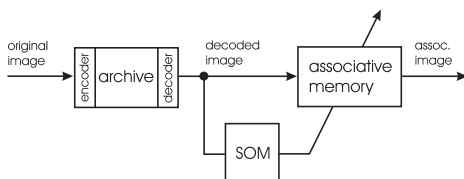


**Fig. 1.** SOM-controlled associative memory

The JPEG procedure (Joint Photographic Expert Group) [2,3] is typical for lossy image compression and an inherent part of image capturing devices such as scanners or digital cameras often implemented in integrated circuits. The classical block-based JPEG procedure formed therefore the basis of our fundamental investigations, but the main ideas of our approach can be applied also to the wavelet-based methods of JPEG 2000. The examples are on the basis

of gray-value images in order to simplify the explanations. The same method can be applied to each component of color images, of course. Consideration of the coupling of the basis colors can improve the results but is not further explained in this paper.

Different approaches exist to describe image degradation [11]. Often, the deviation of the considered and the error-free reference image is assessed by the sum or mean of error squares (or the square root of it: root mean square, RMS) as a quantitative measure. Also the signal-to-noise ratio (SNR) and the mean absolute difference (MAD) are important criterions. The integrating property of these criteria is a serious drawback and the subjective evaluation of an image often deviates from such simple measures. Subjective assessment of image quality depends strongly on the assessing group of persons [11]. In order to reduce the compression artefacts generated by JPEG compression, different solutions have been examined. The quantitative error measure for all investigated approaches has been the sum of error squares. This avoids expensive interviews for a subjective evaluation and the results are easier to be compared. In most cases, a lower quadratic error leads to a better subjective image quality.

An important assumption in our approach is that images of a certain image content can be assigned to classes of images. The variability of an image is limited in many typical cases such as text documents, cheque forms, traffic scenes, nature images etc. Internal coherences exist in the images of an image class, which should be generally exploited for redundancy reduction. This way, the compression procedure is optimised depending on the particular image class. The application of a procedure with well defined parameters for a particular image class to a different (dissimilar) image class can therefore lead to poor results. An image-class-dependent correction seems to be a promising approach to compensate the loss of information caused by image compression. The missing information on the coherences within an image class is recalled from an associative memory after the decompression. This way, the compression artefacts are to be reduced.

## 2 An Auto-associative Recall for Compressed Image Blocks

At first we describe the function of the associative memory. It is applied to the degraded archive images of a certain class. To consider calculation resources and the typical structure of JPEG we have designed associative memories according to image blocks of 8 by 8 pixels. For the  $k$ -th block of an image yields

$$\mathbf{O}_k = \begin{bmatrix} b_{IN_{1,k}} & b_{IN_{9,k}} & \cdots & b_{IN_{57,k}} \\ b_{IN_{2,k}} & b_{IN_{10,k}} & \cdots & b_{IN_{58,k}} \\ \dots & \dots & \dots & \dots \\ b_{IN_{8,k}} & b_{IN_{16,k}} & \cdots & b_{IN_{64,k}} \end{bmatrix}; \quad \mathbf{R}_k = \begin{bmatrix} b_{JPG_{1,k}} & b_{JPG_{9,k}} & \cdots & b_{JPG_{57,k}} \\ b_{JPG_{2,k}} & b_{JPG_{10,k}} & \cdots & b_{JPG_{58,k}} \\ \dots & \dots & \dots & \dots \\ b_{JPG_{8,k}} & b_{JPG_{16,k}} & \cdots & b_{JPG_{64,k}} \end{bmatrix} \quad (1)$$

where  $\mathbf{O}_k$  is the original image block and  $\mathbf{R}_k$  the resulting block after compression/decompression with  $b_{IN_{1\dots 64,k}}$  and  $b_{JPG_{1\dots 64,k}}$  being the  $8 * 8$  gray values of

the  $k$ -th image blocks. The gray values are numbered column-wise obtaining the vectorized original and compressed/decompressed images, respectively:

$$\mathbf{B}_{IN} = \begin{bmatrix} b_{IN_{1,1}} & \dots & b_{IN_{1,k}} & \dots & b_{IN_{1,K}} \\ b_{IN_{2,1}} & \dots & b_{IN_{2,k}} & \dots & b_{IN_{2,K}} \\ \dots & & \dots & & \dots \\ b_{IN_{64,1}} & \dots & \dots & & b_{IN_{64,K}} \end{bmatrix}; \mathbf{B}_{JPG} = \begin{bmatrix} b_{JPG_{1,1}} & \dots & b_{JPG_{1,k}} & \dots & b_{JPG_{1,K}} \\ b_{JPG_{2,1}} & \dots & b_{JPG_{2,k}} & \dots & b_{JPG_{2,K}} \\ \dots & & \dots & & \dots \\ b_{JPG_{64,1}} & \dots & \dots & & b_{JPG_{64,K}} \end{bmatrix}. \quad (2)$$

These  $K$  blocks can originate from the same image or from different images but their contents should possess similar properties to fulfil the desired requirement to represent a certain image class. The selection of suitable sample blocks presenting prototypes of the defined image class is crucial for a good correction. Different strategies to determine the sample blocks have been therefore investigated. For the description of the associative memory approach, we will now use Fig. 2.

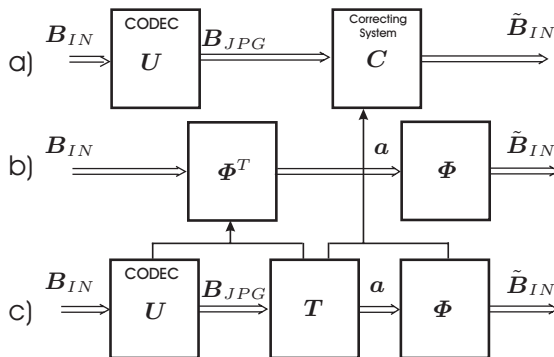


**Fig. 2.** Associative memory for the correction of compression artefacts

Investigations on real image data showed that the relationships between an original and a decompressed image can be approximately described by a set of linear equations. This holds, of course, especially for image classes that are characterized by certain statistic properties. The process of compression/decompression (CODEC) can therefore be approximated by a system matrix  $\mathbf{U}$  for a mathematically simple description (see Fig. 2a). Assuming an approximately linear transfer behaviour of the CODEC, the elements of  $\mathbf{U}$  can be determined by minimisation of the error squares for a test data set. The number of samples must be greater than the number of pixels in the image block. This corresponds to the determination of the pseudo inverse [8,4]:

$$\mathbf{U} = \mathbf{B}_{JPG} \mathbf{B}_{IN}^T \left( \mathbf{B}_{IN} \mathbf{B}_{IN}^T \right)^{-1}. \quad (3)$$

We are looking for a correcting system  $\mathbf{C}$  that compensates the influences caused by  $\mathbf{U}$  as far as possible. This means that our aim is to approximate  $\tilde{\mathbf{B}}_{IN}$

by  $\mathbf{B}_{IN}$ . Such systems can be considered as auto-associative memories. The investigation of the eigenvalues of the transfer matrix  $\mathbf{U}$  resulted in a certain number of eigenvalues with a value zero or close to zero. Here, a direct relationship to the lossy data compression exists where higher frequency components are also often weighted less (reduced code length of JPEG for coefficients of higher frequency components). More eigenvalues of  $\mathbf{U}$  are close to zero with increasing compression rate (lower quality). The relation between number of zero values at higher frequencies and the compression rate is almost linear. This observed behaviour motivates the scheme of classical auto-associative memory [1] according to Fig. 2b that is able to store a-priori knowledge on the image contents. The determination of  $\Phi$  for a certain data set can be considered as a training that approximates  $\tilde{\mathbf{B}}_{IN}$  by  $\mathbf{B}_{IN}$  (auto-association). The training of the auto-associative system can be expressed by

$$\tilde{\mathbf{B}}_{IN} = \Phi \Phi^T \mathbf{B}_{IN} \rightarrow \mathbf{B}_{IN} \quad (4)$$

with a residual error caused by the interpolating behaviour and

$$\tilde{\mathbf{B}}_{IN} = \sum_{\nu} a_{\nu} \varphi_{\nu} = \Phi \mathbf{a} \quad (5)$$

with  $\varphi_{\nu}$  being the  $\nu$ -th line of  $\Phi$  and  $a_{\nu}$  the  $\nu$ -th dimension-reduced signal. The mean square error between  $\tilde{\mathbf{B}}_{IN}$  and  $\mathbf{B}_{IN}$  has to be minimized for each length of vector  $\mathbf{a}$ . An eigenvalue problem results when considering the data of an image class (assuming the number of samples in the data set of this image class is much greater than one) as follows:

$$\mathbf{B}_{IN} \mathbf{B}_{IN}^T \Phi = \Lambda \Phi. \quad (6)$$

The transformation matrix  $\Phi$  is calculated by the solution of the eigenvalue problem [4,6]. The matrix  $\Lambda$  contains the eigenvalues of  $\mathbf{B}_{IN} \mathbf{B}_{IN}^T$  in the main diagonal. This dimension reduction is crucial for the overall system because it stands for the inherent a-priori knowledge that is stored in  $\Phi$ . The corrected image is recalled from the left part of the associative memory (b) by the Karhunen Loëve coefficients  $\mathbf{a}$ .

Because the CODEC produces image data a transfer matrix  $\mathbf{T}$  producing vector  $\mathbf{a}$  (Fig. 2b) is separated from  $\Phi^T$ . The behaviour of the eigenvalues of  $\mathbf{U}$  (increasing compression  $\rightarrow$  fewer eigenvalues  $\neq 0$ ) leads to the conclusion that the first part of the auto-associative memory (Fig. 2b, can be considered as forward transform) models the process of compression/decompression if the length of vector  $\mathbf{a}$  is limited in (Fig. 2c). The same holds for the correcting system  $\mathbf{C}$  consisting of  $\mathbf{T}$  and  $\Phi$ .

$\mathbf{B}_{JPG} = \mathbf{U} \mathbf{B}_{IN}$  models the compression/decompression approximation by the associative memory and from Fig. 2c follows  $\tilde{\mathbf{B}}_{IN} = \Phi \mathbf{T} \mathbf{B}_{JPG}$ . This leads to  $\mathbf{T} = \mathbf{U}^{-1} \Phi^T$ , with  $\mathbf{U}^{-1}$  being the Moore-Penrose inverse [4] and to the resulting correction matrix

$$\mathbf{C} = \mathbf{T} \Phi = (\mathbf{U}^{-1} \Phi^T) \Phi. \quad (7)$$

### 3 An SOM for Image Block Classification

A further improvement of the results of correction can be expected if special transformation matrices  $\Phi$  and  $T$  are determined according to each single image class. An automatic and adaptive classification is desirable. Artificial neural networks are well known and suitable for classification tasks.

Because a direct learning target for the image blocks and the centre of gravity of the classes is hard to define, a SOM seems to be appropriate for this application. The SOM was suggested and developed by Kohonen in the early '80s [5] and was then established as powerful and adaptive tool for clustering and visualization [10]. It belongs to the group of unsupervised trained artificial neural networks with a close relationship to biological signal processing [7]. Due to its inherent properties and biological origin the SOM seems to be predestined to be implemented in the complex image processing system described in this paper.

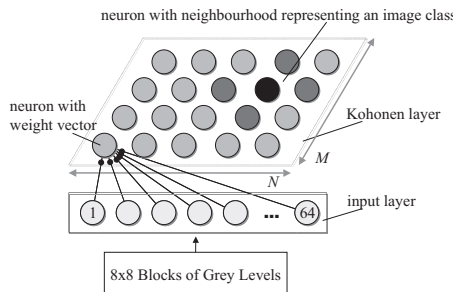


**Fig. 3.** Scheme of the SOM for the creation of image block classes

It performs an ordered non-linear mapping of high-dimensional input data onto a usually two-dimensional rectangular grid of neurons. This reduction of the dimensionality is characterised by an abstraction to important properties contained in the input data. At the same time insignificant information is reduced or even removed. The SOM generally allocates more neurons for inputs that occur more frequently in the input space (magnification factor). This improves the local resolution in these areas. This way the resources, in other words the usage of neurons available for the input data representation, are optimised during the training phase of the network. This is very similar to biological brain maps where for instance in the visual cortex a larger cortical area is allocated for frequently presented observations.

Due to its topology preservation, the SOM, unlike many other clustering algorithms, keeps similarities of the input data by transforming these into neighbourhood relations of the organized map (Fig. 3). In this organizing phase each neuron matures to a prototype for a particular (sub-)cluster by adapting its own properties (weight vector) to those of a group of similar or identical input patterns (input vectors) by using a simple similarity criterion. A neighbourhood

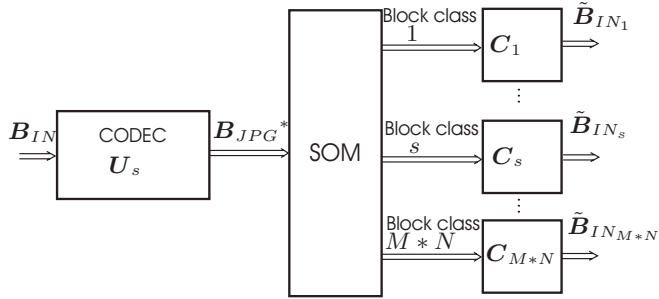


**Fig. 4.** SOM-controlled correction of the compression artefacts

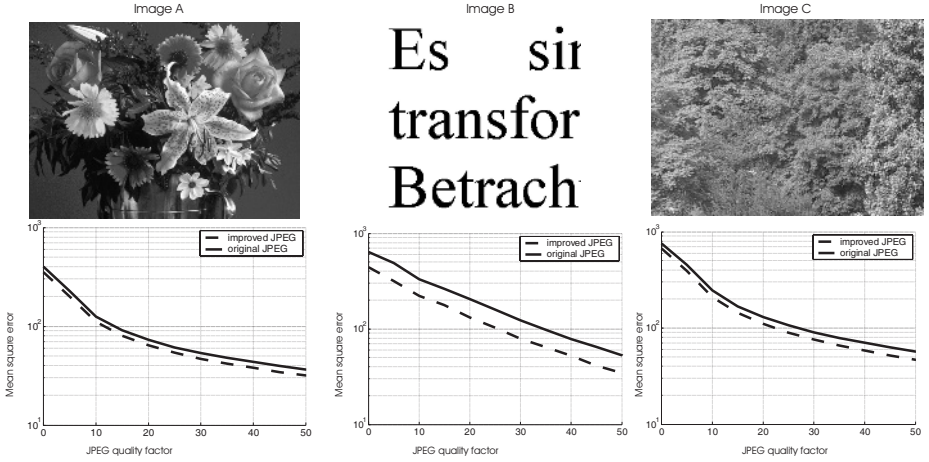


**Fig. 5.** Error reduction on the basis of example images without SOM

function works in such a way that neurons situated close to each other on the map are representing similar properties. In our case the input layer of the SOM is provided by the pixels of the image block. For each input one of the  $M * N$  output neurons - the winner neuron - defines the represented image class. Fig. 4 shows the interaction of the SOM with the CODEC providing its input and the parameter sets  $C_s$  of the auto-associative memory to be activated by the winning neuron. For each block class,  $1 \dots s \dots M * N$ , a parameter set  $\Phi_s$  for the associative memory is calculated by solving the eigenvalue problems and similar to the former considerations (see Eq. 2) yields for each block class  $s$ :

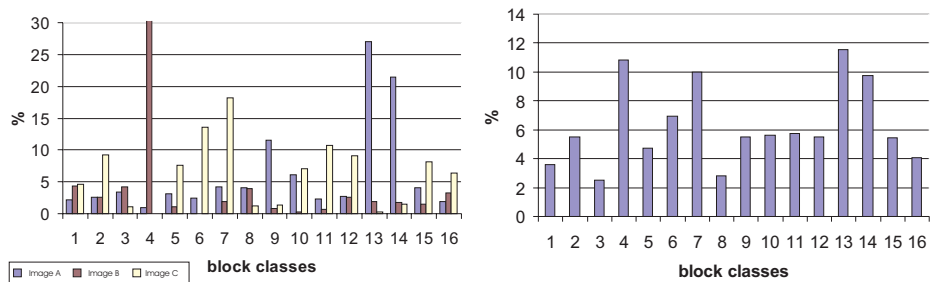
$$C_s = \left( U_s^{-1} \Phi_s^T \right) \Phi_s. \quad (8)$$

## 4 Results

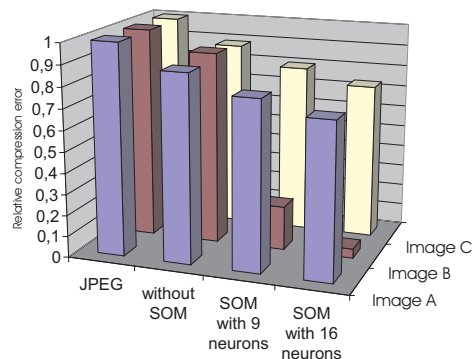
On the basis of three example images the results of the reduction of the compression errors (method of section 2, without SOM) are represented in the following

Fig. 5. The compression error can be reduced by approximately 20 % depending upon the image content and the quality factor or the compression rate can be approximately increased by 25 % without rising up the compression error.

The proposed procedure for the reduction of the compression artefacts has positive effects on further automatic processing of the images. In order to obtain further improvements for the human viewer, other criteria must be additionally included in the selected error measure. The positive effect of reduced compression errors for further automatic processing can be demonstrated by the example of the text recognition. The recognition error can be reduced up to 48 % at higher compression rates (quality factor less than 10). Typical image classes are classified by the SOM. Block-dependent image classes are obtained and the above described method can be applied with varying parameter sets to the associative memory.



**Fig. 6.** Distribution of the image blocks after the training of a 4x4 SOM (left) for all blocks (right) ordered by sample images



**Fig. 7.** Compression error without correction, with correction by associative memory but without SOM and correction error with associative memory controlled by SOM of different sizes, applied to the sample images

Fig. 6 shows a training result of the SOM for the example images of Fig.4. The classifying neurons are well distributed. This is an indication that the SOM is of reasonable size.

Fig. 7 shows the gain of quality by introducing the classifying SOM for the correcting system. With the varying parameter set for the associative memory, the error reduces by about 20...30% for the gray tone images and up to 90 % for the text image. For simplification of the complex diagram, only relative compressions errors are indicated.

## 5 Conclusion

A system for compensation of compression errors by an associative memory has been presented. The performance has been increased considering the image (or block) content introducing a neural network based classification system - a SOM. The SOM enables us to apply the same correcting system to different types of image and also to images with strongly varying image content (for example mixture of text and photographs). The number of different parameter sets needed for correction is equal to the number of neurons in the SOM or the number of introduced image classes. [9] proposes an SOM as a compression scheme as an alternative to vector quantization directly generating the codewords. This interesting approach for compression with an SOM could also be completed with an SOM controlled associative memory as proposed in this paper. Depending on the codeword the associative memory is recalled with different parameter sets.

**Acknowledgments.** The investigations took place in the context of the project "Adaptive Read". The project is sponsored by the Federal Ministry for Education and Research of the Federal Republic of Germany (01 IN 902 J) and by the federal state Sachsen-Anhalt (0032KB099).

## References

1. Abbas H.M., Fahmy, M.M.: A Neural Model for Adaptive Karhunen Loéve Transformation (KLT). Proc. International Joint Conference on Neural Networks, Baltimore, Maryland, vol. 2 (1992)975–980
2. ISO/IEC JTC1 10918-1, ITU-T Rec. T.81, Information technology - Digital compression and coding of continuous-tone still images: Requirements and guidelines (1994)
3. ISO/IEC JTC 1/SC 29/WG 1: Coding of Still Pictures - JPEG 2000. Part 1 Final Committee Draft Version 1.0 (2000)
4. A. Kielbasinski; H. Schwetlick: Numerische Lineare Algebra. Deutscher Verlag der Wissenschaften, Berlin (1988)
5. Kohonen, T.: Self-Organizing Maps. 3rd ed., Springer, London (2001)
6. T. Lilienblum, P. Albrecht, R. Calow, B. Michaelis: Dent Detection in Car Bodies. 15th International Conference on Pattern Recognition (ICPR), Barcelona, 3–8 September 2000, Vol. 4, (2000) 775–778

7. K. Obermayer, T.J. Sejnowski (eds.): Self-Organizing Map Formation – Foundations of Neural Computation. The MIT Press, Cambridge Ma. (2001)
8. R. Rebmann, G. Krell, B. Michaelis: Reduction of Compression Artefacts Caused by JPEG Compression. Proceedings of the VIIP2002 (Sep. 9–12, 2002), ACTA Press, Malaga (2002) 271–275
9. C. Amerijckx and Ph. Thissen: Image Compression by Self-Organized Kohonen Map. IEEE Transactions on Neural Networks, Vol. 9, No. 3, May 1998 (503–507)
10. U. Seiffert, L.C. Jain (eds.): Self-Organizing Neural Networks – Recent Advances and Applications. Springer, Heidelberg (2001)
11. H.R. Tizhoosh, B. Michaelis: Image Enhancement Based on Fuzzy Aggregation techniques. IMTC/99, Proceedings of the 16th IEEE conference (1999) 1813–1817

# A Morphological Methodology for Features Identification in Satellite Images for Semi-automatic Cartographic Updating

Michele Mengucci and Fernando Muge

CRVM Centro de Geo-Sistemas do I.S.T.  
Av.Rovisco Pais 1  
1049-001 Lisboa, Portugal  
Tel. +351 21 841 72 47 – Fax +351 21 841 74 42  
[mmengucci@ist.utl.pt](mailto:mmengucci@ist.utl.pt)

**Abstract.** This work investigates a way to exploit the information of satellite images in order to identify cartographic features, aiming at developing a software tool able to update digital maps automatically. A cartographic feature, like any object present in a multi-channel image, is a set of pixels with similar spectral response and a certain spatial relation between them. The current algorithm works iteratively and mixes the spatial information with the spectral one in an appropriate way to finally detect the whole shape of a cartographic feature starting from a pixel marked previously by the user in a remotely sensed image. It is also shown that Mathematical Morphology (MM) operators can handle the spatial and spectral information decreasing the computational cost. First, the structure of the main algorithm is presented, showing each step of its operational sequence. Then, some application examples are reported and, finally, some remarks illustrate the future possibilities of implementation and development of the algorithm.

## 1 Introduction

Objects in multi-channel images, particularly remotely sensed ones, are set of pixels that can be assembled together by their individual spectral response and by their neighborhood relationship in the spatial domain of each channel. Although there exist in the literature several works that propose to control the segmentation through spectral information [1] [2] [3], there is not a general procedure that combines both types of information. Thus, in this paper, we introduce a novel methodology, whose main objective consists of generating objects by assembling together small elementary regions that are simultaneously spectral and spatial neighbors. Usually the classification procedures are distinguished between *boundary seeking* and *region growing* [4] [5], whether the objects are defined detecting their edge pixels, or as regions in which the pixel values are homogeneous. The proposed algorithm firstly divides the image's spatial domain in small areas and then applies a region growing process to the areas instead than directly to the pixels, so the spectral information is processed in two steps, on the pixel scale and on the elementary region scale.

The first partitioning is performed with a *watershed* [6] transformation on the *spectral gradient* [7] [8] [9], thus obtaining a fine segmentation that preserves the image spectral meaning. Therefore a unique and representative spectral value can be assigned to each area, producing a multispectral *mosaic image* [6]. On the latter a region growing procedure performs an iterative merging of the regions with similar spectral value, starting from the areas marked by the user. The user controls the similarity between regions by a *spectral distance* parameter previously defined. The region merging process is obviously much faster than a pixel merging one, even considering the computational time of the preliminary watershed. Apart from this, objects created with a fixed shape kernel on each pixel usually have a border that reflects this geometry while this procedure maintains the details of the objects morphology as perceived by human vision.

## 2 Fusion Algorithm

This name recalls the merging which is the main operation of this methodology. This algorithm takes the pieces of the mosaic (the basins of the watershed) that are *spatial neighbors*, and merges them into together into a new one.

This idea is meant for any n-dimensional multi-channel image but this article illustrates it in the bi-dimensional case, on a simple set of two images. This simplification maintains the validity of the multi-spectral aspect and is convenient because it worked with less computing expense and it allows a graphical description of the process: indeed we can see the projection of mosaic pieces as points in a two dimensional image, where their coordinates are their grey level in each band, moreover it allows a graphical representation of the concepts of spatial and spectral proximity, which is difficult in a case of a three-dimensional set, and impossible with more dimensions. Finally the bi-dimensionality lets us run the whole algorithm, even when it approaches the multi-spectral data, in terms of MM transforms, as the distances calculations in the spectral space are performed by the binary dilation.

### 2.1 Mosaic Images

A quick remark on the basic support for this procedure has to be done before describing in details the steps of the algorithm. The *mosaic image* to be used is slightly different from the ones found in the literature [6]. Generally a *mosaic image* is created from a grey level image once this is divided in areas and a unique grey value is assigned to each one calculated on the values of its pixels. There are different mosaic versions that differ in the value assigned to object and to the boundary between the areas. Many versions [7] [12] have been used but the one presented here, has two main characteristics: first, the objects are obtained applying the watershed on the multi-spectral gradient, in order to get a detailed separation in catchment basins with homogeneous spectral meaning; second, the watershed line between the adjacent basins has value zero, in order to keep them separated. The binary image with the partition in small areas, viewed as “pieces of the mosaic”, is here called as “pre-mosaic” (Fig.1b).

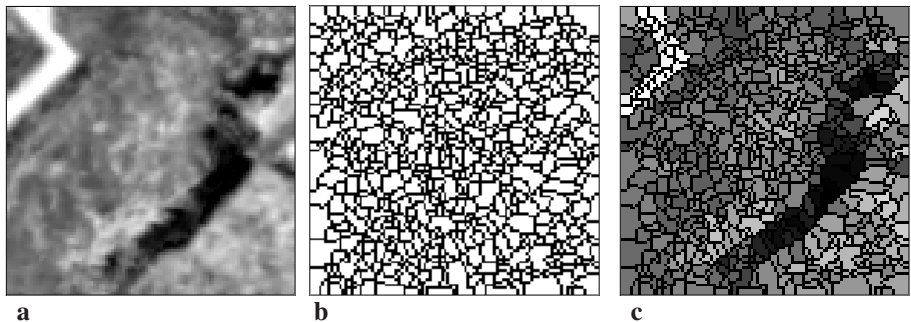


**Fig. 1.** Original image (a), catchment basins or “pre\_mosaic” (b) and mosaic image (c).

## 2.2 Steps of the Algorithm

### Inputs

First, the set of images must be transformed into mosaics. In this case we have two mosaics that were selected from a set of five images. Then a marker image is created. It can be obtained manually, marking some points belonging to the requested object, or automatically, if at least part of the object can be detected in this way. Basically this image should indicate the pieces that belong “a priori” to the required object (Fig.2).

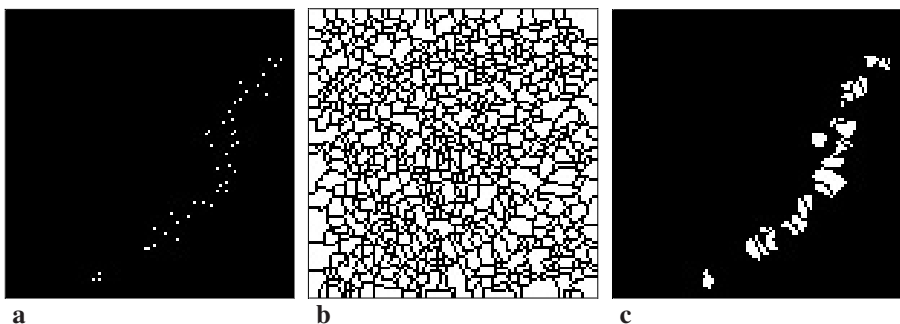


**Fig. 2.** Reconstruction (c) of the pre-mosaic image (b) by the marker image (a).

**Step 1:** Reconstruction of a marker image in the pre mosaic image: only the pieces of the mosaic hit by the marker image (intersection not empty) are considered from the “pre-mosaic” (Fig. 2c).

**Step 2:** The algorithm considers one by one all the pieces marked in the previous step, and for each one of them finds the pieces that are *spatial neighbors* (Fig. 3b).

**Step 3:** The spectral values of a piece, and its spatial neighbors, are visualized as points in the spectral space (Fig. 4a, 4b).

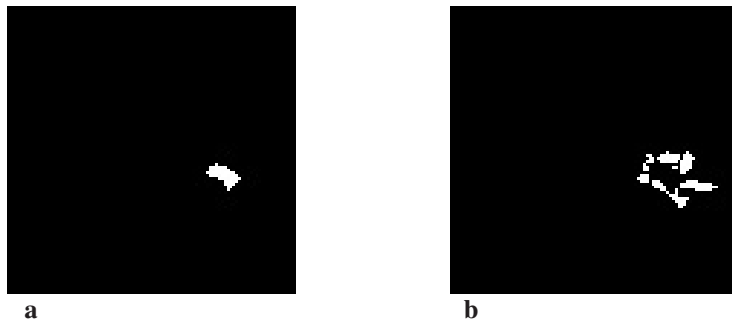


**Fig. 3.** Spatial domain: single piece (a); spatial neighbors (b).

**Step 4:** With an intersection between a dilation of the projection of the piece under evaluation and the projections of its spatial neighbors, only the projections of the *spatial* and *spectral* neighbors are selected. The size of the dilation is the key parameter of this process and it can be different in each channel depending on the contrast relation between the object and the background grey values, which usually varies from one channel to the other. In this case (Fig. 4c) it would mean that the dilation could have different values in the horizontal and the vertical direction.

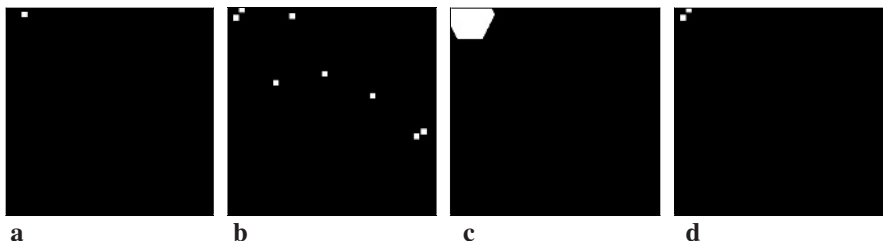


**Fig. 4.** Spectral domain: projections of the single piece in fig. 3a (a); projection of its spatial neighbors (shown in fig. 3b) (b); dilation of the single piece projection (c); intersection to identify the spectral neighbors that are already spatial neighbors (d).

**Step 5:** Knowing the spectral coordinates of the projections of the *spatial* and *spectral* neighbors the algorithm returns to the initial images to identify them (Fig. 5a) and merges them with the initial piece into a new bigger one (Fig. 5b).

**Step 6:** Each piece grows to a larger shape that is the result of the merging procedure. Gradually the new merged pieces modify the mosaics, and update the input images for the next loop of the application. The new pieces of the mosaic images have a grey value that is an average of the grey levels of the merged pieces, weighted on their areas.

These six steps are applied on each previously marked piece and the whole process is looped on all the pieces until the algorithm can find no more spectral neighbors.

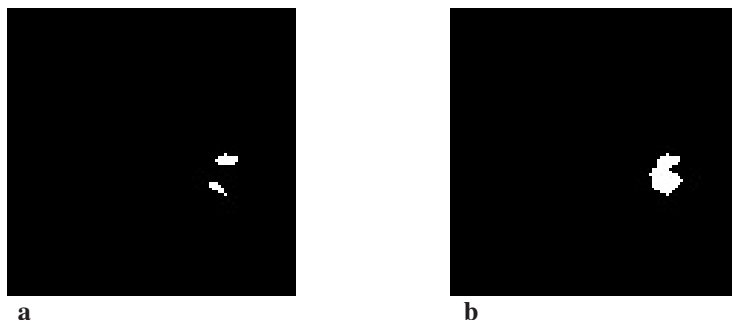


**Fig. 5.** Spatial domain: identification of the spatial neighbors that are spectral neighbors (a); merging procedure (b).

### 3 Case Studies

The developed methodology and algorithms were applied to several remotely sensed images; in particular it has been experimented to detect cartographic features in SPOT satellite images over the area of Luanda (Angola). We present in this paper some examples concerning different cartographic layers. The first one concerns the study of a river (Fig.6a), which is correctly identified (Fig.6b). The contours (Fig.6c) and the medial axis (skeleton) (Fig.6d) of the river, superimposed to the initial image, testify the success of application of our approach. This example also gives a hint on how to use the algorithm results in updating maps, for example this would be the first step towards creating a hydrology GIS layer.

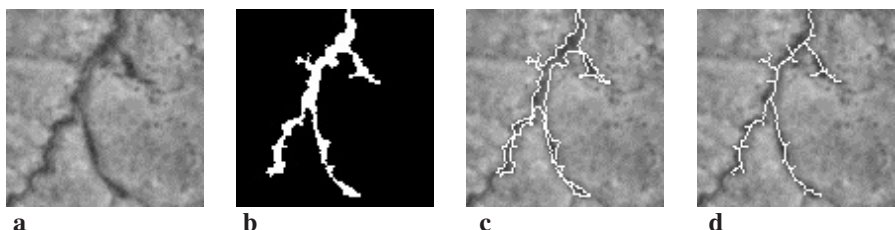


**Fig. 6.** Single channel of cut to object in the original image (a), algorithm detected shape (b), boundaries (c) and skeleton of the object (d).

Using old cartography features as markers to new ones should theoretically work well. Indeed many human built cartographic features (roads, urban areas) tend to expand over the years so the old are included in the recent objects but this procedure can present some drawbacks. For example in Fig.7, because of its slight displacement due to the incorrect registration between the map and the satellite images, the old route could not be used as a marker and forced the use manual markers.

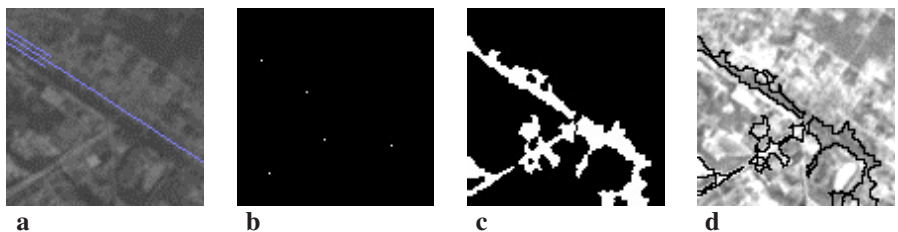


**Fig. 7.** Cut of sub-urban area with old cartography overlaid (a), user made markers (b), algorithm detected shape (c) and boundaries on single channel (d).

The algorithm proved its efficiency in the case of the airport, another object considered relevant as an object to detect. In Fig.8 two input mosaic images are exposed to illustrate the different information between the channels of the remote sensed images and the way that shapes are highlighted and its gray levels simplified. The input channels are the XS3 and XS1, corresponding to the Blue and the Red bands of the SPOT, and they cover almost all the territory occupied by the city of Luanda airport. The marker image is very simple; it has just 4 pixels marked, and has been created specially to extract the shape of the airstrips. As shown in the figure these points were enough to reconstruct the whole shape.

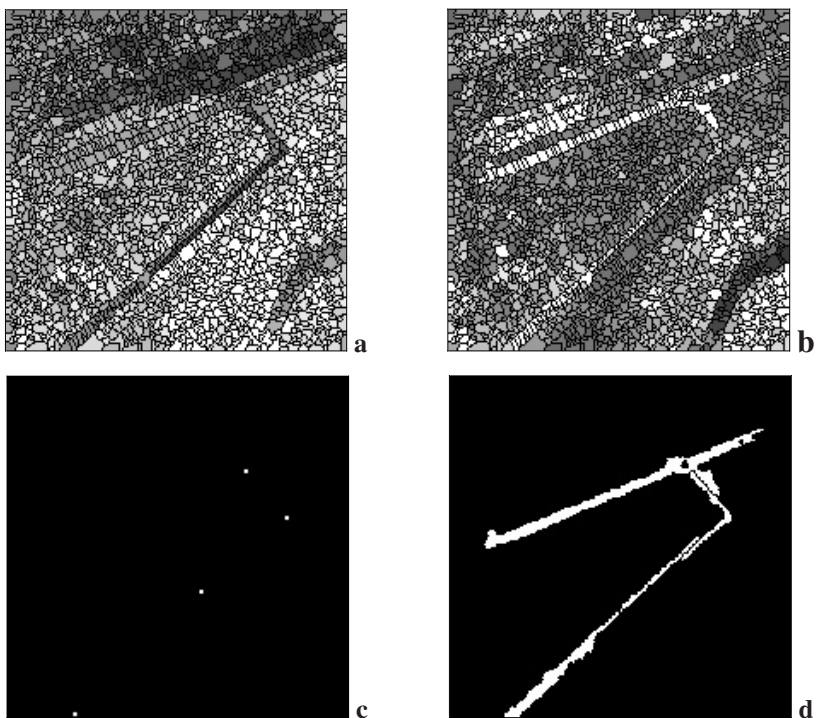


**Fig. 8.** Input mosaics (a and b), marker image (c) and resulting object (d).

## 4 Conclusion and Future Researches

This methodology belongs to the “region growing” procedures’ class but its distinguishing feature is that the elementary regions to be merged are not pixels but pre-segmented “textural elementary units” [13]. The pieces of the mosaic images, obtained with MM operators, can be represented as points in the spectral features space. For this, the region growing procedure becomes much faster and the objects shape found suites better to their morphology as perceived by human vision.

It gives good and useful results and it is actually a good tool to find connected shapes with a spectral meaning, when applied to remotely sensed images. It is not in its definitive version and it is still liable to be modified to improve its efficiency. The future improvements will be done towards a better interaction with users, and to test and compare different modifications to the structure described in 2.2.

Apart from the marker image the algorithm has another aspect where the user interaction is quite important: the spectral distance (2.2 Step 4). This is the parameter that decides whether the projections of the pieces in the spectral space are neighbors or not. It is a distance parameter that has a component in each band. In the future modifications it will be improved the semi-automatic definition of these. The user will be requested to make some click on the object (*object clicks*) in the image and some in the background, in points that do not belong to the object “*a priori*” (*background clicks*). In this way the algorithm can be programmed to read the difference between the values of the clicked pixels in all the bands and calculate statistically the parameters of the spectral distance in the different channels. The whole process could be made fully automatic but the user interaction and understanding is always fundamental. The application of this idea has been mainly dedicated to cartography but the algorithm is an object recognition tool that could work on any other multi-channel digital image.

## References

- [1] Soille, P.: Morphological Partitioning of Multispectral Images, *Journal of Electronic Imaging* 5(3) (July 1996) 252–265
- [2] Ford, S.J., McKeown, D.: Utilization of Multispectral Imagery for Cartographic Feature Extraction, *Proceedings of the DARPA Image Understanding Workshop*, San Diego, CA. (Jan 1992) 805–820
- [3] De Freitas, U.M., Câmara, G.: Developement of a Software for the Remote Sensing Community, *Internal Report at D.P.I. (Divisão de Processamento de Imagem do I.N.P.E. Instituto Nacional de Pesquisas Espaciais)*, Brasil (1997)
- [4] Kettig, R.L., Landgrebe, D.A.: Classification of Multispectral Data by Extraction and Classification of Homogeneous Objects, *IEEE Transactions on Geoscience Electronics*, Vol. GE-14, No.1 (Jan 1976) 19–26
- [5] Cramariuc, B., Gabbouj, M. and Astola Jaakkko, Clustering Based Region Growing Algorithm for Color Image Segmentation, *Digital Signal Processing Proceedings, DSP'97*, Vol.2 (July 1997) 857–860
- [6] Beucher, S.: The Watershed Transformation Applied to Image Segmentation, *10<sup>th</sup> Pfef-ferkorn Conf. On Signal and Image Processing in Microscopy and Microanalysis*, Cambridge UK, Scanning Microscopy International (Sept. 1991).

- [7] Soille, P.: Morphological Image Analysis – Principles and Applications, *Springer Verlag*, Berlin (1998) 266–267
- [8] Di Zenzo, S.: A Note on the Gradient of a Multi-image, *Computer Vision, Graphics, and Image Processing* 33 (1986) 116–125
- [9] Cumani, A.: Edge Detection in Multispectral Images, *Computer Vision, Graphics, and Image Processing: Graphical Models and Image Processing*, 53(1) (1991) 40–51
- [10] Beucher, S. : Segmentation d'Images et Morphologie Matematique, *PhD thesis*, Ecole de Mines de Paris (June 1990)
- [11] Vincent, L., Soille, P.: Watershed On Digital Spaces: An Efficient Solution Based on Immersion Simulation, *IEEE Transactions of Pattern Analysis and Machine Intelligence*, vol.13, n.6, (1991) 593–598
- [12] Soares, F., Muge, F.: Morphological Image Processing for Cartography, *Cartografia e Cadastro, Instituto Português de Cartografia e Cadastro*, Nº9, Portugal (1998) 39–49
- [13] Barata, T., Pina, P.: Construction of Decision Region Borders by Geometric Modelling of Training Sets, *Proceedings of ISMM 200*, CSIRO Publishing, Sydney. (2002) 147–156.

# Morphological Neural Networks with Dendrite Computation: A Geometrical Approach

Ricardo Barrón, Humberto Sossa, and Héctor Cortés

Centro de Investigación en Computación - IPN  
Av. Juan de Dios Bátiz S/N Esq. Miguel Othón de Mendizábal  
Unidad Profesional "Adolfo López Mateos", Zacatenco  
Mexico. D.F. C.P. 07738, MEXICO  
Tel. 57296000 ext. 56560  
 [{rbarron, hsossa}@cic.ipn.mx](mailto:{rbarron, hsossa}@cic.ipn.mx),  [torinja@yahoo.com.mx](mailto:torinja@yahoo.com.mx)

**Abstract.** Morphological neural networks consider that the information entering a neuron is affected additively by a conductivity factor called synaptic weight. They also suppose that the input channels account with a saturation level mathematically modeled by a MAX or MIN operator. This, from a physiological point of view, appears closer to reality than the classical neural model, where the synaptic weight interacts with the input signal by means of a product; the input channel forms an average of the input signals. In this work we introduce some geometrical aspects of dendrite processing that easily allow visualizing the classification regions, providing also an intuitive perspective of the production and training of the net.

## 1 Introduction

Neural networks are today a computational alternative to solve problems where is difficult or does not exist an algorithmic solution. Inspired on the functioning of the nervous system, researchers have postulated different neural processing models.

Recently, it has been found that information processing occurs also at dendrite level and not only at the neuron body [4]. This could be an explanation of the efficiency of the nervous system; due to the information processing practically occurs on the communication channel. This with morphological paradigm is starting point of this research.

### 1.1 Outline of the Paper

The remainder of the paper is organized as follows. In Section 2, we briefly talk about the related work with the present research. In Section 3, we describe the adopted methodology to give a solution to the problem. In Section 4, we provide an example to explain the functioning of the proposed methodology. Finally, in Section 5, we conclude and give directions for future research.

## 2 State of the Art

A neural network can be conceptualized as a non-linear mapping between two pattern-spaces: the input pattern and the output pattern. Normally the internal parameters of this mapping are determined by a training procedure and they are called, in most cases, synaptic weights.

In the decade of the 50's Rosenblatt [1] introduces the Perceptron. This classical model has served a basis of most of the actual developments.

## 3 The Adopted Methodology

### 3.1 Morphological Neural Processing

Morphological processing is based on the lattice algebra:  $(R, \wedge, +)$ , where  $\wedge$  is the MIN operator [2]. The main property of this algebraic structure is distributivity of summation with respect to operator  $\wedge$ , this is:

$$a + (b \wedge c) = (a + b) \wedge (a + c) \quad (1)$$

From the point of view of neural processing, Ritter [4] proposes a model of neuron where the synaptic weights interact additively with the input signals; the dendrites discriminate by taking into account the minimal value of the incident signals, (see Figure 1).

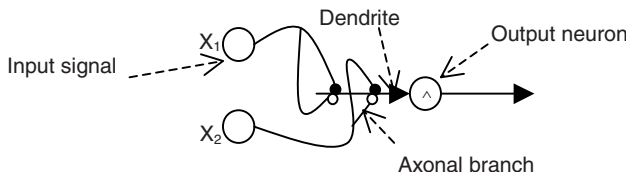


**Fig. 1.** Model of a morphological neuron.

In this model each branch can be of excitation or inhibition (excitation branches end with a black circle). The output neuron might have several dendrites; the output of each one of them can be negated or not.

A fundamental difference with respect to the neuronal classical model is that in morphological processing discrimination among input signals is done by taking into account a threshold that depends on a min value. In the classical model a weighted average of the inputs is taken. Since the physiological point of view it appears more acceptable the threshold criteria, although the quality of the models, it what we want to emulate is a biological process, only could be judged through the insights and scientific experiments in the area.

### 3.2 Dendrite Computation on Morphological Neurons

One of the contributions of the model described in Section 3.1 is the capacity to accomplish processing practically over the same communication channel. In this case the axonal branches can be of excitation or inhibition; only at the moment of contact with the dendrite, just the MIN of the values remains, this is

$$\prod_{l \in L} (-1)^{1-l} (x_i + \omega_{ik}^l), \quad L = \{0,1\} \quad (2)$$

is the value that filters dendrite  $k$ , where  $x_i$  is the input and  $\omega_{ik}^1, \omega_{ik}^0$  are the synaptic excitation and inhibition weights, respectively.

It is worth mentioning that, on this concept of distributed computing over the communication channel, can be the key that explains the efficiency of the nervous system, due to this model underlines the possibility that the fundamental processing of information is not only executed at the cellular bodies.

In summary, the morphological neural computing model with dendrite processing has the following characteristics: We have several input neurons, one of output, the output neuron can have several dendrites, each of the input neurons can excite or inhibit the corresponding axonal branches, thus the result,  $y$ , of the output neuron is computed as (see Figure 2):

$$y = f(\prod_{k=1}^K D_k(\mathbf{x})) \quad (3)$$

where  $D_k(\mathbf{x})$  is the output of the  $k$ -th dendrite when pattern  $\mathbf{x}$  is input. Each  $D_k(\mathbf{x})$  is obtained as follows

$$D_k(\mathbf{x}) = P_k \prod_{i \in I} \prod_{l \in L} (-1)^{(1-l)} (x_i + \omega_{ik}^l), \quad \mathbf{x} = (x_1, \dots, x_n) \in R^n \quad (4)$$

Factor  $P_k \in \{1, -1\}$ . Classification function  $f(\mathbf{x}) = 1$  if and only if its argument is greater or equal to one (on-region) and zero otherwise (off-region). Therefore, the above-mentioned structure provides a solution to a binary classification problem.

It is worth mentioning that the inhibition signal always carries a negative sign independently of the sign of its corresponding synaptic weight.

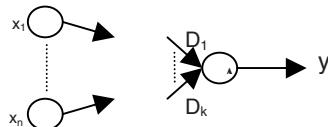


**Fig. 2.** Morphological neural computing model.

### 3.3 Geometric Approach of Dendrite Morphological Computation

In [4], it is enunciated and demonstrated a Theorem that is the base of the neural morphological model with dendrite computation. In a few words this result tells us that if  $X \in R^n$  is a compact set of patterns, then there exists a morphological neural net that classifies  $X$  as its on-region and its complements as its off-region.

The above-mentioned Theorem comes together with an iterative algorithm that allows determining; given a set  $X$ , the parameters of the morphological neural net. For the details refer to [4].

However, the geometrical counterpart of all the analytic and algorithmic statements does not appears completely clear. Since a didactical point of view and of the correct assimilation of the concepts it is desirable to develop until possible an intuitive and geometrical idea of the formal aspects. It is worth mentioning that the proposed intuitive geometrical vision is not only important for a better understanding of the concepts, it will also allow to efficiently to develop a construction algorithm as occurs with the analytical tools as we will next see.

- a. To begin characterizing the geometrical approach, let us consider the effect of the axonal branches over the dendrites:

$$\Lambda_{l \in L} (-1)^{l-1} (x_i + \omega_{ik}^l) = \Lambda \left\{ (x_i + \omega_{ik}^1), -(x_i + \omega_{ik}^0) \right\} \quad (5)$$

This expression is the intersection between two lines that cut axe  $x_i$  at  $-\omega_{ik}^1$  and  $-\omega_{ik}^0$ , respectively (see Figure 3).

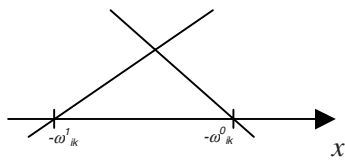


**Fig. 3.** Incidence of axonal branches over a dendrite.

In this case the firing region consists on the base of the triangle that is formed when the lines intersect, the complement constitutes the off-region (in the firing regions operator  $\Lambda$  takes positive or zero values; in the off-region it takes negative values).

- b. At each dendrite fall axonal branches from several input neurons; each of them define an on or off-region; all of them interact according to the following expression

$$D\tau_k(x^\xi) = P_k \Lambda_{i \in I} \Lambda_{l \in L} (-1)^{(l \in L)} (x_i^\xi + \omega_{ik}^l) \quad (6)$$

where  $x^\xi = (x_1^\xi, \dots, x_n^\xi) \in R^n$  is an input pattern,  $\xi = 1, 2, \dots, m$ .

Due to the intersection is given by operator  $\Lambda$  and each pair of axonal branches corresponds to different axes  $x_i (i = 1, \dots, n)$ , this makes that the firing conjoint regions are formed with the Cartesian products of the corresponding firing regions at each input (see Figure 4).

When  $P_k = -1$ , the firing region becomes an off-region and vice versa. It is important to note that the firing border frontier remains on, even when  $P_k = -1$ .

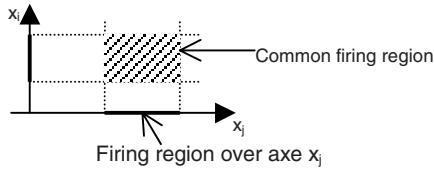


**Fig. 4.** Conjoint firing region.

Finally, the computation of the output is done as:

$$y(\mathbf{x}) = f\left(\bigwedge_{k=1}^K D_k(\mathbf{x})\right) \quad (6)$$

This implies that the firing region of the net is the intersection of the regions of each dendrite (Figure 5).

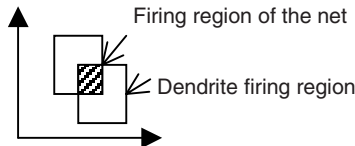


**Fig. 5.** Firing region of the morphological net.

In short, the firing region of all the net, what is what we want to characterize, is obtained by forming the firing regions (one for each input variable), by applying Cartesians products between firing regions or their complements, to finally get in general a hyper-rectangle as the firing region and its complement as the off-region. All the involved parameters in the above process can be synthetized in a table as the one shown in Figure 6.

At each row appear the synaptic weights of the axonal branches that fall on the corresponding dendrite, on last column  $P_k$  specifies if the firing region is complemented or not.

$D_k$	$\omega_{ik}^1$	$\omega_{ik}^0$	$\dots$	$P_k$
$D_1$				
$\vdots$				$\vdots$
$D_K$				

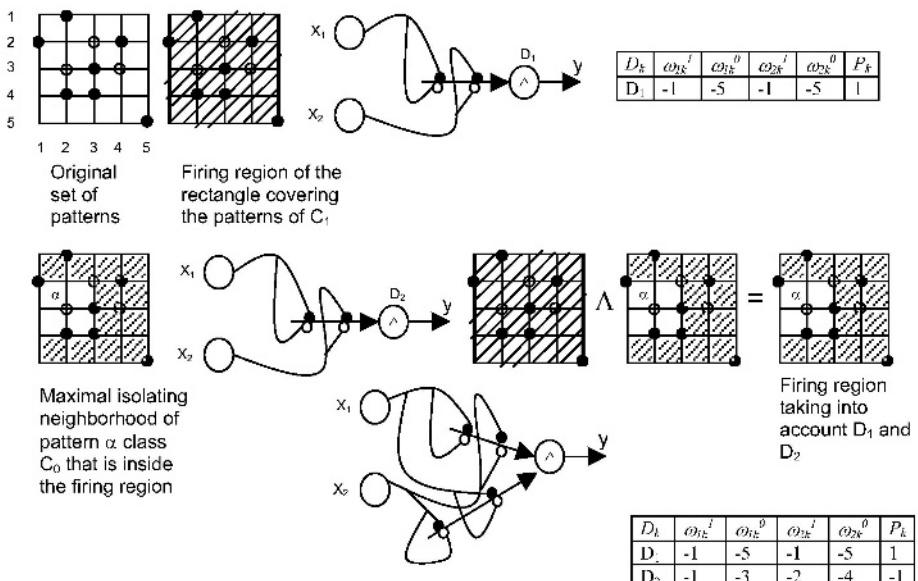
**Fig. 6.** Parameters of the morphological net.

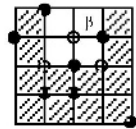
## 4 Experimental Results

The algorithm in geometrical terms is composed of two steps:

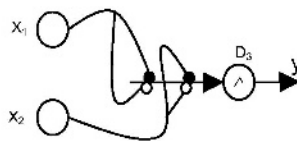
1. Find the hyper-rectangle covering all patterns belonging to class  $C_1$  (firing patterns), although patterns of class  $C_0$  (turn-off patterns) are included.
2. Isolate the points belonging to class  $C_0$  in maximal neighborhoods and take the complement of these neighborhoods so that the neighborhoods become part of the off-region.

**Example 4.1.** Let  $X = [(1,4),(2,5),(2,2),(3,2),(3,3),(4,4),(5,1)]$  patterns of class  $C_1$  (•) and  $X^l = [(2,3),(3,4),(4,3)]$  of class  $C_0$  (o):

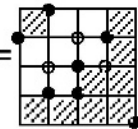
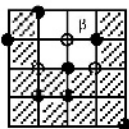
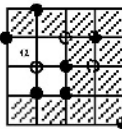




Maximal isolating neighborhood of pattern  $\beta$  class  $C_0$  that is inside the firing region



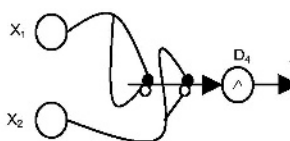
$D_k$	$\omega_{ik}^f$	$\omega_{ik}^g$	$\omega_{2k}^f$	$\omega_{2k}^g$	$P_k$
$D_3$	-2	-4	-3	-5	-1
$D_1$					
$D_2$					



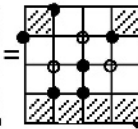
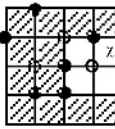
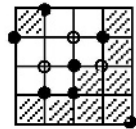
$D_k$	$\omega_{ik}^f$	$\omega_{ik}^g$	$\omega_{2k}^f$	$\omega_{2k}^g$	$P_k$
$D_1$	-5	-1	-5	1	
$D_2$	-3	-2	-4	-1	
$D_3$	-2	-4	-3	-5	-1

Firing region taking into account  $D_1$ ,  $D_2$  and  $D_3$

Maximal isolating neighborhood of pattern  $\chi$  class  $C_0$  that is inside the firing region



$D_k$	$\omega_{ik}^f$	$\omega_{ik}^g$	$\omega_{2k}^f$	$\omega_{2k}^g$	$P_k$
$D_4$	-3	-5	-2	-4	-1
$D_1$					
$D_2$					



$D_k$	$\omega_{ik}^f$	$\omega_{ik}^g$	$\omega_{2k}^f$	$\omega_{2k}^g$	$P_k$
$D_1$	-5	-1	-5	1	
$D_2$	-3	-2	-4	-1	
$D_3$	-2	-4	-3	-5	-1
$D_4$	-3	-5	-2	-4	-1

Firing region taking into account  $D_1$ ,  $D_2$ ,  $D_3$  and  $D_4$ .

To verify that the net has been effectively derived, let us classify patterns: (1,4) and (2,3) belonging to classes  $C_1$ , and  $C_0$ , respectively.

With (1,4), we have:

$$f\left(\begin{bmatrix} 1 \\ 4 \end{bmatrix}\right) = f\left(\bigwedge_{k=1}^4 D_k \begin{bmatrix} 1 \\ 4 \end{bmatrix}\right)$$

$$\begin{aligned} D_1\left(\begin{bmatrix} 1 \\ 4 \end{bmatrix}\right) &= \bigwedge_{i=1}^2 \bigwedge_{l=0}^1 (-1)^{1-l} (x_i + \omega_{i1}^l) \\ &= \bigwedge \{ [(x_1 + \omega_{11}^1) - (x_1 + \omega_{11}^0)] \wedge [(x_2 + \omega_{21}^1) - (x_2 + \omega_{21}^0)] \} \\ &= \bigwedge \{ [(1+1) - (1-5)] \wedge [(4-1) - (4-5)] \} \\ &= \bigwedge \{ [0,4] \wedge [3,1] \} = \bigwedge \{ 0,1 \} = 0 \end{aligned}$$

In the same way,  $D_2\left(\begin{bmatrix} 1 \\ 4 \end{bmatrix}\right) = 0$ ,  $D_3\left(\begin{bmatrix} 1 \\ 4 \end{bmatrix}\right) = 1$  and  $D_4\left(\begin{bmatrix} 1 \\ 4 \end{bmatrix}\right) = 2$ .

Thus  $f\left(\begin{bmatrix} 1 \\ 4 \end{bmatrix}\right) = f\left(\bigwedge_{k=1}^4 D_k \begin{bmatrix} 1 \\ 4 \end{bmatrix}\right) = f(\wedge \{0,0,1,2\}) = f(0) = 1$ , and  $\begin{bmatrix} 1 \\ 4 \end{bmatrix} \in C_1$ .

With (2,3), we have:

$$f\left(\begin{bmatrix} 2 \\ 3 \end{bmatrix}\right) = f\left(\bigwedge_{k=1}^4 D_k \begin{bmatrix} 2 \\ 3 \end{bmatrix}\right)$$

Also  $D_1\left(\begin{bmatrix} 2 \\ 3 \end{bmatrix}\right) = 1$ ,  $D_2\left(\begin{bmatrix} 2 \\ 3 \end{bmatrix}\right) = -1$ ,  $D_3\left(\begin{bmatrix} 2 \\ 3 \end{bmatrix}\right) = 0$  and  $D_4\left(\begin{bmatrix} 2 \\ 3 \end{bmatrix}\right) = 1$ .

Thus  $f\left(\begin{bmatrix} 2 \\ 3 \end{bmatrix}\right) = f\left(\bigwedge_{k=1}^4 D_k \begin{bmatrix} 2 \\ 3 \end{bmatrix}\right) = f(\wedge \{1,-1,0,1\}) = f(-1) = 0$ , and  $\begin{bmatrix} 2 \\ 3 \end{bmatrix} \in C_0$ .

## 5 Conclusions and Future Work

It has been shown that the morphological neural model with dendrite computation is more intuitive from a geometrical point of view, this has been manifested by the given example, where the final table can be also obtained by following the algorithm proposed by Ritter in [4].

As future work we are working on a visual computational tool that automatically allows determining the final parameters of a net as we did in the example; and this with the aim to account with didactic tool to facilitate the training of the morphological neural model with dendrite computation.

**Acknowledgments.** This work was economically supported by the CIC-IPN, the CONACYT under grant 41529, the CGPI-IPN under grant 20020214 and the COFAA-IPN.

## References

1. Donna L. Hudson, Neural Networks and Artificial Intelligence for Biomedical Engineering, IEEE Press, 2000.
2. Gerard X. Ritter, Joseph N. Wilson, Computer Vision Algorithms in Image Algebra, CRC, 2001.
3. Jorge Martínez, Ordered Algebraic Structures, Kluwer Academic, 2002.
4. Gerard X. Ritter, Gonzalo Urcid, Lattice Algebra Approach to Single Neuron Computation, IEEE Transactions on Neural Networks, May 2003.

# A Method for the Automatic Summarization of Topic-Based Clusters of Documents

Aurora Pons-Porrata<sup>1</sup>, José Ruiz-Shulcloper<sup>2</sup>, and Rafael Berlanga-Llavori<sup>3</sup>

<sup>1</sup>Universidad de Oriente, Santiago de Cuba (Cuba),  
aurora@app.uo.edu.cu,

<sup>2</sup>Institute of Cybernetics, Mathematics and Physics, La Habana (Cuba)  
recpat@cidet.icmf.inf.cu

<sup>3</sup>Universitat Jaume I, Castellón (Spain)  
berlanga@lsi.ub.edu.es

**Abstract.** In this paper we propose an effective method to summarize document clusters. This method is based on the Testor Theory, and it is applied to a group of newspaper articles in order to summarize the events that they describe. This method is also applicable to either a very large document collection or a very large document, in order to identify the main themes (topics) of the collection (documents) and to summarize them. The results obtained in the experiments demonstrate the usefulness of the proposed method.

## 1 Introduction

Topic Detection and Tracking (TDT) is a new line of research that comprises three major sub-problems: segmenting speech-recognized TV/radio broadcasts into news stories, detecting novel events, and tracking the development of an event according to a given set of sample stories of that event [1]. An event in the TDT context is something that occurs at a specific place and time associated with some specific actions [2]. For example, the eruption of Mount Pinatubo on June 15<sup>th</sup>, 1991 is consider an event.

Starting from a continuous stream of newspaper articles, the *Event Detection* problem consists in determining for each incoming document, whether it reports on a new event, or it belongs to some previously identified event.

Clustering algorithms have been traditionally used in the *Event Detection* problem, such as the *K-Means*, *Single-Pass* and others [3, 4, 5]. In our approach, we use the *incremental compact algorithm* [6, 7] to solve this problem. This algorithm obtains high quality temporal-semantic clusters of documents, which represent the events of the collection, and it is independent of the document arrival order.

Another important problem that arises in the *event detection systems* is that of providing summaries for the detected events. Apart from the set of the cluster's frequent terms [8] and the relevant news titles [9], these systems do not offer any further information about the events that the generated clusters are representing. Consequently, many times users have to read the documents of the clusters to know the events they report. In the literature, the problem of summarizing a set of input documents (called *multidocument summarization*) has received much attention lately (e.g. [10, 11]).

Basically, a multidocument summarization system tries to determine which sentences must be included in the summary, and then how to organise them to make the summary comprehensible. Many of these approaches are based on a sentence weight function that takes into account the position of the sentences in the documents, the length of the sentences, and the number of frequent keywords of the set of documents they include [12]. In this way, all the sentences in the document cluster must be scored to select the most appropriate for the summary. One of the main drawbacks of the current scoring procedures is that they are slow because the weight of a sentence depends on whether other sentences have been selected or not [13].

In this paper we present a novel and effective method for the multidocument summarization problem, based on the *Testor Theory* [14]. Starting from a set of document clusters, each one representing a different event or topic, our method tries to select the frequent terms of each cluster that are not included in the other clusters (testors). These terms are usually tightly related to the event of the cluster. Once these terms have been selected, the system extracts all the sentences that contain the selected terms. Finally, the system orders the extracted sentences and it produces the cluster's summary from them.

The proposed method computes very fast, and it produces good summaries for the document clusters we have analysed. Unlike the other methods in the literature, the selection of sentences is based on the discriminating frequent terms of each cluster, which can be efficiently computed.

## 2 Document Representation

The incoming stream of documents that feed our system comes from some on-line newspapers available in Internet, which are automatically translated into XML. This representation preserves the original logical structure of the newspapers.

From them, our detection system builds three feature vectors to represent each document  $d^i$ , namely [7]:

- A *vector of weighted terms* ( $TF_1^i, \dots, TF_n^i$ ), where the terms represent the lemmas of the words appearing in the content of the document, and  $TF_k^i$  is the relative frequency of the term  $t_k$  in  $d^i$ . Stop words are disregarded from this vector.
- A *vector of weighted time entities*, where time entities are either dates or date intervals. These time entities are automatically extracted from the content of the documents by using the algorithm presented in [15].
- A *vector of weighted places*. These places are automatically extracted from the content of the documents by using a thesaurus of place names.

The automatic construction of cluster summaries must take into account these three components. In [15], it was shown how the temporal entities of a document (cluster) can be summarized as a date interval called *event-time* period. Places can be easily summarized by taken a representative place from the cluster documents. Thus, in this paper we only focus on the term vector to extract the cluster summaries.

### 3 Basic Concepts

Before presenting our summarization method, we review the main definitions of the *Testor Theory* [14] and we define the basic concepts of this method.

In our problem, the collection of news is partitioned into clusters. Each cluster represents an event. Let  $\zeta$  be a set of detected events in a news collection.

The representative of a cluster  $c \in \zeta$ , denoted as  $\bar{c}$ , is calculated as the union of the documents of that cluster, that is,  $\bar{c} = (TF_1^{\bar{c}}, \dots, TF_n^{\bar{c}})$ , where  $TF_j^{\bar{c}}$  is the relative frequency of term  $t_j$  in the sum vector of the documents of that cluster.

Given a cluster  $c$ , let  $T(c) = \{t_1, \dots, t_{n_c}\}$  be the most frequent terms in the representative  $\bar{c}$ , i.e., the terms  $t_j$  such that  $TF_j^{\bar{c}} \geq \varepsilon$ ,  $j = 1, \dots, n_c$  and  $\varepsilon$  is an user-defined parameter.

For each cluster  $c$ , we construct a matrix  $MR(c)$ , whose columns are the terms of  $T(c)$  and its rows are the representatives of all clusters of  $\zeta$ , described in terms of these columns. Notes that this matrix is different in each cluster.

In the Testor Theory, the set  $\tau = \{x_{i_1}, \dots, x_{i_k}\}$  of features and their corresponding columns  $\{i_1, \dots, i_k\}$  of a matrix  $M$  is called a *testor*, if after deleting from  $M$  all columns except  $\{i_1, \dots, i_k\}$ , all rows of  $M$  corresponding to distinct clusters are different. A testor is called *irreducible (typical)* if none of its proper subsets is a testor [14]. The *length* of the testor is the cardinal of  $\tau$ .

For the calculus of the typical testors of a matrix  $M$ , the key concept is the comparison criterion of the values of each feature. One of these criteria is, for example:

$$d(v_{i_k}, v_{j_k}) = \begin{cases} 1 & \text{if } v_{i_k} - v_{j_k} \geq \delta \\ 0 & \text{otherwise} \end{cases}, \quad (1)$$

where  $v_{i_k}, v_{j_k}$  are the values in the rows  $i$  and  $j$  in the column corresponding to the feature  $x_k$  respectively, and  $\delta$  is an user-defined parameter.

In order to determine all typical testors of a matrix we use the algorithm LEX, which is described in detail in [16]. This algorithm outperforms the other algorithms to calculate the typical testors.

Let a sentence  $S$  of a document  $d$  and  $U$  be a set of terms. We call *maximal co-occurrence* of  $S$  with respect to  $U$ , and we will denote it as  $mc(S, U)$ , to the set of all terms of  $U$  that also occur in  $S$ .

### 4 Method of Summarization

In our opinion, a summary of an event should include the terms that characterize the event, but also those that distinguish this event from the rest.

A summary of an event  $c$  consists of a set of sentences extracted from the documents in  $c$ , in which the highest quantity of terms that belong to typical testors of

the maximum length of the matrix  $MR(c)$  occurs. Moreover, the sentences that cover the calculated typical testor set are also added to the summary.

In order to improve the coherence and organization of the summaries, we sort the extracted sentences according to the publication date of the news and their position in the text.

In order to calculate these typical testors, we considered two classes in the matrix  $MR(c)$ . The first class is only formed by  $\bar{c}$  and the second one is formed by all remaining cluster representatives. The comparison criterion applied to all the features is that of (1). Notice that this criterion requires that the terms frequently appear in the cluster documents but not in the other clusters.

The proposed summarization method is described as follows:

**Algorithm** Summarization of event set

**Input:**  $\zeta$ : a set of events (clusters) of a news collection.

$\varepsilon$ : threshold of term frequencies.

$\delta$ : parameter of the comparison criterion

**Output:** Summary of each event.

For each event  $c \in \zeta$ :

1. Construct the matrix  $MR(c)$ .

2. Calculate the typical testors of the maximum length in the matrix  $MR(c)$ .

3. Let  $U$  be the union of all typical testors found in the step 2.

4. For each document  $d_i$  in the cluster  $c$ :

For each sentence  $S$  in  $d_i$ :

Calculate the maximal co-occurrence  $mc(S, U)$ .

5. Order decreasingly all sentences in terms of the cardinal of its maximal co-occurrence.

Let  $p_1 > p_2 > \dots > p_s$  be these cardinals.

6.  $Summary(c) = \emptyset$

7. Add to  $Summary(c)$  all sentences  $S$  that satisfy  $|mc(S, U)| = p_1$ .

8.  $W = \bigcup_{|mc(S, U)|=p_1} mc(S, U)$ .

9.  $i = 2$ .

10. While  $U \setminus W \neq \emptyset$  do:

$V = \emptyset$ .

For each  $mc(S, U)$  of cardinal  $p_i$ :

If  $mc(S, U) \cap (U \setminus W) \neq \emptyset$  then

Add  $S$  to  $Summary(c)$ .

$V = V \cup mc(S, U)$

$i = i + 1$

$W = W \cup V$

11. Sort all sentences in  $Summary(c)$  according to the publication date of the news in  $c$  and their position in the text.

The paragraph is a useful semantic unit for the construction of the summaries because most writers view a paragraph as a topical unit, and organize their thoughts accordingly. Therefore, if we want to obtain more extensive summaries, we can use the paragraphs instead of the sentences. Thus, we would extract the paragraphs that cover the typical testor set.

## 5 Experiments and Results

The effectiveness of the proposed summarization method has been evaluated using two collections. The first one contains 554 articles published in the Spanish newspaper "El País" during June 1999. We have identified 85 non-unitary events, being their maximum size of 18 documents. The collection covers 21 events associated to the end of the "Kosovo War" along with their immediate consequences, the visit of the Pope to Poland, the elections in several countries like South Africa, Indonesia and the European elections, the events related with the trials to Pinochet and the Kurdish leader Ocalan, among others.

In order to show the quality of the obtained summaries one detected event is selected. It is about the murder of the famous Mexican presenter Paco Stanley. This cluster is formed by 5 documents. Table 1 shows the titles, the publication dates and the length (number of words) of each document in this cluster.

**Table 1.** Documents about the murder of Paco Stanley.

Publication date	Title	Length
1999-6-8	Commotion in Mexico for the murder of a famous presenter.	531
1999-6-9	The Mexican Intelligence declares that the murdered comedian had links with the drug traffic.	748
1999-6-9	The televisions incite the indignation against Cárdenas.	298
1999-6-10	An atmosphere of collective hysteria has been created.	203
1999-6-10	The death of Stanley agitates the political atmosphere in Mexico.	540

The union of the found typical testors for this cluster is: *{murder, Mexican, death}*. The obtained summary of this event by our method is the following one:

Paco Stanley presented several popular variety programs in the Aztec Television, and its death has caused a deep commotion in the Mexican society, in which he was a very appreciated person. Porfirio Muñoz Ledo, the mayor's competitor in the PRD internal fight for the presidential nomination of the party in the presidential elections of the 2000, annotated new causes in the murder of the showman, as he declared that 'it would be immoral' that this notorious death could affect the election process, in which Cárdenas aspires to the Republic presidency. During hours, the reporter Raúl Trejo explained, the only thing that was seen in the Mexican television screens, after murder of Paco Stanley, was a parade of laments, complaints and demands that nothing clarified, but that they became a battering ram.

As we can see, this summary offers a concise vision of the main aspects of the murder of Paco Stanley. This summary has 139 words, in contrast with the 2320 words in total that all documents of the cluster have. That is, a 94% of compression rate. It is worth mentioning that we try to maintain the original fragments in the carried out translation of this summary.

Figure 1 shows the results for the compression rate (in %) at each event with respect to its size (total number of words in the documents of the event). As we can see, there exists a tendency such that the higher event size, the greater the compression rate is.

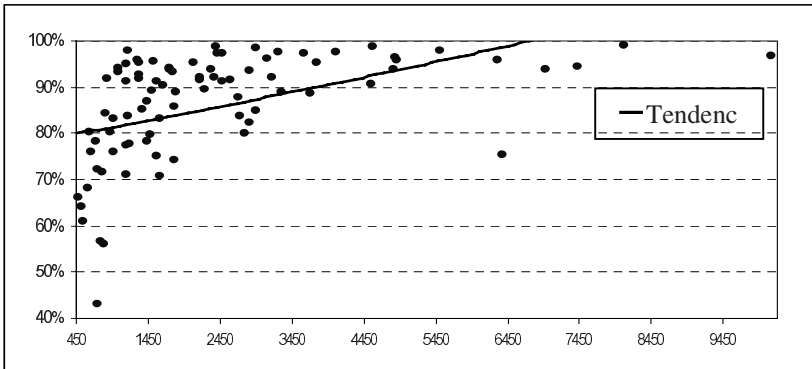


**Fig. 1.** Compression rate against the total number of words in each event.

In order to evaluate the effectiveness of our method, we also used the data (in Spanish) from the TREC-4 conference [17]. This collection contains 693 articles published by AFP agency during 1994. These articles are classified into 23 topics.

Table 2 shows for each topic, its size (number of documents), the size of its typical test set (number of terms) and the obtained compression rate (in %).

**Table 2.** Obtained results in TREC data.

Topic	Size	TT	Rate	Topic	Size	TT	Rate	Topic	Size	TT	Rate
SP51	83	4	96.81	SP60	47	7	97.94	SP69	62	4	98.06
SP52	13	3	98.20	SP62	15	6	85.72	SP70	6	3	74.76
SP53	46	2	99.36	SP63	5	4	83.43	SP71	17	3	99.29
SP54	37	8	94.38	SP64	9	4	83.54	SP72	14	7	91.05
SP55	108	4	99.29	SP65	29	5	96.40	SP73	13	5	93.48
SP57	2	3	82.05	SP66	68	4	97.32	SP74	34	10	97.65
SP58	49	9	97.91	SP67	13	9	87.20	SP75	20	3	94.09
SP59	7	6	93.74	SP68	12	8	93.78				

Again, the obtained summaries capture the main ideas about each topic and an appreciable reduction of words is also achieved. For example, the description given by TREC to the topic SP68 is “AIDS situation in Argentine and what steps is the Argentine government taking to combat the disease”. The union of the found typical testers for this topic is: {Argentine, campaign, prevention, disease, population, drug, case, people}. The summary obtained for this topic is the following one:

The combination of the DDI drugs and hidroxamates against the AIDS disease "could be the only way to remove the virus from the seropositive people", the argentinean doctor Julio Vila, which leads a research group in France, said this Sunday. The Health authorities announced this Friday that the Argentine Government will start a educational campaign to prevent the Acquired Immune Deficiency Syndrome (AIDS). The minister of Health and Social Action, Alberto Mazza, had announced this Friday that the government will start a educational campaign, whose objective is "to instruct the population about the prevention measures that must be adopted to combat the AIDS". The campaign of preventive education

will be started after publishing the results of a national public-opinion poll about the population knowledge on the disease, according to Mazza declarations. Although detected during the last years, the cases were just known now, pointing out that the situation has produced a prevention campaign ordered by the army chief General Martin Balza, which presumes that we are against a "serious but controllable problem". In the same way, the Army Immune Deficiency Center (CEIDE) was created within the Central Army Hospital as an institution that will be in charge of the prevention campaigns, as well as the treatment and monitoring of the AIDS cases.

Indeed, it is hard to evaluate the quality of a summarization method. In spite of this, we consider our summaries readable, coherent and excellent at capturing the main themes of the document sets. Thus, we believe that these summaries can be presented to the user as a meaningful description of the cluster contents.

## 6 Conclusions

In this work we presented an effective method to summarize document clusters generated by Topic Detection Systems. The proposed method employs the calculus of typical testors as its primary operation and from them, it constructs the summaries of each cluster.

The most important novelty is the use of typical testors combined with different techniques and heuristics, to produce all together better summaries.

This method enables construction of a concise representation of the focused cluster. The obtained summaries are much more descriptive than simple sets of frequent words.

The proposed method is applied to a set of newspaper articles in order to summarize the events that they describe. It is helpful to a user in order to determine at a glance whether the content of an event are of interest. The carried out experiments demonstrate the usefulness of the method. The summaries are readable, coherent and well organized. In most cases, the system successfully presents main themes, skips over minor details, and avoids redundancy. Additionally, the proposed summarization algorithm performs efficiently, taking much less time than the clustering process.

To sum up, the summarization method is robust, topic-independent and may easily be applied in other domains and other languages. Additionally, it can be applied to other document collections such as Web pages, books, and so on. For example, in a book we can consider as *clusters* some structural elements of the document (chapters, sections, etc.), being its members the different sub-structures they contain (subsections, paragraphs, etc.)

## References

- [1] Allan, J.; Carbonell, J.; Doddington, G.; Yamron, J. and Yang, Y.: Topic Detection and Tracking Pilot Study: Final Report. In *Proceedings of DARPA Broadcast News Transcription and Understanding Workshop*, pp. 194–218, 1998.

- [2] Yang, Y.; Ault, T.; Pierce, T. and Lattimer, C.W.: Improving text categorization methods for event tracking. In *Proceedings of the ACM SIGIR Conference on Research and Development in Information Retrieval*, SIGIR'00, Athens, pp. 65–72, 2000.
- [3] Carbonell, J.; Yang, Y.; Lafferty, J.; Brown, R.D.; Pierce, T. and Liu, X.: CMU Report on TDT-2: Segmentation, detection and tracking. In *Proceedings of DARPA Broadcast News Workshop*, pp.117–120, 1999.
- [4] Yamron, J.: Dragon's Tracking and Detection Systems for TDT2000 Evaluation. In *Proceedings of Topic Detection & Tracking Workshop*, pp.75–80, 2000.
- [5] Allan, J.; Lavrenko, V.; Frey, D. and Khandelwal, V.: UMASS at TDT 2000. In *Proceedings TDT 2000 Workshop*, 2000.
- [6] Pons-Porrata, A.; Berlanga-Llavori, R. and Ruiz-Shulcloper, J.: Detecting events and topics by using temporal references. *Lecture Notes in Artificial Intelligence* 2527, Springer Verlag, pp.11–20, 2002.
- [7] Pons-Porrata, A.; Berlanga-Llavori, R. and Ruiz-Shulcloper, J.: Building a hierarchy of events and topics for newspaper digital libraries. *Lectures Notes on Computer Sciences* 2633, Springer-Verlag, 2003.
- [8] Zamir, O.; Etzioni, O.; Madani, O. and Karp, R.M.: Fast and Intuitive Clustering of Web Documents. In *Proceedings of KDD'97*, pp. 287–290, 1997.
- [9] Cutting, D.R.; Karger, D.R. and Pedersen, J.O.: Constant Interaction-Time Scatter/Gather Browsing of Very Large Document Collections. In *Proceedings of the 16<sup>th</sup> International ACM SIGIR Conference on Research and Development in Information Retrieval*, 1993.
- [10] Mani, I. and Bloedorn, E.: Multi-Document Summarization by Graph Search and Matching. AAAI/IAAI 1997, pp. 622–628, 1997.
- [11] Barzilay, R.; Elhadad, N. and McKeown, K.: Inferring Strategies for Sentence Ordering in Multidocument News Summarization. *Journal of Artificial Intelligence Research* 17, pp. 35–55, 2002.
- [12] Mani, I.: *Automatic Summarisation*. John Benjamins Publishing Company, 2001.
- [13] Marcu, D.: Discourse-based summarisation in DUC-2001, *Proceedings of Document Understanding Conference*, DUC-2001, 2001.
- [14] Lazo-Cortés, M.; Ruiz-Shulcloper, J. and Alba-Cabrera, E.: An overview of the concept testor. *Pattern Recognition*, Vol. 34, Issue 4, pp.13–21, 2001.
- [15] Llidó, D.; Berlanga R. and Aramburu M.J.: Extracting temporal references to automatically assign document event-time periods. In *Proceedings of Database and Expert System Applications 2001*, Springer-Verlag, Munich, pp. 62–71, 2001.
- [16] Santiesteban, Y. and Pons, A.: LEX: a new algorithm for the calculus of typical testors. *Rev. Ciencias Matemáticas*, Vol. 21, No. 1, (in Spanish), 2003.
- [17] <http://trec.nist.gov>.

# Improving Prepositional Phrase Attachment Disambiguation Using the Web as Corpus\*

Hiram Calvo<sup>1</sup> and Alexander Gelbukh<sup>1,2</sup>

<sup>1</sup> Center for Computing Research, National Polytechnic Institute,  
Av. Juan de Dios Bátiz s/n, esq. Av. Mendizábal, México, D.F., 07738. México  
hcalvo@sagitario.cic.ipn.mx, gelbukh@cic.ipn.mx; www.gelbukh.com  
<sup>2</sup> Department of Computer Science and Engineering, Chung-Ang University,  
221 Huksuk-Dong, DongJak-Ku, Seoul, 156-756, Korea

**Abstract.** The problem of Prepositional Phrase (PP) attachment disambiguation consists in determining if a PP is part of a noun phrase, as in *He sees the room with books*, or an argument of a verb, as in *He fills the room with books*. Volk has proposed two variants of a method that queries an Internet search engine to find the most probable attachment variant. In this paper we apply the latest variant of Volk's method to Spanish with several differences that allow us to attain a better performance close to that of statistical methods using treebanks.

## 1 Introduction

In many languages, prepositional phrases (PP) such as *in the garden* can be attached to noun phrases (NP): *the grasshopper in the garden*, or verb phrases (VP): *plays in the garden*. Sometimes there are several possible variants for attachment of a given PP. For example, in *The police accused the man of robbery* we can consider two possibilities:

- (1) *The police [accused [the man of robbery]]*
- (2) *The police [accused [the man] of robbery]*

In the case (1) the object of the verb is *the man of robbery*, and in (2) the object is *the man*, and the accusation is *of robbery*. An English speaker knows that the second option is the correct one, whereas for a computer we need a method to automatically determine which option is correct.

There are several methods to find the correct PP attachment place that are based on treebank statistics. These methods have been reported to achieve up to 84.5% accuracy [1], [2], [3], [4], [5], [6]. However, resources such as treebanks are not available for many languages and they are difficult to port, so that a less resource-demanding

---

\* Work done under partial support of Mexican Government (CONACyT, SNI), IPN (PIFI, CGEPI), RITOS-2, and Korean Government (KIPA Professorship for Visiting Faculty Positions in Korea). The second author is currently on Sabbatical leave at Chung-Ang University.

method is desirable. Ratnaparkhi [7] describes a method that requires only a part-of-speech tagger and morphological information. His method uses raw text to be trained.

The quality of the training corpus significantly determines the correctness of the results. Specially, to reduce the effects of noise in a corpus and to consider most of the phenomena, a very large corpus is desirable. Eric Brill [8] shows that it is possible to achieve state-of-the-art accuracy with relatively simple methods whose power comes from the plethora of texts available to such systems. His paper also gives examples of several NLP applications that benefit from the use of very large corpora.

Nowadays, large corpora comprise more than 100 million words, whereas the Web can be seen as the largest corpus with more than one billion documents. Particularly for Spanish, Bolshakov and Galicia-Haro [9] report approximately 12,400,000 pages that can be found through Google. We can consider the Web as a corpus that is big and diverse enough to obtain better results with statistical methods for NLP.

Using the Web as corpus is a recently growing trend; an overview of the existing research that tries to harness the potential of the web for NLP can be found in [10]. In particular, for the problem of finding the correct PP attachment, Volk [11], [12] proposes variants of a method that queries an Internet search engine to find the most probable PP attachment.

In this paper we show the results of applying the latest variant of Volk's method with several differences to Spanish. In Section 2 we explain the variants of Volk's method. In Section 3 we present the differences of the method we use with regard to his method. In Section 4 we explain the details of our experiment and the results we obtained, and finally we draw the conclusions.

## 2 Volk's Method

Volk proposes two variants of a method to decide the attachment of a PP to a NP or a verb. In this Section we explain both variants and their results.

### 2.1 First Variant

Volk [11] proposes disambiguating PP attachments using the web as corpus by considering the co-occurrence frequencies (*freq*) of verb + preposition against those of noun + preposition. The formula used to calculate the co-occurrence is:

$$\text{cooc}(X, P) = \text{freq}(X, P) / \text{freq}(X)$$

where X can be either a noun or a verb. For example, for *He fills the room with books*, N = *room*, P = *with*, and V = *fill*. The value of  $\text{cooc}(X, P)$  is between 0 (no co-occurrences found) and 1 (the words always occur together)

The value of  $\text{freq}(X, P)$  is calculated by querying the AltaVista search engine using the NEAR operator:  $\text{freq}(X, P) = \text{query}("X \text{ NEAR } P")$ .

To choose an attachment variant,  $\text{cooc}(N+P)$  and  $\text{cooc}(V+P)$  are calculated, and the variant with the higher value is chosen. If some of the  $\text{cooc}$  values are lower than a *minimum co-occurrence threshold*, the attachment cannot be desambiguated, and thus

**Table 1.** Coverage and Accuracy for Volk's 2000 algorithm

threshold	coverage	accuracy
0.1	99%	68%
0.3	36.7%	75%
0.5	7.7%	82%

it is not covered. By adjusting the *minimum co-occurrence threshold*, Volk's 2000 algorithm can attain very good coverage but poor accuracy, or good accuracy with low coverage. Table 1 shows the coverage / accuracy values for Volk's experiments.

Volk [11] also concludes that using full forms is better than using lemmas.

The same experiment has been done for Dutch by Vandeghinste [13], reaching for a coverage of 100% an accuracy of 58.4%. To obtain an accuracy of 75%, Vandeghinste used a threshold of 0.606, yielding the coverage of only 21.6%.

## 2.2 Second Variant

In a subsequent paper [12], Volk uses a different formula to calculate co-occurrences. Now the head noun of the PP is included within the queries. The formula used is:

$$\text{cooc}(X, P, N_2) = \text{freq}(X, P, N_2) / \text{freq}(X)$$

where  $\text{freq}(X, P, N_2)$  is calculated by querying the AltaVista search engine using the NEAR operator:  $\text{freq}(X, P, N_2) = \text{query}("X \text{ NEAR } P \text{ NEAR } N_2")$ . X can be  $N_1$  or V. For example, for *He fills the room with books*,  $N_1 = \text{room}$ ,  $P = \text{with}$ ,  $N_2 = \text{books}$  and  $V = \text{fill}$ .

Volk experiments first by requiring that both  $\text{cooc}(N_1, P, N_2)$  and  $\text{cooc}(V, P, N_2)$  can be calculated to determine a result. Then, he considers using a threshold to determine the PP attachment when one of  $\text{cooc}(N_1, P, N_2)$  or  $\text{cooc}(V, P, N_2)$  is not known. That is, if  $\text{cooc}(N_1, P, N_2)$  is not known,  $\text{cooc}(V, P, N_2)$  must be higher than the threshold to decide that the PP is attached to the verb, and *vice versa*. Afterwards, by including both lemmas and full forms in queries, Volk attains a better performance, and by defaulting to noun attachment for previously uncovered attachments, he attains the coverage of 100%. The results he found are shown as Table 2.

For Dutch, requiring both  $\text{cooc}(N_1, P, N_2)$  and  $\text{cooc}(V, P, N_2)$ , Vandeghinste

**Table 2.** Results of Volk's 2001 Method

coverage	accuracy	requires both $\text{cooc}(N_1, P, N_2)$ and $\text{cooc}(V, P, N_2)$ ?	threshold when $\text{cooc}(N_1, P, N_2)$ or $\text{cooc}(V, P, N_2)$ is not known	includes both lemmas and full forms in queries?	defaults to noun attachment for uncovered attachments?
55%	74.32%	yes			
63%	75.04%		0.001		
71%	75.59%		0.001	yes	
85%	74.23%		0	yes	
100%	73.08%		0	yes	yes

achieves a coverage of 50.2% with an accuracy of 68.92. Using a threshold and including both lemmas and full forms in queries, he reaches 27% coverage for an accuracy of 75%. For 100% coverage, defaulting the previously uncovered cases to noun attachments, an accuracy of 73.08% is obtained.

### 3 Improving Performance

Methods to resolve PP attachment ambiguity based on treebank statistics achieve by far a better performance than the experiments described above. Nonetheless, we think that there are several elements that could be changed to improve methods based on Web queries. One of the elements to consider is the size of the document database of search engines. Indeed, this is relevant for finding representative co-occurrence frequencies for certain language. It is known that not every search engine yields the same results. For example, Table 3 shows the number of co-occurrences found from different search engines for the same words:

**Table 3.** Number of co-occurrences found in several search engines

	<i>leer en el metro</i>	<i>read in the subway</i>
Google	104	30
All-the-Web	56	23
Altavista	34	16
Teoma	15	19

Google is ranked as search engine with the largest database size by the search engine showdown.<sup>1</sup> Because of its greater document database size, we have determined that using Google to obtain word co-occurrence frequencies can yield to better results.

Another element to consider is the use of the NEAR operator. We decided do not using it since it does not guarantee that the query words appear in the same sentence. Let us consider the following queries from AltaVista:

- (1) wash NEAR with NEAR door 6,395 results
- (2) wash NEAR with NEAR bleach 6,252 results

(1) yields 6,395 pages found, even when books are unrelated to the wash operation. Compared to (2) that yields 6,252 pages found, we can see that there is no clear distinction of when is a preposition + noun related to a verb. On the other hand, using an exact phrase search yields 0, which marks out a clear distinction between *wash with door* and *wash with bleach*. The numbers of the pages found are as follows:

Exact phrase search	AltaVista	Google
“wash with door”	0	0
“wash with bleach”	100	202

Following [12], we use jointly full forms and lemmatized forms of nouns and verbs to obtain better performance. However, as we are not using the NEAR operator, we

<sup>1</sup> Information taken from [www.searchengineshowdown.com](http://www.searchengineshowdown.com), update of December 31st, 2002.

**Table 4.** Queries to determine the PP attachment of Spanish *Veo al gato con un telescopio* and English *I see the cat with a telescope*

veo al gato con un telescopio	hits	I see the cat with a telescope	hits
ver	296,000	see	194,000,000
"ver con telescopio"	8	"see with telescope"	13
"ver con telescopios"	32	"see with telescopes"	76
"ver con un telescopio"	49	"see with a telescope"	403
"ver con el telescopio"	23	"see with the telescope"	148
"ver con unos telescopios"	0	"see with some telescopes"	0
"ver con los telescopios"	7	"see with the telescopes"	14
veo	642,000		
"veo con telescopio"	0		
"veo con telescopios"	0		
"veo con un telescopio"	0	(no such forms in English)	
"veo con unos telescopios"	0		
"veo con el telescopio"	1		
"veo con los telescopios"	0		
$\text{freq}(\text{veo}, \text{con}, \text{telescopio}) = 1.279 \times 10^{-4}$		$\text{freq}(\text{see}, \text{with}, \text{telescope}) = 3.371 \times 10^{-6}$	
gato	185,000	cat	24,100,000
"gato con telescopio"	0	"cat with telescope"	0
"gato con telescopios"	0	"cat with telescopes"	0
"gato con un telescopio"	3	"cat with a telescope"	9
"gato con unos telescopios"	0	"cat with some telescopes"	0
"gato con el telescopio"	6	"cat with the telescope"	2
"gato con los telescopios"	0	"cat with the telescopes"	0
$\text{freq}(\text{gato}, \text{con}, \text{telescopio}) = 0.486 \times 10^{-4}$		$\text{freq}(\text{cat}, \text{with}, \text{telescope}) = 0.456 \times 10^{-6}$	

must consider the determiners that can be placed between the noun or verb and the preposition. Also we consider that the nucleus of the PP might appear in plural, without affecting its use. To illustrate this, consider the following sentence<sup>2</sup>:

*Veo al gato con un telescopio* ‘I see the cat with a telescope’

The attachments are calculated by the queries shown in Table 4. Since  $\text{freq}(\text{veo}, \text{con}, \text{telescopio}) > \text{freq}(\text{gato}, \text{con}, \text{telescopio})$ , the attachment is disambiguated as *veo con telescopio* ‘see with telescope’.

## 4 Experiment and Results

For our evaluation we extracted randomly 100 sentences from the LEXESP corpus of Spanish [15] and the newspaper *Milenio Diario*<sup>3</sup>. All searches were restricted to Spanish pages.

First, we considered not restricting queries to a specific language, given that a benefit could be obtained from similar words across languages, such as French and

<sup>2</sup> Example borrowed from [14].

<sup>3</sup> www.milenio.com

Spanish. For example, the phrase *responsables de la debacle* ‘responsible of the rout’ is used in both languages varying only in its accentuation (*débâcle* in French, *debacle* in Spanish). As Google does not take into account word accentuation, results for both languages are returned by the same query. However, with an unrestricted search, Google returns different count-ups in its API<sup>4</sup> and in its GUI.<sup>5</sup> For example, for *ver* ‘to see’, its GUI shows 270,000 results, whereas its API returns more than 20,000,000, even enabling the “group similar results” filter. This enormous deviation can be reduced by restricting language to a specific language. For Spanish, a restricted search for *ver* ‘to see’ in the GUI returns 258,000 results, whereas in the API it returns 296,000. Currently we are not aware of the reason for this difference; in any case it does not have any serious impact on our experiments.

The sentences of our experiment bear 181 cases of preposition attachment ambiguity. From those, 162 could be automatically resolved. They were verified manually and to determine that 149 of them were resolved correctly and 13 were incorrect.

In terms of coverage and accuracy used by Volk, we obtain the coverage of 89.5% with an accuracy of 91.97%. Without considering coverage, the overall percentage of attachment ambiguities resolved correctly is 82.3%.

## 5 Conclusions

We have found an increase in performance using Volk’s method with the following differences:

- using exact phrase searches instead of NEAR operator;
- using a search engine with a larger document database;
- searching combinations of words that include definite and indefinite articles; and
- searching for singular and plural forms of words when possible.

The results obtained with this method (89.5% coverage, 91.97% accuracy, 82.3% overall) are very close to those obtained by using treebank statistics, without the need of such expensive resources.

A demo version of a program implementing our method can be found at the website [likufanele.com/ppattach](http://likufanele.com/ppattach).

## References

- [1] Adwait Ratnaparkhi, Jeff Reynar, and Salim Roukos. A Maximum Entropy Model for Prepositional Phrase Attachment. In *Proceedings of the Human Language Technology Workshop*, pp 250–255, Plainsboro, N.J. ARPA, 1994.
- [2] Eric Brill and Phil Resnik. A Rule Based Approach to Prepositional Phrase Attachment Disambiguation. In *Proceedings of the Fifteenth International Conference on Computational Linguistics* (COLING), 1994.

---

<sup>4</sup> Google API is a web service that uses the SOAP and WSDL standards to allow a program to query directly the Google search engine. More information can be found at [api.google.com](http://api.google.com).

<sup>5</sup> [www.google.com](http://www.google.com)

- [3] Michael Collins and James Brooks. Prepositional Phrase Attachment through a Backed-of Model. In David Yarowsky and Kenneth Church, eds, *Proceedings of the Third Workshop on Very Large Corpora*, pages 27-38, Cambridge, Massachusetts, June 1995.
- [4] Paola Merlo, Matthew W. Crocker, and Cathy Berthouzoz. Attaching Multiple Prepositional Phrases: Generalized Backer-off Estimation. In Claire Cardie and Ralph Weischedel, editors, *Second Conference on Empirical Methods in Natural Language Processing*, pp 149-155, Providence, R.I., August 1-2, 1997.
- [5] Jakub Zavrel and Walter Daelemans. Memory-Based Learning: Using Similarity for Smoothing. In ACL, 1997.
- [6] Alexander Franz. Independence Assumptions Considered Harmful. In ACL, 1997.
- [7] Adwait Ratnaparkhi. Statistical Models for Unsupervised Prepositional Phrase Attachment. In *Proceedings of the 36th ACL and 17th COLING*, pp. 1079-1085, 1998.
- [8] Eric Brill. Processing Natural Language without Natural Language Processing. In Alexander Gelbukh, ed. *CICLing 2003, Computational Linguistics and Intelligent Text Processing*, Lecture Notes in Computer Science 2588:360-369, Springer-Verlag, 2003.
- [9] Igor A. Bolshakov and Sofia N. Galicia-Haro. Can We Correctly Estimate the Total Number of Pages in Google for a Specific Language?, In Alexander Gelbukh, ed. *CICLing 2003, Computational Linguistics and Intelligent Text Processing*, Lecture Notes in Computer Science 2588:415-419, Springer-Verlag, 2003.
- [10] Frank Keller and Mirella Lapata, Using the Web to Obtain Frequencies for Unseen Bigrams. To appear in *Computational Linguistics* 29:3, 2003.
- [11] Martin Volk. Scaling up. Using the WWW to resolve PP attachment ambiguities. In *Proceedings of Konvens 2000*, Ilmenau, October 2000.
- [12] Martin Volk: Exploiting the WWW as a corpus to resolve PP attachment ambiguities. In *Proceeding of Corpus Linguistics 2001*. Lancaster: 2001.
- [13] Vincent Vandeghinste. Resolving PP Attachment Ambiguities Using the WWW. In the *Thirteenth meeting of Computational Linguistics in the Netherlands*, CLIN 2002 Abstracts, Groningen, 2002.
- [14] Sofia Galicia Haro, Alexander Gelbukh, and Igor A. Bolshakov. Una aproximación para resolución de ambigüedad estructural empleando tres mecanismos diferentes. In *Procesamiento de Lenguaje Natural*, No 27, September 2001. Sociedad Española para el Procesamiento de Lenguaje Natural (SEPLN), Spain, pp. 55-64.
- [15] Fernando Cuetos, Miguel Angel Martí, and Valiña Carreiras, *Léxico informatizado del Español*. Edicions de la Universitat de Barcelona, 2000.

# Determination of Similarity Threshold in Clustering Problems for Large Data Sets

Guillermo Sánchez-Díaz<sup>1</sup> and José F. Martínez-Trinidad<sup>2</sup>

<sup>1</sup> Center of Technologies Research on Information and Systems,  
The Autonomous University of the Hidalgo State  
Carr. Pachuca – Tulancingo Km. 4.5; C.U  
42084 Pachuca, Hgo., Mexico  
[sanchezg@uaeh.edu.mx](mailto:sanchezg@uaeh.edu.mx)

<sup>2</sup> National Institute of Astrophysics, Optics and Electronics,  
Luis Enrique Erro No. 1, Sta. María Tonantzintla,  
72840 Puebla, Mexico  
[fmartine@inaoep.mx](mailto:fmartine@inaoep.mx)

**Abstract.** A new automatic method based on an intra-cluster criterion, to obtain a similarity threshold that generates a well-defined clustering (or near to it) for large data sets, is proposed. This method uses the connected component criterion, and it neither calculates nor stores the similarity matrix of the objects in main memory. The proposed method is focussed on unsupervised Logical Combinatorial Pattern Recognition approach. In addition, some experimentations of the new method with large data sets are presented.

## 1 Introduction

In unsupervised Pattern Recognition area many algorithms have been proposed [1]. Some of them are based on graph theory. In this paper we will consider the approach based on graph proposed in the Logical Combinatorial Pattern Recognition [2, 3].

In this context, it is assumed that the structure of one universe is not known. To find such structure an initial sample is given, then the problem is precisely to find the classes, the groupings.

The main idea consists in consider the data as vertexes in a graph and the similarity among the objects as edges. In this way the problem of unsupervised classification can be seen as finding subgraphs (clusters) in the initial graph (initial sample).

Note that there exists a natural correspondence among data, their similarity and a graph whose vertexes are objects and the weight of their edges is the similarity between adjacent vertexes.

In this context a parameter  $\beta_0$  can be introduced for controlling how many similar a pair of objects must be in order to be considered similar. As result then a new graph containing only edges with weight greater or equal than  $\beta_0$  (the parameter) is obtained.

Therefore depending on the desired closeness in similarity, an appropriate value for this parameter can be chosen by the user and then different graphs are obtained.

Now the problem is reduced to find in the resultant graph certain subgraphs. For example, we can find connected components in the graph fixing a certain  $\beta_o$ , where each vertex is an object of the sample and all the edges have a weight greater than  $\beta_o$ . Note that when the value of  $\beta_o$  is modified the graph may change and then the connected components also can change obtaining a different clustering for each value of  $\beta_o$ . Here rises a natural question, what value of  $\beta_o$  must be chosen?.

There are many criteria to find subgraphs (clustering criteria), in [4] are presented some of them as  $\beta_o$ -connected components,  $\beta_o$ -compact sets,  $\beta_o$ -strictly compact sets, and  $\beta_o$ -complete maximal sets.

The problem of choosing an adequate value for  $\beta_o$ , without neither to calculate nor to store a similarity matrix for the objects, is studied in this paper. A new automatic method to obtain a similarity threshold  $\beta_o$  to generate a well-defined clustering (or near to it) for large data set is proposed. This method is based on the maximum and minimum values of similarity among objects and it calculates an intra-cluster similarity for each cluster. Then the method uses this intra-cluster similarity to obtain a global value, which indicates what clustering has the best average intra-cluster similarity. The new method uses the GLC algorithm [5], which generates a clustering based in connected components criterion for large data sets.

## 2 Related Works

In [6] a method to determine the parameter  $\beta_o$  for a hierarchical algorithm is proposed. This method uses as similarity between two clusters  $C_i$  and  $C_j$  the expression  $\beta(C_i, C_j) = \max_{\substack{o \in C_i \\ o' \in C_j}} \{\beta(o, o')\}$ . Then using a traditional hierarchical algorithm, i.e,

grouping the two clusters more similar in each level, a dendogram is built. Using the dendogram the user can choose the parameter  $\beta_o$  that prefers according to the number of clusters generated by this  $\beta_o$  value.

In this case, the user determines the value of  $\beta_o$  in function of the number of cluster that he want to get analyzing the dendogram, the method automatically not determine the value  $\beta_o$ .

Another related work is [7], where some concepts and theorems to demonstrate the number of forms that a sample of objects can be partitioned in  $\beta_o$ -connected components, are introduced. The values  $\beta_o$  that characterize the different forms of partitioning the sample and the cardinality for each component are also studied.

In this paper, an algorithm such that given a number  $0 < k < m$ , (where  $m$  is the number of objects in the sample), the  $k$   $\beta_o$ -connected components are generated, is proposed.

Note that this method is very useful if the number of  $\beta_o$ -connected components to form is known, otherwise when the number of clusters to form is an incognita in the problem we can not use the method.

Although these techniques were not developed in order to process large data sets.

The problem of determining the value of  $\beta_o$  that generates natural clusters (well-defined clusters) is very important in the context of Logical Combinatory Pattern Recognition approach. Therefore in the next sections a new method to estimate  $\beta_o$  for large data sets is introduced.

### 3 Basic Concepts

In this section, the context of an unsupervised classification problem in the Logical Combinatorial Pattern Recognition is explained and also some basic concepts that our method uses to determine  $\beta_o$  are introduced.

Let  $\Omega=\{O_1, O_2, \dots, O_m\}$  be a set of objects and  $R=\{x_1, x_2, \dots, x_n\}$  a set of features. A description  $I(O)$  is defined for every  $O \in \Omega$  and this is represented by an  $n$ -tuple, e.g.  $I(O)=(x_1(O), \dots, x_n(O)) \in D_1 \times \dots \times D_n$  (initial representation space), where  $x_i(O) \in D_i$ ;  $i=1, \dots, n$ ; and  $D_i$  is the domain of admissible values for the feature  $x_i$ .  $D_i$  can be a set of nominal, ordinal and/or numerical values.

Hereafter we will use  $O$  instead of  $I(O)$  to simplify the notation.

**Definition 1.** A *comparison criterion* [4] is a function  $\varphi_i: D_i \times D_i \rightarrow L_i$  which is associated to each feature  $x_i$  ( $i=1, \dots, n$ ), where:

$\varphi_i(x_i(O), x_i(O)) = \min\{y\}, y \in L_i$ , if  $\varphi_i$  is a *dissimilarity* comparison criterion between values of variable  $x_i$ , or

$\varphi_i(x_i(O), x_i(O)) = \max\{y\}, y \in L_i$ , if  $\varphi_i$  is a *similarity* comparison criterion between values of variable  $x_i$ , for  $i=1, \dots, n$ .  $\varphi_i$  is an evaluation of the similarity or dissimilarity degree between any two values of the variable  $x_i$ .  $L_i$  ( $i=1, \dots, n$ ) is a total ordered set, usually it is considered as  $L_i=[0,1]$ .

**Definition 2.** Let a function  $\beta: (D_1 \times \dots \times D_n)^2 \rightarrow L$ , this function is named similarity function [8], where  $L$  is a total ordered set.

The similarity function is defined using a comparison criterion for each attribute.

**Definition 3.** In a clustering process (also in supervised classification) will understood by Data set (DS) such collection of object descriptions that the size of the set of descriptions together with the size of the result of the comparison of all object descriptions between objects (*similarity matrix*) does not exceed the available memory size. A Large Data Set (LDS) will be called in the case when only the size of the set of descriptions does not exceed the available memory size. And a Very Large Data Set (VLDS) will be called when both sizes exceed the available memory size [9].

**Definition 4.** Let  $\beta$  be a similarity function and  $\beta_o \in L$  a similarity threshold. Then two objects  $O_i, O_j \in \Omega$  are  $\beta_o$ -*similar* if  $\beta(O_i, O_j) \geq \beta_o$ . If for all  $O_j \in \Omega$   $\beta(O_i, O_j) < \beta_o$ , then  $O_i$  is a  $\beta_o$ -*isolated* object.

**Definition 5 (Intra\_i criterion).** Let  $C_1, \dots, C_k$  be  $k$  clusters obtained after apply a clustering criteria with a certain  $\beta_o$ . The intra-cluster similarity criterion (*Intra\_i*) is defined as follows:

$$Intra\_i(C_i) = \begin{cases} \max_s & \text{if } \max_{C_i} = \min_{C_i} = \max_s \\ \max_{C_i} - \min_{C_i} & \text{if } \max_{C_i} \neq \min_{C_i} \\ \min_s & \text{if } \max_{C_i} = \min_{C_i} \neq \max_s \end{cases}$$

where  $\max_s$  and  $\min_s$  are the maximum and minimum similarity values that  $\beta$ , the similarity function, can takes (i.e.  $\max_s=1.0$  and  $\min_s=0.0$ , if  $L=[0, 1]$  for example). Besides,  $\max_{C_i}$  and  $\min_{C_i}$  are the maximum and minimum similarity values among objects belonging to the cluster  $C_i$ .

According to Han and Kamber [10] a good clustering method will produce high quality clusters (well-defined clusters), with high intra-cluster similarity and low inter-cluster similarity.

The proposed *Intra\_i* criterion was inspired in two facts. First, The *Intra\_i* criterion gives a low weight to those clusters where the difference between the maximum and the minimum similarity between objects is low (or null). Also, this criterion gives a high weight to those clusters formed by only one object. This is because these clusters may be outliers or noise, and its global contribution can generates not adequate results.

Second, in this approach of unsupervised classification based in Graph Theory there are two trivial solutions: when  $\beta_0=\min_s$ , obtaining one cluster with all objects of the sample, and when  $\beta_0=\max_s$ , generating  $m$  clusters, each one formed by only one object.

Then, while  $\beta_0$  is increased from 0.0 to 1.0 the *Intra\_i* takes several values in function of the difference between the maximum and the minimum similarity between objects in the different clusters for each clustering. Therefore, we propose that a reasonable way to determine an adequate value of  $\beta_0$  (associated to a well-defined clustering) is considering a clustering (a set of clusters) with minimum average intra-cluster similarity.

## 4 The Method for Determining $\beta_0$

In this section, we describe the proposed method to obtain a threshold  $\beta_0$  such that a well-defined clustering is associated to this value.

### 4.1 Description of the Method

The proposed method works in the following way. First, the threshold  $\beta_0$  is initialized with the minimum value of similarity between objects ( $\beta_0=0.0$ ). After this, in order to generate several clustering, the method handles a loop, which increases the threshold value with a small constant (INC) and then, a clustering using the GLC algorithm is generated with this  $\beta_0$  value. For each cluster in a clustering, the maximum and minimum values of similarity among objects are calculated and the *Intra\_i* criterion is computed. Finally, the method calculates the average *Intra\_i* for each clustering and takes the minimum value obtaining the threshold  $\beta_0$  that generates a well-defined clustering in the data set. This process continues until INC reaches the maximum similarity value  $\beta_0=1.0$ .

The increase value (INC) for  $\beta_0$  can takes several values, depending of the accurate required in the problem (0.1, 0.15, 0.5, 0.01, etc., for example). Two ways to handle this parameter in our method are proposed. The first option simply consists in increase INC until reaches the maximum similarity value. The second option is proposed for similarity functions that depend on comparison functions for features ( $\varphi_t, t=1, \dots, n$ ) that have the form

$$\beta(O_i, O_j) = \left| \{x_t / x_t \in R, x_t(O_i), x_t(O_j) \text{ are similar according to } \varphi_t\} \right| / n \quad \text{or}$$

$$\beta(O_i, O_j) = \sum_{x_t \in R} \varphi(x_t(O_i), x_t(O_j)) / n$$

where  $n$  is the number of attributes. In this case, the value of INC is fixed as  $\text{INC}=1.0/n$ , if  $\beta_0 \in [0.0, 1.0]$ . In this way, the values for  $\beta_0$  among  $1.0/h$  and  $1.0/(h+1)$ ,  $h=1, \dots, n-1$  do not generate any change in the clustering.

The method proposed in this paper is the following:

**Input:**  $\Omega$  (data set), INC ( $\beta_0$  increase value)

**Output:**  $\beta_0$  (threshold calculated)

```

 $\beta_0 = \min_s$ 
Repeat
   $CC_k = GLC(\beta_0)$ 
   $C_{ik} = Clusters(CC_k, i), i=1, \dots, h_k$ 
   $\max_{ci-ik} = Max(C_{ik}, i), i=1, \dots, h_k$ 
   $\min_{ci-ik} = Min(C_{ik}, i), i=1, \dots, h_k$ 
   $value_{ik} = Intra\_i(C_{ik}, \max_{ci-ik}, \min_{ci-ik})$ 
   $meanCC_k = \sum value_{ik} / |CC_k|$ 
   $\beta_0 = \beta_0 + INC$ 
until  $\beta_0 = max_s$ 
 $\beta_0 = \beta_0 - min\_average\_Intra\_i(meanCC_k)$ 

```

The  $GLC(\beta_0)$  function calls to GLC algorithm in order to build a clustering (i.e.  $CC_k$ ) with a specific similarity threshold  $\beta_0$ , applying the connected components criterion. The function  $Clusters(CC_k, i)$  returns the cluster  $i$ , from the clustering  $CC_k$ . The functions  $Max(C_{ik}, i)$  and  $Min(C_{ik}, i)$  return the maximum and minimum values of similarity among objects for the cluster  $i$ , in the clustering  $CC_k$ . The  $Intra\_i(C_{ik}, \max_{ci-ik}, \min_{ci-ik})$  function calculates and return the intra-cluster criterion for the cluster  $i$ .  $|CC_k|$  denotes the number of clusters in a clustering. Finally,  $\beta_0 - min\_mean\_Intra\_i(meanCC_k)$  obtains and return the minimum average value of the  $Intra\_i$  criterion.

The threshold  $\beta_0$  obtained by the method indicates that the clustering associated to  $\beta_0$  is a well-defined clustering.

## 5 Experimental Results

In this section, two examples of applications of the method to data sets and large data sets are presented.

The first data set (DS1) contains 350 numerical objects in 2D, and it is shown in figure 1(a). The clusters shown in this figure have several shapes, sizes and densities, and they are not linearly separable. The method was applied to DS1 and 7 clustering were obtained. The thresholds  $\beta_0$  obtained in each clustering (CC<sub>i</sub>) are as follows:

- CC<sub>1</sub>;  $\beta_0=0.00$ ; No. Clusters = 1; Average *Intra\_i*= 0.8631;
- CC<sub>2</sub>;  $\beta_0=0.89$ ; No. Clusters = 2; Average *Intra\_i*= 0.4777;
- CC<sub>3</sub>;  $\beta_0=0.90$ ; No. Clusters = 3; Average *Intra\_i*= 0.3095;
- CC<sub>4</sub>;  $\beta_0=0.93$ ; No. Clusters = 4; Average *Intra\_i*= 0.2772;
- CC<sub>5</sub>;  $\beta_0=0.94$ ; No. Clusters = 5; Average *Intra\_i*= 0.2378;
- CC<sub>6</sub>;  $\beta_0=0.98$ ; No. Clusters = 86; Average *Intra\_i*= 0.6418;
- CC<sub>7</sub>;  $\beta_0=0.99$ ; No. Clusters = 350; Average *Intra\_i*= 1.0000;

The minimum value of these averages determines the value  $\beta_0=0.94$ , which corresponds to a well-defined clustering (i.e. CC<sub>5</sub>), formed by the clusters shown in the figure 1(b). The same well-defined clustering was obtained in [5]. For this example, the value INC=0.01 was employed.

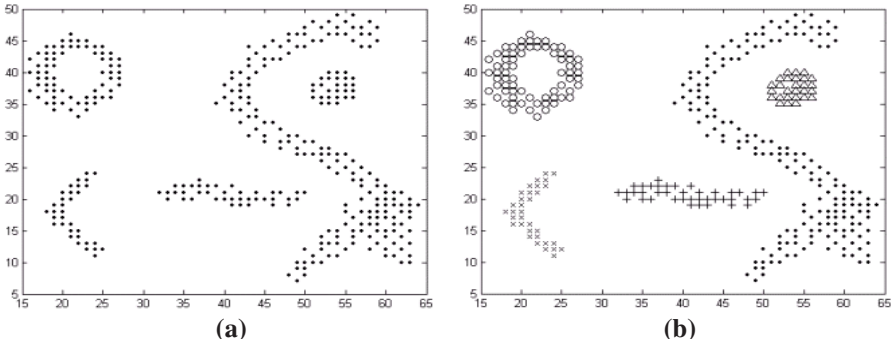


**Fig. 1.** (a) The objects corresponding to DS1; (b) Clustering obtained with  $\beta_0=0.94$ , for DS1 (well defined clustering discovered)

The second data set used for experimentation was a Mushroom database [11]. The mushroom data set (a LDS, according to our definitions) contains records with information that describes the physical characteristics of a single mushroom (e.g. color, odor, shape, etc.). This data set contains 8124 records. All attributes are categorical, and contain missing values. Each record also contains a poisonous or edible label for the mushroom.

In order to show the behavior of the proposed method, several clustering were obtained with their respective  $\beta_0$  and them are presented in tables 1 and 2. Again, we show the well-defined clustering generated for DS2, which corresponds with a

$\beta_0=0.9545$  value, generating 23 clusters, with an average *Intra\_i* value (AIV) of 0.2115. The same well-defined clustering was obtained in [9]. For this experimentation the value INC=0.0454=1.0/22 (number of features = 22) was used.

The cases with  $\beta_0=0.00$ , AIV=0.8182 and  $\beta_0=0.99$ , AIV=1.0 are not shown, because in the first case the clustering obtained has all the objects. And, for the second case each cluster contains only one object.

The notation handled in tables 1 and 2 is as follows: CN denotes the cluster number; NE indicates the number of edible mushrooms; NP denotes the number of poisonous mushrooms, and AIV indicates the average *Intra\_i* value.

The experiments were implemented in C language on a personal computer with Pentium processor at 833 Mhz and 128 RAM Megabytes.

**Table 1.** Clusters obtained for DS2 with  $\beta_0=0.6810$ ;  $\beta_0=0.7273$ ; and  $\beta_0=0.7727$ ;

$\beta_0=0.6810$ , AIV=0.3788			$\beta_0=0.7273$ , AIV=0.2818			$\beta_0=0.7727$ , AIV=0.3182		
CN	NE	NP	CN	NE	NP	CN	NE	NP
1	4016	3880	1	4016	2576	1	392	808
							0	
2	192	0	2	0	1296	2	0	1296
3	0	36	3	192	0	3	48	1768
			4	0	36	4	48	0
			5	0	8	5	192	0
						6	0	36
						7	0	8

**Table 2.** Clusters obtained for DS2 with  $\beta_0=0.8182$ ;  $\beta_0=0.8636$ ;  $\beta_0=0.9091$ ; and  $\beta_0=0.9545$

$\beta_0=0.8182$ , AIV=0.2238			$\beta_0=0.8636$ , AIV=0.2273			$\beta_0=0.9091$ , AIV=0.2208			$\beta_0=0.9545$ , AIV=0.2115		
CN	NE	NP									
1	2848	808	1	896	448	1	0	256	1	0	256
2	768	0	2	768	0	2	704	0	2	512	0
3	0	1296	3	1728	0	3	768	0	3	768	0
4	0	1728	4	0	1296	4	96	0	4	96	0
5	48	0	5	0	288	5	96	0	5	96	0
6	48	0	6	192	0	6	1728	0	6	192	0
7	0	32	7	0	1728	7	0	1296	7	1728	0
8	0	8	8	48	0	8	0	192	8	0	1296
9	192	0	9	32	72	9	0	288	9	0	192
10	288	0	10	48	0	10	192	0	10	0	288
11	0	36	11	0	32	11	0	1728	11	192	0
12	0	8	12	0	8	12	48	0	12	0	1728
13	16	0	13	192	0	13	32	72	13	48	0
			14	288	0	14	48	0	14	0	72
			15	0	36	15	0	32	15	48	0
			16	0	8	16	0	8	16	0	32
			17	16	0	17	192	0	17	0	8
						18	288	0	18	192	0
						19	0	36	19	288	0
						20	0	8	20	32	0
						21	16	0	21	0	36
									22	0	8
									23	16	0

## 6 Conclusions

The method proposed in this paper allows obtaining a well-defined clustering, based in an intra-cluster similarity criterion.

The method gives a threshold value  $\beta_0$  to obtain a well-defined clustering for large data sets.

The method does not establish any assumptions about shape, size or cluster density characteristics of the resultant clusters in each generated clustering. However, the proposed method is still susceptible to noise.

Our method uses the  $\beta_0$ -connected component criterion for clustering. As future work we will work in the generalization of the proposed *Intra\_i* criterion in order to handle other clustering criteria as those exposed in [4].

**Acknowledgement.** This work was financially supported by CONACyT (Mexico) through project J38707-A.

## References

1. Duda R., Hart P., and Stork D.: Pattern Classification (2nd ed). Wiley, New York, NY (2000)
2. Martínez-Trinidad J. F. and Guzmán-Arenas A.: The logical combinatorial approach to pattern recognition an overview through selected works. *Pattern Recognition* 34(4) (2001) 741–751
3. Ruiz-Shulcloper J. and Mongi A.: A Logical Combinatorial Pattern Recognition: A Review. In Recent Research Developments in Pattern Recognition, Ed. Pandalai, Pub. Transword Research Networks, USA. (To appear)
4. Martinez Trinidad J. F., Ruiz Shulcloper J., and Lazo Cortes M.: Structuraliation of universes. *Fuzzy Sets and Systems*. Vol. 112 No. 3 (2000) 485–500
5. Sanchez-Diaz G. and Ruiz-Shulcloper J.: MID mining: a logical combinatorial pattern recognition approach to clustering large data sets. Proc. 5th Iberoamerican Symposium on Pattern Recognition, Lisbon, Portugal (2000) 475–483
6. Pico Peña R.: Determining the similarity threshold for clustering algorithms in the Logical Combinatorial Pattern Recognition through a dendogramme. Proc. 4<sup>th</sup> Iberoamerican Symposium of Pattern Recognition. Havana Cuba (1999) 259–265
7. Reyes Gonzales R. and Ruiz-Shulcloper J.: An algorithm for restricted structuralization of spaces. Proc. 4<sup>th</sup> Iberoamerican Symposium of Pattern Recognition. Havana Cuba (1999) 267–278
8. Ruiz-Shulcloper J. and Montellano-Ballesteros J.: A new model of fuzzy clustering algorithms. Proc. of the 3<sup>rd</sup> EUFIT, Aachen, Germany (1995) 1484–1488
9. Ruiz-Shulcloper J., Sanchez-Diaz G. and Abidi M.: Clustering Mixed Incomplete Data. Heuristics & Optimization for Knowledge Discovery. Idea Group Publishing, USA (2002) 88–106
10. Han J. and Kamber M.: Data mining: concepts and techniques. The Morgan Kaufmann Series in Data Management Systems, Jim Gray Series Editor (2000)
11. Blake C.L. and Merz, C.J.: UCI Repository of machine learning databases [<http://www.ics.uci.edu/~mlearn/MLRepository.html>]. Irvine, CA: University of California, Department of Information and Computer Science (1998)

# Content-Based Retrieval Using Color, Texture, and Shape Information

Ryszard S. Choraś

Faculty of Telecommunications & Electrical Engineering  
University of Technology & Agriculture  
S. Kaliskiego 7, 85-791 Bydgoszcz  
choras@mail.atr.bydgoszcz.pl

**Abstract.** Current technology allows the acquisition, transmission, storing, and manipulation of large collections of images. A way to achieve this goal is the automatic computation of features such as color, texture, shape, and position of objects within images, and the use of the features as query terms.

In this paper we describe some results of a study on similarity evaluation in image retrieval using shape, texture, color and object orientation and relative position as content features. A simple system is also introduced that computes the feature descriptors and performs queries.

## 1 Introduction

Current technology allows the acquisition, transmission, storing, and manipulation of large collections of images. Content based information retrieval is now a widely investigated issue that aims at allowing users of multimedia information systems to retrieve images coherent with a sample image [1]. A way to achieve this goal is the automatic computation of features such as color, texture, shape, and position of objects within images, and the use of the features as query terms.

Content-based retrieval can be divided in the following steps:

*Preprocessing:* The image is first processed in order to extract the features, which describe its contents. The processing involves filtering, normalization, segmentation, and object identification. The output of this stage is a set of significant regions and objects.

*Feature extraction:* Features such as shape, texture, color, etc. are used to describe the content of the image. Image features can be classified into primitive. We can extract features at various levels.

The basic image retrieval system based on this concept is shown in Figure 1.

The main difference between our system and other is the manner in which similarity between a query image and images in a database is computed. For query images, we first compute ROI (Region of Interest) and extract a set of

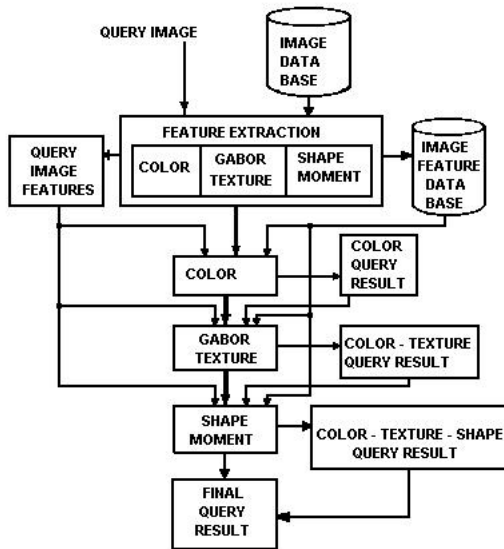


**Fig. 1.** Image retrieval system

color, texture and shape features by applying color histogram computation, Gabor texture extraction and shape parameters computation. The query is processed using color features computation unit, next the Gabor texture unit uses as input the query results of the color features computation unit. Gabor texture unit compares the texture information of the images and discards the images whose color information is similar to that of the query image but the texture information is much different from that of the query image. Next, the shape parameters computation unit is applied to the query results in this stage. The last step is the final query results.

## 2 Feature Extraction

### 2.1 Color Features

We propose a new color feature called color correlogram which describes the global distribution of local spatial correlations of colors and the size of this feature is fairly small [2,3,4].

For a pixel  $p = (x, y) \in F$ , let  $F(p)$  denote its color. The histogram  $h$  of  $F$  is defined for  $i \in [c]$  where  $c$  is number of colors e.g.  $c_1, \dots, c_c$  as

$$h_{c_i}(F) = N \cdot M \Pr_{p \in F} [p \in F_{c_i}] \quad (1)$$

$\frac{h_{c_i}(F)}{N \cdot M}$  gives the probability that the color of the pixel is  $c_i$ .

The correlogram of  $F$  is defined for  $i, j \in [c], k \in [d]$  as

$$\gamma_{c_i c_j}^{(k)}(F) = \Pr_{\substack{p_1 \in F_{c_i} \\ p_2 \in F}} [p_2 \in F_{c_j} \mid |p_1 - p_2| = k] \quad (2)$$

Given any pixel of color  $c_i$  in the image,  $\gamma_{c_i c_j}^{(k)}$  gives the probability that a pixel at distance  $k$  away from the given pixel is of color  $c_j$ . To compute the distance between images  $F$  and  $F'$  we compare histograms and correlograms

$$|F - F'|_h = \sum_{i \in [c]} \frac{|h_{c_i}(F) - h_{c_i}(F')|}{1 + h_{c_i}(F) + h_{c_i}(F')} \quad (3)$$

$$|F - F'|_\gamma = \sum_{\substack{i, j \in [c] \\ k \in [d]}} \frac{|\gamma_{c_i c_j}^{(k)}(F) - \gamma_{c_i c_j}^{(k)}(F')|}{1 + \gamma_{c_i c_j}^{(k)}(F) + \gamma_{c_i c_j}^{(k)}(F')} \quad (4)$$

Given the histograms for a template  $T$  and an image  $F$ , the intersection of these two histograms is defined as

$$H_{c_i}(T \cap F) = \min\{H_{c_i}(T), H_{c_i}(F)\} \quad (5)$$

and

$$h_{c_i}(T \cap F) = \frac{H_{c_i}(T \cap F)}{|T|} \quad (6)$$

The intersection correlogram is defined as the correlogram of the intersection  $T \cap F$ . The intersection correlogram is defined as

$$\gamma_{c_i c_j}^{(k)}(T \cap F) = \frac{\Gamma_{c_i c_j}^{(k)}(T \cap F)}{H_{c_i}(T \cap F) \cdot 8k} \quad (7)$$

where

$$\Gamma_{c_i c_j}^{(k)}(F) = |\{p_1 \in F_{c_i}, p_2 \in F_{c_j} \mid |p_1 - p_2| = k\}| \quad (8)$$

## 2.2 Gabor Features

The differential structure of an image is completely extracted by the convolution with the Gaussian filter family. We use Gabor filters in our image retrieval system. This results in the family of Gabor filters covering the total spatial frequency plane nearly uniformly. Filtering an image with Gabor kernel can be interpreted as local Fourier analysis. The known good characteristics of Gabor filters for image analysis can be justified in scale space framework [5,6]. Gabor filters are used in analysing the property of an object in the selected image because they have optimal joint localization (resolution) in both the spatial and the spatial frequency domains. The frequency tuning of filters allows an axiomatic

characterization of Gabor filters being the linear, shift invariant family of transformations which is (i) parameterized by a scale parameter with a semi-group structure, (ii) is scale invariant i.e. the function that relates the observable is independent of the choice of dimensional units.

Gabor functions are Gaussians modulated by complex sinusoids. In its general form, the two-dimensional Gabor function and its Fourier transform can be written as [7,8]

$$h(x, y) = g(x, y) \exp(j2\pi Fx') \quad (9)$$

$F$  the radial center frequency and  $g(x, y)$  is the 2D Gaussian

$$g(x, y) = \frac{1}{2\pi\sigma_x\sigma_y} \exp\left\{-\frac{1}{2}\left[\left(\frac{x}{\sigma_x}\right)^2 + \left(\frac{y}{\sigma_y}\right)^2\right]\right\} \quad (10)$$

where  $(\sigma_x, \sigma_y)$  characterize the spatial extent and bandwidth of Gabor filter  $h(x, y)$ .

The aspect ratio of  $g(x, y)$  is given by  $\lambda = \sigma_y/\sigma_x$ , which gives a measure of filter's symmetry. In the frequency domain,

$$H(u, v) = \exp\left\{-2\pi^2\sigma^2\left[(u - F)^2\lambda^2 + (v)^2\right]\right\} \quad (11)$$

The set of self-similar Gabor filters is obtained by appropriate rotations and scalings of through the generating function:

$$g_{mn}(x, y) = a^{-m}g(x', y') \quad a > 1 \quad m, n = \text{integer} \quad (12)$$

where

$$(x', y') = (a^{-m}[x \cos \theta + y \sin \theta], a^{-m}[-x \sin \theta + y \cos \theta]) \quad (13)$$

where  $a$  is the scale factor,  $n = 0, 1, \dots, K - 1$  is the current orientation index,  $K$  is the total number of orientations,  $m = 0, 1, \dots, S - 1$  is the current scale index,  $S$  is the total number of scales, and  $\theta = \frac{n\pi}{K}$ .

The scale factor  $a^{-m}$  in equation (12) ensures that the filter energy is independent of  $m$ .

$$E_{mn} = \int \int |g_{mn}(x, y)|^2 dx dy \quad (14)$$

$a = \left(\frac{f_h}{f_l}\right)^{\frac{-1}{S-1}}$ ,  $F = f_h$ ,  $f_l$  and  $f_h$  are the lower and upper center frequencies of interest. In our implementation  $f_l$  and  $f_h$  are equal respectively  $f_l = 0.05$  and  $f_h = 0.4$  and  $a = 2$ .

Gabor filtered output of the image is obtained by the convolution of the image with Gabor function for each of the orientation/spatial frequency (scale) orientation. Given an image  $I(x, y)$ , we filter this image with  $g_{mn}(x, y)$

$$G_{mn} = \sum_k \sum_l I(x - k, y - l) g_{mn}^*(x, y) \quad (15)$$

where \* indicates the complex conjugate.

After applying Gabor filters on the image we obtain an array of magnitudes

$$E_{mn} = \sum_x \sum_y |G_{mn}(x, y)| \quad (16)$$

The magnitudes of the Gabor filter responses are represented by three moments:

- the mean  $\mu_{mn}$

$$\mu_{mn} = \frac{1}{MN} \sum_{x=1}^M \sum_{y=1}^N G_{mn}(x, y) \quad (17)$$

- the standard deviation  $\sigma_{mn}$

$$\sigma_{mn} = \sqrt{\sum_{x=1}^M \sum_{y=1}^N [|G_{mn}(x, y)| - \mu_{mn}]^2} \quad (18)$$

- the skewness  $\kappa_{mn}$

$$\kappa_{mn} = \frac{1}{MN} \sum_{x=1}^M \sum_{y=1}^N \left( \frac{G_{mn}(x, y) - \mu_{mn}}{\sigma_{mn}} \right)^3 \quad (19)$$

The feature vector (*FV*) is represented as follows

$$FV = [\mu_{11}, \sigma_{11}, \kappa_{11}, \dots, \mu_{SK}, \sigma_{SK}, \kappa_{SK}] \quad (20)$$

The similarity of a query image  $Q$  and a image  $T$  in the database is defined as  $T$  where

$$d^{(Q)(T)}(\mu, \sigma, \kappa) = \sum_m \sum_n d_{mn}^{(Q)(T)} \quad (21)$$

where

$$d_{mn}^{QT} = \left| \frac{\mu_{mn}^{(Q)} - \mu_{mn}^{(T)}}{\Xi(\mu_{mn})} \right| + \left| \frac{\sigma_{mn}^{(Q)} - \sigma_{mn}^{(T)}}{\Xi(\sigma_{mn})} \right| + \left| \frac{\kappa_{mn}^{(Q)} - \kappa_{mn}^{(T)}}{\Xi(\kappa_{mn})} \right| \quad (22)$$

where  $\Xi(\mu_{mn})$ ,  $\Xi(\sigma_{mn})$  and  $\Xi(\kappa_{mn})$  are respectively mean, the standard deviation and the skewness of the transform coefficients over the database.

The number of scales chosen is 4 and orientations are 6. Thus 24 Gabor filters are used in the experiments, which give 48 dimensional feature vector texture classification. The proposed features are found to give 94.35% correct classification rates.

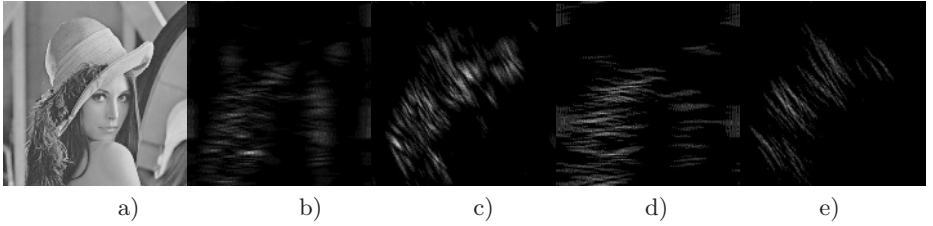


**Fig. 2.** Texture image a). The power spectrum of the Gabor transform with  $0^\circ$  (respectively b) and  $60^\circ$  (respectively c) and e)) orientation for various scale.

### 2.3 Shape Features

Basically, shape based image retrieval is the measuring of similarity between shapes represented by their features. Shape is an important visual feature and it is one of the primitive features for image content description. However, shape content description is a difficult task because it is difficult to define perceptual shape features and measure the similarity between shapes. To make the problem more complex, shape is often corrupted with noise, deflection, arbitrary distortion and occlusion. Therefore, two steps are essential in shape based image retrieval, they are, feature extraction and similarity measurement between the extracted features.

To characterize the shape we used following descriptors: principal axis ratio, compactness, circular variance which are translation, rotation and scale invariant shape descriptors, and seven Hu moments [9,10].

The principal axes ratio (*par*)

$$par = \frac{c_{yy} + c_{xx} - \sqrt{(c_{yy} - c_{xx})^2 - 4(c_{xx}c_{yy} - c_{xy}^2)}}{c_{yy} + c_{xx} + \sqrt{(c_{yy} - c_{xx})^2 - 4(c_{xx}c_{yy} - c_{xy}^2)}} \quad (23)$$

where covariance matrix *C* of a contour is defined

$$C = \begin{bmatrix} c_{xx} & c_{xy} \\ c_{xy} & c_{yy} \end{bmatrix} \quad (24)$$

Compactness (*comp*) is the ratio of the perimeter of a circle with equal area as the original object and the perimeter of original contour

$$comp = \frac{P_{circle}}{P} = \frac{2\sqrt{A_{circle}\pi}}{P} \quad (25)$$

Circular variance (*cv*) is the proportional mean-squared error with respect to a solid circle

$$cv = \frac{1}{N\mu_r^2} \sum_i (||p_i - \underline{\mu}|| - \mu_r)^2 \quad (26)$$

where  $N$  is the number of contour points,  $p_i = (x_i, y_i)^T$  is the contour point,  $\mu$  is the centroid and  $\mu_r$  is the mean radius of the contour.

A object can be represented by the spatial moments of its intensity function. In the spatial case

$$m_{pq} = \sum_{x=1}^m \sum_{y=1}^n x^p y^q f(x, y) \quad (27)$$

The central moments are given by

$$m_{pq} = \sum_{x=1}^m \sum_{y=1}^n (x - X)^p (y - Y)^q f(x, y) \quad (28)$$

where  $(X, Y)$  are

$$X = \frac{m_{10}}{m_{00}} \quad \text{and} \quad Y = \frac{m_{01}}{m_{00}} \quad (29)$$

Normalized central moment  $\mu_{pq}$

$$\mu_{pq} = \frac{m_{pq}}{(m_{00})^\alpha} \quad \alpha = \frac{p+q}{2} + 1 \quad (30)$$

Using nonlinear combinations of the lower order moments, a set of moment invariants (usually called geometric moment), which has the desirable properties of being invariant under translation, scaling and rotation, are derived. Hu [11] employed seven moment invariants, that are invariant under rotation as well as translation and scale change, to recognize characters independent of their position size and orientation.

$$\begin{aligned} \phi_1 &= \mu_{20} + \mu_{02} \\ \phi_2 &= [\mu_{20} - \mu_{02}]^2 + 4\mu_{11}^2 \\ \phi_3 &= [\mu_{30} - 3\mu_{02}]^2 + [3\mu_{21} - \mu_{03}]^2 \\ \phi_4 &= [\mu_{30} + \mu_{12}]^2 + [\mu_{21} + \mu_{03}]^2 \\ \phi_5 &= [\mu_{30} - 3\mu_{12}][\mu_{30} + \mu_{12}] \times [(\mu_{30} + \mu_{12})^2 - 3(\mu_{21} + \mu_{03})^2] + \\ &\quad + [3\mu_{21} - \mu_{03}][\mu_{21} + \mu_{03}] \times [3(\mu_{30} + \mu_{12})^2 - (\mu_{21} + \mu_{03})^2] \\ \phi_6 &= [\mu_{20} - \mu_{02}][(\mu_{30} + \mu_{12})^2 - (\mu_{21} + \mu_{03})^2] + 4\mu_{11}[\mu_{30} + \mu_{12}][\mu_{21} + \mu_{03}] \\ \phi_7 &= [3\mu_{21} - \mu_{03}][\mu_{30} + \mu_{12}] \times [(\mu_{30} + \mu_{12})^2 - 3(\mu_{21} + \mu_{03})^2] \\ &\quad - [\mu_{03} - 3\mu_{12}][\mu_{21} + \mu_{03}] \times [3(\mu_{30} + \mu_{12})^2 - (\mu_{21} + \mu_{03})^2] \end{aligned} \quad (31)$$

To characterize the shape we used a feature vector

$$SFV = (\phi_1, \phi_2, \dots, \phi_7, par, comp, cv) \quad (32)$$

consisting of the seven moment invariants, principal axis ratio, compactness and circular variance descriptors. This vector is used to index each shape in the database. The distance between two feature vectors is determined by city block distance measure.

### 3 Conclusion

A retrieval methodology which integrates color, texture and shape information is presented in this paper. Consequently, the overall image similarity is developed through the similarity based on all the feature components. Experimental evaluation based on our image database shows that our method promisingly outperforms the retrieval systems from the literature.

### References

- [1] M. S. Lew( ed), *Principles of Visual Information Retrieval* (London: Springer-Varlag, 2001).
- [2] M. J. Swain and D. H. Ballard, Color Indexing, *International Journal of Computer Vision*, 7(1), 1991, 11-32.
- [3] A. Drimbarean and P.F. Whelan, Experiments in colour texture analysis, *Pattern Recognition Letters*, 22, 2001, 1161- 1167
- [4] T. Gevers and A.W.M. Smeulders, Colour based object recognition, *Pattern Recognition*, 32, 1999, 453-464.
- [5] George M. Haley and B. S. Manjunath, Rotation-Invariant texture classification using a complete space-frequency model, *IEEE Transactions on Image Processing*, 8(2), 1999, 255-269.
- [6] A. Bovik, M. Clark, W. Geisler, Multichannel texture analysis using localized spatial filters, *IEEE Transactions on Pattern Analysis and Machine Intelligence*, 21(1), 1990, 55-73.
- [7] A. K. Jain and F. Farrokhnia, Unsupervised texture segmentation using Gabor filters, *Pattern Recognition*, 24(12), 1991, 1167-1186.
- [8] B. S. Manjunath and W. Y. Ma, Texture features for browsing and retrieval of data, *IEEE Trans. Pattern Analysis Machine Intelligence*, 18(8), 1996, 837-842.
- [9] F. Mokhtarian and A. Mackworth, Scale-Based Description and Recognition of Planar Curves and Two-Dimensional Shapes, *IEEE Transactions on Pattern Analysis and Machine Intelligence*, 8(1), 1986, 34-43.
- [10] E. Persoon and K. S. Fu, Shape Discrimination Using Fourier Descriptors, *IEEE Trans. On Systems, Man and Cybernetics*, SMC-7(3), 1977, 170-179.
- [11] M. Hu, Visual pattern recognition by moment invariants, *IEEE Trans. on Inf. Theory*, 8, 1962, 179-187.
- [12] R. T. Hu, The revised fundamental theorem of moment invariants, *IEEE Transactions on Pattern Analysis and Machine Intelligence*, 13, 1991, 830-834.
- [13] T. N. Tan, Rotation Invariant Texture Features and Their Use in Automatic Script Identification, *IEEE Transactions on Pattern Analysis and Machine Intelligence*, 20(7), 1998, 751-756.

# Off the Shelf Methods for Robust Portuguese Cadastral Map Analysis

T. Candeias, F. Tomaz, and H. Shahbazkia

Universidade do Algarve – FCT  
BIF laboratory, Campus de Gambelas, 8000-Faro, Portugal  
[{tcandeia, ftomaz, hshah}@ualg.pt](mailto:{tcandeia, ftomaz, hshah}@ualg.pt)

**Abstract.** A document analysis prototype and its application to the automatic Portuguese cadastral map digitalisation is discussed in this paper. Tuning off the shelf methods and sometimes their extension has permitted to obtain applicable results. These algorithms and their tunings as well as the results obtained are given in the paper. The prototype has been approved for further development to an integrated system to be used by some Portuguese entities.

**Keywords:** Cadastral Information System, Map Analysis, Image Processing

## 1 Introduction

In the past years many administrative entities decided to transfer the cadastral information to a numeric format and started using electronic management systems. This is done manually, slowly, and expensively. More than 100000 sheets exist to digitalise in Portugal - one of the smallest countries in Europe.

The process is initiated by a binary scan with a resolution of at least 300dpi. This provides all the necessary information since our map doesn't contain colors or gray scales. The portuguese cadastral map is constrained to several rules, that maintain uniformity explored by our system. Every entity is composed by a closed contour, a numeric identification inserted in a parcel circle, possible dependent plots, separation lines between parcels and a limited word description of each parcel (see figure 1). These are the main guide lines used by our algorithms.

The Portuguese cadastral map authority is pleased with results, that can improve the digitalisation, not only by time saving but also accuracy, since the manual entry of an entire map is tiring and error-prone.

## 2 Processing Methods

The use of various methods for this analysis are mainly conditioned by the enormous computational effort necessary to complete the task, due to the quantity of information (each map has around 500 entities, 800 parcels, 2500 characters and a significant number of miscellaneous information).

Similar problems were also discussed before [1,2], but to obtain a robust application, all the formal aspects of the Portuguese cadastral maps need to be reconsidered (see section 1).

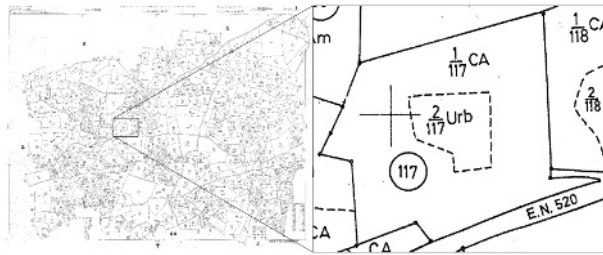


**Fig. 1.** Overview of a cadastral map sample. This typical map is about 85cm x 75cm representing 138 ha of real land. The smaller portion of the map represents 4cm x 4cm @ 300dpi on the paper map.

The legal status of cadastral administration imposes full robustness therefore the applied methods are largely known, tested and are also necessarily fast and accurate [3].

## 2.1 Geo-Referenced Crosses

These crosses are present for reference to the real world position of the map. They are present in small numbers, normally well formed (almost no rotation or distortion), well distributed (constant space among them), making it's recognition and extraction very simple to perform, through template matching of perpendicular lines are scaled in function of the image DPI's. It easily obtains results near 100% for recognition, and only a small percentage of the map is damaged while applying our neighbour algorithm for removing.

## 2.2 Circles

Some problems are associated with circle detection and removal in a common cadastral map: existence of semi-circles, different scales and connection with elements defined as linear (see section 1). This recognition is very important because every parcel is dependent of it's circle recognition.

Hough transform [4,5] is a known process for extraction of parametric defined shapes even in the presence of noise or if the patterns are sparsely digitised. Some changes were made to the original algorithm, and now we are using a simple, but efficient method similar to the algorithm presented in [6].

This method also covers the recognition of semi-circles, due to the initial element labeling (see section 1). To prevent the necessity of large storing and searching associated with Hough's algorithm, local decision is performed for each space point. This however results in a strong circle mismatch recognition near a "true" circle (see figure 2).

This can be easily solved with a post-treatment searching and confirmation algorithm based on the known characteristics of the map and circles, which in most cases are in conformity with a standard. So the peaks represented in figure 2, can be filtered and chosen through its parameters (distance, radius and power). In the example above, only one circle will be filtered due to the proximity of the other.

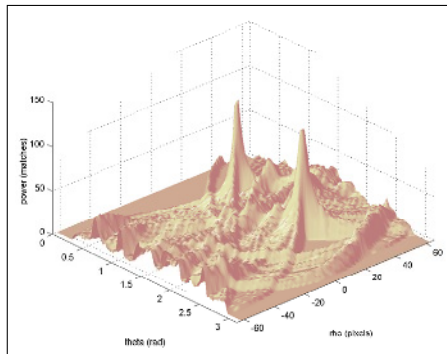


**Fig. 2.** Hough transform, the local decision accepts 2 circles centers

The results are very good, therefore that proves a working solid algorithm. Indeed, in respect to the cadastral standards, we can recognise correctly, for a general map (containing about 300 circles and 90 semi-circles) about 94% of circles and 90% of semi-circles. The percentage of detected, but inexistent circles are below 0.02% in most maps.

### 2.3 Dash

The recognition and extraction of dash elements are imperative for the overall result. Similar to the contour of parcels (see section 2.5) the dash represents inner borders of different land applications. The main difficulty is the similarity of the dashes to other components of the map, noise lines or parts of alpha-numeric elements. A real set of dashes can be easily mistaken with other elements from the map due to its size, shape or context, even to a human's perception.

A density calculation is applied, after a normalization rotation using central moment [7]. In this way, all elements which are not linear and dense are filtered out. A neighbourhood check is also performed to ensure that the dash appears locally in a almost constant frequency.

It's also evident that this method cannot recognise all the dashes (corners or rounded dash), but most important, non-dash elements aren't labelled as a dash by mistake. A pos segmentation is used to join the dash centers and obtain the inner parcel's contour.

### 2.4 Symbol Recognition

Symbol recognition is important to identify parcel's type, its number and also to detect important out of the analysing zone such as the total number of parcels.

The symbols to be recognised are digits and some characters, which can have different sizes. The small set of characters is due to the limited set of words, that describes parcel's type. After analysing different feature extraction methods [8], it was chosen to implement the zoning algorithm [9].

A database was done for all possible characters which are free of noise. The database can have repeated elements to ensure correct recognition, so it's important to consider the database's consistency. This is obtained only allowing addition of a new symbol if its distance to any other is at least 10%.

The classification is implemented using a distance algorithm between two patterns, which measure their dissimilarities. This method is implemented comparing similar squares in patterns - zoning. These squares are found considering the proportional squares inspecting pattern size. Analyzing and comparing each square a punctuation is obtained that could increase or decrease its match. A big size difference between patterns could also decrease its punctuation.

Using this local matching instead of a global approach, it's possible to obtain an invariant size method.

After applying the distance algorithm between testing symbol within each pattern in database, a list is obtained with all matching percentages. This list is later used to enhance the correct hit rate using a cadastral dictionary.

## 2.5 Contour Detection

As in section 2.3, the countour extraction gives a list of points which represent the parcel's coordinates. These points are a list of line segments which constitute a closed polyline.

The contour extraction is composed by three stages: detection, correction and vectorization. The contour lines can have two types: continuous or dashed. Each parcel is separated by continuous lines while dashed lines split sub-parcels. The process of detection and correction is different in each case while vectorization is the same.

The precision of extraction is important and must be considered. To increase precision, two neighbour parcels may have the same common segment line. To contribute for robustness of all the extraction process, a contour is represented by its medial axis points [10], otherwise the line segment wouldn't be equal. So the algorithm of contour extraction is applied to the processed medial axis image.

**Detection.** The main problem of contour detection is the existence of discontinuities which are provided by bad scanning or by noise effect. Two strategies are possible, restore discontinuities or use algorithms which aren't sensible to it. To restore the line following algorithms [11] could be used. But using this kind of algorithm other problems also appear, for example when there are interceptions of lines, the question is which one to follow? Such type of solution would give decision problems that slow down the process. In this way authors have decided to use algorithms which are insensible to discontinuities.

Initially active contour models [12] were considerated, but due to the lack of different energy field, it wasn't possible to apply. As every parcel contains only one circle and this information is reliable, the creation of an algorithm with no sensibility to discontinuities and initial knowledge of a point inside the contour made sense.

The first attempt to solve this problem is a fill algorithm, starting in a point inside of a parcel and then coming to all *critical squares*<sup>1</sup> of the contour while filling square after square.

This is the perfect case which represents the application in an image that was every contour closed. But this isn't the case, so instead of applying a normal fill, it's applied a fill with blocks reaching insensitivity to discontinuities. This means that discontinuities which are smaller or equal to a block square are the perfect case while others can cause problems. Of course that block size is variable but increasing or decreasing it can cause problems in any parcels of the map.

Another approach is to use a quad tree based algorithm for the parcel segmentation. The main idea is similar to the fill algorithm but now squares are of different sizes. The algorithm starts by finding the biggest square inside a parcel in such a way that no collisions exists with black pixels.

The biggest square is filled and, in an interactive way a 4-neighbourhood expansion occurs with the same squares size. Each new empty square is filled until there aren't more possible empty square with the same size. Then for each non empty squares a split is applied in four equal sizes, and this process continues interactively.

This improving is important because it gives sensibility to a square size and discontinuities can be detected because it's possible to know square size at each interaction. The algorithm stops when a larger square, than the current processing one, is detected and empty of contour pixels.

After the detection of critical squares is complete, a detection to contour points is done. This is implemented considering the filled neighbours squares and detecting all contour points in the opposite direction. After all these procedures are complete, a list of points is obtained for each parcel that represents its contour.

The dash's lines which also represent a contour line are detected considering each element already recognised (see section 2.3).

**Correction.** After detecting the contour points some discontinuities are found. These discontinuities are due to the occlusions already existent and so, are necessary to correct.

The contour line of continuous type is corrected using a line follow algorithm [11], making a linear interpolation when there are no neighbour pixels to follow.

The dashed line is corrected in a more complex manner. The extremes of the detected dashes are introduced in a list, then a linear interpolation is done to the near extremes, that can't make part of the current dash. After uniting all the dashed line components, the contour that is united to the dashes can be erased. This erosion is done detecting the extremes that didn't interpolate (absolute extremes).

**Vectorization.** Before applying the vectorization method described in [13,14] its necessary to convert the contour points into chain code.

Once the contour is made by line segments, the chosen method was Rosin & West, considering the split-and-merge approach.

An example of contour extraction can be seen in figure 3.

---

<sup>1</sup> The critical squares in this case are squares which have black pixels, so there can be known that these are squares with contour points.

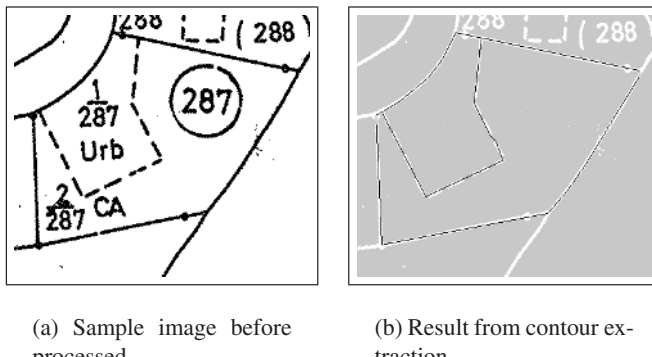


**Fig. 3.** Example of the extraction process of a parcel's contours.

### 3 Results

The results were obtained testing each module with a binary cadastral map, 10784x7853 pixels @ 300 dpi. The time was measured with C internal language's function in a Athlon 1400 processor, 512 Mb DDRam and a HD 7.200 rpm.

The program was compiled with *gcc* version 3.2 (Mandrake Linux 9.0 3.2-1mdk) with *CFLAGS = -O2 -march=i686 -mcpu=i686 -funroll-all-loops*.

The results can be observed in table 1.

**Table 1.** Experimental results of application's modules.

Element	Number of patterns	Performance rate	Processing time
Crosse	35	100%	2:23 min
Circle	386	94%	10:16 min
Semi-circle	94	90%	14:32 min
Symbol	4657	77%	12:56 min
Dashe	2347	84%	4:26 min
Contour	450	82%	30:54 min

The patterns were first manually and then automatically classified to obtain the hit rates. Contour results are qualitative, so each vectorized parcell was compared to the initial map.

Global recognition requires 1 hour and 14 min.

### 4 Discussion

The results obtained at the moment are satisfactory, but can still be improved. In every analysis there are some problems which are resolved increasing consequently the level of the overall results.

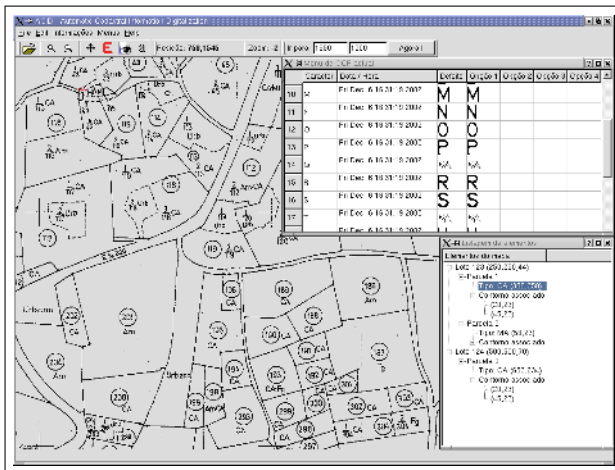
The circle detection is only problematic when processing small circles. This happens because the size of non recognised circles are out of the processing range. This can be solved increasing the processing interval but it will be more time consuming.

The semi-circle detection needs the Hough transform to restore lines, which is computationally expensive. Some problems occur in restoring a parcel's contour related to the size of the Hough transform window.

Symbol detection is the most problematic because there are many different classes to classify. The problem is globally solved because each symbol can be classified alone in a correct way. Problems occur when symbols are connected.

The dash detection is also globally solved, but continue problematic when connected to symbols. This may be solved by splitting unknown elements as in the case of symbols.

The contour extraction could be problematic due to previous processing. Other problems occur when there are two closed discontinuities which are removed after applying a linear element detection. This could be solved applying a filter using size and central moments to non-linear elements to restore them close to the contour, in this way long discontinuities are removed.



problems such as semantic consistency and linking of sections remain a hard task to be addressed. A snapshot of the prototype can be seen in picture 4.

**Acknowledgments.** This work is funded by the FCT (Fundação para a Ciência e Tecnologia), project ACID, contract SRI/34257/99-00 – Automatic Cadastral Information Digitalization.

## References

1. Shahbazkia, H.: Reconnaissance invariante et acquisition de connaissance: application au traitement automatique des plans de cadastre français. PhD thesis, Université Louis Pasteur de Strasbourg (1998)
2. Wenyin, L., Dori, D.: A proposed scheme for performance evaluation of graphics/text separation algorithms. In: GREC. (1997) 359–371
3. Tomber, K., Ah-Soon, C., Dosch, P., Habed, A., Masini, G.: Stable, Robust and Off-the-Shelf Methods for Graphics Recognition. in Proceedings of the 14th International Conference on Pattern Recognition, Brisbane (Australia) (1998) 406–408
4. Duda, R., Hart, P.: Use of the hough transform to detect lines and curves in pictures. Communications of the ACM **15** (1972) 11–15
5. Ballard, D.H.: Generalizing the hough transform to detect arbitrary shapes. Pattern Recognition **13** (1981) 111–122
6. Matas, J., Galambos, C., Kittler, J.: Progressive probabilistic hough transform. Technical report, University of Surrey/Czech Technical University (1998)
7. Kilian, J.: Simple image analysis by moments. Technical report, Freely distributable, version 0.2 (2001)
8. Trier, O., Jain, A., Taxt, T.: Feature extraction methods for character recognition – a survey (1996)
9. Dimauro, G., Impedovo, S., Pirlo, G., Salzo, A.: Zoning design for handwritten numeral recognition. In: ICIAP (2). (1997) 592–599
10. Tombre, K., Tabbone, S.: Vectorization in graphics recognition: To thin or not to thin. Proceedings of 15th International Conference on Pattern Recognition, Barcelona (Spain) **2**, pages 91–96 (September 2000)
11. Jennings, C.: Computer vision for line drawings. Msc Thesis (1993)
12. Kass, M., Witkin, A., Terzopoulos, D.: Snakes: Active contour models. In: Proc. of IEEE Conference on Computer Vision, London, England (1987) 259–268
13. Tombre, K., Ah-Soon, C., et al.: Stable and robust vectorization: How to make the right choices. Proceedings of Third IAPR International Workshop on Graphics Recognition (Jaipur, India), pages 3–16 (September 1999)
14. Eikvil, L., Aas, K., Koren, H.: Tools for interactive map conversion and vectorization. International Conference on Document Analysis and Recognition **2** (August 14–16, 1995)

# Simultaneous Segmentation-Recognition-Vectorization of Meaningful Geographical Objects in Geo-Images

Serguei Levachkine, Miguel Torres, Marco Moreno, and Rolando Quintero

Geoprocessing Laboratory (GEOLAB)

Centre for Computing Research (CIC) - National Polytechnic Institute (IPN)  
`{palych, mtorres, marcomoreno, quintero}@cic.ipn.mx`

**Abstract.** We present an approach to color image segmentation by applying it to recognition and vectorization of geo-images (satellite, cartographic). This is a simultaneous segmentation-recognition system when segmented geographical objects of interest (alphanumeric, punctual, linear, and area) are labeled by the system in same, but are different for each type of objects, gray-level values. We exchange the source image by a number of simplified images. These images are called composites. Every composite image is associated with certain image feature. Some of the composite images that contain the objects of interest are used in the following object detection-recognition by means of association to the segmented objects corresponding “names” from the user-defined subject domain. The specification of features and object names associated with perspective composite representations is regarded as a type of knowledge domain, which allows automatic or interactive system’s learning. The results of gray-level and color image segmentation-recognition and vectorization are shown.

## 1 Introduction

Segmentation is fundamental to the field of image processing because it is used to provide the basic representation on which understanding algorithms operate. The ability to build up a representation from individual pixels of an image, which exploits relationships such as local proximity and highlights the structures of the underlying components, is important for the extraction of features during interpretation and recognition [1]. In general, the nature of this representation is application dependent. In the present work, we developed an application independent segmentation.

Up to the now a great variety of segmentation algorithms for gray-level images has been proposed. The majority of color segmentation approaches are based on mono-chrome segmentation approaches operating in different color spaces [4]. Gray-level segmentation methods can be directly applied to each component of a color space; thus, the results can be combined in some way to obtain a final segmentation result. However, one of the problems is *how to employ the color information as a whole for each pixel*. When the color is projected onto three *RGB* color components, the color information is so scattered that the color image becomes simply multispectral image

and the color information that humans can perceive is lost [2]. Another problem is *how to choose the color representation for segmentation* [3], [4]. There is no single color representation that can surpass others for segmenting all kinds of color images. The use of nonlinear spaces, such as *HSI* and the normalized color space can solve the problem to certain approximation. However, the nonlinear spaces have essential, non-removable singularities and there are spurious modes in the distribution of values [5].

An alternative solution presented in this work is invariant image representation (composite images, or simply *composites*) that does not depend on the choice of particular color space. The processing of a color image is individual segmentation by each color component into image meaningful (or invariant with respect to a given, unnecessary color feature) regions, first and, then – image's joint segmentation-recognition (or “objects of interest designing”). Moreover, the prescribed set of features is regarded as a type of *knowledge domain*. The *composite image technique* includes object-fitting compact hierarchical segmentation, binarization of segmented images, and synthesis of binary representations. The main goal of image synthesis consists of the object linking by its associated names. In the following sections, we build up composite image representations based on object-fitting compact hierarchical segmentation. See also [6], [7], [8], and [9].

## 2 Object-Fitting Compact Hierarchical Segmentation, Recognition, and Vectorization

In our method, the image segments obtained as the result of the iterative procedure of successive increasing of the admitted gray-level and color thresholds in the segment merging form subsequently increasing compact hierarchical structure of the flat segment networks. Each segment of this structure can have the ancestor or a descendant. Thus obtained structure is called *the adaptive dynamic data structure*. The segment of image is a node of the spatial structure, which attributes are primary numbers defined by the averages of color/gray-level segment's features and by a set of pixels that represent the area and the shape of the segment (Section 6). This allows organizing the object-oriented identification of semantically meaningful image's regions. Our system has the interactive procedure of *compulsory restructuration* of the segment relationships as a tool of the semantic analysis of visual data. In other words, the system's learning and self-learning with the prescribed set of associative identifiers are possible in the interactive regime.

Successive segment merging by some criteria leads to the segment structuring in a *multi-level hierarchy* that represents by the dynamic trees [7]. This hierarchy or *the multi-level image partition* is an efficient method of semantic identification of the image's objects. The relationships between the dynamic tree nodes indicate *the neighboring semantically meaningful regions*. Because the image's regions are identified by the corresponding tree nodes, *the neighbor relation* between them can be completely defined by a table of adjacency. A modification (elimination of some edges, i.e. segment relationships) of the dynamic tree allows modifying the resulting region and thus more exact object detection is reached. Each level of the tree of segments can

be considered as alternative image interpretation in different semantics (see Fig. 3, Section 3 and Fig. 5, Section 5).

Adaptive dynamic tree structure regards the search for meaningful objects as the combination of the object features that fit to the corresponding ranges and the following analysis of all admitted areas. This makes possible to use the *automatic learning* algorithms when the set of searched objects is given and it is necessary to define only the corresponding feature ranges (this is natural supposition for geo-images [9]). The learning process can be organized as follows. The user selects the appropriate level of segment hierarchy and points out the set of the suitable areas. These areas can be defined by combining the corresponding segments. Then the program computes the characteristics of the located segments and relationships between them and establishes the formal criterion of the search for the similar objects.

*Object-fitting compact hierarchical segmentation* is a sequence of embedded partitions without repetition of composed segments in different partitions. A partition is obtained by iterative segment splitting or merging. In the merging mode, any segment in each iteration merges into the nearest adjacent segment. The number  $2^i$ , where  $i$  is the number of iteration, is bound total number of segments  $N$ , generated at each iteration [6]. The number  $N$  has to be taken into account for automatic color image analysis. Indeed, the merging of segments into objects defines the image semantics. The image's semantics in this context corresponds to the association of segment fields of different hierarchical levels being identified with identifying conceptions from the subject domain. For example, detection of a segment identifying a coastline or highway becomes semantically meaningful. Further, this set of segments is renamed as "coastline", "highway", etc. (Fig. 1).

Segmented and recognized objects are subsequently vectored by applying a method described in [9] to be finally included into GIS. These three stages (segmentation-recognition-vectorization) are Objected Oriented Data Integration for GIS [9], [12].

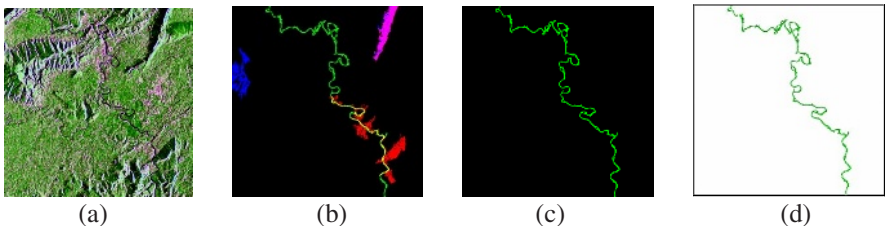


**Fig. 1.** (a) Source image, (b) Segmented image, (c) Recognized image, and (d) Vector image of the river

Precisely all this is what we mean under simultaneous segmentation-recognition-vectorization process. Fig. 1 shows segmentation-recognition-vectorization of the river in a SAR image of Kalimantan Island.

The number of segments  $N$  decreases approximately as  $(4 \div 5)^i$ , where  $i$  is the iteration number (Fig. 2a). From our point of view, deviation from this exponential de-

pendence leads to image's semantics violation. Disclosed regularity can be useful for automatic analysis of gray-level and color images.

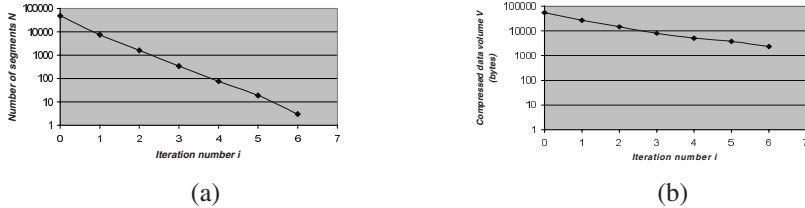


**Fig. 2.** Linear dependences: (a) Number of segments  $N$  on iteration number  $i$ , (b) Compressed image volume  $V$  on iteration number  $i$

Our experiments have shown (Fig. 2b) that the compressed volume of an image is decreased in the same exponential mode (Cf. image compression with information-lossless standard algorithms: RAR, LZH, etc.).

Eliminating the dependence on iteration number  $i$ , we can obtain the exponent-mode relation of compressed data volume  $V$  on number of segments  $N$  as follows:

$$N/N_0 = (V/V_0)^\alpha \quad (1)$$

In equation (1),  $N_0$ ,  $V_0$  denote number of segments and compressed volume of the source image respectively;  $\alpha$  is some real coefficient. We obtained that in the case of object-fitting compact hierarchical segmentation the exponent  $\alpha$  is approximately 2.9. Note that for non-adaptive pyramidal segmentation [3]  $\alpha$  is approximately 1.4. It is known that the volume of compressed data is closely related to the *amount of information into data*. Thus, a theoretical explanation of the obtained experimental dependences (Fig. 2) represents an interesting research topic of Pattern Recognition.

### 3 Composite Image Representation

We have found that in addition to natural decomposition (e.g.,  $R$ ,  $G$  or  $B$  – component splitting) of color images, artificial representations can also be useful for objects of interest detection-recognition [6], [7], [8], and [9]. Our approach provides composite representations of the source image by means of reduced number of color or tone components and segments. Composite image representation is a sequence of binary representations, which are packed into different bit planes. These binary images are the result of two-valued classification of source image by some feature (intensity, area, invariant moments, etc.; Section 6).

A bit component of composite image (Fig. 3) computes by means of global dynamic thresholding of the current segmented image. The threshold is equal to the average all over the image intensity, geometric or other feature, denoted by  $I^{(i)}$ . To threshold the image,  $I^{(i)}$  is compared with its average over the pixels of each segment, denoted by  $I^{(s)}$ , as follows:  $I^{(i)} \geq (\leq) \xi I^{(s)}$ , where  $\xi$  is a tuning parameter.



**Fig. 3.** Bit components of composite images obtained by means of dynamic adaptive thresholding of Lena's source and segmented images

To compose these images, we also used the geometric features from the feature set (Section 6) in addition to intensity feature. The bit components are packed in the resulting representation, where the extrema of intensity indicate the pixels associated with unchanged binary feature. Essentially, the composite images form a “book” in which the objects of interest can be found on appropriated page(s). Thus, a “page number” defines the method of thresholding and the tuning parameter  $\xi$ .

## 4 Color Composites

Compact hierarchical segmentation of a color image is performed by each independent color components ( $R$ ,  $G$ , and  $B$ ) considering these as semi-tone images. In this way, coinciding intensities of resulting  $R$ ,  $G$ , and  $B$  composite images indicate the segments of equal color with respect to using feature. This can be used for invariant color image description. As a rule, compact hierarchical image segmentation implies that color segments are enlarged simultaneously in accordance to regularities presented in Section 2. Due to the self-consistence of  $RGB$ -segmentation behavior, visual quality improvement in composite intensities becomes available [6]. The method requires significant operative memory space. To overcome this disadvantage, we used special data organization in the form of irregular dynamic trees (Section 2 and [6], [7], [8], [9]) that provides optimal in memory space computing for the successive scanning of image scales. Due to data organization, a practical use of our program package does not require further algorithmic development. The user needs only to make adequate choice to carry out task features from prescribed feature set (*knowledge domain*).

## 5 Applications of Composites

Image two-valued classification (binarization) is one of the most important tasks in modern recognition methods. In the frameworks of the composite image technique, we obtained a few solutions for this task [6], [7], [8], and [9]. By applying composites, we

are able to extract cartographic data using  $R$ ,  $G$ , and  $B$ -components of full-size color raster-scanned image (Fig. 4).



**Fig. 4.** Cartographic pattern retrieval from a color map image 1082 x 1406 pixels (extreme left)

Fig. 5 shows how our method insures object detection in the task of recognition of inclined digits embedded in graphics (note that this is old and very difficult problem that has been attracted much attention by image processing specialists [1], [4], [9]). This illustrates that each composite image contains machine-treatable bit-planes for target object detection and also purposeless bit-planes. Indeed, to effectively recognize the objects of interest, it is better to search these objects on appropriated bit-planes. Although, our system can generate some errors in interpretation, it is much more useful for the following understanding algorithms because its output is nearly recognized objects of interest.

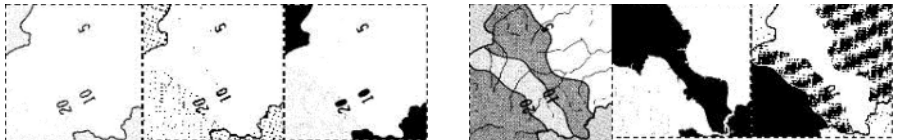


**Fig. 5.** Bit-planes suitable for digit recognition (left side) and other purposes (right side)

## 6 Comments

The presented approach exploits the user's experience providing the knowledge domain in the form of the prescribed feature-attribute set. This set contains a number of attributes and numerous features. The attributes are a primary set of segment characteristics estimated and dynamically stored for all image segments at any level of the composite image representation. This provides a full-value use of object-fitting hierarchical segmentation. The features are numerical segment characteristics, which are obtained as output of data conversion, and are selected in function of the processing stage and the problem context. Thus, prescribed segment attributes are the following -  
*1) Extrema of numerical characteristics: a) global (for the whole image), b) local (for a neighborhood of the segment); 2) Additive: a) integral intensity (the sum of pixel intensities), b) number of pixels, c) integral first and second moments computed with*

*respect to the origin; 3) Non-additive perimeter; 4) Description of the adjacent segments in terms of binary relationships.*

These data provide an estimation of the intensity and geometric segment features: pixel intensity range, average intensity, invariant moments, parameters of linear sizes and shapes, etc. In this manner, the features used in generation of object-fitting hierarchy of the segments can be different from the features used in object recognition [6], [7], [8], and [9]. As a rule, at first step of image processing, only intensity features are useful, because the source image pixels do not form geometrically meaningful segments and objects. Consequently, up to reaching image invariant representation other features are used for object designing and recognition. To our knowledge, this is one of the first attempts to design a segmentation-recognition computer system for complex color images of arbitrary type (Cf. [10] and [12]).

## 7 Conclusion

The problem of *how and to what degree the semantic information should be employed in image segmentation* has led us to the conception of composite image representation for mutual object detection-recognition at low level processing. We conjecture that modern segmentation systems must support mutual object detection-recognition-interpretation, starting at low level, memorizing results at the intermediate level, and effectively communicating these results to the high level. The approach proceeding from this conjecture is called *composite image technique*. The idea is to prepare the source image as much as possible for subsequent high-level processing of image regions. In most of the existing color image segmentation approaches, definition of a region is based on similarity of color. This assumption often makes it difficult for any algorithms to separate the objects with highlights, shadows, shadings or texture, which cause inhomogeneity of colors of the object's surface. Using *HSI* can solve this problem to some extent, except that hue is unstable at low saturation. Some physics-based models have been proposed to solve this problem [4], [11].

We saw an alternative solution of the problem defining image regions by *quantitative, qualitative, and nominal features* (in addition to color feature), which on the whole render the *user's knowledge domain*. We believe that this is a kind of advanced simulation of the human's visual perception. However, it is necessary to emphasize that for optimization of labor-intensive program training a strong formalization of composite image technique is now required. We are under way to solve this problem.

At the same time, automatic interpretation of color images presents certain difficulties for state-of-the art in image processing and also artificial intelligence. To date, it appears unrealistic to obtain fully automatic computer-based interpretation system free of errors [4], [9], and [12].

We believe that only a system approach to the problem can be fruitful. In the context of the present work, this means first, decomposition of source image by multiple hierarchical components to achieve a stable, accurate representation in the presence of degraded images. Second is the segmentation with mutual recognition of appropriate primitives (compression stage) and, if required, their vectorization to be directly in-

cluded into application-oriented database, e.g., GIS (application-dependent stage). Finally, there is the development of a unified knowledge-based trainable and self-trainable system with optimal human-machine interaction for color image treatment.

## References

1. Doermann, D.S.: An Introduction to Vectorization and Segmentation. Lecture Notes in Computer Science, Vol. 1389. Springer-Verlag, Berlin Heidelberg New York (1998) 1–8
2. Gonzalez, R.C., Woods, R.E.: Digital Image Processing. 3<sup>rd</sup> edn. PTR, NJ: Prentice Hall, New York (2002)
3. Alexandrov, V.V., Gorsky, N.D.: Image Representation and Processing: A Recursive Approach. Mathematics and Its Applications, Vol. 261. Kluwer Academic Publishers, Dordrecht Boston London (1993)
4. Cheng, H.D., Jiang, X.H., Sun, Y., Wang, J.: Color Image Segmentation: Advances and Prospects. Pattern Recognition, Vol. 34, No. 12. (2001) 2259–2281
5. Kender, J.: Saturation, Hue, and Normalized Color: Calculation, Digitization Effects, and Use. Computer Science Technical Report, Carnegie Mellon University (1976)
6. Alexandrov, V.V., Kharinov, M.V., Velázquez, A., Levachkine, S.P.: Object-oriented Color Image Segmentation, In: Hamza, M.N. (ed.): Proc. IASTED International Conference on Signal Processing, Pattern Recognition, and Applications (SPPRA 2002) 25–28 June 2002, Crete, Greece, ACTA Press, Anaheim Calgary Zurich (2002) 493–498 (ISBN: 0-88986-338-5; ISSN: 1482–7921)
7. Alexandrov, V.V., Kharinov, M.V., Levachkine, S.P.: Conception of Hierarchical Dynamic Structure in Application to Audio and Video Data Recognition. In: Hamza, M.N. (ed.): Proc. IASTED International Conference on Artificial Intelligence and Soft Computing (ASC 2001) 21–24 May 2001, Cancun, Mexico, ACTA Press, Anaheim Calgary Zurich (2001) 348–353 (ISBN 0-88986-283-4; ISSN 1482–7913)
8. Levachkine, S.P., Velázquez, A., Alexandrov, V.V.: Color Image Segmentation using False Colors and its Applications to Geo-images Treatment: Alphanumeric Character Recognition. Proc. IEEE International Geosciences and Remote Sensing Symposium (IGARSS 2001) 9–13 July 2001, Sydney, Australia (2001) (IEEE Catalog Number (CD-ROM): 01CH37217C; Library of Congress Number: 01-087978; ISBN CD-ROM: 0-7803-7033-3)
9. Levachkine, S.P., Velázquez, A., Alexandrov, V.V., Kharinov, M.V.: Semantic Analysis and Recognition of Raster-scanned Color Cartographic Images. Lecture Notes in Computer Science, Vol. 2390. Springer-Verlag, Berlin Heidelberg New York (2002) 178–189
10. Kumar, K.S., Desai, U.B.: Joint Segmentation and Image Interpretation. Pattern Recognition, Vol. 32, No. 4. (1999) 577–589
11. Levachkine, S.P., Sossa, J.H.: Image Segmentation as an Optimization Problem. Computation and Systems, Vol. 3, No. 4. (2000) 245–263 (ISSN 1405-5546)
12. Benz, U.C., Hofmann, P., Willhauck, G., Lingenfelder, I., Heynen, M.: Multi-resolution, Object-oriented Fuzzy Analysis of Remote Sensing Data for GIS ready Information. In: Levachkine, S., Ruas, A., Bodansky, E. (eds.), Proc. International Workshop on Semantic Processing of Spatial Data (GEOPRO 2002) 3–4 December 2002, Mexico City, Mexico (2002) (ISBN CD-ROM: 970-18-8521-X)

# Geomorphometric Analysis of Raster Image Data to Detect Terrain Ruggedness and Drainage Density

Marco Moreno, Serguei Levachkine, Miguel Torres, and Rolando Quintero

Geoprocessing Laboratory-Centre for Computing Research-National Polytechnic Institute,  
Mexico City, Mexico  
[{marcomoreno, palych, mtorres, quintero}@cic.ipn.mx](mailto:{marcomoreno, palych, mtorres, quintero}@cic.ipn.mx)  
<http://geo.cic.ipn.mx>, <http://geopro.cic.ipn.mx>

**Abstract.** We present an approach to identify some geomorphometrical characteristics of raster geo-images. The identification involves the generation of raster layers, topographic ruggedness and drainage density. The topographic ruggedness is used to express the amount of elevation difference between adjacent cells of Digital Elevation Model (DEM). The topographic ruggedness is presented by means of Terrain Ruggedness Index (TRI). The densities layers are obtained by Spline Interpolation Method. These layers are used to represent the amount of geographic linear objects. The algorithm has been implemented into Geographical Information System (GIS) – ArcInfo, and applied for a GIS of Tamaulipas State, Mexico.

## 1 Introduction

Geomorphometric analysis is the measurement of geometry of the landforms in raster images and has traditionally been applied to watersheds, drainages, hillslopes and other groups of terrain objects. In particular basin morphometric parameters attracted much attention from hydrologists and geomorphologists since watersheds have been used for analysis of different physical ecosystem processes [1]. The geomorphometry represents one set of recommended variables to analyze distribution and concentration of certain spatial objects.

Nowadays, Geographical Information Systems are powerful and useful tools as means of information, visualization and research or as decision making applications [2]. However, contrasting with the traditional topographic map methods, the GIS methods are relatively easy to apply in a consistent way on large areas of landscape, because they allow summation of terrain characteristics for any region. They can be used to provide geomorphometric data and therefore insight the processes affected by terrain morphology for all types of mapping.

Since the mid-1980s, with increasing popularity of GIS technology and availability of Digital Elevation Models (DEM), the potential of using DEM in studies of surface processes has been widely recognized [3]. New methods and algorithms have been developed to automate the procedure of terrain characterization [4]. DEM has been

used to delineate drainage networks and watershed boundaries to compute slope characteristics, and to produce flow paths [5]. In addition, DEM has been incorporated in distributed hydrological models [6].

DEM is playing an increasingly important role in many technical fields of GIS development, including earth and environmental sciences, hazard reduction, civil engineering, forestry, landscape planning, and commercial display. It is difficult to exaggerate the importance of the DEM to geomorphology, because DEM may ultimately replace printed maps as the standard means of portraying landforms. The contour maps remain an important data source for DEM, although techniques for measuring elevation directly from satellite images have been introduced in recent years. Tamaulipas State area is covered by DEM at two resolutions, 50 x 50 m and 250 x 250 m [7].

In this paper, we propose a method to make spatial analysis based on geo-image processing by means of Spatial Analyzer Module (SAM). In Section 2 we present the description of SAM and describe its functionality. In the next sections, we describe how terrain ruggedness and drainage density have been obtained. Some results are shown in Section 5. Section 6 presents our conclusions.

## 2 Spatial Analyzer Module

SAM is a special module, which has been designed to make spatial analysis procedures. SAM uses vector and raster data to make the spatial analysis. This module has been implemented using Arc Macro Language (AML) to ensure portability between computer platforms executing ArcInfo 7.0 or later.

The analysis is based on using different spatial data related to the case of study. SAM contains two components: Analysis Block and List of Procedures. 1) Analysis Block is composed of a set of processes to make data analysis. 2) List of Procedures stores the sequence of steps to execute the processes [8] (see Fig. 1).

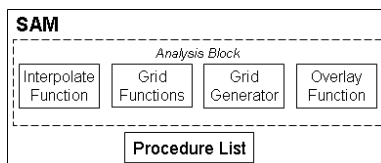


**Fig. 1.** Spatial Analyzer Module is composed of Analysis Block and Procedure List

### 2.1 Analysis Block

It contains the functions to make spatial analysis. These functions are the following:

*Interpolate Function.* The method used is a minimum curvature spline in two dimensions from a set of points. For computational purposes, the entire space of the output grid is divided into blocks or regions of equal size. They are represented in a rectangular shape. The equation 1 shows the spline function that has been used [9]:

$$S(x, y) = T(x, y) + \sum_{j=1}^N \lambda_j R(r_j), \quad (1)$$

where  $j = 1, 2, \dots, N$ ;  $N$  is the number of points;  $\lambda_j$  are the coefficients obtained from the system of equations, which computes the point coordinates;  $R(r_j)$  is the distance from the point  $(x, y)$  to the  $j^{\text{th}}$  point.

To use this function, it is necessary to provide the set of points and tolerances, which depend on the specific case of study.

*Grid Functions.* They contain the set of functions for cell analysis that include operations of the map algebra, and describe how the operations are specified, the data to operate on, and the order in which operations should be processed. In this case the function is SQRT. SQRT calculates the square root of the input grid [10].

*Grid Generator.* It is used to process some analyzed data, especially in density map generation. The vector grids are regular of  $m \times m$  magnitude, in which  $m$  is the cell size. The cell magnitude in the grid is determined by the phenomenon under study characteristics (scale and covered area). Two alternatives can be used to generate the grids. First, specifying the initial and terminal grid coordinates  $((x_0, y_0), (x_1, y_1))$  respectively and establishing the number of required divisions for the grid. The second alternative is to specify the initial coordinate  $(x_0, y_0)$ , cell size, number of columns and rows in the grid [11] (Fig. 2).

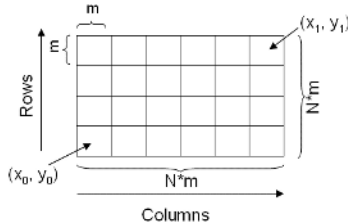


Fig. 2. Specifications of the grid

*Overlay Functions.* This module has been designed to make *topological overlays*, which can be used to identify areas of risk. A set of operations has been defined, and applied to the spatial analysis. This is made to establish the conditions and to combine different information layers using logical operators. These functions combine spatial and attribute data. The implemented operations for topological overlay in this application are: intersection, union and identity, which are represented by the symbols  $\cap$ ,  $\cup$  and  $I$  respectively [10].

## 2.2 List of Procedures

It stores the set of procedures for each one of the analysis processes. It has a description of the required data type and the restrictions. However, the users can change the selection criteria. This provides a list of functions as an alternative for the analysis, in

which the parameters can be modified. SAM has a wide range of applications, not only to make geomorphometric analysis. It is also possible to perform the detection of *landslide* and *flooding* areas [11].

### 3 Generation of Topographic Ruggedness Layer

The Terrain Ruggedness Index (TRI) is a measurement developed by Riley to represent the amount of elevation difference between adjacent cells of a digital elevation grid [12]. The process essentially computes the difference in elevation values from a center cell and the eight cells surrounding it immediately. Then it squares each of the eight elevation difference values to make them all positive and averages the squares. The terrain ruggedness index is then derived by taking the square root of this average, and corresponds to average elevation change between any point on a grid and its surrounding area. The authors of the TRI propose the classification for the values obtained for the index (Table 1):

**Table 1.** Terrain Ruggedness Index Classification

TRI	Interval (m)	Represent
1	0-80	Level terrain surface
2	81-116	Nearly level surface
3	117-161	Slightly rugged surface
4	162-239	Intermediately rugged surface
5	240-497	Moderately rugged
6	498-958	Highly rugged
7	959-4367	Extremely rugged surface

The pseudo-code [12] to generate TRI layer is:

```

program TRI
{dem - Input Grid
tmp1 - Grid to store the Standard elevation
      difference
tmp2 - Grid to calculate the Topographic
      Ruggedness Index
tmp3 - Grid to verifycate tri range
outgrid - Output grid
/* Standard elevation difference */
/*Execute cell by cell*/
tmp1(X,Y) :=((SQRT(dem(x,y)-dem(x-1,y-1))+ 
(SQRT(dem(x,y)-dem(x,y-1))+ (SQRT(dem(x,y)-
dem(x+1,y-1))+ (SQRT(dem(x,y)-dem(x+1,y))+ 
(SQRT(dem(x,y)-dem(x+1,y+1))+ SQRT(dem(x,y)-
dem(x,y))+ (SQRT(dem(x,y)-dem(x-1,y+1))+ 
(SQRT(dem(x,y)-dem(x-1,y)))
/* Evaluate cell-by-cell

```

```

tmp2(X,Y) := SQRT(tmp1(x,y))
/* Evaluate cell-by-cell
   tmp3(X,Y) := If (tmp2(x,y)>=5000)
   then tmp3(x,y) := 5000
   Else tmp3(x,y) :=tmp2(x,y)
/* Evaluate cell-by-cell
outgrid(X,Y) :=( if (tmp3(x,y)>=0 && tmp3(x,y)<=80)
                  then outgrid(x,y) :=1
                  if (tmp3(x,y)>=81 && tmp3(x,y)<=116)
                  then outgrid(x,y) :=2
                  if (tmp3(x,y)>=117 && tmp3(x,y)<=161)
                  then outgrid(x,y) :=3
                  if (tmp3(x,y)>=162 && tmp3(x,y)<=239)
                  then outgrid(x,y) :=4
                  if (tmp3(x,y)>= 240 && tmp3(x,y)<=497)
                  then outgrid(x,y) :=5
                  if (tmp3(x,y)>=498 && tmp3(x,y)<=958)
                  then cell (x,y) :=6
                  if (tmp3(x,y)>=959 && tmp3(x,y)<=5000)
                  then outgrid(x,y) :=7) }

```

## 4 Generation of Drainage Density

Drainage density is defined as the total length of channels divided by area and measured the degree to which a landscape is dissected by channels [13]. To generate the drainage density layer, it is necessary to build a regular grid of 1 km<sup>2</sup> per cell [14]. Using this layer, we can construct the centroid layer. Later, the drainage layer is intersected with the grid layer. For each cell of the grid the lengths by area unit are added into centroid layer. The centroid layer is interpolated and the drainage density layer is obtained. Fig. 3 shows the process to generate the drainage density layer.

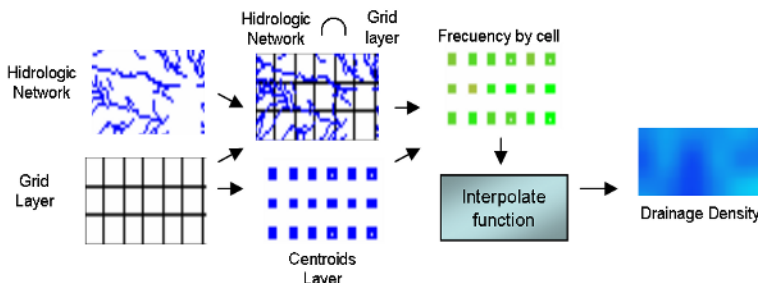


**Fig. 3.** Process to generate the drainage density layer

## 5 Results

Using SAM, we construct drainage density and terrain ruggedness layers. The method has been applied to the Tamaulipas State, Mexico. Some results are presented in this section.

Fig. 4a shows the original DEM. The minimum value is 0 m, maximum value is 3496, mean value of this layer is 227.40 m and the Standard Deviation is 498.469. Fig. 4b shows the Terrain Ruggedness layer constructed by SAM, and the TRI classification of this area. The terrain index layer has the following values; mean is 2.386 m and the Standard Deviation is 2.457. This means that Tamaulipas State has slightly rugged areas in its territory. The extremely rugged areas are principally concentrated at the southwestern part of Tamaulipas State. DEM and TRI Layers are composed by 8000 rows and 2478 columns.

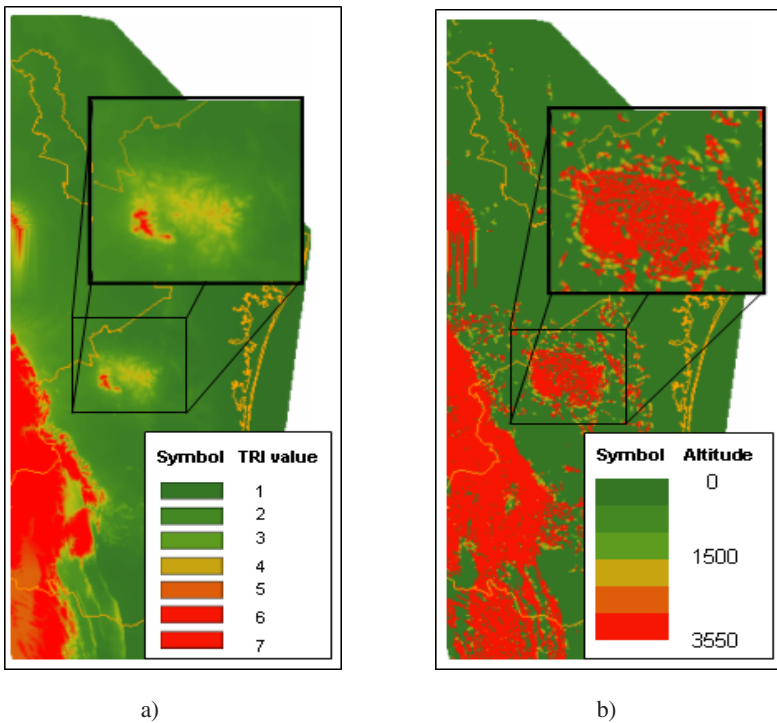
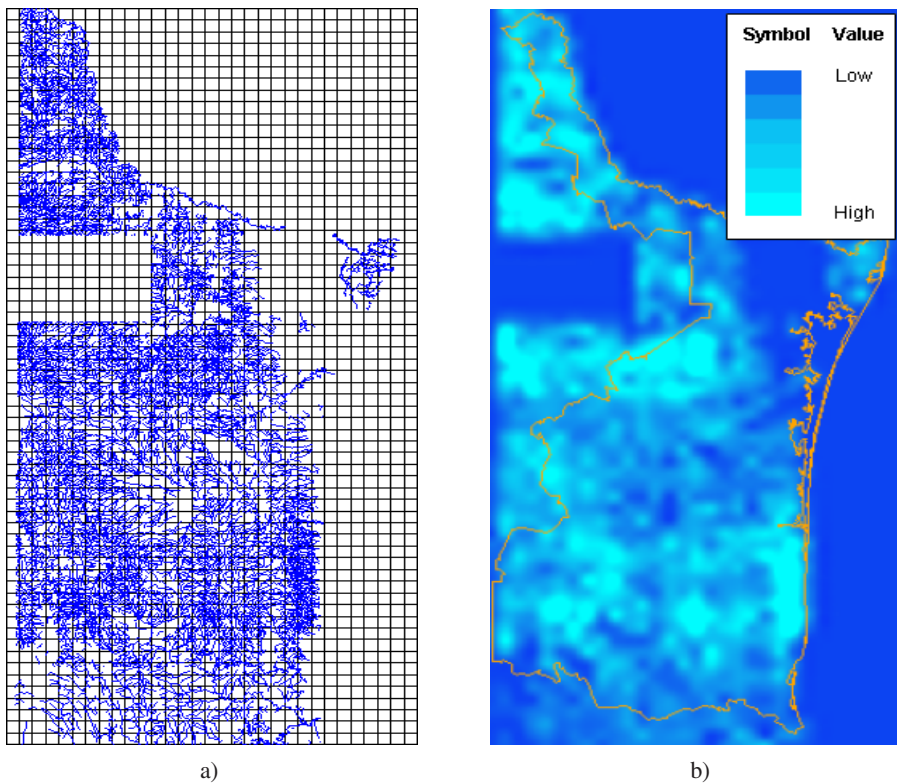


Fig. 4. a) Digital Elevation Model, b) Terrain Ruggedness layer.

Fig. 5a shows the hydrological layer, this layer contains all streams of Tamaulipas State (1:200,000). The drainage density layer is showed in Fig. 5b. The mean value of this layer is 24857, which is nearly to the lower value. The concentrations are represented in blue scale, the dark blue represents higher concentrations and light blue represents the lower concentrations. We can see the highest concentrations of drainage are situated in the south coast, near Tampico City. While the lowest density are presented in the northwestern part of Tamaulipas State.



**Fig. 5.** a) Hydrological Layer, b) Drainage Density

## 6 Conclusion

In this work, a GIS-application (SAM) has been developed to analyze geomorphometric characteristics of geo-images. SAM detects drainage density and terrain ruggedness using raster image data. In this method, spatial and attribute data are used to generate raster data. Using SAM, it is possible to define the *semantic* importance of the characteristics of the spatial data. Users can modify the criteria to have different scenarios to improve the decision making process.

The geomorphometric analysis is traditionally performed using the methods based on topographic map-processing in manual way. Our approach significantly decreases the amount of time and effort required to quantify selected terrain characteristics. Other methods are designed to evaluate additional characteristics, which are different to the properties proposed in our approach. However, these methods can be integrated into SAM.

The generation of drainage density and terrain ruggedness layers facilitates the extraction of spatial characteristics that can be used in other cartographic processes, for instance in the generalization.

**Acknowledgments.** The authors of this paper wish to thank the Centre for Computing Research (CIC-IPN), General Coordination of Postgraduate Study and Research (CGEPI), National Polytechnic Institute (IPN) and the Mexican National Council for Science and Technology (CONACYT) for their support.

## References

1. Bonk, R: Scale-dependent Geomorphometric Analysis for Glacier Mapping at Nanga Parbat: GRASS GIS Approach, Proceedings of the Open source GIS – GRASS User's conference 2002, Italy (2002)
2. Goodchild, M.: Perspective: Browsing metadata, where do we go from here?: Vol. 10 Geo Info Systems (2000) 30–31
3. Wharton, G.: Progress in the use of drainage network indices for rainfall-runoff modelling and runoff prediction. *Progress in Physical Geography*, Vol. 18 (1994) 539–557
4. Desmet, P.J.J., and Govers, G.: Comparison of routing algorithms for digital elevation models and their implications for predicting ephemeral gullies. *International Journal of Geographical Information Systems*, Vol. 10 (1996) 311–331
5. Wiche, G. J., Jenson, S. K., Baglio, J. V., and Dominguez, J. O.: Application of digital elevation models to delineate drainage areas and compute hydrologic characteristics for sites in the James River Basin, North Dakota, U.S. Geological Survey Water-Supply Paper, Vol. 23 (1992)
6. Garrote, L., and Bras, R. L.: A distributed model for real-time flood forecasting using digital elevation models. *Journal of Hydrology*, Vol. 167 (1995) 279–306.
7. Instituto Nacional de Geografía Estadística e Informática (INEGI): Modelos Digitales de Elevación – Generalidades y Especificaciones, INEGI (1999)
8. Torres, M., Moreno, M., Menchaca, R. and Levachkine, S.: Making Spatial Analysis with a Distributed Geographical Information System, Series on APPLIED INFORMATICS – AI 2003, International Conference on Databases and Applications (DBA'2003), International Association of Science and Technology for Development (2003) 1245–1250
9. Mitas, L. and Mitasova, H.: General Variational Approach to the Interpolation Problem, *Journal of Computers and Mathematics with Applications*, Vol. 16 (1988) 983–992
10. Molenaar,, M.: An Introduction to the theory of spatial object modelling for GIS. Taylor & Francis, U.K. (1998)
11. Torres, M., Moreno, M. and Levachkine, S.: SIGETAM: Herramienta GIS de Escritorio enfocada a la Detección de Zonas de Riesgo de Deslave e Inundación, 1st International Congress of Informatics and Computing, Guadalajara, México (2002) 156–168
12. Riley, S. J., DeGloria, S. D., and Elliot, R.: A terrain ruggedness index that quantifies topographic heterogeneity. *Intermountain Journal of Sciences*, Vol. 5 (1999) 23–27
13. Horton, R. E.: Drainage basin characteristics, *Transactions American Geophysical Union*, Vol. 13 (1932) 350–361.
14. Tarboton, D. and Ames, D: Advances in the mapping of flow networks from digital elevation data, World Water and Environmental Resources Congress, Florida, (2001)

# Morphological Applications for Maps Construction in Path Planning Tasks

J. Azorín<sup>1</sup>, G. De Miguel<sup>1</sup>, F.A. Pujol<sup>1</sup>, J.M. García<sup>1</sup>, M. Pujol<sup>2</sup>, and R. Rizo<sup>2</sup>

<sup>1</sup> Depto. Tecnología Informática y Computación,  
Universidad de Alicante Ap. Correos 99, 03080 Alicante, España  
[{jazorin, demiguel, fpujol, juanma}@dtic.ua.es](mailto:{jazorin, demiguel, fpujol, juanma}@dtic.ua.es),

<sup>2</sup> Depto. Ciencia de la Computación e Inteligencia Artificial  
Universidad de Alicante Ap. Correos 99, 03080 Alicante, España  
[{mar, rizo}@dccia.ua.es](mailto:{mar, rizo}@dccia.ua.es)

**Abstract.** The process of taking decisions in an autonomous system has a strong dependence on the information received from the environment in which it works. The path planning process for a mobile robot is a subset of the problems that have to be solved in an automatic system of decisions, where the appropriateness of the method is roughly constrained not only by the achievement of a well-suited information from the environment, but also by how this information is acquired. The main objective of this work is to describe a robust model for robotic path planning in unknown environments. The proposed general model is based on obtaining secure paths where the robot will be able to move so as to complete its task. Thus, from an unknown location, the required information is collected by employing a mobile robot that moves freely through a real world with some generic behaviors that let the robot explore the world.

## 1 Introduction

The growing incorporation of robots to our environment [1] shows the emergent proposal of systems that have an intelligent behavior and, as a result, makes it possible to have a great amount of technical solutions that improve the execution of specialized tasks.

From an Artificial Intelligence point of view, the robotic systems have also an enormous interest when the research is focused on the associated processes that intelligence involves, where *intelligence* refers to an essential feature in some complex systems, such as those ones who involve learning and autonomous control [2]. This way, an autonomous robot can be considered as an embedded system and, in general, as an entity with some reactive and deliberative abilities with adaptive behavior; consequently, it is related to dynamic environments.

The multidisciplinary research in Robotics includes many different approaches in the methods for designing a robot. First, we have the classical point of view that utilizes a three-level architecture: Functional Level, Executive Level and Planning Level, as it can be seen in [3]. On the other hand, a more flexible

characterization is based on some analogies with biological evolution [4]. As a consequence, the first approach implies that these architectures must be simplified quite often since many requests have to be completed at the same time. On the contrary, the second contribution provides a specification based on behaviors that are modelled by means of complex control algorithms that cover a greater range of requests.

Nevertheless, most of the projects proposed for robotic prototypes include architectures based on general criteria of designing in order to solve real-world problems, and also incorporate special features for its adaptation to special environments [5],[6].

In this work, we propose a general model for the recognition of the world in which a robot interacts, in order to follow a collision-free path within the environment. First, we need to define the fundamental concepts for the characterization of the environment and the acquisition of information, as it is described in Section 2. After that, a robust model to generate a map, considering some topological landmarks, is introduced in Section 3. Then, Section 4 explains how the received information is processed and, subsequently, in Section 5 the experimentation is widely illustrated to verify the accomplishment of our research objectives. Finally, we conclude with some important remarks in Section 6.

## 2 Design of a Robust Model

Let us consider a general approach to the situation shown in the previous section. First of all, the problem can be described as the obtaining of safe paths where a mobile robot would be able to wander with no collision, in order to fulfill some objectives. In relation to this, from an unknown world, the robot will obtain information that, once processed, will lead to obstacle-free paths.

To do this, we need to establish theoretically the representation of the factors that would interact with the robot. Since our purpose is obtaining an interpretation function that approximates the environment as good as possible, the suitability of the solution will be mainly determined by the quality of that representation. That is, we want to define a function that synthesizes an image from the perception of the environment; as it is described in the following sections, the synthesis uses Mathematical Morphology methods.

Thus, the algorithm that builds maps of the environment can be divided into a series of independent steps, where each step of lower level provides the necessary information for the upper level processes. This way, it can be considered at the same time as an abstraction of the immediately lower levels.

As a result, this model gives a multi-level architecture that can be divided into the following layers:

- Acquisition of information
  - Positional information
  - Topological information
  - Constraints of the environment

- Information processing
- Generation of knowledge

Next, a more detailed description of these levels will be found.

### 3 Acquisition of Information

As one would expect, the data acquisition depends both on the environment and on a set of features that define the operation of the mobile robot. There are two kind of features:

- The internal sensing capabilities, which are related to obtain the robot location in a real world.
- The external sensing capabilities to acquire information by interacting with the environment (laser, sonar, cameras, . . . ).

In the following sections these features are explained.

#### 3.1 Positional and Topological Information

Considering the internal capabilities, the positional information will be determined mainly by the actual position of the robot in a workspace. Of course, the robot's self-knowledge about what is its location also has a great effect on the final result.

On the other hand, the external capabilities can be calculated by acquiring topological information; these data are extracted from the environment where the robot is interacting to. Thus, the topological landmarks are related to the different zones in which an environment can be divided. Therefore, each of these zones must be located in the world maps and, as a result, the landmarks will establish a possible positioning state of the robot. Let  $e_i$  be all the possible states.

To do this, in our design we will consider that the robot includes a sonar sensor ring, as reading these sensors will give the system enough knowledge to distinguish the topological zones in which a map is divided. Then, the likeness function should be defined; starting from a group of sonar readings, this function provides the probability that the sonar measurements have been created from each one of the states  $e_i$ . The likeness function is determined by:

$$v(r|e_i) = \exp(-dist(r, e_i)/a) . \quad (1)$$

where  $a$  is a correction factor, such that  $a \geq 1$ , and  $dist$  is the euclidean distance between the current sensor reading  $r = (r_1, r_2, \dots, r_n)$  and the representation of each state  $e_i$  in the database:

$$dist(r, e_i) = \sqrt{\sum_{j=1}^n (r_j - e_{i_j})^2} . \quad (2)$$

It is also necessary to establish a model for the robot's movement, which indicates the probability of either changing from a state to another one or keeping on the same state:

$$m(e_i|e_j) . \quad (3)$$

This model has been implemented by using an FSM (Finite State Machine), so that the probability of a transition between states must be estimated according to the environment.

Finally, the acquisition function should be tested. This point can be completed as the robot follows a path, while it avoids obstacles with a constant velocity. Then, we define a probability function  $c_t(e_j|r)$  in order to keep the robot on the same state or to change it, if necessary, when the movement is produced:

$$c_t(e_j|r) = \alpha v(r|e_j) \sum_{i=1}^n m(e_j|e_i) c_{t-1}(e_i|r) . \quad (4)$$

where  $\alpha$  is a real constant.

### 3.2 Topological Landmarks

From the former discussion, it is clear that each landmark will identify a locating state  $(e_1, e_2, \dots, e_n)$ . Let us consider the environment defined in Fig. 1. In this case, the possible landmarks are:

- Corridor: e1
- Corner: e2
- T: e3
- Crossing: e4

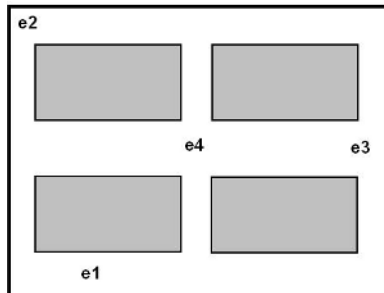


**Fig. 1.** Proposal of environment

Therefore, in this workplace we can find the four landmarks depicted in Fig. 2.

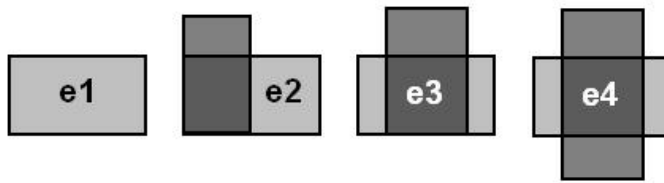


**Fig. 2.** The four topological landmarks

The experimentation is arranged by means of a robot that includes 24 sonar sensors. Then, each reading from the sensors is computed and, afterwards, the robot training is carried out for each landmark that has been previously identified in the map. To perform this, the robot is placed at each landmark and all the possible readings are obtained. From that information, an image of the environment can be created and, as a result, a map is generated; this is explained in the next section.

#### 4 Information Processing and Generation of Knowledge

The next level in the architecture performs a data processing after that the information is received at the lower level. As we have pointed out before, the collected data come from a group of sonar sensors which provide a set of points (i.e., a reading) that makes a representation of the environment.

In order to achieve a reliable image starting from this set of readings, we propose to use a morphological dilation of the obtained points to extract an estimated map (see Fig. 3). Then, the dilation is carried out considering both the robot architecture as well as its physical dimensions. The objective is to find a set of points that provides free paths for a no-collision navigation and, as a result, a synthesized image that contains a map of the environment.

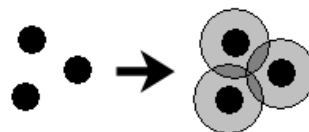


**Fig. 3.** Dilation of a sensor reading

It would be very important to take into account the obtained positional and topological information so that the dilation could create separate regions for the different landmarks and, consequently, could provide a better data representation for the path planning process (Fig. 4).

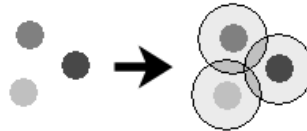


**Fig. 4.** Dilation of points considering topological information

Finally, the highest level includes the generation of an image from the set of regions that are labelled according to the landmarks that exist throughout the environment. This process can also be completed by means of the dilation of the sensor reading points. In the following section we describe some examples of the application of these operations.

## 5 Experiments

Let us consider now the results of some experiments completed for our model. Thus, the tests have been simulated and, afterwards, the robot is supposed to work in the environment built in Fig. 1. As shown before, this world consists of a set of points labelled as corridor, corner, T and crossing points (see Fig. 5 (a)).

Let us assume that the robot moves along a path established by a generic pattern of movement. Then, the positional and topological information is extracted while acquiring points in a planned trajectory, as shown in Fig. 5 (b).

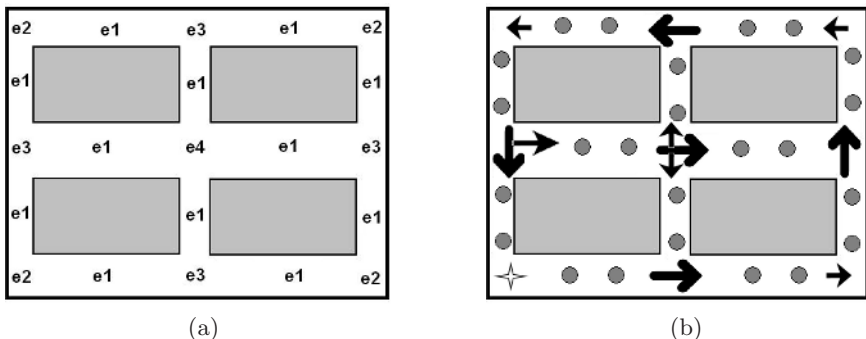


**Fig. 5.** (a) Landmark labelling for an environment. (b) Sample path for the considered environment

This way, when the mobile platform goes along a path, the acquisition of information level provides a series of points where the robot is able to move (see Fig. 6).

As the robot receives the data, the information processing system synthesizes the map of the environment in real time, considering every set of points received.

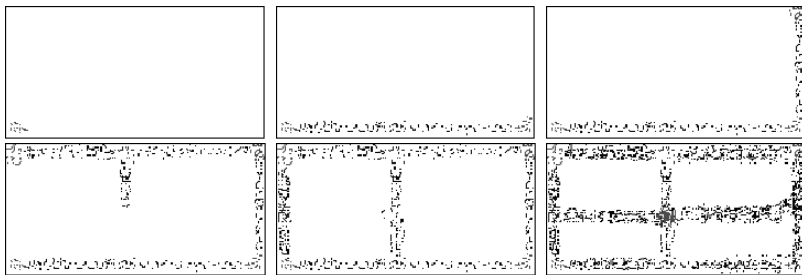


**Fig. 6.** Results of the acquisition level

Consequently, once the system has labelled the points according to one of the possible landmarks, the morphological dilation provides the regions where an object collision has a low probability (Fig. 7).

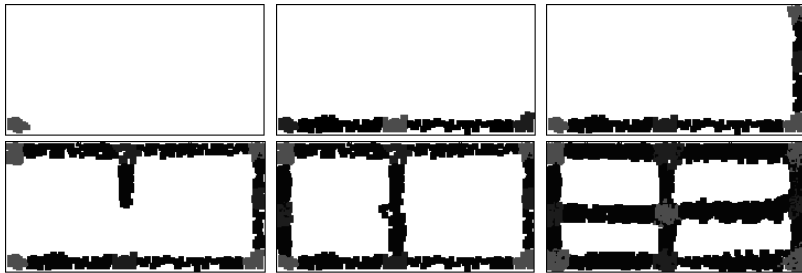


**Fig. 7.** Results of the information processing level

The last images show that the synthesis is completed with an iterative method, where all the information that the sensors provide in real time allows that the map of the environment has a good quality without consuming many resources. As we can see, the main goals of our research task have been accomplished.

## 6 Conclusions

In general terms, the path planning process for a mobile robot is strongly influenced by the precision of the acquisition process. Thus, it can be modified both by the quality of the information obtained from the environment, and the attributes of the system and the environment in which it works.

In this paper, we have developed a proposal of a model for the generation of a map in unknown environments; then we have designed an information acquisition process that allows a representation of the environment for the path planning

process. The experimentation shows that the prototype is quite robust and could be applied in some indoor environments.

As a future work, it would be so desirable the application of the model in a real environment, as well as consider new simulation experiments with different environments. This will lead to a more accurate designing method so that the robot internal hardware could be efficiently implemented. As a result, it can support all the possible requests that the model would have in a real situation and, finally, the function of acquisition can be generalized for other sensing models. Therefore, we can achieve more robustness in the positional and topological acquisition of information and, consequently, in the higher levels of the architecture.

**Acknowledgements.** This work has been supported by the Spanish *Oficina de Ciencia y Tecnología* (OCYT) of the *Generalitat Valenciana*, project number CTIDIA/2002/183 and by the Spanish *Comisión Interministerial de Ciencia y Tecnología* (CICYT), project number TIC2001-0245-C02-02.

## References

1. Parker, L. E.: Lifelong adaptation in heterogeneous multi-robot teams: response to continual variation in individual robot performance. *Autonomous Robots*, **8** (2000) 239–267
2. Brooks, R.A.: Intelligence without reason. In Proc. of the 12th International Joint Conference on Artificial Intelligence, Sydney, Australia, (1991) 569–595
3. Tzafestas, E.S.: Reactive robots in the service of production management, *Journal of Intelligent and Robotic Systems*, **21** (1998) 179–191
4. Arkin, R.C.: Behavior-based robotics. MIT Press (1998)
5. Zomaya, A.Y., Wright, M.R., Nabham, T.M.: On the path planning problem in the vicinity of obstacles. *Cybernetics & Systems*, **29** (1998) 807–868
6. Pujol, F., García Chamizo, J. M., Fuster, A., Pujol, M., Rizo, R.: Use of mathematical morphology in real-time path planning. *Kybernetes*, **31** (2002) 115–123

# Compact Mapping in Plane-Parallel Environments Using Stereo Vision

Juan Manuel Sáez, Antonio Peñalver, and Francisco Escolano

Robot Vision Group

Departamento de Ciencia de la Computación e Inteligencia Artificial

Universidad de Alicante, Spain

{jmsaez, apenalver, sco}@dccia.ua.es

<http://rvg.ua.es>

**Abstract.** In this paper we propose a method for transforming a 3D map of the environment, composed by a cloud of millions of points, into a compact representation in terms of basic geometric primitives, 3D planes in this case. These planes, with their texture, yield a very useful representation in robot navigation tasks like localization and motion control. Our method estimates the main planes in the environment (walls, floor and ceiling) using point classification, based on the orientation of their normal and its relative position. Once we have inferred the 3D planes we map their textures using the appearance information of the observations, obtaining a realistic model of the scene.

## 1 Introduction

Perception is a critical element in robot navigation tasks like map building (mapping) and self-localization. The quality of the map and its post-processing are key for successfully performing these tasks. Early mapping solutions were based on 2D information extracted with sonars [1]. In these cases, the environment is modeled with an occupation grid [2]. In [3] [4] the 3D grids extracted from point clouds are inferred with stereo vision. As these clouds have typically millions of points it is impractical to manage them both in terms of data storage and efficiency. Moreover, it is desirable to obtain representations of higher level of abstractions. Thus, following the idea of “from pixels to geometric primitives” the approach introduced in [5] applies the Hough transform to find the vertical planes (walls) of the environment from stereo data. However, in this case a high-resolution partitioning of the parametric space, which feeds the voting process, is required to find that a good approximation.

Planes have also been estimated using 3D range sensors like laser scans, which produce a more dense information . In [6] it is proposed an adaptation of the EM algorithm [7] for detecting planar patches in an indoor environment. The approach proposed in [8] combines range information and appearance to recover planar representations of outdoor scenes (buildings). However, these two latter approaches require very dense sensors. Here we focus on the case of having a stereo sensor, typically producing very noisy sparse information which is highly

concentrated on high-textured areas. In this paper we obtain the main planes of the scene (walls, floor and ceiling) assuming that the robot is moving in a plane-parallel environment. In order to do so, we first group the 3D points in the map (see [9] and [10] for a complete description of our map-building process) using the direction of their normals. Then, we fit a 3D plane to each group, and finally we perform texture mapping using the information of the initial observations coming from many points of view.

## 2 Sensor and Robot Models

In this paper we use the Digidlops trinocular stereo system mounted on a Pioneer mobile robot controlled with the Saphira library. Given these elements we define an **observation** at time  $t$ , that is  $v_t$  as the set of 3D observed points  $(p_{ij}, n_{ij}, c_{ij})$  collected in matrix  $[v_{ij}]$ , where  $p_{ij}$  are the coordinates of a given point,  $n_{ij}$  a normal vector which has to be estimated, and  $c_{ij}$  is the grey level or color of the point.

Assuming that the robot moves over a plane and that the focal axis of the camera is always parallel to this plane, the **state** or **pose** of the robot at time  $t$  is given by the robot's coordinates at plane  $XZ$  and its relative angle with respect the  $Y$  axis, that is  $\varphi_t = (x_t, z_t, \alpha_t)$ . Similarly, an **action** performed by the robot at time  $t$  is defined in terms of the increment of the current pose  $a_t = (\Delta x_t, \Delta y_t, \Delta \alpha_t)$ , and a **trajectory** performed by the robot is the sequence of  $t$  observations  $V^t = \{v_1, v_2, \dots, v_t\}$  and  $t$  associated actions  $A^t = \{a_1, a_2, \dots, a_t\}$ .

Actions can be robustly estimated from observations, and by integrating the trajectory performed by the robot through robust matching and alignment we obtain a map consisting of a cloud of millions of 3D points (see [9] and [10] for more details).

## 3 Estimating Points Normals

Here we focus on estimating the surface normal  $n_{ij}$  for each point  $p_{ij}$  at a given observation  $v_t$ . In order to do that we consider the 4 or 8 neighbors of the points in the observation matrix  $[v_{ij}]$ , that is, we are exploiting the 2D layout of the points (see Figure 1). In order to improve robustness, instead of consider each neighboring point, we consider neighboring regions of size  $l$ . For each region  $R_i$  we take its centroid  $r_i$ . Then, given the considered point  $p_{ij}$  and the centroids  $\{r_1, r_2, \dots, r_n\}$  of the  $n$  neighboring regions we build the vectors  $\alpha_i = r_i - p_{ij}$ . Then, the normal  $n_{ij}$  results from multiplying adjacent vectors in counterclockwise sense and taking the average:

$$n_{ij} = ((\alpha_n \times \alpha_{n-1}) + (\alpha_{n-1} \times \alpha_{n-2}) + \dots + (\alpha_1 \times \alpha_n))/n \quad (1)$$

As the quality of the latter estimation depends on the number of valid 3D points inside a given region, we consider that the resulting normal is undefined when there is not enough information to provide a robust estimate.

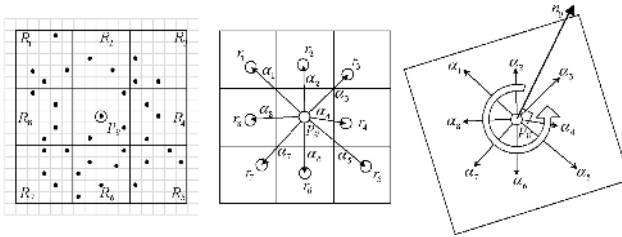


**Fig. 1.** Estimating the normal at a point using 8 regions: Neighboring regions of size  $5 \times 5$  (left), centroid for each region and associated vector (center), normal vector resulting for applying Expression 1.(right)

## 4 Vertical Planes Estimation

### 4.1 Removing Horizontal Planes

Assuming that the floor is flat and also that the height of the camera is constant, and considering the fact that the floor and ceiling planes are usually low textured and in this case their associated stereo points are typically very noisy, we remove these latter planes and we focus on the vertical ones (walls) (see Figure 2).

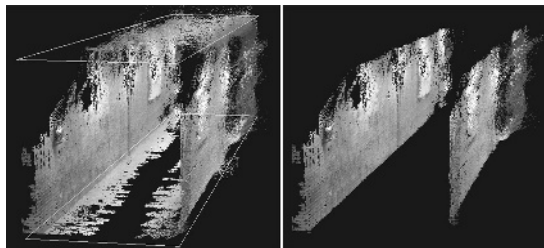


**Fig. 2.** Removing the floor and the ceiling. Complete scene with those planes (left). Resulting scene after removing the planes (right).

Once we have only vertical planes, the problem of estimating these planes can be posed in terms of finding in 2D the segments resulting from their projections on the imaginary horizontal plane. In order to do that, we will build a Gaussian Mixture Model classifier for 2D normals where each class is given by the set of points with similar normals (associated to parallel walls). Next, we build the planes associated to each class with a connected-components process.

### 4.2 Gaussian Mixture Model Classifier

Our one-dimensional mixtures-of-Gaussians classifier [11] is built on a set of  $n$  samples  $X = \{x_1, x_2, \dots, x_n\}$  that we want to fit with  $k$  Gaussian kernels

with unknown parameters  $\{(\mu_1, \sigma_1), (\mu_2, \sigma_2), \dots, (\mu_k, \sigma_k)\}$ . We must estimate the parameters that maximize the log-likelihood function:

$$\ell = \log \prod_{i=1}^n \sum_{j=1}^k \pi_j P(x_i|j) = \sum_{i=1}^n \log \sum_{j=1}^k \pi_j P(x_i|j) \quad (2)$$

where  $\pi_j$  is the prior probability of belonging to the kernel  $j$  and  $P(x_i|j)$  is the probability for  $x_i$  of a Gaussian centered on the kernel  $j$ . In order to find the prior probabilities and the parameters of the kernels we apply the standard EM (Expectation-Maximization) algorithm [7].

In the E-step (Expectation) we update the posterior  $P(j|x_i)$ , that is, the probability that a pattern  $x_i$  is generated by kernel  $j$ :

$$P(j|x_i) = \pi_j P(x_j|j) / \sum_{l=1}^k \pi_l P(x_i|l) \quad (3)$$

In the M-step (Maximization) we proceed to update the priors and the parameters of the kernels given the posteriors computed in the E-step:

$$\pi_j = \frac{\sum_{i=1}^n P(j|x_i)}{n}, \mu_j = \frac{\sum_{i=1}^n P(j|x_i)x_i}{\sum_{i=1}^n P(j|x_i)}, \sigma_j^2 = \frac{\sum_{i=1}^n P(j|x_i)(x_i - \mu_j)^2}{\sum_{i=1}^n P(j|x_i)} \quad (4)$$

Alternating E and M steps the algorithm converges to the closest local maxima with respect to the initialization point. Then, we take the MAP estimate for each normal:  $MAP(x_i) = \arg \max_j P(j|x_i)$ , where  $P(j|x_i) = \pi_j P(x_i|j)/P(x_i)$ .

### 4.3 Classifying Normals

In order to classify each normal, we take the relative angle between the reference vector  $(1,0,0)$  in the  $XZ$  plane. In Figure 3 we represent an example of classification with real data. We represent the original point cloud with the normal of each point, and the directional histogram with four peaks associated to the four types of parallel planes. Also, we show how are classified the points of the scene. We have used  $k = 4$  kernels whose averages have been randomly initialized from the interval  $[0, 360]$ .

When the number of kernels is under 4 (for instance we may have only two classes when the robot is in the middle of a corridor), the algorithm also converges because in this case the prior probabilities of the non-existent classes tend to zero. We illustrate this case in Figure 4. Finally, we also consider the pre-filtering of noisy patterns (normals, in this case) in order to avoid distortions in the final result.

### 4.4 Fitting Vertical Planes

Once we have found the  $k$  classes  $C = \{c_1, c_2, \dots, c_k\}$  associated to the types of wall appearing in the scene, each  $c_j$  contains a set of points  $\{p_i^j\}$  with similar normals. Next, we proceed to divide these sets in different vertical planes.

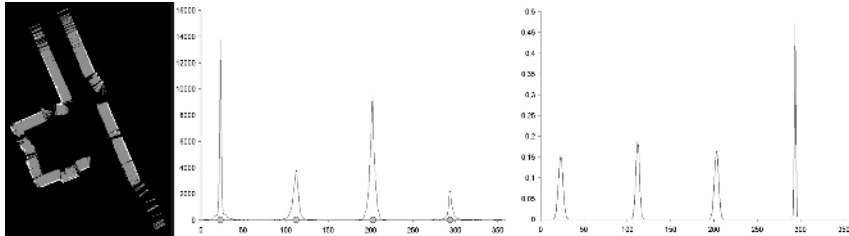


**Fig. 3.** Classification example using EM algorithm. 2D point cloud for a given scene and their normals (left). Directional histogram and final kernels (center). Final Kernels distributions (right).

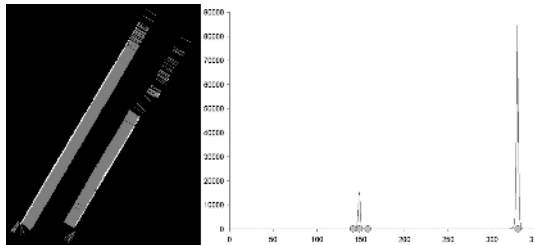


**Fig. 4.** Initial classification of the scene in Figure 2. Normals (left) and final position of the 4 kernels. The prior probabilities are 0.0, 0.42, 0.0 and 0.58 respectively.

Given two points  $p_a^j$  and  $p_b^j$  of class  $c_j$  we consider that they belong to the same plane when the distance between them in the  $XZ$  plane is below a given threshold  $\lambda$ :  $\|p_a^j - p_b^j\|_{xz} < \lambda$ . Given this binary relation we build a graph  $G_j(V, A)$  whose vertices are associated to points in the class and the edges are associated to pairs of vertices that satisfy the previous binary relation. Then we calculate the connected components of this graph which represent the vertical planes.

Once we have computed the connected components we must estimate the parameters of the vertical planes and their bounds. We consider the set of points with their normals  $\{(p_1, n_1), (p_2, n_2), \dots, (p_l, n_l)\}$  that define a given plane  $\psi$ . We take as point and normal of the plane the centroid and the average normal, respectively:  $\psi = (\bar{p}, \bar{n})$ . The plane's bounds are obtained by computing the orthogonal plane  $\psi^\perp = (\bar{p}, \bar{n}^\perp)$ , and these bounds are determined by the most distant points from this orthogonal plane (see Figure 5).

Finally, to consider a plane valid, is necessary to verify that it is sufficiently long and it contains enough points.

Once we have computed the vertical planes in 2D, we must to apply their height in 3D, using the floor and ceiling heights (see Figure 6). In the other hand, the vertical planes bounds (floor and ceiling) are calculated using the bounding-box of the vertical planes set.

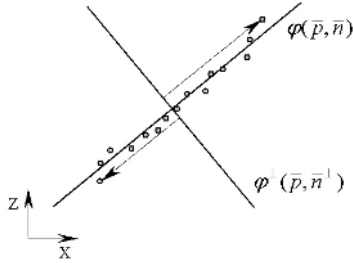


**Fig. 5.** Determining the parameters (point, normal and bounds) of each plane.

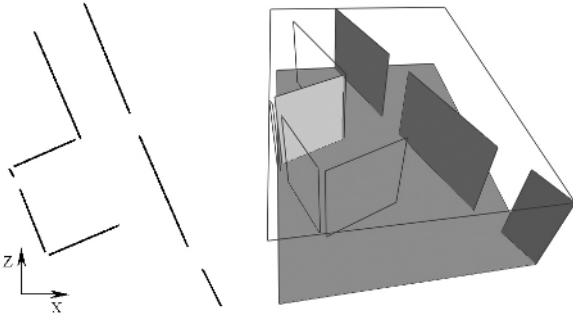


**Fig. 6.** Planes detected from the example of the figure 3. Vertical planes in 2D (left) and corresponding 3D planes with horizontal planes also. The algorithm detects 8 vertical planes.

## 5 Plane Texturization

Once we have found the horizontal and vertical planes, we must texturize them using the appearance information of the observations (reference images).

Each plane defines a rectangular region of the space which can be parametrically crossed in two directions, horizontal ( $\alpha$ ) and vertical ( $\beta$ ). Each 3D point  $p_{\alpha\beta}$  of the plane, can be observed by anyone of the  $t$  observations  $\{v_1, v_2, \dots, v_t\}$ , which we know its respective poses  $\{\varphi_1, \varphi_2, \dots, \varphi_t\}$ .

Using the fundamental matrix of the camera, we project the point on each image. Then, we consult the pixel color in each image, obtaining a set of color candidates for this point  $\{c_1, c_2, \dots, c_t\}$ . We must reject the points of this set that are not visible (because there is a vertical plane between the projection and the 3D point). The final color of the point is calculated like closest to the average of the set:  $\arg \min_{c_i} |c_i - \bar{c}|$ .

The method is able to obtain a quite realistic texture. Nevertheless, an inherent problem resides in the objects in the scene that do not adjust to any plane. We have observed a smooth effect in this objects when they are captured from different points of view (see experiments section)

## 6 Experiments and Validation

In this section, we present a complete experiment in which we have estimated the planes in a real scene. The scene is composed by 68 observations, along an indoor environment located in the facilities of our department. The original point cloud present 2.025.666 points in 3D (Figure 7 left).

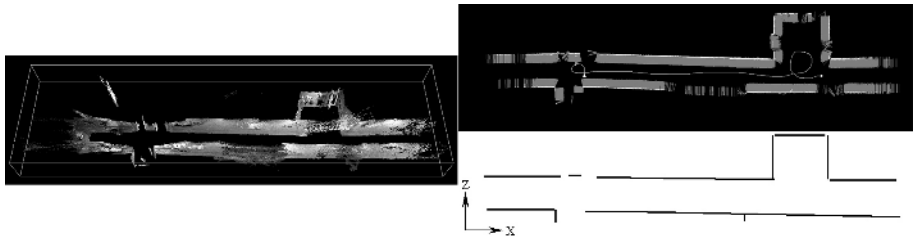


**Fig. 7.** Original point cloud of the experiment (left). Points and normals after horizontal planes removal (top right). Vertical planes detected (Bottom right).

Using the proposed algorithm, we obtain 11 vertical planes (Figure 7 Bottom right). Its corresponding textures, as well as those of ceiling and ground, have been stored in different images. The complete scene (geometric information of the planes and its corresponding textures) occupies 980 Kb of disk space. Comparatively, the original point cloud mentioned previously occupies 31.652 Kb of disk space.

In Figure 8 we show several 3D views of the textured model.

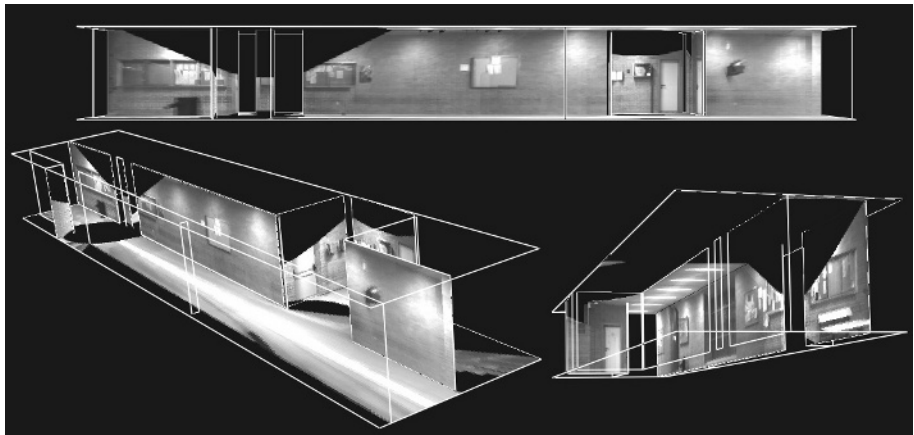


**Fig. 8.** Several 3D views of the final 3D scene.

## 7 Conclusions and Future Work

In this work, we present an algorithm to estimate the principal 3D planes of a scene composed by a set of stereo observations. We have proposed a two-step point classifier based on the normal and the relative positions of the points. Finally, we present an algorithm to estimate the texture of each plane using appearance information of the observations.

We are currently investigating in the construction of non-plane primitives from these planes. Our initial idea is, after estimating planes, we model each one with a free approximation surface. Using this technique, we can obtain more realistic scenes. On the other hand, we are interested in detecting other basic primitives like cylinders and spheres.

## References

1. S. Thrun et al. "Probabilistic Algorithms and the interactive museum tour-guide robot Minerva". International Journal of Robotics Research Vol 19 No. 11. November 2000.
2. F. Dieter, W. Burgard, S. Thrun "The dynamic window approach to collision avoidance". IEEE Robotics and Automation Magazine, 1997
3. H.P. Moravec. "Robot spatial perception by stereoscopic vision and 3D evidence grids". TR The Robotics Institute Carnegie Mellon University. Pittsburgh, Pennsylvania, 1996.
4. S. Se, D. Lowe, J. Little. "Vision-based mobile robot localization and mapping using scale-invariant features" Proc. of IEEE International Conference on Robotics and Automation. Seoul, Korea May 2001.
5. L. Iocchi, K. Konolige, M. Bajracharya. "Visually realistic mapping of planar environment with stereo". Seventh International Symposium on Experimental Robotics (ISER'2000). Hawaii 2000.
6. Y. Liu, R. Emery, D. Chakrabarti, W. Burgard, S. Thrun. "Using EM to learn 3D models of indoor environments with mobile robots". Eighteenth International Conference on Machine Learning. Williams College, June 2001.
7. A. Dempster, A. Laird, D. Rubin. "Maximum likelihood from incomplete data via the EM algorithm". Journal of the Royal Statistical Society, Series B 39, 1 38. 1977
8. I. Stamos, M. Leordeanu. "Automated Feature-Based Range Registration of Urban Scenes of Large Scale". IEEE International Conference of Computer Vision and Pattern Recognition, pp. 555–561, Vol. II, Madison, WI, 2003.
9. J.M. Sáez, F. Escolano "Monte Carlo Localization in 3D Maps Using Stereo Vision". In: Garijo, F.J., Riquelme, J.C., Toro, M.(eds.): Advances in Artificial Intelligence – Iberamia 2002. Lecture Notes in Computer Science, Vol. 2527. Springer-Verlag, Berlin Heidelberg New York (2002) 913–922.
10. J.M. Sáez, A. Peñalver, F. Escolano "Estimación de las acciones de un robot utilizando visión estéreo". IV Workshop de Agentes Físicos (WAF 2003). Alicante, April 2003.
11. R.A. Redner, H.F. Walker. "Mixture Densities, Maximum Likelihood, and the EM Algorithm". SIAM Review, 26(2):195–239, 1984.

# An Oscillatory Neural Network for Image Segmentation

Dênis Fernandes<sup>1</sup> and Philippe Olivier Alexandre Navaux<sup>2</sup>

<sup>1</sup>PUCRS – Faculdade de Engenharia – Pontifícia Universidade Católica do Rio Grande do Sul,  
Av. Ipiranga, 6681, 90619-900 Porto Alegre, RS, Brazil  
[denis@ee.pucrs.br](mailto:denis@ee.pucrs.br)

<sup>2</sup>UFRGS – Instituto de Informática – Universidade Federal do Rio Grande do Sul, Av. Bento  
Gonçalves, 9500, 91501-970 Porto Alegre, RS, Brazil  
[navaux@inf.ufrgs.br](mailto:navaux@inf.ufrgs.br)

**Abstract.** Oscillatory neural networks are a recent approach for applications in image segmentation. Two positive aspects of such networks are its massively parallel topology and the capacity to separate the segments in time. On the other hand, limitations that restrict the practical application are found in the proposed oscillatory networks, such as the use of differential equations, implying high complexity for implementation in digital hardware, and limited capacity of segmentation. In the present paper, an oscillatory neural network suitable for image segmentation in digital vision chips is presented. This network offers several advantages, including unlimited capacity of segmentation. Preliminary results confirm the successful operation of the proposal in image segmentation and its good potential for real time video segmentation.

## 1 Introduction

The increasing demand for artificial vision systems, which implement complex algorithms with high speed, justifies the development of vision chips [10] or silicon retinas [3]. In these chips, the photo detectors corresponding to the pixels of the image are jointly integrated with a massively parallel network of processing elements (PEs) for execution of specific operations over the input image. Analog implementation of vision chips requires simpler circuits than the digital one, presenting, on the other hand, lower flexibility to reprogram the executed function [10]. So, when flexibility is required, the digital implementation is more attractive.

Recently, alternative topologies of artificial neural networks, the oscillatory neural networks, which are inspired on the mechanism of segmentation executed by the human brain, have been applied in image segmentation with satisfactory results [4][6][11][14]. The study of these networks is a fertile field of work, as well as the development of dedicated architectures for efficient implementation [2][6].

The LEGION network (Locally Excitatory Globally Inhibitory Oscillator Network) [15] is the most consistent proposal of oscillatory neural network for image segmentation found in the bibliography. Its applications include segmentation of remote sensing images [12], medical images [8][13], and electronic microscope images [7]. An interesting aspect of this network is the capability to separate the segments of the image in time, facilitating later identification and quantification. Its massively parallel nature is adequate to the implementation of vision chips for image segmentation. The negative aspects include high computational complexity for implementation in digital

hardware as a consequence of the use of differential equations, limited segmentation capacity, and also the high amount of parameters and their little intuitive setting.

This paper introduces a new model of oscillatory neural network inspired on LEGION network, suitable to applications of image segmentation and implementation in vision chips with digital technology. The network presents massively parallel topology and it is able to separate the segments in time. The low complexity and the non-limitation regarding the number of segments to be discriminated are advantages of the network. The use of few parameters with intuitive setting is also a positive aspect, as well as the reduced number of iterations and the easy predictability of the time to reach the results. The digital structure also presents flexibility for easy implementation of more sophisticated segmentation procedures, using different attributes of the image. Results found in practical implementations are presented, proving that the operation of the proposed network was performed according to the expectations, and showing its potential efficiency to real time video segmentation.

## 2 The Proposed Oscillatory Neural Network

In the late 80's, oscillations of approximately 40 Hz were discovered in the visual cortex of the human brain. Such oscillations have strong correlation with the visual stimulus and synchronism of phase occurs between physically near neurons that receive similar stimulus, which can characterize a homogeneous region of the perceived image. Physically near neurons that receive different stimulus or physically distant neurons do not present such synchronism of phase [4][16].

A new oscillatory neural network was conceived [9] using the property of local synchronism between neurons and adding a mechanism of global inhibition implemented with local connections to get anti-synchronism among different groups of neurons. The proposed network is suitable to application in image segmentation and implementation in digital hardware with massively parallel topology.

### 2.1 Structures of Connections

The proposed network is implemented in a two-dimensional topology with the same size of the image to be segmented. Two structures of connections among neurons, called excitatory connections and inhibitory connections, are used.

Figure 1(a) presents an example of the excitatory connection structure. A neuron has its excitatory output  $v_e$  simultaneously connected to the 8 nearest neurons. So, the excitatory output of a neuron will be activated when at least one of its nearest neighbors, with similar input, is active.

Figure 1(b) presents an example of the inhibitory connections structure adopted. Each neuron has its inhibitory output  $v_{io}$  connected to only one neighboring neuron. This structure establishes a priority order and neurons with higher priority inhibit the remainders. The excitatory connections will cause the only neuron qualified by the inhibitory connections to excite the other neurons belonging to same segment. The inhibitory output of the neuron with the lowest priority will be active only when at least one neuron is active. In a practical implementation, this signal can be used to detect images without any segment present at the output of the network.

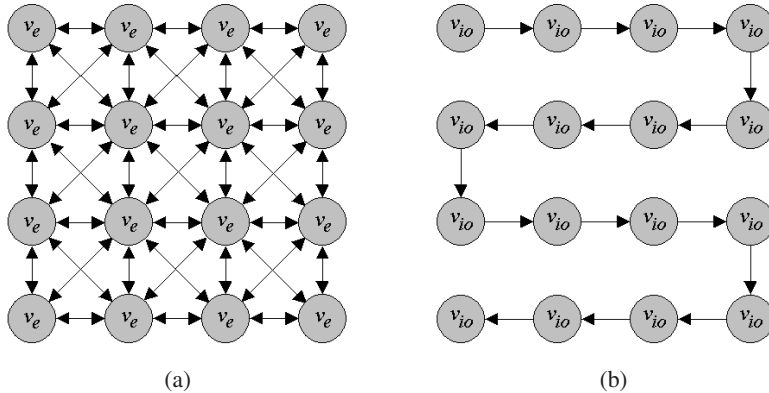


**Fig. 1.** Examples of structures of excitatory connections (a) and inhibitory connections (b)

## 2.2 The Network Neuron

The basic idea for the conception of the proposed neuron consists of associating a binary counter to each of them in a way that neighboring neurons with similar inputs are synchronized in the same state, different from the states of the other groups (Figure 2). The neurons stay inactive, until its counters reach a predefined state.

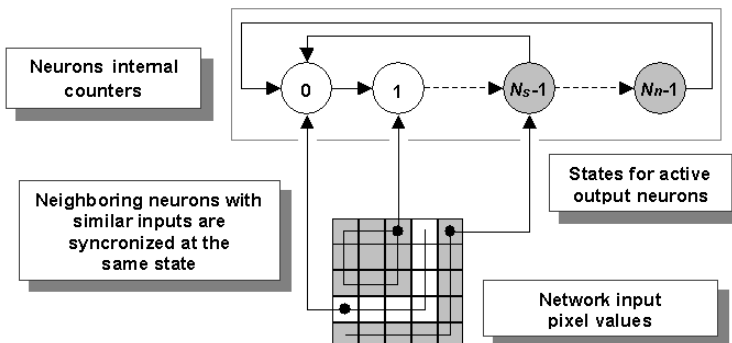


**Fig. 2.** Basic idea behind the conception of the proposed neuron

Figure 3 presents the internal logic structure of the proposed neuron. The definitions of the constants and variables are listed below:

- $N_n$ : total number of neurons in the network;
- $N_s$ : maximum number of segments allowed to be separated by the network;
- $L_w$ : threshold for weight determination;
- $v_c(i,j,t)$ : state of the internal binary counter belonging to the neuron placed at line  $i$  and column  $j$  in time (iteration)  $t$ ;
- $v_o(i,j,t)$ : output signal of the neuron internal comparator;
- $v_e(i,j,t)$ : excitatory output of the neuron;

- $v_{io}(i,j,t)$ : inhibitory output of the neuron;
- $v_{ii}(i,j,t)$ : inhibitory input of the neuron;
- $v_l(i,j,t)$ : leader indication signal;
- $I_a(i,j,t)$ : input signal of the neuron representing a set of features of the related pixel;
- $w(i,j,k,l,t)$ : weight related to the comparison between the input of the neuron placed at line  $i$  and column  $j$  and the input of the neuron placed at line  $k$  and column  $l$ .

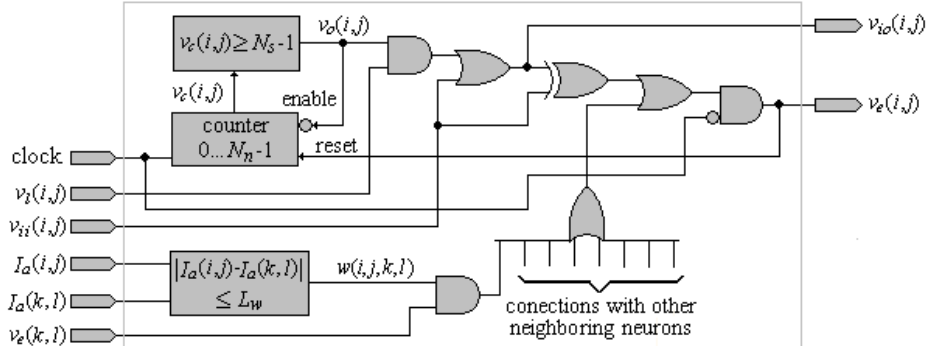


**Fig. 3.** Neuron internal structure of the proposed network

A binary counter with  $N_n$  states defines the neuron state as a function of the time. The counter receives a synchronous reset if the neuron is active ( $v_e(i,j,t)=1$ ), otherwise its state is increased until  $N_s-1$ , remaining there until it is reset. The use of  $N_n$  states makes the discrimination of a maximum of  $N_n$  segments possible, even though, in this case, there is no similarity between any inputs of neighboring neurons. The proposed neuron structure qualifies the network to separate the  $N_s$  first segments according to the sequence established by the structure of inhibitory connections.

The leader signal can be generated internally or externally and only neurons with  $v_l(i,j,t)=1$  will be initially qualified to pass to the active phase (leaders). Neurons with  $v_l(i,j,t)=0$  can be activated through an active neighbor with similar input. In the external generation, some criteria such as the position in the image (for example) can be established. It could be established that neurons in the central region of the image would be the only ones qualified to pass to the active phase, causing the appearance of only that segment at the output of the network. In the internal generation of the signal, one can use, for example, the criteria that a leader must have all the excitatory weights active, which correspond to a pixel in the center of a homogeneous region.

The weights of the network are determined through the comparison of each neuron input attribute intensities with the respective inputs of its neighboring neurons (1). In the cases where the differences between such inputs are, in module, below a threshold  $L_w$ , the respective weights will be unitary. Different attributes of the image can be used to carry through the segmentation. On the other hand,  $I_a(i,j,t)$  can represent vectors of attributes related to the pixels. In this case, the weights can be determined using a measure of vectorial distance, implying more complex structures. In color images, the Euclidean distance could be used to determine the weights, which would result in segmentation by color similarity.

$$w(i, j, k, l, t) = \begin{cases} 0 & \text{if } |I_a(i, j, t) - I_a(k, l, t)| > L_w \\ 1 & \text{if } |I_a(i, j, t) - I_a(k, l, t)| \leq L_w \end{cases} . \quad (1)$$

### 3 Implementation and Results

To verify the functioning of the proposed network, two types of implementation were carried out. The first one is related to the simulation of the behavior of the network through an algorithm implemented in a PC computer. The second one is the use of the Max-plusII program from Altera [1] for simulation of the network and verification of the viability of its implementation in digital devices [9].

#### 3.1 Segmentation of an Artificial Image

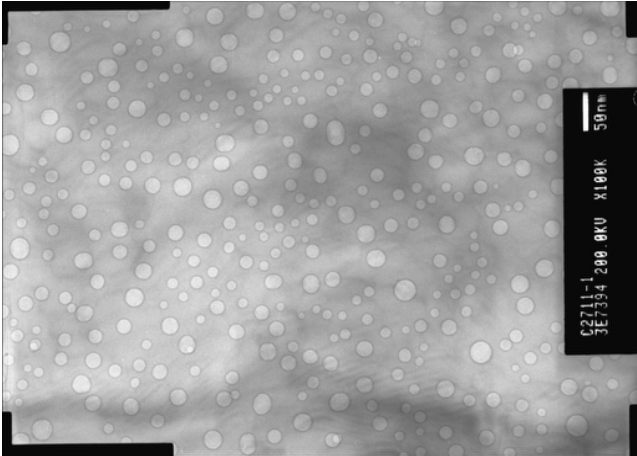
Figure 4 presents an example carried out through the algorithm that simulates the proposed network. The input image, with 100x310 pixels, is placed at the top left position. The additional 7 images are the non-null segments got from the output of a network with 100x310 neurons. In these 7 images, each pixel is a neuron output and the white represents the active neurons. The weights were calculated on the basis of the neighboring pixel intensity differences with  $L_w=0$ . The neurons with all the excitatory weights unitary were considered leaders. The first segment is the background, having the interior parts of the characters “P” and “A” not presented, as they are not physically connected. All the characters were correctly isolated in time, facilitating the application of a character recognition procedure.

FPGA	FPGA	G	A
F	P	•	•

**Fig. 4.** Segmentation using the algorithm that simulates the proposed network operation

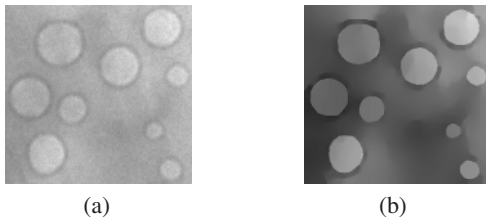
#### 3.2 A Practical Application

Figure 5 presents a gray level image with 1482x2060 pixels and 8 bits, which was obtained through transmission electron microscopy (TEM). This image represents a silicon sample where ions of helium were implanted with the objective to reduce defects in the crystalline structure. The helium accumulates itself in bubbles concentrated in some areas of the silicon. For evaluation of the process, it is necessary to determine the gas volume in the sample. Such volume can be found through the counting of bubbles and estimation of their areas. This procedure must be carried through for several images, being a complex task for human manual execution [7].



**Fig. 5.** Image of TEM representing a silicon sample with helium bubbles

The proposed network was used to segment the helium bubbles and simultaneously separate them in time, facilitating the implementation of an automatic process of counting and area measuring. Figure 6(a) presents a region extracted from Figure 5, which is used to verify the qualitative results of the proposed network.



**Fig. 6.** Region extracted from Figure 5 (a) and filtered with the FPS algorithm (b)

As other segmentation procedures, the proposed network is sensitive to noise in the input image. Such problem makes the use of a smoothing filter necessary. Figure 6(b) presents the result of filtering the Figure 6(a) image using the FPS (Feature Preserving Smoothing) algorithm [5]. The noise reduction and the preservation of the contours of the helium bubbles can be easily observed.

Figure 7 presents the non-null segments got from the output of a network with 1482x2060 neurons. Besides the 9 bubbles, a segment representing the silicon background was also supplied (bottom right position), which can be easily detected and discarded in the automatic procedure of measuring. The network weights were calculated on the basis of the neighboring pixel intensity differences with  $L_w=3$ .

The bubble areas can be obtained computing the ratio between the number of active neurons and the total number of neurons. Knowing the relation in pixel/nm (Figure 5), the helium volume can be estimated. Visual area determination can be inexact

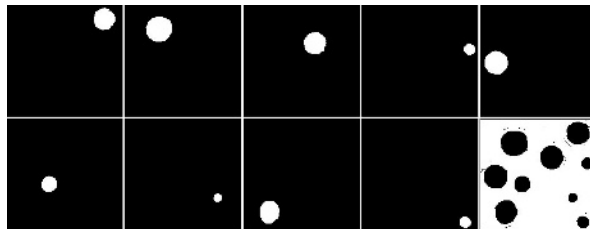


**Fig. 7.** Segments of Figure 6(b) image obtained with the proposed neural network

if the bubbles are not perfectly circular. Such limitation is not observed in the proposed method. Incomplete, degraded and superimposed bubbles can lead to wrong measures. For these situations, the manual process can be used.

## 4 Conclusion

The use of oscillator networks to simulate the capacity of image segmentation of the human brain is a recent proposal with good results. In this context, the LEGION network is the most consolidated model. Its massively parallel topology and the capacity to separate the segments in time are highly attractive. On the other hand, the structure based on differential equations has high complexity for digital machines. Another disadvantage is the limitation to segment a high number of objects simultaneously. The high number of parameters and their little intuitive setting are also drawbacks.

The oscillatory neural network presented by this paper has massively parallel topology and capacity to separate the homogeneous regions of the input image in time. The network does not present limitation related to the number of segments, has lower complexity, is suitable for implementation in digital vision chips, and uses few parameters, with easy setting. Other positive aspects are the easiness of synchronism and the necessity of a low and easily predictable number of iterations to get the result. The addition of a random signal to the inputs, like in the LEGION, is not necessary, which is also a factor of complexity reduction. Since the weights are obtained directly from the attributes of the input image, there is no need of training, in contrast with other neural networks. Finally, the weight determination on the basis of diverse attributes of the input image, can lead to more sophisticated segmentation procedures.

The good results obtained with the proposed network through an algorithm that simulates its behavior prove the consistency and its several positive characteristics. The simulation of a small size network and its implementation in an FPGA chip confirms the correct functioning of the proposal. Also, preliminary statistical analysis have showed that the proposed network can segment images with additive Gaussian noise and 20dB of signal-to-noise ratio with less than 0.02% of misclassified pixels.

As there are no references to implementations of LEGION network using massively parallel digital hardware, the evaluation of the complexity gain of the proposed network is not possible. On the other hand, computational simulations show that the proposed network is much faster than the LEGION network version based on differential equations. Specific studies for complexity reduction are under development in order to implement practical networks using commercial FPGA devices.

Based on the results, it is concluded that the proposed oscillatory neural network is attractive for applications of image segmentation with implementation in massively parallel digital hardware. Its several advantages imply viability for implementation of vision chips using digital technology, allowing high speed in image segmentation.

## References

1. ALTERA, MAX+PLUS II Software Overview, <http://www.altera.com/products/software/maxplus2/mp2-index.html> (20/06/2002)
2. ANDO, H., MIYAKE, M., MORIE, T., NAGATA, M., IWATA, A. A Nonlinear Oscillator Network Circuit for Image Segmentation with Double-threshold Phase Detection, ICANN 99, IEE, Edinburgh, UK, 1999, p. 655–660
3. BARBARO, M., BURGI, P., MORTARA, A., NUSSBAUM, P., HEITGER, F. A 100x100 Pixel Silicon Retina for Gradient Extraction With Steering Filter Capabilities and Temporal Output Coding, IEEE Journal of Solid-State Circuits, 2002, v.37, n.2, p.160–172
4. BUHMAN, J., von der MALSBURG, C. Sensory Segmentation by Neural Oscillators, IJCNN 91, IEEE, Seattle, USA, 1991, p. II603–II607
5. CHEN, Ke; WANG, DeLiang. Image Segmentation Based on a Dynamically Coupled Neural Oscillator Network, IJCNN 99, IEEE, Washington D. C., USA, 1999
6. COSP, J., MADRENAS, J. A Neural Network for Scene Segmentation Based on Compact Astable Oscillators, ICANN 99, IEE, Edinburgh, UK, 1999, p. 690–695
7. FERNANDES, D., NAVAUX, P. O. A., FICHTNER, P. F. P. Segmentation of TEM Images Using Oscillatory Neural Networks, SIBGRAPI 2001, IEEE, Florianópolis, Brazil, 2001, p.289–296
8. FERNANDES, D., SIQUEIRA, M. L., NAVAUX, P. O. A. Segmentation of Fetal Echocardiographic Images Using Self-Organizing Maps and Oscillatory Neural Networks, SIARP 2001, IARP, Florianópolis, Brazil, 2001, p.55–60
9. FERNANDES, D., STEDILE, J. P., NAVAUX, P. O. A. Architecture of Oscillatory Neural Network for Image Segmentation. SBAC-PAD 2002, IEEE, Vitória, Brazil, 2002
10. KOMURO, T., ISHII, I., ISHIKAWA, M. Digital Vision Chips and High-Speed Vision Systems, Symposium on VLSI Circuits Digest of Technical Papers, IEEE, Kyoto, Japan, 2001, p.1–4
11. KUROKAWA, H., MORI, S. A Local Connected Neural Oscillator Network for Sequential Character Segmentation, ICNN 97, IEEE, Texas, USA, 1997, p.838–843
12. LIU, X., CHEN, K., WANG, D. L. Extraction of hydrographic regions from remote sensing images using an oscillator network with weight adaptation, Transactions on GeoScience and Remote Sensing, IEEE, 2001, 39(1), 207–211
13. SHAREEF, N., WANG, D. L., YAGEL, R. Segmentation of Medical Images Using LEGION, Transactions on Medical Imaging, IEEE, 1999, v.18, n.1
14. TERMAN, D., WANG, D. L. Global competition and local cooperation in a network of neural oscillators, Physica D, 1995, v.81(1-2), pp.148–176
15. WANG, D., TERMAN, D. Image Segmentation Based on Oscillatory Correlation, Neural Computation, MIT, 1997, v.9, p.805–836
16. WANG, D. Relaxation Oscillators and Networks. Wiley Encyclopedia of Electrical and Electronics Engineering, Wiley & Sons, 1999, v.18, p.396–405

# Generating Three-Dimensional Neural Cells Based on Bayes Rules and Interpolation with Thin Plate Splines

Regina Célia Coelho<sup>1,2</sup> and Osvaldo Vargas Jaques<sup>2,3,4</sup>

<sup>1</sup>UNIMEP-Universidade Metodista de Piracicaba – Rodovia do Açucar, km 156 – Campus Taquaral – Piracicaba – 13400 – 911, SP, Brazil  
rccoelho@unimep.br

<sup>2</sup>UFPR – Universidade Federal do Paraná, Rua XV de Novembro, 1299, 80060-000, Curitiba, PR, Brazil

<sup>3</sup>UEMS – Universidade Estadual de Mato Grosso do Sul, Caixa Postal 6176, 13083-970 Dourados, MS, Brazil  
ojacques@uembs.br

<sup>4</sup>UNIGRAN – Centro Universitário da Grande Dourados, R. Balbina de Matos, 2121, 79824-900 Dourados, MS, Brazil.  
ojacques@dourados.br

**Abstract.** In this paper the use of Bayes rules and interpolation functions is proposed in order to generate three-dimensional artificial neural cells incorporating realistic biological neural shapes. A conditional vectorial stochastic grammar has been developed to control and facilitate the parallel growth of branching. A L-parser (parser to L-Systems) has also been developed to guarantee that the grammar is free from mistakes before its use. This parser has also the function to generate a group of points corresponding to the morphologic structure of a neural cell. These points are visualized in a three-dimensional viewer especially developed to show the neural cell generated.

## 1 Introduction

The conventional theory-experiment basis for scientific research has been expanded to include computer simulation, which is an increasingly important component of many research lines. Indeed, one of the most important uses of computers in neuroscience is the simulation of neural systems due to the large amount of data that is necessary to be analyzed [1]. Neural modeling has a fundamental role in both experimental and theoretical studies to determine the characteristics of nervous systems. There is an extraordinarily large number of neural cells in our brain as well as a great variety of them. Thus, it is extremely difficult to understand completely how the communications between them occur and how a specific area of the brain responds to a specific stimulus. In this context, there are several studies in the sense of trying to understand the functionality of some neuron types. It is well known that the shape of the cells is a fundamental factor to define the communication between them and to define their respective functions. Consequently, it has been proved that as more complex is the function of the neuron more complex will be its morphology. It is also shown that cells can change their shape redirecting their dendritic branching to

respond some factors acting on them, such as the death of some neighborhood cells or the presence of some attraction/repulsion factor). Therefore, the simulations related to the neural growth should take into account the shape and plasticity of the cells.

Hamilton [2], McCormick and Mulchandani [3], Ascoli and Krichmar [4] have published some works related to simulation of the neural growth. These authors suggest different methods for the growth of cells considering the shape of the natural cells. For instance, Hamilton [2] and Ascoli and Krichmar [3] proposed stochastic L-System and simulated the tropism. On the other hand, McCormick and Mulchandani [3] proposed the growth with stochastic behavior. However, any of these works take into account the historical of the growth or present a easy extension to the growth of different cells considering the shape of them in a neural structure.

The aim of this work is the synthesis of three-dimensional neural cells using interpolation functions and Bayes rules incorporated in stochastic graph grammars. Thus, the neural development considers the little historical about the growth and the shape characteristic that are incorporated by the interpolation functions. These functions are used as a way of generalizing several distribution functions obtained from extracted measures of natural cells, besides allowing the reduction of the amount of stored data. As will be showed, the generated cells present shape very similar to the natural cells. Two tools have been built to assist in this simulation: i) L-Parser, a parser of the graph grammar generated; ii) Neuron-Viewer, used to show the artificial cells.

## 2 The Use of Bayes Rule

The beginning of the generation of a cell corresponds to the first level of growing. In this situation, in which there is not any previous level to consider, the measures to the artificial cells are obtained considering probability density function. However, very often the actual state of a cell depends on its previous state of growing (this is valid just after the cell ramified at least once). For instance, the diameter of the branch can be decreased with its growing. So, it is necessary to verify the previous diameter to determinate the actual, once that diameter has to be smaller than the previous one. The Bayes rule is used to allow this kind of implementation. First of all, it is necessary to obtain a set of shape measures of the natural cells. This work has concentrated on rat pyramidal cells (the files were acquired electronically in Canon [5]). The developed software to obtain the measures considers computer-acquired neuroanatomical files in Eutectic or SWC format [5]. Second, the measures considered in the generation of the artificial cells are calculated. The main shape measures considered are: number of primary branches, length and width of each dendritic segment and arc segment, and branching angles. These measures are organized according to the hierarchical level along the tree [6]. The next step is to estimate the probability density function and then the cumulative distribution functions (CDFs), based on the natural neural cells measures, which characterize the morphological properties of the neural cells. Except for the angles, each measure will generate a bivariated CDF whose random components correspond to the hierarchical level and the respective measure. The angles will generate a trivariated CDFs in which random components correspond to two measures (two angles), besides the hierarchical level. They are related to the torsion and curvature proposed in

McCormick and Mulchandani [3] work to generate three-dimensional cells. Two different groups of CDFs have been generated: one corresponding to the apical branches and another to the basal branches of the pyramidal cells. Fig. 1 presents two examples of CDFs created.

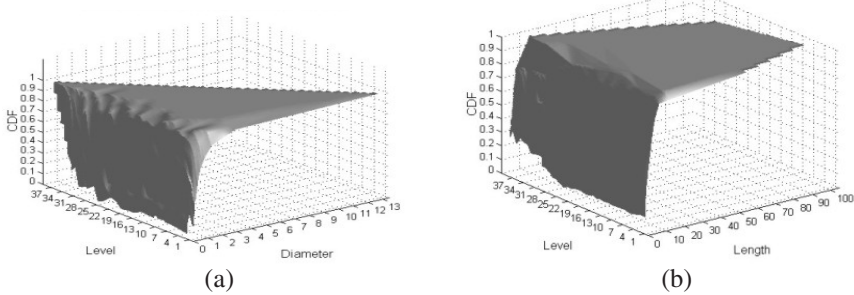


**Fig. 1.** Examples of CDFs used in the generation of splines. (a) CDF of length dendritic segments by hierarchical level; (b) CDF corresponding of dendritic segment diameters by hierarchical level.

Now, it is necessary to use the Bayes rules to generate CDFs that considers the previous measure to calculate the actual measure. According to the Bayes rule, the probability of occurrence of a  $B$  specific event is affected by the fact of another event to have happened or not. Thus, it is necessary to calculate the occurrence of  $B$  conditioned to the previous occurrence of  $A$ , denoted by  $P(B|A)$  (probability of  $B$  given  $A$ ) [7]. Its expression is given by:

$$P(B|A) = \frac{P(A|B)P(B)}{P(A)} = \frac{P(A \cap B)}{P(A)} \quad (1)$$

The implementation was made considering the dependency of measures between two branching levels. Therefore, it was created a CDF of  $B|A$ , once that the occurrence of  $B$  depends on the  $A$ . After that, the calculated  $B$  values are used to find the  $C$  values, generating the CDF of  $C|B$ , and so on. In Fig. 2 is illustrated some examples of generated conditional CDFs. The conditional CDFs have been used to control the length, diameter and angles of dendritic segments. For example, the  $n$  segment length depends on the occurred length in the  $n-1$  segment. In the case of the angles, Bayes rules (or conditional CDFs) were used to control the two different angles considered in this work: torsion and curvature. Fig. 3 illustrates some examples of the graphic resulting of the application of Bayes rules to control these angles.

### 3 Obtaining the Interpolations

The interpolation functions were generated using the CDFs described in the previous section and they are applied in all CDFs. In this paper we have not used these functions to conditional CDFs, but the implementation can be also extended to include the interpolation function with conditional CDFs (this will be implemented in future works). There are several methods of interpolation functions. In this work we used Thin Plate Splines (TPS), which is a linear combination of radial basis functions.

In a TPS, the interpolating surface presents minimal deformation energy related to the known charge points, originating a smooth and continuous surface [8,9].

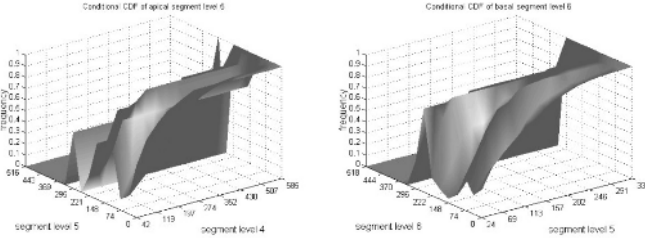


**Fig. 2.** Examples of conditional CDFs used in the generation of splines

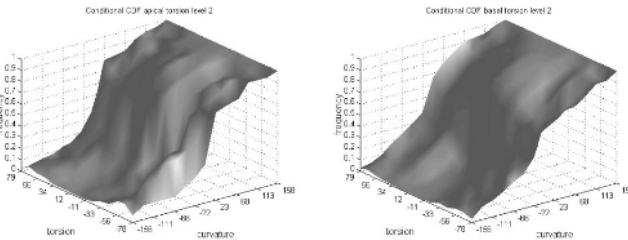


**Fig. 3.** Examples of conditional CDFs used to control the angles of dendritic segment.

Two groups of information are necessary for this interpolation: those known (in this case, the measures of the neural cells) and those we want to know (in this case, the measures that will be used in the generation of the cells in agreement with the probabilities and the level of each branch). The first group of information can be represented by a set of  $n$  vectors  $V = \{\vec{v}_1, \vec{v}_2, \dots, \vec{v}_n\}$ , where  $\vec{v}_i = (c_1, c_2, \dots, c_d)$ ,  $1 \leq i \leq n$  is a d-dimensional vector, and  $n$  is the number of samples of a given measure. Once chosen  $V$ , we have a set  $F(V) = \{f(\vec{v}_1), f(\vec{v}_2), \dots, f(\vec{v}_n)\}$ , where  $f(\vec{v})$  is a result of application on  $\vec{v}$ . We can describe the function interpolation as:

$$F(\vec{v}) = \vec{\alpha}^T \cdot \vec{v} + \beta + \sum_{i=1}^n w_i \Phi(\|\vec{v} - \vec{v}_i\|) \quad (2)$$

where  $\Phi(x)$  corresponds to basic radial basis function,  $w_i$  is the contribution of the function  $\Phi(x)$  in each distance  $x$ ,  $\beta$  is a constant term corresponding to translation of the  $\Phi(x)$  to fit it in the interpolation, and  $\vec{\alpha}$  is a vector used to the rotation of  $\Phi(x)$  in each dimension. The function  $\Phi(x)$  used in this work is defined by:

$$\Phi(x) = \begin{cases} 0 & \text{if } x = 0 \\ x^2 \log(x) & \text{otherwise} \end{cases} \quad (3)$$

By the equation (1) and using the known value of  $V$  and  $F(V)$ , we can calculate  $\alpha$ ,  $\beta$ , and  $w$ . After then, we use the equation (4) together with the calculated variables

in (2) to estimate the unknown values of  $F(\vec{x})$ , being  $\vec{x}$  the values of the measure for which we want to estimate  $F(\vec{x})$ .

$$F(\vec{x}) = \vec{\alpha}^T \cdot \vec{x} + \beta + \sum_{i=1}^n w_i \phi\left(\|\vec{x} - \vec{v}_i\|\right) \quad (4)$$

The axes were transposed to facilitate the implementation, such that, being provided the hierarchical level and a random number (between 0 and 1), the function returns a measure. Therefore,  $F(\vec{v})$  in the equation (2) corresponds to a measure (for example, diameter),  $c_1$  to the probability (CDF) and  $c_2$  to the hierarchical level. In the equation (4),  $\vec{x}$  is a vector with  $x_1$  representing the probability and  $x_2$ , the hierarchical level.

## 4 Generating Neural Cells

To allow the parallel growth, it was created a stochastic graph grammar (a variation of L-Systems) that incorporates the interpolation functions and Bayes rules (or conditional CFDs). Some measures are controlled by interpolation functions (for example, length of dendritic segment and number of branches) and others, by Bayes rules (for example, angles and diameter). They are used to express variation on the growth pattern in terms of the current interaction of the generation process or external influences such as chemical markers or neurotrophic factors. The statistical functions incorporate the precise statistical characterization of the morphological features of the neurons, which can also take into account the stage of the generating process (previous and current stages).

A parser of L-system (L-parser) has also been developed in this work to compile and interpret the grammar. It allows the user to enter with the grammar (L-system) and the result is the object obtained by this grammar. It is very important to eliminate mistakes in the creation of the grammar before its use. This parser facilitates the definition of a specific grammar for each type of cell when is necessary to generate different types of cells in the same neural structure.

The probabilities of each grammar rule have been defined by the probability functions obtained from the measures extracted from biological cells. This means that there is not a fixed probability for each rule production, as commonly found in works that use stochastic L-systems. On the contrary, it is defined a probability function that allows varying a probability depending on the branching level of the branch. The statistical functions used were the CDFs described in section 2, which were incorporated in the grammar using polynomial approximation described in section 3.

It must be emphasized that the grammar results are strongly influenced by the interpolation functions that are related to the L-systems. These functions are used to avoid the necessity to work with several data files, once they generalize a specific measure for all the levels of branching of the cell. So, it is not necessary to have a file of measures for each level, but just the function that describes these measures as a whole.

The grammar below represents a summarized model of our proposal, which includes some control actions (lines 2, 3, 4, 6, 7, 7.1.1, 7.1.2 and 7.2.1). The execution

of a graphic operation is conditioned to the logic value of the expression (lines 6.1, 7.1 and 7.2). In line 4 the ChooseSegmentLength (Level) chooses the dendritic segment length. This function uses the interpolation polynomial described previously referent to the dendritic segment length of each branching level.

Grammar:

```

1. Axiom : X;
2. Level := 1;
3 SumCp := 0;
4. SdLength := ChooseSegmentLength (Level);
5. X → FLengthCp(Level) Curvature(Level) Torsion(Level) Diameter(Level) Y
6. SumCp := SumCp+LengthCp (Level);
   6.1 [SumCp < LengthSd] : Y→X
7. Bprob:=ChooseBranch(Level);
   7.1 [Bprob < BranchProb (Level)] : Y → [-X] [+X]
      7.1.1. Level := Level + 1;
      7.1.2. LengthSd =ChooseSegmentLength(Level);
   7.2 [Bprob > BranchProb (Level)] : Y → NULL
      7.2.1 Level := Level -1;
```

Since the execution of its actions is not only depending on probabilistic functions, we call this model as *Conditional and Stochastic Grammar*.

In line 5, X is responsible for drawing a dendritic arc. The LengthCp(Level), Torsion(Level), Curvature(Level) and Diameter(Level) functions are associated with the F symbol to give information about direction, length and thickness of the arc to be drawn.

The dendritic branching process starts in level 1 with the X axiom and the choice of the dendritic segment length (line 4). Note that there are several CDFs and thin plate splines associated with F in line 5, such as arc length, torsion angle, curvature angle and diameter. While the sum of arcs does not reach the chosen length segment (line 6.1), the branch continues to grow [10]. After this length is reached, it is verified if the branch will ramify or not (line 7). BranchProb(level), in line 7.1, verifies the corresponding value of branching probability in this level. If Bprob is smaller than the branching probability, then two new branches will start to grow starting, thus, a new dendritic segment level. Otherwise, no more new branching will appear in that branch and it will stop growing (line 7.2). The process continues recursively until all the conditions are satisfied (the entire branching stop growing).

Each generated neuron is different from any other previously produced because of the used statistical functions, but all cells present the same general characteristics related to neural shape.

Each neuronal dendrite is described as a series of small cylindrical compartments. Thus, these small compartments will express the tortuosity of the branches. Fig. 4 illustrates some examples of neural cells generated by the proposed method.

An environment of three-dimensional visualization has been generated using OpenGL tool. This environment allows the volumetric visualization, including illumination, transparency, texture, rotations, translations and changes of scale of the generated neural structures. It also includes a menu of options to the variation of visualization parameters such as color, light intensity, properties of the light and of



**Fig. 4.** Neural cells generated by the proposed methods.

the material of the object (in the case, of the neurons), transparency, wire frame visualization, etc, besides being able to include textures. One example of this environment can be seen in Fig. 5. It also allows defining how much percentage of a neuron will be drawn (100%, 90%, etc.). Fig. 6 shows some examples of this option. In those examples it is possible to see that the branches are growing in parallel.



**Fig. 5.** Environment to visualize three-dimensional cells.



**Fig. 6.** Representation of three-dimensional cells drawn in different percentages.

## 5 Conclusion

The study of cells showed in this paper can provide important support to guide the simulation of more complex cells in the future, like Purkinjie cell.

It was shown in this work that the inclusion of Bayes rules in L-system allows that the generation of the current branch takes into account parameters of the previous stages. In addition, these rules allow relating two or more measures. For instance, we can consider that the diameter of the branch depends on its length. Therefore, it is

possible to verify if there is some relationship among the measures or hierarchical levels. It is important to emphasize that this type of conditional statistics is already considered for the angles, once we have to work with two angles by the fact of we are generating three-dimensional cells. In this way, first of all we select a hierarchical level and a random number. Then, using the polynomial approximation of CDF, we can calculate an angle (curvature) and, given the curvature, we used Bayes to calculate the torsion. Additional studies have been initiated about the dynamical growth of the cell including the trophic fields corresponding to varying concentration of ions, chemoattractors or electric fields.

**Acknowledgments.** Regina Célia Coelho is grateful to Fundação de Amparo à Pesquisa do Estado de São Paulo (FAPESP-Brazil Proc. 98/05459-0) for financial help.

## References

1. Seung, S. Neural Coding: Linear Models, 9.29 Lecture, 1, p. 1–6, 2002.
2. Hamilton, P. A language to describe the growth of neurites, *Biological Cybernetics*, 68, p. 559–565, 1992.
3. McCormick, B.H.; Mulchandani K. L-system modeling of neurons visualization. In: I Biomedical Computing Conference Proceedings, p. 693–705, 1994.
4. Ascoli, G.A.; Krichmar, J.L. L-neuron: A modeling tool for the efficient generation and parsimonious description of dendritic morphology, *Neurocomputing*, 32-33, p. 1003–1011, 2000.
5. Cannon, R.C. <http://www.cns.soton.ac.uk/~jchad/cellArchive/idx/toindex>.
6. Coelho, R.C.; Costa, L.F. Realistic Neuromorphic Models and Their Application to Neural Reorganization Simulations, *Neurocomputing*, 48, 555–571, 2002.
7. Arango, H.G. Bioestatística teórica e computacional, Guanabara Koogan, 2001.
8. Mees, A.I.; Jackson, M.F.; Chua, L.O. Device Modeling by Radial Functions, *IEEE Transactions on Circuits and Systems – I: Fundamental Theory and Applications*, 39 (1), p. 19–27, 1992.
9. Costa, L.F.; César Jr, R.M.C. Shape Analysis and Classification, CRC Press, 2001.
10. Costa, L.F.; Cesar Jr., R.M.C.; Coelho, R.C.; Tanaka, J. S. Analysis and Synthesis of Morphologically Realistic Neural Networks, In R. Poznanski (Editor) Modeling in the Neurosciences: From Ionic Channels to Neural Networks, Gordon and Breach Science Publishers, 1999.

# A Maximum Entropy Approach to Sampling in EDA – The Single Connected Case

Alberto Ochoa<sup>1,2</sup>, Robin Höns<sup>1</sup>, Marta Soto<sup>2</sup>, and Heinz Mühlenbein<sup>1</sup>

<sup>1</sup> Fraunhofer Institute for Autonomous Intelligent Systems, Sankt Augustin,  
Germany

<sup>2</sup> Institute of Cybernetics, Mathematics and Physics, Havana, Cuba

**Abstract.** The success of evolutionary algorithms, in particular Factorized Distribution Algorithms (FDA), for many pattern recognition tasks heavily depends on our ability to reduce the number of function evaluations.

This paper introduces a method to reduce the population size overhead. We use low order marginals during the learning step and then compute the maximum entropy joint distributions for the cliques of the graph. The maximum entropy distribution is computed by an Iterative Proportional Fitting embedded in a junction tree message passing scheme to ensure consistency.

We show for the class of single connected FDA that our method outperforms the commonly-used PLS sampling.

## 1 Introduction

In recent years, evolutionary algorithms (EA) have been successfully applied to a wide range of problems in the field of pattern recognition. The critical issue in this application of EA is to reduce as far as possible the number of fitness function evaluations which depends directly of the population size of the EA.

In this paper we introduce a method which helps in reducing the population size for a particular class of EA: the Estimation Distribution Algorithms (EDA) [14], which can be considered as a substantial improvement of the genetic algorithm paradigm [4].

The tractable subclass of EDA, the so-called Factorized Distribution Algorithms (FDA), learn factorizations of the joint distribution, which are trees, polytrees or general directed acyclic graphs. This information is used to construct a model from which new points are efficiently sampled. FDA algorithms use results of Graphical Models research [13].

A critical parameter both for learning and sampling is the required population size which grows exponentially with the size of the cliques of the graph. This paper introduces a method to reduce the population size overhead. We use low order marginals during the learning step and then compute the maximum entropy joint distributions for the cliques marginals of the graph. The maximum entropy distribution is computed by an Iterative Proportional Fitting embedded in a junction tree message passing scheme to ensure consistency.

The outline of the paper is as follows: Section 2 gives a short introduction on Graphical Models and Factorized Distribution Algorithms. Section 3 presents a single connected FDA. In the next section, we introduce our maximum entropy sampling. Then, we present our test bed and discuss the numerical results. Finally, the main conclusions of our research are given.

## 2 Background

### 2.1 Bayesian Networks

A Bayesian network is a directed acyclic graph (DAG) containing nodes, representing the variables, and arcs, representing probabilistic dependencies among nodes. In this paper we will consider binary variables, but the results can be extended to the general discrete case.

Let  $X = \{X_1, \dots, X_n\}$  denote the set of random variables. For any node  $X_i$  and set of parents  $\pi_{X_i}$  the Bayesian network specifies a conditional probability distribution  $p(x_i | \pi_{x_i})$ . We use lower cases to represent the variable values.

In general, Bayesian networks can be multiple connected. In this paper we deal with single connected graphs: these are graphs where no more than one (undirected) path connects every two variables. Examples are chains, trees, forests and polytrees. Whereas in trees each edge is directed away from the root node (so each node has only one parent), in polytrees the direction of edges is not restricted. A polytree generally has many roots (nodes without parents), whereas a tree has only one root.

Polytrees retain many of the computational advantages of trees, but they allow us to describe higher-order interactions than trees, because they allow *head to head* patterns  $X \rightarrow Z \leftarrow Y$ . This type of pattern makes the parents  $X$  and  $Y$  conditionally dependent given  $Z$ , which can not be represented by a tree. A polytree structure can be induced by second-order marginals using a maximum weight spanning tree algorithm, similar to [1].

Given the structure of the probability distribution defined by the Bayesian network, the problem is to find a factorization defining this distribution. This factorization can be determined using a concept called *junction tree*.

### 2.2 Junction Trees

A junction tree [11,9] is an undirected tree the nodes of which are clusters of variables. The clusters satisfy the *junction property*: For any two clusters  $V$  and  $W$  and any cluster  $U$  on the unique path between  $V$  and  $W$  in the junction tree  $V \cap W \subseteq U$ . The edges between the clusters are labeled with the intersection of the adjacent clusters; we call these labels *separating sets* or *separators*.

Junction trees are a very powerful tool for inference in Bayesian networks. For construction of a junction tree, given a general network, we refer to [11,9]. Given a polytree, a junction tree is simple to construct: For each variable that is not a root, create a node containing this variable and all its parents. The separators between the nodes always consist of only one variable.

---

**Algorithm 1** FDA

---

- Step 0 Set  $t \leftarrow 1$ . Generate  $N \gg 0$  points randomly.  
 Step 1 Select  $M \leq N$  points according to a selection method.  
 Step 2 Learn a bayesian factorization of the selected set:

$$p^s(x_1, \dots, x_n) = \prod_{i=1}^n p(x_i | x_{i1}, x_{i2}, \dots, x_{ir})$$

- Step 3 Sample  $N$  new points according to the distribution

$$p(x, t+1) = p^s(x_1, \dots, x_n)$$

- Step 4 Set  $t \leftarrow t + 1$ . If termination criteria are not met, go to Step 1.
- 

### 2.3 The Factorized Distribution Algorihtms

Generally, in an FDA (see algorithm 1) the estimation (step 2) of the probability factorization of the best individuals is used to sample (step 3) the points of the next generation, there are no mutation nor crossover operators.

The computational cost of an FDA implementation is determined by the number of function evaluations, the memory needed to store, and the time spent to update and sample the probabilistic model. This time is often exponential in the maximum number of variables that interact in the problem, or which is the same, the size of the building blocks. FDA algorithms which use only pairwise dependencies are cheap.

## 3 PADA2 – FDA Algorithm with Pairwise Independences

The Polytree Approximation Distribution Algorithm (PADA) [17,16] is a specialization of FDA (see algorithm 1) for single connected Bayesian networks. In this paper we use PADA2 [16], which works with second order marginal distributions. PADA2 is inspired by the algorithm proposed by Rebane and Pearl [15]. We shortly review this algorithm.

A polytree with  $n$  variables has a maximum of  $n - 1$  edges, otherwise it would not be single connected. PADA2 chooses the edges that have the largest values for the *mutual information*  $H(X) + H(Y) - H(X, Y)$  [2]. The selection of the edges is done by a greedy Maximum Weight Spanning Tree algorithm.

Once we have constructed the skeleton a procedure tries to direct the edges of the skeleton by using the following scheme: if  $X - Z - Y \in \text{skeleton}$ , then whenever  $H(X) + H(Y) = H(X, Y)$  we orient the edges to  $Z$ . All other edges are directed at random without introducing new head to head connections.

Another distinguishing feature of PADA2 concerns the sampling step 3 (see algorithm 1). To the best of our knowledge, all FDA algorithms introduced so far that are based on Bayesian networks use the same Monte Carlo sampling

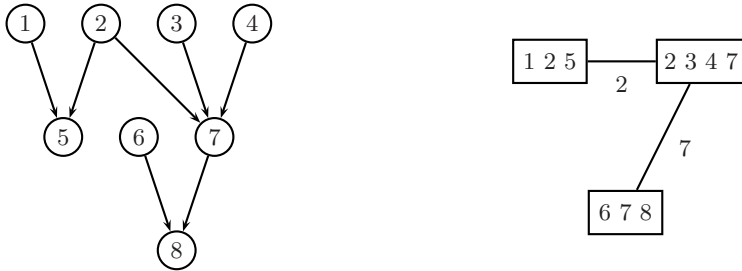


**Fig. 1.** A polytree learned by PADA2 and its junction tree.

algorithm, namely Probabilistic Logic Sampling (PLS) [6]. It is very simple. Given an ancestral ordering of all the variables (parents before children), the method samples  $X_i$  using  $p(X_i | \pi_{X_i})$ . One obvious problem of this method is that the number of points required for estimating the conditional probabilities correctly is exponential in the number of parents.

Both in the process of learning and sampling, FDA that learn general Bayesian networks need a population size which is exponential in the number of parents in order to get reliable estimates of the conditional probabilities. PADA2 is in a different situation: its learning algorithm deals only with second order marginals. Figure 1 shows a polytree learned by PADA2. However, note that the resulting junction tree contains a clique with four variables (7 and its parents 2, 3, 4) and two cliques with 3 variables, so the PLS sampling requires 4-order and 3-order marginals. Therefore, PADA2 is in a very singular situation when it uses PLS: what is gained during learning is then lost during the sampling step.

In the next section we will present a novel method to overcome this problem. We fix some of the second order marginals used in the learning step, and then compute higher order marginals (like the ones in Fig. 1) as the maximum entropy distributions that obey the given second order marginals. It is important to note that, in contrast to PLS, the computation of these marginals does not need a larger sample size (population size) than the one used for learning.

## 4 Maximum Entropy

### 4.1 Entropy and the Maximum Entropy Principle

The *Entropy* [2] of a probability distribution for a random variable  $X$  is given by

$$H(X) = - \sum_x p(x) \log p(x) . \quad (1)$$

If  $p(x) = 0$ , then  $\log p(x)$  is not defined. For this case, we set  $0 \log 0 = 0$ .

The entropy is a measure of the disorder in the distribution, or of our uncertainty about the outcome of a random experiment.

The *Maximum Entropy Principle* states that, supposing we are looking for a probability distribution fulfilling some given constraints, we should choose among the possible solutions the one with the highest entropy. This is historically founded on Bernoulli's "principle of insufficient reason". It was introduced and advocated by Jaynes [7,8]. For a motivation and discussion of Maximum Entropy, see [5].

## 4.2 Maximum Entropy Sampling in PADA2

The method is a variation of previous methods for learning probability distributions on junction trees [10,12].

First we construct a junction tree from the polytree, as described in Sect. 2.2. On each node of the junction tree, we maintain a probability distribution of the contained variables (remember, a child and its parents).

Then we find a closed tour through the junction tree that visits each node at least once. On this tour we perform two steps:

1. Calculate the local distribution by *iterative proportional fitting*,
2. *Pass a message* to the next cluster on the tour, in order to ensure consistency between the clusters.

## 4.3 Iterative Proportional Fitting

The local iteration consists of finding the maximum entropy distribution of a child and its parents, given the second order marginals. This is done by *Iterative Proportional Fitting*. IPF computes iteratively a distribution  $q_\tau(\mathbf{x})$  from the given marginals  $p_k(\mathbf{x}_k)$ ,  $k = 1, \dots, K$ , where  $\mathbf{x}_k$  is a subvector of  $\mathbf{x}$  and  $\tau = 0, 1, 2, \dots$  is the iteration index. Let  $n$  be the dimension of  $\mathbf{x}$  and  $d_k$  be the dimension of  $\mathbf{x}_k$ . Then, starting from the uniform distribution, the update formula is

$$q_{\tau+1}(\mathbf{x}) = q_\tau(\mathbf{x}) - \frac{p_k(\mathbf{x}_k)}{\sum_{y \in \{0,1\}^{n-d_k}} q_\tau(\mathbf{x}_k, \mathbf{y})} \quad (2)$$

with  $k = ((\tau - 1) \bmod K) + 1$ .

For the proof that IPF converges to the maximum entropy solution, see [3] and references therein. Note that the effort is exponential in the clique size.

## 4.4 Message Passing

A message from a cluster  $W$  to a cluster  $V$ , separated by  $S = V \cap W$ , is sent by the following algorithm:

$$q_S^{\text{new}}(\mathbf{x}_S) = \sum_{\mathbf{x}_{W \setminus S}} q_W^{\text{old}}(\mathbf{x}_S, \mathbf{x}_{W \setminus S}) \quad q_V^{\text{new}}(\mathbf{x}) = q_V^{\text{old}}(\mathbf{x}) \frac{q_S^{\text{new}}(\mathbf{x}|S)}{q_S^{\text{old}}(\mathbf{x}|S)}$$

Here  $\mathbf{x}|S$  denotes the vector  $\mathbf{x}$ , restricted to the variables in  $S$ .

#### 4.5 Sampling in the Junction Tree

Using the distributions within the junction tree, the sampling of points works as follows:

Start from any node in the junction tree, sample values for the variables from the local probability distribution. Then, proceed to the neighbors and sample values for the new variables, conditioned on the variables which have already been sampled. When each node has been visited, the sampled individual is complete.

For example, from the structure in Fig. 1, this algorithm samples using the factorization

$$p_{\text{JT}}(\mathbf{x}) = p(x_1, x_2, x_5)p(x_3, x_4, x_7|x_2)p(x_6, x_8|x_7) ,$$

whereas PLS uses the factorization

$$p_{\text{PLS}}(\mathbf{x}) = p(x_1)p(x_2)p(x_3)p(x_4)p(x_5|x_1, x_2)p(x_6)p(x_7|x_2, x_3, x_4)p(x_8|x_6, x_7)$$

which is not an exact factorization of the underlying distribution.

### 5 Numerical Results

Now we present the set of additive decomposable functions (ADF) that will be used in our experiments.

1. The *Deceptive Function* of order  $k$ ,  $F_k^{\text{dec}}$ , is defined as follows.  $u$  denotes the number of 1s in the string. We set  $f_k^{\text{dec}}(u) = k$  if  $u = k$ , and  $f_k^{\text{dec}}(u) = k - 1 - u$  otherwise. The function  $F_k^{\text{dec}}$  is a separable function of subset size  $k$ , with  $n = k * l$ .

$$F_k^{\text{dec}} = \sum_{i=1}^l f_k^{\text{dec}}(x_{ki-k+1} + \dots + x_{ki})$$

2. The next function is also a separable ADF with blocks of length 5. In each block the *FirstPolytree5* function is evaluated. This function has the following property: Its Boltzmann distribution with parameter  $\beta \approx 2$  has a polytree structure with edges  $x_1 \rightarrow x_3$ ,  $x_2 \rightarrow x_3$ ,  $x_3 \rightarrow x_5$  and  $x_4 \rightarrow x_5$ . The reader can easily check this by constructing the Boltzmann distribution and then checking marginal dependencies. The definition of the function is given below.

$\mathbf{x}$	$f_5^{\text{Poly}}(\mathbf{x})$	$\mathbf{x}$	$f_5^{\text{Poly}}(\mathbf{x})$	$\mathbf{x}$	$f_5^{\text{Poly}}(\mathbf{x})$	$\mathbf{x}$	$f_5^{\text{Poly}}(\mathbf{x})$
00000	-1.141	01000	-0.753	10000	-3.527	11000	-6.664
00001	1.334	01001	1.723	10001	-1.051	11001	-4.189
00010	-5.353	01010	-4.964	10010	-7.738	11010	-10.876
00011	-1.700	01011	-1.311	10011	-4.085	11011	-7.223
00100	0.063	01100	1.454	10100	1.002	11100	-1.133
00101	-0.815	01101	0.576	10101	0.124	11101	-2.011
00110	-0.952	01110	0.439	10110	-0.013	11110	-2.148
00111	-0.652	01111	0.739	10111	0.286	11111	-1.849

We recall that the basic claim of our research is that our maximum entropy approach to sampling requires a smaller population size than PLS. In this section we will compare these two sampling methods for PADA2.

All the experiments use a fixed truncation selection pressure ( $\tau = 0.3$ ), do not use elitism and are run until a maximum of 20 generations. We perform 100 runs for each experiment. We use as test functions Deceptive 4 (with 20 variables), Goldberg Deceptive 3 (21 variables) and the FirstPolytree5 (20 variables).

As can be seen in Table 1, the improvement in comparison with conventional PLS is enormous. E. g. for Deceptive 4, our new method finds the optimum in 93 % of the cases for only 800 individuals, whereas PLS even with a population size of 5000 succeeds only in 64 %.

It is also remarkable that the number of generations until success stays the same or even improves. It has also stabilized, as can be seen from the decrease in the standard deviation.

**Table 1.** Numerical results. D4 - Deceptive 4, D3 - Goldberg Deceptive 3, FP5 - First-Polytree 5.  $N$  - population size,  $\%S$  - Success rate,  $G_c$  - generation where the optimum is found,  $MES$  - maximum entropy sampling,  $PLS$  - probabilistic logic sampling.

		$N$	200	600	800	5000
D4	<i>PLS</i>	$\%S$	1	12	16	64
	<i>PLS</i>	$G_c$	$5 \pm 0.0$	$8.0 \pm 3.9$	$8.3 \pm 3.5$	$9.23 \pm 3.5$
	<i>MES</i>	$\%S$	21	76	93	100
	<i>MES</i>	$G_c$	$11.14 \pm 4.5$	$8.6 \pm 3.2$	$8.4 \pm 2.5$	$6.1 \pm 1.3$
D3	<i>PLS</i>	$\%S$	0	8	10	92
	<i>PLS</i>	$G_c$	—	$9.75 \pm 1.5$	$8.7 \pm 3.2$	$7.21 \pm 1.2$
	<i>MES</i>	$\%S$	2	69	90	100
	<i>MES</i>	$G_c$	$8.5 \pm 0.7$	$7.4 \pm 1.1$	$7.0 \pm 1.2$	$5.84 \pm 0.9$
FP5	<i>PLS</i>	$\%S$	25	50	54	55
	<i>PLS</i>	$G_c$	$10.08 \pm 2.08$	$10.42 \pm 2.59$	$10.59 \pm 2.34$	$10.8 \pm 1.5$
	<i>MES</i>	$\%S$	59	100	100	100
	<i>MES</i>	$G_c$	$5.14 \pm 1.07$	$3.93 \pm 0.7$	$3.66 \pm 0.59$	$2.92 \pm 0.44$

## 6 Summary and Conclusions

The paper introduces a new method for sampling individuals in EDA. Here we restrict ourselves to single connected Bayesian networks (polytrees). In a forthcoming paper, we will discuss the multiple connected case.

The polytree induces canonically a junction tree. Its nodes contain the higher-order marginal distributions that are needed in the sampling phase. These are computed from the given second order marginals using the maximum entropy principle. The conventional “Probabilistic Logic Sampling” is replaced by sampling inside the junction tree.

We explore the method by applying it on three benchmark problems. The improvement in comparison with the previous method turns out to be tremendous. We conclude that using this sampling, we can greatly reduce the population size. This results in a big saving of function evaluations which is critical for any pattern recognition application of evolutionary computation.

## References

1. C. K. Chow and C. N. Liu. Approximating discrete probability distributions with dependence trees. *IEEE Trans. on Information Theory*, IT14(3):462–467, 1968.
2. Th. M. Cover and J.A. Thomas. *Elements of Information Theory*. Wiley, New York, 1989.
3. I. Csiszár. I-divergence geometry of probability distributions and minimization problems. *Annals of Probability*, 3:146–158, 1975.
4. D. E. Goldberg. *Genetic Algorithms in search, optimization, and machine learning*. Addison-Wesley, Reading, MA, USA, 1989.
5. P. Grünwald. *The Minimum Description Length Principle and Reasoning under Uncertainty*. PhD thesis, University of Amsterdam, 1998.
6. M. Henrion. Propagating uncertainty in Bayesian networks by probabilistic logic sampling. *Uncertainty in Artificial Intelligence*, 2:317–324, 1988.
7. E. T. Jaynes. Information theory and statistical mechanics. *Phys. Rev*, 6:620–643, 1957.
8. E. T. Jaynes. Where do we stand on maximum entropy? In R. D. Levine and M. Tribus, editors, *The Maximum Entropy Formalism*. MIT Press, Camb., 1978.
9. F. V. Jensen and F. Jensen. Optimal junction trees. In *Proc. of the 10th Conference on Uncertainty in Artificial Intelligence*, pages 360–366, Seattle, Wash., 1994.
10. R. Jiroušek and St. Přeučil. On the effective implementation of the iterative proportional fitting procedure. *Comput. Statistics & Data Analysis*, 19:177–189, 1995.
11. S. L. Lauritzen. *Graphical Models*. Oxford:Clarendon Press, 1996.
12. C.-H. Meyer. *Korrekte Schließen bei unvollständiger Information*. PhD thesis, Fernuniversität Hagen, 1998.
13. H. Mühlenbein, Th. Mahnig, and A. Ochoa. Schemata, distributions and graphical models in evolutionary optimization. *Journal of Heuristics*, 5(2):213–247, 1999.
14. H. Mühlenbein and G. Paaß. From recombination of genes to the estimation of distributions i. binary parameters. In H.-M. Voigt, W. Ebeling, I. Rechenberg, and H.-P. Schwefel, editors, *Lecture Notes in Computer Science 1141: Parallel Problem Solving from Nature – PPSN IV*, pages 178–187, Berlin, 1996. Springer-Verlag.
15. J. Pearl. *Probabilistic reasoning in intelligent systems: Networks of plausible inference*. Morgan Kaufmann, San Mateo, California, 1988.
16. M. Soto. *A Singled Connected Factorized Distribution Algorithm and its cost of evaluation*. PhD thesis, University of Havana, Havana, Cuba, July 2003. (In Spanish, adviser A. Ochoa).
17. M. Soto and A. Ochoa. A Factorized Distribution Algorithm based on polytrees. In *Proceedings of the 2000 Congress on Evolutionary Computation CEC00*, pages 232–237, La Jolla, California, 6–9 July 2000. IEEE Press.

## Author Index

- Aibar, P. 266  
Al-Hamadi, A. 95, 104  
Alarcón, T.E. 291  
Albores, C. 212  
Alexandre, H. 383  
Allende, H. 129  
Alquézar Mancho, R. 180, 188  
Alvarez, L.D. 46  
Álvarez-Borrego, J. 113  
Alvarez-Roca, N.A. 512  
Antequera, T. 359  
Arco, L. 488  
Arlandis, J. 400  
Ayaquica-Martínez, I.O. 472  
Azorín, J. 651
- Badía-Contelles, J.M. 480  
Barandela, R. 424  
Barrón, R. 588  
Bazerque, J. 367  
Berlanga-Llavori, R. 596  
Bloch, I. 71  
Bolea, Y. 221  
Boto, F. 448  
Bottino, A. 153  
Brady, M. 121  
Buxton, B.F. 163
- Caballero, Y. 488  
Caldas Pinto, J. 383  
Calderon, F. 204  
Calera-Rubio, J. 537  
Calvo, H. 604  
Candeias, T. 627  
Caro, A. 359  
Carrasco, R.C. 537  
Carreira, M.J. 306  
Castelán, M. 196  
Castillo Guerra, E. 314  
Castro, M.J. 266  
Cesar, R.M. 71  
Chacón, M. 350  
Chávez, G. 29  
Choraś, R.S. 619  
Ciambelli, J. 367
- Clech, J. 145  
Coelho, R.C. 675  
Cortes, A. 448  
Cortés, H. 588  
Cruz-Alcázar, P.P. 375  
Cuayáhuitl, H. 251
- Dias, M.B. 163  
Durán, M. 359
- Escolano, F. 137, 432, 659  
Espinosa, K. 391  
Ezeiza, A. 244, 259  
Ezeiza, N. 244, 259
- Fernandes, D. 667  
Fernández, M. 329  
Ferri, F.J. 424  
Flores-Méndez, A. 79  
Fuertes, J.M. 54, 87
- García, J.M. 651  
García, M.M. 488  
García, V. 38  
García Garduño, V. 29  
Gelbukh, Alexander 604  
Gibert, K. 464  
Gil-García, R.J. 480  
Goirizelaia, I. 391  
Gómez-Ballester, E. 456  
González, F. 306  
Gordillo, J.L. 212  
Graciano, A.B.V. 71  
Graña, M. 244, 259  
Grau, A. 221  
Guevara, M.A. 282  
Gurevich, I.B. 274, 299, 498, 506
- Hancock, E.R. 196  
Harazishvili, D. 299  
Hernáez, I. 391  
Hernández, M. 244, 259  
Höns, R. 683
- Iancu, L. 1, 563  
Igarza, Juan J. 391

- Jaulin, L. 153  
 Jernova, I. 299  
 Jernova, I.A. 506  
 Kammerer, P. 408  
 Katsaggelos, A.K. 46  
 Khilkov, A. 274  
 Kober, V. 113, 229  
 Krell, G. 571  
 Lafon, S. 367  
 Langs, G. 408  
 Laurentini, A. 153  
 Levachkine, S. 635, 643  
 López de Ipiña, K. 244, 259  
 Lorenzo-Ginori, J.V. 334  
 Lourdes Pereira, M. de 282  
 Lovely, D.F. 314, 334  
 Lozano, M.A. 137  
 Lucena, M. 54, 87  
 Luci, O. 350  
 Marcos de Moraes, R. 440  
 Mariño, C. 306  
 Martínez, U. 38  
 Martínez-Trinidad, J.F. 472, 611  
 Mavilio, A. 329  
 Mecke, R. 104  
 Méndez, R. 391  
 Mengucci, M. 580  
 Michaelis, B. 95, 104, 571  
 Micó, L. 322, 456  
 Miguel, G. De 651  
 Molina, R. 46  
 Montoliu, R. 62  
 Morales, A. 488  
 Morales, E. 416  
 Moreno, M. 635, 643  
 Moreno-Seco, F. 322  
 Morgado, F. 282  
 Mozerov, M. 113  
 Mühlenbein, H. 683  
 Muge, F. 580  
 Mugica, F. 545  
 Murashov, D. 274  
 Navaux, P.O.A. 667  
 Nebot, A. 545, 554  
 Nefyodov, A. 299  
 Niese, R. 95  
 Nolazco-Flores, J.A. 251  
 Nonell, R. 464  
 Ochoa, A. 683  
 Oliveira, H. 282  
 Oliveira de Melo, A.C. 440  
 Oncina, J. 322, 456  
 Orozco-García, J. 342  
 Pacheco, O. 291  
 Padilla, S. 29  
 Palacios, R. 359  
 Peñalver, A. 432, 659  
 Penedo, M.G. 306  
 Pérez-Cortés, J.C. 375, 400  
 Pérez de la Blanca, N. 54, 87  
 Pina Amargós, J. 180, 188  
 Piñero, P. 488  
 Pizarro, L. 129  
 Pla, F. 62  
 Pons-Porrata, A. 480, 596  
 Pujol, F.A. 651  
 Pujol, M. 651  
 Quintero, R. 635, 643  
 Rabal, H. 329  
 Randall, G. 367  
 Rangel, E. 424  
 Rebmann, R. 571  
 Reyes-García, C.A. 342  
 Ritter, G.X. 1, 563  
 Rizo, R. 651  
 Rodriguez, C. 448  
 Rodríguez, P.G. 359  
 Rodríguez, R. 291  
 Romero, L. 204, 416  
 Rueda, L. 521  
 Ruiz-Shulcloper, J. 512, 596  
 Sablatníg, R. 408  
 Sáez, J.M. 432, 659  
 Sánchez, J. 38, 391  
 Sánchez, J.S. 424  
 Sánchez-Díaz, G. 611  
 Sanchis, E. 266  
 Sanchiz-Martí, J.M. 512  
 Sanfeliu, A. 17, 171, 221  
 Santos Machado, L. dos 440  
 Schenk, V.U.B. 121  
 Scuturici, M. 145

- Seiffert, U. 571  
Shahbazkia, H. 627  
Silva, A. 282  
Soraluze, I. 448  
Sossa, H. 588  
Soto, M. 683  
Sousa, J.M. 383  
Sucar, E. 416  
Taboada-Crispí, A. 334  
Tomaz, F. 627  
Torres, I. 236  
Torres, M. 635, 643  
Tovar, C. 244  
Trivi, M. 329  
Trykova, A. 299  
Urcid, G. 1, 563  
Valera, B. 29, 38  
Varela, A. 251  
Vargas Jaques, O. 675  
Varona, A. 236  
Verdú-Mas, J.L. 537  
Vergés-Llahí, J. 171  
Vidal-Ruiz, E. 375  
Vilar, D. 266  
Vorobjev, I. 299  
Yashina, V. 498  
Yzquierdo, R. 488  
Zighed, D.A. 145  
Zolda, E. 408  
Zulueta, E. 244, 259  
Žunić, J. 529